

Jangmyung Lee
Min Cheol Lee
Honghai Liu
Jee-Hwan Ryu (Eds.)

LNAI 8102

Intelligent Robotics and Applications

6th International Conference, ICIRA 2013
Busan, South Korea, September 2013
Proceedings, Part I

1
Part I

 Springer

Lecture Notes in Artificial Intelligence 8102

Subseries of Lecture Notes in Computer Science

LNAI Series Editors

Randy Goebel

University of Alberta, Edmonton, Canada

Yuzuru Tanaka

Hokkaido University, Sapporo, Japan

Wolfgang Wahlster

DFKI and Saarland University, Saarbrücken, Germany

LNAI Founding Series Editor

Joerg Siekmann

DFKI and Saarland University, Saarbrücken, Germany

Jangmyung Lee Min Cheol Lee
Honghai Liu Jee-Hwan Ryu (Eds.)

Intelligent Robotics and Applications

6th International Conference, ICIRA 2013
Busan, South Korea, September 25-28, 2013,
Proceedings, Part I

Preface

The organizing committee for the 6th International Conference on Intelligent Robotics and Applications has been committed to facilitating the interactions among members in the field of intelligent robotics, automation and mechatronics. Through this conference, the committee intends to enhance the sharing of individual experiences and expertise in intelligent robotics with particular emphasis on technical challenges associated with varied applications such as biomedical application, industrial automations, surveillance, and sustainable mobility.

The 6th International Conference on Intelligent Robotics and Applications was most successful in attracting 184 submissions on addressing the state-of-the-art developments in robotics, automation, and mechatronics. Owing to a lot of valuable submission papers, the committee was faced with the difficult challenge of selecting the most deserving papers for inclusion in these lecture notes. For this purpose, the committee undertook a rigorous review process. Despite the high quality of most of the submissions, a total of 147 papers were selected for publication in 2 volumes of Springer's Lecture Notes in Artificial Intelligence as subseries of Lecture Notes in Computer Science. The selected papers will also be presented during the 6th International Conference on Intelligent Robotics and Applications to be held during September 25-28, 2013 in Busan, South Korea.

The selected articles represent the contributions from the scientists from 20 different countries. The contributions of the technical program committee and the referees are deeply appreciated. Most of all, we would like to express our sincere thanks to the authors for submitting their most recent works and the Organizing Committee for their enormous efforts to turn this event into a smoothly-running meeting. Special thanks go to Pusan National University for the generosity and direct support. We particularly thank Mr. Alfred Hofmann and Ms. Anna Kramer of Springer-Verlag for their enthusiastic support in this project.

We sincerely hope that these volumes will prove to be an important resource for the scientific community.

July 2013

Jangmyung Lee
Min Cheol Lee
Honghai Liu
Jee-Hwan Ryu

Conference Organization

International Advisory Committee

Jorge Angeles	McGill University, Canada
Suguru Arimoto	Ritsumeikan University, Japan
Hegao Cai	Harbin Institute of Technology, China
Tianyou Chai	Northeastern University, China
Clarence De Silva	University of British Columbia, Canada
Han Ding	Huazhong University of Science and Technology, China
Sabina Jesehke	RWTH Aachen University, Germany
Ming Li	National Natural Science Foundation of China, China
Zhongqin Lin	Shanghai Jiao Tong University, China
Ding Liu	Xi'an University of Technology, China
Jinping Qu	South China University of Technology, China
Bruno Siciliano	University of Naples, Italy
Mark W. Spong	University of Texas at Dallas, USA
Guobiao Wang	National Natural Science Foundation of China, China
Kevin Warwick	University of Reading, UK
Ming Xie	Nanyang Technological University, Singapore
Youlun Xiong	Huazhong University of Science and Technology, China
Mohammad Siddique	Fayetteville State University, USA

General Chair

Jangmyung Lee	Pusan National University, Korea
---------------	----------------------------------

General Co-chairs

Hee-Je Kim	Pusan National University, Korea
Chun-Yi Su	Concordia University, Canada
Xiangyang Zhu	Shanghai Jiao Tong University, China

Program Chairs

Min Cheol Lee	Pusan National University, Korea
Youngsun Ryuh	KITECH, Korea

Program Co-chairs

Subhash Rakheja	Concordia University, Canada
Shuzhi Sam Ge	National University of Singapore, Singapore

Publicity Chairs

Tongwen Chen	University of Alberta, Canada
Li-Chen Fu	National Taiwan University, Taiwan
Kok-Meng Lee	Georgia Institute of Technology, USA
Hideki Hashimoto	Chuo University, Japan
Ning Xi	City University of Hong Kong, Hong Kong
Xiaohua Xia	University of Pretoria, South Africa
Peter Xu	University of Auckland, New Zealand
Huayong Yang	Zhejiang University, China
Bin Yao	Purdue University, USA
Xinghuo Yu	Royal Melbourne Institute of Technology, Australia
Chaohai Zhang	Harbin Institute of Technology, China
Jae-Bok Song	Korea University, Korea
Jin-Woo Ahn	Kyungsung University, Korea

Organized Session Chairs

Seul Jung	Chungnam University, Korea
Weidong Chen	Shanghai Jiao Tong University, China
Youmin Zhang	Concordia University, Canada
Daniel Schilberg	RWTH Aachen University, Germany
Feng-Li Lian	National Taiwan University, Taiwan
Caihua Xiong	Huazhong University of Science and Technology, China
Kyung Taik Park	KIMM, Korea
In-So Kweon	KAIST, Korea

Exhibition Chairs

Hyunjea Ryu	Busan Robot Industry Association, Korea
Sung-Hyun Han	Kyungnam University, Korea
Samtae Gang	Robotech Co., Ltd., Korea
Young-Im Cho	Suwon University, Korea

Publication Chairs

Honghai Liu	University of Portsmouth, UK
Joonyoung Choi	Pusan National University, Korea
Jee-Hwan Ryu	KOREATECH, Korea

Local Arrangement Chairs

Sungshin Kim	Pusan National University, Korea
Jong-Wook Kim	DongA University, Korea
Byoung-Ho Kim	Kyungsung University, Korea

Finance Chair

Jangmok Kim	Pusan National University, Korea
-------------	----------------------------------

Secretariat

Yunji Kim	SPENALO Center, Korea
Myungja Cho	SPENALO Center, Korea

Organized Session Committee

Shengyong Chen	Zhejiang University of Technology, China
Xinkai Chen	Shibaura Institute of Technology, Japan
Mingcong Deng	Tokyo University of Agriculture and Technology, Japan
Jun Fu	Massachusetts Institute of Technology, USA
Xin Fu	Zhejiang University, China
Haibo Gao	Harbin Institute of Technology, China
Yueming Hu	South China University of Technology, China
Danwei Wang	Nanyang Technological University, Singapore
Limin Zhu	Shanghai Jiao Tong University, China
Joonbum Bae	UNIST, Korea
Hyeungsik Choi	Korea Maritime University, Korea
Jungwon Yun	Gyeongsang National University, Korea
Yangmin Li	University of Macau, Macao
Zhijun Li	South China University of Technology, China
Guangjun Liu	Ryerson University, Canada
Xinjun Liu	Tsinghua University, China
Yandong Tang	Shenyang Institute of Automation, CAS, China
Simon Yang	University of Guelph, Canada
Jianhua Zhang	Shanghai University, China
Enrong Wang	Nanjing Normal University, China
Kang-Bak Park	Korea University, Korea
John M. Dolan	Carnegi Mellon University, USA
Joachim Horn	Helmut-Schmidt-University, Germany

International Program Committee

Amir Aghdam	Concordia University, Canada
Dongpu Cao	Lancaster University, UK
Qixin Cao	Shanghai Jiao Tong University, China
Guangren Duan	Harbin Institute of Technology, China
Shumin Fei	Southeast University, China
Peihua Gu	University of Calgary, Canada
Shuxiang Guo	Kagawa University, Japan
Liu Hsu	Federal University of Rio de Janeiro, Brazil
Chunqing Huang	Xiamen University, China
Sining Liu	Concordia University, Canada
Peter X. Liu	Carleton University, Canada
Derong Liu	University of Illinois at Chicago, USA
Jun Luo	Shanghai University, China
Tao Mao	Dartmouth College, USA
Daniel Miller	University of Waterloo, Canada
Yuichiro Oya	University of Miyazak, Japan
Hailong Pei	South China University of Technology, China
Juntong Qi	Chinese Academy of Sciences, China
Joe Qin	University of Southern California, USA
Yaohong Qu	Northwestern Polytechnical University, China
Gang Tao	University of Virginia, USA
Didier Theilliol	University of Lorraine, France
Hong Wang	University of Manchester, UK
Bugong Xu	South China University of Technology, China
Jianxin Xu	National University of Singapore, Singapore
Deyi Xue	University of Calgary, Canada
Bin Zhang	University of South Carolina, USA
Keitaro Naruse	University of Aizu, Japan
Seok Jo Go	Donggeui institute of Technology, Korea
Jie Chen	Beijing Institute of Technology, China
Zuomin Dong	University of Victoria, Canada
Wei Lin	Case Western Reserve University, USA
Andrew A. Goldenberg	University of Toronto, Canada
Guoying Gu	Shanghai Jiao Tong University, China
Jason J. Gu	Dalhousie University, Canada
Lina Hao	Northeastern University, China
Henry Hong	Concordia University, Canada
Qinglei Hu	Harbin Institute of Technology, China
Min Liu	Tsinghua University, China
Inna Sharf	McGill University, Canada
Yang Shi	Victoria University, Canada
Gangbing Song	University of Houston, USA
Jing Sun	University of Michigan, USA
Yonghong Tan	Shanghai Normal University, China

Yong Tang	South China University of Technology, China
Xingsong Wang	Southeast University, China
Pak Kin Wong	University of Macau, China
Shaorong Xie	Shanghai University, China
Zhenhua Xiong	Shanghai Jiao Tong University, China
Yanzheng Zhao	Shanghai Jiao Tong University, China
Huijun Gao	Harbin Institute of Technology, China
Zijiang Yang	Ibaraki University, Japan
Dingguo Zhang	Shanghai Jiao Tong University, China
Luis E. Garza C.	Tecnológico de Monterrey, Mexico
Ruediger Spillner	Technische University München, Germany
Weidong Chen	Shanghai Jiao Tong University, China
Jaemin Byun	ETRI, Korea

List of Reviewers

We would like to acknowledge the support of the following people who contributed to peer review of articles from ICIRA2013.

Dalei Pan	Derong Liu
Joonyoung Choi	Yinfeng Fang
Keitaro Naruse	Chao Liu
Yanzheng Zhao	Dingguo Zhang
Hailong Pei	John M. Dolan
Yuehui Wang	Bugong Xu
Wei Zeng	Kiattisin Kanjanawanishkul
Zhaojie Ju	Tadeusz Szkodny
Jae Min Byun	Taeyong Choi
Jason J. Gu	Shan Jiang
Hee-Je Kim	Chun-Yi Su
Hui Yu	Mingcong Deng
Ju Jang Lee	Ronglei Sun
Kai Xu	Sungshin Kim
Wenwei Yu	Jong-Wook Kim
Weidong Chen	Weiting Liu
Zhenhua Xiong	Jeehwan Ryu
Min Cheol Lee	Qinchuan Li
Jangmyung Lee	Seok Jo Go
Honghai Liu	Zainah Md Zain
Xuguang Zhang	Mihoko Otake
Po-Ying Lai	Shuzhi Sam Ge
Bin Zhang	Kang-Bak Park
SAM Farhchi	HENTOUT Abdelfetah
Yonghong Tan	Dong-Yun Gu
Mahmod Frajchi	Huayong Yang

Jangmok Kim
Young-Im Cho
Joonbum Bae
Byoung-Ho Kim
Hyeungsik Choi
Hyunmin Do
Dongkyoung Chwa
Caihua Xiong
Chaohai Zhang
Jianhua Zhang
Yaohong Qu
Shitao Zhan
Pi-Ying Cheng
Yangmin Li
Wenlong Li
Seul Jung
Guangren Duan
Feng-Li Lian
Juntong Qi
Enrong Wang
Yuding Cui
Xinjun Sheng
Xinyong Mao

Xinkai Chen
Zicheng Li
Wenbin Chen
Liu Yong-Hua
Guoying Gu
Min-Kyu Park
Jaesung Hong
Zhijun Li
Deqing Mei
Syed Hassan
Zhang Jianjun
Myung-Jin Chung
Jacek Czczot
Taeseok Jin
Joon Young Choi
Can Wang
Guo-Ying Gu
Kalyana Chakravarthy Veluvolu
Xiaogang Duan
Yandong Tang
Tao Mao
Jianjun Meng
Jie Chen

Table of Contents – Part I

Application of High Frequency Systems for Robotics

Development of Power Supply System for Medical Ruby Laser	1
<i>Jae-Hun Jeong, Kook-Sung Hur, and Hee-Je Kim</i>	
Corrosion Protection Using High-Voltage and High-Frequency System	8
<i>Seung-Hwa Baek, Hyun-Min Kim, and Hee-Je Kim</i>	
An Analysis on the Particular Pulse Related to the Human Bio-signal by Using Photoplethysmography(PPG)	18
<i>Myong-hwan Kim and Hee-Je Kim</i>	
Bunker Oil C Heating Using Induction Heating	25
<i>Dong-Hyun Kim, Ki-Ryong Kim, and Hee-Je Kim</i>	
Magnetic Resonance Wireless Power Transmission Using a LLC Resonant Circuit for a Locomotion Robot's Battery Charging	31
<i>Ki-Ryong Kim, Dong-Hyun Kim, and Hee-Je Kim</i>	
Research on the MPPT Simulation of Mini Photovoltaic System for the Robotic Vacuum Cleaner Battery Charging	38
<i>Seong-Min Heo, Ki-Ryong Kim, and Hee-Je Kim</i>	

Intelligent Robots and Autonomous Systems

VDC of In-Wheel EV Simulation Based on Precise Wheel Torque Control	45
<i>Hyunuk Ha, Jongmoo Kim, and Jangmyung Lee</i>	
Vibration Pattern for the Implementation of Haptic Joystick	56
<i>Kyung-Wook Noh, Sun-Kyun Kang, Dong-Hyuk Lee, and Jangmyung Lee</i>	
Outdoor Precision Position Estimation System Using Multi-GPS Receivers	66
<i>Seunghwan Choi, Kijung Kim, Yunki Kim, and Jangmyung Lee</i>	
Low Complexity MAP Algorithm for Turbo Decoder	77
<i>Jonghyun Seo and Jangmyung Lee</i>	
Force Feedback Implementation Based on Recognition of Obstacle for the Mobile Robot Using a Haptic Joystick	85
<i>Dong-Hyuk Lee, Kyoung-Taik Park, Sun-Kyun Kang, and Jangmyung Lee</i>	

Position Detection Performance Improvement for LSM Control in Super Speed Maglev	97
<i>Jinho Lee, Jeongmin Jo, Youngjae Han, and Changyoung Lee</i>	
Network Aware Resource Allocation Scheme for Mobile Ad Hoc Computational Grid	105
<i>Sayed Chhattan Shah, Myong-Soon Park, Wan Sik Choi, Sajjad Hussain, and Ali Kashif Bashir</i>	
Single Camera Motion Estimation: Modification of the 8-Point Method	117
<i>Mohammad Hossein Mirabdollah and Bärbel Mertsching</i>	
A Biomimetic Earthworm-Like Micro Robot Using Nut-Type Piezoelectric Motor	129
<i>Maoying Zhou, Yuebang Tao, Liling Cheng, Wei-ting Liu, and Xin Fu</i>	
A Robust Control of Intelligent Mobile Robot Based on Voice Command	136
<i>Sung Won Jung, Moon Yeol Park, In Man Park, Yang Keun Jung, and Hang Bong Shin</i>	
Vision Based People Tracking Using Stereo Camera and Camshift	145
<i>Kang-Il Park, Chan-Ik Park, and Jangmyung Lee</i>	

Bio-Medical Robotics and Its Application

Analysis of Active Haptic Feedback Effects on Standing Stability	154
<i>Muhammad Raheel Afzal, Yasir Jan, Syed Hassan, and Jungwon Yoon</i>	
Speed Adaptation of a Small Size Treadmill Using Impedance Control Approach for Rehabilitation	165
<i>Jungwon Yoon, Auralius Manurung, and Irfan Hussain</i>	
Design and Simulation of a 3D Actuation System for Magnetic Nano-Particles Delivery System	177
<i>Mohammad Dadkhah, Naveen Kumar, and Jungwon Yoon</i>	
Optimal Kinematic Design of a Novel Robotic Knee Device for Gait Rehabilitation with Stance Control	188
<i>Sanghun Pyo, Mingyun Oh, and Jungwon Yoon</i>	
Neuro Invasive Multi-targeted Drug Delivery Approach Using Swarm of Nano-robotic Carriers	204
<i>Syed Hassan, Ikram Ullah, Myeong Ok Kim, and Jungwon Yoon</i>	

A Novel EMG Control Method for Multi-DOF Prosthetic Hands with Electrical Stimulation Feedback	216
<i>Qi Huang, Li Jiang, Dapeng Yang, and Hong Liu</i>	
Sliding Perturbation Observer Based Reaction Force Estimation Method in Surgical Robot Instrument	227
<i>Sung Min Yoon, Min-Cheol Lee, and Chi Yen Kim</i>	
Design of a Novel Single Incision Laparoscopic Surgery Robot with Increased Tissue Handling Force	237
<i>DaeKeun Ji, Byungsik Cheon, Makoto Hashizume, Morimasa Tomikawa, and Jaesung Hong</i>	
Vertical Collaborative Fuzzy C-Means for Multiple EEG Data Sets	246
<i>Mukesh Prasad, Chin-Teng Lin, Chien-Ting Yang, and Amit Saxena</i>	
Comparison of Exoskeleton Robots and End-Effector Robots on Training Methods and Gait Biomechanics	258
<i>Pi-Ying Cheng and Po-Ying Lai</i>	
TCP Performance in LTE Network	267
<i>Hyun-Chul Yi, Hyoung-Woo Kim, and Joon-Young Choi</i>	
Analysis of Functional Components for a Robotic Patient Lift Based on Chinese Clinical Demands	273
<i>Yu Wu, Dong-Yun Gu, and Jian-He Wei</i>	

Robotics for Rehabilitation and Assistance

Lower Limb Exoskeleton Using Recumbent Cycling Modality for Post-stroke Rehabilitation	284
<i>Hua Yan and Canjun Yang</i>	
An Open-Source Development and Simulation Platform for Smart Wheelchairs	295
<i>Wenlong Liao, Weidong Chen, Zhixuan Wei, Wenxi Zhang, Jingchuan Wang, and Kang Li</i>	
Semantic Mapping for Safe and Comfortable Navigation of a Brain-Controlled Wheelchair	307
<i>Zhixuan Wei, Weidong Chen, Jingchuan Wang, Huiyu Wang, and Kang Li</i>	
Control Strategies and Particle Filter for RGB-D Based Human Subject Tracking and Behavior Recognition by a Bio-monitoring Mobile Robot	318
<i>Nevez Imamoglu, Myagmarbayar Nergui, Yuki Yoshida, Jose Gonzalez, and Wenwei Yu</i>	

CTS Rehabilitation Training Robot Using Motor Control	330
<i>Heein Jeong, Sangyong Lee, and Jangmyung Lee</i>	
A Principle of Mechanical Implementing the Kinematic Synergy for Designing Anthropomorphic Hand	339
<i>Wenbin Chen and Caihua Xiong</i>	
Design Simulations of the SJTU Continuum Arm Exoskeleton (SCAX)	351
<i>Kai Xu, You Wang, and Dong Qiu</i>	
A Novel 10-DoF Exoskeleton Rehabilitation Robot Based on the Postural Synergies of Upper Extremity Movements	363
<i>Kai Liu and Caihua Xiong</i>	
An ANN Based Approach for Gait Prediction of a Lower-Limb Exoskeleton with Plantar Pressure Sensors	373
<i>Yuzhang Liu, Can Wang, Duan Zheng, Gang Wang, and Xinyu Wu</i>	
Optimal Kinematic Calibration of the 6-UPS Parallel Manipulator	384
<i>Genliang Chen, Hao Wang, and Zhongqin Lin</i>	

Bio-Mechatronics

Effects of Long-Term Myoelectric Signals on Pattern Recognition	396
<i>Jiayuan He, Dingguo Zhang, Xinjun Sheng, and Xiangyang Zhu</i>	
Development of a Surface EMG Acquisition System with Novel Electrodes Configuration and Signal Representation	405
<i>Yinfeng Fang, Xiangyang Zhu, and Honghai Liu</i>	
Hybrid Force-Position Fuzzy Control for a Prosthetic Hand	415
<i>Gaoke Zhu, Xiaogang Duan, and Hua Deng</i>	
Simulation of a Hydraulic System Duplicating the Human Circulatory System	427
<i>Feng Huang, Wenwei Qian, Xiaodong Ruan, and Xin Fu</i>	
An Overview of Wearable Sensing and Wearable Feedback for Gait Retraining	434
<i>Pete B. Shull, Wisit Jirattigalachote, and Xiangyang Zhu</i>	
Quantifying Roughness Sensation by an Active Touch Model for Vibrotactile Stimulation	444
<i>Zhongyi Qiu, Dingguo Zhang, and Xiangyang Zhu</i>	
Visual Stimulus Background Effects on SSVEP-Based Brain-Computer Interface	453
<i>Xiaokang Shu, Lin Yao, Jianjun Meng, Xinjun Sheng, and Xiangyang Zhu</i>	

Mechanical Implementation of Postural Synergies of an Underactuated Prosthetic Hand	463
<i>Kai Xu, Yuheng Du, Huan Liu, Xinjun Sheng, and Xiangyang Zhu</i>	
A Micro-wires Based Tactile Sensor for Prosthesis	475
<i>Guanhao Liang, Deqing Mei, Yancheng Wang, Yu Dai, and Zichen Chen</i>	
An Anti-aliasing and De-noising Hybrid Algorithm for Wavelet Transform	484
<i>Yuding Cui, Caihua Xiong, and Ronglei Sun</i>	
Simultaneous and Proportional Estimation of Finger Joint Angles from Surface EMG Signals during Mirrored Bilateral Movements	493
<i>Lizhi Pan, Xinjun Sheng, Dingguo Zhang, and Xiangyang Zhu</i>	
A Mechatronic Platform for Studies of Tactile Sensory System on Prosthesis Hand	500
<i>Xiaoying Cheng, Qingchuan Shan, Ping Yu, Liling Cheng, Wei-ting Liu, and Xin Fu</i>	
Simulation Study of Dipole Localization in MEG-Based BCI Using Magnetic Field Reconstruction	509
<i>Liang Hu, Hui-Min Shen, Wei-ting Liu, Kok-Meng Lee, and Xin Fu</i>	

Environment Recognition and Localization/Navigation

Fully Decentralized Cooperative Localization of a Robot Team: An Efficient and Centralized Equivalent Solution	520
<i>Hua Mu, Mengyuan Dai, Ming Gao, and Xianfei Pan</i>	
Development of a Sound Source Localization System for Assisting Group Conversation	532
<i>Mihoko Otake, Myagmarbayar Nergui, Seong-eun Moon, Kentaro Takagi, Tsutomu Kamashima, and Kazuhiro Nakadai</i>	
Adaptive Tracking Controller Based on the PID for Mobile Robot Path Tracking	540
<i>Hyunjin Chang and Taeseok Jin</i>	
A New Non-Gaussian Filtering Approach to Monocular SLAM Problem	550
<i>Mohammad Hossein Mirabdollah and Bärbel Mertsching</i>	
Object Following Robot Using Vision Camera, Single Curvature Trajectory and Kalman Filters	562
<i>Shin-nyeong Heo, Hyun-Seop Lim, Seungik Hwang, and Jangmyung Lee</i>	

Accurate Localization with COAG Features and Self-adaptive Energy Region	576
<i>Dong-Il Kim and Jae-Bok Song</i>	
2D Multi-class Occupancy Grid Map for a Mobile Security Robot in Urban Environments	584
<i>Yungeun Choe and Myung Jin Chung</i>	
Trajectory Optimization Using Virtual Motion Camouflage and Particle Swarm Optimization	594
<i>Dong Jun Kwak, Byunghun Choi, and H. Jin Kim</i>	
3D Probability Map Building for UGV Navigation in Special Environment	605
<i>Min-Ho Kim, Hee-Mu Lee, and Min-Cheol Lee</i>	
Method and Development of Magnetic Positioning Device for Magnetic Guided Vehicle	615
<i>Hyunhak Cho, Jaeyong Kim, Hajun Song, Moonho Park, and Sungshin Kim</i>	
Relative Pose Estimation for an Integrated UGV-UAV Robot System ...	625
<i>Yongseop Jeong and In So Kweon</i>	
The Algorithm Camera Computing the Object Location	637
<i>Tadeusz Szkodny</i>	
Quantitative Assessment of Uniformity in Particle Distribution	649
<i>Xin Yuan, Lei Jia, Zhengyu Ba, Xinjun Sheng, and Zhenhua Xiong</i>	
Hand Gesture Recognition for Human-Computer Interaction Using Moment Invariants and Neural Network Classifier	661
<i>Ran Chen, Shuangyuan Wang, Liang Gong, and Chengliang Liu</i>	
Sum of Squares Based Range Estimation for Camera Systems	668
<i>Cheol-Joong Kim and Dongkyoung Chwa</i>	
Multi-Agent Fuzzy-Based Control Architecture for Autonomous Mobile Manipulators: Traditional Approaches and Multi-Agent Fuzzy-Based Approaches	679
<i>Abdelfetah Hentout, Mohamed Ayoub Messous, Saliha Oukid, and Brahim Bouzouia</i>	

Robot Motion Analysis and Planning

Geometric Modeling of Any Obstacle Shapes for Robot Motion Planning	693
<i>Md Nasir Uddin Laskar, Seung Y. Choi, Ishtiaq Ahmed, and TaeChoong Chung</i>	

Path Planning Approach for Redundant Manipulator Based on Jacobian Pseudoinverse-RRT Algorithm	706
<i>Yang Qian and Ahmed Rahmani</i>	
Dynamic Research of a Novel Exoskeleton with Level Walking	718
<i>Dalei Pan and Feng Gao</i>	
Mobility Analysis of Two Exechon-Liked Parallel Mechanisms	730
<i>Xinxue Chai, Qiaohong Chen, Jigang Ma, and Qinchuan Li</i>	
A Method for Inverse Kinematic Solutions of 3R Manipulators with Coupling	742
<i>Byoung-Ho Kim</i>	
Author Index	751

Table of Contents – Part II

Mechanism Desing and Control

Design and Inverse Kinematics of Three Degree of Freedom Mine Detection Manipulator	1
<i>Nauman K. Haider, Shiraz Gulraiz, Ayaz Mehmood, and Umer Izhar</i>	
The Modeling and Simulation of Kinetic Analysis of Nonholonomic Systems for the Omni-Directional Wall Climbing Robot	16
<i>W.X. Yan, H.F. Zhou, Yan-Zheng Zhao, Z. Fu, and Y. Wang</i>	
A Rolling Sarrus Mechanism	33
<i>Chao Liu, Hao Wang, Mei-Li Zhai, and Yan-An Yao</i>	
A New Euclidian Distance Based Approach to Measure Closeness to Singularity for Parallel Manipulators	41
<i>Jianyu Mao, Yalei Guo, Jie Ren, and Weizhong Guo</i>	
Framework Based Path Planning, A Novel Approach	54
<i>Morteza Aghaei and Seyyed Mohammad Reza Farshchi</i>	
Kinematics and Dynamics for a 3-DOF Parallel Manipulator with Limbs of Embedding Structures	63
<i>Jianjun Zhang, Xiaohui Wang, Ning Jiang, and Weimin Li</i>	
High-Speed Tracking Control of Parallel Kinematic Machine for Pick-and-Place	74
<i>Hyun Min Do, Chanhun Park, Byung In Kim, Tae Yong Choi, and Jin Ho Kyung</i>	
Ultrasound Based Object Detection for Human-Robot Collaboration . . .	84
<i>Christoph Glowa and Thomas Schlegl</i>	
Exponential Stabilization of Second-Order Nonholonomic Chained Systems	96
<i>Zainah Md. Zain, Keigo Watanabe, Kiyotaka Izumi, and Isaku Nagai</i>	
Development of an Autonomous RC-car	108
<i>Daniel Claes, Joscha Fossel, Bastian Broecker, Daniel Hennes, and Karl Tuyls</i>	
Modeling, Control and Simulation of a 6-DOF Reconfigurable Space Manipulator with Lockable Cylindrical Joints	121
<i>Pooya Merat, Farhad Aghili, and Chun-Yi Su</i>	

Mechanical Design of a Lower Extremity Exoskeleton with Hybrid Legs for Power Augmentation	132
<i>Yunjie Miao, Feng Gao, and Dalei Pan</i>	
Design of Selectively Controllable Micro Actuators Powered by Remote Resonant Magnetic Fields	143
<i>Kai Xu and Guoqing Liu</i>	
Mechanical Home Position Setting Method of the Manipulator with Two Encoders	155
<i>Tae Yong Choi, Hyun-Min Do, Doo-Hyung Kim, Kyung-Taik Park, and Kwangcho Chung</i>	
Using Growth Curve in Trajectory Planning for Industrial Manipulator	166
<i>Hua Jiang, Yonghua Yan, Mingyong Zhang, Jianrong Zhang, and Jiahang Xu</i>	

Motion and Optimal Control

Practical Implementation of the Nonlinear Control of the Liquid Level in the Tank of Irregular Shape	178
<i>Witold Kłopot, Tomasz Kłopot, Piotr Laszczyk, Jacek Czechtot, and Mieczysław Metzger</i>	
An Optimal Feedback Approach for the Stabilization of Linear Systems Subject to Input Saturation and Magnitude-Bounded Disturbances	189
<i>S.T. Zhan, W.X. Yan, Z. Fu, J.H. Liu, W.H. Deng, and Yan-Zheng Zhao</i>	
Estimation of Road Adhesion Coefficient Using Higher-Order Sliding Mode Observer for Torsional Tyre Model	202
<i>J.J. Rath, K.C. Veluvolu, D. Zhang, Q. Zhang, and M. Defoort</i>	
Stability Domain Analysis for Input-Saturated Linear Systems Subject to Disturbance via Popov Criterion: An LMI Approach	214
<i>S.T. Zhan, W.X. Yan, Z. Fu, and Yan-Zheng Zhao</i>	

Humanoid Robot

Synergetic Control Strategy for a Hybrid FES-Exoskeleton System: A Simulation Study	226
<i>Yong Ren, Qing Zhang, and Dingguo Zhang</i>	
A Balance Control Method of a Walking Biped Robot under a Continuous External Force	237
<i>Yeoun-Jae Kim, Joon-Yong Lee, and Ju-Jang Lee</i>	

Design and Control of a Four-Link Mechanism for High Speed and Dynamic Locomotion	246
<i>Huiyang Yu, Ronglei Sun, Hua Nie, and Guohua Qin</i>	
A Six-Legged Walking Robot Inspired by Insect Locomotion	257
<i>Yeongtae Jung and Joonbum Bae</i>	
A Stable Walking Control of Two – Legs Biped Robot	265
<i>Won Sung Ki, Byung Kyun Shim, Won Jun Hwang, Eun Uk Kang, Woo Song Lee, and Sung Hyun Han</i>	

Underwater and Space Robot

Design of a Time-Delayed Controller for Attitude Control of a Quadrotor System	274
<i>Jeong Geun Lim and Seul Jung</i>	
Brain Flow in Application for SYNAP New Robotic Platform	281
<i>Alberto Rovetta</i>	
Design and Analysis on a New Underwater Robot	289
<i>Ngoc-Huy Tran, Hyeung-Sik Choi, Sang-Seob Lee, and Ba-Loc Mai</i>	
Design and Manufacturing a Bio-inspired Variable Stiffness Mechanism in a Robotic Dolphin	302
<i>Yong-Jai Park and Kyu-Jin Cho</i>	
Design and Control of 3-DOF Robotic Fish ‘ICHTHUS V5.5’	310
<i>Gi-Hun Yang, Kyung-Sik Kim, Sang-Hyo Lee, Chullhee Cho, and Youngsun Ryuh</i>	

Power Conversion Technology for Robotics

High Efficiency Isolated Bidirectional AC-DC Power Converter	320
<i>Ho-Sung Kim, Myung-Hyo Ryu, Ju-Won Baek, Jong-Hyun Kim, and Hee-Je Kim</i>	
Dynamic Analysis and Optimal Design of High Efficiency Full Bridge LLC Resonant Converter	327
<i>Dong-Keun Jeong, Myung-Hyo Ryu, Joo-Won Baek, and Hee-Je Kim</i>	
A Boost PFC Rectifier with a Passive Lossless Snubber Circuit Using Coupled Inductors Methodes	334
<i>Hyeok-Jin Yun, Jong-Hyun Kim, Myung-Hyo Ryu, and Hee-Je Kim</i>	
Experimental Investigation on the Hybrid Smart Green Ship	338
<i>Kyoung-Jun Lee, Dongsul Shin, Jong-Pil Lee, Tae-Jin Kim, and Hee-Je Kim</i>	

Hybrid Control Scheme for a Half-Bridge LLC Resonant Converter with a Wide Input Range 345
Dongsul Shin, Kyoung-Jun Lee, Jong-Pil Lee, and Hee-Je Kim

Mechatronics and Automation

A Relay Shaping Method for Servo Mechanical System Identification ... 353
Chao Liu, Jia Liu, Jian-hua Wu, Hui Wang, and Zhenhua Xiong

Optimal Cross-Coupled Synchronization Control of a Precision Motion Stage Driven by Dual Linear Motors 365
Gang Zhang, Jian-hua Wu, Pin-kuan Liu, and Han Ding

Genetic-Based k-Nearest Neighbor for Chaff Echo Detection 375
Jonggeun Kim, HyeYoung Han, Jungwon Yu, Hansoo Lee, and Sungshin Kim

Design and Analysis of a Spatial Remote Center of Compliance Mechanism 385
Lei-Jie Lai, Guo-Ying Gu, Hang Zhou, and Li-Min Zhu

A Novel Conductive Particle Dispersing Method via EHDA for POB-COG Packaging 397
Z. Ba, X. Yuan, L. Jia, X. Sheng, Zhenhua Xiong, and Han Ding

Performance Prediction of Hard Rock TBM Based on Extreme Learning Machine 409
Chengjun Shao, Xiuliang Li, and Hongye Su

A Sensor for Large Strain Deformation Measurement with Automated Grid Method Based on Machine Vision 417
Yi Jin, Mingchi Feng, Tao Luo, and Chao Zhai

A 6-Axis Sensor for Minimally Invasive Robotic Surgery 429
Jun Jiang, Le Xie, and Hailong Yu

Industrial Application of Actuator and Sensor

Mechanical Safety of Automatic Door by Using PFVA Based on 2-Stage Star Compound Gear 436
Min-Kyu Park and Delbert Tesar

Development of Smart Actuator and Its Application 442
Seok-Jo Go, Min-Kyu Park, and Young-Jin Lee

Development of Single Channel Interrogator for Optical Sensors 450
Jang Sik Park, Jong Kwan Song, and Byung Woo Yoon

In-network RFID Data Filtering Scheme in RFID-WSN for RFID Applications	454
<i>Ali Kashif Bashir, Myong-Soon Park, Sang-Il Lee, Jinseop Park, Wongryol Lee, and Sayed Chattan Shah</i>	
Optimal Design of MR Shock Absorber for Passenger Vehicle	466
<i>Kum-Gil Sung and Min-Kyu Park</i>	
Fractional-Order PID Control of Hydraulic Thrust System for Tunneling Boring Machine	470
<i>Ling Fei, Jingcheng Wang, Langwen Zhang, Yang Ge, and Kang Li</i>	
Finite Element Research on Cutting Force and Temperature in Milling 300M Steel	481
<i>Sen Lin, Fangyu Peng, Yizhi Liu, Sheng Yang, and Rong Yan</i>	
Multi-axis NC Machining Dynamics Analysis and Control	
Experimental Study of Surface Integrity of Aluminum Lithium Alloy by Face Milling	491
<i>Haikuo Mou, Xinda Huang, Xiaoming Zhang, and Han Ding</i>	
Research on Active Vibration Control of Thin-Walled Workpiece in Milling Based on Voice Coil Motor	503
<i>Puwei Chen, Jie Zhai, Xiaoming Zhang, Hai-Tao Zhang, and Han Ding</i>	
A Complete Methodology for Estimating Dynamics of the Heavy Machine Tool Structure	513
<i>Hui Cai, Bin Li, Xinyong Mao, Bo Luo, and Fangyu Peng</i>	
Adaptive LQR Control to Attenuate Chatters in Milling Processes	525
<i>Hai-Tao Zhang, Zhiyong Chen, and Han Ding</i>	
Robot Surgery Simulation System for Soft Tissue Cutting	535
<i>Hesheng Wang, Maojiao Cai, Weidong Chen, Meng Li, and Kang Li</i>	
A Novel PWM Scheme for Position Sensorless Control of BLDC Motor Drives Based on Back EMF	545
<i>Zicheng Li, Zhouping Yin, and You-lun Xiong</i>	
Aviation Blade Inspection Based on Optical Measurement	555
<i>Wen-long Li, Li-ping Zhou, and You-lun Xiong</i>	

Computer Integrated Manufacturing and Automation

Programmable Automation of Soccer Ball Sticking through Open Loop Control of a Path Tracing Gripper	569
<i>Majid Munawar, Khurram Butt, Waseem Shahzad, Mehran Ahmad, and Kamal Yousaf</i>	
A Design and Development of Robotics Integrated Curriculum Based on Storytelling for Elementary School Student	580
<i>Ji-Hun Sung, Young-Hoon Sung, and Wae-Shik Moon</i>	
Cutting Force Prediction of Plunge Milling Based on Precise Cutting Geometry	592
<i>Kejia Zhuang, Xiaoming Zhang, and Han Ding</i>	
Distributed Coordination of Multiple Robot Systems Based on Hierarchical Petri Net Models	602
<i>Gen'ichi Yasuda</i>	
Study on Collaborative Simulation of Excavation System of the Shield Machine in Composite Strata	614
<i>Yanmin Zhao, Jianfu Zhang, and Pingfa Feng</i>	

Modeling and Control of Smart Material Actuating Systems

Robust Adaptive Control of a Class of Nonlinear Systems with Unknown Hysteresis Nonlinearity	623
<i>Yong-Hua Liu, Ying Feng, and Chun-Yi Su</i>	
A Prandtl-Ishlinskii Model for Characterizing Asymmetric and Saturated Hysteresis of Smart Material Actuators	635
<i>Omar Aljanaideh, Subhash Rakheja, and Chun-Yi Su</i>	
Improving Tracking Precision of Piezoceramic Actuators Using Feedforward-Feedback Control	644
<i>Guo-Ying Gu, Chun-Xia Li, Lei-Jie Lai, and Li-Min Zhu</i>	
A Novel Analytical Inverse Compensation Approach for Preisach Model	656
<i>Zhi Li, Sining Liu, and Chun-Yi Su</i>	
High Precision Control for Nano-stage Driven by Magnetostrictive Actuator	666
<i>Xinkai Chen and Chun-Yi Su</i>	

Development of a Parallel-Kinematic High-Speed XY Nanopositioning Stage	678
<i>Chun-Xia Li, Guo-Ying Gu, Mei-Ju Yang, and Li-Min Zhu</i>	
Full-Face Tunnel Boring Machine	
Dynamical Behavior of Redundant Thrusting Mechanical System in Shield Machines with Various Grouping Strategies	690
<i>Chunzhang Zhao, Haidong Yu, and Yong Zhao</i>	
Cutters Layout Design of the Full-Face Rock Tunnel Boring Machine Based on Physical Programming	700
<i>Xu Zhang, Wei Sun, Junzhou Huo, and Jingxiu Ling</i>	
Analysis of Multi-sensor Attitude Measurement System on TBM	710
<i>Chuncao Zhang, Guoli Zhu, Jianbo Zhang, and Minghua Pan</i>	
Endocrine Intelligent Control of Thrust Hydraulic System for TBM	720
<i>Jin Yao, Xia Yimin, Cheng Yongliang, and Zhang Huan</i>	
A Cutter Layout Optimization Method for Full-Face Rock Tunnel Boring Machine	727
<i>Geng Qi, Wei Zhengying, Du Jun, and Tang Yiping</i>	
Author Index	739

Development of Power Supply System for Medical Ruby Laser

Jae-Hun Jeong¹, Kook-Sung Hur², and Hee-Je Kim^{2*}

¹ Department of Interdisciplinary Program in Robotics,
Pusan National University, Jangjeon-dong, Geumjung-gu, Korea
jjhoon@pusan.ac.kr

² Department of Electrical Engineering, Pusan National University,
Jangjeon-dong, Geumjung-gu, Korea
hurkooksung@hotmail.com,
heeje@pusan.ac.kr

Abstract. The ruby laser has been used for medical laser. Especially, it is useful for skin regeneration. Medical ruby laser needs light energy more than 1J. Also, it needs to discharge light energy per 1 second. So laser system is necessary to have power supplier more than 2kW for stable operation.

Power system is composed of LLC Resonant Full-bridge converter. Finally, this topic presents power system of ruby laser which discharge light energy with 1J/1.5Hz.

Keywords: Ruby laser, Skin regeneration, Full-bridge converter, LLC resonance, Light energy.

1 Introduction

Laser ray has been widely used in science and technology field, because it has unique character in comparison with general ray. Development of laser technology expanded laser application field toward medical field. Medical laser can replace existing medical devices which have several disadvantages, so it is recognized as most advanced medical device [1].

Medical laser has been developed from 1960s. Kind of medical laser is classed as laser rod called medium. Laser rod decides wavelength of laser which is very important character, because wavelength of laser decides treatment effect. Also, treatment effect is decided by intensity and shape of laser. Especially, ruby laser has 694nm wavelength, it is effective on pigmented lesion like freckle, lentigo, blemish and chlosma.

Generally, repetition rate of medical ruby laser is 1Hz. It is important to increase repetition rate to reduce treatment time. So, this topic presents design procedure of power supplier which can charge and discharge of energy for 1.5Hz.

* Corresponding author.

2 Power System of Ruby Laser

2.1 Configuration of Power System

Power system is composed of three parts [2]. Simmer power generates DC 1kV to operate simmer discharge. It was made by boost transformer. Trigger power generates pk-pk 20kV. Main power supplier generates DC 300~600V to excite laser rod through discharge of flash lamp. Main stage power has to change output voltage, because output voltage decides output of laser.

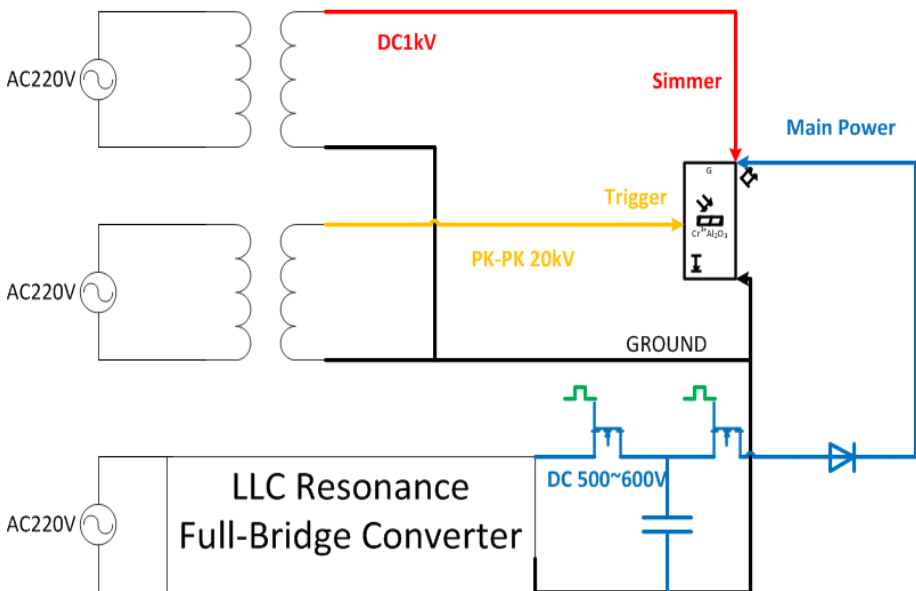


Fig. 1. Configuration of power system

2.2 Simmer Mode Triggering

When high currents flow instantaneously through flash lamp, flash lamp generates strong light. Impedance of flash lamp has to be low for high currents. Simmer mode triggering is a way to make impedance of flash lamp low [3]. It always keeps low current to ionize flash lamp which is condition to generate strong light. Voltage and current applying flash lamp at simmer mode triggering is different by characteristic of flash lamp. Generally, flash lamp is applied 100~150V / 0.1~0.5A. It was applied 186V / 77mA in this experiment. After flash lamp is applied DC 1kV from simmer power, trigger power applies to flash lamp to start simmer mode triggering.

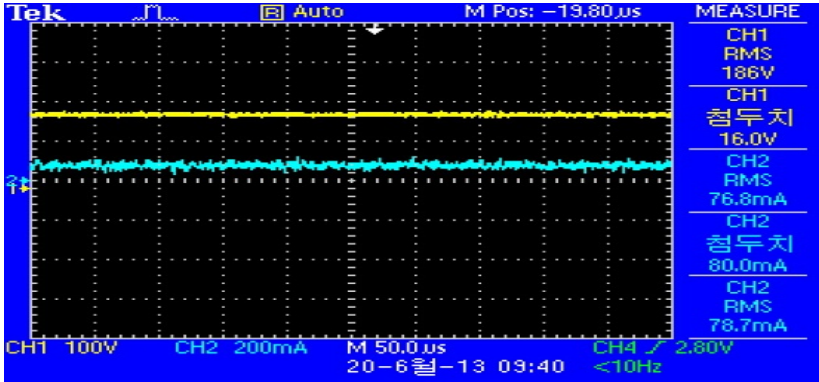


Fig. 2. Result of simmer mode triggering ($V = 186V$, $I = 77mA$)



Fig. 3. Operation of simmer mode triggering

2.3 Design of Main Power Supplier

After simmer mode triggering, main power supplier applies to flash lamp to generate light. Generated light excites ruby rod, and ruby rod finally generates laser beam. Efficiency of light conversion is 0.5~1%. Equation 1 presents charging energy of capacitor to generate laser beam with 1Hz / 1J [4].

$$\begin{aligned}
 P_{peak} &= \frac{0.5 \times C_{load} \times (V_{charge})^2}{T_c} \\
 &= \frac{0.5 \times (30,000 \times 10^{-6}) \times (80)^2}{900 \times 10^{-3}} = 106.6J/sec
 \end{aligned} \quad (1)$$

Main power supplier was designed using LLC resonant Full-Bridge Converter [5]. It charges capacitor by 600V and repeats charging and discharging of 80V.

LLC resonant Full-bridge Converter can realize ZVS(Zero Voltage Switching) to reduce switching loss of MOSFET.

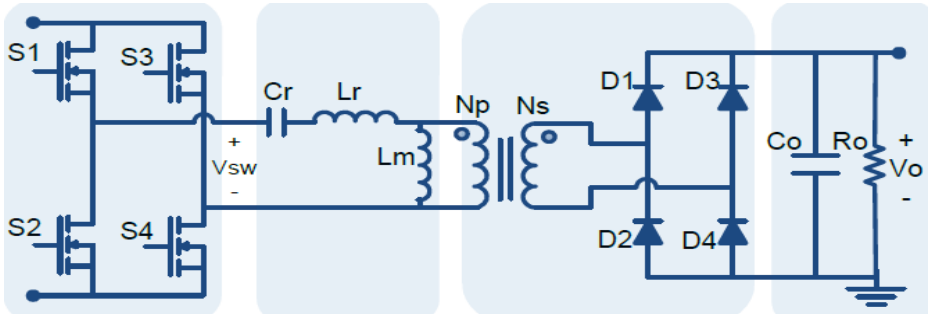


Fig. 4. LLC Resonant Full-Bridge Converter

When flash lamp discharges, impedance of flash lamp is lower. Main power supplier is separated from load by IGBT to protect inrush current.

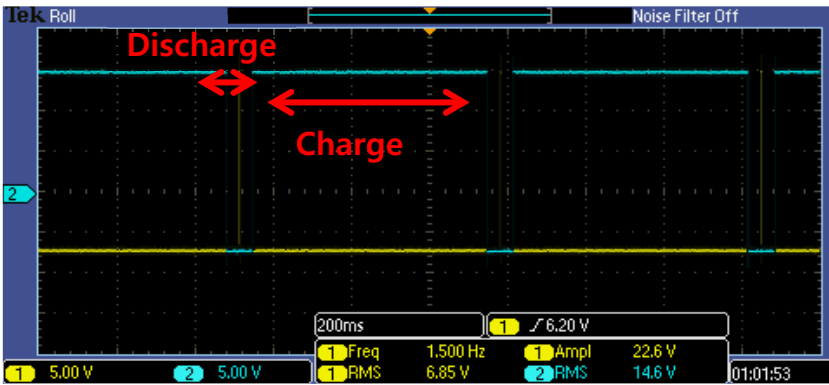


Fig. 5. Separation of charging and discharging time by IGBT(1.5HZ)

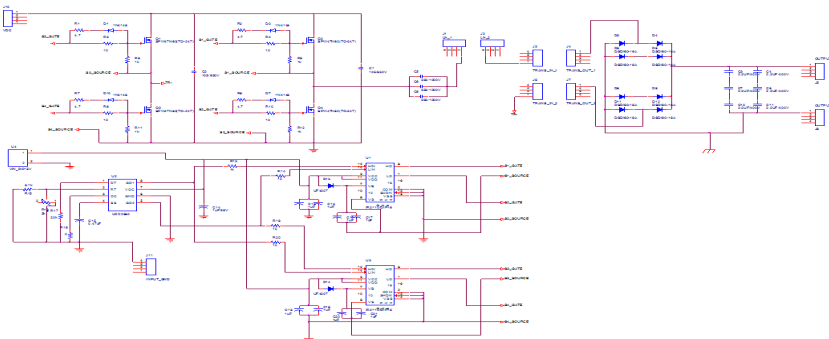


Fig. 6. LLC Resonant Full-Bridge Converter using UCC25600

UCC25600 makes Switching frequency for LLC resonant Full-Bridge Converter and IR2110 makes IGBT control signal for separation of charging and discharging time [6, 7].

3 Experimental Results

It was important that value of maximum voltage decided value of discharging current. However, value of discharging voltage did not affect value of discharging current.

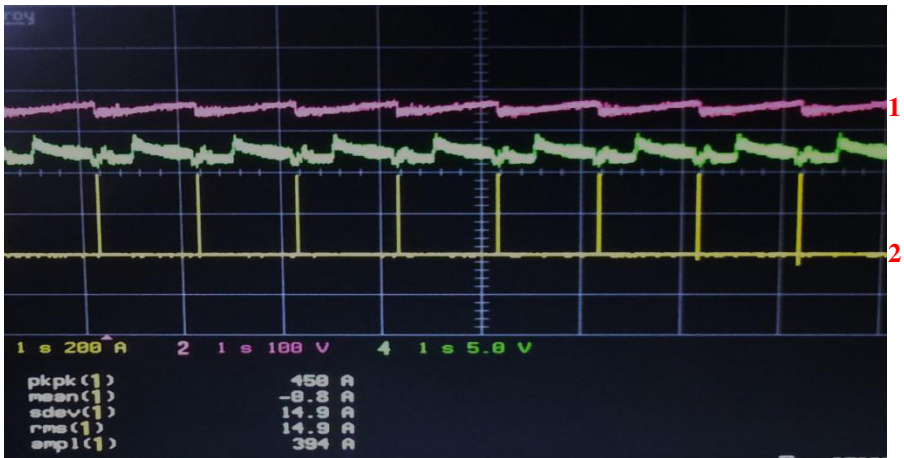


Fig. 7. Result of discharging current at discharging laser beam ($V_{\max} = 371V$ (1), Discharging current = 394A (2))

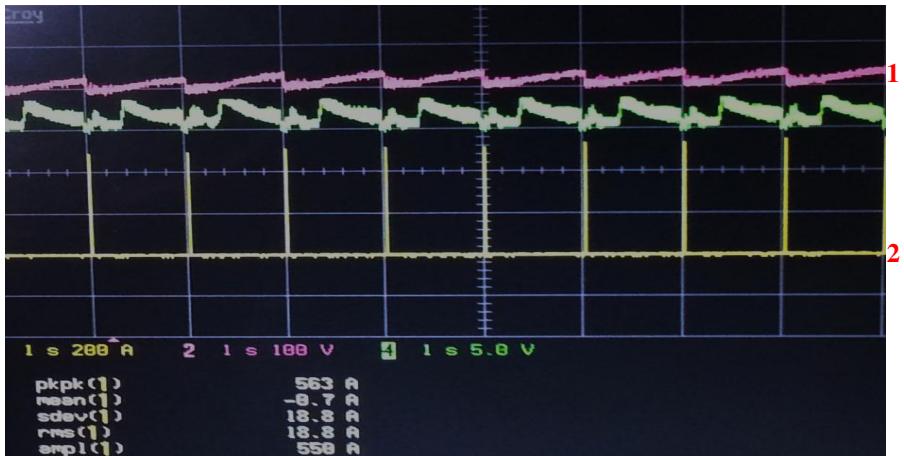


Fig. 8. Result of discharging current at discharging laser beam ($V_{\max} = 438V$ (1), Discharging current = 550A (2))

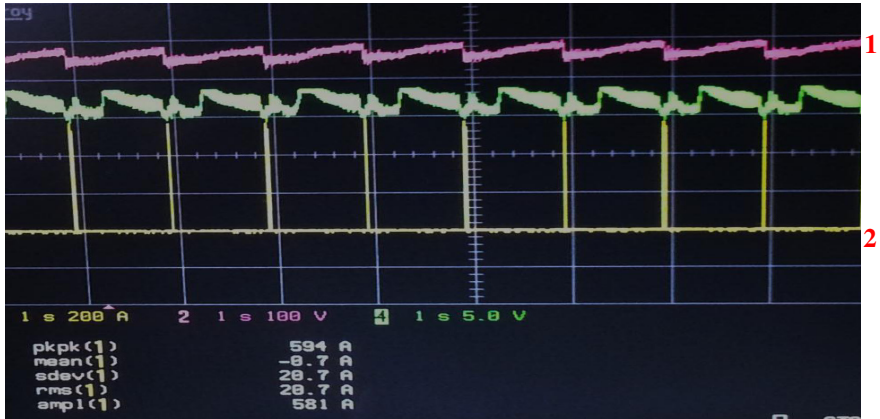


Fig. 9. Result of discharging current at discharging laser beam ($V_{max} = 489V(1)$, Discharging current = $581A(2)$)

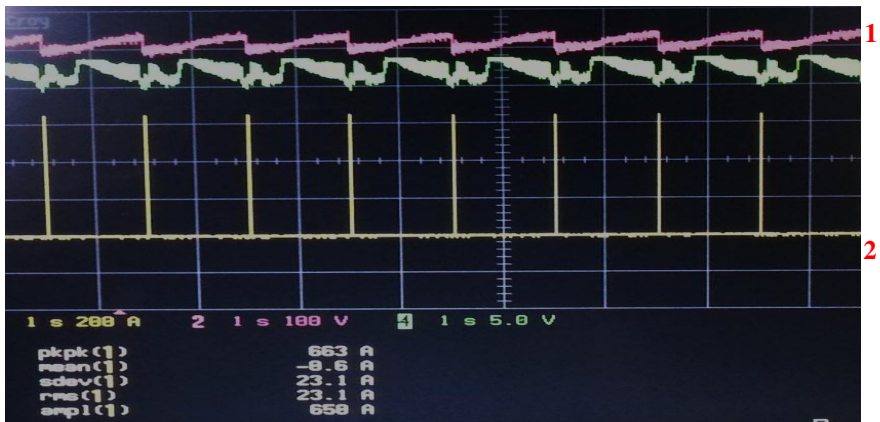


Fig. 10. Result of discharging current at discharging laser beam ($V_{max} = 542V(1)$, Discharging current = $650A(2)$)

Discharging time needed to be short, because value of discharging voltage did not affect value of discharging current. If discharging time is short, discharging voltage also reduces. It is advantage to charge voltage fast.

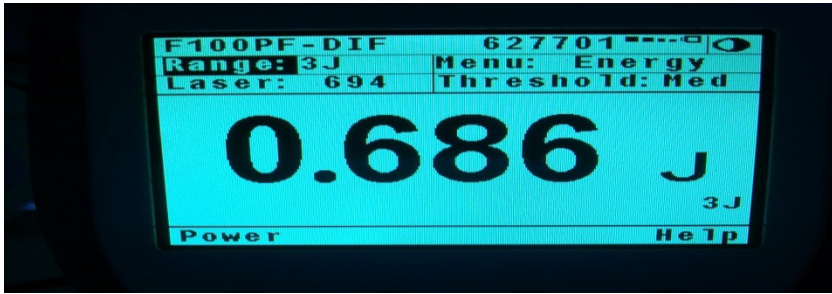


Fig. 11. Output of laser (0.7J / 1.5Hz)

When discharging current was 660A, Output of laser was 0.7J / 1.5Hz.

4 Conclusions

Experiments have presented output of laser according to discharging current. Value of discharging current was decided by charging voltage. In fact, maximum charging voltage can make maximum discharging current.

Discharging time also needed to be short, because value of discharging voltage did not affect value of discharging current. Finally, output of laser was 0.7J / 1.5Hz. To achieve output of laser as 1J / 1.5Hz, maximum charging voltage has to be increased.

Acknowledgement. This research was supported by the MKE(The Ministry of Knowledge Economy), Korea, under the Human Resources Development Program for robotics support program supervised by the NIPA(National IT Industry Promotion Agency) (H1502-13-1001).

References

1. Hecht: The Laser Guidebook, 2nd edn. McGraw-Hill (1992)
2. Koechner, W.: Solid-State Laser Engineering, 3rd edn. Springer (1992)
3. McLeod, A.D.: Design Considerations for Triggering of Flashlamps. PerkinElmer (1998)
4. Application Note 500, Calculating Capacitor Charging Time, TDK-Lambda (2009)
5. Application Note 2012-09, Resonant LLC Converter: Operation and Design, Infineon (2012)
6. UCC25600 Datasheet, Texas Instruments (2011)
7. IR2110 Datasheet, International Rectifier (2005)

Corrosion Protection Using High-Voltage and High-Frequency System

Seung-Hwa Baek¹, Hyun-Min Kim¹, and Hee-Je Kim²

¹Department of Interdisciplinary Program in Robotics,
Pusan National University,

Jangjeon-dong, Geumjung-gu, Korea
{bsh6845, ccaryboy1}@naver.com

²Department of Electrical Engineering,
Pusan National University,
Jangjeon-dong, Geumjung-gu, Korea
heeje@pusan.ac.kr

Abstract. The corrosion of ships and equipment is the issue of shipping transportation and marine pollution. The organotin compound paint such as TBT(Tributyl Tin) or sinking of the ship which has been negligent in maintenance for a long time cause massive contamination of ocean. Therefore, to proof corrosion, maintain and manage the equipment from the electrical corrosion in the seawater becomes more and more significant. The corrosion in the ocean has many causes and there are several ways to prevent the corrosion by now. The main cause of corrosion is the oxidation of metals. Regarding this point, we want to know that application of high-voltage, high-frequency pulsed power technology is how much effective to electrical corrosion in environment of electrolyte that can cause corrosion easily.

Keywords: Electrical corrosion, Marine pollution, High voltage high frequency pulsed power.

1 Introduction

Currently, the prevention of marine pollution is being issued, particularly the pollution resulting from corrosion in salt water. Electrical corrosion has many causes. The aim of this study was to identify ways of reducing corrosion by examining the shape of the output power by comparing the effects of direct current (DC) with those of high voltage pulsed power. Even with the same amount of energy, corrosion differs according to the shape of the signal or frequency. A high voltage high frequency pulse system to the output was used to determine if pulsed power is better in terms of corrosion prevention than DC, and whether a high frequency is more efficient than a low frequency. Electrical corrosion at the electrode or wire differs according to the shape of the input energy, particularly the current.

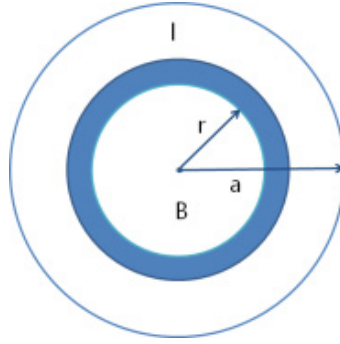


Fig. 1. Circumference

Fig 1 is section of wire that is used in this experiment.
The magnetic flux(Φ) is defined as

$$\Phi = \pi r^2 B_m \sin \omega t \quad (1)$$

When a magnetic field of $B = \sin \omega t$, i.e. the magnetic flux density, is applied in the axial direction of the circumference with a radius of a , length of l , volume of $V(= \pi a^2 l)$, and resistivity of ρ .

The equation for e , which is the induced electromotive force to the circumferential direction, is defined as follows:

$$e = \frac{d\Phi}{dt} = -\pi r^2 B_m \sin \omega t \quad (2)$$

Consider a cylinder with radius of r and thickness of dr , the resistance to a flowing current di , passing through the circumferential, can be expressed as

$$dR = \frac{2\pi\rho}{l dr} \quad (3)$$

Therefore,

$$dI = \frac{e}{dR} = \frac{\omega l B_m \cos \omega t}{2\rho} r dr \quad (4)$$

Current I can be defined from this equation.

$$I = \int_0^a dI = -\frac{\omega a^2 l B_m}{4\rho} \cos \omega t \quad (5)$$

The RMS value of the current I_e can be expressed as

$$I_e = \frac{\omega \alpha^2 l B_m}{4\sqrt{2}\rho} \quad (6)$$

The amount of corrosion will be checked from the different currents and frequencies when high voltage/frequency pulsed power is used.

Pulse power is a technology that allows a very high power output but saves energy. The characteristics are a rapid rise time, and short pulse width concentrated in a narrow space. Hence, it is being utilized in new applications and electromagnetic force energy.

2 Experimental

2.1 Comparison of Electrical Corrosion between DC and High Voltage Pulsed Power

2.1.1 Test Preparation

The degree of rust through an electrochemical reaction of electrolyte was checked to compare the effects of DC and high frequency, high voltage input energy. To maintain constant electrolytes, 5 liters of water and 6 grams of salt were mixed, and 200mL was used in every test. To match the amount of energy, both the DC RMS and high voltage pulsed power, two outputs were fixed to 20V RMS in the water. The experimental time for each test was 10 minutes. The surface of the copper wire and needle were observed by scanning electron microscopy (SEM).



Fig. 2. Test of electrolysis

In fig 2, 5 liters of water and 6 grams of salt are mixed in a test bottle and 200ml of the resulting electrolyte was used for the corrosion test on copper wire and needle.

2.1.2 Circuit and System

The high-frequency, high-voltage pulse system output circuit was made to vary the voltage and frequency. A MC34063 for buck topology, IR2153 for dimming and a 2:200 transformer with Fly-back topology were applied.

The output voltage was varied up to 4kV pk-pk and the output was adjusted to make a RMS value of 20V.



Fig. 3. Main circuit

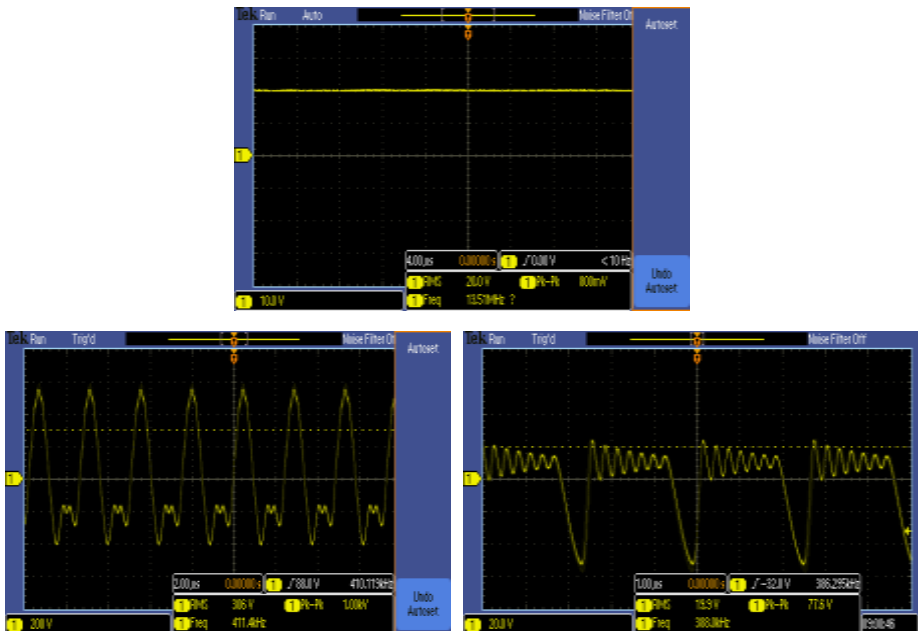


Fig. 4. DC-Pulse and Output waveforms

Fig 3 shows the main circuit for high frequency and high voltage using a 2:200 transformer and Fly-back topology.

A 1kV-400kHz voltage and frequency were used in this experiment. Both DC and pulsed power were applied to the output energy of 20V RMS in the water.

Fig 4 shows the output signals adjusted to 20V RMS for the same energy in the water.

For the same applied voltage, the RMS value was adjusted to 20V in water by applying a high frequency and high voltage pulse of 1kV. Copper wire and needle were weighed before and after the corrosion test, and the surface of the needle was observed by SEM at $\times 500$ magnification to compare the effects of DC and high voltage pulsed power.

2.1.3 Electrochemical Reaction

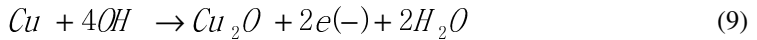
Most of the corrosion proceeds via an electrochemical reaction involving an anode and cathode. The oxidation reaction is can be expressed as



The reduction reaction can be written as follows:



In this study, salt was used as electrolyte to boost corrosion, and the electrical corrosion reaction in salt water can be expressed as



2.1.4 Experimental Results

The DC voltage-applied copper anode underwent an oxidation reaction and electrochemical corrosion, as illustrated by the large difference between before and after the test at 10minutes, which is a relatively short time. Therefore, the progress of electrochemical corrosion can be predicted. The graph of the weight change and SEM images showed that high voltage pulsed power is more efficient on electrical corrosion than DC.

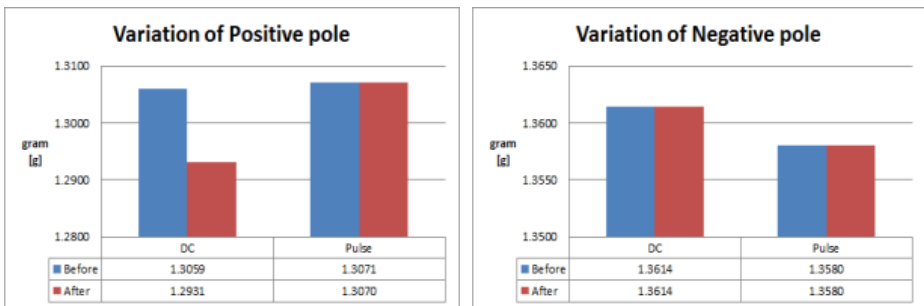


Fig. 5. Weight change in the copper positive pole

Fig 5 shows the weight of copper before and after the test by DC and the pulse voltage.

With the change of weight, as confirmed by surface scan, the needle surface of the DC anode was covered with oxide due to corrosion, forming new surface. In contrast, high frequency, high voltage pulse-applied surface showed considerably less corrosion than the DC applied surface.

Little oxidation was observed and a considerable part of the surface remained in its original state without corrosion. These results show that a high frequency / high voltage pulse is more effective on reducing corrosion than a direct current.

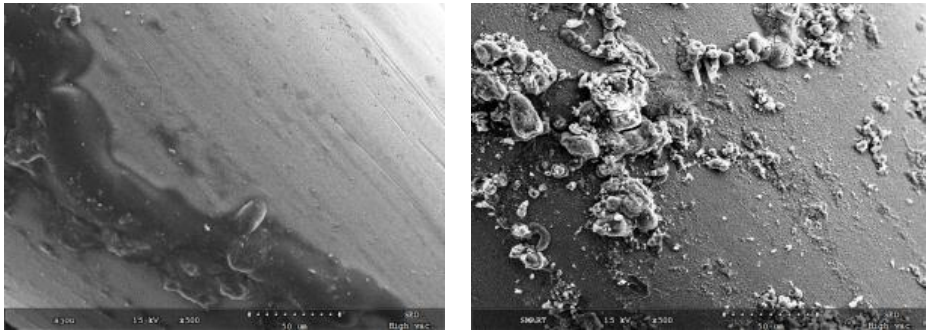


Fig. 6. SEM of DC RMS 20V after corrosion (Positive pole)

Fig 6 shows the surfaces before and after applying DC 20V.

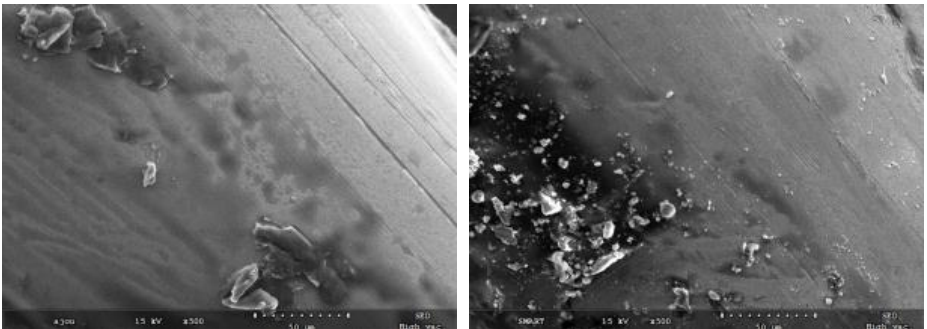


Fig. 7. SEM of the pulse RMS 20V after corrosion (Positive pole)

Fig 7 shows a SEM image of surfaces before and after applying a 20V pulse.

Negative pole showed little change, but the surface of the positive pole using DC power showed more oxidation than the high voltage pulsed power with the same amount of energy. These results suggest that the current focus on the nearest surface

and decreases exponentially toward of the center When the generated current flow in conductor by the input voltage, like a following equation.

$$I_x = I_0 e^{-\frac{x}{P}} \quad (10)$$

where I_0 is the surface current [A] of the cylindrical conductor, I_x is a current at the x [cm] point from the surface, P is the depth that the flowing current value reduces by $\frac{1}{e}$ compared to the surface current.

From the equation 10, P is a penetration depth of high frequency current, μ_r is a non-permeability, ρ [$\mu\Omega \cdot cm$] is a resistivity and f [Hz] is a frequency. The penetration depth can be expressed as

$$P = \frac{\sqrt{\rho \times 10^3}}{2\pi\sqrt{\mu_r f}} = 5.03 \sqrt{\frac{\rho}{\mu_r f}} \text{ [cm]} \quad (11)$$

where P is penetration depth [cm], ρ is the resistivity [$\mu\Omega \cdot cm$], f : frequency and μ_r is the non-permeability.

The level of corrosion is expected to increase with increasing frequency because the penetration depth is reduced and the input energy is concentrated on the surface. On the other hand, at a fixed output voltage, the current decreased with increasing frequency. In terms of energy, as the frequency increases, less power is inputted during the same time. As a result, the pulsed power was confirmed to be more efficient than the DC power, and a high frequency was more efficient than a low frequency.

2.2 Corrosion Degree Based on the Frequency

2.2.1 Frequency Setting

To know the difference in corrosion degree by frequencies, the frequency of the pulse was set by two groups in this experiment. The circuit can make a frequency up to 400kHz. Therefore, 400kHz and 100kHz are selected for the high frequency, 1Hz and 100Hz are selected for the low frequency. Of course, experiments were conducted as same conditions to compare the electrical corrosion between low and high frequency. This time, the voltage was fixed at RMS 10V to lessen the other effects from high voltage. The degree of corrosion was examined by SEM and measuring the weight change.

Fig 8 presents the output signals at approximately 100Hz and 400kHz those are adjusted to RMS 10V for the same energy in the water.

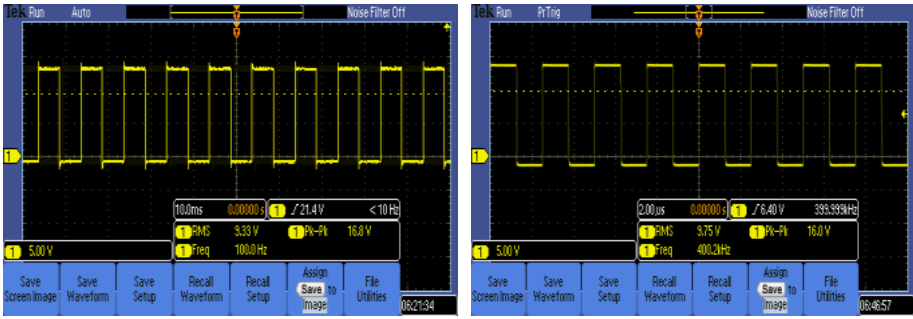


Fig. 8. Difference of input frequency

2.2.2 Experimental Results

The following graph and scan show the experimental results of the frequency change. The results are an average of 5 tests.

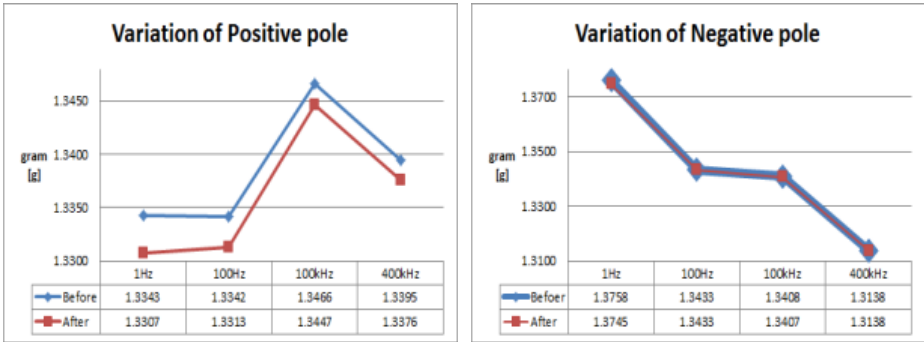


Fig. 9. Graph of weight change

Fig 9 shows weight of copper before and after the test at each frequency [Hz].

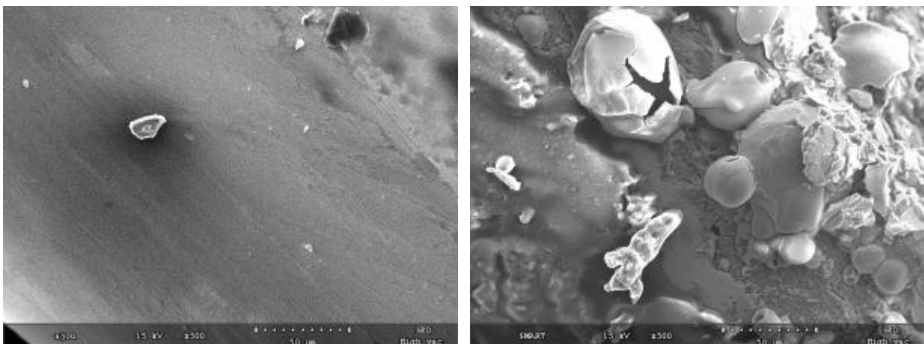


Fig. 10. SEM of 100Hz RMS 10V after corrosion (Positive pole)

Fig 10 presents an SEM image of the surfaces before and after applying 100Hz RMS 10V.

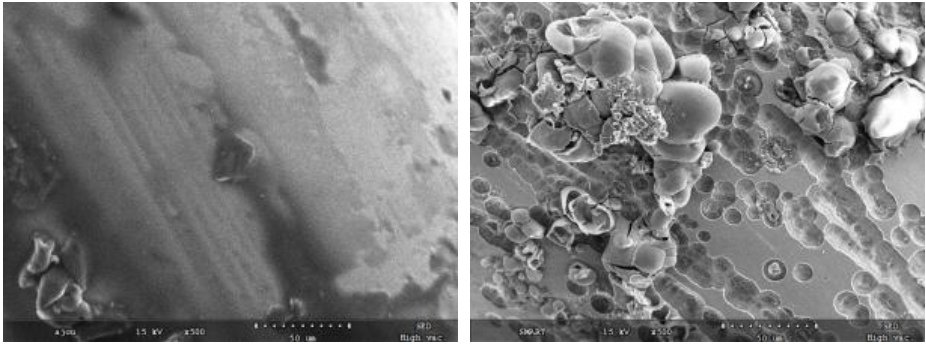


Fig. 11. SEM of 400kHz RMS 10V after corrosion (Positive pole)

Fig 11 shows a SEM image of the surfaces before and after applying 400kHz RMS 10V.

At the positive pole at 100Hz, SEM revealed a surface covered with several oxide layers after corrosion, but very little corrosion was observed at 400kHz for the same test time. Equation 11 showed that a high frequency is more efficient than a low frequency, and less power is inputted during the same time period.

3 Conclusion

The corrosion in the ocean has many causes and there are several ways to prevent the corrosion by now. The main cause of corrosion is the oxidation of metals. Regarding this point, we want to know that application of high-voltage, high-frequency pulsed power technology is how much effective to electrical corrosion in environment of electrolyte that can cause corrosion easily.

Using the results, we also tried to look at the possibilities of an alternative technique that is superior to currently using device such as marine growth prevention system (MGPS).

Once, the current flows through the electrolyte, corrosion of copper starts to occur. At that time, applying high frequency voltage was more effective than applying DC voltage that has the same RMS value with high frequency voltage. In addition, corrosion level decreased with increasing frequency. We expect that as the frequency increases, less power is inputted during the same time. As a result, the pulsed power was confirmed to be more efficient than the DC power, and a high frequency was more efficient than a low frequency.

From this basic experimental results, future studies will further examine the practical effects of high-voltage and high-frequency on electrical corrosion and determine its efficient utilization.

Acknowledgements. This research was supported by the MKE(The Ministry of Knowledge Economy), Korea, under the Human Resources Development Program for robotics support program supervised by the NIPA(National IT Industry Promotion Agency)(NIPA-2012-H1502-12-1002).

References

1. Tullmin, M., Roberge, P.R.: Tutorial Corrosion of Metallic Materials. IEEE Transaction on Reliability 44, 271–272 (1999)
2. Kim, H.-J.: High voltage pulse engineering (2011)
3. Liu, S.-X., Xin, W., Ding, K.-Q.: Simulation of Corrosion on Detection for Pulsed Eddy Current. In: FSKD 2010 (2010)
4. Lin, X.-Y.: Simulation of the corrosion caused by water soluble salt in dust
5. Sommakia, S., Rickus, J.L., Otto, K.J.: Effects of adsorbed protein, an antifouling agent and long-duration DC voltage pulses on the impedance of silicon-based neural microelectrodes
6. Thiele Jr., E.W.: Copper Alloys in the Marine Environment. Copper Development Association, Inc.
7. Kim, S.J.: Ship's marine corrosion and corrosion prevention device. JKISE 44(3), 105, 106, 111 (2011)
8. von Beackmann, W., SchWenk, W., Prinz, W.: Handbook of Cathodic Corrosion Protection, 3rd edn., p. 153. Gulf Publishing (1997)
9. Fang, J., Piao, Z., Zhang, X.: Study on High-voltage Pulsed Electric Field Sterilization Mechanism Experiment. The Journal of American Science 2 (2006)
10. Putri, R.I., Syamsiana, I.N., Hawa, L.C.: Design of High Voltage Pulse Generator for Pasteuization by Pulse Electric Field. International Journal Computer And Electrical engineering 10 (2010)
11. Lee, J.S.: Design of high frequency parallel-resonant inverter for induction heating (2005)

An Analysis on the Particular Pulse Related to the Human Bio-signal by Using Photoplethysmography(PPG)

Myong-hwan Kim and Hee-Je Kim*

Dept. of Electrical Engineering,
Busan National University,
Jangjeon-dong, Geumjung-gu, Busan, Korea
Uboyssg7@nate.com, heeje@pusan.ac.kr

Abstract. The ‘Sajin,’ four diagnostics have been used in Oriental traditional medicine to diagnose a range of diseases. One of the diagnostics, ‘Jinmeak,’ is an analysis of the cardiovascular activity and that is also used an oriental doctor to diagnoses a disease. PPG sensors, a non-invasive method, can make an easy diagnosis by measuring and analyzing the cardiovascular activity. The sensor is composed of a LED and photodiode for monitoring the waveform of pulsation. The human pulse is normally 60 to 150 beat a minute and is approximately 1 to 2.5Hz. The signals have a very low voltage (20mV) and also contain complex information about the patient. The original signals need to be changed to new signals though particle filters and amplifiers in to analyze the signals easily. After conducting an analysis of the signals, as follows, some facts are known. First, people have different voltage levels between 15mV and 20mV. In addition, a particular signal shape can be observed under human conditions. Briefly, if the data of particular signals is collected and generalized, a diagnosis instrument can be developed for making an easy diagnosis of a disease.

Keywords: PPG, Jinmeak, Non-invasive, Signal processing, Generalization about Jinmeak, diagnose a disease, diagnosis instrument.

1 Introduction

The ‘Sajin,’ four diagnostics (seeing a complexion and a tongue, asking the person about their symptoms, hearing the sound of organs, and feeling the pulse) has been used to diagnose diseases when oriental doctors diagnose a disease in the oriental traditional medical [1]. One of the diagnostics, feeling the pulse of people for diagnosis is called ‘Jinmeak’. Jinmeak is a non-invasive method that is simple and inexpensive, so it has been introduced by both oriental traditional and Western medical science. Photoplethysmography (PPG) is currently used to take only the human pulse in Western medicine. On the other hand, the PPG signal provides considerable information on the patient, so if the information is analyzed and generalized, PPG can

* Corresponding author.

be used to feel the pulse for diagnosing a disease [1, 2]. Therefore, a circuit was designed to analyze the PPG signals. The PPG sensor is normally adopted in two ways, transmissive and reflective type, depending on the position of the LED and photodiode [3]. A reflection type can operate at a low voltage (3 to 5V), so that a system size is small and the system's cost is commonly less expensive than the transmissible type. Therefore, the reflection type was selected in this instrument. The PPG system is composed of a sensor part, circuit for transferring the current to voltage, filters and amplifiers. The bio-signals are typically low voltages 20mV and 1 to 2.5 Hz. The voltages show Individual variations. This suggests that human skin and biological tissues might affect the rate of light reflection. In addition, particular waveforms were identified depending on the normal or abnormal condition of the people, and it appears that these signals related to the type of disease. On the other hand, noise artifacts can be produced easily if only little motion occurs during the measurement. Therefore, multi sensors or contact sensors are needed to solve the problem. On the experiment, a PPG system can collect data on the pulse. If more data is collected and generalized, a diagnosis instrument that is more objective and general than an existing subjective method can be developed.

2 Method

The 'Sajin' four diagnostics has been used to diagnose diseases when oriental doctors diagnosed patients in oriental traditional medicine. Briefly, Sajin involves four methods: seeing the complexion and tongue of patients, asking about symptoms, hearing particle sounds of organs and feeling the pulse. Although 'Jinmeak,' feeling the pulse, is a non-invasive and simple way of diagnosing a disease, it is sometimes subjective so doctors can diagnose a different disease when they diagnose the same patient. An objective and general diagnosis needs to be developed to progress the oriental medicine. PPG, a way of measuring the pulse, can be used to diagnose a range of disease.

2.1 Processing PPG Signals

The PPG sensor is normally composed of a LED and photodiode. The signals through the sensor have very low voltages but provide complex information on the human body. On the other hand, only special information is handled on cardiovascular activities. The human pulse is normally between approximately 60 and 150 beats a minute and 1 to 2.5Hz. Therefore, a signal process needs to select only the particular desired signals. The signal commonly has a low voltage 20mV but has different the voltage according to the personal condition. Therefore amplifiers need to identify the signals easily. Figure 1 the steps of the signal process for tiny complicated bio-signals.

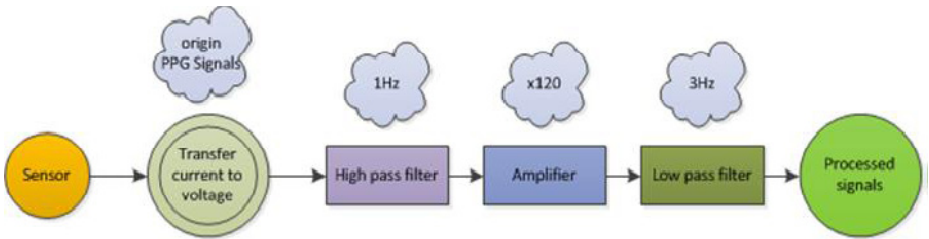


Fig. 1. Process chart of PPG signals

The flow chart contains a converting circuit, high pass filters, low pass filters, and amplifiers. The converting circuit in the system changes the currents to voltages.

Filters are used to select narrow and special frequencies. The amplifiers amplify the signal 120 times to view the signals easily.

2.2 Designed Circuits

As shown in Fig. 2, the figure is a circuit that was designed to analyze the signals, and the sensor was made from a reflective type so that it could operate at low voltages 5V. Only OP amp devices made at the 1st and 2nd order filters, and multiple amplifiers at approximately 120 times were used.

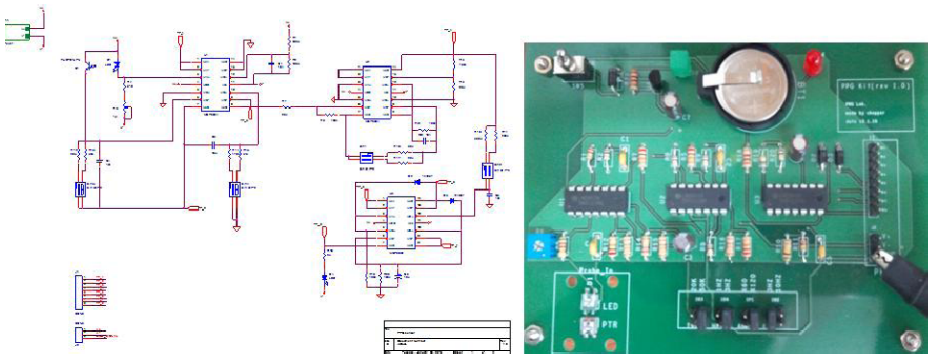


Fig. 2. Design and a circuit for analyzing bio-signals

2.3 Signal Analysis

An infrared LED (~805nm) has commonly been chosen for PPG because melanin inside the human skin absorbs most of the light from the LEDs with the exception of infrared. In addition, the Isosbestic Point, which is one of characteristics of hemoglobin (Hb) and oxidized hemoglobin (HbO₂), is observed at 805nm [4]. Therefore, the frequency of the pulses is commonly approximately 1 to 2.5Hz, and the pulse is complex signal owing to the different rate of absorption and reflection according to the tissues. The pulse of dozen persons was measured and the signals were analyzed.

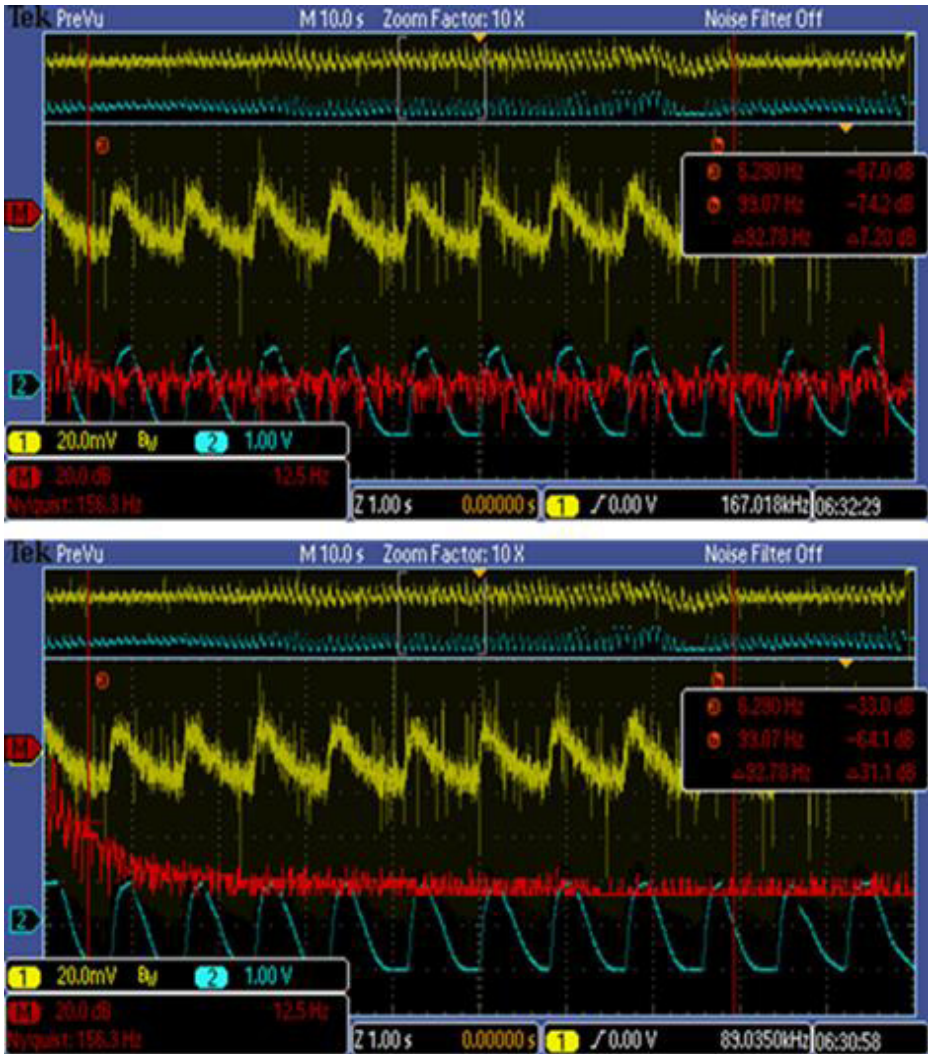


Fig. 3. Origin signals of PPG (yellow, 20mV) and signals after processing (blue, 1V)

In Fig 3 above, the signals were measured for 100 seconds. The yellow waveform is the original pulse with 20mV. After the FFT analysis tool, the most of the energy of the red wave was distributed from 1 to 3.5HZ, and the wave also had moderate energy at about 120Hz. The existed energy at 120Hz can be assumed to have been reflected from affected by tissue by a pulsational artery. In Fig 3, a lower, blue waveform was filtered using a high pass filter (cut frequency (f_c) = 1Hz) and low pass filter (f_c = 3Hz). As a result, the energy existed at less than 3Hz, and moderate energy on 120Hz was no longer in existence. After measuring the pulse, the data was examined again to verify that it had different values, 15to 25mV, according to the person and their conditions. This experiment examined a part of the wave and the repeated form of the

wave. This is why oriental doctors check the intensities and shapes of the pulse when diagnose a disease. The pulses of dozen people were measured and the signals were analyzed. The results showed that a peak shape and pattern of the wave changed according to the symptoms of people. As shown Fig 4, a normal waveform (left-upper) is a regular pulse. Therefore, it has a regular form overall. On the other hand, the waveform (right-upper) of an arthritis patient has the appearance of a gentle repeated wave pattern. This waveform is often observed in patients with inflammation. The waveform (left-mid) of patients who have a cold is normally a low voltage (15~18mV) and the wave frequently moving up and down due to irregular breathing, such as cough, a runny nose, etc., might affect the pulse. Neurogenic gastritis (right-mid) is also irregular and it tends to change its form suddenly. In addition, the wave of headache patients can have a high voltage (20~25mV), Moreover, although it appears regular overall, it suddenly becomes irregular in part, and the peaks of the wave are variable and sharp.

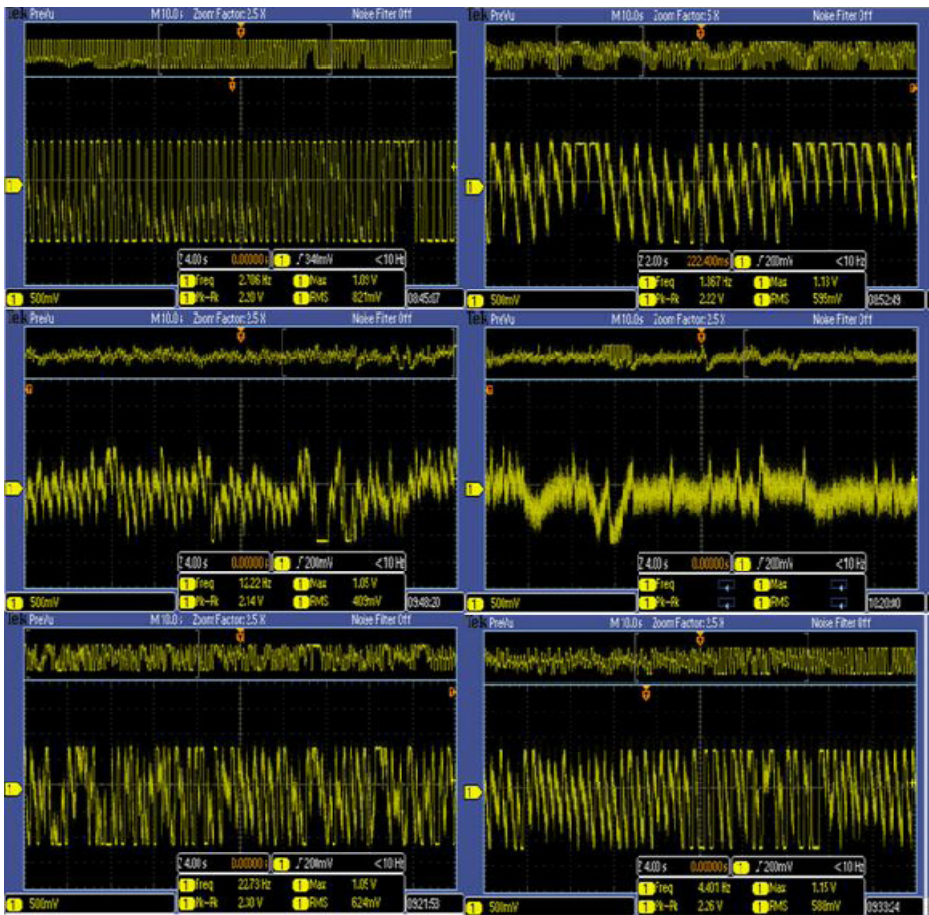


Fig. 4. Normal signal and abnormal signals (left-high: normal, right-high: symptom of joint pain, left-middle: symptom of cold, right-middle: neurogenic gastritis, left-lower and right lower: headache)

3 Result

Complex signals with approximately 20mV, which were measured by the PPG sensor, contain a great deal of information on the human body. The intensity of the pulse can be inferred from the measured voltage. The waveform of the patients with inflammation, a cold, neurogenic gastritis, and headache has specific characteristics but with variable forms. A headache case showed a similar waveform. Therefore, unusual waveforms can show the type of disease. An analysis of the waveform, such as the partial shapes, repeated patterns and whole shape, can provide important information. However, the only unusual waveforms were collected do not generalize clearly due to a lack of the data. Therefore, more data needs to be collected and generalized for a diagnosis.

4 Conclusion

The designed PPG circuit is able to detect and analyze a pulse. The pulses can be classified according to the person's waveforms, such as the form of a part, repeated pattern, entire shape, etc. The data of dozen people was analyzed, but more data should be collected and generalized to obtain general and subjective information. This study provides a technique to change the objective oriental medicine into subjective and scientific medicine. The 'Jinmeak diagnosis instrument' can be developed and commercialized using this technique. Therefore, a part of IT should correspond with oriental medicine to organize the data of the pulse in terms of the diseases of patients and develop new scientific and innovative diagnosis instruments.

References

1. Kang, D.: Oriental diagnosis, Meakjin. *Animal Clinical Medicine* 8(2) (2010)
2. Han, W.T., et al.: Development of plethysmographer & measurement of parameters. The Institute of Electronics Engineers of Korea 16(2) (November 1993)
3. Asada, H.H., et al.: Mobile monitoring with wearable photoplethysmographic biosensors. *IEEE Engineering in Medicine and Biology Magazine* 22(3), 28–40 (2003)
4. John, A.: Photoplethysmography and its application in clinical physiological measurement. *Physiological Measurement* 28(3), 1–39 (2007)
5. Wang, L., et al.: Multichannel reflective PPG earpiece sensor with passive motion cancellation. *IEEE Transaction on Biomedical Circuits and System* 1(4), 235–241 (2007)
6. Han, H., et al.: Development of a reflected Type Photoplethysmograph(PPG) sensor with motion artifacts reduction. *Journal of the Korean Society for Precision Engineering* vol 26(12), 146–153 (2009)
7. Wei, C.-C.: Developing an effective arterial stiffness monitoring system using the spring constant method and photoplethysmography. *IEEE Transaction on Biomedical Engineering* 60(1), 151–154 (2013)

8. Gil, E., et al.: PTT variability for discrimination of sleep apnea rated decrease in the amplitude fluctuations of PPG signal in children. *IEEE Transaction on Biomedical Engineering* 57(5), 1079–1088 (2010)
9. Lee, C., et al.: The optimal attachment position for a fingertip photoplethymographic sensor with low DC. *IEEE Sensor Journal* 12(5), 1253–1254 (2010)
10. Kejia, L., Warren, S., Natarajan, B.: Onboard tagging for real-time quality assessment of PPG acquired by a wireless reflection pulse oximeter. *IEEE Transactions on Biomedical Circuits and Systems* 6(1), 54–63 (2012)

Bunker Oil C Heating Using Induction Heating

Dong-Hyun Kim¹, Ki-Ryong Kim¹, and Hee-Je Kim^{2,*}

¹ Department of Interdisciplinary Program in Robotics,
Pusan National University,
Jangjeon-dong, Geumjung-gu,
Korea

kikkc@naver.com,
kiryong123@gmail.com

² Department of Electrical Engineering,
Pusan National University,
Jangjeon-dong, Geumjung-gu,
Korea

heeje@pusan.ac.kr

Abstract. The purpose of this paper is application of induction heating. Generally, Steam Heating and Resistance Heating are in use to heating Bunker Oil C. however, Heating Machine is hard to maintenance and maintenance cost is expensive, because both method are direct contact with oil.

In this paper, we research for Bunker Oil C heating using induction heating. This way we avoid direct contact with oil and use LLC Resonant Circuit to reduce switching loss.

Keywords: Bunker Oil C, Induction heating, LLC resonant.

1 Introduction

Bunker Oil C is mainly used for marine fuel and Warm up is essential for transport and use Bunker Oil C. Old ways for heating Bunker Oil C are Steam Heating and Resistance Heating. This two ways are easy to realized but maintenance cost is expensive. In this research Induction Heating apparatus place outside, thereby increase convenience and cheap maintenance cost.

2 System Configuration

Total system comprises 3parts. 3parts are Power supply part(1), Control part and electrode part. First, explain the Power supply part. Basic of Power supply part is LLC topology. Circuit design is made up flowing component. MOSFET control frequency is 82kHz and transformer turn ratio is 3:2.

* Corresponding author.

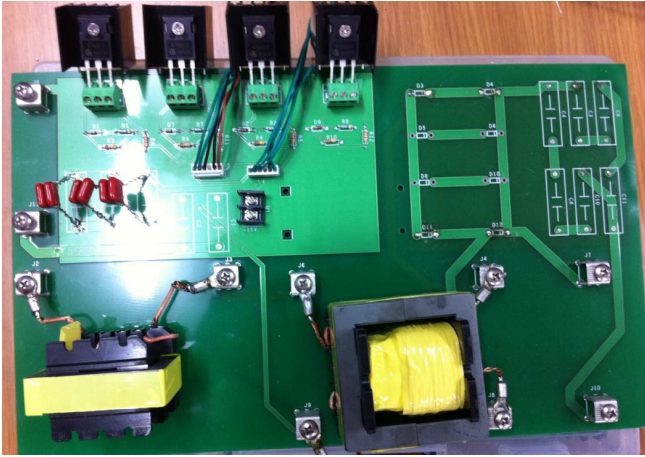


Fig. 1. Main Circuit-LLC

Control port is composed of parts. One of the Control part is MCU. In this research use atmega128. The other of Control part is digital to analog change part. In this case we use IR2110



Fig. 2. Atmega128

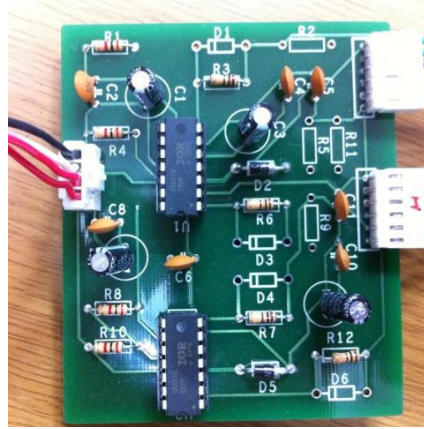


Fig. 3. IR2110

Electrode part is composed of coil form. If it is necessary, we change the Electrode part form

3 Theoretical Background

A electric conductor located current flowing through the coil occur the heat by Hysteresis loss and Eddy Current loss. Using This heat, we can heat the material. This way is called Induction heating.



Fig. 4. Electrode part

First, Hysteresis loss is calculated following formula (1)

$$P_h = nfB_m^{1.6}(\text{wb}/\text{m}^2) \quad (1)$$

Also Eddy Current is calculated following formula (2)

$$W_e = \eta e f^2 B_m^2 \quad (2)$$

Above two formula (1) and (2) we can calculate total energy after that Using psim and flowing three LLC design formulation, try to simulation

$$C_r = \frac{1}{2\pi \times Q_e \times f_0 \times R_e} \quad (3)$$

$$L_r = \frac{1}{(2\pi \times f_0)^2 C_r} \quad (4)$$

$$L_m = L_n \times L_r \quad (5)$$

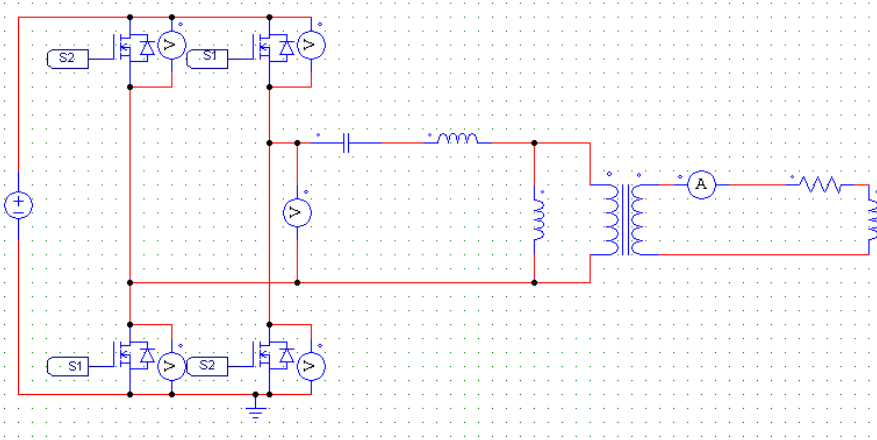


Fig. 5. LLC Resonant Converter PSIM Model

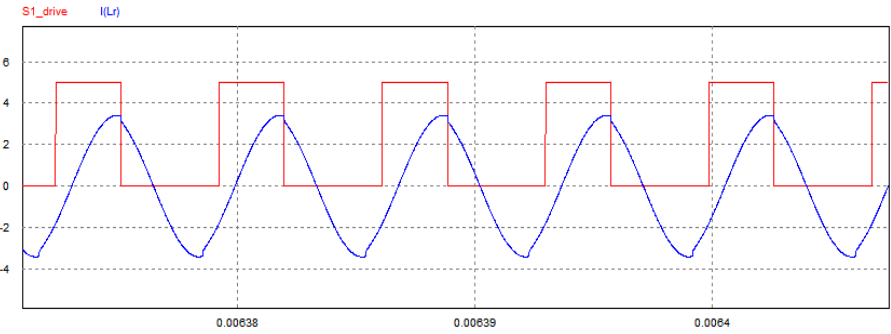


Fig. 6. Simulation Switch waveform

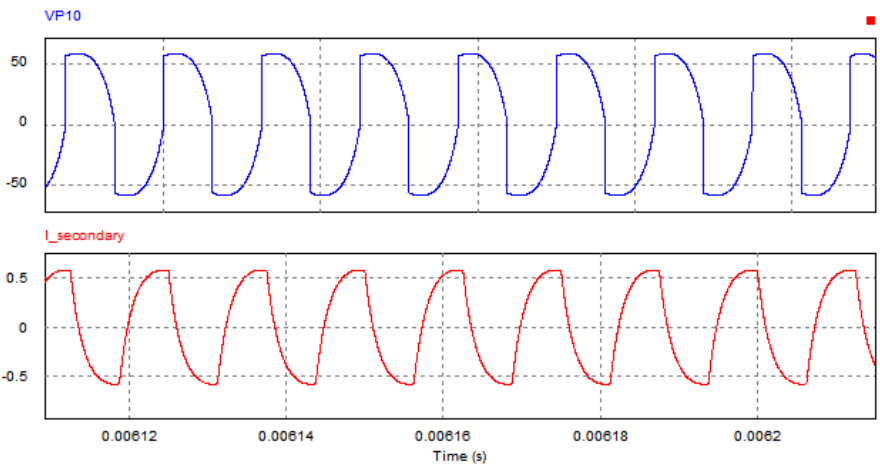


Fig. 7. Simulation Output waveform

4 Result

In this case, Experiment is not directly use system voltage(AC220). Input voltage is slowly increase using Slidacs. On a figure 8, we find that current phase is lagging then voltage phase. Through this figure, we conclude that ZVS is realized well.

When we Measure the MOSFET temperature, There are no problems in connection with heat. And we also noticed that output waveform is similar to simulation waveform on figure 9. But there are one problem. MOSFET Driver is quite hot when operate long-term. So we need additional cooler device.

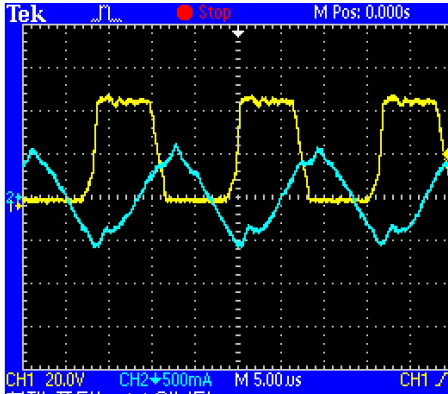


Fig. 8. Switch waveform

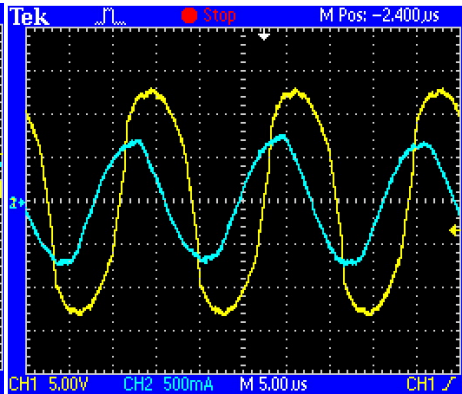


Fig. 9. Output waveform

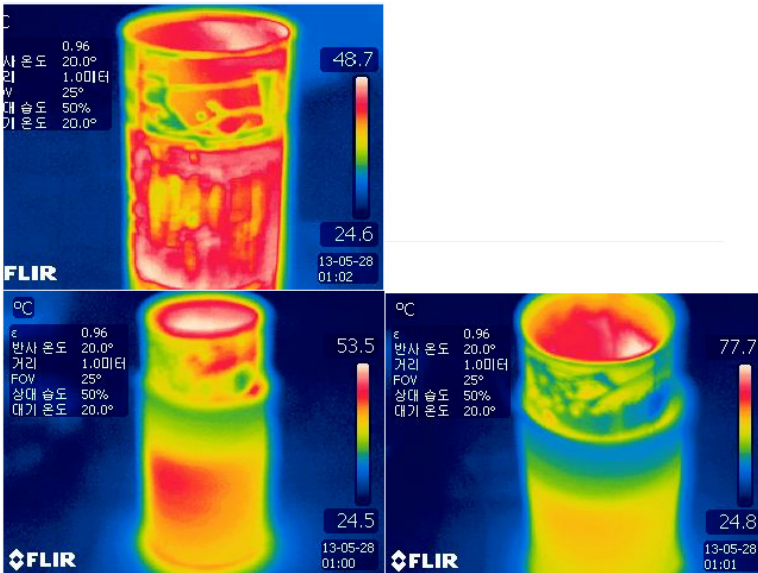


Fig. 10. Thermal Image

Figure 10 is thermal camera image. Counterclockwise, Each figure is passed by 5minutes, 10minutes and 20minutes. Especially last figure has shown us that Bunker Oil C heat was reached the goal.

5 Future Plans

First of all we focus on improving induction heating efficiency by change frequency and electrode form And then compare total circuit cost with expected reduction of maintenance cost. In this way, we examine a hypothesis. If induction heating is better than old way, we change the topology and compare PWM topology with LLC topology. After that we will find what is best way realize a induction heating

Finally we verify effectiveness by real model of storage tank.

Acknowledgement. This research was supported by the MKE (The Ministry of Knowledge Economy), Korea, under the Human Resources Development Program for robotics support program supervised by the NIPA (National IT Industry Promotion Agency) (NIPA-2012-H1502-12-1002).

References

1. Lee, H.G., Kim, E.-S., Hur, D.-Y., Lee, G.-S., Jung, B.-G., Gang, S.-G.: Operating Characteristics of LLC Series Resonant Converter Using A LLT Transformer. The Korean Institute Power Electronics (October 2006)
2. Pressman, A.I., Billings, K., Morey, T.: Switching Power Supply Design, 3rd edn. Mc Graw Hill
3. Namadmalan, A., Moghani, J.S., Milimonfared, J.: A Currend-Fed Parallel Resonant Push-Pull Inverter with a New Cascaded Coil Flux Control for Induction Heating Applications. The Korean Institute Power Electronics (September 2011)
4. Yoo, H., Shim, E., Kang, J., Choi, G., Lee, C., Bang, B.: 100kHz IGBT Inverter Use of LCL Topology for High Power Induction Heating. The Korean Institute Power Electronics (May 2011)
5. Namadmalan, A., Moghani, J.S.: Self-Oscillating Switching Technique for Current Source Parallel Resonant Induction Heating Systems. The Korean Institute Power Electronics (November 2012)

Magnetic Resonance Wireless Power Transmission Using a LLC Resonant Circuit for a Locomotion Robot's Battery Charging

Ki-Ryong Kim¹, Dong-Hyun Kim¹, and Hee-Je Kim^{2,*}

¹ Department of Interdisciplinary Program in Robotics,
Pusan National University, Jangjeon-dong, Geumjung-gu, Korea
kiryong123@gmail.com,
kikkc@naver.com

² Department of Electrical Engineering,
Pusan National University, Jangjeon-dong, Geumjung-gu, Korea
heeje@pusan.ac.kr

Abstract. The purpose of this paper is a locomotion robot's battery charging. Using a LLC resonant circuit and magnetic resonance WPT(Wireless Power Transmission). The proposed this WPT system consists of transmitter and receiver circuits. The transmitter is a LLC resonant circuit and receiver circuit is a LC resonant circuit that has a resonant coil, a capacitor, and full bridge diode rectifier.

Keywords: Magnetic Resonant Wireless Power Transmission, Battery.

1 Introduction

As early as in the late 19th century, Nicola Tesla had put forward the concept of wireless power transfer, and applied for related technology patent in 1902 [1]. After that many scientists have been investigated with respect to the wireless power transfer system. As a result, they found the three big topics on wireless power transmission. The first is an electromagnetic wave, the second is an electromagnetic induction, and the last is a magnetic resonance. However, the first of two methods couldn't get breakthrough progress in the mid-range [2]. In November 2006, Prof. Marin Soljačić and his research team in MIT shows mid-range wireless power transmission based on magnetic resonance on the AIP forum in the United States, and experimentally demonstrated a 60W bulb being lit up over 2m distance in June 2007 [3]. This had a large impact on the wireless power transfer system. However, this system has very complicated formulas and big hardware system to make.

And the frequency that MIT's team use is 13.54Mhz. This frequency is very high and also it is hard that common use electric components are cover.

Moreover, High frequency considers harmfulness to human body.

* Corresponding author.

2 Main Subject

2.1 Background

LC Resonant

The basic theory of this theme is the resonant.

Inductor passes low frequency, and Capacitor passes high frequency.

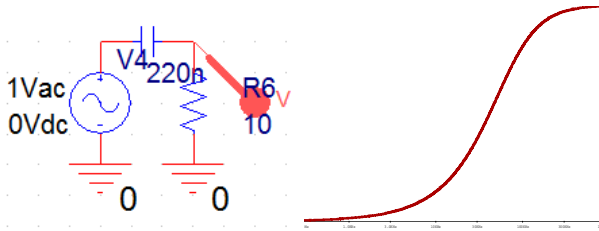


Fig. 1. Characteristic of the capacitor

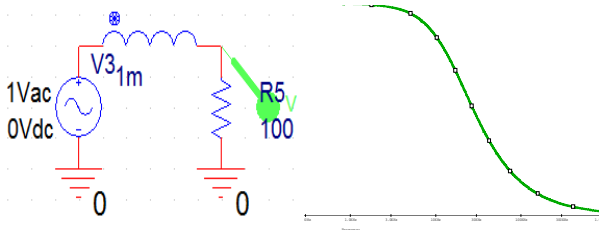


Fig. 2. Characteristic of the inductor

These two components make the resonant frequency.

At the resonant frequency, the impedance is the highest or the lowest.

LC series resonant circuit, the impedance is the lowest at the resonant frequency.

On the other hand, LC parallel resonant circuit's impedance is the highest at the resonant frequency.

So we should select well as the system's characteristic.

2.2 Transmitter

The Half Bridge LLC resonant converter has two inductors and a capacitor.

This resonant network is consist of L_r , L_m , C_r .

L_r is the series resonant inductance, L_m is the transformer's magnetizing inductance, and C_r is the series resonant capacitance.

These components make two resonant frequencies. Two resonant frequencies, f_{r1} and f_{r2} are defined as follows:

$$f_{r1} = \frac{1}{2\pi\sqrt{L_r C_r}} \quad (1)$$

$$f_{r2} = \frac{1}{2\pi\sqrt{(L_r + L_m) C_r}} \quad (2)$$

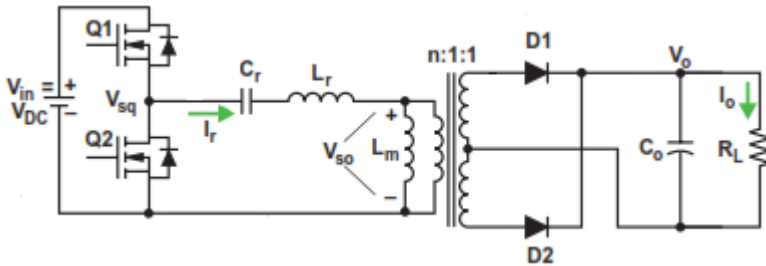


Fig. 3. Half Bridge LLC resonant converter configuration

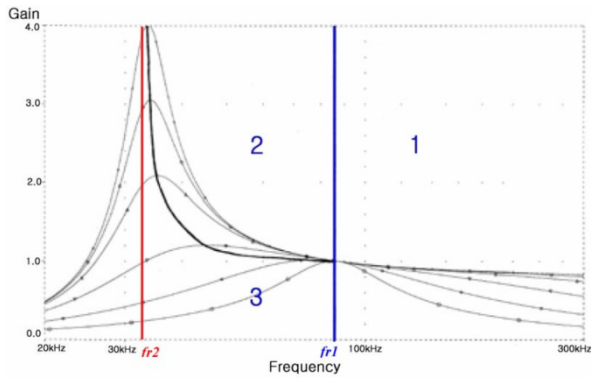


Fig. 4. DC gain characteristic under loads variations

We operate this converter in a region 2. Because the region2 is a ZVS(Zero Voltage Switching) region. In this region, we can minimize a switching loss.

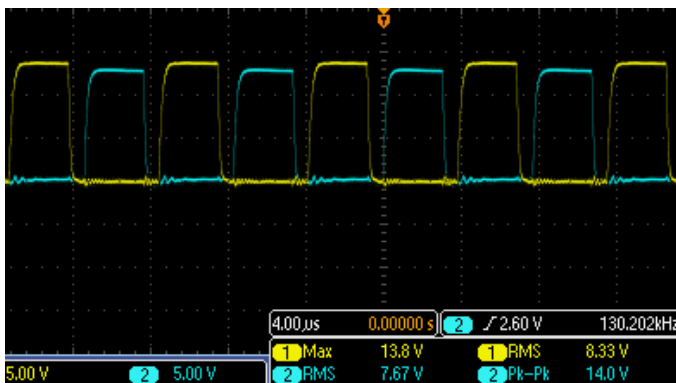


Fig. 5. Waveform of mosfet gate

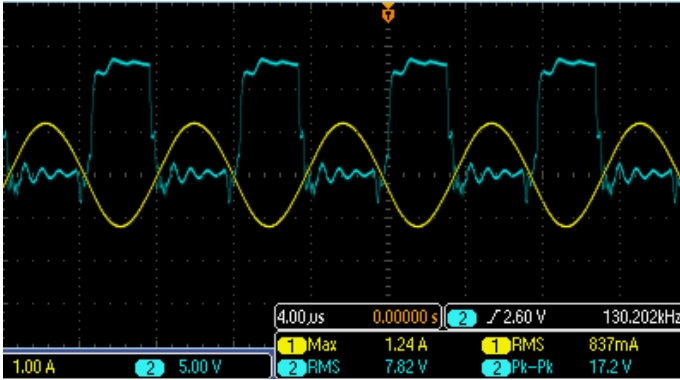


Fig. 6. ZVS wave form

We can find the ZVS is well operating. ZVS means when the gate voltage is on, the current reaches zero or less than zero. This effect prevents the loss.

To analyze frequency vs. gain this circuit, we need an equivalent model.

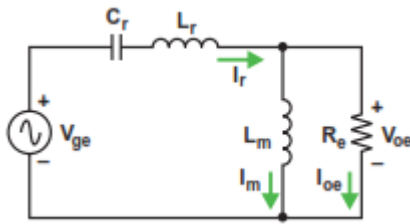


Fig. 7. Equivalent LLC resonant converter

Fig.7. is the equivalent converter model of Fig.3.

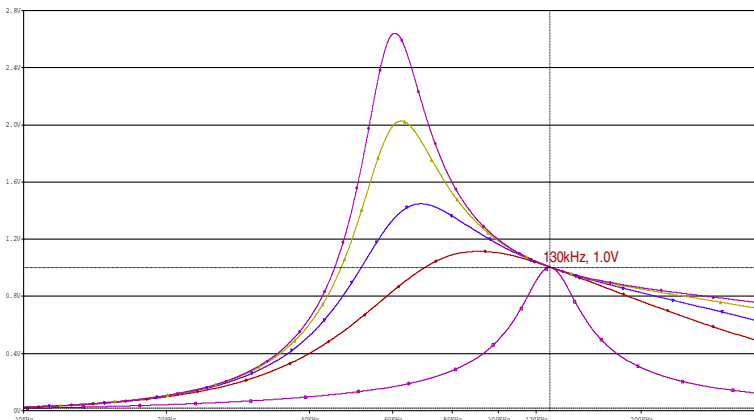


Fig. 8. Frequency vs. Gain wave form

Around the 130kHz, in Fig.8. its gain is almost 1.

The LLC resonant converter design specification is as follows

$V_{in} = 25V$ (Input voltage), $V_{out} = 12V$ (Output voltage),
 $I_{out} = 1A$ (Output current), $f_{r1} = 130kHz$ (the resonant frequency)

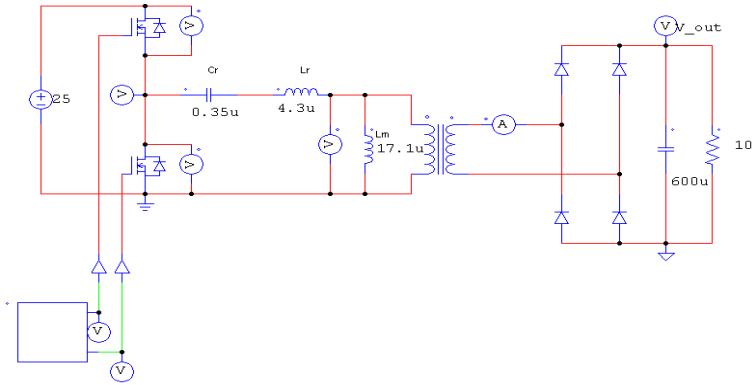


Fig. 9. LLC simulation circuit

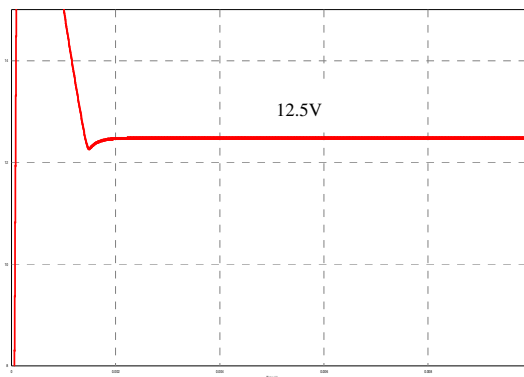


Fig. 10. Simulated voltage output result

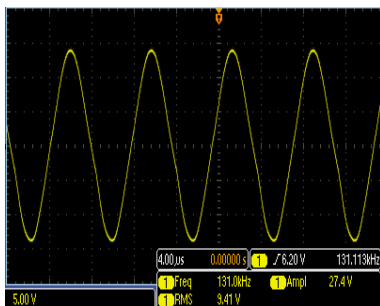


Fig. 11. The secondary output voltage

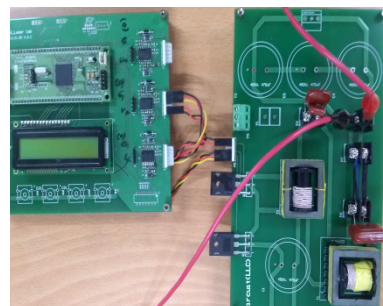


Fig. 12. Transmitter Circuit

$$v_{os} = \frac{4}{\pi} nV_o \sin (2\pi f_{sw}t) \tag{3}$$

As the formula, we can see the sinusoidal wave.

$$V_{os} = \frac{2\sqrt{2}}{\pi} nV_o \tag{4}$$

(Where V_{os} is the secondary output RMS voltage, n is turn ratio, V_o is output voltage)

Substituting in the equation, where n is 1, V_o is 12V, we can get almost the same result as you can see in Fig.11.

2.3 Receiver

The receiver circuit consists of resonant coil, capacitor, and rectifying diode bridge.

This circuit operates around 130kHz. If we use this circuits over or less than resonant frequency, it will not operate.

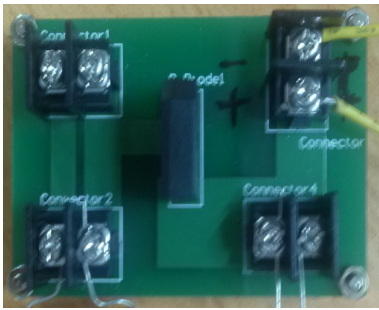


Fig. 13. Receiver Circuit



Fig. 14. Transmitter & Receiver Coils

2.4 Result

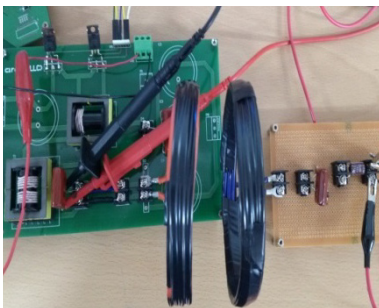


Fig. 15. Experiment



Fig. 16. Output data

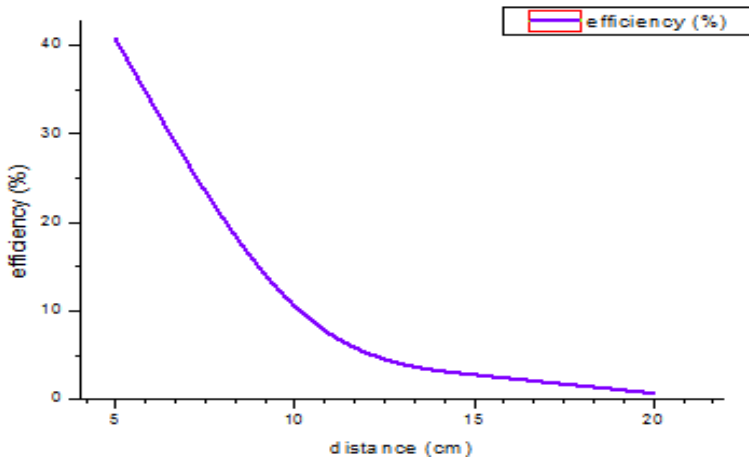


Fig. 17. Output power efficiency vs. distance

The original output specification is 12V, 1A at the load is 12ohm.

However, as an experimental result, the output voltage is about 8V, and the output current is about 0.66A at the load is 12ohm.

There are some errors between the theory and experiment.

These errors maybe occurred by the air loss and low mutual inductance.

We can reduce the air gap loss by making large diameter of coils. However, it makes the system size too big. And depending on the two coils distance, the mutual inductance is changed.

3 Conclusion

The Wireless Power Transfer system need strong coupling between two resonance coils. The main problem in this system is that feedback system doesn't exist and there are not exact data in air gap.

So output specifications are unstable and some errors.

WPT system is very useful because of the wireless. However, in this system will research on the feedback it should be in progress.

References

- [1] Tesla, N.: Apparatus for transmitting electrical energy. US patent number 1,119,732 (issued in December 1914)
- [2] Karalis, A., Joannopoulos, J.D., Soljačić, M.: Wireless non-radiative energy Transfer. The AIP Industrial Physics Forum (November 2006)
- [3] Kurs, A., Karalis, A., Moffatt, R., Joannopoulo, J.D., Fisher, P., Soljačić, M.: Wireless Power Transfer via Strongly Coupled Magnetic Resonances. Science 317, 83-86 (2007)

Research on the MPPT Simulation of Mini Photovoltaic System for the Robotic Vacuum Cleaner Battery Charging

Seong-Min Heo¹, Ki-Ryong Kim¹, and Hee-Je Kim^{2,*}

¹Department of Interdisciplinary Program in Robotics,
Pusan National University,
Jangjeon-dong, Geumjung-gu, Korea
sonyun86@naver.com
kiryong123@gmail.com

²Department of Electrical Engineering,
Pusan National University,
Jangjeon-dong, Geumjung-gu, Korea
heeje@pusan.ac.kr

Abstract. In this paper, we aim to the development of mini solar power system for robot vacuum cleaner battery charging. It has the advantage of being convenient for the robot vacuum cleaner, but at the same time it has the disadvantage like electric shock and inefficient battery charging. In order to overcome these shortcomings, we plan to apply more advanced technology in the development of this system in conjunction with the Wireless power transfer system.

This paper presents to applying to the mini solar battery charging system for the mathematical modeling of solar cells and the 50watt solar array modules MATLAB simulation results.

Keywords: MATLAB simulation, MPPT, Solar cell.

1 Introduction

The renewable energy systems and particularly the photovoltaic systems are now experienced a fast development. As a consequence, a characterization effort is required in these systems, especially concerning photovoltaic modules, generators (groups of modules) and inverters [1], [2]. However, this characterization is quite a difficult issue, due to the variable nature of the weather and operation conditions of these systems. Concerning photovoltaic modules, different types of equipment are used in the laboratories to obtain their – characteristic curves [1]–[3].

In order to improve the efficiency of power converter, we need to understand for output characteristic of the solar cell. The maximum power point control methods

* Corresponding author.

of the solar system is typically called MPPT (Maximum Power Point Tracking), many researcher have been studied about improved MPPT control algorithm.

This paper presents the simulation result of mini photovoltaic system utilized in order to determine whether or not the robotic vacuum cleaner battery charging.

2 Mathematical Modeling of Solar Cells

2.1 Equivalent Circuit of Solar Cells

We are using the single diode model equivalent circuit as shown in [figure 1], in order to understand and interpret the characteristic of solar cell. Because the single diode model equivalent circuit is useful to interpret the physical characteristic of solar cell. It is help us to understand easily and effectively. [4]

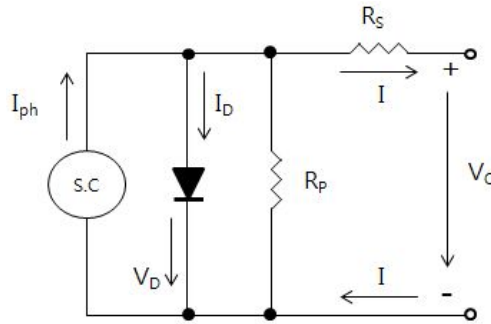


Fig. 1. Equivalent circuit of solar cells

The actual solar modules are expressed to the characteristic for I-V curve according to the equation (1).

$$I = I_{ph} - I_o \left[\exp \left(\frac{V + R_s I}{V_{th} a} \right) - 1 \right] - \frac{V + R_s I}{R_{sh}} \quad (1)$$

- I_{pv} : Photovoltaic current
- I_o : Diode saturation current
- V_{th} : Thermal voltage ($N_s kT/q$)
- q : Quantity of electric charge (1.602×10^{-19} [C])
- k : Boltzmann constant (1.38×10^{-23} [J/K])
- T : Absolute temperature
- a : Diode ideal factor
- R_s : Series resistance
- R_{sh} : Shunt resistance

Both R_s and R_{sh} is internal resistance of solar cell. For this reason, it is difficult to be measured practically. Order to obtain a simplified equation can be defined as $R_s=0$, $R_{sh}=\infty$. The photovoltaic current of a solar cell under insolation and temperature is the same as the equation (2).

$$I_{ph} = (I_{ph,n} + K_I \Delta T) \frac{G}{G_n} \quad (2)$$

- $I_{ph,n}$: Photovoltaic current at STC (25[°C], 1k[W/m²], AM1.5)
- G : Insolation of the solar surface
- G_n : Insolation at STC (25[°C], 1k[W/m²], AM1.5)
- K_I : Short circuit current/temperature coefficient
- ΔT : $T - T_n$
(T and T_n being the actual and nominal temperature [in Kelvin], respectively)

The diode saturation current can be obtained from equation (3).

$$I_o = I_{o,n} \left(\frac{T}{T_n}\right)^3 \exp\left[\frac{qE_g}{ak} \left(\frac{1}{T_n} - \frac{1}{T}\right)\right] \quad (3)$$

- $I_{o,n}$: Diode saturation current at a STC
- E_g : Semiconductor band-gap energy(1.12[eV])

2.2 Fill Factor

In this paper, the MATLAB simulation was used in order to extract the parameters of solar cells. First, in order to extract the value of this parameter should be aware of the specifications of the solar modules. [Table. 1] provide to the specification of solar module ES-50.

Table 1. Specification of the ES-50 solar modules

ES-50	Parameter	Value	Unit
Technical peak power	P_{max}	50	[W]
Open circuit voltage	V_{oc}	1.90	[V]
Short circuit voltage	I_{sc}	2.85	[A]
Voltage at max power	V_{mp}	3.80	[V]
Current at max power	I_{mp}	4.75	[A]

The fill factor is defined as the ratio of the output to the product of the open circuit voltage and shot circuit current corresponds to the area of a rectangle that can be filled up to the voltage-current curve. It is the maximum current and voltage for the short circuit voltage and open circuit voltage of the solar cell. In these conditions, however, the output of the solar cell is zero. FF (Fill Factor) is the factor that determines the maximum of the solar cell, it is a maximum proportion of the output of the solar cell about the multiplication of V_{oc} and I_{sc} .

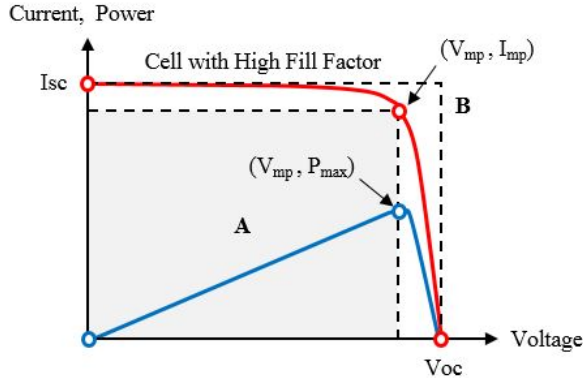


Fig. 2. Characteristic I-V curve of Fill Factor

Figure 1 shows the characteristic I-V curve of Fill Factor, it is represented to equation (4).

$$FF = \frac{I_{mp} \times V_{mp}}{I_{sc} \times V_{oc}} = \frac{\text{area A}}{\text{area B}} \tag{4}$$

Graphically, the FF is a measure of the “square” of the solar cell and is also the area of the largest rectangle which will fit in the I-V curve.

3 The Results of MATLAB Simulation

This section shows the results of MATLAB simulation for the SCM50W solar array module. And they are shown in figure 3, 4.

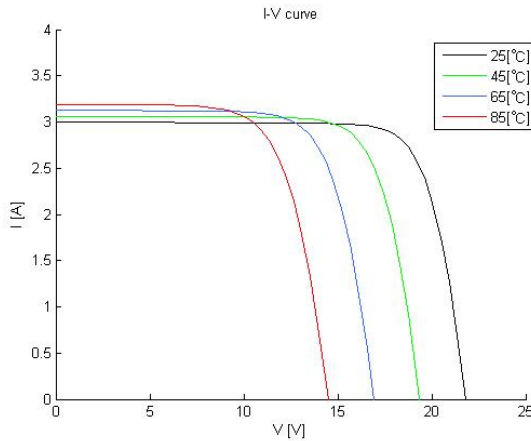


Fig. 3. I-V and P-V model curves and experimental data of the SCM50W at different temperature, 1000[W/m²]

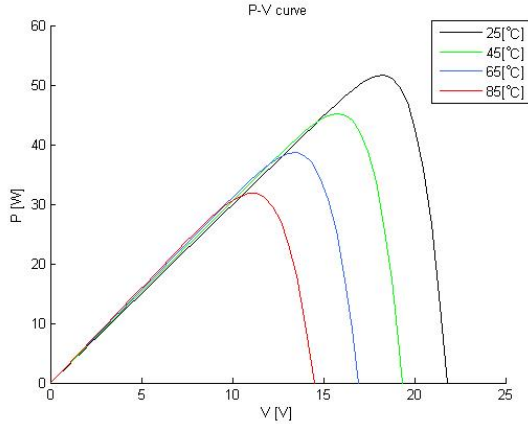


Fig. 3. (continued)

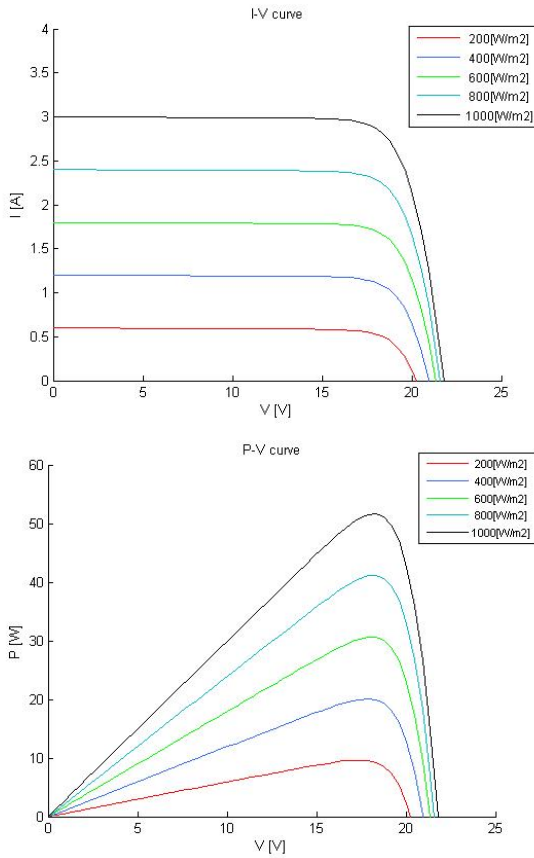


Fig. 4. I-V and P-V model curves and experimental data of the SCM50W at different insolation, 25 [°C]

Table 2 shows the results of the SCM50W PV module simulation data for different temperature and insolation conditions. This data can be extracted by MATLAB simulation.

Table 2. Data of MATLAB simulation at different insolation and temperature

Irradiation [W/m ²]	Temperature[°C]	Voltage [V]	Current [A]	Power[W]
200	25	16.0535	0.6000	9.6321
	45	13.6211	0.6127	8.3457
	65	11.1984	0.6254	7.0035
	85	8.8448	0.6381	5.6439
400	25	16.7336	1.2000	20.0804
	45	14.2614	1.2254	17.4760
	65	11.8265	1.2508	14.7927
	85	9.4547	1.2762	12.0662
600	25	16.9979	1.8000	30.5963
	45	14.5437	1.8381	26.7329
	65	12.1118	1.8763	22.7255
	85	9.7415	1.9144	18.6492
800	25	17.1490	2.4000	41.1577
	45	14.6911	2.4508	36.0050
	65	12.2528	2.5017	30.6529
	85	9.8950	2.5525	25.2570
1000	25	17.2246	3.0000	51.6738
	45	14.7599	3.0635	45.2171
	65	11.3837	3.1271	38.5980
	85	9.9698	3.1907	31.8109

4 Conclusions

PV systems due to the constantly changing temperature, humidity, air quality and is very difficult to compare its performance. Because it is rare operating under the STC (Standard Test Condition) conditions. I-V characteristic curve of PV modules and electrical power will vary depending on temperature and insolation, the load modules is usually only working partially. That power is reduced by half, which caused the decrease of the insolation intensity can be seen through the simulation results. When the temperature increases, the amount of current will rise marginally. However, the width of the voltage variation is very large.

References

1. King, D.L.: Photovoltaic module and array performance characterization methods for all system operating conditions. In: AIP Conf. Proc., pp. 347–368 (1997)
2. Carr, A.J., Pryor, T.L.: A comparison of the performance of different PV module types in temperate climates. *Solar Energy* 76(1), 285–294 (2004)
3. Eikelboom, J.A., Jansen, M.J.: Characterization of PV Modules of New Generations, Results of Tests and Simulations. Netherlands Energy Research Foundation ECN, Report code: ECN-C-00-067 (June 2000)
4. Villalva, M.G., et al.: Comprehensive Approach to Modeling and Simulation of Photovoltaic Arrays. *IEEE Trans. on Power Electronics* 24(5), 1198–1208 (2009)
5. Tai, L., Wang, J., Su, T.: Simulation Research on Photovoltaic Array Output Characteristics and Improved MPPT Control. In: 2012 Fifth International Conference on Intelligent Computation Technology and Qutomation (2012)

VDC of In-Wheel EV Simulation Based on Precise Wheel Torque Control

Hyunuk Ha¹, Jongmoo Kim¹, and Jangmyung Lee²

¹Electric Motor Research Center,
KERI (Korea Electrotechnology Research Institute),
Sungjudong, Sungsan-gu, Changwon-si,
Gyeongsangnam-do, Korea, Republic of
{hyunuk, kimjm}@keri.re.kr

²Dept. of Electronic Engineering,
Pusan National University, Jangjeon-dong, Geumjung-gu,
Pusan, Korea, Republic of
jmlee@pusan.ac.kr

Abstract. Conventional engine based vehicles inevitably have complicated structures due to lots of elements. Because of this characteristic, research, development, and also marketing are mainly conducted by the conglomerate, like GM, BMW, Honda, and Hyundai motors, *etc.* But environmental pollution and fuel exhaustion by the stated vehicle increase the necessity of EV(Electric Vehicle) as a representative of green car. First of all, the structure of EV is relatively simple, and energy transmission ratio of electric motor is more efficient than the engine based power train system. In addition to these, inwheel EV can estimate exact wheel torque, which is the most fundamental information for slip control, such as VDC(Vehicle dynamics control)/TCS(Traction control system)/ABS(Anti-lock brake system). Various kinds of expectable situations during EV's navigation have been simulated through the coordination between 'Carsim' and 'Simulink'.

Keywords: In-wheel EV, Direct torque control, VDC(Vehicle dynamics control), slip control.

1 Introduction

Recently, most of car-manufacturers have concentrated on EV by the social needs to the green vehicles. First of all, EV can significantly decrease fuel consumption which causes serious environmental problems. In addition to this, EV is expected to realize demand oriented production system because of its relatively simple structure. Direct torque transmission structured EVs consist of in-wheel type and in-axis type. Both kinds of structures have their own pros and cons, such as in-wheel EV could be controlled wheel by wheel, so this structure guarantees high stability, smooth cornering and ABS-like system through optimal torque distribution to each wheel.

But it's vulnerable for external disturbances and impulsive shock which contains high frequency, and it requires precise speed control for straight driving. In this paper, various kinds of expectable situations during the EV's navigation have been simulated through the collaboration between 'Carsim' and 'Simulink'. Carsim's fundamental features are highly focused at conventional power-train system, engine torque converter-transmission-differential gear-wheel. In order to simulate in-wheel EV, make practical motor modeling in Simulink, and insert it into the in-wheel EV's power train instead of engine in the conventional power train system. Detailed simulation environment is shown at figure 2 in section 2. This paper consists of four sections, including introduction. Section 2 describe proposed VDC algorithm of in-wheel EV and important simulation environments, section 3 illustrates simulation results for most representative four cases, section 4 finally concludes and presents some future works.

2 VDC Algorithm of In-Wheel EV

2.1 Conventional In-Wheel EV Researches

In-wheel EV is mainly researched by the traditional motor manufacturer, especially Protean[1], Michelin[2], AISIN[3], NTN[4], etc.



Fig. 1. Conventional in-wheel motor of Protean

The most significant technologies for the in-wheel EV is high torque density and robustness against external disturbances, and precise speed/torque control ability. Traditionally, the ratio between sprung mass and un-sprung mass affects vehicle's stability and driving comfort, so heavy weighted wheels diminish these two important vehicle characteristics. Robustness against external disturbances is directly related to maintenance problems and the life cycle of vehicle. Slip control of in-wheel EV is mainly conducted by Hori lab, the university of Tokyo[5]. Hori lab realized TCS by applying MFC(Model Following Control) in 2001[6], and recently proposed MTTE(Maximum transmissible torque estimation)[7] to enhance robustness as well as reliability.

2.2 Proposed VDC Algorithm for In-Wheel EV

Figure 2. illustrates overall block diagram of proposed VDC algorithm.

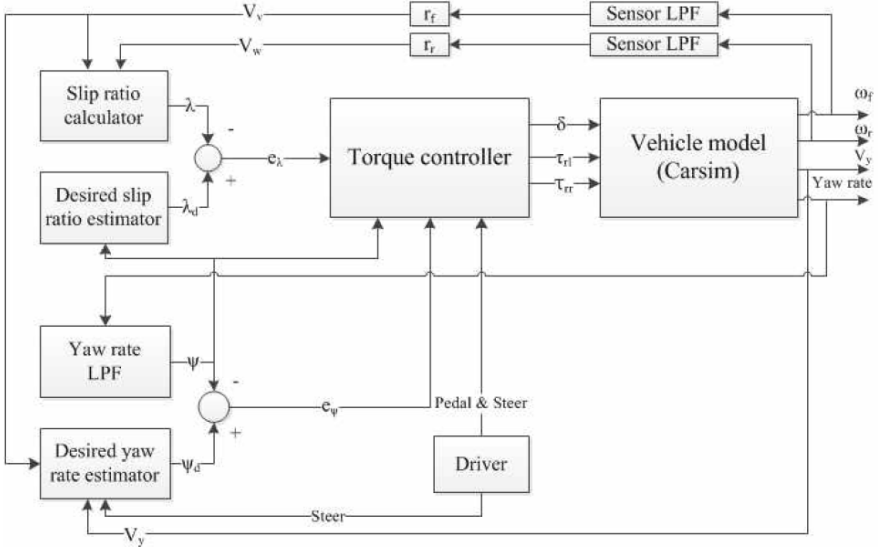


Fig. 2. Proposed VDC algorithm for in-wheel EV

Torque controller calculates wheel torque based on error of slip ratio, yaw rate, and driver's accelerator pedal information. Vehicle model is replaced by Carsim block, slip ratio calculator attains forward wheel speed as estimator for vehicle speed, and rear wheel speed. The ratio between vehicle speed and wheel speed is defined as vehicle's slip ratio, and difference between desired slip ratio and estimated vehicle's slip ratio is controller input along vehicle's longitudinal axis. On the other hand, the between desired yaw rate and vehicle's yaw rate is another controller input along lateral axis. Detailed derivation of desired slip ratio and yaw rate is described in section 2.2.1 and 2.2.2, respectively.

2.2.1 Desired Slip Ratio

Fixed value, generally between 0.15~0.2, is widely utilized in the former researches[8]. Figure 3. illustrates relationship between friction coefficient, mu, and vehicle's slip ratio, lambda by Pacejka's magic formula[9]. Most of the cases, except for cobblestone environment, road's adhesion coefficient is maximized when vehicle's slip ratio is around 0.15. So, conventional researches set desired slip ratio as fixed value, 0.15. But vehicle's adhesion coefficient is varying by the vehicle's rotation elements. In this paper, desired varying slip ratio is determined as,

$$\lambda_d = \lambda_{default} - 0.05 \left| \frac{\dot{\psi}}{\dot{\psi}_{max}} \right| = 0.15 - 0.05 \cdot \left| \frac{\dot{\psi}}{\dot{\psi}_{max}} \right| \quad (1)$$

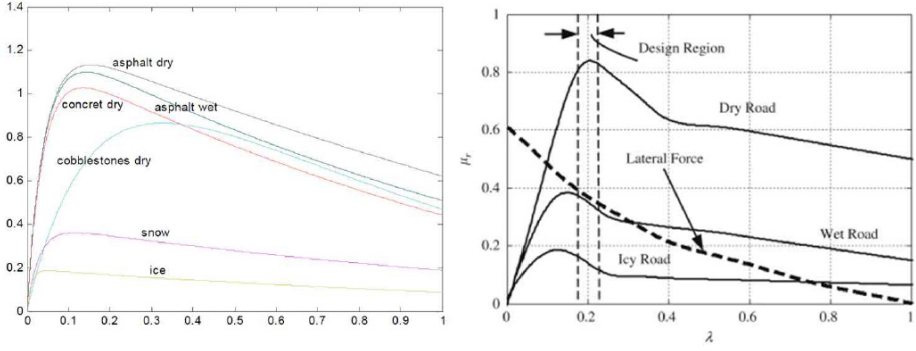


Fig. 3. mu-lambda curve(relationship between friction coefficient and slip ratio)

In default slip ratio is set as 0.15 as usual, and proposed desired slip ratio is varying according to the vehicle’s normalized yaw rate as rotational information. Maximum yaw rate is tentatively selected as 100 rad/s by heuristic method, which is maximum yaw rate during slalom driving.

2.2.2 Desired Yaw Rate

By the vehicle’s lateral dynamics in [10], yaw rate is stated as,

$$\dot{\psi} = \frac{V_x \{ \tan(\delta_f) - \tan(\delta_r) \} \cos(\beta)}{l_f + l_r} \tag{2}$$

Where is V_x is vehicle speed, δ_f and δ_r are front and rear wheel’s steering angle, β is vehicle slip, and finally l_f and l_r are distance between front wheel to COM and rear wheel to COM, respectively. Also from [10], vehicle’s slip angle is derived as,

$$\beta = \tan^{-1} \left[\frac{l_r \tan(\delta_f)}{l_r + l_f} \right] \tag{3}$$

In order to derive vehicle’s desired yaw rate, (3) is substituted into (2). So we can attain vehicle desired yaw rate as in (4), which is a function of steering angle, vehicle’s longitudinal and lateral speed when vehicle’s COM is fixed.

$$\dot{\psi}_d = \frac{V_x \tan(\delta_f) \cos(\tan^{-1}(\frac{V_y}{V_x}))}{l_f + l_r} \tag{4}$$

2.2.3 Wheel Torque Calculation Algorithm

In this paper, proposed wheel torque is calculated with the driver’s accelerator pedal information, slip ratio error, and yaw rate error. Its detailed numerical formula is defined as,

$$\tau_{rl} = T(P) \cdot \left\{1 - (1 - k) \frac{e_{\lambda}}{e_{\lambda \max}}}\right\} \left\{1 - k \frac{e_{\dot{\psi}}}{e_{\dot{\psi} \max}}}\right\} \quad (5)$$

$$\tau_{rr} = T(P) \cdot \left\{1 - (1 - k) \frac{e_{\lambda}}{e_{\lambda \max}}}\right\} \left\{1 + k \frac{e_{\dot{\psi}}}{e_{\dot{\psi} \max}}}\right\} \quad (6)$$

Where T(P) is driver’s accelerator pedal, e_{λ} is slip ratio error, $e_{\dot{\psi}}$ is yaw rate error, k is vehicle’s rotational factor defined as,

$$k = \left| \frac{\dot{\psi}}{\dot{\psi}_{\max}} \right| \quad (7)$$

3 Simulation

3.1 Simulation Environment

As mentioned in introduction, carsim’s default interface is established on engine based powertrain system. So we have to make a suitable motor model to simulate inwheel EV as fig. 4. shows carsim’s internal setting so as tso in-wheel EV simulation and its fundamental simulation scheme. T-N curve(Rpm-torque curve) is designed using user defined function, which is torque command input of motor to Carsim. Other parameters, like tire radius/friction constant/overall length/weight/slanted angle of road is set in the Carsim as shown in table 1.

Table 1. Some important internal Carsim parameters

Category	Value	Unit
Front wheel-COM	1103	mm
Front wheel-Rear wheel	2347	mm
Vehicle mass	747	kg
Slanted angle	0	deg
Tire radius	292	mm
Road friction coefficient	0.85	-

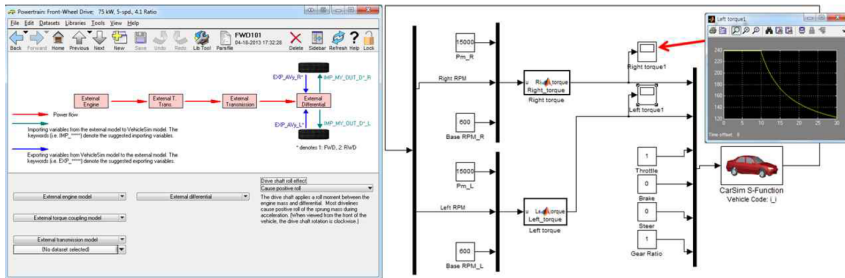


Fig. 4. Internal setting of Carsim for in-wheel EV and fundamental simulation scheme

We propose five most representative environments to simulate in-wheel EV, which is split mu braking test(ISO14512), double lane change(ISO3888), slalom(S-turn), Circle, and J-turn. Our proposed VDC algorithm has been demonstrated under stated five environments by comparing slip ratio, lambda, slip angle, beta, tire’s longitudinal and lateral force, and yaw rate, *etc.*

3.2 Simulation Result

This section describes simulation results for stated environment. Each figure has its own short caption for most distinctive features.

3.2.1 Double Lane Change(ISO3888)

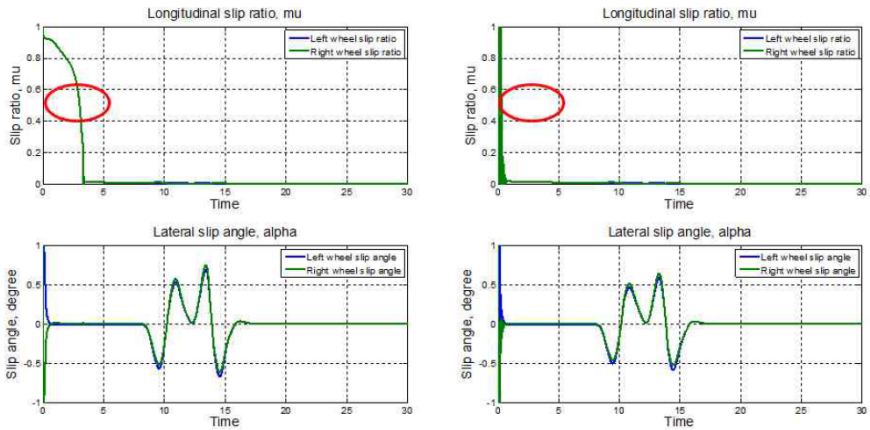


Fig. 5. Slip ratio and slip angle of without VDC/with VDC for double lane change

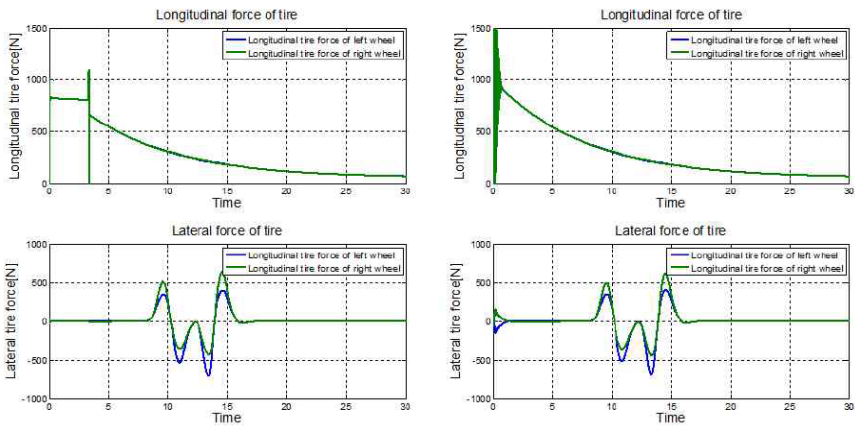


Fig. 6. Tire’s longitudinal/lateral force of without VDC/with VDC

3.2.2 Slalom(S-Turn)

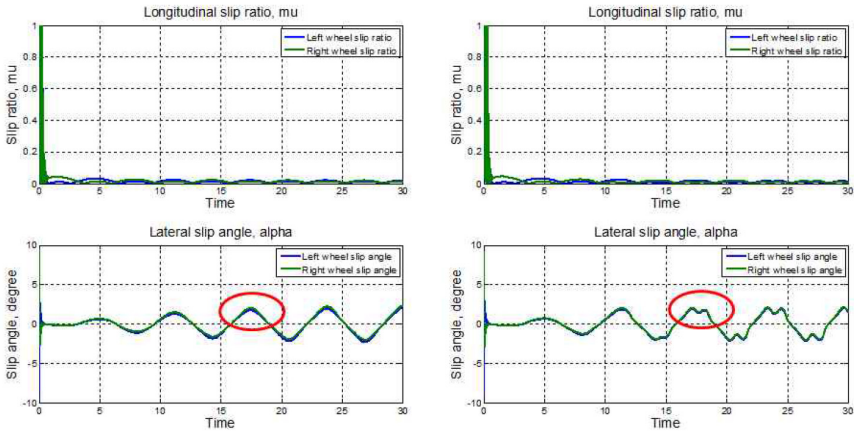


Fig. 7. Slip ratio and slip angle of without VDC/with VDC

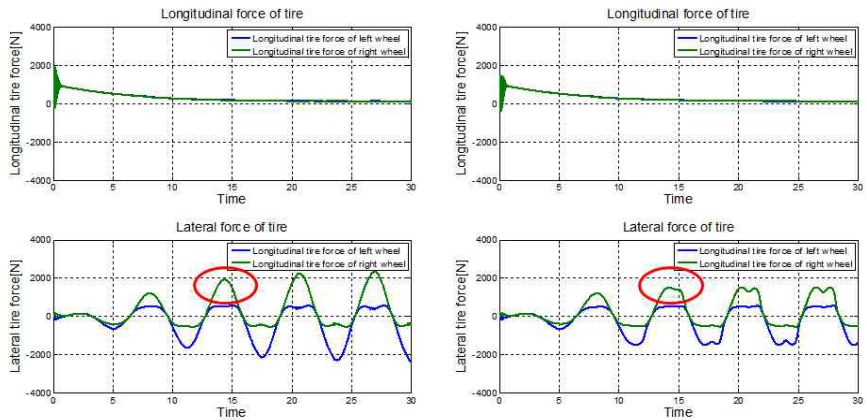


Fig. 8. Tire's longitudinal/lateral force of without VDC/with VDC

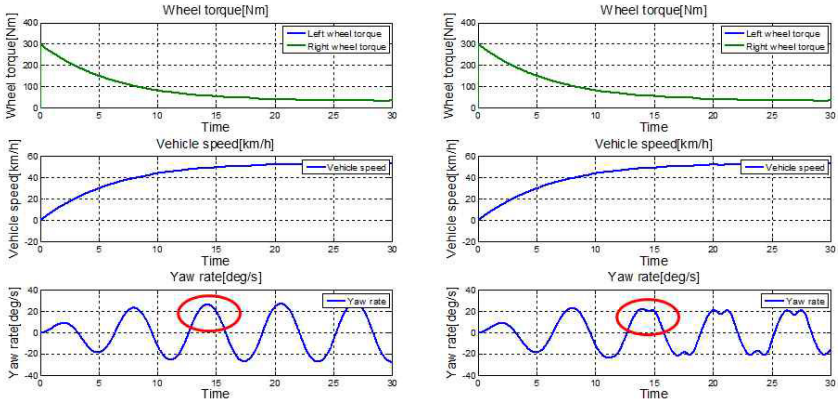


Fig. 9. Wheel torque, vehicle speed, and yaw rate for slalom simulation

3.2.3 Circle

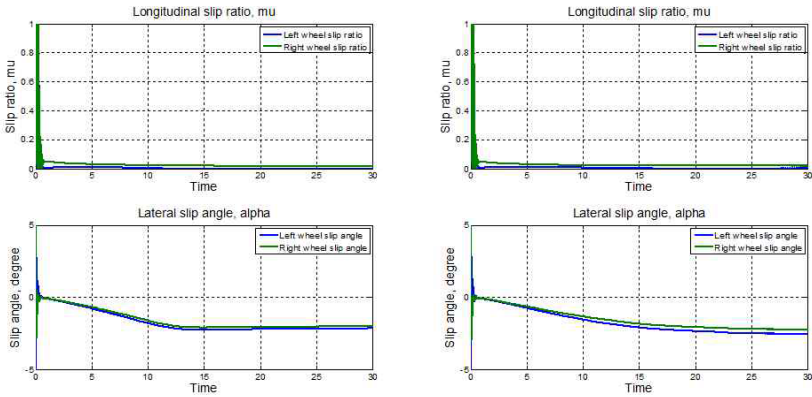


Fig. 10. Slip ratio and slip angle of without VDC/with VDC

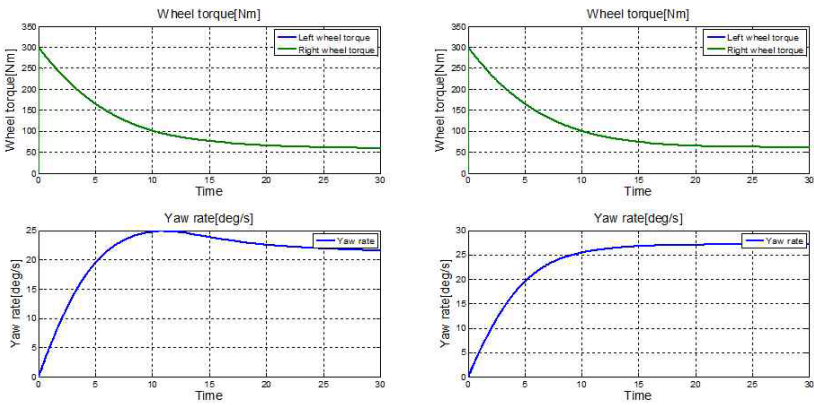


Fig. 11. Wheel torque and yaw rate of circle simulation

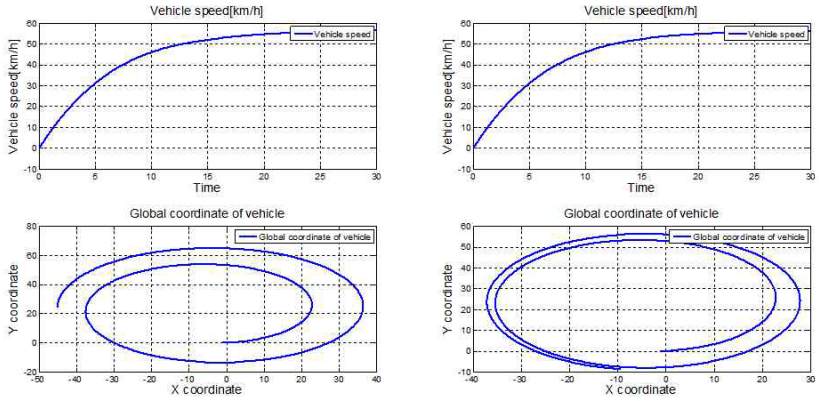


Fig. 12. Vehicle speed and trajectory of circle simulation

3.2.4 J-Turn

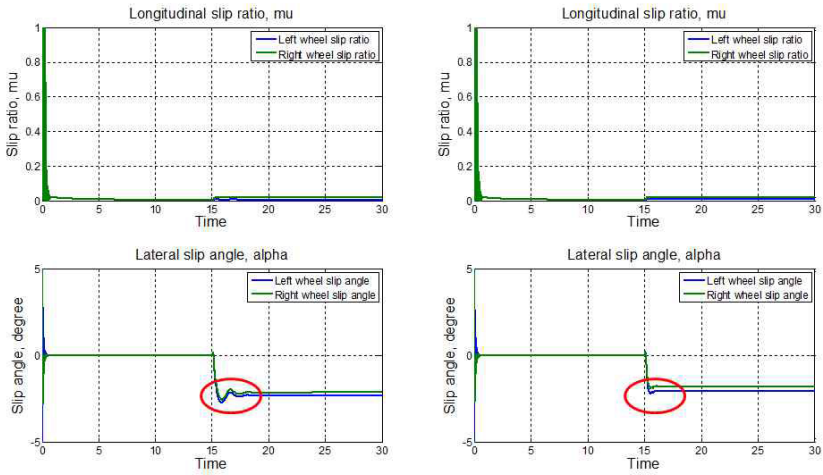


Fig. 13. Slip ratio and slip angle of without VDC/with VDC for J-turn simulation

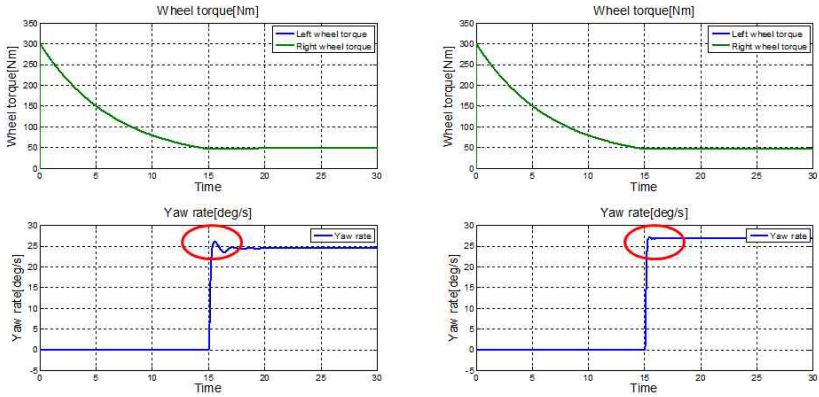


Fig. 14. Wheel torque and yaw rate for J-turn simulation

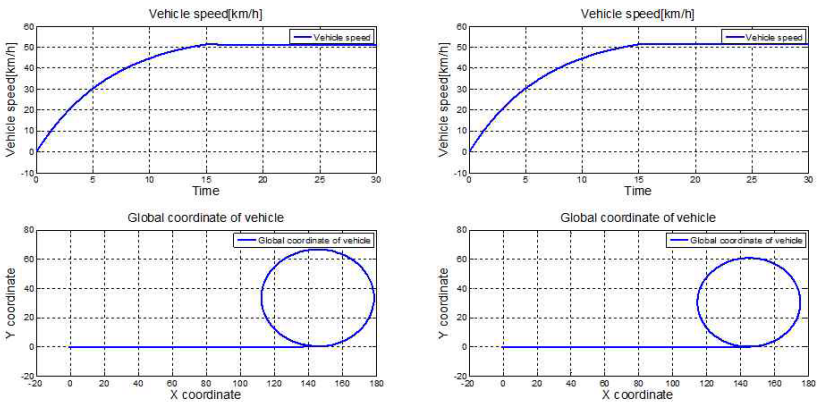


Fig. 15. Vehicle speed and trajectory of J-turn simulation

4 Conclusions

Most EV experts have consentaneously announced that the most significant bottleneck of EV is battery problem. Its low energy density, short driving distance per full charging state, insufficient life cycle, and heavy weight are slowing EV down not to be next generation’s transportation. But EV is an inevitable and huge wave heads for our future. As emphasize on transportation’s conveniences, the reliability and stability issues should be considered concurrently. Moreover, in-wheel EV might be a good and the only solution for specialized EV fields, such as personal mobility system with distinctive chassis. This paper suggests in-wheel EV’s prospective forecasts, and stability problems. As a solution for the suggested issues, efficient VDC algorithm based on precise wheel torque/speed estimation has been proposed. Proposed algorithm has been demonstrated through some practical simulations with Carsim and

Simulink. As some expected future works, 1. Optimal torque distribution to minimize side-slip angle, 2. Substitute motor modeling to real motor to realize HILS(Hardware In the Loop Simulation) system.

Acknowledgement. This research was supported by the MOTIE(The Ministry of Trade, Industry and Energy), Korea, under the Human Resources Development Program for Special Environment Navigation/Localization National Robotics Research Center support program supervised by the NIPA(National IT Industry Promotion Agency)." (H1502-13-1001).

References

1. <http://www.proteanelectric.com/>
2. Espanet, C., Tekin, M., Bernard, R., Miraoui, A., Kauffmann, J.-M.: A new structure of an high torque in-wheel motor. In: Sixth International Conference on Electrical Machines and Systems, ICEMS 2003, vol. 1, pp. 158–162 (2003)
3. Mizutani, R., Nishikamo-gun, Torii, A., Isogai, S.: In-wheel motor capable of efficiently cooling electric motor and reduction gear. United states patents (April 1, 2008)
4. Suzuki, M., Okada, K., Sakai, K., Makino, Y.: Development of an In-Wheel Motor Axle Unit. NTN Technical Review (75) (2007)
5. <http://hflab.k.u-tokyo.ac.jp/>
6. Yin, D., Hori, Y.: A Novel Traction Control for Electric Vehicle without Chassis Velocity
7. Sheng, J., Yin, D., Hori, Y., Hu, F.R.: Electric vehicle traction control. IEEE Trans. on Industry Applications 18(2), 23–31 (2012)
8. Wang, R., Wang, J.: Tire–road friction coefficient and tire cornering stiffness estimation based on longitudinal tire force difference generation. Control Engineering Practice 21(1), 65–75 (2013)
9. Burhaumudin, M.S., Samin, P.M., Jamaluddin, H., Rahman, R.A., Sulaiman, S.: Modeling and Validation of Magic Formula Tire Model. In: International Conference on Automotive, Mechanical and Materials Engineering, ICAMME 2012, Penang (Malaysia), May 19-20 (2012)
10. Rajamani, R.: Vehicle Dynamics and Control, 3rd edn. Mechanical Engineering Series (2011) ISSN 0941-5122

Vibration Pattern for the Implementation of Haptic Joystick

Kyung-Wook Noh¹, Sun-Kyun Kang², Dong-Hyuk Lee², and Jangmyung Lee^{2,*}

¹ Department of Interdisciplinary Program in Robotics, Pusan National University, Korea

² Department of Electrical Engineering, Pusan National University, Korea
{kyungwook7379, sunkyun7379, ldh0917, jmllee}@pusan.ac.kr

Abstract. In this paper, the obstacle recognition research is conducted by using vibration pattern. Remotely, the user can perceive the surroundings sensed by the obstacle recognition unit. The vibration motor was installed at the bottom of the joystick in order to let the user perceive the distance value of the obstacle which can be recognized by ultrasonic sensors. And in the various situations, the operation can be precisely implemented by using the Fuzzy controller.

Keywords: Haptic joystick, Ultrasonic sensor, Vibration pattern, Fuzzy controller.

1 Introduction

Recently, by the development of the robot industry, the Robot is being utilized in a variety of fields. Especially, the necessary in the difficult and dangerous environment that human is difficult to directly access like as the space exploration or the scene of the accident is magnified largely. But, there are limitations of control of the robot using simply the controller. In order to compensate that, requires urgently the introduction of haptic like as the system for Interaction of the between human and robot [1].

The etymology of haptic is originated from, Greek, ‘haptesthai’ that means touching. At 2006, international economic journal FOBES includes one of the method that 10 kinds of way to change we live in the future. The haptic is the technique that feels the tactile, force, sense of movement, and so through input devices that the user used usually. In summary, it is enabled to interact on between the user and the robot without the users do not proceed directly. Through this haptic, it helps to feel and manipulated effectively the objects in the real-environment by increasing the user’s Immersion [2], [3], [4], [5].

Recently, the haptic is taken center stage the education and health care as well as every field that required to remote-control that the users control directly. For example, the practice need to most of the learning has the financial burden because of the consuming materials. In case of the needing practice of the Special environment like as

* Corresponding author.

the driving education and Pilot training, there is a risk of money and physical damage caused by the mistakes[6], [7].

It is the studies of the haptic device are being actively investigated. Typically, PHANTOM Omni, PHANTOM Desktop, PHANTOM Premium, Omega, Falcon etc are developed. However, these kinds of devices aren't for commercialization, so that is very expensive. Because there are difficult problems, it is still in the research. To implement a haptic joystick, the haptic device should be replaced.

In this paper, aiming to implement the haptic vibration motor cost was to complement these issues [8], [9], [10]. Implementation of haptic vibration motor vibration by being equipped with a vibration motor is on joystick. Control method is using fuzzy controller and cycle caused by the vibration of the motor speed is made for detect the haptic vibration through haptic joystick.

First, section 2 describes configuration of overall system for the implementation of haptic, section 3 presents study applying haptic controller briefly, in section 4 presents result of applied controller, and finish with conclusions in section 5.

2 Configuration of Overall System

2.1 Overall System Configuration

Figure 1 is a block diagram of the overall system. Two hall sensors are equipped on joystick express each data of x-axis and y-axis, After A / D conversion at haptic joystick using Bluetooth, send to device, MCU of obstacles. Currently, previous researching is conducted and sends data of hall sensor.

Later, mobile robot will be controlled by the hall sensor data. Obstacles using ultrasonic sensor Ultrasonic sensor to measure the distance information of the obstacles and the measuring device and the measured data is sent to the MCU joystick haptic distance information to control the vibration of the vibration motor is implemented. Measurement device of obstacles is using Ultrasonic sensor to take distance information, measured data can be transferred to joystick MCU to control vibration and implement the haptic [11], [12].

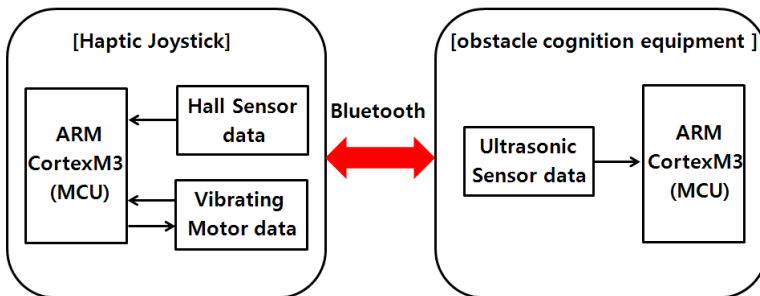


Fig. 1. Block diagram of the overall system

2.2 Haptic Device

Figure 2 shows the configuration of haptic device. Haptic is implemented using vibration motor mounted on the bottom portion of joystick. If the vibration motor rotates, the period of the oscillation occurs. So, Haptic was implemented by controlling the frequency of vibration through the velocity control of vibration motor. The haptic is changed depending on the joystick data and the value of distance between obstacle and obstacle measurement device. When the data value of the joystick is large and the distance of obstacle is near from obstacle measurement to real obstacle, the frequency of the vibration of motor function haptic is higher [13].

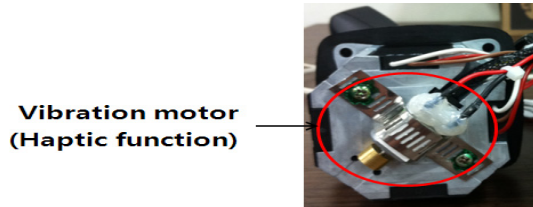


Fig. 2. The haptic device

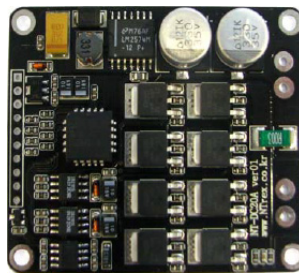


Fig. 3. Motordriver(NT-DC20A)

Figure 3 shows the motor drive is used to drive a vibration motor in this experiment.

Table 1. Specification of Motordriver(NT-DC20A)

Electrical data	
Supply voltage	12V – 36V
Maximum peak current	40A
Maximum continuous current	7A
Temperature range	0°C - 80°C
Logic Level	3.3V – 5V
PWM switching range	8KHz – 24KHz
Current sensing range	0V – 4.5V

Table 1 shows the performance of motor drive.

2.3 Obstacles Measurement Devices

Figure 4 can be represented the distance measurement principle of ultrasonic sensor. By measuring the return time of the reflective ultrasonic signal from the obstacle, obtain the information of obstacle. When the ultrasound is coming back, it compensated errors and figured out the distance. In general, the ultrasonic velocity v in air is represented as equation (1) [14], [15].

$$v = 331.5 + 0.6 \times T \quad (1)$$

$$d = \frac{vt}{2} \quad (2)$$

T : The celsius temperature of air

d : The distance to obstacle

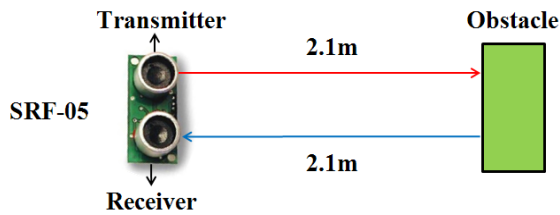


Fig. 4. The distance measurement principle of ultrasonic sensor(SRF-05)

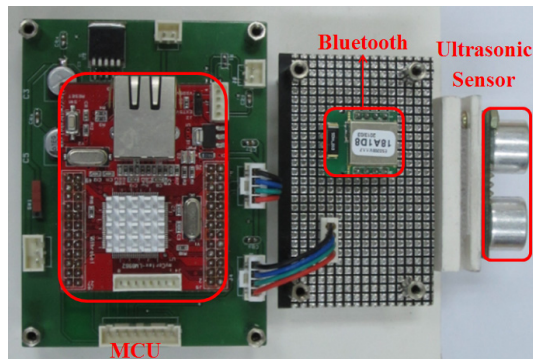


Fig. 5. The obstacle cognition equipment

Figure 5 shows the specification of obstacles measurement devices. The main MCU based on ARM CORTEX-M3-LM8962 controlled overall system. The communication between obstacles measurement devices and haptic joystick is used the BLUETOOTH(ESD200). The ultrasonic sensor(SRF-05) was used to measure the distance between obstacles. This obstacles measurement devices is the prerequisite test devices. later, by replacing the mobile robot, we are going to study the cognition and avoidance of obstacle using the Haptic joystick [16], [17].

3 Haptic System Design

In this study, the haptic vibration motor using Fuzzy control was implemented. For that reason, in order to implement the haptic vibration that occurs will consider two situations. For example, the current speed of the mobile robot during the approach to the obstacle and the distance between mobile robot and obstacle are considered for implementing haptic. The distance between the obstacles and mobile robot is short and the velocity of mobile robot is slow, haptic's reaction does not need to react relatively strong. So, in this study, the consideration of these issues, Fuzzy controllers were used. The fuzzy controller receives as input e and ec . The e is the distance between the obstacles measurement devices and obstacle, ec represents the data of the joystick. The ec represents a variation on the e . However, in this study, e used the data of the joystick because of the influence of haptic implementation depend on the data of joystick. The output set the velocity of vibration motor. Based on the designed rule considering the various action situation of system, the behavior according to the recently inputted e and ec is determined by applying to the IF-Then laws. Finally, Fuzzy output is determined according to the actions defuzzification process. Figure 6 shows used Fuzzy membership function in this study [18], [19], [20].

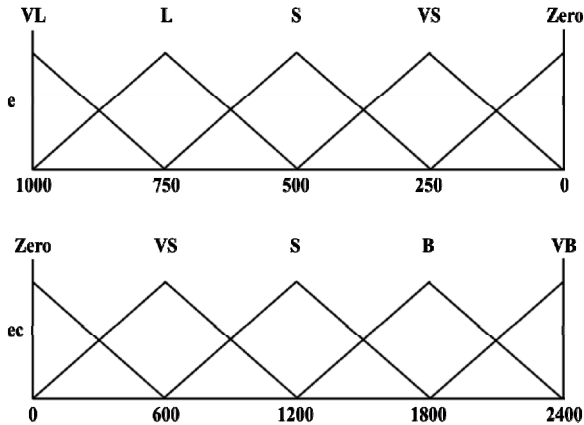


Fig. 6. Fuzzy membership function

Table 2. The Fuzzy rule in order to implement haptic

Motor-input		ec				
		Z	VS	S	B	VB
e	VL	Z	Z	Z	Z	VS
	L	Z	Z	VS	VS	S
	S	Z	S	S	F	F
	VS	Z	F	F	F	VF
	Z	Z	VF	VF	VF	VF

In table 2 , Z, VS, S, B, VB in *ec* mean sequentially Zero, Very Small, Small, Big, Very Big, VL, L, S, VS, Z in *e* mean sequentially Very Long, Long, Short, Very Short, Zero. And VF, F, S, VS, Z in output mean sequentially Very Fast, Fast, Slow, Very Slow, Zero.

4 Experimental Environment and Experimental Results

In this research, we research and experiment in both cases, the vibration pattern changes according to the joystick data is measured and the distance to obstacle from obstacle measurement device. Firstly, changes in the vibration pattern that induced by changes in the joystick data is measured at the same time to maintain the distance to obstacle from obstacle measurement device. Secondly, changes in the vibration pattern that induced by changes in the distance to obstacle from obstacle measurement device at the same time to maintain constant joystick data is measured.

Experiments are performed in two cases that the distance of obstacle is constantly 600mm and 200mm.

Figure 7 shows changes in haptic when the joystick data changes from 0V to 2.5V and constant distance to obstacle is 600mm. 'Haptic' means RPM of vibration motor mounted on the joystick. Haptic occurs according to changes of the joystick data by applying Fuzzy Rule.

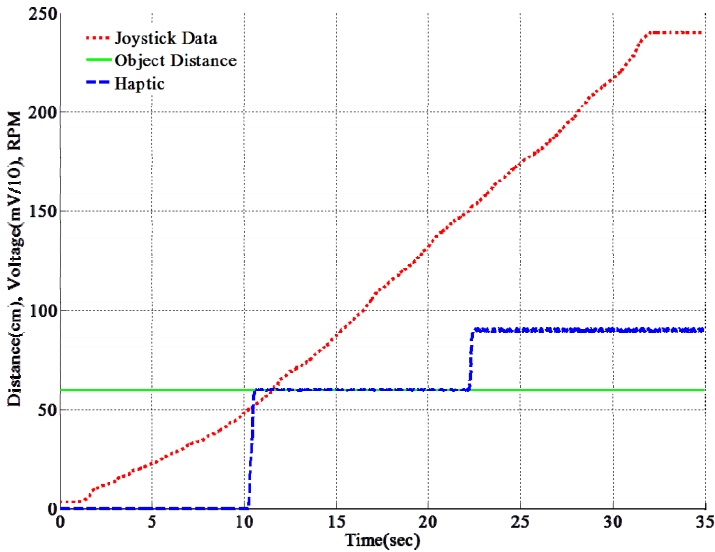


Fig. 7. Haptic response according to joystick data when distance to obstacle is 600mm

Figure 8 shows changes in haptic when the joystick data changes from 0V to 2.5V and constant distance to obstacle is 200mm. In a similar way used in Figure 7, the joystick data has only changed.

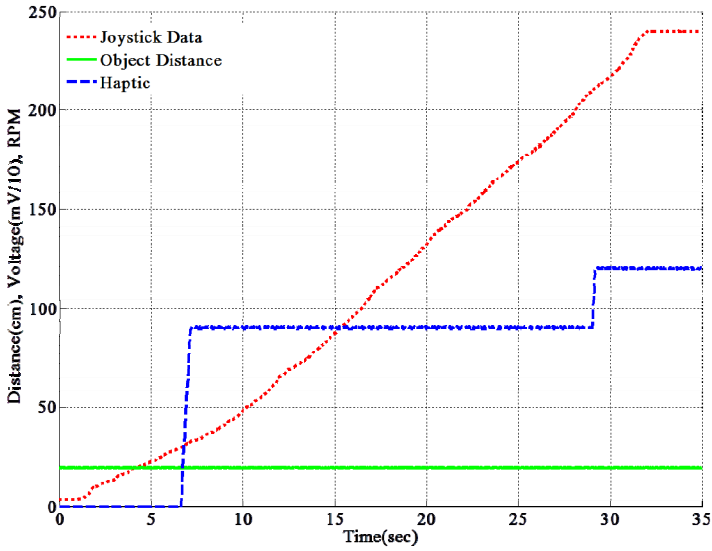


Fig. 8. Haptic response according to the joystick data when distance to obstacle is 200mm

Experiments are performed in two cases that the joystick data is constantly 2.4V and 1.2V.

Figure 9 shows changes in haptic when the distance to the obstacle changes from 1500mm to 100mm and constant joystick data is 2.4V. Haptic occurs according to changes of the distance to obstacle by applying Fuzzy Rule.

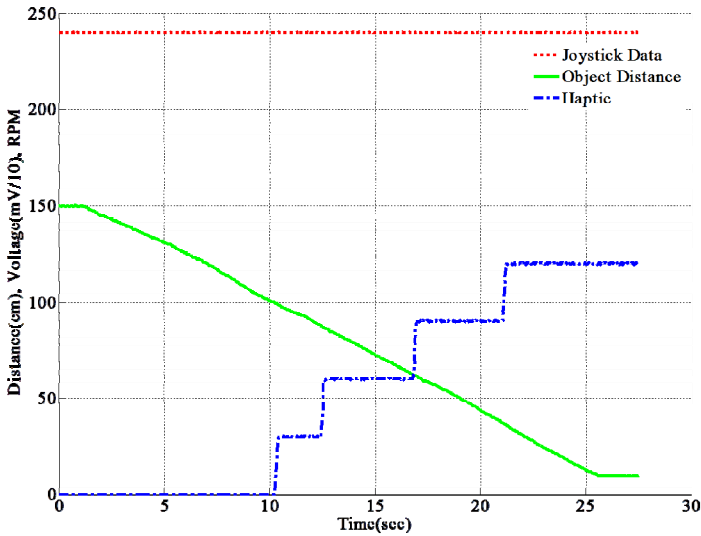


Fig. 9. Haptic response according the distance to obstacle in joystick data to 2.4V

Figure 10 shows changes in haptic when the distance to obstacle changes from 1500mm to 100mm and constant joystick data is 1.2V. In a similar way used in Figure 9, the distance to obstacle has only changed.

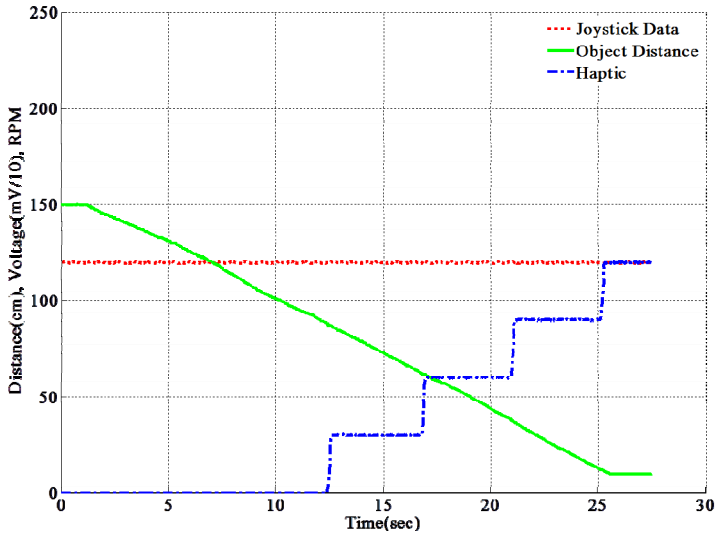


Fig. 10. Haptic response according the distance to obstacle in joystick data to 1.2V

5 Conclusion

In this research, haptic joystick is implemented using vibration pattern. The user perceived the vibration what is caused by motor mounted on the bottom of joystick. The actual strength of the vibration has been represented in Figure 7-10. And it has been analyzed whether the vibration pattern is applied correctly by considering two cases. The results based on the analysis of the experimental indicate that various vibration patterns are applied depending on the situation. Through the experiment, a variety of factors should be supplemented. The first is the response speed of vibration pattern. To apply to a real robot, the faster speed of response than now is need. The second is the position estimation of obstacle using the vibration pattern. The user should perceive the concrete position of the obstacle by the vibration pattern. Finally, the vibration pattern must be accurately implemented so that all users can be aware of the vibration pattern. In this time, only one user participated in this experiment, but the research in near future will be carried out in order to many people can participate in experiment and perceive the vibration pattern. In the future, the vibration pattern is complementary to the above-mentioned problems, and then the vibration pattern will be applied to various robots.

Acknowledgement. "This research was supported by the MOTIE(The Ministry of Trade, Industry and Energy), Korea, under the Human Resources Development Program for Special Environment Navigation/Localization National Robotics Research Center support program supervised by the NIPA(National IT Industry Promotion Agency)." (H1502-13-1001)

"This research was supported by the MSIP(Ministry of Science, ICT & Future Planning), Korea, under the ITRC(Information Technology Research Center) support program (NIPA-2013-H0301-13-2006) supervised by the NIPA(National IT Industry Promotion Agency)"

References

1. Kim, H.-S., Kang, H.-J.: Design of Remote Manipulator Control System using PHANToM Device. In: Power Electronics Conference 2005, pp. 595–597 (July 2005)
2. Kyung, K.U., Park, J.S.: The State of the Art and R&D Perceptives on Haptics. *Electronics and Telecommunications Trends* 21(5), 93–108 (2006)
3. Kim, H., Kyung, K.-U., Park, J., Han, D.: The state-of-the-art on Haptic Interface. *Journal of Information Technology* 8(1), 7–15 (2010)
4. Ryu, J., Kim, J., Seo, C., Lim, Y.-A., Kim, J.-P.: A Survey of Haptic Control Technology. *Journal of the Korean Society of Mechanical Engineers A* 33(4), 283–295 (2009)
5. Kim, M.C.: The present and the future of haptic interfaces. *Weekly Technology Trends* 1204, 28–364 (2005)
6. Rhiu, I., Jin, B., Lee, J., Park, N.-H., Gohng, J., Yun, M.H.: Effect of Haptic Feedback Type on Control Feel of a Thumbwheel Device. In: HCI 2011, pp. 809–812 (January 2011)
7. Jung, H., Kim, D.H.: Control of a mobile Robot Based on a Tangible Interface using iPhone. *Korean Institute of Intelligent Systems* 21(3), 335–340 (2011)
8. Hwang, Y.-S., Lee, J.-M.: Development of Haptic Glove for Remote Control. *The Transactions of the Korean Institute of Electrical Engineers* 60(5), 1030–1035 (2011)
9. Kawasaki, H., Mouri, T., Ikenohata, S., Ohtsuka, Y., Endo, T.: Multi-Fingered Haptic Interface Robot Handling Plural Tool Devices. In: *World Haptics 2007*, pp. 397–402 (March 2007)
10. Lee, K., Lee, D.Y.: Real-Time Haptic Rendering for Multi-contact Interaction with Virtual Environment. *Journal of Institute of Control, Robotics and Systems* 14(7), 663–671 (2008)
11. Ko, A.-K., Choi, J.-Y., Kim, H.-C., Lee, J.-M.: A Haptic Interface Using a Force-Feedback Joystick. *Journal of Institute of Control, Robotics and Systems* 13(12), 1207–1212 (2007)
12. Han, S., Lee, J.: Tele-operation of a Mobile Robot Using a Force Reflection Joystick with a Single Hall Sensor. In: *16th IEEE International Conference on Robot & Human Interactive Communication*, pp. 206–211 (August 2007)
13. Nohmi, M., Ando, A., Bock, T.: Contact Task by Space Teleoperation Using Force Reflection of Communication Time Delay. In: *IEEE International Symposium on CIRA*, pp. 193–198 (2005)
14. Choi, Y.-K., Choi, W.-S., Song, J.-B.: Object Avoidance of a Mobile Robot Using Low-Cost Ultrasonic Sensors with Wide Beam Angle. *Institute of Control, Robotics and Systems* 15(11), 1102–1107 (2009)
15. Kim, H.-N., Kim, H.-J.: A study on the obstacle avoidance using ultrasonic sensors for a mobile robot. In: *Proceedings of KIIS Spring Conference*, vol. 20(1), pp. 373–375 (2010)

16. Jin, T.: Object avoidance of Mobile Robot with Virtual Impedance. In: Proceedings of KIIS Conference, vol. 19(4), pp. 451–456 (2009)
17. Kweon, Y.-T., Kim, M.-K., Kang, H.-J., Roh, Y.-S.: Remote Control of a Mobile Robot using Haptic Device. In: Korean Society of Precision Engineering Autumn Conference, pp. 120–124 (October 2004)
18. Huang, C.-H., Wang, W.-J., Fellow, Chiu, C.-H.: Design and Implementation of Fuzzy Control on a Two-Wheel Inverted Pendulum. *IEEE Transactions on Industrial Electronics* 58(7), 2988–3001 (2011)
19. Lee, Y.-H., Jin, G.-G., Choi, H.-S., Park, H.-I., Jang, H.-L., So, M.-O.: Fuzzy Rule Based Trajectory Control of Mobile Robot. *Journal of the Korean Society of Marine Engineering* 34(1), 109–115 (2010)
20. Lee, W.-H., Lee, H.-W., Kim, S.-H., Jung, J.-Y., Roh, T.-J.: Moving Path following and High Speed Precision Control of Autonomous Mobile Robot Using Fuzzy. *Journal of Fuzzy Logic and Intelligent Systems* 14(7), 907–913 (2004)

Outdoor Precision Position Estimation System Using Multi-GPS Receivers

Seunghwan Choi¹, Kijung Kim¹, Yunki Kim², and Jangmyung Lee^{2,*}

¹ Interdisciplinary Program in Robotics, Pusan National University, South Korea

² Department of Electrical Engineering, Pusan National University, South Korea
{Seunghwan7379, kijung7379, mecha8404, jmlee}@pusan.ac.kr

Abstract. In this paper, tightly coupled system is designed using multi-GPS receivers based on the Extended Kalman Filter(EKF). Typically, GPS has the instantaneous error and INS has the disadvantage that the cumulative error occurs over time. To fill the gap, receiving is stabilized and accuracy is higher position information get using multi-GPS receivers. INS's data is precisely updated through the multi-GPS's position data in the data fusion process of the EKF. Through experiment, it can verify the results compared single GPS and multi-GPS position error, and then calibrated mobile robot position estimation results can be found.

Keywords: Outdoor, Multi-GPS, INS, EKF, Tightly coupled system.

1 Introduction

The fundamental problem of mobile robot is to recognize the position by itself. Now the interest about position recognition technology has been increasing in academia as well as industry field. And, by developing technology of intelligent robotics and unmanned vehicle, research for robot's autonomous driving has been preceded actively. The sensors of position recognition are typically GPS and IMU sensor. GPS calculates own position through satellite out of the Earth. At the beginning of GPS, it was developed for military purposes. However, after applying to real life, it has been gradually expanded from navigation of vehicle to wireless internet and location-based services. GPS calculates the distance from satellite to receiver by using time interval between the signal from satellite and the received signal to receiver. By using the distance among minimum three satellites and the position of each satellite through the three side measurement, the position of receiver is calculated. In case of INS(Inertial Navigation System), it gets information of the posture and the position of the object by using MCU that combine gyro data and acceleration data. INS obtains the acceleration of the object from initial position information, so it calculates the position through double integral equation [1-2]. Recently the research of system that combines the two devices using various filters has been preceded, many system have

* Corresponding author.

been proposed through the combination method and the research of the filter [3]. GPS is calculated by taken time that transmission signal of the satellite arrives to the receiver. At this time, the error is occurred by inconsistency between the satellite and the timer of the receiver. And, the own position is exactly calculated by receiving the signal from at least over 4 GPS satellites. Because the low-cost GPS typically has the 10m distance error, high accuracy DGPS and RTK GPS have been researched. But, these are over ten times more expensive than normal GPS on building the system. In case of INS, it is calculated by position information through integral formulas so error is getting increasing as time goes on [4-6].

1.1 System Combination Method

To supplement the disadvantage of the GPS and the INS, typically system that combine two devices have been widely used. The methods of combination are Loosely Coupled System, Tightly Coupled System and Deeply Coupled System.

Loosely Coupled System use navigation information (position, velocity, posture) and the output of GPS receiver (pseudo range) and their rate of change as measurement of filter. In Tightly Coupled System, first, calculates the pseudo range of GPS satellite and the rate of change of pseudo range from INS navigation information. Second, calculates the pseudo range of GPS receiver and the rate of change of pseudo range. And then, use these intervals as the estimation values of filter. Deeply Coupled System use the In-phase signal and Quadrature In the signal tracking loop of GPS receiver inside and location of the INS, the interval of the estimated I and Q signals from velocity as the estimation value of the filter. Loosely Coupled System is simple and has rapid calculation speed, but it has worse precision than Tightly Coupled System. And Deeply Coupled System is complex and difficult and has a disadvantage that long calculation time through state variables. So, by considering the building of exact outdoor position estimation system in embedded system, Tightly Coupled System is used in this paper [7-9].

1.2 Error Compensation Filter

In the case of the filter, there is the KF(Kalman Filter), EKF(Extended Kalman Filter), UKF(Unscented Kalman Filter), PF(Particle Filter) and so on. KF is simple to configure and fast processing speed. However, the error is severe, because the nonlinear system is assumed to be linear. EKF changes the nonlinear system to the linearization by using the Jacobian. It applies to the process of the KF so that the processing speed is fast, however, the error is large when the nonlinear characteristic is severe. The UKF is a way to obtain the mean and the covariance of the nonlinear function by choosing the sampled sigma point. The precision of the UKF is better than KT and EKF, however, in the case of the UKF, the configuration is complex and the processing speed is slow. If the number of particle is greater, PF can obtain the position more precisely. However, in accordance with the number of particle, the embedded implementation is difficult, because the amount of computation is also increased so that lots of memory is used for calculating and the processing speed is

slow. Therefore, the EKF, which can apply the nonlinear system, and which has simple configuration and fast renewal speed, is used in this paper[10-12].

In this paper, the Multi-GPS is used to develop the precision of the combined system of GPS/INS. With the three of GPS receivers, the exact position information of GPS is obtained using the weight on the satellite reception and the center of the triangular law. Also, the location identification system is built more accurately by combining the INS and GPS through the strongly-connected mode based on EKF.

The organization of this paper is as follows. In section 2, the composition of the system used in this research is covered. In section 3, propose a way how to design the multiple GPS and compare the position error in accordance with the number of the GPS receivers. In section 4, GPS/INS fusion algorithm, we propose, is discussed, and Section 5, the performance of multiple GPS is verified through the experiment compared a single GPS with the multiple GPS. Lastly, in section 6, conclude this paper based on the experimental result.

2 Configuration of the System

In this paper, the two controllers, the three GPS and IMU sensor is used to configure the hardware, as shown in the figure 1. MCU, LM3S8962 of the Cortex-M3 ARM made by TAXAS INSTRUMENT Inc., is used. The GPS sensor, LS20031 made by LOCYSYS Technology Inc., and the EBIMU-9DOF, made by E2BOX sensor is used.

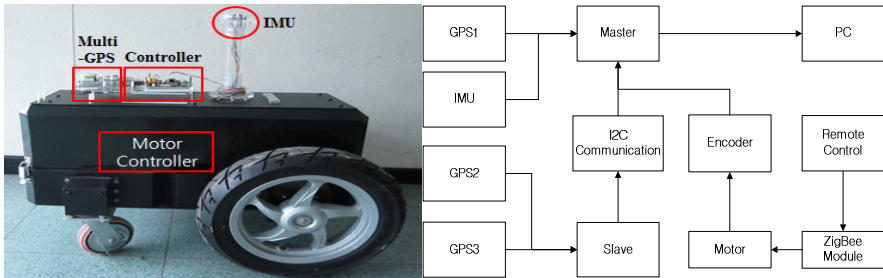


Fig. 1. The Configuration of the hardware and total system block diagram

Figure 1 shows the composition of the system. Each MCU receives the data of GPS receivers and IMU sensor through the UART communications. The main controller gathers the whole data to print out it from the PC at a time.

3 Multi-GPS System

The GPS receiver is got the information, including the time, position, speed, bearing and so forth. In the case of the GPS receiver, it receives more than three satellites to compute the current position using the triangulation method from satellite to receiver distance. Here, it is possible to know the position accurately, as there are a large

number of satellites. However, the received GPS information have the structural error due to the formation of the spatial structure, the geometric error due to the placement of the satellite and SA(Selective Availability) error. Also, if the data is continuously received with the error, the whole data would occur the large error[13-15].

3.1 Configuration of the Multi-GPS

If you use only two GPS receivers, two receiver's location information are calculated by using averaged those position. But it generates instant position error about rotation of station coordinate. Further, In cases that more than four GPS is used, an error range become wider because the number of occurrences of the center of gravity increase to the number $N(N-3)$. Therefore, when only three GPS receivers are used, we can obtain more accurate data, because a position error range becomes minimized and it reduces rotation errors.

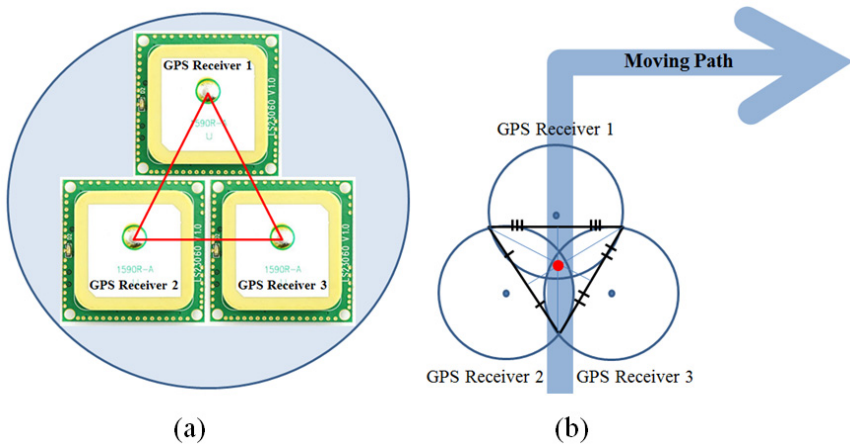


Fig. 2. The Configuration of the GPS receivers

As shown in Figure 2 (a), GPS receivers were applied to trigonometry in the center of the mobile robot. Figure 1 (b) shows the center of gravity according to moving path of the mobile robot. When the mobile robot moves, we can see the range of the position error through the center of gravity at a straight line and rotation.

$$P(G_i) = (x_i, y_i), \quad P(G) = \frac{G_1 \times n_1 + G_2 \times n_2 + G_3 \times n_3}{n_1 + n_2 + n_3} \quad (1)$$

The above equation is the position calculation equation using the multiple GPS receivers. G means the GPS receiver and n means the number of measured satellites at the receiver. In this paper, the transmitted number of satellites from the GPS receiver is weighted for obtaining the improved accuracy of the location information. In addition, that the number of satellites received from receiver is less than four was excluded.

3.2 Multi-GPS Algorithm

A receiving stability of GPS becomes different depending on the weather and environment of outdoor. In addition, there is a little difference in the performance of the receiver. In this paper, the position estimation is determined by distinguishing the receiving stability of the GPS satellites. If the GPS receiver gains data from four or more satellites, the location information is deemed stable and we will collect the data. Therefore, the precise position estimate is executed with position information that obtained through securing the stability by using the center of the triangular.

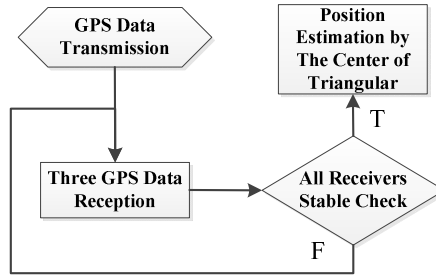


Fig. 3. The block diagram of the Multi-GPS

3.3 Comparison of the Single GPS and Multi-GPS

Obtained in order to compare the performance of single GPS and multiple GPS on Google Earth from a specific position (3514.0941 Latitude:, Longitude: 12904.5011) for 10 minutes to stop the data was obtained.

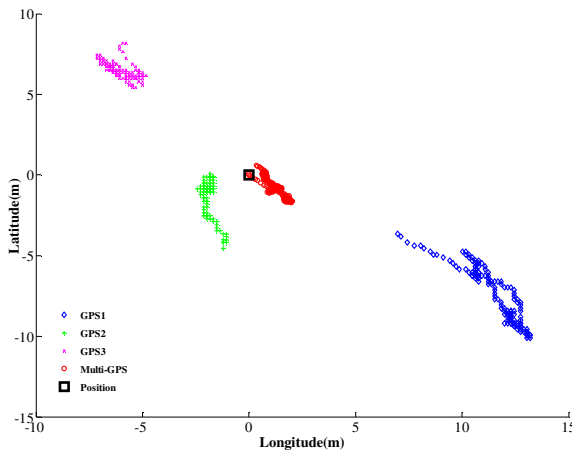


Fig. 4. Comparison of the single GPS & multi-GPS at the stop state

Table 1. The position error of the single GPS and multi-GPS

Sort	Maximum Position Error(m)	Average Position Error(m)
GPS1	8.9791	6.9753
GPS2	4.6624	4.1549
GPS3	2.8108	1.9283
Multi-GPS	2.6217	1.5669

Table 1 shows the maximum position error of the GPS 3 Single-GPS and multi-position error and the average is the result of the calculation. As shown in the table, in the case of a single GPS, position error of up to 8m or more occurred. Average GPS1 and GPS2 error is greater than 4m. In addition, the distribution of the location of the picture, it is difficult to pinpoint the location of the current position point. In case using multi-GPS with center of the triangular law can correct error of each other, so current position information and averaged position error is proved the most excellent.

4 GPS/INS Fusion Algorithm

In this paper, GPS and INS were fused with using tightly-coupled. The tightly-coupled method can get data of sight distance vector through INS' position information and GPS' satellite information. The extended Kalman filter is applied to this system by using estimates of non-linear position error between INS and GPS. In this paper, we improve the precision of a relatively large error of the GPS using multiple GPS. This paper proposes a robust position estimation system of mobile robot through applying the tightly-coupled method based on EKF [16-19].

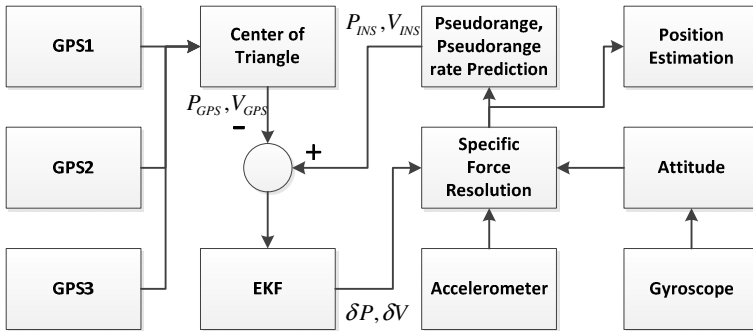


Fig. 5. The block diagram of the GPS/INS fusion Algorithm

Figure 5 is a block diagram of fusion of multiple GPS and INS algorithm. Pseudo distance and change rate of pseudo distance of GPS satellite are obtained through position of INS and information of velocity navigation, GPS satellite pseudo distance. Also, difference between pseudo distance and change rate of pseudo distance obtained from GPS receiver are used as measurement of the EKF.

$$\delta P = P_{INS} - P_{GPS} \quad (2)$$

$$\delta V = V_{INS} - V_{GPS} \quad (3)$$

Using angular velocity from gyro sensor, posture expressed by Quaternion is renewed[20].

$$\hat{q} = \frac{1}{2} q \times (\tilde{\omega}_{ib}^b - \hat{b}_{gyro}) \quad (4)$$

Posture expressed by Quaternion can obtain DCM which change from navigation coordinate system to navigation coordinate system as equation 6.

$$\hat{R}_n^b = \begin{bmatrix} \hat{q}_1^2 + \hat{q}_2^2 - \hat{q}_3^2 - \hat{q}_4^2 & 2(\hat{q}_2^2 \hat{q}_3^2 - \hat{q}_1^2 \hat{q}_4^2) & 2(\hat{q}_1^2 \hat{q}_3^2 + \hat{q}_2^2 \hat{q}_4^2) \\ 2(\hat{q}_2^2 \hat{q}_3^2 + \hat{q}_1^2 \hat{q}_4^2) & \hat{q}_1^2 - \hat{q}_2^2 + \hat{q}_3^2 - \hat{q}_4^2 & 2(\hat{q}_3^2 \hat{q}_4^2 - \hat{q}_1^2 \hat{q}_2^2) \\ 2(\hat{q}_2^2 \hat{q}_4^2 + \hat{q}_1^2 \hat{q}_3^2) & 2(\hat{q}_1^2 \hat{q}_2^2 + \hat{q}_3^2 \hat{q}_4^2) & \hat{q}_1^2 - \hat{q}_2^2 - \hat{q}_3^2 + \hat{q}_4^2 \end{bmatrix} \quad (5)$$

Equation 7 shows that velocity increment value of accelerometer output is changed to navigation coordinate system through DCM.

$$\delta V_f^n = \hat{R}_n^b \begin{bmatrix} 1 & 0.5\delta\theta_z & -0.5\delta\theta_y \\ -0.5\delta\theta_z & 1 & 0.5\delta\theta_x \\ 0.5\delta\theta_y & -0.5\delta\theta_x & 1 \end{bmatrix} \delta V_f^b \quad (6)$$

$$\delta \mathbf{x}_k = f_k(\delta \mathbf{x}_{k-1}) + \omega_k, \quad \delta \mathbf{y}_k = h_k(\delta \mathbf{x}_k) + v_k \quad (7)$$

k 's estimated value is \hat{k} , measurement value is defined as \tilde{k} . f_k is state propagation function, h_k is measurement equation, ω_k is the error of system, v_k is measurement error and $\delta \mathbf{y}_k$ is measurement value.

In this paper, more precise location information than single GPS is shown by using multi GPS based on EKF.

5 Experimental Results

This study uses 3 low-cost GPS receivers as a multiple GPS system. Also, compare single GPS and multiple GPS system for performance verification. GPS with EKF is more precise than tightly-coupled and the experiment was verified.

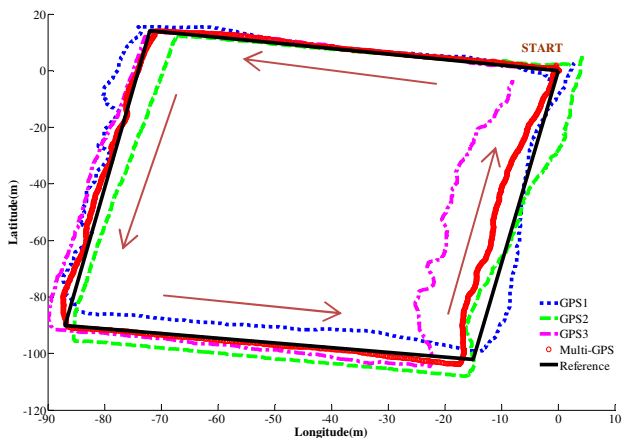


Fig. 6. The result of the single GPS and Multi-GPS

In Figure 6, only GPS data was used to detect location between single GPS and multiple GPS system. Through Google Earth, reference point was defined then drives in the shape of a rectangle. The error occurs at the moment a single GPS 3, as shown in Figure. In case using multi GPS with center of the triangular law can compensate error at the moment.

Table 2. The position estimation error of the single GPS and multi-GPS

Sort	Average Position Error(m)
GPS1	5.2230
GPS2	5.4382
GPS3	7.0857
Multi-GPS	2.5667

Table 2 shows figure 6's averaged position error between single GPS and multiple GPS system. Through this study, multiple GPS system can reduce location error than single GPS, and proved the superiority of multi GPS.

In this paper, EKF is used to combine multi GPS system and INS so that the localization system is more precise. The position error of INS is compensated by precise value of GPS absolute position information.

Figure 7 shows the result of localization by using the GPS/INS fusion system based on EKF. In the case of localization only by using GPS data, there are significant errors sometimes. However, the fusion of GPS and IMU could make the estimation more flexible as shown in figure 7.

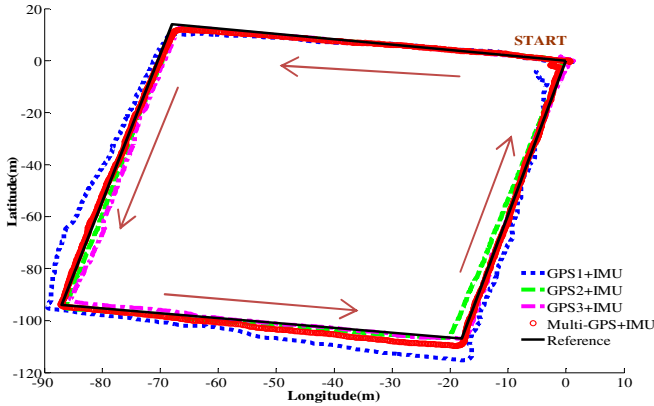


Fig. 7. The result of the fusion of the single GPS and Multi-GPS

Table 3. The position estimation error of the single GPS and multi-GPS

Sort	Average Position Error(m)
GPS1+IMU	1.5113
GPS2+IMU	0.7898
GPS3+IMU	0.9232
Multi-GPS+IMU	0.5298

Table 3 shows the position error of the GPS/IMU fusion system and the data mean the robustness of multi GPS system. Table 3 shows the position error of the GPS/IMU fusion system and the data mean the robustness of multi GPS system. As shown the data of GPS1 in figure 7, the large error of GPS gets the error of position estimation larger. Thus, the more precise GPS data in the fusion system is, the more precise the localization is.

6 Conclusion

In this paper, the GPS/INS fusion system by EKF is proposed in order to estimate outdoor localization precisely. Generally, GPS needs to be precise because the GPS/INS fusion system performs the role that update the position of INS through GPS position information. In many case, DGPS or RTK-GPS is used in order to improving precision of GPS. However DGPS or RTK-GPS requires the use of expensive equipment. For this reason, three low-cost GPS receivers are used to estimate the position by the method of triangular center and the weights depending on the stability of reception. And by using EKF, multi GPS and INS are combined on the assumption that the non-linear features do not appear significant. The experiments proved that the fusion system estimate the position and dramatically reduce the

position error, compared with the use of GPS only. This system decreases the amount of calculation and memory usage and estimate precise position at low cost. Also the system can be applied to all outdoor moving objects or driverless vehicles. In the future, we will configure the system that estimate the position while the mobile robot move outdoor path in real-time.

Acknowledgements. "This research was supported by the MKE(The Ministry of Knowledge Economy), Korea, under the Human Resources Development Program for Special Environment Navigation/Localization National Robotics Research Center support program supervised by the NIPA(National IT Industry Promotion Agency)." (H1502-13-1001)

"This research was supported by the MOTIE(The Ministry of Trade, Industry and Energy), Korea, under the Human Resources Development Program for Special Environment Navigation/Localization National Robotics Research Center support program supervised by the NIPA(National IT Industry Promotion Agency)." (H1502-13-1001)

References

1. Kwon, J.H., Kim, B.G., Lee, D.C., Lee, J.K.: Feasibility Test for the Integration of the Low-degree INS and GPS in Loosely Coupled Mode. *KSCE Journal of Civil Engineering* 7(2), 209–216 (2003)
2. Christensen, R., Fogh, N., la Cour-Harbo, A., Bisgaard, M.: Inertial Navigation System. Department of Control Engineering in Aalborg University (2008)
3. Yi, Y.: On Improving the Accuracy and Reliability of GPS/INS-Based Direct Sensor Georeferencing. The Ohio State University (2007)
4. Seo, J.W., Lee, H.K., Lee, J.G., Park, C.G.: Lever Arm Compensation for GPS/INS/Odometer Integrated System. *Automation, and Systems* 4(2), 247–254 (2006)
5. Chiang, K.-W., Huang, Y.-W.: An intelligent navigator for seamless INS/GPS integrated land vehicle navigation applications. *Applied Soft Computing*, 722–733 (2007)
6. Ohno, K., Tsubouchi, T., Shigematsu, B., Maeyama, S., Yuta, S.: Outdoor Navigation of a Mobile Robot between Buildings based on DGPS and Odometry Data Fusion. In: *IEEE International Conference on Robotics & Automation*, vol. 2, pp. 1978–1984 (2003)
7. Park, Y.B., Lee, J.G., Park, C.G.: Performance Analysis of INS/GPS Integration system. The Korean Institute of Electrical Engineers (July 2000)
8. Zhang, G., Xu, X.: Implementation of tightly coupled GPS/INS navigation algorithm on DSP. In: *International Conference on Computer Design and Applications*, vol. 2, pp. 130–134 (2010)
9. Li, Y., Wang, J., Rizos, C., Mumford, P., Ding, W.: Low-cost Tightly Coupled GPS/INS Integration Based on a Nonlinear Kalman Filtering Design. *The Institute of Navigation*, 958–966 (2006)
10. Park, J.Y., Lee, J.H., Nam, D.K., Kim, D.Y., Sung, S.H.: Investigations on GPS/INS Integration for Land Vehicle Navigation. In: *Proceedings of KIIS Fall Conference*, vol. 19(2) (2009)
11. Cho, S.Y., Kim, B.D., Cho, Y.S., Choi, W.S.: Multi-Filter Fusion Technique for INS/GPS. *The Korean Society for Aeronautical and Space Sciences*, 48–55 (2006)

12. Noureldin, A., Karamat, T.B., Eberts, M.D., El-Shafie, A.: Performance Enhancement of MEMS-Based INS/GPS Integration for Low-Cost Navigation Applications. *IEEE Transactions on Vehicular Technology* 58(3) (2009)
13. Alban, S.: An Inexpensive and Robust GPS/INS Attitude System for Automobiles. *The Institute of Navigation*, 1075–1087 (2002)
14. Moon, H.C., Son, Y.J., Kim, J.H.: The Development of Driving Algorithm for an Unmanned Vehicle with Multiple-GPS's. *Robotics and Systems* 14(1) (2008)
15. Mottaghi, R., Kaess, M., Ranganathan, A., Roberts, R., Dellaert, F.: Place Recognition-based Fixed-Lag Smoothing for Environments with Unreliable GPS. In: *IEEE International Conference on Robotics and Automation*, pp. 1862–1867 (2008)
16. Kim, J.M., Kim, Y.T., Kim, S.S.: An accurate localization for mobile robot using extended Kalman filter and sensor fusion. In: *IEEE International Joint Conference on Neural Networks*, pp. 2928–2933 (2008)
17. Semeniuk, L., Noureldin, A.: Bridging GPS outages using neural network estimates of INS position and velocity errors. *Measurement Science and Technology*, 2783–2798 (2006)
18. Zhou, J., Bolandhemmat, H.: Integrated INS/GPS System for an Autonomous Mobile Vehicle. In: *IEEE International Conference on Mechatronics and Automation*, pp. 694–699 (2007)
19. Huang, D.: Expectation Maximization Based GPS/INS Integration for Land-Vehicle Navigation. *IEEE Transactions on Aerospace and Electronic Systems* 43(3) (2007)
20. Shin, E.H.: Accuracy Improvement of Low Cost INS/GPS for Land Application. MS Thesis, University of Calgary (2001)

Low Complexity MAP Algorithm for Turbo Decoder

Jonghyun Seo and Jangmyung Lee

Dept. of Electronic Engineering, Pusan National University,
Jangjeon-dong, Geumjung-gu, Pusan, Korea, Republic of
{jhseo, jmlee}@pusan.ac.kr

Abstract. As a promising decoding algorithm for turbo codes in terms of relatively low BER, the maximum a posteriori (MAP) algorithm is most widely used. However, the conventional MAP algorithm requires a large number of computations. A modified MAP algorithm is therefore proposed for reduction of the associated memory size and ultimately power saving. A newly introduced block combining is performed for the memory efficiency such that two branch metrics (BMs) are merged into one branch metric. When calculating FSM (Forward State Metric) of the associated state transition, BM is included in the subsequent FSM, and thus when calculating APP (A Posteriori Probability), the BM is exempted and the number of computations for LLR (Log Likelihood Ratio) is reduced. Simulation results demonstrate reduced memory size in use and equivalent performance, compared to the conventional MAP algorithm.

Keywords: Turbo decoder, MAP algorithm.

1 Introduction

Error correcting code has been researched since announcement of Shannon's coding theorem in 1984. And turbo code is one of the error correcting codes proposed in 1993 by Berrou, Glavieux, and Thitimaishima [1].

Turbo code has been researched actively because it has excellent performance of error correction, and there are SOVA (Soft-Output Viterbi Algorithm) or MAP (Maximum A Posteriori) in algorithm of turbo code. Even though SOVA algorithm has less complexity than MAP algorithm, MAP algorithm shows better performance than SOVA algorithm [3]. Thus, MAP algorithm is mainly used in these days [4]. MAP algorithm proposed in 1974 by Bahl, and MAP algorithm calculates to APP from signal of noise.

The following section describes the MAP algorithm for the turbo decoder and then accounts to the block processing technique in section 3. Section 4 describes that efficient MAP algorithm using block combining. Section 5 describes experimental result. Finally section 6 summarizes this paper.

2 Map Algorithm

The MAP algorithm was firstly presented in 1974 by Bahl, Cocke, Jelinik and Raviv. The MAP algorithm aims to calculate the a-posteriori probability (APP) of each state transition [4][5].

Given noisy observation vector, the MAP algorithm finds the probability of each valid state transition as in the Trellis diagram. As shown in Fig.1, the terms, alpha, beta, and Gamma, are defined as the forward state metric and the backward state metric and the branch metric, respectively. Alpha has a systemic bit that means state metric transitioning from the previous state, s' , at time $k-1$ to the next state, s , at time k . Beta can be obtained from the previous one by iterative calculation after receiving all information. The Gamma is defined as the probability that a given transition is chosen given the received sequence at a given state.[7]

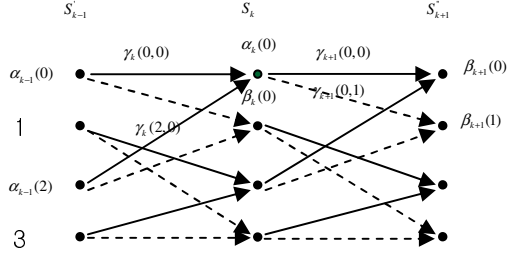


Fig. 1. The Conventional trellis with 4-state from time $k-1$ to time $k+1$

In order to calculate LLR, gamma value is initial needed from received data. Then, alpha and beta value are calculated by using gamma value. Numerical formula (Mathematic method) is shown below. Alpha and beta values are expressed as follows.

$$\alpha_k(s) = \sum_{all\ s'} \gamma_k(s', s) \times \alpha_{k-1}(s') \tag{1}$$

$$\beta_k(s') = \sum_{all\ s} \beta_k(s', s) \times \gamma_k(s', s) \tag{2}$$

$$L(u_k) = \ln \left(\frac{\sum_{\substack{(s,s') \Rightarrow \\ u_k = +1}} \alpha_{k-1}(s') \gamma_k(s', s) \beta_k(s)}{\sum_{\substack{(s,s') \Rightarrow \\ u_k = -1}} \alpha_{k-1}(s') \gamma_k(s', s) \beta_k(s)} \right) \tag{3}$$

$$L(u_{k+1}) = \ln \left(\frac{\sum_{\substack{(s,s'') \Rightarrow \\ u_{k+1} = +1}} \alpha_{k-1}(s) \gamma_k(s, s'') \beta_k(s'')}{\sum_{\substack{(s,s'') \Rightarrow \\ u_{k+1} = -1}} \alpha_{k-1}(s) \gamma_k(s, s'') \beta_k(s'')} \right) \tag{4}$$

Eq. (3) and (4) are LLR computed at time k and $k+1$, respectively. These equations make a decision for the information bit with a maximum probability when transitioning from the previous state to the current state.

3 Using the Block Processing Technique

In this section, we explain a modified MAP algorithm using block processing technique for efficient memory use [2].

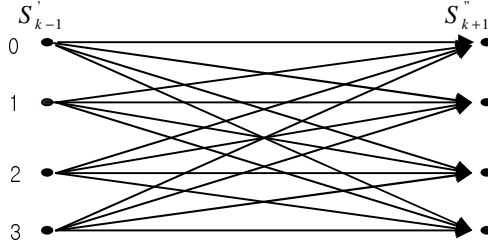


Fig. 2. Block processing trellis with 4-state from time $k-1$ to time $k+1$

The algorithm using the block processing technique does not take into account alpha and beta values at time k , but only at time $k+1$, thereby reducing memory storage for alpha and beta value at time k . Alpha, beta and gamma values are expressed as follows.

$$\alpha_{k+1}(s) = \sum_{\text{all } s'} \gamma(s', s, s'') \times \alpha_{k-1}(s')$$

$$\beta_{k-1}(s') = \sum_{\text{all } s''} \gamma(s'', s, s') \times \beta_{k-1}(s'')$$

$$\gamma(s'', s, s') = \gamma(s'', s) \times \beta_{k-1}(s'')$$

Although the block processing MAP algorithm needs much smaller memory size for the state metric and reduces power consumption, it has a defect that the algorithm needs more multiplication operations than conventional MAP algorithm in LLR calculation.

4 Proposed Scheme for Low Low Complexity Map Algorithm

A. The first proposed scheme

In this section, we explain a modified MAP algorithm using block combining for an efficient turbo decoder.

Fig. 3 shows a combining decoding process from two decoding processes. FSM and BSM are calculated using the combined BM values at each state, and the combined BM value means that two calculated BM values, one value is from time $k-1$ to k and the other is from time k to time $k+1$. The value can be expressed as,

$$\gamma_k^{s', s, s''} = \gamma_k^{s', s} \times \gamma_k^{s, s''} \quad (5)$$

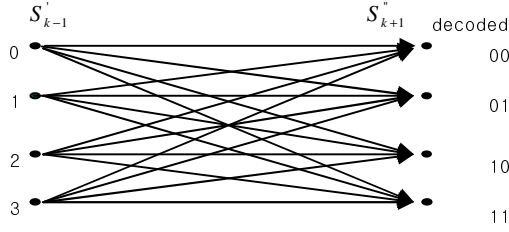


Fig. 3. Block combining trellis with 4-state from time k-1 to time k+1

$$\beta_{k-1}(s') = \sum_{\text{all } s''} \beta_k(s'') \times \gamma_k(s', s'') \tag{6}$$

$$\alpha_{k+1}(s) = \sum_{\text{all } s'} \gamma_k(s', s'') \times \alpha_{k-1}(s') \tag{7}$$

$\gamma_k^{s',s''}$ combining calculate value that transfer to state(S) in time k from state(S') in time k-1. Alpha and beta value in time k+1 calculate with integrated BM value Calculating Alpha and Beta value in this algorithm is as same as conventional MAP algorithm. That is, keep systemic bit to next state (s) at time k from previous state (s') at time k-1. Alpha in the same manner, received all of information bit thereafter current beta value repetitional calculate through next beta value.

To '0' state in time k+1 transfer from all states in time k-1 which receive data (0,0). To '1' state in time k+1 transfer from all states in time k-1 which receive data (0,1). And to '2' state in time k+1 transfer from time k-1 which receive data (1,0). To '3' state in time k+1 transfer from time k-1 which receive data (1,1). Probability values calculate that to each state in time k+1 from time k-1. Express followed below

$$p(u_k = 00 : y_k) = \sum_{0,0} \alpha_{k-1} \gamma_{s',s''} \beta_{k+1} \tag{8}$$

$$p(u_k = 01 : y_k) = \sum_{0,1} \alpha_{k-1} \gamma_{s',s''} \beta_{k+1} \tag{9}$$

$$p(u_k = 10 : y_k) = \sum_{1,0} \alpha_{k-1} \gamma_{s',s''} \beta_{k+1} \tag{10}$$

$$p(u_k = 11 : y_k) = \sum_{1,1} \alpha_{k-1} \gamma_{s',s''} \beta_{k+1} \tag{11}$$

$p(u_k = 00 : y_k)$ display probability likely data (0,0) in received data y_k .
 $p(u_k = 01 : y_k)$ indicates that probability likely data (0,1) in received data y_k .

And $p(u_k = 10: y_k)$ indicates that probability likely (1,0). $p(u_k = 11: y_k)$ indicates that probability likely (1,1).

After calculating their probability values, the maximum value can be determined because decoding calculation is differed according to the maximum value in LLRC. LLRC of the maximum value is as follows.

$$\begin{aligned} & \text{CASE1 } p(u_k = 00: y_k) \\ L(u_k) &= \log\left(\frac{p(u_k = 10: y_k)}{p(u_k = 00: y_k)}\right), \quad L(u_{k+1}) = \log\left(\frac{p(u_k = 01: y_k)}{p(u_k = 00: y_k)}\right) \end{aligned} \quad (12)$$

$$\begin{aligned} & \text{CASE2 } p(u_k = 01: y_k) \\ L(u_k) &= \log\left(\frac{p(u_k = 11: y_k)}{p(u_k = 01: y_k)}\right), \quad L(u_{k+1}) = \log\left(\frac{p(u_k = 01: y_k)}{p(u_k = 00: y_k)}\right) \end{aligned} \quad (13)$$

$$\begin{aligned} & \text{CASE3 } p(u_k = 10: y_k) \\ L(u_k) &= \log\left(\frac{p(u_k = 10: y_k)}{p(u_k = 00: y_k)}\right), \quad L(u_{k+1}) = \log\left(\frac{p(u_k = 11: y_k)}{p(u_k = 10: y_k)}\right) \end{aligned} \quad (14)$$

$$\begin{aligned} & \text{CASE4 } p(u_k = 11: y_k) \\ L(u_k) &= \log\left(\frac{p(u_k = 11: y_k)}{p(u_k = 01: y_k)}\right), \quad L(u_{k+1}) = \log\left(\frac{p(u_k = 11: y_k)}{p(u_k = 10: y_k)}\right) \end{aligned} \quad (15)$$

$L(u_k)$ become decoding value in time k. $L(u_{k+1})$ become decoding value in time k+1. $p(u_k = 00: y_k)$ divide $p(u_k = 10: y_k)$ in $L(u_k)$ of case1. It does divide $p(u_k = 00: y_k)$ by $p(u_k = 10: y_k)$ in $L(u_k)$ of case1. Because it does product of probability value of received data '0' when transfer to time k from time k-1 and probability value of received data '0' when transfer to time k+1 from time k. So, decoding value at time k+1 should make an offset.

Similarly, calculate $L(u_{k+1})$. Also case2 and case3, case4 calculate in the same method. Equation (8) can be simplified.

$$\begin{aligned} p(u_k = 00: y_k) &= \sum_{0,0} \alpha_{k-1} \gamma_{s',s''} \beta_{k+1} \\ &= \alpha_{k-1}(0) \times \gamma_{0,0} \times \beta_{k+1}(0) + \alpha_{k-1}(1) \times \gamma_{1,0} \times \beta_{k+1}(0) + \alpha_{k-1}(2) \times \gamma_{2,0} \times \beta_{k+1}(0) + \alpha_{k-1}(3) \times \gamma_{3,0} \times \beta_{k+1}(0) \\ &= (\alpha_{k-1}(0) \times \gamma_{0,0} + \alpha_{k-1}(1) \times \gamma_{1,0} + \alpha_{k-1}(2) \times \gamma_{2,0} + \alpha_{k-1}(3) \times \gamma_{3,0}) \times \beta_{k+1}(0) \\ &= \alpha_{k+1}(0) \times \beta_{k+1}(0) \end{aligned} \quad (16)$$

Probability of (0,0) that is received data from equation (16) can be simplified by only current state of alpha and beta. Because alpha values at time k+1 include alpha values of all states. Equation (10), (11), (12) also can be simplified by same way.

B. The second proposed scheme

```

If  $p(u_k = 00 : y_k) > p(u_k = 01 : y_k)$  ;
    Then buf = '1';
        If  $p(u_k = 00 : y_k) > p(u_k = 10 : y_k)$ 
            Decoding data = '00';
        Else if  $p(u_k = 00 : y_k) < p(u_k = 10 : y_k)$ 
            Decoding data = '10'
    Else if  $p(u_k = 00 : y_k) < p(u_k = 01 : y_k)$  ;
        Then buf = '0';
            If  $p(u_k = 01 : y_k) > p(u_k = 11 : y_k)$ ;
                Decoding data = '01';
            Else if  $p(u_k = 01 : y_k) < p(u_k = 11 : y_k)$ ;
                Decoding data = '11';
    
```

<Pseudocode>

5 Conclusions

A Multiplication operation can be transferred to an adder operation by using Log-MAP algorithm[7]. To make an easy hardware design, Log-MAP algorithm applies to conventional algorithm and proposed algorithm. After that following the application, compare conventional algorithm with proposed algorithm into LLRC.

Table 1. Compare proposed Algorithm with conventional algorithm using log-MAP Algorithm in LLR Calculation(n:state number, m:data frame)

	Log-MAP algorithm	Pietroben algorithm	Block processing algorithm	Proposed algorithm
Adder Operation	$4*n(m-1)$	$n(m-1)$	$12*n((m-1)/2)$	$1/2*n(m-1)$
Max Operation	$3/2*n(m-1)$	$1/2*n(m-1)$	$3*n(m-1)$	$(n-1)((m-1)/2)$
FSM(or BSM) Memory	$m*n$	$m*n$	$1/2*n(m+1)$	$1/2*n(m+1)$
Number of total memory	$2*n(2*m-1)$	$2*n(2*m-1)$	$n(3*m-1)$	$n(3*m-1)$

Table 2. Compare Proposed Algorithm with conventional algorithm at the number of time for switching(using the Xilinx XST)

	Block processing algorithm	Proposed algorithm	The decrement(%)
Power(mw)	55.41	23.77	56
Area	70.08	28.68	59

Table 3. Compare Proposed Algorithm with conventional at LLRC(using the Xilinx XST)

	Conventional algorithm	Block processing algorithm & Proposed algorithm	The decrement(%)
n=4 m=400	6384	4796	25
n=4 m=800	12792	9596	25

The Proposed scheme has less adder operation than conventional algorithm, and memory uses are as same as block processing technique. However, the operation quantities are far less than block processing technique. Thus, turbo decoder design consist of proposed scheme, the total circuit area can be reduced because it uses small number of adders.

MAP algorithm of turbo decoder has an excellent performance of error correction, but it has very high complexity. In this paper, we proposed an efficient MAP algorithm by using the block combining. 'Block Combining' means that two times of decoding processes are unified with one process and the result both decrease the calculations in memory and operation.

Therefore, proposed MAP algorithm by using block combining can use in efficient memory size and in low power. It is also suitable for low power system or high-speed system.

References

1. Berrou, C., Glavieux, A., Thitimajshima, P.: Near Shannon limit error-correcting coding and decoding: Turbo-Codes. In: Proceeding of IEEE International Conferences on Communications 1993, pp. 1064–1070 (May 1993)
2. Lee, I., Vallejo, M.L., Mujtaba, S.A.: Block Processing Technique for Low Power Turbo Decoder Design. In: IEEE 55th VTC Spring 2002, pp. 1025–1029 (2002)
3. Papke, L., Robertson, P., Villebrun, E.: Improved decoding with the SOVA in a parallel concatenated (turbo-code) scheme. In: Proceeding of ICC 1996, Dallas, TX, USA, pp. 102–106 (June 1996)
4. Bahl, L., Cocke, J., Jelinek, F., Raviv, J.: Optimal decoding of linear codes for minimizing symbol error rate. IEEE Trans. Inform. Theory IT-20, 284–287 (1974)

5. Pietrobon, S., Barbulescu, A.S.: A simplification of the modified Bahl decoding algorithm for systematic convolutional codes. In: Proceeding of ISITA 1994, Sydney, Australia, pp. 875–880 (November 1994)
6. Pietrobon, S., Barbulescu, A.S.: A simplification of the modified Bahl decoding algorithm for systematic convolutional codes. In: Proceeding of ISITA 1994, Sydney, Australia, pp. 875–880 (November 1994)
7. Robertson, P., Villebrun, E., Hoher, P.: A Comparison of Optimal and Sub-Optimal MAP Decoding Algorithms Operating in the Log Domain. In: Proceedings of the International Conference on Communications, pp. 1009–1013 (June 1995)
8. Forney, G.: The Viterbi algorithm. Proceedings of the IEEE 61, 268–278 (1973)
9. Bahl, L.R., Cocke, J., Jelinek, F., Raviv, J.: Optimal Decoding of Linear Codes for Minimising Symbol Error Rate. IEEE Transactions on Information Theory 20, 284–287 (1974)
10. Shrestha, R., Paily, R.: 2013 26th International Conference on VLSI Design and 2013 12th International Conference on Embedded Systems (VLSID), pp. 86–91 (2013)

Force Feedback Implementation Based on Recognition of Obstacle for the Mobile Robot Using a Haptic Joystick

Dong-Hyuk Lee¹, Kyoung-Taik Park², Sun-Kyun Kang¹, and Jangmyung Lee^{1,*}

¹ Department of Electrical Engineering, Pusan National University, Korea

² Research Division of Intelligent Manufacturing System,
Korea Institute of Machinery & Materials
{ldh0917, sunkyun7379, jmlee}@pusan.ac.kr,
ktpark@kimm.re.kr

Abstract. In this paper we have studied a haptic joystick that can recognize the surrounding environment of a mobile robot, which is remotely controlled by using user cognitive vibration pattern. We have realized a haptic joystick that user can remotely control the mobile robot and recognize the position and distance of an obstacle recognized by the operating robot with two vibration motors. We have implemented various situations using collision vector and fuzzy controller of virtual impedance and improved environment recognition accuracy of the mobile robot by overlapping ultrasonic sensors.

Keywords: Haptic joystick, Force Feedback, mobile robot, Haptic.

1 Introduction

Haptic means relating to or based on the sense of touch and it is a technology that can make human feel the power of touch, sense of movement. Human senses mean sight, hearing, touch, taste and smell. A great deal of effort has been made on the implementation of visual and auditory information for a long time, and it has been widely used in the real world[7-9]. Haptic is studied in terms of the delivery and implementation the sense of touches or force feedback. Recently, the necessity of precise implementation the sense of touches and force feedback is emerging to deliver various and accurate information for the industrial robots and unmanned vehicle [1-2]. There is a limit for human to control robots merely using a simple controller. To complement this limit, the interaction system between human and robot, the haptic technology is required. In this paper, we have controlled a mobile robot using haptic joystick and if the robot detects an obstacle while operating, it creates a certain vibration pattern to notify it to the user. The vibration pattern has implemented using Morse code. For hardware, we have mounted duplicated ultrasonic sensors on the mobile robot to detect accurate position of an obstacle, and installed two vibration motors on the joystick to create user cognitive vibration pattern. As software control

* Corresponding author.

methods, we have used collision vector method and fuzzy controller using virtual impedance to make system that delivers haptic to user through speed control of the vibration motor depending on the obstacle position and distance from robot to the obstacle. To begin with, Chapter 2 describes hardware part as total system configuration, and Chapter 3 describes software including virtual impedance, collision vector, and fuzzy controller. Then, Chapter 4 describes experimental environment and the analysis of the various sensors needed for research, and Chapter 5 describes the results of the experiment controller. Finally, Chapter 6 summarizes this paper by presenting the result of this study.

2 Entire System Configuration

2.1 System Configuration

The entire system is configured as figure 1 bellow. The two Hall sensors installed on the joystick represents the X-axis and Y-axis data respectively. The mobile robot operates motor using the Hall sensor data received from the MCU of the joystick. Three ultrasonic sensors are mounted on the front side of the mobile robot to measure the distance and angle between an obstacle and the robot, the measurement data transmitted to the MCU of the joystick and control the vibration motor to implement the haptic.

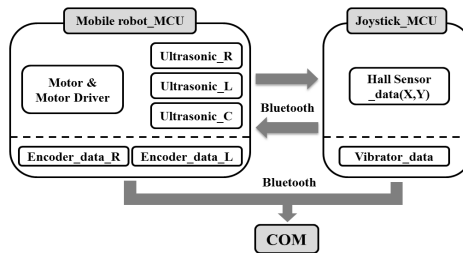


Fig. 1. Entire System

2.2 Mobile Robot Configuration

Figure 2 shows the appearance of the mobile robot designed to perform the test and the three ultrasonic sensors mounted on the front side recognize an obstacle.

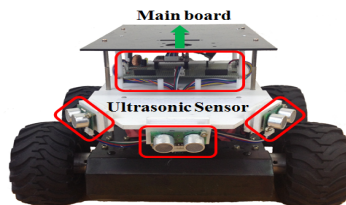


Fig. 2. Design structure of the mobile robot

2.3 Joystick Configuration

Figure 3 represents the axis and coordinate system of the haptic joystick. As shown in the Figure 3 above, if the operator applies force F_h to the joystick, displacement will be created as much as the joystick's location coordinate X_m . This displacement X_m will generate the velocity V_d and the position X_d according to the equation (1) and (2) [3].

$$V_d(s) = K_m \cdot X_m(s) \quad (1)$$

$$X_d(s) = K_v \cdot V_d(s) \cdot ds \quad (2)$$

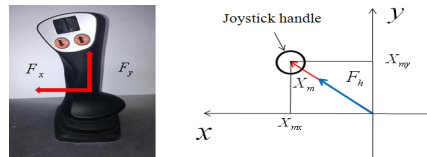


Fig. 3. Haptic Joystick's coordinate system

2.4 Haptic Device Configuration

Figure 4 is the picture of the haptic joystick. Haptic has implemented by mounting a vibration motor on the bottom of the joystick. The faster the mobile robot velocity and the closer the distance from an obstacle, the stronger the vibration of the motor performing haptic function. It was designed to respond immediately according to the current velocity of the mobile robot and distance from an obstacle calculated in real-time. In addition, we have changed the vibration pattern depending on the location of the obstacles. Even if the distance is close, haptic response can be weakened as robot's velocity goes down.

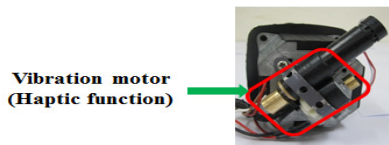


Fig. 4. Haptic Device

2.5 Obstacles Measurement

Figure 5 shows that three ultrasonic sensors are duplicated in order to reduce the uncertainty of the ultrasonic sensor[4-5]. As you can see, same types of N ultrasonic

sensors are placed interval of $\beta \left(= \frac{360^\circ}{N} \right)$ on the circumference with r radius so that

3 ultrasonic sensors are forming a nested ultrasonic sensor ring. When the ultrasonic beam width is α , and the maximum detecting distance is $\rho_{s,max}$, then the Figure 5

represents $\overline{OS_1} = r$, $\lim_{x \rightarrow \infty} \angle CS_1D = \frac{\alpha}{2}$ and $\angle S_1OD = \frac{\beta}{2}$.

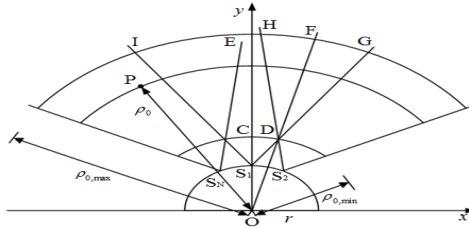


Fig. 5. 3 adjacent ultrasonic sensors with overlapped beam width

Considering the blind spots of the obstacle detection, the obstacle detection range of the nested ultrasonic sensor ring in the Figure 4 can be determined with the following equation (3).

$$\rho_{0,min} \leq \rho_0 \leq \rho_{0,max} \tag{3}$$

Here,

$$\rho_{0,min} = \overline{OD} = d \tag{4}$$

$$\rho_{0,max} = \overline{OE} = r + \rho_{s,max} \tag{5}$$

the $\rho_{0,min}$ of equation (4) is the distance from the center of nested ultrasonic sensor ring to the vertex of the obstacle detection blind spots. The $\rho_{0,max}$ of equation (5) is the maximum distance from the nested ultrasonic sensor ring to the farthest detectable obstacle. In this paper, we have set the maximum detection distance of the ultrasonic sensor as 1 m and performed the tests.

3 Design Haptic System

3.1 Virtual Force Restoration

We have used virtual impedance by applying common impedance method to the field of the mobile robot driving and collision avoidance. As the figure 6 below, the virtual impedance models relationship between mobile robot and obstacles to the relationship between spring and damper and creates virtual power depending on the distance and

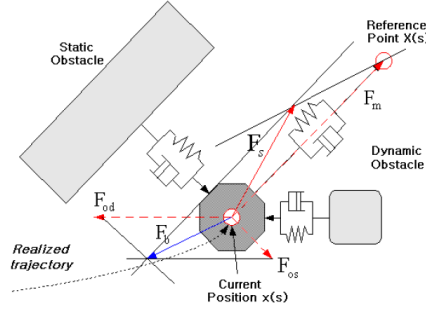


Fig. 6. Virtual Impedance Method

speed information. The virtual force F_b , which will be given to the operator as a feedback is the sum of the repulsive forces for dynamic and static obstacles as the following equation (6).

$$F_b = \left\{ \sum_{i_{od}=0}^{n_{od}} F_{od}(s) + \sum_{i_{os}=0}^{n_{os}} F_{os}(s) \right\} \quad (6)$$

In this paper, the virtual force is implemented only using the sum of repulsive forces for the static obstacles so the sum of repulsive forces for the dynamic obstacles is 0. Therefore, the repulsive force F_{os} for static obstacles from the equation (6) can be obtained by the following equation (7).

$$F_o(s) = K_{s,o}(X_{s,o}(s)) + D_{s,o}(\dot{X}_{s,o}(s)) \quad (7)$$

$$= \begin{cases} \sum_{i=0}^n K_{s,o}(\rho_0 - \|\bar{C}\|)\bar{C}_{unit} - D_{s,o}(\|\Delta\bar{C}\|)\bar{C}_{unit}, & \text{when } \|\bar{C}\| < \rho_0 \\ 0, & \text{otherwise} \end{cases}$$

3.2 Detection of a Collision Vector for an Obstacle

In this paper, three ultrasonic sensors (SRF-04) were placed at intervals of 30° in the front of the mobile robot. We defined a vector, which is facing to the center of the front of the mobile robot and perpendicular to the tangential line of an obstacle as a collision vector (\bar{C}). And it generates the virtual repulsive force by detecting the collision vector for an obstacle through the proposed virtual impedance model[6]. When we detect a collision vector using ultrasonic sensors, the possible cases can be divided into two cases as shown in figure 7. Figure 7. (a), Case 1 A small obstacle which could be a person is detected by only one ultrasonic sensor. Figure 7. (b), Case 2 An obstacle is detected by two ultrasonic sensors because the obstacle is bigger than that of Case 1. In case of Case 1, the collision vector can be obtained by the equation (8).

$$\bar{C} = \bar{L}_c \quad (8)$$

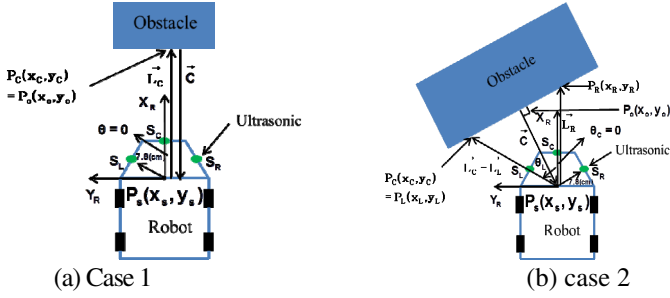


Fig. 7. Collision Vector Detection for an Obstacle

For Case 2, we define a shorter distance from the 2 measured information as $\overline{L_C}$ and the other distance vector is defined as $\overline{L_R}$ or $\overline{L_L}$ depending on the $\overline{L_C}$. For (b) of figure 7, the longer distance vector is defined as $\overline{L_R}$ because it is on the right side and $\overline{L_C}$ is defined as $\overline{L_L}$. Using the points P_L , P_R the lines of $\overline{L_L}$, $\overline{L_R}$ and the tangential line of $\overline{P_L P_R}$ can be measured. And the collision vector that passes by the point P_S can be obtained and the collision vector can be defined as follows.

$$P_L = (x_L, y_L) = (d_L \cos \theta_L, d_L \sin \theta_L) \tag{9}$$

$$P_R = (x_R, y_R) = (d_R \cos \theta_R, d_R \sin \theta_R) \tag{10}$$

$$P_o = (x_o, y_o) = \left(\frac{V \cdot x_L - y_L}{V + \frac{1}{V}}, -\frac{-x_L + \frac{1}{V} \cdot y_L}{V + \frac{1}{V}} \right) \tag{11}$$

$$\overline{C} = \overline{P_o P_S} \tag{12}$$

Here, $v = \frac{y_R - y_L}{x_R - x_L}$, P_S indicates the current position of the mobile robot. θ_L and θ_R represent the angle between the moving direction of the mobile robot, X_R and an ultrasonic sensor[6].

3.3 Fuzzy Algorithms for the Implementation of the Haptic System

The location and distance information of an obstacle calculated by the virtual impedance algorithms is delivered to the operator via the vibration pattern. The vibration pattern requires an algorithm to estimate the position of the obstacle as well as an algorithm for the robot to respond intelligently depending on the current state including the moving direction and the current speed. In this paper, we have generated vibration pattern using fuzzy rules. The performance of the fuzzy may vary depending

on the fuzzy rules configuration method. For better performance, fuzzy rules' optimization process is required. The fuzzy rules are as follows.

Rule: IF Collision Vector is A_C^i and Velocity of Mobile Robot is B_V^i Then Vibration Patton Style X_p^i is and Vibration Strength is Y_S^i

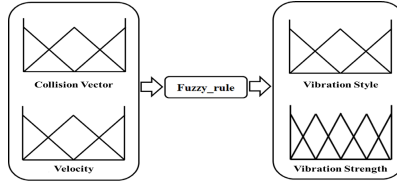


Fig. 8. Structure of Fuzzy Rules

The input variables of fuzzy algorithm to express the virtual force as vibration are the collision vector \vec{c} and the current velocity V of the mobile robot, and the shape and intensity of the vibration reflects the result values. To decide the result value, the Mamdani inference scheme, the center of gravity (COG) defuzzification method is used, and expressed with qualitative language[10-11].

Table 1. Input • output Fuzzy rules

$V \backslash \vec{c} $	Zero	Very Short	Short	Long
Zero	Zero	Zero	Zero	Zero
Very Slow	Zero	Zero	Zero	Zero
Slow	Very Fast	Slow	Very Slow	Very Slow
Fast	Very Fast	Fast	Slow	Very Slow
Very Fast	Very Fast	Very Fast	Fast	Slow

Table 2. Input • output Fuzzy rules

Situation	Presence of Obstacle			Pattern
	Left	Center	Right	
Situation 1	X	X	X	Pattern 0
Situation 2	O	X	X	Pattern 1
Situation 3	O	O	X	Pattern 2
Situation 4	X	O	X	Pattern 3
Situation 5	X	O	O	Pattern 4
Situation 6	X	X	O	Pattern 5
Situation 7	O	O	O	Pattern 6
Situation 8	O	X	O	Pattern 7

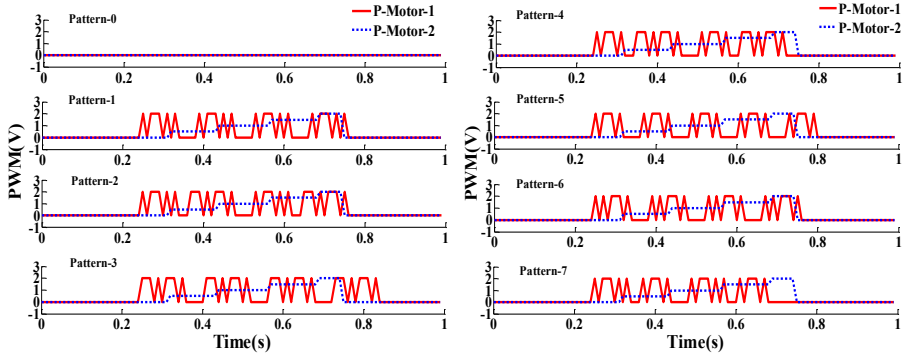
Table 1 shows the designed fuzzy rules. Fuzzy rules are designed into two types by considering the situation. First of all, the risk index between the mobile robot and obstacles to the use, and the risk index reflects the robot’s current velocity and the distance from an obstacle. The size of collision vector is calculated using the distance measured by ultrasonic sensor. We have designed to control the intensity of vibration depending on the speed of the mobile robot and of the collision vector. Secondly, we have provided the user cognitive vibration pattern depending on the obstacle recognition in the Table 2 User can feel the location of an obstacle via the user cognitive pattern in accordance with the data measured by the ultrasonic sensor.

4 Pattern Analysis

The user cognitive vibration pattern has defined in the Table 2 the pattern is realized using Morse code defined in the Table 3. The vibration motor consists of two DC motors. The first motor, P-Motor-1 (Pattern Motor-1) implements pattern depending on the position of the obstacle, and the second motor, P-Motor-2 implements the pattern depending on the distance from the obstacle. Figure 9 (a) shows the pattern 0, 1, 2, 3 of Table 2. Pattern 0 corresponds to the situation 1 which means that the robot detects no obstacle on the front and left and right side of the robot and both motors

Table 3. Input • output Fuzzy rules

	Morse Code
L	● ■ ● ●
LC	● ■ ● ● ■ ● ■ ●
C	■ ● ■ ●
RC	● ■ ● ■ ● ■ ●
R	● ■ ●
F	● ● ■ ●
RL	● ■ ● ● ■ ● ●



(a) pattern(0-3)

(b)pattern(4-7)

Fig. 9. Vibration pattern analysis

does not work. Pattern 1 corresponds to the situation 2 which means that an obstacle detected on the left side of the robot and operates defined pattern. Pattern 2 corresponds to the situation 3 which means that obstacles are detected from the front and left side of the robot. Pattern 2 corresponds to the situation 3 which means that obstacles are detected from the front and left side of the robot. Pattern 3 corresponds to the situation 4 which means that obstacles are detected only from the front of the robot.

Figure 9 (b) shows the pattern 4, 5, 6, and 7. Pattern 4 corresponds to the situation 5 which means that obstacles are detected from the front and right side of the robot. Pattern 5 corresponds to the situation 6 which means that obstacles are detected only from the right side of the robot. Pattern 6 corresponds to the situation 7 which means that obstacles are detected on the front and left and right side of the robot. Pattern 7 corresponds to the situation 8 which means that obstacles are detected on the left and right side. The vibration motor, P-Motor2, representing the distance from an obstacle increases in the shape of staircase. This means that the rotation speed of the motor is getting faster, as the distance from the obstacle is getting closer.

5 Experiment and Result Analysis

Figure 10 shows the experimental environment. This experiment was conducted on the second floor lobby, Samsung educational-industrial complex building of Pusan



Fig. 10. Experimental Environment

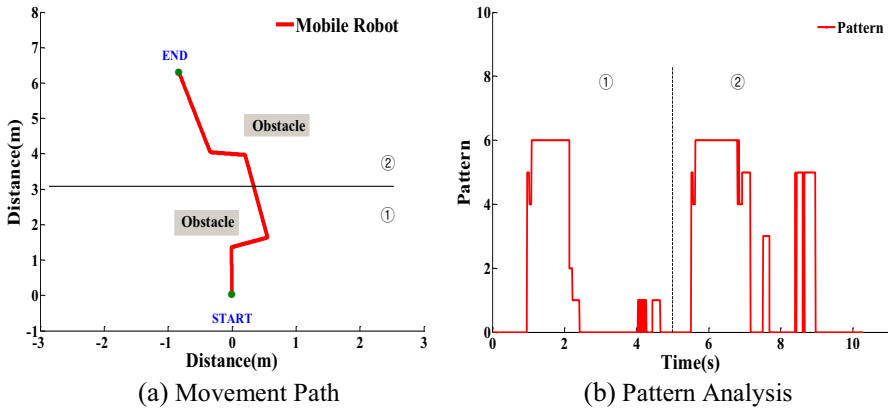


Fig. 11. Experiment 1

National University. We have conducted test under various environments to prove the validity of the vibration pattern suggested in this paper.

Figure 11 (a) shows the movement path that the mobile robot went by avoiding obstacles. We have configured experimental environment by placing the two obstacles, and the mobile robot moved from the start point to the end point. In this case, operator controls the mobile robot with a joystick 5m or more away it, ultrasonic sensors recognize obstacles while the robot is moving along the path and performs force feedback depending on the situation. Figure 11 (b) shows the result of force feedback analysis, which was obtained from the experiment 1 conducted with deploying one obstacle on the robot’s left and right side respectively.

Figure 11(b) shows pattern depending on the situation of the mobile robot and the obstacles, C-vector means the size of collision vector representing the distance between an obstacle and the robot. In the Figure 11 (a), section ① shows that the mobile robot recognizes an obstacle and avoids it according to the vibration pattern, and the vibration pattern is shown in the section ① of the Figure 11 (b) and the last part of the section ① is where noise occurred in the collision and vibration pattern. This noise occurred because the robot detected an obstacle on its left as the robot makes a second turn. The noise on the last part of the section ② of the Figure 11 (b) has occurred with the same reason.

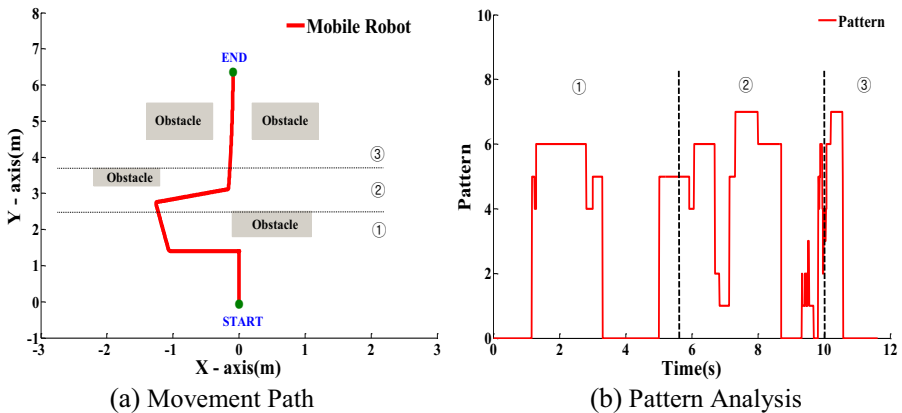


Fig. 12. Experiment 2

Figure 12 (a) shows the movement path that the mobile robot went by avoiding obstacles under the environment of experiment 2. We have placed additional obstacles for experiment 2 to implement more various pattern than experiment 1. We have placed obstacles sequentially like experiment 1 and additional obstacles are placed on the left and right side to check the user cognitive pattern. Figure 12 (b). Shows the analysis of force feedback according to the obstacle recognition on the movement path of the Figure 12 (a). The noise occurred on the last part of section ② in the Figure 12 (b) because the robot detected another obstacle instantly while the

robot makes a turn and cannot recognize the pattern. The noise occurred in the section ③ of the Figure 12 (b) was generated when it is approaching between obstacles. Noise generated because obstacle detected by overlapped ultrasonic sensors, and the pattern could not be recognized instantly. Accurate vibration pattern displays normally after the robot enters between the obstacles.

6 Conclusion

In this study, operator remotely controlled a mobile robot using the user cognitive joystick with vibration pattern and we evaluated the performance of the joystick. We have checked whether the overlapped ultrasonic sensor can detect an obstacle or not and check the accuracy of the measured distances data. We have implemented vibration pattern with the two vibration motors mounted on the bottom of the joystick by adjusting the intensity of vibration depending on the calculated collision vector based on the distance and the velocity of the robot. In addition to this, we have designed fuzzy controller depending on the position of obstacles to create patterns to deal with each situation. We have realized patterns to deal with each situation along the movement path of the mobile robot by placing obstacles to make experimental environment and controlling the robot by operator and we have demonstrated the validity of the pattern by performing the test to recognizing obstacles position and distance. However, while the mobile robot switching the direction, noise occurred and system instability if the robot detects an obstacle. In addition to this, the correct movement path cannot be implemented because the resolution of the encoder used in the experiment was too low. We will figure out the ways to solve these problems and will design the filter to remove the noise to implement more stable Force Feedback in the future.

Acknowledgement. "This research was supported by the MKE(The Ministry of Knowledge Economy), Korea, under the Human Resources Development Program for Specialized Navigation/Localization Technology Research Center support program supervised by the NIPA(National IT Industry Promotion Agency) (NIPA-2012-H1502-12-1002).

This research was financially supported by the Ministry of Trade, Industry & Energy (MOTIE), Korea Institute for Advancement of Technology (KIAT) through the Inter-ER Cooperation Projects.

References

1. Kim, H.-N., Kim, H.-J.: A study on the obstacle avoidance using ultrasonic sensors for a mobile robot. In: Proceedings of KIIS Spring Conference, vol. 20(1), pp. 373–375 (2010)
2. Weinstein, S.: Intensive and extensive aspect of tactile sensitivity as a function of body part, sex, and laterality. In: Kenshalo, D.R. (ed.) *The Skin Sense*, pp. 195–218. Springfield (1968)

3. Jin, T.: Object avoidance of Mobile Robot with Virtual Impedance. In: Proceedings of KIIS Conference, vol. 19(4), pp. 451–456 (2009)
4. Kim, S., Lee, S.: Positional uncertainty reduction of overlapped ultrasonic sensor ring for efficient mobile robot obstacle detection. *J. Institute of Signal Processing and Systems* 10(3), 198–206 (2009)
5. Kim, S., Lee, S.: Design of overlapped ultrasonic sensor ring and its application to obstacle detection. *J. Institute of Signal Processing and Systems* 11(1), 63–73 (2010)
6. Jeon, C.S., Cho, S.K., Lee, J.M.: Tele-operation of a Mobile Robot Using Force Reflection Joystick with Single Hall Sensor. *The Journal of Korea Robotics Society* 1(1), 17–24 (2006)
7. Kyung, K.U., Park, J.S.: The State of the Art and R&D Perceptives on Haptics. *Electronics and Telecommunications Trends* 21(5), 93–108 (2006)
8. Kim, H., Kyung, K.-U., Park, J., Han, D.: The state-of-the-art on Haptic Interface. *Journal of Information Technology* 8(1), 7–15 (2010)
9. Kim, M.C.: The present and the future of haptic interfaces. *Weekly Technology Trends* 1204, 28–364 (2005)
10. Huang, C.-H., Wang, W.-J., Fellow, Chiu, C.-H.: Design and Implementation of Fuzzy Control on a Two-Wheel Inverted Pendulum. *IEEE Transactions on Industrial Electronics* (10-0227-TIE.R2) (2010)
11. Lee, Y.-H., Jin, G.-G., Choi, H.-S., Park, H.-I., Jang, H.-L., So, M.-O.: Fuzzy Rule Based Trajectory Control of Mobile Robot. *Journal of the Korean Society of Marine Engineering* 34(1), 109–115 (2010)

Position Detection Performance Improvement for LSM Control in Super Speed Maglev

Jinho Lee, Jeongmin Jo, Youngjae Han, and Changyoung Lee

Super Speed Maglev Train Research Team,
Korea Railroad Research Institute, Korea
{jinholee, jmjo, yjhan, cylee}@krri.re.kr

Abstract. To control the linear synchronous motor(LSM) which is used for super speed maglev, the precise position data of high speed running train is needed for generation of synchronized current which is supplied to the stator attached on the guideway. Also to reduce the amount of current input to the stator, the whole guideway is divided into several sections and the power is supplied to the only one section which the train is running on. The poor performance of position detection causes the degradation of LSM propulsion efficiency. Also, the poor section change due to bad LSM control causes the fluctuation of vehicle, which decreases the comfortability. In this study, to evaluate the influence of position detection performance on the LSM and section control, the infinite loop type testbed is developed, and improvement method was investigated.

Keywords: Maglev Train, Linear Synchronous Motor, Propulsion, Control, Position Detection, Section Control.

1 Introduction

As a propulsion device for super speed maglev, the linear synchronous motor(LSM) is suitable, since LSM has good performance in several aspects such as rapid acceleration, large capacity and high efficiency. However, to control LSM, the running maglev position information must be fed back to the power inverter to synchronize the output current phase. Therefore, the precise position detection technique is important for higher efficiency and power performance. And since LSM stator is attached on the guideway, to supply the propulsion power to the whole guideway is too much waste of electric power. To minimize the input power, the guideway is divided into several sections and the power is supplied to the only one section which the train is running on. Therefore smooth section change based on the well-controlled propulsion is necessary to mitigate the vibration and noise when train moves from one section to the other section. In this study, to evaluate the influence of position detection performance on the LSM and section control, the infinite loop type testbed is developed, and improvement method was investigated through the experiments.

2 Test Bed

2.1 System Overview

The overall system configuration is shown in Fig. 1. The diameter of the loop type guideway is about 5m and the section is divided into 3. Each inverter provides power to inner and outer guideway alternately by 60 degree. The vehicle has permanent magnets for propulsion and 4 wheels for support and guidance respectively. The position of the maglev is detected through the bar code attached around the guideway side.

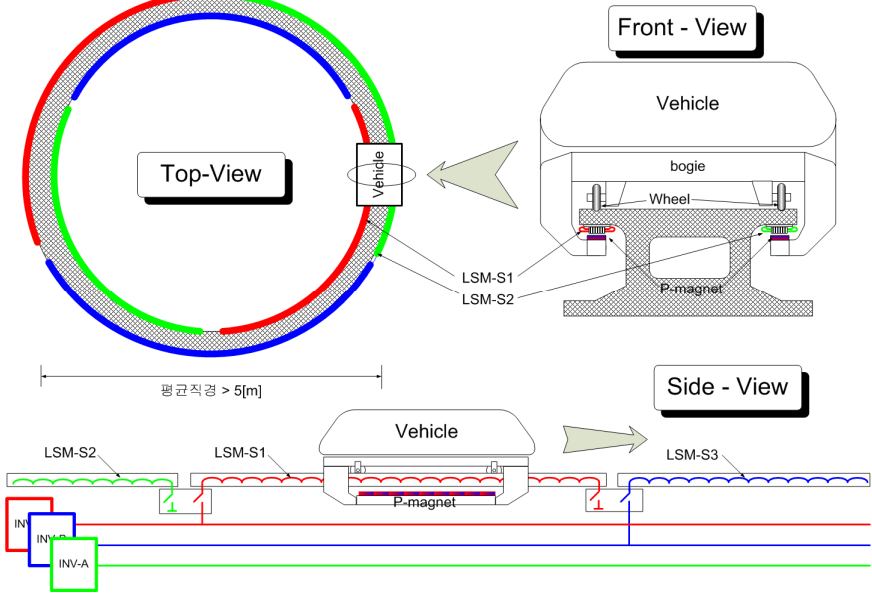


Fig. 1. Overall system configuration of test bed

2.2 Vehicle

For smooth driving, there is a length difference between the inner and outer permanent magnet attached under vehicle as shown in Fig. 2(a). Inside of the mockup frame, acceleration sensors, position detecting device and battery are placed as shown in Fig. 2(b). The final appearance of the manufactured vehicle is shown in Fig. 2(c).

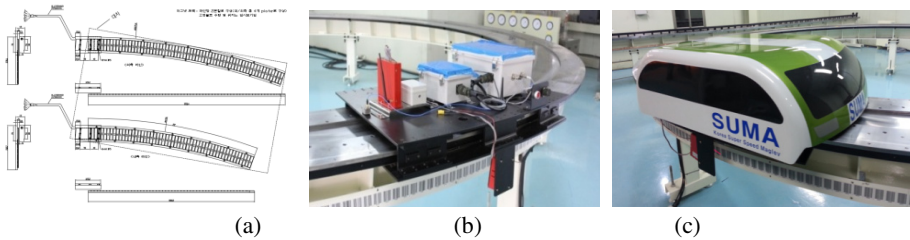


Fig. 2. Vehicle

2.3 Guideway

Whole guideway is made from SS400 and the LSM whose specification is shown in Table 1 is attached under the guideway. Total 36 LSMs are located in the inner and outer side as shown in Fig. 3(a). The bar code for vehicle position detection is attached around the guideway side shown in Fig. 3(b). The final appearance of the manufactured guideway is shown in Fig. 3(c).

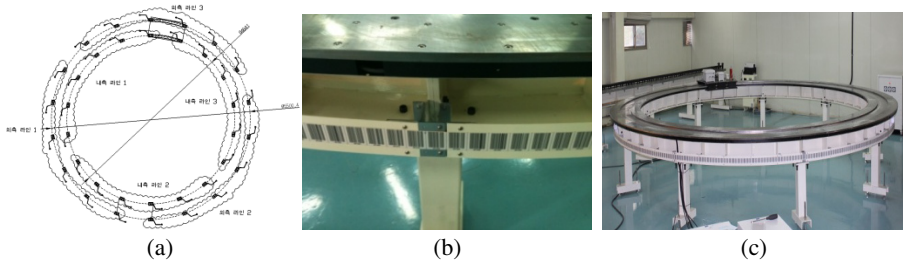


Fig. 3. Guideway

Table 1. Specification of LSM

Peak Force	Continuous Force	Continuous Current	Peak Current	Force Constant	Motor Constant	Thermal Resistance	Attraction Force	Moving Coil Mass
N	N	Arms	Arms	N/Arms	N/W1/2	°C/W	N	kg
138	46	2.4	7.2	19.2	6.6	1.9	110	1.4

2.4 Inverter and Measurement System

As shown in Fig. 4(a) and 4(b), inverters containing the power module, DSP controller, DC link capacitor, power supply, current detecting sensor and heat sink are manufactured. For data monitoring such as vehicle acceleration, output current and inverter input/output command, the measurement system shown in Fig. 4(c) and 4(d) is also developed.

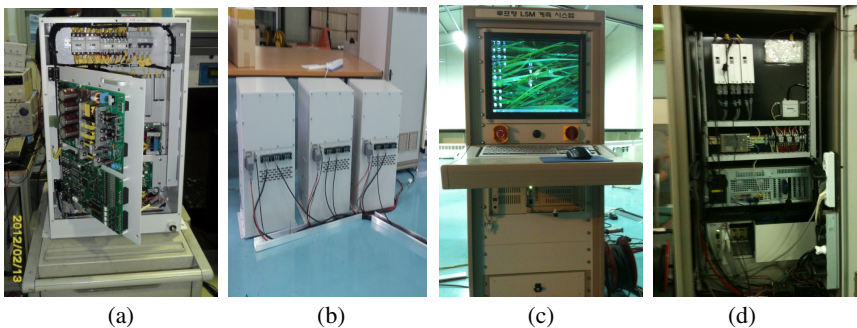


Fig. 4. Inverter and measurement system

2.5 Control Algorithm

As LSM control algorithm, general d-q control logic is applied as shown in Fig. 5. The position data is gathered from bar code and transmitted through the CAN communication. For the section change, by using the current position data of running vehicle, ON/OFF operation of contactor, PWM and current supply from inverter are sequentially provided by DSP controller.

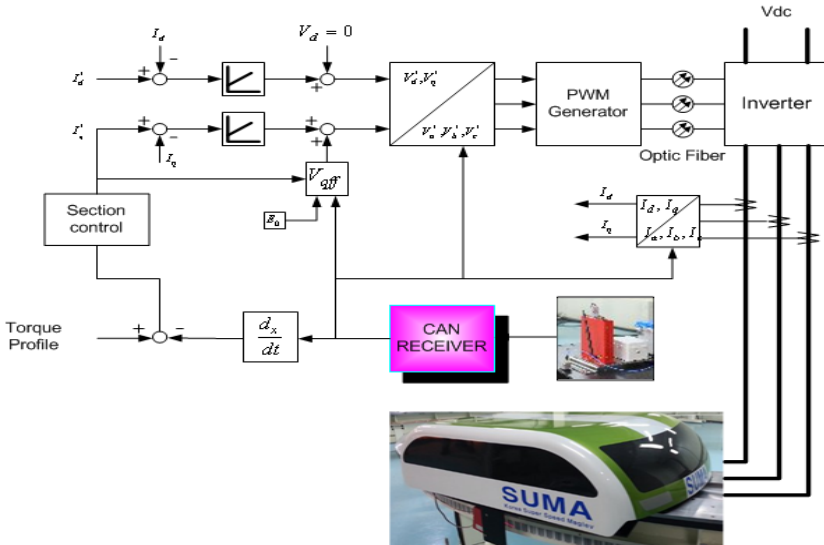


Fig. 5. LSM and section control

Fig. 6 shows the photograph of completely manufactured testbed.

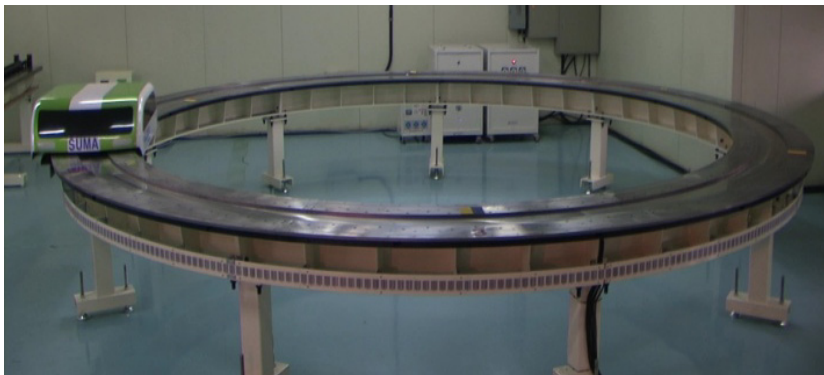


Fig. 6. Testbed for LSM and section control

3 Experiments

3.1 Delay of Position Data Transmission

Fig. 7(a) shows the signal delay of position data from bar code reading. This result indicates that the delay is 2ms and 1% jitter. Since the amount of jitter is negligible, this delay time could be compensated by simple arithmetic calculation. The real position data gathered during 2 turns is shown in Fig. 7(b).

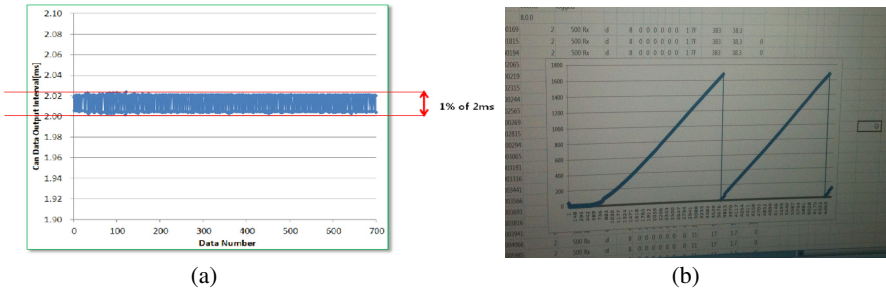


Fig. 7. Position detection through bar code

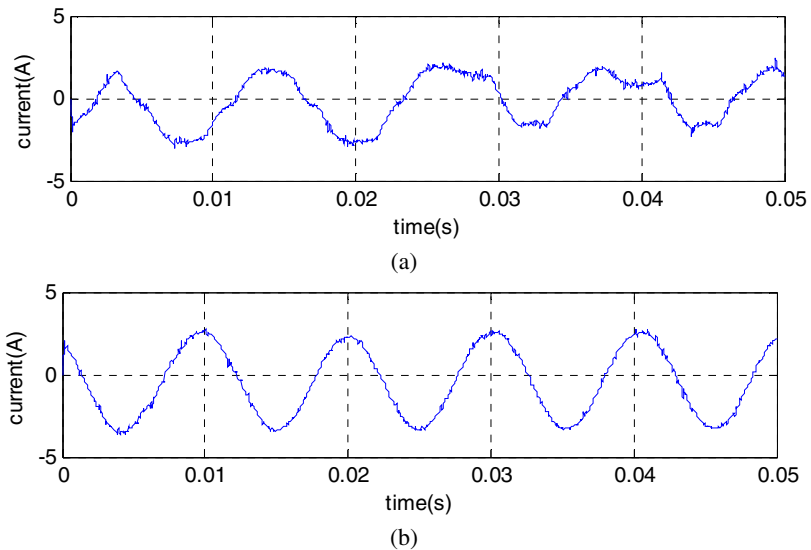


Fig. 8. Compensation of omitted position data

3.2 Compensation of Omitted Position Data

Since the position data receiving rate is much slower than the control rate, only a few position datum are used for current synchronization, resulting the poor output current profile shown in Fig. 8(a). By using predicted equation, more precise position data could be created and consequently the current profile is improved as shown in Fig. 8(b).

3.3 Compensation of the Delayed and Omitted Position Data

Detected position data should be compensated for exact synchronization with current generation. Fig. 9(a) shows the vehicle's acceleration without the compensation of the detected position data in one section. And Fig. 9(b) shows the vehicle's acceleration when in all three sections, the position data is compensated. Due to the uncompensated section, the tangential and radial acceleration is decreased temporarily and this would result in the uncomfortableness. Moreover, the average radial acceleration is decreased due to the overall propulsion power degradation caused by improper position detection.

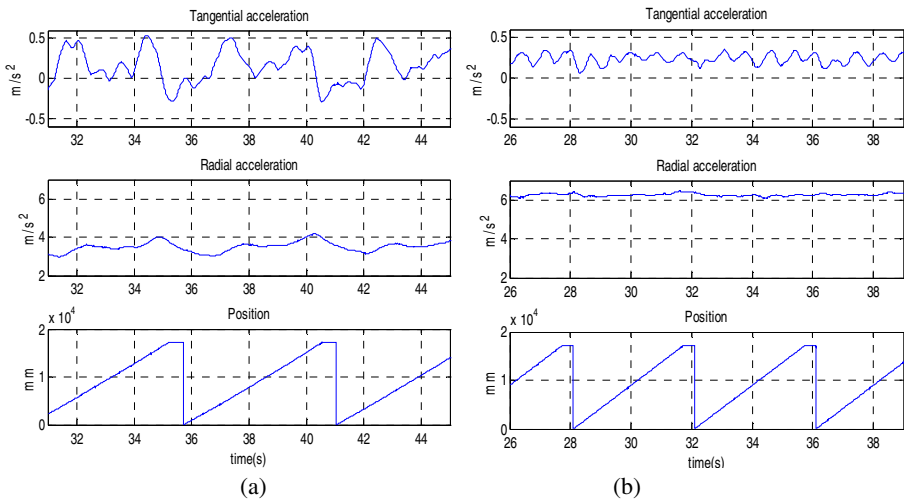


Fig. 9. Vehicle acceleration

3.4 System Performance

After position detection performance is improved, the system performance is evaluated through the running test and the results are shown in Fig. 10. The maximum speed and acceleration is up to $4m/s$ and $1.5m/s^2$ respectively. The Fig. 11 shows the output current from 3 inverters during running, which explains that the section is well changed in sequence.

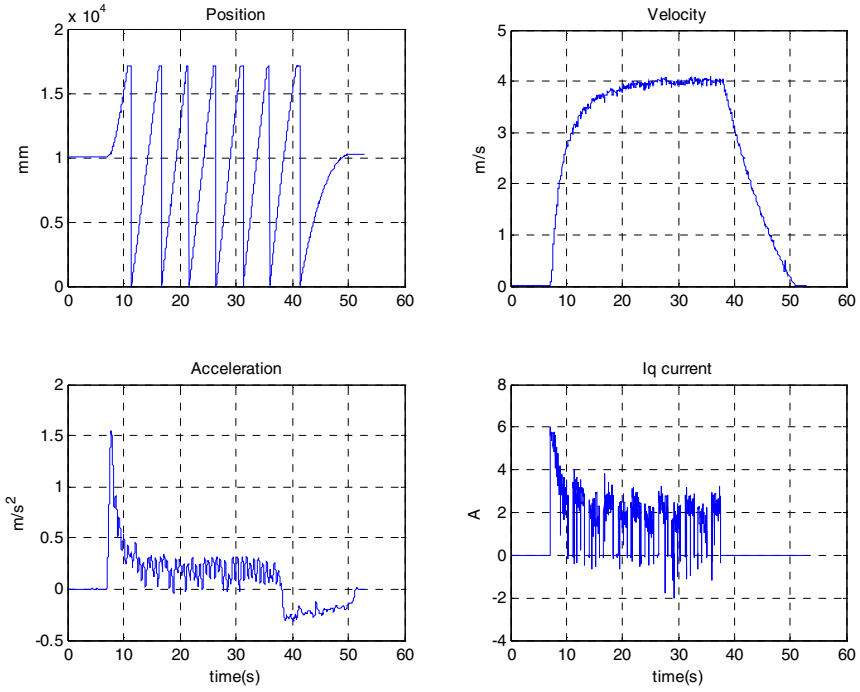


Fig. 10. Running test result

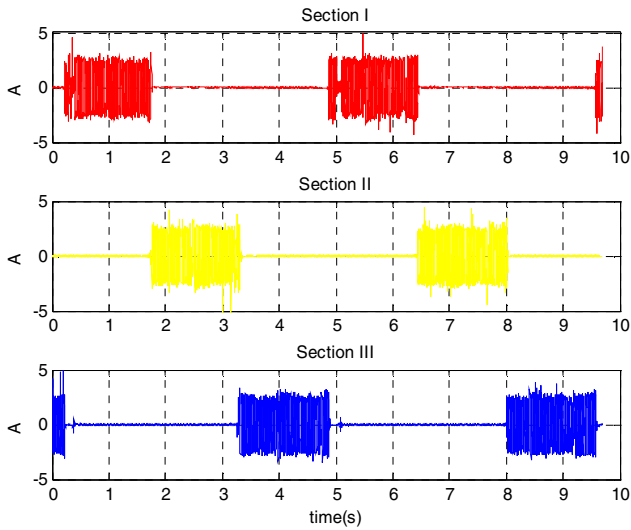


Fig. 11. Section change

4 Conclusion

In this study, to evaluate the influence of position detection performance on the LSM and section control, the infinite loop type testbed is developed, and improvement method was investigated. Experiment results show that the delay and omission of the position data cause the degradation of the LSM propulsion and section change. By applying the compensation method, the system performance such as acceleration was improved. Investigated method in this study would be utilized for the real-size super speed maglev development which is currently being carried out.

Acknowledgments. This work was supported by Core Technology Development Project of Super Speed Maglev Train funded by Ministry of Land, Infrastructure and Transport. (11PRTD-B061485).

References

1. KRRI, Development of Loop-type LSM Testbed and Interface Technology between Maglev and Guideway (completion report) (2012)
2. Lee, J., Han, Y., Jo, J., Lee, C.: Development of Loop Type LSM Testbed for Section Control. In: Spring Conference of the Korean Society for Railway, p. 74 (2012)
3. Qian, C., Wei, R., Wang, X., Ge, Q., Li, Y.: Analysis the Position Signal Problem In Propulsion System With Long Stator Linear Synchronous Motor. In: The 21st International Conference on Magnetically Levitated Systems and Linear Drives (October 2011)
4. Lee, J., Jo, J., Han, Y., Lee, C.: Development of Propulsion Testbed for Super Speed Maglev. In: Spring Conference of the Korean Society for Railway, p. 151 (2013)

Network Aware Resource Allocation Scheme for Mobile Ad Hoc Computational Grid

Sayed Chhattan Shah¹, Myong-Soon Park², Wan Sik Choi¹,
Sajjad Hussain³, and Ali Kashif Bashir⁴

¹ Electronics and Telecommunications Research Institute, South Korea

² Department of Computer Science and Engineering, Korea University, South Korea

³ LS Industrial Systems Co, LTD. Anyang- 431-080, South Korea

⁴ National Fusion Research Institute, Daejeon, South Korea

{Shah, Choiws}@etri.re.kr

Abstract. Mobile ad hoc computational Grids are characterized by unreliable and dynamic communication environment. The bandwidth at different network portions varies over the time and different nodes often experience different connection quality at the same time due to traffic load and constrained communication environment. Therefore, an effective and robust resource allocation scheme should consider connection quality between nodes in addition to other factors such as transmission power, processing speed and task size. In this paper, two resource allocation schemes are described with their pros and cons. The first resource scheme exploits transmission power control mechanism in order to improve energy efficiency and network capacity whereas the second resource allocation scheme takes into account the connection quality and traffic load in order to reduce data transfer time. The relationship between data transfer time and transmission energy consumption has also been investigated in detail. The schemes are validated in a simulated environment using various workloads and parameters.

Keywords: Mobile Grid, Computational Grid, Resource Management.

1 Introduction

We envision a scenario in which a group of miniature autonomous mobile robots are deployed in urban environment to detect, identify, monitor and report a comprehensive range of military and non-military threats. To detect abnormal situations or threats, sophisticated image and video processing algorithms are used [1-2]. In addition to threat detection algorithms, robots also use vision-based navigation algorithms to navigate in environment [3] and perform several other tasks [4]. The processing of such computationally-intensive tasks requires an enormous computational power, often beyond capabilities of single miniature mobile robot. Therefore to process computationally-intensive tasks a distributed computing infrastructure is required to allow mobile robots to share computing resources on demand.

A distributed computing infrastructure which allows mobile robots to share computing resources on demand without pre-existing network infrastructure is known as a mobile ad hoc computational Grid [4]. Mobile ad hoc computational Grid is an integration of computational Grid and mobile ad hoc network. Computational Grid is a software infrastructure that allows distributed computing devices to share computing resources to solve computationally-intensive problems. Whereas mobile ad hoc network is a wireless network of mobile devices that communicate with each other without any pre-existing network infrastructure.

Resource allocation is a central task in any parallel and distributed computing system. Compared to traditional infrastructure-based distributed systems such as Grids and Clusters, mobile ad hoc computational Grids are characterized by shared and unreliable communication medium, low bandwidth, high latency, limited battery power, node mobility and infrastructure-less network environment. Therefore, resource allocation schemes proposed for traditional distributed systems cannot be applied to mobile ad hoc computational Grids.

Previously we proposed a power-based resource allocation scheme [4] to improve energy efficiency and network capacity. The basic idea is to exploit transmission power control mechanism and allocate data-intensive dependent tasks to nodes accessible at minimum transmission power. Since energy consumption is proportional to transmission power, communication at minimum required transmission power reduced energy consumed in transmission of data.

Since mobile ad hoc computational Grids are characterized by unreliable and dynamic communication environment, bandwidth at different network portions varies over the time and different nodes often experience different connection quality at the same time due to traffic load and constrained communication environment. Therefore, an effective and robust resource allocation scheme should consider connection quality between nodes in addition to other factors such as transmission power, processing speed and task size.

In this paper, we describe two resource allocation schemes with their pros and cons. First, we describe our previous resource allocation scheme [4] based on transmission power control mechanism which aims to improve energy efficiency and network capacity. Then, we propose a network aware resource allocation scheme that takes into account the connection quality and traffic load in order to reduce data transfer time. The relationship between data transfer time and transmission energy consumption has also been investigated in detail.

2 System Models

A mobile ad hoc network is modeled as an undirected graph $G_N = (N, L, p, m, b)$ where N is set of vertices representing mobile nodes and L is set of edges representing communication links among them. The nodes within a network can use multiple transmission power levels and are heterogeneous in terms of processing power, memory and battery power. The energy consumption rate for data transmission is same for all nodes. Nodes communicate with each other through message passing and

communication between tasks assigned to same node is negligible. We also assume that nodes do not move across the coverage area and are configured with IEEE 802.11 MAC protocol. Node mobility is addressed in [19].

A parallel application is modeled as a graph $G_A = (T, C)$ where T is the set of vertices representing data-intensive tasks and C is the set of edges representing dependencies between tasks. The tasks within an application are non-preemptive and indivisible work units. The dependencies are divided into two categories: precedence dependencies and parallel execution dependencies. The precedence dependencies are represented by directional edges and parallel execution dependencies are represented by un-directional edges. The tasks with precedence dependencies execute independently but require inputs generated by predecessor tasks while tasks with parallel execution dependencies periodically exchange data with one another and communication between tasks may take place anytime during execution.

3 Resource Allocation

In order to make allocation decisions there are three possible cases:

- (1) Allocation of independent task t_i
- (2) Allocation of task t_i that has dependency on already allocated task t_r
- (3) Allocation of interdependent task set T^*

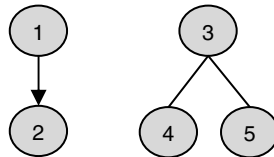


Fig. 1. Three possible cases: task 1 is independent while task 2 has dependency on task 1. Tasks 3, 4 and 5 form an interdependent task set. Task 3 has parallel execution dependency with task 4 and 5 and vice versa.

In this paper our focus is on allocation of interdependent task set. Interdependent task set consists of multiple tasks with parallel execution dependencies. In addition, task set can have dependencies on already allocated task or can be independent. In order to reduce data transfer cost and thus task completion time interdependent tasks in a set should be allocated simultaneously to closely located nodes [4].

When more than one interdependent task needs to be allocated simultaneously to closely located nodes, the basic problem is to search a group of closest nodes within a Grid. More specifically, the problem is to search k closest nodes in a Grid to allocate m interdependent tasks, where $k \geq m$.

3.1 K-Nearest Neighbor Problem

The problem of searching a group of closest nodes in a Grid is modelled as a k-nearest neighbour (kNN) search problem in graph theory. The kNN graph is a weighted directed graph $G(U, E)$ connecting each element to its k-nearest neighbours [5]. A fundamental problem for graphs is to efficiently search the k nodes closest to some specific node.

K-Nearest Neighbor Search Algorithm

In order to search kNN, one option is to use distance-based kNN search algorithms [5-9], whose complexity depends on input graph G . However, a key motivation to search kNN in this study is to reduce energy consumption and communication cost. Therefore, it is not important to search kNN based on distance, because nodes accessible at the same TPL have the same energy consumption and communication cost. For example, when a node that uses fixed and maximum transmission power communicates with two neighbouring nodes, one at a distance of 10 m and the other at a distance of 200 m, the communication with both nodes incurs the same cost [4].

```

Integer i=1
List kNNList = null
While (i<=n) {
    Broadcast a discovery message at  $TPL_i$ 
    Collect replies from nodes accessible at  $TPL_i$ 
    Add nodes to kNNList
    If (number of nodes in kNNList  $\geq$  k) then
        Exit the while loop
    Else
        i++
} Calculate weight using equation given below.

```

Algorithm 1: Pseudo code of kNN search

Therefore, to reduce the energy consumption and communication cost we propose a simple kNN search algorithm based on transmission power control (TPC) mechanism. In order to search kNN, each node broadcasts a discovery message at minimum TPL. When the number of nodes discovered is larger than or equal to k, the search process stops and discovered nodes are declared as kNN; otherwise the node uses the next TPL. For details see Algorithm 1.

After a node finds its kNN, the next step is to search for the optimal node with kNN. For example, Figures 2 and 3 show two source nodes X and Y with four nearest neighbours in green colour. Node X has access to two nodes at TPL 1 and two nodes at TPL 2, while node Y has access to one node at TPL 1, one node at TPL 2, and two

nodes at TPL 4. Since energy consumption is proportional to transmission power, communication consumes less energy at the lower TPL than at the higher TPL. Due to this, the allocation of the task set to node X will consume less energy compared to allocation to node Y.

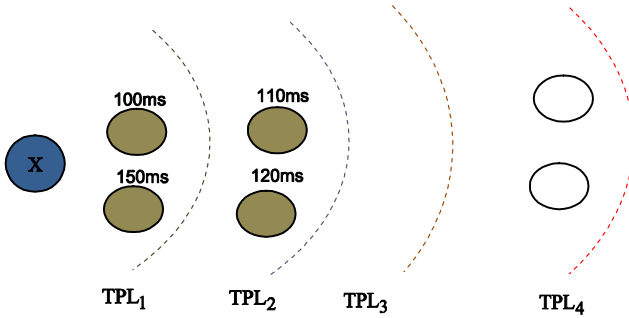


Fig. 2. Node X with 4NN

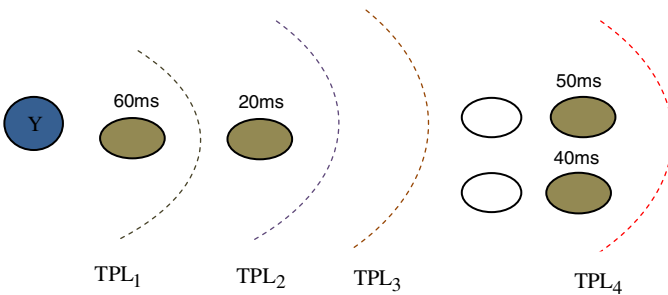


Fig. 3. Node Y with 4NN

In order to distinguish among optimal and suboptimal nodes with kNN, we introduce a weight function based on TPL and the number of nodes accessible at that TPL. The lower TPL has more weight than the higher TPL. Once a node discovers its kNN, it uses the weight function to determine its weight. The highest weight implies that allocation of tasks to this node and its kNN will consume less energy.

$$n_i^w = \sum_{i=1}^l TPL_i^w \cdot N_{TPL_i}$$

TPL_i^w = weight of TPL_i
 n_i^w = weight of node n_i
 l = number of transmission power levels
 N_{TPL_i} = number of nodes accessible at TPL_i

3.2 Transmission Power-Based Allocation Scheme

The basic idea is to allocate interdependent tasks to nodes that accessible at minimum transmission power. In order to allocate tasks, resource allocation service first selects a node with highest weight and then allocates tasks to its kNN.

The allocation based on transmission power offers three key advantages: reduced energy consumption, increased network capacity, and reduced complexity of kNN search algorithm. The tasks executed on two closely located nodes accessible at minimum TPL do not require maximum TP to communicate, which can significantly reduce energy consumption and increase network capacity [10-13]. Moreover, the complexity of the kNN search algorithm depends on the number of TPLs rather than the number of nodes within a Grid. The reader is referred to [4] for a detailed description of the kNN search algorithm and transmission power-based resource allocation scheme.

3.3 Dynamic Bandwidth Problem

Mobile ad hoc computational Grids are characterized by unreliable and dynamic communication environment. The bandwidth at different network portions varies over the time and different nodes often experience different connection quality at the same time due to traffic load and constrained communication environment. This is demonstrated in Figure 4. Since the connection quality between nodes within a Grid is not same and keeps changing an effective and robust resource allocation scheme should consider connection quality between nodes in addition to other factors such as transmission power, processing speed and task size. A resource allocation scheme which does not consider connection quality and network load can lead to performance degradation [4].

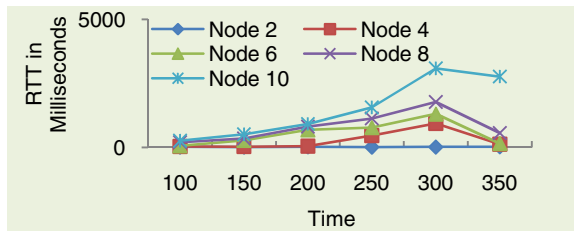


Fig. 4. Demonstrates how connection quality changes over the time. Even nodes at the same time have different performance.

In this section, we first define a term connection quality and then present network aware resource allocation schemes which make allocation decisions based on connection quality between nodes.

Connection Quality

In this study, connection quality is measured in terms of round trip time, packet loss probability and medium access delay. An equation to calculate connection quality is given below:

$$C_j = \left(\frac{P_{\text{size}}}{T_{\text{ready}} - T_{\text{received}}} \right) * P_{\text{loss}}$$

C_j = Connection quality
 P_{size} = Packet Size
 T_{ready} = Time packet is ready to be transmitted
 T_{received} = time acknowledgement received
 P_{loss} = Packet loss ratio

Similar metrics have also been used in [14], [16]. They only differ with respect to number of parameters taken into consideration. For example, a scheme proposed in [14] does not consider time to gain access to medium and also demonstrate that medium access delay does not have significant impact on the performance. The experiments were conducted with medium network size and moderate network load. On other hand, schemes such as [15], [16] have reported that medium access delay plays a significant role as number of nodes and data transfers increase within a network.

3.3.1 Network Aware Resource Allocation Schemes

Naïve Approach: In order to make allocation decisions resource allocation service maintains connection quality information for each pair of nodes. Whenever connection quality changes information maintained at resource allocation service is updated. The key advantage of naïve approach is effective resource allocation decisions due to network-wide view. However, it is very expensive in terms of communication cost. In addition, with small task size and hence data transfers, control traffic may dominate the actual data transfer cost and may degrade the performance of task.

KNN-Based Approach: Instead of maintaining connection quality information for each pair of nodes, kNN-based approach maintains connection quality information of kNN of each node. The nodes in Grid discover their kNN based on transmission power control mechanism and send connection quality information of their kNN to resource allocation service. Resource allocation service decides allocation based on connection quality of nodes and their kNN. This approach reduces communication cost because only kNN information is maintained. However, it increases processing burden on a single node and may result into ineffective allocation decisions due to restricted view of nodes' neighbors.

A Rank-Based Approach: The nodes maintain connection quality information of their kNN. Based on connection quality, they calculate their rank and send that to resource allocation service. The decision making is divided into two levels: at level-1 resource allocation service selects a node with highest rank while at level-2 node

selected at level-1 allocates tasks to its kNN based on connection quality. Since network environment is dynamic, each node calculates its rank at regular intervals. If new calculated rank is greater than threshold it is sent to resource allocation service. It has also been observed that sometime connection quality changes for a short time and then becomes stable. Calculation of rank based on short term information may be misleading. To avoid this problem connection quality is monitored for time interval X and then is compared against a threshold value to decide whether to send it or not. The equation to calculate node's rank is given below:

$$R_i^{\text{total}} = \sum_{j=1}^k C_j$$

C_j = Connection quality between node n_i and n_j
 n_i^r = rank of node n_i
 k = # of nearest neighbors

$$n_i^r = \frac{R_i^{\text{total}}}{k}$$

3.4 Comparison between Transmission Power-Based and Network Aware Resource Allocation Schemes

Compared to transmission power-based allocation, allocation based on connection quality may restrict parallel transmissions and thus network capacity. In addition, it may consume more energy. So there is trade-off between transmission power-based allocation and network-aware allocation. This is demonstrated in Figures 2 and 3. In case of transmission power-based allocation tasks should be allocated to node X because neighbors of node X are accessible at minimum transmission power, which would increase energy efficiency and network capacity. While data transfer cost between tasks would be high due to high latency. In case of network aware allocation, tasks should be allocated to node Y which will improve data transfer times but would reduce network capacity and energy efficiency. The relationship between these two schemes is further explored in section 4.

4 Simulation Results

The performance of network aware rank-based resource allocation scheme is compared with power-based resource allocation scheme [4] which allocates interdependent tasks to nodes based on transmission power control mechanism.

4.1 Simulation Setup

The network simulator NS2 was used for performance evaluation with a wide range of scenarios. In order to make allocation decisions, three key services were implemented: monitoring service, discovery service and resource allocation service. Monitoring service runs on nodes willing to share computing resources while resource allocation and discovery services execute on node that requires additional computing resources. Node monitoring service listens for requests to share computing resources

and keeps track of task's execution. Resource discovery service broadcasts request messages and collects replies while resource allocation service makes allocation decisions based on criteria described in section 3. In addition, each node within a Grid runs a kNN search algorithm, maintains a list of kNN, sends weight or rank to resource allocation service, and also runs a customized version of resource allocation service to allocate tasks to its kNN.

An application submitted to resource allocation service included various number of interdependent tasks with mix workload. Tasks are simple programs that transfer data to their dependent tasks.

4.2 Simulation Results

Scenario 1: Fifteen nodes were deployed in groups of varying size. The largest group consisted of 6 nodes while smallest group had 2 nodes. The distance between nodes within a group was 20-50 m and across the group was 100-250 m. Each node had three nearest neighbors and was able to transmit at three transmission power levels. Before allocation constant bit rate traffic was started between some randomly chosen nodes within a network.

Applications submitted to resource allocation service consisted of interdependent task sets. The maximum numbers of tasks in a set were 3 while smallest task set had 2 interdependent tasks. The ratio of interdependent task set of size 3 to interdependent task set of size 2 was 1:1. Each task transferred data of size 4-8 megabytes. The inter-packet interval was in range of 10ms to 300ms. All tasks had same execution cost because we are only concerned with communication performance of interdependent tasks.

Scenario 2: Twenty nodes were deployed in groups of varying size. The numbers of nodes within each group were in range of 2-3. The distance between nodes within a group was 40-50 m and across the group was 150-250 m. Each node was able to transmit at three transmission power levels. The remaining setup was same as in Scenario 1.

Scenario 3: Twenty nodes were deployed in groups of fixed size. Each group consisted of four nodes. The distance between nodes within group was 50-100 m and across the groups was 100-250 m. Each node was able to transmit at two transmission power levels.

Maximum numbers of tasks in a set were 4 while smallest task set had 3 interdependent tasks. The ratio of interdependent task set of size four to interdependent task set of size three was 2:4. Each task transferred data of size 4-8 megabytes. Inter-packet interval was in range of 10ms to 100ms. Large amount of data transfers were started at some network portions before task allocation process.

Accumulative Application Completion Time - AACT

AACT for Scenarios 1 and 2 is shown in Figures 5 and 6. As results show, rank-based resource allocation scheme improves performance by 3-5% in Scenario 1 and 10-15% in Scenario 2.

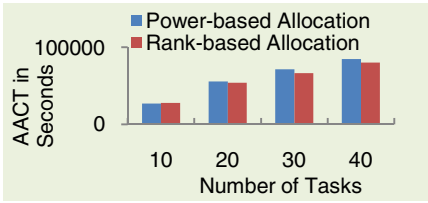


Fig. 5. AACT for Scenario 1

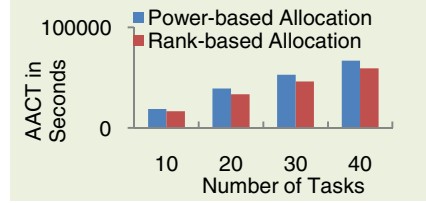


Fig. 6. AACT for Scenario 2

In Scenario 1, 15 nodes divided into two large groups and two small groups were deployed in the region. Due to less number of nodes and group of nodes, there were few choices for allocation. Therefore, performance gains are not significant. While in Scenario 2, large numbers of nodes were deployed into small groups, so there were several choices for allocation. Rank-based allocation scheme allocated task to nodes with better connection quality. Furthermore, when large numbers of tasks such as 30-40 were submitted, tasks were evenly distributed to nodes in order to balance the data transfer load in the network. Power-based allocation scheme allocated tasks to nodes based on transmission power and did not consider network conditions. Therefore, tasks were allocated to same group of nodes because they were accessible at minimum transmission power. This increased the data transfers and degraded the communication performance and connection quality between nodes in that region. Thus completion time of tasks allocated in that region was increased.

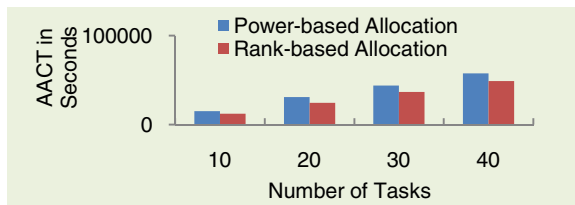


Fig. 7. AACT for Scenario 3

The results for Scenario 3 are given in Figure 7. As results show rank-based resource allocation scheme outperforms power-based allocation scheme and improves performance by 15-20%. This is because before allocation process we started TCP traffic between nodes in few groups to demonstrate an effectiveness of rank-based allocation in varying and rough network configuration. The groups of nodes where TCP traffic was started were experiencing worst communication performance. Rank-based allocation did not allocate task to that region while power-based allocation scheme preferred that region because nodes were accessible at less transmission power. Allocation of tasks to already overloaded network region increased data transfer time of tasks and thus task completion time.

In general, rank-based allocation outperforms power-based allocation when some network portions are highly overloaded and are experiencing worst connection quality.

Transmission Energy Consumption

Transmission energy consumption for Scenarios 1 and 2 is shown in Figures 8 and 9. As results show, performance of both schemes is almost same with 10 tasks, but with 20-40 tasks power-based resource allocation scheme reduces energy consumption by 2-3% in Scenario 1. Whereas in Scenario 2 ranked-based allocation scheme performs better and reduces energy consumption by 2%.

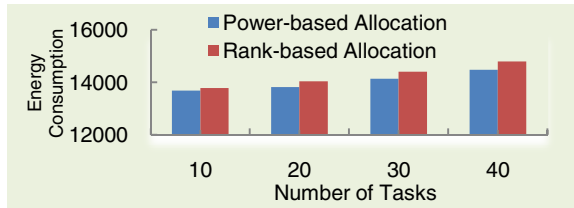


Fig. 8. Energy Consumption for Scenario 1

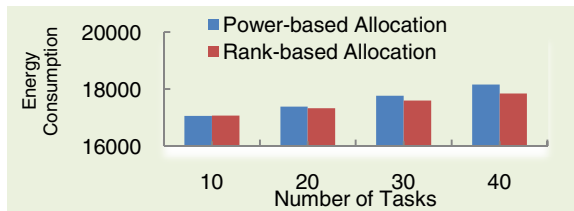


Fig. 9. Energy Consumption for Scenario 2

Since power-based resource allocation scheme allocates task to nodes accessible at minimum transmission power, it reduces energy consumption in Scenarios 1. In Scenario 2 power-based allocation scheme does not perform well because it allocates task to nodes without considering network characteristics. This results into network congestion and increases the number of lost and dropped packets and thus energy consumption. The energy consumed due to communication overhead is the only factor which degrades the performance of power-based allocation scheme.

5 Conclusion

In this paper two resource allocation schemes are described for allocation of data-intensive dependent tasks on mobile ad hoc computational Grids. First resource allocation scheme is based on transmission power control mechanisms and aims to improve energy efficiency and network capacity. The basic idea is to exploit transmission power control mechanism and allocate data-intensive dependent tasks to nodes accessible at minimum transmission power. The second scheme considers network characteristics and connection quality between nodes in order to reduce data transfer time between dependent tasks. Compared to power-based resource allocation

scheme, network aware allocation consumes more energy and restricts the number of parallel transmissions and thus network capacity. While power-based allocation scheme conserve energy but degrades the performance of data-intensive parallel tasks.

Acknowledgments. This research was a part of the project titled “WA-DGNSS Development” funded by the Ministry of Land, Transport and Maritime Affairs, Korea.

References

1. Mashburn, B.C., et al.: Graphics + Robotics + AI = Fast, 3D Scene Construction. In: 10th Midwest Artificial Intelligence and Cognitive Science Conference, April 23-25 (1999)
2. Falcou, J., et al.: A Parallel Implementation of 3D Reconstruction Algorithm for Real-Time Vision. *Parallel Computing* (2005)
3. Se, S., et al.: Vision-based global localization and mapping for mobile robots. *IEEE Transactions on Robotics* 21(3), 364–375
4. Shah, S.C., et al.: Energy-Efficient Resource Allocation Scheme for Mobile Ad Hoc Computational Grids. *Journal of Grid Computing Journal* (April 16, 2011)
5. Paredes, R., Navarro, G.: Practical construction of k nearest neighbor graphs in metric spaces. Technical Report TR/DCC-2005-6, Dept. of Comp. Sci. Univ.
6. Potamias, M., et al.: k -Nearest Neighbors in Uncertain Graphs. *The Proceedings of the VLDB Endowment (PVLDB)* 3 (2010)
7. Callahan, P.: Optimal parallel all-nearest-neighbors using the well-separated pair decomposition. In: Proc. FOCS 1993, pp. 332–340 (1993)
8. Callahan, P., et al.: A decomposition of multidimensional point sets with applications to k nearest neighbors and n body potential fields. *JACM* 42(1), 67–90
9. Vaidya, P.: An $O(n \log n)$ algorithm for the all-nearest-neighbor problem. *Discrete & Computational Geometry* 4, 101–115 (1989)
10. Krunz, M., et al.: Transmission power control in wireless ad hoc networks: challenges, solutions, and open issues. *IEEE Network* (2004)
11. Kubisch, M., et al.: Distributed Algorithms for Transmission Power Control in Wireless Sensor Networks. In: *Wireless Communications and Networking, WCNC* (March 2003)
12. Lin, S., et al.: ATPC: Adaptive Transmission Power Control for Wireless Sensor Networks. In: *Proceedings of SenSys 2006* (November 2006)
13. Kawadia, V., Kumar, P.R.: Principles and protocols for power control in Ad Hoc networks. *IEEE Journal on Selected Areas in Communications* 1, 5–16 (2005)
14. Draves, R., et al.: Routing in multi-radio, multi-hop wireless mesh networks. In: 10th Annual International Conference on Mobile Computing and Networking, pp. 114–128
15. De Couto, D., Aguayo, D., Bicket, J., Morris, R.: High-throughput path metric for multi-hop wireless routing. In: *MOBICOM* (2003)
16. Sakurai, T., Vu, H.L.: MAC access delay of IEEE 802.11 DCF. *IEEE Trans. Wireless Commun.* 6(5), 1702–1710 (2007)
17. Shah, S.C., Park, M.-S.: Resource Allocation Scheme to Minimize Communication Cost in Mobile Ad Hoc Computational Grids. In: *International Conference on Intelligent Networking and Collaborative Systems* (2010)
18. McClatchey, R., et al.: Data Intensive and Network Aware Grid Scheduling. *Journal of Grid Computing* 5(1), 43–64 (2007)
19. Shah, S.C., et al.: An effective and robust two-phase resource allocation scheme for interdependent tasks in mobile ad hoc computational Grids. *Journal of Parallel and Distributed Computing* 2012 (2012)

Single Camera Motion Estimation: Modification of the 8-Point Method

Mohammad Hossein Mirabdollah and Bärbel Mertsching

GET Lab, University of Paderborn,
Pohlwegstr 47-49. 33098 Paderborn, Germany
{mirabdollah,mertsching}@get.upb.de
<http://getwww.upb.de>

Abstract. In this paper, we modify the well-known 8-point method to make it work reliably in outdoor scenarios. It is well-known that the 8-point method is vulnerable against minor measurement noises especially if features are located far from a camera. Such situations occur often in outdoor scenarios. We offer four modifications to the 8-point method in the context of a RANSAC algorithm to make the algorithm robust against the measurement noises up to more than two pixels. The performance of the proposed method will be proved through simulation and practical results.

Keywords: Motion Estimation, 8-point method.

1 Introduction

The motion estimation of a single camera known in literature as ego-motion estimation has been investigated for a long time in many works. An important usage of ego-motion estimations is in monocular SLAM (Simultaneous Localization And Mapping) applications. The applications exploit a rough motion estimation of a camera along with fusion filters or bundle adjustment methods to localize the point features in the space and modify the camera trajectory. The most important approach to an ego-motion estimation is the extraction of a 3×3 matrix (essential matrix) based on some matched points between two consecutive frames. The main work of this family uses eight points and solve a system of eight linear equations to calculate the matrix [5]. Tsai et. al. in [9] showed that the 8-point method in some cases could not provide unique answers. For instance, if seven points of the eight points lie on a plane.

The 8-point method was later criticized to be vulnerable against measurement noises. Therefore, various nonlinear optimization methods were offered to estimate the matrix iteratively [7]. Clearly, the iterative methods require good initial guesses to converge to correct answers; otherwise, they would get stuck in local minima. Hence, these methods have not been used in the relevant applications in the last years. On the other hand, Hartley in [3] claimed that if image coordinates are changed based on the center of the image and they are

normalized with respect to the focal length of the camera, the performance of the 8-point method would improve noticeably. By comparing the results presented in the mentioned works, however, it becomes clear that the 8-point method has still a poor performance for the noises more than 0.15 pixel.

In a more recent work by David Nister [6], it was discussed that five points also suffice to determine an essential matrix. Based on the properties of an essential matrix, the 5-point method extracts a polynomial equation of order ten and by solving the equation, the elements of the essential matrix can be obtained. Nister showed that his method had a better performance rather than the 8-point. Unfortunately, Nister left some unclear points in his work concerning the implementation of the method. This problem has been discussed in [4] and they offered a new solution to obtain the polynomial of order ten. Obviously, implementations of both algorithms require symbolic processing, which makes their implementations inconvenient. Additionally, they would be extremely slow. Another problem concerning the 5-point method is that the polynomial in most of the cases has more than one real root, which gives rise to multiple valid answers for an essential matrix. To alleviate this problem, Nister offered to use multiple views of 5-points instead of two views. Obviously, it gives rise to the multiplication of the computation load by the number of views. Therefore, finding a linear fast method which works robustly against the measurement noise (unlike the 8-point method) could be very interesting and demanded.

The usage of 8-point and 5-point methods has recently been reported in new monocular SLAM algorithms with bundle adjustment methods ([10], [8]). In this works, however, the motion estimation methods have been used for simple scenarios. The 5-point method was used for a case in which the camera had only side motions and the 8-point method was used for an almost planar path.

In this paper, we investigate why the 8-point method and even 5-point method could have poor performances in the presence of the measurement noises. Concerning a practical 8-point or 5-point method which is implemented in the context of a RANSAC algorithm [2], we can consider three steps: first, estimation of several essential matrices from different minimum number of matched points (minimal set), second, selection of the best minimal set and essential matrix and third, selection of the feasible rotation matrix and translation vector from an essential matrix (cheirality test). We show that the conventional methods are vulnerable against measurement noises in each of the three steps and later we offer the proper modifications to address the shortcomings.

This paper is structured as follows: in section 2, the ego-motion estimation problem, the 8-point and 5-point methods are briefly introduced. Inconsistency of 8-point and 5-point method in the presence of measurement noises is discussed in section 3. In section 4, three modifications to make the 8-point method robust will be presented. Section 5 demonstrates the performance of the proposed method through simulations. In section 6, our algorithm is examined for two real outdoor scenarios. Section 7 concludes this paper.

2 Single Camera Motion

Given two camera positions from which a set of space points are observed, the goal is to obtain a rotation matrix and a translation vector which represent the motion of the camera between the two positions. For a space point which has the coordinate $\mathbf{p}_1 = [X_1, Y_1, Z_1]^T$ and $\mathbf{p}_2 = [X_2, Y_2, Z_2]^T$ at the two camera positions, we can write:

$$\mathbf{p}_2 = R(\mathbf{p}_1 - \mathbf{t}) \quad (1)$$

where R^T and $\mathbf{t} = [t_x \ t_y \ t_z]^T$ are the relative camera rotation and translation. We also know that \mathbf{p}_i can be projected on the retina of a camera as follows:

$$x_i = \frac{X_i}{Z_i}; \quad y_i = \frac{Y_i}{Z_i}; \quad i = 1, 2 \quad (2)$$

where x_i and y_i represent the normalized image coordinates with respect to the focal length of the camera. Based on the above setup, the following constraint known as coplanarity constraint is obtained:

$$\mathbf{v}_2^T E \mathbf{v}_1 = 0 \quad (3)$$

where $\mathbf{v}_1 = [x_1, y_1, 1]^T$, $\mathbf{v}_2 = [x_2, y_2, 1]^T$ and E is a 3×3 with the elements $e_1 \dots e_9$. The matrix E is known as an essential matrix in relevant literature and has the following relation with the rotation matrix and translation vector:

$$E = RT \quad (4)$$

where $T = \begin{bmatrix} 0 & t_z & -t_y \\ -t_z & 0 & t_x \\ t_y & -t_x & 0 \end{bmatrix}$.

The elements of the essential matrix can be determined by forming a linear system of equations if at least eight correspondent points are available. It is well-known that using a single camera, we can only extract the direction of the translation but not its amount. Therefore, the recovery of a translation means to find its direction which is a normalized vector in the 3D space.

R and T can be obtained from the singular value decomposition of E . Through this decomposition four different answers are obtained, only one of which can back project the set of given image points into the space in front of the both camera positions. Since, the rotation matrix can be parametrized with three parameters and the translation vector has two degrees of freedom, the motion should be able to be determined with five points. Nister used two extra conditions of essential matrices:

$$\det(E) = 0; \quad EE^T E - \frac{1}{2} \text{trace}(EE^T) E = 0 \quad (5)$$

He wrote the coplanarity constraint for five points. It resulted in five equations of nine unknowns. The solution of the unknowns should lie in the null space of

the matrix of the coefficients of the equations. If the basis of the null space are \mathbf{w} , \mathbf{x} , \mathbf{y} and \mathbf{z} , it can be written:

$$\mathbf{e} = w\mathbf{w} + x\mathbf{x} + y\mathbf{y} + z\mathbf{z} \quad (6)$$

where $\mathbf{e} = [e_1, e_2, \dots, e_9]^T$. Nister discussed that since E can be multiplied by any coefficient, therefore w can be set to one. Consequently, if the three remained unknowns can be determined the essential matrix can also be determined. by plugging Eq. (6) into Eq. (5) an equation system of x , y and z is obtained. By elimination of x and y finally a tenth order polynomial of z is obtained. The real answers of the polynomial give different valid answers for the E matrix.

3 Inconsistency of the 8-Point and 5-Point Methods against Measurement Noises

A practical 8-point or 5-point method in the context of a RANSAC algorithm consists of three steps.

1. Estimation of several essential matrices based on the random selection of the minimum required number of matched points (minimal set).
2. Checking the validity of the estimated essential matrices and selecting the best essential matrix which minimize the coplanarity constraint for all matched points.
3. Extraction of the rotation matrix and translation vector using the SVD decomposition and selection of the feasible answer using the cheirality test.

In the following, we discuss that both methods have shortcomings in each three steps and in the next section we address the shortcomings.

As discussed in previous section, in both 8-point and 5-point methods, to dispose of one of the unknowns, one of them is set to one. In the 8-point method e_9 assumes to be 1 and in 5-point method $w = 1$. Mathematically, however, the assumptions are valid if the parameters are not zero.

In the case of the 8-point method, we show if the camera has a constrained motion similar to the motion of a wheeled vehicle, e_9 will be zero. Under this constraint, the translation vector has only the forward translation at each step: $\mathbf{t} = [0, 0, t_z]^T$. Given this translation vector we have:

$$E = RT = \begin{bmatrix} r_1 & r_2 & r_3 \\ r_4 & r_5 & r_6 \\ r_7 & r_8 & r_9 \end{bmatrix} \begin{bmatrix} 0 & t_z & 0 \\ -t_z & 0 & 0 \\ 0 & 0 & 0 \end{bmatrix} = \begin{bmatrix} -r_2 t_z & r_1 t_z & 0 \\ -r_5 t_z & r_4 t_z & 0 \\ -r_8 t_z & r_7 t_z & 0 \end{bmatrix} \quad (7)$$

It can be seen that the whole third column of E becomes zero and consequently, the coplanarity equation cannot be divided by e_9 . In practice, t_x and t_y may also take very small values which means the other nonzero elements of E should take very large values with respect to e_9 . Considering the sensitivity of the equations with respect to the pixel positions, it can be simply verified that with minor changes of the pixel positions, the E matrix could change noticeably. Therefore,

on the contrary of the previous believes, we find out that the poor performance of the 8-point method in the presence of measurement noise is not due to ignoring the dependencies of the elements of E but it is simply due to forcing e_9 to one.

In the 5-point method a similar problem can occur if w should take a value near to zero. For the 5-point method, this case does not depend on the motion of the camera but it depends on the arrangement of the matched points. Based on the simulation results, the expectation of this case is about 10%. Hence, the 5-point method has a better performance rather than the conventional 8-point method.

The second problem concerns finding the best minimal set in the RANSAC iterations. The conventional methods apply the obtained essential matrices from different minimal sets and all matched points in the coplanarity constraints and then sum up all the absolute values:

$$C_j = \sum_{i=1}^N |\mathbf{v}_{i,2}^T E_j \mathbf{v}_{i,2}|; \quad j = 1 \dots M \quad (8)$$

where N is the number of all matched points and M is the number of minimal sets. Afterwards, the essential matrix associated to the minimum C_j is selected as the best estimation. Looking at Eq. (8), we see that it is the summation of euclidean distances of the term $\mathbf{v}_{i,2}^T E_j \mathbf{v}_{i,2}$ from the origin. It is well-known in noisy cases, we would get better result if we use Mahalanobis distances instead of euclidean distances as it will discussed in the next section.

After obtaining the best E matrix, we can obtain the rotation matrix and the translation vector using the SVD decomposition. This decomposition results in four mathematically valid answers; however, only one of them can back project the image points in the space in front of both camera positions. This measure is known as cheirality test. Unfortunately, this test fails if the space points are located relatively far from the camera and there exist measurement noises. In such cases, the points could be wrongly back projected behind the cameras. This situation occurs in outdoor scenarios very often.

4 A 9-Point Method

In this section we address the shortcomings of the 8-point method mentioned in the previous section. In order to avoid problems occurring by forcing e_9 to one, all nine elements of an essential matrix ($e_1 \dots e_9$) should be estimated. Therefore, we will use nine matched points in the proposed method.

4.1 Essential Matrix Estimation

By using nine matched points, a homogeneous system of 9-equations for the unknowns e_1, \dots, e_9 is obtained. Clearly, the nontrivial non-zero answer is demanded. A well-known method for solving linear homogeneous equation system

is the singular value decomposition. Therefore, by writing the coplanarity constraint for nine matched points, we have:

$$A\mathbf{e} = 0 \quad (9)$$

The above equation system can be solved under the constraint $\mathbf{e}^T\mathbf{e} = 1$. Considering the SVD decomposition of A :

$$A = U\Sigma V^T \quad (10)$$

The column of V^T which is correspondent to the smallest singular value will be the answer of the equation.

4.2 Considering Measurement Noises in the Estimation of E

In fact the SVD approach minimizes the cost function $C = (A\mathbf{e})^T(A\mathbf{e})$, which is the square of euclidean distances between $(A\mathbf{e})$ and the origin. On the other hand, we know if we deal with noisy data, using the Mahalanobis distance gives better results, which means the minimization of the following cost function:

$$C = (A\mathbf{e})^T\Lambda(A\mathbf{e}) \quad (11)$$

where Λ is the inverse of the covariance related to the coplanarity equations.

$$\Lambda_{i,j}^{-1} = \begin{cases} \text{var}(\mathbf{v}_{i,2}^T E \mathbf{v}_{i,1}) & \text{if } i = j \\ 0 & \text{if } i \neq j \end{cases} \quad (12)$$

Since E is not initially known it is not straightforward to calculate the diagonal elements. However, we can consider large uncertainties for the rotation and translation parameters with zero mean values. If we parametrize a rotation matrix with Euler angles $\phi \sim \mathcal{N}(0, \sigma_\phi)$, $\theta \sim \mathcal{N}(0, \sigma_\theta)$ and $\psi \sim \mathcal{N}(0, \sigma_\psi)$ we can write:

$$R = \begin{bmatrix} c\theta c\psi & -c\phi s\psi - s\phi s\theta c\psi & s\phi s\psi - c\phi s\theta c\psi \\ c\theta s\psi & c\phi c\psi - s\phi s\theta s\psi & -s\phi c\psi - c\phi s\theta s\psi \\ s\theta & s\phi c\theta & c\phi c\theta \end{bmatrix} \quad (13)$$

where c and s stands for \cos and \sin consecutively. Since in practical cases the amount of these angles are less than $\frac{\pi}{4}$ rad we can use the following approximation of R based on the Taylor expansion and ignoring terms with the orders more than two:

$$R \approx \begin{bmatrix} 1 - \frac{\theta^2}{2} - \frac{\psi^2}{2} & -\psi - \phi\theta & -\theta + \phi\psi \\ \psi & 1 - \frac{\phi^2}{2} - \frac{\psi^2}{2} & -\phi - \theta\psi \\ \theta & \phi & 1 - \frac{\phi^2}{2} - \frac{\theta^2}{2} \end{bmatrix} \quad (14)$$

Based on the assumptions that rotation amounts are less than $\frac{\pi}{4}$ rad, $\sigma_\phi = \sigma_\theta = \sigma_\psi = 0.5$ are reasonable standard deviation values for the parameters.

Regarding the uncertainty of the translation vector, it can be verified if the equation system is solved using SVD method, the following constraint will be held:

$$t_x^2 + t_y^2 + t_z^2 = \frac{1}{2} \quad (15)$$

Therefore each of the translation parameter should reside in $[-\sqrt{2}/2, \sqrt{2}/2]$ and consequently $\sigma_{t_x} = \sigma_{t_y} = \sigma_{t_z} = 0.5$ will be good selections.

If we consider measurement noises for the image coordinates we have:

$$\begin{aligned} x_i &= \bar{x}_i + \tilde{x}_i \\ y_i &= \bar{y}_i + \tilde{y}_i; \quad i = 1, 2 \end{aligned} \quad (16)$$

where \bar{x}_i and \bar{y}_i are the measured image positions and \tilde{x}_i and \tilde{y}_i are zero mean normal random variables. Based on the mentioned definitions now we are interested to find the following variance:

$$\begin{aligned} \sigma_e^2 &= \text{var}(\mathbf{v}_2^T E \mathbf{v}_1) \\ &\approx \text{var}([x_2, y_2, 1]^T E[\tilde{x}_1 \tilde{y}_1 0]) + \text{var}([\tilde{x}_2, \tilde{y}_2, 0]^T E[x_1 y_1 1]) \end{aligned} \quad (17)$$

Since all the random variables are less than one, the variances of the higher order terms vanish quickly with respect to the lower order terms. Therefore, using Eq. (7) and Eq. (14) and by ignoring the terms with the orders more than three we have:

$$\sigma_e^2 \approx \text{var} \left(\begin{bmatrix} -\psi t_x - t_y + y_1 t_z \\ t_x - \psi t_y - x_1 t_z \end{bmatrix}^T \begin{bmatrix} \tilde{x}_2 \\ \tilde{y}_2 \end{bmatrix} \right) + \text{var} \left(\begin{bmatrix} -t_z(\phi + y_2) + t_y \\ t_z(\theta + x_2) - t_x \end{bmatrix}^T \begin{bmatrix} \tilde{x}_1 \\ \tilde{y}_1 \end{bmatrix} \right) \quad (18)$$

To calculate the above variance, at first, we attempt to find the mean and variance of the multiplication of two independent Gaussian random variables.

The multiplication of two Gaussian random variables is not Gaussian but we can fit acceptably a Gaussian distribution to it. We can use a method offered by unscented Kalman filter for this purpose. Given a one dimensional Gaussian random variable such as $a \sim \mathcal{N}(\bar{a}, \sigma_a)$, we should withdraw three samples as follows :

$$\{\bar{a} - 2\sigma_a, \bar{a}, \bar{a} + 2\sigma_a\} \quad (19)$$

with the weights $\{\frac{1}{8}, \frac{3}{4}, \frac{1}{8}\}$. It can be verified that the mean and variance of the three samples will be the same as the parameters of the Gaussian distribution.

Now, assuming two independent random variables $a \sim \mathcal{N}(\bar{a}, \sigma_a)$ and $b \sim \mathcal{N}(\bar{b}, \sigma_b)$, we are interested to fit a Gaussian distribution to their multiplication: $c = ab$.

By obtaining three samples from each random variable and multiplying all possible combinations of the samples, nine samples for c is obtained. From the obtained samples we can obtain the mean and variance of c as follows:

$$c \sim \mathcal{N}(\bar{c}, \sigma_c^2) \quad (20)$$

where $\bar{c} = \bar{a}\bar{b}$ and $\sigma_c^2 = \bar{a}^2\sigma_b^2 + \bar{b}^2\sigma_a^2 + \sigma_a^2\sigma_b^2$.

Using Eq. (20) and by considering the mentioned standard deviations for rotation and translation parameters, and if $\sigma_{x_1}^2 = \sigma_{x_2}^2 = \sigma_{y_1}^2 = \sigma_{y_2}^2 = \sigma_p^2$, Eq. (18) will be as follows:

$$\sigma_e^2 = (1.25 + 0.25(x_1^2 + y_1^2 + x_2^2 + y_2^2))\sigma_p^2 \quad (21)$$

Since σ_p^2 is a common constant for all equations, it can be removed and then each equation should be divided by its relevant σ_e to solve the equation system Eq. (9) based on the Mahalanobis distance.

4.3 Selection of the Best Essential Matrix

As mentioned in the previous section, we require to find the best essential matrix in a RANSAC context to deal with the outlier problems. Again unlike the conventional 8-point method we use a cost function based on the Mahalanobis distance as follows:

$$C_j = \sum_{i=1}^N \frac{1}{\sigma_{j,i}} |\mathbf{v}_{i,2}^T E_j \mathbf{v}_{i,1}|; \quad j = 1 \dots M \quad (22)$$

where

$$\sigma_{j,i}^2 = [\bar{x}_{i,2}, \bar{y}_{i,2}, 1] E_j \Sigma_p E_j^T [\bar{x}_{i,2}, \bar{y}_{i,2}, 1]^T + [\bar{x}_{i,1}, \bar{y}_{i,1}, 1] E_j \Sigma_p E_j^T [\bar{x}_{i,1}, \bar{y}_{i,1}, 1]^T$$

where

$$\Sigma_p = \begin{bmatrix} \sigma_p^2 & 0 & 0 \\ 0 & \sigma_p^2 & 0 \\ 0 & 0 & 0 \end{bmatrix}$$

We remind that, in the 8-point method the term $\sigma_{j,i}$ is not considered.

4.4 Modified Cheirality Test

The last modification to the 8-point method concerns the cheirality test. After the calculation of E , firstly, it should be decomposed as follows:

$$E = U \Sigma V^T \quad (23)$$

Consequently, the following answers for R and \mathbf{t} is obtained:

$$\begin{aligned} R_1 &= UWV^T; & R_2 &= UW^T V^T \\ T_1 &= VZV^T; & T_2 &= -VZV^T \end{aligned} \quad (24)$$

where

$$W = \begin{bmatrix} 0 & -1 & 0 \\ 1 & 0 & 0 \\ 0 & 0 & 1 \end{bmatrix}; \quad Z = \begin{bmatrix} 0 & -1 & 0 \\ 1 & 0 & 0 \\ 0 & 0 & 0 \end{bmatrix} \quad (25)$$

Given the obtained rotation matrices and translation vectors four valid answers can be obtained: $\{R_1, \mathbf{t}_1\}$, $\{R_1, \mathbf{t}_2\}$, $\{R_2, \mathbf{t}_1\}$ and $\{R_2, \mathbf{t}_2\}$. However, the real answer should back project the image points in front of both camera positions. It means if we Assume $Z_2 > 0$, consequently Z_1 should be also greater than zero. We can calculate Z_1 as follows:

$$Z_1 = \frac{(\mathbf{r}_1 - x_2 \mathbf{r}_3) \cdot \mathbf{t}}{(\mathbf{r}_1 - x_2 \mathbf{r}_3) \cdot \mathbf{v}_1} \quad (26)$$

where \mathbf{r}_i is the i^{th} row of the rotation matrix. The above equation is very unstable if the features are far from the camera and its sign can flip easily between positive and negative in the presence of measurement noises. Hence, the points which are in front of the cameras could be wrongly localized behind the camera.

To solve this problem we consider the elements of the rotation matrix. Considering a rotation matrix which is parameterized by euler angles Eq. (13), we can observe that if the euler angles reside in the interval $[-\frac{\pi}{2}, \frac{\pi}{2}]$, r_1 and r_9 should be always greater than zero. Using this criterion we can easily choose the correct rotation matrix. Then, for the selection of the translation vector we can use Eq. (26). As we will see later in practical experiments, this simple change let the algorithm work robustly in outdoor environments

5 Simulation

To evaluate the performance of the proposed SVD based algorithm with and without consideration of the measurement noise in comparison with the 8-point method, we generated several random paths and random space points. The projections of the space points on the camera screen is added with a Gaussian noise with the standard deviation σ_p . The mean squared error (MSE) between the true path and the estimated paths can be seen in fig. 1.

As it can be seen the 8-point method performance decreases very fast as the measurement noise increases, however, the 9-point SVD methods managed to

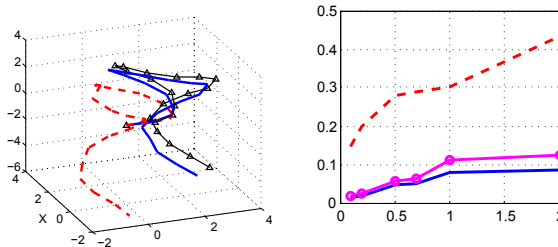


Fig. 1. Left figure: A sample of simulated paths for $\sigma_p = 0.5$ (ground truth(- Δ), 8-point method (- -) and 9 point SVD with Mahalanobis distance consideration(-)). Right figure: Mean squared error between the ground truth and the paths recovered by 8-point(- -), 9-point SVD with (-) and without (o) using Mahalanobis distance.

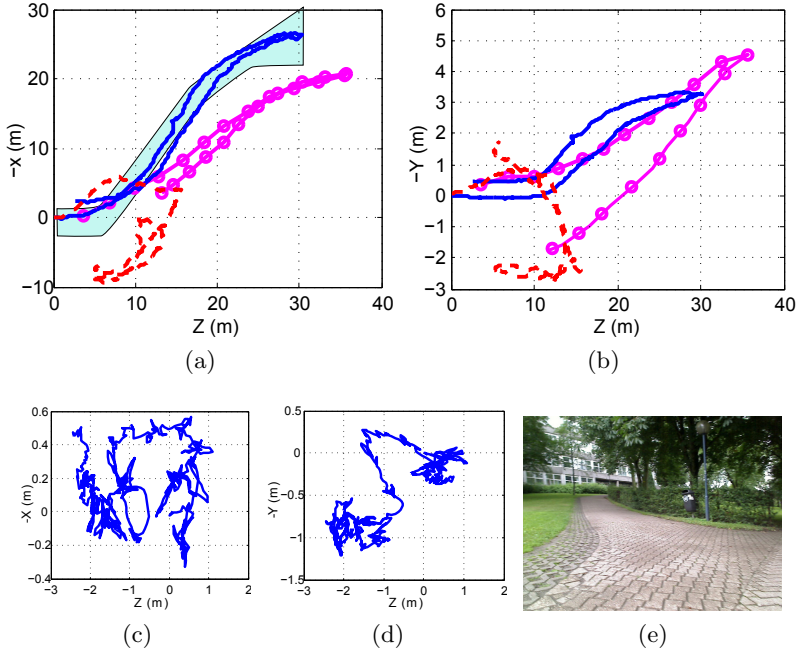


Fig. 3. The run over a ramp: (a): $(Z, -X)$ generated paths, (b): generated $(Z, -Y)$ paths using the 9-point SVD method with(-) and without(-o) noise consideration and the 8-point method (- -). All methods used modified cheirality test to select the feasible rotation Matrix and translation vector. (c) and (d) show the path generated with the 8-point with the usual cheirality test. (e) A view of the ramp.

Regarding the experiment over the ramp, the generated paths using the 9-point SVD method and the 8-point method can be seen in fig. 3. We observe that the 8-point generated again an unacceptable path which had wrong estimations at many points. The 9-point SVD method without the noise effect consideration had much better results rather than the 8-point method but not satisfying. On the other hand, the 9-point method which utilized the Mahalanobis distance for the optimization provided a very nice path. Looking at the $(Z, -X)$ ground truth of the road, we see that the path generated by the last method lies to a great extent on the road. It should be mentioned, that this experiment was a challenging scenario since the robot had very maneuvers on the ramp which gave rise to the excitation of all three euler angles of the rotation matrix simultaneously. Additionally, on the return path, since many of the features were more than a hundred of meters far from the camera, the low resolution of the camera created relatively high amount of systematic measurement noises.

Considering the practical experiments, we see that the 9-point SVD method provided near to perfect paths, whereas, the 8-point method would be useless if it is not used with a SLAM algorithm. It means that landmarks should be observed multiple times and the path get adjusted using the bundle adjustment

methods. However, as we observed for more complex scenarios, the errors some times could be too high and the bundle adjustment methods get possibly stuck in local minima.

7 Conclusion

It was investigated why the 8-point method and 5-point method had a poor performances in the presence of measurement noises. To address the shortcomings, we offered four modification to the conventional 8-point method in the context of a RANSAC algorithm. The high performance of the proposed algorithm was proved through the simulation and practical experiments. Clearly, the main usage of the proposed method is in monocular SLAM applications.

References

1. Bay, H., Tuytelaars, T., Van Gool, L.: Surf: Speeded Up Robust Features. In: European Conference on Computer Vision. pp. 404–417 (2006)
2. Fischler M.A., Bolles, R. C.: Random Sample Consensus: A Paradigm for Model Fitting with Applications to Image Analysis and Automated Cartography. *Commun. ACM* 24(6), 381–395 (1981)
3. Hartley, R.: In Defense of the Eight-Point Algorithm. *IEEE Trans. Pattern Anal. Mach. Intell.* 19(6), 580–593 (1997)
4. Hongdong, L., Richard, H.: Five-Point Motion Estimation Made Easy. In: 18th International Conference on Pattern Recognition. pp. 630–633 (2006)
5. Longuet-Higgins, H.C.: A Computer Algorithm for Reconstructing a Scene from Two Projections. *Readings in computer vision* 293, 133–135 (1981)
6. Nistér, D.: An Efficient Solution to the Five-Point Relative Pose Problem. *IEEE Trans. Pattern Anal. Mach. Intell.* 26(6), 756–777 (2004)
7. Q. Luong, et al.: On Determining the Fundamental Matrix: Analysis of Different Methods and Experimental Results (1993)
8. Strasdat, H.: Scale Drift-Aware Large Scale Monocular SLAM. In: *Proceedings of Robotics: Science and Systems*. Zaragoza, Spain (June 2010)
9. Tsai, R.Y., Huang, T.S.: Uniqueness and Estimation of Three-Dimensional Motion Parameters of Rigid Objects with Curved Surfaces. *IEEE Trans. Pattern Anal. Mach. Intell* 6(1), 13–27 (1984)
10. Zhao, L., et al.: Parallax Angle Parametrization for Monocular SLAM. In: *IEEE International Conference on Robotics and Automation*. pp. 3117–3124 (2011)

A Biomimetic Earthworm-Like Micro Robot Using Nut-Type Piezoelectric Motor

Maoying Zhou¹, Yuebang Tao¹, Liling Cheng², Wei-ting Liu^{1,*}, and Xin Fu¹

¹ The State Key Lab of Fluid Power Transmission and Control, Zhejiang University,
Zheda Rd. 38, 310027, Hangzhou, China

² Zhejiang Academy of Science and Technology for Inspection and Quarantine,
East Fengqi Rd. 99, 310020, Hangzhou, China

Abstract. By investigating the biological locomotion mechanism of natural earthworms, an anchoring-advancing principle has been proposed and a new prototype of micro earthworm-like robots has been designed, fabricated and tested. A miniature piezoelectric linear stepper motor is introduced into the robot actuation. Specialized micro needles are boned to the robot serving as the anchoring points. The prototype dimension is 4.8mm×6.0mm×14.0mm. Preliminary tests have shown the effectiveness of the proposed locomotion principle with demonstration of the maximum characteristic speed of the prototype as approximately 0.36 body length per second, which is better than its natural counterpart. Fair climbing capability of the robot is also validated. Some factors such as surface roughness and hardness are found relevant to the locomotive performance of the robot. Speed and position control of the robot is easily achieved thanks to high accuracy controller.

Keywords: earthworm, anchoring-advancing principle, piezoelectric actuator, locomotion, micro robot.

1 Introduction

Micro robots have shown promising application prospects in such areas as rescue robotics, industrial inspection and medical endoscopy [1]. A number of locomotive mechanisms have been investigated to propose and design new effective mobile robots. While conventional method using rotating wheels indicates insufficient mobility in uneven, slippery or flexible environments, micro robots mimicking and replicating the motions of insects and worms have been widely investigated because of their great adaptability to complex terrain [2]. Earthworm-like mechanisms, which consist of a series of periodic anchoring and advancing sequences, are proved to be quite effective and can be easily achieved using linear actuators. On the other hand, downsizing of the robots needs new principles for actuation and fabrication. Various micro actuators such as ionic polymer metal composite (IPMC) [3], micro motors [3], SMA springs [1] and impact-driven piezoelectric actuators [4] have been studied. Power supply, positioning precision and motion

* Corresponding author.

control have become the basic concerns when designing or choosing micro actuators. A nut-type piezoelectric motor called SQUIGGLE [5] from New Scale Technology adopting bending-wobbling mode achieves promising characteristics with a small dimension of $2.8\text{mm} \times 2.8\text{mm} \times 6\text{mm}$ and is introduced into developing the micro robot. The mechanical characteristics of the robot are investigated. Its motion characteristics under different terrains are also tested in order to verify its locomotive capability.

2 Locomotion Mechanism

From front to rear, the basic shape of an earthworm is a cylindrical tube, divided into a series of segments that compartmentalize the body. Except for the head and anal segments, namely, the first and the last segments [6], each segment carries bristle-like hairs called setae. An earthworm has two kinds of muscles: circular muscles surrounding the body to shrink or expand the segment rapidly and longitudinal muscles mounted along the body to shorten or elongate the segment.

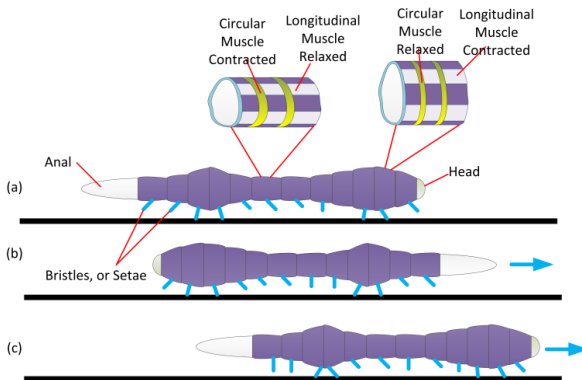


Fig. 1. Locomotion of Earthworm

Crawling action of an earthworm consists of a series of muscles actions and segment movements, as shown in Fig. 1. At first, circular muscles in some segments of the body contracted, shrinking the segments and bringing the bristles erect to anchor the segments. At the same time, longitudinal muscles in other segments extend and elongate the segments to push the whole body one step forward. In the next stage, former extended longitudinal muscles relax, while the circular muscles in the same segment contract, turning the segment into an anchoring segment. Former contracted circular muscles relax, while the longitudinal muscles in the same segment extend, pushing whole body to advance one step. Repeating the sequence of anchoring and advancing actions, an earthworm

will move forward continuously as a result. We may call this kind of motion the anchoring-advancing mechanism.

According to existing research results, body wall strains or moving earthworms are independent of body mass: the segments elongate by approximately 60% during longitudinal muscles contraction and narrow by approximately 25% during circular muscle contraction. Absolute crawling speed increased as a function of body mass, but relative speed (normalized to body length) showed no relationship with body mass. On average, earthworms crawl at a speed of approximately 0.04 body lengths per second, i.e. an average worm traveled one body length in 25 s. [7]

Based on the analysis of earthworm locomotion, a simplified robot prototype has been proposed which consists of two parts: the body and the motor. The robot is initially in the state shown in Fig. 2(a). The motor is then started and drives the shaft to move backward relative to the motor stator. Tilted setae on the head and tail get erect due to the subjected frictional force and anchor the robot. Thus, the motor stator itself will advance a step. This is shown in Fig. 2(b). After that, the motor shaft is driven forward relative to the motor stator in turn. Tilted setae on the motor stator get erect and anchor the stator, resulting in the advance of the body by one step, as shown in Fig. 2(c). At the end of this step, the robot recovers its initial state, getting ready for the second moving sequence. Repeating the anchoring-advancing sequences leads the robot to move forward continuously in one direction. It is easy to expand the prototype to be a multi-segment climbing robot.

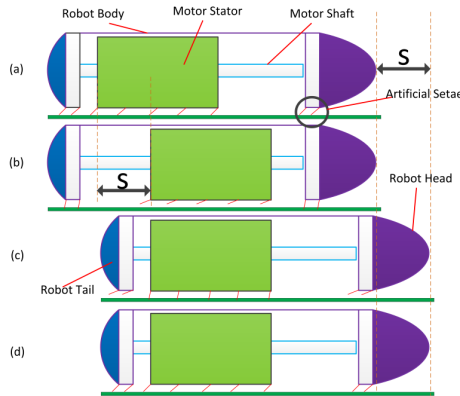


Fig. 2. Locomotion of Earthworm

3 Linear Piezoelectric Nut-Type Actuator

The SQUIGGLE motor (shown in Fig. 3) consists of a screw-type shaft, or the rotor, and a four-prism nut, or the stator. Each lateral face of the stator is covered

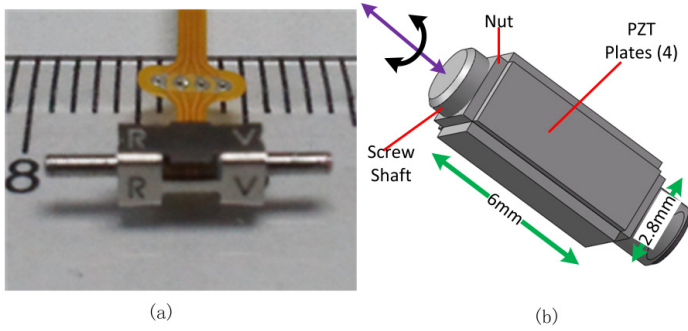


Fig. 3. Locomotion of Earthworm

with a PZT plate. The poling directions of the plates are aligned such that a common driving voltage on opposite pairs of plates produces opposing strain. Housing dimension of the motor is 2.8mm2.8mm6mm, with a shaft 12mm in length.

Driving principle of the motor is shown in Fig.4. When applied alternating driving voltage, strains parallel to the plate surface generate in the PZT plates and bend the nut. According to theoretical analysis, the bending strain excitation is applied at the frequency corresponding to the first bending mode of the tubular stator, aiming to arouse first bending modal resonance in the stator. While two vibrating waves is excited by PZT plate strain in orthogonal plate pairs at given resonant frequency with 90 degree phase shift, hula hoop vibration is created in the stator (as shown in Fig. 4(b)). The screw-threaded fit then transfer the hula hoop vibration of the stator to the sliding motion of the shaft. Both sinusoidal and square driving waveforms are feasible. Positive 90 degree phase shift produces forward movement while negative 90 degrees produces reverse movement.

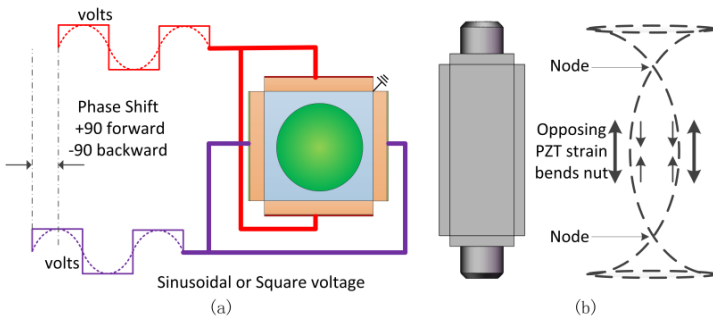


Fig. 4. Locomotion of Earthworm

Because of its ultrasonic wave driving principle, the motor exhibits some great characteristics such as being free of electromagnetic radiation, excellent self-lock performance and low power consumption with low noise. Step resolution of the motor is 0.5m, enabling closed-loop position control with high accuracy. Typically, the shaft moves at a speed of 10mm/s. But the speed can be easily regulated by tuning the duty cycle of the driving square wave applied to the PZT plates of the motor.

4 Robot Fabrication and Experiments

Integrated the earthworm-like anchoring-advancing mechanism with the linear piezoelectric stepper micro motor, we design the simple structure of the micro robot prototype (shown in Fig. 5).

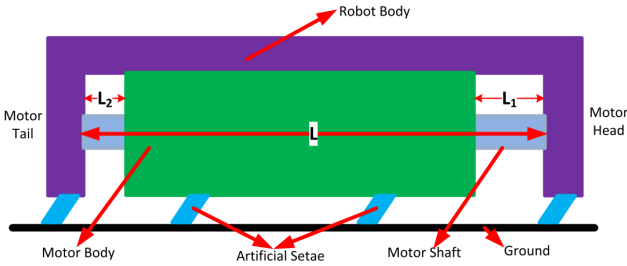


Fig. 5. Locomotion of Earthworm

The prototype is designed into a capsule shape and made of photosensitive resin by 3D printing process. Housing dimension of the prototype is 4.8mm×6.0mm×14.0mm. The motor is mounted into the robot body with the two ends of its shaft contacting against the inner wall of the robot body. In this structure, the calculated stroke of the robot is determined by

$$\Delta L = L_1 \quad (1)$$

Considering that the motor shaft is 6mm longer than the motor body, the stroke varies from zero to 6mm, depending on the initial relative position of the motor body to the motor shaft, which can be easily changed. Adopting square waveform, by adjusting the duty cycle we can regulate the moving speed of the shaft. Here in the experiments, a default speed of 10mm/s is set. Besides, two groups of setae are bonded to the bottom of the outer body of the robot, one on the robot head and the other on the tail. One group of setae is bonded to the bottom of the inner body of the robot. Both groups of setae made from micro needles are in the same tilt direction with an angle of about 45 degree.

Supposing that the initiated stroke of the motor is 3mm, it will cost the robot $\Delta t = \Delta L/v = 0.3s$ to cover a typical step forward. Then the relative speed v_r , in terms of robot length is

$$v_r = \frac{\Delta L}{2L \cdot \Delta t} \approx 0.36s^{-1} \quad (2)$$

That is to say, the robot covers 36% of its whole body length per second theoretically. To test its basic performance and extract some of its important characteristics, the robot was set to move on flat surfaces and sloping surfaces, respectively (shown in Fig. 6).

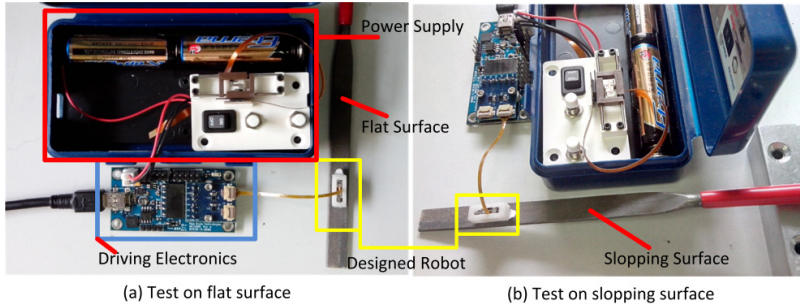


Fig. 6. Locomotion of Earthworm

The tests are conducted on smooth paper surface, rough cloth surface and frosted metal surface, respectively. The locomotion sequence on the frosted metal surface is very efficient and smooth. An absolute speed of about 5mm/s is observed and a stroke of 3mm is obtained, which is consistent with previous theoretical results. Furthermore, the robot has shown fair climbing capability on the sloping surface.

Surface hardness and roughness are found of great influence on the locomotive characteristics of the robot prototype. On paper surface, where the surface roughness is relatively small, the locomotion sequence is irregular and discontinuous, for the steel needle setae do not generate enough contact friction force to push the robot body forward. On cloth surface where surface hardness is relatively small, irregular sequence is also observed and sometimes the robot even gets stuck on the surface, because the steel needles pierce into the soft cloth surface under the action of relatively large output force of the motor.

5 Conclusion and Future Work

An earthworm-like robot driven by a linear piezoelectric stepper motor has been developed. Its locomotive capabilities on flat surface and sloping surface have been investigated. Encouraging results in terms of speed and action frequency is demonstrated, showing that the robot reaches an effective motion way in a manner similar to natural earthworms with low energy consumption. Surface hardness and roughness are found influential on the locomotive characteristics of the robot.

The robot prototype also inspires future research on materials, locomotion mechanisms and control method to improve its performance. A key problem to be addressed is the material and tilt angle of the setae implementation, aiming to improve the friction behaviors of the setae and apply the robot to more terrains. Besides, multi-segment robot is to be investigated based on present single-segment design to adapt to more complex terrains such as rugged surfaces and to achieve more complicated functions such as making turns and navigating obstacles. Mechanical integration and motion control of multiple relatively independent segments is to be given research priority. Whats more, due to its miniature structure, new components such as micro CCD cameras, sensors and manipulator can be added to the robot, which will turn the crawling robot into a sophisticated and powerful micro robot platform.

Acknowledgments. The research presented in this paper has been carried on with the support of the National Basic Research Program (973) of China under Grant No. 2011CB013300.

References

1. Menciasci, A., Gorini, S., Pernorio, G., Dario, P.: A SMA Actuated Artificial Earthworm. In: Proceedings of the 2004 IEEE International Conference on Robotics and Automation, vol. 4, pp. 3282–3287. IEEE Press, New York (2004)
2. Kim, B., Lee, M.G., Lee, Y.P., Kim, Y., Lee, G.: An Earthworm-like Micro Robot Using Shape Memory Alloy Actuator. *Sensors and Actuators A: Physical* 125(2), 429–437 (2006)
3. Kim, B., Ryu, J., Jeong, Y., Tak, Y., Kim, B., Park, J.O.: A Ciliary Based 8-legged Walking Micro Robot Using Cast IPMC Actuators. In: Proceedings of the 2003 IEEE International Conference on Robotics and Automation, vol. 3, pp. 2940–2945. IEEE Press, New York (2003)
4. Kim, B., Park, S., Jee, C.Y., Yoon, S.J.: An Earthworm-like Locomotive Mechanism for Capsule Endoscopes. In: 2005 IEEE/RSJ International Conference on Intelligent Robots and Systems, pp. 2997–3002. IEEE Press, New York (2005)
5. Henderson, D.A.: Simple Ceramic Motor... Inspiring Smaller Products. *Stroke (mm)* 50, 10 (2006)
6. Wikipedia, <http://en.wikipedia.org/wiki/Earthworm>
7. Quillin, K.J.: Kinematic Scaling of Locomotion by Hydrostatic Animals: Ontogeny of Peristaltic Crawling by the Earthworm *Lumbricus Terrestris*. *Journal of Experimental Biology* 202(6), 661–674 (1999)

A Robust Control of Intelligent Mobile Robot Based on Voice Command

Sung Won Jung^{1,*}, Moon Yeol Park¹, In Man Park², Yang Keun Jung³,
and Hang Bong Shin⁴

¹ Dept. of Advanced Eng., Graduate School Kyungnam University
carisma3000@naver.com

² Intem Co. Ltd.

³ Shinla Information Technology Co. Ltd.

⁴ SG Servo Co. Ltd.

Abstract. In general, it is possible to estimate the noise by using information on the robot's own motions and postures, because a type of motion and gesture produces almost the same pattern of noise every time. In this paper, we describe a voice recognition control system for robot (VRCS) system which can robustly recognize voice by adults and children in noisy environments. We evaluate the VRCS system in a communication robot placed in a real noisy environment. Voice is captured using a wireless microphone. To suppress interference and noise and to attenuate reverberation, we implemented a multi-channel system consisting of an outlier-robust generalized side-lobe canceller technique and a feature-space noise suppression using MMSE criteria. Voice activity periods are detected using GMM-based end-point detection

Keywords: Robust voice recognition.

1 Introduction

To make human-robot communication natural, it is necessary for the robot to recognize voice even while it is moving and performing gestures. For example, a robot's gesture is considered to play a crucial role in natural human-robot communication. In addition, robots are expected to perform tasks by physical actions to make a presentation. If the robot can recognize human interruption voice while it is executing physical actions or making a presentation with gestures, it would make the robot more useful.

Each kind of robot motion or gesture produces almost the same noises every time it is performed. By recording the motion and gesture noises in advance, the noises are easily estimated. By using this, we introduce a new method for VRCS under robot motor noise. Our method is based on three techniques, namely, multi-condition training, maximum-likelihood linear regression (MLLR), and missing feature theory

* Corresponding author.

(MFT). These methods can utilize pre-recorded noises as described later. Since each of these techniques has advantages and disadvantages, whether it is effective depends on the types of motion and gesture. Thus, just combining these three techniques would not be effective for voice recognition under noises of all types of motion and gestures. The result of an experiment of isolated word recognition under a variety of motion and gesture noises suggested the effectiveness of this approach. In what follows, Section 2 discusses the design of voice recognition system, and Section 3 explains our method for avoid the obstacles by navigation strategy. Section 4 describes the recognition, navigation experiments, and the results, before conclusion and mentioning future work in Section 5.

2 Paper Preparation

Accounting for the two problems (caused by noisy environments and differences on speaker age) described in Section 1, we developed an RVR system to be robust to both background noise and speakers of different ages. The first block is a front-end processing. It contains a microphone wireless transmitter. The real-time wireless microphone system for suppressing interference and noise and for attenuating reverberation consists of an outlier-robust generalized side-lobe canceller (RGSC) and feature-space noise suppression (MMSE). MMSE noise suppression is applied after RGSC to reduce the residual noise at the RGSC output. After that, the voice activity period detected by the GMM-based end-point detection (GMM-EPD) is transferred to the second block. In the second block, there are two decoders depending on the age of the speaker (adult or child); each decoder works using gender-dependent acoustic models. Noise-suppressed voice at the first block is recognized using these two decoders, and one hypothesis is selected based on posterior probability. The following sub-sections describe each module of our VRCS system acoustic features is estimated correctly. One of the main issues in applying them to VRCS is how to estimate the

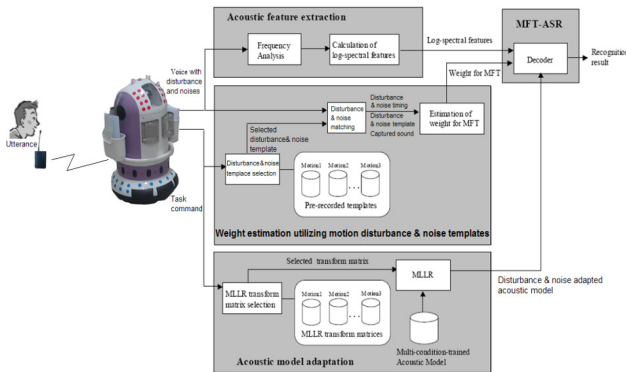


Fig. 1. Block diagram of the proposed method

reliability of input acoustic features correctly. Because the *signal-to-noise ratio (SNR)* and the distortion of input acoustic features are usually unknown, the reliability of the input acoustic features cannot be estimated. So, the SS-based method is not suitable for the robot. In addition, the size of a total system tends to be large. This means that the number of parameters for the system increases and more computational power is required by the system. Because the room and computational power a robot can use are limited, they are hard problems when being applied to a robot. Therefore, we focus on single channel approaches in this paper. Consequently, we use multi-condition acoustic model training, MLLR, and MFT.

2.1 Obstacle Detection and Local Map

The VRCS has three wheels; two driven wheels fixed at both sides of the mobile robot and one castor attached at the front and rear side of the robot. The ultrasonic sensors are mounted around of the mobile robot in middle layer for the detection of obstacles with various heights. In this study, a sonar array composed of 16 ultrasonic sensors cannot be fired simultaneously due to cross talk.

Instead, we adopt a scheduled firing method [9] where sensors are activated in sequence of $\{s_1, s_{12}, s_2, s_{11} \dots\}$. The arrangement of the ultrasonic sensors in upper layer and the sensors are marked as dots in the figure. The distances e_j ($j = 1, 2, \dots, 12$) from the origin of the robot frame $\{R\}$ to obstacles detected by the sensor s_j , can be defined as $e_j = \delta_j + R_r$. Here, R_r is the radius of the robot and the δ_j is the range value measured by the sensor s_j .

A local map is introduced to record the sensory information provided by the 16 sonar sensors with respect to the mobile robot frame $\{R\}$. Sector map defined locally at the current mobile robot frame is introduced. Then, the obstacle position vector se'_j with respect to the frame $\{R'\}$ can be calculated by

$$se'_j = \begin{bmatrix} \cos \delta\theta & \sin \delta\theta & 0 & -\sin \delta\theta / \rho_p \\ -\sin \delta\theta & \cos \delta\theta & 0 & (1 - \cos \delta\theta) / \rho_p \\ 0 & 0 & 1 & 0 \\ 0 & 0 & 0 & 1 \end{bmatrix} \tag{1}$$

where se_j denotes the obstacle position vector defined at the frame $\{R\}$. Hence, when the mobile robot is located at a point O' , the distance value $se'_j = \|se'_j\|$ from the origin of the frame $\{R'\}$ to the obstacle and angle $s\varphi'$ can be calculated by Eq.(1). Here, $\|\cdot\|$ denotes Euclidean norm.

The local map defined at the frame $\{R'\}$ is newly constructed by using the previous local map defined at the frame $\{R\}$ as follows:

$$Se_n \leftarrow Se'_j, n = INT\left(\frac{s\varphi'_j}{\varphi}\right) + \frac{N}{2}; j = 1, 2, \dots, N \tag{2}$$

Where \leftarrow and INT denote the updating operation and integer operation, respectively. Here, se_n , denotes the distance value of n th sector and N represents the number of the sector. If the range values obtained by sensors when the mobile robot is located at a point o' are $e_j = (j = 1, 2, \dots, 12)$, the new local map is partially updated as follows :

$se_j \leftarrow e_j, j = 1, 2, \dots, 12$. The maximum range of the sonar sensor is set to be $\delta_{max} = \delta_{max} - R_r$. Any return range which is larger than is ignored.

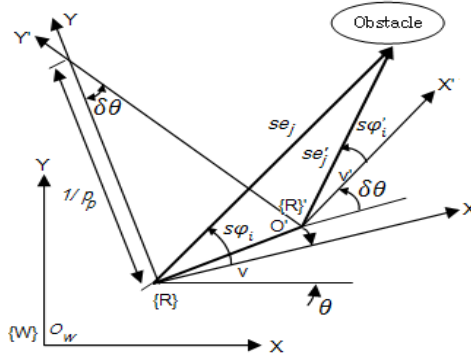


Fig. 2. The coordinate transformation for updating the local map

2.2 Design of Goal-Seeking Behavior and Avoidance Behavior

The primitive behaviors may be divided as follows: goal-seeking behavior, ball-following behavior, keep-away behavior, free space explorer and emergency stop, etc. The output of a primitive behavior is defined by the vector

$$u(t) = (v(t), \Delta\theta(t))^T = (v(t), w(t), Tms)^T \tag{3}$$

where t and Tms denote the time step and the sampling time, respectively. Here, T denotes the transpose and $\omega(t)$ denotes the angular velocity of the robot.

We will divide the primitive behaviors into two basic: avoidance behavior and goal-seeking behavior.

The avoidance behavior is used to avoid the obstacles irrespective of the goal position, while the goal-seeking behavior is used to seek the goal position irrespective of obstacle location. Design of each behavior proceeds in following sequences;

(A) fuzzification of the input/output variables, (B) rule base construction through reinforcement learning, (C) reasoning process, (D) defuzzification of output variables.

In order for the mobile robot to arrive at the goal position without colliding with obstacles, we must control the mobile robot motion in consideration of the obstacle position $X_{oi} = (x_{oi}, y_{oi})$, the mobile robot position $X = (x, y)$ and its heading angle θ with respect to the world coordinate frame $\{W\}$ shown in Fig. 3.

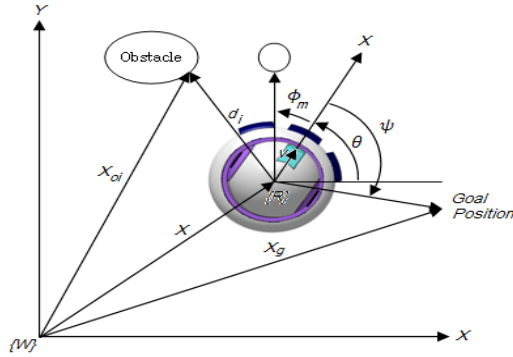


Fig. 3. The coordinate frames and control variables

In order to avoid the increase in the dimension of input space, the distance values d_i , ($i = 1,2,3,4$) are defined by

$$\begin{aligned}
 d_1 &= \min(se_1, se_2, se_3) \\
 d_2 &= \min(se_4, se_5, se_6) & 4a \\
 d_3 &= \min(se_7, se_8, se_9) & 4b \\
 d_4 &= \min(se_{10}, se_{11}, se_{12})
 \end{aligned}$$

As shown in Fig 3. ϕ_m ($-\pi \leq \phi_m \leq \pi$) denotes the orientation of a sector with the shortest range. We choose the input variables for avoidance behavior as ϕ_m and $d_i = \|X_{oi} - X\|$, ($i = 1,2,3,4$) for goal-seeking behavior as heading angle difference ψ and distance to goal $z = \|X_g - X\|$. The input linguistic variables d_i , ψ , ϕ_m and z are expressed by linguistic values (VN, NR, FR), (NB, NM, ZZ, PS, PM, PB), (LT, CT, RT) and (VN, NR, FR, VF), respectively Their membership functions are expressed.

2.3 Fuzzy Decision Maker

New method of selecting an appropriate behavior has been proposed among many primitive behaviors by using a fuzzy decision maker. Let $u = (u_1, u_2, u_3, \dots, u_n)$ be a set of motion commands resulting from the primitive behaviors and $\tilde{G} = (\tilde{G}_1, \tilde{G}_2, \tilde{G}_3, \dots, \tilde{G}_m)$ a set of fuzzy goals by which the suitability of a behavior is judged. The j -th fuzzy goal \tilde{G}_j is characterized by their membership functions $\mu_G(u)$. In what follows, the tilde sign(\sim) representing the fuzzy sets will be dropped for notational simplicity. However, there are some cases where some goals are of greater importance than others. In such cases, fuzzy decision function D might be expressed as the intersection of the goals with the weighting coefficients reflecting

the relative importance of the constituent terms. The problem is then to determine one of alternatives $u_i (i = 1, 2, 3, \dots, n)$ with the highest degree of suitability with respect to all relevant goals $G_j (j = 1, 2, 3, \dots, m)$. To this end, the fuzzy set decision D in discrete space is defined by

$$D = \left[\left\{ u_i, \min \left\{ \mu_{G_j}(u_i) \cdot w_j \right\} \right\} \right]_{i=1, 2, \dots, n; j=1, 2, \dots, m} \tag{5}$$

where $\sum_{j=1}^m w_j = 1.0$. Here, the coefficient w_j denotes the importance of goal G_j . The optimal motion command is defined as the output with the highest degree of membership in D .

When the mobile robot is located at O , as shown in Fig. 4, the repulsive and attractive potentials at the point can be calculated, respectively. Suppose that the mobile robot moves from a point O to a point O' along the path shown in the figure by the output vector of each behavior. The two potentials at a point O' then can be calculated, respectively. Using the above potentials, the differences between potential values at O and O' are calculated. Thus, when the output of each behavior is applied to the mobile robot, the changes of the repulsive and attractive potentials can be calculated by

$$c_{rep}(u_i) = \Delta E_{rep}(u_i) \text{ and } c_{att}(u_i) = \Delta E_{att}(u_i) \text{ , respectively.}$$

The robot motion is controlled by its linear velocity v and rotational velocity w . In order to control the mobile robot, the reference posture $P_r(t) = (x_r, y_r, \theta_r)^T$ and the current posture $P_c(t) = (x_c, y_c, \theta_c)^T$ shown in Fig. 4 are used. The reference posture is calculated by the reference velocity (v_r, w_r) which is determined by the output of a behavior selected by fuzzy decision maker. If the output of the selected behavior is $u = (v, \Delta\theta)$, the velocity (v_r, w_r) is defined as $(v, \Delta\theta)$. In order for mobile robot to have the reference velocity at the reference position, the velocities of two wheels must be controlled.

The purpose of this tracking controller is to make the error posture converge to 0. To achieve this, target velocities are calculated by using the error posture and reference velocities.

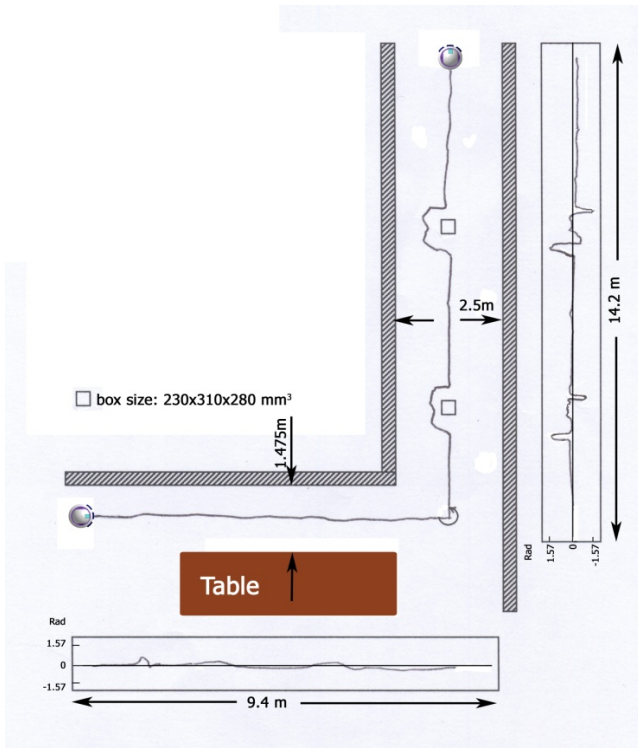
3 Experiments and Result

All the parameters used in the navigation experiments are given in Table 1. The mobile robot has the maximum travel speed of 0.52 m/s and the maximum steering rate of 1.854 rad/sec. Experiments are performed in an indoor with the first experiment for voice recognition without objects and second experiment for both of them: voice recognition and obstacles avoidance. The first experimental space is approximately 9.4m by 1.475m wide, and the second experimental space is approximately 14.2m by 2.5m wide. Fig. 4 shows a sketch of the top view of the room

with the object drawn in the box shape. Since this environment is too simple to test the performance of the overall system, several polygon obstacles were randomly placed in the path of the mobile robot navigation. The mobile robot was initially located at the origin of the world coordinate frame $\{W\}$ and the goal of the first experiment was that robot goes straight until someone speaks “turn left”. Then, the second experiment was active, respectively.

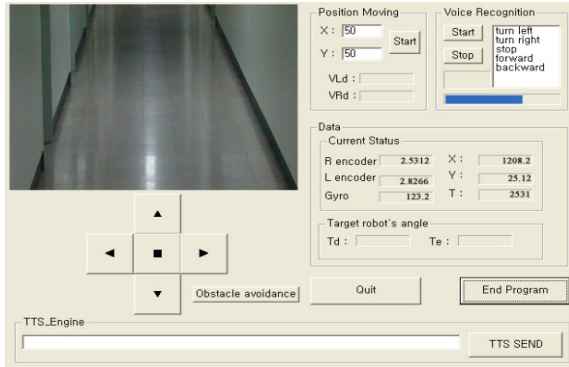
Table 1. The parameter values used for experiments

$D_r = D_l = 0.15m$	Encoder = 512x4
$R_r = 0.4m$	$K_p=0.8, K_i=0.23, K_d=0.04$
$v_{max}=0.55m/s$	$a_{max}=0.2m/sec^2$
$\bar{\varphi} = 11.5^\circ$	$c_j = -0.01N.m$
$c_2 = -0.03N.m$	$E_j = 0.9N.m$
$T_{ms} = 60msec$	$R_{max} = 6.5m$

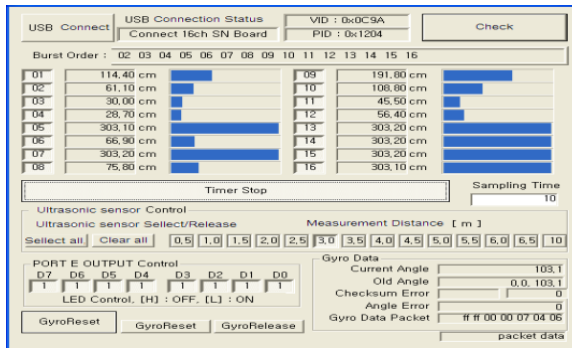


(a) Indoor environment

Fig. 4. The indoor environment for voice recognition and navigation experiments



(b) Voice recognition interface



(c) Obstacle detection using ultrasonic sensors

Fig. 4. (continued)

Through a series of the navigation experiments, it was observed that the heading angle error is a serious problem to mobile robot navigation relying on dead reckoning. The large heading angle error almost resulted from the wheels' slippage when the mobile robot changes its direction. Even if the wheel slippage occurs, the true position and heading angle of the mobile robot could be updated by two beacon pairs and consequently the mobile robot could arrive at the given goal position while avoiding the obstacles.

4 Conclusions

We have proposed the integration of robust voice recognition and navigation system capable of performing autonomous navigation in unknown environments. In order to evaluate the performance of the overall system, a number of experiments have been undertaken in various environments. The experimental results show that the mobile robot with the complete voice recognition and navigation system can arrive at the goal

position according to the desire of speaker even if the wheel slip occurs. From the developed of voice recognition and navigation system, it was observed that the mobile robot can successfully arrive at the desired position through the unknown environments without colliding with obstacles.

References

1. Lippmann, R.P., Martin, E.A., Paul, D.B.: Multi-style training for robust isolated-word speech recognition. In: Proc. of ICASSP 1987, pp. 705–708. IEEE (1987)
2. Blanchet, M., Boudy, J., Lockwood, P.: Environment adaptation for speech recognition in noise. In: Proc. of EUSIPCO 1992, vol. VI, pp. 391–394 (1992)
3. Barker, J., Cooke, M., Green, P.: Robust asr based on clean speech models: An evaluation of missing data techniques for connected digit recognition in noise. In: Proc. of Eurospeech 2001, pp. 213–216. ESCA (2001)
4. Renevey, P., Vetter, R., Kraus, J.: Robust speech recognition using missing feature theory and vector quantization. In: Proc. of Eurospeech 2001, pp. 1107–1110. ESCA (2001)
5. Yamamoto, S., Nakadai, K., Tsujino, H., Okuno, H.: Assessment of general applicability of robot audition system by recognizing three simultaneous speeches. In: Proc. of IEEE/RSJ International Conference on Intelligent Robots and Systems (IROS 2004). IEEE and RSJ (2001) (to appear)
6. Valin, J.-M., Rouat, J., Michaud, F.: Enhanced robot audition based on microphone array source separation with post-filter. In: Proceedings IEEE/RSJ International Conference on Intelligent Robots and Systems (2004)

Vision Based People Tracking Using Stereo Camera and Camshift

Kang-Il Park¹, Chan-Ik Park¹, and Jangmyung Lee^{2,*}

¹ Interdisciplinary Program in Robotics, Pusan National University, South Korea

² Department of Electrical Engineering, Pusan National University, South Korea
{kangil1696, chanik1696, jmlee}@pusan.ac.kr

Abstract. In this paper proposes a visual manipulation method that incorporates computation of 3D object position from characteristic disparity of stereo image. First, we proceed to an image revision work using the calibration. To obtain the characteristic disparity, a set of characteristic points, essential to obtain characteristics like center points or corner points are determined from the CAMShift center of left and right images. By iterative computation and tracking in real time, the algorithm is able to robustly provide accurate 3D position of target objects.

Keywords: Calibration, CAMShift Algorithm, Stereo Camera, People Tracking.

1 Introduction

Technology of detecting and tracking people has been applied in many application systems, such as a mobile robot system, automatic monitoring system, traffic monitoring system and the interaction between humans and robots. In particular, the field of mobile robots as well as on behalf of one human being can do in the future operation without the need for a separate well aware of the circumstances surrounding themselves can perform a variety of roles. And that is being studied harder [1].

In this paper, a method for obtaining three-dimensional information for people tracking is introduced. In robot manipulation, it is very important for vision-based operation to obtain accurate three-dimensional data from the two-dimensional image. For robotic manipulation, three-dimensional object recognition is required; the object recognition is to identify the target information, including the three-dimensional position and orientation. In general, the three-dimensional position is calculated by applying the Disparity of Stereo Camera, and accuracy of Disparity is a very important factor in determining the three-dimensional positional accuracy [2].

In this study, three-dimensional object tracking is performed. For this purpose, first of all, process to recognize objects. In this paper, shift algorithm was used [3]. First, proceed to an image revision work using the calibration. After the object recognition, continually verifying the center point of the object to track similar colors is based on color-based Color-Histogram of the object using CAMShift [4]. Applying this all the

* Corresponding author.

way on the left and right images of the stereo camera, the center point is well-defined. And because of using the average value of a certain area, you will be less of an impact of noise and illumination changes. Eventually, using the result of the CAMShift which is obtained by left and right center point, stable Disparity and the three-dimensional position can be obtained. Using these methods, study was operated with obtaining three-dimensional information for people tracking [5].

In Chapter 2, first, explain the Calibration for an image revision work. And study the CAMShift based algorithm for tracking a person, and then, explain the 3-dimension object tracking using the Stereo Camera.

2 Tracking Algorithm

2.1 Calibration

Camera calibration is one of the most basic, important step in the field of robot vision or computer vision. Specially, if a precise numerical measurement through the video analysis is needed, accurate calibration and calibration of distortion is necessary. The camera calibration means the process which seeks parameter where it explains the conversion relationship between 3D world coordinate and 2D image coordinate or the conversion relationship of this conversion. The conversion relationship is modeled as follows.

$$s \begin{bmatrix} x \\ y \\ 1 \end{bmatrix} = \begin{bmatrix} f_x & skew_cf_x & c_x \\ 0 & f_y & c_y \\ 0 & 0 & 1 \end{bmatrix} \begin{bmatrix} r_{11} & r_{12} & r_{13} & t_1 \\ r_{21} & r_{22} & r_{23} & t_2 \\ r_{31} & r_{32} & r_{33} & t_3 \end{bmatrix} \begin{bmatrix} X \\ Y \\ Z \\ 1 \end{bmatrix} \quad (1)$$

$$A = \begin{bmatrix} f_x & skew_cf_x & c_x \\ 0 & f_y & c_y \\ 0 & 0 & 1 \end{bmatrix}, [R | t] \begin{bmatrix} r_{11} & r_{12} & r_{13} & t_1 \\ r_{21} & r_{22} & r_{23} & t_2 \\ r_{31} & r_{32} & r_{33} & t_3 \end{bmatrix} \quad (2)$$

Here, (X, Y, Z) is the 3D point coordinates of world coordinate system, and [R | t] is the conversion (rotation/movement) matrix which converts world coordinate system with camera coordinate system, and A is the camera matrix.

Camera parameter can be divided into intrinsic parameter and extrinsic parameter on a large scale. From equation (1), A is the intrinsic parameter, and [R | t] is the extrinsic parameter.

Camera intrinsic parameter means the intrinsic parameter of the camera itself, and includes the focal length, principal point, distortion coefficient and non-symmetrical coefficient, etc of the camera. Camera extrinsic parameter is the parameter where it related to the geometric relationship with external space of the camera, and includes the installation height, the direction (fan and slope), etc of the camera [6].

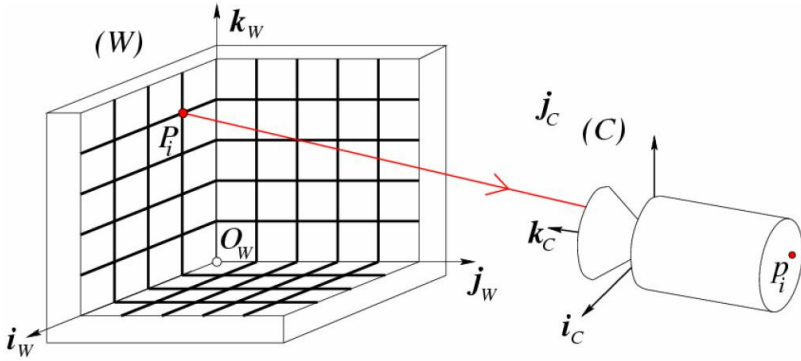


Fig. 1. Quantitative Measurements and Calibration

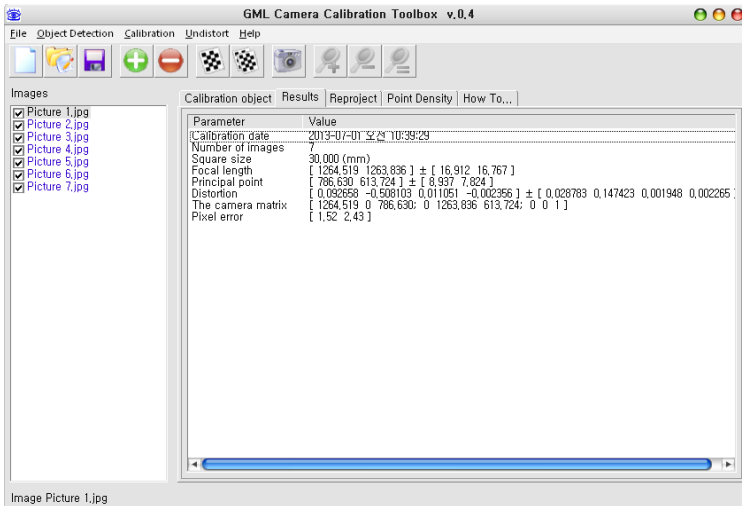


Fig. 2. Calibration Result using GML C++ Calibration Toolbox

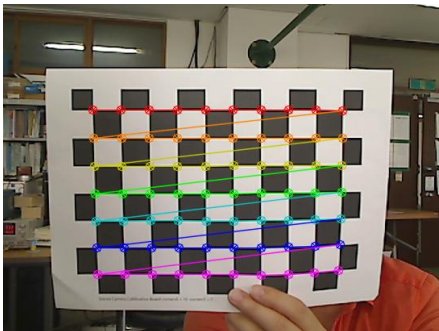


Fig. 3. Calibration from left camera



Fig. 4. Calibration from right camera

2.2 CAMShift Algorithm

The CAMShift stands for (meaning) Continuously Adaptive Mean Shift Algorithm was used for the first time for face detection. The CAMShift algorithm enhanced the success rate of the object tracking by continuously applying Mean Shift Algorithm to every frame and adaptively re-calculating the tracking object or the background. By default, when tracking by camera, object becomes bigger when the object comes closer and object becomes smaller when the object away. CAMShift using Mean Shift Algorithm can calculate the size and angle of the target using Mean Shift Algorithm and is suitable for this research because the algorithm is able to track the change in the size [7].

$$\nabla f(x) = \frac{2c}{nh^{d+2}} \left[\sum_{i=1}^n g_i \right] \left[\frac{\sum_{i=1}^n g_i \cdot x_i}{\sum_{i=1}^n g_i} - x \right] = \frac{2c}{nh^{d+2}} \left[\sum_{i=1}^n g_i \right] m \quad (3)$$

$\sum_{i=1}^n g_i$: Another kernel density estimation

$\bar{x} = \frac{\sum_{i=1}^n g_i \cdot x_i}{\sum_{i=1}^n g_i}$: Weighted average of given data points

$m = \bar{x} - x$: Mean shift

$$m = C \frac{\nabla f(x)}{\sum_{i=1}^n g_i}$$

At location x , the mean shift vector is proportional to the normalized density gradient estimate. The mean shift vector thus always points toward the direction of maximum increase in the density. Intuitively, the local mean is shifted toward the region in which the majority of the points reside.

CAMShift Algorithm

- Step 1. Choose a search window size.
- Step 2. Choose the initial location of the search window.
- Step 3. Compute the mean location (centroid of the data) in the search window.
- Step 4. Center the search window at the mean location computed in Step 3.
- Step 5. Repeat Steps 3 and 4 until convergence.

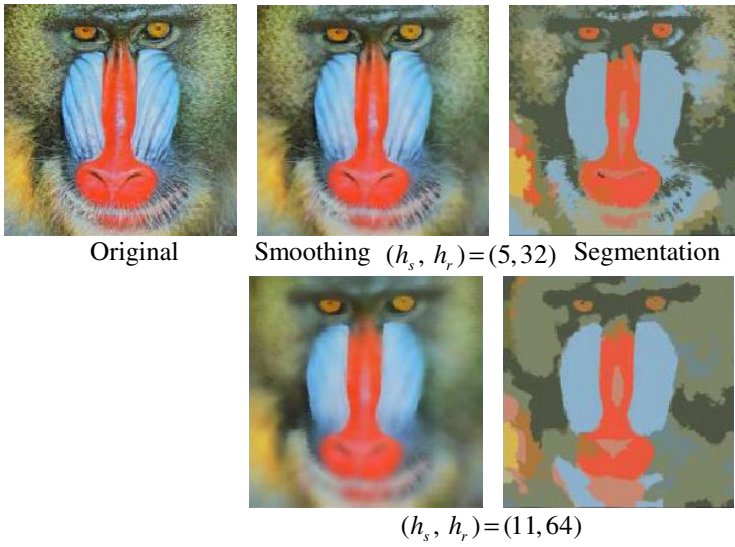


Fig. 5. Smoothing and Segmentation

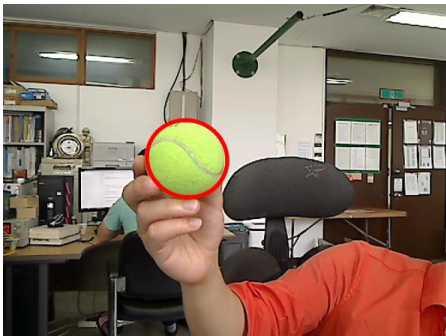


Fig. 6. Camshift from left camera



Fig. 7. Camshift from right camera



Fig. 8. Histogram

2.3 Stereo Camera

To create a stereo image, recall two images and process right and left images. After processing the images, the binarization process for the Gray images is required. Because image binarization processing is required at stereo camera. And, make the Disparity map variables obtained through the two video and image variable processing Disparity video. And then, output the disparity video.

Stereo Imaging



Fig. 9. Image from left camera

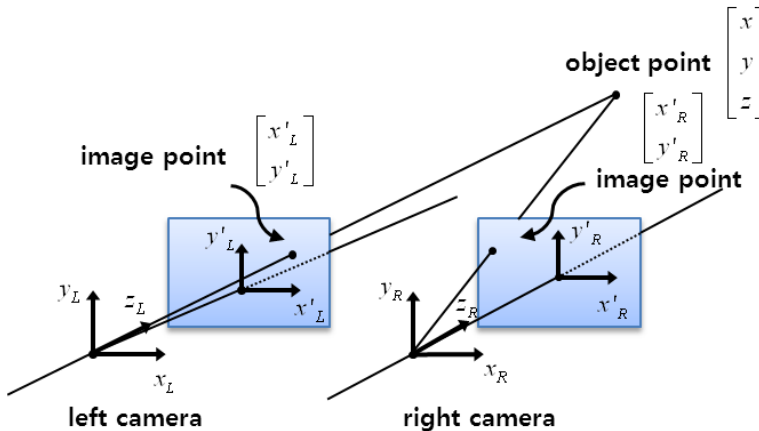


Fig. 10. Image from right camera

Stereo Vision

There are 2 big advantages in having 2 eyes, rather than 1: Redundancy (it's nice to have a backup), Stereopsis

When 2 eyes (or cameras) are placed side by side, they receive slightly different views of a 3D scene



Given : Left and right images
Goal : Determine $[x, y, z]$ wherever possible

Fig. 11. Binocular Stereo

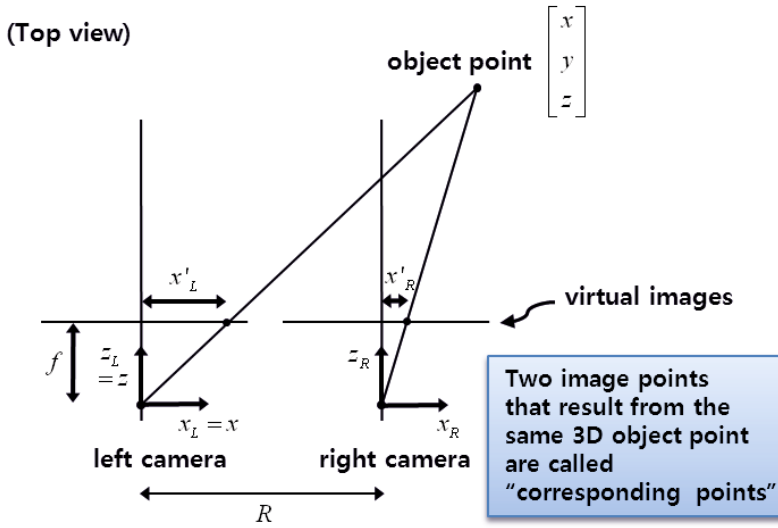


Fig. 12. Binocular Stereo top view

Stereo Algorithm

- Step 1. Acquire stereo image pair
- Step 2. Normalize images
- Step 3. Detect features (e.g., edges) in both images
- Step 4. Search for corresponding feature pairs
- Step 5. Output the image coordinates of the detected stereo pairs
- Step 6. Possibly map those 2D coordinates to 3D locations

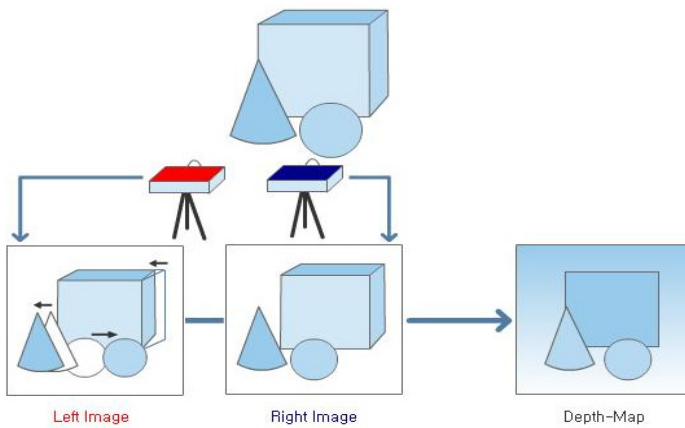


Fig. 13. Stereo camera condition

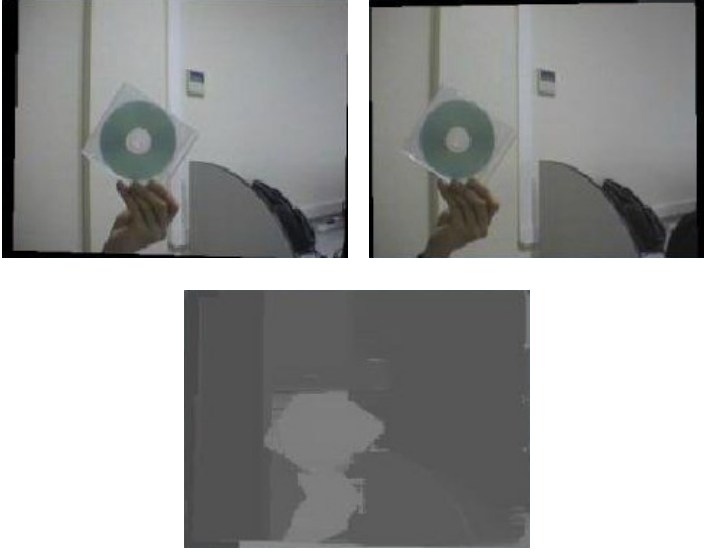


Fig. 14. Stereo camera result

3 Conclusion

In this paper, After separating object that want to track conducting the background removal and object extraction algorithm from the video information, The plan to do a mobile robot track the object via tracking algorithm. Use a stereo camera to obtain three-dimensional location information for tracking people. First, using the Calibration, we proceed to an image revision work, and propose the method of getting the Disparity applying the CAMShift to left and right image of the stereo camera. Applied CAMShift on the left and right images of the stereo camera, suggests ways to get the Disparity. It will be applied to track people utilizing the three-dimensional position information, using the actual robot hardware, and is thought to conduct more research in the future.

Acknowledgments. This research was supported by the MSIP(Ministry of Science, ICT & Future Planning), Korea, under the ITRC(Information Technology Research Center) support program (NIPA-2013-H0301-13-2006) supervised by the NIPA(National IT Industry Promotion Agency).

This research was supported by the MOTIE(The Ministry of Trade, Industry and Energy), Korea, under the Human Resources Development Program for Special Environment Navigation/Localization National Robotics Research Center support program supervised by the NIPA(National IT Industry Promotion Agency). (H1502-13-1001).

References

1. Lee, S.-J., Won, M.-C.: A vision based people tracking algorithm for mobile robots. In: KSME, pp. 871–874 (2011)
2. Shapiro, L.G., Stockman, G.C.: Computer Vision. Prentice-Hall (2001)
3. Lowe, D.G.: Distinctive Image Features from scale-Invariant keypoints. *International Journal of Computer Vision* 60(2), 91–110 (2004)
4. Bradski, G.R.: Computer Vision Face Tracking For Use in a Perceptual User. *Intel Technology Journal* 2(2), 12–26 (1998)
5. Choi, S., Kim, C.-O., Jeong, J.-N., Yang, G.-W., Kim, H.-S.: Robust Object Tracking and Visual Servoing using Stereo Camera and CAMSHIFT. In: ICROS, vol. 36, pp. 164–169 (2007)
6. Lee, J.-Y.: Camera Calibration and Distortion Correction. *KROS* 10(1), 23–29 (2013)
7. Chang, I.-S., An, T.-K., Park, K.-Y., Park, G.-M.: PTZ Camera Tracking Using CAMShift. *KICS* 35(3), 271–277 (2010)
8. Allen, J.G., Xu, R.Y.D., Jin, J.S.: Object Tracking Using CamShift Algorithm and Multiple Quantized Feature Spaces. In: VIP 2003, vol. 36, pp. 3–7 (2003)
9. Eduardo, R., Isabelle, F.C., Anand, S., Guillaume, S.: Optical Flow-Based Controller for Reactive and Relative Navigation dedicated to a Four Rotor Rotorcraft. In: IEEE/RSJ Int. Conference on Intelligent Robots and Systems, pp. 686–689 (2009)
10. Duque, D., Santos, H., Cortez, P.: Moving object detection unaffected by cast shadows, highlights, and ghosts. In: Proc. IEEE Int. Conf. Image Processing, vol. 3, pp. 413–416 (2005)
11. Hartley, R., Zisserman, A.: Multiple View Geometry in Computer Vision. Cambridge Univ. (2000)
12. Jain, R., Kasturi, R., Schunk, B.G.: Machine Vision. McGraw-Hill (1995)
13. Zhang, Z.: A Flexible New Technique for Camera Calibration. *IEEE Trans. Pattern Analysis and Machine Intelligence* 22(11), 1330–1334 (2000)
14. Trucco, E., Verri, A.: Introductory Techniques for 3-D Computer Vision. Prentice-Hall (1998)
15. Open Computer Vision Library | Get Open Computer Vision Library at SourceForge.net, <http://sourceforge.net/projects/opencvlibrary>
16. Middlebury Stereo Vision Page: Data, <http://cat.middlebury.edu/stereo/data.html>

Analysis of Active Haptic Feedback Effects on Standing Stability

Muhammad Raheel Afzal, Yasir Jan, Syed Hassan, and Jungwon Yoon*

Robot and Intelligent Systems Lab,
School of Mechanical & Aerospace Engineering, ReCAPT,
Gyeongsang National University,
Jinju, Republic of Korea
{raheel379,yasirjan}@gmail.com, {hassan,jwyoony}@gnu.ac.kr

Abstract. Upright standing posture is maintained through a continuous sensing and muscle activation by the brain. Any relevant disability may result in an unstable posture and thus increased body sway. To decrease body sway haptic feedback sensing can be used. This paper presents an experimental study about comparison of reduction in body sways using different haptic feedbacks. Anteroposterior (AP) and Mediolateral (ML) body sway were measured through a smartphone, and active feedback was provided using Phantom Omni device. Tests were performed in various postures and the body sway was analyzed with continuous haptic feedbacks. The study shows that active guidance to user produces more stability compared with sensory feedback.

Keywords: Haptics, Standing stability analysis, Smart phone, Body Sway.

1 Introduction

Body sway plays an important role to gain authority of safe and confident locomotion in humans. Human body has multiple sensing inputs including vestibular sensation, vision through eyes, proprioception through leg muscle movements and tactile sensations through soles of the feet for the detection of body sway. The body sway information acts as a feedback to the brain, and based upon the sensed feedback the brain decides in which direction body needs to be tilted to maintain its upright standing posture. Absence or weakening of sensor feedbacks results in higher body sway. Similarly for elder people there is a lack of self-confidence in feeling stable due to the insufficient muscle activation. Therefore, with the increased feedback the brain can make more proper decision about the body tilts and thus reduce body sway.

Human body sway occurs in both sagittal plane i.e. front back movement and frontal plane i.e. sideways left or right movement. In the sagittal plane, center of mass of the body naturally lies in front of the ankle, so the tendency is for anteroposterior (AP) sway [1]. In the frontal plane, the bridge-like frame formed by the legs and pelvis with CoM in the middle appears more stable, however, the slightest sideways

* Corresponding author.

displacement in either direction results in sway in that direction. Body sway has been assessed for static balance and dynamic balance conditions, depending on whether the base is stationary or moving (such as standing or walking) [2].

In order to measure Body sway, various techniques and instruments are being used. Force measurement platforms are widely used as a system to analyze body sway. Taylor et al. [3] Analyzed the usability of pressure sensitive floor sensors along with a processing algorithm for capturing clinical information related to standing stability. Other than the pressure based systems vision based systems are also used. Webcams are relatively much cheaper solution than Vicon motion capture system. Wang et al. [4] Developed a measurement system using low cost web cameras and validated the results with good agreement for body sway during standing using a marker-based Vicon motion capture system. Once the body sway is detected through any system, intelligent algorithms are applied for various analysis of stability. Maatar et al. [5] Presented an analysis of stabilogram using the Principal Component Analysis (PCA) decomposition and also analyzed the effects of different aspects on the human postural stability. The system used to obtain human posture and sway related data is based on an electromagnetic platform; the subject stands on the electromagnetic platform with an electromagnetic sensor mounted on waist to measure changes in position of body posture. All these techniques have their own limitations and mainly use some expensive special equipment. An alternate technique which could be cheaper and based upon easily available equipment would be beneficial.

Now-a-days smartphone is very common in public and using the smartphone for measuring body sway can reduce the cost of many rehabilitation and medical aid systems. Smartphone devices have onboard inertial and magneto sensors which make them a handful for use. He et al. [6] Presented an implementation of a real-time classification of human movement based on smartphone mounted on the waist. Body motions were detected as different patterns i.e. vertical activity, lying, sitting or static standing, horizontal activity and fall.

Light touch refers to a fingertip contact with a stable physical object to provide assistance in reducing body sway. Holden et al. [7] Studied how sensory-motor information about body displacement provided by contact of the index finger with a stationary bar can be used to stabilize balance in the absence of vision. Stabilization equivalent to the contribution conferred by vision was achieved at contact force levels less than 1 N. This value of force is much less than that is necessary to provide significant physical stabilization of the body hence proving the concept of light touch as assistance for human brain to produce better upright balance. Kouzaki et al. [8] made a better observation of this concept. They investigated the light touch effect on postural stability during quiet standing with and without somatosensory input from the fingertip and observed that sway reduction with light touch disappeared when the hand was anaesthetized using a compression block on the upper arm.

Haptic devices are widely used to provide limited feeling of mechanical properties like force, vibration and friction while working in a virtual graphics environment. So they can be used for the light touch feeling to reduce body sway. However Wing et al. [1] used Phantom Premium1.5 device to show that 'light tight touch' contact by the index finger held in the thimble of a haptic device results in increased anteroposterior (AP)

sway with entraining by either simple or complex AP sinusoidal oscillations of the haptic device. Moreover, sway is also increased when the haptic device plays back the prerecorded AP sway path of another person. So there is a difference in human behavior with the difference in haptic feedbacks to the body. A study is required to understand the complex relation between various postures and various types of haptic feedbacks.

This research presents an experimental study on body sway changing with varying haptic feedbacks in different postural conditions. Details of the designed platform for analysis and data collection are discussed in Section 2, while experimental protocol and details of the participants are presented in Section 3. Results from the analysis are documented in Section 4, Section 5 is about the observations and discussion and Section 6 is conclusion derived from this study.

2 Platform Design

In our presented study we measured body sway, i.e. tilt in ML and AP. An smart phone was attached at waist height to the subjects, such that the sagittal plane of the subject's body gets aligned with the XZ plane of the phone for measuring AP tilt angles, while the frontal plane of the subject's body aligns with the XY plane of the phone for measuring ML tilt angles.

An Android application runs on the smartphone which keeps on measuring ML and AP tilt angles from the subject, using its internal orientation sensors. While a socket program based application running on a computer is connected to LAN through Ethernet. The android phone continuously sends data packets through sockets, over wireless network, and the server application continuously listens to the packets received through Ethernet. The transmitted data packet has encoded information about the ML and AP values. That computer program reads the data packet and decodes it to get the ML and AP values.

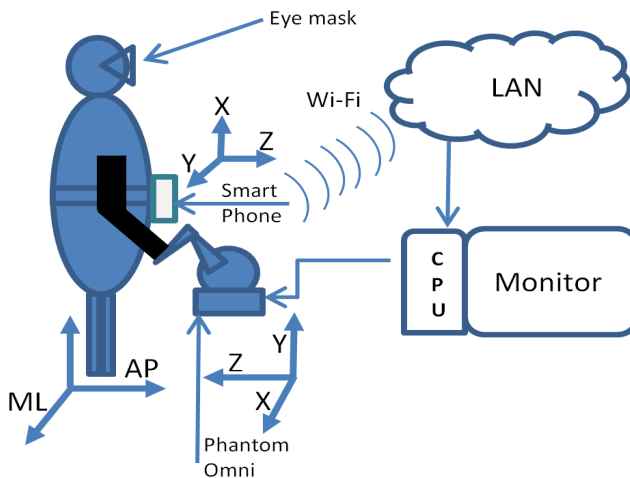


Fig. 1. Hardware setup for experimentation

When the experiment has to initiate, the application has to load the initial ML and AP values, and store the values for the next 30s (single experiment time) in a file. Such operations relevant to the application are controlled by the operator using keyboard keys. The application then makes a decision for the haptic feedback device, based upon the test type, posture and ML and AP values.

The phantom Omni device is used to produce directional force in x and z axis controlled by the application. But its movement is constrained in y axis; a spring force is produced as a reaction to any force trying to move haptic interface point (HIP) in y axis. Phantom Omni stylus handle is grabbed by the subjects to feel light touch through its movement in a specific direction.

The body sway input to the application is mapped linearly over the output haptic device movements. The body sway is supposed to be within the range of positive and negative 15 degrees with respect to the initial position. If it is more tilt than that, the person is considered as out of control and has thus crossed boundary state, thus no need to provide haptic feedback relevant to it. So at this point the haptic device movement is constrained at the last position. The 30 degrees range of ML and AP are mapped to 120 mm range of HIP movement for each respective direction. The output force from the phantom Omni haptic device was always limited to be less than 1N and therefore the HIP could deviate from its position if any subject exerted a force larger than 1N on the device handle. Exact mapping varies with varying postures and tests.

3 Experiment

Various tests were performed on the subjects regarding their stability analysis. These tests were earlier approved by local ethics review committee.

3.1 Testing Protocol

Subjects were instructed to stand barefoot relaxed and still, without speaking to anyone. The experiment needed reduced feedback through other sensors as much as possible, so an eyes mask was used for confirming no feedback through vision during all tests. High density foam with dimensions of 600x600x150 millimeters was used to produce soft ground conditions, for certain tests, causing more unstable surface for upright standing.

The tests were of four types, based upon the subject's body postures and ground conditions.

P1: Standing using one foot on ground and head facing forward.

P2: Standing heel to toe (tandem Romberg stance) on ground and head facing forward

P3: Standing on one foot on foam and head facing forward

P4: Standing heel to toe (tandem Romberg stance) on foam and head facing forward

Each of these posture tests were taken with three different feedback categories of haptic response as described below.

- F1: *No feedback*: The subject did not have any contact with HIP, i.e. both arms were free and near subject's body.
- F2: *Directional sensing feedback*: The subject's contact to HIP moves in a linear way in the direction of tilt, providing information to the subject's hand about body tilt
- F3: *Active guidance feedback*: The subject's contact to HIP is providing an active guidance feedback force to subject's hand for stability.

The three categories of haptic feedbacks (one including no feedback) were provided to the subjects in all the four posture tests. So a total of 12 tests per subject were taken.

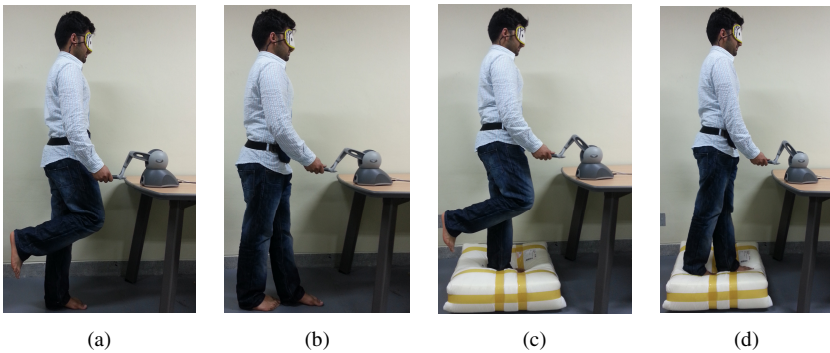


Fig. 2. (a) Posture P1. (b) Posture P2. (c) Posture P3. (d) Posture P4.

3.2 Participants

The physical appearances and other details of the subjects are mentioned in the table.

Table 1. Details about the subjects involved in this research study

Total number of subjects	10
Male / Female	7/3
Range of Age	21-32 years
Range of weights	55-99 kg
Range of heights	158-185cm

4 Results

The ML and AP values are transmitted from smartphone to the application. The speed of data samples received by the application from the smartphone over the network depends upon various factors e.g. smart phone sensing speed, the Wi-Fi transmission speed, the application running speed etc. All these factors vary with time, so a precise

decision about number of samples received over 30 seconds is not easy. Therefore limited number of samples i.e. 300 samples are sampled which is an approximation of the number of samples received. These 300 samples are stored, plotted and analyzed using MATLAB®.

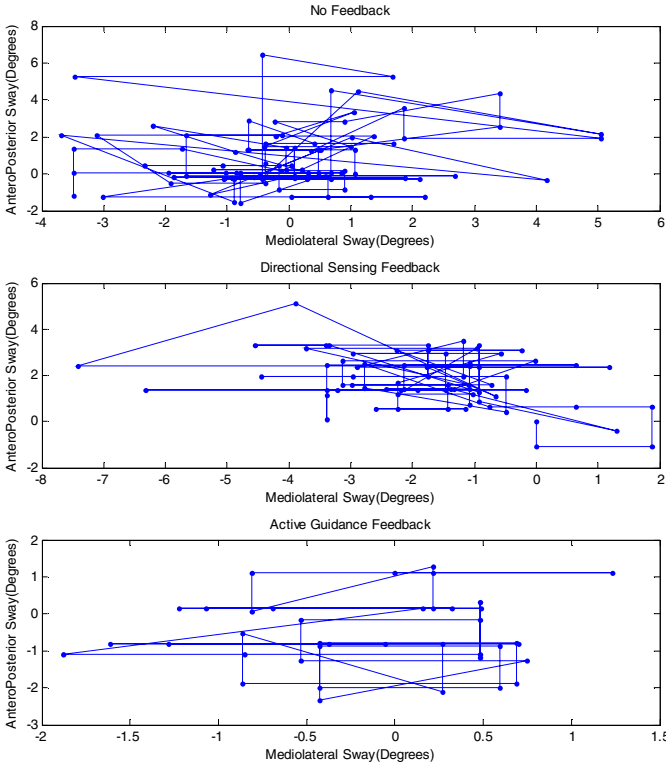


Fig. 3. Graph of ML and AP sway in Posture P1 for all three feedbacks

The graphs (in Fig. 3) show the ML (x-axis) and AP (y-axis) values plotted w.r.t. each other, in various postures and feedbacks. The dots show the tilt angle of the body and lines show the path followed while moving from one position to another. In each graph, initial position is marked as 0 deg ML and 0 deg AP, and with a set of 300 samples the graph is plotted with the followed path.

Other than the graphical analysis, the data was also analyzed numerically to sum up the total body sway (TBS) in each test. Total body sway is calculated by adding the change in tilts after each sample as compared to previous sample. i.e.

$$TBS = \sum |p_{st} - c_{st}|, \text{ for all 300 samples}$$

Where p_{st} = previous sample tilt angle
 c_{st} = current sample tilt angle

The graphs (in Fig 4, 5, 6, 7) show the TBS of all the feedback types, for each subject, for Posture 1,2,3 and 4 respectively.

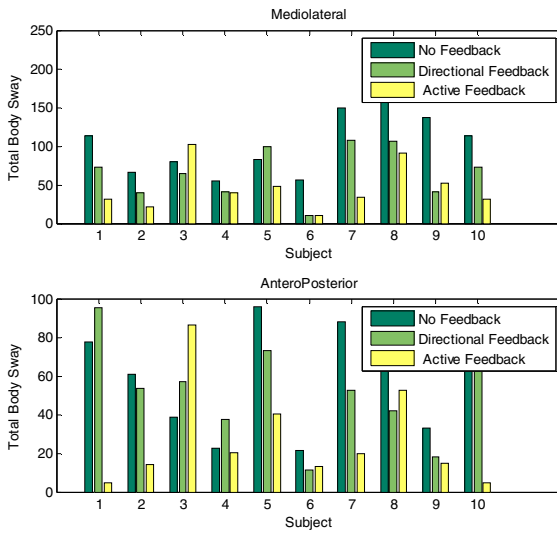


Fig. 4. (a) Posture P1

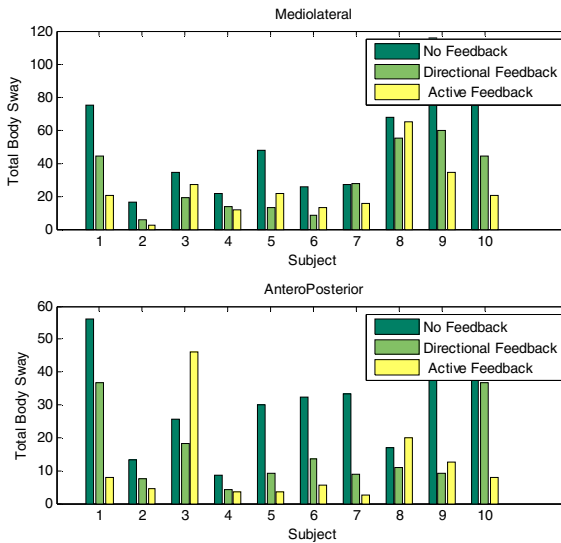


Fig. 5. (a) Posture P2

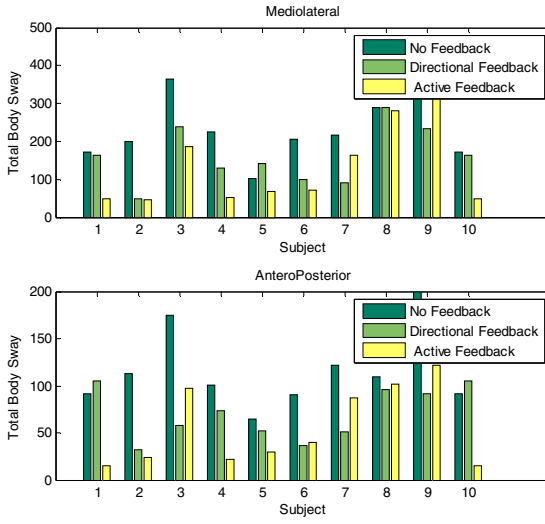


Fig. 6. (a) Posture P3

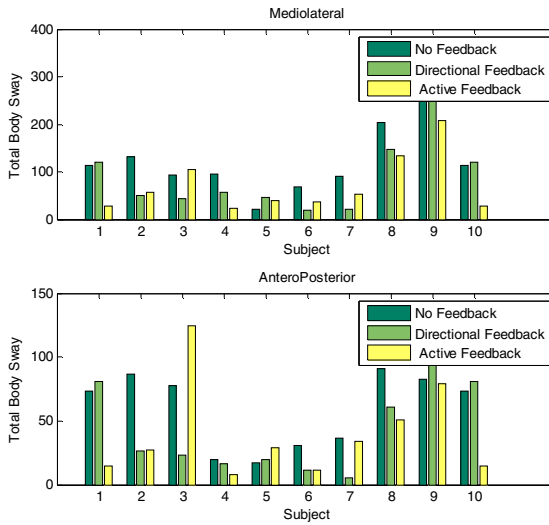


Fig. 7. (a) Posture P4

All these graphs show that the F3 has best results in all scenarios i.e. Total body sway of F3 is least as compared to F1 and F2, in each test.

5 Observations and Discussion

All the experiments lead to the following three observations.

- Observation1: No Feedback (F1) has maximum TBS amongst all
- Observation2: Directional sensing feedback (F2) has more TBS than Active guidancefeedback (F3)
- Observation3: Active guidance feedback (F3) has least TBS amongst all

Each of the three observations, for both ML and AP,so total six observations needs to be verified for all four postures. Therefore a total of 24 observations should be verified. As each experiment was performed on 10 subjects, so each observation was verified based upon the results of all 10 subjects. A net summary about the number of subjects verifying each observation is shown (Fig. 8.).

In the figure 8, Each value represents the percentage of total number of subjects whose results verify the observation. For example left most bar value 80% represents, body sway measurements in 8 out of 10 subjects in posture P1 have maximum ML body sway with No feedback. Hence, the higher value means more confirmation about the observation.

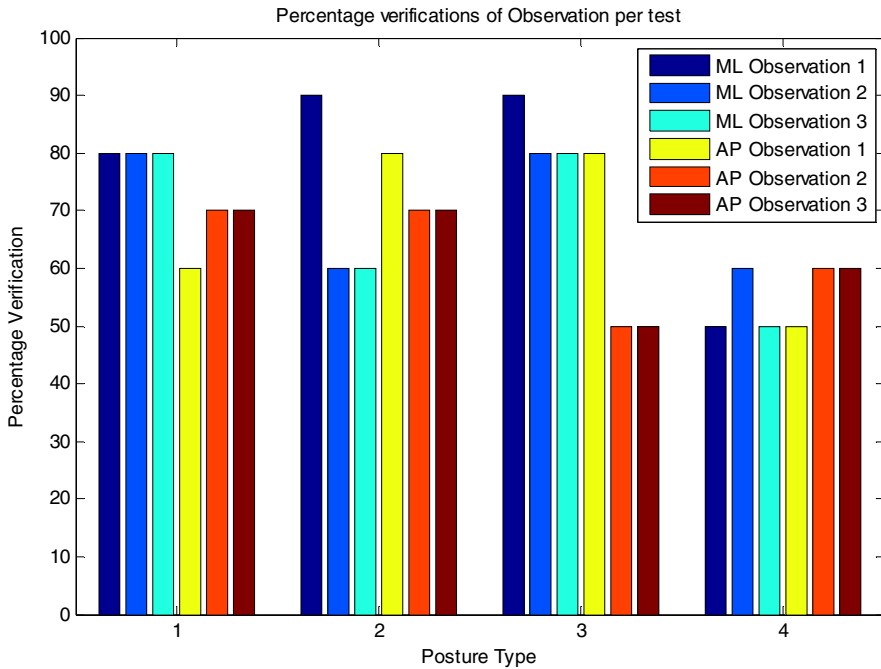


Fig. 8. Percentage verifications of each conclusion per test for all the postures

6 Conclusion

This research presents an experimental study on body sway changing with varying haptic feedbacks in different postural conditions. Results give the comparison between three types of feedbacks. Person with no feedback will have maximum body sway. Person's body sway can be reduced with the help of directional sensing feedback (F2). However, using active guidance feedback (F3) the body sway of that person can be further reduced. These conclusions were based upon percentage verification of the observations(Fig. 9.)

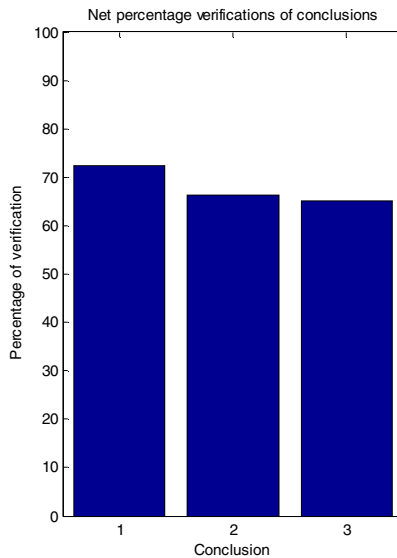


Fig. 9. Net percentage verifications of conclusions

Acknowledgments. This work was supported by National Research Foundation Korea (NRF) (2011-00313832010-0029690 & 2012R1A2A2A01047344) and BK21 PLUS (Brain korea21).

References

1. Wing, A.M., Johannsen, L., Endo, S.: Light touch for balance: influence of a time-varying external driving signal. *Philosophical Transactions of the Royal Society B: Biological Sciences* 366(1581), 3133–3141 (2011)
2. Spirduso, W.W.: *Physical Dimensions of Aging*. Human Kinetics, Champaign Illinois, USA (1995)
3. Taylor, M., et al.: Assessing standing stability of older adults using pressure sensitive arrays. In: *2012 IEEE International Symposium on Medical Measurements and Applications Proceedings (MeMeA)*. IEEE (2012)

4. Wang, F., et al.: Body sway measurement for fall risk assessment using inexpensive webcams. In: 2010 Annual International Conference of the IEEE Engineering in Medicine and Biology Society (EMBC). IEEE (2010)
5. Maatar, D., et al.: Modified PCA Stabilogram Decomposition and Analysis of Fluctuations Phase Diffusion. In: 2012 Spring Congress on Engineering and Technology (S-CET). IEEE (2012)
6. He, Y., Li, Y., Bao, S.-D.: Fall Detection by built-in tri-accelerometer of smartphone. In: 2012 IEEE-EMBS International Conference on Biomedical and Health Informatics (BHI). IEEE (2012)
7. Holden, M., Ventura, J., Lackner, J.R.: Stabilization of posture by precision contact of the index finger. *J. Vestib. Res.* 4(4), 285–301 (1994)
8. Kouzaki, M., Masani, K.: Reduced postural sway during quiet standing by light touch is due to finger tactile feedback but not mechanical support. *Experimental Brain Research* 188(1), 153–158 (2008)

Speed Adaptation of a Small Size Treadmill Using Impedance Control Approach for Rehabilitation

Jungwon Yoon^{*}, Auralius Manurung, and Irfan Hussain

Robot and Intelligent Systems Lab, School of Mechanical Engineering and ReCAPT,
Gyeongsang National University,
Jinju City, South Korea
jwyoona@gnu.ac.kr, auralius@lavabit.com,
irfanmechatronics@gmail.com

Abstract. Automatic speed adaptation in treadmill training plays an important role in gait rehabilitation. To implement automatic speed adaptation of a treadmill belt, we have developed a novel impedance control scheme that accommodates natural movements without mechanical attachments to the user, and can estimate user-treadmill interactive forces to directly detect user intention, while simultaneously maintaining the user's position on the treadmill platform. The experimental results showed that our impedance control scheme can provide a non-intrusive, intuitive method for implementing user-selected speed on a small treadmill. The proposed technique is cost-effective, and could potentially be applied to any type of locomotion interface or gait rehabilitation system, without the use of expensive, sophisticated sensors or special treadmills.

Keywords: Impedance control, treadmill, automatic speed adaptation, gait rehabilitation.

1 Introduction

A treadmill is commonly used in athletic training and clinical assessments such as gait rehabilitation. A treadmill system that automatically adapts its speed to user intention can be very beneficial, since it allows users to interactively participate in training or simulations that involve walking. For rehabilitation purposes, treadmill training with a body weight support system has shown significant success in treating chronic non-ambulatory patients [1]. Recently, there has been increasing demand for self-selected speed adaptation with higher patient intention to enhance the effectiveness of gait training [2].

Most existing schemes for automatic speed adaptation of a treadmill can be categorized as user-position-based controls, user-force-based controls, or gait-parameter-based controls. One traditional method for speed adaptation of a locomotion interface [3] or gait rehabilitation system [4,5] is to update the treadmill

^{*} Corresponding author.

speed via measurement of the physical interaction force between a user and a mechanical system. Since a user feels an inertial force proportional to his/her body weight during acceleration on the overground, a control command for obtaining velocity updates can be derived from force measurements through a mechanical tether [3,4], or can be estimated by measuring the joint torques of a Lokomat [5]. This approach allows user intention to be directly acquired for speed updates, and can be effective for safe navigation of a locomotion interface and safe gait rehabilitation training. However, it can also restrict the user's natural motions during walking, and may not provide realistic proprioceptive feedback from mechanical characteristics for normal users and highly ambulatory patients [6]. It has recently been reported that measuring ground reaction forces on a separate treadmill can provide a self-selected speed scheme [7] for a stroke patient with asymmetric gait, without severely restricting user motions. However, the technique requires an expensive instrumented treadmill and a complicated environment for user position measurements, which presents an obstacle to its widespread use.

Another traditional approach is to employ user position to provide proportional–integral–derivative (PID) control [8–10] of pelvis displacements to obtain treadmill speed updates. Even though this approach is simple and easy to implement, it makes it difficult to detect natural user intention for speed updates, and is hampered by stability problems during human–robot interactions. An advanced control algorithm with a variable reference position [11,12] has been suggested to achieve smooth speed trajectories on a large specialized treadmill (6 meters long), so that the user feels less inertial force during speed changes. However, this scheme may make it difficult to maintain a user's position on a small treadmill, since the reference position changes to reduce user acceleration.

The third approach for obtaining treadmill speed updates utilizes gait parameters such as stance time [13] or the maximum foot-swing velocity [14] to estimate a user's velocity while walking on a treadmill. Even though this type of scheme allows fast velocity estimation (at a half-step of gait), and its feed-forward estimation concept promotes stability, it also requires a motion-capture system to measure gait parameters in real time, and must interpolate the individual gait parameters to obtain the desired velocity estimates. Existing research [3–14] on the automatic control of treadmill adaptation has failed to provide a non-intrusive method for natural human–robot interaction, or else has required the use of complex and expensive integrated systems, or interpolation procedures to acquire the gait patterns of an individual user. Therefore, it is necessary to develop a new approach that provides natural and reliable speed updates in a nonintrusive way, as well as economical and simple installation solutions for widespread use.

In this paper, we propose a novel automatic speed-adaptation scheme with impedance control for a small commercial treadmill, utilizing a virtual spring–damper concept and inexpensive sonar sensors. As simple impedance controller [15] exactly mimics the behavior of a virtual spring and damper, the robot behaves exactly as it would with a real spring and damper connecting it to a constant pose, which guarantees stable interaction with all passive environments. The impedance controller with a virtual spring–damper components makes it possible to avoid restricting user motions while measuring interaction forces, and to obtain treadmill speed updates from estimated forces. Thus, the proposed scheme can control both the desired force

and the position of a user for speed adaptation on a small treadmill (e.g., with a belt length of 1.2 m and a width of 0.5 m). Moreover, the system can conveniently measure user motions with inexpensive sonar sensors and Kalman filter algorithms [16–19]. Therefore, it is nonintrusive, compact and economical, performs satisfactorily, and shows significant potential for application to gait rehabilitation and virtual environment navigation.

2 Speed Adaptation Treadmill System

The treadmill used in this experiment was a conventional exercise treadmill (Healma, South Korea). It was equipped with an alternating current (AC) motor (Eul Ji Electrical Machinery Co., Ltd., Korea), capable of delivering a maximum belt speed of 1.8 m/s. The AC motor was powered by an iG5A inverter drive (LS Industrial Systems Co., Ltd., Korea), with an analog input range of 0–10 volts to provide the desired motor speed.

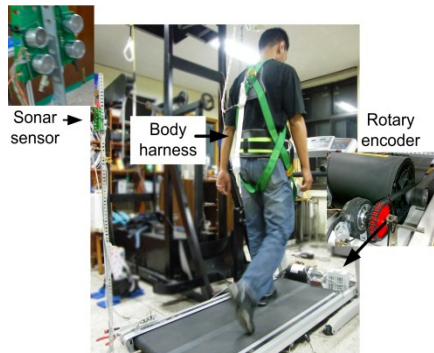


Fig. 1. Treadmill system for walking speed adaptation

The original speed controller from the manufacturer was dismantled and replaced with a CompactRIO real-time controller (National Instruments, USA). A quadrature rotary encoder (Mecapion Co., Ltd., Korea) was attached to the rotating axis of the belt (Fig. 1) to measure the belt speed of the treadmill. The specifications for the control hardware used in this research are summarized in Table 1.

Table 1. Control hardware specifications

Item	Specifications
AC Motor	1.5 kW, 3 ϕ , 220 V, 6.6 A, 60 Hz, 1680 RPM
Inverter Driver	4.5 kVA, 3 ϕ , 200–230 V, 12 A
Encoder	2500 CPR
Controller	NI cRIO 9004, Modules: NI 9401 and 9403, Digital Input/Output, NI 9263 Analog Output

3 Actuator Control of a Treadmill

3.1 Actuator Control

Figure 2 shows the overview of the control systems

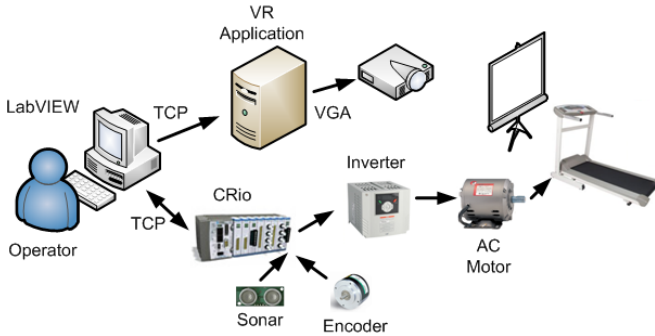


Fig. 2. Overview of the control systems

The purpose of the low-level control is to enable the treadmill motor to track a predefined reference speed with a high degree of precision. The AC servomotor of the treadmill is subject to external disturbances, such as the frictional force between the belt and the motor, which varies according to the body weight of the user. For these reasons, we selected the proportional–integral sliding-mode control (PISMC) from among the available robust control techniques. Sliding-mode control (SMC) is a high-speed switching control that switches between two values in accordance with certain rules. It does not require an exact dynamic model, and hence is easy and practical to implement. The proportional–integral (PI) provides the SMC with an extra tuning parameter, and offers greater flexibility in obtaining the desired performance [4]. The PISMC controller was programmed in the NI CompactRIO controller, with a sampling rate of 500 Hz.

3.2 Kalman Filter

A rotary encoder is used to measure the rotational angles of the belt. In this research, we employ a Kalman filter, which can reliably estimate speed and acceleration values from noisy signals. It has good dynamic behavior and disturbance resistance [16].

A kinematic model describing the relationship between the position, velocity, and acceleration of the treadmill belt can be written as follows [17]:

$$\dot{x} = \begin{bmatrix} 0 & 1 & 0 \\ 0 & 0 & 1 \\ 0 & 0 & 0 \end{bmatrix} x + \begin{bmatrix} 0 \\ 0 \\ 1 \end{bmatrix} w \quad (1)$$

$$y = [1 \quad 0 \quad 0]x + v \quad (2)$$

States x_1 , x_2 , and x_3 are the position, velocity, and acceleration, respectively, of the treadmill belt. The variables w and v are process and measurement noises, with covariances of q and r , respectively. In order to estimate the velocity and acceleration of the treadmill belt, a scalar Kalman filter can be implemented for the kinematic model of Equations (1) and (2). A diagram of the overall low-level control is shown in Fig. 3

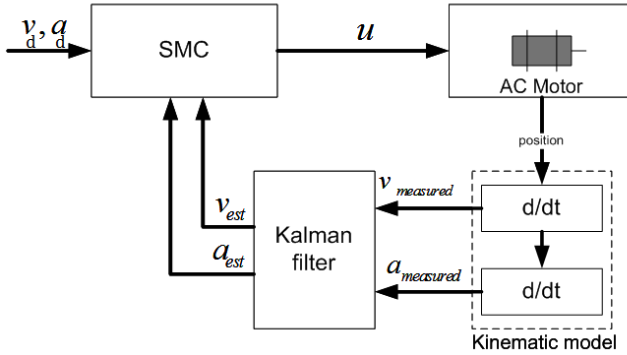


Fig. 3. Sliding-mode control with a Kalman filter for state estimation

4 Impedance Control of a Treadmill

4.1 Measurement of User Motions

4.1.1 Measurement of User Displacement via Sonar Sensor System

In this research, we used a sonar sensor (Devantech SRF05 Ultrasonic Ranger, Devantech, Ltd., England) for distance measurement, since it is inexpensive and offers relatively acceptable performance. As Fig. 1 shows, the sonar sensor was placed at the rear of the treadmill to measure the subject position (x), with a sampling rate of 40 Hz. Figure 4 shows the calibration results for the sonar sensor used in our system, indicating the relationship between the value of the counter (microseconds) and the corresponding distance (cm).

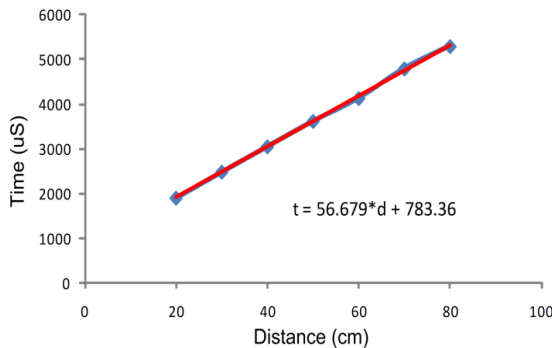


Fig. 4. Calibration results for the sonar sensor SRF05

To reduce the noise levels in the distance measurements, two sonar sensors were combined, using a multiple Kalman filter as a smoother. The sonar sensors were fired sequentially to avoid crosstalk between them. Letting x_1 and x_2 denote the outputs from the local Kalman filters, and P_1 and P_2 their respective error covariances, a multiple Kalman filter was implemented. We used the equation proposed by Drolet et al. [18] to smoothly combine the measurement results of the two sonar sensors:

$$x = \frac{x_1/P_1 + x_2/P_2}{1/P_1 + 1/P_2} \quad (3)$$

In this equation, sensors with smaller error covariances will contribute more to the result. When the subject was walking on the treadmill, the position measurements varied within a range of less than 5 cm, which is the usual trajectory of a pelvis in normal gait [21].

4.2 Speed-Adaptation Control Algorithm

Self-selected speed adaptation on a treadmill can be achieved by allowing the user to interact with a fixed virtual object via the treadmill. Albu-Scaffer et al. [22] utilized a virtual spring–damper concept to allow interaction between a robot and a human in an unknown environment. The virtual spring–damper concept itself has been used in many research areas involving human–robot interaction, such as haptic interfaces [23], grasping [22], and tele-operations [23]. In this study, virtual spring and damper components are applied to an automatic speed-adaptation control for a treadmill with impedance control. The relationship between the user and the treadmill belt can be described by the simple dynamic model shown in Fig. 5.

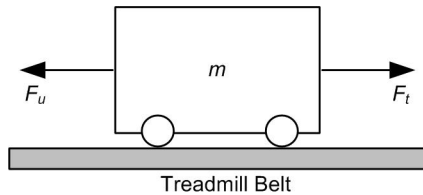


Fig. 5. Interaction between the user and the treadmill belt

In Fig. 5, a treadmill user with mass m is modeled as a wheeled cart [24] that can move freely on the treadmill belt. This is reasonable assumption since the simplest legged locomotion can be modeled based on spoked wheels [25]. The user moves forward by applying force F_u , while the treadmill applies the opposite force F_t to the user by moving its belt. As a result, the user moves at the same velocity as the treadmill belt.

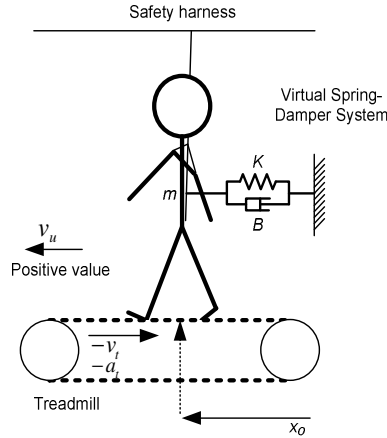


Fig. 6. A user connected to a fixed virtual component by a spring–damper system

Let v_u and v_t are the user and treadmill velocities w.r.t. ground respectively. The relationship between F_u and F_t can be expressed as

$$F_u - F_t = m\dot{v}_{ut}, \quad (4)$$

where, F_u is the user force, F_t is the treadmill force, m is the user mass, and $v_{ut} = v_u - v_t$ is the user velocity with respect to the treadmill. To derive this, we assume that the mass of the treadmill belt is negligible compared to the user mass. In Equation (4), the interaction force error between the user and the treadmill can be defined as $F_s = F_u - F_t$. When the user is walking at a constant velocity, $F_t = F_u$ and $F_s = 0$. If the interaction force error F_s vanishes while the speed is varying, the treadmill will allow the user to walk naturally according to his/her intention, while keeping the user displacement inside the treadmill. On the other hand, if F_s does not vanish, then the user may experience an unexpected inertial force from the treadmill or may fall off the treadmill belt. Since the treadmill belt is carrying a user with mass m , the treadmill-generated force F_t can be expressed as an acceleration term:

$$F_t = m\dot{v}_t, \quad (5)$$

Where, v_t is the treadmill belt velocity with respect to the ground, which has a negative value in unidirectional movement. In order to determine F_u , we assume that the treadmill user is connected to a virtual spring–damper system, illustrated in Fig. 6. When the user starts to move with respect to a reference position, he/she will exert a force F_u on the spring–damper system. The force F_u exerted by the user can then be expressed as

$$F_u = -B\hat{x}_u - K(x_u - x_0), \quad (6)$$

Where K and B denote the stiffness and damping coefficient of the virtual fixed object, x_u and \hat{x}_u denote the user position and velocity with respect to the ground, and x_0 is the reference position on the treadmill.

5 Experimental Results

In order to study the effects of the parameters of the proposed system on the treadmill belt speed, a square function (shown in Fig. 7) was used as the input x , instead of detecting user motions from the sonar sensors.

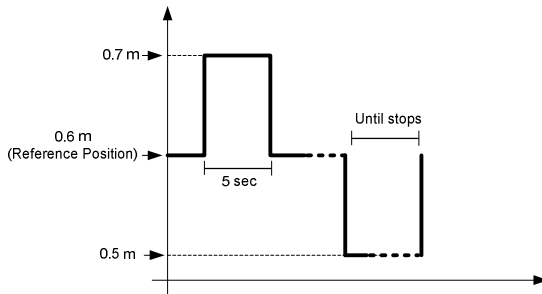


Fig. 7. The square input used to study the control parameters

This step function simulated the way a user increases his/her walking velocity by moving 10 cm ahead of the reference position for five seconds. The user then walked at a constant speed. After that, the user reduced his/her walking speed by moving backward to the reference position, and finally stopped walking.

Figure 8 shows the effects of the proposed controller on the treadmill speed with respect to user displacement. Figure 8(a) shows the speed response of the treadmill belt for different values of the virtual stiffness K . Figure 8(b) shows how user mass M affects treadmill performance. Based on these experimental results, we can summarize the effect of each parameter on the performance of the system as follows: 1) The virtual spring stiffness determines the sensitivity of the system response with respect to user displacement. 2) The virtual damper affects the response time. 3) Increasing the user mass reduces the sensitivity of the system with respect to user displacement.

The appropriate value for the virtual stiffness (K) was found to be 140 to 200 N/m by relating Newton's second law and Hooke's law, taking into account the user mass, the maximum available acceleration of 1 m/s^2 , and possible user displacements of 0.5 m due to the treadmill platform size. The value of the virtual damping was determined heuristically as 10 to 20 Ns/m. Consequently, it should be noted that since the mass m is given, the virtual spring stiffness K mainly affects the steady-state response of the treadmill speed, while the force controller parameters affect the transient response of the treadmill speed.

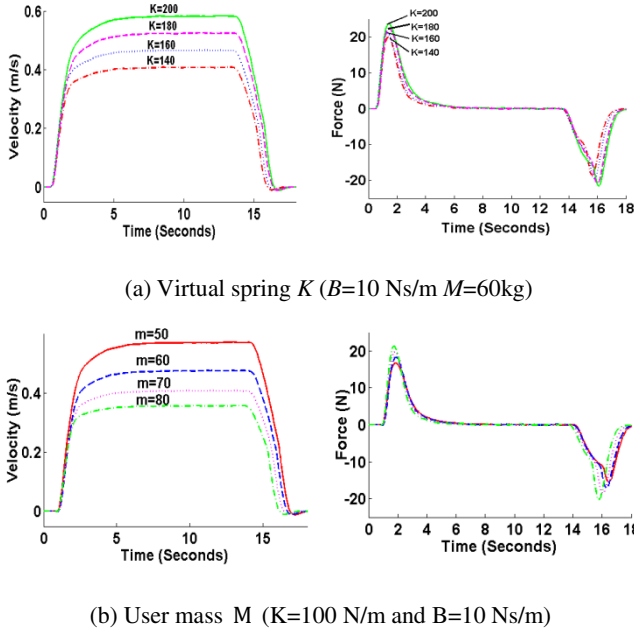


Fig. 8. Effects of the parameters on treadmill speed during speed adaptation

We asked a user to walk on the treadmill and gradually vary his walking speed. Figure 9 shows the resulting belt velocities, accelerations, applied forces, and automatic user displacements during speed adaptation. As Fig. 9 (top) indicates, when the user tried to increase his walking velocity, F_u became negative since he was pulling against the virtual wall. Also, when the user tried to decrease his walking velocity, F_u became positive since he was pushing against the virtual components. This is similar to normal overground walking, where a user also feels inertial forces due to his/her own acceleration. During the experiment, the interaction force error F_s remained close to zero at different velocities, as Fig. 9 (lower middle) shows. The proposed control system also maintained a user displacement close to the reference position, which was set at 0.6 m from the rear of the treadmill (see Fig. 9 (bottom)). When the user tried to stop walking, his displacement lagged behind the reference position. When the user finally stopped, the treadmill brought him back to the home position at a constant slow speed of 0.3 m/s. Since the treadmill could only move bi-directionally during the home positioning period, the treadmill belt moved in a forward direction with a negative value

The interaction force error increased under starting and stopping conditions; this was mainly due to the limitations of the control hardware system. Also, according to Fig. 9 (upper middle), there was a delay of about one second during startup, because at walking velocities lower than 0.3 m/s, the AC motor used to drive the treadmill could not provide enough torque to move the belt due to belt friction.

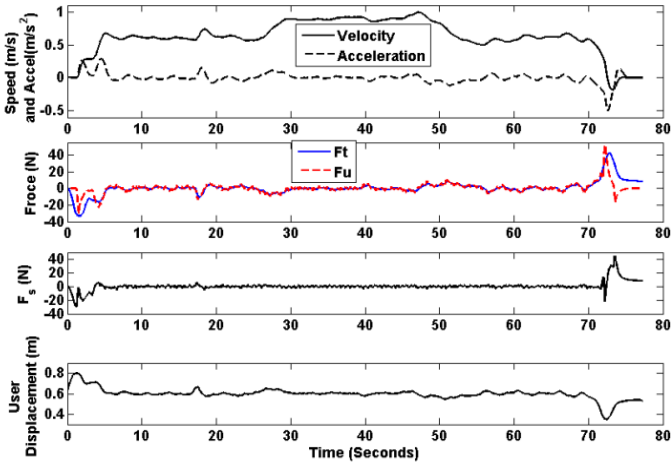


Fig. 9. Belt velocity and acceleration (top), applied forces (upper middle), interaction force error (lower middle), and displacement (bottom) during automatic speed adaptation

These errors could be minimized by using a treadmill actuation system with higher power, no backlash, and no friction, and by increasing the acceleration limits of the treadmill.

6 Conclusions

We introduced a novel speed-adaptation algorithm based on impedance control, and applied it to a small conventional treadmill, commonly used in homes and health centers for exercise purposes, and in hospitals for therapy. The proposed impedance control allows the user to naturally and safely update the speed of a small treadmill, while maintaining a limited user motion range by implementing hybrid position and force control via interaction with a fixed virtual object. The favorable characteristics of the proposed control algorithm indicate its potential use gait rehabilitation with effective training modes. In future work, the interaction forces generated by the treadmill during speed adaptation will be compared via gait analysis to the inertial forces generated during overground walking, and a control system for whole-body haptic interaction during locomotion will be developed by moving the reference position and simulating a virtual wall, based on the proposed control scheme.

Acknowledgments. This work was supported by National Research Foundation Korea (NRF) (2011-00313832010-0029690 & 2012R1A2A2A01047344) and BK21 PLUS (Brain korea21).

References

1. Hesse, S., Bertelt, C., Schaffrin, A., Mauritz, K.H.: Restoration of Gait in Non-ambulatory Hemiparetic Patients by Treadmill Training with Partial Body Weight Support. *Arch. Phys. Med. Rehabil.* 75(10), 87–1093 (1994)
2. Wang, F., et al.: Body sway measurement for fall risk assessment using inexpensive webcams. In: 2010 Annual International Conference of the IEEE Engineering in Medicine and Biology Society (EMBC). IEEE (2010)
3. Christensen, R.R., Hollerbach, J.M., Xu, Y., Meek, S.G.: Inertial force feedback for the treadport locomotion interface. *Presence: Teleoperators and Virtual Environments* 9, 1–14 (2000)
4. von Zitzewitz, J., Bernhardt, M., Riener, R.: A novel methods for automatic treadmill speed adaptation. *IEEE Trans. Neural Syst. and Rehabil. Eng.* 15(3), 401–409 (2007)
5. Koenig, A., Binder, C., von Zitzewitz, J., Omlin, X., Bolliger, M., Riener, R.: Voluntary gait speed adaptation for robot-assisted treadmill training. In: IEEE 11th Int. Conf. on Rehabilitation Robotics, Kyoto, Japan (2009)
6. Checcacci, D., Hollerbach, J.M., Hayward, R., Bergamasco, M.: Design and analysis of a harness for torso force application in locomotion interfaces. In: IEEE EuroHaptics Conference, Los Alamitos, CA, pp. 53–67 (2003)
7. Feasel, J., Whitton, M.C., Kassler, L.P., Brooks Jr., F.P., Lewek, M.D.: The Integrated virtual environment rehabilitation treadmill system. *IEEE Trans. Neural. Syst. Rehabil. Eng.* 19(3), 290–297 (2011)
8. Minetti, A.E., Boldrini, L., Brusamolin, L., Zamparo, P., McKee, T.: A feedback-controlled treadmill (treadmill-on-demand) and the spontaneous speed of walking and running in humans. *J. Appl. Physiol.* 95, 838–843 (2003)
9. Lichtenstein, L., Barabas, J., Woods, R.L., Peli, E.: A feedback control instrument for treadmill locomotion in virtual environments. *ACM Trans. Appl. Percept.* 4(1) (January 2007)
10. Fung, J., Richards, C.L., Malouin, F., McFadyen, B.J., Lamontagne, A.: A treadmill and motion coupled virtual reality system for gait training post-stroke. *Cyberpsychol. Behav.* 9, 157–162 (2006)
11. De Luca, A., Mattone, R., Giordano, P.R., Bulthoff, H.H.: Control Design of the 2D CyberWalk platform. In: IEEE/RSJ Int. Conf. on Intelligent Robots and Systems, St. Louis, MO (October 2009)
12. Souman, J.L., Giordano, P.R., Frissen, I., Luca, A.D., Ernst, M.O.: Making virtual reality real: perceptual evaluation of a new treadmill control algorithm. *ACM Trans. Applied Perception* 7(2) (2010)
13. Noma, H., Miyasato, T.: Design for locomotion interface in a large scale virtual environment ATLAS: ATR locomotion interface for active self motion. In: Proceedings of the IEEE 7th Annual Symposium on Haptic Interface for Virtual Environments and Teleoperated Systems, Los Alamitos CA, pp. 111–118 (1998)
14. Yoon, J., Park, H., Damiano, D.L.: A novel walking speed estimation scheme and its application to treadmill control for gait rehabilitation. *Journal of NeuroEngineering and Rehabilitation* 9(62) (2012)
15. Hogan, N.: On the stability of manipulators performing contact tasks. *IEEE J. Robotics and Automation* 4, 677–686 (1988)
16. Shi, K.L., Chan, T.F., Wong, Y.K., Ho, S.L.: Speed estimation of an induction motor drive using an optimized extended Kalman filter. *IEEE Trans. Industrial Electronics* 49(1) (February 2002)

17. Belanger, P.R.: Estimation of angular velocity and acceleration from shaft encoder measurement. In: IEEE Int. Conf. on Robotics and Automation, Nice, France (1992)
18. Drolet, L., Michaud, F., Cote, J.: Adaptable Sensor Fusion Using Multiple Kalman Filter. In: IEEE/RSJ Int. Conf. on Intelligent Robot and System, Takamatsu, Japan (2000)
19. Busawon, K.K., Kabore, P.: On the Design of Integral and Proportional Integral Observers. In: Proc. of American Control Conf., Chicago, USA (2000)
20. Lee, H., Utkin, V.I.: Chattering suppression methods in sliding mode control systems. *Annual Reviews in Control* 31, 179–188 (2007)
21. Winter, D.A.: *Biomechanics and Motor Control of Human Movement*, 2nd edn. Wiley, New York (1990)
22. Albu-Schaffer, A., Eiberger, O., Grebenstein, M., Haddadin, S., Ott, C., Petit, F., Wimbock, T., Wolf, S., Hirzinger, G.: Soft Robotics: From Torque Feedback Controlled Lightweight Robots to Intrinsically Compliant Systems. In: Int. Conf. on Control, Automation and Systems, Korea (2010)
23. Colgate, J.E., Grafing, P.E., Stanley, M.C., Schenkel, G.: Implementation of Stiff Virtual Walls in Force-Reflecting Interfaces. In: *Virtual Reality Annu. Int. Symposium* (September 1993)
24. Wimboeck, T., Ott, C., Hirzinger, G.: Passivity-based Object Level Impedance Control for Multifingered Hand. In: IEEE/RSJ Int. Conf. on Intelligent Robots and Systems, Beijing, China (2006)
25. Niemeyer, G., Slotine, J.-J.E.: Stable Adaptive Teleoperation. *IEEE Journal of Oceanic Engineering* 16(1), 152–162 (1991)

Design and Simulation of a 3D Actuation System for Magnetic Nano-Particles Delivery System

Mohammad Dadkhah, Naveen Kumar, and Jungwon Yoon*

Robots and Intelligent System Laboratory,
School of Mechanical Engineering and ReCAPT,
Gyeongsang National University, Jinju, Korea
{m.dadkhaht, jwyoona}@gnu.ac.kr, navindma@gmail.com

Abstract. In this paper, a new electromagnetic actuation system is presented for magnetic nano-particles based targeted drug delivery. The system is composed of three sets of coils; each set contains two parallel coils, generate the oriented 3D magnetic gradient field. Differential Current Coil approach is used to calculate the applied current to each coil to ensure that the gradient field, generated in region of interest, is permanently higher than the value needed for saturation of magnetic particles. To investigate the performance of the actuation system, a simulation model, relating to magnetic field distribution and the trajectories of the magnetic particles, has been studied using finite element approach. The proposed actuation system is more compact and cheaper compare to previous systems and simulation results accept that this actuation system can be used effectively for Nano-particles based drug delivery systems.

Keywords: Magnetic Nano-particles, Targeted Drug Delivery, Magnetic Actuation System, Simulation.

1 Introduction

Targeted drug delivery is a method of delivering medication to a patient in a manner that increases the concentration of the medication in disease affected parts of the body relative to others. Magnetic Nano-particles (MNP) can offer several advantages over more traditional drug delivery methods, including Nano size dimensions, biocompatibility, controlled magnetic responsiveness, prolonged circulation lifetime, surface stabilization, and surface recognition. During the last 30 years, magnetic Nano-particles based therapeutics have been investigated and developed for biomedical application for the treatment of cancer and many other diseases [1-3]. Magnetic nano-particles based drug delivery researches are divided into couple of major parts. First part is related to synthesis and characterization of magnetic nano-particles for drug delivery purpose; several groups have been studying and developing magnetic micro/nanoparticles for this purpose [4].

* Corresponding author.

Other part is related to designing the systems to control the locomotion of magnetic nano-particles from injection point to a desired diseased area in the vasculature. To achieve this aim, several different techniques have been proposed in the literature. Initially, magnetic particles were captured by a static magnetic fields produced by permanent magnets [5] or superconducting magnets [6]. However, the application of static magnetic field was not found effective for targeting the magnetic particles deep inside the body.

To reach deep region inside the body, electromagnets are used widely as the actuators [7-10]. Martel et al. have proposed a system to generate the force needed for the propulsion of magnetic particles inside the MRI by using the electromagnets [11-12]. Recently, based on MRI concepts, two sets of coils have been used for each actuating direction in most of the actuation systems which are designed for DDS [13-15]. In such actuation systems, one set of two Helmholtz coils have been used to produce the uniform constant magnetic field in desire direction for saturation of magnetic particles and another set of two Maxwell coils have been applied to generate the gradient magnetic field for producing necessary magnetophoretic force for the propulsion of magnetic particles. To move the particles in 3D by using this design, four coils are necessary for each direction and therefore 12 different coils should be fabricated and supplied by power supplies, which make whole system very heavy and expensive. Due to these problems, some designs were presented in which the magnetophoretic force was just generated in 2D and for third direction mechanical force was added to system [15]. Although it is useful, the system becomes more complex. Moreover, almost all of these researches were applied on the particles with diameter of above $10\mu\text{m}$ and 3D actuation system for Nano-particles is not introduced yet.

In this paper we propose a design with a new approach for actuating the nano-particles in 3D using the electromagnets. The goal of this design is to minimize the size and cost of the system while it is controllable for moving the nano-particle in specified direction. Configuration and specification of the design are presented and its performance is examined using simulation.

2 Theoretical Concepts

2.1 Magnetophoresis

Magnetizable particles are the basis of magnetic nanoparticle drug delivery system (DDS). These particles experience a force in a non-uniform magnetic field which is called magnetophoresis (MAP) and is generated due to difference in permeability of nanoparticles and the medium surrounded them [16].

Considering, the nano-particle as a homogeneous sphere with radius R and net magnetic polarization \mathbf{M} that is suspended in a magnetically linear fluid of permeability μ_1 and subjected to a magnetic intensity \mathbf{H} . The effective magnetic moment of the sphere is calculated by following equation:

$$\mathbf{M}_{\text{eff}} = 4\pi R^3 \left[\frac{\mu_0 - \mu_1}{\mu_0 + 2\mu_1} \mathbf{H} + \frac{\mu_0}{\mu_0 + 2\mu_1} \mathbf{M} \right] \quad (1)$$

where $\mu_0 = 4\pi \cdot 10^{-7} \text{H/m}$ is the permeability of free space. For a magnetically linear particle of permeability μ_2 we have,

$$\mathbf{M} = \chi \mathbf{H} \quad (2)$$

where $\chi = \mu_2/\mu_0 - 1$ is the susceptibility of the particle. In this special case, the effective moment is simplified to:

$$\mathbf{M}_{\text{eff}} = 4\pi R^3 \frac{\mu_2 - \mu_1}{\mu_2 + 2\mu_1} \mathbf{H} \quad (3)$$

Magnetophoretic force (\mathbf{F}_{MAP}) depends on the gradient of the magnetic intensity ($\nabla \mathbf{H}$) and the effective magnetic dipole moment (\mathbf{M}_{eff}) of the particles and is expressed as follow:

$$\mathbf{F}_{\text{MAP}} = \mu_1 \mathbf{M}_{\text{eff}} \cdot \nabla \mathbf{H} \quad (4)$$

Combining this expression with that for the effective moment, the magnetophoretic force for a linear Magnetizable spherical particle in a non-uniform magnetic field may be written as

$$\mathbf{F}_{\text{MAP}} = 2\pi\mu_1 R^3 \frac{\mu_2 - \mu_1}{\mu_2 + 2\mu_1} \nabla \mathbf{H}^2 \quad (5)$$

Magnetizable materials exhibit strongly nonlinear behavior such as paramagnetism and ferromagnetism, which seldom can be ignored in modeling the electromechanics of magnetic particles. The materials with nonlinear magnetic properties are divided to two groups of hard and soft material. In both types, the magnetization is related to magnetic intensity, however, in hard material it also depends on history of magnetization which called hysteresis. The principal manifestation of nonlinearity in magnetically materials is *saturation*, which limits the magnitude of the magnetization vector to a finite value \mathbf{M}_{sat} . The influence of saturation upon the effective moment of a particle should be evident.

Consider a spherical ferromagnetic particle immersed in a linear magnetizable fluid of permeability μ_1 and assume that the particle magnetization is some nonlinear function of the field. Then, Equations (1) and (5) may be used to obtain the MAP force.

$$\mathbf{F}_{\text{MAP}} = 2\pi\mu_1 R^3 \left[\frac{\mu_0 - \mu_1}{\mu_0 + 2\mu_1} \nabla \mathbf{H}^2 + \frac{2\mu_0}{\mu_0 + 2\mu_1} \mathbf{M}(\mathbf{H}) \cdot \nabla \mathbf{H} \right] \quad (6)$$

If the permeability of the medium surrounded the particles could satisfy the relation $\mu_0 \cong \mu_1$ then MAP force simplifies to:

$$\mathbf{F}_{\text{MAP}} = \frac{4}{3}\pi\mu_0 R^3 \mathbf{M}(\mathbf{H}) \cdot \nabla \mathbf{H} \quad (7)$$

If the particle is magnetically soft and the magnetic field is strong, then the particle will saturate so that $\mathbf{M}(\mathbf{H}) \rightarrow \mathbf{M}_{\text{sat}}$.

2.2 Particle Trajectories

There are many forces which acting on moving particles in blood vessels such as hydrodynamic drag force, inertia, buoyancy, gravitational and particle-particle interaction. However, only major forces are taken for consideration. Using Newton's law, the trajectory of a particle in fluid caused by total force \mathbf{F} can be described as:

$$m_p \frac{d\mathbf{v}_p}{dt} = \mathbf{F} \quad (8)$$

where m_p and \mathbf{v}_p are the mass and velocity of the particle, respectively. There are many forces which acting on moving particles in vessels. The forces which have the major impact on total force are hydrodynamic drag force and magnetophoretic force. The other forces such as inertia, buoyancy, gravitational and particle-particle interaction forces are ignored in model because they are several orders of magnitude lower than the magnetic force. Ignoring these low impact forces, total force on particle may be expressed as follow:

$$\mathbf{F} = \mathbf{F}_{\text{MAP}} + \mathbf{F}_{\text{drag}} \quad (9)$$

The hydrodynamic drag forces (\mathbf{F}_{drag}) is given by Stoke's law as

$$\mathbf{F}_{\text{drag}} = -6\pi\eta R(\mathbf{V}_p - \mathbf{V}_f) \quad (10)$$

where η is the fluid viscosity, R is the particle radius, \mathbf{V}_p is the particle velocity and \mathbf{V}_f is the fluid velocity. Based on equation (7) to (10) we can obtain:

$$m_p \frac{d\mathbf{v}_p}{dt} = \frac{4}{3}\pi\mu_0 R^3 \mathbf{M}(\mathbf{H}) \cdot \nabla \mathbf{H} - 6\pi\eta R(\mathbf{V}_p - \mathbf{V}_f) \quad (11)$$

By solving this equation the trajectory of the particles could be calculated.

3 Actuation System Design

3.1 Design Basis

The magnetic field generated by the coils at any point is inversely proportional to the square of the distance of the point from the coils. As a result, the compact coils system design will be more sufficient and should be considered in the actuation system design process.

Magnetophoretic force depends on the gradient of the magnetic field and the magnetization of the particles. Magnetization is related only to magnetic intensity and gradient of magnetic field has no effect on it. The magnetic intensity of about 4×10^5 A/m is needed to saturate the magnetite (most common material used in magnetic nano-particles). Magnetic field gradient, though, have no theoretical limit but it have experimental limitations. The gradient field could be increased by increasing the currents of the coils. Unfortunately, cross sectional area of the wires limit the current of the coils. This means that to increase the current of the coils, the wires with bigger cross-section area should be used which makes the coils bigger and

heavier. Other solution is to increase the number of the wire turns of the coils which similarly increase the size and weight of the coils. However, the power equation (12) shows that the current have more effect on power consumption of the coils than the number of wire turns.

$$P = RI^2 \quad (12)$$

In equation (12), I is the current of coils wires and R is the coils resistance which is proportional to wire length and rise directly by adding the wire turns to coil. Thus, improving the magnetic intensity and gradient of the system by increasing the number of wire turns is more sufficient than increasing the current.

3.2 Differential Current Coils Approach

As it is mentioned before, in most of recent researches, the combination of Helmholtz and Maxwell coils have been used for the actuation of the particles. Fig. 1 shows the sample model of this system which moving the particles in one direction (here Y-axis). Magnetic flux density generated by each sets of the Helmholtz coils and Maxwell coils as well as the combination of all coils are shown in Fig. 2. To produce these fields, the Helmholtz and Maxwell coils were assigned 7000 A Turns and 10000 A Turns, respectively. However, current in Maxwell coils are in reverse direction. It can be seen that Helmholtz coils generates the uniform magnetic field while Maxwell coils generate the smooth gradient field. By applying both set of coils, their magnetic fields were superimposed.

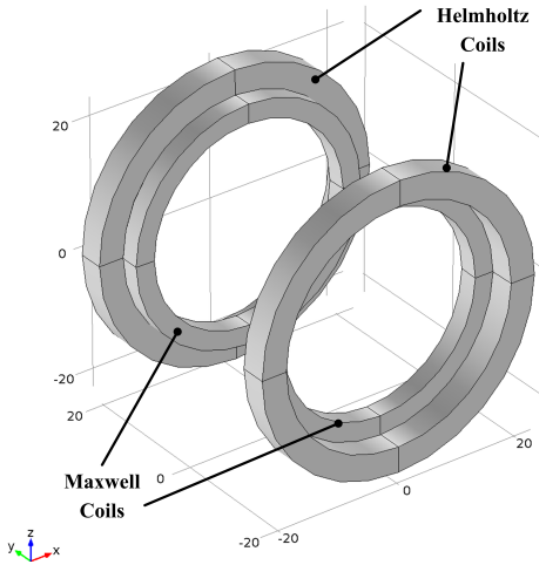


Fig. 1. Sample model of Helmholtz and Maxwell coils system

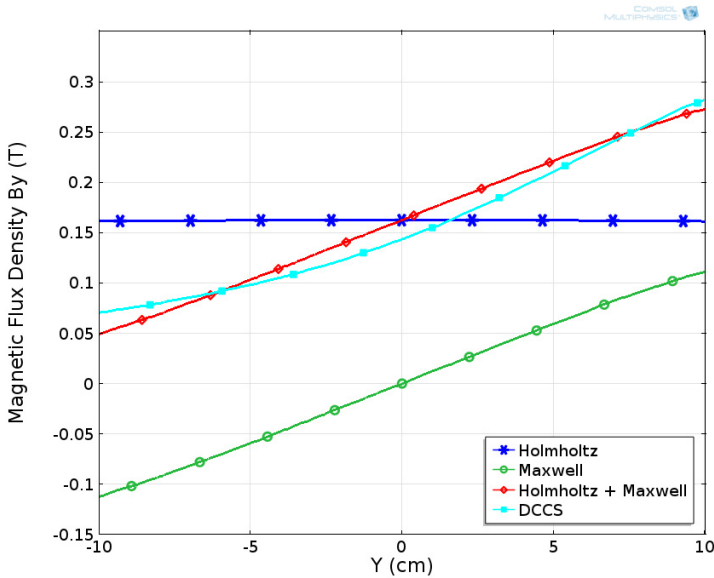


Fig. 2. Magnetic flux density generated by the Helmholtz coils and Maxwell coils

In our actuation system design, the Helmholtz coils are avoided and only the Maxwell coils are used with differential currents method and therefore we call it differential current coils approach (DCC). The principle of DCC approach is based on the fact that magnetic particles are always moving toward the points with higher magnetic intensity. In our system, by increasing the current density in one coil and decreasing the current density in other coil, the gradient field is generated which attracts the particles towards the coil with higher current density. Besides, since both of coils have current in the same direction, the field intensity could be kept higher than the value needed for saturation.

The magnetic field generated using DCC for sample structure of Fig. 1 is plotted in Fig. 2. The Maxwell coils were assigned 20000 A Turns and 1000 A Turns whereas the Helmholtz 1 coils are off. From this figure, it is clear that differential current coils system is suitable for generating the desire magnetic field. Though there is some non-linearity in magnetic field, its effect on Nano-particle delivery system is slight.

3.3 3D Setup Idea

Our proposed 3D actuation system consists of three sets of coils and is shown in 3. Each set is composed of two circular coils, placed perpendicular to one axis and generated the magnetic field in one direction using DCC approach. Therefore, three sets of coils can generate the magnetic field in all the three directions of the Cartesian coordinate system.

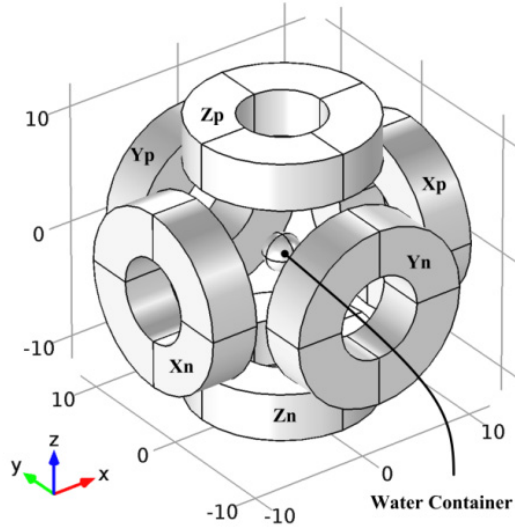


Fig. 3. Proposed 3D actuation system

For moving the particles in desire direction, the current magnitude of all the coils should be properly calculated at each moment. For better investigation, we named the current in each coil as I_{jk} , where j represents the perpendicular axis to coil which could be x , y or z and k represents the directional position of the coil in relation to the center of the setup. Assuming the coordinate system origin at the center of the coils setup, k would be p if the coil positioned on the positive side of its normal axis and n if the coil placed on the negative side. For instance, I_{xp} refers to current of the coil placed on the positive side of the x -axis and I_{zn} states the current of the z -axis, negative side coil.

4 Simulation

4.1 Modeling

To investigate the proposed setup, particle tracking simulation using numerical method was performed. The COMSOL Multiphysics Software package was used for the modeling of the setup as well as for the solution of the differential equation. The meshed model which was used for simulation is shown in Fig. 4. All the coils were modeled symmetrically by hollow cylinders with the same size. The inner diameter, width and height of the coils are 7 cm, 4 cm and 4 cm respectively and each pair of the coils are separated by a distance of 16 cm. Considering the wire with diameter of 1 mm, 1600 turns of wire could be fitted in modeled coils. Accounting fabrication tolerance and errors, the wire turns was kept equal for all coils as 1500 turns.

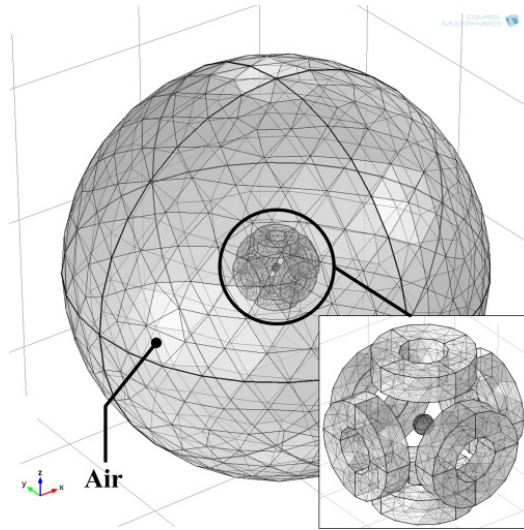


Fig. 4. Meshed model of actuation system used for simulation

The magnetic field generated by the coils was calculated using AC/DC module of COMSOL in steady state. The surrounding environment was assumed as air; however, a 30 mm diameter sphere was modeled at the center of the setup as a water container. The container was supposed to be full of water and therefore the water was considered stable.

The particles were released at the origin and their moving path due to calculated magnetic field and drag force in water was tracked using Particle-Tracking module of COMSOL. The particles are supposed as spherical magnetite particle with diameter of 900 nm and the saturation magnetization of 1.69×10^6 A/m. For realistic results, B-H curve for particle's material is applied to model.

4.2 Results

Sample 3D and surface plots for magnetic field simulation of the setup is shown in Fig. 5 whereas, I_{xp} , I_{yn} and I_{zp} are assigned 15 A and I_{xn} , I_{yp} and I_{zn} are given 2 A. These plots show that the model can calculate the magnetic field accurately.

Fig. 6 shows the particle trajectory in the calculated magnetic field for 60 second. As it is clear, the particle was moved toward the positive direction of x-axis and z-axis and negative direction of the y-axis, the same direction which was designed by the applied current. It could be mentioned that the maximum velocity of 4500 nm/s was achieved.

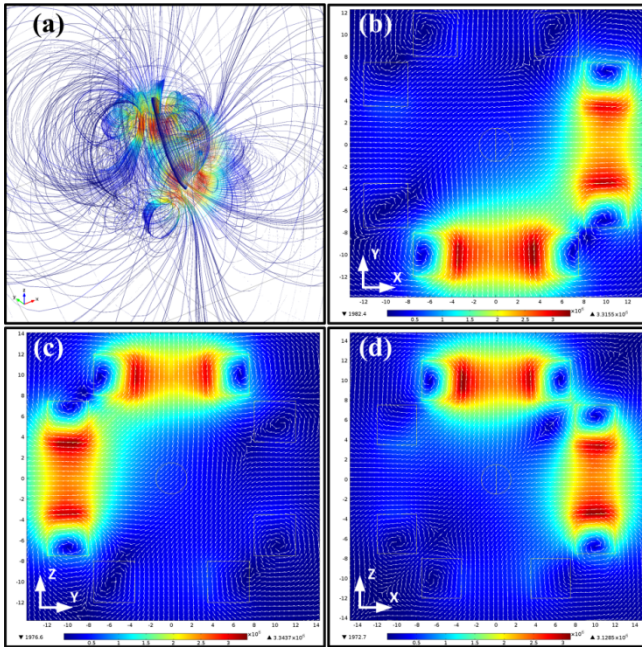


Fig. 5. Simulation result for Magnetic field and flux density, (a) 3D, (b) x-y surface, (c) y-z surface, (d) x-z surface

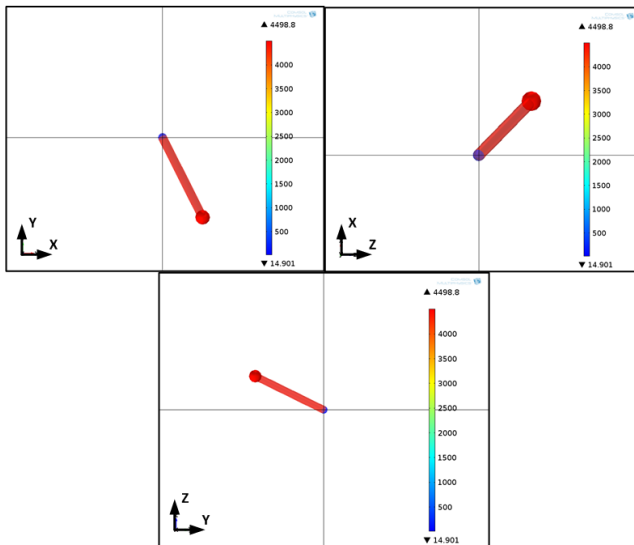


Fig. 6. Particle trajectory in calculated magnetic field in different views. The colors shows the particle velocity.

5 Conclusion

In this paper, a new actuation system was presented which could be used as a low cost and compact experimental setup for researches in the field of magnetic Nano-particles drug delivery systems. Configuration and dimensions of this system was chosen in such a way that could cover the size of the mouse brain, as an initial target of experiments. Moreover, to achieve realistic results, the currents and number of the electromagnet coils turns are considered realistic. In our proposed system, the numbers of the electromagnets and consequently number of the required power suppliers and fabrication cost was decreased. The simulation results were approved that this system could generate the desire magnetic field for Nano-particle propulsion. Moreover, it was accepted that there is a possibility to perform suitable control on particle trajectory.

Acknowledgment. This work was supported by National Research Foundation Korea (NRF) (2011-00313832010-0029690 & 20120009524).

References

- [1] Pankhurst, Q., Connolly, J., Jones, S.K., Dobson, J.: Applications of magnetic nanoparticles in biomedicine. *Journal of Physics D, Applied Physics* 36, 167–181 (2003)
- [2] Johannsen, L., Blanchette, J.O.: Nanoparticle and targeted systems for cancer therapy. *Advanced Drug Delivery Reviews* 56, 1649–1659 (2004)
- [3] Davis, M.E., Chen, Z., Shin, D.M.: Nanoparticle therapeutics: an emerging treatment modality for cancer. *Nature Reviews Drug Discovery* 7, 771–782 (2008)
- [4] Arruebo, M., Fernandez-Pacheco, R., Ibarra, M.R., Santamaria, J.: Review: Magnetic nanoparticles for drug delivery. *NanoToday* 2, 22–32 (2007)
- [5] Alexiou, C., Jurgons, R., Seliger, C., Brunke, O., Iro, H., Odenbach, S.: Delivery of Superparamagnetic Nanoparticles for Local Chemotherapy after Intraarterial Infusion and Magnetic Drug Targeting. *Anticancer Research* 27, 2019–2022 (2007)
- [6] Takeda, S.I., Mishima, F., Fujimoto, S., Izumi, Y., Nishijima, S.: Development of magnetically targeted drug delivery system using superconducting magnet. *Journal of Magnetism and Magnetic Materials* 311, 367–371 (2006)
- [7] Yesin, K.B., Vollmers, K., Nelson, B.J.: Modeling and control of untethered biomicrobots in a fluidic environment using electromagnetic fields. *Int. J. Robot. Res.* 25, 527–536 (2006)
- [8] Abbott, J.J., Ergeneman, O., Kummer, M.P., Hirt, A.M., Nelson, B.J.: Modeling Magnetic Torque and Force for Controlled Manipulation of Soft-Magnetic Bodies. *IEEE Transactions on Robotics* 23, 1247–1252 (2007)
- [9] Alexiou, C., Diehl, D., Henninger, P., Iro, H., Rockelein, R., Schmidt, W., Weber, H.: A High Field Gradient Magnet for Magnetic Drug Targeting. *IEEE Transactions on Applied Superconductivity* 16, 1527–1530 (2006)
- [10] Han, X., Cao, Q., Li, L.: Design and Evaluation of Three-Dimensional Electromagnetic Guide System for Magnetic Drug Delivery. *IEEE Transactions on Applied Superconductivity* 22, 4401404 (2012)
- [11] Mathieu, J.-B., Martel, S.: Magnetic microparticle steering within the constraints of an MRI system: proof of concept of a novel targeting approach. *Biomedical Microdevices* 9, 801–808 (2007)

- [12] Martel, S., Felfoul, O., Mathieu, J.-B., Chanu, A., Tamaz, S., Mohammadi, M., Mankiewicz, M., Tabatabaei, N.: MRI-based Medical Nanorobotic Platform for the Control of Magnetic Nanoparticles and Flagellated Bacteria for Target Interventions in Human Capillaries. *The International Journal of Robotics Research* 28, 1169–1182 (2009)
- [13] Choi, H., Choi, J., Jang, G., Park, J., Park, S.: Two-dimensional actuation of a microrobot with a stationary two-pair coil system. *Smart Materials and Structures* 18, 055007 (2009)
- [14] Jeon, S., Jang, G., Choi, H., Park, S.: Magnetic Navigation System With Gradient and Uniform Saddle Coils for the Wireless Manipulation of Micro-Robots in Human Blood Vessels. *IEEE Transactions on Magnetics* 46, 1943–1946 (2010)
- [15] Choi, H., Cha, K., Choi, J., Jeong, S., Jeon, S., Jang, G., Park, J., Park, S.: EMA system with gradient and uniform saddle coils for 3D locomotion of microrobot. *Sensors and Actuators A: Physical* 163, 410–417 (2010)
- [16] Jones, T.B.: Dielectrophoresis and magnetophoresis. In: *Electromechanics of Particles*, pp. 34–82. Cambridge University Press (1995)

Optimal Kinematic Design of a Novel Robotic Knee Device for Gait Rehabilitation with Stance Control

Sanghun Pyo¹, Mingyun Oh², and Jungwon Yoon¹

¹ School of Mechanical Engineering, Gyeongsang National University,
Jinju Gyeongnam, Korea

² Department of Physical Medicine & Rehabilitation, College of Medicine,
Gyeongsang National University, Republic of Korea
jwyoong@gnu.ac.kr

Abstract. In this paper, we have proposed a novel robotic knee device with a five-bar linkage to allow low impedance voluntary knee motions within a specified rotation range during swing phase and to assist knee extension motions during stance phase after reaching the boundary of the rotation range. The proposed device can provide free knee motions through the five-bar linkage with 2-DOF (degree of freedom) actuations by a patient's shank and a linear actuator, and can assist knee extension at any controlled knee angle during weight bearing by a geared five-bar linkage with 1-DOF actuation of the linear actuator. The kinematic transition between two modes can be implemented by contact mechanism of a circular structure (knee joint) and a linear link (patella), and the resultant knee rotation range can be determined by the linear actuator. A weight optimization scheme with a simple genetic algorithm (SGA) is performed to increase portability of the proposed device and minimize the side-effects of increased link numbers as compared to existing four-bar mechanisms. The cost function is composed of sums of normalized total link lengths and normalized motor powers. The optimization results show that the total link length and motor power were reduced to 47% and 43% respectively, as compared to initial design. The proposed robotic knee device can provide a new rehabilitation mode for a stroke patient to allow safe and self-motivated overground walking with minimum concern of falling down.

Keywords: kinematics, genetic algorithm, rehabilitation, bio-mechanics.

1 Introduction

A stroke or cerebrovascular accident (CVA), is the rapid loss of brain function(s) due to disturbance in the blood supply to the brain [1]. As a consequence, stroke patients may lose lots of body functions because of injury in brain, including the walking ability especially. Subsequently, if spontaneous recovery is not possible, the patient needs to take a rehabilitation phase of the treatment to recover their physical ability [2-3]. Thus, to support gait rehabilitation for patients, suffering from the paralysis as a consequence of stroke or other neurological diseases, active type orthosis or exoskeletons have been actively proposed in these days [4]. In a traditional way to

support a stroke patient, reciprocating gait orthosis (RGO) are commonly used [5]. The RGO can support patient's weight during stance phase through buckling of knee joint so that it can help patients with paretic limb walk by themselves. However, such devices can cause asymmetry during gait as result of the irregular and sudden impulsive compulsion supports. Kobetic et al. [6] suggested an active knee orthosis system to allow exoskeletal bracing and multichannel functional electrical stimulation. The knee mechanism consisted of electro-mechanical joint locks to provide upright stability during only stance phase. However, simple locking mechanism by electronic switching can't provide active assistance to the knee joint.

Jin et al. [7] designed a knee prosthetic device based on optimization of six-bar linkages to generate closer trajectories to normal gait. "Roboknee" [8] is a robotic exoskeleton based on a four-bar linkage consisted of slide-crank to enhance human strength, endurance, and speed using a series elastic actuator. Colombo et al. [9] developed a rehabilitation system based on treadmill, whose mechanism on knee joint is consisted of simple four-bar linkages system. Mefoued et al. [10] suggested a 1-DOF knee actuation system with chain drive controlled by high order sliding mode controller. Nikitzuk et al. [11] developed a knee brace consisting of planetary gear mechanism and variable damper component and Belforte et al. [12] used a direct drive based on a chain mechanism with a pneumatic cylinder for knee joint support.

Even though it is possible to augment knee power through existing 1-DOF robotic knee systems [7-12], it is hard to apply the existing systems directly to patients with neurologic diseases. As main reasons, the existing 1 DOF systems simultaneously do not satisfy requirements of sufficient knee torque to support a patient's weight during stance phase as well as do not provide back-drivability and small weight of actuators for wearable conditions.

To overcome these problems, Veneman et al. [13] designed a new actuation system for knee joint. It consists of a servomotor, a flexible Bowden cable transmission, and a force feedback loop based on a series elastic element to support just torque to knee joint. The actuation system aims for an impedance controlled gait rehabilitation robot for treadmill-training. Similarly, Ackermann and Cozman [14] and Sulzer et al. [15] developed a powered knee orthosis which can provide knee flexion torque in swing phase to compensate gait disability known as stiff-knee gait (SKG). Even though both knee actuation systems could allow high torque with small impedance, which are limited to only treadmill training applications since the actuators should be located on the fixed base.

Recent clinical studies [16] for gait rehabilitation showed that the treadmill gait training is not very efficient than traditional gait training on over-ground. Also, less assistance may increase more efficiency of the training with larger variation of motions [17]. Therefore, it is important to develop a new gait rehabilitation system that can provide high impedance for safe supports as well as low impedance for free voluntary motions, while allowing overground training.

Even though a recent new type of stance-control knee-ankle-foot orthosis [18] (SCKAFOs) can allow wearers to flex their knee when swinging the leg forward, while preventing knee flexion during weight-bearing, existing SCKAFOs cannot provide powered knee extension assist at any desired knee angle, which is important for adapting different walking conditions such as slope and stairs, or handling unexpected conditions like stumbling.



Fig. 1. A robotic knee device with a five-bar linkage for stance control

In this paper, we suggest a novel robotic knee device as shown by Fig. 1. This can provide free knee rotations during swing phase and assist knee extension during stance phase at any desired knee angle. Voluntary motions with minimum impedance can be achieved by a 2-DOF five-bar linkage of a patient's shank and a linear actuator. In addition, a novel 1-DOF geared five-bar linkage with the linear actuator can provide necessary impedance for the patient's weight support. These functions can be implemented by kinematic transition through contact condition between the 2-DOF five-bar linkage and the 1-DOF geared five-bar linkage.

However, the proposed active knee device must use additional linkages than a simple four-bar mechanism. To maximize the benefit of the proposed device, it is necessary to minimize total weight of the device, while keeping necessary actuator performances for required torques and angular velocities during gait. For this purpose, we use a SGA (Simple Genetic Algorithm) to minimize sum of total link lengths and motor power by reducing the weight of the novel knee device. The proposed weight optimization scheme can reduce total weight of the suggested system and enhance its portability compared to an existing four-bar mechanism.

2 Design Concept for Portable Stance Control

In biomechanics of knee, the moment to support the weight of human body is mainly generated by the compressive force of quadriceps. When the contraction of quadriceps occurs at knee joint, a reaction force is produced by the patella ligament, which finally generates resultant moments at the knee [19-20]. So the conceptual design of an active knee orthosis can be realized by taking into account human biomechanics of knee joint as shown in Fig. 2. Since the mechanical functioning of quadriceps muscles resembles to linear movements by actuation, the proposed 5-bar knee device is designed so that the angle between the femur and the tibia links can be determined with the displacement of the linear quadriceps actuator (see Fig. 2 for each link). The proposed design mainly aims to support patient's lower limb

movements during stance phase, especially when the quadriceps muscle of a patient can't provide necessary knee moments due to his/her body weight. When a patient can walk by him/herself, the actuator will operate in free mode with minimum impedance by frictions of revolute joints. For these purposes, the maximum allowable motion ranges of a knee joint can be determined depending on patient's conditions and the corresponding displacement of the quadriceps actuator can be calculated to satisfy the specified motion range based on kinematics of the proposed device, which will be explained in Section 3.

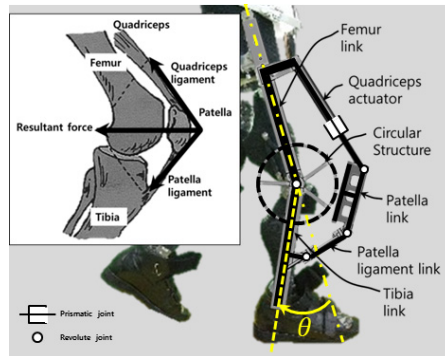


Fig. 2. A robotic knee device with a five-bar linkage for stance control

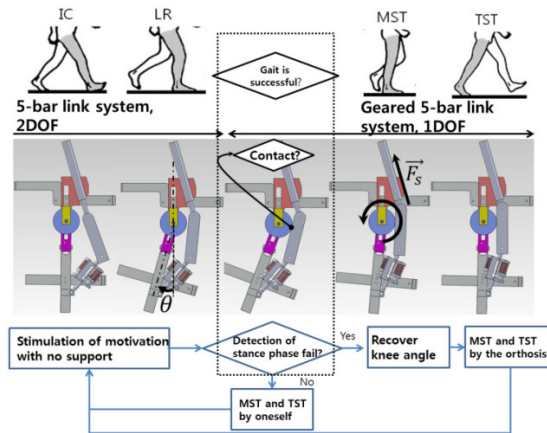


Fig. 3. Transition from the 2-DOF five-bar linkage to the 1-DOF geared five-bar linkage by mechanical contact

Within the specified motion ranges, a wearer can move the knee joint freely with a 2-DOF 5-bar mechanism as non-contact condition before the patella link contacts with the circular structure as shown in Fig. 3. In this case, a shank of human body and

the quadriceps actuator can be considered as active actuators. When a patient loses gait stability and the resultant knee angle exceeds an allowable knee motion range during stance phase, the 5-bar linkage will be changed to a 1-DOF geared 5-bar linkage by mechanical contact between the patella link and the circular structure (see the Section 3.) for detail description of the geared five-bar linkage). After this contact situation, the knee joint angle and the shank of lower limb are only controlled by the quadriceps linear actuator, which can provide mechanical assistance by active actuation.

Hence, the active knee device with contact and non-contact modes can provide additional supportive motions as well as providing voluntary unrestricted motions for better gait therapy.

Even though the contact mechanism is mechanically generated by motions of wearers, the contact condition can also be electrically detected by measuring currents of the quadriceps actuator with a linear DC motor. So this contact condition can be used for evaluating whether patient can successfully walk within adequate knee motion ranges and the quadriceps actuator can provide adequate control assistance through the actuated geared five-bar linkage. On the other hand, if the contact condition from the quadriceps actuator is not detected, the device does not provide any assistance to knee motions, which means a patient-driven walking for better gait therapy.

3 Kinematic Analysis of the Knee Device

Fig. 4 shows the kinematic model of the knee device during the non-contact condition. The l_{bar} represents the link length to connect the quadriceps actuator with the femur link vertically, l_{q} is the length from the tibia link to the connecting part with the patella link, λ is the assembling angle with the l_{bar} linkage, s is the displacement of the quadriceps actuator, θ is the wear's knee joint angle with respect to a vertical line to ground. When the quadriceps actuator is in the non-contact condition, the mechanism will keep the five-bar linkage as shown in Fig 4.

The degree of freedom (DOF) of the proposed knee mechanism can be determined by mechanical contact between the patella link and the circular structure as explained in section 2. To analyse kinematic features of the knee device, Grübler-Kutzbach criterion is utilized as Eq. 1.

$$m = 3(n - 1) - 2j_1 - j_2 \quad (1)$$

where m is the DOF of the mechanism, n is the number of links, j_1 is the number of 1DOF(full) joints and j_2 is the number of the 2 DOF (half) joints.

For non-contact conditions, since the mechanism is composed of 5 links and 4 revolute joints and 1 prismatic joint, the degree of freedom (m_q) becomes finally two. ($j_1 = 5, j_2 = 0, n = 5, m = 2$)

For this condition, a wearer can move his/her knee joint freely and independently because the quadriceps actuator does not directly affect the knee joint driven by wearer.

When the quadriceps actuation is under the mechanical contact condition, the mechanism will be changed to the geared five-bar linkage as shown in Fig. 5. In this contact condition, the patella link is connected and constrained with the circular structure. The contact condition between the patella link and the circular structure can be considered as a half joint with 2-DOF joints of rolling and sliding. Thus, the contact condition can transfer unidirectional motions for knee extension. Since the tibia link and the circular structure are also rigidly connected, the knee joint can be finally controlled by the quadriceps actuator. Thus, the novel knee device mechanism is composed of four revolute and one prismatic joints (one active and one passive), and one half joint (sliding-rolling joint). From equation (1), then, the degree of freedom (m_q) becomes finally one. ($j_1 = 5, j_2 = 1, n = 5, m = 2$)

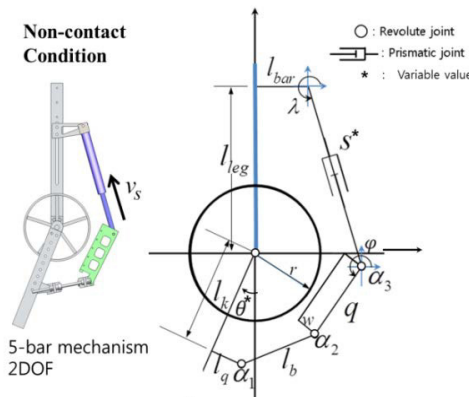


Fig. 4. Geared 5-bar mechanism with the contact condition

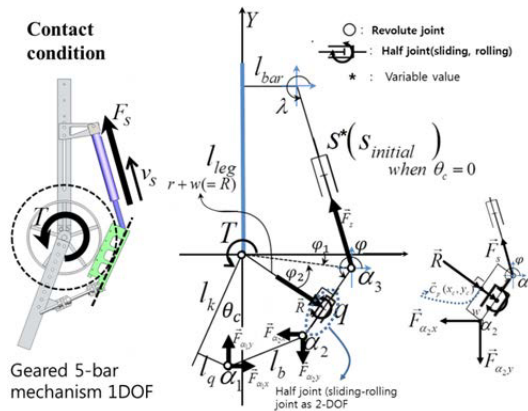


Fig. 5. Five-bar linkage of active knee orthosis under non-contact condition

In Fig. 5, the dynamics factors as v_s , F_s and T represent the velocity, force, and resultant torque of the quadriceps actuator respectively. The θ_c represents the angle of the tibia link by the linear actuator under the contact condition. The geared five-bar kinematics of the proposed knee device can be represented by θ_c and s as:

$$\begin{aligned}\theta_c &= f(s) \quad (0^\circ \leq \theta_c \leq 50^\circ) \\ \because 0^\circ &= f(s_{initial})\end{aligned}\quad (2)$$

where s is the displacement of the quadriceps actuator and θ_c is the controlled tibia angle. To solve (2), the position vectors of each revolute joint described by $\vec{\alpha}_n$ can be expressed by (3) as:

$$\begin{aligned}\vec{\alpha}_1 &= (-l_k \sin \theta_c + l_q \cos \theta_c) \vec{i} + (-l_k \cos \theta_c - l_q \sin \theta_c) \vec{j} \\ \vec{\alpha}_3 &= (l_{bar} + s \cos \lambda) \vec{i} + (l_{leg} + s \sin \lambda) \vec{j}\end{aligned}\quad (3)$$

The angles (φ_1 , φ_2) shown in Fig. 5 can be represented by (4) and (5) as:

$$\varphi_1 = \tan^{-1} \left(\frac{l_{leg} + s \sin \lambda}{l_{bar} + s \cos \lambda} \right) \quad (4)$$

$$\varphi_2 = \cos^{-1} \left(\frac{r + w}{\sqrt{(l_{bar} + s \cos \lambda)^2 + (l_{leg} + s \sin \lambda)^2}} \right) \quad (5)$$

Meanwhile, φ is related as follows;

$$\varphi = \frac{3}{2} \pi - \varphi_2 + \varphi_1 \quad (6)$$

The position vector of $\vec{\alpha}_2$ can be solved by (7) as:

$$\vec{\alpha}_2 = (l_{bar} + s \cos \lambda + q \cos \varphi) \vec{i} + (l_{leg} + s \sin \lambda + q \sin \varphi) \vec{j} \quad (7)$$

The kinematic relationship of both $\vec{\alpha}_1$ and $\vec{\alpha}_2$ can be defined as distance constraint by physical length of linkage (l_b). Using this constraint, the relation between the displacement of the quadriceps actuator and the angle of tibia link (θ_c) can be defined as follows;

$$\begin{aligned}l_b^2 &= (l_{bar} + s \cos \lambda - l_q \cos \theta_c + l_q \cos \varphi + l_k \sin \theta_c)^2 \\ &\quad + (l_{leg} + l_k \cos \theta_c + s \sin \lambda + l_q \sin \theta_c + q \sin \varphi)^2\end{aligned}\quad (8)$$

By using Eq. (8), the relationship between the displacement of the quadriceps actuator and the tibia link angle (θ_c) can be calculated by initial values from the conceptual design parameters as shown by Table 1 and the relation between θ_c and s is presented in Fig. 6. The thick line in Fig. 6 represents the knee angle of the 1-DOF geared five-bar linkage, while the lower part of the line covers motions of the 2-DOF five-bar linkage and the upper part of the line is the “unfeasible” region of the proposed kinematic mechanism. The displacement of the quadriceps actuator can determine how much the knee joint angle can move freely. Therefore, the main concept of the suggested mechanism is to automatically lock the knee angle by the adjusted displacement of the quadriceps actuator and prevent the knee falling down due to patient’s weak muscle strengths.

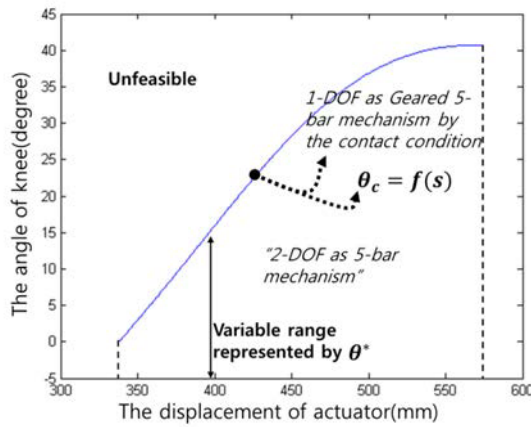


Fig. 6. The relation between quadriceps actuator and knee angle

Table 1. The value of conceptual design parameters

	Parameter	Initial Value	Parameter	Initial Value
Linkages	l_k	248mm	q	217mm
	l_q	65mm	l_b	175.87mm
	l_{bar}	110mm	l_{leg}	419mm
	R	196mm	$s_{initial}$	332mm
Actuator	v_s	320mm/s	F_s	218.8N

4 Optimal Design

The proposed novel knee orthosis needs to have more linkages as compared to existing four-bar linkage [8], besides it also needs the special parts like the circular structure to generate contact situation. Therefore, it is desirable to reduce the total

length of linkages for the knee device, which will be directly proportional to total weight of the device. At the same time, a proper actuator should be selected with the power that can provide the necessary torque and angular velocity enough to support normal gait during stance phase. In this section, a weight optimization scheme will be explained.

4.1 Genetic Algorithm

Since the proposed knee device composed of many linkages and their relations for performance are highly non-linear and complex, it is not easy to find optimal kinematic parameters of the device. Thus, Holland’s simple genetic algorithm (SGA) [21] has been used to find the optimal kinematic design of the proposed knee device. The SGA algorithm has been successfully applied to optimum design [22] of a 6 DOF haptic device and assembly algorithms [23-24] with path planning for active haptic guidance.

The individuals in the proposed mechanism are composed of the linkage lengths L_{gen} ($l_{leg}, l_k, l_q, l_b, q, l_{bar}, R, s$) and the actuator specification (F_s, \dot{s}). Table 2 shows the parameters used for the genetic algorithm.

Table 2. Parameters used for genetic algorithm

	Genetic Algorithm Parameters			
	The number of population	The maximum number of one generation	The crossover chance(P_c)	The mutation chance(P_m)
Value	100	50	0.85	0.05

4.2 Cost Function

The cost function (f) for weight optimization can be represented by (9) as:

$$\min f = \left(\frac{\sum L_{gen}}{\sum L_{initial}} + \frac{F_{gen}}{F_{initial}} \cdot \frac{v_{gen}}{v_{initial}} + SP + GP \right) \tag{9}$$

where $L_{initial}$ is the length of links of initial design, L_{gen} means the union set containiNng the linkages set created by GA, and $F_{initial}$, F_{gen} , $v_{initial}$, v_{gen} mean the chromosome related to the power of the quadriceps actuator. In addition, the specification condition (SP) and geometrical constraint condition (GP) can be defined by (10) as:

$$Penalty = SP + GP = \sum_{i=1}^k r_i g_+^{(i)} + \sum_{i=k+1} r_i \left(g_+^{(i)} \right) \tag{10}$$

$$g_+^{(i)} = \max(0, g^{(i)})$$

In case of SP as in (11), the angular velocity should be under $1.35rad/s$ and the generating torque should be under $35Nm$ in the range of knee angle ($0^\circ \sim 40^\circ$) to fit the specification of the knee device. The desired specifications are selected for stance phase support of a wearer with body weight of $73kg$ and height of $174cm$ and for $1.12m/s$ gait velocity supports [25].

$$\begin{aligned}
 SP &= \sum_{i=1}^3 10^3 \left(g_{q+}^{(i)} \right) \\
 g_q^{(1)} &= 1 - \frac{\max(\theta_c)}{50^\circ}, \quad g_q^{(2)} = 1 - \frac{\min(\dot{\theta}_c)}{1.35rad/s} \\
 g_q^{(3)} &= 1 - \frac{\min(T)}{35Nm} \quad (0^\circ \leq \theta_c \leq 40^\circ)
 \end{aligned} \tag{11}$$

Eq. 12 represents the penalty considered for the geometry constraint of the knee device to avoid unfeasible designs. Its geometrical configurations can be shown in Fig. 7(a). The constraints in (12) make $\vec{\alpha}_2$ as position vector be located in the triangular area so that the contact condition should exist. The constraint in (13) guarantees feasible solutions for possible mechanism generation and its desirable configuration is shown in Fig. 7(b)

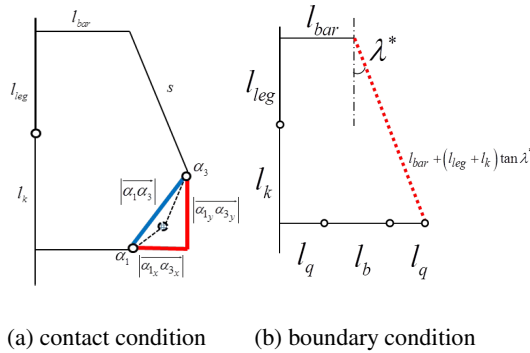


Fig. 7. The geometrical constraints for feasible geometric solutions

$$\begin{aligned}
 GP &= \sum_{i=4}^{11} 10^7 \left(g_{q+}^{(i)} \right) \\
 \left\{ \begin{aligned}
 g_q^{(4)} &= -(\alpha_{3y} + l_k), \quad g_q^{(5)} = l_q - \alpha_{3x} \\
 g_q^{(6)} &= l_q - |\alpha_{1y} \alpha_{3y}|, \quad g_q^{(7)} = l_b - |\alpha_{1x} \alpha_{3x}| \\
 g_q^{(8)} &= |\alpha_1 \alpha_3| < (l_q + l_b) \\
 g_q^{(9)} &= \alpha_2 \vec{i} < x_c \vec{i} < \alpha_3 \vec{i} \\
 g_q^{(10)} &= \alpha_2 \vec{j} < y_c \vec{j} < \alpha_3 \vec{j}
 \end{aligned} \right. \tag{12}
 \end{aligned}$$

$$g_q^{(11)} = l_{bar} + (l_{leg} + l_k) \tan \lambda^* - (l_q + l_b + q) \tag{13}$$

The suggested multi-objective function will then satisfy the desired constraint conditions for feasible solutions and will minimize the weight of the device through the optimization process as shown in Fig. 8.

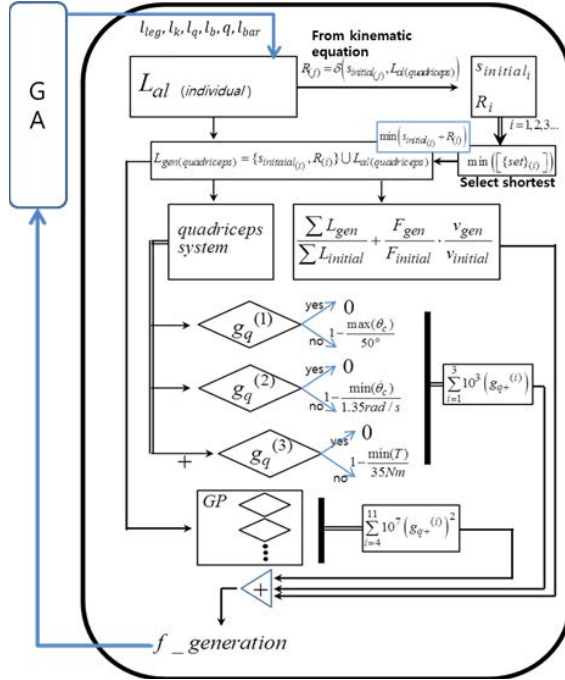


Fig. 8. Flowchart of the weight optimization process

4.3 Optimization Result

Table 3 shows the optimization results by using the SGA, the results satisfies all constraints of (11)-(13). The relative size of kinematic models of the initial design and optimal design are compared to each model in Fig. 9. The kinematic parameters from the optimization result can also satisfy required actuation performances as shown in Fig. 10.

In the initial design, the summation of total linkages including the initial displacement of the actuator and radius of circular structure is 1768.87mm while the summation from the result of optimal design is only 930.45mm and it reduced to 47.4% of the initial design. The actuator power has been also reduced to 40W and is

only 43% of the initial motor power of 70W. It should be noted that the resultant maximum power 40W from the optimization is much smaller than 160W of the Robonee [8].

In addition, the offset value of the linear actuator in Fig.10 (a) has reduced to 100mm, which provides more feasible solution for real implementation. The velocity and torque of the optimized design can also satisfy the requirements in the wider range of the knee angle and more consistent values as compared to initial design as shown in Fig. 10(b)-(c). Finally, Fig. 1 shows that the real fabricated device based on the optimization result can be successfully equipped to a normal person.

Table 3. The value of conceptual design parameters

	Parameter	Optimal Value	Parameter	Optimal Value
Linkages	l_k	257.5mm	q	145.99mm
	l_q	21.61mm	l_b	169.3mm
	l_{bar}	38.83mm	l_{leg}	145.09mm
	R	196mm	$s_{initial}$	332mm
Actuator	v_s	106.36mm/s	F_s	374.7N

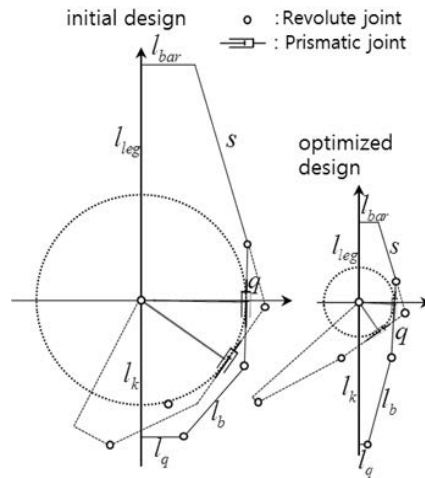


Fig. 9. The relative size between initial and optimized systems

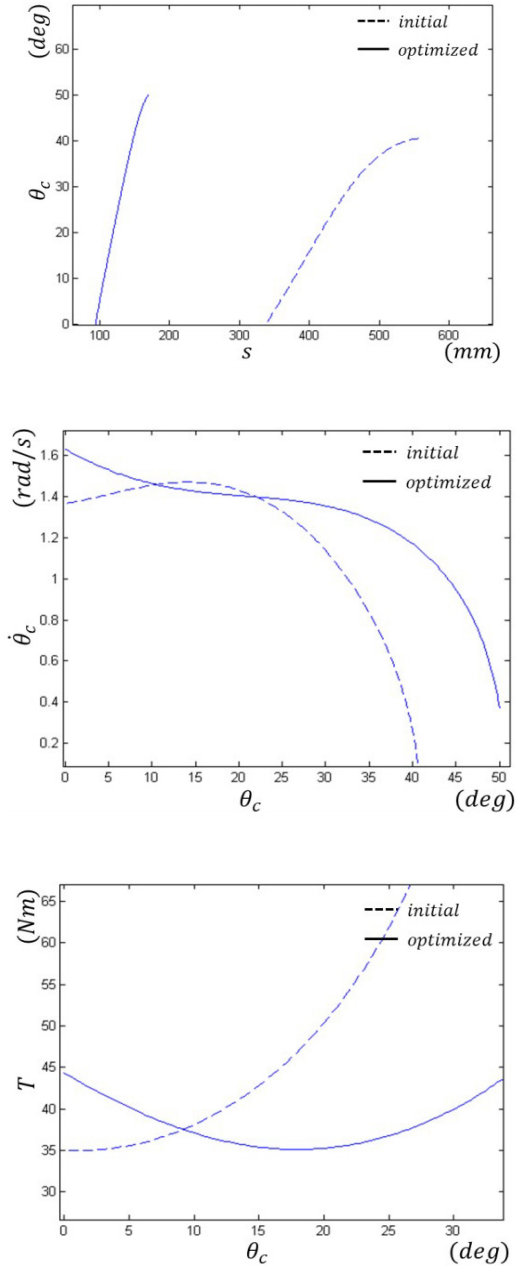


Fig. 10. The performance comparisons between initial and optimized systems

5 Discussion

The necessity of robotic wearable assistive devices or exoskeletons is greatly increasing to provide adequate movement therapy for patients with lower limb incapability. But, the main difficulties that current wearable exoskeleton robots face are to detect a patient's movement intention and to enhance a patient's motivation for overground gait with higher safety during training. The proposed device utilizes mechanical contacts and its operation modes can be changed based on patients motions. Thus, the proposed device can be intermediate solutions between robotic exoskeletons and passive orthoses. Similar to existing SCKAFOs[18], the proposed device utilizes a locking mechanism to provide necessary gait supports during weight bearing and to reduce the weight of the device with smaller actuator power, which can overcome the limitations of exoskeleton approaches. In addition, since the proposed device utilizes active actuations, it can provide more functions compared to existing SCKAFOs.

The achievable design features for the proposed device can be summarized as follows;

- Locking the knee flexion at any desired knee angle rather than just at full knee extension (to ascent or descend stairs, to stand with a flex knee, and to stabilize after stumbling).
- Unlocking the knee at any knee desired angle regardless of the braced limb loading.
- Assisting knee-extension at any desired knee angle during stance
- Reducing the device weight and necessary motor power compared to powered exoskeleton.
- Switching stance-swing mode without requiring knee extension moment to unload the joint.

In results, the proposed device may allow efficient gait training modes in portable environments by providing low impedance for voluntary motions and high impedance during weight-bearing periods as well as assisting knee extensions at any desired knee angles.

6 Conclusion

In this paper, the suggested kinematic model will allow a robotic knee device to use compact and light actuators with full support during walking. However, the proposed device must use additional linkages than a simple four-bar mechanism. In this paper, we use the SGA to minimize sum of total link lengths and motor power by reducing the weight of the novel knee device. To find feasible parameters, kinematic constraints have been applied to the algorithm. The proposed optimization scheme reduces total link lengths and a necessary motor power to about half of the initial values. The proposed optimization scheme can be applied to reduce total weight of general multi-linkages while keeping necessary actuator specifications. In addition, it is expected that the proposed robotic knee device can provide a new rehabilitation

mode for a stroke patient to allow safe and self-motivated overground walking with minimum concern of falling down by providing adequate control supports of the device. For future development, a controller for the proposed concepts will be implemented and clinical trials will be performed to determine the clinical effects of the proposed rehabilitation modes.

References

1. Lee, H.J., Lee, M.S.: Middle-aged patients after stroke- The process of adaptation. *Journal of Nursing* (36), Article 5, 792–802 (2007)
2. Dong-Yu, G.: Acute phase of stroke rehabilitation. In: *The Annual Fall Meeting of the Korean Stroke Society*, vol. 10, pp. 39–40 (2005)
3. Yoon, J., Novandy, B., Yoon, C., Park, K.: A 6-dof gait rehabilitation robot with upper and lower-limb connections that allows walking velocity updates on various terrains. *IEEE/ASME Transaction on Mechatronics* 15(2) (2010)
4. Nene, A.V., Hermens, H.J., Zilvold, G.: Paraplegic locomotion: a review. *Spinal Cord* (34), 507–524 (1996)
5. <http://www.fillauer.com/pdf/M009-RGO.pdf>
6. Kobetic, R., To, C.S., Schnellenberger, J.R., Audu, M.L., Bulea, T.C.: Development of hybrid orthosis for standing, walking, and stair climbing after spinal cord injury. *Journal of Rehabilitation Research & Development* 46(3), 447–462 (2009)
7. Jin, D., Zhang, R., Dimo, H.O., Wang, R., Zhang, J.: Kinematic and dynamic performance of prosthetic knee joint using six-bar mechanism. *Journal of Rehabilitation Research and Development* 40(1), 39–48 (2003)
8. Pratt, J.E., Krupp, B.T., Morse, C.J., Collins, S.H.: The RoboKnee: An Exoskeleton for Enhancing Strength and Endurance During Walking. In: *Proceedings of the 2004 IEEE International Conference on Robotics & Automation*, pp. 2430–2435 (2004)
9. Colombo, G., Joerg, M., Schreier, R., Dietz, V.: Treadmill training of paraplegic patients using a robotic orthosis. *Journal of Rehabilitation Research and Development* 37(6), 693–700 (2000)
10. Mefoued, S., Mohammed, S., Amirat, Y.: Knee Joint Movement Assistance Through Robust Control of an Actuated Orthosis. In: *2011 IEEE/RSJ International Conference on Intelligent Robots and Systems, San Francisco, CA, USA, September 25-30 (2011)*
11. Nikitczuk, J., Weinberg, B., Canavan, P.K., Mavroidis, C.: Active Knee Rehabilitation Orthotic Device With Variable Damping Characteristics Implemented via an Electrorheological Fluid. *IEEE/ASME Transactions on Mechatronics* 15(6), 952–960 (2010)
12. Belforte, G., Gastaldi, L., Sorli, M.: Pneumatic active gait orthosis. *Mechatronics* 11, 301–323 (2001)
13. Veneman, J.F., Ekkelenkamp, R., Kruidhof, R., van der Helm, F.C.T., van der Kooij, H.: A Series Elastic- and Bowden-Cable-Based, Actuation System for Use as Torque Actuator, in Exoskeleton-Type Robots. *The International Journal of Robotics Research* 25(3), 261–281 (2006)
14. Ackermann, M., Cozman, F.G.: Automatic Knee Flexion in Lower Limb Orthoses. *ABCM* 31(4), 305–311 (2009)
15. Sulzer, J.S., Roiz, R.A., Peshkin, M.A., Patton, J.L.: A Highly Backdrivable, Lightweight Knee Actuator for Investigating Gait in Stroke. *IEEE Transaction on Robotics* 25(3) (June 2009)

16. Duncan, P.W., et al.: Body-Weight-Supported Treadmill Rehabilitation after Stroke. *N. Engl. J. Med.* 364(21), 2026–2036 (2011)
17. Hornby, T.G., Campbell, D.D., Kahn, J.H., Demott, T., Moore, J.L., Roth, H.R.: Enhanced gait-related improvements after therapist- versus robotic-assisted locomotor training in subjects with chronic stroke: a randomized controlled study. *Stroke* 39(6), 1786–1792 (2008)
18. Yakimovich, T., Lemaire, E.D., Kofman, J.: Engineering design review of stance-control knee-ankle-foot orthoses. *Journal of Rehabilitation Research and Development* 46(2), 257–268 (2009)
19. Gage, J.R., Deluca, P.A., Renshaw, T.S.: Gait Analysis: Principles and Applications. *Journal of Bone & Joint Surgery* 77-A(10), 1607–1623 (1995)
20. Kramers de Quervain, N.A., Simon, S.R., Leurgans, S., Pease, W.S., McAllister, D.: Gait Pattern in the Early Recovery Period after Stroke. *The Journal of Bone and Joint Surgery* 78(10) (1996)
21. Holland, J.H.: *Adaptation in natural and artificial systems*. The University of Michigan Press, Michigan (1975)
22. Hwang, Y., Yoon, J., Christiand, Ryu, J.: The Optimum Design of a 6-DOF Parallel Manipulator with Large Orientation Workspace. In: *IEEE International Conference on Robotics and Automation 2007 (ICRA 2007)*, Italia, Rome (2007)
23. Christiand, Yoon, J.: A Novel Optimal Assembly Algorithm for the Haptic Interface Application of a Virtual Maintenance System. In: *IEEE International Conference on Robotics and Automation 2008 (ICRA 2008)*, LA (2008)
24. Hassan, S., Yoon, J.: Virtual Maintenance System with a Two-Stage Ant colony Optimization Algorithm. In: *2011 IEEE International Conference on Robotics and Automation (ICRA 2011)*, Shanghai International Conference Center, Shanghai, China, May 9-13 (2011)
25. Winter, D.A.: *The Biomechanics and Motor Control of Human Gait: Normal, Elderly, and Pathological*. Univ. of Waterloo Press, Waterloo (1991)

Neuro Invasive Multi-targeted Drug Delivery Approach Using Swarm of Nano-robotic Carriers

Syed Hassan¹, Ikram Ullah², Myeong Ok Kim², and Jungwon Yoon^{1,*}

¹ School of Mechanical and Aerospace Engineering & ReCAPT
² College of Natural Sciences (RINS) and Applied Life Sciences,
Gyeongsang National University, 660701 Jinju, Korea
{hassan, jwyoony}@gnu.ac.kr, mokim@gsnu.ac.kr

Abstract. This research presents multipath planning scheme for drug loaded nano carriers (virtual robots) based targeted drug delivery. Initially, magnetic field based local path planner algorithm is investigated for its viability within CNS (Central Nervous System) brain capillaries. Furthermore, Optimized Swarm based technologies in hybrid with the local path planner is applied to deal with the complexity of the neuronal blood capillaries system. Globally optimized swarm trajectories for the nano carriers to target multiple neuro-invasive diseases are obtained as a result from the proposed approach. For demonstration purpose the presented scheme is simulated in a 3d virtual environment, results showed that the optimized swarming was successfully performed in closer to real-time (online). Moreover, the drug delivery performance of the carrier robots was more targeted (directional path) and shorter in length and in uniform velocity keeping the overall drug release time controlled than the conventional (oral \ intravenous) drug delivery procedures.

Keywords: targeted drug delivery, nano technology, nano robots, swarm.

1 Introduction

Conventional (oral/intravenous) drug delivery systems are based upon simple drug injection and they rely upon natural blood flow to target the diseased area. These delivery systems have their limitations due to their target locations and type of drugs. One of the major limitations for the traditional technique is also high precision and accuracy of the methods. Frist et al. [1] suggests that the research and development of nanorobots with embedded nano-biosensors and actuators is considered to provide a new possibility to provide health specialists with new high-precision tools. These tools and equipments aim towards efficient methods for patient treatment [2]. For example, among other medical instrumentation, catheterization has been used successfully as an important methodology for intracranial surgery [3].

In early 80's, the development of micro-technology led to new medical instruments, but with the advancement in nanotechnology and embedded electronics

* Corresponding author.

another big step has been taken. The miniaturization instrument along with the nano technology has been very useful in this field. Andrew et al. [4] tells how the advent of bio-molecular science and new manufacturing techniques is helping to advance the miniaturization of devices from microelectronics to nano-electronics. The manufacturing of nano-electronics [5-6], has permitted further advances in nano technologies in these fields. Therefore, the researches lead to continuous advancements in the nano technologies aspect.

Nanotechnologies comprises of nano sized sensors, actuators and eventually nano robots. Nano sensors and actuators have been used together for fabrication of hardware architectures [7]. In recent years some researchers have been reported to have ability to integrate nano robots with biosensors [8-9]. These nano robots are being used in medical field. Many researchers have focused on targeting of nanocarrier based robots for drug delivery system and health monitoring. Adriano et al. [7] successfully developed an IC based nano robot for brain aneurysm and simulated results in the virtual 3d environment. Furlani and Furlani [10] developed a mathematical model for studying magnetic targeting of therapeutic carrier particles in the microvasculature and concluded that magnetic targeting can be achieved using sub-micron carrier particles when the tumor is within a few centimeters of the surface of the body. Vartholomeos et al. [11] studied the use of the innovative concept of MRI targeted drug delivery platform for robotic targeting of magnetized aerosol in the lungs. The problems related to usage of magnetization are the control and precision of the desired magnetic field. Cherry et al. [12] developed a physics-based model of a general magnetic drug targeting (MDT) system with the goal of realizing the practical limitations of MDT when electromagnets are the source of the magnetic field. David et al, [13] studied a combined theoretical and in vitro modeling approach for predicting the magnetic capture and retention of MNPs in vivo and concluded that this combination can potentially assist with parametric evaluations of magnetic targeting, and enable rapid enhancement and optimization of magnetic targeting methodologies. The magnetic particles also get affected with the fluids already present in the body. Therefore a proper analysis of fluid dynamics is desired. Yue et al. [14] developed a stochastic ODE model for the motion of a super-paramagnetic cluster suspended in a Hagen-Poiseuille flow and guided by an external magnet to travel to a target with the application of magnetic drug targeting, with clusters in the range of 10-200 nm radii. Heidsieck et al. [15] presented a model for vascular targeting with a full three-dimensional analysis of the magnetic and fluidic forces and subsequently evaluated the resulting trajectories of the complexes.

Tabatabaei et al. [17] demonstrated the possibility of automatically navigating untethered microdevices to conduct target endovascular interventions with the computer-controlled displacement of a magnetic sphere along a pre-planned path inside the carotid artery of a living swine using a clinical MRI system. Fu and Yan [18] proposed DNA nanobot for targeted drug delivery. The nanobot opens in the presence of the correct combination of antigen keys and the molecular payload is then released to bind to target cells and activate signaling pathways. Thamma wongsa et al. [19] proposed a new technique of microsurgery using a nanorobot controlled by light. A nanorobot is trapped and transported (moved) by the rotational optical tweezers

within the microtubule. In operation, nanorobots are stably trapped by the dynamic potential wells and transported to the required surgical targets for treatment.

From the above literature, it is clear that the development and application of nanorobots has provided remarkable advances in biomedical applications through medical target identification, to improve diagnosis and provide new therapeutic procedures. A large number of nanorobots can be controlled through various techniques and could be efficiently utilized for treatment of disease such as Cancer, Alzheimer etc.

1.1 Epilepsy Disease (ED)

Epilepsy is a common neurological disorder characterized by a number of recurrent and spontaneous seizures [20]. It's already known that 60-70% of patients respond to conventional antiepileptic drugs but 30-40 % of patients need combined therapeutic approach [21]. The majority of patients suffering from epilepsy generally suffer from focal seizures, which start in one part of the brain and then spread. Epilepsy starting with seizures is due to excessive hypersynchronous discharges from a group of neurons in the brain and spread to the surrounding neurons and affects one or both hemisphere of the brain [22].

1.2 Alzheimer Disease (AD)

Alzheimer's disease (AD) is the most common form of senile dementia, characterized by progressive memory loss. AD was first described by Alois Alzheimer, a German physician, in 1906 [23]. AD leads to a decreased quality of life and an increased burden on caregivers and it is the most common brain disease of adulthood. Samanta et al. have shown that, it is 1.5 times more common than stroke or epilepsy and is as common as congestive heart failure [24]. Amatniek et al. and Mendez et al. showed how "The risk of seizures is high in patients with Alzheimer's disease (AD), with up to 87- fold increase compared with an age-matched reference population" [25-26]. The primary pathological hallmarks of AD are the presence of amyloid plaques containing the β -amyloid peptide and neurofibrillary tangles composed of hyperphosphorylated tau protein, shown by Galimberti et al. [27].

2 Motivation

In this research drug loaded nano carriers (NC's) were used for delivery purpose. NCs are very small objects, less than 1/1,000 the width of an average human hair, which can interact with individual human cells, proteins and even single molecules. The drug loaded NC's were prepared using biopolymer method in spherical shape method [28]. The current approach to drug therapy of seizures and degeneration of cells because of Alzheimer disease (AD) involves producing high levels of Anti Epileptic drugs (AEDs) and Anti Alzheimer drugs (AADs) in the blood, through the use of conventional methods like, orally taken pills or intravenous (IV) injections. In

both situations, the objective is to let the drug reach the brain and pass through the blood brain barrier reaching brain tissues.

The neuronal system contains billions of capillaries within millimeters of distance producing complex bifurcations of intracranial vessels, through which the drug circulate in whole brain. Though, these are very well established traditional methods for drug up taking but now days it is well established that these methods are very limited and avert the drugs from reaching the brain at therapeutic concentrations that are aimed overtime [17].

From the above literature, it is well established that the possibilities of integration and fabrication of nano electronics (nano biotech) to produce nano robots is advancing continuously and references are found for bio and electro nano level enabling technologies for robot carriers in this aspect.

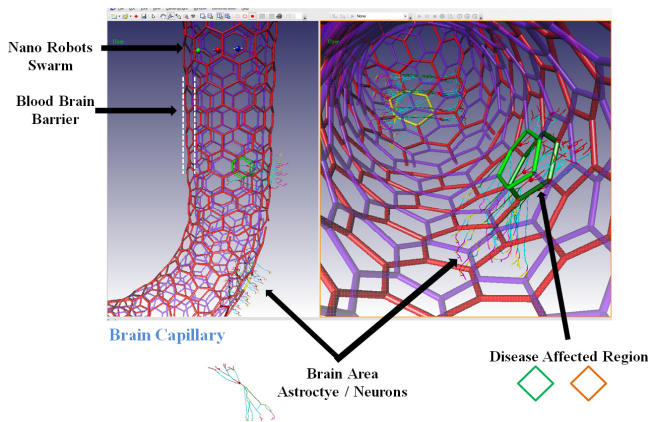


Fig. 1. A Simulation view from inside the brain capillary surrounded by the BBB (Virtual nano level simulator designed for virtual experiments)

3 Nano Level Simulations

Simulations for nanotechnology allows researcher now a days to develop potent tools for developing and testing nano level operations. The virtual simulation environment virtualizes the process of anticipation to measure the performance of the designed system as well as can demonstrate a pre analysis data to the researchers.

Targeted drug delivery system for multi targeting of more than one disease needs advance technologies for monitoring and analysis due to the complexity of the neuronal structures. Furthermore, the size of the nano level carrier robots and their swarming behavior makes it difficult to visualize the manipulation process in real time. To overcome these issues, a virtual simulator framework is developed and utilized multi targeting of nano robots in a 3d virtual blood vessel as shown in figure 1. The simulator framework settings reflect the perceived needs of the nano level operations such as target identification, its targeting, swarming towards the target and providing visual feedback about aspects of technical ability to researchers.

3.1 Virtual Nano Robots

In this research nano robots are considered as active agents that travel with the uniformity of blood flow. The nano robots swarm their trajectory towards the induced target already identified as shown above the presence of disease in hippocampus area of brain. The virtual nanorobot carriers modeled for this research were between ranges of 100 to 150 nano meters. The carriers were of enough diameters to carry drug loaded particles (molecules) in container. The robots were developed to swarm towards the disease area and sense for specific binder (disease affected area). Once the binder is identified the robots bind with the disease affected cell proteins.

3.2 Artificial Potential Field Path Planner

Artificial potential field (APF) [29] is a path planning technique based on obstacles as repelling force sources, and goals as attracting force sources. Potential field approach has been successfully applied to various problems to find an obstacle free path [30]. An object is driven by the accumulation of the two forces; the artificial attractive and repulsive forces. This method is commonly known as local path planning which handles a single object travelling between initial and final position. A force field is generated between the initial and final target where the object moves towards the target because of the attractive field. Whereas, a negative force field is applied in a given radius to repel the object from colliding with obstacles. Hence, accumulating both the attractive and repulsive forces the particle will travel towards the attractive object, hence resulting in a trajectory which is obstacle free and directed towards the target.

The positions of a particle and its bounding box in a frame of origin O can be represented as the transformed points of particles vertex using a 3d homogenous transformation matrix (1).

$$\begin{aligned}
 q_{11} &= \cos\theta_i \cos\phi_i, \quad q_{12} = \cos\theta_i \sin\phi_i \sin\psi_i - \sin\theta_i \cos\psi_i \\
 q_{13} &= \cos\theta_i \sin\phi_i \cos\psi_i + \sin\theta_i \sin\psi_i, \quad q_{21} = \sin\theta_i \cos\phi_i \\
 q_{22} &= \sin\theta_i \sin\phi_i \sin\psi_i + \cos\theta_i \cos\psi_i, \quad q_{23} = \sin\theta_i \sin\phi_i \cos\psi_i - \cos\theta_i \sin\psi_i \\
 q_{31} &= -\sin\phi_i, \quad q_{32} = \cos\phi_i \sin\psi_i, \quad q_{33} = \cos\phi_i \cos\psi_i
 \end{aligned}$$

$$q = \begin{bmatrix} q_{11} & q_{12} & q_{13} & d_{xi} \\ q_{21} & q_{22} & q_{23} & d_{yi} \\ q_{31} & q_{32} & q_{33} & d_{zi} \\ 0 & 0 & 0 & 1 \end{bmatrix} \tag{1}$$

The configuration of the robots is represented by $q = [d_{xi} \ d_{yi} \ d_{zi} \ \theta_i]$, and d_{xi} , d_{yi} , d_{zi} is translation along the x-axis, y-axis and z-axis of the workspace coordinate. The summation of the attractive and repulsive forces gives the direction for movement as a normalized vector as follows:

$$q = [q_x, q_y, q_z, \theta] \tag{2}$$

$$\vec{f} = \Delta q \frac{F_{att} + F_{rep}}{|F_{att} + F_{rep}|} S \tag{3}$$

Where q define the coordinates of the force applied to move the object, S is step size between path points.

The 3d path planning process based on 3d potential field method is further assisted by the PSO for optimization process in finding optimal path. In potential field scheme only valid path is planned and it is not considered as optimal as in an environment there can be many paths from initial to final position. Therefore, in order to deal with this scenario as suggested by Wahid et al. [31] swarm optimization is opted to perform optimization among all available valid paths resultant by applying potential field concepts.

3.3 Particle Swarm Optimization PSO

Many artificial intelligence techniques have been utilized as an optimization tool in various applications, ranging from biological and medical applications to computer graphics. Particle swarm optimization (PSO) technique, introduced by Kennedy and Eberhart [16] is an artificial intelligence (AI) technique that can be used to find approximate solutions to extremely difficult or impossible numeric maximization and minimization problems. The traditional PSO algorithm is based on behavior of the swarms of particles. The best strategy for particle to reach the destination is to follow the particle, which is very close to the destination. The optimization solution of the problem is regarded as the progressive paths of the particles towards the destination.

The fitness of each particle is computed by the fitness function. Each particle proceeds with a velocity, which determines its direction and distance.

3.4 Multi Targeted Swarm Planner

In case of path planning for targeted drug delivery, optimization process is defined as process of finding the best feasible path to achieve targeted drug delivery for specific disease site. Since path planning is multimodal optimization problem which means there can be multiple routes to find solution for one problem. Therefore, our proposed approach is a hybrid approach of APF and traditional PSO. In this algorithm, the premature convergence of the traditional PSO scheme is undermined and the convergence rate is accelerated by utilizing the APF planner.

As a result, the performance to accomplish the global optimization is observed to be improved with subject to the optimization method. First, the principal drug delivery process constraints are specified to the algorithm, targets are identified for individual robots in swarm and the optimization model of virtual blood vessels is investigated. The PSO algorithm forms a swarm of multiple robots which includes the robots with multiple drug loaded to target multi disease. For each particle, the APF path planner initially investigates the disease target (In this scenario the Hippocampus area) and plans the path based on an attractive artificial magnetic field and hydrodynamic drag force. The velocities of swarm particles are based on the investigated forces. Followed by the PSO, planner performs the optimization for all the possible paths outlined by APF planner to find one best optimal path reported as *gbest*.

The proposed algorithm performs path planning in virtual environment initially by loading the 3D CAD models of bio nanorobots swarm with their initial and final position identified, where all the robots are placed in a swarm group on the starting point at random. In the beginning considering that the robots velocity is equal to the blood flow velocity, (V_i^k) is initialized for every particle. In the swarm (population) every individual robot results in a path from initial to final position. When the robot reaches the final position its *pbest* and swarm *gbest* is calculated and a list of path value is maintained for each robot. Traditional rules are followed to keep the list of previous best robot position *pbest*. Finally, the *gbest* robot is considered as the global solution.

The process starts by simulating the robots injection in to the virtual blood vessel. The movement of the robots is affected by accumulation of three types of forces, the attractive forces F_{att} and the repulsive forces F_{rep} and the drag forces F_{drag} . The hydrodynamic drag forces (F_{drag}) are given by Stoke’s law as:

$$F_{drag} = -6\pi\eta R_p (V_p - V_f) \tag{4}$$

Where η is the fluid viscosity, R_p is the radius of nanorobot carrier, V_p is the robot velocity and V_f is the fluid velocity.

$$V_{apf} = \Delta q \frac{F_{att} + F_{rep} + F_{drag}}{\|F_{att} + F_{rep} + F_{drag}\|} \tag{5}$$

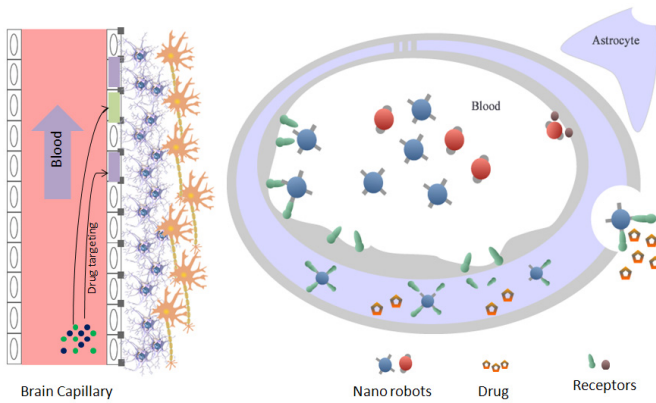


Fig. 2. Nano robot carriers binding with the receptors and passing through the BBB

Disease (target) Identification

In a given model, the biosensors detect the energy level of the cells. Since both the Alzheimer disease (AD) and Epilepsy (EP) cause degeneration of the neuronal cells, the overall energy level of the affected area is lower as compared to other regions. Experimental analysis has shown that in case of AD and EP, the neuronal cell death is common whereas, EP disease further produce seizures (high level of voltage bursts in neuronal cells). The drug target is identified by the planner algorithm by measuring the voltage level in neuronal cells. In case of higher levels the EP disease is detected anti EP drug loaded nanorobots perform the drug delivery. For AD, anti AD loaded

nano particles are unloaded by the robot and specific binders collect the drug molecules to carry them passing through the BBB as shown in figure 2.

Anti-Agglomeration Rule

The purpose of this rule was to ensure that the robots carry a delicate repulsion charge to avoid agglomeration. If the robot approaches within the charge field of other robot in a swarm, this rule maintains a repelling distance between robots. Anti-agglomeration is the urge to steer away robots from an imminent repelling impact.

If $|P_i - P_j| < 10\mu\text{m}$

$$Alogg = \sum_{i=1}^N Alogg_i - (P_i - P_j) \tag{6}$$

Where, $10\mu\text{m}$ was taken as zeta potential radius, P_i and P_j are the position of i^{th} and j^{th} particle respectively and $i \neq j$.

Velocity Saturation Rule

This rule ensures that the flow between the robot remain invariant with respect to the blood flow. Therefore, the velocities were averaged to keep the robots intact in a swarm and flow with an average velocity inside the blood vessel.

$$Vavg_i = (\sum_{j=1}^N Vel_j / N) - Vel_i \text{ Where, } Vel_i \text{ is velocity of } i^{\text{th}} \text{ particle; } i \neq j \tag{7}$$

Proposed Algorithm

The proposed algorithm is derived from above equations and can be written as:

$$V_i^{k+1} = wV_i^k + Vapf + Vavg_i + c_1 (pbest_i - S_i^k) + c_2 (gbest - S_i^k) \tag{8}$$

$$w = W_{Max} - [(W_{Max} - W_{min}) Iter] / MaxIter \tag{9}$$

If $V_i^{k+1} > Vmax$, then limit (V_i^{k+1})

$$S_i^k = S_i^k + Alogg \tag{10}$$

$$S_i^{k+1} = S_i^k + V_i^{k+1} \tag{11}$$

$$F(S) = \sum_i^{k-1} 200 ((S_{i+1} - S_i)^2 + (1 - S_i)^2) \tag{12}$$

For global minimum: $F(S) = 0$; and $S(i) = 1, i = 1:k$

Where, i is number of total robots and $F(S)$ is the fitness function which takes real numbers and V_{max} is maximum velocity a constant value to limit the flow of robots. The attractive magnetic force pulls the robots towards its final position. If the $pbest$ of the path is greater than the previous $pbest$, the new $pbest$ value is ignored. The loop mechanism in traditional PSO for updating $gbest$ and $pbest$ were used. When the swarm reaches the final position the $gbest$ which indicates the path of one of the robot among the swarm is reported as optimal solution. The $gbest$ is considered as the robot at best position within the swarm.

4 Experiments and Results

The proposed approach produces a path between the initial injected position to the final binding position, assisted by the swarm handler to produce and optimized path for the whole swarm to travel within the dynamic central nervous system CNS environment travelling inside the brain blood capillaries. Initially, an attractive gradient field (pull forces) is produced which attracts the swarm of nano robots towards the targeted delivery area. The resultant forces are accumulation of attractive forces, repulsion force, hydrodynamic drag forces and attractive force which are produced by the flow of blood within blood vessel. For more realistic approach APF was applied which is based on artificial magnetic field attraction force producing virtual gradient field of magneto static coils in virtual environment. Whereas, hydrodynamic drag forces were considered which are present in the blood vessel due to blood flow. The combination of hydrodynamic and attractive gradient field resulted in nano robots trajectory planning and swarm behavior study.

A single computer with a Pentium (2.14 GHz-D'Core) CPU and 3 GB ram is used to run the simulations of nano robots swarm and a computed workspace (4.0x4.0x4.0)cm. The constant parametric values for the simulation were considered as: viscosity $\eta = 0.001\text{Nm/s}^2$, diameter of carrier's $d_{robot} = 200\text{nm}\sim\text{aprox}$. The value of c_1 c_2 and w for PSO was taken to be 0.3, 0.4 and 0.2 respectively. The velocities were measured in millimeters/second and distance was measured in millimeter. The anti-agglomeration distance of nanorobots was taken $10\mu\text{m}$ (physically zeta potential value) in the range of -18 to -27mV [28].

The experiment was carried out in normal blood flow rate of about 0.19mm/s, the swarm was divided in group of 500, 1000, 5000 and 10,000 robots injected into the virtual brain capillary. The simulation view of the movement of nano robots swarm from initial to final position is shown in Figure 3.

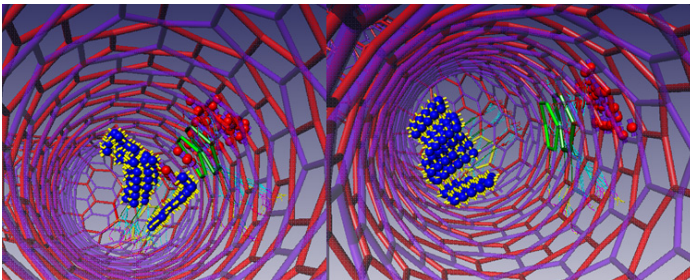


Fig. 3. Shows the Swarm loaded with AEDs drug binds with green channel and the remaining swarm travels to the yellow channel carrying AADs

The results obtained from the virtual simulation demonstrated that the swarm was successful in reaching the target towards hippocampus BBB area. The proposed path planner converged faster, in average it took 50 generations to synchronize optimization process and resulting in optimal or near optimal solution. The

optimization process reduced the path length initially planned by the APF planner, therefore, consuming less transportation towards the target as shown in figure 4 the optimized path(trajjectory) results for each swarm. The initial results without optimization shows a path length above 15 millimeters, whereas optimizing potential field, the path length was highly optimized as shown in figure 4. Optimizing the swarm to adapt an efficient (optimal) path the results showed that overall transportation time and average path cost of the swarm was reduced. Several other forces acting on nano carrier robots in the drug targeting system including gravitational force, buoyancy forces and inertial forces were considered negligible as these are relatively small for nano level carriers [32].

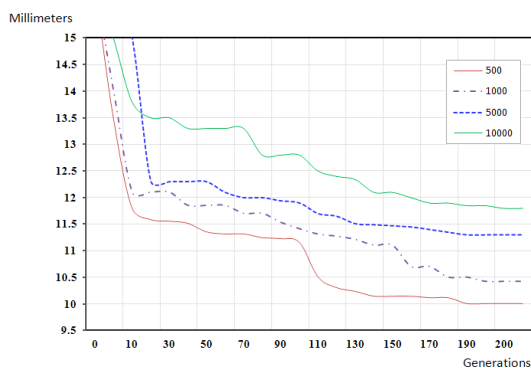


Fig. 4. Path optimization value graph for robot at best (leading) position in swarm

5 Conclusion

In this research, a novel prototype approach is presented based on the real time swarming of nano carrier robots for multi targeted drug delivery process within the virtual 3D invivo environment. The optimization results and the efficiency index showed that the proposed scheme reduced the overall transportation time and path length of the swarm. Simulation results further showed that a higher success rate in targeting the drugs with a faster convergence rate towards the optimal target can be achieved by applying swarm optimization process. The swarm optimization enhanced the sustainability and site targeting of nano carriers further enabling the future directions for broad range of nano medicine applications.

The prototype scheme is developed to contest the neuro invasive disease causing the degeneration of neuronal cells. The current implementations are done in 3D virtual environment to experiment the swarming behavior of nano carriers. For this research a small portion of nano carrier robots is selected initially, the swarm of nano carrier robots is injected into the brain capillary, the carriers flow along with (in direction of) the blood flow with an initial velocity determined by the accumulation of flow velocity and forces in equation (8). The localized artificial magnetic field plays a vital role in projecting the carriers towards the targeted area. The attractive forces affect movement of carries towards the disease affected area. The role of swarming

approach is to keep the particles within a swarm and allow them to share the information for every individual carrier status. Applying the intelligent particle swarm optimization technology allows the carriers to follow the optimized path to reduce the path cost and keeping the drug in sustained manner.

Acknowledgement. This work was supported by National Research Foundation Korea (NRF) (2011-00313832010-0029690 & 20120009524).

References

1. Frist, W.H.: Health care in the 21st century. *New England Journal of Medicine* 3, 267–272 (2005)
2. LaVan, D.A., McGuire, T., Langer, R.: Small scale systems for in vivo drug delivery. *Nature Biotechnol.* 21, 1184–1191 (2003)
3. Ikeda, S., Arai, F., Fukuda, T., Negoro, M., Irie, K., Takahashi, I.: Patient-specific neurovascular simulator for evaluating the performance of medical robots and instruments. In: *IEEE International Conference on Robotics and Automation (ICRA)*, pp. 625–630 (2006)
4. Andrews, R.J.: Neuroprotection at the nanolevel—Part I introduction to nanoneurosurgery. *Annals of the New York Academy of Sciences*, 169–184 (2007)
5. Chau, R., Doyle, B., Datta, S., Kavalieros, J., Zhang, K.: Integrated nanoelectronics for the future. *Nature Materials* 6, 810–812 (2007)
6. Elder, J.B., Liu, C.Y., Apuzzo, M.L.J.: Neurosurgery in the realm of 10-9, Part 2: Applications of nanotechnology to neurosurgery-present and future. *Neurosurgery* 2, 269–284 (2008)
7. Cavalcanti, A., Shirinzadeh, B., Freitas Jr., R.A., Hogg, T.: Nanorobot architecture for medical target identification. *Nanotechnology* 19, 15 (2008)
8. Montemagno, C., Bachand, G.: Constructing nanomechanical devices powered by biomolecular motors. *Nanotechnology* 3, 225 (1999)
9. Hill, C., Amodeo, A., Joseph, J.V., Patel, H.R.H.: Nano and microrobotics: how far is reality. *Expert Rev., Anticancer Ther.* 8, 1891–1897 (2008)
10. Furlani, E.J., Furlani, E.P.: A model for predicting magnetic targeting of multifunctional particles in the microvasculature. *Journal of Magnetism and Magnetic Materials* 312(1), 187–193 (2007)
11. Vartholomeos, P., Mavroidis, C.: Magnetic targeting of aggregated nanoparticles for advanced lung therapies: A robotics approach. In: *Proceedings of the 3rd IEEE RAS & EMBS International Conference on Biomedical Robotics and Biomechanics*, Tokyo, pp. 861–868 (2010)
12. Cherry, E.M., Maxim, P.G., Eaton, J.K.: Particle size, magnetic field, and blood velocity effects on particle retention in magnetic drug targeting. *Med. Phys.* 37(1), 175–182 (2010)
13. David, E., Cole, A.J., Chertok, B., Park, Y.S., Yang, V.C.: A combined theoretical and in vitro modeling approach for predicting the magnetic capture and retention of magnetic nanoparticles in vivo. *Journal of Controlled Release* 152(1), 67–75 (2011)
14. Yue, P., Lee, S., Afkhami, S., Renardy, Y.: On the motion of super-paramagnetic particles in magnetic drug targeting. *Acta Mechanica* 223(3), 505–527 (2012)

15. Heidsieck, A., Vosen, S., Zimmermann, K., Wenzel, D., Gleich, B.: Analysis of Trajectories for Targeting of Magnetic Nanoparticles in Blood Vessels. *Mol. Pharmaceutics* 9, 2029–2038 (2012)
16. Kennedy, J., Eberhart, R.: Particle Swarm Optimization. In: Proceedings of the IEEE International Conference on Neural Networks, Tokyo, pp. 1942–1948 (1995)
17. Tabatabaei, S.N., Duchemin, S., Girouard, H., Martel, S.: Towards MR-navigable nanorobotic carriers for drug delivery into the brain. In: IEEE International Conference on Robotics and Automation (ICRA), May 14–18, pp. 727–732 (2012)
18. Fu, J., Yan, H.: Controlled drug release by a nanorobot. *Nature Biotechnology* 30, 407–408 (2012)
19. Thammasawongsa, N., Zainol, F.D., Mitatha, S., Ali, J., Yupapin, P.P.: Nanorobot Controlled by Optical Tweezer Spin for Microsurgical Use. *IEEE Transactions on Nanotechnology* 12(1), 29–34 (2013)
20. Duncan, J.S., et al.: Adult epilepsy. *Lancet* (London, England) 367, 1087–1100 (2006)
21. Prisco, L., et al.: Trigeminal neuralgia: successful antiepileptic drug combination therapy in three refractory cases. *Drug, Healthcare and Patient Safety* 3, 43 (2011)
22. Vedula, S.S., Bero, L., Scherer, R.W., Dickersin, K.: Outcome reporting in industry-sponsored trials of gabapentin for off-label use. *The New England Journal of Medicine* 361(20), 1963–1971 (2009)
23. Berchtold, N.C., Cotman, C.W.: Evolution in the Conceptualization of Dementia and Alzheimer's disease. Greco-Roman Period to the 1960s. *Neurobiol. Aging*. 19(3), 173–189 (1998)
24. Samanta, M.K., et al.: Alzheimer disease and its management: a review. *American Journal of Therapeutics* 13(6), 516–526 (2006)
25. Amatniek, J.C., Hauser, W.A., DelCastillo-Castaneda, C., Jacobs, D.M., Marder, K., Bell, K., Albert, M., Brandt, J., Stern, Y.: Incidence and predictors of seizures in patients with Alzheimer's disease. *Epilepsia* 47, 867–872 (2006)
26. Mendez, M.F., Catanzaro, P., Doss, R.C., Arquello, R., Frey, W.H.: Seizures in Alzheimer's disease: Clinicopathologic study. *J. Geriatr. Psychiatry Neurology* 7, 230–233 (1994)
27. Galimberti, D., Scarpini, E.: Disease-modifying treatments for Alzheimer's disease. *Ther. Adv. Neurol. Disord.* 4, 203–216 (2011)
28. Shah, M., et al.: Amphiphilic PHA–mPEG copolymeric nanocontainers for drug delivery: Preparation, characterization and in vitro evaluation. *International Journal of Pharmaceutics* 400(1), 165–175 (2010)
29. Khatib, O.: Real-time obstacle avoidance for manipulators and mobile robots. *The International Journal of Robotics Research* 5, 90–98 (1986)
30. Park, M.G., Jeon, J.H., Lee, M.C.: Obstacle avoidance for mobile robots using artificial potential field approach with simulated annealing. In: Proceedings of the IEEE International Symposium on Industrial Electronics (ISIE 2001), vol. 3. IEEE (2001)
31. Abdel Wahid, M.H.M., McInnes Colin, R.: Wall following to escape local minima for swarms of agents using internal states and emergent behavior. In: International Conference of Computational Intelligence and Intelligent Systems (ICCIIS 2008) (2008)
32. Gleich, B., Hellwig, N., Bridell, H., Jurgons, R., Seliger, C., Alexiou, C., et al.: Design and evaluation of magnetic fields for nanoparticle drug targeting in cancer. *IEEE Transactions on Nanotechnology* 6, 164–170 (2007)

A Novel EMG Control Method for Multi-DOF Prosthetic Hands with Electrical Stimulation Feedback

Qi Huang, Li Jiang, Dapeng Yang, and Hong Liu

State Key Laboratory of Robotics and System, Harbin Institute of Technology,
150001 Harbin, China
yangdapeng@hit.edu.cn

Abstract. In this paper a novel bidirectional control scheme for multigrasp prosthetic hands with forward EMG control and backward sensory feedback is proposed. Based on the knowledge of grasp taxonomy and the principle of finite state machine (FSM), users can control multi-DOF prosthetic hands with the EMG control strategy to accomplish 7 most frequently used hand gestures, which occupy 85% of hand usage in activities of daily life. Besides, to restore the comprehensive sense of control, the transcutaneous electrical nerve stimulation (TENS) is adopted to apperceive the gripping force. Experiments were conducted on a 5-DOF prosthetic hand to evaluate both the grasp success rate and the average grasp time, according to each grasp task. The results show that the proposed method can effectively recognize the contraction patterns with the grasp success rate of nearly 95%, and the control state can be rapidly switched with the average operation time less than 20 seconds, which in all ensures fluent hand grasps.

Keywords: Prosthetic Hand, EMG Control, Electrical Stimulation.

1 Introduction

In those days, numerous sophisticated robot hands have been developed for improving the rehabilitation therapy for the upper limb amputees [1]. However, finding a proper myoelectric control method for these dexterous hands still seems to be a challenge for those amputees with limited electromyography (EMG) activities.

At present, approaches established on EMG pattern recognition turn out to be an effective method in controlling the multi-DOF prosthetic hands. However, the user generally needs a number of active muscles and has to concentrate his mind on the muscle contractions, which is very difficult for high-level amputees. Besides, the performance of the controller would be easily affected by the variations of electrode-skin interface and muscle fatigue [2-4].

To overcome these shortcomings, a method based on the mechanism of finite state machine (FSM) comes to light, which divides the controlling process into a series of interconnected states that uniquely defined by the controller [5-7].

On the other hand, sensory feedback about the variety of the command signal and operation status of the prosthetic hand can help the users compensate for their inherent deficiencies of the control system [8]. Experiments based on brain functional magnetic resonance imaging indicate that mutual adaption between the human body and the prosthetic can be achieved with the help of sensory feedback [9]. Compared to other forms of sensory feedback, such as mechanical vibration or acoustic clue, electrical stimulation has the advantages of small size and low power consumption [10] that make it be easily integrated in portable prostheses.

This paper presents the design and preliminary experimental validation of a myoelectric control methodology for multi-DOF hand prostheses with sensory feedback. The FSM method is utilized in the control strategy, while the electrical stimulation is applied to the human body in order to provide sensory information. The control system divides the control states based on statistical data of grasp taxonomy, and encodes the EMG signals with their endurance and magnitude.

The result of preliminary experimental validation shows that, with 2 EMG electrodes placed on a pair of agonist/antagonist muscles, this approach can accomplish a combined position and force control of the prosthetic hand imitating 85% human hand gestures in activities of daily life (ADLs). The average operation time for 6 typical objects and one hand gesture is less than 20 seconds with the success rate as high as 95%. The sensory feedback channel endows the subject with feeling about their “hands”, thus a more precise and stable grasp can be ensured.

2 Materials and Methods

2.1 The HIT-IV Hand

Fig. 1 shows the proposed HIT-IV prosthetic hand and its control system. The HIT-IV hand is a kind of 5-DOF anthropomorphic prosthetic hand with humanoid finger layout and palm shape. Each finger of the HIT-IV hand is actuated by a DC motor, respectively, via a coupling rod mechanism [11]. The control system is composed of two subsystems: the robot motion control subsystem and the sensory subsystem.

The motion control system is mainly integrated in a low-level controller inside the HIT-IV hand, in charge of processing the data of torque sensors and position sensors and driving the motors under the instruction of the sensory subsystem. The core of this system is a digital signal processor (DSP, TMS320F2810, Texas Instruments). It communicates to the sensory subsystem via the eCAN bus.

The sensory subsystem consists of a high-level controller and an electrical stimulator. The high-level controller is in charge of processing the data from EMG electrodes, generating motion instructions for the motion control system, as well as sending out stimulus information to the electrical stimulator (via the SPI bus). Similar to traditional pattern recognition-based myoelectric controller, the high-level controller works in two phases: Phase 1 for acquiring samples and training the classifier; and Phase 2 for classifying the incoming EMG signals and generating motion codes. However, the working style of the high-level controller in Phase 2 is slightly different (that will be discussed in next section).

The core of the electrical stimulator is a DDS chip (AD9959, Analog Devices) that can generate 4 channel synchronized modulation waveforms. After power amplifying, the waveforms are applied to the human body in the form of current source.

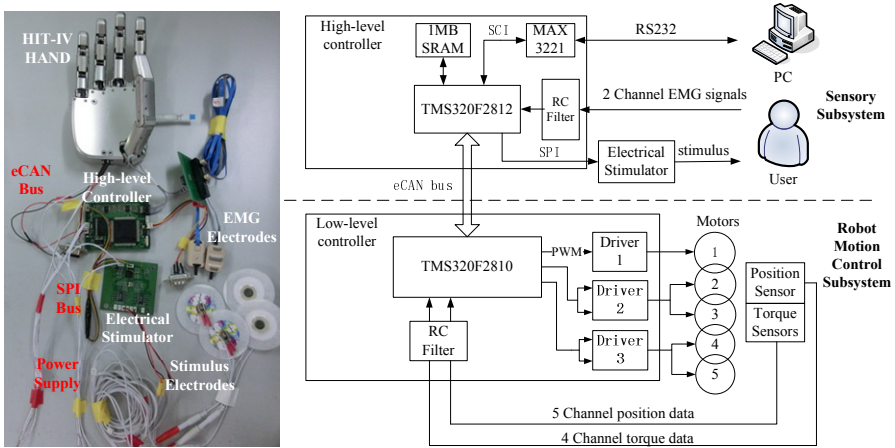









Fig. 1. HIT-IV prosthetic hand and its control system

2.2 Control Structure of the High-Level Controller

Theoretically, a multigrasp prosthetic hand should enable amputees to perform all ADLs. However, since some operation types play much more important roles than the others, a practical method is to give a high priority to the operation types which are used more frequently. According to [12-17], studies have been conducted to categorize human hand postures and analyze the usage frequency of different gesture types in ADLs. Although these researchers have different starting points (for example, Sollerman et al. [14] assorted the hand operations based on the relative movements of the thumb and the other fingers, while Napier et al. [13] assorted them based on their demands of precision and power) and the statistics about the usage frequency are also different, they indeed share some common points that we can outline as a clear map about the usage frequency of different operation types. Table 1 lists 7 most commonly used hand gestures and their usage frequency.

Table 1. Seven most commonly used hand gestures [12,15,17]

Hand Gesture	Usage Frequency (Gesture Name)	Hand Gesture	Usage Frequency (Gesture Name)
	28.7% (Cylindrical)		13.6% (Spherical)
	13.8% (Palmar)		10.5% (Lateral)
	7.3% (Pointing)		7.3% (Tipping)
	4.7% (Hooking)	Total	85%

Two commercial surface EMG electrodes (Otto Bock, 13E200=50) are adopted to sample the EMG signals. This type of electrode outputs an envelope signal of the raw EMG signal (after amplification, filtering and rectification), with the signal energy concentrated in a lower frequency band (0~50Hz) [18]. Therefore, the sample rate is fixed at 100 Hz and the normalized output signals (digital, 0~5V) of the A/D converter are directly used for classification.

According to the contraction states of the forearm muscles, the EMG signals can be categorized into 3 classes: flexion, rest and extension. It has been proved that, with an appropriate feature representation, the classification task is essentially a linear problem [3]. To simplify the algorithm and improve computing speed, the linear discriminant analysis (LDA) method is chosen to classify EMG signals with common one-against-one strategy.

We define the period, starting at the time when the acquired data first classified to flexion (or extension) to the time when the acquired data classified to non-flexion (or non-extension), as the persistence time of flexion (or extension). Ignoring the classifying error, the persistence time of flexion and extension can be regarded as the contraction time of muscles. According to the persistence time, the EMG signals are divided into short extension (noted as " e "), short flexion (noted as " f "), long extension (noted as " E "), and long flexion (noted as " F ") as shown in Fig. 2. In the figure, " L_f ", " L_e ", " L_F " and " L_E " denote the persistence time of short flexion, short extension, long flexion and long extension respectively. Parameters d_1, d_2, d_3 are used to determine the length of persistence time.

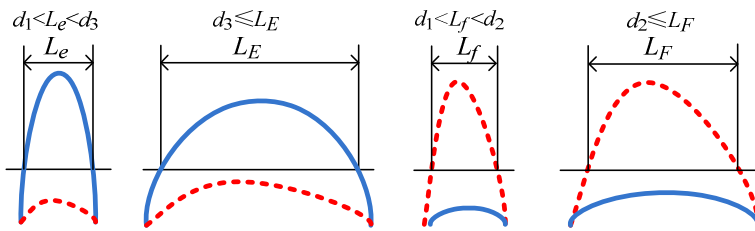


Fig. 2. Encoding of EMG signals. The continual blue line represents the extensor activity, while the dotted red line represents the flexor activity.

Parameter d_1 is the shortest persistence time of valid short contractions; while, d_2 and d_3 are the shortest persistence time of valid long contractions. From the relationships demonstrated in Fig. 1, it can be seen that, as d_1 reduces, chance of noise and artifacts classifying into muscle contractions rises; while, as d_2 and d_3 reduce, the length difference between short contractions and long contractions becomes diminutive. On the other hand, if d_1, d_2 and d_3 are overlarge, it will lower the encoding success rate as well as the efficiency, as users have to keep the contraction leading to fatigue. Therefore, the time parameters d_1, d_2 and d_3 should be suited to user practice.

We map each hand posture to a series of EMG signals, as shown in Table 2.

Table 2. EMG signal sequence of each gesture

Gesture Name	EMG Signal Sequence	Gesture Name	EMG Signal Sequence
Cylindrical	Default	Palmar	e
Spherical	f	Pointing	$e \rightarrow e$
Lateral	$f \rightarrow f$	Hooking	$e \rightarrow f$
Tipping	$f \rightarrow e$		

To achieve the administration of both hand gesture and gripping force, the controller is constituted of two separate states: 1) the coding state for gesture selection; and 2) the control state for proportional control. Fig. 2 shows the topography of the controller. The working flow of the EMG control procedure can be summarized as 4 main steps:

Step 1. When the system is in the gesture coding state, users wave their hands to emerge a series of short EMG signals (Signal e or f) to generate the gesture code listed in Table 1 (users can clear the gesture code by producing a signal E);

Step 2. After a gesture code is achieved, the users produce a Signal F , and then the system gets into the proportional control state;

Step 3. When the system is in the proportional control state, users contract the flexor (or extensor) to make the prosthetic hand move forward (or backward) along a predetermined trajectory from the full open state to a successful grasp gesture with an adjustable force;

Step 4. After the grasp is done, users contract the extensor to make the prosthetic hand move back to the fully open state, and hold on to produce a Signal E making the system get back to the gesture coding state.

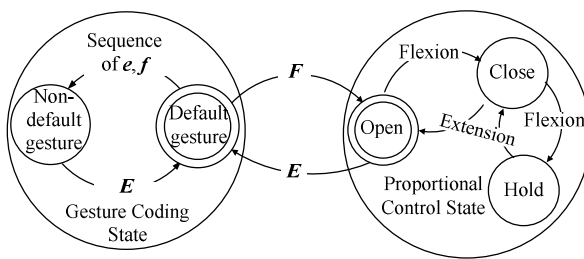


Fig. 3. States and transitions of the FSM

Here we take a palmar pinch for example. At the beginning, the system is in the gesture coding state. The user rapidly contracts the extensor to generate a Signal e which corresponds to the palmar gesture (see Table 1), and then contracts the flexor for a while to produce a Signal F making the system get into the proportional control state. After the system getting into the proportional control state, torque sensors installed in the based joint of each finger judge whether the prosthetic hand has

touched the object. If not, the controller moves each finger of the prosthetic hand forward or backward a few degrees along the trajectory predetermined in the gesture coding state. Position sensors installed in each finger help to achieve precise position control. If touched, the control message integrating the information from LDA classifier, torque sensors and position sensors is sent to each motor of the fingers to achieve a reliable and flexible grasping. Finally, when the gripping is over, the user continuously contracts the extensor to drive the prosthetic hand back to its origin state and then, to make the controller back to the gesture coding state waiting for the next motion.

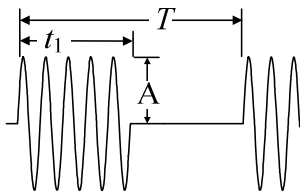
2.3 Sensory Feedback Based on Electrical Stimulus

The HIT-IV hand is equipped with 5 position sensors for each finger and 4 torque sensors for the thumb, index, middle and ring fingers which bear the main gripping force. As the user can easily figure out the position of each finger by their eyes, the sensory feedback system is designed with expectation of feeding back the information of the total torque sensors. The four channels feedback, one for each torque sensor, is not fully deployed because too many feedback channels may confuse the controlling intension of the user. Noticing the difference between the movement of thumb and other fingers, two channels of stimulus waveforms are applied to the human body, denoting the forces of thumb, as well as the other three fingers, respectively. The force data is acquired and graded by the robot motion control subsystem, and then transmitted to the high-level controller via eCAN bus.

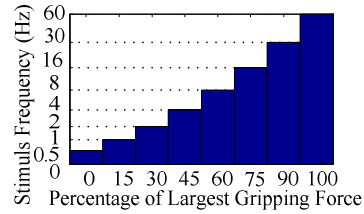
The core of the electrical stimulator is a DDS chip (AD9959, Analog Devices Instruments), which can carry out the frequency, phase, and amplitude modulation on a sine wave independently for each channel. The electrical stimulation method employed in this paper is the transcutaneous electrical nerve stimulation (TENS). It utilizes the intermediate frequency signal as a carrier carrying the low-frequency modulation wave and has advantages of strong penetration, adjustable parameters, and little charge accumulation [19]. Specific to outer electrical stimulator, the 4000Hz sinusoidal signal is selected as the carrier, where the 0-100Hz square wave signal is used as the modulated wave. Fig. 4 (a) shows the stimulus waveform. Adjustable parameters are the amplitude A , the occupation time t_1 and the modulation cycle T .

According to former experiments [20], due to the huge differences in the tolerance of electrical stimulation of individuals, the intensity and the occupation period are not practical to be widely applied. On the contrary, the individuals share the same sense about the frequency at appropriate stimulus intensity. Therefore, in this paper the modulated waveform frequency is employed to transmit the force information, as shown in Fig. 4(b).

When the high level controller gets into the proportional control state, the stimulus waveform of each channel starts at the frequency of 0.5 Hz. After the fingers touching the object and moving forward, outputs of the torque sensors increase. We define the stall torque of the motor as 1F. The frequency of the stimulus increases one grade with the outputs of torque sensors increase 15% of the range. When the high level controller gets back to the gesture coding state, the stimulus stops to avoid interrupting the coding process.



a) The stimulus waveform

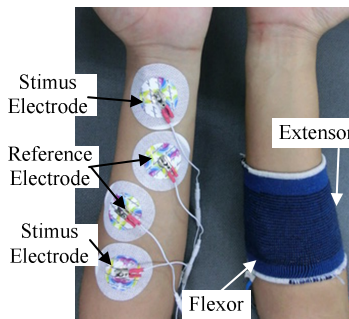


b) The relationship between the stimulus frequency and gripping force

Fig. 4. Parameters of the stimulation

3 Experiments Setup

In order to evaluate the efficiency and success rate of the control method with electrical stimulation, a series of experiments were carried out. Ten healthy subjects were invited in the experiments. The subjects were 6 men and 4 women, right-handed, age 30-35 years, weight 50-80kg, height 160-190 cm. All subjects signed the informed consent before the experiments and all experimental was approved by the university's ethics board. The experiments were conducted under a general living environment with normal temperature, humidity, and electromagnetic interference. The subjects were instructed to sit beside a desk with their arms suitably lying on the desk. One arm of the subject was used to produce EMG signals, while the other arm was applied the electrical stimulus (Fig. 5). Two commercial EMG electrodes (Otto Bock, 13E200=50) were slightly clamped on the flexor and extensor respectively by an elastic bandage. The sample rate was set at 100 Hz. Four disposable Ag/AgCl electrodes were employed as two stimulus electrodes and two reference electrodes for all two channels (one stimulus electrode and one reference channel for each).

**Fig. 5.** Layout of the EMG electrodes and stimulus electrodes








The experiments were conducted in 2 steps.

Step 1. The subjects should firstly get familiar with the experimental process. The two electrodes were attached on the forearms of the subjects. The experimenter instructed

the subject to perform some grasp rehearsals in which the time parameters (d_1 , d_2 and d_3) and the stimulus parameters (amplitude A and occupation time t_1) were adjusted to make the subjects feel most comfortable.

Step 2. Each subject conducted a total of 70 hand motions with each kind of hand motion 10 times. The 70 motions were randomly arranged and the subjects had no idea about what to do next before the instruction from the experimenter. The experimenter recorded the time from the beginning of the order to the point the prosthetic hand accomplishing the motions (listed in Table 3). If the grasp was failed, the experimenter recorded the failed motion and the subject was asked to recode the controller until the prosthetic hand completing the motion, while the timer kept on timing.

Table 3. Stable state of each operation

Cylindrical	Spherical	Palmar	Lateral	Pointing	Tipping	Hooking
						

4 Results and Discussions

In order to evaluate the efficiency and reliability of the control method, we define success rate SR and operation time t_1 as the measure of the experimental results. Since each type of operation was conducted 10 times, the SR for each operation is defined as following:

$$SR = \frac{\text{Operation Succeed Times}}{10} \tag{1}$$

The operation time of operation i , noted as t_i is defined as the period from the time the experimenter giving out the order to the time the subject accomplishing the operation. If the subject failed at the first time, he or she should recode the controller immediately while the timer continuously counted.

Fig. 6 shows the SR statistics for each subject. It can be seen that there is little difference among the operation success rates of different subjects. The success rate of certain operation is highly related to the complexity of the EMG signal sequence (EMG code). The default gesture, cylindrical grasping, which needs no short contraction, had the highest success rate of $95\% \pm 5.27\%$ (Mean \pm Standard Deviation). While, the operations of lateral grasping, pointing, tipping and hooking, which need two short contractions, shared a lower success rate. The worst performing operation, hooking, has the success rate greater than 88%, attributing to the proper selection of the time parameters.

Fig. 7 shows the operation time of different operation types. On each statistic box, the central line is the median and the edges are the 25th and 75th percentiles respectively (draw with Matlab). One can see a clear trend that, which is similar to Fig. 6, the simpler the EMG code is, the better the performance is. Operations with

simple EMG code (short contraction is no more than one) can be accomplished within 10 seconds while the others need longer. This is not only because the coding itself needs more executing time, but also it has a low success rate.

	Subjects									
	1	2	3	4	5	6	7	8	9	10
Hooking	90	90	80	90	90	100	80	90	80	90
Tipping	80	100	90	80	70	100	90	90	90	90
Pointing	80	90	90	100	90	90	90	100	80	90
Lateral	100	90	90	90	80	90	90	90	100	100
Palmar	90	90	90	100	90	90	80	90	100	90
Spherical	80	90	90	100	100	90	90	100	90	90
Cylindrical	90	100	90	100	90	100	100	100	90	90

Fig. 6. Success rate of each subject with each operation

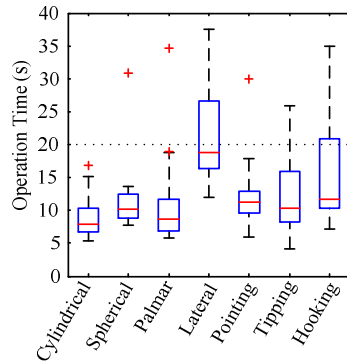


Fig. 7. Operation time of different gestures

In order to work out a unified operation time, we define T_1 as the average operation time:

$$T_1 = \sum_{i=1}^7 t_i \frac{p_i}{p} \tag{2}$$

where t_i is the operation time of different operations, p_i is the usage frequency of the operation i listed in Table 1 ($p = 0.85$). Finally, the average operation time of 10 subjects is 12.3 ± 2.4 (Mean \pm Standard Deviation) seconds. According to Sollerman’s hand function test [14], the operation completed within 20 seconds can be seen as "fluent operation". Therefore, the control method proposed can help the high-level amputees achieve "fluent operation" with sensory feedback.

Fig. 8 presents the stimulation waveform applied on the subject when gripping force changing. In the experiment, the subjects can clearly perceive the intensity of the electrical stimulation (thus they can relate these sensing to the grasp force of the fingers) and have no other discomfort feelings.

It seemed that the visual attention in the experiment is highly reduced when the subject holding the object. It is obviously that the stimulation feedback provides the user alternative sensory channel about the operation, which in large probability can promise a visual-free prosthesis operation in the future. We also found that, since the stimulation feedback only occurred when force sensor is activated, it cannot provide the current motion information about the prosthetic hand. Feedback carrying more information or interacting with the EMG control method will be investigated in the future.

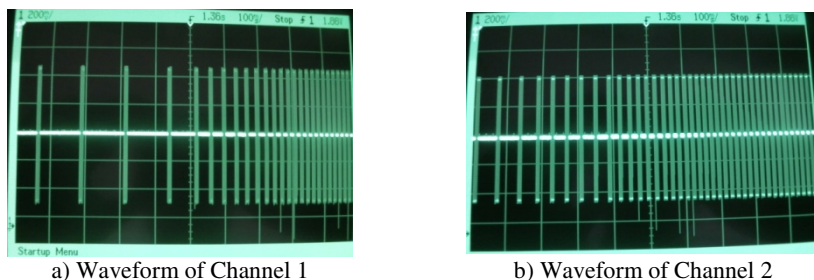


Fig. 8. The actual waveform applied on the subject when gripping force changing (measured by 54622D Mixed Signal Oscilloscope, Agilent Technologies)

5 Conclusions

The paper proposed a novel EMG control method for the multi-DOF prosthetic hand utilizing 2 channel of EMG signals, which adopts the length character (short or long) of the EMG activities for decoding the motions. Through properly correlating the time series and the grasp gestures, nearly 85% of the hand operations in activities of daily life can be actualized. The multi-subject experiment validated that most operation can be accomplished within 20 seconds by deploying the proposed forward EMG control and backward feedback method. It needs only a pair of flexor/extensor muscles on the forearm which can be found on the stump of most upper-limb amputees. Different to traditional FSM methods, new method can realize a multi-finger operation, which will advantage the grasp rapidness and stability. In addition, according to the description of the subjects, the electrical stimulation has moderate stimulus intensity without discomfort. The subjects can perceive the gripping force according to the frequency modulation of stimulus waveform, which contributes to the adjustment of the finger movement direction and the hand proprioception.

Further, we will experiment on amputees to verify the actual efficiency and reliability of the control method. Moreover, we will continue to research on the kinematics of human hands in grasping operation to improve the mapping relationships between the EMG codes and hand gestures.

Acknowledgments. This work is in part supported by the National Program on Key Basic Research Project (973 Program, No. 2011CB013306, 2011CB013305), the National Natural Science Foundation of China (No. 51205080), and the Self-planned Task of State Key Laboratory of Robotics and System (HIT, No. SKLRS201201A03).

References

1. Joseph, B., Aaron, D.: Performance Characteristics of Anthropomorphic Prosthetic Hands. In: Proceedings of IEEE International Conference on Rehabilitation Robotics, pp. 1–7. ETH Zurich Science City, Switzerland (2011)
2. Ju, Z., Zhu, X., Liu, H.: Empirical Copula-Based Templates to Recognize Surface EMG Signals of Hand Motions. *International Journal of Humanoid Robotics* 8(4), 725–741 (2011)

3. Scheme, E., Englehart, K.: Electromyogram pattern recognition for control of powered upper-limb prostheses: state of the art and challenges for clinical use. *The Journal of Rehabilitation Research and Development* 48(6), 643–660 (2011)
4. Ju, Z., Liu, H.: Human Hand Motion Analysis With Multisensory Information. *IEEE/ASME Transactions on Mechatronics* 99(2), 1–11 (2013)
5. Fougner, A., Stavdahl, Ø., Kyberd, P., et al.: Control of upper Limb Prostheses: terminology and proportional myoelectric control: a review. *IEEE Transactions on Neural Systems And Rehabilitation Engineering* 20(5), 663–676 (2012)
6. Pilarski, P., Dawson, M., Degris, T., et al.: Dynamic switching and real-time machine learning for improved human control of assistive biomedical robot. In: *Proceedings of the 4th IEEE RAS/EMBS International Conference on Biomedical Robotics and Biomechanics*, Roma, Italy, pp. 296–302 (2012)
7. Dalley, S., Varol, H., Goldfarb, M.: A Method for the Control of Multigrasp Myoelectric Prosthetic Hands. *IEEE Transactions on Neural Systems and Rehabilitation Engineering* 20, 58–67 (2012)
8. Riso, R., Ignagni, R., Keith, W.: Cognitive feedback for use with FES upper extremity neuroprostheses. *IEEE Transactions on Biomedical Engineering* 38(1), 29–38 (1991)
9. Kato, R., Yokoi, H., Hernandez, A., et al.: Mutual adaptation among man and machine by using f-MRI analysis. *Robotics and Autonomous Systems* 57(2), 161–166 (2009)
10. Kaczmarek, A., Webster, G., Bach-y-Rita, P., et al.: Electrotactile and vibrotactile displays for sensory substitution systems. *IEEE Transactions on Biomedical Engineering* 38(1), 1–16 (1991)
11. Li, N., Jiang, L., Yang, D., Wang, X., Fan, S., Liu, H.: Development of an Anthropomorphic Prosthetic Hand for Man-Machine Interaction. In: Liu, H., Ding, H., Xiong, Z., Zhu, X. (eds.) *ICIRA 2010, Part I. LNCS*, vol. 6424, pp. 38–46. Springer, Heidelberg (2010)
12. Taylor, C., Schwarz, R.: The anatomy and mechanics of the human hand. *Artificial Limbs* 2, 22–35 (1955)
13. Napier, J.: The prehensile movements of the human hand. *The Journal of Bone and Joint Surgery* 38, 902–913 (1956)
14. Sollerman, C., Ejeskär, A.: Sollerman hand function test: a standardised method and its use in tetraplegic patients. *Scand. J. Plast. Reconstr. Hand Surg.* 29(2), 167–176 (1995)
15. Cutkosky, M.: On grasp choice, grasp models, and the design of hands for manufacturing tasks. *IEEE Transactions on Robotics and Automation* 5(3), 269–279 (1989)
16. Kilbreath, S., Heard, R.: Frequency of hand use in healthy older persons. *Australian Journal of Physiotherapy* 51, 119–122 (2005)
17. Zheng, J., Rosa, S., Dollar, A.: An investigation of grasp type and frequency in daily household and machine shop tasks. In: *Proceedings of 2011 IEEE International Conference on Robotics and Automation*, Shanghai, China, pp. 4169–4175 (2011)
18. Bitzer, S., Smagt, P.: Learning EMG Control of a Robotic Hand: towards Active Prostheses. In: *Proceedings of International Conference on Robotics and Automation*, Florida, USA, pp. 2819–2823 (2006)
19. Mulveya, R., Fawkner, J., Radford, H., et al.: The Use of Transcutaneous Electrical Nerve Stimulation (TENS) to Aid Perceptual Embodiment of Prosthetic Limbs. *Medical Hypotheses* 72, 140–142 (2009)
20. Li, N.: Research On Interactive Control System And Multi-Motion Recognition Based On Pressure Distribution For Prosthetic Hand: [Ph. D dissertation], Harbin, Harbin Institute of Technology, School of Mechatronics Engineering, pp. 53–57 (2012)

Sliding Perturbation Observer Based Reaction Force Estimation Method in Surgical Robot Instrument

Sung Min Yoon, Min-Cheol Lee^{*}, and Chi Yen Kim

School of Mechanical Engineering, Pusan National University and RIMT,
San 30, Jangjeon-dong, Geumjeong-gu, Busan, South Korea, 609-735
mclee@pusan.ac.kr

Abstract. Previous research applied SMCSPO (sliding mode control with sliding perturbation observer) algorithm as robust controller to control the instrument and found that the value of SPO (sliding perturbation observer) followed force disturbance, reaction force loaded on the tip very similarly. However, in fact, some factors like friction which are not easy to find model parameters beforehand can make an effect on reaction force estimation because the factors are included in any perturbation. This paper addresses the SPO based reaction force estimation method to extract a reaction force on the surgical robot instrument in case of including Coulomb friction due to operation of cable-pulley structure. The Coulomb friction can be estimated by experiment and compensated from the estimated perturbation. To prove the suggested estimation method, experimental evaluation is performed. The results show that it is possible to substitute SPO for sensors to measure the reaction force. This estimated reaction force will be used to realize haptic function by sending the reaction force to a master device for a surgeon. The results will contribute to create surgical benefit such as shortening the practice time of a surgeon and giving haptic information to surgeon by using it as haptic signal to protect an organ by making force boundary.

Keywords: Surgical robot, Instrument, Sliding perturbation observer, Reaction force estimation.

1 Introduction

Surgical robot instrument is the device to perform operation in human bodies instead of surgeon's hands. Therefore, the system requires the high degree of freedom to describe human hand motions. However, it should be manufactured by the small size to put it into small-sized trocar holes of less than 10mm according to reduction of dangerousness of infection, safety, and needs of minimally invasive surgery (MIS) and there is the problem of consumables that should be discarded after it is restrictively used. Cable driven system is now adopted in surgical robot instrument

^{*} Corresponding author.

because of this problem[1][2]. However cable driven mechanism and the structure which are manufactured by the small are impossible to attach any electric or magnetic sensor for measuring force. Thus, surgeons cannot feel the touch of organ and so has to depend only on the information by visual feedback, which occur some problems [3].

The previous research applied SMCSPO (sliding mode control with sliding perturbation observer) algorithm as robust controller to control the instrument and showed the improved control result[4]. In the previous research, SPO(Sliding Perturbation Observer) was supposed to estimate all undesired terms, such as nonlinearities, an error of model, a friction in cable system, and a disturbance of outer force like reaction force[5][6]. However, in fact, some factors like friction which are not easy to find model parameters beforehand can make an effect on reaction force estimation because the factors are included in any perturbation. Especially, in cable-pulley structures, in case of pretension that is applied to solve a slack phenomenon, it not only increases the Coulomb friction on rotation axis, but also can have an effect on the reaction force estimation[7].

This paper addresses the SPO based reaction force estimation method to extract a reaction force on the surgical robot instrument in case of including Coulomb friction due to operation of cable-pulley structure. To suggest a possibility of reaction force, applying a suggested method in a real surgical robot instrument, experimental evaluation will be implemented. Also, applying the suggested method in not only tips of instrument but rolling and pitching motion, the possibility of the reaction force estimation will be shown in all degrees of freedom of the instrument.

This estimated reaction force will be used to realize haptic function by sending the reaction force to a master device for a surgeon. The results will contribute to create surgical benefit such as shortening the practice time of a surgeon and giving haptic information to surgeon by using it as haptic signal to protect an organ by making force boundary.

This paper is organized as follows: In Chapter 2, dynamic model of cable driven system of surgical robot instrument is derived. In Chapter 3, SPO based reaction force estimation method is introduced. In Chapter 4, A possibility of estimation of reaction force is evaluated through experiment. This paper concludes in Chapter 5.

2 Dynamics of Surgical Robot Instrument

2.1 Tendon Driven System in Surgical Robot Instrument

To estimate the reaction force in surgical robot instrument, it is required to understand the dynamics. Fig. 1 shows the representative commercial surgical robot instrument manufactured by Intuitive Surgical, Inc[8]. The end effect of surgical robot instrument conducts an operation in the body instead of the surgeon's hand. There are various shape and size of end-effect which are specialized for operation use. General surgical robot instrument has 3+1 DOF to simulate the motion of surgeon's two fingers, thumb and index finger. These are two fingers(tips) and additional 2 DOF for the fingers, pitching and rolling. Cause interference to grasping and pitching, but driving mechanism for each motion is basically the same. It is cable pulley power transmission mechanism.

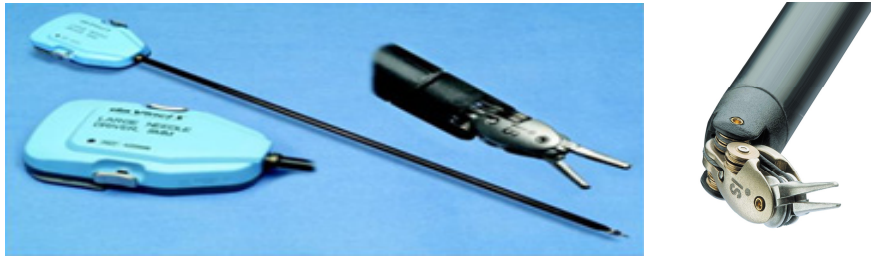


Fig. 1. Surgical robot instrument

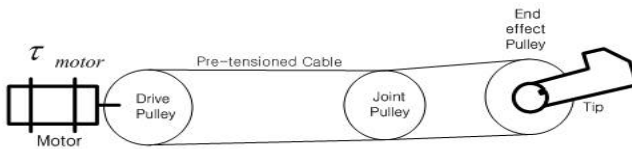


Fig. 2. The basic structure of surgical robot instrument

Fig. 2 describes inner structure of instrument. In cable-pulley structure, driving force of driving pulley is transmitted to the pulley of an end effect by the difference between two tensions. Basically, there are three pulleys in commercial instrument. Driving pulley attached to motor shaft supplies a driving force into cable with tension. The pulley in end-effect works at the joint of the tip which plays a role in finger. Another pulley changes the direction of cable without loss of tension. Generally, the slip and slag phenomenon are occurred in a device of cable-pulley structure. A problem of slip phenomenon is solved by using pull-pull structure. Also, the slack phenomenon which is caused by the elasticity of cable is being supplemented by pretension. So pretension is an important factor in the design of a surgical instrument. However, the pretension related to friction when the normal force at the driving shaft pulley is inputted[7]. It would be able to consider Coulomb friction force.

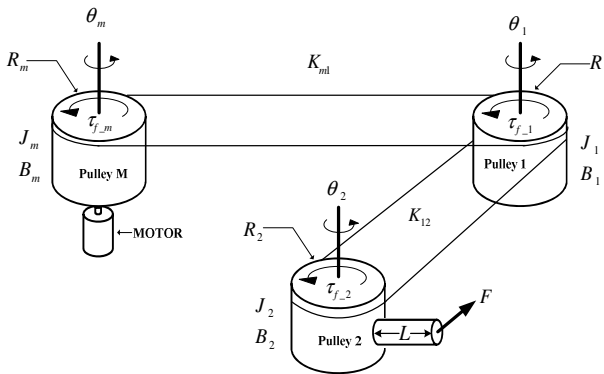


Fig. 3. Pulley dynamic analysis

2.2 Governing Dynamic Equation

In this paper, plant dynamics is derived based on Fig. 3. In Fig. 3 and following Eq. (1), (2) and (3), J_m , J_1 , J_2 and B_m , B_1 , B_2 represent inertia and damping value of the pulley parts respectively. R_m , R_1 , R_2 are the radius of pulleys. K_{m1} , K_{12} are constant spring coefficient. It is assumed that the cable tension shows a tendency of linear spring. τ_{f_m} , τ_{f_1} , τ_{f_2} represent friction torque which are caused by Coulomb friction due to a pretension.

If the weight of cable is assumed to be ignorable, the driving part connected with motor is expressed as following equation.

$$J_m \ddot{\theta}_m + B_m \dot{\theta}_m + R_m K_{m1} (R_m \theta_m - R_1 \theta_1) + \tau_{f_m} \operatorname{sgn}(\dot{\theta}_m) = u_m \quad (1)$$

where, u_m is input torque from motor.

At pulley 1, the dynamic equation has to consider movement of pulley M and end-effect pulley 2 and is expressed as following :

$$J_1 \ddot{\theta}_1 + B_1 \dot{\theta}_1 + R_1 K_{12} (R_1 \theta_1 - R_2 \theta_2) + \tau_{f_1} \operatorname{sgn}(\dot{\theta}_1) = R_1 K_{m1} (R_m \theta_m - R_1 \theta_1) \quad (2)$$

At pulley 2, the working force on the end-effect F is included into dynamic equation.

$$J_2 \ddot{\theta}_2 + B_2 \dot{\theta}_2 + \tau_{f_2} \operatorname{sgn}(\dot{\theta}_2) + LF = R_2 K_{12} (R_1 \theta_1 - R_2 \theta_2) \quad (3)$$

The purpose of this research is to show that reaction force F loaded on the end effector of instrument in Eq. (3) can be estimated by using SPO. However, it is difficult to apply Eq. (1), (2) and (3) to SPO. The angle sensor can be attached to the only driving pulley. So, it is difficult to measure the angle of other pulleys except the driving pulley. Also, cable tension has spring characteristic, spring coefficients in Eq. (1), (2) and (3) are not certain and it is not easy to identify the system characteristic clearly. Thus, to simplify the model equation it is assumed that the cable length elongation of the instrument driven by the cable pulley mechanism is very small and negligible. This means that each joint angle is same, $\theta_m \approx \theta_1 \approx \theta_2$. Therefore the simplified dynamic equation is obtained from Eq. (1), (2) and (3) as

$$J \ddot{\theta}_m + B \dot{\theta}_m + \tau_f \operatorname{sgn}(\dot{\theta}_m) + LF = u_m \quad (4)$$

where, $J = J_m + J_1 + J_2$, $B = B_m + B_1 + B_2$ and $\tau_f = \tau_{f_m} + \tau_{f_1} + \tau_{f_2}$

3 Reaction Force Estimation Based on SPO

In this chapter, addresses the SPO based reaction force estimation method. The perturbation is related to the reaction force of instrument. The reaction force can be calculated to estimate the value of the perturbation using SPO.

3.1 Sliding Perturbation Observer(SPO)

From Eq. (4), considering the errors of the model parameters the equation of surgical robot instrument is expressed as following :

$$\ddot{\theta}_m = -\left(\frac{B}{J} + \Delta\frac{B}{J}\right)\dot{\theta} + \left(\frac{1}{J} + \Delta\frac{1}{J}\right)u - \frac{1}{J}\tau_f \operatorname{sgn}(\dot{\theta}_m) - \frac{1}{J}LF \quad (5)$$

Perturbation is defined as the combination of the model parameter error, Coulomb friction, and the reaction force.

$$\Psi = -\Delta\frac{B}{J}\dot{\theta}_m + \Delta\frac{1}{J}u_m - \frac{1}{J}\tau_f \operatorname{sgn}(\dot{\theta}_m) - \frac{1}{J}LF \quad (6)$$

The now control variable which is used in order to decouple the control of Eq. (5) is defined as

$$-\frac{B}{J}\dot{\hat{x}} + \frac{1}{J}u = \alpha_3\bar{u} \quad (7)$$

where \hat{x} is the estimated state vector, α_3 is an arbitrary positive number and \bar{u} is the new control variable[9]. Throughout the text, “ \sim ”, refers to estimation errors whereas “ \wedge ” symbolizes the estimated quantity.

Transformation of Eq. (3) simply allows us to write the system dynamics. The state representation of the simplified dynamics is given by

$$\dot{x}_1 = x_2 \quad (8.1)$$

$$\dot{x}_2 = \alpha_3\bar{u} + \Psi \quad (8.2)$$

$$y = x_1 \quad (8.3)$$

Let x_3 be a new state variable defined as

$$x_3 = \alpha_3x_2 - \Psi / \alpha_3 \quad (9)$$

It is desirable to observe the variable x_3 and consequently calculate Ψ using Eq. (9) instead of estimating the directly. The structure of the sliding perturbation observer consists of the perturbation observer and sliding one. This structure can be achieved by writing the observer equation as

$$\dot{\hat{x}}_1 = \hat{x}_2 - k_1\operatorname{sat}(\tilde{x}_1) - \alpha_1\tilde{x}_1 \quad (10.1)$$

$$\dot{\hat{x}}_2 = \alpha_3\bar{u} - k_2\operatorname{sat}(\tilde{x}_1) - \alpha_2\tilde{x}_1 + \hat{\Psi} \quad (10.2)$$

$$\dot{\hat{x}}_3 = \alpha_3^2 (-\hat{x}_3 + \alpha_3 \hat{x}_2 + \bar{u}) \quad (10.3)$$

where $\hat{\Psi}$ is derived as

$$\hat{\Psi} = \alpha_3 (-\hat{x}_3 + \alpha_3 \hat{x}_2) \quad (11)$$

$k_1, k_2, \alpha_1, \alpha_2$ are positive numbers, $\tilde{x}_1 = \hat{x}_1 - x_1$ is the estimation error of the measurable state, and $sat(\tilde{x}_1)$ is the saturation function for the existence of sliding mode[10].

3.2 Reaction Force Estimation

The estimated perturbation includes not only outer force but also the model parameter error and Coulomb friction. Especially, in cable-pulley structures, in case of pretension that is applied to solve a slack phenomenon, it not only increases the Coulomb friction on rotation axis, but also can have effect on the reaction force estimation. Therefore, it should be removed from the influence of the Coulomb friction due to pretension. The reaction forces can be calculated using Eq. (12)

$$\hat{F}_{reaction} = \frac{g_{reac}}{s + g_{reac}} \frac{J}{L} \left\{ \hat{\Psi} + \tau_f \operatorname{sgn}(\dot{\theta}) \right\} \quad (12)$$

However, in order to calculate the reaction force, the Coulomb friction due to pretension should be measured. The friction effects due to pretension can be measured in advance by using the estimated perturbation of the SPO. Where, g_{reac} is cut-off frequency of a low-pass filter.

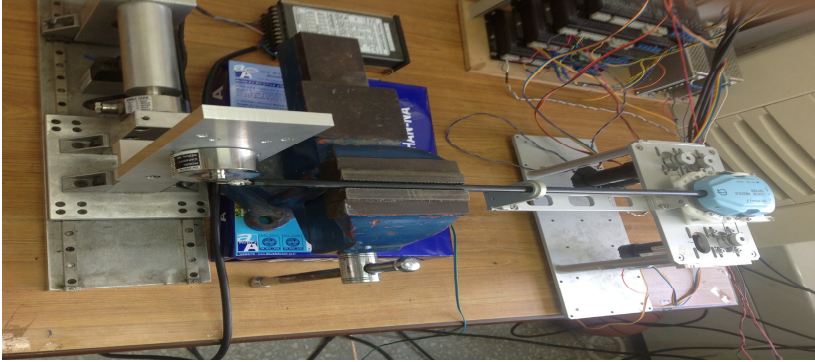


Fig. 4. Experimental system for the reaction force estimation

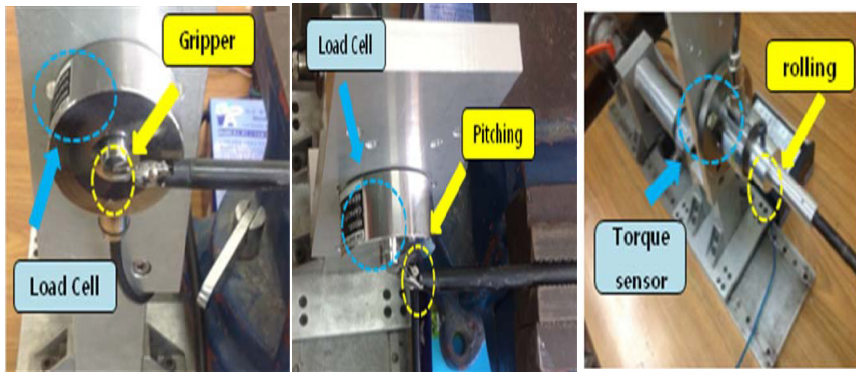


Fig. 5. Experiment for the reaction force estimation of each motions(gripping, pitching, rolling)

4 Experiment

4.1 Experimental System

The experimental system to verify the reaction force estimation of surgical robot instrument is illustrated Fig. 4. Endo Wrist Instrument (Large Needle driver) used in currently commercialized surgical robot Da Vinci was used in this.

To evaluate the possibility of reaction force which occurs according to the motion of a fingers(tips), a roll, and a pitch of the instrument, the force/torque measured by a load cell/ torque sensor and the method that was described in chapter 3 could be compared. Also, we implemented comparative evaluation with perturbation value which was merely estimated by only SPO. With the estimation of reaction occurring when end-effect of the instrument contacts with a load cell by the motion of the finger and the pitch, we compared estimated reaction force and a measured value by the load cell. Left and center side of Fig. 5 show the experiment of the reaction force estimation according to the motions of the finger and the pitch, respectively. Also, the estimated reaction force that occurs by a roll motion was structured to compare with the measured values by a torque sensor, shown in the right side of Fig. 5.

4.2 Experimental Results

Fig. 6, Fig.7 and Fig.8 are the experiment results of estimation reaction force according to the motions of the finger, the pitch, and the roll, respectively. The upper graph of each figure represents trajectory for the movement of each joint, and the graph below represents a comparative outcome of estimation for reaction. The force measured by a sensor changes according to the input trajectory, the estimated reaction can also be confirmed in similar forms. But, the perturbation estimation result only observed by the SPO shows some errors occurring influenced by undesired factor such as the Coulomb friction due to pretension when the result is compared with the measured value by sensor . However, in case of estimating reaction force in the explained method of chapter 3, undesired factors were compensated and the errors

were reduced, so we can confirm the accuracy of the reaction force estimation was increased. The experimental results show that reaction force loaded on the surgical robot instrument can be estimated only using perturbation observer without using any sensors; we anticipate that this is utilized in making some haptic function of surgical robots in the future.

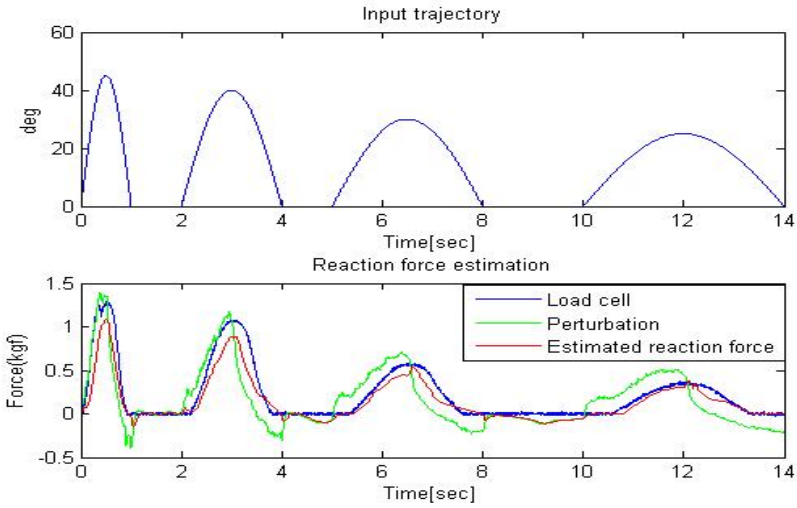


Fig. 6. Experiment result of the reaction force estimation of gasping motion

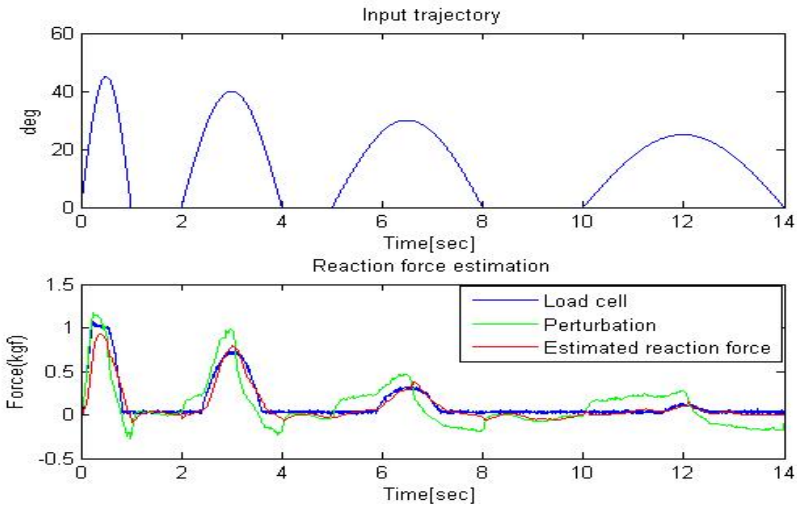


Fig. 7. Experiment result of the reaction force estimation of pitchig motion

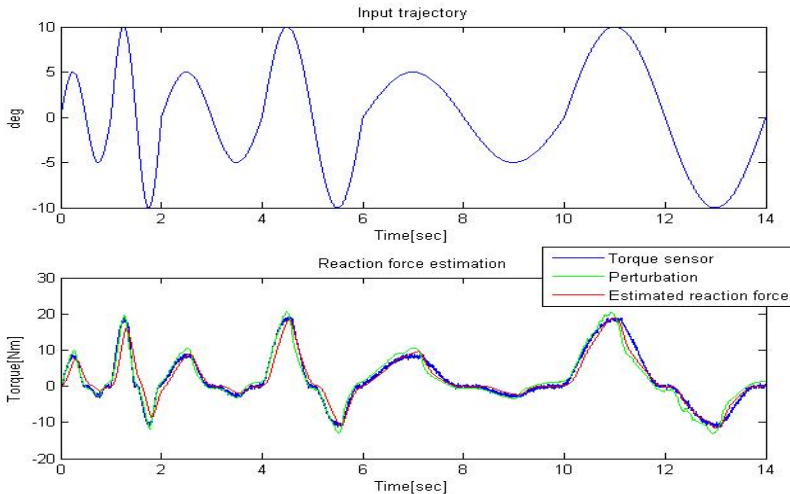


Fig. 8. Experiment result of the reaction force estimation of rolling motion

5 Conclusions

In this paper, an estimation method of reaction force based on SPO was dealt. To verify the possibility of the estimated reaction force, experimental evaluation which was applied by a suggested method for 3DOF of surgical robot instrument was performed. From the result of the experiment, compared with the estimated perturbation by only SPO, it confirms that the accuracy of estimated reaction force was increased because the undesired terms such as the Coulomb friction due to pretension were compensated. Therefore, as shown in this research, to estimate reaction force of surgical robot instrument only with perturbation observer will ensure the safety of surgery by enabling the implementation of haptic function of a surgical robot. And, due to sensorless force measurement, increased effectiveness can be expected. In the future, studies of applying estimated reaction to the surgical robot haptic system will be conducted.

Acknowledgments. This research was supported by Basic Science Research Program through the National Research Foundation of Korea(NRF) funded by the Ministry of Education, Science and Technology(2011-0014915) and financially supported by the Ministry of Education, Science Technology (MEST) and National Research Foundation of Korea(NRF) through the Human Resource Training Project for Regional Innovation.

References

1. Guthart, G.S., Salisbury, J.K.: The Intuitive telesurgery system: Overview and applications. In: Proc. IEEE Int. Conf. Robotics and Automation, vol. 1, pp. 618–621 (2000)

2. Fanzino, R.J.: The Laprotek surgical system and the next generation of robotics. *Surgical Clinics of North America* 83(6), 1317–1320 (2003)
3. Giulianotti, P., Coratti, A., Angelini, M., Sbrana, F., Cecconi, S., Balestracci, T., Caravaglios, G.: Robotics in General Surgery- Personal Experience in a Large Community Hospital. *Archives of Surgery* (238), 777–784 (2003)
4. Song, Y.E., Lee, M.C., Kim, C.Y.: Sliding Mode Control with Sliding Perturbation Observer for Surgical Robots. In: *Proceedings of ISIE 2009*, pp. 2153–2158 (July 2009)
5. Kim, C.Y., Lee, M.C., Go, S.J.: The Workability of Sliding Perturbation Observer as Haptic Signal at the Surgical Robot Instrument. In: *Proceeding of SICE 2010*, pp. 465–470 (2010)
6. Kim, C.Y., Lee, M.C., Yoon, S.M., Knag, B.H.: A Study on State and Perturbation Observers of the Controller of Surgical Robot Instrument. In: *Proceedings of ASCC 2011*, pp. 553–557 (2011)
7. Lee, T.K., Kim, C.Y., Lee, M.C.: Friction Analysis According to Pretension of Laparoscopy Surgical Robot Instrument. *International Journal of Precision Engineering and Manufacturing* 12(2), 259–266 (2011)
8. Intuitive Surgical Inc., EndoWrist Instrument catalogue, <http://www.intuitivesurgical.com>
9. Terra, M.J., Elmali, H., Olgac, N.: Sliding Mode Control With Perturbation Observer. *Journal of Dynamic System, Measurement, and Control* 119, 657–665 (1997)
10. Slotine, J.J., Hedrick, J.K., Misawa, E.A.: On Sliding Observers for Non-Linear Systems. *ASME Journal of Dynamic System, Measurement and Control* 109, 245–252 (1987)

Design of a Novel Single Incision Laparoscopic Surgery Robot with Increased Tissue Handling Force

DaeKeun Ji¹, Byungsik Cheon¹, Makoto Hashizume²,
Morimasa Tomikawa², and Jaesung Hong¹

¹ Department of Robotics Engineering,

Daegu Gyeongbuk Institute of Science & Technology, Korea

² Department of Advanced Medical Initiatives, Kyushu University, Fukuoka
jhong@dgist.ac.kr

Abstract. Recently, the number of single port laparoscopic surgery (SILS) that can easily conceal postoperative scars is increasing, and robotic SILS platforms are being developed to overcome inconvenient maneuverability of manual SILS. However, the drive mechanism of most robotic SILS platforms existing uses the wire, therefore it cannot afford to deliver sufficient force, and the wire is mechanically deformed, thus causing negative effects on movement accuracy. Due to this limitation, a precious operation cannot be conducted by using conventional robotic SILS platforms. This paper presents the design of a novel single incision surgery robot that is actuated by using plate spring driven mechanisms with relatively high force transmission and larger workspace. Evaluations of PLAS were performed and its feasibility as a novel effective robotic SILS platform was proved.

Keywords: Single incision laparoscopic surgery, Plate spring mechanism, Robotic surgery.

1 Introduction

In accordance with emerging many applications in medical field, medical industry is in the spotlight for blue chip. Laparoscopic surgery has been proven as one of the most successful and considerable advance in the medical field. By operating laparoscopic surgery with tiny incisions on the abdominal surface, operations result in less blood loss, reduced postoperative scarring, fewer complications, and faster recovery periods when compared with standard open surgery [1]. In light of this pursuit, natural orifice transluminal endoscopic surgery (NOTES) and single incision laparoscopic surgery (SILS) have been proposed. Although both methods are same in terms of minimal invasiveness, NOTES uses a natural orifice entry and makes incisions inside the body, whereas SILS uses a single incision on the abdominal surface, preferably the umbilicus. However, several problems unsolved and difficulties have been reported in clinical NOTES trials [2, 3, 4]. In consequence, SILS operations are increasing in both popularity and feasibility. Currently many

clinical operations can be carried out by SILS procedure, such as cholecystectomy, appendectomy, hysterectomy, tubal ligation, ovarian cystectomy, nephrectomy, partial nephrectomy [5], ureterolithotomy [6], and prostatectomy.

In spite of the fact that SILS can be used in many medical fields, surgeons have difficulties to conduct SILS operations as technical challenges remain. One of these challenges is the counter-intuitive usage, where forceps are needed to be crossed to increase operation workspace. To solving the counter-intuitive usage, SILS robots have developed, where they offer a natural sense of laparoscopic operations from a single port [7]. However, due to the incision diameter limitation and mechanical constraints in transmissions, other problems have emerged, such as limitation of workspace, the overall sizes of robot and insufficient force. In addition, as most of robotic systems for laparoscopic surgery adopt the wire driven mechanisms, they have failed to reach the tissue handling force requirement. Considering the problems behind the previous studies, this paper proposes a novel robotic SILS platform design that has relatively higher force transmission values during tissue handling by utilizing plate springs in its structure. Its system has 12 degrees of freedom in both arms and the structure of the design that permits more stable and precise operations in an expanded workspace.

2 Method

2.1 Plate Spring Mechanism

As both wire driven mechanism and tool with large volume requirements cannot satisfy required tissue handling force with reduced size, this studies utilizes plate spring driven mechanisms to find an optimum place in its novel single incision laparoscopic surgery robot design. Plate spring driven mechanisms can afford to deliver tension such as wires, additionally also deliver compressional forces without a large increase in system size provided that they have placed in a guide (Fig. 1). Additionally, since it does not need a structure for rewinding like wires, where simple structure is provided and more force can be delivered as their cross sectional areas are larger than wires that conventional SILS platforms are using. However, in delivering compressional forces, compressive force is absorbed to elasticity energy due to buckling, and thus it is not able to deliver the force to the end of the opposite side. In this situation, if a guide preventing buckling in both sides of spring is installed such as (Fig. 1A), compressive force does not become absorbed to elastic energy and therefore plate spring comes to deliver the compressive force. Consequently, plate spring driven mechanism can deliver not only tension but compressive force at the same time (Fig. 1B). To confirm the feasibility of plate spring driven mechanisms, the tissue handling force of the tool tips are measured by using force gage.

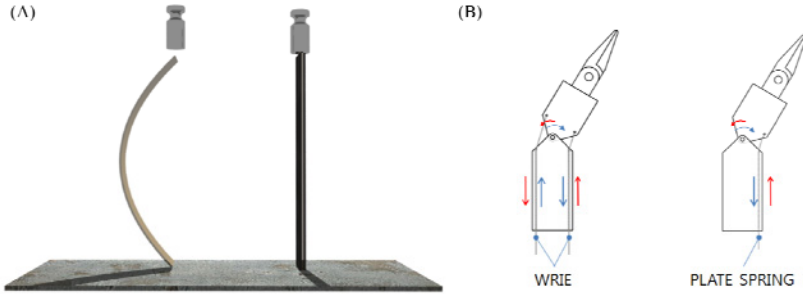


Fig. 1. (A) An example of buckling and preventing buckling and (B) Comparison of wire & plate spring driven mechanism

2.2 Workspace and Degrees of Freedom Considerations

Commonly, SILS robots of type Y are incompetent to treat for relatively large organs such as livers and intestines because their starting point where they are opening to expand the workspace are fixed. SILS robots of type of Y have much smaller workspace than SILS robots of type of X owing to this constraint. To solve this constraint, two individual prismatic joints are added for each arm. Also, this additional degree of freedom provides a larger efficient workspace with increased posture possibilities of the forceps (Fig. 2). The remaining movement of the robot manipulator is decided by maintaining the four degrees of freedom from classical configuration of Type Y SILS robots. Adding two individual prismatic joint, totals a 12 degrees of freedom is reached in the design.

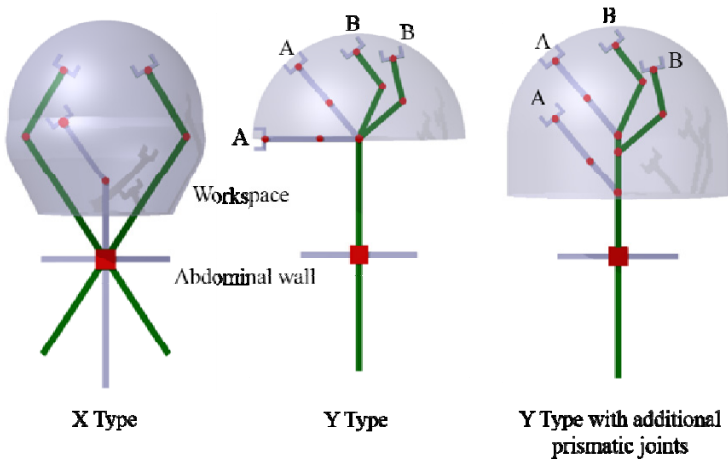


Fig. 2. Comparison of workspace configurations and possible postures: X type, Y type and modified Y type SILS robot with additional prismatic joints

2.3 Kinematic of SILS Robot

The SILS robot in this paper is designed for closed loop linkages to drive the second and the third joints of each arm, throughout this section, it will be considered as two distinct six-degrees-of-freedom serial manipulators and only one arm will be analyzed. In addition, the fifth and the sixth joints are regarded as the linear and the rotational motion of the forceps that will be inserted into the system, such as Fig. 3(A).

A kinematic representation of the left arm of the system is shown in Fig. 3(B) and its axes are labeled with respect to the distal denavit Hartenberg convention. The corresponding Denavit Hartenberg parameters are also contributed in Table 1.

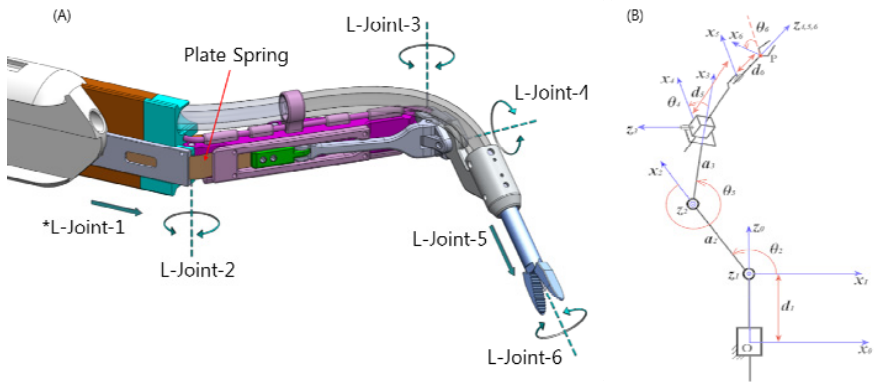


Fig. 3. (A) A structure of degrees of freedom, L=left and (B) Kinematic representation of 6-DoF serial manipulator

Table 1. D-H Parameters of the serial manipulator

<i>Joint i</i>	α_i	a_i	d_i	θ_i
1	$\pi/2$	0	$d_1 = \text{variable}$	0
2	0	a_2	0	$\theta_2 = \text{variable}$
3	$3\pi/2$	a_3	0	$\theta_3 = \text{variable}$
4	$\pi/2$	0	0	$\theta_4 = \text{variable}$
5	0	0	$d_5 = \text{variable}$	0
6	0	0	d_6	$\theta_6 = \text{variable}$

2.4 The SILS Robot Prototype

After the decision of the construction parameters, the prototype of the SILS robot is modeled by 3D modeling software. The construction parameters are tabulated in Table 2. The proposed robot was named “PLAS” which stands for *Plate spring*

mechanism based *L*aparoscopic Surgery robot. This PLAS consist of two parts: one is a surgery part, conducting operations, with to be inserted to the body of patients and the diameter of surgery part of PLAS is 33mm. The other is an actuation part, delivering forces to the surgery part such as Fig. 4 and includes the actuators that will implement the 12 degrees of freedom to the PLAS. The actuation part of the PLAS will always remain outside of the body. Each arm of surgery part of PLAS has six-degrees-of-freedom that includes two prismatic and four revolute joints as already mentioned before. The grasping motion of the end effector is excluded from degrees of freedom calculation and the plate spring mechanism is only used in third joint. The second joint and the forth joint are actuated by link and wire mechanism. After the completion of the 3D part modeling, a final prototype of the PLAS is manufactured and assembled in Fig. 5.

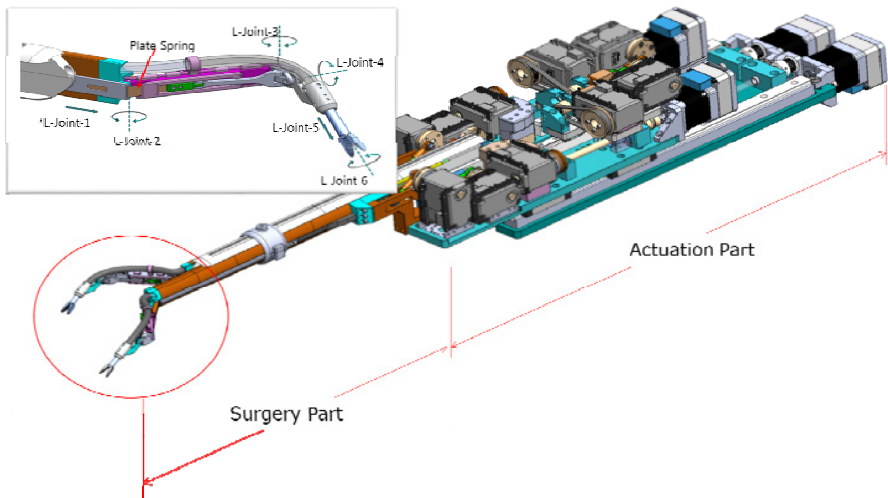


Fig. 4. The structure of Plate spring mechanism based *L*aparoscopic Surgery robot (PLAS)

Table 2. The construction parameter of PLAS

Parameters	d_1 (mm)	a_2 (mm)	a_3 (mm)	d_5 (mm)	d_6 (mm)
Value	0↔215	70	13	60	0↔35
Parameters	θ_2 (degrees)	θ_3 (degrees)	θ_4 (degrees)	θ_6 (degrees)	
Value	0↔80	0↔110	-50↔50	0↔360	



Fig. 5. Final prototype of SILS robot, PLAS

3 Experiment and Results

To evaluate force transmission capabilities of the joints, the laboratory test was conducted by using force gage that was fixed firmly on to the vibration free table by the help of magnetic bases. In each joint, the test that measures the force was performed by repeating 5 trials. The experimental setup containing force gage tip distance measured from the rotation axis of the related joints and posture of the PLAS arm during the experiments can be shown in Table 3. In addition, the results are shown in Fig. 6.

Table 3. Force transmission experimental setup details

<i>Joint i</i>	<i>PLAS Arm Posture</i>	<i>Force Gage Tip Distance (mm)</i>
1	Straight	-
2	Angled	60
3	Angled	15
4	Angled	15
5	Straight	-
6	Angled	20
Grasping	Straight	15

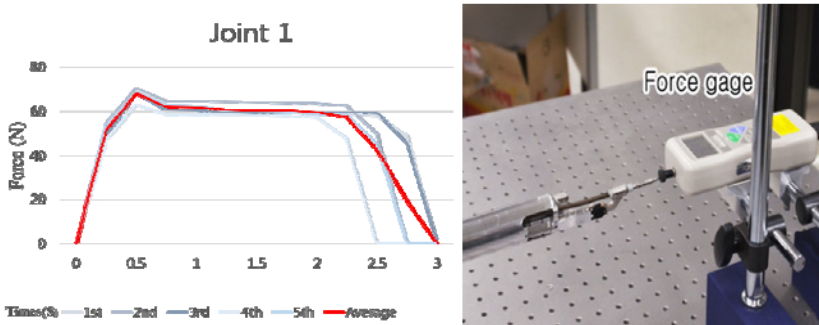


Fig. 6. Force transmission measured at each joint with a force gage

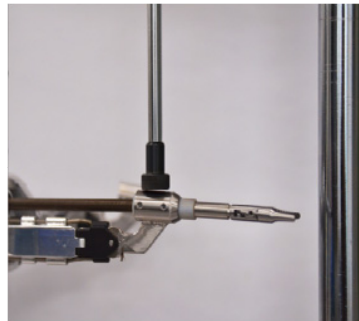
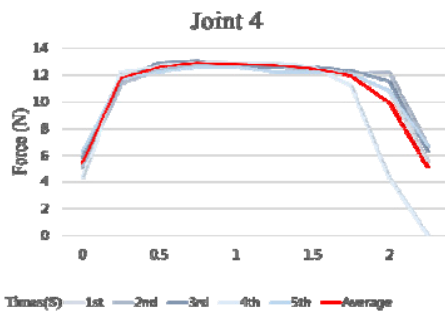
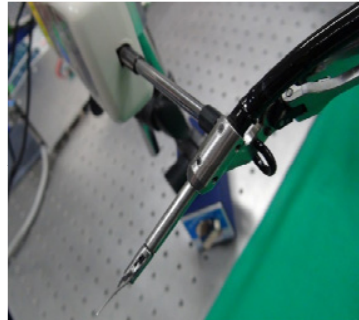
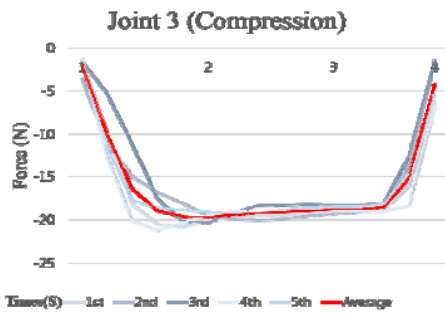
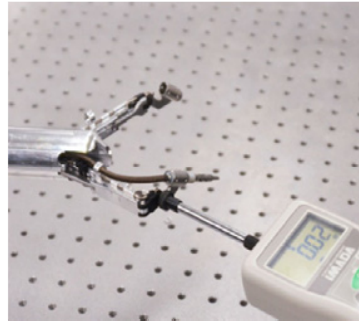
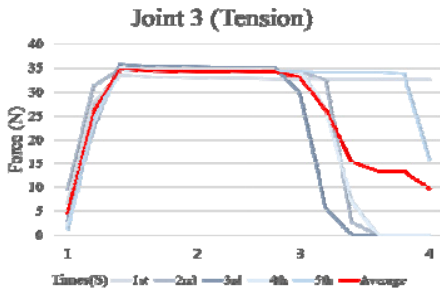
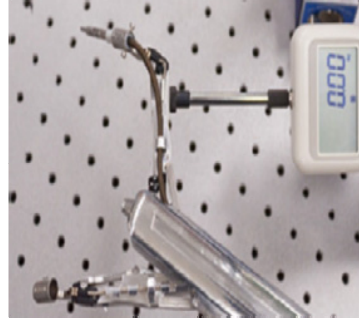
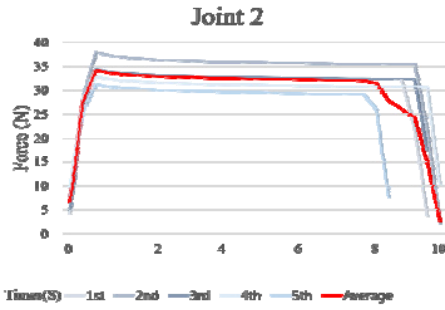


Fig. 6. (continued)

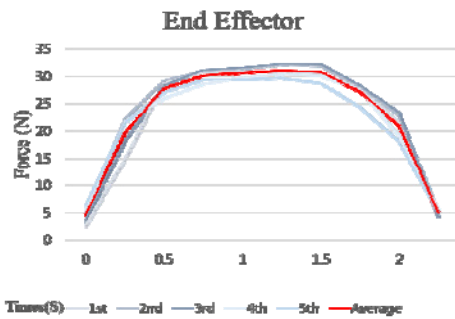
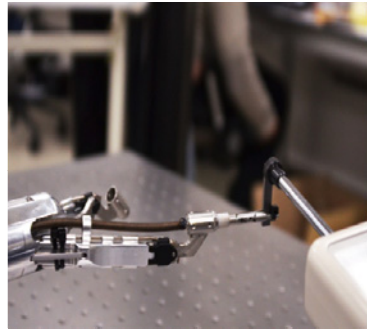
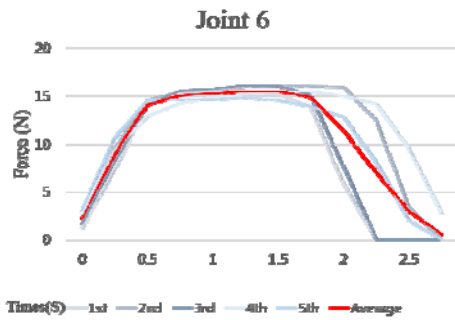
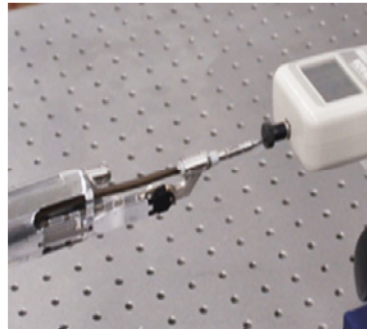
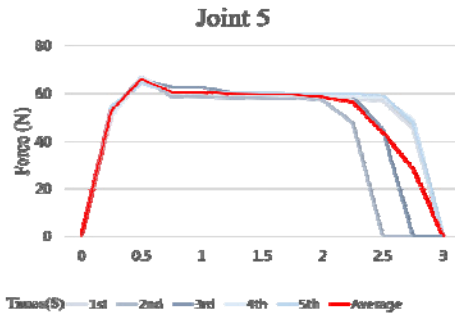


Fig. 6. (continued)

4 Discussion and Conclusion

The force transmission capabilities can be obtained through force transmission experimental that measure the force of each joint by force gage. Force readings from the force gage experiments reveal that PLAS has sufficient force to achieve 10N goal at the end effector even though single contributions from each joint instead of whole motion. In comparison with third joint that use the plate spring and forth joint that use wire, we can confirm that third joint deliver higher forces than forth joint. It should be

refined by using another spring drive or other kinds of mechanism in forth joint in future prototypes.

In light of these results, these studies have introduced a new type of single port surgery robot to overcome the problems, such as insufficient force, by using plate spring driven mechanisms. Also it is confirmed in the experiments that plate spring driven mechanisms have considerable potential in force transmission.

However, the plate spring mechanism has disadvantage, which may be plastic deformation at the small radius of curvature and it should be prevented by modifying structure of SILS robot on future prototype because the plastic deformation can affect the movement of SILS robot. To make the prototyping easier and cheaper, we had to use aluminum, instead of pre-planned stainless steel. According to the selected material, we had to increase the diameter of the surgery part of PLAS, to meet the stiffness requirement. If we change material to stainless steel, future prototypes is below the 25mm goal.

In conclusion, these studies have proposed a new type of single port surgery robot to develop the conventional SILS robot that use wire in terms of the force and workspace. The result of experiments has shown promising possibility that will be further enhanced in future prototypes.

Acknowledgments. This work was supported by DGIST Convergence science center (13-BD-0401). It was also supported by MIREBrain project.

References

1. WooJung, L.: Single port laparoscopic surgery. *Journal of the Korean Medical Association* 53(9), 793–806 (2010)
2. Gettman, M.T., Lotan, Y., Napper, C.A., Cadeddu, J.A.: Transvaginal laparoscopic nephrectomy: development and feasibility in the porcine model. *Urology* 59(3), 446–450 (2002)
3. Clayman, R.V., Box, G.N., Abraham, J.B.: Rapid communication: transvaginal single-port NOTES nephrectomy: initial laboratory experience. *Journal of Endourology* 21(6), 640–644 (2007)
4. Lima, E., Rolanda, C., Pego, J.M.: Third-generation nephrectomy by natural orifice transluminal endoscopic surgery. *Journal of Urology* 178(6), 2648–2654 (2007)
5. Kaouk, J.H., Goel, R.K.: Single-port laparoscopic and robotic partial nephrectomy. *European Urology* 55(5), 1163–1169 (2009)
6. Gettman, M.T., White, W.M., Aron, M.: Where do we really stand with LESS and NOTES. *European Urology* 59(2), 231–234 (2011)
7. Autorino, R., Kaouk, J.H., Stolzenburg, J.U.: Current Status and Future Directions of Robotic Single-Site Surgery: A Systematic Review. *European Urology* (2012)

Vertical Collaborative Fuzzy C-Means for Multiple EEG Data Sets

Mukesh Prasad¹, Chin-Teng Lin², Chien-Ting Yang², and Amit Saxena³

¹ Dept. of Computer Science,

² Dept. of Electrical Engineering

National Chiao Tung University, Hsinchu, Taiwan

³ Dept. of Computer Science & IT

Guru Ghasidas Vishwavidyalaya, Bilaspur, India

mukeshnctu.cs99g@nctu.edu.tw

Abstract. Vertical Collaborative Fuzzy C-Means (VC-FCM) is a clustering method that performs clustering on a data set of having some set of patterns with the collaboration of some knowledge which is obtained from other data set having the same number of features but different set of patterns. Uncertain relationship lies in data between the data sets as well as within a dataset. Practically data of the same group of objects are usually stored in different datasets; in each data set, the data dimensions are not necessarily the same and unreal data may exist. Fuzzy clustering of a single data set would bring about less reliable results. And these data sets cannot be integrated for some reasons.

An interesting application of vertical clustering occurs when dealing with huge data sets. Instead of clustering them in a single pass, we split them into individual data sets, cluster each of them separately, and reconcile the results through the collaborative exchange of prototypes. Vertical collaborative fuzzy C-Means is a useful tool for dealing collaborative clustering problems where a feature space is described in different pattern-sets.

In this paper we use collaborative fuzzy clustering, first we cluster each data set individually and then optimize in accordance with the dependency of these datasets is adopted so as to improve the quality of fuzzy clustering of a single data set with the help of other data sets, taking personal privacy and security of data into consideration.

Keywords: Fuzzy Clustering, Fuzzy C-means, Collaborative Fuzzy Clustering, Feature Space, Pattern set, Prototype.

1 Introduction

Clustering especially fuzzy clustering is an efficient tool for data analysis for understanding and visualizing data structures. The well-known Fuzzy C-means (FCM) [1, 2] algorithm is a typical one instance of Fuzzy clustering methods, which is very effective for a single dataset clustering and analysis. Fuzzy C-means is an extension of classical k-means which supports that every object must belong exclusively to a single cluster. On the other hand, FCM assumes that every object

belongs with some degree to every cluster. There are numerous modifications and several appealing clustering methods have been proposed in recent years.

The main quest is to assure that fuzzy clustering operates not only on data but takes full advantage of various sources of knowledge available when dealing with the problem at hand. A group of patterns in different fields has diverse information. To get a comprehensive study of these patterns, knowledge based clustering is recommended and collaborative clustering [3] between dataset is introduced by Pedrycz. The main objective of this study is to introduce and explore various scenarios where knowledge could be seamlessly included in the algorithmic architecture of fuzzy clustering.

Because of data confidentiality and some security problem we cannot access information of data directly from the dataset. To deal with this kind of problem Pedrycz introduced collaborative clustering [4, 5]. In this clustering algorithm several subsets of patterns can be processed together with an objective of finding a structure that is common to all of them.

The rest of the paper is organized as follows: Section 2 gives a simple introduction of Collaborative clustering along with horizontal collaborative clustering and vertical collaborative clustering and also explains the mathematical equation by expanding on optimization function and pseudo code of collaborative clustering. Section 3 shows the experimental results on sleep stage data and compares it changes in prototypes and partition matrices before and after collaboration. Section 4 brings a small discussion of effect of collaboration. Section 5 shows the effect of collaboration on cluster when we apply validation method and finally the conclusions are covered in Section 6.

2 Collaborative Clustering

In this section we presented a brief overview of Collaborative Fuzzy C-means and deal with the some mathematical equation which is the root of this technique. Collaborative clustering has two typical forms called horizontal collaborative clustering and vertical collaborative clustering. Horizontal collaborative clustering has been used in most of the papers with some experiments on it. But there is no such experiment result based on vertical collaborative clustering.

In this paper we focused more on vertical collaborative clustering instead of horizontal collaborative clustering and performed some experiment with sleep stage data. Section 3 and section 4, presents how the prototypes and partition matrix values are changing with the effect of vertical collaborative clustering.

To accommodate the collaboration technique in the optimization process, the objective function is explained in the form

$$Q[l] = \sum_{k=1}^N \sum_{i=1}^c u_{ik}^2[l] d_{ik}^2[l] + \sum_{\substack{m=1 \\ m \neq l}}^c \alpha[l, m] \sum_{k=1}^N \sum_{i=1}^n \{u_{ik}[l] - u_{ik}[m]\}^2 d_{ik}^2[l] \quad (1)$$

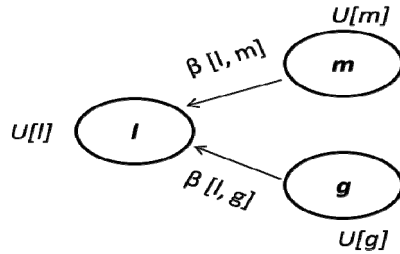


Fig. 1. Collaborative clustering scheme

2.1 Horizontal Collaborative Clustering

In horizontal collaborative clustering we deal with the same patterns but different feature spaces, probably disjoint subsets of feature space. The communication platform is based on the partition matrix.

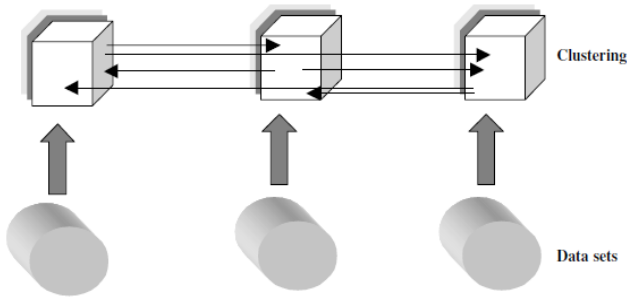


Fig. 2. A General scheme of Horizontal Clustering

2.2 Vertical Collaborative Clustering

In vertical collaborative clustering we are concerned with different patterns usually disjoint subsets of patterns but the same feature space. Hence the communication platform is based on the level of the prototypes.

The proposed objective function governing a search for structure in the l^{th} data set is

$$Q_{ii} = \sum_{k=1}^{M[l]} \sum_{i=1}^c u_{ik}^2 [l] d_{ik}^2 [l] + \sum_{\substack{m=1 \\ m \neq l}}^P \beta[l, m] \sum_{i=1}^c \sum_{k=1}^{M[l]} u_{ik}^2 [l] \|v_i[l] - v_i[m]\|^2 \tag{2}$$

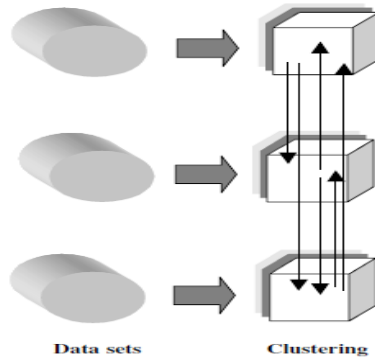


Fig. 3. A General scheme of Vertical Clustering

Where $\beta [l, m]$ is a collaboration coefficient supporting an impact of the m^{th} data set and affecting the structure to be determined in the l^{th} data set. The first term is the objective function used to search for the structure of the l^{th} data set as same as FCM does, and the second term articulates the differences between the prototypes. Number of clusters denoted by C . P is the total no. Of datasets involve in the collaborative process.

The optimization of $Q[l]$ involves the determination of the partition matrix $U[l]$ and the prototypes $V_i[l]$. First we solve the problem for each data set separately and allow the results to interact, forming thereby collaboration between the sets. The minimization of the objective function with respect to the partition matrix requires the use of Lagrange multipliers because of the existence of the standard constraints imposed on the partition matrix. We form an augmented objective function V incorporates the Lagrange multiplier λ and deal with each individual pattern ($t=1, 2, \dots, N[l]$):

$$V = \sum_{i=1}^c u_{it}^2[l] d_{it}^2[l] + \sum_{\substack{m=1 \\ m \neq l}}^p \beta[l, m] \times \sum_{i=1}^c u_{it}^2[l] \| v_i[l] - v_i[m] \|^2 - \lambda \left(\sum_{i=1}^c u_{it} - 1 \right) \quad (3)$$

Taking the derivative of V with respect to $u_{st}[l]$ and making it 0, we have

$$\frac{\partial V}{\partial u_{st}} = 2 v_{st}[l] d_{it}^2[l] + 2 \sum_{\substack{m=1 \\ m \neq l}}^p \beta[l, m] u_{st}[l] \| v_s[l] - v_s[m] \|^2 - \lambda = 0 \quad (4)$$

For notational convenience, let us introduce the shorthand expression

$$D_{l, m} = \| v_s[l] - v_s[m] \|^2 \quad (5)$$

From the above equation, we derive

$$u_{st}[l] = \frac{\lambda}{2 \left(d_{st}^2[l] + \sum_{\substack{m=1 \\ m \neq l}}^p \beta[l, m] D_{l, m, s} \right)} \quad (6)$$

Given the standard normalization condition

$$\sum_{j=1}^c u_{jt} [l] = 1, \text{ One has}$$

$$\frac{\lambda}{2} = \frac{1}{\sum_{j=1}^c \frac{1}{d_{jt}^2 [l] + \sum_{\substack{m=1 \\ m \neq l}}^p \beta [l, m] D_{l, m, j}}} \tag{7}$$

With the consideration of following abbreviated notation

$$\varphi [l] = \sum_{m \neq l}^p \beta [l, m] D_{l, m, j} \tag{8}$$

The partition matrix is

$$u_{st} [l] = \frac{1}{\sum_{j=1}^c \frac{d_{st}^2 [l] + \varphi_s [l]}{d_{jt}^2 [l] + \varphi_j [l]}} \tag{9}$$

For the prototypes, we complete calculations of the gradients of Q with respect to the coordinates of the prototype v[l] and solve the following equations:

$$\frac{\partial Q [l]}{\partial v_{st} [l]} = 0, \quad s=1, 2, \dots, c; t = 1, 2, \dots, n$$

We obtain

$$\frac{\partial Q [l]}{\partial v_{st} [l]} = 2 \sum_{k=1}^N u_{sk}^2 [l] (x_{kt} - v_{st} [l]) + 2 \sum_{m \neq l}^p \beta [l, m] \times \sum_{k=1}^N u_{sk}^2 [l] (v_{st} [l] - v_{st} [m]) = 0 \tag{11}$$

Next,

$$v_{st} [l] \left(\sum_{m \neq l}^p \beta [l, m] \sum_{k=1}^{N[l]} u_{sk}^2 [l] - \sum_{k=1}^{N[l]} u_{sk}^2 [l] \right) = \sum_{m \neq l}^p \beta [l, m] \sum_{k=1}^{N[l]} u_{sk}^2 [l] v_{st} [m] - \sum_{k=1}^{N[l]} u_{sk}^2 [l] x_{kt} \tag{12}$$

Finally, we get

$$v_{st} [l] = \frac{\sum_{m \neq l}^p \beta [l, m] \sum_{k=1}^{N[l]} u_{sk}^2 [l] v_{st} [m] - \sum_{k=1}^{N[l]} u_{sk}^2 [l] x_{kt}}{\left(\sum_{m \neq l}^p \beta [l, m] \sum_{k=1}^{N[l]} u_{sk}^2 [l] - \sum_{k=1}^{N[l]} u_{sk}^2 [l] \right)} \tag{13}$$

2.3 The Algorithm of VC-FCM

The computation details are organized into following fashion:

```

Given: subsets of patterns  $X_1, X_2, X_3, \dots, X_p$ .
Select: distance function, number of clusters ( $c$ ),
        Termination condition, and collaboration matrix
         $\beta[l, m]$ .
Compute: initiate randomly all partition matrices
         $U[1], U[2], \dots, U[P]$ 
Phase I
For each data
    Repeat
        Compute prototypes  $\{V_i[l], i=1, 2, \dots, C$  and
        partition matrices  $U[l]$  for all subsets of
        patterns}
    Until a termination condition has been satisfied
Phase II
    Repeat
        For the matrix of collaborative links  $\beta[l, m]$ 
        compute prototypes  $V_i[l]$  and partition
        matrices  $U[l]$  by using (9) and (13)
    Until a termination condition has been satisfied.

```

The termination criterion relies on the changes to the partition matrices obtained in successive iterations of the clustering method, for instance a Tchebyschev distance could serve as a sound measure of changes in the partition matrices. Subsequently, when this distance is lower than an assumed threshold value ($\epsilon > 0$), the optimization is terminated.

3 Experiment Result

In our study, we used the FP1 and FP2 EEG channels to identify the sleep stages [6]. For each epoch, there are 12 extracted features, because six features were extracted in each EEG channel. For each extracted feature, we make brief descriptions as follow

- The features (No. 1~6) were extracted from the FP1 EEG channel.
- The features (No. 7~12) were extracted from the FP2 EEG channel.

We applied vertical collaborative clustering on two subjects only. As we know vertical collaborative clustering is applicable one dataset having the same number of feature spaces and different number of patterns. Keeping this property in mind sleep stage data is suitable for this technique. We consider one subject as one dataset. The total numbers of feature spaces are 12 for both datasets and total numbers of patterns are 890 and 690 for dataset1 (S1 in Table 1) and dataset2 (S2 in Table 2) respectively and having 5 clusters each.

The sleep stages of these two subjects, S1 and S2, were scored by an experienced sleep expert through visual scoring with the manual scoring of the American Academy of Sleep Medicine (AASM) [7], and each 30-second epoch would assign a state.

The sleep stages defined are as follows: Wake, REM (rapid eye movement), NREM (Non-rapid eye movement) including Stage 1 (N1), Stage 2 (N2), and Stage 3 (N3).

Table 1. Number of sleep epoch for each sleeps stage

SC*	Wake	N1	N2	N3	REM	Total
S1	286 32.13%	132 14.83%	263 29.55%	117 13.15%	92 10.34%	890
S2	138 20.00%	46 6.67%	356 51.59%	69 10.00%	81 11.74%	690
S3	214 35.31%	85 14.03%	182 30.03%	111 18.32%	14 2.31%	606
....
S10	103 10.27%	121 12.06%	491 48.95%	132 13.16%	156 15.55%	1003
Total	1518 18.40%	1084 13.14%	3119 37.80%	1283 15.55%	1247 15.11%	8251

*SC means the subject code

3.1 The Prototypes and Partition Matrix of Dataset1 Before Collaboration as Follow

Prototypes:

$$\begin{aligned}
 V_1[1] &= \begin{bmatrix} 0.6756, 0.9173, 0.0579, 0.0548, 0.0453, 0.1130, \\ 0.6620, 0.9190, 0.0527, 0.0526, 0.0405, 0.1178 \end{bmatrix} \\
 V_2[1] &= \begin{bmatrix} 0.8950, 0.9849, 0.0362, 0.0168, 0.0072, 0.0259, \\ 0.8856, 0.9846, 0.0361, 0.0166, 0.0071, 0.0270 \end{bmatrix} \\
 V_3[1] &= \begin{bmatrix} 0.6602, 0.9216, 0.0493, 0.0398, 0.0393, 0.0769, \\ 0.6499, 0.9235, 0.0432, 0.0362, 0.0346, 0.0741 \end{bmatrix} \\
 V_4[1] &= \begin{bmatrix} 0.8013, 0.9629, 0.0500, 0.0453, 0.0236, 0.0799, \\ 0.7903, 0.9623, 0.0466, 0.0407, 0.0205, 0.0745 \end{bmatrix} \\
 V_5[1] &= \begin{bmatrix} 0.6004, 0.8855, 0.0521, 0.0435, 0.0480, 0.0821, \\ 0.5802, 0.8774, 0.0465, 0.0388, 0.0433, 0.0735 \end{bmatrix}
 \end{aligned}$$

Partition matrix:

$$U [1] = \begin{bmatrix} 0.2507 & 0.0465 & 0.2740 & 0.0925 & 0.3361 \\ 0.3149 & 0.0411 & 0.2606 & 0.0869 & 0.2962 \\ \dots & \dots & \dots & \dots & \dots \\ \dots & \dots & \dots & \dots & \dots \\ 0.2054 & 0.0624 & 0.4164 & 0.1390 & 0.1766 \\ 0.2128 & 0.1626 & 0.2116 & 0.1822 & 0.2306 \end{bmatrix}$$

3.2 The Prototypes and Partition Matrix of Dataset1 After Collaboration

Prototypes:

$$\begin{aligned} V_1'[1] &= [0.7144, 0.9298, 0.0665, 0.07461, 0.0407, 0.1665, \\ & 0.6961, 0.9309, 0.06184, 0.0732, 0.0374, 0.1736] \\ V_2'[1] &= [0.7558, 0.9429, 0.0471, 0.0391, 0.0320, 0.0729, \\ & 0.7410, 0.9414, 0.0428, 0.0356, 0.0277, 0.0691] \\ V_3'[1] &= [0.8136, 0.9708, 0.0338, 0.0181, 0.0133, 0.0323, \\ & 0.8051, 0.9686, 0.0324, 0.0173, 0.0130, 0.0325] \\ V_4'[1] &= [0.7744, 0.9501, 0.0466, 0.0362, 0.0232, 0.0674, \\ & 0.7645, 0.9493, 0.0444, 0.0347, 0.0218, 0.0718] \\ V_5'[1] &= [0.6401, 0.8976, 0.0496, 0.0386, 0.0505, 0.0696, \\ & 0.6250, 0.8929, 0.0440, 0.0340, 0.0446, 0.0638] \end{aligned}$$

Partition matrix:

$$U [1] = \begin{bmatrix} 0.0243 & 0.0040 & 0.0273 & 0.0081 & 0.9360 \\ 0.0309 & 0.0036 & 0.0254 & 0.0076 & 0.9323 \\ \dots & \dots & \dots & \dots & \dots \\ \dots & \dots & \dots & \dots & \dots \\ 0.0193 & 0.0064 & 0.7937 & 0.0212 & 0.1591 \\ 0.0187 & 0.0142 & 0.0186 & 0.0160 & 0.9323 \end{bmatrix}$$

3.3 The Prototypes and Partition Matrix of Dataset2 Before Collaboration

Prototypes:

$$\begin{aligned} V_1[2] &= [0.5744, 0.8708, 0.0329, 0.0377, 0.0493, 0.0753, \\ & 0.5683, 0.8612, 0.0300, 0.0321, 0.0547, 0.0687] \\ V_2[2] &= [0.5329, 0.8229, 0.0313, 0.0394, 0.0516, 0.0753, \\ & 0.5470, 0.8392, 0.0307, 0.0348, 0.0582, 0.0715] \\ V_3[2] &= [0.6810, 0.9296, 0.0360, 0.0328, 0.0387, 0.0662, \\ & 0.6727, 0.9301, 0.0291, 0.0263, 0.0417, 0.0562] \end{aligned}$$

$$V_4[2] = \begin{bmatrix} 0.8936, 0.9837, 0.0285, 0.0156, 0.0104, 0.0283, \\ 0.8759, 0.9799, 0.0285, 0.0148, 0.0138, 0.0259 \end{bmatrix}$$

$$V_5[2] = \begin{bmatrix} 0.5964, 0.8883, 0.0334, 0.0351, 0.0464, 0.0722, \\ 0.5910, 0.8825, 0.0297, 0.0300, 0.0513, 0.0646 \end{bmatrix}$$

We used collaboration coefficient $\beta(1,2)=2$ and $\beta(2,1)=2$ for collaboration process to see the impact of dataset1 on dataset2 and impact of dataset2 on dataset1 and we found that how Prototype and partition matrix changes their values due to this collaboration process.

Partition matrix:

$$U [2] = \begin{bmatrix} 0.0514 & 0.2187 & 0.2877 & 0.2368 & 0.2052 \\ 0.0595 & 0.2853 & 0.2199 & 0.1421 & 0.2930 \\ \\ \\ 0.0315 & 0.1851 & 0.3691 & 0.2527 & 0.1613 \\ 0.0214 & 0.2897 & 0.2940 & 0.1251 & 0.2695 \end{bmatrix}$$

3.4 The Prototypes and Partition Matrix of Dataset2 After Collaboration

Prototypes:

$$V_1'[2] = \begin{bmatrix} 0.6785, 0.9037, 0.0314, 0.0305, 0.0327, 0.0616, \\ 0.6812, 0.9096, 0.0308, 0.0289, 0.0378, 0.0534 \end{bmatrix}$$

$$V_2'[2] = \begin{bmatrix} 0.5840, 0.8503, 0.0361, 0.0463, 0.0546, 0.0862, \\ 0.5889, 0.8551, 0.0344, 0.0395, 0.0608, 0.0804 \end{bmatrix}$$

$$V_3'[2] = \begin{bmatrix} 0.7161, 0.9180, 0.0339, 0.0273, 0.0302, 0.0536, \\ 0.7093, 0.9212, 0.0322, 0.0241, 0.0341, 0.0501 \end{bmatrix}$$

$$V_4'[2] = \begin{bmatrix} 0.8606, 0.9720, 0.0265, 0.0169, 0.0150, 0.0291, \\ 0.8433, 0.9654, 0.0263, 0.0157, 0.0192, 0.0272 \end{bmatrix}$$

$$V_5'[2] = \begin{bmatrix} 0.6924, 0.9157, 0.0323, 0.0303, 0.0371, 0.0596, \\ 0.6826, 0.9098, 0.0293, 0.0257, 0.0392, 0.0551 \end{bmatrix}$$

Partition matrix:

$$U '[2] = \begin{bmatrix} 0.0045 & 0.8348 & 0.0284 & 0.0208 & 0.1112 \\ 0.0052 & 0.8401 & 0.0193 & 0.0124 & 0.1227 \\ \\ \\ 0.0028 & 0.1038 & 0.2342 & 0.2521 & 0.4069 \\ 0.0018 & 0.7076 & 0.0684 & 0.0243 & 0.1976 \end{bmatrix}$$

4 Quantifying the Collaboration Effect

The effect of collaboration between datasets can be evaluated at two levels.

4.1 At the Level of Data

The collaboration effect can be evaluated by the degree of collaboration influence over the numeric representation of prototypes (centroids). The collaboration impact is expressed in the changes of prototypes obtaining over the result of the collaboration.

4.2 At the Level of Information Granules

The collaboration effect can be evaluated by the degree of collaboration influence over the partition matrix. Calculate the average distance between the partition matrices $U^{[1]} = u_{ik} [1]$ and $U^{[2]} = u_{ik} [2]$, that is

$$\sigma = \frac{1}{Nc} \sum_{k=1}^N \sum_{i=1}^c |u_{ik} [1] - u_{ik} [2]| \tag{14}$$

By Table 2 we can see clearly that the stronger the collaboration (higher value of β), the lower the values of σ .

Table 2. value of σ with different level of β

β	0.1	0.3	0.5	0.8	1	3
σ	0.2752	0.2650	0.2574	0.2496	0.2460	0.2345

5 Cluster Validity

In the case of fuzzy clustering algorithms, some validity indices such as partition coefficient and classification entropy are designed by Bezdek [8] use only information of fuzzy membership grades to evaluate the clustering results.

5.1 Partition Coefficient (PC)

To measure the amount of “overlaps” between clusters. Partition coefficient defined as follows:

$$PC(c) = \frac{1}{N} \sum_{i=1}^c \sum_{j=1}^N (u_{ij})^2 \tag{15}$$

Where, $u_{ij}(i = 1, 2, \dots, c; j = 1, 2, \dots, N)$ is the membership of data point j in cluster i . The value is closer to one, the data are better classified.

5.2 Classification Entropy (CE)

It is a measurement for the fuzziness of a cluster partition only, which is similar to partition coefficient. Classification entropy is defined as

$$CE(c) = \frac{1}{N} \sum_{i=1}^c \sum_{j=1}^N u_{ij} \log(u_{ij}) \quad (16)$$

The value near to one indicates membership spread between several classes, while value closer to zero indicates the more complete classification into a single class.

Table 3. shows that how the value of Partition Coefficient and Classification Entropy are changing and affecting the clusters through collaboration mechanism. After collaboration the data are better classified and complete classification into a single class.

Table 3. PC and CE value comparison before and after Collaboration

For $\beta=0.2$	Dataset1		Dataset2	
	PC	CE	PC	CE
Before Collaboration	0.3522	1.2563	0.3682	1.2410
After Collaboration	0.7907	0.4039	0.8592	0.2532

6 Conclusion

In this paper we discussed about vertical collaborative fuzzy clustering which is useful for clustering of multiple databases derived from several datasets. Vertical collaborative clustering helps to bring the information about interaction of different sources, and reveal the basic internal structures and rules of the datasets with incomplete or unreal data. The vertical collaborative fuzzy clustering is adapted for vertical collaboration datasets that describe the same feature spaces but different patterns. An interesting application of vertical clustering occurs when dealing with huge data sets. Instead of clustering them in a single pass, we split them into individual data sets, cluster each of them separately, and reconcile the results through the collaborative exchange of prototypes.

During the collaboration process each data set is collaborated with all maps during the local phase. So the data confidentiality and safety is preserved. The purpose of collaborative clustering is to get clustering results closer to the original, and any external information is used to improve the clusters of the given data set which have been revealed. The quantification of the collaboration effect can be realized either the level of prototypes or the partition matrices. For future work we wanted to use this collaborative clustering method to deal with bigger database problems.

References

1. Bezdek, J.C.: Pattern recognition with fuzzy objective function algorithms. Plenum Press, New York (1981)
2. Bezdek, J.C., Ehrlich, R., Full, W.: FCM: the fuzzy C-means clustering algorithm. *Computers and Geosciences*
3. Pedrycz, W.: Collaborative fuzzy clustering. *Pattern Recognition Letters* 23(14), 1675–1686 (2002)
4. Pedrycz, W.: Knowledge-based clustering: from data to information granules. A John Wiley & Sons, Inc. (2005)
5. Pedrycz, W., Rai, P.: Collaborative Fuzzy Clustering with the use of Fuzzy C-Means and its Quantification. *Fuzzy Sets and Systems* (2008), doi:10.1016/j. fuss. 2007.12.030
6. Fraiwan, L., Lweesy, K., Khasawneh, N., Wenz, H., Dickaus, H.: Automate sleep stage identification system based on time-frequency analysis of a single EEG channel and random forest classifier. *ELSEVIER Computer Methods and Programs in Biomedine* 108, 10–19 (2012)
7. Iber, C., A-Israel, S., Chesson Jr., A.L., Quan, S.F.: *AASM manual For Scoring Sleep* (2007)
8. Bezdek, J.C.: Numerical taxonomy with fuzzy sets. *J. Math. Biol.* 1, 57–71 (1974)

Comparison of Exoskeleton Robots and End-Effector Robots on Training Methods and Gait Biomechanics

Pi-Ying Cheng and Po-Ying Lai*

Department of Mechanical Engineering, National Chiao-Tung University, Taiwan
lpy928@gmail.com

Abstract. Rehabilitation robot positively improves walking ability of patients with gait disorders. Over the last decade, rehabilitation robot devices replaced the training of overground and treadmill. In this paper, our discussion focuses on exoskeleton robot and end-effector robot. The purpose of this study was to compare the training methods, gait Kinematic trajectories and muscle activity patterns on subjects when training on exoskeleton robot and end-effector robot.

Keywords: Rehabilitation robot, exoskeleton robot, end-effector robot.

1 Introduction

In traditional locomotor training on overground walking, patients practice gait using walking aids such as, crutches, canes, and walkers. Three or more therapists are required to guide the patient with leg movement and stabilize the patient's pelvis during the process. Over the last decades, training system that incorporates treadmill with a suspension support has been in practice clinically [1]. Studies have shown improved results in terms of the patient's walking ability, walking speed, balance, and symmetric walking control comparative to the traditional methods. Patient's body weight is partly supported by the suspension system on the treadmill to prevent the risk of falling [2]. During the gait training, two therapists are required to assist the patient's movement. One of the therapists stabilizes the patient's pelvis, while the other therapist must control the treadmill speed. Despite of the effectiveness in rehabilitation in traditional locomotor training or the treadmill-suspension system, clinical practice of both methods are still limited by the manpower of therapists. Thus, the duration of the patient's exercise is usually limited by the physical availability of therapists [3].

In the recent years, robotic devices have been widely utilized to replace the manpower and physical needs of therapists in the field of neurological rehabilitation. It also allows patients with nerve damage to receive a lot of exercising. Robotic rehabilitation devices can be divided based on the driven principles: exoskeleton robot (e.g. Lokomat, AutoAmbulator, LOPES, ALEX) [4]-[7], and end-effector robot(e.g. G-EO-systems, Gait Trainer, Gait Master)Type [8]-[10]. A number of research on exoskeleton robot and end-effector robot are studied and will be discussed in this

* Corresponding author.

study. The proven evidences from many of the studies show the effectiveness of robotic rehabilitation devices in terms of improving gait ability and physiological functions.

Most of the studies are based on the comparison between rehabilitation robots, overground walking and treadmill training. Therefore, three main purposes of this study are: (1) comparison of the training methods between exoskeleton robots and end-effector robots. (2) comparison of the gait activities between exoskeleton robots and end-effector robots. (3) comparison of the muscle activity between exoskeleton robots and end-effector robots.

2 Rehabilitation Robot Device

2.1 Rehabilitation of Exoskeleton Robot

1) Lokomat: Lokomat (Hocoma SA, Switzerland) is the most widely utilized rehabilitation robotic system in the current field of exoskeleton gait training clinically. This system is commonly used to improve gait function of patients with lower limb disorders that are caused by stroke, spinal cord injury, traumatic brain injury, and multiple sclerosis. The structure is composed of driven gait orthosis (DGO), Lokolift, and Andago®. The pelvis joint and the knee joint of DGO are made of a combination of DC motor and lead screws[4]. Before the use of Lokomat, the therapist must pre-measure the lengths of the subject's thighs and lower legs, and the width of the subject's pelvis. This allows the therapist to adjust the exoskeleton robot's upper legs, lower legs and the frame on both sides accordingly to match with the subject. After that, subject's thighs and lower legs are strapped and stabilized on to the exoskeleton's robotic upper legs and lower legs. The dorsiflexion of the subject's feet is controlled by two elastic straps. First, the gait function and the level of damage of the patient are evaluated by the therapist to avoid circumstances such as orthopedic problems and muscle diseases problems. Based on the evaluation result, the gait speed of the exoskeleton and the strength of the suspension support are adjusted in accordance to the patient's weight by the therapist. In the beginning of the training, each subject first walks in the Lokomat for up to 5 minutes in order to acclimate to the device and for the therapist to make minor adjustments for tighten leg cuff straps and optimize joint alignment. Each subject is exercised passively on the Lokomat and the kinematic trajectories of the Lokomat are fully programmable. On the same token, gait speed, frequency, distance, duration can all be controlled. At the current state, several studies have proven that Lokomat improves not only the patient's gait function but also slows down muscle atrophy and reduces the problem of muscle tone [11], [12].

2) AutoAmbulator: The AutoAmbulator (HealthSouth, Houston, Texas, USA) is a rehabilitation robotic device located in Health South, USA. Detail specification related to this device has not been released up-to-date. In the previous study by Fisher et al, it is stated that 20 hemiplegic stroke patients were randomly selected to receive regular physiotherapy and rehabilitation robotic therapy. The result stated that patients who received training by the AutoAmbulator showed dramatic improvement on gait function and body balance [5].

3) LOPES: In 2007, lower extremity powered exoskeleton (LOPES), a new gait rehabilitation device was published by Veneman et al. Evaluation measures show that the device allows both “patient-in-charge” mode and “robot-in-charge” mode, in which the robot is controlled either to follow or to guide a patient, respectively. This device integrates the first study of LOPES, which focused on the clinical trials on 5 stroke patients. The patients received a 6-week training, with sessions of 3 times a week, and at maximum of 45 minutes per session. The post-training result stated that 4 of the patients were improved on foot clearance, gait speed and endurance [6].

4) ALEX: Active leg exoskeleton (ALEX), an unilateral exoskeleton robot for stroke patients with side hemiplegic legs was invented at the University of Delaware. The overall setup has four main components to aid the unaffected leg. Two stroke patients received a 6-week training. During the training the speed of the treadmill was increased. The result showed substantial improvement of the patients’ gait pattern after the training [7], [13].

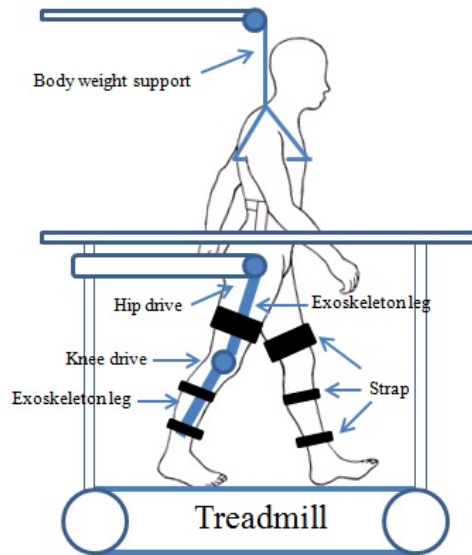


Fig. 1. Rehabilitation of exoskeleton robot

2.2 Rehabilitation of Exoskeleton Robot

1) GT I: The development of mechanized gait trainer(MGT or GT I), for restoration of gait, was based on a doubled crank and rocker gear system. It consists of two footplates positioned on bars, cranks and rockers. The crank propulsion is modified by a gear to provide a ratio of 60 percent to 40 percent between the gait of stance and swing phases. GT I has successfully treated children with cerebral palsy and a large number of stroke patients in the past studies. In most cases, the patients’ gait ability and body balance were both improved [9].

2) GM 2: Current commercially available gait machines, such as Lokomat, AutoAmbulator, LokoHelp and GT I, are limited to repetitive exercises of walking on the floor. Hiroaki et al. from University of Tsukuba in Japan released a publication regarding an end-effector rehabilitation device, called Gait Master 2 (GM2). The structural motion principle is based on the relative positions of the base connecting bars, which allows the pedals to move forward and back, up and down. Subject on GM2 is able to perform gait training on normal walking, climbing up and down the stairs. Due to the lack of body support and the lack of fixation of the feet on GM2, the subject can be trained both passively and actively. 3 assessments on 9 healthy subjects were performed on GM2 by Hiroaki et al.: (1) actual overground walking; (2) passive simulated walking on GM2; (3) active simulated walking on GM2. During the tests, the subjects' Physiological Cost index (PCI) and lower limb electromyography (EMG) were being recorded. The result showed no significant differences between actual overground walking and walking passively on GM2. PCI result was most significantly different when subjects were actively walking on GM2. Due to the fact that actual overground walking was more relaxed, and the subjects were driven significantly by the pedal board on GM2, the subjects would involuntarily lift their legs to coordinate with the movement of the pedal boards while the subjects were actively trained. In regards to the lower limb EMG, the result was more significant when the subjects were actively trained on GM2 [10].

3) HapticWalker: HapticWalker is an end-effector based gait rehabilitation robot, which was designed in references to the programmable footplate concept [23]. Each of the two manipulators comprises a hybrid serial-parallel robot and a footplate for permanent foot attachment at its end-effector. The subject's feet are fixed to the footplates via safety release bindings, in addition to the use of safety harness to prevent falls and also to enable body weight support.

4) G-EO Systems: Hesse et al. introduced a newly developed gait robot for training gait of stroke patients, called the G-EO Systems. In the report of G-EO Systems, four tests were performed on 6 sub-acute stroke patients: (1)actual overground walking, (2)simulation of overground walking on G-EO-Systems, (3)actual upward stairs climbing, (4)simulation upward stairs climbing on G-EO-Systems. Under the four test circumstances, patients were required to continue for 30 seconds or at least 10 steps, in order to record the lower limb EMG. The study showed very similar muscle activities for stroke patients under actual and simulation walking, as well as actual and simulation stairs climbing on G-EO-Systems. The slight differences found were: (1) thigh muscles activity was initiated slower on stimulated overground walking (compared to actual overground walking), and muscle activity duration was longer, (2)in comparison to the actual upward stairs climbing motion, the gastrocnemius muscles were being most active, while the activity of the lower legs' anterior muscles showed adjustments overtime for 3 of the patients. Step length, step frequency, step height and step speed could be adjusted according to the patients' gait ability [8].

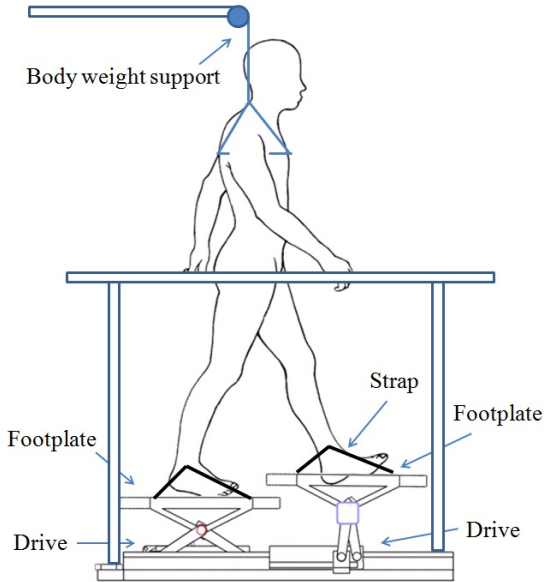


Fig. 2. Rehabilitation of end-effector robot

3 Discussion

3.1 Robot-Assisted Gait Training Methods

In the current robot-assisted gait trainings, training duration, distance and speed are regulated by the therapists in accordance to the patient's degree of injury. As the patient shows improvement, the percentage of body weight support by the suspension system can be gradually decreased. Due to the limitation of structural design, all of the exoskeleton robots only allow overground walking training. These exoskeleton robot gait training lack variations in the gait patterns. End-effector robots of GM2, HapticWalker and G-EO-Systems utilize 6 degrees of freedom in the mechanism design [8], [10]. Therefore, they allow subjects to perform gait training on overground walking, upward and downward stairs climbing, such as Table I. In order to overcome the single training method of the exoskeleton robots, Brüttsch et al. integrated virtual reality (VR) with Lokomat, through the so-called biofeedback values, which allowed 10 gait nerve-damaged children to have interaction with VR using very little spontaneous force[14]. In addition, end-effector robots, GM2 device is capable of carrying out 3 training modes: enforced, semi-voluntary and real [10]. Inactive training decreases learning and recovery of walking motion in comparison to active training [15], [16].

Table 1. Rehabilitation robot

Device	DOF	Gait simulation	Training modes
Lokomat	2	Overground walking	Combined virtual reality [14].
AutoAmb-ulator	2	Overground walking	---
LOPES	4	Overground walking	1)Patient-in-charge mode. 2)Robot-in-charge mode [24].
ALEX	2	Overground walking	---
GT I	1	Overground walking	---
GM2	6	Overground walking Stair climbing up Stair climbing down	1)Actual overground walking. 2)Passive simulated walking. 3)Active simulated walking [10].
HapticWal-ker	6	Overground walking Stair climbing up Stair climbing down	---
G-EO-Systems	6	Overground walking Stair climbing up Stair climbing down	---

3.2 Kinematic Trajectories

Previous study showed that Lokomat changed the hip range of motion by almost 7° on healthy subjects. This would not cause much harm on patients whose hip range of motion are severely impaired [12]. Human hip joint, which is usually modeled as a ball-socket joint, is different from other joints since it provides three dimensional motions. The sagittal plane motion is most important for walking, in which hip flexion prepares the clearance for swinging, while the transition from hip flexion to extension facilitates limb advancement during swing phase and it also provides propulsion force in stance phase [25]. As the patient is using the robotic legs, the speed of the motor drive for the exoskeleton must match with speed of the treadmill, in order to ensure the safety of the patient. Further, the knee joints are moving three-dimensionally as human walks, whereas they are restricted to sagittal plane when using the exoskeleton. Patients could be affected by the potential shear forces during alignment between hip joints and the exoskeleton joints [26]. Hidler indicated that Locomat System often runs with 100% guidance force, with which a particular gait pattern would be enforced regardless of the subject’s intentions [12]. Thus, with the inability to vary the kinematic patters, the subject could only go from step to step. Hidler found that misalignment of the subject’s and Lokomat’s knee and hip joints occurred as the subject intentionally alter their gait actively in Lokomat [12]. Any resistance and inertia movements are refrained from the hemiplegic subjects by the Exoskeleton.

In end-effector robots, therapist must pay close attention to the patient's knee motion to prevent knee hyperextension while training on GT I. Knee support is particular important to patients with severe spinal cord injury. Patients may wear any kind of ankle-foot orthosis (AFO) or knee ankle-foot orthosis (KAFO) to prevent knee instability [9], [17].

3.3 Muscle Activation Patterns

Hidler reported the cause of erroneous muscle pattern of healthy subjects as a result of reduced shank muscle activity and falsely bearing of proximal weight on muscles in the swing phase on Lokomat. Minor changes occurred during the terminal swing phase and the loading phase. During terminal swing, the subject's ankle was less dorsiflexed on the gain trainer. That is due to the geometrical constraints of the chosen mechanical solution, thus the rear of the footplate was lowered only minimally [12], [18]. The antagonistic tibialis anterior muscle was remarkably less active on the GT I, possibly due to patient reliance on the mechanical support during the swing phase. The activity of the tibialis anterior muscle was reduced when comparing exoskeleton robot with end-effector robot [9], [17].

Hesse et al. stated that, the activation of the quadriceps muscles was delayed throughout the whole stance phase on the G-EO-Systems during the floor walking condition. The thigh muscles of hemiplegic subjects were inactive during the swing phase on the G-EO-Systems [8]. Subjects' knees are supported by exoskeleton-based system during the stance phase, whereas stabilization of the knees is assisted manually or by stimulating the quadriceps using FES in end-effector based machine. Although FES may be utilized to facilitate quadriceps muscles, it may cause rapid muscle fatigue and often insufficient muscle responses [9], [12].

The tibialis anterior muscle activity is reduced accordingly when patients take advantage of the plates support on the feet during swing phase. Patient's feet have direct contact to the treadmill on the exoskeleton robot. The impact strength of the direct contact is usually unnoticeable to severe or total lower limb disability, thus patient would not be unaware of new injury during training [8], [9], [12]. In comparison to the previous two methods, better performances of vastus muscle, gastrocnemius, and tibialis are observed when subjects were actively walking on GM2. The activity of tibialis, which control the subject's plantar flexion and dorsiflexion is the most essential. Gastrocnemius and tibialis could be strengthened through gait training, hence improve the problem of foot drop [10].

References

1. Finch, L., Barbeau, H., Arsenuault, B.: Influence of body weight support on normal human gait: development to fagaitre training strategy. *Physical Therapy* 71(11), 842–855 (1991)
2. Behrman, A.L., Harkema, S.J.: Locomotor training after human spinal cord injury: a series of case studies. *Physical Therapy* 80(7), 688–700 (2000)
3. Westlake, K.P., Patten, C.: Pilot study of Lokomat versus manual-assisted treadmill training for locomotor recovery post-stroke. *NeuroEngineering and Rehabilitation* 6(18) (June 2009)

4. Colombo, G., Joerg, M., Schreier, R., Dietz, V.: Treadmill training of paraplegic patients using a robotic orthosis. *Rehabilitation Research and Development* 37(6), 693–700 (2000)
5. Fisher, S., Lucas, L., Thrasher, T.A.: Robot-Assisted Gait Training for Patients with Hemiparesis Due to Stroke. *Topics in Stroke Rehabilitation* 18(3), 269–276 (2011)
6. van Asseldonk, E.H., Veneman, J.F., Ekkelenkamp, R., Buurke, J.H., van der Helm, F.C., van der Kooij, H.: The Effects on Kinematics and Muscle Activity of Walking in a Robotic Gait Trainer During Zero-Force Control. *IEEE Trans. Neural Syst. Rehabil. Eng.* 16(4), 360–370 (2008)
7. Banala, S., Kulpe, A., Agrawal, S.K.: A Powered Leg Orthosis for Gait Rehabilitation of Motor-Impaired Patients. In: *Proceedings of IEEE International Conference on Robotics and Automation*, pp. 4140–4145 (April 2007)
8. Stefan, H., Andreas, W., Christopher, T.: Innovative gait robot for the repetitive practice of floor walking and stair climbing up and down in stroke patients. *NeuroEngineering and Rehabilitation* 7, 30 (2010)
9. Werner, C., Von Frankenberg, S., Treig, T., Konrad, M., Hesse, S.: Treadmill training with partial body weight support and an electromechanical gait trainer for restoration of gait in subacute stroke patients. *A Randomized Crossover Study* 33, 2895–2901 (2002)
10. Yano, H., Kasai, K., Saito, H., Iwata, H.: Sharing Sense of Walking With Locomotion Interfaces. *International Journal of Human-Computer Interaction* 17(4), 447–462 (2009)
11. Wirz, M., Zemon, D., Rupp, R., Scheel, A., Colobo, G., Dietz, V., Hornby, T.G.: Effectiveness of automated locomotor training in patients with chronic incomplete spinal cord injury: a multicenter trial. *Arch. Phys. Med. Rehabil.* 86(4), 672–680 (2005)
12. Hidler, J., Nichols, D., Pelliccio, M., Brady, K.: Advances in the understanding and treatment of stroke impairment using robotic devices. *Top Stroke Rehabil.* 12(2), 21–33 (2005)
13. Banala, S., Kim, S., Agrawal, S.K., Scholz, J.P.: Robot Assisted Gait Training with Active Leg Exoskeleton (ALEX). *IEEE Trans. Neural Syst. Rehabil. Eng.* 17(1), 2–8 (2009)
14. Brüttsch, K., Schuler, T., Koenig, A., Zimmerli, L., -Koencke, S.M., Lünenburger, L., Riener, R., Jäncke, L., Meyer-Heim, A.: Influence of virtual reality soccer game on walking performance in robotic assisted gait training for children. *Journal of NeuroEngineering and Rehabilitation* 7(1), 323–366 (2010)
15. Adamovich, S.V., Fluet, G.G., Tunik, E., Merians, A.S.: Sensorimotor training in virtual reality: a review. *Neuro Rehabilitation* 25, 29–44 (2009)
16. Lotze, M., Braun, C., Birbaumer, N., Anders, S., Cohen, L.G.: Motor learning elicited by voluntary drive. *Brain* 126, 866–872 (2003)
17. Hesse, S., Werner, C.: Connecting research to the needs of patients and clinicians. *Brain Research Bulletin* 78, 26–34 (2009)
18. Hidler, J.M., Wall, A.E.: Alterations in muscle activation patterns during robotic-assisted walking. *Clin. Biomech.* 20, 184–193 (2005)
19. Adamovich, S.V., Fluet, G.G., Tunik, E., Merians, A.S.: Sensorimotor training in virtual reality: a review. *Neuro Rehabilitation* 25, 29–44 (2009)
20. Lotze, M., Braun, C., Birbaumer, N., Anders, S., Cohen, L.G.: Motor learning elicited by voluntary drive. *Brain* 126, 866–872 (2003)
21. Hesse, S., Werner, C.: Connecting research to the needs of patients and clinicians. *Brain Research Bulletin* 78, 26–34 (2009)
22. Hidler, J.M., Wall, A.E.: Alterations in muscle activation patterns during robotic-assisted walking. *Clin. Biomech.* 20, 184–193 (2005)

23. Hussein, S., Schmidt, H., Volkmar, M., Werner, C., Helmich, I., Piorko, F., Krüger, J., Hesse, S.: Muscle coordination in healthy subjects during floor walking and stair climbing in robot assisted gait training. In: Conf. Proc. IEEE Eng. Med. Biol. Soc., pp. 1961–1964 (2008)
24. van der Kooij, H., Veneman, J., Ekkelenkamp, R.: Design of a compliantly actuated exoskeleton for an impedance controlled gait trainer robot. In: Annual International Conference of the IEEE Engineering in Medicine and Biology Society, vol. 1, pp. 189–193 (2006)
25. Perry, J., Burnfield, J.M.: Gait Analysis: Normal and Pathological Function, 2nd edn. S. Incorporated (2010)
26. Pons, J.L.: Wearable Robots: Biomechatronic Exoskeletons. Wiley (2008)

TCP Performance in LTE Network

Hyun-Chul Yi, Hyoung-Woo Kim, and Joon-Young Choi

Department of Electrical Engineering, Pusan National University,
Pusan, Korea

{hcy,hwkim0314,jyc}@pusan.ac.kr

Abstract. In this paper, in order to analyze the dynamic property of data traffics in LTE (Long Term Evolution) mobile communication network, we build a dynamic model for LTE network in the packet level and implement the model based on NS-2 simulator. Using the implemented dynamic model for LTE network, we simulate TCP Reno with packet loss congestion measure and FAST TCP with queuing delay congestion measure in various LTE network environments and analyze the stability and performance of each TCP. The simulation results show that FAST TCP is superior to TCP Reno in performance over twice and illustrate that queuing delays contain more effective information on the network congestion than packet losses in the LTE network.

Keywords: Fast TCP, LTE, Congestion Control.

1 Introduction

LTE is called 3GPP Long Term Evolution, it is a high-speed wireless data packet communication standard for the advanced mobile phone from HSDPA (High Speed Downlink Packet Access). It is based on the Release 8 that finalized on December 2008 from 3rd asynchronous mobile communication technology standard organization, 3GPP(3rd Generation Partnership Project). LTE uses important techniques, OFDM(Orthogonal Frequency Division Multiplexing) and MIMO(multi-input multi-output) for communicate at a rate of 12 times more than HSDPA [1,2].

In Korea, SK Telecom and LG U + launched the LTE service in June 2011 and KT start in January 2012 [3]. LTE subscribers in about 7.09 million people of June 2012(16.1% increase from the previous month), which accounted for 13.4 percent of whole the mobile communication subscribers(about 5,299 million people). The number of subscribers in the month rapidly increased [4]. The mobile communication base station systems of the previous generation made in the foreign companies, but from LTE network system, Korea companies as Samsung Electronics, LG Electronics, ETRI, and etc increased the share of standard patents [5].

In the case of an overseas, LTE mobile communication system is commercialized first by TeliaSonera in Sweden in December 2009, and it has services in many countries in North America and Europe, and Japan. January 8 2013 now, the service providers of 145 has begun the commercial LTE services in the 66 countries around the world, the service providers of 381 are investing in LTE in 114 countries. Until the end of 2013, the

providers of 234 in 83 countries expected to build a commercial LTE network [6]. Because of the number of LTE service subscribers increases, the market of base station systems, parts, and devices related with the LTE service has also increased [5].

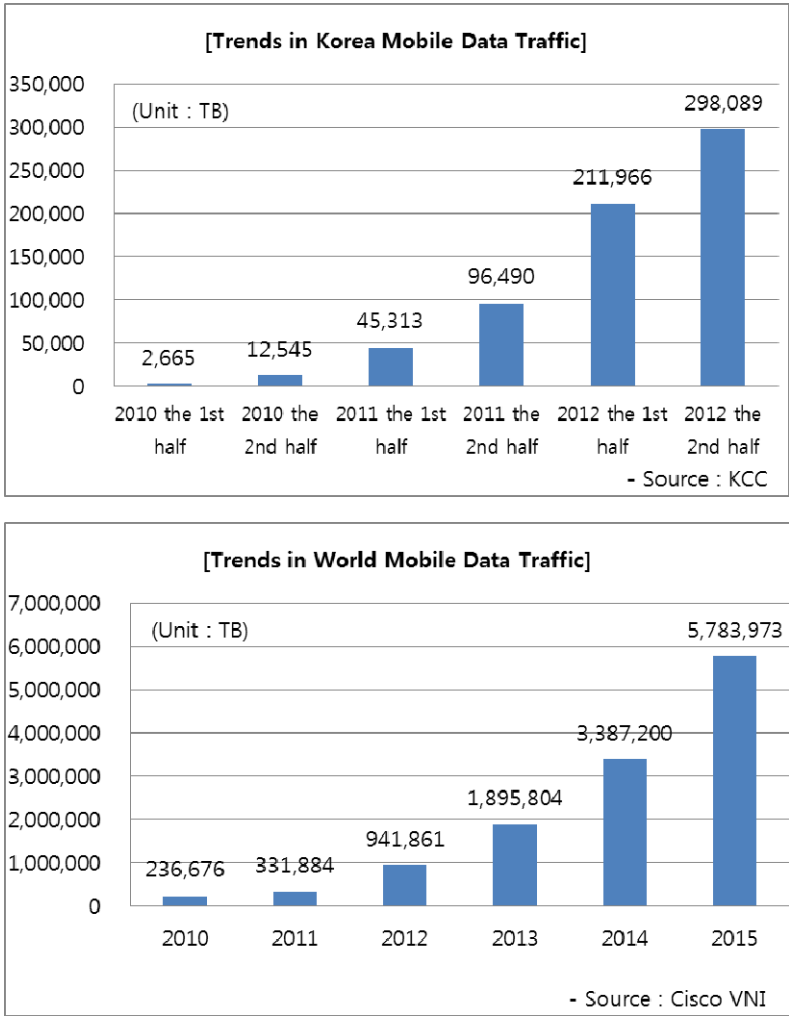


Fig. 1. Trends in Korea and World Mobile Traffic

It is estimated that the global mobile data traffic has increased rapidly and increase more and more to the increased use of mobile devices such as the smartphones and the tablet PC. Therefore, the data communication services are the main causes of the traffic load in the mobile communication network. This situation is illustrated as statistical data in Figure 1. The side effects that increased burden of the service providers and the user cost, and quality loss of data services and voice calls have become a real problem already.

Almost the data application programs that use the LTE mobile communication network was designed and operated base on TCP(Transmission Control Protocol), has designed in a wired link with the steady bandwidth and the network delay. However, the wireless network link includes the mobile communication network, that has the characteristic as network delay and bandwidth can be vary continuously along the flow of time. Applied to a wireless network as a previous existing TCP caused the performance of the wireless network decrease abnormally [7, 8].

Therefore, the communication services based on TCP efficiency providing is considered as an important factor in determining the success of the LTE mobile communication. It is important to optimize stability and performance of TCP in the LTE mobile communication network. In this paper, we modeling the LTE mobile communication network by using NS-2 network simulator. We simulate Fast TCP and TCP Reno in the network model that has been implemented, and analyze the performance and reliability of each TCP protocols.

2 TCP Reno and Fast TCP

TCP Reno has AIMD(Additive Increase and Multiplicative Decrease) and the slow-start characteristics. Currently, this protocol is commonly used as TCP protocol in the network of the wired and the wireless. The congestion window(CWND) and the window threshold information was calculated every times to send the appropriate data to the available bandwidth[10,11]. This congestion control scheme works by taking into account the congestion packet loss information. Since the variety of transmission medium, the transmission rates, and the routing paths, the status of the network is changed according to the time. The response of the entire network is slow and inefficient in TCP Reno [12].

In the case of Fast TCP, without a way to reduce half of the congestion window size as well as TCP Reno, by calculating the appropriate congestion window size in each situation for each, Fast TCP is to maximize the using of the bandwidth [13]. Fast TCP uses the queuing delay information as congestion means to calculate the congestion window, represents the status of the entire network directly, and the response rate of the network is faster than TCP Reno.

3 Experiments

3.1 Simulation Environment

Implement Fast TCP and TCP Reno in the LTE network model by using NS-2 network simulator and measure the CWND respectively. Further, to measure the CWND of TCP algorithm by changing the operating conditions of QoS in the same condition. The LTE network topology and the simulation parameters used in the performance evaluation are shown in Figure 4 and Table 2 [14]. In the topology, UE use the 10, each of UE are assumed to use the voice calls, the streaming, the web search, and the download service of data. The bandwidth is 10Mbps, the delay time is 2ms between Cell and eNB. The bandwidth is 100Mbps, the delay time is 2ms between eNB and aGW. The bandwidth is 100Mbps, the delay time is 2ms between aGW and Server.

Table 1. Types of Traffic in LTE

Traffics(Class ID)	Example
Conversational(0)	Session/RTP Session/RTP Agent
Streaming(1)	CBR/UDP Agent
Interactive(2)	HTTP/TCP Agent HTTP/Client HTTP/Cache HTTP/Server
Background(3)	FTP/TCP Agetn

Table 2. Simulation Parameters

Parameters	Value
Simulation Time	30 Sec
Multicast	On
Buffer Size	100 Pakets

3.2 Comparison of CWND in LTE Network

CWND change measurments of Fast TCP and TCP Reno, depending on whether QoS behavior in the simulation are shown in Figure 5 and 6. In the figure, by setting to half of the threshold value of the window when a packet loss occurs, TCP Reno has a lower CWND than Fast TCP. On the other hand, Fast TCP has CWND twice or more than TCP Reno and uses network bandwidth efficiently, using the queing delay as a congestion control variable.

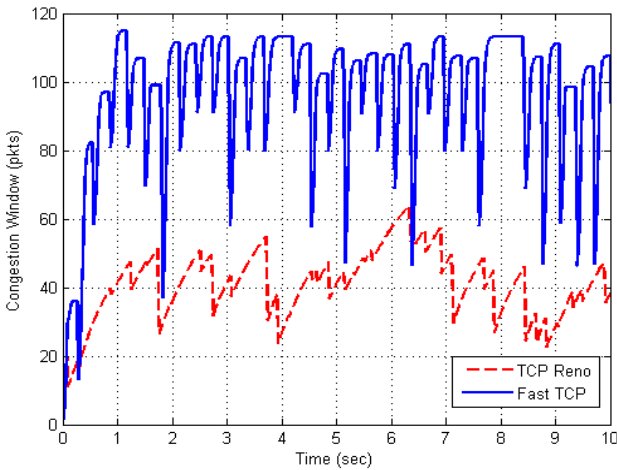


Fig. 2. Comparison of the Mean Value of CWND with QoS Off

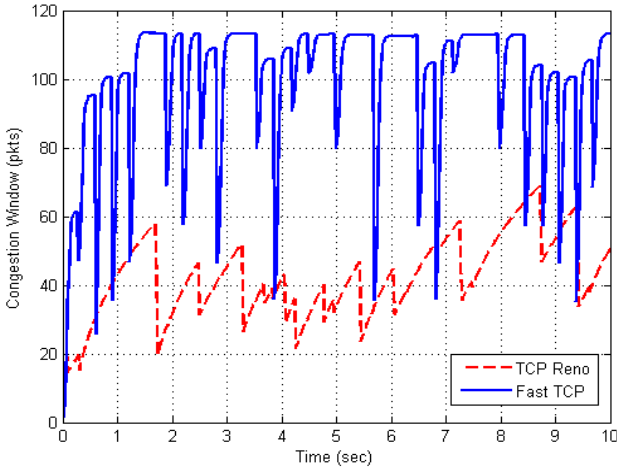


Fig. 3. Comparison of the Mean Value of CWND with QoS On

Table 3. Comparison of the Mean Value of CWND

Types of TCP	CWND Mean (Pakets)	
	QoS Off	QoS On
TCP Reno	46.07	38.88
Fast TCP	95.86	97.36

Table 3 shows the mean value of CWND while an 1 second. TCP Reno has a lower value of CWND than QoS Off, and Fast TCP has a higher CWND value than using QoS Off.

4 Results

In this paper, we design the LTE network model by using NS-2 simulator, and compared the performance of Fast TCP and TCP Reno depending on QoS condition. The results of the simulation shown that the performance of Fast TCP is the two times or more than TCP Reno and the use of QoS has a higher value CWND. In the LTE network, the queuing delay included more effective information than the packet loss about the network congestion.

References

1. LTE, <http://www.3gpp.org/LTE>
2. 3GPP TS 36.300 v.8.3.0, Evolved UTRA and Evolved UTRAN (E-UTRAN). In: 3GPP, pp. 1–120 (November 2007)
3. LTE MAPS, <http://www.ltemaps.org>

4. KISDI, Evaluation of the Competition Status in the Telecommunications Markets (November 2012)
5. Lee, K.S., Seok, W.H., Song, Y.K.: Current Status and Prospect of LET Market. *Electronics and Telecommunications Trends* 26(4), 152–164 (2011)
6. GSA, <http://gsacom.com>
7. Choi, Y.R.: The data traffic of the mobile communication is increasing rapidly, how works with? Nice Credit, Korea (November 2010)
8. Park, Y.J., Park, A.S., Kang, S.Y., Kim, Y.K., Ryu, S.: Trends on Development of Network Capacity in LTE-Advanced to Support Increasing Mobile Data Traffic. *Electronics and Telecommunications Trends* 27(1), 122–135 (2012)
9. Qiu, Q.-L., et al.: LTE/SAE Model and its Implementation in NS-2. In: 2009 Fifth International Conference on Mobile Ad-hoc and Sensor Networks, pp. 299–303 (December 2009)
10. Allman, M., Paxson, V., Stevens, W.: TCP Congestion control. RFC 2581, pp. 1–17 (April 1999)
11. Chiu, D., Jain, R.: Analysis of the Increase and Decrease Algorithms for Congestion Avoidance in Computer Networks. *J. Compute Networks* 17(1), 1–14 (1989)
12. Balakrishnan, H., Padmanabhan, V., Kats, R.: The Effects of Asymmetry on TCP Performance. In: *Proc. ACM/IEEE Mobicom*, pp. 77–89 (September 1997)
13. Wei, D.X., Jin, C., Low, S.H., Hegde, S.: FAST TCP: motivation, architecture, algorithms, performance. *IEEE/ACM Trans. Networking* 14, 1246–1259 (2006)
14. Han, J.S., Bae, S.S.: *Network Simulator*, pp. 253–285. Seahwa Publication (2009)

Analysis of Functional Components for a Robotic Patient Lift Based on Chinese Clinical Demands

Yu Wu^{1,2}, Dong-Yun Gu^{1,2,3,*}, and Jian-He Wei^{1,2}

¹ Engineering Research Center of Digital Medicine and Clinical Translation, Ministry of Education of P.R. China, Shanghai Jiaotong University, Shanghai, 200030, China

² School of Biomedical Engineering, Shanghai Jiaotong University, Shanghai, 200030, China

³ Department of Orthopedic Surgery, Shanghai Ninth People's Hospital,

Shanghai Jiaotong University, Shanghai, 200011, China

dongyungu@gmail.com

Abstract. This study aimed to offer suggestions to the design of robotic patient lift based on Chinese clinical demands by investigating the Chinese medical institutions at different levels, and assessing the current caregivers' low back load during manual patient handling tasks.

The space, spatial distribution and structure of seven equipped patient beds in four Chinese medical institutions at different levels were investigated. Kinetic data and rating of perceived exertion were also calculated and recorded from nine caregivers performing six patient handling tasks with three "actor" patients.

We recommend that the robotic patient lift designed for Chinese medical institutions should be of more compact size with more flexible features. Biomechanical loading characteristics during different handling tasks and the patient weight should be taken into consideration in the robotic lift design.

Keywords: Robotic patient lift, patient handling tasks, biomechanical analysis, spinal loading.

1 Introduction

Occupational low back injury is a growing concern among nursing personnel, which were caused by manual patient handling [1-6]. Epidemiological studies show that the manual ways of patient handling are popular in most medical institutions of China, causing a high prevalence of musculoskeletal complaints. The low back was the most commonly reported body site (56%) [7], and over 70% of Chinese nurses suffered from low back injuries [8].

Biomechanical researches on manual patient handling tasks prove that excessive load is imposed on the caregivers' lumbar spine during these hazardous jobs [9-12]. At the same time, frequent trunk bending and twisting cause high low back load in different anatomical directions due to different tasks including lifting, turning and

* Corresponding author.

repositioning [10]. That means different patient handling tasks have their own risks, which are not merely resulted from one injury index (e.g., compression force).

A wide range of mechanical lifting and transfer solutions have evolved to enable safe patient lifting and handling since the 'No Lift Policy' is prevalent in many countries. The robotic lifting systems (floor lifts, ceiling lifts, standing aids etc.) have yet to reach the commercial market in North America and Europe, and considerably decreased the low back load of caregivers[11, 13-15]. Bostelman et.al designed an advanced home lift, position, and rehabilitation chair to help the patients with potential neural and cognitive impairments [16]. Lee et.al designed a patient transportation robot's lifting arms without a sheet and tested the comfort and safety of the machine [17]. However, due to the unique clinical settings, few robotic patient lifts were developed based on the Chinese clinical demand. Additionally, a specific patient lift considering different loading characteristics of Chinese patient during different manual handling tasks is quite necessary in Chinese medical institutions. It can effectively relieve the low back injury risks of caregivers in a comprehensive way.

In order to provide specific and comprehensive guides to the design of robotic patient lift based on Chinese clinical demand, we investigated the space, spatial distribution and structure of equipped patient bed in Chinese medical institutions at different levels, and evaluated the risk of low back injuries for Chinese caregivers by analyzing the peak force and moment on lumbar 5th vertebra to sacral 1st vertebra (L5/S1) level and psychophysical stress during manual patient handling tasks.

2 Method

2.1 Investigation of the Size of Wards and Inside Beds

The sizes of five wards and the inside seven clinical beds in four clinical institutions (including two hospitals of first level, one hospital of second level, and a community health center) in Shanghai were investigated. The measuring parameters included the length/width of wards and beds, distance between beds, distance between bed end and wall, and detailed size of other parts of bed (including bed height, foot/bar/footboard height).

2.2 Biomechanical and Psychophysical Study of Manual Patient Handling Tasks

2.2.1 Subjects

This study protocol was approved by the Bioethics Committee from School of Biomedical Engineering, Shanghai Jiaotong University. Caregiver and agent patient subject contents were obtained prior to the scheduled test date.

Nine female nursing assistants were chosen as the caregivers (with 48 ± 6 years old, 63.09 ± 5.27 kg and 160.67 ± 5.66 cm.) They had over 2 years (10.22 ± 5.95 years) of patient handling experience but carried no prior injury history on their lower lumbar.

Three agent patients in good health with lower body dependence and upper body independence (able to bear weight) are chosen: the lightest patient is a male that

weighs 53kg; a female with medium weight of 71kg; and the heaviest patient is a male of 79kg.

2.2.2 Experimental Design

The experiments consisted of six common manual patient handling tasks in Figure 1:

- a) Turning away: turning patient in bed away from caregiver from back to the other side;
- b) Moving to bedside: repositioning patient from lying in middle of the bed to bedside;
- c) Raising up to sitting: elevating patient from supine position to sitting on edge of the bed;
- d) Lying down to bed: moving patient from sitting on the bed to supine position;
- e) Moving to bed head: reposition the supine patient towards the head of the bed;
- f) Transferring: transferring the patient from sitting on the bed to sitting in a chair.

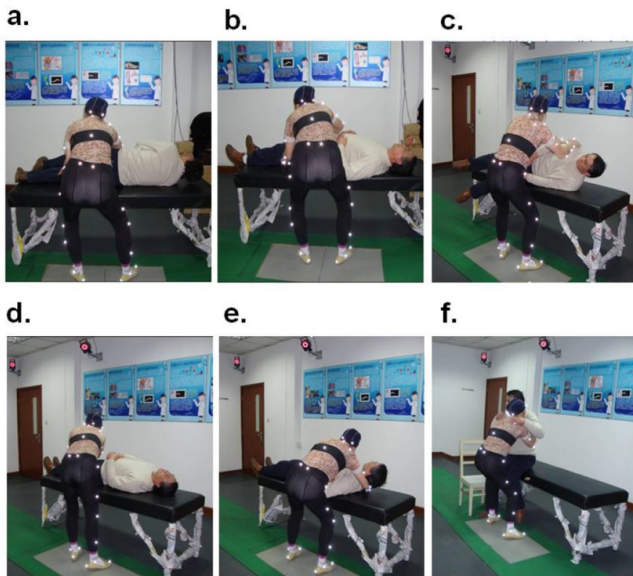


Fig. 1. The manual patient handling tasks: a) Turning away; b) Moving to bedside; c) Raising up to sitting; d) Lying down to bed; e) Moving to bed head and f) Transferring

Caregivers were asked to perform the tasks with each ‘patient’ three times, and rested for 1 minute after each trial. Before the data collection, the subjects performed practice trials to familiarize them with each task. On account of the limited conditions, an examination couch of 63cm height and an ordinary chair without armrests 45cm in height are used as the bed and chair in clinics.

2.2.3 Data Collection Techniques

Vicon® T40 3D Motion Capture with 10 cameras were used to capture the body posture of the caregivers. Two forceplates (AMTI® OR6-7) were placed side by side to register the ground reaction force. The cameras and forceplates were time-synchronized.

Thirty-nine reflective markers were placed on the caregivers' bodies. Most of the markers were placed on the anatomical landmarks of the caregivers along with the rest to form the rigid bodies to track: the upper trunk, pelvis, left and right thighs, left and right shanks, left and right feet. Thus the segment lengths, joint centers and body fixed coordinate system were determined.

After finishing each trial, rating of perceived exertion (RPE) from each caregiver was recorded by Borg CR-10 scale. Caregivers were asked to describe 'How stressful do you (themselves) feel during each task?' by using the number from 0 ('not stressful at all') to 10 ('using the maximum' effort).

2.2.4 Model Development and Data Analysis

A linked eight-segment model was built to estimate net reaction forces and moment at low back. The L5/S1 joint was defined by the joint of the upper trunk and pelvis. The reaction load for each joint was estimated by inverse dynamic approach. In this study, peak force and moment of caregivers' low back spine in three anatomical directions were calculated and compared for each task, representing the instant maximum load on L5/S1 level during the manual handling process.

The effects of each task and patient's body weight on peak moment were examined by two-way repeated measures ANOVA tests and Turkey HSD for multiple comparisons ($P=0.05$). Kruskal-Wallis non-parametrical rank test was employed to determine whether significant main effects ($P<0.05$) of RPE were observed.

3 Result

3.1 The Space, Spatial Distribution and Structure of Equipped Patient Beds in Four Chinese Medical Institutions

Beds investigated in this study included a three-handle and a four-handle bed in orthopedic and neurosurgery wards of hospital A (a first level hospital), an ordinary and an extra bed in a thoracic surgery ward of hospital B (a first level hospital), a bed in a orthopedic ward in hospital C (a second level hospital) and a bed in a general surgery ward in a community health center.

The space size of wards was within the range of 313~357 cm in width and 510~593 cm in length. The distance between two beds in Chinese wards was within the range of 60~85 cm, and the width of corridors (i.e. the space between the bed end to the wall, or between the extra bed and an ordinary bed) for robotic patient lift running was within the range of 108~155cm. The size of patient bed was within the range of 75~95 cm in width and 194~205 cm in length with an extra fixing bar normally setting underneath the foot of bed (in Fig.2 and Fig.3). Detailed size of the wards and the beds inside were concluded in Table 1.

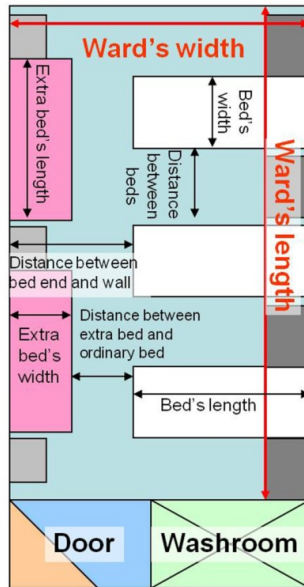


Fig. 2. Graphic top-view of a thoracic surgery ward in hospital B (a first level hospital)

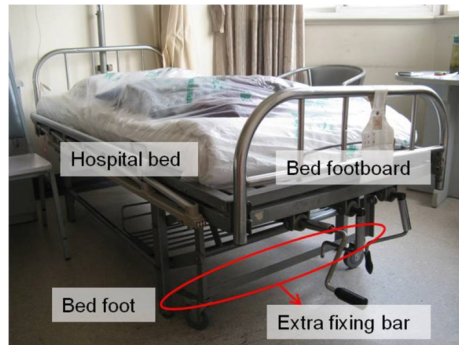


Fig. 3. Hospital bed with an extra fixing bar setting underneath the foot of bed

3.2 Peak Low Back Force in Three Anatomical Directions

The peak axis force (i.e. compression) on L5/S1 level during the six manual patient-handling tasks were above the back-compression criterion limit of 3400N (as shown in Fig.3), which was recommended by National Institute for Occupational Safety and Health [18]; Additionally, the peak A-P shear force during task b (512.37 ± 63.87 N) and e (534.74 ± 65.22 N) were over the recommend caution level of 500N [19], while the others all surpassed 400N.

Task f had the highest axis force (i.e. compression, 4833.57 ± 905.24 N) ($P < 0.01$). Task b and e resulted in highest A-P shear force (512.37 ± 63.87 N/ 534.74 ± 65.22 N) ($P < 0.05$). Highest lateral shear forces were found in the mean value of task c ($P < 0.05$)

and d ($P<0.005$). Task a cost the lowest load on L5/S1 motion segment in three directions ($P<0.05$).

Table 1. Size of wards and the clinical beds from various hospital levels in Shanghai

Medical institutions	Ward size (cm)		Space in wards (except beds) (cm)		Basic size for bed (cm)		Detailed size for bed and other parts of bed (cm)			
	Length	Width	Distance between beds	Distance between bed end and wall	Length	Width	Height /increasing to	Foot height	Bar at bed end/beneath /increasing to	Footboard height
Hospital A (Orth., three-handle bed)			80	120	200	90	62/55	44	13/17	76
Hospital A (Orth., four-handle bed)	510	320	79	117	197	93	63/72	47	11/24	80
Hospital A (Neur. Surg.)			60	125	196	93	68/--	50	17	85
Hospital B (Thro. Surg.)			85	155	202	85	63/--	42	23	89
Hospital B (Thro. Surg., extra bed)	593	357	53 (between extra beds)	80 (between extra bed and ordinary bed)	194	75	44/--	34	--	--
Hospital C (Orth.)	568	313	70	108	205	90	66/80	43	14/--	81
Community health center (Gen Surg.)	550	330	67	125	205	89	70/--	46	15/--	86

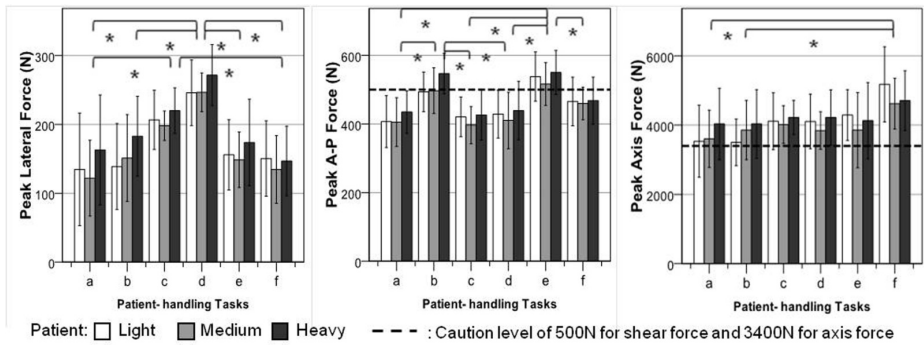


Fig. 4. Peak low back force calculated in six patient-handling tasks in three directions

Significant difference in values of force existed between light and heavy ‘patients’ ($P<0.05$), and between medium and heavy ‘patients’ as well ($P<0.05$). However, no difference between light and medium patients was noticed ($p>0.1$).

3.3 Peak Low Back Moment in Three Anatomical Directions

Task c, d and f in Fig.4 had the highest peak moments in twisting directions ($P<0.05$), while Task a and b showed the significant lowest moments ($P<0.05$). Moreover, significant difference did not exist in peak extension-flexion and lateral (left-right) bending moment.

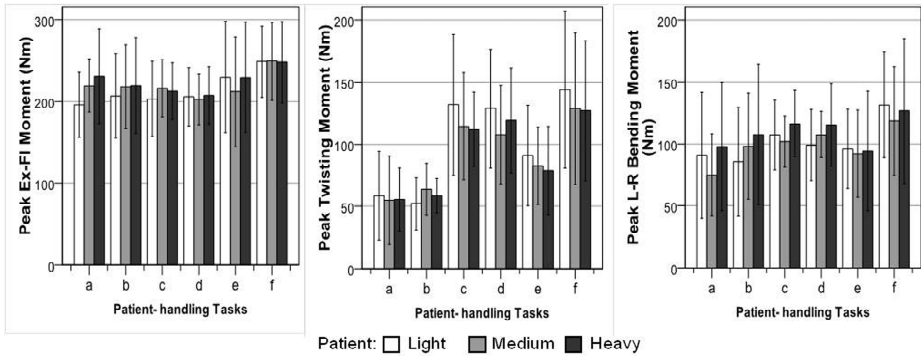


Fig. 5. Peak low back force calculated in six patient-handling tasks in three directions

There were no significant differences in peak low back moment of three anatomical directions among the three levels of ‘patient’ weight ($p>0.05$). Furthermore, the cross effect of weight and task could be ignored ($p>0.1$).

3.4 Caregivers’ Rating of Perceived Exertion

The ratings of perceived exertion on low back during six manual patient handling tasks were between 3~6 (Fig.5), which means the perceived exertion were from the degree of ‘medium’ to ‘stressful’. Difference existed among these tasks: mean rank of Task e and f were significantly higher than other tasks ($P<0.05$), while Task a and c had the lowest rank (56.46 and 68.89) ($P<0.05$).

Significant difference of RPE was found among three patient weight levels ($P<0.05$). The patient with medium weight caused ‘moderate’ strength of caregivers ($RPE\geq 3$) during all tasks, while the heaviest patient made caregivers ‘a bit of stressful’($RPE>4$) and even more ‘stressful’ during task b, e and f ($RPE>5$).

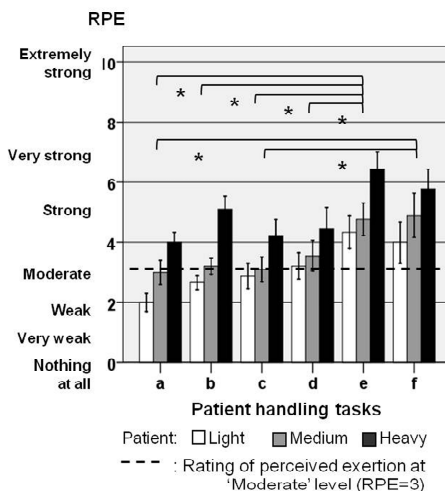


Fig. 6. Ratings of perceived exertion on spinal low back during six patient handling tasks

4 Discussion

Few patient lifts based on Chinese clinical demand are designed and applied because of the limited medical resources and restricted clinical area. Thus, handling and moving patients manually are still popular in many Chinese medical institutions with the restricted clinical conditions. In order to offer suggestions to design a robotic patient lift specifically for Chinese medical institutions, the space, spatial distribution and structure of equipped patient bed of five wards in four Chinese medical institutions at different levels were investigated in this study. The current injury risks for Chinese caregivers' lower back during their manual patient handling were also evaluated by biomechanical and psychophysical method.

4.1 Overall Dimensions of Robotic Patient Lift Designed for Chinese Clinical Demand

To avoid the collision with the other beds, the robotic patient lift designed for Chinese medical institutions should be of more compact size. The overall dimensions of the machine should range 108~155cm so as to move smoothly through corridors. Sensors are suggested to set on the robotic patient lift to detect the nearby obstacles and give immediate feedback during moving and turning in the wards.

Additionally, the distance between two beds in Chinese wards was 60~85 cm, which was not wide enough for the operation of a lift. Most clinical beds had bars at the bottom of bed ends which may block the moving path of lifts. Therefore, we suggest another trajectory for the robotic patient lift to approach the clinical bed, rather than operating at the bedside. Retractable lift mast, boom and fork would also be necessary to support the operation of the robotic patient lift.

4.2 Robotic Patient Lift Designed to Reduce Different Low Back Injury Risks

We find that peak loads of compression during all handling tasks were higher than the generally accepted limit of 3400N. At the same time, tasks of Repositioning caused the high A-P shear force over the caution level of 500N. This means jobs on manual patient handling are quite demanding and complex.

No significant differences in values of L5/S1 force and moment were found between task b and e, as well as between task c and d in all directions of all the metric values tested. Thus, these manual patient-handling tasks were suggested to be grouped into 4 classes according to the above biomechanical results and with the characteristics of caregivers' actions. The features of resultant force and moment during all these tasks were summarized.

- Group I: Turning, including task a 'Turning away', operated by pushing or pulling patients by ordinary elastic force, cost lowest force, twisting and lateral bending moment.
- Group II: Repositioning, including task b 'Moving to bedside' and task e 'Moving to bed head', operated by moving patients against friction force, cost highest A-P force.

- Group III: Lifting/Lowering, including task c ‘Raising up to sitting’ and task d ‘Lying down to bed’, operated by lifting or lowering patients with part of their weight, cost highest lateral force.
- Group IV: Transferring, including task f ‘Transferring’, operated by carrying patients with most of their weight, cost highest compression, twisting and lateral bending moment.

We suggest that biomechanical injury characteristics during different manual handling tasks and the patient weight should be taken into consideration. Multiple operation modes are recommended during different handling tasks to effectively relieve the low back injury risks of caregivers in a comprehensive way.

4.3 Patients’ Weight Effect on the Design of Robotic Patient Lift

It is noted that manual handling tasks performed in China are not the same with those in other countries, due to the shorter height and lighter weight of both Chinese caregivers and patients (with the average height of 1.67~1.71m and weight of 65.6~68.5kg for adult male, 1.56~1.59m and 53~59.7kg for adult female [20]).

‘Patients’ weight was proved to have an effect on caregivers’ low back force: significant differences existed between light (53kg) and heavy (79kg) ‘patients’ ($P<0.05$), and also between medium (71kg) and heavy patients ($P<0.05$). There was no difference between light and medium weight patients ($p>0.1$). It is interesting to find that the weight gap between medium and heavy ‘patients’ (8kg) was quite smaller than between the medium and light patient (26kg). However, load difference existed between the smaller weight difference rather than the larger difference in patients’ weight. This can be explained by the uncontrolled factor of the resultant load on caregivers, which was depended on the patient’s body size/weight as well as the performance of the agent patient, etc. We estimated that the lighter ‘patients’ acted as a totally dependent person, while the medium patient may act more ‘actively’ than was asked.

We also assessed the ‘patient’ weight effect on caregivers’ psychophysical stress by collecting their ratings of perceived exertion (RPE) to verify the biomechanical results. Within each pair of the two levels, significant difference of RPE was found. This may imply that the psychophysical index would be more sensitive to the caregivers than the biomechanical one.

Since the patient weight was a significant index of injury risk, an overweight patient may cause the potential falling accident due to the unstable structure or components of the lift. Therefore, designers of the robotic patient lift should note the stiffness of the machine, and install protective devices to ensure the safety of patients.

4.4 Limitations

There are two noteworthy limitations of this study. Firstly, a limited number of wards and beds were investigated. Limited subjects were recruited, and only six common patient handling tasks were evaluated. Thus, more trials are needed to achieve a more logical and statistically convincing result. Secondly, considering the limited area of the lab, a less realistic experimental environment was built to simulate the real-life scenario, which may influence the process and the result of this study.

5 Conclusion

In conclusion, the robotic patient lift based on Chinese clinical demand should be designed into a more compact size. The moving trajectory of the machine may choose a more flexible way due to the limited space in Chinese wards. The lift should also be designed to operate in multiple modes, so as to effectively reduce caregivers' injury risks during different handling tasks with different biomechanical characteristics.

Acknowledgements. This work was supported by the International Scientific and Technological Cooperation Grant (2009DFA32500). The authors thank the nursing assistants and agent patients who participated in this laboratory study. Special thanks go to Dr. Yue Li for her help with experiment design, data processing and manuscript revision.

References

1. Waters, T.R.: When is it safe to manually lift a patient? *Am. J. Nurs.* 107, 53 (2007)
2. Personick, M.E.: Nursing home aides experience increase in serious injuries. *Mon. Labor. Rev.* 113, 30–37 (1990)
3. Smedley, J., Egger, P., Cooper, C., et al.: Manual handling activities and risk of low back pain in nurses. *Occup. Environ. Med.* 52, 160–163 (1995)
4. Kjellberg, K., Lagerstrom, M., Hagberg, M.: Work technique of nurses in patient transfer tasks and associations with personal factors. *Scand. J. Work Environ. Health.* 29, 468–477 (2003)
5. Owen, B.D., Keene, K., Olson, S.: An ergonomic approach to reducing back/shoulder stress in hospital nursing personnel: a five year follow up. *Int. J. Nurs. Stud.* 39, 295–302 (2002)
6. Mitchell, T., O'sullivan, P.B., Smith, A., et al.: Biopsychosocial factors are associated with low back pain in female nursing students: a cross-sectional study. *Int. J. Nurs. Stud.* 46, 678–688 (2009)
7. Smith, D.R., Wei, N., Zhao, L., et al.: Musculoskeletal complaints and psychosocial risk factors among Chinese hospital nurses. *Occup. Med.* 54, 579–582 (2004)
8. Chiou, W.K., Wong, M.K., Lee, Y.H.: Epidemiology of low back pain in Chinese nurses. *Int. J. Nurs. Stud.* 31, 361–368 (1994)
9. Claus, J., Alwin, L., Andreas, T., et al.: Characteristic values of the lumbar load of manual patient handling for the application in workers' compensation procedures. *J. Occup. Med.* 6 (2011)
10. Marras, W., Davis, K., Kirking, B., et al.: A comprehensive analysis of low-back disorder risk and spinal loading during the transferring and repositioning of patients using different techniques. *Ergo.* 42, 904–926 (1999)
11. Zhuang, Z., Stobbe, T.J., Hsiao, H., et al.: Biomechanical evaluation of assistive devices for transferring residents. *Appl. Ergon.* 30, 285–294 (1999)
12. Skotte, J., Fallentin, N.: Low back injury risk during repositioning of patients in bed: the influence of handling technique, patient weight and disability. *Ergo.* 51, 1042–1052 (2008)
13. Marras, W., Knapik, G., Ferguson, S.: Lumbar spine forces during manoeuvring of ceiling-based and floor-based patient transfer devices. *Ergo.* 52, 384–397 (2009)

14. Santaguida, P.L., Pierrynowski, M., Goldsmith, C., et al.: Comparison of cumulative low back loads of caregivers when transferring patients using overhead and floor mechanical lifting devices. *Clin. Biomech.* 20, 906–916 (2005)
15. Engkvist, I.L.: Evaluation of an intervention comprising a No Lifting Policy in Australian hospitals. *Appl. Ergon.* 37, 141–148 (2006)
16. Bostelman, R., Ryu, J.-C., Chang, T., et al.: An Advanced Patient Lift and Transfer Device for the Home. *Journal of Medical Devices* 4
17. Lee, Y.-H., Bae, B.-S., Yim, H.J., et al.: The Design of a Patient Transportation Robot's Lifting Arms Considering Comfort and Safety without the Presence of a Sheet. *Journal of Robotics* (2011)
18. Niosh. *Work practices guide for manual lifting* (1981)
19. McGill, S., Norman, R., Yingling, V., et al.: Shear happens! Suggested guidelines for ergonomists to reduce the risk of low back injury from shear loading. In: *Proceedings of the 30th Annual Conference of the Human Factors Association of Canada* (1998)
20. Department of Mass Sports, G. A. O. S. O. C. 2010 Chinese national bulletin fitness and health monitoring (2010)

Lower Limb Exoskeleton Using Recumbent Cycling Modality for Post-stroke Rehabilitation

Hua Yan and Canjun Yang

The State Key Laboratory of Fluid Power Transmission and Control, Zhejiang University, Hangzhou 310027, Zhejiang, China
{wereyh, ycj}@zju.edu.cn

Abstract. This paper presents a compact exoskeleton robot for post-stroke patients at the early stage of lower limb rehabilitation as soon as they become stable. Unlike the usual walking gait, a new training modality mimicking the popular exercise named recumbent cycling is implemented to provide safe and comfortable assistance for the patients lacking active motor ability as a result of very low muscle power. To realize the recumbent cycling gait pattern, the exoskeleton robot mounted on a wheelchair possesses two pairs of hip and knee joints on right and left legs respectively, and each joint has one degree-of-freedom actuated in the sagittal plane. Joint position and velocity for recumbent cycling modality are calculated based on a simplified kinematic model of the exoskeleton. Clinical experiments are conducted with two post-stroke patients, and the preliminary results show a promising application of recumbent cycling modality in robotic rehabilitation.

Keywords: Exoskeleton, Recumbent Cycling, Lower Limb, Rehabilitation, Wheelchair.

1 Introduction

Patients following a stroke need repetitive and intensive movement training to regain motor ability [1]. In addition, National Institutes of Health (NIH) suggests that physical therapy begins as soon as a patient is stable [2]. Some clinical researches have confirmed that post-stroke patients could expect a better recovery if physical therapy started early after motor injury [3, 4]. Moreover, even the patients in the acute phase could benefit from physical therapy [5]. So a safe and comfortable training modality for patients of severely impaired motor ability, e.g. patients with grade 0 or 1 according to Medical Research Council (MRC) Scale [6] shown in Table 1, is a main concern of the implementation of physical therapy.

Table 1. MRC scale for evaluation of muscle power [6]

Grade	Description
0	No contraction
1	Flicker or trace of contraction
2	Active movement, with gravity eliminated
3	Active movement against gravity
4	Active movement against gravity and resistance
5	Normal power

Body weight supported treadmill training for motor rehabilitation has already been established with manual or robotic assistance [7, 8]. Nevertheless, the regular walking modality may seem difficult for patients with grade 0 or 1 at the early post-stroke stage. Meanwhile, special attention should be paid to the suspension system [9] for comfort and safety. As a popular exercise to enhance muscular ability, recumbent cycling contains a more convenient joint range of motion to prevent spasm occurrence, especially for hip joint, and the patient's weight is distributed comfortably over a large area, supported by the backrest. Mazzocchio et al. [10] conducted cycling on healthy subjects, the results indicated that cycling effectively improved performance and induced lasting changes in locomotor activity. Johnston [11] showed that cycling could address impairments through potentially minimizing stress on joints by considering factors influencing the biomechanics of cycling, which benefited patients with physical disability. Gregor et al. [12] calculated the general muscle moment patterns in younger and older healthy adults from recorded joint kinematic and kinetic data in order to more properly and efficiently use recumbent cycling as a rehabilitation tool. Additionally, Kerr et al. [13] collected electromyographic and kinematic signals from 12 healthy participants during recumbent cycling, the results suggested there was sufficient agreement to support the use of recumbent cycling as a specific training modality in the early stage of rehabilitation. The researches above revealed the potential application that recumbent cycling may provide a safe, task-oriented locomotor intervention. As a complementary training modality, recumbent cycling offers an alternative option to the severe post-stroke patients with very low motor ability.

Exoskeleton robots used for rehabilitation in post-stroke patients with motor disabilities are getting more and more attention in recent decades. Most lower limb exoskeleton robots, e.g. HapticWalker [14], Lokomat [8] and Lopes [15], adopted the normal walking modality of healthy subject to provide patients with a biomimetic training pattern. In our previous work [16], a 4-DOF gait rehabilitation exoskeleton was developed for body weight supported treadmill training. An important prerequisite for these exoskeleton robots is that patients have to partially support body weight by themselves [17], which is difficult for those with very low muscle power. As mentioned above, recumbent cycling can solve these problems by uniformly distributing weight of upper-body over patient's back. Besides the low load and range of joint motion has an intrinsic advantage to prevent spasm occurrence. To the authors' knowledge, few exoskeleton robots developed employed the recumbent cycling modality [18, 19]. One of them named "MoreGait" [19] utilized the recumbent posture to provide an intensive and durable training through actuating the man-made shoes along a straight line, and simulating a force field on the foot pad to enhance neural plasticity.

Therefore, this paper introduces an alternative exoskeleton robot using the recumbent cycling modality for lower limb rehabilitation. In the next section, a brief description of the exoskeleton robot is presented. Section 3 introduced the characteristic and implementation of the recumbent cycling modality. In section 4, clinic trials are conducted with 2 stroke patients to evaluate the design concept and performance of the exoskeleton robot, followed by discussion and conclusion.

2 Lower Limb Exoskeleton Robot

Exoskeleton robots realize movement therapy by physically attaching to human limbs, and passing motion and force through the interaction ports. Therefore an anthropomorphic structure is needed to form a compatible kinematic chain with human limb, which is the guarantee to a comfortable and safe training. Three anatomical joints are responsible for the movements of lower limb, i.e. the hip, knee and ankle, the motion of which are achieved through the contraction and expansion of corresponding flexors and extensors shown in Fig. 1. It's assumed that hip and knee joints play a primary role during recumbent cycling. So in this research the developed lower limb exoskeleton robot has 4 actuated degrees-of-freedom (DOFs) in the sagittal plane, i.e. the hip flexion/extension and knee flexion/extension of two legs respectively, as indicated in Fig. 1. Meanwhile, mechanical ankle joint is passive to accommodate motion of the anatomical one.

Both the knee and hip joints are driven by custom-made linear actuators comprising precision ball screws, timing belts and pulleys. The pulleys are driven by DC motors. Encoders are mounted at all motors to measure the hip and knee angles. Flexible straps for physically connecting the patient and exoskeleton are distributed over the shank and thigh links of two legs, the lengths of which are adjustable according to human dimensions standard [20].

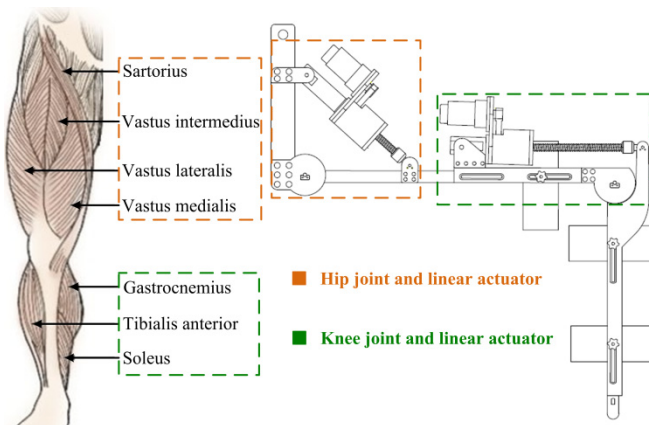


Fig. 1. Lower limb muscles and corresponding structure of exoskeleton

The robotic exoskeleton moves synchronously to assist human lower limb training, which indicates that the mechanical joints ROM should be no more than the corresponding one of anatomical joints. Meanwhile, some specific constraints should be added considering the posture of recumbent cycling. Table 2 shows the human physiological ROM during activities of daily life (ADLs) [21] and recumbent cycling; also the designed mechanical limits are shown.

Table 2. Human’s ROM and the designed joint limits

Joint	Motion	Phy. ROM	Rec. Cyc. ROM	Mech. limits
Hip	Flexion	120°	78°~ 120°	75°~ 120°
	Extension	30°	—	—
Knee	Flexion	150°	40°~ 86°	90°
	Extension	0°	0°	0°

During the movement training, the weight of upper body is distributed over the backrest of wheelchair, the inclination of which can be adjusted based on patient’s preference. Meanwhile, a pair of armrests is mounted over the right and left thigh link respectively to stabilize human body. The patients could place their upper limbs on the armrests and maintain a comfortable position. Foot drop, as a common phenomenon in stroke patient [22], is a crucial factor hindering recumbent cycling that needs a dexterous ankle joint. However, the range of ankle flexion/extension in weak patient is limited [21], so a pair of foot pads are passively connected to the shank links to prevent foot drop and offer a small range of motion to the ankle joint.

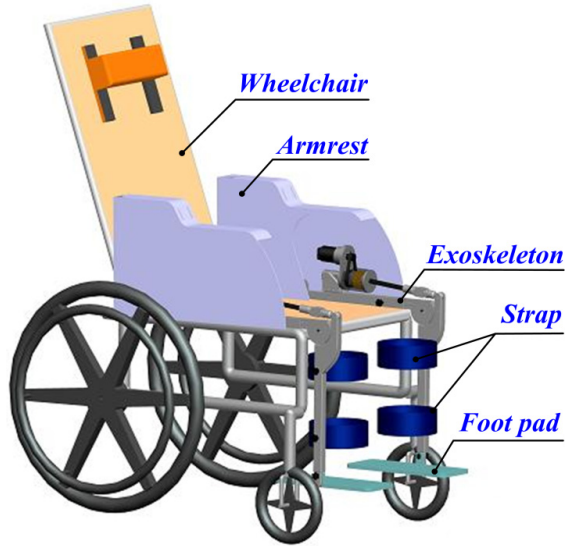


Fig. 2. Basic components of the exoskeleton robot

A hierarchically distributed architecture is employed by the control system, as shown in Fig. 3. It comprises three hardware parts: the high level PC, low level control unit and exoskeleton. Considering different gaits are needed to adapt to the patients, all four driven joints of the exoskeleton can be precisely controlled independently. For each driver, an individual position-velocity-current controller loop has been implemented on the distributed micro servo motor amplifiers. The close-loop control runs on each amplifier in real time. The information of limit switches on each joint is collected by the I/O port on the micro servo motor amplifiers. Host PC and distributed micro servo motor amplifiers communicate with each other through the CAN bus.

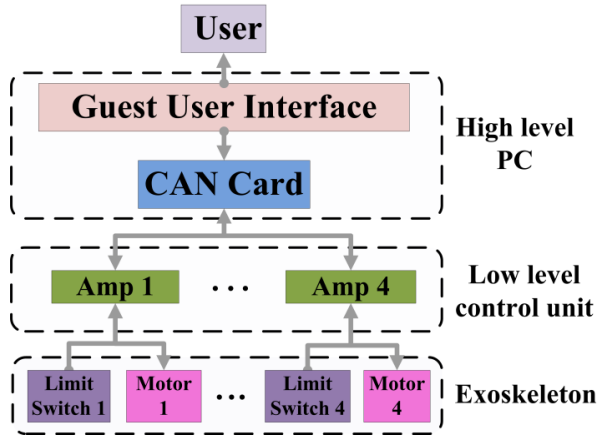


Fig. 3. Control system architecture of lower limb exoskeleton

Safety is one of the most important issues in human-machine system design. The safety of this exoskeleton robot is guaranteed by both hardware and software assurance. The hardware assurance includes mechanical angle limitation and limit switch in each joint according to human motion data and an emergency switch easily handled by the therapist. The software assurance sets up the angle and current limitations in four motors respectively, and an emergency program to deal with mechanical or motor failures.

3 Implementation of Recumbent Cycling Modality

An anthropomorphic and comfortable gait pattern is crucial to the therapeutic outcome during training session [23]. Other than the walking gait pattern obtained from healthy people through motion capture system, the standard recumbent cycling gait pattern can be calculated from the simplified kinematic model of one leg since the two legs have the same structure, as shown in Fig. 4.

The kinematic model includes two actuated joints, i.e. hip joint O_1 and knee joint O_2 , and two links representing thigh and shank. The trajectory of ankle joint O_3 forms a virtual circle, the center of which is C . Since the positions of hip joint O_1 and centre of circle C are fixed, and ankle joint O_3 moves along the virtual circle, the vector equation of the closed chain is shown as:

$$\overline{O_1O_2} + \overline{O_2O_3} + \overline{O_3C} = \overline{O_1O} + \overline{OC} \tag{1}$$

Projecting equation (1) onto the X and Y axis respectively obtains:

$$l_1 \cos \theta_1 + l_2 \cos \theta_2 + l_3 \cos \theta_3 = l_3 \tag{2}$$

$$l_1 \sin \theta_1 - l_2 \sin \theta_2 - l_3 \sin \theta_3 = -l_4 \tag{3}$$

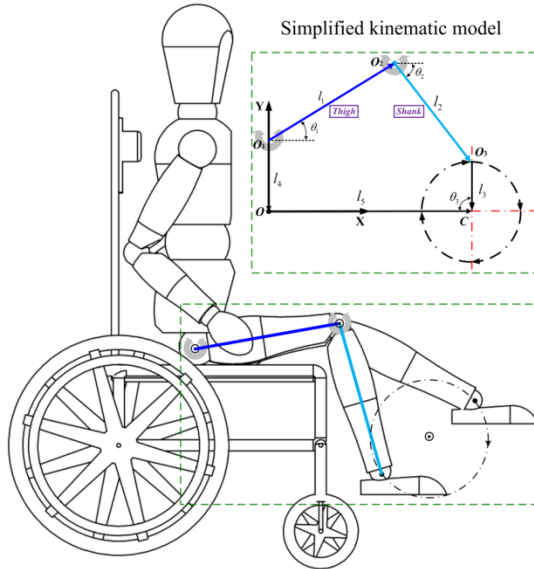
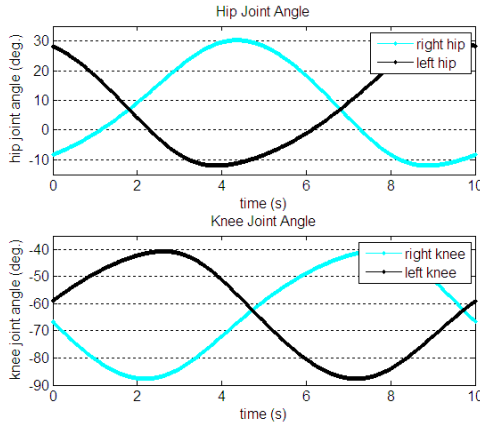
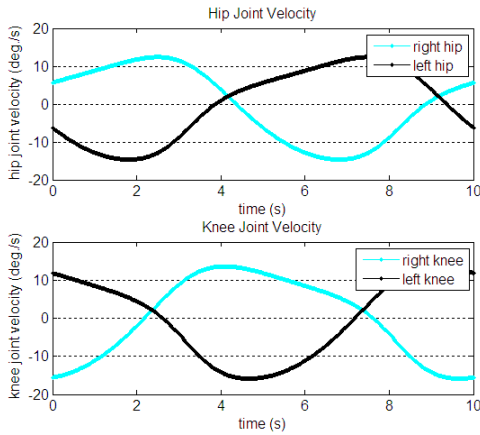


Fig. 4. Simplified kinematic model of lower limb exoskeleton

Where l_1 , l_2 , l_3 , l_4 and l_5 are length of thigh, length of shank, radius of virtual circle, vertical and horizontal distance between hip joint O_1 and center of virtual circle C . According to human dimensions standard [20], different combinations of l_1 and l_2 are used to accommodate to the different human body sizes. l_3 , l_4 and l_5 are determined by the position and radius of the virtual circle, here $l_3=150mm$, $l_4=230mm$ and $l_5=650mm$. Ankle joint θ_3 is determined by the angular velocity of circular motion of O_3 expressed as w , which is set according to the assessment of patient’s motor ability. Hence given a set of length of thigh, length of shank and angular velocity respectively, i.e. l_1 , l_2 and w , the joint angle θ_1 and θ_2 can be calculated through equation (2) and (3). Once the joint motion of one leg is obtained, the other leg can be calculated easily by phase-lag of π . Here the right leg ahead of left one is chosen. Fig. 5 shows the hip and knee joint angle (a) and velocity (b) of two legs respectively when $l_1=465mm$, $l_2=400mm$ and $w=\pi/5rad/s$. The obtained position-velocity-time (PVT) data of four joints is served as input to four motors respectively, which controls the execution of recumbent cycling modality.



(a)



(b)

Fig. 5. Hip and knee joint angle (a) and velocity (b) profile

4 Experiment and Discussion

Clinical experiments were carried out to testify the feasibility and effectiveness of the lower limb exoskeleton using recumbent cycling modality. Two stable post-stroke patients (see Table 3) participated in the experiments under the supervision of professional therapist. Informed consent was obtained. The training procedure of each patient lasted for 30 minutes.

Table 3. Patients information

Rank	Gender	Age	Height (cm)	Weight (kg)	MRC grade
1	M	85	162	51	Left: 3 Right: 0
2	F	61	157	56	Left: 1 Right: 4

Fig. 6 shows the male patient wearing the lower limb exoskeleton during rehabilitation training. This patient is right hemiplegia with right MRC grade 0, which means the right leg couldn't generate any active movement. The preparation procedure before training was simple and less time consuming when compared with body weight suspension. During the training procedure, the patient followed the recumbent cycling gait pattern passively and no joint or muscle pain appeared. The comfort and safety of exoskeleton system and recumbent cycling modality are verified.

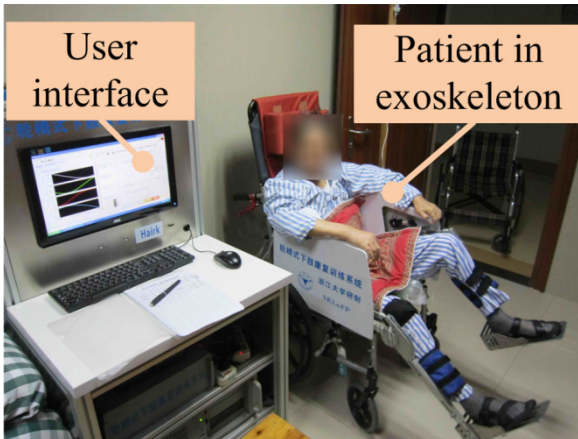


Fig. 6. Experiment setup of lower limb exoskeleton system

Fig. 7 shows the motor torque of hip and knee joints in female patient during movement training. An interesting phenomenon can be discovered that motor torque of the unaffected leg showed more fluctuation than the hemiplegic one. This may attribute to the active motion during leg movement when the patients were asked to move freely according to their own wishes. The preliminary results obtained are encouraging, and more experiments are in progress to provide more clinical data for further analysis.

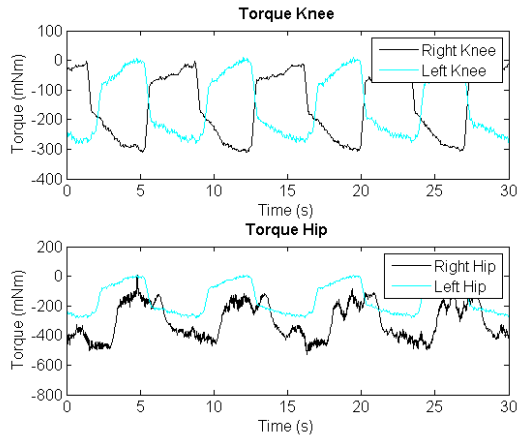


Fig. 7. Motor torque of knee and hip joints of the female patient

5 Conclusion

A lower limb exoskeleton mounted on a wheelchair for motor rehabilitation of severe post-stroke patients was presented. Unlike the common walking gait pattern, the exoskeleton employed recumbent cycling modality to provide more comfortable and safe training through supporting most of human upper body weight with adjustable inclination backrest. Hardware and software assurance were implemented to ensure training safety. A simplified kinematic model of the exoskeleton mechanism was obtained to calculate the recumbent cycling gait. Two post-stroke patients involved in the clinical experiments under the supervision of therapist to testify the exoskeleton system. The preparation procedure was simple when compared with suspension in body weight support treadmill training. Both patients accomplished the experiments successfully and showed no discomfort or pain. The results encourage the promising application of recumbent cycling modality in robotic rehabilitation.

In future work, an active ankle joint to provide more natural recumbent cycling gait pattern is needed. Besides, passive movement training is not suitable for patients regaining some motor ability. To stimulate the locomotor potential and initiative participation of these patients, active control strategy combing with virtual reality may provide better solution.

Acknowledgment. The authors would like to thank Science Fund for Creative Research Groups of National Natural Science Foundation of China under Grant No. 51221004. Also, the suggestion and help during clinical experiments provided by Dr. Bing Xu, Jie Chen, Donghai Wang and Qian Bi are greatly appreciated.

References

1. Kwakkel, G., Wagenaar, R.C., Twisk, J.W., Lankhorst, G.J., Koetsier, J.C.: Intensity of leg and arm training after primary middle-cerebral-artery stroke: a randomised trial. *The Lancet* 354, 191–196 (1999)
2. Post-Stroke Rehabilitation Fact Sheet, <http://www.ninds.nih.gov>
3. Musicco, M., Emberti, L., Nappi, G., Caltagirone, C.: Early and long-term outcome of rehabilitation in stroke patients: the role of patient characteristics, time of initiation, and duration of interventions. *Archives of Physical Medicine and Rehabilitation* 84, 551–558 (2003)
4. Smith, M., Garraway, W., Smith, D., Akhtar, A.: Therapy impact on functional outcome in a controlled trial of stroke rehabilitation. *Archives of Physical Medicine and Rehabilitation* 63, 21–25 (1982)
5. Freburger, J.K.: An analysis of the relationship between the utilization of physical therapy services and outcomes for patients with acute stroke. *Physical Therapy* 79, 906–918 (1999)
6. Committee, M.R.C.N.I., Riddoch, G.: Aids to the investigation of peripheral nerve injuries. HM Stationery Off. (1943)
7. Hesse, S., Bertelt, C., Schaffrin, A., Malezic, M., Mauritz, K.-H.: Restoration of gait in nonambulatory hemiparetic patients by treadmill training with partial body-weight support. *Archives of Physical Medicine and Rehabilitation* 75, 1087–1094 (1994)
8. Jezernik, S., Colombo, G., Keller, T., Frueh, H., Morari, M.: Robotic Orthosis Lokomat: A rehabilitation and research tool. *Neuromodulation: Technology at the Neural Interface* 6, 108–115 (2003)
9. Frey, M., Colombo, G., Vaglio, M., Bucher, R., Jorg, M., Riener, R.: A novel mechatronic body weight support system. *IEEE Transactions on Neural Systems and Rehabilitation Engineering* 14, 311–321 (2006)
10. Mazzocchio, R., Meunier, S., Ferrante, S., Molteni, F., Cohen, L.G.: Cycling, a tool for locomotor recovery after motor lesions? *NeuroRehabilitation* 23, 67–80 (2008)
11. Johnston, T.E.: Biomechanical considerations for cycling interventions in rehabilitation. *Physical Therapy* 87, 1243–1252 (2007)
12. Gregor, S.M., Perell, K.L., Rushatakankovit, S., Miyamoto, E., Muffoletto, R., Gregor, R.J.: Lower extremity general muscle moment patterns in healthy individuals during recumbent cycling. *Clinical Biomechanics* 17, 123–129 (2002)
13. Kerr, A., Rafferty, D., Moffat, F., Morlan, G.: Specificity of recumbent cycling as a training modality for the functional movements; sit-to-stand and step-up. *Clinical Biomechanics* 22, 1104–1111 (2007)
14. Schmidt, H., Piorko, F., Bernhardt, R., Kruger, J., Hesse, S.: Synthesis of perturbations for gait rehabilitation robots, pp. 74–77. *IEEE* (2005)
15. Veneman, J.F., Kruidhof, R., Hekman, E.E.G., Ekkelenkamp, R., Van Asseldonk, E.H.F., van der Kooij, H.: Design and evaluation of the LOPES exoskeleton robot for interactive gait rehabilitation. *IEEE Transactions on Neural Systems and Rehabilitation Engineering* 15, 379–386 (2007)
16. Ym, D.: Study and realization of the training control system of a rehabilitation exoskeleton orthosis for lower limbs. Master. Zhejiang University (2008)
17. Hesse, S.: Treadmill training with partial body weight support after stroke: a review. *NeuroRehabilitation* 23, 55–65 (2008)
18. Hwang, B., Jeon, D.: A wheelchair integrated lower limb exercise/rehabilitation system: Design and experimental results on the knee joint. In: 2012 IEEE/SICE International Symposium on System Integration (SII), pp. 164–169. *IEEE* (2012)

19. Rupp, R., Plewa, H., Hofer, E.P., Knestel, M.: MotionTherapy@ Home-A robotic device for automated locomotion therapy at home, pp. 395–400. IEEE (2009)
20. China, S.B.o.T.S.o.: Human dimensions of Chinese adults. GB 10000-88 (1989)
21. Pons, J.L.: Wearable robots: biomechatronic exoskeletons. Wiley Online Library (2008)
22. Basmajian, J., Kukulka, C., Narayan, M., Takebe, K.: Biofeedback treatment of foot-drop after stroke compared with standard rehabilitation technique: effects on voluntary control and strength. *Archives of Physical Medicine and Rehabilitation* 56, 231–238 (1975)
23. Hidler, J., Wisman, W., Neckel, N.: Kinematic trajectories while walking within the Lokomat robotic gait-orthosis. *Clinical Biomechanics* 23, 1251–1259 (2008)

An Open-Source Development and Simulation Platform for Smart Wheelchairs

Wenlong Liao^{1,2}, Weidong Chen^{1,2}, Zhixuan Wei^{1,2}, Wenxi Zhang^{1,2},
Jingchuan Wang^{1,2}, and Kang Li³

¹ Department of Automation, Shanghai Jiao Tong University,
and Key Laboratory of System Control and Information Processing,
Ministry of Education of China, Shanghai 200240, China

² State Key Laboratory of Robotics and System (HIT), Harbin 150001, China

³ Electrical Engineering and Computer Science,
Queen's University Belfast, Belfast BT9 5AH, UK
wdchen@sjtu.edu.cn

Abstract. Simulator for smart wheelchairs is of great significance for both driver training and algorithm design. A development and simulation platform for wheelchairs is presented in this paper. On this platform, simulations of kinematics, dynamics and sensors are integrated, and a virtual prototype of wheelchair and virtual world are modded also. The sensors include encoders, a laser range finder and a set of Kinect. This platform is implemented in Gazebo and ROS, and is completely open source and freely available. Experiments verifies that this platform can be used as a valid tool for driver training and algorithm design.

Keywords: Simulation, Smart Wheelchair, Driver Training, Algorithm Design.

1 Introduction

Increasing the mobility of individuals with mobile dysfunction, powered wheelchairs can ensure them a more independently life. However, enough driving skills are required to assure them of operating wheelchairs safely. A simulation system providing driver training is urgently necessary for these users. On the other hand, due to the insufficient of powered ones, several smart wheelchairs have been developed over the past decades [1-4]. However, high costs of hardware equipment and poor test repeatability make it difficult to design and optimize the algorithms for smart wheelchairs. The development and simulation platform for smart wheelchairs can meet the demands for shortening the development cycle of a new algorithm and reducing the costs of experiments.

A virtual reality based 3D simulator for wheelchairs was presented in [5]. However, the simulator only works in 2D world, without including dynamics and sensor modeling. In [6], a stair climbing wheelchair was modeled and simulated to validate the stair climbing feasibility. It only focuses on stair climbing wheelchair which is different with powered one. An interactive wheelchair training system that adjusted the position of the wheelchair on the screen according to the rotation speeds of wheelchair's wheels was developed in [7]. Nevertheless, the system only takes kinematics into

consideration, which is very rough in nature. In [8] and [9], a multi-agent based simulator for hardware test and development was described. It created a mixed reality and achieved an interaction between the real and virtual worlds. However, without physical engine, its collision detection and dynamics are limited to a specified case: the robot's shape has to be defined in mathematical equations, and the model of wheelchair is simplified as a mass point with motors. Another limitation is that only proximity sensors are implemented.

Integrating simulations of kinematics, dynamics and sensors, a comprehensive platform for both driver training and algorithm design of wheelchair is presented in this paper. It realistically mimics the characteristics of wheelchair, and takes care of the interactions between the wheelchair and the world. Different from previous works, this platform is completely open source and freely available. Therefore, smart wheelchair developers can quickly modify the package to meet their ever-changing needs. Driver training and shared control algorithm experiments, which are carried out on this platform, validates its feasibility.

2 System Structure

Based on heavily modified, commercially available power wheelchairs [10], the majority of smart wheelchairs are quite similar in hardware. Generally, they have two differentially driven rear wheels with motors and encoders. Laser range finders (LRF) and vision sensors are the common sensors for smart wheelchairs [10]. As to vision sensors, only the Kinect is taken into consideration since it consists of an IR camera and a RGB camera. As shown in Fig. 1, the hardware structure of JiaoLong smart wheelchair [11-13] is presented. It is a common structure that smart wheelchairs adopt.

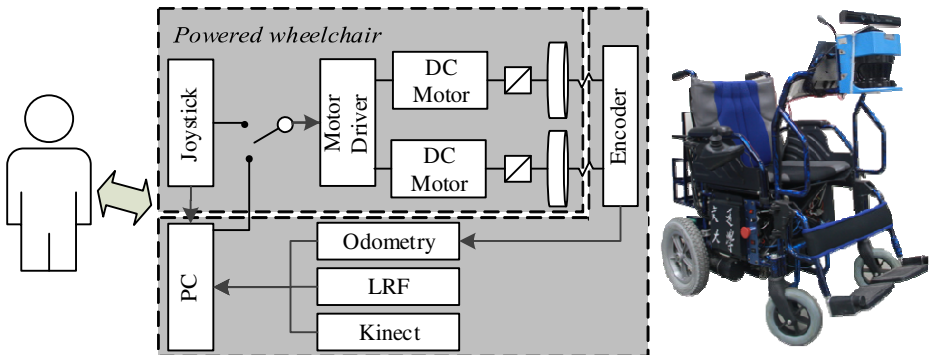


Fig. 1. Hardware structure of JiaoLong smart wheelchair

Fig. 2 shows the software structure of the proposed development and simulation platform. This platform combines a real joystick, virtual wheelchair and virtual world, and achieves a real-time simulation. In a loosely coupling way, client program accesses to the platform through a topic-based pub/sub communication, including getting sensors' data and controlling the speed of wheelchair.

The implementation of this platform makes a use of Gazebo [14, 15] and ROS [16]: the calculations of dynamics and sensors are vastly based on the physical engine ODE and rendering engine OGRE in Gazebo; communication between client programs is implemented in ROS. The modules excluding GUI are dynamically loaded, and can be modified or replaced conveniently according to the specified wheelchair simulated (especially sensors). Since the smart wheelchairs are ever-changing, a platform whose code is not available may not works in such situations. Following the principles established by Gazebo and ROS, this platform is completely open-source, and maintains a brief API for developer and a friendly GUI for end user.

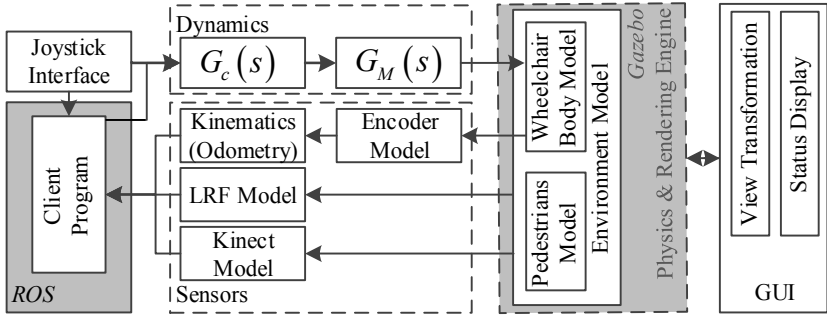


Fig. 2. Software structure of the development and simulation platform

3 Kinematics and Dynamics

3.1 Kinematics

The kinematics equation for the wheelchair is described as follows:

$$\begin{bmatrix} \dot{x} \\ \dot{y} \\ \dot{\theta} \end{bmatrix} = \begin{bmatrix} \cos \theta & 0 \\ \sin \theta & 0 \\ 0 & 1 \end{bmatrix} \begin{bmatrix} v \\ \omega \end{bmatrix} . \tag{1}$$

Where, (x, y, θ) is the position of the wheelchair, and (v, ω) the linear velocity and angular velocity of the wheelchair.

(v, ω) is derived from rotating speeds of two driving wheels which is treated as the controlled variables:

$$\begin{bmatrix} v \\ \omega \end{bmatrix} = \begin{bmatrix} \frac{r}{2} & \frac{r}{2} \\ \frac{r}{b} & -\frac{r}{b} \end{bmatrix} \begin{bmatrix} \omega_R \\ \omega_L \end{bmatrix} . \tag{2}$$

Where (r, b) is the diameter and spacing of two driving wheels.

3.2 Dynamics

There are a couple of approaches for mobile robot dynamic simulation. The whole physical process is simulated by physical engine in the first approach, such as ODE, Bullet, etc. The precise simulated effect (such as collision process) can be achieved by this approach when the physical quantity within the dynamic model is known. However in practice, part of physical quantity is difficult to obtain, and some characteristics of simulated object cannot be indicated through rigid body dynamics, such as time delay.

In the second approach, through collections of the identification of model parameters of system responses, the entirety of a robot is simulated. Being simplified, the approach avoids the measurement of all parts of a robot, and the error depends on the fitting precision of the established model. However, constant payload, and no external collisional force involved are assumed in this approach, which leads to inapplicability in practice.

Based on the synthesization of these approaches, modeling analysis of the wheelchair is carried out at first in this paper, and then the wheelchair dynamic model is divided into electric machinery model, wheelchair body model (WBM), and regulated model, where the regulated model not only compensates the errors within the electric machinery and WBM, and mirrors the characteristics of coupling of wheelchair system, and time delay, etc. as well.

The powered wheelchair can be expressed as a multivariable system, and its dynamic equation [17] is described as:

$$\begin{bmatrix} \omega_R(s) \\ \omega_L(s) \end{bmatrix} = \begin{bmatrix} g_{11}(s) & g_{12}(s) \\ g_{21}(s) & g_{22}(s) \end{bmatrix} \begin{bmatrix} u_R(s) \\ u_L(s) \end{bmatrix} = G(s) u(s) . \tag{3}$$

Where, $u = [u_R(s) \quad u_L(s)]^T$ is the input of actuator.

The wheelchair is regarded as a servo system, and each term of (3) is obtained as:

$$g_{ij} = \frac{M(s)}{N(s)} e^{-\tau_{ij}s}; i, j = 1, 2 . \tag{4}$$

The influences from payload and the external force to the dynamics of the wheelchair can be amounted to the electric machinery model. Thus, the system is separated into three parts: electric machinery (with reduce) $G_M(s)$, WBM $G_0(s)$ and regulated part $G_c(s)$, depicted as whole as:

$$G(s) = G_c(s) G_M(s) G_0(s) . \tag{5}$$

It is clear that $G_0(s)$ and $G_c(s)$ remain constant in different situations.

The output moment model from electric machinery model is described by the follow equations, with ignorance of the inductance of electric machinery:

$$\begin{cases} T_R = K_r (u_R - K_{fr} \omega_R) \\ T_L = K_L (u_L - K_{fL} \omega_L) \end{cases} \quad (6)$$

Where, T_* is the output torque of the left or right motor, K_* the torque constant, and K_{f*} the back EMF constant.

With WBM taken account, we have:

$$\begin{cases} J_z \dot{\omega} = \frac{b}{2r} (T_R - T_L) \\ M \begin{bmatrix} \ddot{x} \\ \ddot{y} \end{bmatrix} = \frac{1}{r} \begin{bmatrix} \cos \theta & \cos \theta \\ \sin \theta & \sin \theta \end{bmatrix} \begin{bmatrix} T_R \\ T_L \end{bmatrix} \end{cases} \quad (7)$$

Where, M and J_z are the mass and moment of inertia of the wheelchair body respectively.

Equation (3) and (4) describe the dynamics of the whole wheelchair model, which is determined by the input-output data fitting from the experiments, and where K_{f*} and M are obtained from measurements, K_* , J_z from identifications. With the compensation of $G_C(s)$, errors to some extent are allowed for the physical quantities just mentioned.

3.3 Parameter Identification

The parameter identification is carried out on JiaoLong smart wheelchair. Parameters of kinematics are simple to acquire, with $r = 0.153 \text{ m}$ and $b = 0.580 \text{ m}$.

As shown in Fig. 3, an uncertain multivariable model for this system is developed through applying inputs (ranges between 0 V and 1 V) to the wheelchair. Classified in two situations, the dynamic models are obtained, where $G(s)|_a$ stands for the start of wheelchair (the wheelchair is stopped at present, and is ordered to move), and $G(s)|_b$ for the normal mode. These models are described as follows:

$$\begin{aligned} G(s)|_a &= e^{-1.143s} G(s)|_b \\ G(s)|_b &= \frac{1}{1.468s^2 + 2.095s + 1} \begin{bmatrix} (1.355s + 1)e^{-0.2s} & 0.551se^{-0.1s} \\ 0.551se^{-0.1s} & (1.355s + 1)e^{-0.2s} \end{bmatrix} \end{aligned} \quad (8)$$

It can be found that the difference between $G(s)|_a$ and $G(s)|_b$ is the 1.143 seconds delay, which is designed to prevent abnormal start caused by misuse.

Table 1 shows the main physical parameters of the proposed model. M and J_z are adjusted to the user's weight (61 kg), in which J_z is estimated based on the method presented in [18].

Table 1. Parameter of wheelchair dynamics

K_*	K_{f*}	M	J_z
4.22 $V \cdot s^{-1}$	1.031 $N \cdot m \cdot V^{-1}$	112 kg	16.45 $kg \cdot m^2$

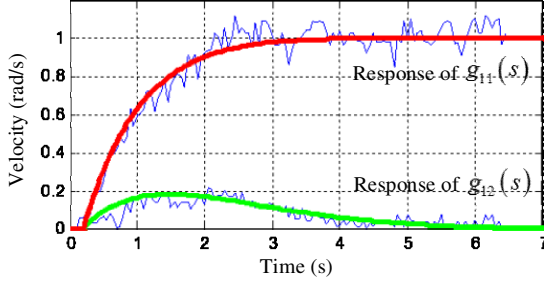


Fig. 3. The responses of simulation and real system in normal mode

According to the equation (5), the regulated model can be expressed as:

$$G_c(s) \Big|_a = e^{-1.143s} G_c(s) \Big|_b$$

$$G_c(s) \Big|_b = \frac{(2.404s + 1)(0.302s + 1)}{1.468s^2 + 2.095s + 1} \begin{bmatrix} e^{-0.2s} & 0.5241e^{-0.1s} \\ 0.524e^{-0.1s} & e^{-0.2s} \end{bmatrix}. \tag{9}$$

This transfer matrix and motor model are discretized and then implemented.

4 Sensor Models

Sensor noise is always inevitable in the real situation. Therefore, the error model of the sensors should be built to handle the measurement in the simulation.

4.1 Encoder

Encoders are used to measure the speed of driving wheels, and the lines per period (LPP) method [19] is commonly used. The model of velocity measurement can be derived as follows:

$$\hat{\omega}_k = \frac{2\pi}{nN\Delta T} \left(\text{floor} \left(\frac{nN\theta_k}{2\pi} \right) - \text{floor} \left(\frac{nN\theta_{k-1}}{2\pi} \right) \right). \tag{10}$$

Where, ω is the angular speed of the wheel, n the transmission ratio between the wheel and encoder, θ the angle of wheel, ΔT the measurement cycle, and $\text{floor}(\cdot)$ the rounded down function.

4.2 Laser Range Finder

The error of laser range finder mainly consists of flicker noise and white noise [20]:

$$\begin{cases} \delta r = x + v \\ T\ddot{x}(t) + x(t) = \varepsilon(t), \varepsilon \sim N(0, \mu_\varepsilon) \end{cases} \quad (11)$$

Where, x is a Gauss-Markov process, and v a white noise whose mean is 0 and variance is μ .

4.3 Kinect

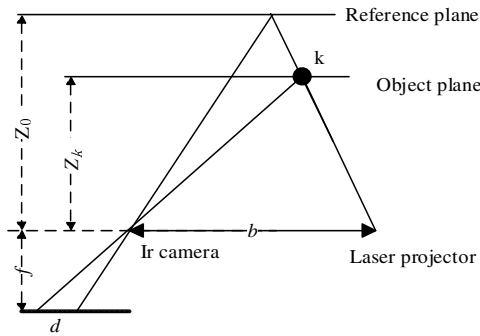


Fig. 4. Operating principle of the Kinect [21]

The Kinect is simulated and replaced by depth camera of Gazebo in the platform. Its' principle can be described as Fig. 4, and the calculation process [21] is shown as:

$$\begin{cases} Z_k = \frac{Z_0 \cdot f \cdot b}{fb + Z_0 d} \\ X_k = -\frac{Z_k}{f} x_k \\ Y_k = -\frac{Z_k}{f} y_k \end{cases} \quad (12)$$

Where, (X_k, Y_k, Z_k) is the coordinates of the measured point k , Z_0 the depth of reference plane, f the focal length of the infrared camera, b the base length, d the observed disparity in image space, and (x_k, y_k) the coordinates of point k in the image plane.

Noting the geometric relationship, we have:

$$d = \sqrt{x_k^2 + y_k^2} \quad (13)$$

To facilitate the analysis, that x_k and y_k follow the normal distribution, and are independent of the other is assumed. According to the error propagation model, the error of the Kinect can be described as:

$$\begin{cases} \delta Z_k = -\frac{z_0}{fd\eta^2}(x_k \delta x_k + y_k \delta y_k), \eta = 1 + \frac{Z_0 d}{fb} \\ \delta X_k = \frac{z_0}{fd\eta^2}((x_k - \eta d) \delta x_k + y_k \delta y_k) \\ \delta Y_k = \frac{z_0}{fd\eta^2}(x_k \delta x_k + (y_k - \eta d) \delta y_k) \end{cases} \quad (14)$$

Where, δx_k and δy_k are the error of x_k and y_k respectively.

5 3D Model of Wheelchair and World

Various tools can be used to design the CAD model of wheelchair and world. SolidWorks is chosen to draw the 3D model of wheelchair, which is shown in Fig. 5-a. In order to control the six joints of the wheelchair, the body, shafts, front and rear wheels are drawn separately.



a) 3D model of the wheelchair.

b) 3D model of Virtual World.

Fig. 5. 3D wheelchair model and world model

It should be noted that all processes including rendering and dynamics must be finished in a step cycle (1 millisecond on this platform). To reduce the computational complexity, two different models are designed for the rendering engine and physics engine. A complex model with many triangle meshes is used for rendering. The other model composed of simple shapes including boxes and cylinders is used for collision detection and dynamics calculation. In this way, computing load can be reduced significantly without sacrificing the simulation precision.

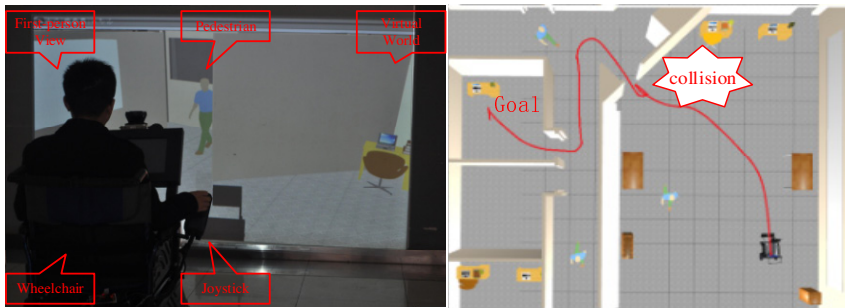
In order to simulate the actual scene, both the static and dynamic characteristics of world are modeled. The static characteristics refer to stationary objects such as furniture, doors and walls. Described in the COLLADA format [22], these objects are composed of complex shapes and materials with transparency and texture. Some popular 3D modeling software including Google SketchUp and 3D Studio Max are used to synthesize them in a same scene. As the dynamic characteristics, random pedestrians are modeled in the scene, and their behavior is roaming with obstacle avoidance.

6 Applications

The proposed platform can be used in many contexts. Two examples that applies it to driver training and designing control algorithm are presented below.

6.1 Driver Training

As shown in Fig. 6-a, the development and simulation platform combined with JiaoLong smart wheelchair and a projector can be used for driver training. User moves the joystick of the wheelchair whose signal is sampled by the platform. According to the user's command, the motion of wheelchair is simulated and the first person view is projected. Simultaneously, user's operations, navigation path and collisions are recorded to evaluate the driving habits and skills.



a) The driver training system.

b) The virtual world and navigation path.

Fig. 6. Driver training on the development and simulation platform

As shown in Fig. 6-b, an indoor simulation scene where some pedestrians are roaming is designed to train the user. The user is asked to drive the wheelchair from the initial position, pass the door and corridor, and dock at the desk. During this period, the user should avoid the pedestrians and other obstacles. The navigation path driven by a newbie is shown in Fig. 6-b. There is a collision occurred because the user cannot turn the wheelchair with large inertial promptly.

6.2 Development of Client Program

Due to the limitation of test environments and available users, design and optimization of new algorithms for smart wheelchair is somehow difficult. In this situation, the proposed platform can shorten the development cycle and reduce the experimental costs. This part takes the semantic map based shared controller [23], which is tested and verified on the platform, as an example.

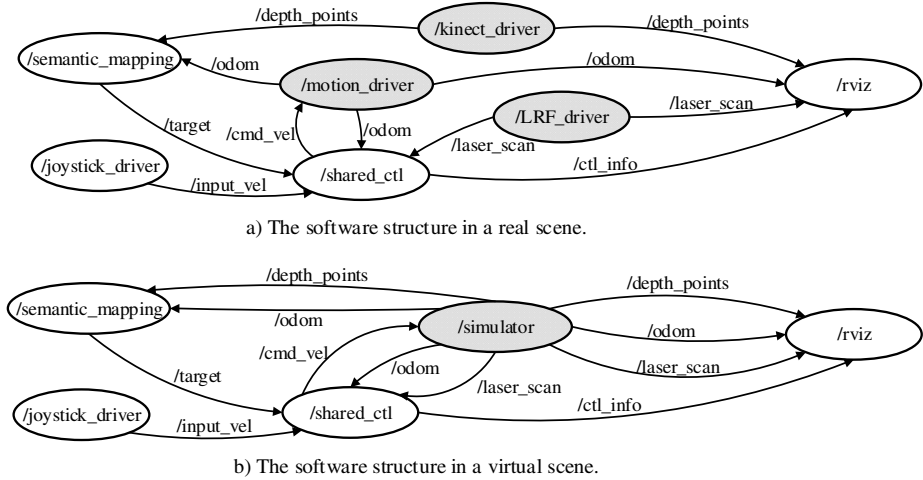


Fig. 7. The software structures of the system combined with the shared controller

The software structures of the system in real and virtual scene can be found in Fig. 7. Obviously, the only difference between them is that the simulator replaces the hardware related modules in the real scene. In this sense, the steps to develop a new algorithm can be described as follows:

- a) Implement the algorithm in ROS (just like the way in a real scene);
- b) Simulate and optimize the algorithm on the platform until the goal is achieved;
- c) Replace the simulator with the drivers for hardware (only the executable files), and the algorithm is applicable now.

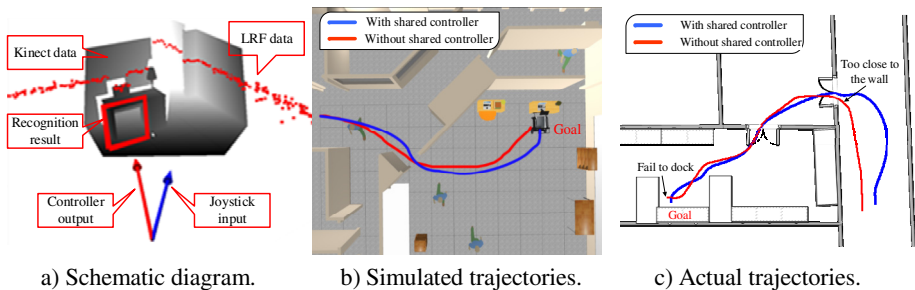


Fig. 8. The results of the wheelchair with and without application of the controller

Fig. 8-a illustrates how the controller works. It builds a local 3D semantic map through the Kinect. Combining this map and the joystick input, the controller achieves an object related navigation with obstacle avoidance. As shown in Fig. 8-b, the user tries to drive and dock the wheelchair at the destination desk from the initial position. Both of the trajectories of the wheelchair with and without the application of the controller can be found in Fig. 8-b. The wheelchair with the controller can pass through

the doorway safely and dock precisely, while it turns to a danger or a failure when the controller is not used.

Compared with the trajectories in a real scene shown in Fig. 8-c, the characteristics that have been described above are similar. Some differences between the experiments in a real and a virtual scene should be pointed out as well: a) the real-time performance of the platform depends on the computer hardware, especially when the Kinect is simulated, so a computer with high performance is recommended; b) the results of the simulation is seemly better with less noise of sensors (for example, the slip of wheels is ignored in the virtual scene). Despite these drawbacks, the platform can be a useful tool for algorithm design with sensors and dynamics implemented in the platform.

7 Conclusion

A development and simulation platform for both drive training and algorithm design is designed and implemented in this paper. The software structure is proposed with the analysis of the hardware of smart wheelchairs, followed by a detail modeling for dynamics, sensors and world. The platform is implemented in Gazebo and ROS, and is completely open source and freely available. Both developers and end users of smart wheelchairs can benefit from this platform.

Two applications including driver training and algorithm design are presented. Experiments show the effectiveness of the proposed platform, and it can be used for driver training and algorithm design.

Acknowledgments. This work is partly supported by the National High Technology Research and Development Program of China under grant 2012AA041403, the Natural Science Foundation of China under grant 60934006 and 61175088, the State Key Laboratory of Robotics and System (HIT), the Research Fund for the Doctoral Program of Higher Education under grant 20100073110018.

References

1. Rebsamen, B., Guan, C., Zhang, H.H., Wang, C.C., Teo, C., Ang, M.H., Burdet, E.: A Brain Controlled Wheelchair to Navigate in Familiar Environments. *IEEE Trans. Neural Syst. Rehabil. Eng.* 18(6), 590–598 (2010)
2. Li, Q.N., Chen, W.D., Wang, J.C.: Dynamic Shared Control for Human-Wheelchair Cooperation. In: *IEEE International Conference on Robotics and Automation*, pp. 4278–4283. IEEE Press, Shanghai (2011)
3. Levine, S.P., Bell, D.A., Jaros, L.A., Simpson, R.C., Koren, Y., Borenstein, J.: The NavChair Assistive Wheelchair Navigation System. *IEEE Trans. Rehabil. Eng.* 7(4), 443–451 (1999)
4. Simpson, R., LoPresti, E., Hayashi, S., Nourbakhsh, I., Miller, D.: The Smart Wheelchair Component System. *J. Rehabil. Res. Dev.* 41(3B), 429–442 (2004)
5. Niniss, H., Nadif, A.: Simulation of the Behaviour of a Powered Wheelchair Using Virtual Reality. In: *3rd International Conference on Disability, Virtual Reality and Associated Technologies*, pp. 9–14. University of Reading Press, Algher (2000)

6. Ito, T.: Simulation-Based Study Using a Stair Climbing Wheelchair. In: 3rd Asia International Conference on Modelling and Simulation, pp. 537–542. IEEE Press, Baiti (2009)
7. Lin, C.-S., Chang, C.-C., Chen, W.-L.: Design and Application of an Interactive Wheelchair Training System. *Biomed. Eng. App. Bas. C.* 20(6), 377–385 (2008)
8. Braga, R.A.M., Malheiro, P., Reis, L.P.: Development of a Realistic Simulator for Robotic Intelligent Wheelchairs in a Hospital Environment. In: Baltes, J., Lagoudakis, M.G., Naruse, T., Ghidary, S.S. (eds.) *RoboCup 2009*. LNCS, vol. 5949, pp. 23–34. Springer, Heidelberg (2010)
9. Braga, R., Petry, M., Reis, L.P., Moreira, A.: IntellWheels: Modular Development Platform for Intelligent Wheelchairs. *J. Rehabil. Res. Dev.* 48(9), 1061–1076 (2011)
10. Simpson, R.C.: Smart Wheelchairs: A Literature Review. *J. Rehabil. Res. Dev.* 42(4), 423–438 (2005)
11. Wang, Y., Chen, W.D.: Hybrid Map-Based Navigation for Intelligent Wheelchair. In: IEEE International Conference on Robotics and Automation, pp. 637–642. IEEE Press, Shanghai (2011)
12. Wang, W., Chen, W.D., Wang, Y.: Probabilistic Grid Map Based Localizability Estimation for Mobile Robots. *Robot* 34(4), 485–491 (2012) (in Chinese)
13. Wang, Y., Chen, W.D., Wang, J.C., Wang, W.: Improved Particle Filter Localization in Crowded Environments for Mobile Robots. *Robot* 34(5), 596–603 (2012) (in Chinese)
14. Koenig, N., Howard, A.: Design and Use Paradigms for Gazebo, An Open-Source Multi-Robot Simulator. In: IEEE/RSJ International Conference on Intelligent Robots and Systems, pp. 2149–2154. IEEE Press, Sendai (2004)
15. Gazebo, <http://gazebo.org>
16. Robot Operating System (ROS), <http://www.ros.org/wiki>
17. Nguyen, T.N., Su, S.W., Nguyen, H.T.: Robust Neuro-Sliding Mode Multivariable Control Strategy for Powered Wheelchairs. *IEEE Trans. Neural Syst. Rehabil. Eng.* 19(1), 105–111 (2011)
18. GB/T 17245—2004, Inertial Parameters of Adult HumanBody (in Chinese)
19. Brown, R.H., Schneider, S.C., Mulligan, M.G.: Analysis of Algorithms for Velocity Estimation from Discrete Position Versus Time Data. *IEEE Trans. Ind. Electron.* 39(1), 11–19 (1992)
20. Jain, S., Nandy, S., Chakraborty, G., Kumar, C.S., Ray, R., Shome, S.N.: Error Modeling of Laser Range Finder for Robotic Application Using Time Domain Technique. In: IEEE Conference on Signal Processing, Communications and Computation, pp. 1–5. IEEE Press, Xi'an (2011)
21. Khoshelham, K.: Accuracy Analysis of Kinect Depth Data. In: ISPRS Workshop Laser Scanning, pp. 133–138. CRC Press, Calgary (2011)
22. COLLADA - Digital Asset and FX Exchange Schema, <http://collada.org>
23. Wei, Z., Chen, W., Wang, J.: 3D Semantic Map-Based Shared Control for Smart Wheelchair. In: Su, C.-Y., Rakheja, S., Liu, H. (eds.) *ICIRA 2012, Part II*. LNCS, vol. 7507, pp. 41–51. Springer, Heidelberg (2012)

Semantic Mapping for Safe and Comfortable Navigation of a Brain-Controlled Wheelchair

Zhixuan Wei^{1,2}, Weidong Chen^{1,2}, Jingchuan Wang^{1,2}, Huiyu Wang^{1,2}, and Kang Li³

¹ Department of Automation, Shanghai Jiao Tong University, and Key Laboratory of System Control and Information Processing, Ministry of Education of China, Shanghai 200240, China

² State Key Laboratory of Robotics and System (HIT), Harbin 150001, China

³ Electrical Engineering and Computer Science,
Queen's University Belfast, Belfast BT9 5AH, UK
wdchen@sjtu.edu.cn

Abstract. This paper presents a novel navigation system designed for a brain-controlled wheelchair, which interacts with human user by the low throughput interface. The navigation system proposes the semantic map, which is integrated with the navigation points, semantic targets and local 3D map, to a human user who can choose one of the navigation points as a goal for navigation. The semantic targets provide category, geometry and functionality information of the recognized objects, such as a table which can be docked. The local 3D map provides the navigation points in the traversable areas. The human-wheelchair interactive system shows the semantic map to user, and the user selects the goal via a brain-computer interfaces (BCI). Therefore, this method can help the wheelchair implement accurate navigation (e.g. docking) with a low throughput interface and the safety and comfortability are improved. Our navigation system is successfully tested in real environment.

Keyword: Smart Wheelchair, 3D Semantic Map, Brain-Computer Interfaces.

1 Introduction

The smart wheelchairs play more and more important roles in disabled and elderly people's life. Most wheelchairs are controlled by the interface such as joystick, touch screen or voice. For the people who cannot control these interfaces, the brain-computer interfaces (BCI) based on electroencephalography (EEG) is made. But BCI is a low throughput device, whose result is only in a limited number of classes and determined in 0.5-1 Hz [1]. Therefore, it is difficult to control a wheelchair safely and comfortable, using only the outputs of a BCI.

In this paper, a navigation system integrated with semantic mapping is proposed. Semantic mapping is used to extract obstacle, provide the navigation points at the traversable areas, and analyze environment to recognize objects, in order to propose probable action (e.g. docking, door passage) to the user [2, 3]. The user's workload is reduced to choose either a navigation point or a probable action via BCI to control the

wheelchair. In addition, a wheelchair controlled by the navigation system is safer than controlled directly by human user command.

In these years, many brain-controlled wheelchairs were proposed. Carlson et al. [4] developed a vision-based shared control for a BCI wheelchair, in which method, the vision system provided obstacle avoidance and the wheelchair interpreted the high-level BCI commands such as go left and go right. Mandel et al. [5] proposed the combination of a BCI interpreting steady-state visual evoked potentials and an environment analyzing system. This system analyzed a local 2D map to extract the route graphs. The user could choose a route with the four commands of BCI. Iturrate et al. [6] described a brain-controlled wheelchair, on which a screen displayed a real-time virtual reconstruction of the environment and the target location that wheelchair could arrive. The EEG signals of user were processed to detect which target location the user wanted to choose. And then an autonomous navigation system controlled the wheelchair move to the target while avoiding collisions with obstacles. Perrin et al. [7] presented a semi-autonomous navigation for the robot by analyzing the environment to determine the probable action of robot, and the human user can decide whether to implement the action or not. The probable action of robot was extracted by recognizing the places of interest where a human-robot interaction should take place (e.g. crossings). The user could choose the target by means of a button or a brain-computer interface (BCI).

All the methods above can analyze the environment and provide probable routes or actions to user who will choose one of them to drive the wheelchair. But the routes or actions those providing are crude, such as follow a route or turn left. They can hardly implement accurate navigation of the wheelchair, such as docking, which is our aim. Consequently, our navigation system can reduce the operation of user and improve comfortability. Furthermore, as pose and category of the target is known, our navigation system can plan an optimum trajectory, which is safer than the passive obstacle avoidance.

In this article, system architecture of semantic mapping for safe and comfortable navigation of a brain-controlled wheelchair is presented. A local 3D map is built online using Rao-Blackwellized particle filter (RBPF). The local 3D map is used to extract navigation points and semantic targets. The user selects the goal from the navigation points or semantic targets. And the wheelchair is autonomous navigated to the goal. A smart wheelchair equipped with a RGB-D sensor and a laser range finder (LRF) is developed as experimental platform for studying the effectiveness of the proposed method.

2 System Architecture

As shown in Fig. 1, our approach has two loops: human loop and machine loop, and semantic map is the bridge between these two loops. In machine loop, a semantic map including a real-time virtual reconstruction of the local environment, combined with navigation points and semantic targets, is built. In human loop, the user faces a screen displaying the semantic map, and uses EEG signals to select a goal from the navigation points and semantic targets in the semantic map. Once the goal is selected, the motion control module will calculate the speed of wheelchair considering with obstacles.

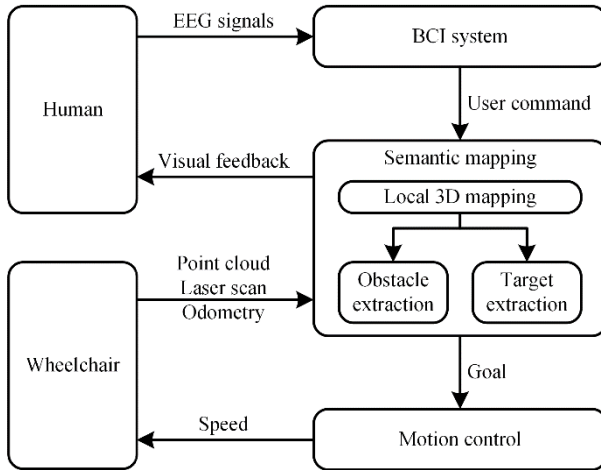


Fig. 1. System architecture

3 BCI System

EEG is one type of biological electrical signals. EEG can be divided into four types of wave: delta (1-3Hz), theta (4-7Hz), alpha (8-13Hz), beta (14-30Hz). The expressions of user have relationship with beta waves, since beta waves with multiple and varying frequencies are often associated with active, busy, or anxious thinking and active concentration [8]. Consequently, the expressions of user can be recognized by BCI to control the navigation system.

A linear classifier is used to recognize the expressions of user. The feature is the integral of energy of a set of channels in a period of time. The first step is feature selection, that we select one set of channels of EEG whose changing are conspicuously associated to one expression. For different expressions, several sets of channels are selected. The second step is to train the system via offline experiments, where user makes some kind of expression several times. The data of selected channels are recorded and used to train the linear classifier. Finally, the trained linear classifier is used to recognize the expression. In this article, four commands (forward, backward, left, right) are recognized and used in our navigation system.

4 Semantic Mapping

The semantic map is a bridge connecting user and machine. It presents a virtual reconstruction of environment additional with navigation information including obstacles, navigation points and semantic targets. The user can select the goal interactively via BCI, referencing the feedback shown on the semantic map, and the motion control module will navigate the wheelchair to the goal.

4.1 Local 3D Mapping

To extract the traversable area and obstacles around the wheelchair, a local 3D map is needed. In this paper, Rao-Blackwellization particle filter (RBPF) [9, 10], an implementation of SLAM problem, is used to localize the pose of wheelchair and build local 3D map. SLAM is a problem that estimates $p(x_{1:t}, m|z_{1:t}, u_{1:t-1})$, the joint distribution over the wheelchair trajectory $x_{1:t}$ and the map m , by sensor observations (laser scans) $z_{1:t}$ and control signals (odometry) $u_{1:t-1}$. Rao-Blackwellization is expressed by the following equality:

$$p(x_{1:t}, m|z_{1:t}, u_{1:t-1}) = p(m|x_{1:t}, z_{1:t}) \cdot p(x_{1:t}|z_{1:t}, u_{1:t-1}). \quad (1)$$

which decouples the trajectory estimation problem $p(x_{1:t}|z_{1:t}, u_{1:t-1})$ from the map computation $p(m|x_{1:t}, z_{1:t})$.

The map computation problem can be solved by assuming that wheelchair trajectory is known and using inverse laser range finder model. The map is stored in a grid map. Each cell of the grid map expresses the probability of occupancy. The occupancy probability of each cell is updated by sensor observations [11]. Rather than directly register the raw data of sensor, the occupancy probability representation can reduce noise of sensor and ignore the dynamic obstacles such as people.

For the trajectory estimation problem above, a non-parametric implementation of the Bayes filter is implemented. The Bayes filter is based on a set of particles. Each particle associates with a weight, and each particle represents a trajectory hypothesis for the wheelchair up to time t . Since we assume that the movement of our wheelchair is restricted in the 2D plane, the trajectory of wheelchair consists of a set of poses $x_{1:t-1} = (x, y, \theta)$, including position and orientation. The particle filter performs following three steps between $p(x_{1:t-1}|z_{1:t-1}, u_{1:t-1})$ and $p(x_{1:t}|z_{1:t}, u_{1:t})$: predicting the pose of wheelchair by the motion model and odometry, updating the weight of particles by matching laser scans, and resampling the distribution of particles if necessary.

In order to building local 3D map online, at each time the SLAM updating the pose of wheelchair, a frame of point cloud obtained by RGB-D sensor is inserted into the local 3D map, and the point clouds, which are obtained far from the current position, are discarded.

4.2 Obstacle Extraction

The obstacles are extracted from the local 3D map in order to mark the navigation points. Since the wheelchair only travel in the 2D ground, the wheelchair can be considered as a cube and all obstacles can be project to the ground. Supposing the wheelchair can go through the obstacle lower than H_{\min} and the height of wheelchair is H_{\max} , the obstacles can be represented by the follow equation:

$$P_{obstacle} = \{(x, y) | (x, y, z) \in P_{3D}, H_{\min} < z < H_{\max}\}. \quad (2)$$

where P_{3D} is the points of local 3D map.

4.3 Semantic Target Extraction

The shape-based method is used to build 3D semantic map, referencing to our previous work [2, 3]. The local 3D map is processed by three steps:

- 1) Data preprocessing: using pass through filter and down-sample to reduce the amount of data;
- 2) Segmentation: using RANSAC algorithm and European clustering to segment the point cloud into horizontal planes and vertical planes;
- 3) Recognition: matching the segments to a priori model library in order to identify the semantic targets.

Finally, the semantic targets are marked on the local 3D map.

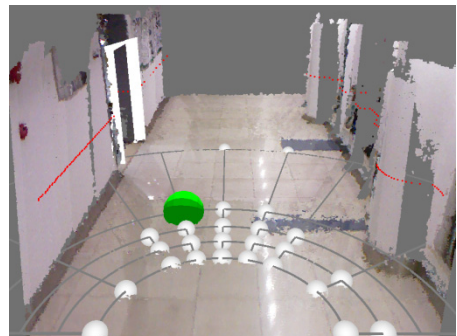
4.4 Visual Feedback

The semantic map integrated with local 3D map, semantic targets and navigation points is displayed on the screen as a visual feedback to the user (Fig. 2). The user can control the wheelchair by selecting the goal from the navigation points via BCI.

The distribution of navigation points is inspired by the article [6]. The ground is divided by a grid, and each intersection between circular arcs and radial lines is a possible position that a navigation point can locate. Considering both accurate control and fast move ability of wheelchair, the closer from the wheelchair, the thicker distribution of navigation points is, and vice versa. So the appropriate grid is like Fig. 2-b. On each intersection, if the minimum distance to the obstacle is larger than a threshold, this point is a navigation point (the white points in Fig. 2-b). And the semantic target (the white frame in Fig. 2-b) is binding on the nearest navigation point. The goal, as a selected navigation point (the green point in Fig. 2-b), will be delivered to the motion control module for driving the wheelchair.



(a)



(b)

Fig. 2. (a) Snapshot of a user navigating along a corridor; (b) Detail of the screen displayed in (a)

5 Motion Control

Driving the wheelchair to a normal navigation point and a semantic target are different, because the pose of a semantic target includes position and orientation meanwhile a navigation point only contains position.

The navigation system controls the wheelchair to a semantic target according to the relative position of the wheelchair and the semantic target. A real-state feedback controller [12] is used to calculate the linear and angular velocity (v and ω) (Eq. 3).

$$\begin{cases} v = k_r r \\ \omega = k_a a + k_b b \\ r = \sqrt{\Delta x^2 + \Delta y^2} \\ a = -\theta + \text{atan2}(\Delta x, \Delta y) \\ b = -\theta - a \end{cases} \quad (3)$$

where Δx and Δy are position error between the wheelchair and the semantic target, θ is the orientation of wheelchair, r is the distance between the wheelchair and the semantic target, a and b are intermediate variables. k_r , k_a and k_b are constants.

The method to navigate the wheelchair to a normal navigation point is a simplification of above method as shown in Eq. 4.

$$\begin{cases} v = k_r r \\ \omega = k_a \text{atan2}(\Delta x, \Delta y) \\ r = \sqrt{\Delta x^2 + \Delta y^2} \end{cases} \quad (4)$$

where the meanings of all parameters are similar with above.

In order to guarantee the safety of motion, MVFH&VFF methods [13, 14] are used to implement obstacle avoidance, as modifying the linear and angular velocity command according to the laser scan.

6 Experiment and Results

6.1 Wheelchair Prototype

The wheelchair prototype [2, 3] based on an ordinary electric wheelchair, equipped with several mobile robot sensors including a Kinect, a LMS200 LRF, odometry, and an Emotiv EPOC EEG Neuroheadset etc., is shown in Fig. 3. There are two computer on the wheelchair, one runs Linux to implement semantic mapping and motion control, and another one runs Windows for BCI. And these two computer communicate with each other by Ethernet. The motion control commands are executed by the Smart Motion Controller (SMC) of wheelchair in 20Hz. Both laser scans of LRF and point clouds of Kinect are obtained for semantic mapping. The local 3D mapping algorithm is performed using a ROS implementation of GMapping [10] from OpenSLAM. The semantic map update frequency is 1Hz. The EPOC is connected to the computer by Bluetooth for obtaining BCI commands in 3Hz. The system software is developed based on ROS [15] and PCL [16].

The 14 channels of the EPOC distribute in accordance with International 10-20 system [17] as shown in Fig. 4. Three sets of channels are used in our system: [AF3, AF4, F7, F8], [T7, F7, FC5], [T8, F8, FC6] (Fig. 4). The period of integral is 0.3 second. Four expressions are recognized in our system: lifting brows, biting the teeth on the left, biting the teeth on the right, and biting the teeth on both side. These expressions can lead to significant changes in EEG, and do not affect the user operating the wheelchair (e.g. moving eyes will affect the user observing screen).

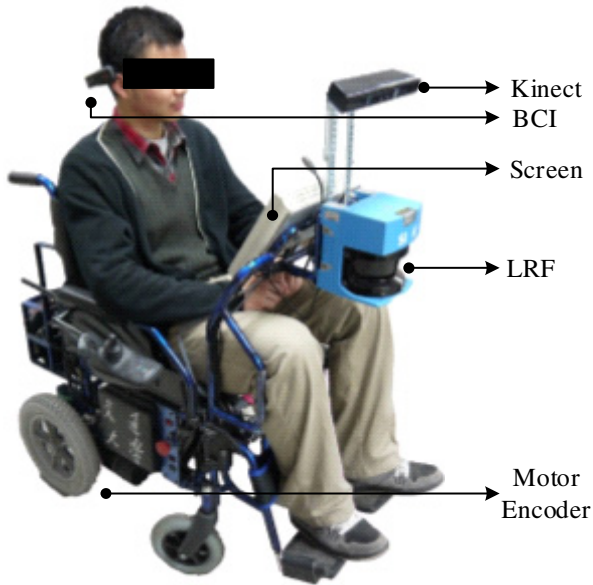


Fig. 3. Wheelchair prototype

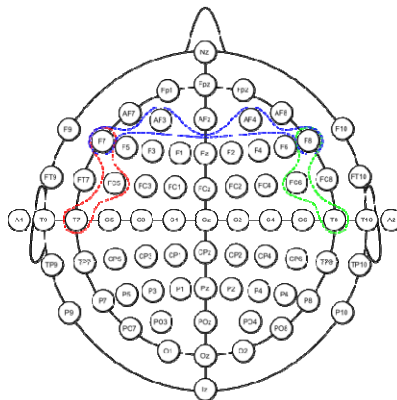


Fig. 4. Electrodes of International 10-20 system for EEG [18]

6.2 Experimental Environment and Task

The environment for experiment is shown in Fig. 6-a. The tasks include passing through a doorway and docking into the table.

The blue line in Fig. 6-a is the path of wheelchair. The path of wheelchair controlled automatically, when the user selects a semantic target, is marked as dashed.

6.3 Semantic Mapping

Fig. 5 illuminates an example of semantic mapping test. Fig. 5-a is a snapshot of experimental environment, and Fig. 5-b is the screenshot of semantic map at that moment. In the semantic map, the white points are navigation points, the green point is the goal, and the white frame marks the semantic target (a table).

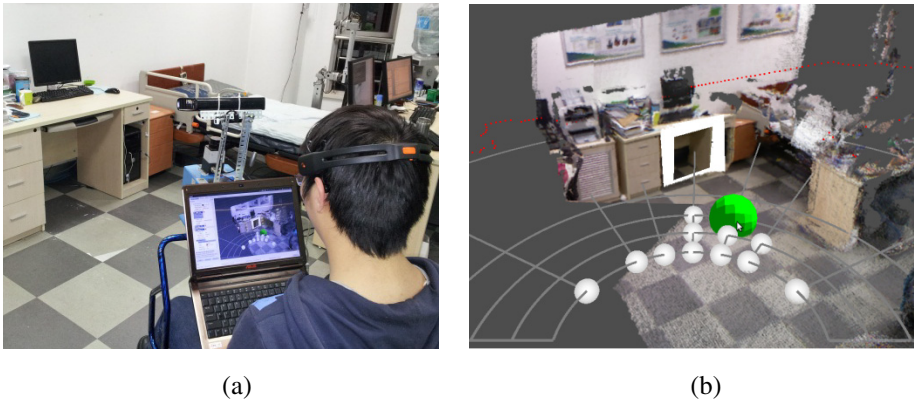


Fig. 5. (a) Snapshot of a user preparing to dock into table; (b) Detail of the screen displayed in (a)

6.4 Performance Evaluation

This section describes a general evaluation of the brain-controlled wheelchair and compares our navigation system with the similar system only controlled with navigation points excluding semantic targets. We call our navigation system as system I and the comparative system as system II. The metrics to evaluate the wheelchair performance are:

- 1) Task success: degree of accomplishment of the navigation task;
- 2) Path length: distance traveled to accomplish the task;
- 3) Time: time taken to accomplish the task.

The metrics to evaluate the comfortability are:

- 1) High ω ratio: the ratio of the control steps whose angular velocity is higher than 8 deg/s to the total control steps;
- 2) BCI commands: number of BCI commands.

The metrics to evaluate the safety are:

- 1) Collisions: number of collisions;
- 2) Obstacle clearance: minimum and mean distance to the obstacles.

Fig. 6-b shows the comparison of trajectories two systems and the results are summarized in Table 1 to Table 3. In five experiments of each system, all experiments succeed with system I but only once succeeds with system II, since it's barely docking into the table without semantic map. The path of system I is longer, because the autonomous navigation to the semantic target needs a longer path which is far from obstacles and smooth (the ratio of high angular velocity is lower), in order to guaranteeing the safety and comfortability. System II costs more time to complete the task since manual control need more adjustment by the user. Similarly, the user sends more BCI commands to system II to control the wheelchair. And both of these two systems are safe enough to protect wheelchair from collisions. The obstacle clearance is measured when the wheelchair is passing through a door.

Table 1. Metrics to evaluate the wheelchair performance

	System I		System II	
	mean	std.	mean	std.
Task success	1	-	0.2	-
Path length (m)	28.5	0.3	23.2	0.6
Time (s)	96	8	116	10

Table 2. Metrics to evaluate the comfortability

	System I		System II	
	mean	std.	mean	std.
High ω ratio (%)	3.4	1.1	7.6	1.2
BCI commands	19	2	37	5

Table 3. Metrics to evaluate the safety

	System I		System II	
	mean	std.	mean	std.
Collisions	0	0	0	0
Clearance mean (m)	1.56	0.03	1.33	0.03
Clearance min (m)	0.65	0.07	0.44	0.16

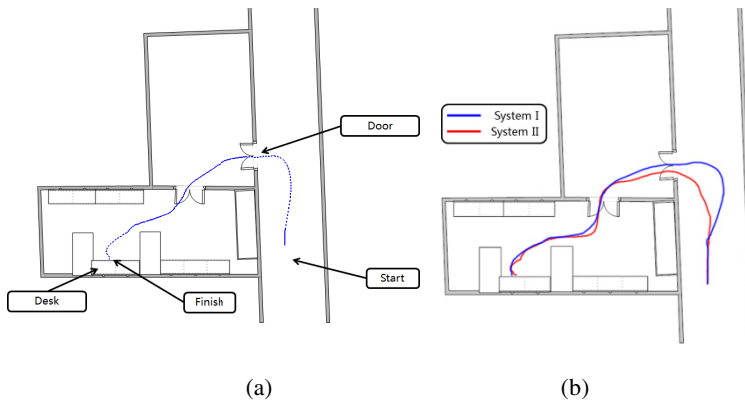


Fig. 6. (a) Experimental environment and tasks; (b) Comparative experiment

7 Conclusion and Future Works

This paper presents a smart wheelchair navigation system relying on semantic map controlled via brain-computer interface. Semantic map is used to analyze the environment and extract semantic targets. When the user selects the semantic target, our system can actively navigate the wheelchair, which plans a smooth path far from obstacles and accurately navigate the wheelchair to the goal. And autonomous navigation to the semantic target significantly reduces operation of user. Consequently, both safety and comfortability are improved. The experiments validate the proposed method with the real wheelchair and in the real world. In the future, the BCI will be improved to adapt different people, and the robustness and stability of semantic mapping should be enhance.

Acknowledgments. This work is partly supported by the National High Technology Research and Development Program of China under grant 2012AA041403, the Natural Science Foundation of China under grant 60934006 and 61175088, the State Key Laboratory of Robotics and System (HIT), the Research Fund for the Doctoral Program of Higher Education under grant 20100073110018.

References

1. del Milan, J.R., Carmena, J.: Invasive or Noninvasive: Understanding Brain-Machine Interface Technology. *IEEE Engineering in Medicine and Biology Magazine* 29, 16–22 (2010)
2. Wei, Z., Chen, W., Wang, J.: 3D semantic map-based shared control for smart wheelchair. In: Su, C.-Y., Rakheja, S., Liu, H. (eds.) *ICIRA 2012, Part II. LNCS*, vol. 7507, pp. 41–51. Springer, Heidelberg (2012)

3. Wei, Z., Chen, W., Wang, J.: Semantic Mapping for Smart Wheelchairs Using RGB-D Camera. *Journal of Medical Imaging and Health Informatics* 3, 94–100 (2013)
4. Carlson, T., Monnard, G., del Millán, J.R.: Vision-based shared control for a BCI wheelchair. *International Journal of Bioelectromagnetism* 13, 20–21 (2011)
5. Mandel, C., Luth, T., Laue, T., Rofer, T., Graser, A., Krieg-Bruckner, B.: Navigating a smart wheelchair with a brain-computer interface interpreting steady-state visual evoked potentials. In: *IEEE/RSJ International Conference on Intelligent Robots and Systems*, pp. 1118–1125. IEEE Press, St. Louis (2009)
6. Iturrate, I., Antelis, J.M., Kubler, A., Mínguez, J.: A noninvasive brain-actuated wheelchair based on a P300 neurophysiological protocol and automated navigation. *IEEE Transactions on Robotics* 25, 614–627 (2009)
7. Perrin, X., Chavarriaga, R., Colas, F., Siegwart, R., del Millán, J.R.: Brain-coupled interaction for semi-autonomous navigation of an assistive robot. *Robotics and Autonomous Systems* 58, 1246–1255 (2010)
8. Baumeister, J., Barthel, T., Geiss, K., Weiss, M.: Influence of phosphatidylserine on cognitive performance and cortical activity after induced stress. *Nutritional Neuroscience* 11, 103–112 (2008)
9. Murphy, K.: Bayesian map learning in dynamic environments. *Advances in Neural Information Processing Systems* 12, 1015–1021 (1999)
10. Grisetti, G., Stachniss, C., Burgard, W.: Improved techniques for grid mapping with rao-blackwellized particle filters. *IEEE Transactions on Robotics* 23, 34–46 (2007)
11. Thrun, S., Burgard, W., Fox, D.: Probabilistic robotics, vol. 1. The MIT Press, Cambridge (2005)
12. Siegwart, R., Nourbakhsh, I.R.: Introduction to autonomous mobile robots. The MIT Press, Cambridge (2004)
13. Parikh, S.P., Grassi Jr, V., Kumar, V., Okamoto Jr, J.: Integrating human inputs with autonomous behaviors on an intelligent wheelchair platform. *IEEE intelligent systems* 22, 33–41 (2007)
14. Carlson, T., Demiris, Y.: Human-wheelchair collaboration through prediction of intention and adaptive assistance. In: *IEEE International Conference on Robotics and Automation*, pp. 3926–3931. IEEE Press, Pasadena (2008)
15. Robot Operating System (ROS), <http://www.ros.org>
16. Rusu, R.B., Cousins, S.: 3D is here: Point Cloud Library (PCL). In: *IEEE International Conference on Robotics and Automation*, pp. 1–4. IEEE Press, Shanghai (2011)
17. Niedermeyer, E., da Silva, F.H.L.: *Electroencephalography: basic principles, clinical applications, and related fields*. Lippincott Williams & Wilkins, Hagerstown (2005)
18. International 10-20 system, [http://en.wikipedia.org/wiki/10-20_system_\(EEG\)](http://en.wikipedia.org/wiki/10-20_system_(EEG))

Control Strategies and Particle Filter for RGB-D Based Human Subject Tracking and Behavior Recognition by a Bio-monitoring Mobile Robot

Nevrez Imamoglu¹, Myagmarbayar Nergui², Yuki Yoshida³,
Jose Gonzalez⁴, and Wenwei Yu¹

¹ Medical System Engineering, Graduate School of Engineering

² Mechanical Engineering

³ Medical System Engineering

⁴ Research Center for Frontier Medical Engineering, Chiba University, 1-33 Yayoi-cho,
Inage-ku, Chiba 263-8522 Japan
yuwill@faculty.chiba-u.jp

Abstract. Our ultimate goal is to develop autonomous mobile home healthcare robots which closely monitor and evaluate the patients' motor function, and their at-home training therapy process, providing automatically calling for medical personnel in emergency situations. In our previous study, we developed basic algorithms for tracking, measuring, and behavior recognition of human subjects by a mobile robot, thus, demonstrated the feasibility of the idea of bio-monitoring home healthcare mobile robots. In this study, in order to realize effective bio-monitoring robots, we investigated 1) color based particle filter subject tracking with proposed depth likelihood integration to control the weights of particles; 2) control schemes for acquiring stable image sources for further human motion analysis, especially, the algorithms for reducing the camera vibration due to the acceleration and deceleration of the robot; 3) human activity recognition using contour data of the tracked human subjects extracted from depth images. Results showed that, depending on depth data can be quite useful as an observation by simplifying state space in 2D rather than 3D state space, and, a fuzzy control algorithm could decrease the vibration due to the acceleration and deceleration. Finally, the human activity recognition could be achieved with a high correct rate, by using geometric parameters extracted from contour data.

Keywords: Mobile robot, home healthcare, human behavior recognition, tracking strategies, fuzzy control, contour data.

1 Introduction

Recently, due to increasing elderly population, and the improvement of medical treatment and prevention of lifestyle diseases, the home healthcare is more on demand. The aim of home healthcare is to reduce hospital admissions and to make it possible for Motor-function Impaired Persons (MIPs) to remain at home rather than

using residential, long-term, or institutional-based nursing care. Human motion, such as gait, is usually measured by using motion capture systems. However, motion capture systems are costly and only effective in limited areas, thus not suitable for at-home monitoring.

One solution of monitoring systems for MIPs can be a bio-monitoring robot, which is capable of tracking the human subject appropriately, and observe and analyze human activities. Using mobile robots to track and follow human subjects is not a new research topic. There have been research works using mobile robots equipped with various sensors such as vision sensors, laser range finders, audio sensor and integration of them [2-5]. Most of these systems aimed to only tracking and following persons. Moreover, the sensors used are expensive.

Our ultimate goal is to develop autonomous mobile home healthcare and rehabilitation robots which closely monitor and evaluate the motor function of MIPs, and their at-home training therapy process, providing automatically calling for medical personnel in emergency situations. This required not only tracking and following, but also accurately measuring and recognizing the motion of MIPs in an indoor environment.

In our previous study, we used a mobile robot equipped with a Kinect sensor, which contains a RGB camera, a Depth sensor, and a multi-array microphone. We developed a set of algorithms to improve the accuracy of the skeletal points extracted from the color and depth images. Furthermore, we developed basic algorithms for tracking, measuring, and behavior recognition of human subjects by a mobile robot, thus, demonstrated the feasibility of the idea of bio-monitoring home healthcare mobile robots [1]. Especially, for recognizing human behavior, we applied Hidden Markov Model (HMM [6]) for human joint angle data, because that statistical nature of the HMM could render overall robustness to gait representation and recognition. Compared with the other classification algorithms applied for image sequence features [7-10], the HMM based method could give a higher recognition rate.

Although, in the previous feasibility study, satisfactory recognition results were acquired, subject detection and image based tracking were handled by the Microsoft Kinect SDK on the scene where the active subject tracking was by following subject with the robot motion and Kinect sensor rotation control. However, Kinect SDK for RGB-D based subject tracking was not very robust by causing subject loss during tracking by sudden environmental changes or vibration on the Kinect sensor due to the motion. Hence, a better tracking model is required to solve this problem in order to realize ultimately a bio-monitoring robot that could work in the real daily living environment. The second problem is that, since the task of robot is to observe human subject, the camera should be put at a certain height from the moving platform of the robot. So that, uneven terrain existed even in the indoor environment would could vibration of the camera, consequently, the image source would be very unstable and difficult to recognize. Another problem is that, in the previous research, the measurement accuracy was relying on the color markers, which give subjects constraints, meanwhile, are subject to the influence of the motion of the robot and human subjects.

For the first problem, we investigated color-based particle filter tracking [11, 12] to be able to track detected subject on the scene in consequent frames. But, since the particle state space have some randomness due to motion model, there is a possibility

of losing the subject if the color distribution of the new particle states are not consistent with the reference color model. For a successful tracking, it is important to use particles with high probability, therefore, we added depth likelihood data too in order to eliminate particles with very low depth likelihood observation to support the color distribution. For the second problem, we realized a hybrid control architecture (Fig. 5), in which 3 controllers were integrated to realize 1) speed control to decrease the vibration due to acceleration and deceleration; 2) reactive control to enable the robot move while avoid obstacles; 3) PID control for the robot to follow the subject. For the third problem, we realized the human activity recognition using contour data of the tracked human subjects extracted from depth images. Several geometric parameters (the ratio of height to weight of the tracked human subject, and distance between centroid of upper and lower parts of human body) were calculated from the contour data, and used as the features for the activity recognition.

The paper is organized as follows: in section 2, in order to show a complete scenario of our approach, we briefly explained part of our previous work on human tracking, measurement and behavior recognition. In section 3, we described the proposed depth integration for color-based particle filter which is a simple but efficient model to achieve subject tracking. In section 4, a fuzzy control scheme was introduced. In section 5, the human activity recognition based on contour data was explained. In section 6, results were shown with discussion. Finally, conclusions were drawn.

2 Feasibility Study of a Bio-monitoring Mobile Robot

2.1 The Mobile Robot Used for Experiment, and Measurement

The robot we employed is a Pioneer 3-DX, with a Microsoft Kinect as vision sensor (Fig. 1) [1]. In order to acquire high measurement accuracy, color markers were attached to the knee and ankle joints of human subjects (Fig. 2)[1]. The measurement experiment was conducted in an experiment room, with a simple setting of obstacles.



Fig. 1. Robot used in the studies

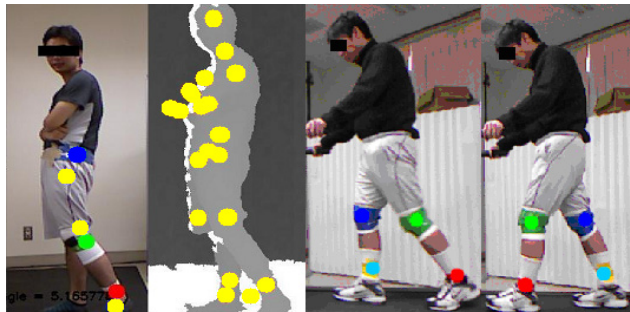


Fig. 2. RGB image with skeleton points (yellow ones are original skeleton points, others are the corrected points)

2.2 Human Behavior Recognition Procedure

After the joint trajectories were calculated, they were discretized and fed into one Hidden Markov Model (HMM), with trunk tilt angle. The HMM model Hidden Markov Model is a statistical model. In the HMM [13, 14], the system being processed is considered as a Markov process, which has unknown parameters. HMM were built from one series data. Different series of joint and body angle data were performed to recognize the gait gesture using HMM and to find the most likely decoded paths (Viterbi paths). Feasibility of the research is approved from the results in our previous work in which for 6 subjects, 6 motions (walking, sitting, running, impaired walking, falling down, standing), the human behavior recognition process could achieve a high accuracy (98-99%).

3 RGB-D Particle Filter Based Subject Tracking

In this section, we investigated the utilization of RGB-D sensor for color tracking using particle filter on region of interest (RoI) which is defined by an ellipse. The employment of the particle filter is using recursive Bayesian filter based on the distributed samples around a RoI given the state and observations [11, 12]. Due to the randomness in the distribution and motion model of the particles, it can handle non-linearity of the system and non-Gaussian noise conditions. Therefore, particle filter applications can create a robust framework for vision based object or subject tracking in dynamical environments [11] that can be replaced by SDK for subject tracking.

First of all, manually given a selected region where the subject locates, a reference distribution of the color probability density function (pdf) is computed from selected RoI [11, 12, 15]. Then, for the given ellipse RoI, random particle distribution is done with a state definition as below [15]:

$$\mathbf{s}_t = \{x_t, y_t, \dot{x}_t, \dot{y}_t, Hx_t, Hy_t, \theta_t\} \quad (1)$$

where x, y represents the centroid of the reference ellipse or each particle representing the center of an ellipse for computing the observation color pdf value followed by their motion values as the derivative representations, and Hx and Hy are the half axes values with ellipse angle θ [15, 11]. State update definition over time is given as follows [11, 12, 15]:

$$\mathbf{s}_t = A \times \mathbf{s}_{t-1} + \delta_{t-1} \quad (2)$$

where A is the transformation matrix for the motion model for the new state, and δ_{t-1} the random noise on the new state prediction where the color pdf of each particle can be obtained by a Gaussian model. Then, the Bhattacharyya coefficient (3) can be used to calculate likelihood of the particles [11, 15]:

$$\rho[p, q] = \sum p[n]q[n]; \quad n \in \{1, \dots, N\} \quad (3)$$

In addition to the color similarity, we propose to use depth likelihood based on a Gaussian function to update the weights which can eliminate the particles out of subject boundaries during tracking task. Therefore, the weights can be kept as the color likelihood update or can be assigned to zero if the particle does not fall on the estimated subject depth region. In Fig.3, a depth image is given with its respective subject depth likelihood and threshold binary data to eliminate particles out of subject depth likelihood region. By this way, we can keep the surviving particles on the subject body which increases robustness of the tracking without the necessity of 3D state space usage as used in the work [12]. Hence, with a simple and fast depth observation integration, 2D state space for particles can achieve the tracking with RGB-D sensor.



Fig. 3. (a) Depth image from Kinect sensor, (b) depth likelihood image computed from the sample on subject depth value, (c) binary segmentation of (b), (d)

Then, the weights of each particle can be calculated as

$$w_t = N(d_t c_t w_{t-1}) \quad (4)$$

where $N(\cdot)$ is the normalizing function to make the sum of weights to 1, w is the particle weight and c is the color likelihood for each particle, d is the depth based particle elimination weight in which d is 1 if the particle inside the segmented depth subject estimation as in Fig.3(c), otherwise 0. Therefore, in Fig.3(d) color image, the weights of particles fall on the background regions will be zero. So, after this update all the updated particles will be on the tracked foreground region.

4 Enhancement on Data Acquisition During Robot Motion

The mobile robot control is the processing result of several equipment such as Kinect sensor used for subject detection and tracking, a rotating table (mount of the Kinect sensor and providing rotation flexibility on horizontal direction for it), eight ultrasound sensors on the front end of the robot used for avoiding obstacles. The idea is to track the subject detected by the Kinect sensor in which subject distance and pose are taken into consideration as well as with the obstacle data around the surrounding environment of the robot.

The subject detection is relying on the Microsoft Research product Kinect SDK that labels the detected human subject with color pixels on depth image where the object depth values are assigned with gray-scale color map (Fig.4). Initial distance and pose detection of the human subject should be as accurate as possible to achieve better robot motion behavior for the subject tracing task in indoor environment. Kinect sensor and SDK is mostly stable for stationary usage; however, the mobile usage has might have problems such as the noisy irrelevant regions detected as false detection for the subject boundaries (Fig.4(b)).

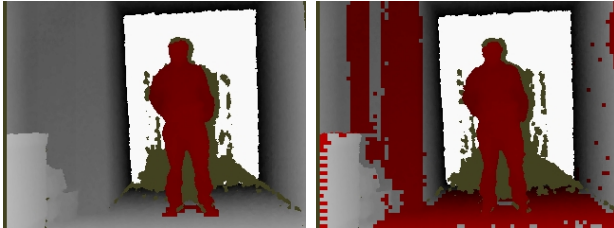


Fig. 4. Human subject detection samples by Kinect SDK software (a) subject correctly detected (b) subject with irrelevant false detections

There are several reasons that can be stated as the cause of false detections such as high illumination or lighting condition changes in the environment, high-speed motion or loss of the subject on the scene, or vibration on Kinect sensor caused by the robot and rotating table motion. In this paper, vibration on Kinect sensor is examined, and we build a control approach as in [14] to reduce the effect of vibration on Kinect SDK data acquisition. Fig.5 shows the flowchart of the mobile robot system that try to keep a stable distance between the subject while tracking the subject and avoiding obstacles [14]. Based on the work in [14], it can be seen that robot speed is decided by the distance between the robot and the detected human subject, so rather than using that desired speed directly, we tried to use incrementing the speed until reaching desired speed by utilizing a fuzzy approach as in Fig.5 and Fig.6 [14]. Ultrasound sensors are used for obstacle detection, and subject pose is decided by the pose of rotating table that rotates the Kinect sensor to keep the detected subject in the center of the image. So, combining all these information, a rule based reactive controller is implemented for subject tracking and activity recognition of the subject [14]. Since we try to decrease the effect of vibration by the robot motion on the detection of subject by Kinect SDK, we made the experimentation on a simplified and stable case where environmental conditions can be controlled. Hence, we compared the constant

speed assignment or fuzzy speed controller in a straight track of the subject without any obstacle with stable lighting conditions. By this way, we can observe how the fuzzy controller improve the data acquisition and subject detection of the Kinect SDK by reducing the vibration effect on Kinect sensor. The simplified fuzzy system for the straight forward motion can be seen in Fig.6(a), and corresponding fuzzy membership functions are given in Fig.6(b). We used normalized error (Fig.6(b)) to compute the membership values which enables the system to respond around same time duration for acceleration values or deceleration according the fuzzy output.

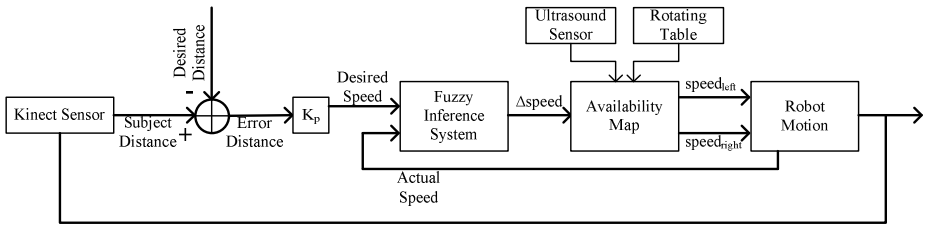


Fig. 5. Flowchart of the robot motion control for the subject tracking system

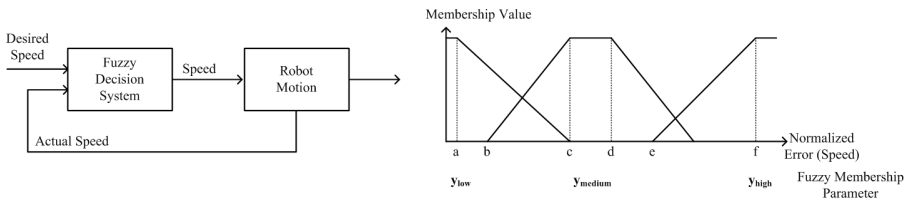


Fig. 6. (a) Simplified flowchart of fuzzy speed control, (b) membership functions for the error speed

In Fig.6(b), y_{low} , y_{medium} , and y_{high} are the fuzzy weights for the membership functions. The parameters of the membership functions of the fuzzy block are a , b , c , d , e , and f . Based on the inputs, fuzzy system decides how much the current speed should be increased according to the normalized error speed that is calculated by the difference of desired speed and actual speed. Desired speed is computed based on the distance between mobile robot and subject of interest on the scene as shown in Fig.5.

5 Feature Extraction for Activity Recognition

For the activity recognition, we are using our latest implementation as in [13]. First, feature extraction from depth images is required to represent the activity of the subject over time. To be able create a feature space, we utilize the model stated in our recent work [13] which only considers the image processing part of the whole mobile robot system. Simply, the model takes advantage of color information on the depth image that labels the human subject. In Fig.7(a) and Fig.7(b), sample Kinect sensor data for color and depth images are give. Here, we only use the depth image that is labeled

with a specific color information on the human subject. Using the color likelihood, first we obtain a binary subject likelihood image, and some morphological operations are applied to remove the noise and irrelevant regions [13]. Then, binary human body shape extracted from the depth image as in Fig.7(c).



Fig. 7. (a) Color image, (b) depth image with color map, (c) binary human body extraction based on (b)

To be able to create the feature space to represent each possible activity, some geometric parameters are calculated from the shape of the human subject on the binary image. For that reason, we utilize three vertical regions as in Fig.8, and for each region of the body following data obtained : i) ratio of height to weight of the boundary of the human subject, ii) centroid points of upper and lower regions of the human shape (one/green and third/blue boxes of human shape), iii) distance in pixels between centroid points of upper part and lower part.

Fig.8 represents several possible daily activity of a human subject in indoor environment such as standing, sitting, bending, and lying down [13]. In Fig.8, h and w are the height and weight of the shape for each selected region on human body, and d is the distance (pixels) between centroid points of upper and lower parts of shape [13].

Then, the ratio parameter can be calculated by h/w for each selected region which can distinguish several patterns such as standing, walking and lying down [13]. And as for the last feature d , horizontal distance between the centroid of upper and lower body regions are extracted to improve the classification of sitting and bending activities that can cause false detection since the ratio feature for these two activities can be similar based on the view point [13]. In sum, we can create four features; three ratio features for the upper, middle and lower regions of the binary image, and one distance feature to represent the difference of upper and lower body shape.

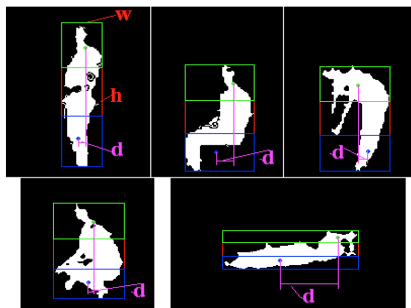


Fig. 8. Samples for the feature extraction model from binary subject images for different types of activities

6 Results

6.1 Tracking

The experiments for the particle filter tracking of the depth-color based proposed integrated model was done in such a condition where selected subject and Kinect sensor are dynamic. The experiments showed that depth information as observation data to particle filter algorithm is good enough to handle tracking in dynamic environment. In Fig.9, tracking samples by several frames are given from the experimental recordings. The images represent the foreground regions with RGB data in which background regions on the scene are removed by the depth likelihood estimation. And, particles are shown with the ellipse ROI in which ellipse state space is estimated by the weighted average of the particle states [15].

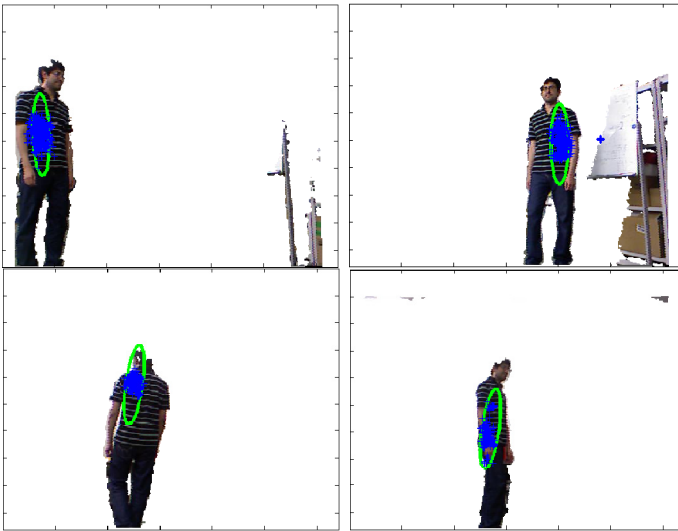


Fig. 9. Several sample frames for tracking frames where the estimated ellipsoid region on subject body segmented from the depth likelihood

6.2 The Effect of Fuzzy Control Scheme

We used a rotating table to control the movement of the Kinect camera in a horizontal plane. We installed the rotating table between the base of The Kinect sensor and stand-up tool of the Kinect. The Kinect sensor itself has a vertical tilt. Thus, the Kinect sensor is able to rotate in vertical and horizontal plane. Now, we have 2 dimension movement of the Kinect camera. Why we needed 2D movement is to manage different kinds of human tracking and following by a mobile robot while keeping the tracking human inside the vision area in case that the robot avoiding obstacles and can not come near by tracked human.

However, to be able to observe the vibration affect, the subject is asked to walk in a straight line for the experiment while the robot tries to keep the stable distance

during the tracking; therefore, both the rotating table and robot pose is in the same direction with the subject [14]. So, we can check effect of the fuzzy speed controller by minimizing the external disturbances. We tried two different case as the constant speed assignment directly and fuzzy speed controller approach to see the noise conditions on the Kinect sensor images for the subject detections.

In Fig.10 (a), it can be seen subject regions are labeled with red color where many false detections on several sequences can be observed around the subject, on the floor, or on the wall due to the sudden speed acceleration to a constant value [14]. On the other hand, fuzzy speed controller improved the image acquisition with subject detection by decreasing the number of false detections on the acquired image sequences (Fig.10(b)) [14]. This is because of the incremental fuzzy speed assignment over time which helps to reduce the vibration effect on the Kinect sensor.



Fig. 10. Kinect SDK subject detection with (a) constant speed assignment, (b) fuzzy speed controller

Also, as another evaluation metric, we made a graph over image sequences by using the number of red pixels that defines the detected subject regions as in Fig.11 [14]. In Fig.11 the spikes means that there is sudden increase on the subject image region boundaries that is due to the false detections of subject regions as in Fig.11(b) [14]. The number of spikes with fuzzy speed controller (Fig.11(b)) compared to error of constant desired speed assignment (Fig.11(a)) are decreasing due to the decrease in vibration effect since the fuzzy speed controller prevents sudden speed changes that result in more false detections [14].

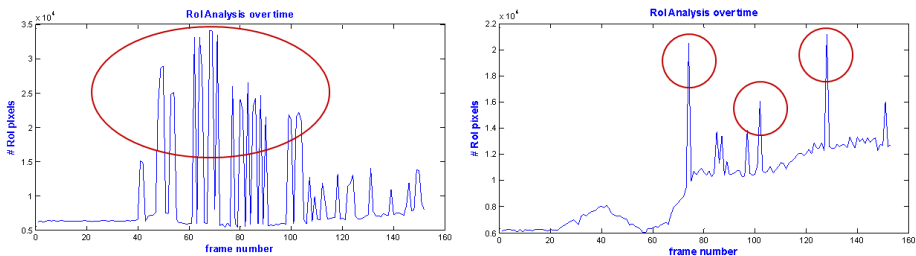


Fig. 11. Number of red pixels to define the subject region on each image sequence with (a) constant speed assignment, (b) fuzzy speed controller

6.3 The Effect of Feature Extraction

The Mobile Robotics Programming Toolkit (MRPT) was used as the software platform for section 3. The MRPT is an open source and it is released under the GPL. The MRPT is basically writing on C++ programming language. We have written our full program for the real environment in Microsoft Visual C++/C# 2010 Express and Matlab on a laptop computer mounted on the robot. There are many kinds of libraries and SDK available for the Kinect sensor. For example, OpenKinect, OpenNI, NITE, FFAST, Official windows SDK of Microsoft and so on in different platforms. The natural user interface (NUI) API in the Kinect for Windows® Software Developer Kit (SDK) enables applications to access and manipulate these data. Notebook computer is a Macbook Pro (2.2GHz quad-core Intel Core i7).

Activity recognition of the human subject is tested as implemented in [13, 14] since this paper focuses on the control strategies as in section 3 and 4. However, using the model in [13, 14], we are able to classify five different daily activities such as walking, standing, sitting, bending and lying down. Based on the four features stochastic model as HMM, high accuracy was obtained for each daily activity. Standing and lying down activities were recognized with %100 detection rate. Also, walking, sitting and bending activities recognized with high performance as %98.2, %97.3, and %99.2 respectively [13, 14].

7 Conclusion

In this study, we tried to build a reliable bio-monitoring mobile robot system; therefore, several modules are examined. First we proposed a simple and fast way of integrating depth likelihood observation to color-based particle filter subject tracking. Then, based on our previous experiences, control schemes are given for acquiring stable image sources for further human motion analysis, especially, the algorithms for reducing the camera vibration due to the acceleration and deceleration of the robot. Finally, using appropriate feature representation of the human subject, activity recognition is achieved by contour data of the tracked human subjects extracted from depth images.

Experimental analysis demonstrated that adapting depth and color observation for particle filter tracking can be beneficial for active tracking in dynamical environment, and, a fuzzy control algorithm could decrease the vibration instead of using sudden acceleration and deceleration commands for the mobile robot. Finally, the human activity recognition could be achieved with a high correct rate while the robot tracks the human subject, in which using geometric parameters extracted from contour data is a good candidate for feature representation. However, more work is needed to be done to create a robust system which can handle subject detection, tracking and activity recognition.

References

- [1] Nergui, M., Yoshida, Y., Gonzalez, J., Koike, Y., Sekine, M., Yu, W.: Human Motion Tracking and Measurement by a Mobile Robot. In: *Intelligent Robotics and Applications*, pp. P21–P30 (2012)
- [2] Kwon, H., Yoon, Y., Park, J.B., et al.: Person tracking with a mobile robot using two uncalibrated independently moving cameras. In: *IEEE International Conference on Robotics and Automation*, Barcelona, Spain, pp. 2877–2883 (2005)
- [3] Gupta, M., Behera, L., et al.: A Novel Approach of Human Motion Tracking with the Mobile Robotic Platform. In: *International Conference on Modelling and Simulation*, UKSim (2011)
- [4] Cunha, J., Pedrosa, E., et al.: Using a Depth Camera for Indoor Robot Localization and Navigation. In: *Robotics Science and Systems (RSS) Conference on Campus at the University of Southern California*, Poster Presentation, p. P5 (2011)
- [5] Biswas, J., Veloso, M.: Depth Camera based Localization and Navigation for Indoor Mobile Robots (2011), <http://www.cs.cmu.edu/~mmv/papers/11rssw-KinectLocalization.pdf>
- [6] Rabiner, L.R.: A Tutorial on Hidden Markov Models and Selected Applications in Speech Recognition. *Proceedings of the IEEE* 77(2) (February 1989)
- [7] Wang, L., Tan, T., et al.: Silhouette Analysis-Based Gait Recognition for Human Identification. *IEEE Transactions on Pattern Analysis and Machine Intelligence* 25(12) (December 2003)
- [8] Uddin, M.Z., Kim, T.S., et al.: Video-based Human Gait Recognition Using Depth Imaging and Hidden Markov Model: A Smart System for Smart Home. In: *SHB2010 - 3rd International Symposium on Sustainable Healthy Buildings*, Seoul, Korea (May 27, 2010)
- [9] Rohila, N., et al.: Abnormal Gait Recognition. *International Journal on Computer Science and Engineering* 2(5), 1544–1551 (2010)
- [10] Pushpa Rani, M., et al.: An efficient gait recognition system for human identification using modified ICA. *International Journal of Computer Science & Information Technology* 2(1) (February 2010)
- [11] Nummiaro, K., Koller-Meier, E., Van Gool, L.: Object Tracking with an Adaptive Color-Based Particle Filter. In: Van Gool, L. (ed.) *DAGM 2002*. LNCS, vol. 2449, pp. 353–360. Springer, Heidelberg (2002)
- [12] García, G.M., Klein, D.A., Stückler, J., Frintrop, S., Cremers, A.B.: Adaptive Multi-cue 3D Tracking of Arbitrary Objects. In: Pinz, A., Pock, T., Bischof, H., Leberl, F. (eds.) *DAGM and OAGM 2012*. LNCS, vol. 7476, pp. 357–366. Springer, Heidelberg (2012)
- [13] Nergui, M., Yoshida, Y., Imamoglu, N., Gonzalez, J., Otake, M., Yu, W.: Human Body Contour Data Based Activity Recognition. In: *35th Annual International Conference of the IEEE Engineering in Medicine and Biology Society, EMBC 2013* (accepted, 2013)
- [14] Nergui, M., Yoshida, Y., Imamoglu, N., Gonzalez, J., Otake, M., Yu, W.: Human Activity Recognition Using Body Contour Parameters Extracted from Depth Images. *Journal of Medical Imaging and Health Informatics* (accepted)
- [15] Paris, S.: Particle Filter Color Tracker. In: *Mathworks File Exchange* (2011), <http://www.mathworks.com/matlabcentral/fileexchange/17960-particle-filtSer-color-tracker>

CTS Rehabilitation Training Robot Using Motor Control

Heein Jeong, Sangyong Lee, and Jangmyung Lee

Pusan National University, Korea
{heein1696, jmlee}@pusan.ac.kr

Abstract. Wrist, perform an important function to the daily life. Company employee that time in response to changes in the work environment, you are working in front of a computer longer, feel the burden of the wrist is not small. Patients by 10% or more each year have increased distribution carpal tunnel syndrome. Indeed, the importance of prevention has been emphasized. In addition, carpal tunnel syndrome needs consistent rehabilitation. But it is hard without having to visit a professional rehabilitation center, to achieve this in daily life. Therefore, it is trying to develop a robot which can prevent the carpal tunnel syndrome. Robot has the goal here is a wearable rehabilitation robot wrist with two degrees of freedom using the motor. It help the prevention and rehabilitation of carpal tunnel syndrome, this robot is equipped with auxiliary muscle function and muscle strength exercise some.

Keywords: Rehabilitation training robot.

1 Introduction

Carpal tunnel syndrome, and a disease that occurs it is Rodriguez is located in the base of the wrist, nerve pressed on the tunnel site nerves and blood vessels pass through, one in 20 Americans is to occur. Carpal tunnel syndrome is a disease susceptible relatively surgical therapy. Fortunately, most treatment it is possible through non-surgical physical therapy that adjust the paresthesia and pain to recover the function of the hand. Median nerve and tendon of muscle to bend your finger are passing to carpal tunnel, space of about the thickness of a finger which is located on the palm side of the wrist. If it is squeezed or pressed, you will feel which paralyzed and numb comes fingers, hand and wrist. It often occurs in people who work force to enter a lot of hand or repetitive operation of the finger (playing stringed instruments, typing, handicrafts, manufacturing assembly plants, sewing, handicrafts etc.) in inefficient posture of the wrist (most of all posture broken wrist). Pain caused by carpal tunnel syndrome is started slowly. At night, more intense, when many people feel numbness and pain I looks like the show mainly massaged and confessed hands and wrists that attempts to reduce pain. Except severe cases, the initial treatment of carpal tunnel syndrome, and to use the method of non-surgical most, it is important that not only the wrist, to correct the posture of the head and upper body at this time. Carpal Tunnel Syndrome is often caused by repeated load on the wrist. So, It is important that correct the incorrect usage of the hand in daily work, and take the

stretch breaks frequently. This robot is a rehabilitation robot of the wrist to help stretch the wrist. What has 3 D.O.F. The robot is not only to simple vertical motion but also rotational and left - right motion. Further, it is possible to follow the desired strength, speed and position using the impedance control.

2 Paper Preparation

Upper limb, including the wrist, perform an important function to the daily life. However, recently according to the aging society, Patients with upper extremity hemiplegia due to stroke or an increase in the elderly with reduced upper limb function. For patients with upper extremity function such decrease, or suffering from hemiplegia, it is possible to recover the function by continuous regeneration. Also, company employee that time in response to changes in the work environment, you are working in front of a computer longer, feel a burden on the wrist is not small. If such a case, it is not performed frequently, stretching to release stress of the wrist, may be diseases such as carpal tunnel syndrome occurs. The carpal tunnel syndrome actual patients by 10% or more each year is increasing, research for regeneration has also been actively products considered various for preventing this are released. Wrist or paralyzed by disease and a variety of causes, rehabilitation stable is necessary for patients with state pursuant to it, but without having to visit a rehabilitation center professional, to make it happen in real life it is not easy. Therefore, it is trying to develop a robot which can be automatic stretching, regeneration and simple muscular exercise is possible easily in real life. Various reasons to increase the pressure in the carpal canal, carpal tunnel syndrome is an entrapment neuropathy the most common upper limb to induce pain and sensory deficit ischemia of the median nerve occurs. In the United States, it is a loss to the business by CTS from injury or illness of fully private company (mean 28), and that is the second most followed is a loss to the business by fractures (average 30 days) were reported. In this way, the reasons that there are many work defect days caused by CTS are a lack of complex preventive intervention and an absence of appropriate therapeutic intervention through an early diagnosis. Thus, if the proper intervention is not implemented for the patients that have already happened, symptom aggravation can accelerate the work defect days. It is known that 50% of the medically diagnosed CTS are associated with the work, and recently the studies that present the need for preventive intervention, considering the occupational characteristic of CTS monitoring system, have been reported. CTS patients can be rehabilitated by behavior as shown in Fig.1.

Therefore, we will try to develop a robot to assist the prevention and rehabilitation of CTS. It is provided as a wearable, this robot comprises essentially a function of reducing wrist stress and then to move up-down left-right side to the wearer's wrist with a two degree of freedom. Also has a function to grasp the movement of the patient using the sensor to assist the strength. You can assist in muscle strength or light strength training is to be able. help the prevention of water pipe muscle syndrome that can occur easily in daily life.

Carpal Tunnel Rehabilitation Exercises

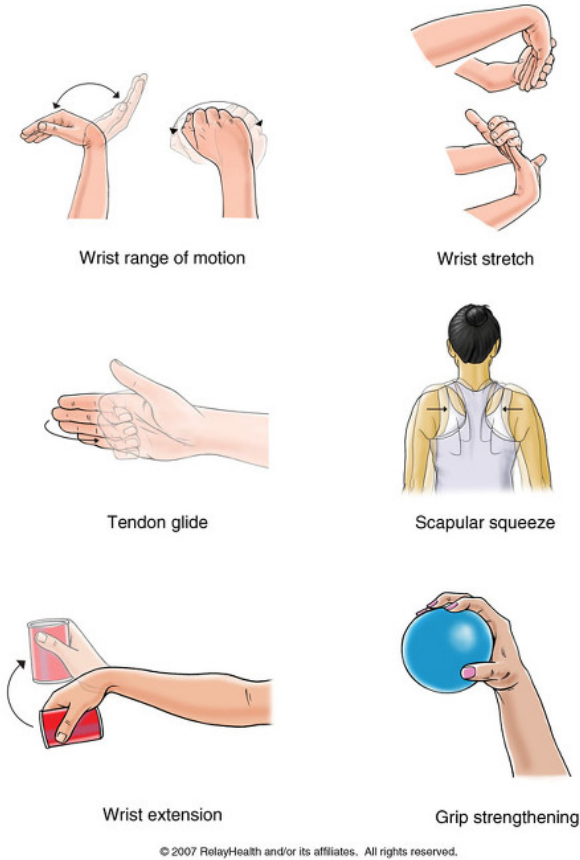


Fig. 1. CTS rehabilitation exercises

The robot performs behavior Wrist Range of Motion and Wrist Extension of Fig.1. The following is a description of each motion. Function of active range of motion, help to be able to recover the muscle in a no power state, is a simple repetitive motion and stretch of the wrist muscles. It is move to perpendicularly, horizontally, oval.

Function of Wrist flexion exercise is operation, which enhance the strength in a state where the strength of the wrist has recovered to some extent.

Table 1. Description of each motion of Fig.1

name	motion
Wrist Range of Motion	<p>A. Flexion: Gently bend your wrist forward. Hold for 5 seconds. Do 3 sets of 10.</p> <p>B. Extension: Gently bend your wrist backward. Hold this position 5 seconds. Do 3 sets of 10.</p> <p>C. Side to side: Gently move your wrist from side to side (a handshake motion). Hold 5 seconds at each end. Do 3 sets.</p>
Wrist stretch	<p>With one hand, help to bend the opposite wrist down by pressing the back of your hand and holding it down for 15 to 30 seconds. Next, stretch the hand back by pressing the fingers in a backward direction and holding it for 15 to 30 seconds. Keep your elbow straight during this exercise. Do 3 sets on each hand.</p>
Tendon glide	<p>Start with the fingers of your hand held out straight. Gently bend the middle joints of your fingers down toward your upper palm. Hold for 5 seconds. Do 3 sets of 10.</p>
Scapular squeeze	<p>While sitting or standing with your arms by your sides, squeeze your shoulder blades together and hold for 5 seconds. Do 3 sets of 10.</p>
Wrist extension:	<p>Hold a soup can or hammer handle in your hand with your palm facing down. Slowly bend your wrist upward. Slowly lower the weight down into the starting position. Do 3 sets of 10. Gradually increase the weight of the object you are holding.</p>
Grip strengthening	<p>Squeeze a rubber ball and hold for 5 seconds. Do 3 sets of 10</p>

Part of the number 1 in Figure 2 is spanned to the wrist and part of the number2 is place four-finger enters. Putting a hand through number 1, It can possible to put the finger at number2. Red color of the number 3 is part of the motor. It is placed at the top and side of the wrist one by one. The motor attached to the side part moves up-and-down motion and the motor attached to the upper part moves left-and-right motion. The number of 4 is the cylinder. While the hand moves, It decrease or increase to be able to move depending on the location. The number of 5 is the part of band. It helps robot clasp the wrist considering different size of hand and thickness of the wrist regardless different people.

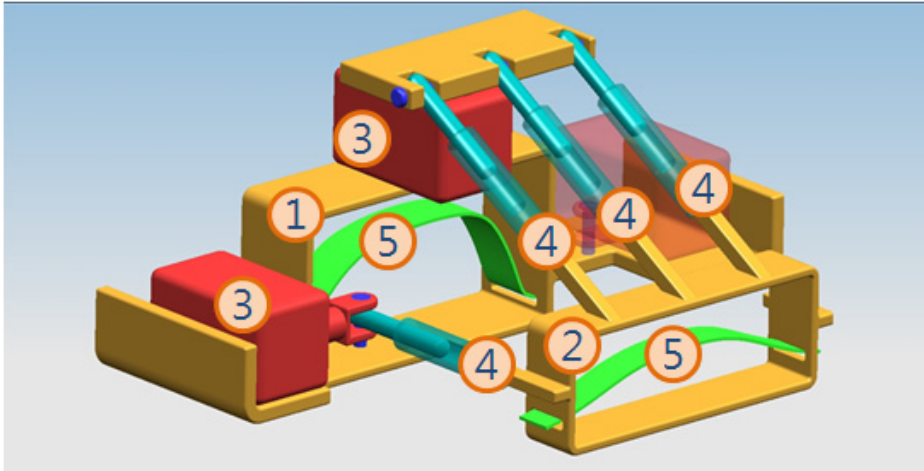


Fig. 2. View of rehabilitation robot

Function of Active range of motion is just control angle for simple repetition exercise.

Wrist flexion exercise function track the location using impedance control.

Assume that external object having mass M , the dynamics of entire system can be expressed as follows.

$$mx'' + k_e(x - x_e) = f \tag{1}$$

here, f is a force applied of the robot.

if using the PD control law about x^d , force f can be expressed as follows.

$$f = k_p(x^d - x) - k_v x' \tag{2}$$

If the gain is positive value, this PD control system is always stable system.

Force of the steady state to be given to the surrounding environment can read off x_{ss} form $x'' = x' = 0$ as equation (1) and (2).

By substituting the formulas used the PD control law, it is possible to determine the expression of the steady state as follows.

$$x_{ss} = \frac{k_p \cdot x^d + k_e \cdot x_e}{k_e + k_p} \tag{3}$$

finally,

$$f_c = k_e \frac{k_p(x^d - x_e)}{k_e + k_p} \tag{4}$$

The impedance control function expression can be expressed as follows..

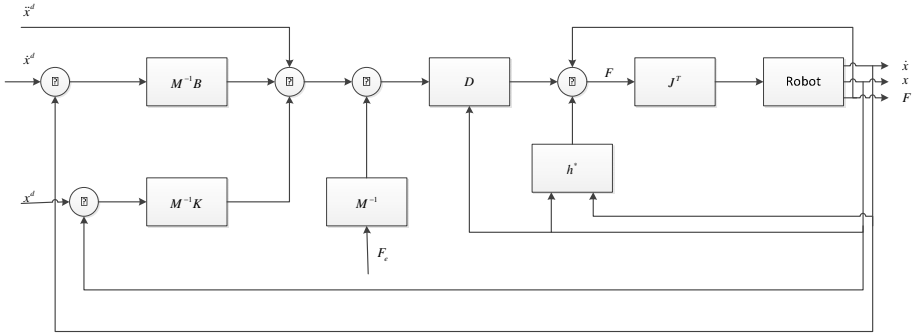


Fig. 3. Impedance control block diagram

$$F = D(\ddot{X}^d + M^{-1}B\dot{E} + M^{-1}KE - M^{-1}F_e) + C + G + F_e \tag{5}$$

The following expression for the dynamics of the robot manipulator is expressed in Cartesian space.

$$D(X)\ddot{X} + C(X, \dot{X}) + G(X) = F - F_e \tag{6}$$

Here, X is the distal position, $D(X)$ is the inertia matrix in the Cartesian space, $C(X, \dot{X})$ is the coriolis and the centrifugal forces in the Cartesian space,

$G(X)$ is the gravity in the Cartesian space, F_e is the exerted force from the outside,

F is the input power to the control. In other words, received force F from the sensor of the wrist, F_e is the exerted force by the motor. Therefore motor is moving to get the desired power of the wrist. While the robot moves along the trajectory, F_e is controlled.

Impedance control, the objective impedance function is defined as follows.

$$M\ddot{E} + BE + KE = F_e \tag{7}$$

Here, M , B , K a positive definite diagonal matrix, $E = X^d - X$, X^d is the reference trajectory. Contact force F_e is defined by the following equation.

$$F_e = K_e(X - X_e) \tag{8}$$

Here, K_e is the stiffness of the target, X_e is the position of the target.

In this case, the reference trajectory X_d is calculated according to equation(4). Using F_d, X_e, K, K_e .

$$x^d = x_e + \Delta x^d, \Delta x^d = \frac{f_d}{k_{eff}} \quad (9)$$

$$k_{eff} = \frac{kk_e}{k + k_e} \quad (10)$$

Here x^d, x_e, f_d, k, k_e is the factor of X^d, X_e, F_d, K, K_e .

But we do not exactly know the stiffness k_e of the target.

Therefore clear the objects stiffness k_e using the f_e as following

$$f_e = k_e(x - x_e) \quad (11)$$

Solving for k_e as follows

$$k_e = \frac{f_e}{(x - x_e)} \quad (12)$$

Here, k_e means one component of contact force F_e estimated by wrist force sensor. Substituting,

$$k_{eff} = \frac{k \frac{f_e}{(x - x_e)}}{k + \frac{f_e}{(x - x_e)}} = \frac{kf_e}{k(x - x_e) + f_e} \quad (13)$$

$$x^d = x_e + f_d \left[\frac{k(x - x_e) + f_e}{kf_e} \right] \quad (14)$$

Therefore, reference trajectory x^d can be won from equation (15). Reference trajectory x^d is calculated by x_e . Suppose that we know values of f^d, f_e, k, x, x_e for total time. By the way, supposing $f_e = 0$ in equation (15), Δx that is a part modifying the reference trajectory goes infinity. In other words,

$$\Delta x = f^d \frac{k(x - x_e) + f_e}{kf_e} \rightarrow f_e = 0 \rightarrow \infty \quad (15)$$

This case represents the state that robot does not receive force of the motor, $x = x_e$.

Using the L'hospital's theory to solve this problem, compute partial derivatives with respect to f_e and substitute $f_e \rightarrow 0$, when the state of robot is $x - x_e = 0, f_e = 0$.

$$\lim_{f_e \rightarrow 0} \Delta x = \frac{f^d}{k}$$

Combining this and equation (15), the results are as follows:

$$x^d = \begin{cases} x_e + \frac{f^d}{k} \\ x_e + f^d \left[\frac{k(x - x_e) + f_e}{kf_e} \right] \end{cases} \quad (16)$$

Giving force to the wrist, the force value is obtained by sensor. Using this value, robot can be moved through the force of the desired value. It works like holding a dumbbell in wrist movement for patients. Therefore, setting the force as the desired weight of the dumbbell, the movement of the robot can be determined by the force value of wrist which obtained from sensor.

Dynamixel has a 260Ncm torque, if average 10cm to a length of the palm from the wrist, it is possible to give the average force 26N.

We're planning to use the motor rather than a pneumatic cylinder, to design a wearable rehabilitation training machine of 3 DOF. Select by motor that uses a Dynamixel with a light weight as compared to DC motors general put out sufficient force. In order to move the wrist, a constant torque is required, the robot is struck by the weight of the wrist when the torque greater than the gravitational force due to the weight of the wrist does not do anything necessary, phenomenon does not occur. And is to have the convenience of movement and carry it to production to be able to use without the help of peripheral devices. Also, It has a weight 68g, minimum control angle is 0.29°. It can be controlled relatively precise.

3 Conclusion

Through motor control, use carpal tunnel syndrome rehabilitation robot to help patient convenient and safe treatment. Also, use it to protect carpal tunnel syndrome in daily life. This robot can be used at everywhere because of light weight basing on simple design and high mobility. Depending on the hands' position, robot can control proper force. There are some effects like exercising with dumbbell with impedance control by controlling designed force, velocity, position. Therefore, this machine can help

patient not only stretching but also strength training. This robot has 3 D.O.F, so can help patient's top and bottom, left and right and rotational stretching of wrist. The robot is operated without the help of other peripherals. Thus, there are some advantages mobility and easy to produce instead of using Pneumatic cylinder motor. Pneumatic cylinder is more powerful than motor, but just using motor's force is enough to control wrist force. Additional features to consider are emergency stop function and angular alignment control function. Emergency stop function is considered because of patient's safety and malfunction. If emergency stop function is operated, the robot will stop acting and reinstated. Also, alignment angle can be different from each person, so the angular alignment control function is made to customize for every user. All in all, if you set up the range of movement of the wrist, according to a person stretching effect is expected to appear.

Acknowledgments. "This research was supported by the MOTIE(The Ministry of Trade, Industry and Energy), Korea, under the Human Resources Development Program for Special Environment Navigation/Localization National Robotics Research Center support program supervised by the NIPA(National IT Industry Promotion Agency)." (H1502-13-1001)

"This research was supported by the MSIP(Ministry of Science, ICT & Future Planning), Korea, under the ITRC(Information Technology Research Center) support program (NIPA-2013-H0301-13-2006) supervised by the NIPA(National IT Industry Promotion Agency)"

References

1. Smith, T.F., Waterman, M.S.: Identification of Common Molecular Subsequences. *J. Mol. Biol.* 147, 195–197 (1981)
2. May, P., Ehrlich, H.-C., Steinke, T.: ZIB Structure Prediction Pipeline: Composing a Complex Biological Workflow through Web Services. In: Nagel, W.E., Walter, W.V., Lehner, W. (eds.) *Euro-Par 2006. LNCS*, vol. 4128, pp. 1148–1158. Springer, Heidelberg (2006)
3. Almeida, F., Lopes, A., Abreu, P.: IForce-Impedance Control: a new control strategy of robotic manipulators
4. Koo, D.H.: Design of Exoskeleton Robot for Arm Rehabilitation in Stroke Patients (2010)
5. Song, K.W.: Synchronization Control of Single Link Manipulators. In: *CICS 2010* (2010)
6. Anderson, R., Spong, M.W.: Hybrid impedance control of robotic manipulators: *Robotics and Automation. IEEE Journal* 4(5)
7. Xu, W., Yin, M., Zou, Y.: Time-varying force tracking in impedance control. In: *2012 IEEE 51st Annual Conference on Decision and Control (CDC)* (2012)
8. Li, Y., Ge, S.S., Tee, K.P.: Adaptive impedance control for natural human-robot collaboration: WASA 2012. In: *Proceedings of the Workshop at SIGGRAPH Asia*, pp. 91–96 (2012)
9. Mehdi, H., Boubaker, O.: Stiffness and Impedance Control Using Lyapunov Theory for Robot-Aided Rehabilitation. *International Journal of Social Robotics* 4(1), 107–119 (2012)
10. Forte, F., Naldi, R., Macchelli, A., Marconi, L.: Impedance control of an aerial manipulator. In: *American Control Conference, ACC* (2012)

A Principle of Mechanical Implementing the Kinematic Synergy for Designing Anthropomorphic Hand

Wenbin Chen* and Caihua Xiong

State Key Lab of Digital Manufacturing Equipment and Technology
Institute of Rehabilitation and Medical Robotics
Huazhong University of Science and Technology, Wuhan 430074, China
wbchen@hust.edu.cn

Abstract. The kinematic synergy observed in angular velocity profile are employed by human hand in skilled grasping movement. Comparing to the static posture synergy, the reconstruction error of hand shape from kinematic synergy is obviously smaller when both using two most significant principle components. What's more, the whole process of hand dynamic movement can be reconstructed just by several constant parameters as weight coefficient to linear combine the kinematic synergies. However, no work in literature mechanically implement the kinematic synergy for designing anthropomorphic hand. In this paper, real-world data of hand grasping process is collected using a data glove, and two most important kinematic synergies are extracted. A novel mechanical designing principle is proposed to synthesize the synergies by groups of cams. The mechanism design has the potentially attractive benefit to greatly reduce the complexity of motion control of anthropomorphic hand. The full grasping process of anthropomorphic hand can be implemented just by keeping input-shaft rotate one cycle at constant velocity.

Keywords: kinematic synergy, mechanical implementation, anthropomorphic hand, design principle.

1 Introduction

The human hand has a large number of mechanical DOF, which offers great flexibility to perform skilled grasping and manipulation. It is a particularly challenging to design an anthropomorphic prosthetic hand controlled by bio-signals, such as sEMG(surface electro-myography) and EEG(electro-encephalography), that can replicate the dexterous movement of human hand. To achieve this goal, the particular mechanism employed should be able to implement statistical information of the dexterous movement as much as possible. On the other hand, the number of input channels for controlling anthropomorphic prosthetic hand should be compatible with the bio-signal interface. However, due to the limited bandwidth of bio-signal interface, the versatility and controllability seems to be incompatible if each degree of

* Corresponding author.

freedom of the anthropomorphic hand require individual control to perform grasping task or manipulation.

The neurophysiological researches about the principle of CNS (Central Nervous System) coordinate the fingers motion provide an alternative strategy to address this problem. It is showed that the coordination of available degree of freedom follow the synergy manner. Each posture or motion procedure of hand can be represented as linear combination of several principle components. This principle component correspond to static or temporal flexion/extension actuation statuses of several involved muscles. In literature, the static status is referred as to posture synergy whose component value is scalar corresponding to the joint angle, and the temporal status is referred as to kinematic synergy or dynamic synergy whose component value is vector corresponding to the temporal angular velocity or torque. Comparing to the related low approximation (80% of the total variance) [1] of static posture synergy, the kinematic synergy have higher approximation (89% of the total variance) [2] to the original movement. What's more, the kinematic synergies contain spatiotemporal information which is attractive to design more versatile anthropomorphic hand with fewer inputs.

Much work have been done to deal with coordinating multi-joints of robotic hand via a few inputs. These inputs are the coefficient for combining static posture synergies. For example, two and three postural synergies were used to control 24 actuators in the ACT hand to perform writing and piano playing [3, 4]. Other examples include the use of two synergies in the DLR II hand [5], the use of three synergies in the SAH hand [6], the use of two synergies in the UB hand [7], etc. Two extracted patterns of sEMG from wrist movement were used to control the CyberHand in real-time[8]. Different from above works, the posture synergies were implemented via mechanical design. The input rotation were transmitted to several sub-rotation by different radius pulleys. These sub-rotation were used to drive the finger joints[9].

However, these works are totally based on the static postural synergies without the temporal information. Since the fixed ratio in each synergy create fixed velocity and grasping force among joints, the static posture synergies are not suitable for flexible and dynamic motion. The temporal characteristic among joints is key to realize the delicate and skilled motion for anthropomorphic hand. Up to now, no work has exploited this fact mechanically on robotic hand design.

To address this issue, this paper proposes a mechanical method to implement the kinematic synergy. The kinematic synergy is generated by groups of cam mechanism. The design use only two input-shafts which rotate at constant velocity to produce temporal varying hand postures. We develop a principle of how to design appropriate cam contour to fit the time vary angular velocity. A improvement of the mechanism design is also presented in this paper.

2 Kinematic Synergy and Mechanical Principle

Kinematic synergy is derived from angular velocities of the finger joints of the human hand during grasping tasks by SVD procedure. Before giving the mechanism implementation, we begin with a brief overview of the mathematical form of kinematic synergy.

If the period of hand grasping or manipulation is averagely sampled t_s times in one trial, the angular velocity evolvment of hand's n joints at the duration can be represented

$$\mathbf{v} = [\omega_1(t_1) \cdots \omega_1(t_s) \cdots \omega_n(t_1) \cdots \omega_n(t_s)] \quad (1)$$

where the element $\omega_i(t_j)$ is the i th joint velocity at the t_j th sample (t_1 represents the first sample at initial time and t_s represents the final sample at end time). Given N trials for grasping or manipulating different objects, a velocity matrix can be defined by:

$$\mathbf{V} = \begin{bmatrix} \mathbf{v}_1 \\ \vdots \\ \mathbf{v}_N \end{bmatrix} \quad (2)$$

where \mathbf{v}_i ($i=1 \cdots N$) is the i th trial of grasping or manipulation. Then, this joint velocity matrix can be rewritten as product of three smaller matrices by singular value decomposition, which is illustrated by Eq.(3). Each row of the third matrix \mathbf{S} is called a principle component (or called a synergy). The associated weight of each synergy is the corresponding diagonal element of the second matrix whose diagonal elements are ranked from largest to smallest.

$$\mathbf{V} = \mathbf{U} \text{diag}\{\lambda_1 \cdots \lambda_m\} \mathbf{S} \quad (3)$$

According to the importance of elements of the diagonal matrix, the matrix \mathbf{V} can be approximated by $\hat{\mathbf{V}}$ if the first k diagonal elements are selected.

$$\mathbf{V} \approx \hat{\mathbf{V}} = \mathbf{W} \mathbf{S}_k \quad (4)$$

where $\mathbf{W} = \mathbf{U}_k \text{diag}\{\lambda_1 \cdots \lambda_k\}$, \mathbf{U}_k is the first k columns of matrix \mathbf{U} , \mathbf{S}_k is the first k rows of matrix \mathbf{S} . Here we use the first two diagonal elements, i.e. λ_1 and λ_2 , and then :

$$\begin{aligned} \mathbf{V} \approx \hat{\mathbf{V}} &= \begin{bmatrix} w_1^1 & w_1^2 \\ \vdots & \vdots \\ w_q^1 & w_q^2 \\ \vdots & \vdots \\ w_N^1 & w_N^2 \end{bmatrix} \begin{bmatrix} S_1^1(t_1) & \cdots & S_1^1(t_s) & \cdots & S_n^1(t_1) & \cdots & S_n^1(t_s) \\ S_1^2(t_1) & \cdots & S_1^2(t_s) & \cdots & S_n^2(t_1) & \cdots & S_n^2(t_s) \end{bmatrix} \\ &= \begin{bmatrix} w_1^1 & w_1^2 \\ \vdots & \vdots \\ w_q^1 & w_q^2 \\ \vdots & \vdots \\ w_N^1 & w_N^2 \end{bmatrix} \begin{bmatrix} \mathbf{S}^1 \\ \mathbf{S}^2 \end{bmatrix} \end{aligned} \quad (5)$$

where w_i^1 and w_i^2 are weight coefficients associated with \mathbf{S}^1 and \mathbf{S}^2 for the i th row of matrix \mathbf{V} . The two principle components \mathbf{S}^1 and \mathbf{S}^2 are the angular velocity synergy of the joints over the entire movement. Each row of \mathbf{V} corresponding to one trial can be written as

$$\mathbf{v}_i \approx \begin{bmatrix} w_i^1 & w_i^2 \end{bmatrix} \begin{bmatrix} \mathbf{S}^1 \\ \mathbf{S}^2 \end{bmatrix} \quad (6)$$

or rewritten in following form:

$$\begin{bmatrix} \omega_1(t_1) & \cdots & \omega_1(t_s) \\ \vdots & & \vdots \\ \omega_n(t_1) & \cdots & \omega_n(t_s) \end{bmatrix} \approx w_i^1 \begin{bmatrix} S_1^1(t_1) & \cdots & S_1^1(t_s) \\ \vdots & & \vdots \\ S_n^1(t_1) & \cdots & S_n^1(t_s) \end{bmatrix} + w_i^2 \begin{bmatrix} S_1^2(t_1) & \cdots & S_1^2(t_s) \\ \vdots & & \vdots \\ S_n^2(t_1) & \cdots & S_n^2(t_s) \end{bmatrix} \quad (7)$$

where each row of the matrices at the two sides of Eq.(7) corresponds to one joint velocity evolution at the duration of hand movement. The reduced form of Eq.(7) for the i th joint is:

$$\omega_i|_{t_1}^{t_s} \approx w_i^1 S_i^1|_{t_1}^{t_s} + w_i^2 S_i^2|_{t_1}^{t_s} \quad i = 1, \dots, n \quad (8)$$

It must be noted that the element of kinematic synergy represented by angular velocity is a continuously varying function of time. This characteristic of kinematic synergy is obviously different from the static posture synergy whose element is scalar value. When initial hand posture is specified as the naturally full extended fingers, the hand posture at each time during the given period can be got by integrating kinematic synergy. The mechanical realization of kinematic synergy is implemented by properly designing transmission mechanism whose output velocity has the same profile and amplitude with the kinematic synergy described in Eq.(7).

3 Mechanism Design

3.1 Hand Grasping and Kinematic Synergy Extraction

Here we use the CyberGloveTM to measure the time-varying joint angles of hand from initial posture to grasp objects with different shapes using in daily living. The final grasping patterns for each object follow the grasp taxonomy proposed by Cutkosky[10]. In total 322 grasping trials are used to extract kinematic synergies. We only consider ten of the sensors that correspond to the metacarpophalangeal (MCP) and interphalangeal (IP) joints of the thumb and the MCP and proximal interphalangeal (PIP) joints of the other four fingers. These ten joints can capture most characteristics of the hand in grasping tasks. Note that the distal interphalangeal (DIP) joints are not considered because the flexion of the DIP joint of a finger is about two-thirds of that of the PIP joint [11]. The most two important kinematic synergy are extracted as shown in Fig. 1. For analysis compliance, the trajectories are filtered and the duration time is normalized to one second.

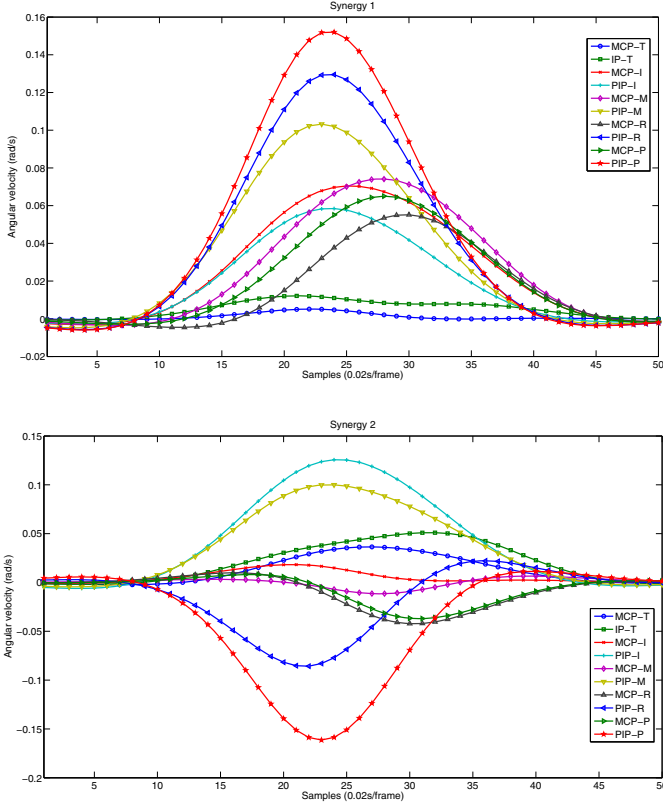


Fig. 1. Two kinematic synergies extracted from 322 grasping trials. The abbreviated letters T, I, M, R and P correspond to thumb, index finger, middle finger, ring finger and pinky finger respectively.

3.2 Transmission Mechanism

Cam Design

The angular velocity profile in each synergy is realized by a combined mechanism consisting of a cam, disc and pulley. As shown in Fig. 2, the cam and disc are fixed together. The radius of the cam is dependent on the rotational angle. When the input shaft rotates at constant angular velocity, the differential motion between input angle and output translation is :

$$r_b(\alpha)d\alpha - r_a d\alpha = 2dy \tag{9}$$

Here, the dy is described in tendon space and it can be mapped to joint space just by winding a rope around the disc of a revolutionary joint. In this subsection, we call this revolutionary joint *design-reference-finger-joint* whose disc radius and differential rotation are denoted by r_s and $d\alpha_s$ respectively. Thus, if the output translation dy in tendon space is applied to the design-reference-joint, the dy can be represented as $dy = r_s d\alpha_s$. Put it into Eq.(9), we get

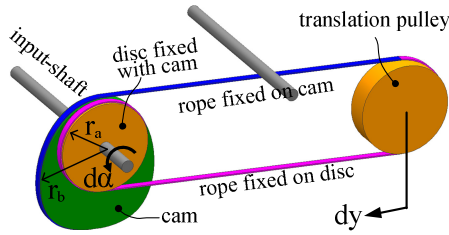


Fig. 2. Mechanism generating time-varying translation in tendon space. The cam is rigidly attached to the shaft. The axes of disc and cam are aligned. Notice that there is only one single rope in this mechanism which two end-tips of the rope are fixed with cam and disc respectively. The different color of the rope is just for conveniently illustrating winding manner.

$$r_b(\alpha)d\alpha - r_a d\alpha = 2r_s d\alpha_s \tag{10}$$

Dividing both sides of Eq.(10) by differential time dt , the expression about the radius of cam is got

$$r_b(\alpha) = 2r_s \frac{S}{\bar{\omega}} + r_a \tag{11}$$

where $S = d\alpha_s/dt$ can be considered to be the angular velocity of one joint in kinematic synergy. $\bar{\omega} = d\alpha/dt$ is the angular velocity of input axis with constant value. In this subsection, we call $\bar{\omega}$ *input-reference-rotation*. According to Eq.(11), if the radii of cam’s disc and *design-reference-finger-joint* disc, e.g., r_a and r_s , are respectively specified, the cam with resulted radius will ensure the *design-reference-finger-joint* follow the corresponding velocity profile of the kinematic synergy under averagely rotating the input-shaft certain angle at constant velocity $\bar{\omega}$.

Considering the continuous requirement of cam contour on the initial time (0 degree) and end time (360 degree), here, we assume that the *design-reference-finger-joint* posture change from initial shape to the final grasping shape when input-shaft rotate one cycle. This assumption means that the maximum rotational angle of the input-shaft should be 360 degree. When input-shaft rotates back to 0 degree from its maximum allowed angle, the hand joint return to its initial shape by the torsional springs set at finger joint axes.

For example, if the radii of cam’s disc r_a and *design-reference-finger-joint* disc r_s are set to be $r_a = r_s = 10\text{mm}$, and the *input-reference-rotation* $\bar{\omega} = 0.5 \text{ rad/s}$, using the first kinematic synergy shown in Fig. 1 as the value of S , the resulting radii of cam and its associated disc for the first kinematic synergy are given in Fig. 3.

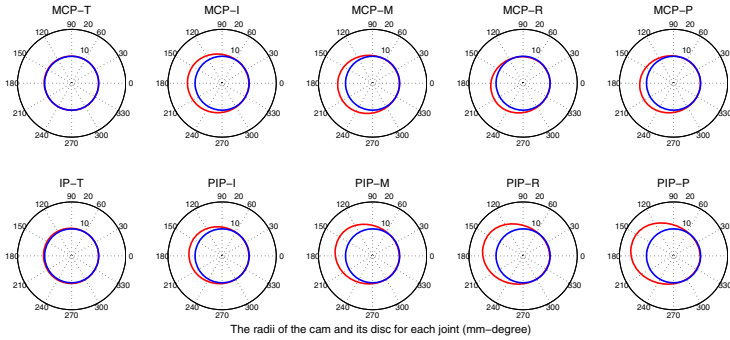


Fig. 3. The radii of the cam and its associated disc related to rotational angle in polar coordinate (radius-angle) for each joint corresponding to the first kinematic synergy. The red curves represent the cam contour and the blue cycles represent the disc rigidly attached to cam.

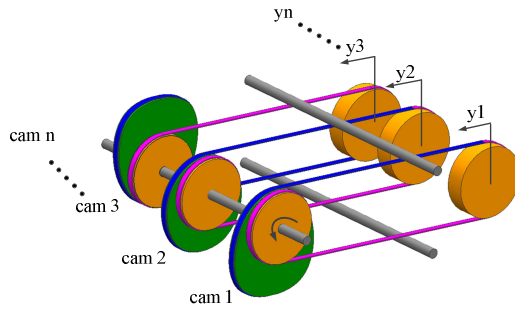


Fig. 4. The cams attach on the input-shaft. Notice that the cam 3 rotates 180 degree around the input-shaft and the rope winding around the cam and associated disc is in reverse order, which is to generate obviously minus velocity profile of some joints in kinematic synergy.

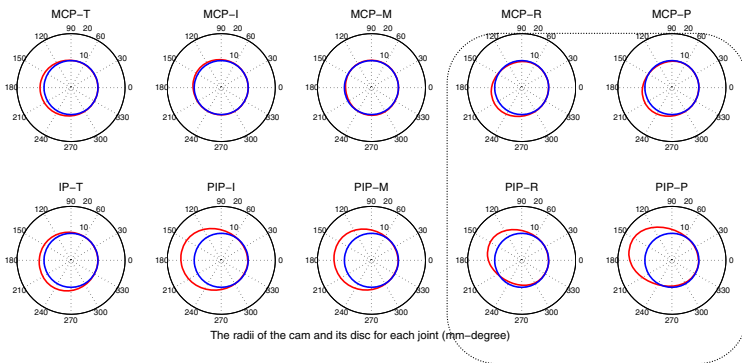


Fig. 5. The radii of the cam and its associated disc related to rotational angle in polar coordinate (radius-angle) for each joint corresponding to the second kinematic synergy. Notice that the last four cams marked out by dashed line are the result by changing shaft-attached manner and reverse rope winding.

Notice that some joints in the kinematic synergy, e.g. the second kinematic synergy, have greatly minus velocity profile, which will result the corresponding cam with concave contour according to Eq.(11). To avoid this phenomenon, the corresponding cam can attach the input-shaft in opposition direction and change the rope winding in reverse manner. For illustration, see the cam 3 shown in Fig. 4. After this process, the resulting radii of cam and its associated disc for the second kinematic synergy are all convex and the results are given in Fig. 5.

Synergy Synthesis

In this subsection, we will use the designed cams proposed in above section and show how to realize the synthesis of kinematic synergies in Eq.(7).

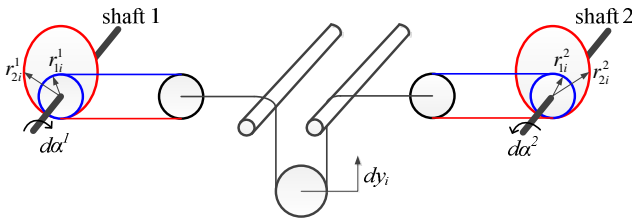


Fig. 6. Combining the two cam mechanisms to implement kinematic synergy analysis

As shown in Fig. 6, the output dy_i is given by

$$r_{2i}^1 d\alpha^1 - r_{1i}^1 d\alpha^1 + r_{2i}^2 d\alpha^2 - r_{1i}^2 d\alpha^2 = 4dy_i \quad i = 1, \dots, 10 \tag{12}$$

Here the dy_i is directly applied to drive the i th finger joint of anthropomorphic hand. Thus $dy_i = r_i^0 d\alpha_i^0$ in which r_i^0 and $d\alpha_i^0$ represent radius of disc and differential rotation of the i th finger joint respectively. Put it into Eq.(12) and rewrite Eq.(12) in following form:

$$\frac{\omega^1}{4r_i^0} (r_{2i}^1 - r_{1i}^1) + \frac{\omega^2}{4r_i^0} (r_{2i}^2 - r_{1i}^2) = \omega_i^0 \tag{13}$$

where $\omega^1 = d\alpha^1/dt$, $\omega^2 = d\alpha^2/dt$ and $\omega_i^0 = d\alpha_i^0/dt$. ω^1 and ω^2 are scalar and represent the rotational velocity of shaft 1 and 2 respectively. According to Eq.(11), we have $r_{2i}^1 - r_{1i}^1 = 2r_s S_i^1/\bar{\omega}$ and $r_{2i}^2 - r_{1i}^2 = 2r_s S_i^2/\bar{\omega}$, where S_i^1 and S_i^2 represent the i th row of the first kinematic synergy and the second kinematic synergy in (7) respectively. Put them into Eq.(13), the angular velocity of i th joint of anthropomorphic hand related to the two kinematic synergy is given by:

$$\omega_i^0 = \frac{r_s}{2\bar{\omega}r_i^0} \omega^1 \cdot S_i^1 + \frac{r_s}{2\bar{\omega}r_i^0} \omega^2 \cdot S_i^2 \quad i = 1, \dots, 10 \tag{14}$$

Comparing (8) and (14), we basically implement the kinematic synergy synthesis via the proposed cam mechanism. To perform one grasping task in predefined

duration from initial fully extended hand posture, it only need to specify the constant rotational velocity for two input-shafts , e.g. ω^1 and ω^2 .

Among the mechanical implementation of hand kinematic synergy, there are four independent parameters are needed to specify, e.g. r_s the disc radius of design-reference-joint, r_a the disc radius associated with cam, $\bar{\omega}$ the reference-angular-velocity, and r_i^O the disc radius of the i th finger joint, when the r_i^O for each finger joint are assumed to be the same value. Changing r_s , $\bar{\omega}$ and r_i^O will effect the rotational velocity of input-shaft. The maximum radius of cams and disc radius of the finger joint should be in appropriate limit for designing and friendly using the anthropomorphic hand. The optimal value of the four parameters r_s , r_a , r_i^O and $\bar{\omega}$ corresponding to one synergy can be solved by following optimal procedure:

$$\begin{aligned} \min : r_b &= f(r_s, r_a, r_i^O, \bar{\omega}) = 2r_s \frac{|S^1|_{\max}}{\bar{\omega}} + r_a \\ \text{subject to:} \\ 0 \leq \omega^1 &= |w^1|_{\max} \Big/ \frac{r_s}{2\bar{\omega}r_i^O} \leq \omega_{\max} \\ r_{\min}^O &\leq r_i^O \leq r_{\max}^O \\ r_{S \min} &\leq r_s \leq r_{S \max} \\ r_{a \min} &\leq r_a \leq r_{a \max} \\ \bar{\omega} &> 0 \end{aligned} \tag{15}$$

where the meaning of objective function is to limit the maximum radius of cam corresponding to the joint with most maximum velocity peak in kinematic synergy. $|S^1|_{\max}$ is found to be 0.152rad/s according to the motion data. The first constraint condition is to limit the rotational velocity of the input-shafts. According to the SVD decomposition of motion data, the maximum coefficient $|w^1|_{\max}$ is found to be 60.453. Other boundary values for optimization are given in Table 1

Table 1. Value of boundary condition for optimization

Boundary parameters	value	Boundary parameters	value
ω_{\max}	4π rad/s	$r_{S \max}, r_{S \min}$	10 mm, 5 mm
r_{\max}^O, r_{\min}^O	10 mm, 5 mm	$r_{a \max}, r_{a \min}$	15 mm, 10 mm

Using the global optimization procedure in Matlab, the optimal results of the design parameters (15) are given in Table 2. Similarly, we can obtain the optimal cam mechanism using procedure (15), and the required parameter for optimization are $|S^2|_{\max} = 0.126$ rad/s, $|w^2|_{\max} = 20.421$. The optimal results are also given in Table 2.

Table 2. The optimal result for the cam mechanism

kinematic synergy 1		kinematic synergy 2	
Parameters	value	Parameters	value
r_s	8.03 mm	r_s	9.25 mm
r_a	10.00 mm	r_a	10.00 mm
r_i^O	5.00 mm	r_i^O	5.00 mm
$\bar{\omega}$	0.17 rad/s	$\bar{\omega}$	0.57 rad/s
optimal value of objective function	24.6mm	optimal value of objective function	14.1 mm

Based on these optimal, the final cam mechanisms for synergy synthesis can be obtained. According to the optimal result, the radius of disc associated with cams in synergy 1 and synergy 2 are the same value. The same radius of disc of all finger joints simplify the finger design. Notice that the contour of final cam mechanism are different from the illustrated result shown in Fig. 3 and Fig. 5. Due to the page limit, these optimal cam mechanism are not shown here. However, for illustrating how the mechanism working, here we give the developed prototype of anthropomorphic hand driven by the mechanism according to implementation of the kinematic synergy, as shown in Fig. 7

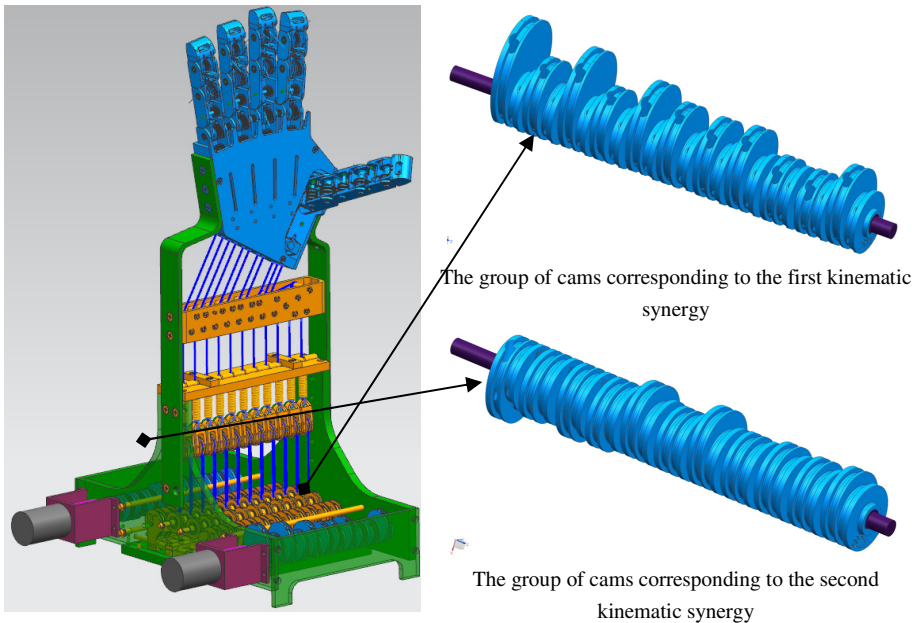


Fig. 7. The developed prototype of anthropomorphic hand driven by the mechanism according to implementation of the kinematic synergy

4 Conclusion

We have presented a novel design principle for realizing the kinematic synergy of multiply fingers of human hand perform grasping task most using in daily living. This mechanism implementation can be used to guide the design of driving mechanism and fingers of prosthetic hand controlled by patient's bio-signal, such as EMG. Since the channels of bio-interface is extremely limited, realizing the dynamic motion control in real-time with only two input is the most attractive of our method. Through mechanism implementing the kinematic synergy, the grasping process of anthropomorphic hand can easily be implemented just by keeping input-shaft rotate one cycle at constant velocity. These characteristic of the proposed mechanism greatly reduces the control complexity.

We also discussed the a meaningful design improvement to allow miniaturization of hand finger and drive mechanism. This is very important for the anthropomorphic hand in practical using in daily living. Another benefit of the improvement is to appropriately limit the grasping force, since moment arm of input force, e.g. radius of cam, is controlled. Because the kinematic synergy observed in angular velocity profile has higher precision on reconstructing hand posture, especially for time varying posture in grasp, than that of static posture synergy[2], it is promising for perform more flexible movement. How to further reduce the reconstruction error via mechanism manner is our future scope.

Acknowledgments. This work was supported by the National Basic Research Program of China (973 Program) (Granted No. 2011CB013301), National Science Fund for Distinguished Young Scholars of China (Grant No. 51025518), and the National Natural Science Foundation of China (NSFC) under Grant No. 51121002.

References

- [1] Santello, M., Flanders, M., Soechting, J.F.: Postural Hand Synergies for Tool Use. *The Journal of Neuroscience* 18(23), 10105–10115 (1998)
- [2] Vinjamuri, R., Mingui, S., Cheng-Chun, C., Heung-No, L., Sciabassi, R.J., Zhi-Hong, M.: Dimensionality Reduction in Control and Coordination of the Human Hand. *IEEE Transactions on Biomedical Engineering* 57(2), 284–295 (2010)
- [3] Rombokas, E., Malhotra, M., Matsuoka, Y.: Task-specific Demonstration and Practiced Synergies for Writing with the ACT Hand. In: *IEEE International Conference on Robotics and Automation (ICRA)*, Shanghai, pp. 5363–5368 (2011)
- [4] Zhang, A., Malhotra, M., Matsuoka, Y.: Musical Piano Performance by the ACT Hand. In: *IEEE International Conference on Robotics and Automation (ICRA)*, Shanghai, pp. 3536–3541 (2011)
- [5] Wimböck, T., Jahn, B., Hirzinger, G.: Synergy Level Impedance Control for Multifingered Hands. In: *IEEE/RSJ International Conference on Intelligent Robots and Systems (IROS)*, San Francisco, pp. 973–979 (2011)

- [6] Rosell, J., Suárez, R., Rosales, C., Pérez, A.: Autonomous Motion Planning of a Hand-Arm Robotic System Based on Captured Human-like Hand Postures. *Autonomous Robots* 31(1), 87–102 (2011)
- [7] Ficuciello, F., Palli, G., Melchiorri, C., Siciliano, B.: Experimental evaluation of Postural Synergies during Reach to Grasp with the UB Hand IV. In: *IEEE/RSJ International Conference on Intelligent Robots and Systems (IROS)*, San Francisco, pp. 1775–1780 (2011)
- [8] Matrone, G., Cipriani, C., Carrozza, M., Magenes, G.: Real-time myoelectric control of a multi-fingered hand prosthesis using principal components analysis. *Journal of NeuroEngineering and Rehabilitation* 9(40), 1–13 (2012)
- [9] Brown, C.Y., Asada, H.H.: Inter-finger coordination and postural synergies in robot hands via mechanical implementation of principal components analysis. In: *IEEE/RSJ International Conference on Intelligent Robots and Systems*, pp. 2877–2882 (2007)
- [10] Cutkosky, M.R.: On grasp choice, grasp models, and the design of hands for manufacturing tasks. *IEEE Transactions on Robotics and Automation* 5(3), 269–279 (1989)
- [11] Yi, B., Harris Jr, F.C., Wang, L., Yan, Y.: Real-time natural hand gestures. *Computing in Science & Engineering* 7(3), 92–96 (2005)

Design Simulations of the SJTU Continuum Arm Exoskeleton (SCAX)

Kai Xu, You Wang, and Dong Qiu

RII Lab (Lab of Robotics Innovation and Intervention), UM-SJTU Joint Institute,
Shanghai Jiao Tong University, Shanghai, 200240, China
{k.xu,youwang,d.qiu}@sjtu.edu.cn

Abstract. In a clinical environment for rehabilitation therapy, one exoskeleton is usually shared by multiple patients. If the exoskeleton has a rigid structure which is actuated to mobilize a patient, it will be challenging to guarantee these on-site adjustments can make the rigid exoskeleton fit each patient kinematically perfectly. This paper proposes to design an exoskeleton using compliant continuum mechanisms. Its intrinsic flexibility allows the adaption to different human anatomies passively. The design concept, kinematics and design simulations are elaborated for this SJTU Continuum Arm Exoskeleton (SCAX). Combining previous experimental results for a proof-of-concept shoulder exoskeleton, the SCAX could effectively achieve consistent Anatomy Adaptive Assistances (AAA) for different patients with their limb motions.

Keywords: Exoskeleton, continuum mechanisms, kinematics, SCAX (SJTU Continuum Arm Exoskeleton), AAA (Anatomy Adaptive Assistances).

1 Introduction

Research on exoskeletons has been quite active in the past decades. Numerous exoskeleton systems were developed for upper and lower limbs for military and medical applications (e.g. [1, 2]). These exoskeleton systems either aim to augment a healthy wearer's physical performance with robotic actuation or to deliver rehabilitation therapies to patients with neuromuscular defects after stroke or injury. Examples include the performance-augmenting exoskeleton from UC Berkeley [3], the load-carrying exoskeleton from MIT [4], rehabilitation exoskeletons for lower limbs [5-9], and those for upper limbs [10-17]. Actuation schemes of these systems include hydraulic cylinders [3] or pneumatic cylinders [5, 15, 18], pneumatic muscle actuators [10], cables [7, 11, 17], parallel mechanisms [8, 12, 14], gearmotors [19] and so on.

Besides these systems, research was also about enabling technologies, such as inertia compensation [20], sensing & control [4, 21-24], and most importantly ergonomics [25-27].

Many of the existing exoskeleton systems shared one similar design methodology: an articulated rigid kinematic chain is actuated to move an attached wearer. The use of rigid mechanisms in an exoskeleton might be suitable for applications for strength augmentation so that excessive external loads can be undertaken so as to shield the

wearer. But the use of rigid mechanisms introduces drawbacks such as bulkiness, high inertia, and most importantly the difficulty of maintaining kinematic compatibility between the exoskeleton and a human anatomy. In a clinical environment for rehabilitation therapy, one exoskeleton is usually shared by a group of patients. If the exoskeleton has a rigid structure, it will be challenging to guarantee these on-site adjustments can make the rigid exoskeleton fit each patient kinematically perfectly. Hence, design possibilities of using compliant components could be investigated. These attempts include a simulation work that used elastic cords to assist walking [28], an upper body exoskeleton using pneumatic artificial muscles [29], a cable-driven upper-limb exoskeleton [16, 17], and a proof-of concept continuum shoulder exoskeleton [30-32].

This paper presents the design concept, kinematics and simulation verifications of the SJTU Continuum Arm Exoskeleton (SCAX) as shown in Fig. 1. The contribution of this paper is mainly the proposal of designing an arm exoskeleton for rehabilitation using continuum mechanisms. Intrinsic compliance of such a continuum exoskeleton adapts to different human anatomies passively and can always assure the kinematic compatibility between itself and a group of patients.

The paper is organized as follows. Section 2 presents the design concept. Section 3 presents nomenclature and kinematics so that the simulation verifications can be presented in Section 4. Conclusions and future work are summarized in Section 5.

2 Design Concept

The continuum shoulder exoskeleton as in Fig. 1 consists of i) a rigid forearm sleeve, ii) a flexible elbow brace, iii) a rigid upper arm sleeve, iv) a flexible shoulder brace, v) a body vest, vi) a set of guiding cannulae, and vii) an actuation unit. Actuation of the continuum elbow brace and the continuum shoulder brace orients a patient's arm accordingly. This work is inspired by the designs from [33-35] where downscaled such continuum structures were used in surgical robots.

Structures of the continuum elbow brace and the continuum shoulder brace are similar. A schematic structure is also depicted in Fig. 2. Each brace consists of an end ring, a base ring, a few spacer rings and several secondary backbones. All the backbones are made from thin NiTi (Nickel-Titanium alloy) rods.

For either the shoulder brace or the elbow brace, the secondary backbones are only attached to the end ring and can slide in holes of the spacer rings and the base ring. The backbones for the elbow brace are routed through the upper arm sleeve and the shoulder brace. The backbones for the elbow and the shoulder braces are all routed through the set of guiding cannulae to the actuation unit, which simultaneously pulls and pushes these backbones to bend the continuum braces to orient a patient's upper arm and forearm. Miniature springs are used to keep the spacer rings evenly distributed to prevent buckling of the secondary backbones.

Advantages of the continuum exoskeleton include: i) safety and comfort introduced by the inherent compliance, ii) passive adaptation to different patient anatomies, iii) size scalability, iv) a redundant backbone arrangement for load redistribution and reduced buckling risks, and v) design compactness achieved by dual roles of these backbones as both the structural components and the motion output members.

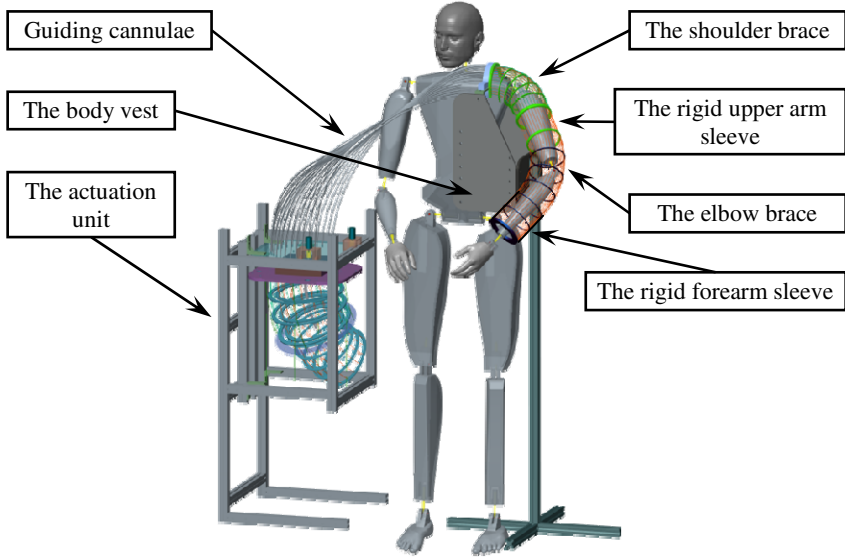


Fig. 1. Design concept of the SJTU Continuum Arm Exoskeleton (SCAX)

3 Nomenclature and Kinematics

The nomenclature and the kinematics assume that the continuum braces (the shoulder and the elbow braces) bend into a planar shape within the bending plane as shown in Fig. 2. Shapes of the secondary backbones are assumed by a sweeping motion of the structure's cross section along the primary backbone. The cross section is assumed rigid and perpendicular to the primary backbone. Different from previously published results [34, 36, 37], this work doesn't assume shape of the imaginary primary backbone to be circular, which has been experimentally verified in [31].

3.1 Nomenclature and Coordinate Systems

Since the shoulder brace and the elbow brace are structurally similar, the structure in Fig 2 could be applied as the shoulder brace or the elbow brace with different arrangement of the backbones.

To describe the structure, nomenclatures are defined in Table I, while coordinate systems of the continuum brace are defined as below

- *Base Ring Coordinate System (BRS)* is designated as $\{tb\} \equiv \{\hat{\mathbf{x}}_{tb}, \hat{\mathbf{y}}_{tb}, \hat{\mathbf{z}}_{tb}\}$. It is attached to the base ring of the continuum brace, whose XY plane coincides with the base ring and its origin is at the center of the base disk. $\hat{\mathbf{x}}_{tb}$ points from the center of the base disk to the first secondary backbone while $\hat{\mathbf{z}}_{tb}$ is perpendicular to the base ring. The secondary backbones are numbered according to the definition of δ_i .

- *Bending Plane Coordinate System 1* (BPS1) is designated as $\{t1\} \equiv \{\hat{\mathbf{x}}_{t1}, \hat{\mathbf{y}}_{t1}, \hat{\mathbf{z}}_{t1}\}$ which shares its origin with $\{tb\}$ and has the brace bending in its XZ plane.
- *Bending Plane Coordinate System 2* (BPS2) is designated as $\{t2\} \equiv \{\hat{\mathbf{x}}_{t2}, \hat{\mathbf{y}}_{t2}, \hat{\mathbf{z}}_{t2}\}$ obtained from $\{t1\}$ by a rotation about $\hat{\mathbf{y}}_{t1}$ such that $\hat{\mathbf{z}}_{t1}$ becomes backbone tangent at the end ring. Origin of $\{t2\}$ is at center of the end ring.
- *End Ring Coordinate System* (ERS) $\{te\} \equiv \{\hat{\mathbf{x}}_{te}, \hat{\mathbf{y}}_{te}, \hat{\mathbf{z}}_{te}\}$ is fixed to the end ring. $\hat{\mathbf{x}}_{te}$ points from center of the end ring to the first secondary backbone and $\hat{\mathbf{z}}_{te}$ is normal to the end ring. $\{te\}$ is obtained from $\{t2\}$ by a rotation about $\hat{\mathbf{z}}_{t2}$.

Table 1. Nomenclature used in this paper

t	Index of the continuum braces: $t = 1$ for the shoulder brace and $t = 2$ for the elbow brace
m	Index of the secondary backbones, $i = 1, 2, \dots, m$
r_{ii}	In the indicated brace, distance from the imaginary primary backbone to the i th secondary backbone. r_{ii} can be different for different t and i .
β_{ii}	In the indicated brace, β_{ii} characterizes the division angle from the i th secondary backbone to the first secondary backbone. $\beta_{ii} \equiv 0$ and β_{ii} remain constant once the braces are built.
L_t, L_{ii}	In the indicated brace, lengths of the imaginary primary and the i th secondary backbones measured from the base ring to the end ring.
$\rho_t(s), \rho_{ii}(s_{ii})$	In the indicated brace, radius of curvature of the primary and the i th secondary backbones.
\mathbf{q}_t	In the indicated brace, $\mathbf{q}_t = [q_{t1} \ q_{t2} \ \dots \ q_{tm}]^T$ is the actuation lengths for the secondary backbones and $q_{ii} \equiv L_{ii} - L_t$.
$\theta_t(s)$	In the indicated brace, angle of the tangent to the imaginary primary backbone in the bending plane. $\theta_t(L)$ and $\theta_t(0)$ are designated by θ_{tL} and θ_0 , respectively. $\theta_0 = \pi/2$
δ_{ii}	In the indicated brace, a right-handed rotation angle about $\hat{\mathbf{z}}_{t1}$ from $\hat{\mathbf{x}}_{t1}$ to a ray passing through the imaginary primary backbone and the i th secondary backbone.
δ_t	$\delta_t \equiv \delta_{t1}$ and $\delta_{ii} = \delta_t + \beta_{ii}$
Ψ_t	$\Psi_t \equiv [\theta_{tL} \ \delta_t]^T$ defines the configuration of the indicated brace.
${}^{tb}\mathbf{p}_t(s)$	In the indicated brace, position vector of a point along the primary backbone in $\{tb\}$. ${}^{tb}\mathbf{p}_t(L)$ is the tip position and is designated by ${}^{tb}\mathbf{p}_{tL}$.

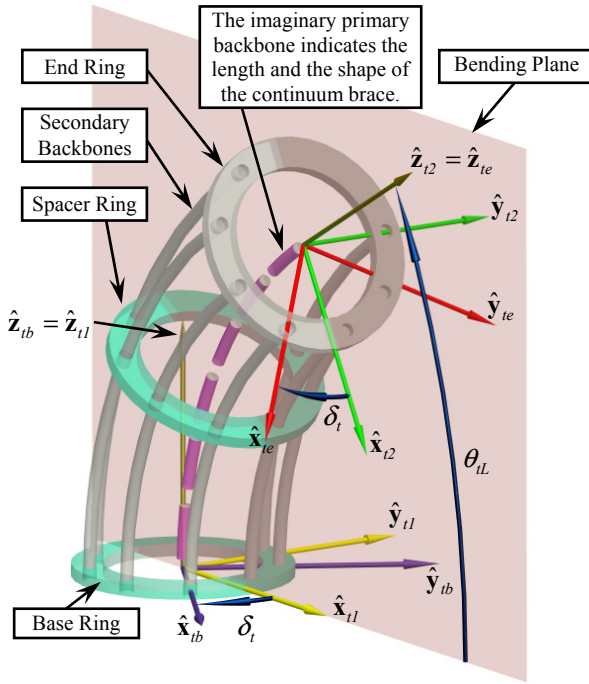


Fig. 2. Nomenclature and coordinates of the continuum brace

3.2 Kinematics

Thorough kinematics analysis of such a continuum brace can be found in [34, 36, 37]. This work here emphasizes the shape of the primary backbone to be non-circular (the result also applies if the shape is circular) and arrangements of the secondary backbones to be arbitrary (assigning different values to r_{ii} and β_{ii}).

Configuration of the continuum brace is parameterized by $\psi_i = [\theta_{iL} \ \delta_i]^T$. Since shapes of the secondary backbones are assumed by a sweeping motion of the structure's cross section along the primary backbone, projection of the i th secondary backbone on the bending plane is a curve which is offset by Δ_{ii} from the primary backbone. Its radius of curvature and arc-length are indicated by $\rho_{ii}(s_{ii})$ and s_{ii} . They are related to the parameters of the primary backbone as follows:

$$\rho_i(s) = \rho_{ii}(s_{ii}) + \Delta_{ii} \quad (1)$$

Where $\Delta_{ii} \equiv r_{ii} \cos \delta_{ii}$

The length of the primary backbone and the length of the i th backbone are related according to:

$$L_i = \int ds_{ii} = \int (ds_{ii} - ds_t + ds_t) = \int (ds_{ii} - ds_t) + L_t \quad (2)$$

The integral above can be rewritten as in Eq. (3). Substituting Eq. (1) into Eq. (3) gives Eq.(4), which leads to the result as in Eq. (5):

$$\int (ds_{ii} - ds_t) = \int_0^{\theta_0 - \theta_{iL}} (\rho_{ii}(s_{ii}) - \rho_t(s_t)) d\theta \quad (3)$$

$$\int_0^{\theta_0 - \theta_{iL}} (\rho_{ii}(s_{ii}) - \rho_t(s_t)) d\theta = - \int_0^{\theta_0 - \theta_{iL}} \Delta_{ii} d\theta \quad (4)$$

$$L_i = L_t - r_{ii} \cos \delta_{ii} (\theta_0 - \theta_{iL}) = L_t + r_{ii} \cos \delta_{ii} (\theta_{iL} - \theta_0) \quad (5)$$

Referring to the definition of q_{ii} in Table 1, Eq. (5) gives:

$$q_{ii} = r_{ii} \cos \delta_{ii} (\theta_{iL} - \theta_0), \quad i = 1, 2, \dots, m \quad (6)$$

Equation (6) states that actuation of this continuum brace only depends on the values of θ_{iL} and δ_t , no matter what the actual shape of the primary backbone is. This characteristics provides a particular advantage: when the brace is put on different patients, different anatomies give different shapes of the primary backbone, but the actuation remains the same while orienting the limb to the same direction (the direction is characterized by θ_{iL} and δ_t).

Rotation matrix ${}^b\mathbf{R}_e$ associates $\{te\}$ and $\{tb\}$:

$${}^{tb}\mathbf{R}_{te} = \mathbf{R}(\hat{\mathbf{z}}_{tb}, -\delta_t) \mathbf{R}(\hat{\mathbf{y}}_{t1}, \theta_0 - \theta_{iL}) \mathbf{R}(\hat{\mathbf{z}}_{t2}, \delta_t) \quad (7)$$

Where $\mathbf{R}(\hat{\mathbf{n}}, \gamma)$ represents rotation about $\hat{\mathbf{n}}$ by an angle γ .

Tip position of the continuum brace is given by:

$${}^{tb}\mathbf{p}_{iL} = {}^{tb}\mathbf{R}_{te} \left[\int_0^{L_t} \cos(\theta_t(s_t)) ds_t \quad 0 \quad \int_0^{L_t} \sin(\theta_t(s_t)) ds_t \right]^T \quad (8)$$

Where ${}^{tb}\mathbf{R}_{te} = \mathbf{R}(\hat{\mathbf{z}}_{tb}, -\delta_t)$ and the integrals depend on the actual shape of the primary backbone.

4 Design Simulations

Actual shapes of the shoulder and the elbow braces depend on a minimal of the total potential energy of the exoskeleton-arm system (elastic potential energy of the continuum exoskeleton and the gravitational potential energy of the arm). The shapes would also be affected by the anatomical parameters (such as shoulder widths and arm lengths) of a patient.

Demonstrated experimentally as in [31], the shapes of the braces' secondary backbones were different from circular arcs. In fact the actual shapes kept changing during the motions of assisting a patient's limb. In order to verify the kinematics of the SCAX exoskeleton, the simulations are conducted with an assumption that the shape of one secondary backbone within the braces could be characterized as one circular arc plus a straight line, as shown in Fig. 3.

The arm in Fig. 3 consist of a shoulder joint, an upper arm, an elbow joint and a forearm with hand. The shoulder joint is represented by a spherical joint whereas the elbow joint is represented by a revolute joint.

The axis of the upper arm is aligned with $\hat{\mathbf{z}}_{1e}$ and the axis of the forearm is aligned with $\hat{\mathbf{z}}_{2e}$. Since the wearer's hand can be considered rigidly attached to the forearm sleeve, the position and the orientation of the hand can be characterized by ${}^{1b}\mathbf{p}_{hand}$ and ${}^{1b}\mathbf{R}_{2e}$ respectively as follows:

$${}^{1b}\mathbf{p}_{hand} = {}^{1b}\mathbf{p}_{1L} + {}^{1b}\mathbf{R}_{1e} \left\{ {}^{1e}\mathbf{p}_{\{1e\}\{2b\}} + {}^{2b}\mathbf{R}_{2e} {}^{2e}\mathbf{p}_{hand} \right\} . \quad (9)$$

Where ${}^{2e}\mathbf{p}_{hand}$ is an arbitrary point within the hand described in $\{2e\}$ and ${}^{1e}\mathbf{p}_{\{1e\}\{2b\}}$ is the position vector from the origin of $\{1e\}$ to the origin of $\{2b\}$.

$${}^{1b}\mathbf{R}_{2e} = {}^{1b}\mathbf{R}_{1e} {}^{2b}\mathbf{R}_{2e} . \quad (10)$$

Once the arm exoskeleton is built, lengths of the continuum braces and the sleeves will be kept constant. Structural parameters of the SCAX exoskeleton are listed in Table 2. L_{1s} and L_{2s} are the lengths of the upper arm sleeve and the forearm sleeve respectively.

Motion simulations were conducted for the four poses with the following configuration variables as shown in Fig. 4.

- ✧ $[\theta_{1L} = \pi/2 \ \delta_1 = 0 \ \theta_{2L} = \pi/2 \ \delta_2 = 0]^T$
- ✧ $[\theta_{1L} = \pi/3 \ \delta_1 = 3\pi/4 \ \theta_{2L} = \pi/2 \ \delta_2 = 0]^T$
- ✧ $[\theta_{1L} = \pi/6 \ \delta_1 = 3\pi/4 \ \theta_{2L} = \pi/2 \ \delta_2 = 0]^T$
- ✧ $[\theta_{1L} = \pi/6 \ \delta_1 = 3\pi/4 \ \theta_{2L} = \pi/3 \ \delta_2 = 3\pi/4]^T$

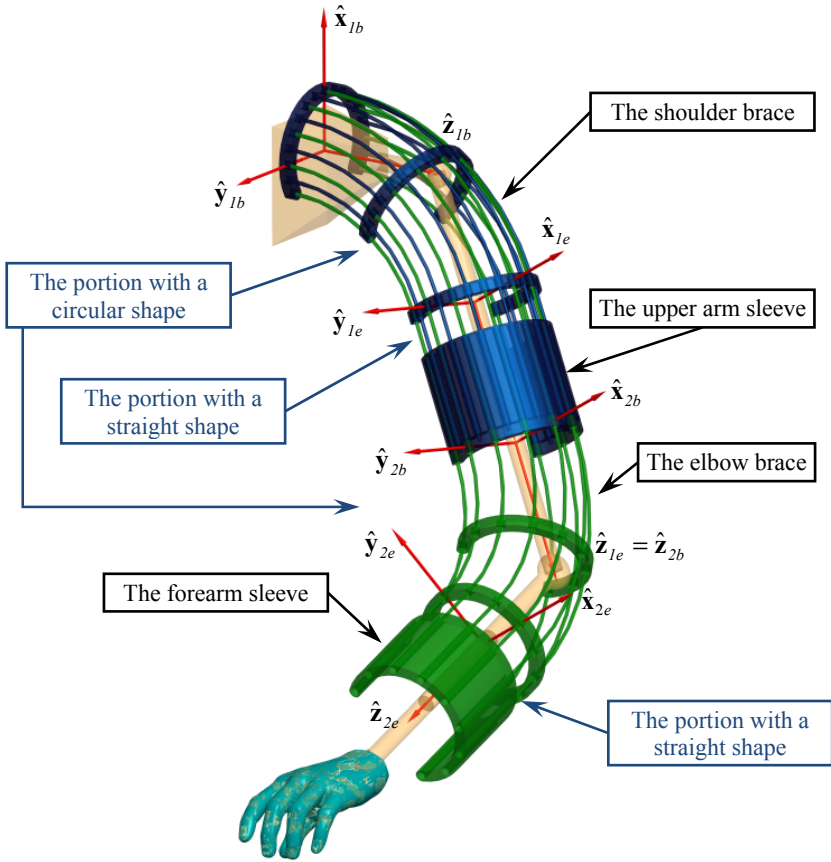


Fig. 3. Coordinate assignments of the SCAX exoskeleton

Table 2. Structural parameters of the SCAX exoskeleton

$L_1 = 280mm$	$r_{1i} = 65mm$	$L_{1s} = 80mm$	
$L_2 = 260mm$	$r_{2i} = 65mm$	$L_{2s} = 80mm$	
$\theta_{1L} \in [0 \ \pi/2]^T$	$\delta_1 \in [-\pi \ \pi]^T$	$\theta_{2L} \in [0 \ \pi/2]^T$	$\delta_2 \in [-\pi \ \pi]^T$

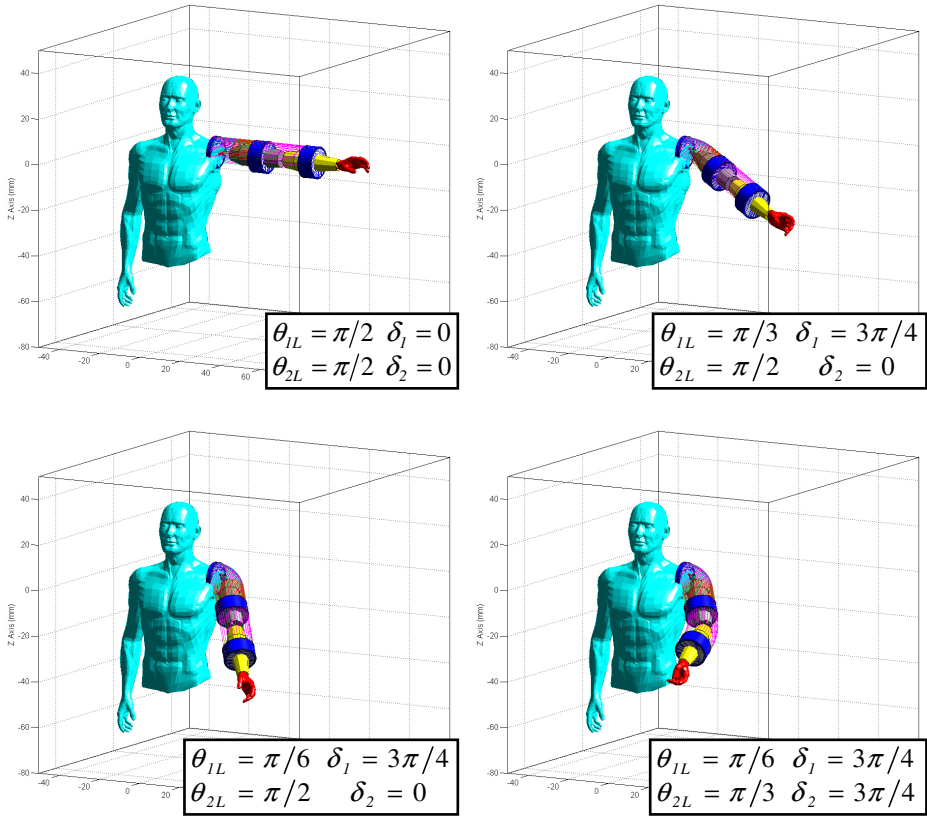


Fig. 4. Motion simulations of the SCAX exoskeleton

5 Conclusions and Future Work

This paper presented the design concept, kinematics and motion simulations of the SJTU Continuum Arm Exoskeleton (SCAX) which utilizes continuum braces to orient a patient wearer's arm for rehabilitation therapies. The secondary backbones in the continuum braces were pushed and pulled to achieve the actuation so as to assist a patient with upper arm motions.

During the assisted motions, the continuum braces in the exoskeleton were deformed and they passively adapted to different anatomies because of the intrinsic flexibility. Although shapes of the exoskeleton were different for different anatomies, the same actuation was able to assist the anatomically different arms with similar motions. This is a particular advantage for the exoskeleton's application in a clinical setting. When the exoskeleton is shared by a group of patients, without performing any hardware adjustments, the exoskeleton can match each patient's anatomy passively and assist his/her arm motions.

No firm attachment between the arm sleeves and the arm is needed. When the arm sleeves are oriented by the shoulder brace and the elbow brace, the arm rests in the sleeves naturally, preventing the exoskeleton from exerting excessive forces on the shoulder joint and on the elbow joint. In other words, the proposed design could potentially provide safe and effective rehabilitation to a group of anatomically different patients in an operation-friendly manner, where is hence referred as to a rehabilitation with Anatomy Adaptive Assistances (AAA rehabilitation).

Based on a general framework of the kinematics of the continuum braces, motion simulations were conducted to verify the motion capabilities of the SCAX exoskeleton while assisting an arm.

Future work mainly lies on two aspects. The first aspect is to design an effective and compact actuation unit to drive the shoulder and the elbow braces. The second aspect is to improve the ergonomics so that it can be used by impaired subjects. A possible solution is to design the continuum braces as two separable pieces which can be quickly assembled while putting on a patient. In this way the exoskeleton can also be conveniently peeled off when a therapeutic session is finished.

Acknowledgments. This work was supported in part by the National Program on Key Basic Research Projects (the 973 Program) #2011CB013300, and in part by Program for New Century Excellent Talents in University (the NCET Program).

References

1. Brewer, B.R., McDowell, S.K., Worthen-Chaudhari, L.C.: Poststroke Upper Extremity Rehabilitation: A Review of Robotic Systems and Clinical Results. *Topics in Stroke Rehabilitation* 14(6), 22–44 (2007)
2. Dollar, A.M., Herr, H.: Lower Extremity Exoskeletons and Active Orthoses: Challenges and State-of-the-Art. *IEEE Transactions on Robotics* 24(1), 144–158 (2008)
3. Zoss, A.B., Kazerooni, H., Chu, A.: Biomechanical Design of the Berkeley Extremity Exoskeleton (BLEEX). *IEEE/ASME Transaction on Mechatronics* 11(2), 128–138 (2006)
4. Walsh, C.J., Paluska, D., Pasch, K., Grand, W., Valiente, A., Herr, H.: Development of a Lightweight, Underactuated Exoskeleton for Load-Carrying Augmentation. In: *IEEE International Conference on Robotics and Automation (ICRA)*, Orlando, Florida, USA (2006)
5. Durfee, W.K., Rivard, A.: Preliminary Design and Simulation of a Pneumatic, Stored-Energy, Hybrid Orthosis for Gait Restoration. In: *ASME International Mechanical Engineering Congress*, Anaheim, California, USA, pp. 1–7 (2004)
6. Banala, S.K., Agrawal, S.K., Fattah, A., Krishnamoorthy, V., Hsu, W.-L., Scholz, J., Rudolph, K.: Gravity-Balancing Leg Orthosis and Its Performance Evaluation. *IEEE Transactions on Robotics* 22(6), 1228–1239 (2006)
7. Veneman, J.F., Ekkelenkamp, R., Kruidhof, R., van der Helm, F.C.T., van der Kooij, H.: A Series Elastic- and Bowden-Cable-Based Actuation System for Use as Torque Actuator in Exoskeleton-Type Robots. *International Journal of Robotics Research* 25(3), 261–281 (2006)

8. Saglia, J.A., Tsagarakis, N.G., Dai, J.S., Caldwell, D.G.: A High Performance 2-dof Over-Actuated Parallel Mechanism for Ankle Rehabilitation. In: IEEE International Conference on Robotics and Automation (ICRA), Kobe, Japan, pp. 2180–2186 (2009)
9. Farris, R.J., Quintero, H.A., Goldfarb, M.: Preliminary Evaluation of a Powered Lower Limb Orthosis to Aid Walking in Paraplegic Individuals. *IEEE Transactions on Neural Systems and Rehabilitation Engineering* 19(6), 652–659 (2011)
10. Tsagarakis, N.G., Caldwell, D.G.: Development and Control of a ‘Soft-Actuated’ Exoskeleton for Use in Physiotherapy and Training. *Autonomous Robots* 15(1), 21–33 (2003)
11. Perry, J.C., Rosen, J., Burns, S.: Upper-Limb Powered Exoskeleton Design. *IEEE/ASME Transaction on Mechatronics* 12(4), 408–417 (2007)
12. Gupta, A., O’Malley, M.K., Patoglu, V., Burgar, C.: Design, Control and Performance of RiceWrist: A Force Feedback Wrist Exoskeleton for Rehabilitation and Training. *International Journal of Robotics Research* 27(2), 233–251 (2008)
13. Stienen, A.H.A., Hekman, E.E.G., Prange, G.B., Jannink, M.J.A., Aalsma, A.M.M., van der Helm, F.C.T., van der Kooij, H.: Dampace: Design of an Exoskeleton for Force-Coordination Training in Upper-Extremity Rehabilitation. *Journal of Medical Devices* 3(031003), 1–10 (2009)
14. Klein, J., Spencer, S., Allington, J., Bobrow, J.E., Reinkensmeyer, D.J.: Optimization of a Parallel Shoulder Mechanism to Achieve a High-Force, Low-Mass, Robotic-Arm Exoskeleton. *IEEE Transactions on Robotics* 26(4), 710–715 (2010)
15. Wolbrecht, E.T., Reinkensmeyer, D.J., Bobrow, J.E.: Pneumatic Control of Robots for Rehabilitation. *International Journal of Robotics Research* 29(1), 23–38 (2010)
16. Agrawal, S.K., Dubey, V.N., Gangloff, J.J., Brackbill, E., Mao, Y., Sangwan, V.: Design and Optimization of a Cable Driven Upper Arm Exoskeleton. *Journal of Medical Devices* 3(031004), 1–8 (2009)
17. Mao, Y., Agrawal, S.K.: Design of a Cable-Driven Arm Exoskeleton (CAREX) for Neural Rehabilitation. *IEEE Transactions on Robotics* 28(4), 922–931 (2012)
18. Vukobratovic, M., Hristic, D., Stojiljkovic, Z.: Development of Active Anthropomorphic Exoskeletons. *Medical and Biological Engineering and Computing* 12(1), 66–80 (1974)
19. Loureiro, R.C.V., Harwin, W.S.: Reach & Grasp Therapy: Design and Control of a 9-DOF Robotic Neuro-rehabilitation System. In: IEEE International Conference on Rehabilitation Robotics (ICORR), Noordwijk, The Netherlands, pp. 757–763 (2007)
20. Aguirre-Ollinger, G., Colgate, J.E., Peshkin, M.A., Goswami, A.: Design of an Active One-Degree-of-Freedom Lower-Limb Exoskeleton with Inertia Compensation. *International Journal of Robotics Research* (2010) (onlinefirst)
21. Kawamoto, H., Lee, S., Kanbe, S., Sankai, Y.: Power Assist Method for HAL-3 using EMG-based Feedback Controller. In: IEEE International Conference on Systems, Man and Cybernetics (IEEE SMC), Washington, D.C, USA, pp. 1648–1653 (2003)
22. Yamamoto, K., Ishii, M., Noborisaka, H., Hyodo, K.: Stand Alone Wearable Power Assisting Suit: Sensing and Control Systems. In: IEEE International Workshop on Robot and Human Interactive Communication, Kurashiki, Okayama, Japan (2004)
23. Fleischer, C., Hommel, G.: A Human–Exoskeleton Interface Utilizing Electromyography. *IEEE Transactions on Robotics* 24(4), 872–882 (2008)
24. Sharma, V., McCreery, D.B., Han, M., Pikov, V.: Bidirectional Telemetry Controller for Neuroprosthetic Devices. *IEEE Transactions on Neural Systems and Rehabilitation Engineering* 18(1), 67–74 (2010)

25. Schiele, A., van der Helm, F.C.T.: Kinematic Design to Improve Ergonomics in Human Machine Interaction. *IEEE Transactions on Neural Systems and Rehabilitation Engineering* 14(4), 456–469 (2006)
26. Kim, H., Miller, L.M., Byl, N., Abrams, G.M., Rosen, J.: Redundancy Resolution of the Human Arm and an Upper Limb Exoskeleton. *IEEE Transactions on Biomedical Engineering* 59(6), 1770–1779 (2012)
27. Jarrassé, N., Morel, G.: Connecting a Human Limb to an Exoskeleton. *IEEE Transactions on Robotics* 28(3), 697–709 (2012)
28. van den Bogert, A.J.: Exotendons for assistance of human locomotion. *Biomedical Engineering Online* 2(17) (2003)
29. Kobayashi, H., Hiramatsu, K.: Development of Muscle Suit for Upper Limb. In: *IEEE International Conference on Robotics and Automation (ICRA)*, New Orleans, LA, USA, pp. 2480–2485 (2004)
30. Xu, K., Qiu, D., Simaan, N.: A Pilot Investigation of Continuum Robots as a Design Alternative for Upper Extremity Exoskeletons. In: *IEEE International Conference on Robotics and Biomimetics (ROBIO)*, Phuket, Thailand, pp. 656–662 (2011)
31. Xu, K., Qiu, D.: Experimental Design Verification of a Compliant Shoulder Exoskeleton. In: *IEEE International Conference on Robotics and Automation (ICRA)*, Karlsruhe, Germany (accepted for presentation, 2013)
32. Xu, K., Zhao, J., Qiu, D., Wang, Y.: A Pilot Investigation of a Continuum Shoulder Exoskeleton for Anatomy Adaptive Assistancess. *IEEE Transactions on Robotics* (2013)
33. Xu, K., Simaan, N.: An Investigation of the Intrinsic Force Sensing Capabilities of Continuum Robots. *IEEE Transactions on Robotics* 24(3), 576–587 (2008)
34. Simaan, N., Xu, K., Kapoor, A., Wei, W., Kazanzides, P., Flint, P., Taylor, R.H.: Design and Integration of a Telerobotic System for Minimally Invasive Surgery of the Throat. *International Journal of Robotics Research* 28(9), 1134–1153 (2009)
35. Ding, J., Goldman, R.E., Xu, K., Allen, P.K., Fowler, D.L., Simaan, N.: Design and Coordination Kinematics of an Insertable Robotic Effectors Platform for Single-Port Access Surgery. *IEEE/ASME Transactions on Mechatronics, Early Access Articles* (2012)
36. Xu, K., Goldman, R.E., Ding, J., Allen, P.K., Fowler, D.L., Simaan, N.: System Design of an Insertable Robotic Effector Platform for Single Port Access (SPA) Surgery. In: *IEEE/RSJ International Conference on Intelligent Robots and Systems (IROS)*, St. Louis, MO, USA, pp. 5546–5552 (2009)
37. Xu, K., Simaan, N.: Analytic Formulation for the Kinematics, Statics and Shape Restoration of Multibackbone Continuum Robots via Elliptic Integrals. *Journal of Mechanisms and Robotics* 2 (2010)

A Novel 10-DoF Exoskeleton Rehabilitation Robot Based on the Postural Synergies of Upper Extremity Movements

Kai Liu* and Caihua Xiong

State Key Lab of Digital Manufacturing Equipment and Technology
Institute of Rehabilitation and Medical Robotics
Huazhong University of Science and Technology
Luoyu Road 1037, Wuhan, 430074, China
liukai050325@163.com

Abstract. Muscular and postural synergies are the major embodiments of motor coordination of the human's limbs. Muscular and postural synergies analyses are widely employed in clinical evaluation, control of multi-DOF prosthesis and mechanical design of multifingered hand recently. But there are few research reports about the application of postural synergies in the mechanical design of exoskeleton robot. In this paper, the real-world data on a specific set of movements of the upper limb was recorded by the motion capture system, and principal components analysis was used to reveal the synergies. A novel exoskeleton robot actuated by artificial air muscles for upper extremity was proposed based on the postural synergies. The robot has 10 degrees of freedom (five active and five passive) with only two pairs of artificial air muscles in the drive mechanism, which is helpful to simplify the control of the robot.

Keywords: postural synergies, exoskeleton robot, principal components analysis, mechanical design.

1 Introduction

Stroke is considered as one of the top three diseases which threaten the human's health. Recent study estimates that the number of people in China suffering from stroke is increasing by 2 million yearly, and above two thirds of the survivors have hemiparesis or paralysis [1]. It is proved that quite a few of them could regain their motor ability through extensive and repetitive task-oriented exercises. But this will bring heavy burdens to the society and families because a large number of medical staff needed in the rehabilitation trainings driving up the cost of therapy. The researchers suggest that roboticized rehabilitation trainings could provide a good solution to the problem, and they have investigated how to improve the effect of rehabilitation trainings by use of robots for more than 30 years. From the earlier

* Corresponding author.

representative devices, such as MIT-Manus [2], MEMS [3] and GENTLE/s [4], to recently proposed prototypes CADEN-7 [5], ARMin-III [6] and Salford University “Soft Actuated” Exoskeleton robot [7], we can make a conclusion that exoskeleton is becoming the major direction of mechanical design of the rehabilitation robots.

Accompanied by the exoskeletons with multi-DOFs, the patients could finish almost all movement patterns the activities of daily life need during the trainings. In order to make a more scientific and targeted therapeutic regimen, communications between the patients and robots must be taken into consideration. Mostly, the physiological information is used as the source of signals for control system because of their superiority of reflecting the patients’ intentions. For example, Kazuo Kiguchi and Yoshiaki Hayashi has proposed an 7-DOF exoskeleton robot SUEFUL-7 with EMG-based control strategy[8]. In order to identify the motions of the 7-DOF robot, the EMG signals of sixteen locations on the arms are measured through an amplifier. But it’s hard to derive sixteen channels of EMG signals which are available from the patient’s arms. Apparently, this will impede the implement of EMG signals in the control of the robot.

In order to simplify the controlling process, it is imperative to design a compact and underactuated mechanism that needs limited signals to regulate. Postural synergies have been widely employed control of multi-DOF prosthesis and mechanical design of multifingered hand recently. But there are few research reports about the application of postural synergies in the mechanical design of multi-DOF exoskeleton robot. The purpose of this paper is to introduce the mechanical design method of a novel exoskeleton robot for upper extremity rehabilitation. The robot could achieve several typical motions with just two channels of signals, which is meaningful to simplify the use of rehabilitation robot for the patients themselves.

2 Synergies Analysis

Motor coordination is defined as the combination of several limbs or body parts in a manner that is well synchronous, fluent, and efficient in order to finish the intended goal. It’s the result of that human should fulfill repetition of many tasks, such as eating, drinking and dressing day by day. The repeated and continuous stimulation leads the brain to activate muscles in optimal and predictable patterns, which gives rise to muscular and postural synergies. A Muscular synergy is considered as a neural strategy of simplifying the control of multiple degrees of freedom. And a postural synergy is a preferred pattern of muscle co-activation that is used by the nervous system to maintain standing balance. Gelfand and Latash [10] proposed that the central nervous system does not eliminate the redundant degrees of freedom, but instead it uses all of them to ensure flexible and stable performance of motor tasks. Correspondingly, we can employ the postural synergies in our design to make the robot have good performance.

2.1 Overview of Principal Component Analysis

In order to study the postural synergies of the upper extremity, we used principal components analysis (PCA) method to indicate the pertinence of the variables which

represented the motion angles of each joint. Here is a brief overview of PCA employed in our investigation, the specification of it shown in [11] [12].

The posture of the upper extremity is represented by a posture vector:

$$\mathbf{X}_i = [p_1 \cdots p_j \cdots p_n] \tag{1}$$

The element p_j of the posture vector is defined as the angular displacement of some DOF located in the arm, and n is the number of the DOF considered. As \mathbf{X}_i is the posture of the arm at a given time, a m -row posture matrix with the data of the whole motion can be represented by

$$\mathbf{X} = [\mathbf{X}_1 \cdots \mathbf{X}_i \cdots \mathbf{X}_m]^T \tag{2}$$

Employing PCA method, we can reconstruct the posture matrix \mathbf{X} with k principal components, so:

$$\mathbf{X} \approx \tilde{\mathbf{X}} = \begin{bmatrix} p_{1,1} & p_{1,2} & \cdots & p_{1,k} \\ & \vdots & & \\ p_{i,1} & p_{i,2} & \cdots & p_{i,k} \\ & \vdots & & \\ p_{m,1} & p_{m,2} & \cdots & p_{m,k} \end{bmatrix} \begin{bmatrix} \mathbf{a}_1^T \\ \mathbf{a}_2^T \\ \vdots \\ \mathbf{a}_k^T \end{bmatrix} + \bar{\mathbf{X}} \tag{3}$$

Where the value $p_{i,k}$ is the scalar weight of principal component $\mathbf{a}_k^T = [\delta_{k,1} \cdots \delta_{k,j} \cdots \delta_{k,n}]$ quantizes the proportion of the angles of the joints in the motion.

2.2 Data Collection and Analysis

Clinical tests indicate that a special series of motions selected to activate the impaired muscles of the patient is enough for the rehabilitation trainings, the resulting reduction of function movements is not significant for the therapy. As a result, in the experiment that was needed to analysis the postural synergies of the upper extremity. We chose a set of movements for the right arm, shown in Fig.1, and three subjects took part in our experiment. In the experiment, three subjects were requested to finish the designated five types of movement within the same time respectively, meanwhile, the angles of the targeted motions of joints were measured by an optical motion capture system (VICON F-20).The targeted motions were distributed in the shoulder complex and elbow complex, the shoulder complex possesses 3DOF: flexion/extension, abduction/adduction and internal/external rotation, and the elbow complex possesses 2DOF: flexion/extension and supination/pronation.



Fig. 1. Five types of Movements in the experiment, (a)original posture, (b)touching the left ear, (c)touching the mouth, (d)touching the right ear, (e)touching the left shoulder, (f)touching the calvaria

Generally, it’s very hard to design a compact and self-contained joint to provide a motion, whose velocity is compounded of two or more different components, just by mechanical structure. The posture matrix \mathbf{X} needed at least two principal components to reconstruct the motions if we set the contribution of the principal components as more than 80%. So there is a need to make a partial analysis of the data, then we could reconstruct the new posture sub-matrixes with only one component. According to our analysis, the initial 5-volume posture matrix \mathbf{X} was divided into 2-column matrix \mathbf{M} and 3-column matrix \mathbf{N} , they were reconstructed by principal component \mathbf{e}_1 and \mathbf{e}_2 respectively as

$$\mathbf{M} \approx \tilde{\mathbf{M}} = \begin{bmatrix} p_{1,1} \\ \vdots \\ p_{i,1} \\ \vdots \\ p_{m,1} \end{bmatrix} \mathbf{e}_1^T + \bar{\mathbf{M}} \tag{4}$$

$$\mathbf{N} \approx \tilde{\mathbf{N}} = \begin{bmatrix} p_{1,2} \\ \vdots \\ p_{i,2} \\ \vdots \\ p_{m,2} \end{bmatrix} \mathbf{e}_2^T + \bar{\mathbf{N}} \tag{5}$$

$$\mathbf{e}_1 = [\delta_{1,1} \ \delta_{1,2}]^T \tag{6}$$

$$\mathbf{e}_2 = [\delta_{2,1} \ \delta_{2,2} \ \delta_{2,3}]^T \quad (7)$$

During PCA process, we could calculate the eigenvectors and eigenvalues of the covariance matrix \mathbf{M} and \mathbf{N} . The weight of an eigenvalue in the sum of all eigenvalues reveals the contribution of its eigenvector during the reconstruction of the motions. And here, the eigenvector is considered as principal component. According to the analysis of data, we got the percent of information explained by the principal components, shown in Fig. 2, which supported our hypothesis.

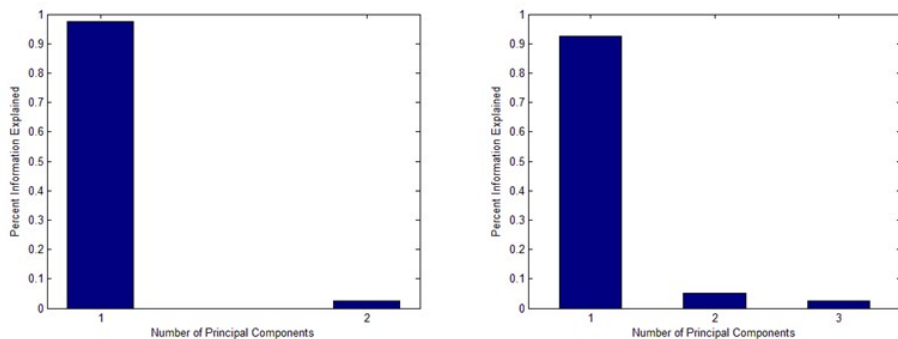


Fig. 2. Percent of information explained by the components after we divided the posture matrix \mathbf{X} into \mathbf{M} , \mathbf{N}

3 Mechanism Design

Our goal is to design a 10-DOF exoskeleton rehabilitation robot that could provide necessary motions for the physical therapy of patients with motor impairment. The robot has five active DOFs actuated by pneumatic muscles, three for shoulder complex and two for elbow complex.

3.1 Principle of Design

According to postural synergies analyzed in part 2, in our design, the joints with actuation were divided into two groups, one consisted of shoulder abduction/adduction and internal/external rotation, the other consisted of shoulder flexion/extension, elbow flexion/extension and supination/pronation. The joints in one group can be combined in a coupling way, which is helpful to reduce the number of actuators. As a result, the robot could achieve the pre-established motions with only two channel of signals inputted.

Considering the contractile mechanism of the artificial air muscle, fine steel cable was used to transfer the motions to the individual joint through driving wheels. Quantification of the radii of the driving wheels was the key point in our design.

In the equation (6) and (7), $\delta_{i,j}$ actually indicates the relationship between the radii of the driving wheels. So the mechanism of the joints was designed to distribute the motions provided by artificial to specific joint, shown in Fig. 2 and Fig. 3.

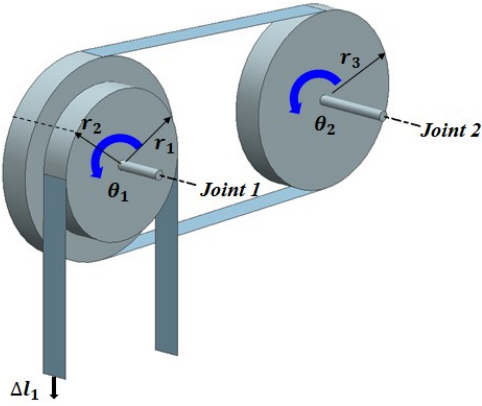


Fig. 3. Coupling structure for the joints of shoulder abduction/adduction and internal/external rotation

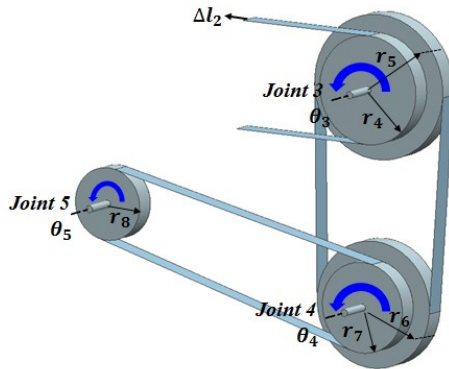


Fig. 4. Coupling structure for joints of shoulder flexion/extension, elbow flexion/extension and supination/pronation

In our scheme, the radii of the actuated joints must satisfy the conditions below:

$$\frac{r_3}{r_2} = \frac{\delta_{1,1}}{\delta_{1,2}} \tag{8}$$

$$\frac{r_6}{r_5} = \frac{\delta_{2,1}}{\delta_{2,2}} \tag{9}$$

$$\frac{r_8}{r_7} = \frac{\delta_{2,2}}{\delta_{2,3}} \tag{10}$$

And the value of $r_i (i=1,2,\dots,8)$ was calculated in view of the stroke of the artificial muscle, the motion range of the joint and the minimum bending radius allowed by the steel cable. If we define the inputs of the artificial air muscles as Δl_1 , Δl_2 for the moment t_i , the posture vector of the upper extremity can be written as:

$$\mathbf{X}_i = g(\mathbf{M}_i, \mathbf{N}_i) = f(\Delta l_1(t_i) \cdot \mathbf{e}_1^T, \Delta l_2(t_i) \cdot \mathbf{e}_2^T) \tag{11}$$

While,

$$\mathbf{M}_i = [\theta_1(t_i) \ \theta_2(t_i)] = \frac{\Delta l_1(t_i)}{r_1} \begin{bmatrix} 1 & \delta_{1,2} \\ & \delta_{1,1} \end{bmatrix} \tag{12}$$

$$\mathbf{N}_i = [\theta_3(t_i) \ \theta_4(t_i) \ \theta_5(t_i)] = \frac{\Delta l_2(t_i)}{r_4} \begin{bmatrix} 1 & \delta_{2,2} & \delta_{2,3} \\ & \delta_{2,1} & \delta_{2,1} \end{bmatrix} \tag{13}$$

3.2 Prototype Design Overview

The upper extremity of human is a complicated and dexterous biomechanical system with seven degrees of freedom (three in the shoulder complex, two in the elbow complex and two in the wrist joint) [13]. The inspiration of the following exoskeleton robot was from the anatomy of the human’s upper extremity. To construct a mechanism to replicate the motions of human’s extremity is the goal of research on rehabilitation robot. Here, we present a novel 10 DOF exoskeleton robot based on the postural synergies of the upper extremity, shown in Fig. 5.

Joint 1, 2, 3 are located around the shoulder complex, and joint 4, 5 is located in elbow complex. The axes of joint 1 and joint 2 are orthogonal, the motion of joint 2 is synchronous to joint 1. So when the steel cable connected to the artificial muscle drives the wheel in joint 1, a complex motion comprised of joint 1 and joint 2 occurs around the shoulder complex. The axes of joint 3, joint 4 are parallel, and the axis of joint 5 is orthogonal to them. This makes it convenient to transfer the movement from joint 3 to joint 5. In order to reproduce the motions customized for the upper extremity, the joint 3 must rotate with the joint 2, which will be realized by the control algorithms. The range of motion of the five active joints is shown in table 1.

Table 1. Range of motion (ROM) of the active joints

Joint 1	Joint 2	Joint 3	Joint 4	Joint 5
0~90°	0~90°	0~135°	0~135°	-45~90°

Except the five active joints, five passive joints are set up to make the motions of the exoskeleton more flexible and stable. Joint 6, 7 and 8 provide moderate linear

displacement on the sagittal plane, coronal plane, and transverse plane respectively, which plays a part in offsetting the spatial movement of the center of the glenohumeral joint. Joint 9 and 10 are designed to accommodate the movements located in the wrist joint of the robot to the human's. The range of motion of the five active joints is shown in table 2.

Table 2. Range of motion (ROM) of the passive joints

Joint 6	Joint 7	Joint 8	Joint 9	Joint 10
0~50mm	0~40mm	0~40mm	0~30mm	-45~45°

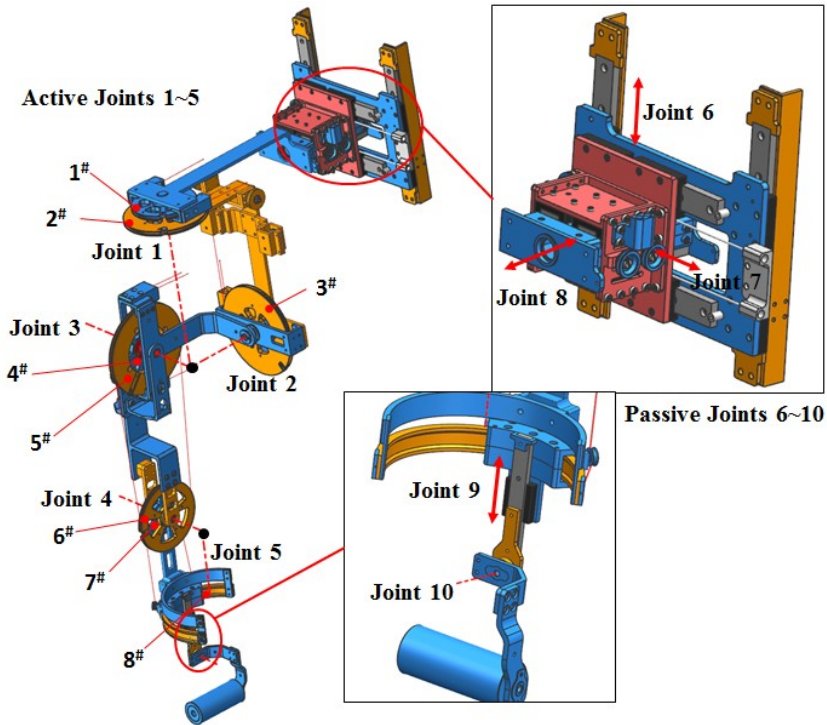


Fig. 5. The solid model of the exoskeleton robot, the driving wheels are numbered from 1[#] to 8[#]

According to equation (8), (9) and (10), we could calculate the radii of the driving wheels considering the stroke of the artificial muscle, the motion range of the joint and the minimum bending radius allowed by the steel cable. Here, the driving wheel in joint 5 was substituted by curved rail for eliminating the potential conflicts between the robot and human's arm. The radii of the driving wheels is shown in table 3.

Table 3. Radii of the driving wheels (mm)

1 [#]	2 [#]	3 [#]	4 [#]	5 [#]	6 [#]	7 [#]	8 [#]
50	66	75	50	74	56	37	74

4 Conclusion

In this paper, we propose a novel design scheme for the exoskeleton robot of upper extremity. It has five active degrees of freedom with only two actuators, which means only two channels of peripheral signals are needed to control the robot. This will greatly simplify the power supply and control system of the robot, and makes it easy to operate for the patients themselves. Also, the reduction of the control signals will promote the use of physiological signals, such as sEMG, during real-time control.

The coupling design of the five actuated joints could reconstruct the motions depicted by equation (12) and (13), we call it “hardware synergy”. If we want to reconstruct the motions depicted by equation (11), a novel algorithm for control is necessary. And testing the synergy algorithm on the prototype is our future work.

Acknowledgments. This work was supported by the National Basic Research Program of China (973 Program) (Granted No. 2011CB013301), National Science Fund for Distinguished Young Scholars of China (Grant No. 51025518), and the National Natural Science Foundation of China (NSFC) under Grant No. 51121002.

References

1. Cardiovascular Disease Prevention Research Center of the Ministry of Health: Chinese Cardiovascular Disease Report for 2011 (2012)
2. Hogan, N., Krebs, H.I., Charnnarong, J., Srikrishna, P., Sharon, A.: MIT-Manus: a workstation for manual therapy and training I. In: Proceedings of IEEE International Workshop on Robot and Human Communication, pp. 161–165 (1992)
3. Lum, P.S., Burgar, G.G., Shor, P.C.: Evidence for improved muscle activation patterns after retraining of reaching movements with the MIME robotic system in subjects with poststroke hemiparesis. *IEEE Transactions on Neural System and Rehabilitation Engineering* 12(2), 186–194 (2004)
4. Coote, S., Stokes, E., Murphy, B., Harwin, W.: The effect of GENTLE/s robot-mediated therapy on upper extremity dysfunction post stroke. In: Proceedings of the 8th International Conference on Rehabilitation Robotics (2003)
5. Perry, J.C., Rosen, J., Burns, S.: Upper-Limb Powered Exoskeleton Design. *IEEE/AMSE Trans. on Mechatronics* 12(4), 408–417 (2007)
6. Nef, T., Guidali, M., Riener, R.: ARMin III – arm therapy exoskeleton with an ergonomic shoulder actuation. *Applied Bionics and Biomechanics* 6(2), 127–142 (2009)
7. Tsagarakis, N.G., Caldwell, D.C.: Development and Control of a ‘Soft-Actuated’ Exoskeleton for Use in Physiotherapy and Training. *J. Autonomous Robots* 15, 21–23 (2003)

8. Kazuo, K., Yoshiaki, H.: An EMG-Based Control for an Upper-Limb Power-Assist Exoskeleton Robot. *IEEE Transactions on Systems, Man and System-Part B: Cybernetics* 42(4), 1064–1071 (2012)
9. Mihelj, M., Nef, T., Riener, R.: ARMin II-7 DOF Rehabilitation Robot: Mechanics and Kinematics. In: *IEEE International Conference on Robotics and Automation*, Roma, Italy (2007)
10. Gelfand, I.M., Latash, M.L.: On the problem of adequate language in movement science. *Motor Control* 2, 306–313 (1998)
11. Smith, L.I.: A tutorial on principle components analysis (February 26, 2002)
12. Jonathon, S.: A tutorial on principal components analysis (April 22, 2009)
13. Martini, F.H., Timmons, M.J., Tallitsch, R.B.: *Human Anatomy*, ch. 8. Prentice Hall, Person Education, Inc. (2003)

An ANN Based Approach for Gait Prediction of a Lower-Limb Exoskeleton with Plantar Pressure Sensors

Yuzhang Liu, Can Wang, Duan Zheng, Gang Wang, and Xinyu Wu

Guangdong Provincial Key Laboratory of Robotics and Intelligent System
Shenzhen Institutes of Advanced Technology, Chinese Academy of Sciences
{yz.liu, can.wang, duan.zheng, gang.wang, xy.wu}@siat.ac.cn

Abstract. This paper proposes an approach based on Artificial Neural Network (ANN) method for gait prediction of a lower-limb exoskeleton equipped with plantar pressure sensors and a pair of crutches. This approach can be implemented to predict the exact moment to change gait motion status. Further, the proposed approach can help to decide the starting movement speed of the pilot, through predictions on angular velocities of joints of both knees and hips. In this way, the exoskeleton can cope better with the pilot. Experimental results show that the new approach can capture the starting point of a new move, as well as predict the starting movement speed based on inputs from pressure sensors installed under pilot's plantar and crutches.

Keywords: gait prediction, Artificial Neural Network, exoskeleton.

1 Introduction

Exoskeleton robots, mainly constructed by mechanical parts and electronic parts, have emerged in recent years for its ability to enhance peoples' performance or assist disabled people who survived from stroke or who are not strong enough to move their limbs freely [1][2][3]. The whole system of the robot is a cross-field research subject concerning automation, artificial intelligence, medical treatment, and of which, one of the core ideas is to make the robot cooperate with the wearer, regarded as a robot-pilot, harmoniously [4].

From the aspect of energy transform, the robot drives its pilot. From that of signal transform, however, we can see an opposite picture: the robot is driven by its pilot by means of various sensor-information. [5][6] The more advanced the sensor-signal-processing system turns out, (including the quantities and the precision of sensors, the bandwidth of communication, the signal processing algorithms) the more the pilot feels like he is driving himself with feeble strength [7][8].

Hence, self-learning algorithms were introduced. There are two main approaches of self-learning, one is fuzzy control, and the other is artificial neural network (ANN). A new gait recognition method based on a fuzzy inference system was introduced in [9]. And classification purposes of gait events were elaborated in [10]. In a robot

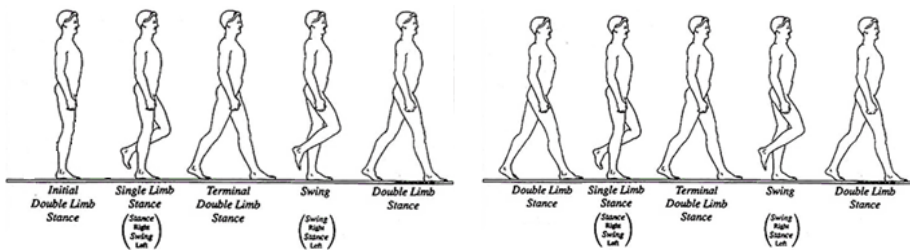
game, the localization system of the soccer robot is the key technology. With the ANN technology, the robot can learn and adjust its location adaptively [11]. In a mobile robot navigation system, the motion planning problem of constructing a collision free path can be solved based on ANN [12]. In [13], quantitative analysis of inter joint coordination at various walking speeds is presented. In this system, high-dimensionality, temporal dependence, and nonlinear relationships of the gait patterns are overcome by ANN.

ANN is a parallel distributed special signal processing system by simulating the construction and functions of human brain, in which parallelism, distributed storage, high fault tolerance, adaptive and learning ability are the most significant advantages for a better biological imitation control. Our research is focused on constructing an ANN based approach by means of detecting and measuring pressure from pilot’s plantar and from the two crutches, where the crutch pressure was regarded as an adviser to help decide the starting moment of each motion. And through angular velocity predication, the robot side can coordinate with its pilot much better. In section 2, a 6-state-cycle controlling together with the entire ANN for gait prediction were interpreted. The experimental results in section 3 show how the gait feature changed by self-learning with ANN. Section 4 concludes the paper and outlines directions for future research.

2 The Approach

2.1 Gait Analysis

A single gait cycle of an average person can be divided into 6 states (see Fig. 1), from which, a dynamic, geometrical pattern was abstracted as a leadership of gait trend for the motion of the exoskeleton.



a) an initial gait cycle

b) an intermediate gait cycle

IDLS: Initial Double Limb Stance;

SLSR: Single Limb Stance Right

TDLS: Terminal Double Limb Stance;

SLSL: Single Limb Stance Left (Swing)

DLS: Double Limb Stance;

Fig. 1. A single gait cycle

(Notes: Reference picture from Google, key word: gait cycle)

In Fig. 2, Θ_0 was a tiny angle for the pilot's bending to shift his centre of gravity forward in the state of Initial Double Limb Stance (IDLS). Between the Initial Double Limb Stance (IDLS) and the Single Limb Stance right (SLS right), the motion of left hip joint and left knee joint was operated, where ω_{lhr} and ω_{lkr} represent the angular velocity of both left hip joint and left knee joint respectively until it goes into Single Limb Stance right (SLS right), where both the left hip joint and left knee joint meet their limit angles Θ_{lhmx} and Θ_{lkmx} . And between the SLS right and the Terminal Double Limb Stance (TDLS), the motion of hip joint and knee joint was operated as well, but with opposite directions, which were represented by ω_{lhf} and ω_{lkf} until it goes into TDLS where both the left hip joint and left knee joint meet their limit angles, Θ_{lhmn} and 0. Between TDLS and SLS left, the motion of right hip joint and right knee joint was operated, where ω_{rhr} and ω_{rkr} represent the angular velocity of both right hip joint and right knee joint respectively. At the mean time, the motion of left hip joint was operated, with the velocity of ω_{lhb} until it goes into SLS left, all the limit angles Θ_{rhmx} , Θ_{rkmx} and Θ_0 . And between the SLS left and the Terminal Double Limb Stance (TDLS), the motion of hip joint and knee joint was operated as well, but with opposite directions, which were represented by ω_{rhf} and ω_{rkf} until it goes into TDLS again where both the right hip joint and right knee joint meet their limit angles, Θ_{rhmn} and 0. Then a gait cycle was finished.

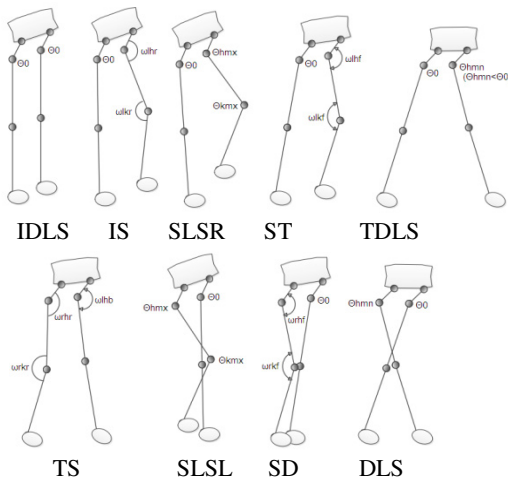
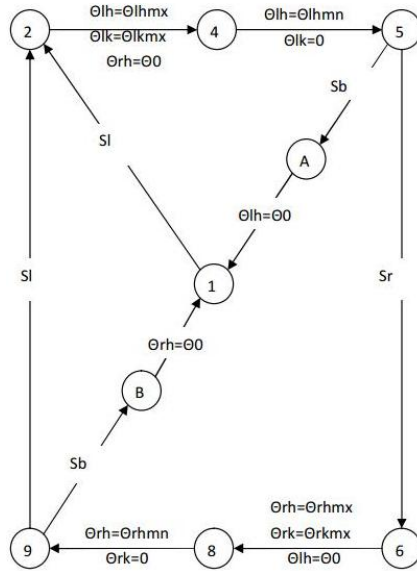


Fig. 2. Gait trend diagram

2.2 Gait States Transform Algorithm

See Fig. 3, state 1 is the initial double limb stance. Once triggered by S_1 , it jumps to State 2, in which, the left leg lifts, until the hip angle and the knee angle meet their limitation: Θ_{lhmx} and Θ_{lkmx} . And here comes state 4, in which the left leg falls down from Θ_{lhmx} and Θ_{lkmx} to Θ_{lhmn} and 0. At the mean time, it jumps to state 5, which is the terminal double limb stance. Once triggered by S_b , Θ_{lh} turns back to Θ_0 , it finally jumps

back to state 1, known as the initial double limb stance. But once triggered by S_r , it jumps to State 6, in which, the right leg lifts, until the hip angle and the knee angle meet their limitation: Θ_{rhmx} and Θ_{rkmx} . And as the hip angle of the left leg Θ_{lh} turns back into Θ_0 , in which case, the pilot moves forward. And here comes state 8, in which the right leg falls down from Θ_{rhmx} and Θ_{rkmx} to Θ_{rhmn} and 0, respectively. At the mean time, it jumps to state 9, which is the double limb state. Once triggered by S_b , Θ_{rh} turns back to Θ_0 , it finally jumps back to state 1, the initial double limb stance. If triggered by S_l , it jumps to State 2, in which case, the left leg lifts, and another cycle is beginning.



Notes: 1:IDLS; 2: IS; 4: ST; 5: TDLS; 6: DS; 8: SD; 9: DLS

Fig. 3. Gait states transform diagram

2.3 An ANN Based Gait Motion Modification Algorithm

Fig. 4 represents the exact location of the 4 plantar pressure sensors beneath the feet, which, FSR_{lh} , FSR_{ll} , FSR_{rh} , and FSR_{rl} represent the upper and lower spots of the left foot and right foot, respectively.

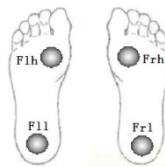


Fig. 4. Plantar Pressure Sensors

Fig. 5 illustrates the ANN map built up for the exoskeleton to define and update the angular velocity of each joints, both hips and knees, in which, FSR_{lh} , FSR_{ll} , FSR_{rh} , FSR_{rl} and FSR_{crl} , FSR_{crr} represent plantar pressure of each foot, upper spot and lower spot and the left crutch and right crutch, respectively. Of the time derivative, they turned into $dFSR_{lh}/dt$, $dFSR_{rh}/dt$, $dFSR_{rl}/dt$, $dFSR_{rl}/dt$ and $dFSR_{crl}/dt$, $dFSR_{crr}/dt$ respectively.

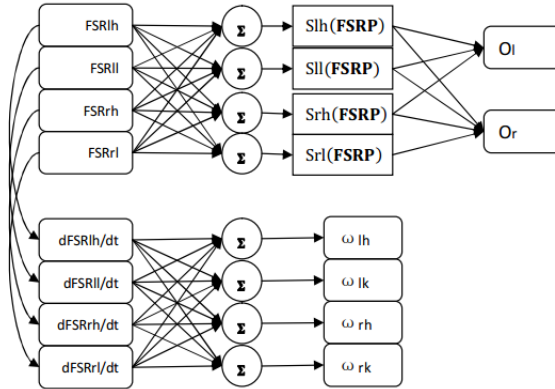


Fig. 5. Gait motion modification based on ANN

A typical artificial neuron can be described as

$$y_i = f \left(\sum_{j=0}^n w_{ij} y_{ij} \right)$$

Where $f(*)$ is an activation function that can sometimes be described as a switching function with its outputs 1 or 0. Vector w , which includes bunches of parameters such as w_{xx} can be adjusted based on corresponding experiences. In our research, vector w was obtained from homogeneous transformation of $(ulh, ull, urh, url)^T$. And the functions $Slh(*)$, $Srl(*)$, $Srh(*)$ and $Srl(*)$ indicating when-to-rise-the-leg are all regarded as activation switching functions.

As we know, the value of all the pressure sensors, which include plantar pressure sensors and crutch pressure sensors, represents the body weight of the pilot. The threshold value of when-to-rise-the-leg is roughly proportional to the body weight. Thus, the inequality is obtained as below:

$$FSR_{lh} > \eta_{lh} \bullet ulh \bullet FSR \tag{1}$$

$$FSR_{ll} > \eta_{ll} \bullet ull \bullet FSR \tag{2}$$

$$FSR_{rh} > \eta_{rh} \bullet urh \bullet FSR \tag{3}$$

$$FSR_{rl} > \eta_{rl} \bullet url \bullet FSR \tag{4}$$

Where

$$\begin{pmatrix} \mathbf{ulh} \\ \mathbf{ull} \\ \mathbf{urh} \\ \mathbf{url} \end{pmatrix} = \begin{pmatrix} u_{11} & u_{12} & u_{13} & u_{14} & u_{15} & u_{16} \\ u_{21} & u_{22} & u_{23} & u_{24} & u_{25} & u_{26} \\ u_{31} & u_{32} & u_{33} & u_{34} & u_{35} & u_{36} \\ u_{41} & u_{42} & u_{43} & u_{44} & u_{45} & u_{46} \end{pmatrix} \quad (5)$$

$\mathbf{FSRP} = (FSRlh \ FSRll \ FSRrh \ FSRrl \ FSRcrl \ FSRcrr)^T$
 inequality (1)~ (4) can be transformed into switching functions as below:

$$Slh(\mathbf{FSRP}) = \begin{cases} 1, & \mathbf{wlh} \bullet \mathbf{FSR} < 0 \\ 0, & \mathbf{wlh} \bullet \mathbf{FSR} \geq 0 \end{cases} \quad (6)$$

$$Sll(\mathbf{FSRP}) = \begin{cases} 1, & \mathbf{wll} \bullet \mathbf{FSR} < 0 \\ 0, & \mathbf{wll} \bullet \mathbf{FSR} \geq 0 \end{cases} \quad (7)$$

$$Srh(\mathbf{FSRP}) = \begin{cases} 1, & \mathbf{wrh} \bullet \mathbf{FSR} < 0 \\ 0, & \mathbf{wrh} \bullet \mathbf{FSR} \geq 0 \end{cases} \quad (8)$$

$$Srl(\mathbf{FSRP}) = \begin{cases} 1, & \mathbf{wrl} \bullet \mathbf{FSR} < 0 \\ 0, & \mathbf{wrl} \bullet \mathbf{FSR} \geq 0 \end{cases} \quad (9)$$

where

$$\begin{pmatrix} \mathbf{wlh} \\ \mathbf{wll} \\ \mathbf{wrh} \\ \mathbf{wrl} \end{pmatrix} = \begin{pmatrix} \eta lh \bullet \mathbf{ulh} \\ \eta ll \bullet \mathbf{ull} \\ \eta rh \bullet \mathbf{urh} \\ \eta rl \bullet \mathbf{url} \end{pmatrix} - \begin{pmatrix} 1 & 0 & 0 & 0 & 0 & 0 \\ 0 & 1 & 0 & 0 & 0 & 0 \\ 0 & 0 & 1 & 0 & 0 & 0 \\ 0 & 0 & 0 & 1 & 0 & 0 \end{pmatrix} \quad (10)$$

Assuming $Scrl$ and $Scrr$ are switching functions for both crutches as below:

$$Scrl(\mathbf{FSRcrl}) = \begin{cases} 1, & \mathbf{FSRcrl} > \delta \\ 0, & \mathbf{FSRcrl} < \delta \end{cases} \quad (11)$$

$$Scrr(\mathbf{FSRcrr}) = \begin{cases} 1, & \mathbf{FSRcrr} > \delta \\ 0, & \mathbf{FSRcrr} < \delta \end{cases} \quad (12)$$

where δ is a constant threshold value obtained from average persons exerting their force upon the crutches. Thus, a true value table, in which O_l and O_r are regarded as outputs, with the rest inputs can be expressed:

Table 1.

INPUTS						OUTPUTS	
$Scrl$	$Scrr$	Slh	Sll	Srh	Srl	O_l	O_r
1	X	0	0	1	1	1	0
X	1	1	1	0	0	0	1
1	0	X	X	1	1	1	0
0	1	1	1	X	X	0	1
0	0	X	X	X	X	0	0
X	X	X	0	X	0	0	0
X	X	X	0	0	X	0	0
X	X	0	X	X	0	0	0
X	X	0	X	0	X	0	0

Since the angular velocity of each joint is roughly linear dependence to the $dFSR_{lh}/dt$, $dFSR_{rh}/dt$, $dFSR_{rl}/dt$, and $dFSR_{rr}/dt$, we can build up the whole network, in which $\omega_{lh}(*), \omega_{lk}(*), \omega_{rh}(*)$ and $\omega_{rk}(*)$ represent the switching functions to the linear outputs in the hidden layer.

The whole network is adaptive by means of the variation of the crutches. For instance, if the right leg rises earlier than it is supposed to, the left crutch presses harder to the ground. If the left leg rises later, however, the right crutch presses harder to the ground. Thus, the ANN can finally seek out the fittest threshold value to for each plantar pressure sensor to yield the best moment to rise the leg. And the angular velocity of each joint is adaptive as well. For instance, if the right leg rises faster than it is supposed to, the left crutch presses faster to the ground. If the right leg rises faster than it is supposed to, the left crutch presses faster to the ground. If the left leg rises faster than it is supposed to, however, the right crutch presses faster to the ground. Thus, we can first build up functions as below:

$$Scrl' = \begin{cases} 1, & \frac{dFSR_{crl}}{dt} > \sigma \\ 0, & \frac{dFSR_{crl}}{dt} < \sigma \end{cases} \quad (13)$$

$$Scrr' = \begin{cases} 1, & \frac{dFSR_{crr}}{dt} > \sigma \\ 0, & \frac{dFSR_{crr}}{dt} < \sigma \end{cases} \quad (14)$$

Table 2.

INPUTS					OUTPUTS			
State	Scrl'	Scrr'	OI	Or	Sl	Sr	η	ω
IDLS	0	0	0	0	0	0		
IDLS	1	0	X	0	1	0	η_{l--}	
IDLS	0	1	0	X	0	1	η_{r--}	
IDLS	X	X	0	1	0	1		
IDLS	X	X	1	0	1	0		
SLSR	1	X	X	X				ω_{l++}
SLSR	0	1	X	X				ω_{l--}
SLSR	1	1	X	X			η_{l++}	
TDLS	X	0	X	0	0	0		
TDLS	X	1	X	X	0	1		
TDLS	X	0	X	1	0	1		
SLSL	X	1	X	X				ω_{r++}
SLSL	1	0	X	X				ω_{r--}
SLSL	1	1	X	X			η_{r++}	
DLS	0	X	0	X	0	0		
DLS	1	X	X	X	1	0		
DLS	0	X	1	X	1	0		

Where σ is a constant threshold value obtained from average persons about the variance ratio of exerting their force upon the crutches(See Fig. 3 again), a true value table, in which S_l and S_r are regarded as outputs, with the rest inputs can be expressed:

3 Experimental Results

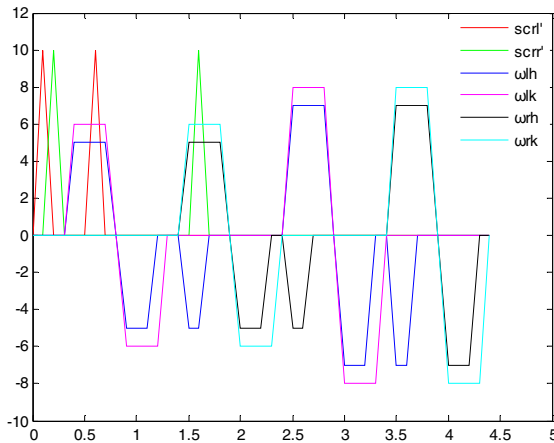
The variation of ω_{lh} , ω_{lk} , ω_{rh} and ω_{rk} of 2 gait cycles was described in Fig. 6. Except for the computer speed of the architecture of the hardware bearing the algorithms, the learning time during the process depends on the proper step length of the dynamic change of $\Delta \eta(t)$ or $\Delta \omega(t)$.

In Fig. 6.a, First, the Scr_l' and Scr_r' were both sensed by the ANN in the IDLS state in the first cycle. And they were respectively sensed by ANN in SLSR and SLSL in the SLSR and SLSL in the first cycle as well. Hence the angular velocity and the right moment to start a new gait were adjusted from $\Delta \omega(t)$ and $\Delta \eta(t)$ in the second gait cycle, which makes the pilot rise his leg earlier than he used to, and walk in a faster speed, which situation is more adaptive to the pilot. In Fig. 6.b, the Scr_l' and Scr_r' were respectively sensed by ANN in SLSL and SLSR with a different order, compared with the situation in Fig. 6.a. Thus, the new gait were adjusted from $\Delta \omega(t)$ and $\Delta \eta(t)$ in the second gait cycle, but with an opposite direction, leading the pilot walk in a lower speed.

The step length of η : $\Delta \eta(t) = \Delta \eta_0 \cdot k^{-2}$ ($k = 0, 1, 2, \dots$),

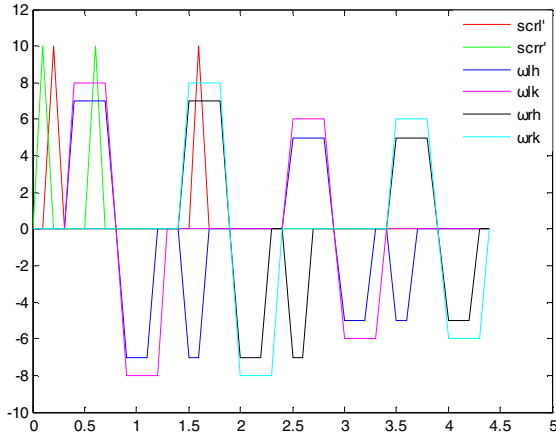
where $\Delta \eta_0$ is a constant

The step length of ω : $\Delta \omega(t) = \Delta \omega_0 \cdot k^{-2}$ ($k = 0, 1, 2, \dots$), where $\Delta \omega_0$ is a constant.



a

Fig. 6.



b

Fig. 6. (continued)

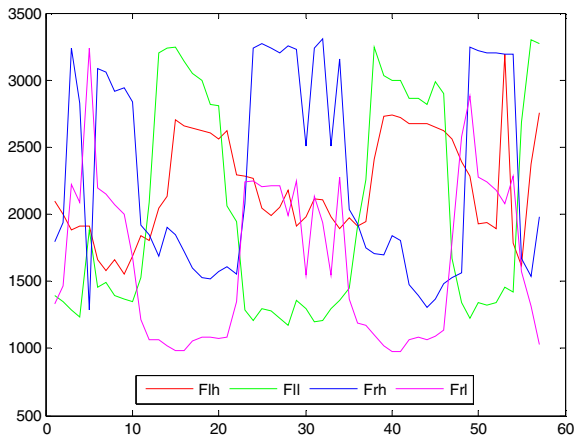


Fig. 7. Plantar pressure in 3 gait cycles with low speed

Fig. 7~9 depict Plantar Pressure Sensors in 3 gait cycles with different angular speed.

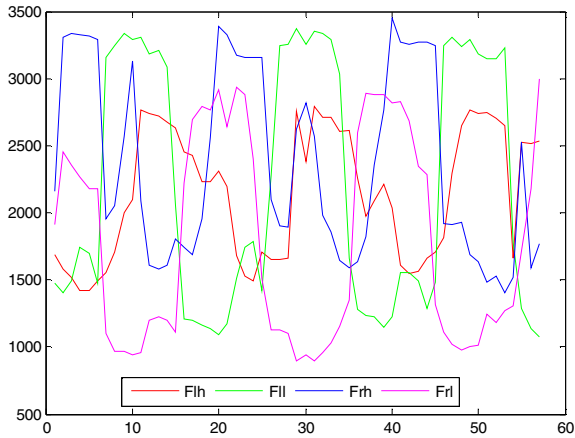


Fig. 8. Plantar pressure in 3 gait cycles with intermediate speed

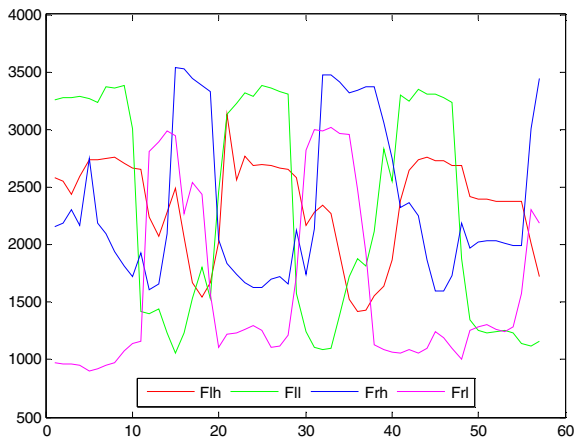


Fig. 9. Plantar pressure in 3 gait cycles with fast speed

4 Conclusion

In this manuscript, we proposed an ANN-based approach for gait prediction of a lower-limb exoskeleton equipped with pressure sensors installed under pilot's plantar and crutches. As experimental results show, this approach can predict the start point of a gait motion. As well as help to decide the movement speed of the pilot. The future work will be focused on intensive training under various robot-pilot interactive situations.

Acknowledgments. This work was supported by a grant from Shenzhen Science and Technology Project [Reference No. ZDSY20120617113312191] and was partially supported by Guangdong Innovative Research Team Program [Reference No. 201001D0104648280].

References

- [1] Huo, W., Huang, J., Wang, Y., Wu, J.: Control of A Rehabilitation Robotic Exoskeleton Based on Intentional Reaching. In: MHS 2010, Micro-Nano GCOE 2010, Bio-Manipulation 2010, pp. 357–362 (2010)
- [2] Banala, S.K., Kim, S.H., Agrawal, S.K., Scholz, J.P.: Robot Assisted Gait Training With Active Leg Exoskeleton (ALEX). *IEEE Transactions on Neural Systems and Rehabilitation Engineering* 17(1), 2–8 (2009)
- [3] Banala, S.K., Agrawal, S.K., Scholz, J.P.: Active Leg Exoskeleton (ALEX) for Gait Rehabilitation of Motor-Impaired Patients. In: *Proceedings of the 2007 IEEE 10th International Conference on Rehabilitation Robotics*, pp. 401–407 (June 2007)
- [4] Veneman, J.F., Kruidhof, R., Hekman, E.E.G., Ekkelenkamp, R., Van Asseldonk, E.H.F., van der Kooij, H.: Design and Evaluation of the LOPES Exoskeleton Robot for Interactive Gait Rehabilitation. *IEEE Transactions on Neural Systems and Rehabilitation Engineering* 15, 379–386 (2007)
- [5] Che, D., Kwon, O., Shim, J., Park, J.H.: Design of Multipurpose Sensing System for Human Gait Analysis. In: *SICE-ICASE International Joint Conference, Bexco, Busan, Korea*, pp. 1168–1173 (October 18-21, 2006)
- [6] Chen, F., Yu, Y., Ge, Y., Sun, J., Deng, X.: A PAWL for Enhancing Strength and Endurance during Walking Using Interaction Force and Dynamical Information. In: *IEEE International Conference on Robotics and Biomimetics, ROBIO 2006*, pp. 654–659 (December 2006)
- [7] Yang, C., Niu, B., Chen, Y.: Adaptive Neuro-Fuzzy Control Based Development of a Wearable Exoskeleton Leg for Human Walking Power Augmentation. In: *Proceedings of the 2005 IEEE/ASME International Conference on Advanced Intelligent Mechatronics, Monterey, California, USA, July 24-28*, pp. 467–472 (2005)
- [8] Cao, H., Ling, Z., Zhu, J., Wang, Y., Wang, W.: Design Frame of a Leg Exoskeleton for Load-Carrying Augmentation. In: *Proceedings of the 2009 IEEE International Conference on Robotics and Biomimetics, Guilin, China*, pp. 426–431 (December 2009)
- [9] Roy, A., Sural, S.: A Fuzzy Inferencing System for Gait Recognition. In: *Annual Conference of the North American Fuzzy Information Processing Society -NAFIPS 2009 Annual Meeting of the North American Fuzzy Information Processing Society* (2009)
- [10] Ng, S.K., Chizeck, H.J.: Fuzzy Model Identification For Classification of Gait Events in Paraplegics. *IEEE Transactions on Fuzzy Systems* 5, 536–544 (1997)
- [11] Chang, S.-H., Chang, W.-H., Hsia, C.-H., Ye, F., Chiang, J.-S.: Efficient neural network approach of self-localization for humanoid robot. In: *Joint Conferences on Pervasive Computing, JCPC 2009*, pp. 149–154 (2009)
- [12] Wahab, W.: Autonomous Mobile Robot Navigation Using a Dual Artificial Neural Network. In: *Proceedings of the IEEE Region 10 Annual International Conference, TENCON 2009* (2009)
- [13] Dejnabadi, H., Jolles, B.M., Aminian, K.: A New Approach for Quantitative Analysis of Inter-Joint Coordination During Gait. *IEEE Transactions on Biomedical Engineering* 55(2), 755–764 (2008)

Optimal Kinematic Calibration of the 6-UPS Parallel Manipulator

Genliang Chen, Hao Wang*, and Zhongqin Lin

State Key Laboratory of Mechanical System and Vibration (Shanghai Jiao Tong University), Dongchuan Road 800, Minhang District, 200240 Shanghai, P.R. China
{leungchan, wanghao, zqlin}@sjtu.edu.cn

Abstract. This paper presents the optimal kinematic calibration of the Hexapod (6-UPS) parallel manipulator based on a new observability index. The polytope description, rather than the widely used ellipsoid one, is introduced to depict the inaccuracy of the identified parameters. Then, the infinity-norm of the residual errors is utilized to assess the calibration precision of the kinematic parameters, which should be minimized during the process of measurement configurations selection. In order to find the optimal configurations, the Particle Swarm Optimization (PSO) algorithm is employed in the proposed method and a collision mechanism is added to cope with the joint space boundary constraint of the studied manipulator. In the end, a numerical example is studied to verify the correctness and effectiveness of the proposed approach.

Keywords: Optimal kinematic calibration, Observability index, Particle Swarm Optimization algorithm, Hexapod manipulator.

1 Introduction

Due to the inevitable defects in manufacturing and assembly, the manipulators' kinematic parameters do not exactly match the design goal, which influences the positioning accuracy significantly. Therefore, kinematic calibration is always carried out as an economical and efficient way to overcome this problem by compensating the errored parameters [1]. However, due to the existence of measurement errors, the kinematic parameters cannot be perfectly calibrated. Moreover, the identification precision is sensitive to the sensor noise in some cases.

To minimize the effects of the sensor noise on the calibration quality, much research work has been done in the past few decades, which are mainly concerning their investigations on the determination of the optimal measurement configurations for robot calibration [2]-[7]. Then, the problem can be expressed as to choose a particular set of measurement configurations to minimize some specific observability indices, which are used to evaluate the goodness of the selected configurations. All these indices are derived based on the singular value decomposition (SVD) of the identification matrix \mathbf{J}_P whose inverse linearly transforms the measurement errors to the inaccuracy of the identified parameters.

* Corresponding author.

Borm and Menq [8] selected the geometric mean of all the identification Jacobian matrix's non-zero singular values as the observability index (termed as $O_1 = m^{-\frac{1}{2}}(\delta_1 \cdots \delta_L)^{\frac{1}{L}}$, where $\delta_1, \dots, \delta_L$ represent the singular values and m is the number of the measured configurations). It can also be related to the determinate of the symmetric matrix $\mathbf{M}_p = \mathbf{J}_p^T \mathbf{J}_p$. Driels and Pathre [2] suggested the condition number of \mathbf{J}_p as the observability index (expressed as $O_2 = \delta_L/\delta_1$). In addition, Nahvi and Hollerbach used the minimal singular value of \mathbf{J}_p (denoted as $O_3 = \delta_L$ [9]) and the multiplication of O_2 and O_3 (namely $O_4 = \delta_L^2/\delta_1$ as the noise amplification index [10]) as the observability indices, respectively. Sun and Hollerbach [11] have systematically compared these observability indices to the alphabet optimalities from experimental design literatures and proposed some useful criteria for observability index option in the light of different purposes.

However, from the viewpoint of optimal experiment design, all these indices are based on the statistics of redundant datum measurements [11]. They just indicate a possibility for estimation precision. No guarantee can be made for the robot's identified parameters that the residual errors are no more than specific quantities, which is important to assess the accuracy performance of robot manipulators.

Otherwise, all the above indices are obtained under the assumption of unit hypersphere constraint for sensor noise, namely $\|\varepsilon \mathbf{Y}\|_2 \leq 1$ (where $\varepsilon \mathbf{Y}$ is the composed measurement error vector). As a matter of fact, the pose sensor performs the measurements individually at different configurations during the calibration process. Consequently, a hypercube will be generated for the constraint of sensor noise. And an error polytope, rather than the ellipsoid, can be obtained for the identified parameters through the linear mapping with \mathbf{J}_p .

For the above reasons, this paper presents a new observability index to evaluate the goodness of the selected measurement configurations for robot calibration. It is derived based on the polytope description of the residual errors and a bounding box is generated to estimate the inaccuracy of the identified parameters. The l_∞ -norm of the residual errors, also known as the worst situation of parameter identification, is defined as a new index O_∞ which should be minimized in the optimal configurations selection. The PSO algorithm is introduced and modified to determine the optimal configurations. A collision mechanism is employed into the searching process to cope with the input boundary constraint of the manipulator's actuated joints. With the proposed method, the worst case of parameter identification can be obtained. As a result, the calibration precision of the identified parameters can be guaranteed, which is essential to predict the absolute positioning accuracy of robot manipulators.

The rest of this paper is organized as follows. In Sec.2, the polytope and the ellipsoid descriptions for residual errors are compared via an intuitive example. Then, Sec.3 presents the definition and derivation of the proposed observability index for configuration selection. The PSO algorithm with collision mechanism is introduced in Sec.4 to search for the optimal configurations. In Sec.5, the Hexapod manipulator is studied as a numerical example to verify effectiveness of the proposed method. In the end, some conclusions are drawn in Sec.6.

2 Polytope versus Ellipsoid for Error Description

Generally, the task velocity vector of a robot manipulator in the workspace can be obtained through the linear mapping

$$\dot{\mathbf{y}} = \mathbf{J}\dot{\mathbf{q}} \tag{1}$$

where $\mathbf{q} \in \mathbb{R}^n$ and $\mathbf{y} \in \mathbb{R}^m$ denote the input and the output vectors in the robot's joint and task spaces, respectively. $\mathbf{J} \in \mathbb{R}^{m \times n}$ is the Jacobian matrix. And the robots studied here are assumed not under-actuated, which yields $n \leq m$.

The manipulability ellipsoid and polytope have been systematically studied and compared as dexterity measurements for robot manipulators [12]. The manipulability ellipsoid can be obtained conveniently based on the l_2 -norm estimation of the input velocities (namely $\|\dot{\mathbf{q}}\|_2 \leq 1$) as

$$\|\dot{\mathbf{q}}\|_2 = \dot{\mathbf{q}}^T \dot{\mathbf{q}} = \dot{\mathbf{y}}^T \mathbf{J}^{+T} \mathbf{J}^+ \dot{\mathbf{y}} \leq 1 \tag{2}$$

where $\mathbf{J}^+ = \mathbf{J}^T(\mathbf{J}\mathbf{J}^T)^{-1}$ denotes the pseudo-inverse of the Jacobian matrix \mathbf{J} .

However, each active joint has its own velocity constraint in practice. Thus, the joint velocity vector will be confined within $\|\dot{\mathbf{q}}\|_\infty = \max |q_i| \leq \dot{q}_{\max}$ rather than $\|\dot{\mathbf{q}}\|_2 \leq 1$. Therefore, the ellipsoid approach does not transform the exact velocity constraint from the joint space to the task space. Consequently, Lee [12] introduced the concept of the manipulability polytope as a more accurate and practical description of the dexterity for robot manipulators. And several concise methods [13] have been proposed to compute the corresponding polytope associated with the ∞ -norm constraints of the active joints' input velocities.

Actually, the precision estimation for robot calibration suffers from the same problem. The robot's extended kinematic model can be generally expressed as

$$\mathbf{y} = \mathbf{f}(\mathbf{p}, \mathbf{q}) \tag{3}$$

where \mathbf{p} represent the kinematic-parameter vector.

Then, the linearized calibration model can be represented as

$$\Delta \mathbf{Y} + \varepsilon \mathbf{Y} = \mathbf{J}_P \Delta \mathbf{p} \tag{4}$$

where $\Delta \mathbf{Y} = [\Delta \mathbf{y}_1^T, \Delta \mathbf{y}_2^T, \dots, \Delta \mathbf{y}_m^T]^T$ is the composed deviation of the measured poses \mathbf{y}_i from their nominal ones $\hat{\mathbf{y}}_i$, namely $\Delta \mathbf{y}_i = \mathbf{y}_i - \hat{\mathbf{y}}_i, i = 1, 2, \dots, m$. $\varepsilon \mathbf{Y} = [\varepsilon \mathbf{y}_1^T, \varepsilon \mathbf{y}_2^T, \dots, \varepsilon \mathbf{y}_m^T]^T$ represents the composed random error vector during pose measurements. And $\Delta \mathbf{p}$ denotes the deviation of the kinematic parameters' actual values from their nominal ones. The identification Jacobian matrix is defined as $\mathbf{J}_P = [\mathbf{J}_{P,1}^T, \mathbf{J}_{P,2}^T, \dots, \mathbf{J}_{P,m}^T]^T$, which can be obtained as

$$\mathbf{J}_{P,i} = \left. \frac{\partial \mathbf{f}}{\partial \mathbf{p}} \right|_{\mathbf{y}=\hat{\mathbf{y}}_i}, i = 1, 2, \dots, m \tag{5}$$

Since the exact values of the measurement noise cannot be determined absolutely, the deviation of the parameters' actual values from their nominal ones can only be obtained according to the simplified form of Eq.4 as

$$\Delta \mathbf{Y} = \mathbf{J}_P \Delta \mathbf{p} \tag{6}$$

Comparing Eq.6 to Eq.4, it is obvious that the residual errors of the identified parameters satisfy the following relation.

$$\mathbf{J}_P \varepsilon \mathbf{p} = \varepsilon \mathbf{Y} \quad (7)$$

where $\varepsilon \mathbf{p} = \Delta \hat{\mathbf{p}} - \Delta \mathbf{p}^*$ denotes the residual errors, namely the difference between the identified values of the kinematic parameters from their actual ones.

Then, the estimation of the residual errors can be obtained as

$$\varepsilon \hat{\mathbf{p}} = \mathbf{J}_P^+ \varepsilon \mathbf{Y} \quad (8)$$

where $\mathbf{J}_P^+ = (\mathbf{J}_P \mathbf{J}_P^T)^{-1} \mathbf{J}_P^T$ is the Moore-Penrose inverse of \mathbf{J}_P .

All the aforementioned observability indices O_i ($i = 1, \dots, 4$) can be obtained based on the singular values of the identification Jacobian matrix \mathbf{J}_P and related to some indices of the error ellipsoid, such as volume, eccentricity and maximum axis. Analogously, these results are derived under the assumption that the measurement error forms a hypersphere constraint, namely $\|\varepsilon \mathbf{Y}\|_2 \leq 1$. However, in practice the pose sensor performs the measurements independently at different configurations. As a result, the sensor noise will be bounded by $\|\varepsilon \mathbf{Y}\|_\infty = \max |\varepsilon y_i| \leq \varepsilon y_{i,max}$. Instead of the hypersphere, a hypercube can be obtained as the variable constraint (namely the domain) of Eq.8. According to the linear mapping of \mathbf{J}_P , a polytope will be derived as the range of the linear function. Obviously, it is the exact bound of the residual errors of the identified kinematic parameters, within which the real calibration errors will be confined.

Take the simple planar 2-R serial robot as an example. There are four kinematic parameters in this robot, namely the position of the fixed joint and the lengths of the links. To simplify the expression of discussion, but without loss of generality, only the length errors of the links are taken into consideration in this particular case.

Supposing three different configurations are measured for identifying the actual lengths of the links. For each configuration, a two-dimensional error vector is employed into the calibration model due to the sensor noise. Therefore, the total sensor noise will be constrained within a 6-hypercube. According to the linear mapping defined in Eq.8, the exact bound of the identified links' residual errors can be obtained in the form of a polygon, as illustrated in Fig.1.

From the figure, it is obvious that the exact error bound can be obtained as the convex hull of the image points mapped from the vertices of the measurement error's constraint hypercube. And most of the image points are transformed onto the inner points of the identified error polytope. The error ellipse is also illustrated in the figure for comparison. It shows that the error ellipse is smaller than the polygon both in volume and maximum magnitude. Additionally, the ellipse's maximum axis, known as the worst direction for error transmission, does not point to a certain vertex of the obtained error polygon. It means that the error ellipse just presents a qualitative evaluation for the residual errors and can not provide the quantitative estimation how accurate the kinematic parameters would be after identification. Thus, it can be stated that the polytope description is more direct and accurate than the ellipsoid one to evaluate the identification quality of the kinematic parameters.

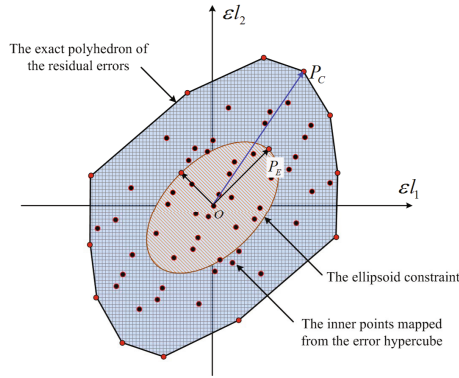


Fig. 1. Error polytope v.s. ellipsoid for the identified parameters

3 Observability Index Based on the l_∞ -Norm Evaluation

As indicated in the above section, the precision estimation for robot calibration can be solved conveniently once the exact error bound of the identified parameters is determined absolutely. However, it is not an easy task to completely specify the error polytope due to the high dimension of the identified parameters and the excessive measurement datum.

Suppose the dimension of the robot’s output vector is n and p kinematic parameters need to be calibrated with m different measured configurations. Then, the constraint of the measurement errors can be represented by a hypercube in the Euclidean space \mathbb{R}^{mn} . And the dimension of the identification Jacobian matrix satisfies $\mathbf{J}_P \in \mathbb{R}^{mn \times p}$. As a result, the problem of estimating the residual errors of the calibrated parameters has been transformed to the one of determining the error polytope in \mathbb{R}^p mapped from the mn -hypercube through \mathbf{J}_P .

In the case of the six degree-of-freedom (DOF) Hexapod manipulator, there are totally 42 kinematic parameters to be calibrated and more than seven different configurations to be measured for reliable parameter identification [14]. The dimension of the composed error vector $\varepsilon \mathbf{Y}$ will be increased by six for each more measurement. Therefore, the least dimension of $\varepsilon \mathbf{Y}$ would be 48. Then, the total number of the vertices of the error hypercube will be $2^{mn} = 2^{48} \doteq 2.8147 \times 10^{14}$. Even for the kinematic parameter, the number of the error hypercube’s vertices will exceed $2^p = 2^{42} \doteq 4.3980 \times 10^{12}$. It is an extremely big, even impossible, problem to completely determine the exact bound of the residual errors in such high dimension situation. Thus, it is necessary to define some indices to estimate the inaccuracy of the identified parameters.

As discussed in the above sections, the observability indices $O_i (i = 1, 2, 3, 4)$ are derived based on the 2-norm constraint for the measurement errors, as

$$\|\varepsilon \mathbf{Y}\|_2^2 = \varepsilon \mathbf{Y}^T \varepsilon \mathbf{Y} = \varepsilon \hat{\mathbf{p}}^T \mathbf{J}_P^T \mathbf{J}_P \varepsilon \hat{\mathbf{p}} = \varepsilon \hat{\mathbf{p}}^T \mathbf{M}_P \varepsilon \hat{\mathbf{p}} \leq 1 \tag{9}$$

where $\mathbf{M}_P = \mathbf{J}_P^T \mathbf{J}_P$.

As indicated in the literatures [15], the l_2 -norm constraint is usually used in many robotics applications more because it is mathematically tractable than physically desirable. Since the pose sensor performs the measurement independently at different configuration during robot calibration, the l_∞ -norm constraint is more practical than the l_2 -norm one for the measurement errors.

Therefore, an alternative observability index is defined based on the ∞ -norm of the identified parameters' residual errors as

$$O_\infty \triangleq \|\varepsilon \hat{\mathbf{p}}\|_\infty = \|\mathbf{J}_P^+ \varepsilon \mathbf{Y}\|_\infty \tag{10}$$

According to the definitions of the ∞ -norm (the maximum row sum of absolute values) of vectors and matrices, the new index can be rewritten as

$$O_\infty = \max_{1 \leq i \leq p} |\varepsilon \hat{\mathbf{p}}_i| = \max_{1 \leq i \leq p} \left| \sum_{j=1}^{mn} (\mathbf{J}_P^+)_{i,j} \varepsilon \mathbf{Y}_j \right| \tag{11}$$

where $\varepsilon \hat{\mathbf{p}}_i$ and $\varepsilon \mathbf{Y}_j$ are the i^{th} and j^{th} components of the error vector $\varepsilon \hat{\mathbf{p}}$ and $\varepsilon \mathbf{Y}$ respectively. $(\mathbf{J}_P^+)_{i,j}$ denotes the entry in the i^{th} row and j^{th} column of \mathbf{J}_P^+ .

For the vertices of the measurement error hypercube, the components of $\varepsilon \mathbf{Y}$ would be either 1 or -1 (namely $\varepsilon \mathbf{Y}_j = \pm 1$). Let $\varepsilon \mathbf{Y}_j$ have the same sign as the entry $(\mathbf{J}_P^+)_{i,j}$. Then, the observability index can be finally determined as

$$O_\infty = \max_{1 \leq i \leq p} |\varepsilon \hat{\mathbf{p}}_i| = \max_{1 \leq i \leq p} \sum_{j=1}^{mn} |(\mathbf{J}_P^+)_{i,j}| = \|\mathbf{J}_P^+\|_\infty \tag{12}$$

From Eq.12, O_∞ can be simply the l_∞ -norm of \mathbf{J}_P^+ . Its physical meaning is the maximum absolute value of the components in the identified parameters' residual errors. For a given planar vector $\mathbf{r}_p = (x_p, y_p)^T$, the ∞ -norm produces a square constraint with the side equal to the maximal component of the vector, namely $\|\mathbf{r}_p\|_\infty = \max\{|x_p|, |y_p|\}$. Using this concept, Eq.8 can be interpreted in a geometric manner. Still take the planar case as an example. As shown in Fig.2, based on the image points transformed from the measurement errors' constraint hypercube, different estimations for the error bound of the identified parameters can be obtained according to different criterions.

On one hand, a circular area can be obtained according to the l_2 -norm evaluation. From the figure, it is obvious that this circle is inscribed by the exact error polygon. Based on this criterion, it can be guaranteed that the l_2 -norm values of the residual errors will not exceed the radius of the bounding circle. It sounds a reasonable evaluation for the inaccuracy of the kinematic parameters for robot calibration. However, it is difficult to identify the vertex with maximum l_2 -norm in high dimensional cases, such as the spatial parallel manipulators.

On the other hand, a square region can also be obtained based on the l_∞ -norm evaluation of the residual errors, as shown in the figure. The physical meaning of this estimation is that each component of the residual errors will not be larger than this magnitude. And it is easy to calculate the side length of this bounding square according to Eq.12. Moreover, a smaller bounding box can be specified by

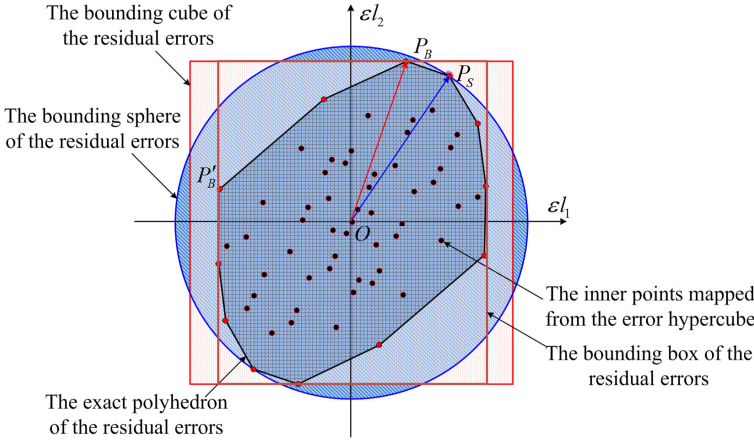


Fig. 2. Comparison of the 2-norm and infinity-norm evaluations for the residual errors

computing each row sum of absolute values of \mathbf{J}_P^+ , namely the l_1 -norm of the row vectors, which binds the residual errors. As a result, for a given matrix \mathbf{J}_P^+ there exist individual assessments for the error bound of all identified parameters. And the observability index O_∞ is defined as the largest one for the overall evaluation of the identification inaccuracy.

4 PSO Algorithm with Collision Mechanism

In this section, the PSO algorithm [16,17] is introduced to search for the optimal configuration set according the observability index O_∞ . Taking the active joints' boundary constraints into account, a collision-mechanism is employed into the standard PSO algorithm to cope with boundary constraint problem.

The actual position of one particle in the swarm is associated with a particular design vector \mathbf{x} , the dimension of which equals to the number of design variables in the studied problem. The trajectory of the i^{th} particle at iteration k can be described with the position update equation as

$$\mathbf{x}_i^{k+1} = \mathbf{x}_i^k + \Delta\mathbf{x}_i^{k+1} \tag{13}$$

where the velocity update equation for the particle can be determined as

$$\Delta\mathbf{x}_i^{k+1} = \omega\Delta\mathbf{x}_i^k + c_1r_{1,i}^k(\mathbf{x}_i^{b,k} - \mathbf{x}_i^k) + c_2r_{2,i}^k(\mathbf{x}_*^{b,k} - \mathbf{x}_i^k) \tag{14}$$

where $\mathbf{x}_i^{b,k}$ denotes the best previously obtained position of the particle i before the current iteration and $\mathbf{x}_*^{b,k}$ is the previously best one among the entire swarm. The random numbers $r_{1,i}^k$ and $r_{2,i}^k$ are uniformly distributed in $[0, 1]$. c_1 and c_2 are referred to as the intelligent particles' cognitive and the social scaling factors. And ω denotes the inertia factor.

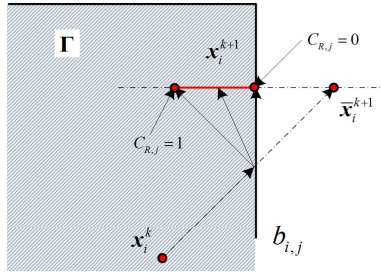


Fig. 3. The collision mechanism of PSO algorithm

Applying the algorithm to our problem, each particle among the swarm corresponds to a set of measurement configurations. Then, the problem can be set up conveniently and the updating theme of the swarm can be implemented readily. However, the standard PSO algorithm is usually applied to solve unconstrained optimization problems. In order to handle the motion constraint of the robot’s active joints, a collision-mechanism is introduced to maintain a feasible population when some particles cross across the searching boundary.

Suppose the particles are constrained within the feasible searching region Γ , as shown in Fig.3. Then, a collision will occur when the updated position of a particle reaches outside. It is natural and intuitive to regard Γ as a cage made of glass. Although the particles are with intelligence, they cannot realize the existence of the transparent boundary. When they find better positions based on their cognitive and social intelligence, they will fly towards them without any hesitation. Then, infeasible individuals will be generated among the population if no handling strategy is introduced.

The basic idea of the collision-mechanism is based on the inelastic behavior of two colliding objects. The searching particles are supposed to be bounced back when they hit the boundary of Γ . Then, the position update theme of the flying particles can be rewritten as follows if collision happens.

$$\mathbf{x}_{i,j}^{k+1} = b_j - C_{R,j} (\mathbf{x}_i^k + \Delta\mathbf{x}_{i,j}^{k+1} - b_j) \tag{15}$$

where b_j represents the limitation of the j^{th} component of the design vector \mathbf{x} . And $0 \leq C_{R,j} \leq 1$ is the coefficient of restitution. $C_{R,j} = 0$ and $C_{R,j} = 1$ are associated with the perfectly inelastic and elastic collisions, respectively.

Based on the modified updating theme, the evolving population will search the best position for the particles within the feasible region all the time to guarantee the algorithm proceed successfully. Additionally, the restitution coefficient can be modified flexibly between 0 and 1 in different cases. As pointed by Nategh [14], the maximum observability index is potentially obtained at the extreme boundary of the robots’ motion constraints. Then, for our optimal configurations selection problem, the collisions are supposed to be perfectly inelastic ones, namely $C_{R,j} = 0$, to make the algorithm quickly converge.

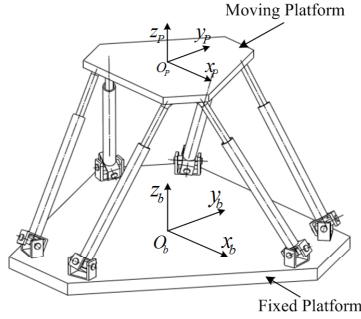


Fig. 4. The hexapod (6-UPS) parallel manipulator

5 Numerical Simulations

In this section, the hexapod (6-UPS) parallel manipulator, as shown in Fig.4, is studied as a numerical example to demonstrate the proposed calibration method. There are 7 independent kinematic parameters to be identified in each limb, namely the position vector of the universal joint on the fixed platform u_i , the initial length of the prismatic joint l_i and the position of the spherical joint on the moving platform s_i . Thus, there are totally 42 parameters to be identified during the kinematic calibration, whose nominal values are listed in Tab.1.

Each measurement generates six constraint equations to the calibration system. Therefore, at least 8 measurement configurations are required for reliable parameter identification. In order to reduce the influence of the sensor noise, 14 different configurations are measured. The pose sensor’s measurement errors are assumed to be uniformly distributed in $\varepsilon_p \in [-0.010, 0.010] mm$ for position and $\varepsilon_o \in [-0.001, 0.001] rad$ for orientation. Otherwise, the motion ranges of the actuated prismatic joints lie in $q_i \in [-200.00, 200.00] mm, i = 1, \dots, 6$.

Using the modified PSO algorithm, the optimal measurement configurations for kinematic calibration can be determined conveniently based on the proposed observability index O_∞ whose iterative improvement is illustrates in Fig.5. From

Table 1. Nominal values of kinematic parameters (mm)

Limb No.	u_i	l_i	s_i
1	(1931.8517, 517.6381, 0) ^T	3757.4884	(565.6854, 565.6854, 0) ^T
2	(-517.6381, 1931.8517, 0) ^T	3757.4884	(207.0552, 772.7407, 0) ^T
3	(-1414.2136, 1414.2136, 0) ^T	3757.4884	(-772.7407, 207.0552, 0) ^T
4	(-1414.2136, -1414.2136, 0) ^T	3757.4884	(-772.7407, -207.0552, 0) ^T
5	(-517.6381, -1931.8517, 0) ^T	3757.4884	(207.0552, -772.7407, 0) ^T
6	(1931.8517, -517.6381, 0) ^T	3757.4884	(565.6854, -565.6854, 0) ^T

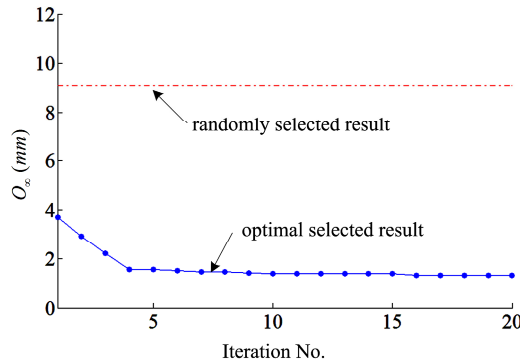


Fig. 5. Improvement of the observation index O_∞ during the searching process

the figure, it is obvious that the observability index is reduced significantly by the properly selected configurations than that by the random ones.

In order to validate the obtained result, numerical simulations are carried out. Random errors ranged in $[-5.0, 5.0]$ mm are added to the nominal parameters to obtain the presumed actual ones. The robot’s simulated actual poses is obtained by means of a numerical method to the forward kinematics analysis. Additionally, uniformly distributed measurement errors are introduced to simulate the sensor noise.

As shown in Fig.6, the residual errors of the robot’s identified parameters are much smaller than the manufacturing and assembly tolerances before calibration. Moreover, the identification precision can be further improved by choosing a set of optimal measurement configurations. In the numerical example, mean value of the residual errors has been reduced from 0.370 mm to 0.047 mm.

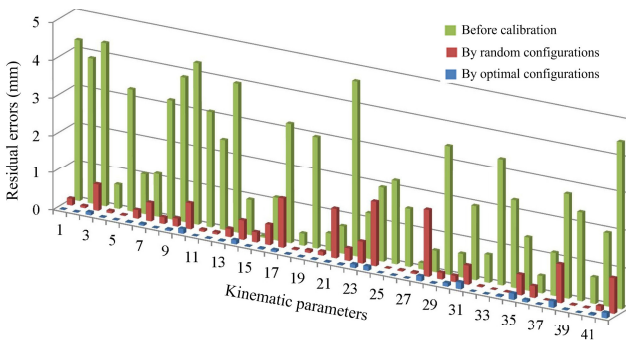


Fig. 6. Residual errors of the identified parameters

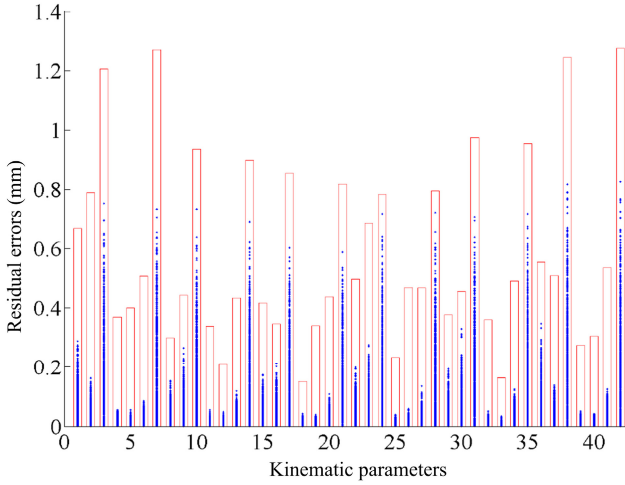


Fig. 7. Residual errors of the identified parameters in numerical experiments

Otherwise, the boundary for all parameters' residual errors can also be obtained by calculating all rows' l_1 -norm of \mathbf{J}_p^+ , which can be regarded as a threshold for identification inaccuracy. To verify this property, another numerical experiment is designed by repeating the above calibration simulation for thousands of times, as shown in Fig.7. It is evident that none of the maximal residual errors of the identified parameters exceeds this theoretical maximum. But in some cases, the maximal residual errors are close to this threshold, which means that the worst situation for parameter-identification may arise due to unfortunate distribution of the random measurement errors for the end-effector's poses. Therefore, the final accuracy performance of the calibrated manipulator can be obtained with this estimation for the parameters' identification inaccuracy.

6 Conclusion

In this paper, a new observability index is proposed for the optimal configurations selection for robot calibration. The concept of the error polytope is introduced to describe the inaccuracy of the identified parameters based on the l_∞ -norm evaluation, which provides a deterministic estimation for residual errors. The new index is not only mathematically tractable but also with intuitive physical meanings. It has ascertained the absolute bound of the potential residual errors and then guaranteed the identification inaccuracy not exceed some specific thresholds. The results of the numerical simulation have verified the correctness and effectiveness of the proposed approach.

Acknowledgments. This research work is supported by the National Science Foundation of China (NSFC) under Grant No. 51075259 and 51121063.

References

1. Mooring, B., Roth, Z., Driels, M.: *Fundamentals of Manipulator Calibration*. John Wiley & Sons (1991)
2. Driels, M., Pathre, U.: Significance of observation strategy on the design of robot calibration experiments. *Journal of Robotic Systems* 7(2), 197–223 (1990)
3. Borm, J., Meng, C.: Determination of optimal measurement configurations for robot calibration based on observability measure. *International Journal of Robotics Research* 10(1), 51–63 (1991)
4. Khalil, W., Gautier, M., Enguehard, C.: Identifiable parameters and optimum configurations for robot calibration. *Robotica* 9(1), 63–70 (1991)
5. Zhuang, H., Wang, K., Roth, Z.: Optimal selection of measurement configurations for robot calibration using simulated annealing. In: *1994 IEEE International Conference on Robotics and Automation*, pp. 393–398 (1994)
6. Daney, D., Papegay, Y., Madeline, B.: Choosing measurement poses for robot calibration with the local convergence method and tabu search. *International Journal of Robotics Research* 24(6), 501–518 (2005)
7. Verl, A., Boye, T., Pott, A.: Measurement pose selection and calibration forecast for manipulators with complex kinematic structures. *CIRP Annals-Manufacturing Technology* 57(1), 425–428 (2005)
8. Menq, C., Borm, J., Lai, J.: Identification and observability measure of a basis set of error parameters in robot calibration. *Journal of Mechanical Transmission, Automation Design* 111(4), 513–518 (1989)
9. Nahvi, A., Hollerbach, J.: The noise amplification index for optimal pose selection in robot calibration. In: *1996 IEEE International Conference on Robotics and Automation*, pp. 647–654 (1996)
10. Nahvi, A., Hollerbach, J., Hayward, V.: Calibration of a parallel robot using multiple kinematic closed loops. In: *1994 IEEE International Conference on Robotics and Automation*, pp. 407–412 (1994)
11. Sun, Y., Hollerbach, J.: Observability index selection for robot calibration. In: *2008 IEEE International Conference on Robotics and Automation*, pp. 831–836 (2008)
12. Lee, J.: A study on the manipulability measures for robot manipulators. In: *1997 IEEE International Conference on Intelligent Robots and Systems*, pp. 1458–1464 (1997)
13. Hwang, Y., Lee, J., Hsia, T.: A recursive dimension-growing method for computing robotic manipulability polytope. In: *2000 IEEE International Conference on Robotics and Automation*, pp. 2569C–2574C (2000)
14. Nategh, M., Agheli, M.: A total solution to kinematic calibration of hexapod machine tools with a minimum number of measurement configurations and superior accuracies. *International Journal of Machine Tools and Manufacture* 49(15), 1155–1164 (2009)
15. Shim, I., Yoon, Y.: Stabilized minimum infinity-norm torque solution for redundant manipulators. *Robotica* 16(2), 193C–205C (1998)
16. Kennedy, J., Eberhart, R.: Particle swarm optimization. In: *1995 IEEE International Conference on Neural Network*, pp. 1942–1948 (1995)
17. Coath, G., Hargamuge, S.: A comparison of constraint-handling methods for the application of particle swarm optimization to constrained nonlinear optimization problems. In: *2003 IEEE Congress on Evolutionary Computation*, pp. 2419–2425 (2003)

Effects of Long-Term Myoelectric Signals on Pattern Recognition

Jiayuan He, Dingguo Zhang, Xinjun Sheng, and Xiangyang Zhu

State Key Laboratory of Mechanical System and Vibration,
Shanghai Jiao Tong University, Shanghai 200240, China
{hejiayuan,dgzhang,xjsheng,mexyzhu}@sjtu.edu.cn

Abstract. The long-term electromyography (EMG) signal can make significant effect on prosthesis control based on pattern recognition. In this paper, we collected myoelectric signals lasting twelve days and compared the performance of six different features in time and frequency domains. They showed the same tendency and all led to degradation of recognition accuracy over time. Quantification method was used to measure changes in EMG feature space. It showed that distinctness of classes was increased after the long experiment and variability of patterns between days was larger than that within one day. The results of the study can help to investigate practical use of pattern recognition based prostheses.

Keywords: electromyography, long-term signals, nonstationarity, prosthesis, pattern recognition.

1 Introduction

Electrically powered prostheses, controlled by myoelectric signals, can be classified into two groups, conventional control and pattern recognition control [1]. Conventional control scheme is based on the amplitude of myoelectric signals and provides only one degree of freedom (DOF) control. However, because of its robustness, it is widely used in commercially available prostheses.

Pattern recognition control uses features describing the myoelectric signals. It is based on the assumption that features will be repeatable for the same muscle contraction and different between different contractions [2]. This scheme can control more DOFs than conventional method because more information is extracted. There are many researchers investigating pattern recognition based control scheme and many promising results have been achieved [3][4][5]. However, due to the nonstationary property of EMG signals, most of them are achieved in laboratory settings, and the experiment time is not very long, usually between 1 to 2 hours.

In order to make pattern recognition control clinically viable, some researchers have made efforts towards the robustness of this scheme. Liu [6] investigated effects of arm position on EMG recognition. Hargrove [7] developed a training strategy to decrease electrode displacement effects.

Our previous work studied the nonstationary effects on myoelectric signals within one day and developed an unsupervised method to solve this problem [8]. The error rate was decreased by about 8 percents and the result was promising. However, signals may be more fluctuant between days and performance will be deteriorated, which influences prostheses using over days.

So in this work we concentrate on the effects of myoelectric signals recorded over twelve days and try to analyze it with the quantification method. The paper is organized as follows. Section 2 describes the experiment procedure and methods. Section 3 presents major results and discussion, and the last part is the conclusion.

2 Methods

Informed consent was obtained from all the subjects. The procedures were in accordance with the Declaration of Helsinki.

2.1 Data Acquisition

A total of five healthy able-bodied subjects took part in the experiments. One of the subjects had no prior experience of EMG-based motion classification. The experiment experience of the others was from a little to moderate.

Four wireless electrodes were placed on the extensor carpi ulnaris, flexor carpi radialis, extensor carpi radialis longus and flexor carpi ulnaris, which was shown in Fig.1. The four muscles mainly controlled human wrist and hand motion. Before attaching electrodes, the skin was cleaned with alcohol to reduce impedance. After the initial calibration, electrode positions were marked to help reestablish the experimental setup on different days.

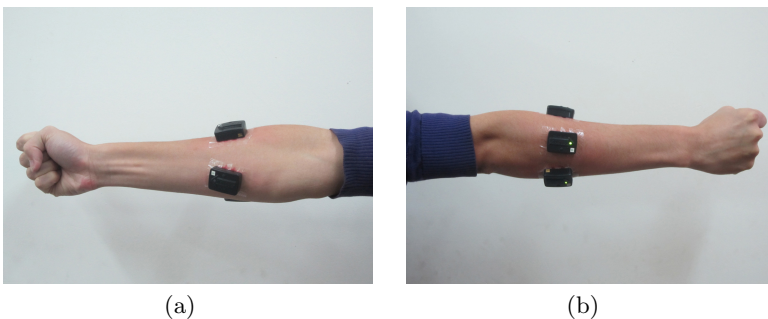


Fig. 1. Four electrodes are placed on the extensor carpi ulnaris, flexor carpi radialis, extensor carpi radialis longus and flexor carpi ulnaris: (a) anterior view, (b) posterior view

We used one of commercial myoelectric signal systems, Trigno™ Wireless system (Delsys Inc.), to collect EMG data. The system included a band pass filter from 20 to 450 Hz. The sampling frequency was set to 2 kHz.

Thirteen motion classes were considered in this study, which were pronation, supination, hand close, hand open, radial flexion, ulnar flexion, flexion, extension, fine pinch, cylindrical grasp, spherical grasp, lateral prehension and a resting class. The motions were shown in Fig.2. The subjects stood before the device and naturally extended their arms toward the ground before the experiment. Then, they were instructed to perform motions with a consistent level of effort. Each contraction was sustained for 5s and subjects had a 5-s rest between subsequent motions to avoid fatigue. Every motion needed to be performed once in one trial. For each subject, there were totally 20 trials per day and the time between experiments of two subsequent days was kept about 24h. The entire experiment lasted 12 days.

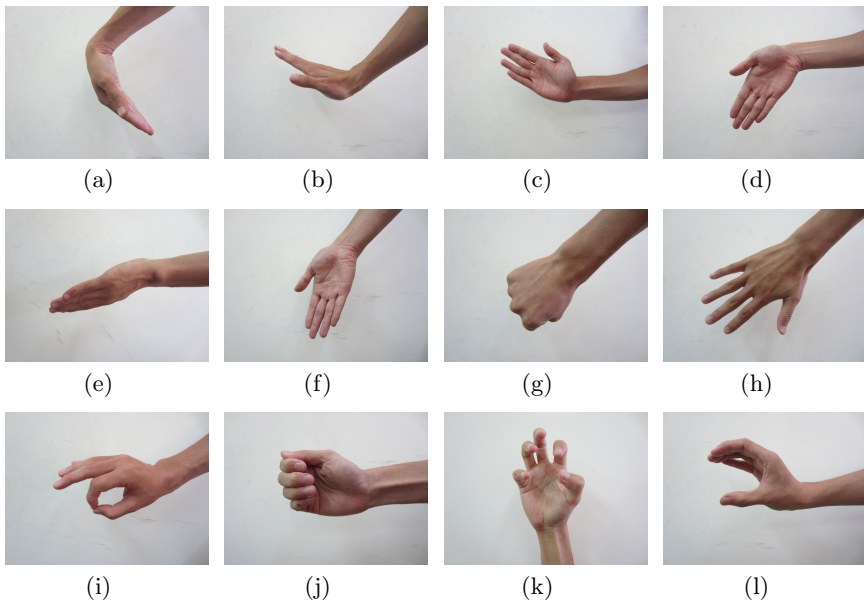


Fig. 2. Twelve active motions are considered: (a) flexion, (b) extension, (c) radial flexion, (d) ulnar flexion, (e) pronation, (f) supination, (g) hand close, (h) hand open, (i) fine pinch, (j) lateral prehension, (k) spherical grasp, (l) cylindrical grasp

2.2 Data Processing

Pattern recognition scheme had two major parts: feature extraction and classification.

In this work, we compared the long-term performances of six different feature extraction methods, which were time-domain (TD) feature [2], bispectrum (BS) feature [9], discriminant Fourier-derived cepstrum (FC) [3], improved discrete Fourier transform (iDFT) [10], auto regression (AR) [11] and cepstral coefficients (Ceps) [5]. They extracted information from time and frequency domain, respectively.

As for classifiers, previous study [12] showed that classification method had little effect on the performance of myoelectric pattern recognition system. Englehart [4] found that linear discriminant analysis (LDA) was an effective real-time myoelectric control scheme. And it was adopted in our study for its low computation cost and high performance.

Data were segmented using 200 ms windows, with processing increments of 50 ms. The first ten trials of the first day were assigned as the training set and the others were the testing set.

The classification error was used to compare the performance of different features, which was defined as

$$\text{Error Rate} = \left(1 - \frac{\text{Number of correctly classified samples}}{\text{Total number of testing samples}}\right) \times 100\% \quad (1)$$

2.3 Quantifying Feature Space Changes

Features were characteristics of EMG signals. In order to monitor the differences of signals between different days, three metrics were used to quantify feature space changes [13]. A sketch of these metrics was shown in Fig.3.

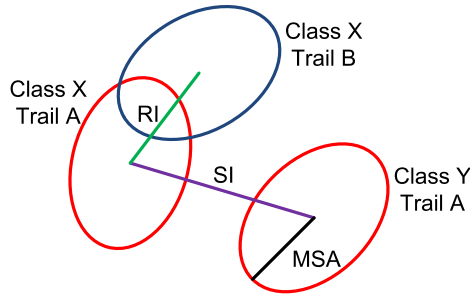


Fig. 3. A sketch of three quantification metrics. Repeatability index (RI) describes distance between different trials of the same class. Separability index (SI) measures distance between different classes of the same trial. Mean semi-principal axis (MSA) represents intraclass distance.

Repeatability index (RI) measured how well subjects reproduced feature patterns. The RI is calculated as half of the average Mahalanobis distance between the centroid of the reference trail set (u_r) and a testing trial (u_k), averaged across the testing trial set and twelve active motion classes

$$RI = \frac{1}{12} \sum_{i=1}^{12} \left(\frac{1}{T} \sum_{k=1}^P \frac{1}{2} \sqrt{(u_{ri} - u_{ki})^T S_{ri}^{-1} (u_{ri} - u_{ki})} \right) \quad (2)$$

where P is the number of trails for one testing data set, and S_{r_i} is the covariance of the reference data for class i . Greater RI means lower consistency between reference and testing trials.

Separability index (SI) monitored the distance between different classes of one trial set. It is defined as

$$SI = \frac{1}{12} \sum_{i=1}^{12} \left(\min_{j=1, j \neq i}^{j=T} \frac{1}{2} \sqrt{(u_i - u_j)^T S_i^2 (u_i - u_j)} \right) \quad (3)$$

where u_k is the centroid of a trial, k denoting i or j , and P is the number of trials in one data set.

Mean semi-principal axis (MSA) indicated the size of the class. We supposed that the motion class conformed to Gaussian distribution, and it constructed a hyperellipsoid in the feature space. The MSA is calculated as the geometric mean of the semi-principal axes (a_j) of the hyperellipsoid averaged across active motion classes

$$MSA = \frac{1}{12} \sum_{i=1}^{12} \left(\left(\prod_{j=1}^D a_{ij} \right)^{1/D} \right) \quad (4)$$

SI and MSA represent interclass and intraclass distance, respectively. Larger SI and smaller MSA indicate more distinct classes. And in this work, number of trials for one data set was set to be five. The analysis of variances (ANOVA) were used to assess the differences between different data sets statistically.

3 Results and Discussion

The average classification error was shown in Fig.4. It could be seen that performance of all features degraded over time. The error rates increased about 35 percent during 12 days. Even on the second day, it was above 15 percent and that made people hard to control prostheses. Meanwhile, the slopes of curves became small over time. It implied that the descent speed became slow. After 8 days, the error rate was stable at 40 percent. Trends of all the curves were similar, though they extracted different aspects of information from EMG signals. And iDFT got the best performance among six features.

The RI index of iDFT feature for five subjects was shown in Fig.5. The testing data set was the following five trails of the reference data. We could see that the RI of testing and reference data from different days was larger than that from the same day ($p = 0.0002$). Meanwhile, the RI values were similar for trials belonging to one day ($p = 0.2263$). It meant that variability of patterns generated between days were greater than that within one day. Considering reattaching electrodes every day, that may be caused by changes of impedance between electrodes and skin, human electrophysiological changes after a night, or other potential factors [14].

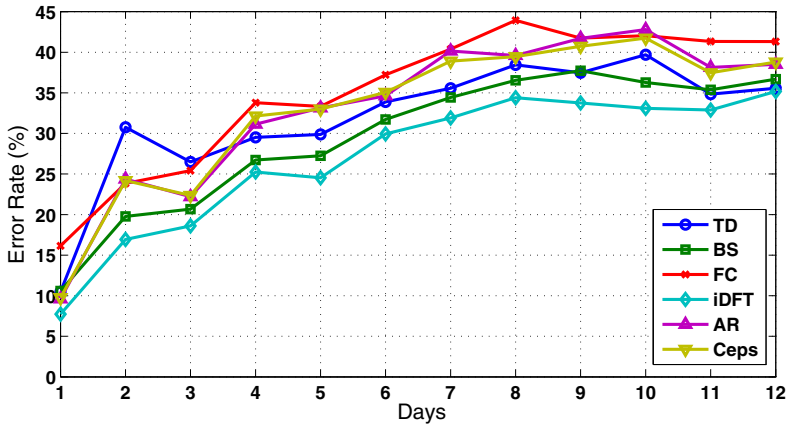


Fig. 4. The error rates of features all increased over time. Among six different time and frequency domain features, iDFT shows the best performance.

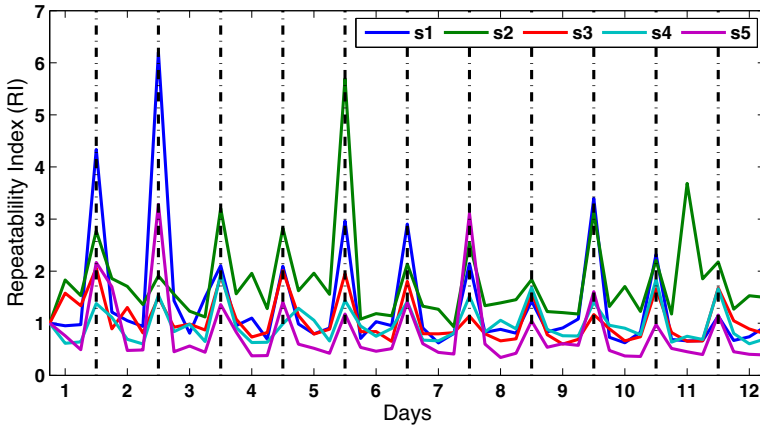


Fig. 5. The RI for data set from different days is larger than that from the same day. The values are normalized with the first one.

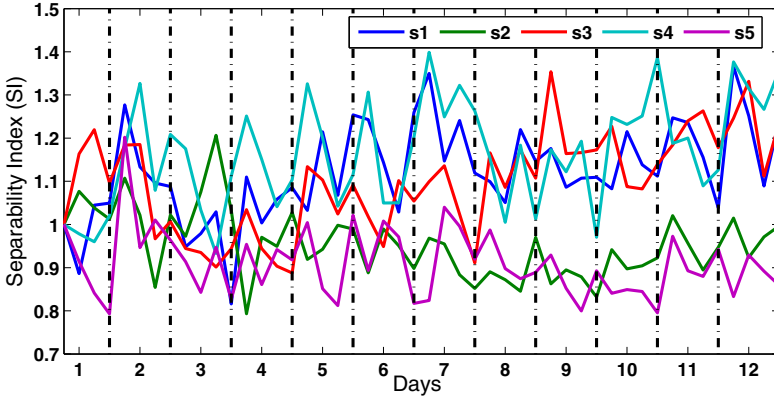


Fig. 6. The SI of three subjects increases during twelve days, indicating the variability between classes was reduced. The values are normalized with the first one.

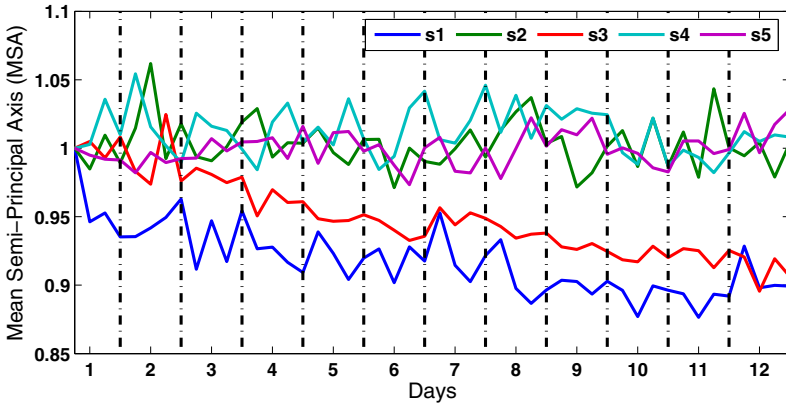


Fig. 7. The MSA of two subjects decreases during twelve days. It means the intraclass distance is reduced after the long time experiment. The values are normalized with the first value.

Notice that S3 had no experience of EMG experiment, but his RI curve did not show significant difference with others. Subjects variation had little effect on RI values ($p = 0.1544$)

Fig.6 was the results of SI index for iDFT feature. Three of five subjects, S1, S3, and S4, showed increase tendency over time. That meant their interclass variability was reduced. The other two curves fluctuated around one. The MSA of iDFT feature of five subjects could be seen in Fig.6. The values of S1 and S3 decreased during twelve days, indicating decrease of intraclass distance. With decreasing of MSA and increasing of SI, the hyperellipsoids for motion classes became smaller and were farther apart. The distinctness of classes for S1, S3, S4,

was increased after the experiment. On the other hand, curves of SI and MSA stayed around one for S2 and S5. Their class separability did not change much. Since S1 was a novice, we guessed that long-term experiment made inexperienced subjects generate more distinct classes. And it had little effect on experienced ones.

4 Conclusion

This paper investigated the effects of long-term myoelectric signals on pattern-recognition based control. Performance of different features were compared and iDFT feature got the best. But they all degraded over time due to the non-stationary property of long-term EMG. By quantifying pattern feature space, we found that distinctness of classes for three subjects, including a novice, was increased after the long-term experiment. The variability of patterns between different days was larger than that within one day. Our future work will focus on the factors causing the variations and try to contain their impacts.

Acknowledgments. This work was supported by the National Basic Research Program (973 Program) of China (Grant No.:2011CB013305), the National Natural Science Foundation of China (Grant No.51075265), and the Science and Technology Commission of Shanghai Municipality (Grant No.11JC1406000, 13430721600).

References

1. Hargrove, L.J., Scheme, E.J., Englehart, K.B., Hudgins, B.S.: Multiple binary classifications via linear discriminant analysis for improved controllability of a powered prosthesis. *IEEE Transactions on Neural Systems and Rehabilitation Engineering* 18(1), 49–57 (2010)
2. Hudgins, B., Parker, P., Scott, R.: A new strategy for multifunction myoelectric control. *IEEE Transactions on Biomedical Engineering* 40(1), 82–94 (1993)
3. Chen, X., Zhu, X., Zhang, D.: Use of the discriminant fourier-derived cepstrum with feature-level post-processing for surface electromyographic signal classification. *Physiological Measurement* 30(12), 1399 (2009)
4. Englehart, K., Hudgins, B.: A robust, real-time control scheme for multifunction myoelectric control. *IEEE Transactions on Biomedical Engineering* 50(7), 848–854 (2003)
5. Kang, W., Shiu, J., Cheng, C., Lai, J., Tsao, H., Kuo, T.: The application of cepstral coefficients and maximum likelihood method in emg pattern recognition [movements classification]. *IEEE Transactions on Biomedical Engineering* 42(8), 777–785 (1995)
6. Liu, J., Zhang, D., He, J., Zhu, X.: Effect of dynamic change of arm position on myoelectric pattern recognition. In: *IEEE Proceedings of the 2012 IEEE International Conference on Robotics and Biomimetics* (2012)
7. Hargrove, L., Englehart, K., Hudgins, B.: A training strategy to reduce classification degradation due to electrode displacements in pattern recognition based myoelectric control. *Biomedical Signal Processing and Control* 3(2), 175–180 (2008)

8. He, J., Zhang, D., Zhu, X.: Adaptive pattern recognition of myoelectric signal towards practical multifunctional prosthesis control. In: Su, C.-Y., Rakheja, S., Liu, H. (eds.) ICIRA 2012, Part I. LNCS, vol. 7506, pp. 518–525. Springer, Heidelberg (2012)
9. Chen, X., Zhu, X., Zhang, D.: A discriminant bispectrum feature for surface electromyogram signal classification. *Medical Engineering & Physics* 32(2), 126–135 (2010)
10. He, J., Zhang, D., Sheng, X., Zhu, X.: Improved discrete fourier transform based spectral feature for surface electromyogram signal classification. In: 2013 Annual International Conference of the IEEE Engineering in Medicine and Biology Society, EMBC (accepted, 2013)
11. Graupe, D., Salahi, J., Kohn, K.: Multifunctional prosthesis and orthosis control via microcomputer identification of temporal pattern differences in single-site myoelectric signals. *Journal of Biomedical Engineering* 4(1), 17–22 (1982)
12. Hargrove, L., Englehart, K., Hudgins, B.: A comparison of surface and intramuscular myoelectric signal classification. *IEEE Transactions on Biomedical Engineering* 54(5), 847–853 (2007)
13. Bunderson, N., Kuiken, T.: Quantification of feature space changes with experience during electromyogram pattern recognition control. *IEEE Transactions on Neural Systems and Rehabilitation Engineering* 20(3), 239–246 (2012)
14. De Luca, C.J.: Physiology and mathematics of myoelectric signals. *IEEE Transactions on Biomedical Engineering* (6), 313–325 (1979)

Development of a Surface EMG Acquisition System with Novel Electrodes Configuration and Signal Representation

Yinfeng Fang¹, Xiangyang Zhu², and Honghai Liu¹

¹ Group of Intelligent System and Biomedical Robotics
School of Creative Technologies, University of Portsmouth
Portsmouth, United Kingdom

{yinfeng.fang,honghai.liu}@port.ac.uk

² State Key Laboratory of Mechanical System and Vibration,
Shanghai Jiao Tong University, Shanghai, P.R. China
mexyzhu@sjtu.edu.cn

Abstract. Surface EMG signal is a quite useful tool for both the clinical application and human-machine interface. This paper proposes a multi-channel sEMG acquisition system with a novel sEMG electrodes array using improved bipolar montage. The proposed array employs elastic fabric to fix 18 dry electrodes, which make it own the advantages of reusability, wearability and flexibility. Moreover, a new graphic presentation of forearm sEMG signal is proposed, from which muscular activities can be observed instinctively in the form of round image patterns. At the end of this paper, several groups of hand gestures are studied to show the potential of the proposed system.

Keywords: surface EMG, dry electrodes, forearm, EMG array, sEMG map.

1 Introduction

With advances in sensing technologies and miniaturisation of instrumentation, biomedical practitioners such as ergonomists, physiotherapists and occupational therapists are looking to measure sEMG with wearable devices for applications. To some extent, sEMG applications have already penetrated ergonomics, sport science and rehabilitation, mostly as a means of qualitative assessment [1] and clinical neurophysiology [2]. Recent decades, surface EMG is widely used as a human machine interface to control prosthetic extremes[3–6]. However, the performance of these prosthetic hands is still romanticised and clumsy and one of the most impediments is the lack of a stable human-machine interface. Therefore, this paper focuses on developing a sEMG acquisition system to fill this gap.

The placement of sEMG electrodes is a critical issue for the successful identification of hand motions. Traditionally, identification is highly dependent on proper alignment and failure in doing so results in false identification. Moreover, the placement of electrodes is highly inefficient and inconvenient because

users typically have no knowledge about muscle distribution[7]. In some new strategies of electrodes configuration, muscle location is ignored, which certainly reduces the difficulty of pinpoint the accurate position of muscles. However, a new problem also appeared, the lower discrimination of EMG signals. One possible approach to compensate it is to utilise more channels[8, 9] and make the best of the redundant information from massive channels. Thus we need to address two more questions, how many channels are enough and how to distribute these channels. As far as we know, the number of channels is considerably limited in most systems[10, 11], which certainly restricts the quantity of information that can be abstracted from sEMG signals.

One reason restricts the channel number is the widely use of disposable electrodes that occupied a large area on the limited field of the forearm [12, 13]. Another reason is that most researchers thought a few channels can already describe most information using some data analysis tools, like PCA. One more important reason is the lack of proper device to capture multi-channel sEMG signal, which is one of aims of this paper. Some related works were completed by other researchers, for instance, [14] proposed a multi-channel sensors with 7 channels and [7] proposed a 6 channel EMG sensor ring. Another aim of this paper is to design a proper sEMG electrodes array with 16 channels for capture forearm muscular activity, which we think is the tradeoff among many practical factors, like the distance between electrodes, the size of the arm, the mess of connecting wires and the cost.

The remainder of the paper is organised as follows. Section II describes the materials and methods for multi-channel sEMG array design, including electrodes configurations and analogy circuits. Section III presents the structure of the data acquisition software system, where some details of software design are involved. Section IV describes a novel representation of sEMG array. Section V gives the experimental results, where graphic patterns of several groups of hands gestures are demonstrated.

2 Materials and Methods

2.1 The Configuration of 16-Channel sEMG Electrodes Array

Typically, EMG data collection guidelines aim to increase signal amplitude while minimising noise, thus increasing the signal-to-noise ratio [15, 16]. Monopolar montage and bipolar montage are two usual methods to pick up sEMG signal. Experiments of Staudenmann *et al.*[17] have demonstrated that monopolar montage signals show a strongly homogeneous pattern over the muscle, but the bipolar montage show a less homogeneous pattern. In other words, bipolar montage signal has a better discrimination than bipolar montage signal. In terms of noise suppression, bipolar montage has better performance than monopolar montage due to the shorter distance between two electrodes. On the other hand, with the same number of single electrodes, monopolar montage can obtain more sEMG channels than bipolar, which reduce the complexity of electrodes layout. This paper proposes a novel electrodes distribution with bipolar montage and

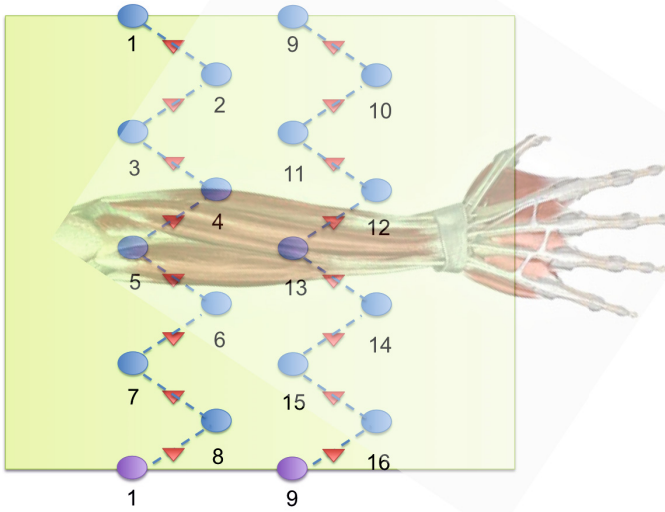


Fig. 1. This figure shows the distribution of electrodes on a 2-D space. Blue solid circles are the sEMG electrodes labelled from 1 to 16. The red triangle indicates a bipolar channel that amplifies two neighbouring electrodes connected by dot lines.

meanwhile keeps the number of channels as the same as monopolar montage by way of sharing one electrode in neighbouring channels as shown in Fig.1.

The electrodes in our system are modified from standard disposable Ag/AgCl ECG electrodes, which is widely used for EMG signal collection (The original Ag/AgCl electrodes were bought from Ebay). Two reasons spur us to modify the traditional Ag/AgCl electrodes. On one hand, one disposable Ag/AgCl ECG electrode cover too much area of the skin and result in low density of electrodes array. On the other hand, disposability would generate a big waste because of the large use of electrodes in one electrodes array.

2.2 SEMG Analogy Circuit

The aim of the sEMG analogy circuit is to extract clean EMG signal from a noisy background. The noise source includes power line interference [18], baseline wander and motion artefact [19], amplifier saturation, poor electrode contact and physiologic interference and so forth, among which power line noise is the main contamination source. This paper use differential mode amplifiers as first-stage amplifiers, and thus the common mode noises (e.g., power line noise) can be suppressed dramatically. Because the frequency band of sEMG signal is relatively narrow, ranging from 20 Hz to 500 Hz, a band pass is designed to reduce the frequent components beyond that range. Fig. 2 shows the circuit diagram. The use of In-Amps can dramatically suppress common mode noise due to the high common-mode rejection ratio (CMRR). Following the In-Amp, two Sallen-Key filters are used to compose the band pass filter with a bandwidth ranging from

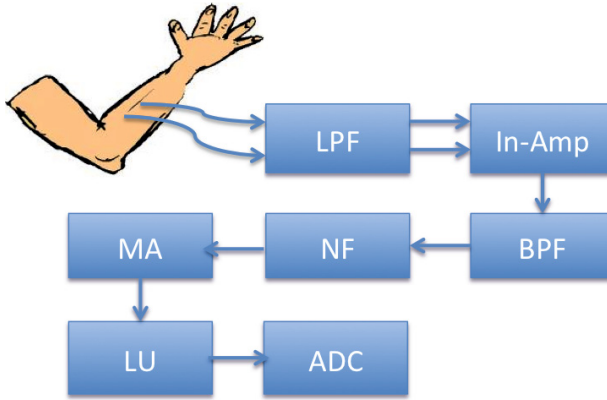


Fig. 2. The framework of sEMG analog circuit. LPF, BPF and NF indicate the low-pass filter, band pass filter and a notch filter, respectively. In-Amp and MA are the instrumentation amplifier and the main amplifier. LU denotes level uplifting circuit.

20 Hz to 500 Hz, which can help to remove baseline wander and motion artefact as well as the white noise.

In ideal conditions, power line noise is common, thus can be removed by an In-Amp. But the imbalance of tissue resistance and skin-electrodes resistance transfer common noise to differential noise easily. Therefore, a notch filter with 50 Hz (UK power line frequency) center frequency is added to suppress distortion common noise. This filter consists of a multiple feedback band-pass filter and an adding circuit. Once the 50 Hz noise removed, the possibility of saturation distortion decrease, thus a main amplifier can follow to enhance EMG signal further. Finally, a level uplifting circuit is placed to adjust the output voltage to be compatible with the AD converter.

As mentioned above, monopolar montage and bipolar montage are two different combinations of EMG electrodes for multi-channel sEMG signal acquisition. In this paper, bipolar montage is adopted to build up two 8-channel sEMG rings (seen in Fig.3). The circled configuration of electrodes and amplifiers makes the system be suitable to capture sEMG signals on forearms with different size.

3 Data Capturing and Display

In this paper, micro-controller STM32L151V8 (STMicroelectronics Inc.) is used to complete the task of converting analog signals to digital signals, which integrated up to 20 channels of AD converters and a USB signal processing unit. Fig.4 demonstrates the data stream of sEMG signal after being sampled by ADC.

After being processed by analog circuits, sEMG signals are sampled by ADC at 1 kHz frequency that is two times of the maximum frequency of the sEMG signal, conforming to Nyquist sampling theorem. Discrete sEMG data will be kept in a buffer with a customised format. When the buffer is full, the data will

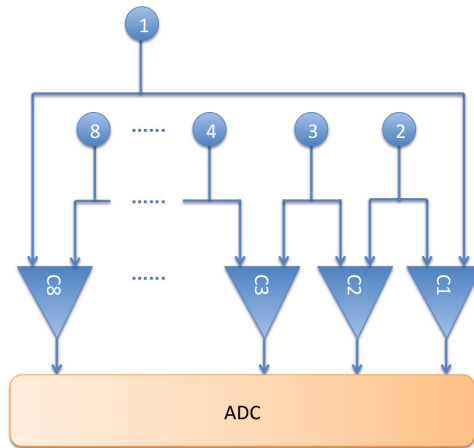


Fig. 3. This is the system diagram of an 8-channel sEMG ring. Single channel sEMG amplifiers are indicated by triangles ordered from C1 to C8 and electrodes are indicated by dots ordered from 1 to 8.

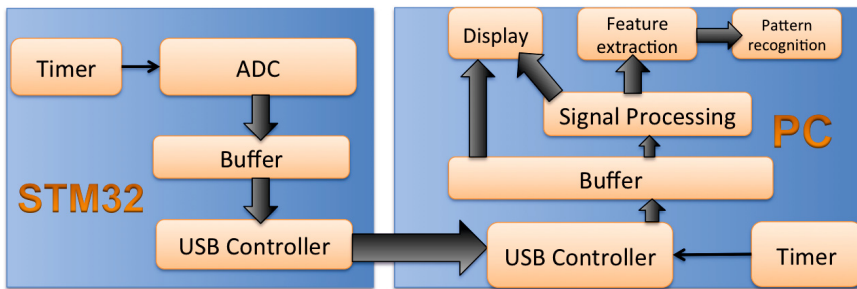


Fig. 4. This picture shows the sEMG data stream direction, where a STM32 micro-controller and a PC are included

be copied to a special buffer in the USB unit and prepared to be read by the USB host (seen in Fig.4). In order to guarantee real time processing, the USB buffer would be updated no matter whether the data are read. Calculated from ADC resolution, the number of channels and sampling frequency, the minimum transfer speed should be no lower than 16 KB/S, which can be achieved by the cooperation of reading period (controlled by the Multimedia Timer in Visual C++) and the buffer size in both PC software and STM32 firmware.

In the PC, a USB driver is designed to recognise the sEMG capture device (USB unit in micro-controller) and keep transfer protocol consistent. Visual Studio 6.0 and Driverstudio are utilised to develop the USB driver and the driver runs in a PC with Windows XP operating system. For easy operating the sEMG device, we designed an application software to display, save and process the sEMG signal. In the software, a multimedia timer is used to read the data from the USB port periodically to keep synchronization with the device (seen in Fig.4).

4 Graphic Representation of Multi-channel sEMG Signals

This paper proposes a novel method to represent forearm multi-channel sEMG signal in the form of images (seen in Fig.5). The colour of each block is determined by the root mean square (RMS) of sEMG signal that can be calculated by Equ.1,

$$RMS(j) = \sqrt{\frac{1}{N} \sum_{i=jL+1}^{N+jL} x_i^2}, \quad (1)$$

where x_i is the raw sEMG value, N is the length of the window, L is the size of the window shift.

To obtain stable and smooth patterns of forearm muscular activities, some tricks are conceived. Firstly, this paper applies a logarithmic scale to the RMS value, which is used to reduce the impact of the transient EMG signal and highlight the steady-state EMG signal. In the graphic representation, the steady-state of the EMG signal is easy to be observed and keep the whole pattern being stable. Secondly, the processed RMS values will be calculated and be mapped

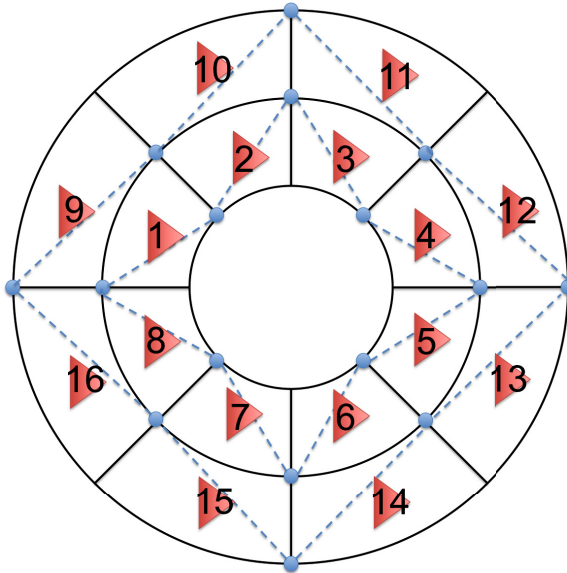


Fig. 5. This is the graphical representation of a 16-channel sEMG signal. One blue solid circle indicates one electrode and one red triangle denotes one sEMG channel. There are total 16 electrodes and 16 channels in the map. The inner belt labelled from 1 to 8 denotes the sEMG ring near the hand and the outer belt is near to the body trunk. Each block that divided by black curves will be brushed in different colours that present the strength of the corresponding sEMG signal.

to a scale from 0 to 255 further (seen in Equ.2), and each value corresponds to an RGB colour in the JET colour map.

$$RMS_{normalized} = \frac{\ln(RMS) - \ln(RMS_{min})}{\ln(RMS_{max}) - \ln(RMS_{min})} \times 255 \quad (2)$$

5 Results and Discussions

Experiments have been carried out to verify the hardware device, PC software and the sEMG graphic representation (seen in Fig.6). In the experiment, the window size N is set to 300 ms, which has been widely accepted to guarantee the real-time performance of the system [9, 20] and the shift size L is set to 20 ms. The software runs in a PC installed Windows XP Service Pack 3 with 3GHz Core 2 CPU, 3 GB memory space.

We use two groups of hand gestures to carry out the experiments. The first group is to test all the channels with two hand status: relax status and fist status(seen in Fig.7).The second group is to show the changes of graphic patterns with two wrist states: wrist up and wrist down(seen in Fig.8).



Fig. 6. This picture shows the experimental scene. A subject wears the proposed sEMG electrodes on the right forearm and sits in a chair with the elbow on the armrest. Electrodes are connected to the sEMG device that connects to a PC via a USB port. The software GUI is used to process 16 sEMG signal channels and display it in graphic patterns in real time.

In Fig.8, it is easy to find the borders that separate the image into two sets. One set contributes to make wrist upward, which is highlighted by dot line in range A. The other set contributes to keep wrist downwards in range B. These two wrist motions can be used to calibrate some pattern recognition methods in further applications due to the clear distinguish-ability.

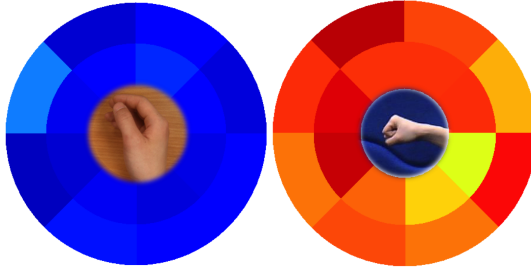


Fig. 7. It shows the graphic patterns of a fist gesture and relax status

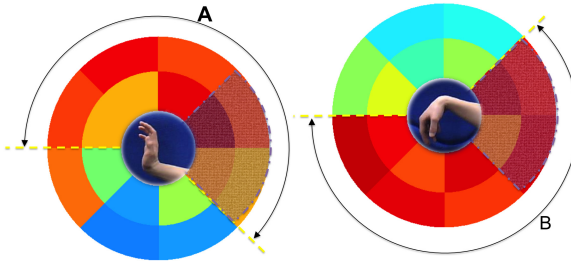


Fig. 8. These two figures show the sEMG graphic patterns of two wrist motions

6 Conclusion

In this paper, a variety of existing sEMG acquisition systems are investigated in literature, which lead us to design a new sEMG acquisition system to capture the sEMG signal on the forearm with a novel wearable electrodes array. Both the hardware and software are developed to meet this specific application. According to the structural characteristic of the sEMG array, this paper presents a graphic presentation to demonstrate the muscle activities on the forearm. Some experiments were completed to show the potential of the new graphic presentation. In the graphic patterns, the strength and location of the muscular activities can be observed clearly, which will certainly contribute to further pattern recognition algorithm.

Acknowledgments. This research was supported by grants of the UK Engineering and Physical Science Research Council (Grant No. EP/G041377/1), the National Basic Research Program (973 Program) of China (Grant No. 2011CB013305) and the Science and Technology Commission of Shanghai Municipality (Grant No. 13430721600).

References

1. Chan, A.D., MacIsaac, D.: Cleanemg: Assessing the quality of emg signals. In: 34th Conference of the Canadian Medical Biological Engineering Society and Festival of International Conferences on Caregiving, Disability, Aging and Technology, pp. 1–4.
2. Lapatki, B.G., van Dijk, J.P., Jonas, I.E., Zwartz, M.J., Stegeman, D.F.: A thin, flexible multielectrode grid for high-density surface EMG. *Journal of Applied Physiology* 96(1), 327–336 (2004)
3. Zaini, M.H.M., Ahmad, S.A.: Surgical and non-surgical prosthetic hands control: A review, September 25–28, pp. 634–637 (2011)
4. Hargrove, L., Englehart, K., Hudgins, B.: A training strategy to reduce classification degradation due to electrode displacements in pattern recognition based myoelectric control. *Biomed Signal Process Control* 3(2), 175–180 (2008)
5. Ju, Z.J., Liu, H.H.: A unified fuzzy framework for human-hand motion recognition. *IEEE Transactions on Fuzzy Systems* 19(5), 901–913 (2011)
6. Ju, Z., Liu, H.: Recognizing hand grasp and manipulation through empirical copula. *International Journal of Social Robotics* 2(3), 321–328 (2010)
7. Tang, X., Liu, Y., Lv, C., Sun, D.: Hand motion classification using a multichannel surface electromyography sensor. *Sensors (Basel)* 12(2), 1130–1147 (2012)
8. Oskoei, M.A., Hu, H.S.: Myoelectric control systems—a survey. *Biomed Signal Process Control* 2(4), 275–294 (2007)
9. Englehart, K., Hudgins, B.: A robust, real-time control scheme for multifunction myoelectric control. *IEEE Transactions on Biomedical Engineering* 50(7), 848–854 (2003)
10. Saponas, T.S., Tan, D.S., Morris, D., Balakrishnan, R.: Demonstrating the feasibility of using forearm electromyography for muscle-computer interfaces. In: Conference Proceeding of the Chi 2008: 26th Annual Chi Conference on Human Factors in Computing Systems, vol. 1 and 2, pp. 515–524 (2008)
11. Rojas-Martinez, M., Mananas, M.A., Alonso, J.F.: High-density surface emg maps from upper-arm and forearm muscles. *J. Neuroeng. Rehabil.* 9, 85 (2012)
12. Al-Timemy, A.H., Bugmann, G., Escudero, J., Outram, N.: Classification of Finger movements for the dexterous hand prosthesis control with surface electromyography (2013)
13. Tenore, F.V.G., Ramos, A., Fahmy, A., Acharya, S., Etienne-Cummings, R., Thakor, N.V.: Decoding of individuated finger movements using surface electromyography. *IEEE Transactions on Biomedical Engineering* 56(5), 1427–1434 (2009)
14. Du, Y.C., Lin, C.H., Shyu, L.Y., Chen, T.S.: Portable hand motion classifier for multi-channel surface electromyography recognition using grey relational analysis. *Expert Systems with Applications* 37(6), 4283–4291 (2010)
15. Kendell, C., Lemaire, E.D., Losier, Y., Wilson, A., Chan, A., Hudgins, B.: A novel approach to surface electromyography: an exploratory study of electrode-pair selection based on signal characteristics. *J. Neuroeng. Rehabil.* 9, 24 (2012)
16. Day, S.: Important factors in surface emg measurement, pp. 1–17. Bortec Biomedical Ltd publishers (2002)
17. Staudenmann, D., Kingma, I., Stegeman, D.F., van Dieen, J.H.: Towards optimal multi-channel emg electrode configurations in muscle force estimation: a high density emg study. *J. Electromyogr Kinesiol* 15(1), 1–11 (2005)

18. Malboubi, M., Razzazi, F., Aliyari, S.M.: Elimination of power line noise from emg signals using an efficient adaptive laguerre filter. In: 2010 International Conference on Signals and Electronic Systems (ICSES), pp. 49–52 (2010)
19. De Luca, C.J., Gilmore, L.D., Kuznetsov, M., Roy, S.H.: Filtering the surface emg signal: Movement artifact and baseline noise contamination. *J. Biomech.* 43(8), 1573–1579 (2010)
20. Momen, K., Krishnan, S., Chau, T.: Real-time classification of forearm electromyographic signals corresponding to user-selected intentional movements for multifunction prosthesis control. *IEEE Transactions on Neural Systems and Rehabilitation Engineering* 15(4), 535–542 (2007)

Hybrid Force-Position Fuzzy Control for a Prosthetic Hand

Gaoke Zhu¹, Xiaogang Duan^{2,*}, and Hua Deng²

¹ School of Mechanical and Electrical Engineering,
Central South University, Changsha 410083, China
zhgk888@163.com

² State Key Laboratory of High Performance Complex Manufacturing,
School of Mechanical and Electrical Engineering,
Central South University, Changsha 410083, China
{xgduan, hdeng}@csu.edu.cn

Abstract. A hybrid force-position fuzzy control strategy is proposed to control a four-link prosthetic hand. Firstly, a dynamics model of the prosthetic hand system is obtained by using Newton-Euler method. Then, a control strategy is designed by combining a PD and a fuzzy logic controllers. The PD controller in the outer-loop is used to control the grasping force. The fuzzy controller in the inner-loop is adopted to control the grasping position. Finally, the prosthesis system with the proposed controller is simulated by pinching different virtual springs and compared with a hybrid force-velocity controller. The simulation results show the hybrid force-position fuzzy control method is more effective.

Keywords: Prosthetic hand, force-position control, fuzzy logic control.

1 Introduction

Amputees expect to own prosthesis with rich functionality looking like a real limb long on their own bodies. Although researchers present many control methods for prosthetic hands, the prostheses' dexterity is still far away from human hands'. The design and the low-level control architecture of these prostheses are strictly limited due to technology [1].

For prosthetic hands, one of important works is to design a proper control strategy. A prosthetic hand described in [2] is considered to be the world's oldest dexterous hand. The hand has two level controls: a movement control and a simple adaptive control circuit. Early control method is usually position or velocity control. Until 1972, Groome used force feedback control in a teleoperator system [3]. The force control started to be researched for industrial robots. In 1981, Raibert and Craig proposed the classic hybrid position /force control strategy [4]. This compliance control method realizes the force control and position control on two different channels.

* Corresponding author.

For a dexterous prosthetic hand, the control system is usually composed of two parts: an upper-layer control and a low-layer control. The upper-layer control is the interface between prostheses and users. Typically the input to the system is electromyographic (EMG) signals of human skin surface [5]. The bottom-layer control is often based on position/velocity or force feedback from the prosthetic hand to fulfill effective actions expected by amputees.

When a prosthetic hand grasps an object, there are usually two procedures: no-contact step before touching the object and grasping step. In the no-contact step, the distance between fingers and the object is unknown. Amputees expect the prosthetic hand to close quickly. When the hand almost contacts the object, the hand should touch it smoothly to avoid impulsion. In the grasping step, the weight of the object is also unknown. No enough grasping power will lead to objects sliding from the prosthesis. An excessive grasping force may damage some delicate objects. For these problems, the prosthetic hand needs an effective control strategy.

The hybrid control technique applied in prostheses shows very good application prospects [6][7][8]. Engeberg proposed a hybrid force-velocity sliding mode controller with an outer force control loop and an inner position/velocity control loop that uses a sliding mode controller [9]. The controller is effective to prevent unwanted force overshoot but is out of work to reach the desired force in gripping steady state so the grasped object is prone to slipping down.

In this paper, a hybrid force-position controller is proposed to realize accurate force control with almost no overshoot. The proposed control strategy addresses the dual nature of prosthetic hand control by the use of a single input to control not only the position and velocity of the fingers and the thumb before they contact the environment, but also the force exerted upon the environment once contact is established [9]. The hybrid force-position fuzzy controller has an exterior force feedback loop that uses a proportional-derivative (PD) control technique to minimize the error between the actual and desired forces and an interior position feedback loop that uses a fuzzy logic controller (FLC) described in [10] and [11]. A dynamics model is presented for a prosthetic hand composed of a four-link system, a DC micro motor, a gear train and a virtual spring. Based on the model, the force-position fuzzy controller is implemented. In simulation, we set three kinds of spring to simulate different gripping environment. And the control performance of hybrid force-position controller is compared with a hybrid force-velocity controller presented in [9].

2 System Modeling

As shown in Fig. 1, the basic structure of the prosthetic hand presented includes a DC micro motor, a gear train and a linkage system. The hand has one degree of freedom. The micro motor drives the sector gear through a reduction gear and a transition gear. The thumb link and the sector gear are connected into a whole through a hinge shaft. The index finger is derived by the sector gear through a connecting rod (BC). Thus, the closing and opening function is realized. The point A and ray AD are settled as the origin and the x -axis of the Cartesian coordinate system, respectively.

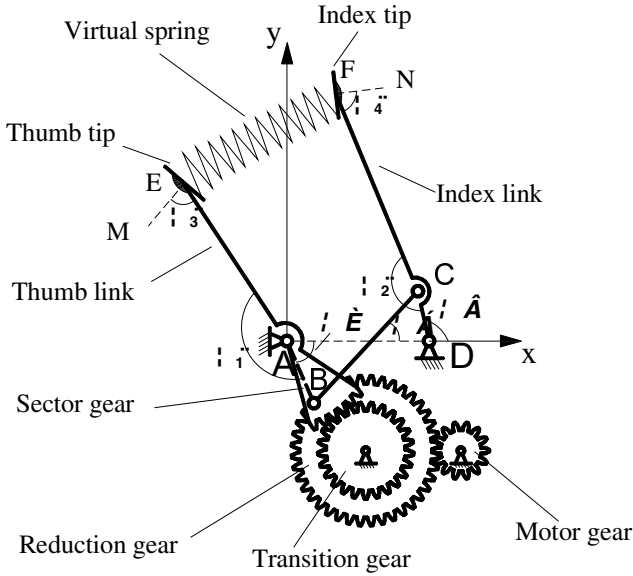


Fig. 1. Schematic diagram of a prosthetic hand

Table 1. Nomenclature of the motor and four-link system parameters

Nomenclature	Meaning	Nomenclature	Meaning
R_a	Terminal resistance of motor	R_0	Radius of sector gear
K_e	Back-EMF constant	U_N	Nominal voltage of motor
K_t	Tongue constant	w_N	Nominal speed of motor
L_a	Rotor inductance	m_3	Mass of BC
J_m	Rotor inertia	J_A	Inertia of thumb link to A
T_f	Friction torque of motor	J_D	Inertia of index link to D
B	Viscosity coefficient of motor	J_{C3}	Inertia of BC to centroid
u	Input voltage to motor	θ	Angle from x -axis to AB
ω	Rotor speed	α	Angle from x -axis to BC
i	Current of armature circuit	β	Angle from x -axis to CD
T_L	Load torque on motor	s	Distance from tip E to F
i_1	Ratio between motor gear & reduction gear		
i_2	Ratio between transition gear & sector gear		
L_k	The length of link k . k is 1~6 corresponding to link AD, AB, BC, CD, AE, CF		
θ_j	The j th angle. j is 1~4 corresponding to $\angle BAE$, $\angle FCD$, $\angle MEA$, $\angle NFC$		

To facilitate the modeling process, the nomenclature of the motor and linkage parameters are listed in Table 1. All the parameters' units are used the international system of units (SI), such as mass [kg], length [m], time [s], current [A], angle [rad].

We will build a mathematical model of the prosthetic hand system by the method of classical mechanics. The model scheme of the model is shown in Fig. 2, where u is the

input voltage to DC motor; T_L is the load torque on the motor; F_1 is the acting force between the transition and sector gears; F_2 denotes the force exerted by the environment; and s denotes the distance between the thumb and index tips.

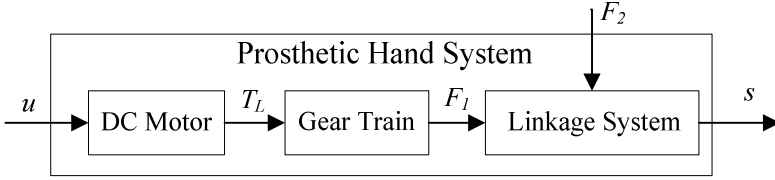


Fig. 2. Model scheme of a prosthetic hand system

The DC micro motor has a precious metal commutation. Here, the friction torque (Coulomb friction and Static Friction) is considered as a constant and its direction is opposite to that of motor angular velocity.

The dynamic model of the motor is given as follows:

$$J_m \dot{\omega} = K_t i - B\omega - T_L - \text{sgn}(\omega) \cdot T_f, \tag{1}$$

$$u = L_a \dot{i} + K_e \omega + R_a i, \tag{2}$$

where $\text{sgn}(\omega)$ is defined as 0, -1, or +1, depending on if ω is zero, negative or positive, respectively (The counterclockwise is positive direction).

Based on gear transmission properties, the angular velocity and acceleration of thumb link (i.e. ABE, see in Fig. 1(b)) are:

$$\dot{\theta} = \omega / (i_1 i_2), \quad \ddot{\theta} = \dot{\omega} / (i_1 i_2). \tag{3}$$

According to geometric properties of the four-link mechanism, it's easy to get the equations described below:

$$L_2 \cos \theta + L_3 \cos \alpha = L_1 + L_4 \cos \beta, \tag{4}$$

$$L_2 \sin \theta + L_3 \sin \alpha = L_4 \sin \beta. \tag{5}$$

Then, the Eq. 6 and Eq. 7 are easily derived based on Eq. 4 and Eq. 5 as follows:

$$\begin{bmatrix} \dot{\alpha} \\ \dot{\beta} \end{bmatrix} = \begin{bmatrix} L_4 \cos \beta & L_4 \sin \beta \\ L_3 \cos \alpha & L_3 \sin \alpha \end{bmatrix} \begin{bmatrix} \sin \theta \\ -\cos \theta \end{bmatrix} g_d L_2 \dot{\theta}, \tag{6}$$

$$\begin{bmatrix} \ddot{\alpha} \\ \ddot{\beta} \end{bmatrix} = \begin{bmatrix} L_4 \cos \beta & L_4 \sin \beta \\ L_3 \cos \alpha & L_3 \sin \alpha \end{bmatrix} \left(\begin{bmatrix} \sin \theta \\ -\cos \theta \end{bmatrix} L_2 \ddot{\theta} + \begin{bmatrix} \cos \theta \\ \sin \theta \end{bmatrix} L_2 \dot{\theta}^2 - \begin{bmatrix} -L_3 \cos \alpha & L_4 \cos \beta \\ -L_3 \sin \alpha & L_4 \sin \beta \end{bmatrix} \begin{bmatrix} \dot{\alpha}^2 \\ \dot{\beta}^2 \end{bmatrix} \right) g_d, \tag{7}$$

where $g_d = 1 / [L_3 L_4 (\sin \beta \cos \alpha - \cos \beta \sin \alpha)]$.

In order to establish moment equilibrium equations of different links in the prosthetic hand system, the mechanics analysis are shown Fig. 3.

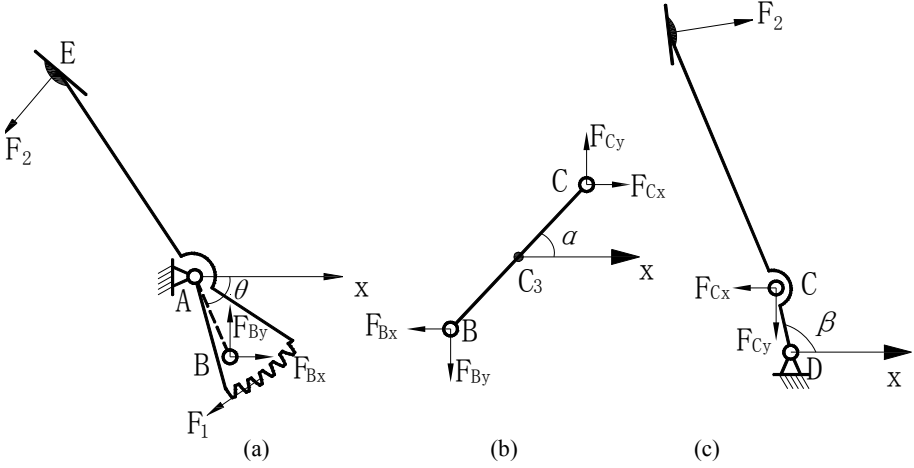


Fig. 3. The mechanics analysis of links (a) Thumb link (b) Connecting rod (c) Index link

Based on Newton's classical laws of mechanics, the equilibrium equations are derived as follows:

$$J_A \ddot{\theta} = F_1 R_0 - F_2 L_5 \sin \Theta_3 - F_{Bx} L_2 \sin(-\theta) - F_{By} L_2 \cos \theta, \quad (8)$$

$$J_{C_3} \ddot{\alpha} = F_{Bx} L_{C_3} \sin \alpha + F_{Cx} (L_3 - L_{C_3}) \sin \alpha - F_{By} L_{C_3} \cos \alpha - F_{Cy} (L_3 - L_{C_3}) \cos \alpha, \quad (9)$$

$$J_D \ddot{\beta} = F_{Cx} L_4 \sin \beta + F_{Cy} L_4 \cos(\pi - \beta) - F_2 \sin \Theta_4 [L_6 + L_4 \sin(\Theta_2 - \frac{\pi}{2})], \quad (10)$$

where F_1 is the driving force on the thumb link but the resistance on transition gear. Similarly, F_{Bx} , F_{By} , F_{Cx} and F_{Cy} are the forces on the related hinge joints, as shown in Fig. 3. F_2 is the force on fingertips, perpendicular to the surface of fingertips. L_{C_3} is the distance between point B and point C_3 . Point C_3 is the center of mass for link BC.

In addition, the acceleration of centroid C_3 can be derived by the same means that used to get Eq. 7. The acceleration axial component of centroid C_3 is:

$$\begin{bmatrix} a_{C_3x} \\ a_{C_3y} \end{bmatrix} = \begin{bmatrix} \ddot{x}_{C_3} \\ \ddot{y}_{C_3} \end{bmatrix} = \begin{bmatrix} -(\cos \theta) \dot{\theta}^2 - (\sin \theta) \ddot{\theta} \\ -(\sin \theta) \dot{\theta}^2 + (\cos \theta) \ddot{\theta} \end{bmatrix} L_2 + \begin{bmatrix} -(\cos \alpha) \dot{\alpha}^2 - (\sin \alpha) \ddot{\alpha} \\ -(\sin \alpha) \dot{\alpha}^2 + (\cos \alpha) \ddot{\alpha} \end{bmatrix} L_{C_3}. \quad (11)$$

To the link BC, the force balance equations are:

$$m_3 a_{C_3x} = F_{Cx} - F_{Bx}, \quad m_3 a_{C_3y} = F_{Cy} - F_{By}. \quad (12)$$

Combining Eq. 6~Eq. 12 and eliminating intermediate variables, we can obtain the dynamics model of the four-link system in the form:

$$f(\theta) \cdot \ddot{\theta} + g(\theta) \cdot \dot{\theta}^2 = F_1 \cdot h_1(\theta) + F_2 \cdot h_2(\theta), \quad (13)$$

where $f(\theta)$ and $g(\theta)$ are very complex nonlinear functions of variable θ , respectively. The $h_1(\theta)$ and $h_2(\theta)$ are also nonlinear functions. (Here to save space, the details are omitted).

Based on gear transmission properties, the load torque on the motor is:

$$T_L = F_1 R_0 / (i_1 i_2). \tag{14}$$

The dynamics model of the prosthetic hand system composed of the motor model and the four-link system model is built by Eq. 1, Eq. 2, Eq. 13 and Eq. 14.

Assigning state variables x_1, x_2 and x_3 corresponding to i, θ and $\dot{\theta}$, respectively, yields the following form of the system model:

$$\dot{x}_1 = (u - K_e i_1 i_2 x_3 - R_a x_1) / L_a, \tag{15}$$

$$\dot{x}_2 = x_3, \tag{16}$$

$$\dot{x}_3 = \frac{J_m i_1 i_2 [K_t x_1 - B i_1 i_2 x_3 - \text{sgn}(x_3) T_f] - R_0 g(x_2) x_3^2 - F_2 R_0 h_2(x_2)}{J_m (i_1 i_2)^2 h_1(x_2) + R_0 f(x_2)}. \tag{17}$$

Define the coordinates of thumb tip and index tip as E (x_e, y_e) and F (x_f, y_f), respectively. According to the geometric relationship, the distance between fingertip E and fingertip F is given as:

$$s = |EF| = \sqrt{(x_e - x_f)^2 + (y_e - y_f)^2} = s(x_2), \tag{18}$$

where $s(x_2)$ is a function of state variable x_2 , the detail isn't shown to save space.

The four-link prosthetic hand is similar to a second-order system [9], but the linkage system is coupled and the external force F_2 is uncertain. Actually, the prosthetic hand is a highly non-linear system as shown in Eq. 17. The damping effects of the linkages are neglected because the linkages are all at a lower speed. The friction torques in the hinge joints are assumed to be zero.

3 Hybrid Force-Position Fuzzy Control

A hybrid force-position fuzzy control is designed as shown in Fig. 4 with dual feedback loops: the outer force control loop and the inner position fuzzy control loop. Only a single input (i.e. desired force) is used to control the prosthesis. In the outer force feedback loop, a classical PD controller is described by the following model

$$s_d = K_{Fp} e_F + K_{Fd} \dot{e}_F, \tag{19}$$

where e_F is the force error, s_d is the desired distance, K_{Fp} is proportional gain and K_{Fd} is derivative gain [12]. The output s_d of the PD controller is used to specify the desired distance between the thumb and index tips.

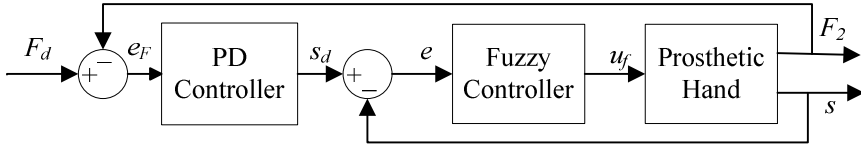


Fig. 4. Hybrid force-position fuzzy controller

In the inner loop, a fuzzy logic controller (FLC) [10] is used to improve anti-interference and parameter adaptability of the system. The input to the fuzzy controller is the position error. The position error e is defined as:

$$e = s_d - s, \tag{20}$$

where s is the actual distance between the thumb and index tips.

The detail design of the FLC was discussed in [10] and [11]. Here, only the structure of the FLC is shown in Fig. 5. Generally, for a FLC, the fuzzy rule adopts

“If E is A_i and R is B_j then \tilde{u} is G_{i+j} ”

where E, R and $A_i, B_j (i, j = -N, \dots, -1, 0, 1, \dots, N)$ denote input variables and input fuzzy sets, respectively; \tilde{u} and G_{i+j} denote the control action and output fuzzy set, respectively; N denotes the number of input fuzzy sets.

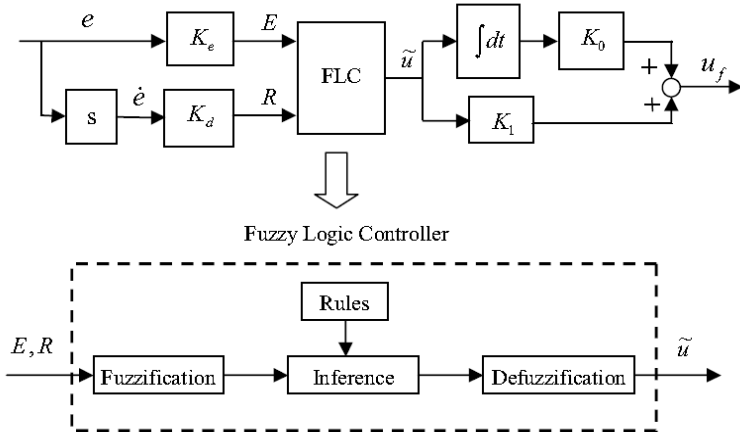


Fig. 5. Structure of the fuzzy logic controller

Practically, rules are always finite in real-world application, i.e., N is finite. Here, we select $N=3$, as shown in Table 2, where the linguistic labels are negative large (NL), negative medium (NM), negative small (NS), zero (ZO), positive small (PS), positive medium (PM) and positive large (PL).

Table 2. Fuzzy rule base in finite rules

R/E	NL	NM	NS	ZR	PS	PM	PL
PL	ZR	PS	PM	PL	PL	PL	PL
PM	NS	ZR	PS	PM	PL	PL	PL
PS	NM	NS	ZR	PS	PM	PL	PL
ZR	NL	NM	NS	ZR	PS	PM	PL
NS	NL	NL	NM	NS	ZR	PS	PM
NM	NL	NL	NL	NM	NS	ZR	PS
NL	NL	NL	NL	NL	NM	NS	ZR

The standard triangular membership functions(MFs), as shown in Fig. 6, are used.

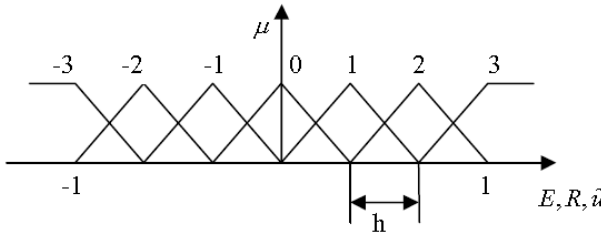


Fig. 6. Membership functions of input and output variable

When there are infinite rules, the output model of the rule base becomes [10]

$$\tilde{u} = sat(\sigma) = \begin{cases} \text{sgn}(\sigma), |\sigma| > 1 \\ g(\sigma), |\sigma| < 1 \end{cases}, \tag{21}$$

with

$$g(\sigma) = \sigma + (1 - \gamma)(kh - \sigma), \tag{22}$$

where $\sigma = E + R$

Thus, the mathematical model of the fuzzy PID controller can be easily derived as

$$u_f = K_0 \int \tilde{u} dt + K_1 \tilde{u} = K_0 \int sat(\sigma) dt + K_1 sat(\sigma), \tag{23}$$

where \tilde{u} is given in Eq. 21.

4 Simulations

Here, we assumed a five centimeters compression spring that can be pinched by the prosthetic hand. For convenience, the reaction force of the spring on the fingertips is assumed always perpendicular to the surface of the tips. And every time the prosthesis moves from the fully opening. Until the distance between the thumb and index tips reduces to 5 centimeters, the tips start to contact the virtual spring. Thus, the process has two procedures: no-contact step before touching the spring and pinching step. The values of the prosthetic hand system parameters are listed in Table 3. As comparison, a hybrid force-velocity controller is applied on our prosthetic hand as shown in Fig. 7 [9].

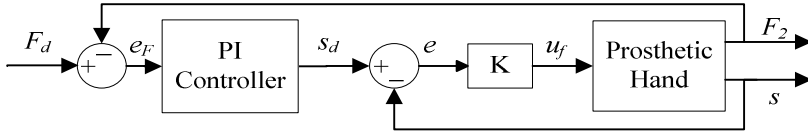


Fig. 7. Hybrid force-velocity controller

Three kinds of stiffness have settled: a spring with constant stiffness k_1 , a spring with a non-linear stiffness k_2 and a damping spring with stiffness k_3 and damping coefficient D .

Case 1: Consider a spring with constant stiffness. The stiffness k_1 is defined as:

$$k_1 = 200N / m, 0 \leq l_1 \leq 0.05m \tag{24}$$

where l_1 is the length of the first spring.

The force on the tips F_2 can be easily derived as:

$$F_2 = \begin{cases} 0, s_0 < s \leq s_m \\ k_1(s - s_0), 0 \leq s \leq s_0 \end{cases}, \tag{25}$$

where s_0 is the position contacting the spring firstly i.e. 0.05m; s_m is the maximum distance between tips i.e. 0.10m. For the pinched spring with stiffness k_1 , the control performance of step response is shown in Fig.8. The parameters of the outer PD force controller are chosen as $K_{Fp}=1, K_{Fd}=0.0005$. The parameters of the FLC are selected as $K_e=0.6, K_d=0.3, K_0=0.8, K_l=0.56$. And a sinusoidal force tracking is shown in Fig. 9 with the first spring.

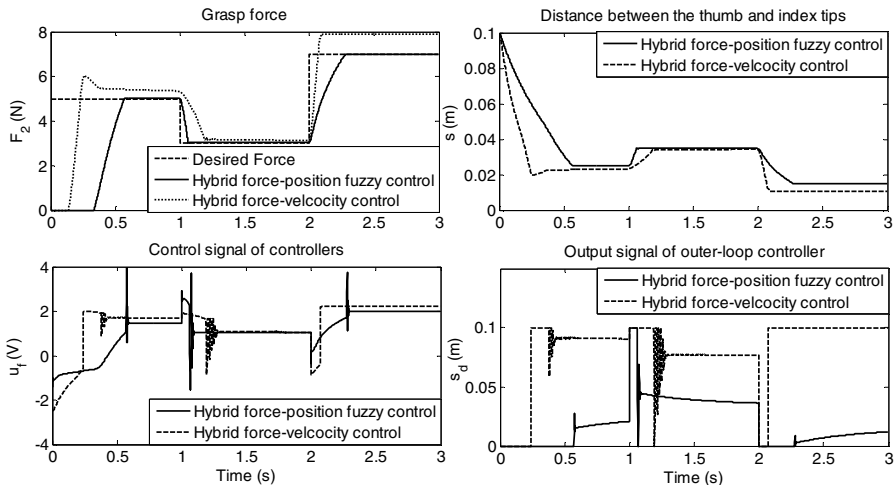


Fig. 8. Control performance of controllers for case 1

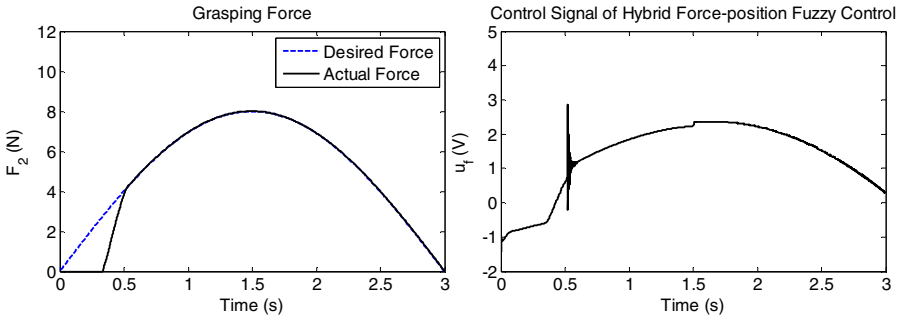


Fig. 9. Sinusoid force tracking performance of hybrid force-position fuzzy controller for case 1

Case 2: Consider a spring with non-linear stiffness. The non-linear stiffness k_2 is defined as:

$$k_2 = (a - b \cdot l_2^2) N / m, 0 \leq l_2 \leq 0.05 m, \tag{26}$$

where l_2 is the length of the second spring, $a=500N/m$, $b=60000N/m^3$. The force on tips is similar to Eq.25. For the spring with non-linear stiffness k_2 , a step response is shown in Fig. 10. The parameters of the outer PD force controller and FLC are set as $K_{Fp}=0.3$, $K_{Fd}=0.0001$ and $K_e=1$, $K_d=0.4$, $K_0=0.8$, $K_I=0.5$, respectively.

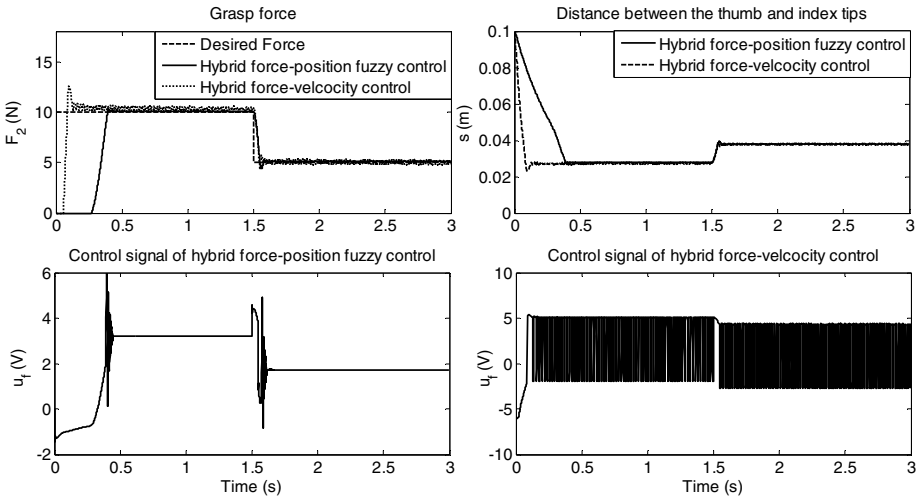


Fig. 10. Control performance of hybrid force-position fuzzy controller for case 2

Case 3: Consider a damping spring. For the damping spring, the force exerted by the third spring is given by:

$$F_2 = \begin{cases} 0, & s_0 < s \leq s_m \\ k_3(s - s_0) + D\dot{s}, & 0 \leq s \leq s_0 \end{cases} \tag{27}$$

where $k_3 = 300$ N/m; the value of damping coefficient D is 0.3 N*s/m when $s_0 - d_{max} \leq s \leq s_0$, or $D = 0$ with $d_{max} = 0.01$ m. A step response is shown for the damping spring in Fig. 11. The parameters of the outer PD force controller and FLC are chosen as $K_{Fp} = 0.1$, $K_{Fd} = 0.0001$ and $K_e = 1$, $K_d = 0.4$, $K_\theta = 0.8$, $K_f = 0.5$, respectively.

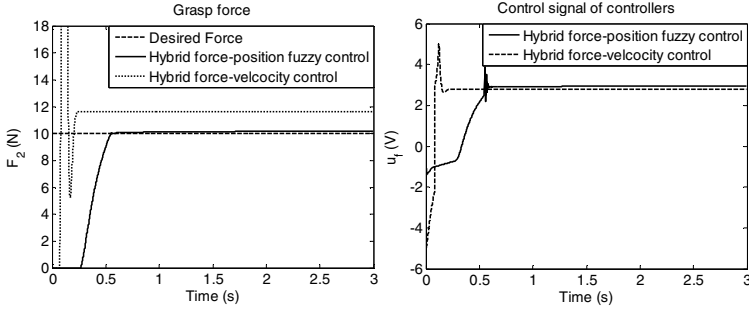


Fig. 11. Control performance of hybrid force-position fuzzy controller for case 3

Table 3. The value of the prosthetic hand system parameters

i_1	i_2	R_a [Ω]	K_e [Vs/wad]	K_t [Nm/A]	L_a [H]	J_m [kgm ²]	T_f [Nm]	B [Nms/rad]
10:1	12.5:1	1.94	6.92×10^{-3}	6.92×10^{-3}	4.5×10^{-5}	2.7×10^{-7}	2×10^{-4}	1×10^{-8}
L_1 [m]	L_2 [m]	L_3 [m]	L_4 [m]	L_5 [m]	L_6 [m]	R_θ [m]	Θ_1 [rad]	Θ_2 [rad]
0.0402	0.0190	0.0430	0.0143	0.0537	0.0600	0.0252	3.32	2.97
Θ_3 [rad]	Θ_4 [rad]	m_3 [kg]	J_A [kgm ²]	J_D [kgm ²]	θ [rad]	s [m]	U_N [V]	ω_N [rad/s]
1.27	1.27	0.007	3.1×10^{-5}	1.5×10^{-4}	-1.51~0.88	0~0.1	6	837.8

The simulation results in different situations (Fig. 8~Fig. 11) show that the hybrid force-position fuzzy control we proposed has a good control performance on our prosthetic hand system. From fully opening to contacting the virtual spring, the spent time is about 0.3s and the whole time from opening to reaching the desired force is about 0.5s in all situations. Note that the forces have almost no overshoot by the fast speed. And the prosthetic hand can grasp objects with rather accurate force. Obviously, the new controller is better than the hybrid force-velocity controller.

There is a little impact of the control signals when the prosthesis contacts the spring. The motor has a very large deadband because of Coulomb friction, viscous friction, and backlash. And it's hard to modulate grip force once that is excessive because the motor have to be given negative voltages. Thus, to maintain the accurate gripping force, the control signal will change drastically.

5 Conclusion

A hybrid force-position fuzzy control method is proposed to control a prosthetic hand. Only use a single input to control not only the position and velocity of the thumb and index fingers by an inner position feedback loop but also the grasping force on objects

by an outer force feedback loop. The inner loop adopts a fuzzy logic control strategy and the outer loop uses the PD technique. Three kinds of environment are simulated by different springs. And the proposed control strategy is applied to control the prosthesis. The simulation results demonstrate the effectiveness of the hybrid force-position fuzzy control method. In the future, we will apply the proposed control strategy in our experiments to verify its effectiveness.

Acknowledgments. The work described in this paper was partially supported by the grants from National Basic Research Program 973 of China (Grant Nos. 2011CB013302), a Postdoctoral Foundation of Central South University, China.

References

1. Carrozza, M.C., Cappiello, G., Stellin, G., Zaccone, F., Vecchi, F., Micera, S., Dario, P.: On the development of a novel adaptive prosthetic hand with compliant joints: experimental platform and EMG control. In: Proceedings of the IEEE/RSJ International Conference on Intelligent Robots and Systems, pp. 3951–3956 (2005)
2. Tomovic, R., Boni, G.M.: An adaptive artificial hand. *IRE Transactions on Automatic Control* 7(3), 3–10 (1962)
3. Groome, R.C.T.: Force Feedback Steering of teleoperator System. Master's Thesis, Massachusetts Institute of Technology (1972)
4. Raibert, M.H., Craig, J.J.: Hybrid position/force control of manipulator. *Transactions of the ASME, Journal of Dynamic Systems, Measurement, and Control* 103(2), 126–133 (1981)
5. Muzumdar, A.: *Powered Upper Limb Prostheses*. Springer, Berlin (2004)
6. Sciavicco, L., Siciliano, B.: *Modeling and Control of Robot Manipulators*, 2nd edn. Springer, New York (2000)
7. Dillon, G., Horch, K.: Direct neural sensory feedback and control of a prosthetic arm. *IEEE Trans. Neural Syst. Rehabil. Eng.* 13(4), 468–472 (2005)
8. Scherillo, P., Siciliano, B., Zollo, L., Carrozza, M., Guglielmelli, M., Dario, P.: Parallel force/position control of a novel biomechatronic hand prosthesis. In: Proc. IEEE/ASME Int. Conf. Adv. Intell. Mechatron, pp. 920–925 (2003)
9. Engeberg, E.D., Meek, S.G., Minor, M.A.: Hybrid force-velocity sliding mode control of a prosthetic hand. *IEEE Trans. Biomed. Eng.* 55(5), 1572–1581 (2008)
10. Li, H.X., Gatland, H.B., Green, A.W.: Fuzzy variable structure control. *IEEE Trans. Syst. Man, Cybern. B* 27(2), 306–312 (1997)
11. Duan, X.G., Li, H.X., Deng, H.: Effective tuning method for fuzzy PID with internal model control. *Ind. Eng. Chem. Res.* 47(21), 8317–8323 (2008)
12. Li, Y., Kiam, H.A., Gregory, C.Y.: PID Control System Analysis and Design. *IEEE Contr. Syst. Mag.*, 32–41 (2006)
13. Duan, X.G., Li, H.X., Deng, H.: Robustness of fuzzy PID controller due to its inherent saturation. *Journal of Process Control* 22(2), 470–476 (2012)

Simulation of a Hydraulic System Duplicating the Human Circulatory System

Feng Huang^{1,*}, Wenwei Qian², Xiaodong Ruan¹, and Xin Fu¹

¹ State Key Laboratory of Fluid Power Transmission and Control,
Zhejiang University, Hangzhou, China

huangfe001@zju.edu.cn

² Cardiothoracic Surgery Department of Zhejiang Provincial People's Hospital,
Hangzhou, China

Abstract. Mock circulatory system has been an essential tool for ventricular assist device (VAD) developing. It can replicate the characteristics of the natural human circulatory system, such as the flow and pressure of the aortic root. In this study a new method to establish a mock circulatory system using basic hydraulic elements is proposed. The system consists of a self-designed centrifugal pump, one electromagnetic switch valve, three vessels with a certain volume and a throttling valve. All of the hydraulic elements are modeled by means of fluid dynamics and ideal gas law. Once combining the components to form a system, numerical calculation is employed to get the results. Then the results are compared to the data obtained from the human circulatory system to validate the effectiveness of the new mock circulatory system. It can be found that this system is simple but valuable for VAD evaluating.

Keywords: hydraulic system, mock circulatory system, modeling, simulation.

1 Introduction

Heart failure has become a severe disease. It contributes to a large number of patients, most of whom will face a danger of death. For now, there is only one way to cure the end stage heart failure, which is called heart transplantation. But the heart donors are rare, only about a few thousandths of the patients who need a new heart. Ventricular assist devices (VAD) as an effective method of transition can solve the problem of donor shortage. VAD developing is a costly, time consuming process, needing to continually adjust the design according to the animal experiments. Although a mock circulatory system can't replace the animal experiments completely, it will reduce the number of the animal tests, thus decreasing the expenses and development cycle.

As a mock circulatory system, it must be capable of reproducing the main characteristics of the human blood circulation. By physiology knowledge, the heart is the core of the blood circulation, playing a role as a power source. Blood is ejected from the heart into the vascular network which has the property of resistance,

* Corresponding author.

compliance and inertance. At last, blood returns to the heart, making the blood system a complete circulation. The mock circulatory system should repeat this process and meanwhile replicate the pressure and flow of the human circulatory system.

There have been some mock circulatory systems for VAD testing in the world. The most difference between them is the realization of the cardiac function. G. Ferrari utilized a cylinder-piston system to reproduce the ventricular function [1], and Romano Zannoli etc. used this method as well [2]. In addition, Daniel Timms and F. M. Colacino employed a pneumatic system as the ventricle respectively [3] [4]. These mock systems are good but have the limitation of complexity or large volume because of the introduction of transmission or air supply devices.

In this research we propose a new system to reproduce the characteristics of the human blood circulatory system, and establish the mathematical model of the system, and then use Simulink (Mathworks Inc., Massachusetts, USA) to get the results.

2 Methods and Materials

The schematic diagram of the mock circulatory system is shown in Fig. 1. The system consists of a self-designed centrifugal pump, an electromagnetic switch valve, three vessels and a throttling valve. For simplicity, the pulmonary circulation is ignored. It is just included in the component of veins and atrium reservoir. The pump pumps the fluid into the sealed ventricle chamber, compressing the air above the liquid level. While the switch valve is open, the fluid is ejected into the sealed aorta chamber which also contains a certain volume of air. The air in these two chambers is used to reproduce the compliance property of the ventricle and the vessels. The switch valve is controlled by a signal with a frequency of heart rate (HR). And the throttling valve represents the resistance of the vascular network.

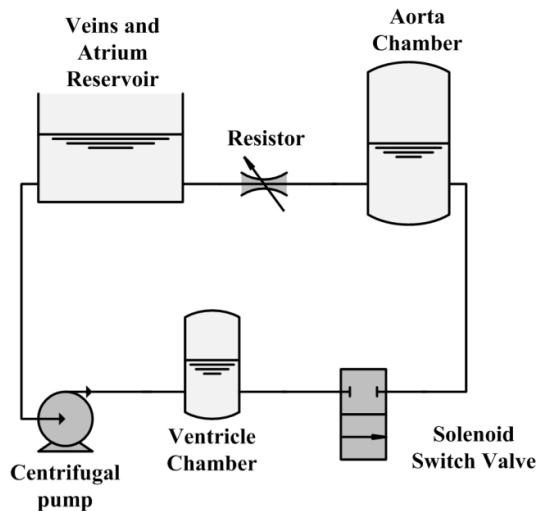


Fig. 1. The schematic diagram of the mock circulatory system

According to the work of Simon Mushi et al., the centrifugal pump can be modeled as the following equation [5]:

$$\Delta p_{pump} = (k_0 + k_1\omega)Q_{pump} + k_2\omega^2 \tag{1}$$

where Δp_{pump} is the pressure drop across the pump head, ω is the pump rotational speed in revolutions per minute (rpm), and Q_{pump} is the pump flow rate in liters per minute (L/min). The parameters $k_0 = 7.9, k_1 = -8.4 \times 10^{-3}, k_2 = 2.1 \times 10^{-5}$ are get from the fitting of the CFD simulation data listed in TABLE 1. The fitting analysis uses the least square method. Fig. 2 shows the fitting curves of the pump according to the simulation data.

Table 1. The CFD simulation data of the pump

$\omega=3000rpm$		$\omega=2500rpm$	
$Q(L/min)$	$\Delta p(mmHg)$	$Q(L/min)$	$\Delta p(mmHg)$
1	176.5	1	114.2
2	161.2	2	99.8
3	145.5	3	89.0
4	130.3	4	77.2
5	113.5	5	64.7
6	93.6	6	50.0
7	70.8	7	33.1

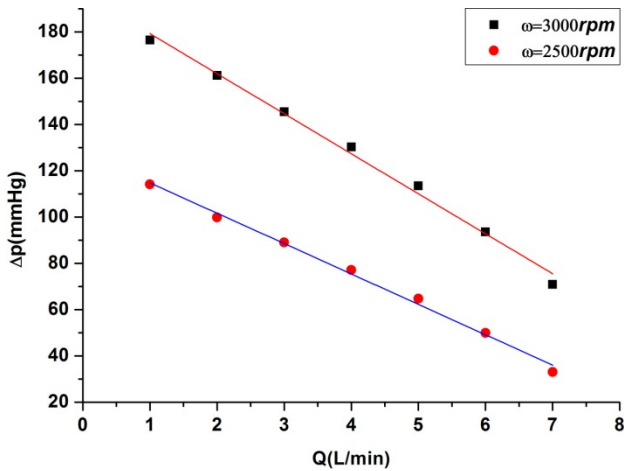


Fig. 2. The linear fitting of the data of the pump, to obtain the values of k_0, k_1, k_2

The model of the switch valve is regarded as an orifice, and can be expressed as

$$Q_{svalve} = \begin{cases} C_d A_0 \sqrt{2\Delta p_{svalve} / \rho}, & kT \leq t \leq kT + t_{sys} \\ 0, & kT + t_{sys} \leq t \leq (k + 1)T \end{cases} \tag{2}$$

Where Δp_{svalve} and Q_{svalve} are the pressure drop across the valve and the flow through the valve, respectively. During the systolic period, the valve is open and the flow rate is Q_{svalve} . At other time, the flow through the switch valve is always zero. The systolic period t_{sys} and the cardiac cycle T are set differently in normal and heart failure conditions. And other parameters such as the fluid density ρ in this equation are with constant values.

Compliance is a very important characteristic of both ventricles and vessels. When referring to the ventricle, we often call this characteristic with another name - the elastance. It is a classical method to use a chamber with a certain volume of air to reproduce compliance [3] [6]. When this method is applied, the pressures distributing in the arterial segments are regarded as a constant. That is, the artery is a lumped parameter model. The modeling of the chamber, using ideal gas law and continuity equation, can be expressed as

$$\int \Delta Q dt = V_0 - V_{gas} \quad (3)$$

$$p_{gas} \cdot V_{gas}^n = p_0 \cdot V_0^n \quad (4)$$

$$C = dV_{gas}/dp_{gas} \quad (5)$$

Where C is the instantaneous compliance of a chamber, n is the air polytropic exponent value, ΔQ is the difference between the inlet and outlet flow rate, V_0 and V_{gas} are the initial and instantaneous volume of the air in the chamber, p_0 and p_{gas} are the initial and instantaneous pressure of the air. The initial value of p_0 is set according to the physiological parameters, for example 80mmHg for the aorta chamber in normal condition. And the value of V_0 is calculated from the maximum compliance, using the equation as follow

$$V_0 = \sqrt[n]{np_0 C_{max}} \quad (6)$$

Where C_{max} is the maximum compliance. The other parameters are with the same meaning of those mentioned before.

The throttling valve, which is used as the vascular resistance, is simply described by

$$\Delta p_{tvalve} = R_{tvalve} \cdot Q_{tvalve} \quad (7)$$

Where Δp_{tvalve} is the pressure drop across the throttling valve, and Q_{tvalve} is the flow through the valve.

3 Implementation, Results and Discussion

The previous models of the system components are combined together in Simulink, and the parameter sets for normal and pathological conditions can be found in TABLE 2. When all of the parameters set properly, simulation is implemented for 10 seconds with the ode45 solver in normal mode.

Table 2. Parameter sets for normal and pathological conditions

	Normal condition	Pathological condition
Pump speed ω (rpm)	3000	2200
Cardiac cycle T (s)	0.8	0.5
Systolic period t_{sys} (s)	0.3	0.2
The initial pressure of the air in ventricle chamber p_{v0} (mmHg)	10	30
The initial volume of the air in ventricle chamber V_{v0} (mL)	18.6	21.8
The initial pressure of the air in aorta chamber p_{a00} (mmHg)	80	100
The initial volume of the air in aorta chamber V_{a00} (mL)	47.8	38.8
Fluid density ρ (kg/m ³)	1055	1055
Valve coefficient $C_d A_0$ (cm ²)	1.5	1.5
Vascular resistance R_{tvalve} (mmHg·s/mL)	1.25	4.0

Results obtained from the simulation of this mock circulatory system for the normal and pathological conditions are shown in Fig.3 and Fig. 4, respectively. In the normal condition, the aortic pressure varies from 80mmHg to about 120 mmHg, with an average flow of about 4 L/min. when the heart fails to eject enough blood, the aortic average flow decreases to only about 1.5 L/min. Although the vascular resistance rises, the pressure reduces to the range of about 60~80 mmHg. The heart rates in these two conditions are different. It's in accordance with the fact that the heart will beat more quickly if the body can't get enough blood. All of the results are within physiologic levels.

This is a preliminary simulation study about using the off-the-shelf hydraulic products to reproduce the hemodynamics of the natural blood circulatory system. The results show that this method is feasible. Compared to other mimicking method, it's simpler and economical, which will save a lot of time and expense. Due to the controllability of the components, this system is expected to replicate more characteristics such as the preload and afterload sensitivities of the mock ventricle, which will benefit the testing of the VADs. More work about the experiments will be carried out in the future.

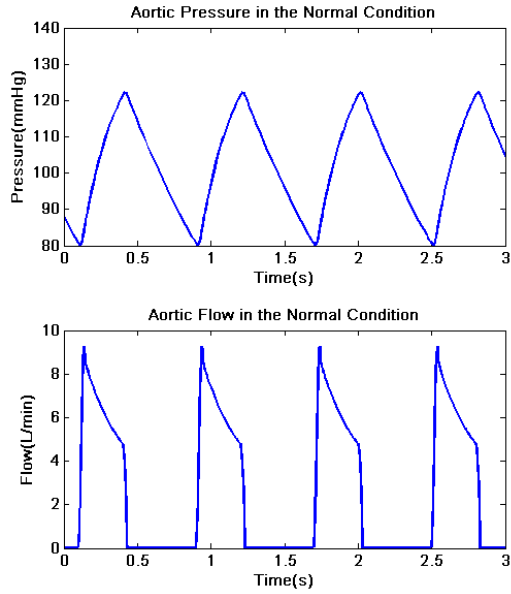


Fig. 3. Simulation results in the normal condition

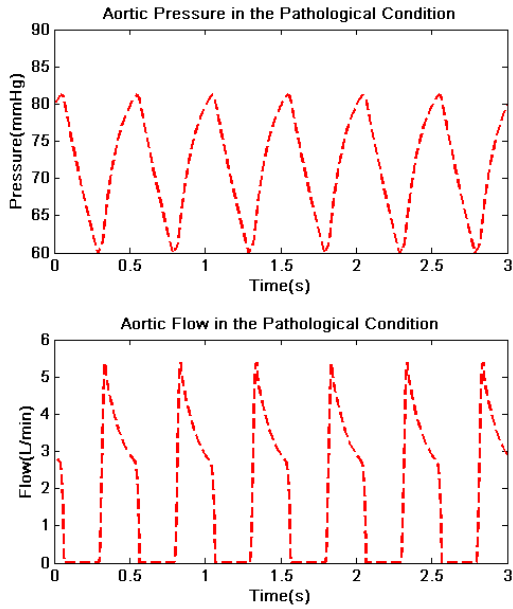


Fig. 4. Simulation results in the pathological condition

4 Conclusions

A mock circulatory system has become a useful tool for VAD evaluating. This paper provides a new method to construct a mock circulatory system. The numerical simulation demonstrates the effectiveness of the system. By changing the parameters of this system, some other conditions can also be reproduced, such as the hypertension status. In the future, experiments will be carried out, validating the ability of the mock circulatory system. It will be a strong support for VAD and artificial heart developing.

Acknowledgments. The authors are grateful to National Science Foundation of China (Grant No. 51275461), Zhejiang Provincial Natural Science Foundation of China (Grant No. Z1110189).

References

1. Ferrari, G., Delazzari, C., Mimmo, R., Ambrosi, D., Tosti, G.: Mock Circulatory-System for in-Vitro Reproduction of the Left-Ventricle, the Arterial Tree and Their Interaction with a Left-Ventricular Assist Device. *J. Med. Eng. Technol.* 18(3), 87–95 (1994)
2. Zannoli, R., Corazza, I., Branzi, A.: Mechanical simulator of the cardiovascular system. *Phys. Medica* 25(2), 94–100 (2009)
3. Timms, D., Hayne, M., McNeil, K., Galbraith, A.: A complete mock circulation loop for the evaluation of left, right, and biventricular assist devices. *Artif. Organs* 29(7), 564–572 (2005)
4. Colacino, F., Arabia, M., Moscato, F., Danieli, G.: Modeling, analysis, and validation of a pneumatically driven left ventricle for use in mock circulatory systems. *Med. Eng. Phys.* 29(8), 829–839 (2007)
5. Mushi, S., Yu, Y.C.: IEEE Control of a mock circulatory system to simulate the short-term baroreflex. In: *American Control Conference*, vol. 1-12, pp. 844–849 (2008)
6. Bowles, C.T., Shah, S.S., Nishimura, K., et al.: Development of mock circulation models for the assessment of counterpulsation systems. *Cardiovasc. Res.* 25(11), 901–908 (1991)

An Overview of Wearable Sensing and Wearable Feedback for Gait Retraining

Pete B. Shull^{1*}, Wisit Jirattigalachote², and Xiangyang Zhu¹

¹ State Key Laboratory of Mechanical System and Vibration,
Institute of Robotics, School of Mechanical Engineering,
Shanghai Jiao Tong University,
800 Dongchuan Rd, Shanghai 200240, China

² Department of Mechanical Engineering,
Stanford University,
424 Panama Mall, Bldg 560, Stanford, California, USA
pshull@sjtu.edu.cn

Abstract. Wearable gait retraining could enable benefits from laboratory retraining systems to extend to a broad portion of the population, which doesn't live near or have access to laboratory gait retraining testing facilities. While few portable gait retraining systems utilize both wearable sensing and wearable feedback, several systems employ critical components. The purpose of this paper is to provide a brief overview of various wearable sensing and wearable feedback components for gait retraining. We discuss wearable inertial sensors including accelerometers, gyroscopes, and magnetometers to estimate gait kinematics, wearable haptic feedback for retraining gait kinematics, wearable goniometers for measuring 2D and 3D ankle kinematics, and wearable measures of foot force and foot pressure. We conclude with a look at the future of wearable gait retraining systems and possible applications.

Keywords: Real-time training, rehabilitation, gait, feedback.

1 Introduction

Technological advances in computing power have enabled human movement to be measured and relevant biomechanical parameters to be calculated in real-time. Concurrently, wearable haptic (touch) feedback devices have been shown to be particularly effective for informing humans to move in new ways. By combining real-time motion sensing with real-time haptic feedback, humans can in theory be trained to move in ways that prevent injury, increase athletic performance, or treat musculoskeletal or neurological disease. Real-time movement training has often been used for relatively slow movements, such as upper extremity reaching tasks where haptic sensations can provide direct feedback regarding trajectory errors [1], [2], [3]. Recent research has shown that real-time feedback can be used to train relatively faster movements such as gait [4], [5], [6]. However, most real-time gait retraining

* Corresponding author.

systems do not provide wearable sensing and wearable feedback [7], but rather are performed in a laboratory setting with equipment which is tethered to the ground. While this type of biofeedback has been clinically effective, such as reducing knee loading and pain for knee osteoarthritis patients [8], the benefits are limited to populations living near facilities equipped with the necessary and specialized equipment. Thus, wearable gait retraining systems could provide the same benefits seen in the laboratory to a much wider populous. While few portable gait retraining systems with both wearable sensing and wearable feedback exist, several systems have employed necessary components. The purpose of this paper is to provide a brief overview of various systems with either wearable sensing or wearable feedback for gait retraining. We discuss wearable sensor arrays of accelerometers, gyroscopes, and magnetometers to estimate gait kinematics, wearable haptic feedback for training gait kinematics, wearable goniometers for measuring 2D and 3D ankle kinematics, and finally, wearable measures of foot force and foot pressure. We conclude with a look at the future of wearable gait retraining systems and possible applications.

2 Overview of Real-Time Movement Retraining

Real-time movement retraining through wearable systems requires several components: a human user, sensing, real-time biomechanics model, desired biomechanics, and feedback (Fig. 1).

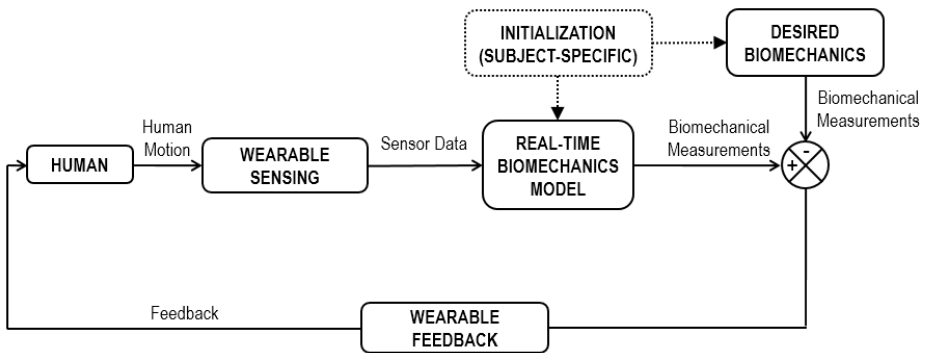


Fig. 1. Block diagram and information flow for real-time movement retraining systems

Human movements are sensed with wearable sensors such as accelerometers, gyroscopes, or goniometer (more details in Section 3), and this data is sent to the real-time biomechanics model. The model converts sensor signals into relevant biomechanical parameters of interest. The model could be as simple as a unity gain or as complex as a full-body musculoskeletal real-time simulation. Sensed biomechanical measurements are then compared with the desired biomechanical measurements and the error signal is used to provide wearable feedback to the user to alert a movement correction. The real-time biomechanics model and the desired biomechanics may be initialized in a way that is specific to each subject, though this

is optional and could also be the same for all subjects. It is also possible for the real-time biomechanics model and the desired biomechanics to be updated throughout testing [9]. While the above block diagram is general for any movement retraining, it is relevant for gait retraining in this paper.

3 Wearable Sensing and Feedback for Gait Retraining

While there are many types of wearable sensors for measuring human movement parameters, we choose to highlight some of the most common including: inertial sensors, goniometers, foot force, and foot pressure sensors. We also highlight wearable auditory and haptic feedback for informing kinematic gait changes.

3.1 Accelerometers, Gyroscopes and Magnetometers

Accelerometers, gyroscopes and magnetometers are miniaturized motion sensors that can be seen in many mobile devices such as smartphones and tablets. These sensors are responsible for sensing orientation when you tilt your smartphone and your device display rotates accordingly. Over the last few decades, Micro-Electro-Mechanical Systems (MEMS) technology has been responsible for the dramatic advance of these types of motion sensors. The sensors have become smaller, cheaper, more energy efficient, and more accurate. However, these sensors still has some shortcomings.

Accelerometers can sense the accelerations of an object it is attached to. Typically, accelerometers have higher signal-to-noise ratio at higher frequencies than at low frequencies. Thus, position estimates at higher frequencies will yield better results than at low frequencies where bias error from small to no movement becomes an issue. Gyroscopes can sense angular rates, or rate of turning, of an object. By integrating the signal, orientations (roll, pitch, and yaw angles) can be computed for a given object. However, over time, gyroscope signal drift errors accumulate and result in reduced accuracy. Magnetometers can sense the earth's magnetic field strength. Similar to a compass, it can be used to calculate the North Pole direction as an absolute reference direction. Magnetometers are susceptible to signal interference when ferrous material is present nearby. Due to some of these shortcomings, researchers usually use accelerometers, gyroscopes, and magnetometers in combination to leverage the strength of each. When accelerometers and gyroscopes are packaged together, they are sometimes called inertial measurement units (IMUs), and when all three sensors are present, some may refer to them as MARG (magnetic, angular rate, and gravitational) sensor. By combining multiple sensors together, we can achieve better performance than from each sensor alone through sensor fusion algorithms. Over the years, many algorithms have been developed and implemented to help improve the accuracy such as various kinds of Kalman filters [11, 15, 16, 17] or machine learning algorithms [12].

Due to their small size, portability, high accuracy, and low power consumption, these types of body-fixed sensors give rise to the possibility of bringing gait-lab quality measurements outside the traditional laboratory settings [10]. Several systems

have been developed over the years, both wired and wireless. For example, Simcox et al. [13] developed a wired body-fixed sensor pack using accelerometers and gyroscopes to measure the trunk and lower-limb sagittal plane angles, as seen in Fig. 2A. Similarly, Watanabe et al. [18] developed a wireless version of this type of system that can also be used to estimate stride length. In addition, some researchers have developed calibration procedures and algorithms to accurately measure three dimensional knee angles, which is particularly important for evaluating knee anterior cruciate ligament (ACL) injury [14]. The challenge in using these miniaturized motion sensors lies in finding a robust sensor fusion algorithm that can achieve good accuracy over a long period of time.

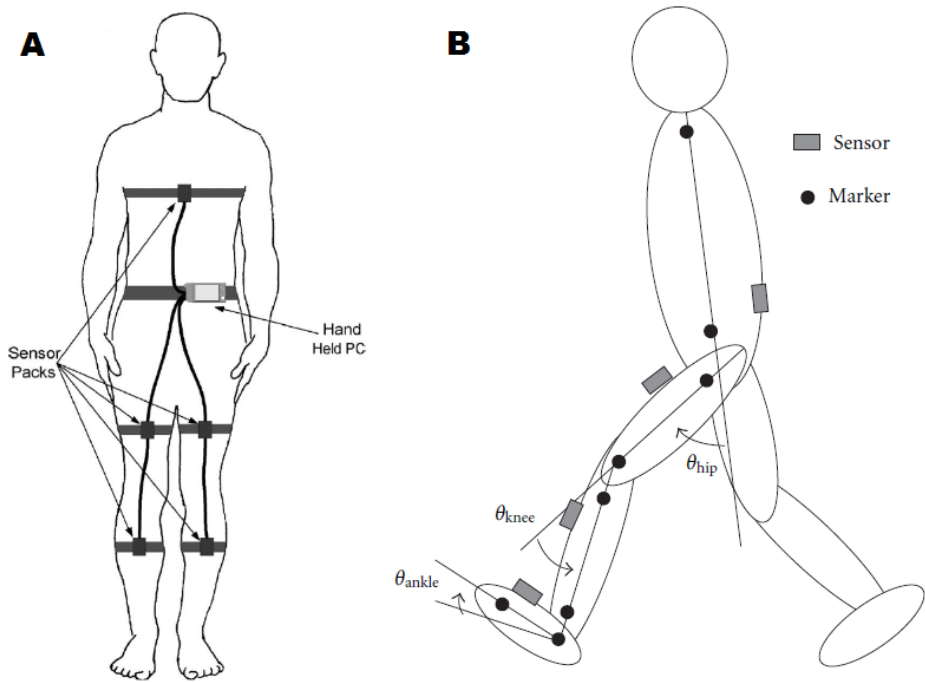


Fig. 2. A.) Wired body-fixed sensor packs. Image modified from [13]. B.) Placement of inertial sensors on the human body with joint angles definitions. Image modified from [18]

3.2 Wearable Feedback

Compared to wearable sensing, there are relatively fewer studies employing wearable feedback for gait retraining. The most common human sensations for wearable feedback of gait retraining are auditory and haptic, while vision, sight, and smell are less common. Basaglia et al. [19] used audio biofeedback to control knee recurvation during gait for patients with neurological diseases. An electrogoniometer was used to measure knee flexion angle and an audio signal alerted the user when knee flexion exceeded a threshold of 180 degrees. Riskowski et al. [20] used an instrumented knee

brace to provide auditory biofeedback for the rate of loading. Once the rate of loading exceeded a specified threshold during gait an auditory signal would be sent to the user to alert a needed change. Shull et al. [4,21] retrained trunk sway, tibia angle, and foot progression angle by placing a wearable skin stretch device [22] and/or C2 factor vibration motors near the location of desired kinematics change (Fig. 3). Wheeler

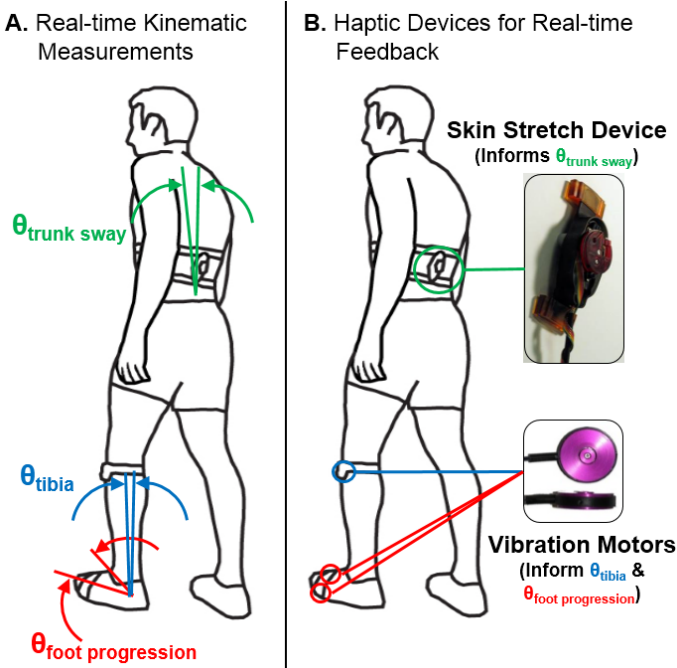


Fig. 3. (A) Real-time sensing and (B) haptic feedback to retrain gait kinematics. A rotational skin stretch device [22] on the lower back applies rotational skin stretch via two contact points on the skin to inform lateral trunk sway adjustments. One vibration motor on the lateral knee joint and two motors on the foot inform lateral tibia angle and foot progression angle, respectively. Image modified from [4].

et al. [23] strapped a vibration motor to the forearm to give feedback on the knee adduction moment (estimate of medial compartment loading). This alerted the user to choose a kinematic change to reduce the knee adduction moment. Finally, Dowling et al. [24] used a vibration motor on the shoe to retrain foot center of pressure during gait, which in turn changed the knee adduction moment. The challenge with wearable feedback is designing and selecting appropriate feedback devices and body locations to present intuitive feedback which encourages the user to move in a more optimal way.

3.3 Goniometers

Goniometers have long been used to measure human kinematics [25], [26]. Unlike some inertial sensors such as accelerometers or gyroscopes, which require integration

to obtain kinematic positions, goniometers directly measure angular changes. There are several types of goniometer sensing elements: potentiometer, strain gauge, mechanical-flexible, inductive, and optical. Rigid goniometer sensing is most often performed with one or more potentiometers located at the desired axis of interest (Fig. 4). Alternatively, flexible goniometers use strain gauges, changes in elongation between multiple wires, and optical fiber to measure changes in bending angles. The challenge with goniometers is designing a sensor that is both accurate and comfortable.

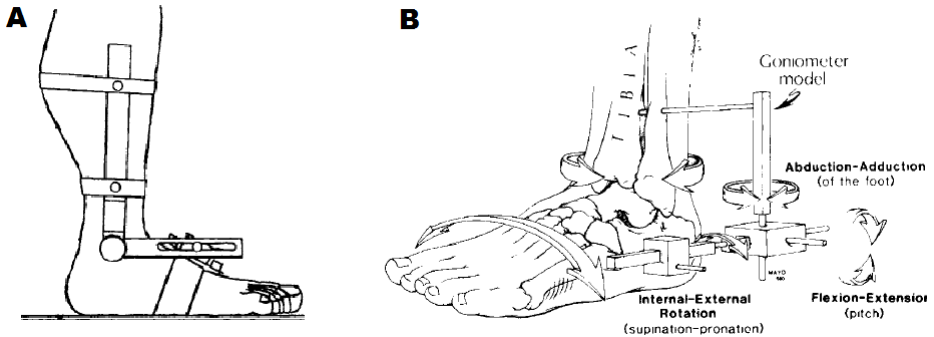


Fig. 4. (A) One degree-of-freedom goniometer to measure ankle flexion-extension. Image modified from [25]. (B) Three degree-of-freedom goniometer to measure ankle flexion-extension, internal-external rotation, and abduction-adduction. Image modified from [26].

3.4 Foot Force and Pressure

In a typical gait laboratory, there are usually force plates embedded into the ground or underneath a treadmill to measure ground reaction forces. This measurement allows researchers to analyze different walking characteristics such as their center of pressure and joint forces and moments via inverse dynamics. In order to obtain the same measurements outside the gait laboratory, researchers have developed several systems to capture ground reaction forces and moments or other correlated parameters [28, 31].

One simple version of foot force sensing comes in the form of force-sensing resistors (FSRs), seen in Fig. 5B. As its name suggested, the resistance changes as the force changes. Despite the non-linearity of the signal, FSRs are quite robust and accurate for gait phase detection such as foot strike, swing, and stance [27]. For pathological gait disorders, the detection may become more difficult and less accurate. Still, FSRs have proven to be useful in many other applications. Redd et al. [32] developed FSR-embedded insoles to be used with a smartphone and successfully induced gait asymmetry in normal subjects. This may lead to the possibility of using it in rehabilitation for patients with asymmetry problem. De Leon Rodriguez et al. [33] demonstrated the use of in-shoe foot pressure sensing to minimize the new at-risk foot area for diabetes patients.

A high accuracy version of foot force measurement unit is a miniaturized force plate, as seen in Fig. 5A. This type of sensor gives more information than FSRs do. It can measure three axes of forces and three axes of moments, thus providing researchers with the ability to estimate joint forces and moments when coupled with other motion sensors such as IMUs [30]. However, the higher accuracy and more information come at a price. The sensor cost is several thousands dollars or more for one unit. Furthermore, the weight of these instrumented force plate shoes is still relatively high and has a slight effect on normal gait [29]. The challenge with this type of sensor lies in the tradeoff among its accuracy of measurement, cost, weight, robustness, and ease of use.

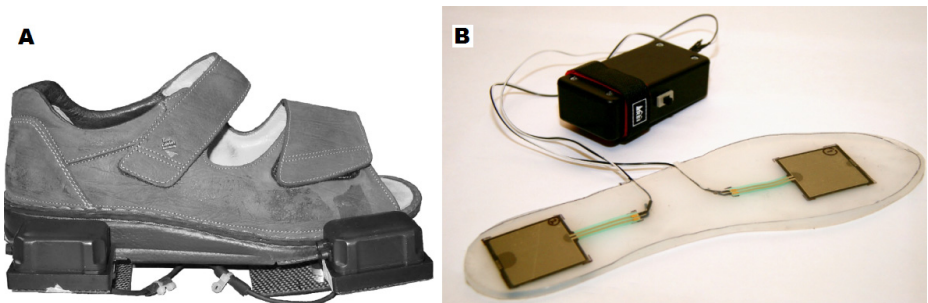


Fig. 5. A.) Instrumented shoe with miniaturized force plates and inertial measurement units (IMUs). Image modified from [30]. B.) Force-sensing resistors (FSRs) embedded insole Image modified from [32].

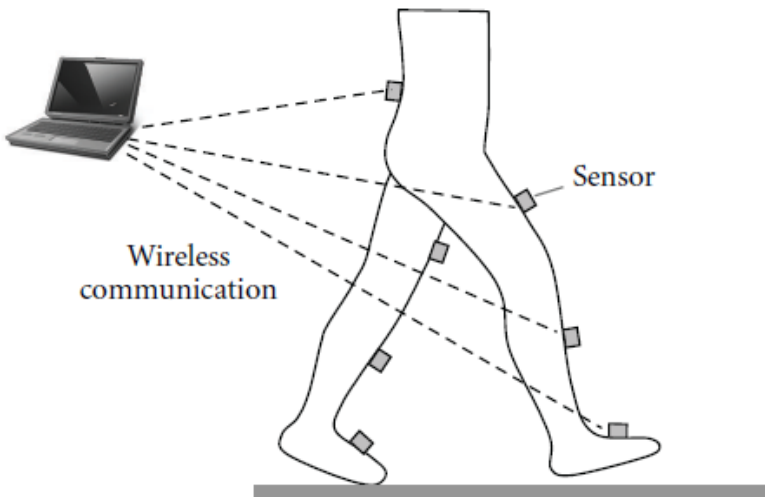


Fig. 6. An array of wireless sensors could potentially be linked to networks for analysis by a clinical professional in a remote location. Image modified from [18]

4 Conclusion and Future Work

This article provided a brief overview of several key components for wearable gait retraining systems. While there are few completely portable systems with wearable sensing and wearable feedback, much research has proven the effectiveness of key components. Combining these various components into a cohesive wearable system could provide gait retraining benefits to a diverse patient population. Furthermore, with the increased connectivity of portable computing devices such as smart phones, it may soon be possible to stream movement performance data from the user to a clinical professional in a remote location (Fig. 6), which could potentially expand the expertise of clinical professionals as far as the internet can extend.

References

1. Lieberman, J., Breazeal, C.: TIKL: Development of a Wearable Vibrotactile Feedback Suit for Improved Human Motor Learning. *IEEE Trans. on Robotics* 23, 919–926 (2007)
2. Bloomfield, A., Badler, N.I.: Virtual Training via Vibrotactile Arrays. *Presence: Teleoperators & Virtual Environments* 17, 103–120 (2008)
3. Kapur, P., Premakumar, S., Jax, S.A., Buxbaum, L.J., Dawson, A.M., Kuchenbecker, K.J.: Vibrotactile Feedback System for Intuitive Upper-limb Rehabilitation. *IEEE World Haptics*, 621–622 (2009)
4. Shull, P.B., Lurie, K., Cutkosky, M., Besier, T.: Training multi-parameter gaits to reduce the knee adduction moment with data-driven models and haptic feedback. *J. Biomech.* 44, 1605–1609 (2011)
5. Barrios, J.A., Crossley, K.M., Davis, I.S.: Gait Retraining to Reduce the Knee Adduction Moment through Real-time Visual Feedback of Dynamic Knee Alignment. *J. Biomech.* 43, 2208–2213 (2010)
6. Hunt, M.A., Simic, M., Hinman, R.S., Bennell, K.L., Wrigley, T.V.: Feasibility of a Gait Retraining Strategy for Reducing Knee Joint Loading: Increased Trunk Lean Guided by Real-time Biofeedback. *J. Biomech.* 44, 943–947 (2011)
7. Tate, J.J., Milner, C.E.: Real-time Kinematic, Temporospatial, and Kinetic Biofeedback During Gait Retraining in Patients: A Systematic Review. *Phys. Ther.* 90, 1123–1134 (2010)
8. Shull, P.B., Silder, A., Shultz, R., Dragoo, J.L., Besier, T.F., Delp, S.L., Cutkosky, M.R.: Six-Week Gait Retraining Program Reduces Knee Adduction Moment, Reduces Pain, and Improves Function for Individuals with Medial Compartment Knee Osteoarthritis. *J. Ortho. Res.* 31(7), 1020–1025 (2013)
9. Shull, P.B., Lurie, K., Shin, M., Besier, T., Cutkosky, M.: Haptic Gait Retraining for Knee Osteoarthritis Treatment. In: *IEEE Haptics Symposium*, pp. 409–416. IEEE Press, New York (2010)
10. Mayagoitia, R.E., Nene, A.V., Veltink, P.H.: Accelerometer and rate gyroscope measurement of kinematics: an inexpensive alternative to optical motion analysis systems. *Journal of Biomechanics* 35(4), 537–542 (2002)
11. Zhu, R., Zhou, Z.: A real-time articulated human motion tracking using tri-axis inertial/magnetic sensors package. *IEEE Transactions on Neural Systems and Rehabilitation Engineering* 12(2), 295–302 (2004)

12. Goulermas, J.Y., Howard, D., Nester, C.J., Jones, R.K., Ren, L.: Regression techniques for the prediction of lower limb kinematics. *Journal of Biomechanical Engineering* 127(6), 1020 (2005)
13. Simcox, S., Parker, S., Davis, G.M., Smith, R.W., Middleton, J.W.: Performance of orientation sensors for use with a functional electrical stimulation mobility system. *Journal of Biomechanics* 38(5), 1185–1190 (2005)
14. Favre, J., Luthi, F., Jolles, B.M., Siegrist, O., Najafi, B., Aminian, K.: A new ambulatory system for comparative evaluation of the three-dimensional knee kinematics, applied to anterior cruciate ligament injuries. *Knee Surgery, Sports Traumatology, Arthroscopy* 14(7), 592–604 (2006)
15. Yun, X., Bachmann, E.R.: Design, implementation, and experimental results of a quaternion-based Kalman filter for human body motion tracking. *IEEE Transactions on Robotics* 22(6), 1216–1227 (2006)
16. Roetenberg, D., Slycke, P.J., Veltink, P.H.: Ambulatory position and orientation tracking fusing magnetic and inertial sensing. *IEEE Transactions on Biomedical Engineering* 54(5), 883–890 (2007)
17. Sabatini, A.M.: Estimating three-dimensional orientation of human body parts by inertial/magnetic sensing. *Sensors* 11(2), 1489–1525 (2011)
18. Watanabe, T., Saito, H., Koike, E., Nitta, K.: A preliminary test of measurement of joint angles and stride length with wireless inertial sensors for wearable gait evaluation system. *Computational Intelligence and Neuroscience* 2011, 6 (2011)
19. Basaglia, N., Mazzini, N., Boldrini, P., Bacciglieri, P., Contenti, E., Ferraresi, G.: Biofeedback Treatment of Genu-Recurvatum Using an Electrogoniometric Device with an Acoustic Signal. *Scand. J. Rehab. Med.* 21, 125–130 (1989)
20. Riskowski, J.L., Mikesky, A.E., Bahamonde, R.E., Burr, D.B.: Design and Validation of a Knee Brace with Feedback to Reduce the rate of Loading. *J. Biomech. Engr.* 131, 84503–84506 (2009)
21. Shull, P.B., Shultz, R., Silder, A., Dragoo, J.L., Besier, T.F., Cutkosky, M.R., Delp, S.L.: Toe-in Gait Reduces the First Peak Knee Adduction Moment in Patients with Medial Compartment Knee Osteoarthritis. *J. Biomech.* 46, 122–128 (2013)
22. Bark, K., Wheeler, J., Shull, P.B., Savall, J., Cutkosky, M.R.: Rotational Skin Stretch Feedback: A Wearable Haptic Display for Motion. *IEEE Trans. on Haptics* 3, 166–176 (2010)
23. Wheeler, J.W., Shull, P.B., Besier, T.: Real-time Knee Adduction Moment Feedback for Gait Retraining through Visual and Tactile Displays. *J. Biomech. Engr.* 133, 041007-5 (2011)
24. Dowling, A.V., Fisher, D.S., Andriacchi, T.P.: Gait Modification via Verbal Instruction and an Active Feedback System to Reduce Peak Knee Adduction Moment. *J. Biomech. Engr.* 132, 071007-5 (2010)
25. Carmines, D.V., Nunley, J.A., McElhaney, J.H.: Effects of Ankle Taping on the Motion and Loading Pattern of the Foot for Walking Subjects. *J. Ortho. Res.* 6, 223–229 (1988)
26. Laughman, R.K., Carr, T.A., Chao, E.Y., Youdas, J.W., Sim, F.H.: Three-Dimensional Kinematics of the Taped Ankle Before and After Exercise. *Amer. J. Sports Med.* 8, 425–431 (1980)
27. Pappas, I.P., Popovic, M.R., Keller, T., Dietz, V., Morari, M.: A reliable gait phase detection system. *IEEE Transactions on Neural Systems and Rehabilitation Engineering* 9(2), 113–125 (2001)

28. Veltink, P.H., Liedtke, C., Droog, E., van der Kooij, H.: Ambulatory measurement of ground reaction forces. *IEEE Transactions on Neural Systems and Rehabilitation Engineering* 13(3), 423–427 (2005)
29. Liedtke, C., Fokkenrood, S.A., Menger, J.T., van der Kooij, H., Veltink, P.H.: Evaluation of instrumented shoes for ambulatory assessment of ground reaction forces. *Gait & Posture* 26(1), 39–47 (2007)
30. Schepers, H.M., Koopman, H.F.J.M., Veltink, P.H.: Ambulatory assessment of ankle and foot dynamics. *IEEE Transactions on Biomedical Engineering* 54(5), 895–902 (2007)
31. Bamberg, S., Benbasat, A.Y., Scarborough, D.M., Krebs, D.E., Paradiso, J.A.: Gait analysis using a shoe-integrated wireless sensor system. *IEEE Transactions on Information Technology in Biomedicine* 12(4), 413–423 (2008)
32. Redd, C.B., Bamberg, S.J.M.: A wireless sensory feedback device for real-time gait feedback and training. *IEEE/ASME Transactions on Mechatronics* 17(3), 425–433 (2012)
33. De León Rodríguez, D., Allet, L., Golay, A., Philippe, J., Assal, J.P., Hauert, C.A., Pataky, Z.: Biofeedback can reduce foot pressure to a safe level and without causing new at-risk zones in patients with diabetes and peripheral neuropathy. *Diabetes/Metabolism Research and Reviews* 29(2), 139–144 (2013)

Quantifying Roughness Sensation by an Active Touch Model for Vibrotactile Stimulation

Zhongyi Qiu, Dingguo Zhang, and Xiangyang Zhu

State Key Laboratory of Mechanical System and Vibration
Shanghai Jiao Tong University
Shanghai, China, 200240

qzy09421@126.com, {dgzhang,mexyzhu}@sjtu.edu.cn

Abstract. Vibrotactile stimulation has been widely used in haptics. This paper describes a method of quantifying roughness sensation by performing assigned patterns of vibrotactile stimuli on human finger pads. In order to design the stimulus parameters, an active touch model for human finger pad is fabricated. To validate the model, a roughness sensation experiment is conducted using 11 selected types of sandpapers. The frequencies and amplitudes of vibrotactile stimuli are derived from the active touch model. The results show that a strong relationship exists between the stimulus patterns and perceived roughness sensation. Also, we prove that the correlation between the rates of growth in human sensation and increasing stimuli intensities matches psychological disciplines.

Keywords: Haptics, Skin model, Vibrotactile stimulation, Roughness, Active touch.

1 Introduction

Haptic technology is intimately connected with robotics through its reliance on dexterous mechatronic devices and draws heavily on the theoretical foundations of manipulator design, actuation, sensing, and control [1]. In the field of haptics, vibrotactile, electrotactile and mechanotactile [2] are three main methods. Vibrotactile stimulation evokes tactile sensations using mechanical vibration of skin, typically at frequencies of 10-500Hz [3]. Tactile perception is complex, and its neurophysiology and perceptual basis are still under active research. It is reported that glabrous human skin contains four types of mechanoreceptors (see Table 1).

Roughness sensation usually concerns about the texture and material features of real objects. In order to render more realistic roughness sensation to human, many studies have been conducted to make tactile feelings actively using vibrotactile stimulation. Masashi Konyo et al. proposed representing Virtual Touch by stimulating the mechanoreceptors selectively [4]. They developed a useful tactile synthesis method that controlled three sensations related with roughness, softness, and friction as tunable parameters of texture feel. Especially they mentioned that roughness sensation can be evoked by stimulating FAI. Ki-Uk Kyung et al. studied on the correlation of perceived

roughness and vibrotactile stimuli and found that frequency and amplitude played an important role in vibrotactile sensation [5]. Seung-Chan Kim et al. proposed using sandpapers as a method to evaluate human sensibility on perceived texture under variations of vibrotactile stimuli [6]. Takashi Maeno et al. introduced ultrasonic vibration to texture sensation to generate the realistic surface of touching materials [7].

Table 1. Basic properties of four types of mechanoreceptors.

Mechanoreceptors	SAI	SAII	FAI	FAII
End Organ	Merkel Disk	Ruffini Ending	Meissner Corpuscle	Pacinian Corpuscle
Sensory Adaptation	Slow	Slow	Fast	Fast
Receptive Field	Small	Large	Small	Large
Frequency Range	5~15Hz	15~400Hz	3~100Hz	10~500Hz
Perceiving Property	Pressure	Stretch	Flutter	Vibration

Although vibrotactile stimulation has been studied and applied in some aspects, the basic mechanisms are rarely discussed or explored. In previous studies, researchers attempted to create various roughness sensations by combinations of several kinds of frequencies and amplitudes. As a result, they always had to find complex relationships between stimulation and sensation in a trial-and-error way, which is not convincible some times. In this paper, we propose an active touch model to set up the vibrotactile stimulation parameters to quantify the perceived roughness sensation. The primary objective of this research is to use specific stimulation patterns for different roughness sensation evaluation.

2 Mathematical Model of Active Touch

In this part we designed to construct a theoretical touching model to obtain the parameters of vibrotactile stimuli and then evaluate perceived roughness sensation. According to the duplex theory of tactile texture perception [8], active touch is more sensible for human than passive touch so we consider the case in which a human finger moves on the sandpaper. As sandpapers are selected as touching materials, the numerical features of sandpapers are considered to define roughness. Grit number and particle size are two main properties of sandpapers. Grit number refers to the number of abrasive particles per square inch of paper. The larger the grit number, the more particles per square inch. Particle size refers to the average diameter of abrasive particles. In this way, we will approximately define the surface of sandpapers as a sinusoidal surface, which the wavelength λ and the amplitude A can be deduced from grit number and particle size respectively.

When the finger moves on the sandpapers, a dynamic longitudinal deformation occurs on the finger pad. As the sandpaper has been considered as sinusoidal surface, this deformation will be a kind of periodical vibrational movement. When the finger slides on the sinusoidal surface at a given velocity v , the period of the stimuli generated on the surface of finger τ is expressed by a wave equation as follows,

$$\tau = \frac{\lambda}{v} \tag{1}$$

In this paper, we set the value of v to be 0.1 m/s in order to simulate the actual touching speed. Therefore, a displacement of stimulus $y_s(t)$ at a given time t is expressed as a sinusoidal function as follows,

$$y_s(t) = A \sin\left(\frac{2\pi v}{\lambda} t\right) \tag{2}$$

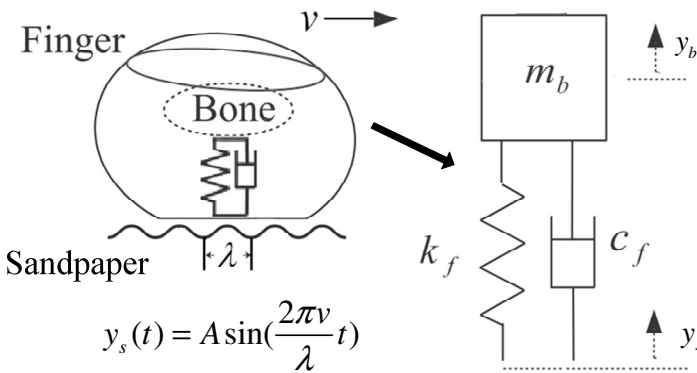


Fig. 1. Ski model for numerical analysis of the deformation of a finger pad when touching the sandpaper actively. Left figure is a schematic model of finger moving on sandpaper. Right figure shows a simple dynamic structure of finger pad vibration.

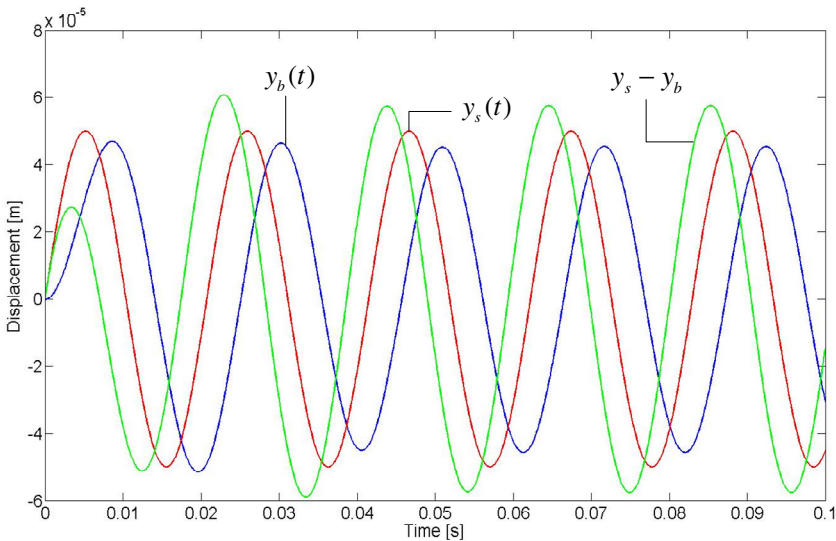


Fig. 2. Finger pad motion trajectory derived from the active touch model

In this model, we try to obtain the vibrational features of the finger when applying the sinusoidal stimulus. And we ignore the force caused by pressing the finger and the gravity of the finger. As shown in Fig. 1, the finger is expressed as a mass point with a spring and damper connected by a simple Kelvin model. The equation of finger sliding is expressed as follows,

$$m_b \ddot{y}_b + c_f (\dot{y}_b - \dot{y}_s) + k_f (y_b - y_s) = 0 \quad (3)$$

In this equation, m_b represents the mass of the finger, k_f is the spring coefficient and c_f is the damper coefficient. The movement of the finger mass point is expressed as $y_b(t)$ and $y_s(t)$ is the sandpaper stimulus mentioned above. Some physical parameters are based on the report of [9]. By solving this equation, we obtain the actual finger motion and then we can get the longitudinal skin stretch $y_s - y_b$. Fig. 2 shows the diagram of the finger motion curve on a kind of typical sandpaper.

3 Roughness Sensation Experiment

3.1 Subjects

Six subjects participated in the experiment and none of them had any knowledge about the field of haptic research. All of them were right-handed and none of them had any sensory or motor impairment in their index fingers.

3.2 Apparatus and Stimuli

Vibrotactile stimuli are delivered through a linear resonant actuator (Model C10-100, Precision Microdrives, UK). A power amplifier (Serenade HP, Tempotec Corporation) is used to adjust the vibrating strength of the actuator. Instead of setting the vibration amplitude of the actuator, we transfer the amplitude into acceleration for control convenience and an accelerometer (Biometrics, UK) is used.

Sandpapers of grit size 120,150,180,220,240,280,320,500,800,1200,2000 is used. According to the Weber fraction [5], the log scale of the sandpaper grit should be linearly with the grit number so that subjects can better discriminate the roughness sensation of different sandpaper. Fig. 3 displays the grit size and log-scaled size. The sandpaper specimens have dimensions of 10cm*3cm.

The two basic parameters of the vibrotactile stimuli are amplitude and frequency. From the roughness sensation model we described above, we can control the amplitude (acceleration) and frequency of the actuator. The vibration curve of the actuator is expressed by $\ddot{y}_s - \ddot{y}_b$. And the vibration parameters of the actuator specific to every kind of sandpapers are shown in Table 2.

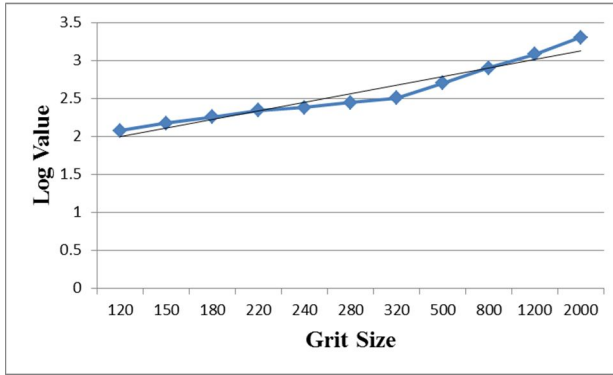


Fig. 3. The log values of grit size of 11 selected types of sandpaper. The black fitted line shows that the sandpaper specimens are suitable for human roughness sensation experiment.

Table 2. Properties of sandpaper specimens and stimulus parameters derived from the active touch model. As sandpaper feels less rough with the increasing of grit number, we set the roughness magnitude for each sandpaper type for experiment convenience. Also, the frequency and amplitude provide the unique features of stimuli, so we use stimulus pattern numbers to mark the stimuli we use in the experiment.

Grit number	Roughness magnitude	Particle size(um)	Stimulus frequency(Hz)	Stimulus acceleration amplitude(G)	Stimulus pattern number
120	11	124	43.1	0.491837	1
150	10	100	48.2	0.426531	2
180	9	83	52.8	0.37449	3
220	8	65	58.4	0.311224	4
240	7	59	61	0.290816	5
280	6	51	65.9	0.264286	6
320	5	44	70.4	0.231633	7
500	4	28	88	0.178571	8
800	3	19	111.4	0.146939	9
1200	2	12	136.4	0.110204	10
2000	1	6.5	176.1	0.07551	11

3.3 Procedure

The subjects had to sit comfortably on a chair with their arms extended toward the experiment platform. Their hands rested while only the index fingers were extended towards the stimulus. The subjects were instructed to do active touch with their right index fingers by touching the 10cm sandpaper bar in one second each time. In this way, this experiment situation meets the hypothesis of touching speed in the touching model. And their left index fingers were exposed to a vibrotactile stimulus with the linear resonant actuator (Fig. 4).

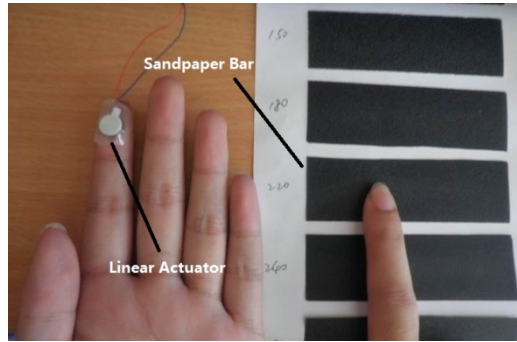


Fig. 4. Experiment Setup. The right index finger touches the sandpaper bar while the left index finger receives the vibrotactile stimuli.

The subjects were trained to experience the eleven vibrotactile stimulus and try to match the touch feeling with the corresponding sandpapers first. After that 4 sets of eleven vibrotactile stimulus (44 trials in all) were randomly presented to the subjects and the period of each stimulus was 20 seconds. During that time, the subjects could actively touch the sandpaper bars and choose the one which matched the feeling of the vibrotactile stimulus. The subjects took a 10-second break before the next trial.

3.4 Results and Discussion

In order to quantify the perceived roughness sensation, we classify sandpapers of different grit numbers into roughness degrees. As the roughness sensation decreases with the grit number, we graded grit 120 as roughness 11, grit 150 as roughness 10, and so on (see Table 2). We averaged the responses of all the subjects and the results are shown in Fig. 5. The stimulus number means the specific stimulation pattern we derived from the mathematical model corresponding to the specific sandpaper. And the theoretical linear trend is what we expect the perceived roughness to be. Generally, the experimental results show that the perceived roughness decrease with the stimulus pattern number. As the stimulus parameters are all calculated from the active touch model, it is proved that both the frequency and amplitude have relationships with roughness sensation.

Our goal is to stimulate FAI selectively to produce roughness sensation, but actually it hard to stimulate only one kind of mechanoreceptor. So from the experimental results we see that around stimulus pattern 3 and stimulus pattern 9 the errors are relatively large. The corresponding stimulus frequencies are around 50Hz and 110Hz. From Table 1 we see that the vibrotactile stimuli are also likely to stimulate SAI and FAII in these two frequencies. So this phenomenon brings subjects of sensation illusion and finally leads to wrong responses.

To further analyze the experiment data, we introduce Stevens' Power Law [10]. Stevens' Power Law relates sensation magnitude to stimulus intensity:

$$\psi(I) = kI^e \quad (4)$$

In this equation, $\psi(I)$ stands for sensation magnitude, I stands for stimulus intensity, e is a power exponent dependent on modality and k is constant. The exponent e determines the growth rate of the perceived magnitude, and it ranges from 0.35 to 0.86 for vibrotactile stimuli [11]. As in our experiment, we can calculate the stimulus intensity of every stimulus pattern to verify the results of the experiment. Fig. 6 shows the relationship of perceived roughness sensation magnitude and stimulus intensity. We fit this plot with a curve:

$$y = 23.742x^{0.5306} \tag{5}$$

We observe that this fitted curve perfectly matches the form of Stevens' Power Law and the power exponent 0.5306 is within the vibrotactile stimuli modality range. This result shows that the stimuli pattern derived from the touching model can be used to correlate with human perceived roughness sensation.

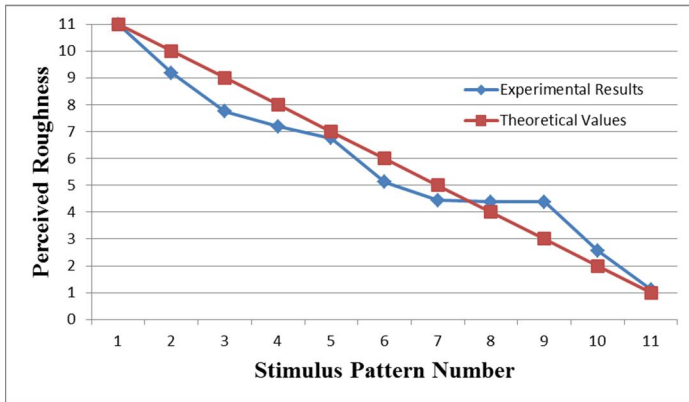


Fig. 5. Experimental results of all subjects

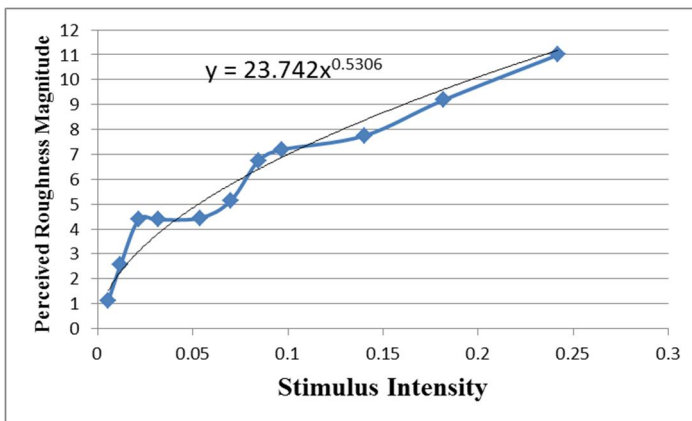


Fig. 6. The relationship of perceived roughness magnitude and stimulus intensity. The black curve fits the original experiment data and gives out the equation.

4 Conclusion and Future Work

The objective of this research was to quantify perceived roughness sensation by constructing human active touch model. From the experimental results, the active touch model proved to be useful in roughness sensation by setting the stimulus frequencies and amplitudes. In addition, the stimulus intensity is matched with perceived roughness magnitude. Through the active touch model, roughness sensation can be correlated with the physical properties of touching materials.

In this paper we adopt sandpapers as experiment materials because its parameters are easy to be obtained and calculated. The next-stage work will consider several kinds of different materials to better verify our physical model. Touching force is not considered in our current experiment, so we will consider putting touching force into model construction and using force sensors in the future.

Acknowledgement. This work is supported by the National Basic Research Program (973 Program) of China (Grant No.2011CB013305), the National Natural Science Foundation of China (Grant No.51075265), and the Science and Technology Commission of Shanghai Municipality (Grant No. 11JC1406000, 13430721600).

References

1. Hannaford, B., Okamura, A.M.: Haptics. Handbook of Robotics, 719–739 (2008)
2. Antfolk, C., D’Alonzo, M., Controzzi, M., Lundborg, G., Rosen, B., Sebelius, F., Cipriani, C.: Artificial Redirection of Sensation From Prosthetic Fingers to the Phantom Hand Map on Transradial Amputees: Vibrotactile Versus Mechanotactile Sensory Feedback. *IEEE Transactions on Neural System and Rehabilitation Engineering* 21, 112–120 (2013)
3. Kaczmarek, K.A.: Electrotactile and vibrotactile displays for sensory substitution systems. *IEEE Transactions on Biomedical Engineering* 38(1), 1–16 (1991)
4. Konyo, M., Tadokoro, S., Yoshida, A.: A tactile synthesis method using multiple frequency vibrations for representing virtual touch. In: *IEEE/RSJ International Conference on Intelligent Robots and Systems (IROS)*, pp. 3965–3971 (2005)
5. Kyung, K.U., Kwon, D.S.: Perceived roughness and correlation with frequency and amplitude of vibrotactile stimuli. In: *Proc. EuroHaptics 2006*, pp. 277–282 (2006)
6. Kim, S.C., Kyung, K.U., Sohn, J.H.: An evaluation of human sensibility on perceived texture under variation of vibrotactile stimuli using a tactile display system. In: *2006 14th Symposium on Haptic Interfaces for Virtual Environment and Teleoperator Systems*, pp. 429–436. *IEEE* (2006)
7. Maeno, T.K., Otokawa, M.: Tactile Display of Surface Texture by use of Amplitude Modulation of Ultrasonic Vibration. In: *IEEE Ultrasonics Symposium* (2006)
8. Hollins, M., Risner, S.R.: Evidence for the duplex theory of tactile texture perception. *Percept. Psychophys.* 62(4), 695–705 (2000)

9. Okamoto, S., Konyo, M., Tadokoro, S.: Vibrotactile Stimuli Applied to Finger Pads as Biases for Perceived Inertial and Viscous Loads. *IEEE Transactions on Haptics* 4(4), 307–315 (2011)
10. Miyuki, M., Griffin, M.J.: Magnitude-dependence of equivalent comfort contours for fore-and-aft, lateral and vertical hand-transmitted vibration. *Journal of Sound and Vibration* 295(3), 633–648 (2006)
11. Ryu, J., et al.: Psychophysical model for vibrotactile rendering in mobile devices. *Presence: Teleoperators and Virtual Environments* 19(4), 364–387 (2010)

Visual Stimulus Background Effects on SSVEP-Based Brain-Computer Interface

Xiaokang Shu, Lin Yao, Jianjun Meng, Xinjun Sheng, and Xiangyang Zhu

State Key Laboratory of Mechanical System and Vibration
Shanghai Jiao Tong University
Shanghai, China, 200240

{shu.x.k89, ylin01iny, mengjianjunxs008}@gmail.com,
{xjsheng, mexyzhu}@sjtu.edu.cn

Abstract. The flickering source is an indispensable component in steady-state visual evoked potentials based brain-computer interface, and its background severely influences the potentials evoked by the repetitive stimuli. In this paper, we designed the experiment paradigm under three different backgrounds in the context of the SSVEP controlled small car, including black screen, static scene of the environment, and dynamic scene of the environment. From the spectrogram analysis of the EEG signals at occipital cortex, we found apparent decrease in SSVEP amplitude in dynamic scene condition comparing to the reference condition black screen. And the SSVEP amplitude changes under these three conditions further resulted in identification accuracy decreasing in dynamic scene condition as compared to black screen reference condition, which was evaluated from 10×10 cross validation. Besides, in real-time control of the small car, our results indicated that training in static scene condition exhibited better performance than that in black screen.

Keywords: SSVEP, LDA, Stimulation Background, Power Spectrum.

1 Introduction

A brain computer interface (BCI) provides a non-muscular channel for communication and control with external world, which facilitates people who suffer from some sort of locked-in syndrome or amyotrophic lateral sclerosis [1]. Up to now, various BCI modalities have been proposed, such as motor imagery based BCI, steady-state visual evoked potentials (SSVEPs) based BCI, P300 evoked potentials based BCI, sensory motor rhythm (SMR) based BCI. These systems can be divided into different categories according to their inputs, feature extraction, outputs, and other characteristics. Among them, the SSVEP-based BCI with much higher information transfer rate, little or no subject training, receives much attention, and has been adopted in applications, such as cursor movement [2], letter or icon selection [3], and device control [4].

Brain controlled wheelchair is especially useful for those people with severely disabled mobility [5]. While brain driven small car control takes a first step towards

the wheelchair control. Various detection algorithm, as well as local machine control strategy could be extensively evaluated before real-life application such as the wheelchair control [6].

As we utilized the SSVEP based BCI as the interface between the subject and the machine, the SSVEP amplitude is largely determined by the characteristics of the flickering sources, including the frequencies of the flickering blocks, duty cycles, colors of the flickering sources [7]. The surrounding environment around the flickering sources receives less attention, although it has an important impact on subject's attention. Attention effects may further influence the flickering light processing of the brain's visual cortex. This is a critical issue, especially in the real-time control of the small car. As we use the real-time video captured from the camera fixed in the car to guide the subject's control, the change of the environment will affect the subject's attention to the flicker blocks in front of the video pictures. Therefore, this study focuses on the background effect of the flickering source on the decoding of SSVEP-based BCI, and characteristic changes of these neurophysiologic signals.

2 System Overview

The schematic of the experiment system is shown in Fig.1. There are three flickering blocks of separate frequencies which are mapped to different control command of the car. Accordingly, the gazed target can be identified by finding the visual stimulus, which contributes to the major frequency component in the induced SSVEP. As we designed, the major frequency component detected from EEG were 12.5hz, 9.37hz and 8.33hz, and they were separately used to control the forward, left and right movements of the small car correspondingly. Then the command will be transmitted from computer to the car through a wireless transmitter. As a feedback, the scene captured by the camera will be delivered to the computer's monitor.

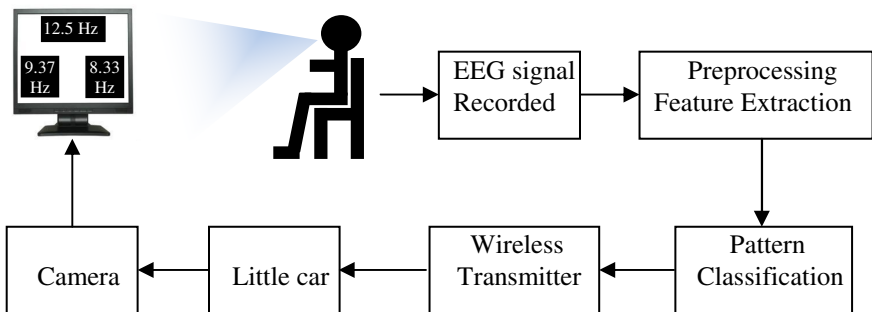


Fig. 1. Schematic diagram of the SSVEP controlled car experiment

3 Methodology

The Neurophysiology and electrophysiology experiments give the result that when the human continuously focuses on instantaneous visual stimuli with constant time interval, steady state visual evoked potential (SSVEP) will occur in primary visual cortex of the brain. And the collected EEG signals will show corresponding stimuli frequency and its harmonic wave components obviously in frequency domain. That is the EEG signal is modulated with the stimulus frequency in aspect to signal modulation theory. Then the signal processing is aimed to obtain the features relating to stimuli frequency from the complex modulated EEG signal.

In terms of the result of the Neurophysiology and electrophysiology experiments, stimuli frequency and its first harmonic wave component should be extracted as the classification features in SSVEP [8]. Fig.2 shows the EEG spectrum of channel CB2 on primary visual cortex when the subject is staring at the flicking light at 9.37Hz. It is clear that the 9.37Hz flicking frequency and its harmonic component are sticking out in frequency domain.

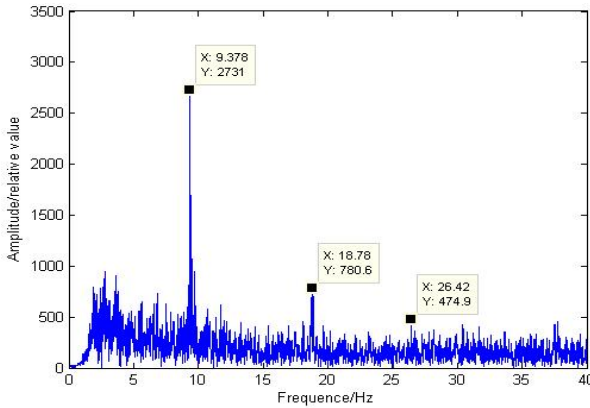


Fig. 2. The EEG spectrum at Channel CB2

3.1 Feature Extraction and Classification

Suppose $S_i(t)$ is the EEG signal from channel i with $i=1\dots N$, and f_j is the j th stimuli frequency with $j=1\dots M$, and $W(t-c)$ is the window function with the center at c . We apply inner product to extract the specified frequency as projecting the signal to sine and cosine space. The continuous form of feature extractions as follows:

$$A_j(c) = \sqrt{\left| \langle S_i(t)W(t-c), \cos(2\pi f_j t) \rangle \right|^2 + \left| \langle S_i(t)W(t-c), \sin(2\pi f_j t) \rangle \right|^2}$$

$$B_j(c) = \sqrt{\left| \langle S_i(t)W(t-c), \cos(2\pi * 2f_j t) \rangle \right|^2 + \left| \langle S_i(t)W(t-c), \sin(2\pi * 2f_j t) \rangle \right|^2}$$

$A_{ij}(c)$ is the j th frequency component from EEG channel i at time point c ;
 $B_{ij}(c)$ is the harmonic wave component of j th frequency from EEG channel i at
time point c .

Combining following experiment setup in section 4, with the sampling interval
 $\Delta T = 1/f_s$, and window sliding length $p = 1000 * \Delta T$, the continuous form could be
converted to the discrete form as follows:

$$A_{ij}(n) = \sqrt{L_1(n) + L_2(n)}$$

$$A_{ij}(n) = \sqrt{H_1(n) + H_2(n)}$$

where

$$L_1(n) = \left| \left\langle S_i(m\Delta T)W(m\Delta T - np), \cos(2\pi f_j m\Delta T) \right\rangle \right|^2$$

$$L_2(n) = \left| \left\langle S_i(m\Delta T)W(m\Delta T - np), \sin(2\pi f_j m\Delta T) \right\rangle \right|^2$$

$$H_1(n) = \left| \left\langle S_i(m\Delta T)W(m\Delta T - np), \cos(2\pi * 2f_j m\Delta T) \right\rangle \right|^2$$

$$H_2(n) = \left| \left\langle S_i(m\Delta T)W(m\Delta T - np), \sin(2\pi * 2f_j m\Delta T) \right\rangle \right|^2$$

So the feature vector for the classification could be expressed as follows:

$$F = (A_{11}, A_{12}, \dots, A_{1M}, B_{11}, B_{12}, \dots, B_{1M}, A_{21}, A_{22}, \dots, A_{2M}, B_{21}, B_{22}, \dots, B_{2M}, \dots, A_{N1}, A_{N2}, \dots, A_{NM}, B_{N1}, B_{N2}, \dots, B_{NM})^T$$

There are three classes to be classified, we apply Linear Discriminant Analysis
(LDA) in pairwise strategy based on the considerations that the features to different
categories are quite discriminable and the training samples are relatively large
enough.

Take i th and j th categories classification problem for example, Suppose F^i and
 F^j be i th and j th training feature sets. The average feature of each sets are as
follows:

$$\mu_i = E(F^i)$$

$$\mu_j = E(F^j)$$

E denotes the Expectation operator. And the within class covariance is defined as

$$S_w^{ij} = E[(F^i - \mu_i)(F^i - \mu_i)^T] + E[(F^j - \mu_j)(F^j - \mu_j)^T]$$

The parameters of the LDA classification could be derived from Fisher method
which tries to find an optimal projection direction that maximizes the difference
between the two classes while minimize the difference within the class.

The discriminant plane could be expressed in the linear formulation as follows:

$$y = w^T x + b$$

Where

$$w = (S_w^{ij})^{-1}(\mu_1 - \mu_2)$$

$$b = -w^T \frac{\mu_1 + \mu_2}{2}$$

4 Experimental Validations

There are five healthy subjects participating in the experiment. Only one of these subjects has been trained for SSVEP experiments before. All of them were informed of the whole experiment process.

4.1 Experiment Setup

Hardware of the experiment is shown in Fig.3. The computer with a LCD screen is used to display the on-line video transferred from the camera fixed in the small car, and meanwhile three flickering blocks mapped to different control orders will be displayed in front of the scene.

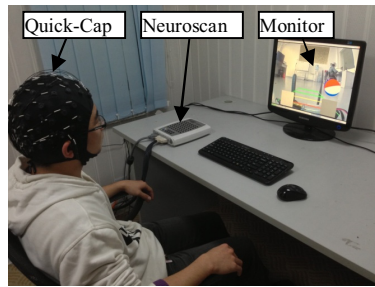


Fig. 3. Hardware of the experiment

EEG signals are recorded from primary visual cortex of the brain with a SynAmps system (Neuroscan, U.S.A). Eight channels useful in our experiment are PO3, POz, PO4, O1, Oz, O2, CB1, CB2. The reference electrode locates between Cz and CPz, and ground electrode locates on forehead. An analog high-pass filter with 2Hz was applied, and sampling frequency is 1000Hz. The flickering frequencies of three blocks representing left, right and forward are 8.33Hz, 9.37Hz and 12.5Hz.

The experimental target is to control the small car mentioned before. The car is simply combined with two motors, two lithium batteries, a Single Chip Mickey, a camera and a wireless transmission. Commands are transmitted to the SCM through a Bluetooth. The camera is used to deliver the scene around the car to the subject. The whole structure is shown in Fig.4.

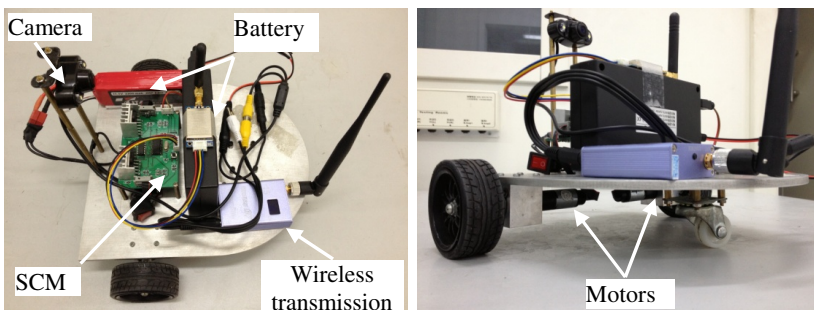


Fig. 4. The structure of the little car

4.2 Experiment Paradigm

This experiment includes two runs: Training run and on-line controlling run. In the former one, the subject will be introduced to gaze at one of the three flickering blocks. A color ball appears randomly besides one of the three flicking blocks, indicating which the subject should gaze at. Each indicating cue lasts for 5 seconds. Three trials make up a session, and each trial will be done under different stimulation background. Those three stimulation background are shown in Fig.5. In the first trial, the background is black screen, the second one is a static picture and the last one is a dynamic video. Three sessions are performed as a training run, and there is a short rest between two sessions. During the experiment process, EEG signals are recorded for the further analysis. Therefore, the main purpose of this study is to compare the training result of different stimulation background.

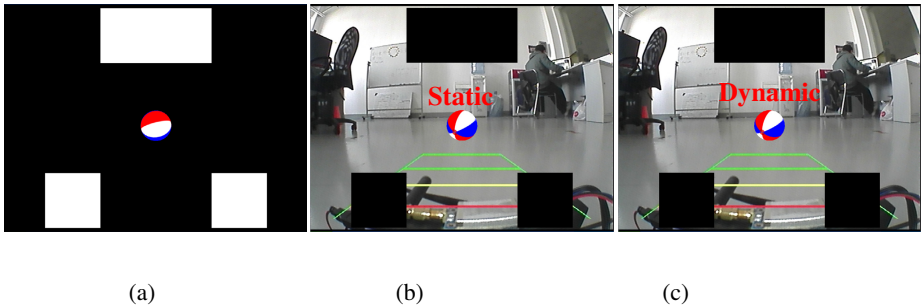


Fig. 5. Three kinds of stimulation background: (a) black screen; (b) static scene; (c) dynamic scene

In the on-line controlling run, subjects will be introduced to control the car to orbit around piles. Locations of the piles are shown in Fig.6. The subject should control the car to travel across the piles, if he or she can make the car to go through the piles one by one, then we can regard the system as effective. Otherwise, we should check the experiment system or give up the subject. In the on-line controlling run no data will be recorded. The whole experiment was carried out as in Fig.7.

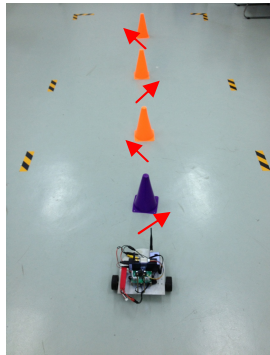


Fig. 6. Locations of the piles in the online-control run. The subject should control the car to travel across the piles and the result will be regarded as a criterion of the system's workability.

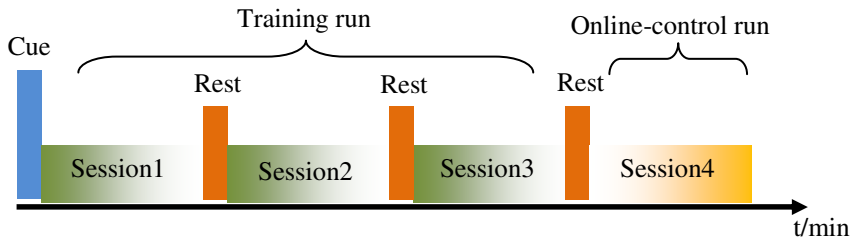


Fig. 7. The experiment paradigm

5 Results and Discussion

5.1 Results of the Experiment

In the online-control run, all of the five subjects are able to control the car freely, so we conclude that the BCI system is working and the subjects are suitable for the SSVEP experiment. In this case, we can use the training data to analyze the impact of different stimulation background. We firstly separate the filtered data into three sections and each section is corresponding to one of the three stimulation frequencies: 12.5Hz, 9.37Hz and 8.33Hz. Then we draw the frequency spectrum of three sections to check out whether the fundamental frequency and its first and second harmonic component are sticking out. We can find in Fig.8 that the signal feature is distinct.

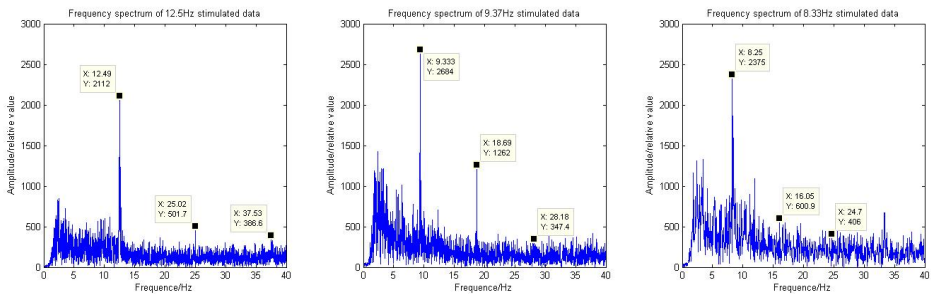


Fig. 8. Frequency spectrum of different stimulation frequency from one specific subject

In the following analysis, the window size for feature extraction and classification was 1s, and the moving step size was 0.1s. Firstly, we combined all the data from three sessions according to the stimulation background, and secondly we carried out a 10-fold cross validation for ten times with each data set. Then we can get the average accuracy for three different kinds of stimulation background. The results are shown in

Table 1. Average accuracy for 10-fold cross validation

Stimulation background	Black screen	Static scene	Dynamic scene
Subject1	97.62	95.44	94.91
Subject2	97.48	98.55	96.15
Subject3	96.49	94.96	91.98
Subject4	98.53	98.22	93.81
Subject5	97.4	91.91	86.4

Table 2. Recognition accuracy of a single trial

Subject index	Stimulation background	session1	session2	session3
Subject1	Black Screen	92.91	89.53	92.91
	Static Scene	95.16	91.22	95.50
Subject2	Black Screen	96.62	92.12	92.00
	Static Scene	98.76	93.36	92.45
Subject3	Black Screen	78.60	74.10	80.18
	Static Scene	83.78	79.73	84.91
Subject4	Black Screen	83.11	79.05	84.68
	Static Scene	81.76	81.19	90.09
Subject5	Black Screen	76.91	79.62	81.42
	Static Scene	73.20	83.33	84.80

It is clear that the stimulation background has large impact on the recognition accuracy. Except for subject2, the other subjects had a distinct drop in their accuracy when the stimulation background was changed to static scene or dynamic scene. And the dynamic scene has an even worse performance.

However, we separately compared the accuracy between black screen and static scene while using the data of dynamic scene as testing set. In detail, the testing data and training data are from an identical session to overcome the influences of time. The result is listed in Table.2. It is interesting that we got higher recognition accuracies when the subject was stimulated under the static background rather than the black screen.

5.2 Discussions

Stimulation background seems to have large impact on the recognition accuracy according to the results above. Firstly, the additional scene background will reduce the differentiation of the EEG signals. As shown in Table.1, if we carry out a 10-fold cross validation on the data from an identical stimulation background, then the accuracy with static scene or dynamic scene will drop. What's more, in the power spectrum figures from five subjects we find that an obvious decrease of the amplitude appeared. The comparable result from subject1 is shown in figure.9. Such being the case, we may attribute the impact of recognition accuracy to the change of the power spectrum induced by visual distractions with different stimulation background.

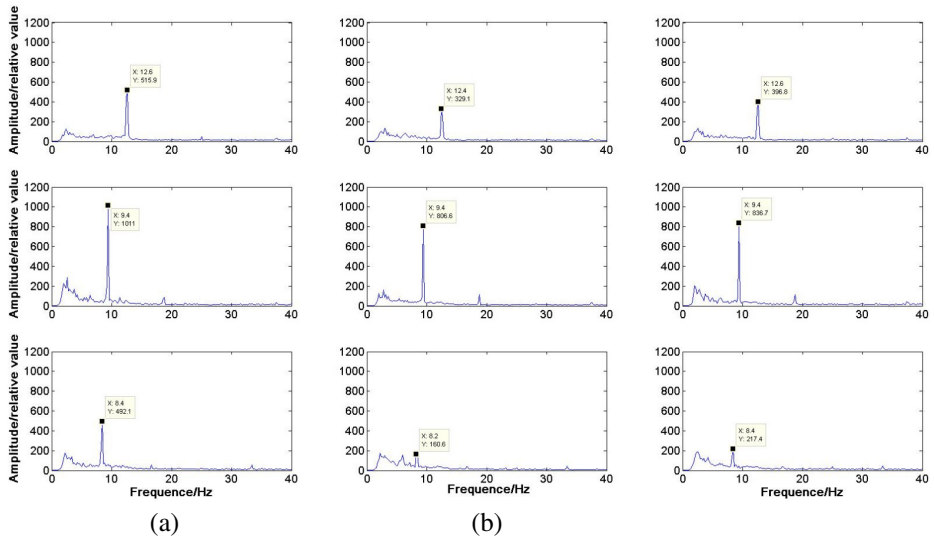


Fig. 9. Comparative result of the power spectrum with subject1: (a) is the power spectrum corresponding to black screen stimulation background; (b) and (c) separately corresponds to static and dynamic scene stimulation background. And each row shows one of the three stimulation frequencies

But when the data sets from different stimulation background were tested with an identical data set from dynamic scene, the static scene seems to have a positive effect on the accuracy. We can see an improvement of the accuracy in most sessions of the five subjects (Table.2). To compare with the results from Table.1, we may have a conclusion that a static scene relative to the experiment surroundings will not only reduce the EEG signal’s power spectrum, but also has an improvement of the recognition accuracy than black screen.

6 Conclusion and Future Work

In this work, we have investigated the background effect of visual stimulus on the characteristics of the SSVEP signals. The experiment showed that dynamic scene takes the most serious distractions for the users, and followed by the static scene. To explore the essential reason of the impact, we drew up the power spectrum figures for every subject. In the power spectrum, we find out an obvious decrease of the amplitude, so we get the conclusion that visual distractions will impact the power spectrum of the SSVEP signals.

In the future, more sophisticated algorithms should be adopted to better trace the changes of the SSVEP signals according to the change in environment factors relating to the flickering visual sources. Our next work will move the current research on controlling the small car to the real-life control of the wheelchair for people with locomotion disabilities.

Acknowledgement. This work is supported by the National Basic Research Program (973 Program) of China (Grant No. 2011CB013305), the National Natural Science Foundation of China (Grant No.51075265), and the Science and Technology Commission of Shanghai Municipality (Grant No. 11JC1406000, 13430721600)

References

1. Wolpaw, J.R., et al.: Brain-computer interfaces for communication and control. *Clinical Neurophysiology* 113(6), 767–791 (2002)
2. Lee, P.-L., et al.: An SSVEP-actuated brain computer interface using phase-tagged flickering sequences: A cursor system. *Annals of Biomedical Engineering* 38(7), 2383–2397 (2010)
3. Cecotti, H.: A self-paced and calibration-less SSVEP-based brain–computer interface speller. *IEEE Transactions on Neural Systems and Rehabilitation Engineering* 18(2), 127–133 (2010)
4. Cheng, M., et al.: Design and implementation of a brain-computer interface with high transfer rates. *IEEE Transactions on Biomedical Engineering* 49(10), 1181–1186 (2002)
5. Rebsamen, B., et al.: Controlling a wheelchair indoors using thought. *IEEE Intelligent Systems* 22(2), 18–24 (2007)
6. Lee, P.-L., et al.: A brain-wave-actuated small robot car using ensemble empirical mode decomposition-based approach. *IEEE Transactions on Systems, Man and Cybernetics, Part A: Systems and Humans* 42(5), 1053–1064 (2012)
7. Zhu, D., et al.: A survey of stimulation methods used in SSVEP-based BCIs. *Computational Intelligence and Neuroscience*, 1 (2010)
8. Wang, Y., et al.: Brain-computer interfaces based on visual evoked potentials. *IEEE Engineering in Medicine and Biology Magazine* 27(5), 64–71 (2008)

Mechanical Implementation of Postural Synergies of an Underactuated Prosthetic Hand

Kai Xu¹, Yuheng Du¹, Huan Liu¹, Xinjun Sheng², and Xiangyang Zhu²

¹ RII Lab (Lab of Robotics Innovation and Intervention), UM-SJTU Joint Institute,

² Robotics Institute, School of Mechanical Engineering

Shanghai Jiao Tong University,

Shanghai, 200240, China

{k.xu, dyh, h.liu, xjsheng, mexyzhu}@sjtu.edu.cn

Abstract. Recent advances in neurology showed that human controls dozens of muscles for hand motions in a coordinated manner. Such coordination is referred as to a postural synergy and synergies could be combined to form various hand poses. Implementing the synergies digitally in the controller, 6 to 12 motors of a robotic prosthetic hand can be controlled by a few synergy inputs from an amputee's bio-signal interfaces. This paper proposes to implement the synergies via a mechanical transmission unit so that two rotation inputs can be scaled, combined and mapped to 13 rotary outputs to enable not only grasping but also manipulation of a prosthetic hand. Synthesis of the postural synergies and design of the prosthetic hand are briefly reviewed, whereas the transmission design is elaborated as the implementation of the postural synergies. Tests were performed to quantify how well the synergies could be reproduced via the transmission. Experiments that follows are expected to demonstrate the effectiveness of constructing a low cost yet versatile prosthetic hand by mechanically implementing the postural synergies.

Keywords: Prosthetic hand, postural synergies, underactuated mechanisms, planetary gears.

1 Introduction

It is a challenging task to construct an anthropomorphic prosthetic hand that can reproduce the delicate motions of the biological original. In order to achieve this goal, the prosthetic hand shall be versatile enough for various daily tasks and controllable through a bio-signal interface, such as EMG (electro-myography) or EEG (electro-encephalography). However limited bandwidth of these interfaces used to prevent fully actuated robotic hands from being applied as prostheses if each DoF (Degree of Freedom) requires individual control, even though many designs were absolutely the state-of-the-art (e.g. the ones in [1-4]).

Recent advances in neurology suggested a possible way of achieving dexterous control of a prosthetic hand via limited inputs. It was showed that CNS (Central Nervous System) controls dozens of muscles for hand poses in a coordinated manner.

Such coordination is referred as to a postural synergy, which corresponds to flexion and/or extension actuation statuses of the involved muscles. CNS combines postural synergies, adjusting each synergy's coefficient (weight), to realize various hand motions. Combination of two primary postural synergies accounts for about 84% of the variance of dozens of different grasping postures [5]. What's more, CNS switches between different sets of postural synergies for distinct grasping and manipulations tasks [6].

These findings have led to the application of a robotic hand with many actuators as prosthesis. Two channels of the bio signals as synergy inputs would act as coefficients while combining two postural synergies. Several existing designs have practiced this idea, such as the DLR II Hand with two synergies [7], the SAH hand with three synergies [8], the UB hand with two synergies [9], and the ACT hand which uses two and three postural synergies to control 24 actuators to perform writing and piano playing [10, 11]. The aforementioned designs are certainly functional but the cost of such a prosthetic hand could also be quite high (multiple sets of miniature servomotors with amplifiers, feedback sensors and controllers). If postural synergies could be mechanically implemented, such a prosthetic hand could potentially be more affordable with a low cost.

Mechanical implementation of postural synergies was attempted by Brown and Asada using differential pulleys [12]. Various postures of the hand were formed. However, grasping performance and effectiveness of the mechanically implemented postural synergies were not studied. This paper proposes a different approach to realize the mechanical implementation of the postural synergies using planetary gears. Positive results of this paper could prove the effectiveness of implementing postural synergies mechanically.

Synthesis of the postural synergies are briefly summarized in Section 2, which was detailed in [13]. Mechanism designs of the prosthetic hands and the transmission as a mechanical implementation of the posture synergies are elaborated in Section 3. Tests and experiments are presented in Section 4 with conclusions and future work followed in Section 5.

2 Postural Synergy Synthesis

Unlike referring to the discrete grasp taxonomy as in [14-16], using the postural synergies introduced a new way to reproduce various hand grasping motions. As shown in a milestone work by Ciocarlie and Allen [17], poses of several different hands were optimized to achieve various grasping tasks. Since two synergy inputs can be optimized for the grasping of distinct objects, they could also be used to perform manipulation of the same object (manipulating one object is essentially a smooth transition between consecutive grasping patterns of the same object). It's possible to upgrade the motion capability of a prosthetic hand from grasping to manipulation using the concept of the postural synergies.

The postural synergies are usually extracted as the first two principal components from a series recorded hand poses. If the synergies are implemented digitally, the controller would map the two synergy inputs q_1 and q_2 to the actuator outputs \mathbf{p}

as shown in Eq. (1), where \mathbf{u}_1 and \mathbf{u}_2 are the postural synergies, and $\bar{\mathbf{p}}$ is an average output. If the prosthetic hand has n actuators, \mathbf{p} , \mathbf{u}_1 , \mathbf{u}_2 and $\bar{\mathbf{p}}$ are all $n \times 1$ vectors.

$$\mathbf{p} = \bar{\mathbf{p}} + q_1 \mathbf{u}_1 + q_2 \mathbf{u}_2 \quad . \quad (1)$$

While performing grasping tasks as in [7-9, 17], the synergy inputs were optimized to properly form poses of the hand. As a matter of fact, these adjustments essentially compensated for the discrepancy between the original postural synergies and their implementations. While planning a manipulation task for a prosthetic hand, the synergy inputs will be mainly used to transform the hand from one pose to another in a continuous manner, limiting their roles in compensating the implemented postural synergies. Hence, the synergy discrepancy should be minimized to satisfactorily reproduce the specific sequenced motions via only two synergy inputs.

In order to minimize the synergy discrepancy, this paper introduces a novel technique of synthesizing the postural synergies by constructing a dummy hand. Instead of inviting 5 to 10 human subjects, asking them to manipulate one or more objects, recording and analyzing the human hand motions using sophisticated systems such as CyberGlove™ or the Vicon™ cameras, this dummy hand was constructed and manually posed for manipulation tasks with each pose measured. Constructing a dummy hand and measuring its poses could produce direct results for the synergy synthesis in a very cost-efficient way. More importantly it avoided unnecessary errors while designing prosthetic mechanisms with lower kinematic pairs (e.g. revolute joints) based on measurements of human hands whose joints are essentially higher kinematic pairs (e.g. the carpometacarpal joint, the metacarpophalangeal joints).

The dummy hand was constructed as in Fig. 1-(a). All the joints were passive with enough friction against external disturbance (e.g. gravity). The arrangement of its revolute joints provided motion capabilities similar to a human hand. The joints are named as follows. Letters *T*, *M*, *R*, *L* and *I* before the underscore indicate the joints for the thumb, the middle finger, the ring finger and the little finger respectively. Abbreviations of *rot*, *mcp*, *ip*, *abd*, *pip* and *dip* after the underscore indicate the rotation joint, the metacarpophalangeal joint, the interphalangeal joint, the abduction joint, the proximal and the distal interphalangeal joint respectively.

The specific motion paradigm is the manipulation of two rehabilitation training balls on the palm in a cyclic way, as shown in Fig. 1. This exercise helps the seniors or mild-stroke patients to maintain or recover their hand motor function. Although this paradigm might not seem practically meaningful to amputees, the motivation is to demonstrate the effectiveness of this presented synergy synthesis.

In each pose, joint angles were measured using an optical tracker (MicronTracker SX60 from Claron Technology Inc) as shown in Fig. 1-(b). The two intersecting surfaces of the two adjacent phalanxes were first characterized by obtaining coordinates of three points on the surfaces. The joint angle was then obtained from the dot product of the two surface normals. Six key poses as in Fig. 1-(c) to Fig. 1-(h) are identified and recorded. With detailed processes and numerical values available in [13], results of the postural synergies are briefly summarized.

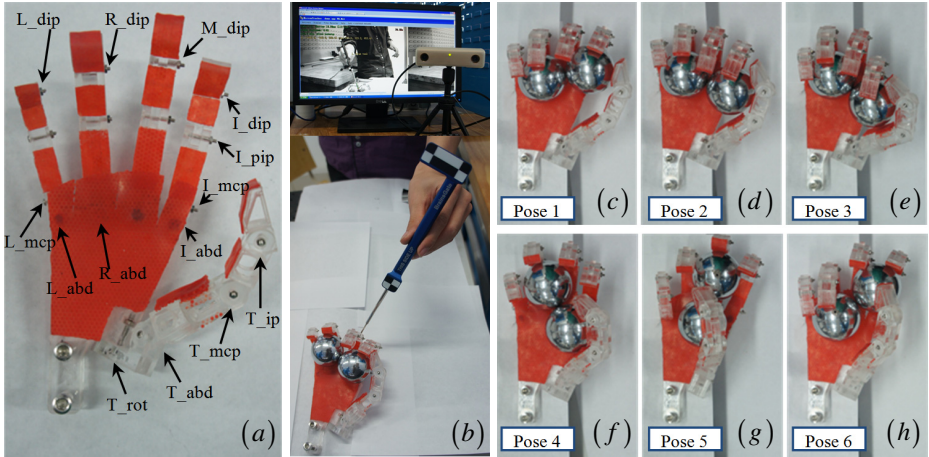


Fig. 1. The dummy and its poses: (a) construction, (b) measurement process of the joint angles using an optical tracker, (c) to (h) six key poses for manipulating two training balls

Each pose in Fig. 1-(c)~(h) corresponds to a pose vector $\mathbf{p}_i \in \mathfrak{R}_{19 \times 1}$, $i = 1, 2, \dots, 6$. Since motions of the four distal interphalangeal joints (I_dip, M_dip, R_dip and L_dip) were coupled to the motions of the four proximal interphalangeal joints (I_pip, M_pip, R_pip and L_pip), dimension of the pose vector can be reduced, $\mathbf{p}_i \in \mathfrak{R}_{15 \times 1}$.

Six poses in Fig. 1-(c)~(h) can be put side to side to form a pose matrix \mathbf{P} . Singular value decomposition of the pose matrix \mathbf{P} is as in Eq. (2).

$$\begin{aligned}
 \mathbf{P}_{15 \times 6} &= [\mathbf{p}_1 \quad \mathbf{p}_2 \quad \dots \quad \mathbf{p}_6] = \bar{\mathbf{P}} + \mathbf{U}_{15 \times 15} \boldsymbol{\Sigma}_{15 \times 6} \mathbf{V}_{6 \times 6}^T \\
 &= \bar{\mathbf{P}} + [\mathbf{u}_1 \quad \mathbf{u}_2 \quad \dots \quad \mathbf{u}_{15}] \cdot \begin{bmatrix} \text{diag}(\delta_1, \delta_2, \dots, \delta_6) \\ \mathbf{0}_{9 \times 6} \end{bmatrix} \begin{bmatrix} \mathbf{v}_1^T \\ \mathbf{v}_2^T \\ \vdots \\ \mathbf{v}_6^T \end{bmatrix}. \tag{2}
 \end{aligned}$$

Where $\bar{\mathbf{P}} = [\bar{\mathbf{p}} \quad \bar{\mathbf{p}} \quad \bar{\mathbf{p}} \quad \bar{\mathbf{p}} \quad \bar{\mathbf{p}} \quad \bar{\mathbf{p}}]$ is the average pose and $\bar{\mathbf{p}} = \frac{1}{6} \sum_{i=1}^6 \mathbf{p}_i$.

By neglecting the singular values δ_i ($i = 3, 4, 5, 6$), hand poses (the pose matrix $\tilde{\mathbf{P}}$ and the individual pose vector $\tilde{\mathbf{p}}_i$) can be reproduced as in Eq. (3) and Eq. (4). Vectors \mathbf{u}_1 and \mathbf{u}_2 are referred to as the postural synergies. With q_{1i} and q_{2i} as synergy inputs, various hand poses could be approximated. The average pose vector

$\bar{\mathbf{p}}$, the postural synergies \mathbf{u}_1 and \mathbf{u}_2 , and inputs q_{ki} ($k=1,2$ and $i=1,2,\dots,6$) are summarized in Table 1.

$$\tilde{\mathbf{P}} = \bar{\mathbf{P}} + [\mathbf{u}_1 \quad \mathbf{u}_2] \begin{bmatrix} \delta_1 \mathbf{v}_1^T \\ \delta_2 \mathbf{v}_2^T \end{bmatrix} = \bar{\mathbf{P}} + [\mathbf{u}_1 \quad \mathbf{u}_2] \begin{bmatrix} q_{11} & q_{12} & \cdots & q_{16} \\ q_{21} & q_{22} & \cdots & q_{26} \end{bmatrix}. \quad (3)$$

$$\tilde{\mathbf{p}}_i = \bar{\mathbf{p}} + q_{1i} \mathbf{u}_1 + q_{2i} \mathbf{u}_2, \quad i = 1, 2, \dots, 6. \quad (4)$$

Table 1. The average pose, the postural synergies and the synergy inputs

Joints	Average pose (°)	Postural synergies		Synergy inputs (°)
		\mathbf{u}_1	\mathbf{u}_2	
T_rot	59.7	-0.49	0.24	$q_{11} = 36.2^\circ$
T_mcp	38.7	-0.16	-0.21	$q_{21} = 21.0^\circ$
T_ip	44.0	-0.15	-0.23	$q_{12} = 28.1^\circ$
T_abd	43.0	-0.2	-0.17	$q_{22} = -1.1^\circ$
L_mcp	44.8	0.34	-0.66	$q_{13} = 37.6^\circ$
M_mcp	28.2	0.56	0.12	$q_{23} = -31.5^\circ$
R_mcp	35.8	0.44	0.5	$q_{14} = -38.5^\circ$
L_mcp	58.3	0.15	-0.25	$q_{24} = -25.1^\circ$
L_pip	54.8	0.01	0.06	$q_{15} = -52.4^\circ$
M_pip	72.0	-0.01	-0.11	$q_{25} = 2.6^\circ$
R_pip	72.5	-0.02	0.08	$q_{16} = -11.0^\circ$
L_pip	70	-0.13	0.14	$q_{26} = 34.1^\circ$
I_abd	8.7	0.03	0.08	
R_abd	9.7	-0.05	-0.02	
L_abd	15.5	-0.02	0.07	

3 Design Descriptions of the Prosthetic Hand

3.1 Design Overview

This paper proposes to implement postural synergies mechanically. According to Eq. (4), a pair of synergy control inputs q_{1i} and q_{2i} shall be combined and scaled, then mapped to the outputs through a transmission to drive the prosthetic hand from its average pose $\bar{\mathbf{p}}$. This transmission is referred as to the mechanical implementation of the postural synergies.

This mechanical implementation of synergies could be installed in forearm since it is unlikely such a complicated transmission could be fully embedded in palm. All the outputs from the transmission will be connected to the prosthetic hand to drive the finger joints using flexible shafts, as shown in Fig. 2. Decisions on i) how to realize the mechanical implementation of synergies, ii) how to actuate finger joints, and iii) how to connect the transmission outputs to the finger joint axes, should be made consistently and compatibly.

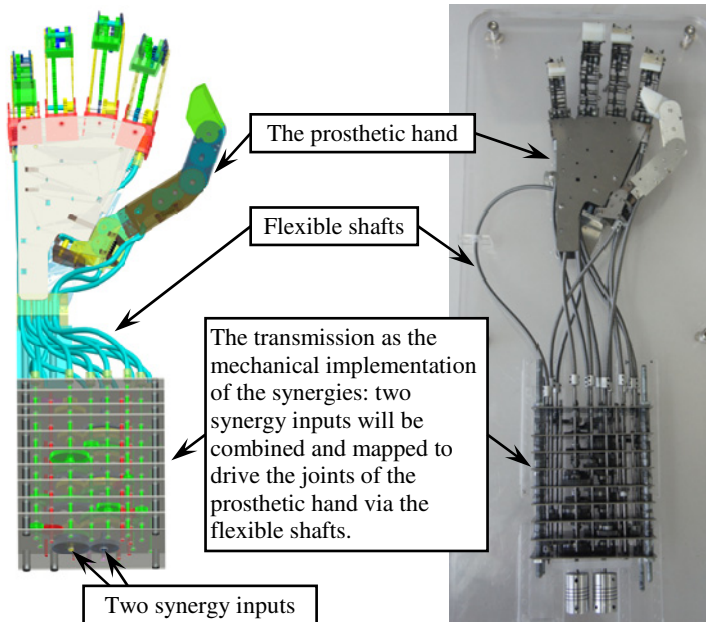


Fig. 2. Design overview of the prosthetic hand and the mechanical synergy implementation

Since inputs q_{1i} and q_{2i} ($i = 1, 2, \dots, 6$) shall be combined and scaled, there are only a few options to realize this function mechanically. Possible options include designing a differential hydraulic system, using differential pulleys (as in [12]), using planetary gears, etc. This paper chose to use planetary gears because this option might provide better accuracy than that of using differential pulleys and might be easier to fabricate than that of designing a differential hydraulic system. Then the synergy outputs will be rotations (instead of being translations as in the other two options). The most direct way to connect these synergy outputs to the finger joint axes is to use flexible shafts. What's more, rotations of these flexible shafts would not be affected by a future presence of possible wrist motions. Using worm gears and gears, rotations of these flexible shafts will drive all the finger joints.

Section 3.2 summaries the transmission and actuation designs of the prosthetic hand which were detailed in [13], whereas Section 3.3 elaborates the design of the

mechanical implementation of synergies. The prosthetic hand and the mechanical synergy implementation were then fabricated, assembled and connected. Two actuators are expected to drive all the joints of the prosthetic hand to realize the desired motion sequence.

3.2 Design of the Prosthetic Hand

As shown in Fig. 3, several flexible shafts were connected to the worms to the drive worm gears. Then the worm gears were attached to a train of spur gears to actuate the hand joints. The train of spur gears was used to allow proper positioning of the worms and worm gears so that they could be fully housed inside the thumb. All the worm gears used had a gear ratio of 20:1.

As shown in Fig. 3-(a), a dual arrangement of worm gears introduced coupling between the T_{mcp} and the T_{ip} joints. Once the worm gear for the T_{mcp} joint was actuated, in order to keep the thumb distal phalanx stationary with respect to the thumb proximal phalanx, the worm gear for the T_{ip} joint should be actuated accordingly. This coupling should be accommodated while designing the transmission.

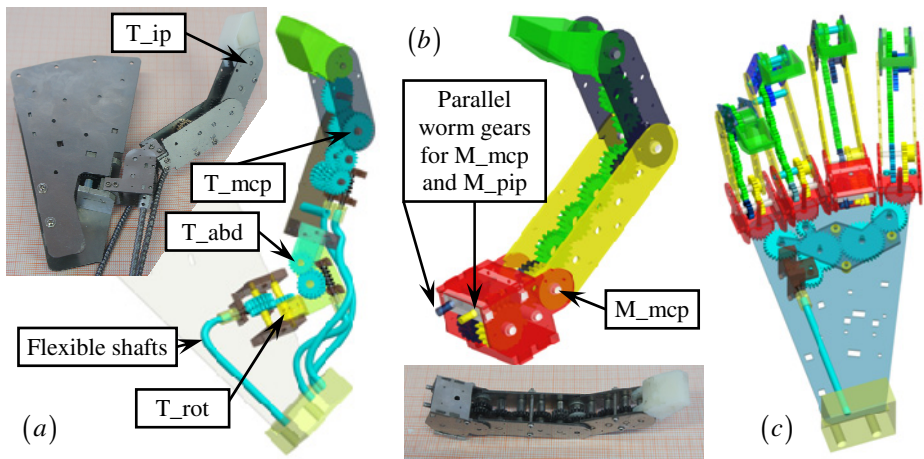


Fig. 3. Design of the prosthetic hand: (a) structure of the thumb, (b) structure of the middle finger, and (c) the structure for the abduction of the fingers

Similar to the actuation of the thumb joints, flexible shafts were connected to the worms and the spur gears to drive the metacarpophalangeal and interphalangeal joints. Since actuation of the index, the middle, the ring and the little fingers are essentially similar, Fig. 3-(b) only shows the structure of the middle finger. Coupling between the distal interphalangeal joint and the proximal interphalangeal joint was realized using trains of spur gears inside the fingers. Axes of these gears were offset to accommodate their specific pitch radiuses.

According to Eq. (4) and Table 1, abduction motions of the index, the ring and the little fingers were also subjected to inputs q_{1i} and q_{2i} . However, their synergies values (abd rows for \mathbf{u}_i) are substantially smaller than those of other joints. In order to reduce the complicity of the transmission, abduction motions of the three fingers were made coupled. Gear profiles were fabricated on components of the finger subassemblies so that one set of worm & worm gear will drive abduction motions of the index, the ring and the little fingers through a train of spur gears.

3.3 Implementation of the Postural Synergies via a Mechanical Transmission

This paper proposes to implement the postural synergies mechanically. In other words, two synergy inputs will be scaled, combined and mapped to the synergy outputs through a mechanical transmission unit. Due to the coupling between the four distal interphalangeal joints and the respective proximal interphalangeal joints, 19 joints of the prosthetic hand originally required 15 synergy outputs from the transmission. The abduction motions of the index, the ring and the little fingers were made coupled and hence these three joints only required one synergy output. In total, 13 synergy outputs would be needed to drive the prosthetic hand. All the synergy outputs will be connected to the corresponding worms using flexible shafts.

A schematic of the planetary-gear-based transmission for the implementation of the postural synergies is shown in Fig. 4. Two inputs q_1 and q_2 were shared by multiple sets of planetary gears. q_2 was connected to all the sun gears, while q_1 was connected to all the ring gears (annuluses). Idlers were added to make up for the distance between the two input axes. Rotations of the planet carriers were used as outputs which were connected to joint worms through the flexible shafts.

An overall transmission can be derived as in Eq. (5), where q_o is a synergy output, z_i and z_{ki} are the numbers of the indicated gear teeth. The gear teeth can be adjusted so that Eq. (5) is consistent with the numerical values from Table 1.

$$q_o = -\frac{z_5 z_3}{z_6 z_4} \frac{z_1 (z_{k1} + 2z_{k2}) q_1 + z_{k2} q_2}{2(z_{k1} + z_{k2})} . \quad (5)$$

4 Preliminary Experiments and Tests

All the components of the prosthetic hand were fabricated and assembled. Four rotations are needed for the T_rot, the T_abd, the T_mcp and the T_ip joints of the thumb. Two rotations are needed for the metacarpophalangeal joint and the proximal interphalangeal joint of the four fingers (their distal interphalangeal joints are actuated by the proximal interphalangeal joints though couple gear trains). One more rotation

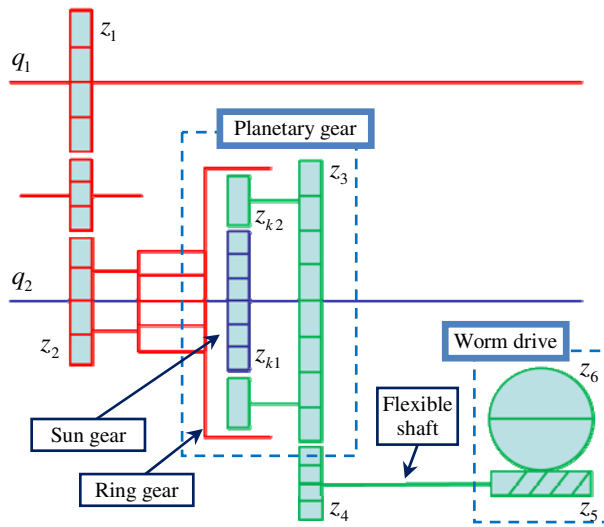


Fig. 4. A schematic of the transmission as a mechanical synergy implementation

is needed for the abductions of the fingers. In total, 13 rotational outputs are needed from the transmission to drive the 19 joints in the prosthetic hand (abduction of the middle finger is fixed).

4.1 Motion Capabilities of the Hand

The prosthetic hand was manually posed by rotating its flexible shafts, to verify motion ranges of the joints as in Fig. 5. It can be seen that the prosthetic hand can be successfully posed for the six key postures which are needed for manipulating the two rehabilitation training balls.

The experiments performed here only tried to show motion ranges of the prosthetic hand design to qualitatively verify its capability for this intended task. Since the manual actuation of the flexible shafts doesn't correspond to the coupled outputs from the transmission, these poses are naturally different from the ones shown in Fig. 1.

4.2 Transmission Error Quantification

The transmission as the mechanical implementation of the postural synergies was designed, fabricated and assembled as a set of planetary gears, as shown in Fig. 6.

Two Maxon DC servomotors were controlled by a Matlab xPC Target to drive the two synergy inputs. Motion control cards included the D/A card PCL-727 from the AdvanTech Inc and the counter card CNT32-8M from the Contec Inc. The synergy outputs were examined one by one using an encoder. Readings from the encoder for one synergy output was plotted with respect to the two synergy inputs, as in Fig. 7.

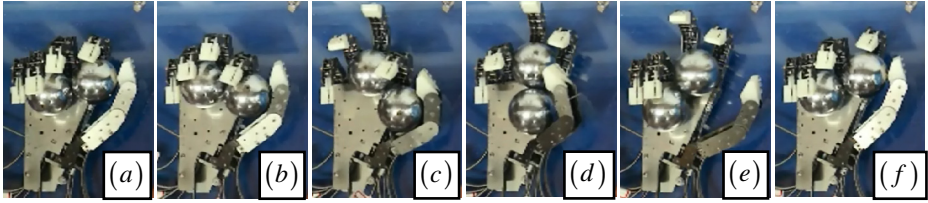


Fig. 5. The assembled prosthetic hand was manually posed by rotating the flexible shafts to qualitatively verify its motion capability for the intended task of manipulating two training balls

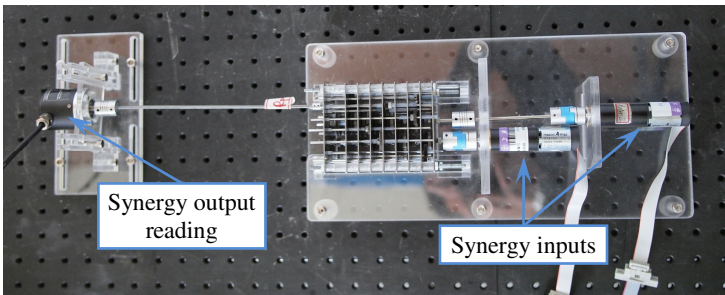


Fig. 6. An experimental setup for quantifying transmission errors of the planetary gears

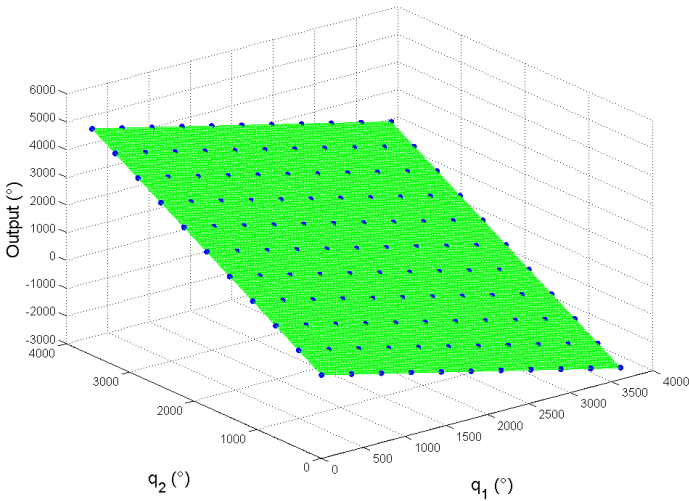


Fig. 7. The synergy output with respect to the two synergy inputs

According to the Eq. (4), a synergy output can be visualized as a plane while plotted with respect to the two synergy inputs, which could be seen in Fig. 7. The blue dots represent the measured rotary outputs. The distances between the dots and the plane are transmission errors. According to the experiments, all the errors have been kept under 0.25%. These errors come from the backlash of the gear system.

5 Conclusions and Future Work

This paper presents the latest results of a prosthetic hand project regarding the mechanical implementation of the postural synergies, summarizing the structural design and the postural synergy synthesis from previously published results. This project attempts to upgrade motion capability of a prosthetic hand from object grasping to more delicate motions (such as manipulation of objects) using the concept of the postural synergies. A specific manipulation paradigm is the manipulation of two rehabilitation training balls in a cyclic manner using two synergy inputs.

The postural synergies synthesized from several key poses of a dummy hand were implemented mechanically via a transmission unit. The transmission unit combines, scales and maps two synergy inputs to 13 synergy outputs and the outputs are routed to the prosthetic hand via flexible shafts to drive the prosthetic hand. The transmission unit was tested through a series of experiments and the transmission errors were quantified.

Future work includes several aspects. The first aspect is to further improve the kinematic performance of the prosthetic hand. Currently the hand joints have quite some backlash which should be eliminated by preloading the joints using a spring. Secondly inter-pose planning of the synergy inputs will be investigated, trying to realize the proposed manipulation task in a continuous manner. Thirdly, motion capabilities of additional grasping and manipulating tasks will be explored using the same transmission and the prosthetic hand.

Acknowledgments. This work was supported by the Chinese National Program on Key Basic Research Projects (the 973 Program) #2011CB013300.

References

1. Bicchi, A.: Hands for Dexterous Manipulation and Robust Grasping: a Difficult Road toward Simplicity. *IEEE Transactions on Robotics and Automation* 16(6), 652–662 (2000)
2. Gazeau, J.P., Zegloul, S., Arsicault, M., Lallemand, J.P.: The LMS Hand: Force and Position Controls in the Aim of the Fine Manipulation of Objects. In: *IEEE International Conference on Robotics and Automation (ICRA)*, Seoul, Korea (2001)
3. Liu, H., Meusel, P., Seitz, N., Willberg, B., Hirzinger, G., Jin, M.H., Liu, Y.W., Wei, R., Xie, Z.W.: The Modular Multisensory DLR-HIT-Hand. *Mechanism and Machine Theory* 42(5), 612–625 (2007)
4. Grebenstein, M., Chalon, M., Friedl, W., Haddadin, S., Wimböck, T., Hirzinger, G., Siegwart, R.: The Hand of the DLR Hand Arm System: Designed for Interaction. *International Journal of Robotics Research* 31(13), 1531–1555 (2012)

5. Santello, M., Flanders, M., Soechting, J.F.: Postural Hand Synergies for Tool Use. *The Journal of Neuroscience* 18(23), 10105–10115 (1998)
6. Weiss, E.J., Flanders, M.: Muscular and Postural Synergies of the Human Hand. *Journal of Neurophysiology* 92(1), 523–535 (2004)
7. Wimböck, T., Jahn, B., Hirzinger, G.: Synergy Level Impedance Control for Multifingered Hands. In: *IEEE/RSJ International Conference on Intelligent Robots and Systems (IROS)*, San Francisco, CA, USA, pp. 973–979 (2011)
8. Rosell, J., Suárez, R., Rosales, C., Pérez, A.: Autonomous Motion Planning of a Hand-Arm Robotic System Based on Captured Human-like Hand Postures. *Autonomous Robots* 31(1), 87–102 (2011)
9. Ficuciello, F., Palli, G., Melchiorri, C., Siciliano, B.: Experimental evaluation of Postural Synergies during Reach to Grasp with the UB Hand IV. In: *IEEE/RSJ International Conference on Intelligent Robots and Systems (IROS)*, San Francisco, CA, USA, pp. 1775–1780 (2011)
10. Rombokas, E., Malhotra, M., Matsuoka, Y.: Task-specific Demonstration and Practiced Synergies for Writing with the ACT Hand. In: *IEEE International Conference on Robotics and Automation (ICRA)*, Shanghai, China, pp. 5363–5368 (2011)
11. Zhang, A., Malhotra, M., Matsuoka, Y.: Musical Piano Performance by the ACT Hand. In: *IEEE International Conference on Robotics and Automation (ICRA)*, Shanghai, China, pp. 3536–3541 (2011)
12. Brown, C.Y., Asada, H.H.: Inter-Finger Coordination and Postural Synergies in Robot Hands via Mechanical Implementation of Principal Components Analysis. In: *IEEE/RSJ International Conference on Intelligent Robots and Systems (IROS)*, San Diego, CA, USA, pp. 2877–2882 (2007)
13. Xu, K., Zhao, J., Du, Y., Zhu, X.: Design and Postural Synergy Synthesis of a Prosthetic Hand for a Manipulation Task. In: *IEEE/ASME International Conference on Advanced Intelligent Mechatronics (AIM)*, Wollongong, Australia (2013)
14. Cutkosky, M.R.: On Grasp Choice, Grasp Models, and the Design of Hands for Manufacturing Tasks. *IEEE Transactions on Robotics and Automation* 5(3), 269–279 (1989)
15. Feix, T., Pawlik, R., Schmiedmayer, H.-B., Romero, J., Kragić, D.: A Comprehensive Grasp Taxonomy. In: *Robotics, Science and Systems Conference (RSS)*, Seattle, Washington, USA (2009)
16. Zheng, J.Z., De La Rosa, S., Dollar, A.M.: An Investigation of Grasp Type and Frequency in Daily Household and Machine Shop Tasks. In: *IEEE International Conference on Robotics and Automation (ICRA)*, Shanghai, China, pp. 4169–4175 (2011)
17. Ciocarlie, M.T., Allen, P.K.: Hand Posture Subspaces for Dexterous Robotic Grasping. *The International Journal of Robotics Research* 28(7), 851–867 (2009)

A Micro-wires Based Tactile Sensor for Prosthesis

Guanhao Liang, Deqing Mei^{*}, Yancheng Wang,
Yu Dai, and Zichen Chen

The State Key Laboratory of Fluid Power Transmission and Control,
Department of Mechanical Engineering,
Zhejiang University, Hangzhou, Zhejiang, 310027, China
medqmei@zju.edu.cn

Abstract. Tactile sensor is indispensable in prosthesis for object manipulation. This study presented a novel tactile sensor based on the conductive micro-wires that can measure the normal and shear forces. The developed sensor consists of four layers, from bottom to top are the substrate supporting, polyimide based matrix circuit, micro-wire based sensing, and top surface bump layers, respectively. To improve the sensing performance, structural dimensions were optimized. According to the optimization results, analytical models and finite element analysis (FEA) were conducted to study the normal and shear force sensing performance of the sensor. To develop the tactile sensor, the carbon-black based conductive polymer was firstly fabricated, and then the conductive micro-wires were manufactured by using the method of micro-contact printing (μ CP). The results demonstrate that the machined micro-wires have dimensions of 250 μ m in width and 50 μ m in height.

Keywords: tactile sensor, normal force, shear force, micro-wires, prosthesis.

1 Introduction

The tremendous development of the prosthesis has proposed great demands for high-sensitivity flexible tactile sensors. Tactile sensor that capable of normal and shear force measuring is indispensable in prosthesis for object manipulation. To manipulate object, gentle touch is a very important function to determine whether the prosthesis get in touch with some object or not. With a high-sensitive tactile sensor, the prosthesis can perceive the environment as the skin of human being, which will largely improve the performance of gentle touch and tactile sensitivity.

So far, several kinds of tactile sensors have been developed with the sensing principles of piezoresistive [1-3], capacitive [4-5], piezoelectric [6-7], optical [8], etc. Organic field-effect transistors (OFETs), due to its flexibility and high sensitivity, have been preferred by researchers to develop flexible tactile sensor [9-11], especially with nano-wires field-effect transistors (NW FETs) [12] to amplify the sensing signals. In addition, there exist tactile sensor that compose of two sensing layers, which are capacitive layer to detect gentle touch and piezoresistive layer to detect

^{*} Corresponding author.

common static force [13]. These studies have proposed many useful ways to increase the sensitivity of tactile sensor, but there still exists some problems to be solved, such as the flexibility. And the sensitivity of tactile sensor needs to be improved more to achieve better performance of the prosthesis.

Taking advantage of high sensitivity of the conductive micro-wires, this paper presented a micro-wire based tactile sensor to measure the normal and shear force. Structural optimization was conducted to improve the sensing performance. Then, analytical models and FEA were conducted to study the normal and shear forces measuring behavior. This was followed by the manufacture of the carbon-black based polymers. The conducted micro-wires were fabricated by the method of μ CP [13-15]. Finally, the results and conclusions were conducted, respectively.

2 Design of the Tactile Sensor

As shown in Fig. 1, the designed tactile sensor mainly consists of four layers: substrate supporting layer, polyimide based matrix circuits layer, conductive micro-wires sensing layer, and top surface bump layer. One sensing element consists of four arrayed micro-wires with the substrate made of PDMS at 10:1 of monomer to curing agent, and laminated by a thin polyimide film, on which the matrix circuits are deposited by magnetron sputtering. The conductive micro-wires generated on the matrix circuits can measure the normal and shear forces. The total view of the tactile sensor is shown in Fig. 2, and the force applied on the surface of the bump can be decomposed into F_x , F_y , and F_z in x , y , z axis respectively.

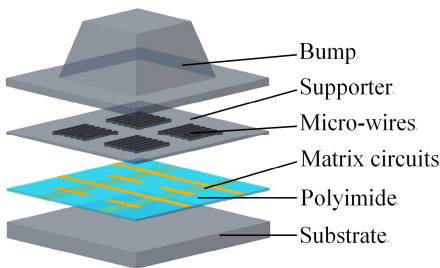


Fig. 1. Sensing layers of tactile sensor

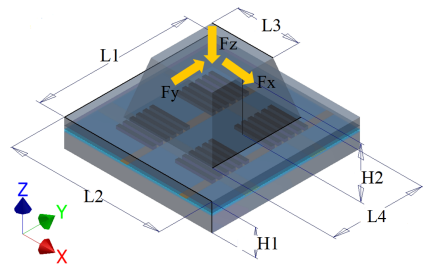


Fig. 2. Total view of the tactile sensor

The original state of the tactile sensor is shown in Fig. 3(a). When applying the normal force on the top surface bump, four micro-wires arrays will be compressed uniformly as shown in Fig. 3(b), which induces the decreasing of the resistivity of the micro-wires, thus can measure the normal force. When applying the shear force, two micro-wires arrays on the left side are stretched and the other two arrays on the right side are compressed, which lead to the increasing and decreasing of the resistivity of the micro-wires, respectively, as shown in Fig. 3(c).

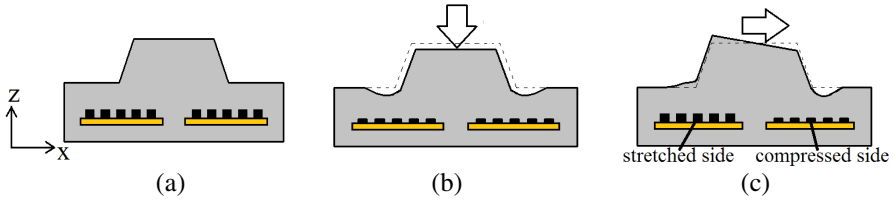


Fig. 3. Force sensing principle of the tactile sensor: (a) original state, (b) normal, and (c) shear force

3 Optimization and Modeling of the Tactile Sensor

To improve the sensing performance, structural dimensions of the tactile sensor need to be optimized. And according to the optimal dimensions, analytical models and finite element analysis (FEA) need to be conducted to establish relationship between the external force that applied on the tactile sensor and the forces that acting on the micro-wires.

3.1 Optimization of the Bump of the Tactile Sensor

The external forces are directly applied on the top surface bump, thus the dimensions of the surface bump are critical to the sensing performance of the tactile sensor. As shown in Fig. 2, one element of the tactile sensor is designed with dimension of 2 mm \times 2 mm and with height of 0.36 mm. The bump is designed with height of 0.7 mm, the top square surface with dimensions of 0.82 mm \times 0.82 mm. Totally, we can get dimensions $L1 = L2 = 2$ mm, $L3 = 0.82$ mm, $H1 = 0.36$ mm, $H2 = 0.7$ mm. The dimensions of the bottom surface bump $L4$ (as shown in Fig. 2) need to be optimized to increase the sensing performance of the sensor.

To optimize the surface bump geometry, FEA was conducted to find out an optimal $L4$ as shown in Fig. 2 using ANSYS software. With the optimal bump geometry, the micro-wires will be deformed largest when applying the same force, which means that the micro-wires are more sensitive to the force. The material properties values used in FEA model had been obtained by stretching and compression tests, as shown in Table. 1.

Fig. 4(a) and (b) show the average deformation in z direction of the micro-wires varies with the $L4$ of the bump when applying 0.5 N normal force in z direction and 0.5 N shear force in x direction, respectively. The deformation of the micro-wires increases as the $L4$ of the bump increase and reaches a peak value and then decrease. For the normal force, the peak value occurs at 1.3 mm (Fig. 4(a)), while for the shear force, the maximum deformation of the micro-wires I, III, and II, IV (Fig. 5(b)) occurs at $L4 = 1.2$ mm (Fig. 4(b)). When $L4$ of the bump is at small value, the

deformation of the micro-wires is mainly concentrated on the central area. As $L4$ increase, the surface bump becomes larger, making the micro-wires receive less force and lead to a smaller average deformation. Thus, the peak value of the average deformation occurs at the optimal $L4$ of the bump. From Figs. 4(a) and (b), the optimal $L4$ of the bump equals 1.2 mm or 1.3 mm. In the following sections, $L4$ that equals 1.2 mm will be adopted.

Table 1. Material properties used for FEA

Material	Young's modulus(Mpa)	Poisson's ratio
PDMS(7.5:1)	2.90	0.49
PDMS(10:1)	1.97	0.49
PDMS(20:1)	0.55	0.49
Polyimide	3500	0.34
Conductive micro-wires	2.90	0.49

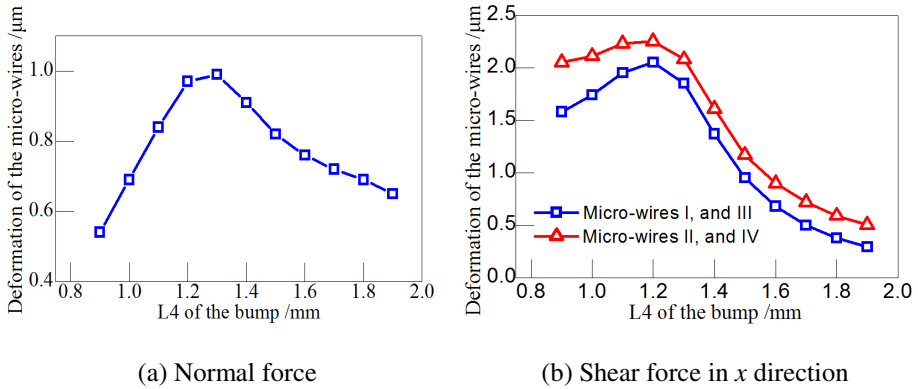


Fig. 4. Dimension effects of the bump on the micro-wires deformation

3.2 Analytical Modeling of the Tactile Sensor

To measure the changes of the resistance of the micro-wires when the external force applied, analytical models need to be developed. Assuming the force is applied on the top surface of the bump, the force can be decomposed into three components: F_x , F_y , and F_z in x , y , and z directions, respectively, as shown in Fig. 5(a). F_1 , F_2 , F_3 , and F_4 are the forces acting on each of the micro-wires I, II, III, IV. Figs. 5(b) – (d) show the force component acting on each of the micro-wires when applying F_x , F_y , and F_z separately. F_{xj} , F_{yj} , and F_{zj} ($j=1, 2, 3, 4$) are the forces acting on the micro-wires when applying F_x , F_y , and F_z respectively.

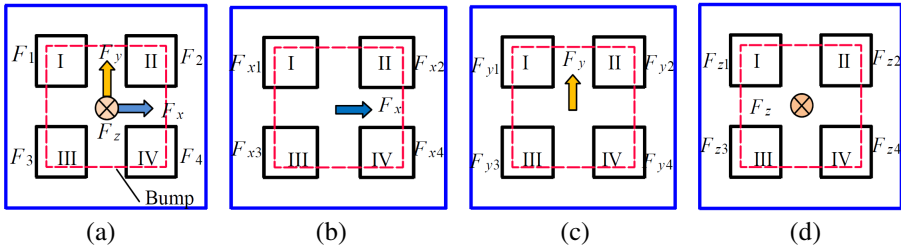


Fig. 5. Force distribution of the micro-wires when applying (a) 3D force, (b) F_x in x axis, (c) F_y in y axis and (d) F_z in z axis

As applying F_x , micro-wires I and III feature the same deformation, and micro-wires II and IV feature the same deformation as shown in Fig. 5(b). As applying F_y , micro-wires I and II feature the same deformation, and micro-wires III and IV feature the same deformation as shown in Fig. 5(c). And when applying F_z , micro-wires I, II, III, and IV feature the same deformation. Consider that the deformations of the tactile sensor are small, the tactile sensor can be considered as deforming linearly, so it can be inferred that there exists a linear relation between the force applied on the bump and the force acting on the micro-wires. So the following equations can be assumed:

$$\begin{cases} F_{x1} = F_{x3} = k_l F_x \\ F_{y1} = F_{y2} = k_u F_y \\ F_{x2} = F_{x4} = k_r F_x \\ F_{y3} = F_{y4} = k_d F_y \\ F_{z1} = F_{z2} = F_{z3} = F_{z4} = k_a F_z \end{cases} \quad (1)$$

where k_l , k_u , k_r , k_d , k_a are coefficients that are assumed and to be calculated though FEA.

According to the force superposition, Eq. 2 can be obtained:

$$F_{xj} + F_{yj} + F_{zj} = F_j \quad (2)$$

where $j = 1, 2, 3, 4$.

The relationship of the forces that acting on the micro-wires and their deformations can be expressed as:

$$F_{xi} = F_{yi} = F_{zi} = E \cdot \varepsilon \cdot S = E \cdot \frac{d_{DEF}}{l} \cdot S \quad (3)$$

where $i = 1, 2, 3, 4$; E is the Young's modulus of the micro-wires; ε is the average strain of the micro-wires; S is the top surface area of one array of the micro-wires; l is the height of the micro-wires; d_{DEF} is the deformation in z direction of the micro-wires.

To obtain the relationship between F_i ($i = 1, 2, 3, 4$) and F_x , F_y , F_z , FEA were conducted to calculate the coefficients k_b , k_w , k_r , k_d , and k_a . When normal force in z direction and shear force in x direction applied separately as shown in Fig. 5(b) and

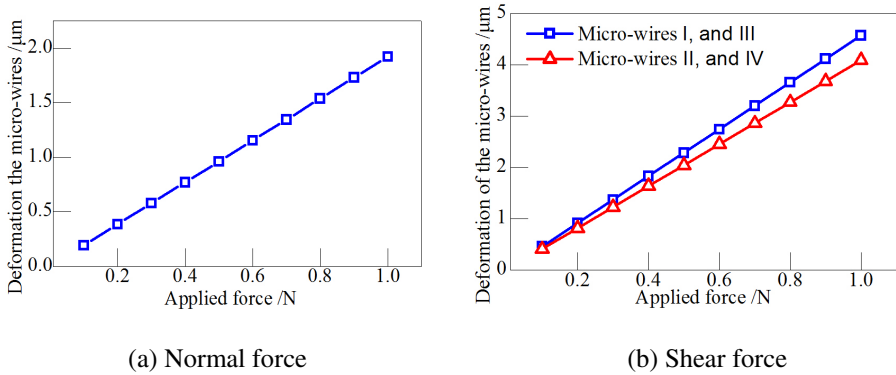


Fig. 6. Force effects on the deformation of the micro-wires

(d), the deformations of the micro-wires are shown in Fig. 6. As the normal force increase, four micro-wires arrays deform linearly with the increasing of the normal force as shown in Fig. 6(a). From Fig. 6(b), micro-wires II and IV are compressed and micro-wires I and III are stretched, and they both deform linearly with the increasing of the shear force.

In this FEA, $E = 3 \text{ MPa}$, $S = 0.15 \text{ mm}^2$, and $l = 100 \text{ }\mu\text{m}$. And the slope of the line in Fig. 6(a) can be expressed as follows according to Eqs. (1) and (3):

$$\frac{d_{DEF}}{F_z} = \frac{k_a \cdot l}{E \cdot S} = 1.922 \tag{4}$$

So k_a can be calculated from Eq. (4). In the same way, from Fig. 6(b) and Eqs. (1) and (3), k_l , k_u , k_r , k_d can be obtained as follows:

$$\begin{cases} k_a = 0.008649 \\ k_l = 0.02057 \\ k_u = 0.01340 \\ k_r = 0.01340 \\ k_d = 0.02057 \end{cases} \tag{5}$$

From Eqs. (1) – (5), the following expressions can be obtained:

$$\begin{cases} F_x = \frac{F_1 - F_2}{0.00717} \\ F_y = \frac{F_3 - F_1}{0.00717} \\ F_z = \frac{1.535F_2 - F_3}{0.004628} \end{cases} \tag{6}$$

where F_1, F_2, F_3 are the forces acting on micro-wires I, II, III.

From Eq. 6, the relationship between F_i ($i=1, 2, 3, 4$) and the force applied on the bump are developed. But we can notice that F_4 do not appear in Eq. (6), that's

because three arrays of micro-wires are already enough to calculate the force applied on the bump, and for the fourth micro-wires, its deformation can be used to increase the accuracy of the force measurement. The relation between F_i ($i=1, 2, 3, 4$) and resistance of the micro-wires can be linear in our designed range and it will not be discussed here. By measuring the F_i ($i=1, 2, 3, 4$) on each micro-wire array, the normal and shear forces can be calculated by using Eq. 6.

4 Fabrication of the Conductive Micro-wires

Nano-wires used in the tactile sensor have high sensitivity [12]. It can be inferred that if the conductive wires scale down to micron or even nanometer, they represent high sensitivity. Thus, the conductive micro-wires with high sensitivity are critical component of the designed tactile sensor. How to fabricate micro-wires that is as small as possible is challenging. This paper presents a μ CP method [14-16] to fabricate the micro-wires.

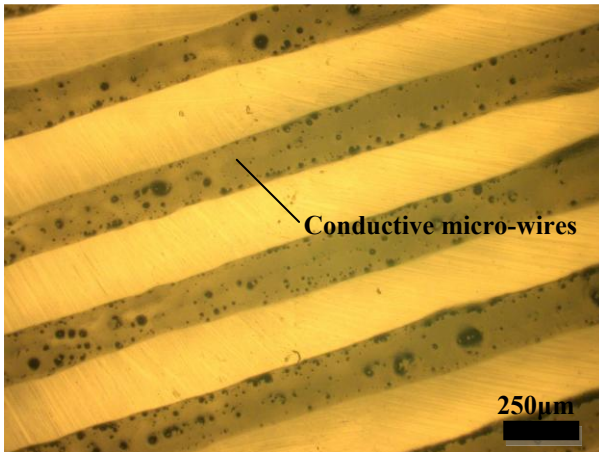


Fig. 7. Micro-wires fabricated on the slide glass

The fabrication process is as follows: 1) the carbon black with diameter of 30 nm were dispersed in toluene solution at 1:15 weight ratio, and magnetically stirred for 2 hours; 2) ultrasonic dispersion for 3 minutes to make the carbon black disperse more uniformly in toluene solution; 3) PDMS base polymer was added into toluene at 1:3 weight ratio, 4) these two solutions were mixed together and placed on magnetic stirring instrument (75 °C) to evaporate the toluene completely, forming the liquid-state conductive polymer nano-composites; 5) the composite was spin coated on a silicon wafer; 6) a micro-wires patterned mold was placed on the composite thin layer for 10 seconds before lifting the mold up, leaving a thin layer of nano-composites on the patterns of the mold; 7) the mold was then stamped onto a slide glass to transfer the nano-composite pattern, forming the arrays of micro-wires on the slide glass; 8) then place the slide glass in the oven to cure the micro-wires at 80 °C for 3 hours.

The fabricated micro-wires are shown in Fig. 7, the width and height of the micro-wires are 250 μm and 50 μm , respectively. Electrical characteristics will be tested in the future work.

5 Conclusions and Future Works

This paper presented a novel micro-wires based tactile sensor and μCP method to fabricate the micro-wires. The four micro-wires arrays using as the sensing element can measure the normal and shear force. To increase the sensing performance of the tactile sensor, the top surface bump geometries were optimized by using the FEA modeling. The optimal dimensions of the bump are 1.2 mm side length and 0.7 mm height. Based on the optimal surface bump, analytical models for the tactile sensor to measure the normal and shear forces were developed. The results show that the tactile sensor can measure the applied forces by measuring the resistance changes of the four micro-wires. To fabricate the micro-wires, μCP method and its fabrication process were proposed, the manufactured micro-wires features width of 250 μm and height of 50 μm . Conclusion can be drawn that micro-wire array based tactile sensor is feasible and can measure the normal and shear forces.

Future work will be to characterize the conductive ability of the micro-wires and sensing performance of the tactile sensor. Smaller micro-wires will be fabricated to achieve a higher sensitivity and utilized as the sensing element to develop a tactile sensor.

Acknowledgments. The author would like to acknowledge the supports from the National Basic Research Program (973) of China under Grant No. 2011CB013300, the National Natural Science Foundation of China under Grant No. 51105333, and the Postdoctoral Science Foundation of China under Grant No. 2011M500995.

References

1. Kim, K., Lee, K.R., Kim, W.H.: Polymer-based flexible tactile sensor up to 32 \times 32 arrays integrated with interconnection terminals. *Sens. Actuators A: Phys.* 156, 284–291 (2009)
2. Noda, K., Hoshino, K., Matsumoto, K.: A shear stress sensor for tactile sensing with the piezoresistive cantilever standing in elastic material. *Sens. Actuators A: Phys.* 127, 295–301 (2006)
3. Yu, S., Chang, D., Tsao, L.: Porous nylon with electro-active dopants as flexible sensors and actuators. In: *Proceedings of the IEEE 21st International Conference on Micro Electro Mechanical Systems (MEMS)*, Tucson, AZ, USA, pp. 908–911 (2008)
4. Lee, H., Chung, J., Chang, S.: Normal and shear force measurement using a flexible polymer tactile sensor with embedded multiple capacitors. *J. Microelectromech. Syst.* 17, 934–942 (2008)
5. Ying, M., Bonifas, A.P., Lu, N.: Silicon nanomembranes for fingertip electronics. *Nanotechnology* 23(34), 344004-1 (2012)

6. Hosoda, K., Tada, Y., Asada, M.: Anthropomorphic robotic soft fingertip with randomly distributed receptors. *Robot Auton. Syst.* 54, 104–109 (2006)
7. Dahiya, R.S., Valle, M., Metta, G.: Bio-inspired tactile sensing arrays. In: *Proceedings of Bioengineered and Bioinspired Systems IV*, Dresden, Germany, pp. 73650D-9 (2009)
8. Hoshino, K., Mori, D.: Three-dimensional tactile sensor with thin and soft elastic body. In: *Proceedings of the IEEE Workshop on Advanced Robotics and Its Social Impacts*, Taipei, Taiwan, pp. 1–6 (2008)
9. Mannsfeld, S.C.B., Tee, B.C., Stoltenberg, R.M.: Highly sensitive flexible pressure sensors with microstructured rubber dielectric layers. *Nat. Mater.* 9(10), 859–864 (2010)
10. Kawaguchi, H., Someya, T., Sekitani, T.: Cut-and-paste customization of organic FET integrated circuit and its application to electronic artificial skin. In: *IEEE International Solid-State Circuits Conference*, San Francisco, Canada, vol. 40(1), pp. 177–185 (2005)
11. Someya, T., Kato, Y., Sekitani, T.: Conformable, flexible, large-area networks of pressure and thermal sensors with organic transistor active matrixes. *Proc. Natl. Acad. Sci.* 102(35), 12321–12325 (2005)
12. Takei, K., Takahashi, T., Ho, J.C.: Nanowire active-matrix circuitry for low-voltage macroscale artificial skin. *Nat. Mater.* 9(10), 821–826 (2010)
13. Liang, G., Mei, D., Wang, Y., Dai, Y., Chen, Z.: Design and simulation of bio-inspired flexible tactile sensor for prosthesis. In: Su, C.-Y., Rakheja, S., Liu, H. (eds.) *ICIRA 2012, Part III. LNCS (LNAI)*, vol. 7508, pp. 32–41. Springer, Heidelberg (2012)
14. Xia, Y.N., Whitesides, G.M.: Soft Lithography. *Annu. Rev. Mater. Sci.* 28, 153–184 (1998)
15. Zhong, C., Kapetanovic, A., Deng, Y.: A Chitin Nanofiber Ink for Airbrushing, Replica Molding, and Microcontact Printing of Self-assembled Macro-, Micro-, and Nanostructures. *Adv. Mater.* 23, 4776–4781 (2011)
16. Chakra, E.B., Hannes, B., Dilosquer, G.: A new instrument for automated microcontact printing with stamp load adjustment. *Review of Scientific Instruments* 79, 64101–64102 (2008)

An Anti-aliasing and De-noising Hybrid Algorithm for Wavelet Transform

Yuding Cui*, Caihua Xiong, and Ronglei Sun

State Key Lab of Digital Manufacturing Equipment and Technology,
Institute of Rehabilitation and Medical Robotics,
Huazhong University of Science and Technology, Wuhan 430074, China
hjhbuick@hust.edu.cn

Abstract. The purpose of this research is to eliminate the noise of sEMG signal which it used to control the upper arm rehabilitation robot. In this paper, we propose an anti-aliasing and de-noising hybrid algorithm for signal processing based on wavelets theory and FFT. Experimental results showed that the hybrid algorithm is quite effective for signal anti-aliasing and de-noising.

Keywords: Rehabilitation robot, De-noising, Anti-aliasing, DWT, FFT, Hybrid algorithm.

1 Introduction

Signal processing techniques are mathematical procedures that can be usefully applied to extract information from biomedical signals. The more popular methods include fast fourier transform(FFT), discrete wavelet transform(DWT) and wavelet package transform(WPT). These mathematical representations are powerful tools used to detect and quantitatively describe the recorded signal resulting from physiological events. But a raw signal often corrupted by noise in its acquirement and transmission because of interference of environment and internal factors of circuit. Therefore de-noising becomes a first importance question in signal processing, in essence, signal de-noising used all kinds of circuits or algorithms to eliminate the noise while retaining as much as possible the important signal features.

We can find that in some wavelets literature one often used the term just is de-noising. For example, articles by Mallat and Hwang[1]. Wavelet provides an appropriate basis for separating noisy signal from the raw signal, the small coefficient are more likely due to noise and large coefficient due to important signal features[2].

Threshold plays an important role in each scale using wavelet de-noising. Donoho and Johnstone [3] [4] proposed several thresholds, which work excellent for signal de-noising such as universal threshold. Universal threshold is at least as smooth as the target function and it achieves minimax convergence rates up to a logarithmic penalty over a wide range of function classes[4]. However, it has its own drawbacks, it removes too many terms in the wavelet series by having the threshold value higher than what ought to be. Thus we propose level dependent thresholds since these offer greater flexibility.

* Corresponding author.

There is heavy aliasing in mallat’s fast algorithm since the low-pass filter and high-pass filter used in wavelet transform is not properly band-limited, then we propose an hybrid algorithm for signal anti-aliasing and de-noising based on wavelets theory and FFT.

The remainder of this paper is organized as follows: A brief review of WT is provided in Section 2. Detailed analysis of aliasing causes in down-sampling and soft threshold de-noising, then we proposed a hybrid algorithm for signal anti-aliasing and de-noising based on wavelet and FFT in Section 3. Section 4 we gave the experiment results and discussions. Finally, conclusions are presented in Section 5.

2 Wavelet Analysis

Multiresolution theory was developed by Meyer[5], Mallat[6] and Daubechies [7], the concept of multiresolution analysis play a central role in Mallat’s fast pyramid algorithm for the decomposition and reconstruction of signal. Using this algorithm, we are able to compute the DWT and inverse DWT for the signal much faster than FFT. Such a multiresolution analysis(MRA) requires a description of two basic functions: the scaling function $\phi(x)$ and the wavelet function $\psi(x)$. A scaling function $\phi(x)$ gives a set of approximations of the signal as a set of resolution levels j , by projecting it on a set of subspaces V_j which are generated by stretched and translated versions of $\phi(x)$. For a given resolution level j , the subset V_j is spanned by the base of scaling functions:

$$\phi_{j,k}(x) = 2^{\frac{j}{2}} \phi(2^j x - k), j, k \in \mathbb{Z}. \tag{1}$$

Given a discrete signal $x[n], n = 1, \dots, N$; the approximation coefficients yield:

$$c_{j,k} = \langle x, \phi_{j,k} \rangle \tag{2}$$

By setting stretching factor equal to 2, we have $\phi(x)$ corresponding to

$$\phi(x) = \frac{1}{\sqrt{2}} \sum_{k \in \mathbb{Z}} h_k \phi(2x - k). \tag{3}$$

where

$$h_k = \frac{1}{\sqrt{2}} \langle \phi(x), \phi(2x - k) \rangle. \tag{4}$$

it is called low-pass filter. The MRA is completely defined by the function $\phi(x)$ or equivalently by the sequence h_k from equation (4). The scale function always defines the low frequency signal components.

The information lost between two successive approximations is called a detail, it is obtained by projecting the signal on the complement of V_j , denoted by $W_j(W_j + V_j = V_{j+1})$, it defined by the wavelet functions:

$$\psi_{j,k}(x) = 2^{\frac{j}{2}} \psi(2^j x - k), j, k \in z. \quad (5)$$

where $\psi(x)$ is the mother wavelet

$$\psi(x) = \sqrt{2} \sum_{k \in z} g_k \psi(2x - k). \quad (6)$$

where

$$g_k = 1/\sqrt{2} \langle \psi(x), \psi(2x - k) \rangle. \quad (7)$$

It is called high-pass filter. The detail coefficients are computed as follows:

$$d_{j,k} = \langle x, \psi_{j,k} \rangle. \quad (8)$$

The signal can be reconstructed from the approximation of resolution level J_0 and the details of lower levels:

$$\tilde{x}(t) = \sum_k c_{J_0,k} \tilde{\phi}_{J_0,k}(t) + \sum_{j \leq J_0} \sum_k d_{j,k} \tilde{\psi}_{j,k}(t) \quad (9)$$

where $\tilde{x}(t)$ is a reconstructed signal, $\tilde{\phi}_{j,k}(t)$ $j, k \in z$ and $\tilde{\psi}_{j,k}(t)$ $j, k \in z$ are scaling functions and wavelet functions for signal reconstruction respectively.

3 Method for Anti-aliasing and De-noising

There are a number of practical considerations such as choice of wavelet filter and the low-resolution cut-off J_0 of DWT that must be addressed in order to come up with a useful wavelet analysis of a signal. Furthermore, since the wavelet filter bank is not an ideal filter bank, it should be lead to heavy aliasing in fast pyramid algorithm. Each of these problems we shall discuss in more detail as following:

3.1 Choice of Wavelet Filter and the Low-Resolution Cut-Off J_0 of DWT

The first practical problem in constructing a wavelet analysis is how to choose a wavelet filter from all the wavelet filters. A reasonable choice depends very much on the practical application, this paper our choice is dictated by a desire to balance two considerations: firstly, wavelet filters of the very shortest widths can sometimes introduce undesirable artifacts into the resulting analyses (such as unrealistic blocks, sharks' fins and triangles). On the other hand, while wavelet filters with large support width N can be a better match to the characteristic features in a signal. But their use can result in (i) more coefficients being unduly influenced by boundary conditions (ii) some decrease in the degree of localization of the DWT coefficients (iii) an increase in computational cost.

A reasonable overall strategy is thus to use the smallest wavelet support width N that gives reasonable results, we keep increasing wavelet support width N until we come to an analysis that is free of any artifacts attributable to the wavelet filter alone.

The second practical problem is the choice of low resolution cut-off level J_0 of DWT. As was true for the choice of the wavelet filter, a reasonable selection of the

level J_0 for DWT must take into account the application in practical. It should also be noted that the support width N of the wavelet filter can impact the choice of J_0 somewhat. A default for J_0 is to set it such that [9].

$$(2^{J_0} - 1)(2N - 1) + 1 \leq N_0 < (2^{J_0+1} - 1)(2N - 1), \tag{10}$$

where N_0 is the number of original sampling points. We are able to calculate the level J_0 of partial DWT.

3.2 Remove Aliasing during Getting Approximations and Details Coefficients

The process of signal decomposed based Mallat’s fast pyramid algorithm[8] include two step: the first step is convolution approximation coefficients $A_{j,k}$ with low-pass filter $\{h_i\}$ or high-pass filter $\{g_i\}$; second, to do a down-sampling after convolution. However, as a key step, down-sampling can lead to heavy aliasing.

Down-sampling in the time domain is direct: $V = (\downarrow 2)X$ (operator \downarrow represent down-sampling) means $V(k) = X(2k)$, but in the frequency domain, $V = (\downarrow 2)X$ has transform $V(\omega) = [X(\omega/2) + X(\omega/2 + \pi)]/2$, so ω enters the down-sampled vector V not only by doubling $\omega/2$ but also by doubling $\omega/2 + \pi$ [10].

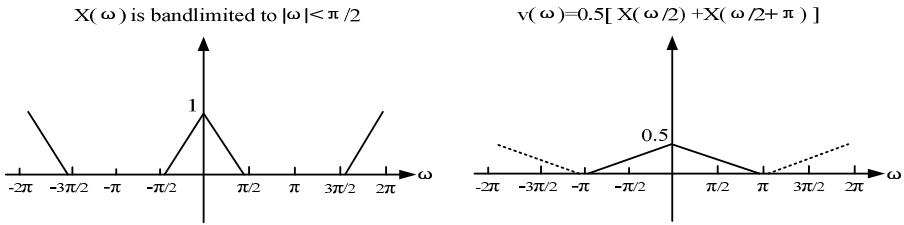


Fig. 1. Down-sampling this band-limited signal no aliasing

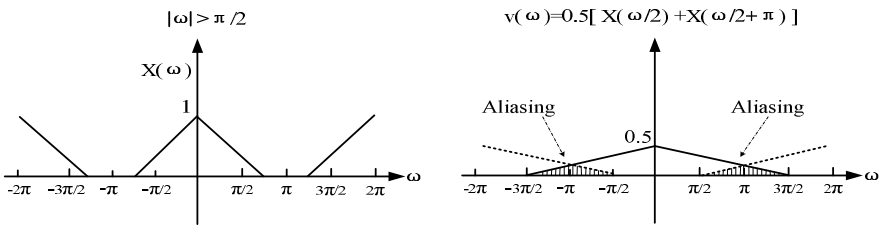


Fig. 2. $(\downarrow 2)X$ cause of typical aliasing

In Fig.1, the input $X(\omega)$ is properly band-limited. that is, $|\omega| < \pi/2$. The stretched transform $X(\omega/2)$ does not overlap the aliasing term $X(\omega/2 + \pi)$. The output $V(\omega)$ from down-sampling still contain this aliasing part. But a non-overlapping alias can be filtered away, so down-sampling ($|\omega| < \pi/2$) does not lead to aliasing. But in Fig.2, the input $X(\omega/2)$ is not band-limited $|\omega| < \pi/2$, that is $\max|\omega| > \pi/2$. The stretched transform $X(\omega/2)$ overlaps the aliasing term $X(\omega/2 + \pi)$. The output

$V(\omega)$ from down-sampling should cause typical aliasing, it should be symmetrical and centered on points which $|\omega| = \pi$. In order to do down-sampling for the input $X(\omega)$ without aliasing, the input $X(\omega)$ should correspond to $|\omega| < \pi/2$.

The same situation happened in the process of convoluting time signal $\{X(t)\}$ with high-pass filter $\{g_j\}$, the process of down-sampling should not lead to aliasing if the input $X(\omega)$ is properly band-limited to $\pi/2 < |\omega| < \pi$.

The Method of Remove Aliasing in the Process of Obtaining the A_{j-1}

Based on the above analysis, we proposed an anti-aliasing algorithm for the process of DWT as following:

(1) To apply fast fourier transform (*FFT*) to A'_j which is convolutional result of approximation coefficients A_{j-1} with lower-pass filter $\{h_j\}$;

(2) The result of the *FFT* in step (1) which is greater than $f_s/2^{j+1}$ would be set to zeros. That is, to set $A'_j(k) = 0$ if $N_{j-1}/4 < k < 3N_{j-1}/4$, where N_{j-1} is the number of approximation coefficients A_{j-1} ;

$$A'_j(k) = \begin{cases} \sum_{n=0}^{N_{j-1}} X(n)\omega_{N_{j-1}}^{(n-1)(k-1)} & \text{otherwise} \\ 0 & N_{j-1}/4 < k < 3N_{j-1}/4 \end{cases} \quad (11)$$

where $\omega_{N_{j-1}} = e^{(-2i\pi)/N_{j-1}}$.

(3) Apply inverse fast fourier transform (*IFFT*) to the result in step (2), we down-sampled to the results of IFFT and obtained the approximation coefficients A_j . Go on the next decomposition until $j = J_0$.

The Method of Remove Aliasing in the Process of Obtaining the D_j

(1) To apply fast fourier transform (*FFT*) to D'_j which is convolutional result of approximation coefficients A_{j-1} with filter $\{g_h\}$;

(2) The result of the *FFT* in step (1) which is less than $f_s/2^{j+1}$ would be set to zeros. That is, we shall set $D'_j(k) = 0$ if $0 < k < N_{j-1}/4$ or $3N_{j-1}/4 < k < N_{j-1}$, where N_{j-1} is number of approximation coefficients A_{j-1} ;

$$D'_j(k) = \begin{cases} \sum_{n=0}^{N_{j-1}} X(n)\omega_{N_{j-1}}^{(n-1)(k-1)} & \text{otherwise} \\ 0 & k < N_{j-1}/4 \text{ and } 3N_{j-1}/4 < k < N_{j-1} \end{cases} \quad (12)$$

where $\omega_{N_{j-1}} = e^{(-2i\pi)/N_{j-1}}$.

(3) Apply inverse fast fourier transform (*IFFT*) to the result in step (2). Don't down-sampled to the results of IFFT and obtained the detail coefficients D_j .

3.3 Apply Soft Threshold Function to High Frequency Coefficients and Reconstruct Signal with Wavelet Transform

To get $\{A_{j-1,n}\}$ from $\{A_{j,k}\}$ and $\{D_{j,k}\}$ is called reconstruct algorithm. And we have the reconstruction equation as following:

$$A_{j-1,n} = \sum_k A_{j,k} h_{n-2k} + \sum_k D_{j,k} g_{n-2k} \tag{13}$$

where h_{n-2k} $n, k \in z$ is the low-pass reconstruct filter and g_{n-2k} $n, k \in z$ is the high-pass reconstruct filter. $A_{j,k}$ and $D_{j,k}$ had been obtained according to the algorithm as mentioned in the section 3.2.

Before the calculation of approximation coefficients $A_{j-1,k}$ $j, k \in z$, we should apply soft threshold function to the wavelet coefficients $D_{j-1,k}$ $j, k \in z$ in each resolution level. The soft threshold function $\eta_{j,k}$ is defined as following :

$$\eta_{j,k} = \begin{cases} \text{sign}\{D_{j,k}\} \{ |D_{j,k}| - \lambda_j \} & \text{if } |D_{j,k}| > \lambda_j \\ 0 & \text{if } |D_{j,k}| \leq \lambda_j \end{cases} \tag{14}$$

where λ_j is the sub-band level dependent threshold of wavelet coefficients in the j -th level. In order to eliminate noise, we proposed level dependent thresholds as follows:

$$\lambda_j = \sqrt{2\sigma_\epsilon^2 \ln(n_j)} / \ln(j+1) \tag{15}$$

For practical use, it is important to estimate the noise level σ_ϵ from the data rather than to assume that the noise level is known. In practical we derive an estimate standard deviation from the D_j , this standard deviation estimator was given by Donoho and Johnstone[3] :

$$\sigma_\epsilon = \frac{\text{median}\{ |D_{j,0}|, \dots, |D_{j, \frac{N_j}{2}-1}| \}}{0.6745} \tag{16}$$

We chosen the threshold as this that can be interpreted with the reason as the following :

$$P[\max_l \{ |e_l| \} > \lambda_j] \leq \frac{1}{4\pi \ln(N)} \tag{17}$$

where N is the sample size of the original signal, this threshold thus ensures with high probability, that the reconstruction is as smooth as or smoother than the true deterministic signal.

After all the wavelet coefficients are filtered by soft threshold functions we can recover the signal using equation (9).

4 Results and Discussion

In order to validate the performance of hybrid algorithm which proposed in section 3, let us use this algorithm to analyse a typical signal y . The signal y is defined as:

$$y = \sin(30\pi t) + \sin(60\pi t) + \sin(90\pi t) + \sin(120\pi t) + \sin(150\pi t) + \sin(180\pi t) + \sin(240\pi t) + \sin(300\pi t) + \sin(500\pi t) + \sin(600\pi t) \quad t \in [0, 0.5] \tag{18}$$

Choosing 4096 points from y with 800Hz sampling rate and using wavelet sym10 and calling related functions from Matlab wavelet toolbox, the signal y is decomposed to level 3. Ideal components in each sub-band after applying DWT are given in Table 1. Figure 3 shows the spectra of sub-band signals after applying DWT with sym10 to signal y . From Fig.3 we can find heavy aliasing appears. Figure 4 shows the spectra of sub-band signals after applying anti-aliasing algorithm. Contrasting every sub-band spectra in the Fig.4 with Table1, we can find that the frequency components at each sub-band are exactly the same. The aliasing is avoided rather effectively by the anti-aliasing algorithm.

According to the rule mentioned in the section 3. We chose wavelet function named ‘‘Symlets’’(sym10) and $J_0 = 7$ for signal de-noising. In Figure 4, the first is the raw signal, and the second is the signal corrupted with white noise, the third showed the noised signal have been removed noise utilizing hybrid algorithm proposed in previous section. In figure 4, we can see that the reconstruction signal is as smooth as the raw signal.

All of results show that wavelet-based method for de-noising and we proposed anti-aliasing algorithm in wavelet decomposition is suitable for processing signals.

Table 1. Ideal components in each sub-band of signal y (Hz)

Level	1	2	3
a	15,30,45,60,75,90,120,150	15,30,45,60,75,90	15,30,45
d	250,300	120,150	60,75,90

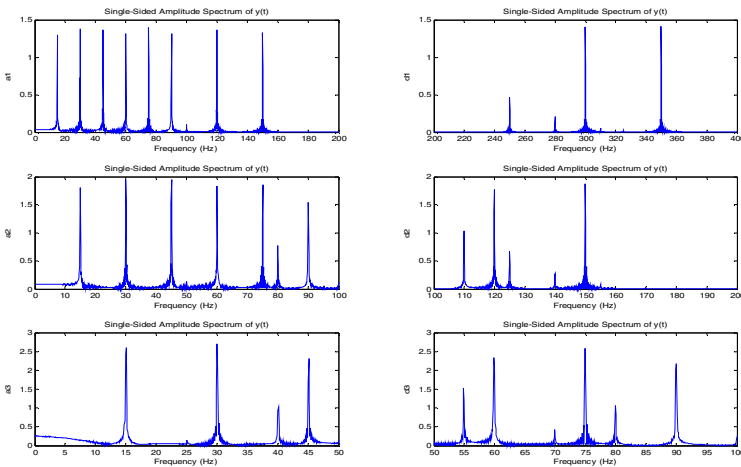


Fig. 3. The spectra of sub-band signals after applying the DWT with sym10 to signal y

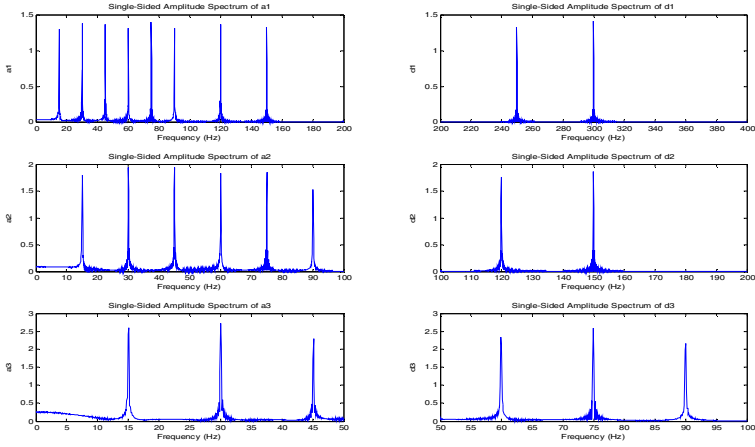


Fig. 4. The spectra of sub-band signals after applying the anti-aliasing with sym10 to signal y

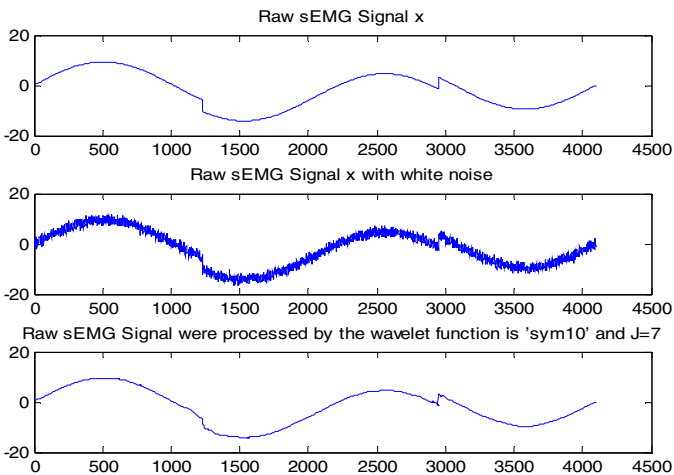


Fig. 5. Raw signal and reconstructions using hybrid anti-aliasing and denoising algorithm

5 Conclusion

This paper has presented a hybrid algorithm for signal anti-aliasing and de-noising based-on wavelet transform and FFT. Experimental results demonstrated that anti-aliasing could effective for avoiding aliasing and level dependent threshold performs good for signal de-noising. We suggest that it is used as a pre-filter technique for sEMG signal, which been used to control rehabilitation robot after action pattern recognition.

Acknowledgement. This work was supported by the National Key Technology R&D Program of China under Grant 2008BAI50B04, the National Natural Science Found for Distinguished Young Scholars of China under Grant 51025518, and the '863' Hi-Tech Research and Development Program of China under Grant 2008AA040202.

References

1. Mallat, S.G., Hwang, W.L.: Singularity detection and processing with wavelets. *IEEE Transactions Information Theory* 38(2), 617–643 (1992)
2. Jansen, M.: *Noise Reduction by Wavelet Thresholding*. Springer, New York (2001)
3. Donoho, D.L., Johnstone, I.M.: Ideal spatial adaptation via wavelet shrinkage. *Biometrika* 81, 425–455 (1994)
4. Donoho, D.L.: De-noising by soft-thresholding. *IEEE Transactions on Information Theory* 41, 613–627 (1995)
5. Meyer, Y.: *Ondelettes et fonctions splines*. Seminaire EDP, Ecole Polytechnique, Paris (1986)
6. Mallat, S.G.: *Multiresolution representation and wavelets*. Ph.D. Thesis, University of Pennsylvania, Philadelphia, PA (1988)
7. Daubechies, I.: Orthonormal bases of compactly supported wavelets. *Communications on Pure and Applied Mathematics* 41, 909–996 (1988)
8. Mallat, S.G.: A theory of multiresolution signal decomposition: the wavelet Representation. *IEEE Transaction on Pattern Analysis Machine Intelligence* 11, 674–693 (1989)
9. Percival, D.B., Walden, A.T.: *Wavelet Methods for Time Series Analysis*, pp. 96–96. Cambridge University Press (2000)
10. Strang, G., Nguyen, T.: *Wavelets and Filter Banks*, pp. 91–93. Wellesley-Cambridge Press, Wellesley (1996)

Simultaneous and Proportional Estimation of Finger Joint Angles from Surface EMG Signals during Mirrored Bilateral Movements

Lizhi Pan, Xinjun Sheng, Dingguo Zhang, and Xiangyang Zhu

State Key Laboratory of Mechanical System and Vibration,
Shanghai Jiao Tong University, Shanghai 200240, China
{melzpan, xjsheng, dgzhang, mexyzhu}@sjtu.edu.cn

Abstract. This paper studies the continuous estimation of finger angles with state-space model to realize the simultaneous and proportional control of finger joint motions, where the test model of mirrored bilateral movements is first applied to decode the fingers' continuous motion. First a linear method was proposed for simultaneous and proportional estimation of 10 degrees of freedom (DOFs) finger joint angle with surface electromyography (EMG). The state-space model was adopted to estimate one finger joint angle from 8 channel surface EMG signals recorded from contralateral limb mirrored bilateral movements. The average estimation performance of 8 DOFs of the hand except little finger can achieve 0.824(index R^2), while the index R^2 can achieve as high as 0.924 with the estimation thumb metacarpophalangeal joint (MCP). Although the estimation performance of the little finger was not good enough, the results demonstrate that state-space model is a feasible method to estimate the finger joint angles. Because the proposed method requires only the contralateral finger joint angles as the model identification reference, there is a great potential application for unilateral amputees in control of dexterous myoelectric prosthesis with multiple DOFs.

Keywords: EMG, state-space model, continuous, finger, estimation.

1 Introduction

Surface electromyography (EMG) signals collected from the residual muscles have been widely used as the inputs of a human-machine interface (HMI). The pattern recognition method has been clinically applied in upper limb amputees for 30 years[1]. However, the clinical receptance of powered upper limb prostheses based on pattern recognition is still limited, even though the recognition accuracy rate could attain > 0.96 by using current technology[2]. The material causes are the relative fewer functions that can be classified with acceptable recognition rate, in addition it is not continuous and is inherent sequential with ON/OFF control mode[3].

As dexterous myoelectric prosthesis with multiple degrees of freedom (DOFs) developed pretty fast in recent years, there is a growing need for continuous estimation of finger joint angles. Simultaneous and proportional control signals for

a dexterous myoelectric prosthesis with multiple DOFs is one of the most significant challenges in myoelectric control[4]. The simultaneous and proportional control for multiple DOFs of the wrist movements has been analyzed[5][6]. Although mirrored bilateral movements has been used in simultaneous and proportional estimation wrist force and kinematics[3][6], there is no work on continuous estimation finger joint angle using mirrored bilateral movements before. As artificial neural network (ANN) was widely used in continuous estimation of finger joint angles from EMG signals[7][8][9], linear model has never been taken into consideration in finger joint angles estimation area.

In this work, a linear state-space model used for continuous estimation of 10 DOFs finger joint angles was proposed. Both finger joint angles and EMG signals of contralateral arm were concurrently recorded. Mirrored bilateral training was first adopted to continuously decode the finger joint angles.

2 Methodology

2.1 Subjects

As a preliminary study, the proposed method in a limbed normal subject was analyzed, which is a necessary basis for future testing in disabled subjects. One limbed normal (man, age25) took part in the experiment. The subject participated in the experiment had signed the informed consent and the procedures accorded with declaration of Helsinki.

2.2 Experimental Setup

As shown in Fig. 1, a limbed normal subject was asked to sit in the chair with his arm along the body resting on the armrests. The subject was instructed to reproduce a series of mirrored bilateral finger movements starting from the neutral position. The subject was instructed to move one single finger while holding the rest of fingers in a neutral position. The subject was told to move the finger reaching the maximum angle of flexion and extension in the following order: thumb, index, middle, ring and little finger.

2.3 Data Acquisition

For surface EMG signals acquisition, a Trigno Wireless System (Delsys Inc., USA) was used in this work. As shown in Fig. 1, eight channel EMG signals were recorded from six finger movement-related muscles: 1. Flexor Pollicis Longus, 2. Flexor Pollicis Longus, 3. Flexor Digitorum Superficialis, 4. Flexor Digitorum Profundus, 5. Extensor pollicis Brevis, 6. Abductor Pollicis Longus, 7. Extensor Digitorum, 8. Extensor Digitorum[8]. Eight wireless noninvasive surface electrodes were placed over the target muscles using medical adhesive tape. The electrodes were wirelessly connected to the Trigno Base Station which communicating with a computer through the USB link. The EMG signals were band-pass filtered(pass band 20-450Hz) and sampled at 2000Hz by the EMG data acquisition system.



Fig. 1. Sitting position of a subject and position of the EMG electrodes. EMG signals were acquired from the right arm and finger joint angles were recorded from left hand.

For finger joint angles acquisition, a 5DT Data Glove 14 Ultra (5DT Inc., USA) was used in this work. As shown in Fig. 2, the subject wore the 5DT Data Glove on the left hand and the metacarpophalangeal joint (MCP) and the proximal interphalangeal joint (PIP) of each finger was measured. The scaled finger joint angle from the 5DT Data Glove was used in this work.

Software Development Kits (SDKs) of Trigno Wireless System and 5DT Data Glove 14 Ultra were used to compile an *c#* program that can simultaneously sample EMG signals and finger joint angles at 2000Hz and write the data to a *txt* file.

2.4 Data Preprocessing

The EMG signals were full-waved rectified and low-pass filtered (2th order zero-lag Butterworth digital filter, cut-off frequency 10Hz) to obtain the muscle activity envelopes. And the finger joint angles were low-pass filtered (2th order zero-lag Butterworth digital filter, cut-off frequency 10Hz) as well. Then the filtered EMG signals and the angle data were used as the inputs and output for the EMG-angle model identification to get the model set 1. In order to explore how normalization of the data can affect the performance of model identification, the filtered EMG signals and the angle data were normalized before used for EMG-angle model identification to get the model set 2. For model set 3 and 4, moving window was used to compute the mean absolute value(MAV) and the



Fig. 2. Finger joint angles acquired by the 5DT Data Glove 14 Ultra from the left arm

root mean square(RMS) of the normalized data. The window length was set to 200ms and the window increment was set to 50ms.

2.5 Estimation of Finger Joint Angles from EMG

As we have done estimation of wrist kinematics from EMG in previous work, state-space model was feasible to estimate 2 DOFs of wrist movements. In this work, a state-space model was also used to estimate the finger joint angles from EMG signals.

$$\begin{aligned} x(k+1) &= Ax(k) + Bu(k) \\ y(k) &= Cx(k) \end{aligned} \quad (1)$$

where x is the hidden state vector, y is the finger joint angle, u is the muscle activations, A is the system matrix that represents the dynamic behavior of the hidden state vector x , B is the matrix that maps the EMG signal u to the state vector x , and C is the matrix that represents the relationship between the finger joint angle y and the state vector x . We used different state-space models for different finger joint angles to obtain a better estimation performance for each DOF. Therefore, ten state-space models were used to estimate the MCP and PIP of each finger of contralateral hand. Each state-space model had the EMG signals as input and one of the finger joint angles as output. The state-space models were identified using the 'N4SID' algorithm[10], which is a subspace method for estimation of state-space models.

For all state-space models, the first half data was used for model parameters identification and the rest half for estimation. In order to evaluate the estimation performance of the state-space model in each finger joint angle, the coefficient of determination R^2 [11] was used. The index R^2 is defined as follows:

$$R^2 = 1 - \frac{\sum_{t=0}^N (\widehat{f(t)} - f(t))^2}{\sum_{t=0}^N (f(t) - \overline{f(t)})^2} \tag{2}$$

where N is the number of data samples, $f(t)$ is finger joint angle function, $\widehat{f(t)}$ is the corresponding estimated finger joint angle from the state-space model, and $\overline{f(t)}$ is the temporal average of $f(t)$.

3 Result and Discussion

Fig. 3 demonstrates the R-squared value (index R^2) between the estimation angle and real angle: the index R^2 of thumb is higher than others; and index R^2 of model 1, 2, 3 and 4 is 0.717, 0.701, 0.727 and 0.724, respectively. The above results show that normalization of filtered EMG signal has no effect on improving the estimation performance of finger joint angle. But MAV and RMS of filtered EMG signal has a positive effect on prediction of finger joint angles. As can be seen in Fig 3, although the estimation performance of the little finger was not good enough, that of the other four fingers is much higher. Thus the state-space model is feasible for continuous motion decoding for finger joint angles.

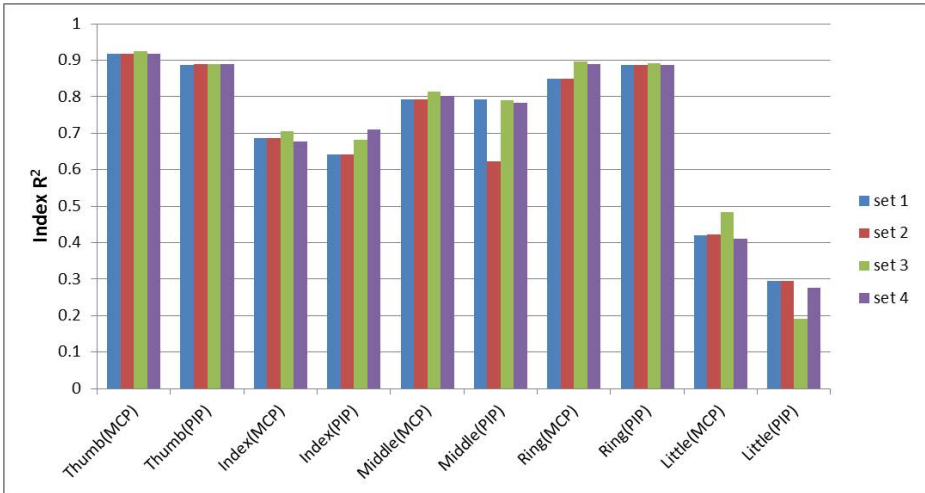


Fig. 3. Index R^2 for each MCP and PIP joints of five fingers from model set 1 to set 4

Fig. 4 demonstrates that, although the motion of other fingers causes the coupled motion of thumb partly, the state-space model still is capable of estimating the MCP angle and PIP angle of thumb very well. Therefore, it goes to show that, the state-space model used in this work is feasible for simultaneous and proportional estimate of finger joint angles.

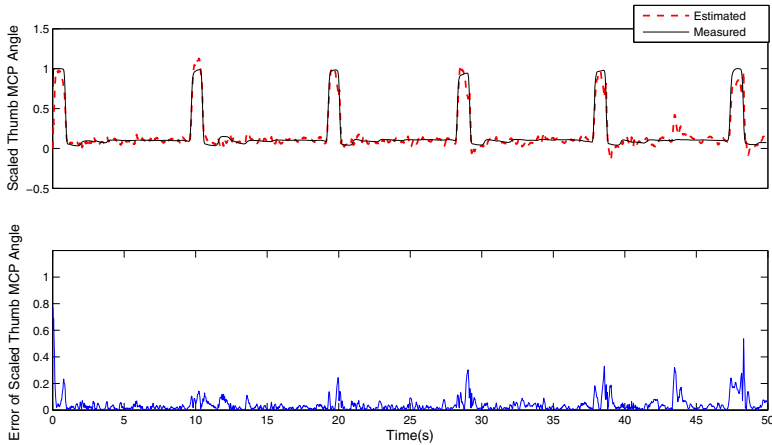


Fig. 4. Measured and estimated MCP joint angles of thumb in model set3. In this example, the index R^2 achieved as high as 0.924.

In this work, the order of all the state-space models were chosen used the default choice of the algorithm n4sid. But maybe the default choice is not the best order for the estimation finger joint angle. More analysis on the state-space model order chosen should be done in our future work.

In order to improve the finger joint angle prediction performance, more electrodes like electrodes array should be adopted in continuous decoding finger joint angle experiments. And we would like to use the cross-correlation analysis between finger joint angles and EMG signals to choose the most relevant EMG channels as the model inputs for each DOF of finger joints. We think that would be helpful to improve the estimation performance.

4 Conclusions

This paper proposed a linear method for continuous estimation 10 DOFs finger joint angle from EMG signals of contralateral arm using mirrored bilateral training. This study has shown that linear model like state-space model used in this work can fit the problem estimating finger joint angle from contralateral EMG signals well. It has a great potential application for unilateral transradial amputees on simultaneously and proportionally controlling a dexterous myoelectric prosthesis. In the future, we would like to do the experiments on more normal-limb subjects and extend the experiment to the unilateral limb amputees.

Acknowledgments. This work was supported by the National Basic Research Program (973 Program) of China (Grant No. 2011CB013305), the Science and Technology Commission of Shanghai Municipality (Grant No. 11JC1406000, 13430721600), and the State Key Laboratory of Robotics and System of HIT (SKLRS-2012-ZD-04).

References

1. Hudgins, B., Parker, P., Scott, R.: A new strategy for multifunction myoelectric control. *IEEE Transactions on Biomedical Engineering* 40(1), 82–94 (1993)
2. Chen, X., Zhu, X., Zhang, D.: Use of the discriminant fourier-derived cepstrum with feature-level post-processing for surface electromyographic signal classification. *Physiological Measurement* 30(12), 1399 (2009)
3. Nielsen, J., Holmgaard, S., Jiang, N., Englehart, K., Farina, D., Parker, P.: Simultaneous and proportional force estimation for multifunction myoelectric prostheses using mirrored bilateral training. *IEEE Transactions on Biomedical Engineering* 58(3), 681–688 (2011)
4. Fougner, A., Staudahl, O., Kyberd, P., Losier, Y., Parker, P.: Control of upper limb prostheses: Terminology and proportional myoelectric control—a review. *IEEE Transactions on Neural Systems and Rehabilitation Engineering* 20(5), 663–677 (2012)
5. Jiang, N., Englehart, K., Parker, P.: Extracting simultaneous and proportional neural control information for multiple-dof prostheses from the surface electromyographic signal. *IEEE Transactions on Biomedical Engineering* 56(4), 1070–1080 (2009)
6. Muceli, S., Farina, D.: Simultaneous and proportional estimation of hand kinematics from emg during mirrored movements at multiple degrees-of-freedom. *IEEE Transactions on Neural Systems and Rehabilitation Engineering* 20(3), 371–378 (2012)
7. Smith, R.J., Tenore, F., Huberdeau, D., Etienne-Cummings, R., Thakor, N.V.: Continuous decoding of finger position from surface emg signals for the control of powered prostheses. In: 30th Annual International Conference of the IEEE Engineering in Medicine and Biology Society, EMBS 2008, pp. 197–200. IEEE (2008)
8. Hioki, M., Kawasaki, H.: Estimation of finger joint angles from semg using a recurrent neural network with time-delayed input vectors. In: IEEE International Conference on Rehabilitation Robotics, ICORR 2009, pp. 289–294. IEEE (2009)
9. Ngeo, J., Tamei, T., Shibata, T.: Continuous estimation of finger joint angles using muscle activation inputs from surface emg signals. In: 2012 Annual International Conference of the IEEE Engineering in Medicine and Biology Society (EMBC), pp. 2756–2759. IEEE (2012)
10. Ljung, L.: System identification. Wiley Online Library (1999)
11. Draper, N.R., Smith, H., Pownell, E.: Applied regression analysis, vol. 3. Wiley, New York (1966)

A Mechatronic Platform for Studies of Tactile Sensory System on Prosthesis Hand

Xiaoying Cheng¹, Qingchuan Shan¹, Ping Yu¹, Liling Cheng²,
Wei-ting Liu^{1,*}, and Xin Fu¹

¹ The State Key Lab of Fluid Power Transmission and Control,
Zheda Rd. 38, 310027, Hangzhou, China

² Zhejiang Academy of Science and Technology for Inspection and Quarantine,
East Fengqi Rd. 99, 310020, Hangzhou, China

Abstract. This paper focuses on developing a mechatronic platform for smart prosthesis touch studies of tactile sensory system. The platform was designed for stimulation of the tactile sensor arrays using multiple indenters driven by an auto positioner, providing repeatable stimuli with controlled force. Particular requirements were addressed to make the platform suitable for curved sensitive flat surface on fingertip of smart prosthesis hand. The design of the mechatronic platform is presented, as well as its performance in stimulating process.

Keywords: Flexible tactile sensor, mechatronic stimulator, prosthesis hand.

1 Introduction

Tactile sensing of human represents many aspects of detections which include shape of object, texture, temperature, moisture, friction, force and many other physical properties [1]. In this paper, we are primarily interested in the tactile sensors that are sensitive to mechanical properties (such as friction and force), and the functions of measuring other properties have not been integrated on the proposed platform. To study these kinds of tactile sensors for prosthesis hand, active and passive methods are adopted [2]. In active test prosthesis hand grasps the target covered with calibrated force sensor array, while in passive method prosthesis hand is kept still and stimuli are introduced by the test platform [3-5]. Both two protocols require stimuli standardized and repeatable to acquire useful data and to achieve this there should be a mechatronic stimulator mounted on the passive test platform to control parameters needed during the process of stimulation.

This paper presents the development of a mechatronic system that could stimulate flexible tactile sensors attached on fingertip of a prosthesis hand with controllable indenting and sliding. While the stimulation is repeated, the system records both normal and tangential force applied on the fingertip and simultaneously the singles of

* Corresponding author.

tactile sensors are acquired. The mechatronic system is designed to be programmable and is capable of being used in analysis of the performance of flexible tactile sensor after deformed and integrated on prosthesis hand.

For testing tactile sensors which are applied on prosthesis hand, several of requirements should be followed in design of this mechatronic device. Firstly, the parameters involved should be controllable, such as indent force and sliding velocity. Secondly, the system should be able to produce stimuli that cover the measuring range of tactile sensors. Thanks to these sensors are designed to mimic human touch, so most of them have the same measuring range value as the perception of human hand: force sensitivity is about 0.1N-10N, spatial resolution is less than 1mm at fingertip [6]. Thirdly, it is necessary to record vibration during the sliding process because vibration sensors are usually used for detecting sliding movement in grasping task [7]. Fourth, due to the finger of prosthesis hand will not operate during the test and indenter should be perpendicular to the surface of contact area, the artificial hand will be rotated and its position should be adapted before the test.

Heretofore, most of the stimulator reported have been developed mainly for the neurological study of tactile perception of human [2-5] and the mechatronic system could solve the problems mentioned above has not been specifically researched or addressed in scientific paper. In this work, a platform is proposed and presented that can meet all these requirements during research of tactile sensory arrays for prosthesis. A series of tests is applied on standard commercial sensors which are regarded as targets by this system, including static and dynamic indentation, sliding vibration and friction. By comparing data from target and stimulator, the performances of these tactile sensors are assessed.

2 Materials and Setup of System

2.1 Mechanism and Stimulator

The mechatronic platform proposed in this paper has the function of indenting and sliding tactical stimuli towards the sensors on prosthesis hand (Fig.1). The indenter is driven by a linear guide (driven by a step motor) and the artificial hand is manipulated by an automation positioner (VP-25XYZL, Newport) associated with a step motor served as a rotator. In indention movement, positioner keeps the prosthesis steady and linear guide produces indenting force while in sliding movement, linear guide presses a rough surface on the finger and positioner will move prosthesis hand horizontally to cause vibration. Before each test, it has to adjust the spatial position of prosthesis hand by positioner and rotator to assure the contact force is perpendicular to touch surface.

To stimulate prosthesis a series of rigid indenters are prepared with two type of ends, cylinder with plat or half spherical end for indentation and flat square with rough sandpaper attached for slide. The former indenters are manufactured in different diameter while the latters are attached by sandpaper with different roughness.

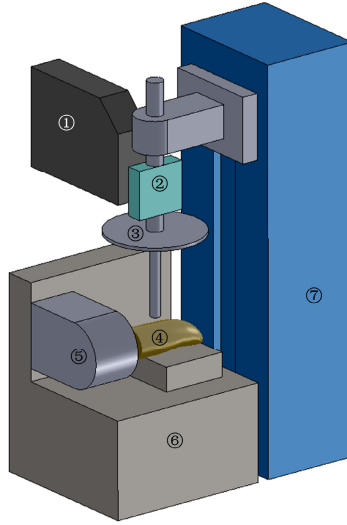


Fig. 1. Demonstration of mechatronic stimulator system with indenter head mounted (① laser distance sensor head, ② force gauge, ③ indenter head, ④ artificial finger with extrinsic sensors attached, ⑤ rotating step motor, ⑥ 3-DoF positioner, ⑦ liner guide)

2.2 Sensors and Feedback

The experiments require the force applied on target sensors is controlled and measurable. It is also necessary to measure the frequency of indenter when slide motion occurred. Between the linear guide and indenter a force gauge (EVT-14C-2kg, China) is implemented to measure the indentation force and the data are stored in PC. To record the vibration during slide motion, a piezoelectric stripe (PVDF) sensor (LDT0-028K, MEAS) is attached between sandpaper and rigid flat surface. The data from target sensors are acquired by a DAQ device (USB6212BNC, NI). Moreover, the rigid indenter of mechatronic stimulator is driven by a linear guide through a compressible force gauge, regarding the relatively low stiffness of the force gauge and elastic layer covered on artificial hand (which can improve the effectiveness of the grasping function and protect the frangible tactile sensors), a laser distance sensor (LK-G30, KEYENCE) is used for measuring the real indentation depth during the passive test to remove the effect of deformation (Fig.1).

However, what the force gauge reads is not equal to the force applied on the surface of contact area which can be derived from follow equation,

$$F_{FG}(t) = F_{IF}(t) + M_{IH}\ddot{z}(t) - M_{IH}g, \quad (1)$$

where $F_{FG}(t)$ is the value measured by force gauge, M_{IH} is the mass of indenter head, $z(t)$ is the indentation depth, g is gravitational acceleration and $F_{IF}(t)$ is the real indentation force caused by elastic layer over the rigid.

2.3 Control of System

The control architecture of whole mechatronic system is divided into two parts, high level for human interaction and low level for bottom control of system.

The high level control layer is used to input commands such as motion type (indentation or slipping), indentation force, frequency, position, slipping speed, *etc.* and output test results including data acquired from force gauge, distance sensor and target sensors. It not only saved some typical movement, like ramp of different speed, sine wave of different frequency and amplitude, but also could reproduce customized motions.

The task of low level layer is mainly on exciting the commands received from high level. It is in charge of controlling the 3-DoF positioner and the liner guide producing target indentation force. It is also able to acquire data from sensors in the system and recording signals from target sensor.

The indentation force (or normal pressure in sliding motion) is generated by liner guide driven by a step motor through a screw mandrel, so the low level layer is controlling the force in z direction by modifying the rotating speed of the step motor. The block diagram of closed-loop indentation force controller is shown in Fig.2.

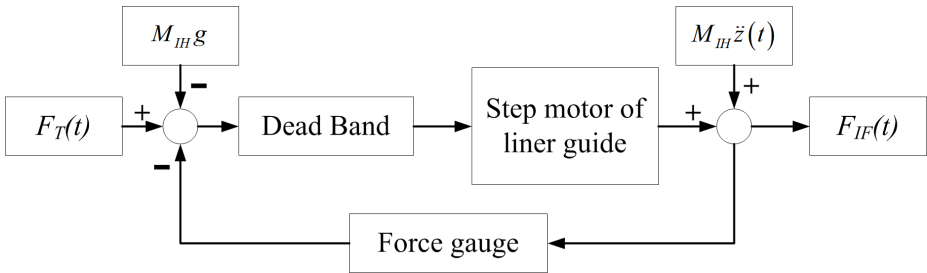


Fig. 2. The block diagram of closed-loop indentation force controller

3 Experiments and Results

3.1 Experiment Setup

Indenting Motion. In indentation test, 3-DoF manipulation stage is used to adjusting the position of prosthesis hand and liner guide is the source of the indentation force (Fig.3a). When artificial hand is steady and contact area is right under the indenter head, the liner guide begins to drive the stimulator in low speed (around 0.1mm/s) until the contact happens (when force gauge can read out minimum force). Then the step motor is operating under controlled so that the indenting motion is performed as experimenter commands, such as ramp, sine wave or other combination movement. All the data from sensors in mechatronic system and the signals of target sensor are recorded contemporaneously in PC.

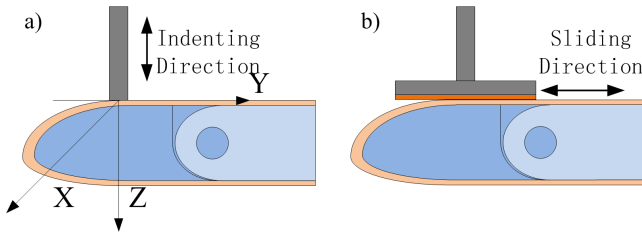


Fig. 3. The diagram of contact methods in indenting motion (a) and sliding motion (b)

Sliding Motion. In sliding test, the liner guide is driving a rigid flat with different sandpapers covered to produce normal pressure and texture contact while 3-DoF manipulation stage not only ensures the contact position but also slides the prosthesis hand in horizontal direction (Fig 3b). A series of experiment can be carried out with contact force and motion speed varying and the data from sensors are storage as in indenting test.

3.2 Data Acquired from Tactile Sensors

In the experiment section of this paper, two kind of commercial sensors is involved, a piezoresistive force sensor and a piezoelectric vibration sensor. Normally, piezoresistive sensor is placed under cover layer for static force detection and piezoelectric sensor is applied on the surface to catch dynamic vibration [7-8]. In this paper, several combinations of these two kinds of sensors are implemented as shown in Fig.4. The flexible cover layer is made of polydimethylsiloxane (PDMS) with a mixing ratio of curing agent and prepolymer is 1:10 in weight.

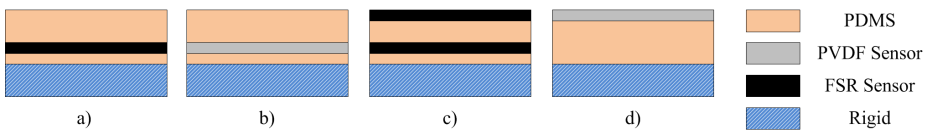


Fig. 4. The diagram of different combinations of PVDF and FSR sensors with PDMS covered

In the indentation test, two indenting movements are performed, ramp motion with speed varying from 0.1mm/s to 0.5mm/s through a stroke of 1mm and sine wave motion with fixed frequency and different peak forces. Ramp test is carried out on FSR sensors in Fig.4a and 4c, sine wave test is on both piezoresistive and piezoelectric sensors in Fig.4a and 4b. Data results are shown in Fig.5.

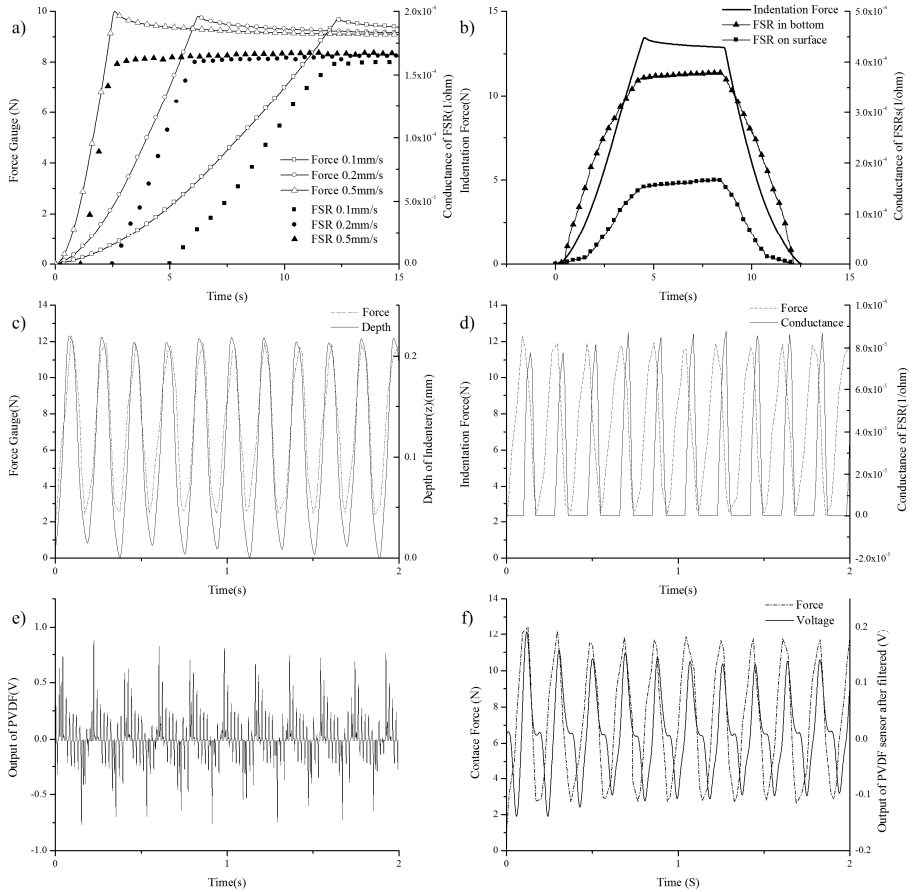


Fig. 5. Data results in indentation test. a) Ramp motion on the FSR as in Fig.4a at different speed. b) Ramp motion on FSRs as in Fig.4c at 0.2mm/s. c) Value read from force gauge and laser distance sensor in sine wave motion. d) Real contact force calculated from Eq.1 and the response from FSR. e) Voltage output of PVDF sensor as in Fig.4b after amplified in sine wave test. f) A low pass filter is added to get rid of industrial-frequency noise.

For FSR sensor, a voltage divider circuit is prepared and the output voltage calculated is described by

$$V_{out} = \frac{R_M V_+}{R_M + R_{FSR}}, \quad (2)$$

where V_+ is 5V and R_M is 5.1k Ω and the conductance of FSR is proportional to the force applied while the charge generated by PVDF sensor is amplified by a charge amplifier (DH5862, China,) and voltage outputs of these sensors are acquired by NI device synchronously.

From Fig.5a is shown that the PDMS layer (2mm) reduced the minimum sensitivity of FSR to 2N (a standard FSR400 is 0.1N). In Fig.5b, with the equivalent pressure applied, resistant change of FSR on surface is 2 times of its counterpart in the bottom. The mass of the indenter head used is 40g and the curve of real contact force is calculated by Equ.1 from the data in Fig.5c. Due to the reason mentioned above, the response curve of FSR in Fig.5d is not like that of contact force but in a spinous shape and also a lag between two waves is observed. A charge amplifier with a gain of 10mv/pC is implemented to get the result in Fig.5e. Due to high sensitivity to dynamic motion of piezoelectric sensors, it has to add a low pass filter (with passband edge at 10Hz and stopband edge at 20Hz) to get rid of power frequency(50Hz) noise and still a lag is generated.

In the sliding test, the artificial finger is stroke for a distance (8mm) at different speed (from 1mm/s to 5mm/s) while it is being indented by a rigid plane with sandpaper covered. This test is only carried out on PVDF sensor on surface (Fig.4d). The result curves are drawn in Fig.6

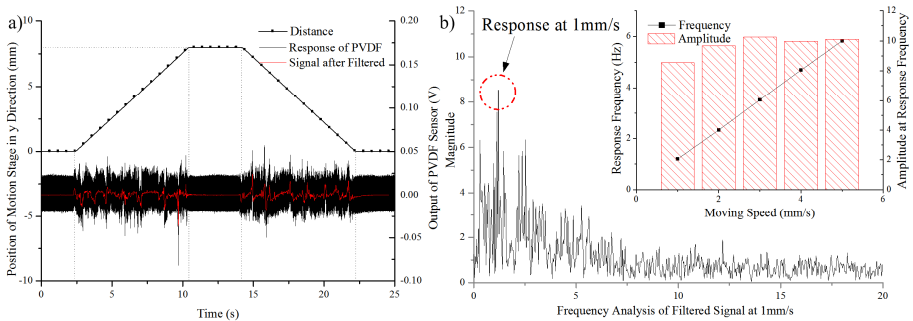


Fig. 6. Data results from sliding test. a) Motion stage position and voltage response of PVDF Sensor in 1mm/s test and a filter is used for noise removal. b) Frequency analysis of filtered signal from a). The same method is applied on results of the rest sliding tests and response frequency and amplitude related are shown in a graph.

After being processed by a filter with 20Hz cutoff frequency, the signal from PVDF sensor when motion stage was operating at 1mm/s is much effective. To analysis the frequency property of this filtered curve in Fig.6a, a FFT method is used and the amplitude versus frequency is drawn in Fig.6b and in this graph, max amplitude can be found at 1.2Hz. Repeating this method on other sliding tests, we can get max amplitude and related frequency in each motion and the result is also in Fig.6b. It is obviously the response frequency is proportional to sliding speed and the reason is the texture pattern of sandpaper is fixed and vibration is caused by relative slip between contact surfaces, therefore the frequency of vibration is proportional to relative speed and so is the response of PVDF sensor.

3.3 Analysis of Mechatronic Platform

To analyze the performance of the mechatronic stimulator, it is necessary to evaluate the effectiveness of motion control function of the developed system. In this analysis, several errors parameters related to indentation force are considered.

In sine wave motion of indentation test, error parameter is defined to quantitatively evaluate the dynamic performance of this system as followed,

$$\sigma_{force_peak}(1, N) = \sqrt{\frac{1}{N} \sum_{i=1}^N (F_{peak} - F_{des})^2}, \tag{3}$$

where σ_{force_peak} is the root mean square error in the interval of N peak, F_{peak} and F_{des} are applied and target contact force peak respectively. In ramp motion, error parameters of linearity and static drift are calculated by

$$\sigma_{nonlinearity} = \Delta F_{Max} / F_{des} \times 100\%, \tag{4}$$

$$\sigma_{drift}(t_a, t_b) = \sqrt{\frac{1}{t_b - t_a} \int_{t_a}^{t_b} (F_{gauge} - F_{des})^2 dt}, \tag{5}$$

where $\sigma_{nonlinearity}$ is the nonlinear error in ramp section, ΔF_{Max} is max difference between contact force and linear value, σ_{drift} is the static drift error during (t_a, t_b) , t_a is the time when indentation force stops increasing, F_{gauge} is the value read from force gauge and F_{des} is the target indentation force. Several error parameters are calculated for each motion and given in Table.1.

Table 1. Error parameters calculated for each motion

Error parameter	Motion type	Motion property	Error value
σ_{force_peak}	Sine wave motion	$F_{des}=9N$	0.1119N
		$F_{des}=12N$	0.1445N
		$F_{des}=15N$	0.1652N
$\sigma_{nonlinearity}$	Ramp motion	Speed=0.1mm/s	17.07%
		Speed=0.2mm/s	16.91%
		Speed=0.5mm/s	18.6%
σ_{drift}	Ramp motion	Speed=0.1mm/s	0.3206N
		Speed=0.2mm/s	0.4431N
		Speed=0.5mm/s	0.6387N

In sine wave motion, the stimulator can keep the error value under 0.2N when peak force is no more than 15N. The nonlinearity in ramp motion is mainly caused by elasticity of the cover layer (PDMS) on sensors so it did not change much when motion speed was increased. The t_b in drift error calculation equals to t_a+3s , and besides velocity of ramp, property of force gauge is another reason of this error. By

increasing the performances of liner guide and force sensor, these errors related to indentation force can still be reduced.

4 Conclusions

The development and validation of a mechatronic stimulator platform is presented in this work for research of tactile sensors on prosthesis hand. This system is able to produce precise repeatable and programmable stimulus in indenting and sliding motion on the surface of artificial hand with tactile sensors embedded. Future work will focus on fulfilling the function of active measurement which means the system could validate the sensors in prosthesis hand while the latter is operating. Meanwhile, the performance of indentation process will be improved with the means of replacing the liner guide by a controlled voice-coil motor associated with related controller.

Acknowledgments. This work was supported in part by National Basic Research Program of China (973 Program, 2011CB013303) and Science Fund for Creative Research Groups of National Natural Science Foundation of China (No.: 51221004).

References

1. Lee, M.H., Nicholls, H.R.: Tactile sensing for mechatronics-a state of the art survey. *Mechatronics* 9, 1–31 (1999)
2. Oddo, C.M., Beccai, L., Vitiello, N., Wasling, H.B., Wessberg, J., Carrozza, M.C.: A mechatronic platform for human touch studies. *Mechatronics* 21, 604–613 (2011)
3. Byrne, J.: A feedback controlled stimulator that delivers controlled displacements or forces to cutaneous mechanoreceptors. *IEEE Trans. Biomed. Eng.* 22, 66–69 (1975)
4. LaMotte, R.H., Whitehouse, G.M., Robinson, C.J., Davis, F.: A tactile stimulator for controlled movements of textured surfaces across the skin. *J. Electrophysiol. Tech.* 10, 1–17 (1983)
5. Goodwin, A.W., Morley, J.W., Clarke, C., Lumaksana, B., Darian-Smith, I.: A stimulator for moving textured surfaces sinusoidally across the skin. *J. Neurosci. Methods* 14, 121–125 (1985)
6. Jones, L.A., Lederman, S.J.: *Human Hand Function*. Oxford University Press (2006)
7. Edwards, J., Lawry, J., Rossiter, J., Melhuish, C.: Extracting textural features from tactile sensors. *Bioinspir. Biomim.* 3, 1–12 (2008)
8. Vászárhelyi, G., Ádám, M., Vázsonyi, É., Bársony, I., Dücső, C.: Effects of the elastic cover on tactile sensor arrays. *Sens. Actuat. A* 132, 245–251 (2006)

Simulation Study of Dipole Localization in MEG-Based BCI Using Magnetic Field Reconstruction

Liang Hu¹, Hui-min Shen¹, Wei-ting Liu¹, Kok-Meng Lee^{2,*}, and Xin Fu¹

¹ State Key Laboratory of Fluid Power Transmission and Control, Zhejiang University,
310027 Hangzhou, China

² George W. Woodruff School of Mechanical Engineering, Georgia Institute of Technology,
Atlanta, USA

{cmeehuli, hmshen, liuwt, xfu}@zju.edu.cn,
kokmeng.lee@me.gatech.edu

Abstract. Brain-computer interface (BCI) based on magnetoencephalography (MEG) provides intentional signals with high spatial resolution for communications of patients suffering severe motor dysfunctions. However, the incomplete measurements of the extremely weak magnetic field outside head bring significant uncertainties to active neural source (ANS) localization. This paper presents a novel computational method to improve the ANS localization accuracy. Based on the fact that the external magnetic field obeys the Maxwell equations quasistatic, the field can be reconstructed via solving a Laplace's equation with measured boundary conditions. By numerically solving Laplace's equation with finite element method (FEM), the signal-to-noise ratio of the reconstruction can be improved with high-order interference eliminated. The inverse estimation model, the reconstructions, and reconstruction selection are presented, and validated via simulation. Results show that about half of the dipole localization error is eliminated compared with method utilizing only measurements.

Keywords: Brain-computer interface (BCI), Magnetoencephalography (MEG), localization, magnetic field reconstruction, inverse computation.

1 Introduction

Brain-computer interface (BCI) provides a direct communication way by monitoring brain activities, and has brought great improvements to the life qualities of patients suffering severe motor dysfunction and loss of muscle control (such as spinal cord injury, locked-in syndrome and stroke). The detection methods of brain activity signals served for BCI include electroencephalography (EEG) [1], electrocorticogram (ECoG) [2], positron emission tomography (PET), functional magnetic resonance imaging (fMRI), and magnetoencephalography (MEG) [3]. Although technically demanding, the non-invasive MEG directly reflects the primary neuronal currents,

* Corresponding author.

combines high spatial/temporal resolution, and requires little time for training; thus, attracts researches to develop MEG-based BCI [4-6]. In MEG-based BCI studies, the information researchers would typically to extract from the surface measurements is approximate location of active neural source (ANS) for communication. Since the active neural region extension is small enough compared to its distance to sensors, the point-like model of equivalent current dipole (ECD) is always employed for ANS model. With appropriate constraints, the inverse problem is reduced into nonlinear optimization problem of estimating unknown parameters of ECD, and can be solved through least-square (LS) technique from measurements.

Considering high equipment cost, stringent requirements for measuring neural signals, simulation-based methods to improve ANS localization accuracy have become an effective way and been widely adopted [7, 8]. Various technologies have been developed for improving ANS localization accuracy, including whole-head superconducting quantum interference device (SQUID), signal space projection [9], independent component analysis [10], and signal space separation [8, 11].

This paper presents a synergistically computational and experimental method to enhance information associated to the estimated ANS via simulation. Unlike other estimation methods that rely solely on measurements, this synergistic method provides with reconstructed nearby magnetic field distribution with better signal-to-noise ratio (SNR) and requires no additional measurements for the estimation and no alteration to existing measuring equipment. The remainder of this paper offers the followings:

- 1) The principle and model of ANS localization are presented along with a statistical study on the selecting criterion of reconstruction for superimposing.
- 2) The improvements brought by superimposing the numerically reconstructed external field with improved SNR have been analyzed using simulated MEG data from a single ECD in a spherical symmetric head model. It is shown that about half of the dipole localization error (DLE) in ECD location estimation is eliminated by superimposed RD. Estimation results for different SNR (in range of 3 to 10) are additionally evaluated to validate the method.

2 Methodology

2.1 Inverse ANS Localization

Based on the fact that MEG is absolutely insensitive to the number shells [12], the head can be modeled as spherically symmetric conductor, and the ECD presented here represents a fixed neuroanatomical structure with fixed locations and orientations in different time slices [13]. As illustrated in Fig. 1(a), the neural activities are restricted in the sphere head (the black solid line) and the uniformly spaced sensor array (the blue dot-dashed line) measures the distribution of the normal flux density $\mathbf{D}_{r,m}$ on the upper half surface. Fig. 1(b) defines the spherical coordinates (r, θ, φ) .

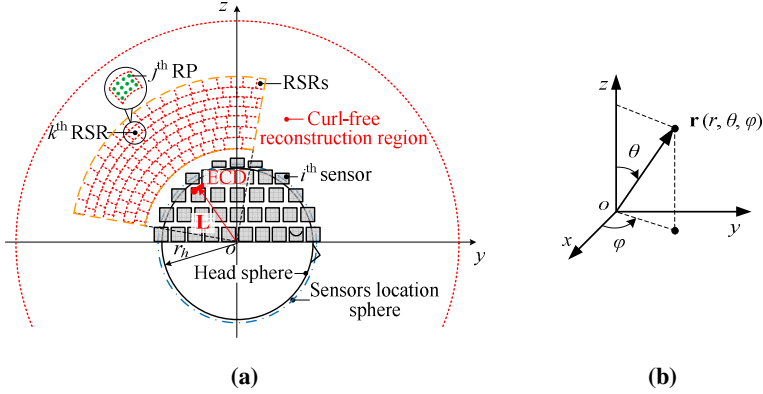


Fig. 1. (a). Cross-section on y - z plane illustrates an ECD locates at $\mathbf{L}(L_x, L_y, L_z)$ in a spherical head model which is modeled as a spherical symmetric conductor of radius r_h (the black solid line), N mutually independent single-axis sensors are uniformly spaced on the outer surface of spherical head (the blue dot-dashed line) and measure the normal component of magnetic field, and the curl-free reconstructed region (the red dashed line) with its division; x axis of rectangular coordinate system is orthogonal to y - z plane pointing into the paper; there are M reconstructed points (RPs) in the curl-free reconstructed region which is divided into K reconstructed subregions (RSRs) with J points in each; (b). Corresponding spherical coordinates of sensing system, zenith direction is z axis and azimuth axis is x axis; the polar angle θ is the angle between the zenith direction and vector \mathbf{r} , and the azimuth angle φ is the signed angle measured from the azimuth reference direction to the orthogonal projection of \mathbf{r} on the reference plane.

The forward mathematic model for magnetic field distribution $\mathbf{D}_{r,f}$ in Fig. 1(a) is presented below [12]:

$$D_{r,f}(\mathbf{L}, \mathbf{Q}, \mathbf{r}) = \frac{\mu_0 Q}{4\pi} \frac{(\mathbf{r} - \mathbf{L}) \times \mathbf{r}}{|\mathbf{r} - \mathbf{L}|^3} \cdot \mathbf{q} \quad (1)$$

As shown in Fig. 1(a), the vector \mathbf{L} defines the location of the ECD (moment $\mathbf{Q} = Q\mathbf{q}$ with magnitude Q along unit vector \mathbf{q}); as shown in Fig. 1(b), \mathbf{r} defines the i^{th} measured location or the j^{th} RP position.

Numerical approaches to the estimation of unknown source parameters are generally based on the widely used LS technique which attempts to find a set of parameters that minimizes the square of the difference between the observations and the predictions from the forward model in Eq. (1), as follows:

$$\min f(\mathbf{L}, \mathbf{Q}) = \min \left(\sum_{i=1}^N \|D_{r,m}(i) - D_{r,f}(\mathbf{L}, \mathbf{Q}, i)\|^2 \right) \quad (2)$$

where $D_{r,m}(i)$ is the normal magnetic flux density recorded by the i^{th} sensor; $D_{r,f}(\mathbf{L}, \mathbf{Q}, i)$ is the normal component of instantaneous magnetic field at the i^{th} measured position computed from Eq. (1).

2.2 Numerical Computation of External Magnetic Field

Though MEG signals are time-varying, their variation is relatively slow so that induction effects can be neglected, and MEG measuring systems (such as SQUID) are constructed that sensors, their container (called Dewar), and the adjacent space around them are free of magnetic sources and materials, strictly nonmagnetic [3]; thus, the biophysically generated magnetic field outside the head can be treated as quasi-static in current-free space as illustrated in Fig. 1 (the red dashed line) and presented as a gradient of a scalar magnetic potential obeying Laplace's equation. In physics, any potential field obeying Laplace's equation can be uniquely determined once the boundary conditions (BCs) are specified.

As shown in Fig. 1(a), the sensor measurements provide the necessary Neumann boundary condition on the upper half for reconstructing the field outside the head. Based on the biophysiology fact that the ANSs generally occur on the cerebral cortex close to the upper half surface, it is reasonable to assume the lower half has negligible field and the field strength of the unmeasured lower half surface to be zero. Additionally, the potential at the outer spherical surface (or the far field) of the reconstructed region approaches zero. We employ a finite element (FE) software COMSOL Multiphysics to numerically solve Laplace's equation with the mixed BCs. In the numerical computation procedure, the high-order noise is eliminated, leaving the computed external magnetic field with improved SNR.

With the reconstructed magnetic field distribution outside the head, the unknown ECD parameters are estimated by minimizing the objective function which relates to two contributions: measurements $\mathbf{D}_{r,m}$ and reconstruction $\mathbf{D}_{r,r}$

$$\min f(\mathbf{L}, \mathbf{Q}) = \min \left(\sum_{i=1}^N \|D_{r,m}(i) - D_{r,f}(\mathbf{L}, \mathbf{Q}, i)\|^2 + \sum_{j=1}^M \|D_{r,r}(j) - D_{r,f}(\mathbf{L}, \mathbf{Q}, j)\|^2 \right) \quad (3)$$

where $D_{r,r}(j)$ is the reconstructed normal magnetic flux density at the j^{th} RP; $D_{r,f}(\mathbf{L}, \mathbf{Q}, j)$ is the normal component of instantaneous magnetic field at the j^{th} RP computed from Eq. (1).

According to the principle of LS estimation [14], the objective function can be seen as the residual sum of squares between the real and observation quality, thus the introduction of reconstruction in the second part of Eq. (3) with improved SNR brings more veracity to the estimation of ECD location than traditional method based only on measurements.

In order to ensure both computational efficiency and high estimation accuracy, RSRs with more contribution to estimation improvement are needed to be selected. This selection procedure is detailed below:

Step 1: As shown in Fig. 1(a), the equally spaced M RPs in the reconstructed region outside the head are divided into K small subregions $\Omega_1, \dots, \Omega_K$ (called RSR) for pre-superimposing RSRs selection in next step, with each containing J RPs.

Step 2: The goodness of each RSR is evaluated by the mean dipole localization error (mDLE), which is defined as the mean distance between the location parameters estimated from measurements combined a RSR and the real source locations. Those effective RSRs (eff_RSRs) with goodness smaller than that computed from measurements are selected out and ranked in ascending order for superimposing.

Step 3: The first RSR for superimposing (called “sup_RSR”) is the one with the smallest mDLE; then the rest of the sup_RSRs are chosen from the eff_RSRs as follows:

- a) The rest of the sup_RSRs are superimposed to the selected sup_RSRs and measurements separately following the ascending order to estimate the location parameters, and the one with the smallest mDLE is chosen out as the next member of sup_RSRs;
- b) When choosing the $(w+1)^{\text{th}}$ sup_RSR, if each mDLE computed from combinations of each of the left eff_RSRs, measurements and the selected w sup_RSRs, is larger than mDLE computed from measurements combined the selected w sup_RSRs, the selection procedure for the sup_RSR stops.

3 Simulation and Results

3.1 Simulation

This method using reconstructions with the surface field measurements synergistically for ANS localization is evaluated by using simulated measurements. The head is modeled as spherically symmetric conductor of radius 95.0 mm [15]. The simulated instantaneous MEG data employed for estimation is composed of synthetically computed noise-free magnetic field and uniform zero-mean uncorrelated random Gaussian white noise with certain standard deviation. The mutually independent sensors are placed on a homocentric spherical surface at 16.0 mm above the surface of the head, sensor number $N=55$. Their locations are presented in Table 1, and the arc length between two adjacent sensors is approximately 40mm.

Table 1. Sensors locations, $S(i, j)=(R, \theta, \varphi)$ stands for the j^{th} sensor on θ - φ plane of the i^{th} level on the θ - z plane with radius R ($N=55$)

$S(i, j)$	$\Delta\varphi$	
$i=1, j=1, \dots, 17$	$2\pi/17$	$\theta = \pi/2 - (i-1)(\Delta\theta)$; $\Delta\theta = 0.37$; $\varphi = j(\Delta\varphi)$; $R=111.0$ mm;
$i=2, j=1, \dots, 16$	$2\pi/16$	
$i=3, j=1, \dots, 13$	$2\pi/13$	
$i=4, j=1, \dots, 8$	$2\pi/8$	
$i=5, j=1$	$\theta=0, \varphi=0$	

The uncertainty of estimation was analyzed statistically with total 100 samples, and the set of repetitions can be viewed as a set of independent realizations of MEG. In order to analyze the dependency between different levels of noise corruption and the corresponding achieved improvement, SNR ranging from 3 to 10 are simulated according to recorded MEG trials [16]. The SNR is defined as the ratio of the peak value of the computed noise-free results to the standard deviation of stated Gaussian white noise.

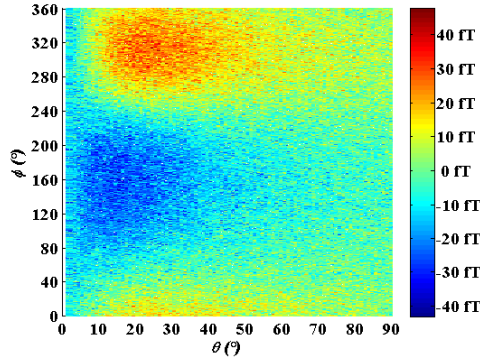


Fig. 2. Normal components distribution of the simulated magnetic field measurements with SNR=3

A unity magnitude ECD is assumed to locate in the cortical areas responsive to somatosensory inputs (in the primary somatosensory cortex in the post central gyrus [17]), and its location is ($L_x=-19.0$ mm, $L_y=5.0$ mm, $L_z=87.0$ mm) and moment orientation is ($\theta=0.287$, $\varphi=1.28$). The simulated MEG data with SNR=3 is shown in Fig. 2.

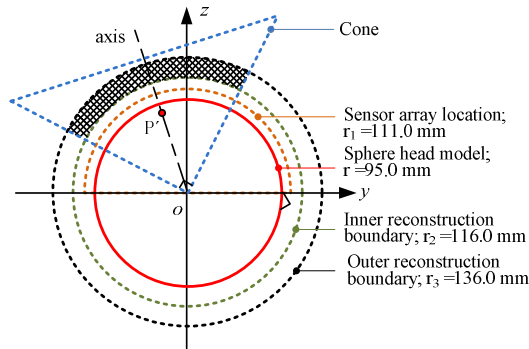


Fig. 3. Derivation geometric model of reconstructed points on y-z plane view

The derivation geometric model for reconstructed region is presented in Fig. 3. Based on the pre-estimated ECD location P' from measurements, the reconstructed region is chosen as the overlapping shaded part of a cone and the intersection of two homocentric spheres. As to the cone, its vertex lays at the origin of coordinate o , axis on the line directs from the origin of coordinate o to P' , and the angle of the top of the cone is 90° . There are 1350 reconstructed sample points evenly distributed in the intersection space of two homocentric spheres (with outer boundary radius of 136.0 mm, inner boundary radius of 116.0 mm) and the cone (the shaded region illustrated in Fig. 3). And the RPs are divided into 450 RSRs with 3 sample points in each RSR. To keep the completeness of information contained in RSR, the arc of each RSR on reconstructed sphere approximately equals the distance between each detecting sensor.

With simulated measurements as illustrated in Fig. 2, the magnetic field outside head was reconstructed via finite-element software COMSOL Multiphysics. In the discretization, we chose quadratic Lagrange elements, and the appropriate function $\tilde{\psi}$ is second-order polynomials on each mesh tetrahedron

3.2 Results

The proposed method combining measurements and reconstructed magnetic field outside the head are validated based on the simulation model aforementioned, with results presented below.

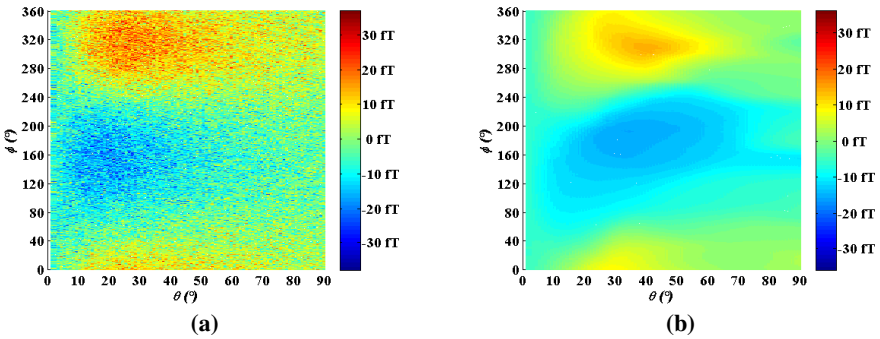


Fig. 4. (a) The observations contaminated by Gaussian white noise of the same level (SNR 3) of that on sensors on surface of radius 116.0 mm in the reconstructed region; (b) The reconstructed magnetic field distribution (normal component) on surface of radius 116.0 mm in the reconstructed region.

The simulated observations and reconstructed magnetic field of the same region (points distributed on surface of radius 116.0mm in the reconstructed region) are presented in Fig. 4: the simulated observations which are contaminated by Gaussian white noise of the same level with that in measurements (SNR=3) are illustrated in Fig. 4(a); the reconstructed magnetic field distribution computed according to Eqs. 3, 4 and 5 are presented in Fig. 4(b). The SNR of the reconstructed magnetic field in Fig. 4(b) equals 6, which is improved greatly and twice of the measurement (SNR=3). The estimation results computed from measurements with different levels of SNR (SNR=3, 5 and 10) are presented in Table 2.

The estimation results computed from measurements with different levels of SNR (SNR=3, 5 and 10) are presented in Table 2. The RSR selection results are illustrated in condition of SNR=3. According to *step 1* of the RSRs selection criterion mentioned above, totally 437 eff_RSRs are picked out firstly. The ECD parameters are estimated again utilizing measurements superimposed each chosen eff_RSR, and those eff_RSRs are evaluated and ranked by goodness mDLE from small to large. Then the ranked RSRs are superimposed to measurements continuously following the principle in *step 3* of the criterion. When looking for the 13th sup_RSR, the minimum mDLE of measurements superimposed all the previous 12 sup_RSRs together with each of the left eff_RSRs is larger than that computed from measurements superimposed the

previous 12 sup_RSRs, indicating the stop of superimposition. The selected 12 sup_RSRs central location, their goodness of estimation (mDLE) and distance (d_j) to simulated real ECD are presented in Table 2.

Table 2. Central locations (L_{RSR-x} , L_{RSR-y} , L_{RSR-z}), estimation goodness mDLE and distance from estimated ECD d_j of sup_RSRs, SNR=3

RSR NO.	Central location of RSRs (mm)			mDLE ^a	d_j (mm)
	L_{RSR-x}	L_{RSR-y}	L_{RSR-z}		
1	-11.8	16.0	124.4	10.4	39.7
2	-39.4	-14.8	108.1	10.0	35.4
3	2.7	13.2	23.3	9.5	36.5
4	-51.9	-13.2	102.9	9.2	40.8
5	-15.5	49.9	103.6	9.1	48.0
6	0	-44.9	107.0	9.0	56.8
7	-81.2	-27.1	92.4	8.9	66.3
8	58.8	-30.7	95.2	8.8	86.0
9	-60.0	-55.2	82.5	8.8	73.0
10	-66.7	86.6	81.0	8.8	94.6
11	67.9	30.3	107.8	8.7	92.9
12	-54.3	-63.6	107.3	8.7	79.7

^a mDLE is the goodness computed from measurements combining RD of the j^{th} superimposed RSR continuously.

The improvements of 12 sup_RSRs δ defined as the difference of mDLE computed from measurements and mDLE computed from combination of measurements and sup_RSRs divided by mDLE computed from measurements are presented in Fig. 5, and the maximum improvement is 30.3% compared to estimated result only from measurements. From Fig. 5 we can see that the trend of improvements brought by superimposing RSRs is smooth with the increase of sup_RSRs, suggesting different contribution of RSRs to ECD estimation improvement and the necessary of RSRs selection.

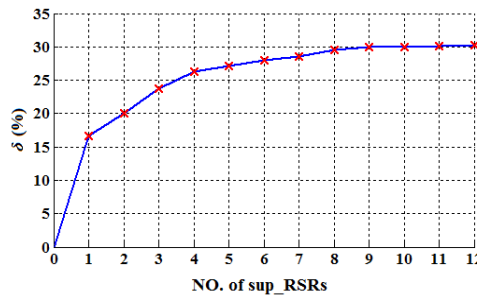


Fig. 5. δ of measurements combining 12 sup_RSRs sequentially, SNR=3

To evaluate the feasibility of this method with various SNRs, this method is applied to SNR=5 and 10 with 55 sensors. The estimation results along with the improvements of estimation are displayed in Table 3. The results in Table 3 suggest

that superimposing RD improves the estimation accuracy in the same way with different levels of noise; the goodness of measurements superimposed RD with SNR=3 (mDLE=8.7mm) approximates to that computed from measurements with SNR=5 (mDLE=8.5mm), indicating the improvement of SNR from superimposing sup_RSRs.

Table 3. The simulated real ECD location L_r , estimated localization L_m and goodness e_m computed from measurements, and estimated localization L_s and goodness e_s computed from measurements combining sup_RSRs with sensor number $N=55$ s and different levels of SNR (SNR=3, 5 and 10)

SNR	10	5	3
L_r (mm)		(- 19.0, 5.0, 87.0)	
L_m (mm)	(-18.5, 5.0, 87.3)	(-19.5, 6.6, 87.3)	(-19.6, 7.2, 86.7)
L_s (mm)	(-18.8, 5.3, 86.3)	(-19.5, 6.8, 84.5)	(-19.6, 6.9, 83.2)
e_m (mm)	4.4	8.5	12.5
e_s (mm)	2.7	6.0	8.7
δ (%)	38.6	29.4	43.4

In order to evaluate the proposed method, an example of estimation goodness computed from simulated measurements of 98 sensors (distributed in the same area on the sphere of 55 sensors, but has a higher distribution density) is conducted, and the mDLE estimated from 98 measurements is 7.1mm. Compared with mDLE of 55 sensors, we can see that estimation result with better goodness is possible to achieve by computing from fewer sensors through improved method, making the feasibility of sensor number decrease for compact MEG device.

4 Discussion and Conclusion

A novel approach for ECD estimation in MEG utilizing synergistic reconstructed magnetic field outside the head and measurements has been presented. The biophysically generated magnetic field outside the head can be treated as quasi-static in current-free space, thus the magnetic field is reconstructed by solving the Laplace's equation with measured BCs on the outer surface of head and expressed as a linear combination in terms of infinite series of magnetic field derived from measurements compromising ANS and noises. With truncated series the external noise can be greatly eliminated from reconstructed external magnetic field with interested magnetic field preserved. Then, external magnetic field with better SNR are selected out, and superimposed to the measurements for improved localization accuracy and reliability.

Simulation results show that the synergistic use of measurements along with reconstructed field improves ANS estimation accuracy. Twice SNR of the measurements can be achieved by exploiting the proposed method of magnetic field reconstruction. The inverse computation cost and time is greatly reduced by only 3%

of the RD involved the screening. The reduction of goodness mDLE by superimposing selected sup_RSRs with better SNR information eliminates nearly half of error in estimation compared with traditional estimation methods based on measurements solely. The approximate goodness of traditional method with signals SNR=3 equaling to proposed one with signals SNR=5, and the approximate goodness of traditional method with measurements of 98 sensors equaling to proposed one with 55 sensors, clearly makes the synergistically computational and experimental method applicable in study of ANS estimation and implies better localization accuracy.

In this paper, the sup_RSRs are off-line selected with the knowledge of real source location by simulations. Database of effective RSRs corresponding to different source locations will be created with systematic study in future work without dependence on real source location in sup_RSRs selection. Except that, replacement of measurement samples with less noisy reconstructed sample, investigation of the effects of sensor count, novel partitioning method of reconstructed region, and novel optimization algorithms on the efficiency and accuracy of the estimation, related to the improvement of ANS estimation will be carried out.

Besides, the localization method proposed in this paper can also be applied to other areas including medicine and industry, such as magnetic localization of capsule endoscopy and localization of excitation system.

Acknowledgments. The authors are grateful to the financial support of the National Basic Research Program (973) of China (No. 2011CB013300), the National Natural Science Foundation of China (No. 51105329), and the Key Scientific and Technological Innovation Team of Zhejiang Province (No. 2009R50011).

References

1. Graimann, B., Allison, B., Pfurtscheller, G.: *Brain-Computer Interfaces: Revolutionizing Human-Computer Interaction*. Springer, Heidelberg (2010)
2. Felton, E.A., Wilson, J.A., Williams, J.C., Garell, C.P.: Electrocorticographically Controlled Brain-Computer Interfaces using Motor and Sensory Imagery in Patients with Temporary Subdural Electrode Implants. Report of four cases. *J. Neurosurg.* 106, 495–500 (2007)
3. Hansen, P.C., Kringelbach, M.L., Salmelin, R.H.: *MEG: an Introduction to Methods*. Oxford University, New York (2010)
4. Mellinger, J., Schalk, G., Braun, C., Preissl, H., Rosenstiel, W., Birbaumer, N., Kubler, A.: An MEG-based brain-computer interface (BCI). *Neuroimage* 36(3), 581–593 (2007)
5. Buch, E., Weber, C., Cohen, L.G.: Think to Move: a Neuromagnetic Brain-Computer Interface (BCI) System for Chronic Stroke. *Stroke* 39, 910–917 (2008)
6. Wang, W., Sudre, G.P., Xu, Y., Kass, R.E., Collinger, J.L., Degenhart, A.D.: Decoding and Cortical Source Localization for Intended Movement Direction with MEG. *J. Neurophysiol.* 104(5), 2451–2461 (2010)
7. Babiloni, F., Babiloni, C., Carducci, F., Romani, G.L., Rossini, P.M., Angelone, L.M., Cincotti, F.: Multimodal Integration of EEG and MEG Data: a Simulation Study with Variable Signal-to-noise Ratio and Number of Sensors. *Hum. Brain Mapp.* 22, 52–62 (2004)

8. Taulu, S., Simola, J.: Spatiotemporal Signal Space Separation Method for Rejecting Nearby Interference in MEG Measurements. *Phys. Med. Biol.* 51, 1759–1768 (2006)
9. Uusitalo M. A., Ilmoniemi R. J.: Signal-space Projection Method for Separating MEG or EEG into Components. *Med. Biol. Eng. Comput.* 35, 135–140 (1997)
10. Vigário, R., Särelä, J., Jousmäki, V., Hämäläinen, M., Oja, E.: Independent Component Approach to the Analysis of EEG and MEG Recordings. *IEEE Trans. Biomed. Eng.* 47(5), 589–593 (2000)
11. Song, T., Gaa, K., Cui, L., Feffer, L., Lee, R.R., Huang, M.X.: Evaluation of Signal Space Separation Via Simulation. *Med. Biol. Eng. Comput.* 46, 923–932 (2008)
12. Hämäläinen, M., Hari, R., Ilmoniemi, R.J., Knuutila, J., Lounasmaa, O.V.: Magnetoencephalography: Theory, Instrumentation and Applications to Non-Invasive Studies of the Working Human Brain. *Rev. Mod. Phys.* 65(2), 413–498 (1993)
13. Scherg, M., Crannon, D.V.: Two Bilateral Sources of the Late AEP as Identified by a Spatio-Temporal Dipole Model. *Electroencephalogr. Clin. Neurophysiol.* 62(1), 32–44 (1985)
14. Casella, G.: *Statistical Inference*, 2nd edn. Duxbury, Pacific Grove (2002)
15. Cuffin, B.N.: Effects of Local Variations in Skull and Scalp Thickness on EEGs and MEGs. *IEEE Trans. Biomed. Eng.* 40(1), 28–42 (1993)
16. Regan, D.: *Human Brain Electrophysiology. Evoked Potentials and Evoked Magnetic Fields in Science and Medicine*. Elsevier Press, New York (1989)
17. Mauguière, F., Merlet, I., Forss, N., Vanni, S., Jousmäki, V., Adeleine, P., Hari, R.: Activation of a Distributed Somatosensory Cortical Network in the Human Brain. A Dipole Modelling Study of Magnetic Fields Evoked by Median Nerve Stimulation. Part I: Location and Activation Timing of SEF Sources. *Electroencephalogr. Clin. Neurophysiol.* 104, 281–289 (1997)

Fully Decentralized Cooperative Localization of a Robot Team: An Efficient and Centralized Equivalent Solution

Hua Mu, Mengyuan Dai, Ming Gao, and Xianfei Pan

College of Mechatronics and Automation,
National University of Defense Technology, Hunan 410073, P.R. China
huamu08@gmail.com

Abstract. This paper presents an efficient, centralized equivalent and fully decentralized solution to the cooperative localization of mobile robot teams. Formulating the cooperative localization problem in the framework of Bayesian estimation, the decentralized solution is designed by interlacing the calculation steps of *prediction* and *update* in a proper sequence. In the proposed solution, each robot fuses only the sensor data relevant to itself; information is shared among the robots by a chain communication topology. The solution yields linear minimum mean-square error estimates, equivalent to a centralized extended Kalman filter. There is no information redundancy and computation duplication among the robots. The solution can also be viewed from the perspective of implementing inference on a specific junction tree. The performance of the proposed algorithm is evaluated with simulation experiments.

Keywords: cooperative localization, decentralized solution, mobile robot team, Bayesian estimation, junction tree.

1 Introduction

In recent years, the cooperative localization of a robot team has received significant attention from the robotics community[1-3]. When the same external landmarks are used by different robots for self-localization or inter-robot observations are made, the states of the relevant robots are correlated. Cooperative localization is a joint estimation problem state over the time-history of the robot team, allowing the robots to share the localization resources and achieve higher overall performance.

A centralized solution to the cooperative localization problem is straightforward yet expensive and lack of robustness. Various decentralized solutions are proposed by many researchers. A decentralized Kalman filter approach is proposed in [4]. The essence of this method is to distribute the expectation vector and the covariance matrix of the joint probability among the robots; each robot is allocated its state expectation and the covariance block-row related to itself. The prediction of the covariance block-row involves each robot *broadcasting* the state transition matrix. The fusion of each measurement, either a measurement regarding only one robot or an

inter-robot measurement, updates the parameters allocated to each robot, which requires the observer and the observed robot to *broadcast* the measurement information and the covariance block-rows. The operation scales poorly with the number of the robots and the number of the measurements. Actually, the update operation in standard Kalman filter framework is difficult to be distributed since the states are correlated to each other.

The information filter with delayed states [5] is appealing since both the prediction and the update are local operations to each robot and can be easily distributed. The moment recovery, however, manipulates global information and seems to be an obstacle to a decentralized solution. The solution proposed in [6] employs the incremental Cholesky modifications for efficient moment recovery. The sparse Cholesky factors of the joint state estimate are pipelined from robot to robot and the moment recovery for a group of states is accomplished at some robot who accumulates enough Cholesky factors. The solution is communication expensive since the Cholesky factors are duplicated at each robot in fact. The solution presented in [7] reduces the communication cost at the price of lower localization accuracy. In [7], each robot maintains a set of information parameters with the same size of the parameters for the joint delayed states. Each robot only integrates data from its own sensors. When an inter-robot measurement occurs, the two robots exchange their stored data and fuse the data based on convex combination. The moment recovery can be implemented in a centralized manner at each robot. The result is consistent and unbiased, yet not a minimum mean square error estimate.

Very recently another decentralized solution is presented in [8]. It achieves centralized-equivalent estimates, yet requiring a robot to transmit all odometric data to its neighbors, and to duplicate the data fusion effort.

In [9], a decentralized approach based on junction tree algorithm is designed to solve the cooperative localization problem. In the decentralized formulation, the local sensor data at each robot are integrated into potentials of the cliques of junction trees; the information is shared among the robots through message passing between cliques. The information parameterization of Gaussian distributions is utilized. The decentralized junction tree approach actually provides a general framework, within which there are a number of implementations for a fixed problem due to multiple choices of the junction tree.

This paper introduces a decentralized solution to the cooperative localization problem which could be deduced within the framework of the junction tree. Different from the work in [9], this work utilizes the moments form parameterization. The moments parameters have explicit physical meaning and the moments parameterization avoids the troubles brought by the moment recovery. We point out that the solution can be illustrated outside the context of the junction tree, instead from the perspective of Bayesian estimation.

2 Problem Formulation

This section formulates the problem of cooperative localization in the framework of Bayesian estimation. Consider a team of mobile robots. Each robot is equipped with

dead-reckoning sensors to measure self-motion; odometer or inertial measurement unit for example. Some robots carry sensors that provide relative position measurements (range and/or bearing) among robots or between robots and the environment; such as cameras, laser range-finders. Some robots can correct its dead-reckoning error. In the case that the environment map is known, the measurements between a robot and the environment can be utilized to bound the dead-reckoning error. Otherwise, the sensor like GPS can provide absolute localization information. The robots can communicate with each other. The cooperative localization task is to estimate the state (position, orientation, velocity etc.) of each robot making use of both its own observations and those observations made by and of other robots. The robots are identified by capitals A, B, C , etc .

2.1 State Space Model

The state of robot A at time instance k is denoted by x_k^A . Assume the motion model of robot A is given as

$$x_{k+1}^A = f(x_k^A, u_k) + G_k w_k \quad (1)$$

where u_k is the system input at time step k , w_k is the process noise, $w_k \sim \mathbb{N}_m(w_k; 0, Q)$, and G_k is a matrix with proper dimensions. $\mathbb{N}_m(v; \mu, P)$ represents a Gaussian distribution over v with mean μ and covariance P .

The GPS-like measurement of robot A at time step k is denoted z_k^A . The observation model is given as

$$z_k^A = h_1(x_k^A) + r_{1k} \quad (2)$$

where r_{1k} is the measurement noise, $r_{1k} \sim \mathbb{N}_m(r_{1k}; 0, R_1)$.

The measurement that robot B makes to robot A at time step k is denoted by z_k^{BA} . The observation model is defined as

$$z_k^{BA} = h_2(x_k^A, x_k^B) + r_{2k} \quad (3)$$

where r_{2k} is the measurement noise, $r_{2k} \sim \mathbb{N}_m(r_{2k}; 0, R_2)$.

If functions $f(\cdot)$, $h_1(\cdot)$ and $h_2(\cdot)$ are nonlinear, Taylor expansions are used to linearize the models to make the inference tractable. The linearized system is given in Table 1., where μ_k^A is the best available mean estimate of x_k^A .

Table 1. The linearized space model

model	linearized model	meaning of symbols
(1)	$x_{k+1}^A = f(\mu_k^A, u_k) + F(x_k^A - \mu_k^A) + G_k w_k$	$F = \left. \frac{\partial f}{\partial x_k^A} \right _{x_k^A = \mu_k^A}$
(2)	$z_k^A = h_1(\mu_k^A) + H_1(x_k^A - \mu_k^A) + r_{1k}$	$H_1 = \left. \frac{\partial h_1}{\partial x_k^A} \right _{x_k^A = \mu_k^A}$
(3)	$z_k^{BA} = h_2(\mu_k^A, \mu_k^B) + H_2^A(x_k^A - \mu_k^A) + H_2^B(x_k^B - \mu_k^B) + r_{2k}$	$H_2^A = \left. \frac{\partial h_2}{\partial x_k^A} \right _{x_k^A = \mu_k^A, x_k^B = \mu_k^B}$, $H_2^B = \left. \frac{\partial h_2}{\partial x_k^B} \right _{x_k^A = \mu_k^A, x_k^B = \mu_k^B}$

Assume the initial state of each robot is a Gaussian variable. The linearized system in Table 1. defines the following conditional distributions

$$p(x_{k+1}^A | x_k^A) = \mathbb{N}_m(x_{k+1}^A; Fx_k^A + f(\mu_k^A, u_k) - F\mu_k^A, \bar{Q}) \quad (4)$$

$$p(z_k^A | x_k^A) = \mathbb{N}_m(z_k^A; H_1 x_k^A + h_1(\mu_k^A) - H_1 \mu_k^A, R_1) \quad (5)$$

$$p(z_k^{BA} | x_k^A, x_k^B) = \mathbb{N}_m(z_k^{BA}; H_2^A x_k^A + H_2^B x_k^B + h_2(\mu_k^A, \mu_k^B) - H_2^A \mu_k^A - H_2^B \mu_k^B, R_2) \quad (6)$$

where $\bar{Q} = G_k Q G_k^T$.

2.2 Bayesian Estimation

Let Z_k denote the collection of the measurements made at time step k , including the inter-robot measurements and the intro-robot measurements. Let \mathbb{Z}_k denote the collection of the measurements up to time step k , namely, $\mathbb{Z}_k = \{Z_1, Z_2, \dots, Z_k\}$. The task of cooperative localization is to estimate the posterior state for each robot, which can be given by $p(x_k^A, x_k^B, x_k^C, \dots | \mathbb{Z}_k)$. The estimation is implemented iteratively as follows:

$$\text{prediction: } p(x_{k+1}^{R1}, \dots, x_{k+1}^{RN} | \mathbb{Z}_k) = \int p(x_k^{R1}, \dots, x_k^{RN}) p(x_{k+1}^{R1} | x_k^{R1}) \dots p(x_{k+1}^{RN} | x_k^{RN}) dx_k^{R1} \dots dx_k^{RN} \quad (7)$$

$$\text{update: } p(x_{k+1}^{R1}, \dots, x_{k+1}^{RN} | \mathbb{Z}_{k+1}) = \frac{p(x_{k+1}^{R1}, \dots, x_{k+1}^{RN}) \prod_{i=1}^N p(z_{k+1}^{Ri} | x_{k+1}^{Ri}) \prod_{j \neq i} p(z_{k+1}^{RiRj} | x_{k+1}^{Ri}, x_{k+1}^{Rj})}{\prod_{i=1}^N p(z_{k+1}^{Ri}) \prod_{j \neq i} p(z_{k+1}^{RiRj})} \quad (8)$$

In each cycle, the computation is composed of two parts: *prediction* and *update*. In the *prediction* part, the joint state probability is propagated from time step $k-1$ to time step k . In the *update* part, the inter-robot measurements and the intro-robot

measurements are fused. With the Gaussian assumption, the inference for the linearized system can be accomplished by the extended Kalman filter (EKF), providing the expectation and covariance of the probability distribution of the joint states.

Inspecting that both *prediction* and *update* are actually multi-step calculations, a fully decentralized solution is proposed in the paper by arranging the calculation steps of *prediction* and *update* in a proper sequence. In the decentralized solution, *prediction* is accomplished by each robot predicting its own state and *update* is accomplished by each robot fusing the measurements relevant to itself; the state predictions and the measurements fusions are implemented by turns. The messages passed between robots are the joint probabilities where only part of robots doing predictions and measurement updates. The posterior joint probability is obtained by a certain robot.

3 A Fully Decentralized Solution: An Example

Example. Consider the cooperative localization of three robots which are labeled as *A*, *B* and *C*. Each robot is equipped with an odometry. Robot *A* is equipped with a GPS receiver to obtain its position. Robot *B* has a laser range-finder which can make range measurements to the other two robots (See Fig.1). The three robots can communicate with each other by a local wireless network.

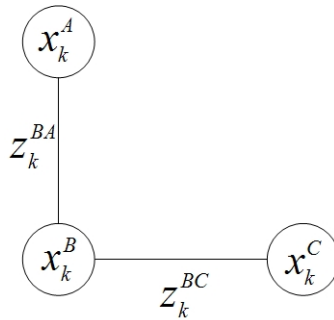


Fig. 1. The inter-robot measurements

3.1 Estimation at Time Step $k = 1$

In the beginning, the robot states are irrelevant to each other. The state prediction and the fusion of the intro-robot measurement are implemented in the same way at each robot. Take robot *A* for example.

$$\text{prediction: } p(x_1^A) = \int p(x_0^A) p(x_1^A | x_0^A) dx_0^A$$

$$\text{update(if needed): } p(x_1^A | z_1^A) = \frac{p(x_1^A) p(z_1^A | x_1^A)}{p(z_1^A)}$$

To fuse the inter-robot measurements, the joint state probability should be constructed and this involves the communication of the state estimation between

robots. The joint state can be constructed incrementally if the robots communicate in a chain. An inter-robot measurement can be fused either at the observer or the observed when the two relevant states are included into the joint state. The order of the robots on the communication chain is not critical. Assume robot B sends a message of $p(x_1^B)$ to robot C and robot C constructs a joint state as follows,

$$p(x_1^B, x_1^C) = p(x_1^B)p(x_1^C) \quad (9)$$

Then robot C can fuse the observation z_1^{BC} :

$$p(x_1^B, x_1^C | z_1^{BC}) = \frac{p(x_1^B, x_1^C)p(z_1^{BC} | x_1^B, x_1^C)}{p(z_1^{BC})} \quad (10)$$

Robot C then sends its estimation to Robot A . After receiving the estimation message, robot A carries on the joint state construction and the inter-robot measurement fusion, just like robot C .

$$p(x_1^A, x_1^B, x_1^C | z_1^A, z_1^{BC}) = p(x_1^A | z_1^A)p(x_1^B, x_1^C | z_1^{BC}) \quad (11)$$

$$p(x_1^A, x_1^B, x_1^C | z_1^A, z_1^{BC}, z_1^{BA}) = \frac{p(x_1^A, x_1^B, x_1^C | z_1^A, z_1^{BC})p(z_1^{BA} | x_1^B, x_1^A)}{p(z_1^{BA})} \quad (12)$$

3.2 Estimation with Correlated States

The robot states become correlated due to the fusion of the inter-robot measurement, which is clearly shown in the above subsection. Without loss of generality, we assume the states are correlated to each other when estimating the states of time step $k+1$ ($k \geq 1$). The prior joint state is represented by $p(x_k^A, x_k^B, x_k^C | Z_k)$.

The robot team satisfies the following assumptions before implementing the $k+1$ estimation:

1. The prior is held by a robot, say robot A .
2. The intro-robot measurements are held by the robot who makes the measurements. That is to say, there is no communication among the robots about the intro-robot measurements.
3. The inter-robot measurements are held by the two relevant robots. For example, the measurement z_k^{BA} is stored at both robot A and robot B . This requires a measuring robot to send the inter-robot measurement information to the observed robot.

Assume $Z_k = \{z_k^A, z_k^{BA}, z_k^{BC}\}$. Again the robots need to communicate in a chain. It's better for robot A to start the estimation since it holds the prior joint state. The decentralized solution places no constraint on the locations of the other two robots at the communication chain. Take the communication topology of $A \rightarrow B \rightarrow C$ for

example. The computations implemented by each robot in the fully decentralized solution are as follows.

Robot A:

$$\text{prediction: } p(x_k^B, x_k^C, x_{k+1}^A | \mathbb{Z}_k) = \int p(x_k^A, x_k^B, x_k^C | \mathbb{Z}_k) p(x_{k+1}^A | x_k^A) dx_k^A \quad (13)$$

$$\text{update: } p(x_k^B, x_k^C, x_{k+1}^A | \mathbb{Z}_k, z_{k+1}^A) = \frac{p(x_k^B, x_k^C, x_{k+1}^A | \mathbb{Z}_k) p(z_{k+1}^A | x_{k+1}^A)}{p(z_{k+1}^A)} \quad (14)$$

Robot B:

$$\text{prediction: } p(x_{k+1}^B, x_k^C, x_{k+1}^A | \mathbb{Z}_k, z_{k+1}^A) = \int p(x_k^B, x_k^C, x_{k+1}^A | \mathbb{Z}_k, z_{k+1}^A) p(x_{k+1}^B | x_k^B) dx_k^B \quad (15)$$

$$\text{update: } p(x_{k+1}^B, x_k^C, x_{k+1}^A | \mathbb{Z}_k, z_{k+1}^A, z_{k+1}^{BA}) = \frac{p(x_{k+1}^B, x_k^C, x_{k+1}^A | \mathbb{Z}_k, z_{k+1}^A) p(z_{k+1}^{BA} | x_{k+1}^B, x_{k+1}^A)}{p(z_{k+1}^{BA})} \quad (16)$$

Robot C:

$$\text{prediction: } p(x_{k+1}^B, x_{k+1}^C, x_{k+1}^A | \mathbb{Z}_k, z_{k+1}^A, z_{k+1}^{BA}) = \int p(x_{k+1}^B, x_{k+1}^C, x_{k+1}^A | \mathbb{Z}_k, z_{k+1}^A, z_{k+1}^{BA}) p(x_{k+1}^C | x_{k+1}^B) dx_{k+1}^C \quad (17)$$

$$\text{update: } p(x_{k+1}^B, x_{k+1}^C, x_{k+1}^A | \mathbb{Z}_{k+1}) = \frac{p(x_{k+1}^B, x_{k+1}^C, x_{k+1}^A | \mathbb{Z}_k, z_{k+1}^A, z_{k+1}^{BA}) p(z_{k+1}^{BC} | x_{k+1}^B, x_{k+1}^C)}{p(z_{k+1}^{BC})} \quad (18)$$

At the end of $k+1$ estimation, robot C achieves the posterior state estimation for each robot. It can send the results to the other robots. To estimate the states at next time step, it's better to start the calculations from robot C to avoid unnecessary communication.

4 A Fully Decentralized Solution: General Cases

4.1 Perspective of the Bayesian Estimation

The solution for the example of three robots in Section 3 can be generalized to a team of N robots. The observer who made an inter-robot measurement is required to send a measurement message to the observed robot, which ensures the measurement can always be fused by one of the two robots. Except the communication of the inter-robot measurements, the communication of the state estimation requires a chain topology. The only thing a robot should know about other robots is the IDs (identifications) of its neighbors. In the applications where there exists a fixed communication chain, the neighbors' IDs can be downloaded to each robot as prior information. In the cases where it is hard to find a fixed communication chain due to the movements of the robots, the communication chain can be built dynamically for different estimation cycles. Each robot acts in a modular way described as follows.

1. For time step $k = 1$:

- Predicting its own state since the states are irrelevant at the moment.
- Updating its own state by fusing intro-robot measurements if there is any.
- If there is an estimation message sending from a neighbor:
 - receiving the message and then calculates the joint state probability;
 - updating the joint state by fusing the inter-robot measurements that the relevant states appear in the joint state.
- Sending an estimation message to a neighbor with whom it has not communicated any estimation message in this estimation cycle. If a robot can not find such a neighbor, the estimation finishes up and the robot is identified as the starting robot for the next estimation cycle.

2. For time step $k + 1 (k = 1, 2, \dots)$:

If the robot is the starting robot or if the robot receives an estimation message from its neighbor:

- Predicting its own state in the joint state probability.
- Updating the joint state by fusing intro-robot measurements if there is any.
- Updating the joint state by fusing the inter-robot measurements that the relevant states appear in the joint state.
- Sending an estimation message to a neighbor with whom it has not communicated any estimation message in this estimation cycle. If a robot can not find such a neighbor, the estimation finishes up and the robot is identified as the starting robot for the next estimation cycle.

In the Bayesian estimation framework, both the *prediction* and the *update* are composed of multiple steps. The decentralized solution interlaces these steps to make each robot fuse its local sensor data and share its information across the team with proper communication strategy. For a linearized system model, the estimates generated by the decentralized solution achieve the same accuracy as a centralized EKF, if given the same data. In this sense, the decentralized solution is optimal since it yields minimum mean-square error estimation.

4.2 Perspective of the Junction Tree Algorithm

The proposed solution is actually a special implementation of the junction tree solution in [9]. The junction tree used for inference is specific. Firstly, the cliques of the junction tree are formulated using the elimination order as follows. The measurement variables are eliminated before the state variables and the state variables at time step $k - 1$ are eliminated before the states at time step k . The elimination order of the state variables at time step $k - 1$ determines the communication chain of robots. The construction of a junction tree is still not unique from the cliques. An optimal junction tree in terms of the minimum communication cost among the robots can be determined by making the initialization of cliques local to each robot. The junction tree for the cooperative localization at time step k for the example in Section 3 is depicted in Fig.2.

The standard Hugin strategy is adopted as the message passing strategy for the inference on the junction tree. Assume the states of robots are irrelevant with each other at the beginning. The overall decentralized solution is implemented in terms of Hugin algorithm as follows.

1. Initialization

Each robot is informed the IDs of its neighbors in the communication chain. The potentials of the measurement cliques are initialized as the measurement likelihoods.

For $k=1$, the state potentials of all the robots are initialized in the same way. Take robot A for example. The state potential of robot A is initialized as $p(x_0^A)p(x_1^A | x_0^A)$.

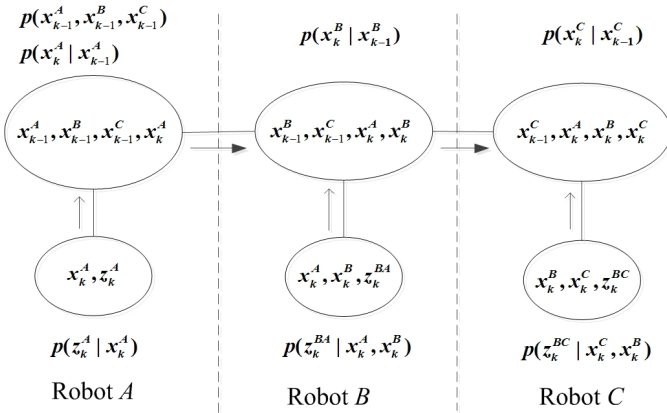


Fig. 2. The junction tree for inference for time step k ($k \geq 1$) for the example in Section 3, with the initial potentials of the cliques given for $k \geq 2$. The dotted lines illustrates the allocation of the cliques to the robots. The arrows with dark head stand for the message passing involving communication between robots, while the arrows with simple head represent the message passing between cliques held by the same robot.

For $k \geq 2$, the state potential of the robot who holds the prior, take robot A for example, is initialized as $p(x_{k-1}^A, x_{k-1}^B, \dots | \mathbb{Z}_{k-1})p(x_k^A | x_{k-1}^A)$. The state potential for other robots, take robot B for example, is initialized as $p(x_k^B | x_{k-1}^B)$.

2. Inference, $k \geq 1$

When a robot makes an inter-robot measurement, it sends a measurement message to the observed robot. Each robot manipulates its state potential by the following operations.

- (1) Multiplying in the estimation message passed to it if there is any, and denoting the ID of the robot who passed the message to it as X.
- (2) Incorporating the measurement likelihoods if there is any, including intro-robot measurements and inter-robot measurements.

(3) Eliminating the older own state from the state potential. If there is another neighbor different from X , formulating an estimation message from the resultant potential and transmitting to that neighbor. Otherwise, the resultant potential gives the required state estimates of time instance k for all the robots. The state of this robot should be eliminated first when constructing junction tree for next cycle inference.

5 Performance Evaluation and Analysis

In this section, we perform simulations to validate our approach and analyze the performance in terms of accuracy, modularity, scalability and robustness.

5.1 Simulation

A conventional two-wheel vehicle model is used and the trajectories of robots are generated by setting waypoints. Three robots (labeled with A , B and C) are considered. Assume each robot has odometer for motion measurement. Robot A and robot B each has a range finder which can make range measurements to other robots lying within 150m. Robot B also has a GPS receiver. The standard deviations are: initial positions, 8m; velocity measurements, 0.6m/s; steering angle measurements, 10degree; GPS measurements, 2m; range measurements, 0.1m. Data association for the range observations is assumed known.

Fig. 3 provides the robot trajectories with and without cooperative localization, together with the ground truth. The cooperative localization errors for robot A in x -axis and y -axis are given in Fig.4, together with the 3σ uncertainty. There is no inter-robot range measurement relevant to robot A before 15s, since the distances to the other robots are larger than 150m, beyond the limit of the range finder. After 15s, the localization error for robot A is reduced sharply and maintained small due to the fusion of the range measurements. The benefit of the cooperative localization is obvious. The accuracy of our decentralized solution is the same with a centralized EKF.

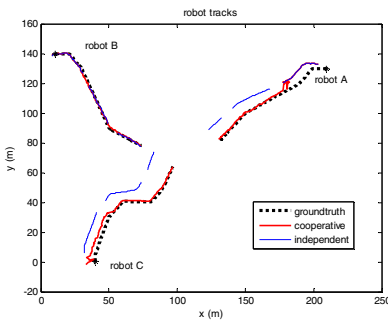


Fig. 3. The robot trajectories

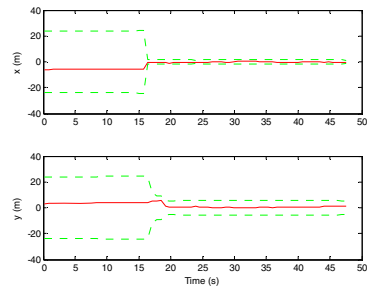


Fig. 4. The cooperative localization error for robot A

5.2 Analysis

The proposed solution has following advantages.

(1) Accuracy. The proposed solution is optimal in terms of the linearized system model of the cooperative navigation problem. However, the problem itself is actually a nonlinear problem, especially the observation equations of the inter-robot measurements. The loss of the accuracy due to the linearization can be reduced utilizing the relinearization technique. Each iteration of relinearization repeats the whole estimation process except the linearization points are updated as estimates of last iteration.

(2) Modularity. No global knowledge of the robots team is required a priori, each robot can be constructed and programmed in a modular fashion, allowing dynamic system configuration. In the decentralized cooperative navigation solution, the communication requirements between robots are allowed to change dynamically, as long as the whole team can communicate in a chain structure.

(3) Scalability. The proposed solution has good scalability especially among the centralized-equivalent solutions. The computation of data fusion is distributed to each robot pretty much evenly without any duplication. No broadcast is involved. The communication load is not only lower than most of the other centralized-equivalent solutions, but also is comparable with the solution in [7]. The communication of the inter-robot measurements in the two solutions is the same. The bulk of the communication of estimates is $2m(Nd)^2$ for the solution in [7] and $(N-1)(Nd)^2$ for the solution in this work, where m is the number of the inter-robot measurements, N is the number of the robots, and d is the state dimension for single robot. When it satisfies $m > (N-1)/2$, which are common cases, our solution has lower communication costs.

(4) Robustness. The communication chain can be built dynamically in each estimation cycle, imposing the least requirements on the connectivity of the robots. Each robot has a joint state estimate for the team, at most one estimation cycle earlier. As a result the cooperative localization could be restarted at any other robot when a robot fails.

6 Conclusions

In the paper, a novel decentralized solution to the cooperative localization problems of robot teams is investigated. The solution is designed by interlacing the calculation steps of *prediction* and *update* in a proper sequence. In the proposed solution, each robot fuses only the sensor data relevant to itself and shares estimation information with its neighbors on a chain communication topology. The solution is centralized-equivalent, in the sense that it yields linear minimum mean-square error estimates, equivalent to a centralized extended Kalman filter given the same data. The solution has good scalability since there is no information redundancy and computation duplication among the robots. Each robot acts in a modular manner and the solution is robust to robot failure. The solution can also be viewed from the perspective of implementing inference on a specific junction tree.

A simulation scenario of three ground robots is designed to verify our approach. Our simulated system has time-synchronous measurements. However, the decentralized algorithm applies equally to real-world asynchronous systems, in which case time-alignment is performed by projecting forward the platform states (according to the motion model) to match the observation time-stamps. This is the same approach as is routinely applied in centralized filtering systems. The approach is not limited to the scenario described here; it can be applied to multiple aerial vehicles and multiple underwater vehicles as well. Also, the decentralized structure appears to be a general paradigm for decentralized estimation, like cooperative target tracking, cooperative exploration, etc.

References

1. Bahr, A., Leonard, J.J., Maurice, F.F.: Cooperative Localization for Autonomous Underwater Vehicles. *The International Journal of Robotics Research* 28(6), 714–728 (2009)
2. Sharma, R.: Bearing-only Cooperative-Localization and Path-Planning of Ground and Aerial Robots. PhD thesis, Brigham Young University (2011)
3. Savic, V., Zazo, S.: Cooperative localization in mobile networks using nonparametric variants of belief propagation. *Ad Hoc Networks* 11(1), 138–150 (2013)
4. Roumeliotis, S.I., Bekey, G.A.: Distributed Multi-Robot Localization. *IEEE Transactions on Robotics and Automation* 18(5), 781–795 (2002)
5. Eustice, R.M., Singh, H., Leonard, J.J.: Exactly Sparse Delayed-State Filters for View-Based SLAM. *IEEE Trans. on Robotics* 22(6), 1100–1114 (2006)
6. Mu, H., Bailey, T., Durrant-Whyte, H., et al.: Decentralised Solutions to the Cooperative Multi-Platform Navigation Problem. *IEEE Transactions on Aerospace and Electronic Systems* 47(2), 1433–1449 (2011)
7. Cristofaro, A., Renzaglia, A., Martinelli, A. (eds.): Distributed Information Filters for MAV Cooperative Localization. *Distributed Autonomous Robotic Systems*. Springer, Heidelberg (2013)
8. Leung, K.Y.K., Barfoot, T.D., Liu, H.H.T.: Decentralized localization of sparsely-communicating robot networks: A centralized equivalent approach. *IEEE Transactions on Robotics* 26(1), 62–77 (2010)
9. Mu, H., Wu, M., Ma, H., Wu, W.: A Decentralized Junction Tree Approach to Mobile Robots Cooperative Localization. In: Liu, H., Ding, H., Xiong, Z., Zhu, X. (eds.) *ICIRA 2010, Part I. LNCS*, vol. 6424, pp. 736–748. Springer, Heidelberg (2010)

Development of a Sound Source Localization System for Assisting Group Conversation

Mihoko Otake¹, Myagmarbayar Nergui¹, Seong-eun Moon¹,
Kentaro Takagi², Tsutomu Kamashima², and Kazuhiro Nakadai^{3,4}

¹ Chiba University, Graduate School of Engineering,
1-33 Yayoi-cho, Inage-ku, Chiba, 263-8522, Japan

² System in Frontter Inc.

³ Tokyo Institute of Technology

⁴ Honda Research Institute

{otake,myagaa}@chiba-u.jp

Abstract. In this study, we developed a sound source localization system, which consists of Jellyfish-02 and HARK robot audition software, in order to reduce the number of wires for evaluating speech duration. Sound source localization performance of Jellyfish-02 is evaluated by precision, recall, and F-measure. Performance of Jellyfish-02 is superior to conventional microphone arrays. During the experiment, we found that F-measure becomes smaller as the number of speakers increases. We investigated the percentage of speech overlapped periods in natural conversation for the purpose of examining the applicability of the system to measure speech duration in group conversation. From the results, Jellyfish-02 surpasses conventional microphone array in design and usability. It is potentially applicable for assisting group conversation by measuring duration of speech for each participant.

Keywords: sound source localization system, group conversation, microphone array, communication support.

1 Introduction

Human beings are communicating with each other through conversation in daily life. In super aged society, group conversation plays very important role in order to achieve interactive communication. By sharing their experiences for collaborative learning may improve their cognitive function. In our previous study, we developed a system that assists group conversation of older adults by evaluating speech duration and facial expression of each participant during conversation. Each participant in the system needs to wear a wired headphone. If the number of the participants increases, this system will become more complicated and cumbersome.

In order to reduce the number of wires used for headphones in the system, we developed the robot, which is capable of artificial hearing function by localizing sound source. The sense of hearing has evolved and been maintained so that organisms can make use of sound in their environment not only for communication,

but also to glean information about the general acoustic milieu that enhances general survival [1]. Animals and human beings are able to estimate sound source localization as a first step in behaving appropriately in response to the sound. In order to make an artificial hearing system for robots, the robots should be capable of hearing their surrounding world by recognizing and understanding sound source environment by using microphones installed to them. In [2], researchers developed a real-time 3D sound localization system with a miniature microphone array for virtual reality. There have been many research works and applications related to sound source localization [3-5]. Research works [6], [7] aimed to develop a capability of artificial listening to the robot, which is called by “robot audition”. Robot audition is considered as an essential function to understand the surrounding auditory world such as human voices, music, and other environmental sounds. In this study, our developed sound source localization robot system, which is called Jellyfish, consists of microphone arrays, programmed by robot audition software HARK (HRI-JP Audition for Robots with Kyoto University). We developed two versions of Jellyfish robot, which surpasses existing microphone arrays in design and usability. Jellyfish-01 is without cover and connected to the system by a wire, Jellyfish-02 is with a dome-shaped cover and connected to the system by wireless.

In this study, we evaluated sound source localization performance of Jellyfish-01 and Jellyfish-02 robot by precision, recall and F-measure. We also investigated the percentage of speech overlapped periods in natural conversation for the purpose of examining the applicability of the system to measure speech duration in group conversation [8].

This paper is structured as follows. Section 2 explains about a sound source localization Jellyfish robot to assist group conversation. Section 3 shows the experiment we conducted during this study. Section 4 demonstrates the results of this system. Section 5 concludes this paper.

2 Jellyfish Shaped Sound Source Localization System

In this study, our developed sound source localization system comprises a Jellyfish shaped robot and robot audition software, called HARK shown in Fig. 1.



Fig. 1. Sound source localization system

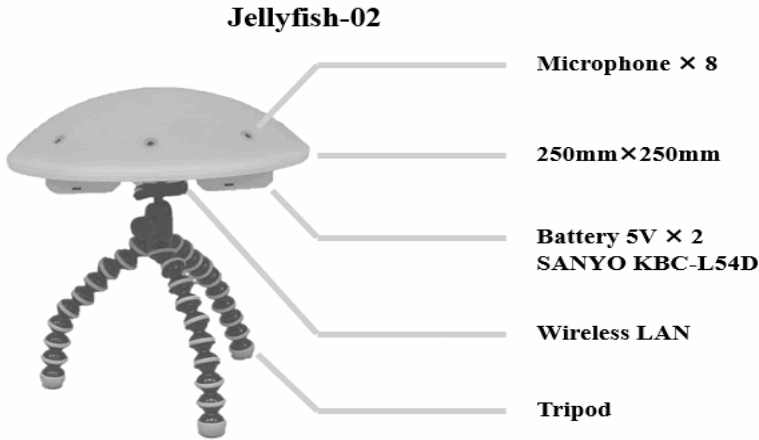


Fig. 2. Microphone array used for sound source localization

2.1 Jellyfish Shaped Robot

We developed two version of Jellyfish robot, which is capable of localizing sound sources by microphone array. Version 1 of Jellyfish shaped robot was connected to the system by a wire and without top cover. Version 2 of Jellyfish robot is shown in Fig.1, and making wireless connection to the system with covered dome-shaped like the umbrella of a jellyfish. We programmed the Jellyfish robot by using HARK software platform.

Jellyfish-02 shown in Fig.2 is a robot whose top is covered with a dome like the umbrella of a jellyfish with a diameter of 250 mm. It consists of eight microphone arrays, two batteries of 5V (SANYO KBC-L54D), wireless LAN (IEEE 802.11) and stand-up tool such as a tripod shown in Fig.2. In the system, sampling rate is 16 kHz, and sampling resolution is 24bit. The tripod is attached below the packaged microphone arrays.

2.2 “HARK” Robot Audition Software [6, 7]

The HARK robot audition software system developed by HRI-JP Audition for Robots with Kyoto University is an open-sourced robot audition software consisting of sound source localization modules, sound source separation modules and automatic speech recognition modules of separated speech signals that works on any robot with any microphone configuration.

Since a robot with ears may be deployed to various auditory environments, the robot audition system should provide an easy way to adapt to them. HARK provides a set of modules to cope with various auditory environments by using an open-sourced middleware, FlowDesigner, and reduces the overheads of data transfer between modules.

HARK has been open-sourced since April 2008. The resulting implementation of HARK with MUSIC-based sound source localization, GHDSS-based sound source separation and Missing-Feature-Theory-based automatic speech recognition (ASR) on several robots like HRP-2, SIG, SIG2, and Robovie R2. Recognition of three simultaneous utterances in real time has been achieved.

HARK has following features,

- Audio Signal Input
- Sound Source Localization
- Sound Source Separation
- Acoustic Feature Extraction
- Automatic Missing Feature Mask Generation
- Speech Recognition Client

3 Experiments

In order to compare our developed systems, which include Jellyfish-01 and Jellyfish-02, with conventional microphone array, we did several experiments. Jellyfish-02 is improved by some characteristics, such as design and communication method from Jellyfish-01. We examined the developed system, which is sound source localization system used for a tool of assisting to group conversation in design and usability. In order to verify the system, we evaluated performance of sound source localization of Jellyfish-01 and 02 by precision, recall and F-measure with the same specifications.

Fig.3 shows experimental setup conducted during the experiments.



Fig. 3. Experimental setup

In the experiments of evaluating performance of sound source localization, a speaker is assumed that one to three people conducted to the experiment. Utterance used in the experiment is the following text, which is often used in a meeting, it was measured using the Jellyfish-01 and Jellyfish-02 by telling several times loudly these sentences.

- I will start the meeting now.
- I will describe the projects today.
- Do you have any questions?
- We would like to hear the opinions of other people.
- I will end the meeting with this.

During all the experiments, we installed a video camera, in order to have reference system, each participant asked to wear IC recorder. In the middle of hexagonal table with a radius of around 1m, Jellyfish robot, sound source localization system is put and distance of 1m from the subject. Sound localization resolution of HARK is 5 degree. Seat arrangements of the experiments are shown in Fig.4, in which the subject asked to sit in interval by 30 degrees between seats. Seat arrangements are also measured combination of angles, which are summarized in Table.1.

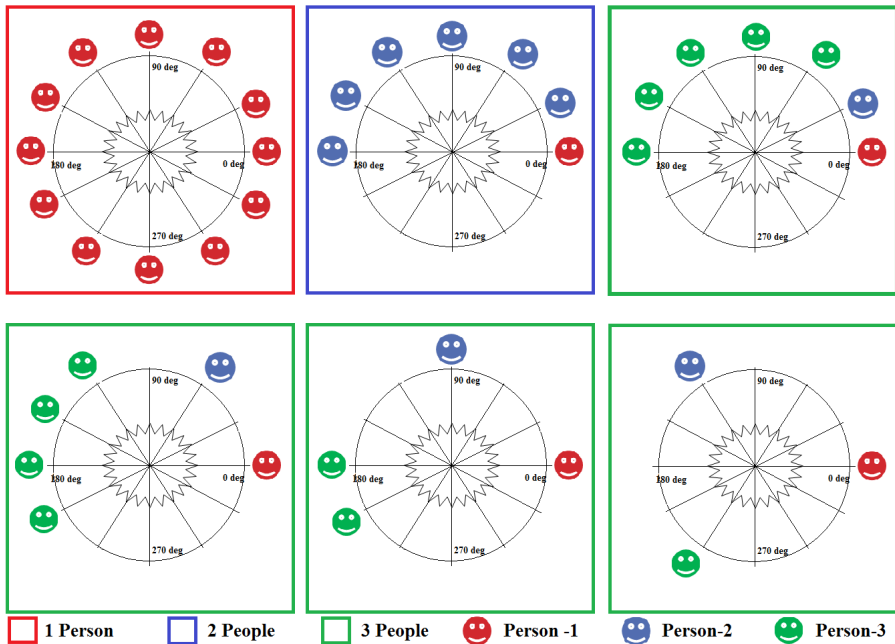


Fig. 4. Seat arrangements of the experiments

Table 1. Measured Combinations of Angles

1 Person	2 People		3 People		
	Person-1	Person-2	Person-1	Person-2	Person-3
0 ⁰	0 ⁰	30 ⁰	0 ⁰	30 ⁰	60 ⁰
30 ⁰	0 ⁰	60 ⁰	0 ⁰	30 ⁰	90 ⁰
60 ⁰	0 ⁰	90 ⁰	0 ⁰	30 ⁰	120 ⁰
90 ⁰	0 ⁰	120 ⁰	0 ⁰	30 ⁰	150 ⁰
120 ⁰	0 ⁰	150 ⁰	0 ⁰	30 ⁰	180 ⁰
150 ⁰	0 ⁰	180 ⁰	0 ⁰	60 ⁰	120 ⁰
180 ⁰			0 ⁰	60 ⁰	150 ⁰
210 ⁰			0 ⁰	60 ⁰	180 ⁰
240 ⁰			0 ⁰	60 ⁰	210 ⁰
270 ⁰			0 ⁰	60 ⁰	180 ⁰
300			0 ⁰	90 ⁰	210 ⁰
330			0 ⁰	120 ⁰	240 ⁰

Table 2. F-measure of Sound Source Localization

	1 Person	2 People	3 People
Jellyfish-01	0.85	0.62	0.35
Jellyfish-02	0.89	0.71	0.62

4 Results

In order to investigate the effect on sound source localization performance, we calculated F-measure of two developed system (Jellyfish-01 and Jellyfish-02) with same specification features. Experimental results are shown in Table 2.

From this table, we could see easily F-measure of Jellyfish-02 is greater than that of Jellyfish-01 in all the experiments. It can be said that the accuracy of source localization of Jellyfish-02 is better than Jellyfish-01 from the results. From the performance evaluation of the sound source localization experiments, Jellyfish-02 is effective to use as a tool for group conversation support compared to traditional microphone array.

In addition, when the number of people conducted to the experiment increases, F-measure decreases in both systems. It shows that performance of sound source localization is depending on how overlapping speech conversation.

Therefore, we conducted sound source localization experiments in natural conversation, to determine speech duration of each participant and overlapped period among group conversation. This experiment was carried out using the co-imagination method [9-10]. Co-imagination method supports interactive conversation through bringing feelings with images according to the theme, where allocated periods and turns for each participant are predetermined, so that all participants play both roles of speakers and listeners.

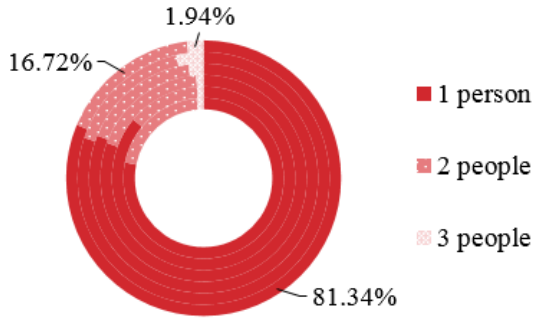


Fig. 5. Results of overlapped periods

Table 3. Adjusted F-measure of Sound Source Localization

	Jellyfish-01	Jellyfish-02
F-means	0.80	0.85

In this experiment, the subjects sat on the position of 0° , 120° , 240° degree of table with a radius of 1m, as well as performance evaluation experiment of sound source localization is conducted by 6 times. The results of this experiment is shown in Fig.5.

From Fig.5, we could see that the percentage of the period where only one person spoke was 81.3% among whole period of the conversation. That is the period where two people uttered simultaneously was 16.7%. That of the period where three people spoke overlapped was 1.94%. Adjusted F-measure of sound source localization is determined in Table 3. From these results, Jellyfish-02 is possible to assist the group conversation by measuring duration of speech for each participant based on its capability of sound source localization.

5 Conclusions

In this study, we developed a sound source localization system, which consists of Jellyfish-02 wireless microphone array and HARK robot audition software, to assist the group conversation. Several experiments are conducted to evaluate performance of the sound source localization. It was shown that the sound source localization accuracy of Jellyfish-02 is superior to conventional microphone arrays by evaluating precision, recall, and F-measure. However, the F-measure decreases when the number of subjects increases. This means that degradation of sound source localization accuracy is depending on how overlapping speech of conversation.

Therefore, we conducted a sound source localization experiments in natural conversation to investigate the ratio of multiple utterances of human overlap among natural conversation. As a result, overlapping speech duration among three people is less, and can be used for feedback of the group conversation in future.

This study shows that the sound source localization system using Jellyfish microphone array is effective for measuring speech duration based on localized speech, and can be applicable for assisting tool of group conversation.

In the future, we will integrate this system with eye tracking system and acceleration sensors such as respiration sensors in order to make an effective algorithm to analyze and support an interactive conversation system for older adults.

Acknowledgments. This work was supported by a Grant-in-Aid for Scientific Research on priority area founding a creative society via collaboration between humans and systems (#4101) from the Ministry of Education, Culture, Sports, Science and Technology of Japan (MEXT).

References

1. Fay, R.R., Popper, A.N.: Evolution of hearing in vertebrates: The inner ears and processing. *Hear. Res.* 149, 1–10 (2000)
2. Zhao, S., Ahmed, S., Liang, Y., Rupnow, K., Chen, D., Jones, D.L.: A Real-Time 3D Sound Localization System with Miniature Microphone Array for Virtual Reality. In: 2012 7th IEEE Conference on Industrial Electronics and Applications (ICIEA), pp. 1853–1857 (2012)
3. Nakamura, K., Nakadai, K., Ince, G.: Real-time super-resolution Sound Source Localization for robots. In: 2012 IEEE/RSJ International Conference on Intelligent Robots and Systems (IROS), pp. 694–699 (2012)
4. Nakashima, H., Mukai, T.: 3D Sound Source Localization System Based on Learning of Binaural Hearing. In: 2005 IEEE International Conference on Man and Cybernetics, Systems, pp. 3534–3539 (2005)
5. Cho, Y., Yook, D., Chang, S., Kim, H.: Sound Source Localization for Robot Auditory Systems. *IEEE Transactions on Consumer Electronics* 55(3), 1663–16692 (2009)
6. Nakadai, K., Takahashi, T., Okuno, H.G., Nakajima, H., Hasegawa, Y., Tsujino, H.: Design and Implementation of Robot Audition System 'HARK'- Open Source Software for Listening to Three Simultaneous Speakers. *Advanced Robotics* 24(5-6), 739–761 (2010)
7. Yamamoto, S., Nakadai, K., Nakano, M., Tsujino, H., Valin, J.-M., Komatani, K., Ogata, T., Okuno, H.G.: Design and implementation of a robot audition system for automatic Speech recognition of simultaneous speech. In: *Proc. of ASRU*, pp. 11–116 (2007)
8. Yamaguchi, T., Ota, J., Otake, M.: A system that assists group conversation of older adults by evaluating speech duration and facial expression of each participant during conversation. In: *Proc. of 2012 IEEE International Conference on Robotics and Automation*, pp. 4481–4487 (2012)
9. Otake, M.: Coimagination method: Sharing imagination with images and time limit. In: *Proceedings of the International Reminiscence and Life Review Conference*, pp. 97–103 (2009)
10. Otake, M., Kato, M., Takagi, T., Asama, H.: Coimagination method: supporting interactive conversation for activation, of episodic memory, division of attention, planning function, and its evaluation via conversation interactivity measuring method. In: *Proceedings of the 2009 International Symposium on Early Detection and Rehabilitation Technology of Dementia*, pp. 167–170 (2009)

Adaptive Tracking Controller Based on the PID for Mobile Robot Path Tracking

Hyunjin Chang and Taeseok Jin

Dept. of Mechatronics Engineering, DongSeo University,
San 69-1 Churye-dong, Sasang-ku, Busan 617-716, Korea
{hjchang, jintse}@dongseo.ac.kr

Abstract. In this paper, we present a simple and effective way of implementing an adaptive tracking controller based on the PID for mobile robot trajectory tracking. The method uses a non-linear model of mobile robot kinematics and thus allows an accurate prediction of the future trajectories. The proposed controller has a parallel structure that consists of PID controller with a fixed gain. The control law is constructed on the basis of Lyapunov stability theory. Computer simulation for a differentially driven non-holonomic mobile robot is carried out in the velocity and orientation tracking control of the non-holonomic WMR. The simulation results of wheel type mobile robot platform show that the proposed controller is more robust than the conventional back-stepping controller to show the effectiveness of the proposed algorithm.

Keywords: Trajectory tracking, Mobile robot, Lyapunov, Non-holonomic, Kinematics.

1 Introduction

In the last decade years, wheeled mobile robots have many application fields in industrial and service robotics, particularly when flexible motion capabilities are required on reasonably smooth grounds and surfaces (Wang, 1994). They are especially necessary for tasks that are difficult and dangerous for men to perform. Many researchers have shown interest in mobile robots. Most of them have focused on trajectory tracking—to control the robot to follow a desired trajectory, and point stabilization—to stabilize a robot at a desired point (Wang, 1994 ; Dixon et al., 2001).

In this paper, the adaptive following control is used as a following controller of mobile robot (Ge et al., 2003; Slotine et al., 1991; Pourboghrat et al., 2000). And also, a classical PID approach is applied for the path-following controller, which is the control strategy most frequently used in the industry. A very simple model of the mobile robot kinematics is used and thus a robust PID tuning is necessary. PID's advantages include simplicity, robustness and their familiarity in the control community. Because of this, a great deal of effort has been spent to find the best choice of PID parameters for different process models. The structure of the newly proposed control algorithm of nonlinear PID-based adaptive control is shown

in Fig. 3. This control algorithm has the characteristics such as simple structure, little computation time, and continuous auto-tuning method of the PID controller.

The paper is organized as follows: In Section 2, we discuss the model transformation of the systems including the kinematics of the mobile robot and the problem of designing controller based on Lyapunov techniques and PID, and Section 3 deals with several results to show that the proposed method is effective. Finally, some conclusions are drawn in Section 4.

2 Designing Controller of Mobile Robot

A two-wheel differential drive mobile robot was chosen as the object in this paper. Its wheel rotation is limited to one axis. Therefore, the navigation is controlled by the speed a change on either side of the robot. This kind of robot has non-holonomic constraints. The kinematics scheme of a two-wheel differential drive mobile robot is as shown in Fig. 1, where $\{O, X, Y\}$ is the global coordinate, v_m is the velocity of the robot centroid, ω is the angular velocity of the robot centroid, v_l is the velocity of the left driving wheel, v_r is the velocity of the right driving wheel, L is the distance between two driving wheels, R is the radius of each driving wheel, x_i and y_i are the position of the robot, θ_i is the orientation of the robot, and ω_m is the angular velocity. According to the motion principle of rigid body kinematics, the motion of a two-wheel differential drive mobile robot can be described using equations (1) and (2), where $\omega_{m,l}$ and $\omega_{m,r}$ are angular velocities of the left and right driving wheels respectively.

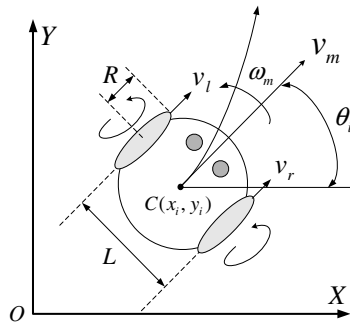


Fig. 1. Kinematics scheme of differential drive mobile robot

$$\begin{aligned} v_l &= \omega_{m,l}R \\ v_r &= \omega_{m,r}R \end{aligned} \quad (1)$$

$$\begin{aligned} v_m &= (v_r + v_l) / 2 \\ \omega_m &= (v_r - v_l) / L \end{aligned} \tag{2}$$

The non-holonomic constraint equation of the robot is as tracking:

$$\dot{x}_i \sin \theta - \dot{y}_i \cos \theta = 0 \tag{3}$$

Moreover, we can define the dynamic function of the robot as formula (4).

$$\begin{aligned} \dot{x}_i &= v_m \cos \theta_i = \frac{R}{2} (\omega_{m,r} + \omega_{m,l}) \cos \theta_i \\ \dot{y}_i &= v_m \sin \theta_i = \frac{R}{2} (\omega_{m,r} + \omega_{m,l}) \sin \theta_i \\ \dot{\theta}_i &= \omega_m = \frac{R}{L} (\omega_{m,r} - \omega_{m,l}) \end{aligned} \tag{4}$$

Rewriting the equation (4), we can express the Jacobian matrix as (5)

$$\begin{bmatrix} \dot{x}_i \\ \dot{y}_i \\ \dot{\theta}_i \end{bmatrix} = \begin{bmatrix} \frac{R}{2} \cos \theta_i & \frac{R}{2} \cos \theta_i \\ \frac{R}{2} \sin \theta_i & \frac{R}{2} \sin \theta_i \\ -\frac{R}{L} & \frac{R}{L} \end{bmatrix} \begin{bmatrix} \omega_{m,l} \\ \omega_{m,r} \end{bmatrix} \tag{5}$$

All variables are interrelated in equation (5), which causes the controller design to be more complex. Therefore, equation (5) should be decoupled. For θ_i is only related to ω_m , x_i and y_i are only related to v_m .

Let us denote the current position of the mobile robot as p_m , the velocity as \dot{p}_m . The Cartesian velocity \dot{p}_m , is represented in terms of joint variables as (6). So, the kinematics model of the robot is as tracking:

$$\dot{p}_m = J(p_m) \dot{q}_m \tag{6}$$

$$\begin{bmatrix} \dot{x}_i \\ \dot{y}_i \\ \dot{\theta}_i \end{bmatrix} = \begin{bmatrix} \cos \theta_i & 0 \\ \sin \theta_i & 0 \\ 0 & 1 \end{bmatrix} \begin{bmatrix} v_m \\ \omega_m \end{bmatrix} = J(p_m) \dot{q}_m \tag{7}$$

Therefore, in order to obtain the real-time position of the robot, we can control the control law as $\dot{q}_m = [v_m, \omega_m]^T$.

The tracking is the way to get the desired inputs of the mobile robot system mathematically. The issue of mobile robot trajectory tracking can generally be transformed into tracking one reference mobile robot. To assume the robot current position to be $p_m = [x_i, y_i, \theta_i]^T$, and the speed to be $\dot{q}_m = [v_m, \omega_m]^T$, the reference mobile robot position is $p_{m,r} = [x_r, y_r, \theta_r]^T$, and the speed to be $\dot{q}_{m,r} = [v_r, \omega_r]^T$, as shown in Fig. 2.

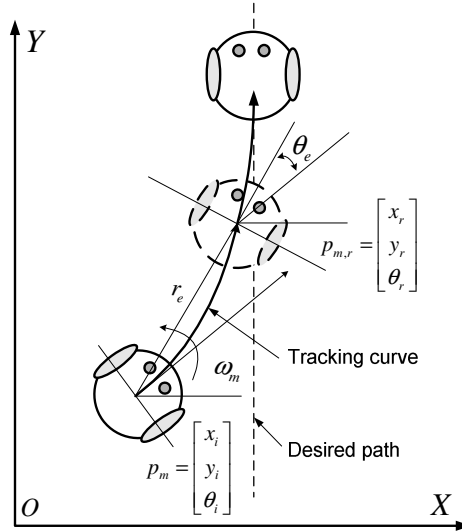


Fig. 2. Position error of mobile robot under Cartesian coordinate

To order $p_e = [x_e, y_e, \theta_e]^T = [x_r - x_i, y_r - y_i, \theta_r - \theta_i]^T$, and the mobile robot position error equation (8) is obtained from the geometric relationship shown in Fig. 2. The reference state in the robot coordinate is expressed as follow by the transformation from the world coordinate to the robot coordinate.

$$\begin{aligned}
 p_e = \begin{bmatrix} x_e \\ y_e \\ \theta_e \end{bmatrix} &= \begin{bmatrix} \cos \theta & \sin \theta & 0 \\ -\sin \theta & \cos \theta & 0 \\ 0 & 0 & 1 \end{bmatrix} (p_{m,r} - p_m) \\
 &= T_e (p_{m,r} - p_m)
 \end{aligned} \tag{8}$$

Then the position error differential equation is as tracking:

$$\dot{p}_e = \begin{bmatrix} \dot{x}_e \\ \dot{y}_e \\ \dot{\theta}_e \end{bmatrix} = \begin{bmatrix} y_e \omega_m - v + v_r \cos \theta_e \\ -x_e \omega_m + v_r \sin \theta_e \\ \omega_r - \omega_m \end{bmatrix} \tag{9}$$

Trajectory tracking of mobile robot based on kinematics model is to search the bounded input as $\dot{q} = [v_m, \omega_m]^T$, that causes position error vector, $p_e = [x_e, y_e, \theta_e]^T$ to be bounded, and $\lim_{t \rightarrow \infty} \|[x_e, y_e, \theta_e]^T\| = 0$, with arbitrary initial error and the equation (9) controlled by the control law.

By using the error vector $p_e = (x_e, y_e, \theta_e)$, the tracking curve in the robot coordinate can be calculated as follow;

$$\begin{aligned} \dot{r}_e &= -v_m \cos \theta_e \\ \dot{\theta}_e &= -\omega_m + \frac{v_m \sin \theta_e}{r_e} \\ \dot{\theta}_r &= \frac{v_m \sin \theta_e}{r_e} \end{aligned} \tag{10}$$

A Lyapunov candidate function is defined as in equation (11).

$$V = V_1 + V_2 = \frac{1}{2} \lambda r_e^2 + \frac{1}{2} (\theta_e^2 + h \theta_r^2) \tag{11}$$

$$\dot{V} = \dot{V}_1 + \dot{V}_2 = \lambda r_e \dot{r}_e + (\theta_e \dot{\theta}_e + h \theta_r \dot{\theta}_r) \tag{12}$$

$$\dot{V} = -\lambda r_e v_m \cos \theta_e + \theta_e \left[-\omega_m + \frac{v_m \sin \theta_e}{r_e} \cdot \frac{(\theta_e + h \theta_r)}{r_e} \right] \tag{13}$$

where V_1 means the error energy to the distance and V_2 means the error energy in the direction.

Let us substitute equation (12) into the corresponding part in equation (12), it results in equation (13). Note that $\dot{V} < 0$ is required for a given V to be a stable system. On this basis, we can design the nonlinear controller of the mobile robot as in equation (14),(15).

$$v_m = \gamma (r_e \cos \theta_e), \quad (\gamma > 0) \tag{14}$$

$$\omega_m = k \theta_e + \gamma \frac{\cos \theta_e \cdot \sin \theta_e}{\theta_e} (\theta_e + h \theta_r), \quad (k, h > 0) \tag{15}$$

Therefore, using this controller for the mobile robot, \dot{V} approaches to zero as $t \rightarrow \infty$; r_e and θ_e also approach almost to zero as shown in (16).

$$\dot{V} = -\lambda(\gamma \cos^2 \theta_e) r_e^2 - k \theta_e^2 \leq 0 \quad (16)$$

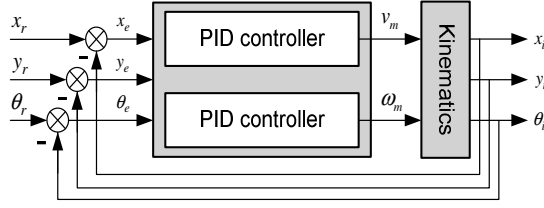


Fig. 3. Control system diagram

In this paper, we use a PID algorithm for controlling position and velocity of the mobile robot platform. Using the PID algorithm, we can control the important system characteristics, let say us, rising time, steady state error, system stability, etc. Each term in the control algorithm has a different effect on the system characteristics (Yu et al., 2012). In the PID control, the input for control of a standard PID controller in continuous time is stated as in equation (17).

$$\begin{aligned} m(t) &= K \left[e(t) + \frac{1}{T_i} \int_0^t e(\tau) d\tau + T_d \frac{de(t)}{dt} \right] \\ &= K_p e(t) + K_i \int_0^t e(\tau) d\tau + K \frac{de(t)}{dt} \end{aligned} \quad (17)$$

where $e(t)$ represents error signal that is the difference between desired input and output signal. For the digital control PID equation in discrete time is expressed as equation (18).

$$\Delta m(k) = K_p \Delta e(k) + K_i e(k) + K_d \Delta^2 e(k) \quad (18)$$

$$\Delta m(k) = v_0 e(k) + v_1 e(k-1) + v_2 e(k-2) \quad (19)$$

where $v_0 = K_p + K_i + K_d$, $v_1 = -K_p - 2K_d$, and $v_2 = 2K_d$.

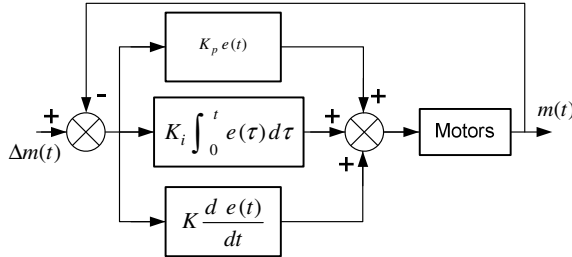


Fig. 4. PID controller diagram

3 Mobile Robot Experiments

The reference track is as, straight line of $y = x$ and curveline of $(x-0)^2 + (y-0.5)^2 = 1.25^2$ respectively, the reference velocity is as $v_r = 0.5[m/s]$, and the reference angular velocity is as $\omega_r = 0.2[rad/s]$. While the initial velocity of the mobile robot is as $v_m = 0.5$, and the initial angular velocity of the mobile robot is as $\omega_m = 0.3$, the initial position for the mobile robot is as $x = 1, y = 1.5$.

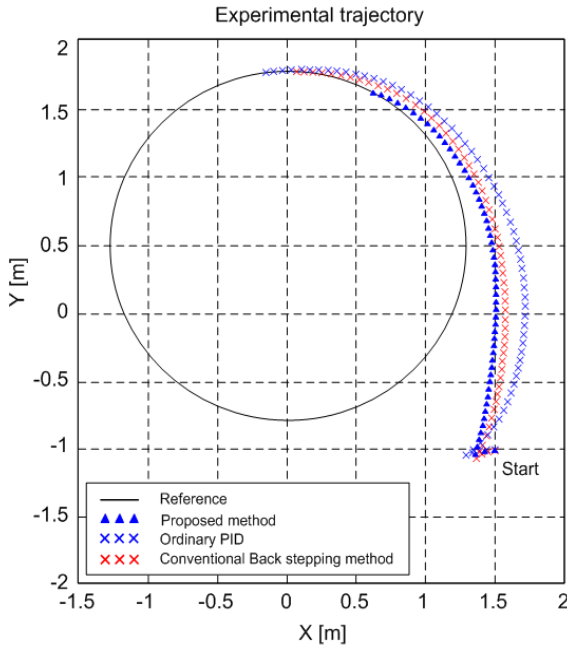
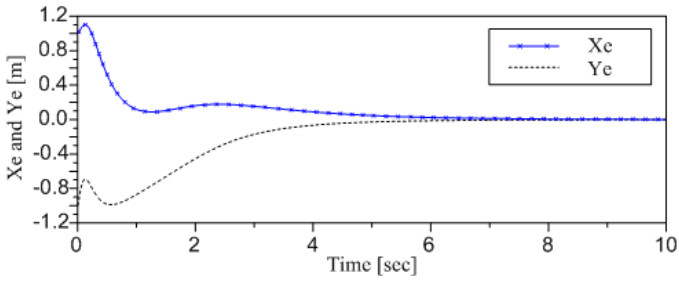


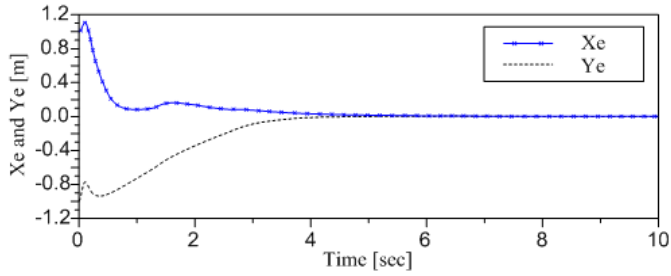
Fig. 5. Compared experiment results of robust PID tuning with ordinary PID and Conventional back-stepping method

The experimental results are shown in Fig. 5. The proposed algorithm in this paper compares with ordinary PID and conventional back-stepping method, we can see clearly from Fig. 5. When a mobile robot tracks a straight line, proposed method and conventional back-stepping method has the similar effect from Fig. 5, however ordinary PID and the conventional back-stepping method aren't stability. Meanwhile, from Fig. 5, we can see it clearly that proposed method has less error and more smoothness than conventional back-stepping method and ordinary PID. So the former has better stability and better tracking precision than the latter.

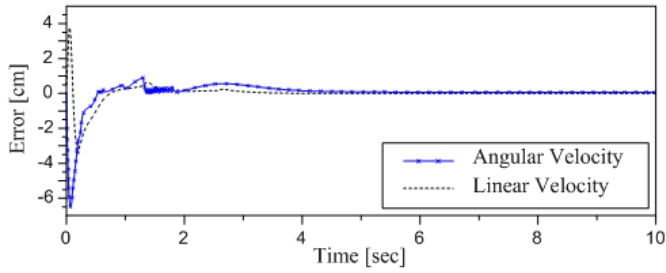
It is important to note the good performance of the controller in spite of the very simple non-linear model used for the computation of the control law. This type of model simplification is very important when a simple and low-time consuming control law is needed because of processor limitations.



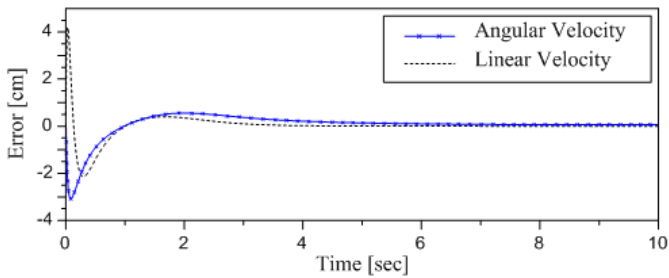
(a) Conventional back-stepping method



(b) Proposed method

Fig. 6. Trajectory error of mobile robot

(a) Conventional back-stepping method



(b) Proposed method

Fig. 7. Angular and Linear velocity error of mobile robot

Figure 6 shows the outputs and control inputs that make the mobile robot follow desired trajectory. It should be noted that the proposed method and conventional back-stepping method displacements are brought to zero in 3 [sec] and 7 [sec] in Fig. 8, respectively. Figure 7 shows the convergence of the tracking error variables with proposed method. It is clear that the performance of the system has been improved with respect to conventional back-stepping method. As the proposed controller requires no prior information about the dynamics of the vehicle. The validity of the proposed controller has been evidently verified.

4 Conclusion

This paper presents an adaptive tracking controller for mobile robot based on a robust PID method. The proposed controller has a parallel structure that consists of PID controller with a fixed gain. The principal advantage of the present methodology is that it uses a very simple model for the mobile robot which allows the tuning of a simple PID controller. The new method for the robust tuning of the PID controller is based on classical concepts and can be applied to integrative process plus a delay. The simple and clear control laws lead to simplicity of adjusting the parameters to achieve the desired performance including the tracking error and control signals. Stability of system has been guaranteed by appropriate choice of Lyapunov functions. Simulations have shown robustness and efficiency of this method. For the future work, robust tuning and position estimation should be considered to realize more accurate motions of mobile robots.

Acknowledgement. This journal was supported by the Basic Science Research Program through the National Research Foundation of Korea(NRF) funded by the Ministry of Education, Science and Technology(No. 2010-0021054).

References

1. Fierro, R., Lewis, F.L.: Control of a nonholonomic mobile robot: back-stepping kinematics into dynamics. In: Proceeding of the IEEE Conference on Decision and Control (CDC 1995), pp. 3805–3810 (1995)
2. Wang, L.X.: Adaptive fuzzy systems and control – design and stability analysis. Prentice-Hall (1994)
3. Dixon, W.E., Dawson, D.M., Zergeroglu, E., Behal, A.: Nonlinear Control of Wheeled Mobile Robots. Springer (2001)
4. Samson, C.: Time-varying feedback stabilization of a nonholonomic wheeled mobile robot. International Journal of Robotics Research 12, 55–66 (1993)
5. Kolmanovsky, I., McClamroch, N.: Development in nonholonomic control problem. IEEE Control System Magazine 15, 20–36 (1995)
6. Xinzhe, P.E.I.: Research on trajectory tracking and stabilization of nonholonomic mobile robots. Phd. dissertation, Dept. control theory and control engineering, Harbin Institute of Technology (2003)

7. Astolfi, A.: Discontinuous control of nonholonomic systems. *System and Control Letters* 27, 37–45 (1996)
8. Jiang, Z.P.: Robust exponential regulation of nonholonomic systems with uncertainties. *Automatica* 36, 189–209 (2000)
9. Ge, S.S., Wang, Z.P., Lee, T.H.: Adaptive stabilization of uncertain nonholonomic systems by state and output feedback. *Automatica* 39, 1451–1460 (2003)
10. Slotine, J.J., Li, W.: *Applied nonlinear control*. Prentice-Hall, Englewood Cliffs (1991)
11. Pourboghraat, F., Karlsson, M.P.: Adaptive control of dynamic mobile robots with nonholonomic constraints. *Computer Electric Engineering* 28, 241–253 (2000)
12. Thanh, T.D.C., Ahn, K.K.: Nonlinear PID control to improve the control performance of 2 axes pneumatic artificial muscle manipulator using neural network. *Mechatronics* 16, 577–587 (2006)
13. Astrom, K.J., Hagglund, T.: Revisiting the ziegler-nichols step response method for PID control. *Journal of Process Control* 14, 635–650 (2004)
14. Fadaei, A., Salahshoor, K.: A Novel Real-time Fuzzy Adaptive Auto-Tuning Scheme for Cascade PID Controllers. *International Journal of Control, Automation, and Systems* 9(5), 822–823 (2011)

A New Non-Gaussian Filtering Approach to Monocular SLAM Problem

Mohammad Hossein Mirabdollah and Bärbel Mertsching

GET Lab, University of Paderborn,
Pohlwegstr 47-49. 33098 Paderborn, Germany
{mirabdollah,mertsching}@get.upb.de
<http://getwww.upb.de>

Abstract. In this paper we present a new method to address the monocular SLAM problem by a non-Gaussian filtering approach. In the proposed method, the distribution of a robot position is efficiently sampled based on the method offered by the unscented Kalman filter. Attached to each sample, for each landmark, a line segment is considered to represent the uncertainty of the landmark. In another word, the robot position distribution is acceptably assumed Gaussian and the distributions of landmarks are assumed to be uniform over line segments. We offer a near to optimal method to trim the line segments and reduce their uncertainties (lengths) at each time step. The high performance of the algorithm will be proved through simulation and experimental results.

1 Introduction

The monocular SLAM problem in which only bearing measurements of landmarks are available have been addressed in many works in recent years. However, each of them has its own shortcomings. The main problem concerning the bearing SLAM is how to deal with the large uncertainties of landmarks which varies between zero and infinity at their initialization times.

Previous approaches to handle the fusion problem of bearing-only SLAM are divided into the delayed and un-delayed methods. Delayed methods postpone the modification of the hypothesized robot position until they get a reliable depth measurement of landmarks [1]; whereas, un-delayed methods which are more recent try to decrease the uncertainty of the robot position from the beginning. Most of the proposed un-delayed methods are based on Extended Kalman filters.

Sola et al. assumed separate entries for different depth hypotheses of a landmark in the estimated vector of the EKF filter [8]. Clearly, this method can cause ambiguities if two different landmarks lie on the same ray. Therefore, Kwok et al. in [4] proposed another method based on the Gaussian Sum filter (GSF) which is the extension of the EKF if the uncertainties can be expressed as a weighted sum of a set of individual Gaussians. In their method, the uncertainty of each landmark is modeled by the summation of a set of Gaussians placed along the ray by which the landmark is observed. Depending on the maximum depth uncertainties, the number of the Gaussians is increased. Hence, the GSF based method has

an exponentially growing complexity with respect to the number of landmarks and the maximum depth uncertainties. As a result, using this method in outdoor environments in which the depth uncertainties are high, could be impractical.

Civera et al. [2] offered a new perspective to use inverse depth parametrization of landmark positions in the estimated vector. This method works well if the landmarks are initialized far from the camera depending on the speed of the robot. In other word, if the robot approaches a close landmark before its uncertainty is reduced enough, the landmark can be localized behind the camera (negative depth) and the algorithm diverges. Additionally, for the landmarks which have distances less than one meter and half, the algorithm diverges in the first steps. The explanation of this behavior is simple, the inverse depth method maps all distances between 1 to infinity to the interval $[0,1]$, whereas, depths between 0 and 1 will be mapped the interval $[1, +\infty]$ which gives rise to a severe non-linearity which cannot be handled by EKF filters. Parsly et al. claimed in [7] that the problem of the negative depth can be tackled by applying a logarithmic parametrization for the depth. But, obviously, this method still suffers from the problem of close landmarks due to the extreme nonlinearity of the logarithm function about one. On the other hand, they did not also provide any practical results to support their claims.

Recently, some methods have also been offered which utilize a sole camera to solve the monocular SLAM problem up to a scale factor. They use camera motion estimation methods ([6]) to estimate the motion of a camera up to a scale factor. Then, by bundle adjustment methods, they modify the path and the landmark positions up to a scale. Strasdat et al. offered a monocular SLAM method for the relatively simple case that the camera has mostly side motions [9]. They also used inverse depth parametrization to initialize features. Zaho et al. in [10] offered a delayed method named parallax angle parametrization, in which they have relied on a high quality visual odometry which is not realistic in most of practical cases.

In this paper, we offer a robust method for 2D scenarios in which the landmark uncertainties are modeled by line segments of which orientations have small uncertainties (proportional to measurement noises). In our algorithm, a robot position is sampled in a way similar to the unscented Kalman filter method [3]. Attached to each sample, a set of line segments is considered to present the uncertainties of the landmark positions. The line segment angles are kept almost constant as their values at their initialization times. To reduce the uncertainty of a landmark position, the length of a line segment is reduced near to optimally by calculating the PDF of the intersection points of the line segment and the lines through which the related landmark is observed at the other robot positions. Furthermore, inspired from Fast SLAM 2.0 method [5], we incorporate recent measurements to obtain posterior distributions for the odometry data and to determine the weights of samples. It should be mentioned that UKF filters cannot be applied directly if we are dealing with high depth uncertainties. Since a landmark position uncertainty cannot be represented in a Gaussian form, but it looks like a distribution over a trapezoid. On the other hand, as the number

of landmarks increases, the computation load increases extremely in such a way that they cannot be used online.

The paper is organized as follows: In section II, the setup of the monocular SLAM problem using line segments is introduced. Section III formulates a recursive algorithm including three steps to localize robot and landmarks simultaneously. Section IV shows the performance of the proposed algorithm in comparison with the inverse and logarithmic depth parametrization methods through the simulation. In section V, the results of the real time implementation of the algorithm on a real robot is presented. Section VI concludes this paper.

2 Statement of Monocular SLAM Using Line Segments

Assuming a mobile robot in a 2D space, the robot position can be stated by three parameters x^R, y^R, θ^R , where x^R, y^R show the absolute location of the robot on the $X - Y$ plane and θ^R gives the orientation of the robot with respect to the X axis. The motion of the robot is controlled by the linear velocity $u_{f,k}$ (m/step) and the angular velocity $u_{r,k}$ (rad/step). Considering these parameters, the motion model of the robot in a discrete time case will be as follows:

$$\begin{aligned} x_{k+1}^R &= x_k^R + u_{f,k} \cos \theta_k^R \\ y_{k+1}^R &= y_k^R + u_{f,k} \sin \theta_k^R; \quad k = 0, 1, 2, \dots \\ \theta_{k+1}^R &= \theta_k^R + u_{r,k} \end{aligned} \quad (1)$$

$u_{f,k}$ and $u_{r,k}$ are usually provided by odometry or IMU sensors and as we know the measurements they provide includes some uncertainties. Therefore we can write:

$$u_{f,k} = \bar{u}_{f,k} + \tilde{u}_{f,k}; \quad u_{r,k} = \bar{u}_{r,k} + \tilde{u}_{r,k} \quad (2)$$

where $\bar{u}_{f,k}$ and $\bar{u}_{r,k}$ are the measured speeds and $\tilde{u}_{f,k} \sim \mathcal{N}(0, \sigma_{\tilde{u}_f}^2)$ and $\tilde{u}_{r,k} \sim \mathcal{N}(0, \sigma_{\tilde{u}_r}^2)$ are their uncertainties modeled as Gaussian processes.

In the case of bearing only measurements (e.g. using a monocular camera), if a set of landmarks such as $\{L_1, \dots, L_M\}$ which are uniquely identifiable can be extracted, the available measurements will be $\{\phi_{1,k}, \dots, \phi_{M,k}\}$. Then, the mathematical model of the measurement is obtained as follows:

$$\phi_{j,k} = \tan^{-1} \frac{y_j^L - y_k^R}{x_j^L - x_k^R} - \theta_k^R + v_k; \quad j = 1, \dots, M \quad (3)$$

where (x_j^L, y_j^L) s represent the absolute positions of the j^{th} landmark (initially unknown), v_k is the measurement noise assumed to be normal $\mathcal{N}(0, \sigma_v^2)$.

Now, the problem is the estimation of the robot and the landmark positions, given the following measurement sequence:

$$\{\Phi_{j,k}\} \equiv \{\Phi_{1,k}, \dots, \Phi_{M,k}\}; \quad \Phi_{j,k} = \{\phi_{j,k}, \phi_{j,k-1}, \dots, \phi_{j,0}\}$$

Speaking in probabilistic terms, by definition of the vectors $\mathbf{x}_k^R = [x_k^R \ y_k^R \ \theta_k^R]^T$ and $\mathbf{x}_j^L = [x_j^L \ y_j^L]^T$ and considering the fact that the landmark positions are independent the following PDF (probability density function) should be estimated:

$$p(\mathbf{x}_k^R, \{\mathbf{x}_{j,k}^L\} | \{\Phi_{j,k}\}) = p(\{\mathbf{x}_{j,k}^L\} | \mathbf{x}_k^R, \{\Phi_{j,k}\})p(\mathbf{x}_k^R | \{\Phi_{j,k}\}) \tag{4}$$

The above decomposition can be simply verified using the Bayesian rule. The term $p(\mathbf{x}_k^R | \{\Phi_{j,k}\})$ can be presented by a set of N weighted samples as follows:

$$p(\mathbf{x}_k^R | \cdot) \approx \sum_{i=1}^N w_i x_{k,i}^R; \quad \sum_{i=1}^N w_i = 1 \tag{5}$$

Now assuming that the robot observes a landmark such as L_j for the first time at the time step l , from Eq. (4) it can be inferred that given the sample $x_{l,i}^R$, the landmark should lie on a line which starts at $(x_{l,i}^R, y_{l,i}^R)$ and goes to infinity at the angle $\alpha_{j,i,l} = \theta_{l,i}^R + \phi_{j,l}$. Obviously, given $\theta_{l,i}^R$, the uncertainty of $\alpha_{j,i,l}$ will only be related to the measurement noise.

Before proceeding the development of the algorithm, we define the following notation for the line segment related to L_j :

$$\bar{\mathbf{x}}_j^L \equiv \Gamma(\mathbf{x}_{j,0}^L, \lambda_j, \alpha_j) \tag{6}$$

where $\mathbf{x}_{j,0}^L = [x_{j,0}^L \ y_{j,0}^L]^T$ represents the starting point of the line segment with the length λ_j and the angle $\alpha_{j,l}$ with respect to the X axis.

3 Simultaneous Modification of Line Segments and Robot Position

The estimation of Eq. (4) can be done in a recursive algorithm which consists of three steps as follows:

- Using line segments $\{\bar{\mathbf{x}}_{j,l,k}^L\}$, new measurements $\{\Phi_{j,k+1}\}$ and the prior distributions of control inputs $\tilde{u}_{f,k}$ and $\tilde{u}_{r,k}$, to obtain their posterior distributions such as $\tilde{u}_{f,k}^p$ and $\tilde{u}_{r,k}^p$ and also to weight the samples.
- Using the posterior distributions of the input controls, to trim line segments given the new measurements.
- Resampling the obtained posterior distribution.

3.1 Sampling

Since our method is based on the sampling of the distribution of a robot position, we discuss briefly the sampling method which utilizes a minimal number of samples. A well established method for efficient sampling of a Gaussian distribution is utilized by unscented Kalman filter in which the sigma points of a joint Gaussian distribution are chosen as samples. In the UKF sampling method, from a vector with the length n , $2n + 1$ samples are obtained. Consequently, given the

robot position vector $[x_k^R, y_k^R, \theta_k^R]^T$ with the distribution $\mathbf{x}_k^R \sim \mathcal{N}(\bar{\mathbf{x}}_k^R, \Sigma)$, seven samples can be obtained as follows:

$$\mathbf{x}_{k,0}^R = \bar{\mathbf{x}}_k^R; \mathbf{x}_{k,r}^R = \bar{\mathbf{x}}_k^R + \left(\sqrt{\frac{3}{1-w_0}} \Sigma \right)_r; \mathbf{x}_{k,r+3}^R = \bar{\mathbf{x}}_k^R - \left(\sqrt{\frac{3}{1-w_0}} \Sigma \right)_r \quad (7)$$

where $w_0 = \frac{1}{3}$, $w_r = w_{r+3} = \frac{1}{9}$, $r = 1, 2, 3$ and $(\cdot)_r$ is the r^{th} column of the matrix.

3.2 Intersection of Two Line Segments under the Uncertainties of Parameters

From Geometry, we know that a point in a space can be localized if it can be observed from two different known positions. Clearly, the point will be on the intersection of two lines through which it is observed. However, if the two positions have uncertainties, it is required to approach the problem in a probabilistic context.

In the following, we discuss given a sample such as $\mathbf{x}_{k,i}^R$ from $p(\mathbf{x}_k^R|\cdot)$, $u_{f,k}$, $u_{r,k}$ and $\{\Phi_{j,k}\}$, what would be the distribution of the intersection points. We know that a line equation can be presented in a vector form as follows:

$$\mathbf{x} = \mathbf{x}_0 + d\mathbf{p} \quad (8)$$

where $\mathbf{x} = [x \ y]^T$ represents the point locations on the line, $\mathbf{x}_0 = [x_0 \ y_0]^T$ is a known point of the line, d is a scalar depth variable and $\mathbf{p} = [p_1 \ p_2]^T$ is a vector which stands for the orientation of the line. In a line equation, the depth parameter varies between $-\infty$ and $+\infty$. For a line segment, however, it lies in a limited interval such as $[d_{min}, d_{max}]$.

We should mention that in the line segment method once a landmark at the time step l is initialized with a line segment such as $\bar{\mathbf{x}}_{j,l,k}^L$, its orientation is kept almost constant but its starting point and the depth parameter will be changed by receiving the new measurements. The changes of these parameters are based on the intersection point of the two lines: $\bar{\mathbf{x}}_{j,l,k,i}^L$ and the line at where the same landmark at the new robot position is observed ($\bar{\mathbf{x}}_{j,k+1,i}^L$). For the simplicity, we remove the index i and also replace the indexes (j, l, k) and $(j, k + 1)$ with 1 and 2. Therefore, based on Eq. (8), the line equations will be as follows:

$$\mathbf{x}_1^L = \mathbf{x}_{1,0}^L + d_1\mathbf{p}_1; \quad \mathbf{x}_2^L = \mathbf{x}_{2,0}^L + d_2\mathbf{p}_2 \quad (9)$$

where $\mathbf{x}_{2,0}^L = [x_{k+1}^R \ y_{k+1}^R]^T$, $\mathbf{p}_1 = [\cos \alpha_1 \ \sin \alpha_1]^T$ with $\alpha_1 = \theta_l^R + \phi_{j,l}$ and $\mathbf{p}_2 = [\cos \alpha_2 \ \sin \alpha_2]^T$ with $\alpha_2 = \theta_{k+1}^R + \phi_{j,k+1}$.

Eq. (9) can be solved for d_1 as follows:

$$[\mathbf{p}_1 | -\mathbf{p}_2] \begin{bmatrix} d_1 \\ d_2 \end{bmatrix} = \begin{bmatrix} \Delta x^L \\ \Delta y^L \end{bmatrix} \quad (10)$$

where $\Delta x^L = x_{2,0}^L - x_{1,0}^L$, $\Delta y^L = y_{2,0}^L - y_{1,0}^L$. The solution for d_1 is:

$$d_1 = \frac{\Delta x^L \sin \alpha_2 - \Delta y^L \cos \alpha_2}{\sin(\alpha_2 - \alpha_1)} \tag{11}$$

Using Eq. (1) and Eq. (11), the following equation can be obtained:

$$d_1 = \frac{\Delta x \sin(\bar{\alpha}_2 + \tilde{\alpha}_2) - \Delta y \cos(\bar{\alpha}_2 + \tilde{\alpha}_2) + (\tilde{u}_{f,k} + \tilde{u}_{r,k}) \sin(\bar{\alpha}_2 - \theta_k^R + \tilde{\alpha}_2)}{\sin(\Delta\bar{\alpha} + \Delta\tilde{\alpha})} \tag{12}$$

where $\Delta x = x_k^R - x_{1,0}^L$, $\Delta y = y_k^R - y_{1,0}^L$, $\Delta\bar{\alpha} = \bar{\alpha}_2 - \bar{\alpha}_1$ and $\Delta\tilde{\alpha} = \tilde{\alpha}_2 - \tilde{\alpha}_1$. $\bar{\alpha}_1 = \bar{\theta}_l^R + \bar{\phi}_{j,l}$, $\tilde{\alpha}_1 \sim \mathcal{N}(0, \sigma_v^2)$ and $\bar{\alpha}_2 = \theta_k^R + \bar{u}_{r,k} + \bar{\phi}_{j,k+1}$, $\tilde{\alpha}_2 \sim \mathcal{N}(0, \sigma_v^2 + \sigma_{\tilde{u}_r}^2)$.

3.3 Posterior Distributions of $\tilde{u}_{f,k}$ and $\tilde{\alpha}_2$ Given the Landmark Positions

To minimize the uncertainty of the robot position at each time step, we use Eq. (11) to obtain posterior distributions for $\tilde{u}_{f,k}$ and $\tilde{\alpha}_2$. Solving Eq. (12) for $\tilde{u}_{f,k}$ and $\tilde{\alpha}_2$ results in the following equations:

$$\tilde{u}_{f,k} = \frac{d_1 \sin(\Delta\bar{\alpha} + \Delta\tilde{\alpha}) - \Delta x \sin(\bar{\alpha}_2 + \tilde{\alpha}_2) + \Delta y \cos(\bar{\alpha}_2 + \tilde{\alpha}_2) - \tilde{u}_f \sin(\bar{\alpha}_2 - \theta_k^R + \tilde{\alpha}_2)}{\sin(\bar{\alpha}_2 - \theta_k^R + \tilde{\alpha}_2)} \tag{13}$$

$$\tilde{\alpha}_2 = \tan^{-1} \frac{\Delta x \sin \bar{\alpha}_2 - \Delta y \cos \bar{\alpha}_2 + (\tilde{u}_{f,k} + \tilde{u}_{r,k}) \sin(\bar{\alpha}_2 - \theta_k^R) - d_1 \sin(\Delta\bar{\alpha} - \tilde{\alpha}_1)}{-\Delta x \cos \bar{\alpha}_2 + \Delta y \sin \bar{\alpha}_2 + u_f \cos(\bar{\alpha}_2 - \theta_k^R) + d_1 \cos(\Delta\bar{\alpha} - \tilde{\alpha}_1)} \tag{14}$$

Calculation of the posterior distributions of $\tilde{u}_{f,k}$ and $\tilde{u}_{r,k}$ from the above equations are not straight forward. Nevertheless we can calculate 2σ equivalent boundaries for them. Given the 2σ borders of $\tilde{u}_{f,k}$, $\tilde{\alpha}_1$, $\tilde{\alpha}_2$ and a line segment such as $\tilde{\mathbf{x}}_{j,l,k,i}^L$, we define the following intervals:

$$\begin{aligned} \Sigma_{u_f} &= [-2\sigma_{\tilde{u}_f}, 2\sigma_{\tilde{u}_f}]; & \Sigma_{\alpha_1} &= [-2\sigma_{\tilde{\alpha}_1}, 2\sigma_{\tilde{\alpha}_1}] \\ \Sigma_{\alpha_2} &= [-2\sigma_{\tilde{\alpha}_2}, 2\sigma_{\tilde{\alpha}_2}]; & \Sigma_{d,j,i} &= [0, \lambda_{j,l,i,k}] \end{aligned}$$

By plugging the eight combinations of the borders of Σ_{α_1} , Σ_{α_2} and $\Sigma_{d,j,i}$ into Eq. (13), eight values for $\tilde{u}_{f,k}$ are obtained. Consequently, an interval including the minimum and maximum of the eight values can be formed as follows:

$$R_{\tilde{u}_{f,k,j}} = [\tilde{u}_{f,k,j,min}, \tilde{u}_{f,k,j,max}]$$

For each landmark a similar interval can be obtained. Obviously, the best valid interval can be obtained by the intersection of all these intervals with the prior interval of $\tilde{u}_{f,k}$:

$R_{\tilde{u}_{f,k}} = [\tilde{u}_{f,k,1}, \tilde{u}_{f,k,2}] = (\bigcap_{j=1}^M R_{\tilde{u}_{f,k,j}}) \cap \Sigma_{\tilde{u}_{f,k}}$. Using $R_{\tilde{u}_{f,k}}$, finally we can obtain the following posterior distribution for $\tilde{u}_{f,k}$

$$\tilde{u}_{f,k}^p \sim \mathcal{N}\left(\frac{\tilde{u}_{f,k,1} + \tilde{u}_{f,k,2}}{2}, \frac{(\tilde{u}_{f,k,1} - \tilde{u}_{f,k,2})^2}{4}\right) \tag{15}$$

Using the same procedure, a posterior distribution for $\tilde{\alpha}_2$ denoted as $\tilde{\alpha}_2^p$ is obtained. Since $\tilde{\alpha}_2 = \tilde{u}_{r,k} + \tilde{\phi}_{j,k}$ and since $\tilde{\phi}_{j,k}$ is a zero mean random Gaussian variable, the best posterior estimation $\tilde{u}_{r,k}^p$ is equal to $\tilde{\alpha}_2^p$.

To weight the samples, we utilize the Mahalanobis distance between the prior and posterior distributions. We should remind that the obtained posterior distributions are for a given sample. To be more specified, we add the index i to posterior distributions $\tilde{u}_{f,k,i}^p$ and $\tilde{\alpha}_{2,i}^p$. Consequently, the weight of the sample i will be:

$$w_{i,k+1} = \eta w_{i,k} \exp\left[-\frac{(\tilde{u}_{f,k,i}^p - \tilde{u}_{f,k})^2}{2\sigma_{f,i}^2} - \frac{(\tilde{\alpha}_{2,i}^p - \tilde{\alpha}_{2,i})^2}{2\sigma_{r,i}^2}\right] \tag{16}$$

where $\sigma_{f,i}^2 = \sigma_{\tilde{u}_{f,k,i}^p}^2 + \sigma_{\tilde{u}_{f,k}}^2$, $\sigma_{r,i}^2 = \sigma_{\tilde{\alpha}_2^p}^2 + \sigma_{\tilde{\alpha}_2}^2$ and η is a normalization factor.

3.4 Optimal Trimming of Line Segments

After obtaining the posterior distributions for $\tilde{u}_{f,k}^p$ and $\tilde{u}_{r,k}^p$, now we should obtain the projection of $p(\mathbf{x}_{k+1}^R | \mathbf{x}_k^R, \tilde{u}_{f,k}^p, \tilde{u}_{r,k}^p)$ on each line segment. We drop the upper index p in the following for the sake of simplicity.

d_1 is a random variable which is a function of three random variables $\tilde{\alpha}_1$, $\tilde{\alpha}_2$ and $\tilde{u}_{f,k}$. If $|\tilde{\alpha}_1|, |\Delta\tilde{\alpha}| < 0.15$, Eq. (11) can be written as follows:

$$d_1 \approx \frac{A}{B + C\Delta\tilde{\alpha}} = \frac{\bar{A} + \tilde{A}}{B + C\Delta\tilde{\alpha}} \tag{17}$$

where

$$\begin{aligned} \bar{A} &= \Delta y \cos \bar{\alpha}_1 - \Delta x \sin \bar{\alpha}_1 + \bar{u}_{f,k} \sin(\bar{\alpha}_1 - \theta_k^R), \\ \tilde{A} &= (-\Delta y \sin \bar{\alpha}_1 - \Delta x \cos \bar{\alpha}_1 + \bar{u}_{f,k} \cos(\bar{\alpha}_1 - \theta_k^R))\tilde{\alpha}_1 + \tilde{u}_{f,k} \sin(\bar{\alpha}_1 - \theta_k^R) \\ &= \gamma_1 \tilde{\alpha}_1 + \gamma_2 \tilde{u}_{f,k}, \\ B &= \sin \Delta\bar{\alpha}, \quad C = \cos \Delta\bar{\alpha} \end{aligned}$$

The above approximations for larger $\Delta\tilde{\alpha}$ will be gradually violated. However, since $\sin(\cdot)$ function compresses a zero mean random variable towards zero, using the approximation in the derivation of the equations means that we considered larger uncertainties rather than the real case which makes our calculation still valid but not optimal.

In Eq. (17) A has a Gaussian distribution: $\mathcal{N}(\bar{A}, \gamma_1^2 \sigma_{\alpha_1}^2 + \gamma_2^2 \sigma_{\bar{u}_{f,k}}^2)$. If we obtain the distribution of $p(d_1|A)$ then $p(d_1)$ can be calculated as follows:

$$p(d_1) = \int p(d_1|A)p(A)dA \tag{18}$$

The above equation means to convolve $p(d_1|\bar{A})$ with a Gaussian kernel $\mathcal{N}(0, \gamma_1^2 \sigma_{\alpha_1}^2 + \gamma_2^2 \sigma_{\bar{u}_{f,k}}^2)$. The convolution smooths and expands $p(d_1|A)$ proportional to the standard deviation of the Gaussian. Therefore, we firstly calculate $p(d_1|\bar{A})$ and with the mentioned consideration, trim the line segment optimally. Using the random variable algebra, the PDF of d_1 given \bar{A} can be obtained as follows:

$$p(d_1|\bar{A}) = \frac{1}{\sqrt{2\pi}C^2\sigma_{\Delta\bar{\alpha}}^3} \left| \frac{\bar{A}(\bar{A} - Bd_1)}{d_1^3} \right| \exp\left(-\frac{(\bar{A} - Bd_1)^2}{2C^2\sigma_{\Delta\bar{\alpha}}^2 d_1^2}\right) \tag{19}$$

In Fig. 1a, the PDF for $A = 1$, $\sigma_{\Delta\bar{\alpha}} = 0.1$ and $\Delta\bar{\alpha} = 0, 0.1$ can be seen. The integral in Eq. (18) cannot be solved analytically. However, as we already mentioned, it should look like $p(d_1|\bar{A})$ but smoothed and expanded (Fig. 1b). The extrema points of $p(d_1)$ are the key-points to trim a line segment, considering the fact that d_1 should be always non negative.

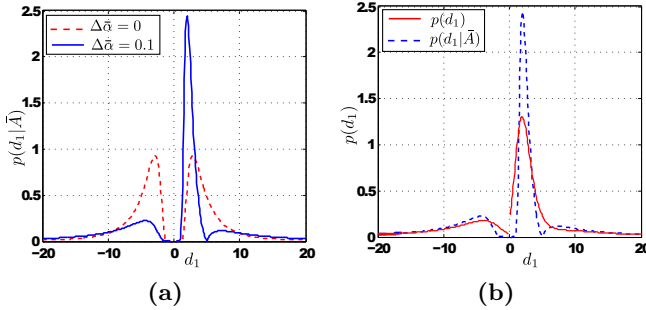


Fig. 1. (a) $p(d_1|\bar{A})$ for two different parallax angles. (b) $p(d_1|\bar{A})$ and $p(d_1)$ for $\Delta\bar{\alpha} = 0.1$. In both cases, the standard deviation of the random variables are: $\sigma_{\bar{u}_{f,k}} = \sigma_{\bar{\alpha}_2} = 0.1$ and $\sigma_{\bar{\alpha}_1} = 0.001$.

The PDF $p(d_1)$ has three extrema points if $B \neq 0$. The extrema points can be obtained by solving the equation $\frac{\partial p(d_2)}{\partial d_2} = 0$. Since the closed form of $p(d_1)$ is not available, based on the above discussions, We firstly calculate the extrema of $p(d_1|\bar{A})$ and then consider the effect of the uncertainty of \bar{A} . Therefore we have:

$$\frac{\partial p(d_1|\bar{A})}{\partial d_1} = 4\sigma^2 C^2 B d_1^3 + (\bar{A} B^2 - 6\sigma_{\Delta\bar{\alpha}}^2 C^2 \bar{A}) d_1^2 - 2\bar{A}^2 B d_1 + \bar{A}^3 = 0 \tag{20}$$

Fortunately, there are analytic solutions to cubic equations. The solution of this equation always results in real roots one of which is at least positive. By back substitution of the three roots in Eq. (17) three answers for $\Delta\tilde{\alpha}$ such as $\Delta_1\tilde{\alpha}$, $\Delta_2\tilde{\alpha}$ and $\Delta_3\tilde{\alpha}$ are obtained. We can compensate the effect of $\Delta\tilde{\alpha}$ by recalculation of Eq. (17) given $\Delta_r\tilde{\alpha}$ ($r = 1, 2, 3$). It results in three distances such as $d_{2,1} < d_{2,2} < d_{2,3}$. To compensate the effect of $\tilde{u}_{f,k}$ we use its 2σ confidence region to obtain the following term:

$$b_{j,r} = \left| \frac{2\sigma_{\tilde{u}_{f,k}} \sin(\bar{\alpha}_2 - \theta_k^R)}{\sin(\Delta\bar{\alpha} + \Delta_r\tilde{\alpha})} \right|; \quad r = 1, 2, 3 \tag{21}$$

Then we modify $d_{1,r}$ as follows:

$$d_{1,j,r} = \begin{cases} d_{1,j,r} - b_{j,r}, & \text{if } d_{1,j,r} \geq 0 \\ d_{1,j,r} + b_{j,r}, & \text{if } d_{1,j,r} < 0 \end{cases} \tag{22}$$

We sort the obtained values ascending: $d_{1,j,1} < d_{1,j,2} < d_{1,j,3}$ and define the following interval based on the two greatest values:

$$\bar{d}_1 = [d_{1,j,2}, 2 \frac{d_{1,j,3} - d_{1,j,2}}{u(|\Delta\alpha| - 2\sigma_{\Delta\tilde{\alpha}})}] \tag{23}$$

where $u(\cdot)$ is a step function. After the calculation of the above interval, \bar{d}_1 is intersected with the interval $[0, \lambda_{j,l,i}]$ to obtain the updated line segment. In Eq. (23), the infinity depth is preserved if the parallax angle is less than the confidence region of $\Delta\tilde{\alpha}$.

3.5 Resampling

We can fit a Gaussian distribution to the statistics including seven weighted samples. To obtain a Gaussian distribution for the robot position based on the statistics and also preserve the dependency between the robot position and landmark positions, we define the following vector for each set of robot sample and the parameters of the line segment:

$$\mathbf{x}_{i,j} = [x_i, y_i, \theta_i, x_{j,i}^L, y_{j,i}^L, \alpha_{j,i}^L, \lambda_{j,i}^L]^T \tag{24}$$

Consequently, the following mean vector and covariance matrix can be obtained:

$$\mathbf{x}_j = \sum_{i=1}^7 w_i \mathbf{x}_{i,j}; \quad \Sigma_j = \sum_{i=1}^7 w_i (\mathbf{x}_{i,j} - \mathbf{x}_j)(\mathbf{x}_{i,j} - \mathbf{x}_j)^T \tag{25}$$

Then the new samples can be obtained as follows:

$$\mathbf{x}_{0,j} = \mathbf{x}_j; \quad \mathbf{x}_{r,j} = \mathbf{x}_j - \left(\sqrt{\frac{9}{2}\Sigma_j} \right)_r; \quad \mathbf{x}_{3+r,j} = \mathbf{x}_j + \left(\sqrt{\frac{9}{2}\Sigma_j} \right)_r$$

where $r = 1, 2, 3$. Obviously, for all robot and landmark combinations the mean and covariance of the robot position will be the same but we have to calculate the mean vector and covariance matrices the way mentioned above, in order not to lose the dependency between the robot position and the landmark positions.

4 Simulation

To show the performance of the proposed algorithm, an environment including one robot and 81 landmarks was simulated. The robot was driven on a long path including a straight and a circular parts. It is known that if a robot moves linearly, it mostly meets the landmarks on low parallax angles which is the most challenging case for monocular SLAM algorithms, we allowed the robot also rotate to see its performance in circular paths. In this simulation, the odometry data is added with zero mean Gaussian noises with the standard deviations 0.1. As observed in Fig. 2a, the proposed algorithm performed perfectly both in making a path very close to the real path and also making a proper map of the landmarks. On the other hand, the inverse depth parametrization method diverged in the first steps due to the close landmarks (Fig. 2b). The logarithmic parametrization method had a better performance than the inverse depth method but it also diverged to a great extent from the real path (Fig. 2c). In different simulations setup, we observed that the inverse depth parametrization method diverged quickly if there existed any landmark closer than 1.5 m to the camera at the initialization time. It could gradually diverge if there were any landmarks less than 3 m. Another case in which the algorithm diverged was when the robot approached one or more landmarks in low parallax angles.

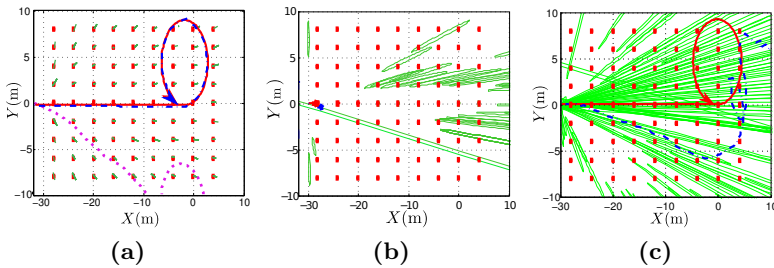


Fig. 2. Localization and mapping: (a) Line segment method at $k = 200$. (b) Inverse depth parametrization method at $k = 4$. (c) Logarithmic parametrization method. In all figures the red pluses are the real positions of landmarks and the red paths are also the real robot paths. The green line segments or ellipses and the dashed blue paths show the estimated landmark positions and the estimated robot path. The dotted path show the estimated path based on odometry data. In all cases the noises were $\tilde{u}_{f,k}, \tilde{u}_{r,k} \sim \mathcal{N}(0, 0.1)$ and $\sigma_v = 0.001$.

5 Practical Results

We implemented the proposed algorithm on a pioneer four wheeled robot which was equipped with a laptop with an Intel Core 2 Duo (3.33 GHz) processor. A consumer webcam with a resolution of 960x720 and the field of view about 60° was also installed on the robot. We conducted one outdoor and one indoor experiments. The features we used to track within the frames were Harris corners. The features were extracted from a frame and tracked in the next frames until 70% of them disappeared. Then again new landmarks were extracted and tracked repeatedly. The applied tracking algorithm was the Lucas-Kanade method (implemented in the OpenCv library). The initial number of landmarks was thirty by which our algorithm managed to work online at the frame rate 20 Hz.

For the outdoor scenario, the robot was driven two times about an square. The robot passed the starting point two times. The generated path by the odometry and the modified path using our algorithm in addition to the extracted landmarks with the length uncertainties less than 15 m can be seen in Fig. 3a. It can be observed that the proposed method had a high performance such that it managed to correct a relatively high amount of odometry errors and close the loop with a high precision in both turns. Our method extracted and registered about 2000 landmarks (Fig. 3b). The landmark uncertainties are presented as line segments. It should be mentioned that although the life time of the tracks of the landmarks were mostly short (in average less than ten frames), and also in outdoor scenarios we should consider relatively high measurement noises due to the vibration of the camera, the proposed algorithm managed to extract many landmarks with the length uncertainties less than 15 m.

The second experiment was conducted in an indoor hallway. The run included both straight and rotational motions. The map of the hallway, the odometry and modified paths and additionally the landmarks with the length uncertainties

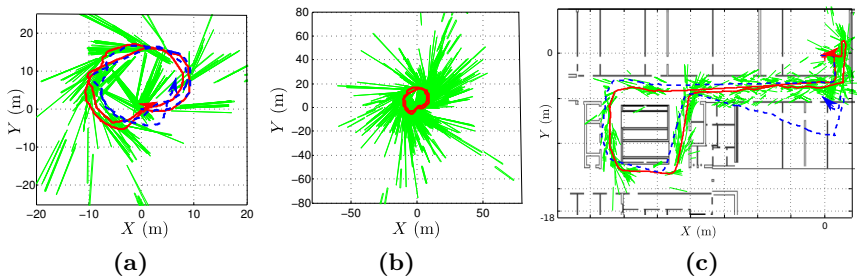


Fig. 3. Outdoor experiment: (a) Odometry path (dashed curve), modified path generated by our method (continuous curve) and extracted landmarks with length uncertainties less than 15 m. (b) Extracted landmarks (length uncertainties less than 60 m). (c) Indoor experiment: Odometry path (dashed curve), modified path generated by our method (continuous curve) and extracted landmarks with length uncertainties less than 1 m.

less than one meter can be seen in Fig. 3c. We can observe that the algorithm managed again to correct the odometry path perfectly and also localized lots of landmarks with low uncertainties.

6 Conclusion

A new non-Gaussian filtering algorithm was proposed to address the bearing-only SLAM problem. The algorithm can deal with both close and far landmarks. The proposed method works based on the sampling of the robot position distribution. Unlike the particle filter based methods in which the number of particles should increase with respect to the odometry noises, we used an efficient sampling method offered by UKF filters to let the algorithm work in a wide range of odometry noises with only seven samples. Additionally, unlike, the exponentially increasing complexity of EKF based methods, the complexity of the proposed method increases linearly with respect to the landmark numbers. The high performance of the algorithm was verified through the simulation and practical experiments. As the next works, we intend to extend this idea for the three dimensional scenarios.

References

1. Bailey, T.: Constrained Initialisation For Bearing-only SLAM. In: International Conference on Robotics and Automation, pp. 1966–1971. IEEE (2003)
2. Civera, J., et al.: Inverse Depth Parametrization for Monocular SLAM. *IEEE Transactions on Robotics* 24(5), 932–945 (2008)
3. Julier, S.J., Uhlmann, J.K.: Unscented Filtering and Nonlinear Estimation. *Proceedings of the IEEE*, 401–422 (2004)
4. Kwok, N.M., Dissanayake, G.: Bearing-only Slam Using a SPRT Based Gaussian Sum Filter. In: International Conference on Robotics and Automation, pp. 1109–1114. IEEE (2006)
5. Montemerlo, M., et al.: FastSLAM 2.0: An Improved Particle Filtering Algorithm for Simultaneous Localization and Mapping that Provably Converges. In: *Proceedings of the Sixteenth International Joint Conference on Artificial Intelligence, IJCAI* (2003)
6. Nistér, D.: An Efficient Solution to the Five-Point Relative Pose Problem. *IEEE Trans. Pattern Anal. Mach. Intell.* 26(6), 756–777 (2004)
7. Parsley, M.P., Julier, S.J.: Avoiding Negative Depth in Inverse Depth Bearing-only SLAM. In: International Conference on Intelligent Robots and Systems, pp. 2066–2071. IEEE (2008)
8. Sola, J., et al.: Undelayed Initialization in Bearing-only SLAM. In: International Conference on Intelligent Robots and Systems, pp. 2499–2504. IEEE (2005)
9. Strasdat, H., et al.: Scale Drift-Aware Large Scale Monocular SLAM. In: *Proceedings of Robotics: Science and Systems* (2010)
10. Zhao, L., et al.: Parallax angle Parametrization for Monocular SLAM. In: International Conference on Robotics and Automation, pp. 3117–3124 (2011)

Object Following Robot Using Vision Camera, Single Curvature Trajectory and Kalman Filters

Shin-nyeong Heo¹, Hyun-Seop Lim², Seungik Hwang², and Jangmyung Lee^{2,*}

¹ Interdisciplinary Program in Robotics,
Pusan National University, South Korea

² Department of Electrical Engineering,
Pusan National University, South Korea

{snheo7379, goodguy12, seunik7379, jmlee}@pusan.ac.kr

Abstract. Path planning of mobile robot has a purpose to design an optimal path from an initial position to a target point. Minimum driving time, minimum driving distance and minimum driving error might be considered in choosing the optimal path and they are correlated to each other. In this paper, an efficient driving trajectory is planned in a real situation where a mobile robot follows a moving object. Position and distance of the moving object are obtained using a web camera; the rotation angular and linear velocities are estimated using Kalman filters to predict the trajectory of the moving object. Finally the mobile robot follows the moving object using a single curvature trajectory by estimating trajectory of the moving object. Using the estimation by Kalman filters and the single curvature in the trajectory planning, the total tracking distance and error rate have been saved about 7 %.

Keywords: Kalman filter, Robot trajectory, Single Curvature, Object Following.

1 Introduction

In the past, robot was mainly used industrial automation for industrial locus. This robot is shape of manipulator. So, workspace was limited. Recently, various features of intelligent mobile robot have been studied while mobile robot is driving. Intelligent mobile robot usability and necessity is growing in each field. For example, industrial automation, unmanned industrial warehouse system, materials transportation, cleaning and guide robot and etc. Especially, service robot part is quickly growing in our daily lives [1][2]. The mobile robot to perform a given task while driving. Because of that, many things can be taken into consideration such as position measurement, speed and acceleration, obstacle recognition, and set the path to move [3].

In particular, the objective of the trajectory path planning of mobile robot from the initial position to the target point is to design the optimal path. In general, when set the optimal path can be considered minimum driving distance. So, it is necessary to reduce these elements.

* Corresponding author.

2 The Design of the Mobile Robot

2.1 The Configuration of Mobile Robot

The System Configuration consists of MCU, IMU sensor, motor driver, Web Camera and PC. This is shown in Figure 1. Using USB 2.0 Communication, data sent to the PC in real-time and PC calculates the distance and angles. The drive command is sent to the MCU using UART communication. MCU is control the mobile robot's motor using driving command. Also, Position data from motor encoder and Yaw data from IMU sensor is sent to PC using UART communication for driving motion.

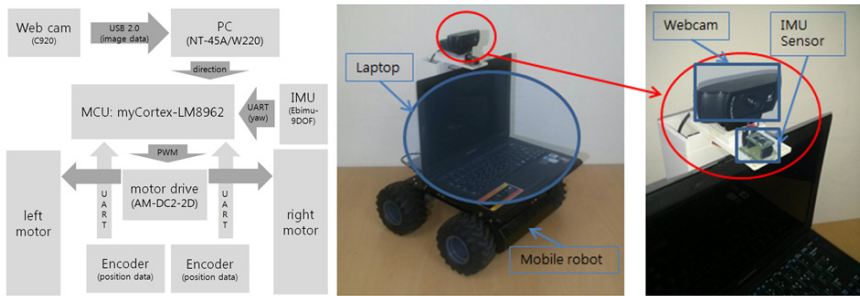


Fig. 1. The Configuration of System and Real mobile robot

2.2 The Modeling of Mobile Robot

To find out the location of a moving object on a coordinate plane XY , uses the camera's image data. To the object's distance and direction from the image data of each position is computed. Figure 2 shows coordinate of mobile robot and X_1-Y_1 is the absolute coordinates of a reference point on the outside of the mobile robot. X_2-Y_2 coordinate system has the origin as center point of the mobile robot and is based on a X axis it is mobile robot heading direction. To analyze the structure of the mobile robot, define position P in equation (2.1).

$$p = (x \quad y \quad \theta) \tag{2.1}$$

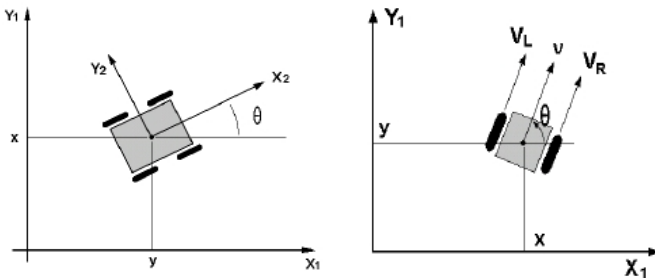


Fig. 2. Kinetic model

Kinetic model is shown in figure 2. Define the left wheel and right wheel angular velocity as ω_L, ω_R and this is shown in equation (2.2). Kinetic model represent equation (2.3).

$$V_R = r\omega_R, V_L = r\omega_L \tag{2.2}$$

$$\omega = \frac{V_R - V_L}{L} = r \frac{\omega_R - \omega_L}{L} \tag{2.3}$$

$$v = \frac{V_R + V_L}{2} = r \frac{\omega_R + \omega_L}{2}$$

Based on this kinetic model, mobile robot can be controlled to track moving object.

2.3 The Driving Principle of the Mobile Robot

The mobile robot motion status is determined by the value of both wheels speed. The mobile robot move forward if both side of the wheel's speed is same. The mobile robot rotates on the spot if the right wheel speed is 1m/s and the speed of the left wheel is -1m/s. In this case, the center of rotation is called Instantaneous Center of Curvature (ICC). ICC position is determined by speed ratio of both wheels. Equation (2.4) shows that ICC in the wheel speed and the robot is proportional to the distance.

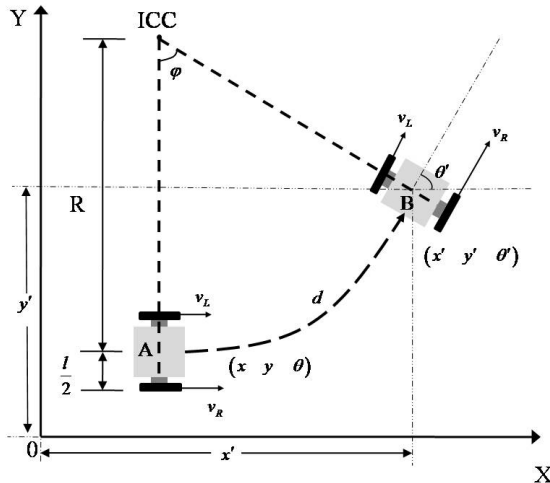


Fig. 3. ICC of mobile robot

$$v_L : v_R = R - \frac{l}{2} : R + \frac{l}{2} \tag{2.4}$$

The equation (2.4) can be summarized as equation (2.5) and l is the width of the robot. R is the mobile robot turning radius that determines the movement of the distance, or the radius of curvature.

$$R = \frac{1}{2} \left(\frac{v_R + v_L}{v_R - v_L} \right) \tag{2.5}$$

Turning radius of the mobile robot is determined by the value of both wheels speed. The mobile robot having straight movement if $R = \infty (v_R = v_L)$. The mobile robot having rotational motion if $v_R \neq v_L$. ICC coordinates is defined as the equation (2.6). In Figure 3, If the mobile robot moves from A to B, $(x \ y \ \theta)$ is the position when time is t and $(x' \ y' \ \theta')$ is the position when time is $t + \delta t$.

$$ICC = [x' - R \sin(\varphi), y' + R \cos(\varphi)] \tag{2.6}$$

The mobile robot position $(x' \ y' \ \theta')$ is as follows.

$$\begin{aligned} \begin{bmatrix} x' \\ y' \\ \theta' \end{bmatrix} &= \begin{bmatrix} \cos(\varphi\delta t) & -\sin(\varphi\delta t) & 0 \\ \sin(\varphi\delta t) & \cos(\varphi\delta t) & 0 \\ 0 & 0 & 1 \end{bmatrix} \begin{bmatrix} x - ICC_x \\ y - ICC_y \\ \theta \end{bmatrix} + \begin{bmatrix} ICC_x \\ ICC_y \\ \varphi\delta t \end{bmatrix} \\ \begin{bmatrix} x' \\ y' \\ \theta' \end{bmatrix} &= \begin{bmatrix} R \sin(\varphi\delta t) + ICC_x \\ -R \cos(\varphi\delta t) + ICC_y \\ \theta + \varphi\delta t \end{bmatrix} \end{aligned} \tag{2.7}$$

In equation (2.7), $x - ICC_x$ is 0 and $y - ICC_y$ is $-R$ as figure 3. Equation (2.7) is position of mobile robot. This expression is about rotation angle. Distance d from A to B and rotation angle φ is shown in equation (2.8), (2.9).

$$d = \int_t^{t+\delta t} v_1 dt = \int_t^{t+\delta t} \frac{v_L + v_R}{2} dt \tag{2.8}$$

$$\varphi = \frac{d}{R} = \frac{\int_t^{t+\delta t} (v_L + v_R) dt}{l(v_L + v_R)} (v_R - v_L) \tag{2.9}$$

The turning radius of the robot, moving distance, rotation angle, and the linear speed and rotational speed values can be obtained from equation (2.8), (2.9).

3 Single-Curvature Trajectory

3.1 Single-Curvature

Curvature means how fast rotate curve when moved along the curve at a point P to another point Q as shown in Figure 4. Curvature K can be expressed as follows.

$$k = \lim_{\Delta s \rightarrow 0} \left| \frac{\Delta \theta}{\Delta s} \right| = \left| \frac{d\theta}{ds} \right| \tag{3.1}$$

Curvature radius have constant curvature radius of the circle and it is called radius of gyration. Equation (3.2) means Curvature radius ρ .

$$\rho = 1 / k \tag{3.2}$$

Here K is $K > 0$ and total moving distance Δs is arc length in equation (3.1). So, curvature k is inversely proportional to the radius of curve. Radius of curvature is infinite if $K = 0$, so it can be assumed a circle with an infinite radius.

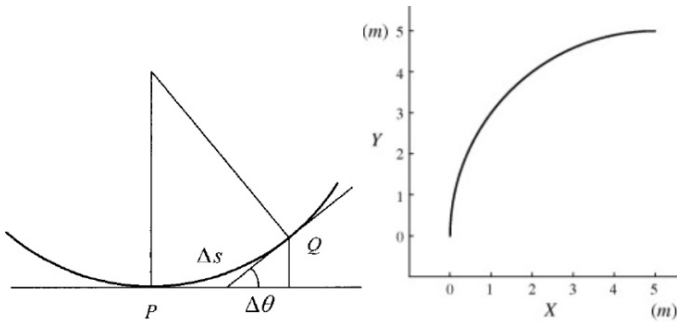


Fig. 4. The curvature of a curve and The single curvature trajectory

When the mobile robot driving along curvature trajectory, curvature radius greatly affect the driving error. Errors are more caused when curve driving ($k \neq 0$) than straight driving ($k = 0$). Driving errors are more when small rotation radius and faster speed. Figure 4 shows the trajectory of a single curvature. Smaller the turning radius and faster moving speed, error will increase when the mobile robot is using single curvature trajectory [4].

3.2 Single-Curvature Path Planning

As shown in Figure 5, the mobile robot to move to a single curvature, the trajectory path. The radius of left wheel is $r1 - (l/2)$ and right wheel is $r1 + (l/2)$. The speed of the left wheel must be fast than the speed of the right wheel. ($v_L > v_R$).

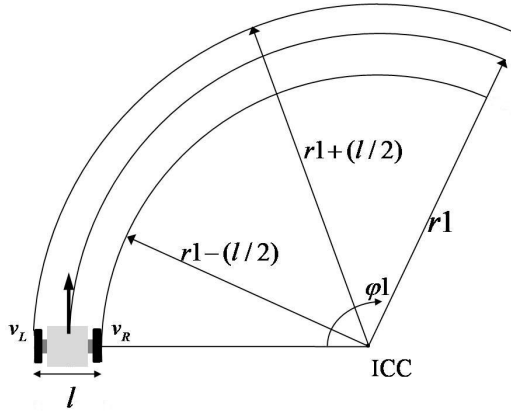


Fig. 5. Path planning of single curvature

$$v_R = \int_0^t a_R(\tau) d\tau = a_R t \tag{3.3}$$

$$v_L = \int_0^t a_L(\tau) d\tau = a_L t \tag{3.4}$$

Equation (3.3) and (3.4) are the relation between velocity and acceleration. Speed and acceleration is proportional because of $a_L > a_R$. Acceleration of left wheel is $a_L = a_{max}$ to get the minimum estimation time. ($v_L = v_R$) in a straight line trajectory. Set the value of $r1$, $\dot{\phi}l$ from this.

$$v_L = (r1 + \frac{1}{2})\dot{\phi}l \tag{3.5}$$

$$v_R = (r1 - \frac{1}{2})\dot{\phi}l \tag{3.6}$$

From equation (3.5) and (3.6), rotation radius(radius of curvature) $r1$ is expressed as equation (3.7)

$$r1 = \frac{1}{2} \left(\frac{v_L + v_R}{v_L - v_R} \right), r1 \geq \frac{1}{2} \tag{3.7}$$

4 State Estimation of Moving Object

4.1 Kalman Filter

The Kalman filter is an algorithm that uses a series of measurements observed over time, containing noise (random variations) and other inaccuracies, and produces estimates of unknown variables that tend to be more precise than those based on a single measurement alone. More formally, the Kalman filter operates recursively on streams of noisy input data to produce a statistically optimal estimate of the underlying system state. The filter is named for Rudolf (Rudy) E. Kálmán, one of the primary developers of its theory. Kalman filter is used many areas like computer vision, robotics, radar. In this paper, Kalman filter is used for trajectory prediction of moving object on image frame to robust state estimation. Image frame size is 640x480. The proposed markers on the Cartesian coordinates of the image frame is moving, as shown in Figure 6. The coordinates of the moving object in the direction of the x-axis has the coordinates from 0-640. Y-axis has the coordinates to 0-480. x,y position, direction, speed, rotation, angular velocity is estimate through Kalman filter. From the moving object (proposed markers) x,y coordinates.

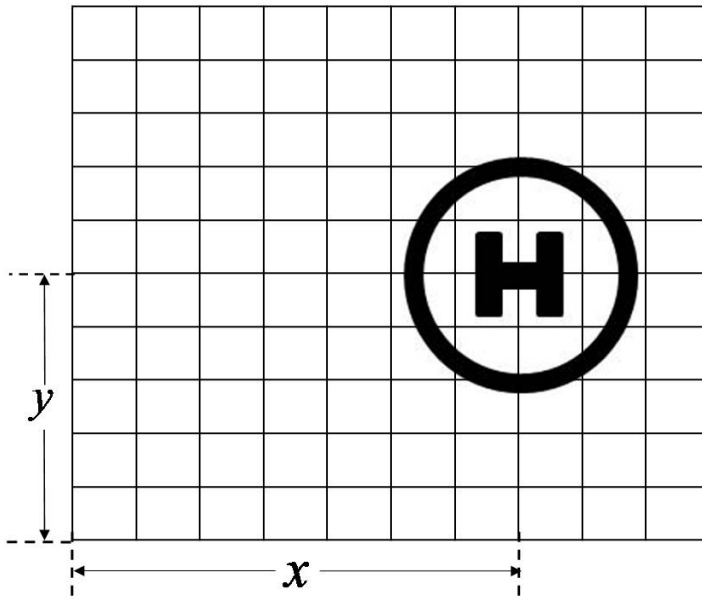


Fig. 6. A coordinate of moving object(proposed mark) on image frame

4.2 Steps of Kalman Filter

Kalman filter is consists of 6 steps (A~E) as shown in figure 6.

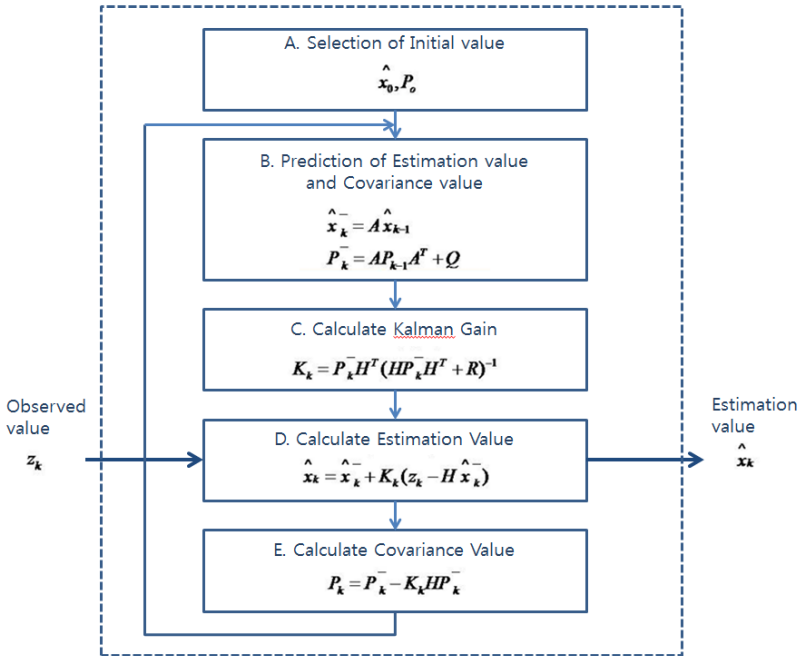


Fig. 7. Kalman Filter

Step A is the selection of the initial value. Input is the measurements value(z). Output is the estimation value. Calculate Kalman gain(K) in step C using estimation value and Covariance value in step B. Step D, calculate the estimate value using the input measurements value. Finally, in step E the estimate error covariance shows how accurate estimation value. It can be determined that using estimation value or not. In other words, estimate value of error covariance and compensate between measurement value and estimation value. Then, get the new estimation value. In this paper, the trajectory of a moving object using Kalman filter to predict the rotational angular velocity and the linear velocity of the moving object is estimated.

4.3 Position Estimation for Moving Objects

Estimation position of moving objects is as follows.

$$\hat{P}_{x+\delta t} = \hat{P}_x + \hat{V}_x \delta t + \frac{1}{2} \hat{A}_y \delta t^2 \quad (4.1)$$

$$\hat{P}_{y+\delta t} = \hat{P}_y + \hat{V}_y \delta t + \frac{1}{2} \hat{A}_y \delta t^2 \quad (4.2)$$

$$\hat{P}_{z+\delta t} = \hat{P}_z + \hat{V}_z \delta t + \frac{1}{2} \hat{A}_z \delta t^2 \tag{4.3}$$

δt is sampling time and $(P_x, P_y)(V_x, V_y)(A_x, A_y)$ shows the estimates of position, velocity and acceleration of mobbing object. Equation (4.7)~(4.8), such as a random movement is defined that causing the movement of the moving object changes in V_k and w_k .

$$\begin{aligned} \delta x_{k+\delta t} &= v_k \delta t \cos(\theta_k + \frac{1}{2} \omega_k \delta t) \\ &\approx v_k \cos(\theta_k) \delta t - \frac{1}{2} \omega_k v_k \sin(\theta_k) \delta t^2 \end{aligned} \tag{4.4}$$

$$\begin{aligned} \delta y_{k+\delta t,k} &= v_k \delta t \sin(\theta_k + \frac{1}{2} \omega_k \delta t) \\ &\approx v_k \sin(\theta_k) \delta t + \frac{1}{2} \omega_k v_k \cos(\theta_k) \delta t^2 \end{aligned} \tag{4.5}$$

$$\delta \theta_{k+\delta t,k} = \omega_k \delta t \tag{4.6}$$

$$\delta v_{k+\delta t,k} = \zeta_v \tag{4.7}$$

$$\delta \omega_{k+\delta t,k} = \zeta_\omega \tag{4.8}$$

Where ζ_v, ζ_ω are Gaussian random variables [5][6].

4.4 State Estimation of a Moving Object Using Kalman Filter

In order to apply the Kalman filter to estimate the state of moving objects, equation (4.9),(4.10) of the discrete- time state transition model is required .

$$x_k = \Phi_{k,k-1} x_{k-1} + \omega_{k-1} \tag{4.9}$$

$$z_k = H_k x_k + v_k \tag{4.10}$$

$$\begin{bmatrix} x_k \\ y_k \\ \theta_k \\ v_k \\ \omega_k \end{bmatrix} = \begin{bmatrix} 1 & 0 & 0 & \delta t \cos(\theta_{k-1}) & -\frac{1}{2} v_{k-1} \delta t^2 \sin(\theta_{k-1}) \\ 0 & 1 & 0 & \delta t \sin(\theta_{k-1}) & \frac{1}{2} v_{k-1} \delta t^2 \cos(\theta_{k-1}) \\ 0 & 0 & 1 & 0 & \delta t \\ 0 & 0 & 0 & 1 & 0 \\ 0 & 0 & 0 & 0 & 1 \end{bmatrix} \begin{bmatrix} x_{k-1} \\ y_{k-1} \\ \theta_{k-1} \\ v_{k-1} \\ \omega_{k-1} \end{bmatrix} + \begin{bmatrix} 0 \\ 0 \\ 0 \\ \zeta_v \\ \zeta_\omega \end{bmatrix} \tag{4.11}$$

$$\begin{bmatrix} x_k \\ y_k \end{bmatrix} = \begin{bmatrix} 1 & 0 & 0 & 0 & 0 \\ 0 & 1 & 0 & 0 & 0 \end{bmatrix} \begin{bmatrix} x_k \\ y_k \\ \theta_k \\ v_k \\ \omega_k \end{bmatrix} + \begin{bmatrix} \gamma_k \\ \gamma_k \end{bmatrix} \quad (4.12)$$

Covariance matrix of the estimation error is required to obtain the filter gain. Equation (4.13) shows covariance matrix of the estimation error. The optimal filter gain K_k is the equation (4.14).

$$P'_k = \Phi_{k,k-1} P_{k-1} \Phi_{k,k-1}^T + Q_{k-1} \quad (4.13)$$

$$K_k = P'_k H_k^T [H_k P'_k H_k^T + R_k]^{-1} \quad (4.14)$$

Equation (4.15) is the process of estimating the state

$$\hat{x}_k = \Phi_{k,k-1} \hat{x}_{k-1} + K_k [z_k - H_k \Phi_{k,k-1} \hat{x}_{k-1}] \quad (4.15)$$

Finally, Equation (4.16) go through the process of modifying the covariance matrix of the estimation error. And re-circulate the process of equation (4.13) [7].

$$P_k = P'_k - K_k H_k P'_k \quad (4.16)$$

4.5 Moving Object Trajectory Prediction

Approximation modeled as a function from the state estimator to estimate the speed and the rotational angular velocity of the moving object using Kalman filter. Equation (4.17)~(4.18) is modeled after the input is predicted.

$$v_{k+n} = \hat{v}_k + \hat{a}_{lk} nT \quad (4.17)$$

$$\omega_{k+n} = \hat{\omega}_k + \hat{a}_{\omega k} nT \quad (4.18)$$

Finally, equation (4.17) shows for the trajectory of a moving object.

$$\begin{aligned} \hat{x}_{k+m} &= x_k \sum_{h=0}^m v(h) \cos[\theta(h)]T, \quad \hat{y}_{k+m} = y_k + \sum_{h=0}^m v(h) \sin[\theta(h)]T \\ v(h) &= \hat{v}_k + \hat{a}_{lk} hT, \quad \theta(h) = \hat{\theta}_k + \omega_k hT + \frac{1}{2} \hat{a}_{\omega k} hT^2 \end{aligned} \quad (4.19)$$

5 Experimental Results

In this paper, proposed forecasting the trajectory of a moving object about minimum driving distance using image frame. The proposed test environment running in real time to predict the trajectory of a moving object trajectories run to investigate how they affect the experiment as shown in the following Table 1 A, B, each experiment was performed five times. Experiment A is calculated the position of a moving object through image processing. After, calculate the turning radius and distance, driving using position value from encoder.

Experiment B is the position of moving objects through image processing is obtained as same as Experiment A. Forecast the trajectory of the moving object on image frame after estimate rotational angular velocity and the linear velocity of the moving object using Kalman filter state estimation. Finally, turning radius, distance to calculate the position of the encoder is run through the values.

Table 1. The test composition

Experiment A	Mobile robot following a moving object using only single-curvature trajectory.
Experiment B	Mobile robot following a moving object using single curvature trajectory and Kalman filters



Fig. 8. The image frame detecting the identification mark

Figure 8 shows the actual experiment on the recognition of the image frame to detect the marker. Experimenter was holding the actual recognition marker and moved along the S-shaped course.

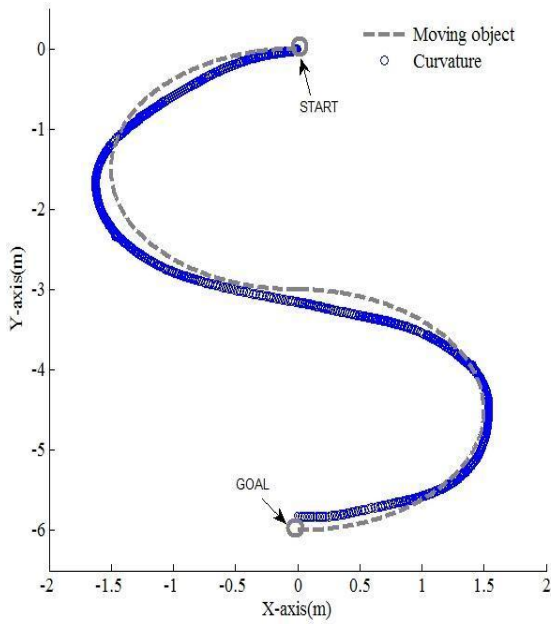


Fig. 9. Trajectory of mobile robot of second test A

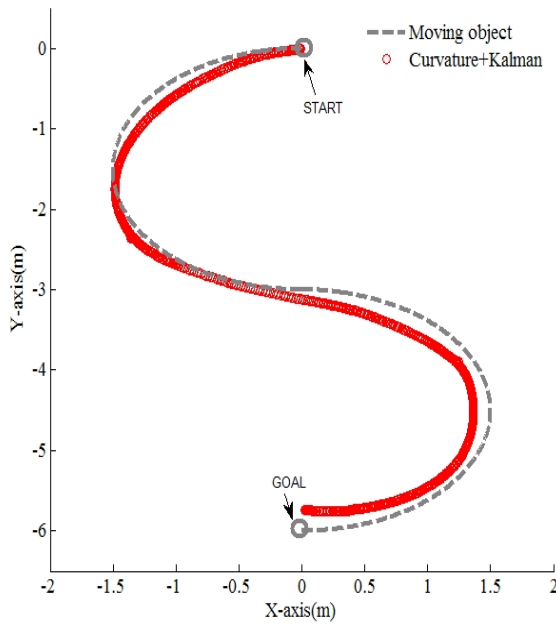


Fig. 10. Trajectory of mobile robot of second test B

Figure 9 shows the results of the second experiment A. Trajectory of moving objects is gray, trajectory of the mobile robot is blue. First curve area of experiment A, The mobile robot is driving 144mm outer from reference course. Straight sections from (-0.5, -3) to (0.5, -3), K is almost 0. So, the mobile robot driving maximum speed and minimum distance(straight line). Also, the mobile robot driving outer from reference course at second curve section of experiment A. Figure 10 is result of second experiment B. Trajectory of moving objects is gray, trajectory of the mobile robot is red. The moving object tends to move following the trajectory the first curve section at Experiment B. A straight course is the same as the experiment the shortest distance (straight line) was run with. Also, second curve section is estimated well. So, experiment B has better performance than the experiment A.

Table 2. The total driving distance (m)

	result1	result2	result3	result4	result5	Average
Experiment A	9.86	9.57	9.45	9.94	9.76	9.72
Experiment B	8.98	9.06	9.24	8.96	9.21	9.09

Total reference driving distance is 9.42m. Driving distance of experiment A,B are shown in Table 2. Driving distance of Experiment A is average 9.72m and Experiment B is average 9.09. Experiment A is longer than Experiment B. So, proposed methods have better performance.

6 Conclusion

Need the mobile robot path plan to find the optimal driving trajectory. Path planning is required considering the Minimum driving time, minimum driving distance and minimum driving error. In this paper, mobile robot for tracking moving objects in real-time driving trajectory is described. The driving purpose of the trajectory is a minimum of distance. Single curvature trajectory is applied for tracking moving objects and Kalman filter was used for reduce the distance to find the optimal trajectory. Experiment was done at curve course for occurs more errors. So, It can show how to reduce the distance. Finally, using a Kalman filter with a single curvature trajectory is better than only using single curvature trajectory.

Acknowledgements. This research was supported by the MSIP(Ministry of Science, ICT & Future Planning), Korea, under the ITRC(Information Technology Research Center) support program (NIPA-2013-H0301-13-2006) supervised by the NIPA(National IT Industry Promotion Agency).

This research was supported by the MOTIE(The Ministry of Trade, Industry and Energy), Korea, under the Human Resources Development Program for Special Environment Navigation/Localization National Robotics Research Center support program supervised by the NIPA(National IT Industry Promotion Agency). (H1502-13-1001).

References

- [1] Jin, T.-S., Lee, J.-M.: Object Position Estimation and Optimal Moving Planning of Mobile Manipulator based on Active Camera. *The Institute of Electronics Engineers of Korea* 42(5), 1–12 (2005)
- [2] Ko, N.-Y., Seo, D.-J., Moon, Y.-S.: A method for Real Time Target Following of a Mobile Robot Using Heading and Distance Information. *Korean Institute of Intelligent Systems* 18(5), 624–631 (2008)
- [3] Choi, B.-S., Lee, J.-M.: A Capturing Algorithm of Moving Object using Single Curvature Trajectory. *The Institute of Control, Robotics and Systems* 12(2) (February 2006)
- [4] Jin, T.-S., Lee, J.-M.: Localization and Navigation of a Mobile Robot using Single Ultrasonic Sensor Module. *The Institute of Control, Robotics and Systems*, vol. 12(2) (February 2006)
- [5] Hwang, C.-H., Lee, S.-H., Cho, B.-T., Lee, J.-M.: Optimal Trajectory Planning for Capturing a Mobile Object. *The Institute of Control, Robotics and Systems* 10(8) (August 2004)
- [6] Park, J.-W., Park, J.-H., Yun, K.-S., Lee, J.-M.: Tracking and Capturing a Moving Object Using Active Camera Mounted on a Mobile Robot. *The Institute of Control, Robotics and Systems* 7(9) (September 2001)
- [7] Yi, H.-J., Choi, Y.-K.: A Navigation Algorithm for Mobile Robots in Unknown Environments. *Korean Institute of Intelligent Systems* 16(3), 275–284 (2006)

Accurate Localization with COAG Features and Self-adaptive Energy Region

Dong-Il Kim^{*} and Jae-Bok Song

Department of Mechanical Engineering, Korea University, Korea
{astronovic, jbsong}@korea.ac.kr

Abstract. Localization is very important for autonomous navigation of a mobile robot. For outdoor localization, Monte Carlo Localization (MCL) is used with the digital surface model. In order to develop an improved localization technique, in this study, commonly observed from air and ground (COAG) features are incorporated into an MCL localization system by means of an energy function to determine candidates. Experiments in real environments show improved localization accuracy over methods using MCL with COAG features.

Keywords: Monte Carlo Localization, MCL.

1 Introduction

An effective localization technique is essential to perform autonomous navigation. Commonly, global positioning system (GPS) information is incorporated to solve the outdoor localization problem. However, GPS signals can be occluded by obstacles in places such as forests. Therefore, localization techniques with range sensors have been researched. In such situations, a mobile robot has to estimate its pose in the environments from the reference map. One of the most popular reference maps is the digital surface map (DSM) [1, 2]. In DSMs, a single height measurement is stored in a two-dimensional (2D) grid as shown in Fig. 1. Maps can be generated using an aerial mapping system equipped with GPS and range sensors. This type of map can be used for various applications such as military navigation in large outdoor environments [3].

Monte Carlo Localization (MCL), which is commonly used with range sensors, has been studied in the previous works [4]. MCL could be improved using more detailed maps [5] and feature extraction. One such feature extraction technique - commonly observed air and ground (COAG) feature extraction - was proposed in [6]. COAG feature extraction classifies the grids on the map with respect to the viewpoint of the robot. Therefore, COAG can be used to determine whether the sensor data and predicted data are the same or not. However, if the sample distribution in the particle filter does not include the real robot pose, the pose error increases significantly. Therefore, in this study, the energy function known as self-adaptive Monte Carlo

^{*} Corresponding author.

localization (SAMCL) [7] is used to generate points initially, and the resampling and importance weighting processes are modified so that they use this function. Through the modification of MCL, the samples were able to be distributed reasonably, and the accuracy of MCL was improved.

This paper is organized as follows. Section 2 introduces COAG features briefly. Modification of MCL with the energy function and COAG feature extraction is explained in section 3, and the improvement of localization performance through the proposed method is analyzed in section 4. Finally, the conclusions of this study are presented in section 5.

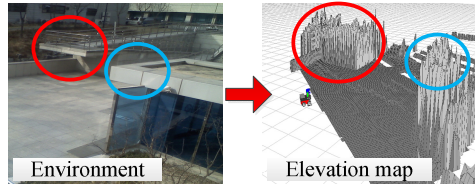


Fig. 1. An example of an environment modeled as an elevation map

2 COAG Features

In this chapter, COAG features [6] are briefly described. Figure 2 shows some disadvantages of a 2.5D elevation map: the range measured by the sensor can be significantly different from the range predicted by the map. Therefore, the elevation map cannot describe the 3D outdoor environment well, but it is still widely used for applications such as military vehicles, land surveying, and geography.

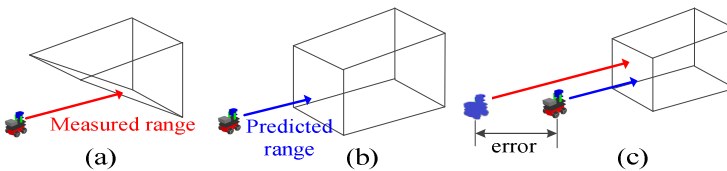


Fig. 2. Difference between measured range and range predicted from an elevation map. If the range is measured from the robot's perspective (a), the range map is predicted as (b) from the elevation map. Therefore, the error pictured in (c) occurs.

To cope with the disadvantage described above, COAG features are classified into 4 groups: commonly observed (CO), potentially commonly observed (PCO), not commonly observed (NCO), and unknown (UN). COAG points are extracted with a laser rangefinder and a DC tilt motor. As shown in Fig. 3, CO points are extracted for the grids commonly observed from both the air and the ground, so the range to CO point is predicted from the DSM, and the range is very close to the range measured by a laser rangefinder. The grids higher than the PCO point are not properly sensed because the tilt angle of a laser rangefinder is limited. Probably, the PCO point is

likely to be on the vertical surface, but we cannot assure the grid of PCO point is correctly sensed. As shown in Fig. 3(c), NCO points are extracted for the grids unable to be sensed from the air. So, the range predicted from the DSM is different from the range measured by a laser rangefinder. For features of these categories, range data can be observed from the air but not from the ground, so we use only CO points for matching, because they most suit the purposes of our research.

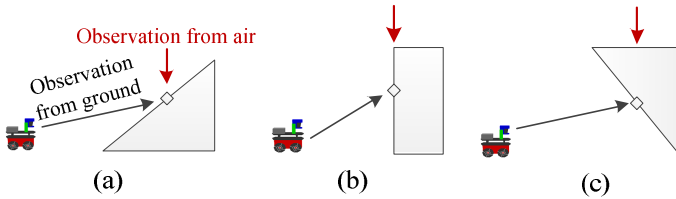


Fig. 3. Examples of COAG Features. (a) is an example of CO point. (b) and (c) are examples of PCO and NCO features.

3 Modified Monte Carlo Localization

A similar energy region (SER) [7] was used to express the viability of the samples in the studies using a 2D grid map and range data. However, SER is not applicable to localization methods using DSM. Therefore, in this study, the energy of each sample is calculated with COAG feature extraction.

3.1 Energy Function

In this paper, we adopt the energy function used in self-adaptive Monte Carlo Localization (SAMCL). As mentioned in section 2, CO points are the most meaningful for localization with DSMs. The energy function considers the point type as a criterion which determines if the samples are in a reasonable place on the DSM.

To start, the energy for range measurements is defined as:

$$a_i = 1 - d_i/d_{\max} \quad (1)$$

where d_i is range measurement i with respect to a CO point and d_{\max} is the maximum measurement of the range sensor. Using a_i , the total energy of each sample is calculated as the sum over all energy values and normalized.

$$E(n) = (\sum_{i=1}^I a_i^{[n]}) / I \quad (2)$$

where I is the number of samples—used as a normalizer—and n is the sample index. By calculating the discrepancy between $E(n)$ and the energy from the real sensor data E , it is determined whether the samples are in a reasonable place. The overall procedure for calculating the discrepancy is described in Algorithm 1.

Algorithm 1. Energy Function. m_{CO} is a measurement between the robot and a CO point, and E is the energy calculated with real sensor data, where δ is the threshold value.

```

1: Input :  $m_{CO}$ 
2: for all samples  $n$  do
3:   for all measurements to CO point  $i$ 
     each measurement  $d_i < d_{max}$  do
4:      $a_i^{[n]} = 1 - d_i^{[n]}/d_{max}$ 
5:   end for
6:    $E(n) = \sum_{i=1}^I a_i^{[n]}$ 
7:   normalize  $E(n) = E(n)/I$ 
8:   if  $|E(n) - E| > \delta$  then
9:      $E(n) = 0$ 
10:  end if
11: end for
12: Output:  $E(n)$ 

```

3.2 Modified Monte Carlo Localization

By using the energy function, the samples can be distributed reasonably over the DSM as shown in Fig. 4. For the initial sampling, the CO points were extracted from the initial sensor data for use by the energy function.

With the samples distributed reasonably, other processes of MCL were performed. In this paper, the sampling importance resampling (SIR) algorithm is adopted [8, 9]. This algorithm consists of three steps: sampling, importance weighting, and resampling. After the initial sampling, these steps are repeated. Before the sampling process, COAG point extraction is also accomplished.

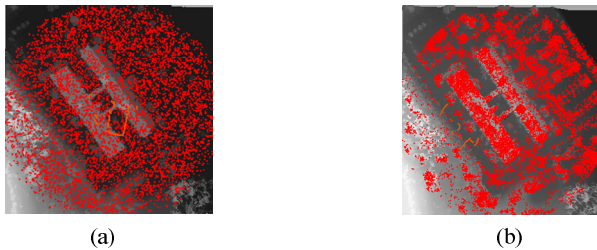


Fig. 4. Difference of initial sampling process for global localization in the conventional and proposed methods. (a) initial sampling of the conventional method, and (b) sampling using the proposed method.

After the sampling step according to the motion input, the weights are assigned to each sample by the importance weighting process. The sensor model and weight from the energy function are used along with the motion model. The importance weighting factor is calculated from the sensor model as follows:

$$\omega_t^{(n)} = \frac{bel(x_i^{(n)})}{bel^-(x_i^{(n)})} = \eta \cdot p(z_t | x_t^{(n)}) \quad (3)$$

where η is the normalization constant, $\omega_t^{(n)}$ is the importance factor of the weight, z_t is the sensor measurement and x_t is the pose at time t . Using (2) and (3), the weight of the sample can be derived as follows:

$$\omega_{t_final}^{(n)} = E(n) \times \omega_t^{(n)} \quad (4)$$

where ω_{t_final} , the weight of each sample, is finally calculated. After the weight is calculated, it is normalized, and the resampling process is performed for the next step. Through this process, the samples with the higher importance weight are selected more frequently. Clusters naturally form, and one of them is near the true robot pose; the true robot pose is estimated by iteration of the SIR algorithm. Algorithm 2 shows the entire modified MCL algorithm.

Algorithm 2. Algorithm of modified MCL. χ_{t-1} is the set of particles.

```

1: Input :  $\chi_{t-1}, u_t, z_t, m$ 
2:  $z_{t\_co} = \text{coag\_points\_extraction}(z_t)$ 
3: for  $m = 1$  to  $M$  do
4:    $x_t^{[m]} = \text{sample\_motion\_model}(u_t, x_{t-1}^{[m]})$ 
5:    $\omega_t^{[m]} = \text{sensor\_model}(z_{t\_co}, x_t^{[m]}, m)$ 
6:    $E(m) = \text{energy\_function}(z_{t\_co}, m)$ 
7:    $\omega_{t\_total}^{(m)} = E(n) \times \omega_t^{(m)}$ 
8:    $\bar{\chi}_t = \bar{\chi}_t + \langle x_t^{[m]}, \omega_{t\_total}^{[m]} \rangle$ 
9: end for
10: for  $m = 1$  to  $M$  do
11:   draw  $i$  with probability  $\propto \omega_{t\_total}^{[i]}$ 
12:   add  $x_i$  to  $\chi_t$ 
13: end for

```

4 Results

Fig. 5 represents a reference map of a testing ground at Changwon, Korea, and the map consists of 25cm x 25cm grid cells. Experiments were conducted using a Pioneer 3-AT platform (Adept MobileRobots) equipped with a laser rangefinder (SICK LMS 291) and a DC Tilt motor.

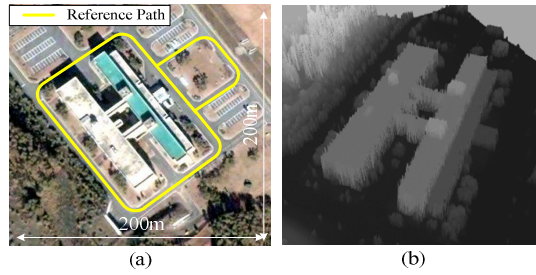


Fig. 5. Testing ground and modeled elevation map

Global localization was performed with 20,000 samples. Localization was considered successful if the number of samples was under 500, and the heading of the robot was similar to the real heading. As shown in Fig. 6(a), 20,000 samples were initially distributed over the reasonable region. From the iterative update and resampling process, the samples were redistributed around the samples that had high probability as shown in Fig. 6(b). As a result, the samples converged around the real position of the robot as shown in Fig. 6(c). After the several experiments, the success rate was about 65%.

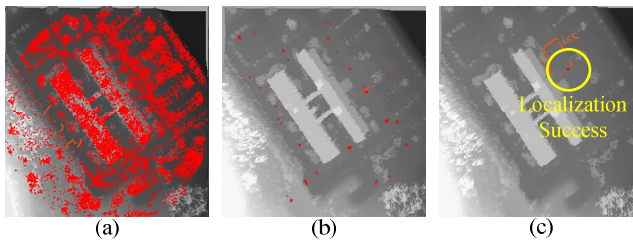


Fig. 6. Process of global localization with the proposed method

Local tracking is the process that estimates the robot pose in the local area. Fig. 7(a) shows a distribution of 500 samples around the initial pose. Fig. 7(b) shows the estimated path from the proposed scheme, and Fig. 7(c) shows the result from 100 repetitive experiments.

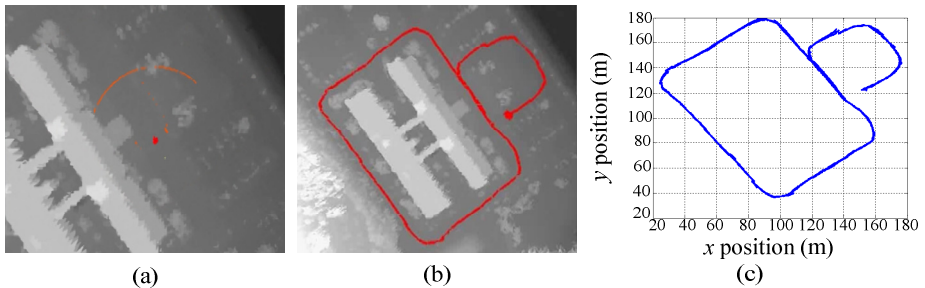


Fig. 7. Results of local tracking with the proposed method

The estimated pose errors from local tracking are represented in Fig. 8. The result from the proposed scheme is compared with the conventional method using DSM and COAG features. The average error from the method using DSM and COAG features is 1.9m and the average error from the proposed method is 0.8m, which indicates that the estimation accuracy is improved by the proposed method.

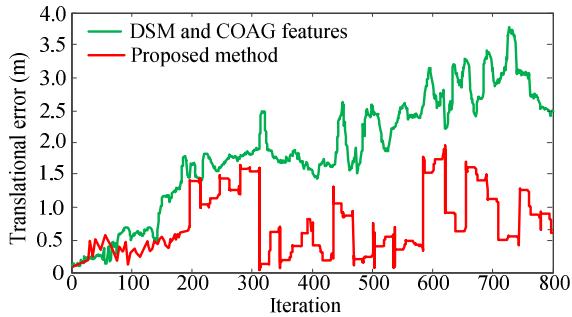


Fig. 8. Comparison between the results of the methods. The graph shows the translation error for MCL iteration.

5 Conclusion

In this paper, an improved MCL for robust outdoor localization was proposed. By using COAG features and the energy function, the samples were distributed in a reasonable area of the reference map. The proposed scheme was validated by the experiments conducted in the real environment.

The results show that the proposed method improved estimation accuracy, so it is useful for DSM-based MCL. The proposed algorithm reduced localization failures since the samples were reliably distributed. In addition, the proposed method can be applied to various environments since DSMs can be built by an aerial LIDAR system.

Acknowledgements. The authors gratefully acknowledge the support from UTRC (Unmanned Technology Research Center) at KAIST, originally funded by DAPA and ADD.

References

1. Nashashibi, F., Fillatreau, P., Dacre-Wright, B., Simeon, T.: 3-D Autonomous Navigation in a Natural Environment. In: IEEE International Conference of Robotics and Automation, pp. 433–439 (1994)
2. Parra, C., Murrieta-Cid, R., Devy, M., Briot, M.: 3-D Modelling and Robot Localization from Visual and Range Data in Natural Scenes. In: Christensen, H.I. (ed.) ICVS 1999. LNCS, vol. 1542, pp. 450–468. Springer, Heidelberg (1998)

3. Frederick, P., Kania, R., Rose, M.D., Ward, D., Benz, U., Baylot, A., Willis, M.J., Yamauchi, H.: Spaceborne Path Planning for Unmanned Ground Vehicles (UGVs). In: IEEE Conference of Military Communications (MILCOM), pp. 3134–3141 (2005)
4. Fox, D.: Monte Carlo Localization: Efficient Position Estimation for Mobile Robots. In: Proc. Of AAAI 1999, Orlando, FL (1999)
5. Kummerle, R., Triebel, R., Pfaff, P., Burgard, W.: Monte Carlo Localization in Outdoor Terrains Using Multilevel Surface Maps. *Journal of Field Robotics* 25(6-7), 346–359 (2008)
6. Kwon, T.B., Song, J.B.: A New Feature Commonly Observed from Air and Ground for Outdoor Localization with Elevation Map Built by Aerial Mapping System. *Journal of Field Robotics* 28(2), 227–240 (2011)
7. Zhang, L., Zapata, R., Lepinay, P.: Self-adaptive Monte Carlo Localization for Mobile Robots using Range Sensors. In: IEEE/RSJ International Conference on Intelligent Robots and Systems, pp. 1541–1546 (2009)
8. Doucet, A.: On Sequential Monte Carlo Sampling Methods for Bayesian Filtering. In: *Statistics and Computing*, vol. 10, pp. 197–208 (2000)
9. Doucet, A.: *Sequential Monte Carlo methods in practice*. Springer, Berlin (2001)

2D Multi-class Occupancy Grid Map for a Mobile Security Robot in Urban Environments

Yungeun Choe and Myung Jin Chung

Robotics Program, Korea Advanced Institute of Science and Technology,
Daejeon, Republic of Korea
yungeun@kaist.ac.kr, mjchung@ee.kaist.ac.kr

Abstract. Previously developed our 3D sematic perception and mapping technique can provide semantic information of the urban structures. In this paper we propose 2D MOG map to integrate semantic information of the urban structures and its change detection method for the sake of security patrol robot surveillance. Occupancy of 3D objects can be simply represented in 2D grids according to classes. Since 2D MOG Map follows probability properties, we showed that 2D MOG Map can be adopted for updating map and change detection.

Keywords: Semantic mapping, Change Detection, Surveillance Robot, Laser Scanner, Point Cloud, Urban Environment.

1 Introduction

3D semantic perception ability in urban environments, which can determine kinds of urban object such as car, building, tree, and road, is crucial for high level autonomous robotic tasks. The main examples of utilizing the perception ability are safety, security, and rescue robotics (SSRR). This paper deals with an application of semantic perception ability for a mobile security robot.

It spends high costs for employing security guards. The use of mobile security robots can save time and costs for patrols. The goal of this paper is to suggest a mobile security robot system and its algorithms based on the semantic perception ability, in order to substitute patrol missions of security guards in urban environments.

In patrol mission scenario, we aim that mobile robots perform mission level teleoperation [1] for fully autonomous surveillance. In mission level teleoperation, an operator can give a command by simple way, for instance: find parking cars in front of the building. To perform the scenario, security robots should prepare various robotic techniques as shown in Figure 1. Recent SLAM techniques [2] in robotics community have shown that it can perform autonomous navigation of a mobile robot. Similarly semantic perception [3] has been studied for recent years since semantic perception plays an important role to perform the surveillance mission.

In previous work of surveillance, a main source of sensing the environments is images or videos collected by cameras. There are many previous works based on image analysis [4]. However cameras cannot be installed in everywhere and are not suitable

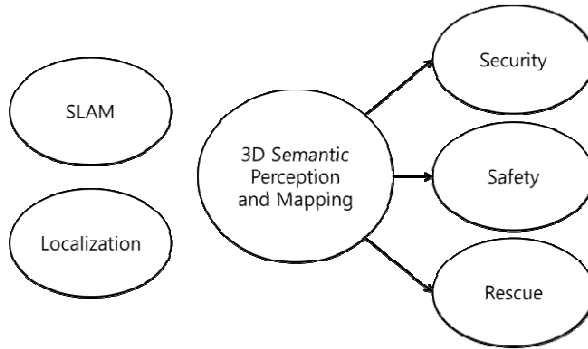


Fig. 1. Robot technologies for urban surveillance robot

for urban environments. For the surveillance mission in urban environments, 2D or 3D laser scanner is a more preferable solution than camera since laser scanner is robust to illumination changes.

To achieve the surveillance mission, we designed a mobile security robot (Figure 2) and its system software architecture (Figure 3). When a security robot is driving in urban environments, for surveillance, they should recognize the objects in urban environments such as building, road, car, tree and etc.

Previously developed our 3D semantic perception and mapping technique [5] can provide semantic information of the urban structures. As shown in Figure 3 and 4, for the surveillance mission, recognized objects need to be determined if they are changed or not. In robotics community the technique is referred to as change or novelty detection. Among the changed objects, it requires to pick out strange objects (Anomaly Detection).

In this paper we propose the change detection method. In that case, semantic perception results are accumulated in the proposed 2D multi-class occupancy grid map.

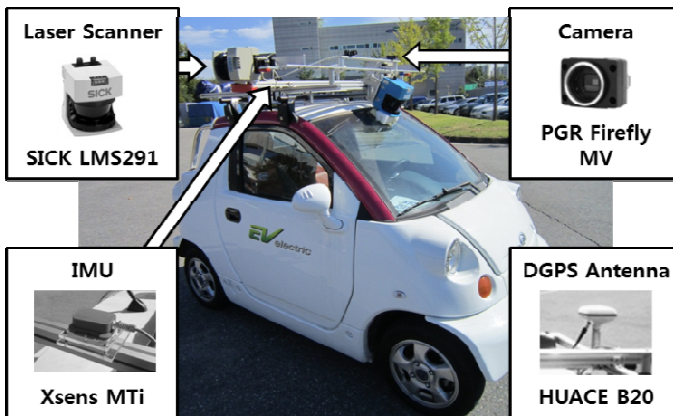


Fig. 2. System hardware of our urban surveillance robot

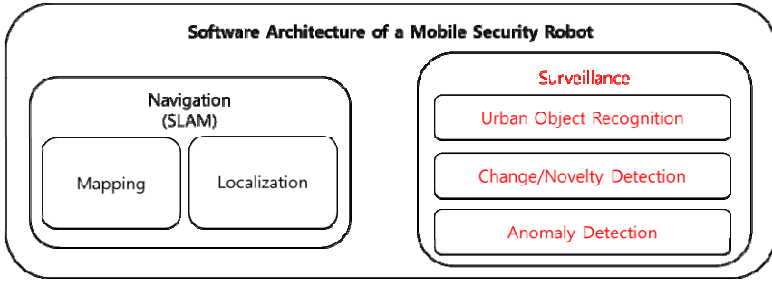


Fig. 3. Software architecture for autonomous surveillance

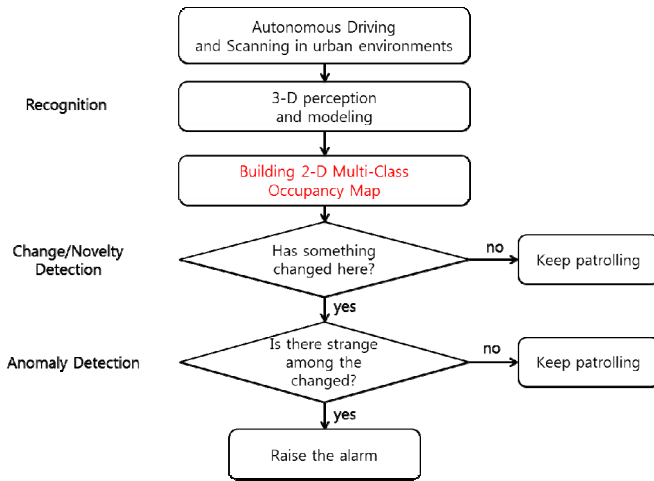


Fig. 4. Flow Chart of autonomous surveillance algorithm

2 Related Work

In a previous research of change detection [6], the 3D Gaussian distribution [7] representation used with adaptive cell size is to efficiently represent both the spatial and color aspects of the reference model. In [7], changes are detected over the point clouds using a combination of the Gaussian Mixture Model (GMM) and the Earth Mover’s Distance (EMD) algorithms. The shape retrieval is achieved using two different algorithms. The set of geometric primitives has been limited to the set, i.e., sphere, cylinder, plane.

A disadvantage of the previous change detection algorithms ([6], [7]) is that previous works only deal with change detection in 3-D space for surveillance. The change detection results do not include semantic information such as the kinds of urban structures. For anomaly detection, semantic information of the urban structures is required. e.g.) Is a car moved? Is a road broken?

In this paper, we propose a map structure named 2D multi-class occupancy grid map (MOG map) that include semantic information. The proposed MOG map

integrates semantic information and can be also applied to change detection and anomaly detection as well. MOG map plays important role for surveillance and simply the procedure.

3 2D Multi-Class Occupancy Grid Map (2D MOG Map)

2D occupancy grid map [8] is a popular mapping algorithm to integrate sensor information collected from laser scanner or sonar sensor. In 2D occupancy grid map [8], there are two states, occupied or non-occupied. The probability of occupancy in each grid is denoted by coloring from black (occupied) to white (non-occupied) as shown in Figure 5. In 2D occupancy grid map however it supports only occupancy information of occupied objects without considering various kinds of objects.

$$X = \{\text{occupied, non-occupied}\}: \text{map occupancy in one grid} \quad (1)$$

$$P(X | Z_{1:t}): \text{occupancy given the observations}$$

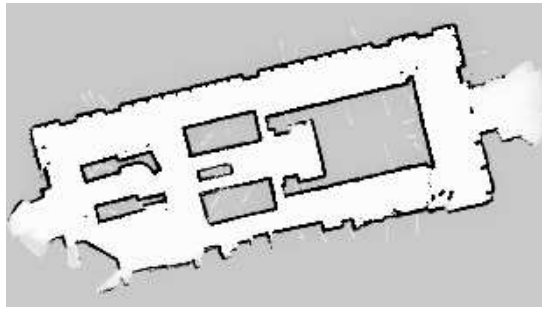


Fig. 5. An example of 2D Occupancy Grid Map [8]

The purpose of 2D MOG map is to integrate occupancy information of multi-class objects in 2D grids. Occupancy of 3D objects can be simply represented in 2D grids according to classes as shown in Figure 6 and 7. Where points are labeled with one of urban classes [3], occupied points are projected onto 2D grids as shown in Figure 6.

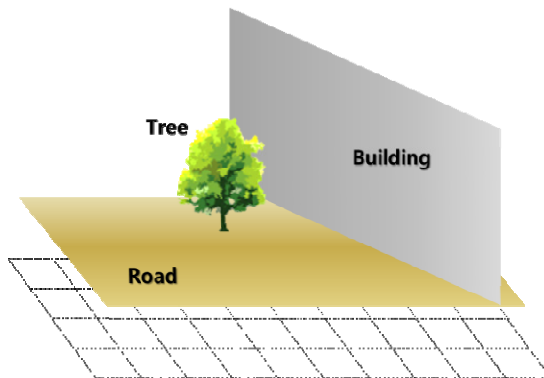


Fig. 6. Illustration of 3D scanning points are projected onto 2D grids

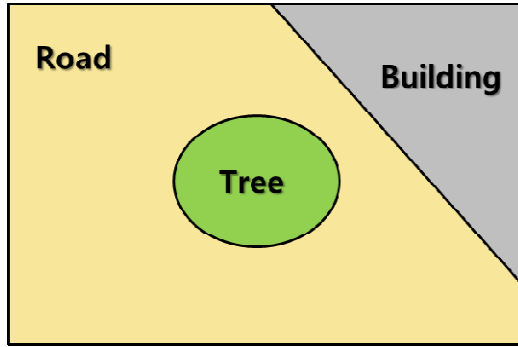


Fig. 7. Illustration of 2D Multi-class Occupancy Grid(MOG) Map

While in 2D occupancy grid map there are two states, occupied or non-occupied, in 2D MCG map there are five states such that building, tree, road, car, and others (5 classes) as follow:

$$X = \{x_1, x_2, \dots, x_{N_c}\}$$

$$N_c = 5 : \text{number of classes}$$

In 2D MCG Map, all grids are always occupied ('non-occupied' $\notin X$). This map is distinguished with occupancy grid map in terms of that 2D MOG maps are always occupied due to being grounds. Assume that a map is static during one patrol. Since 2D MOG Map follows probability properties, probability theorems can be adopted.

e.g. Bayesian filter, KL divergence. Given 2D MOG Maps, the structures of urban environments can be simply represented and adapted to probabilistic approach for surveillance mobile robots. This map supports dynamic object filtering as incoming scan points with class labels. Bayesian filter for updating MOG map is as below:

$X = \{x_1, x_2, \dots, x_{N_c}\}$: state of multi class occupancy (time invariant)

$Z_{1:t} = \{z_1, z_2, \dots, z_t\}$: the set of observations until t

t : the number of scanning in the grid

For simplicity $P(X = x_k | Z_{1:t})$ is denoted by $P(x_k | Z_{1:t})$.

$$\begin{aligned}
 P(x_k | Z_{1:t}) &= \frac{P(z_t | x_k, Z_{1:t-1})P(x_k | Z_{1:t-1})}{P(z_t | Z_{1:t-1})} \\
 &= \frac{P(z_t | x_k)P(x_k | Z_{1:t-1})}{P(z_t | Z_{1:t-1})} \\
 &= \eta P(z_t | x_k)P(x_k | Z_{1:t-1})
 \end{aligned}$$

$$\begin{aligned}\eta &= P(z_t | Z_{1:t-1})^{-1} \\ &= \left(\sum_{i=1}^{N_c} P(z_t | x_i, Z_{1:t-1}) P(x_i | Z_{1:t-1}) \right)^{-1}\end{aligned}$$

For triggering Bayesian filter, initial probability is required. The initial probability can be defined as below.

$$P(x_k) = \frac{1}{N_c}, \quad k = 1, \dots, N_c, \quad \text{where } N_c \text{ is the number of classes.}$$

where N_k is the number of points corresponding to the k -th class on a 2D grid and N_{all} is the number of all points on a 2D grid. Assume that points in 2D grids are uniformly scanned in the direction of Z axis.

$$P(z_t | x_k) = \frac{N_k}{N_{\text{all}}}, \quad \sum_{i=1}^{N_c} P(z_t | x_i) = 1.$$

To design change detection algorithm using 2D MOG maps, Kullback–Leibler (KL) divergence is calculated. KL divergence is non-symmetric measure of the difference between two probability distributions P and Q. P and Q of a discrete random variable their K–L divergence is defined to be:

$$D_{\text{KL}}(P \parallel Q) = \sum_i P(i) \ln \frac{P(i)}{Q(i)}.$$

If two probabilities in 2D MOG maps are the same, $D_{\text{KL}} = 0$. As two probability are differ, D_{KL} will be increased. Therefore the higher KL divergence means a large difference between the changing in two maps.

4 Experimental Result

To validate the proposed 2D MOG map, our surveillance robot (Figure 2) was patrolled in KAIST campus. In Figure 8, collected point clouds are shown. Each point is colored by specific colors according to urban object classes by hand labeling. In practice, urban object classes can be obtained from the previous semantic mapping methods [5]. In our experiments, we assumed that urban object classes are given in order to only test the proposed 2D MOG map and change detection algorithm.

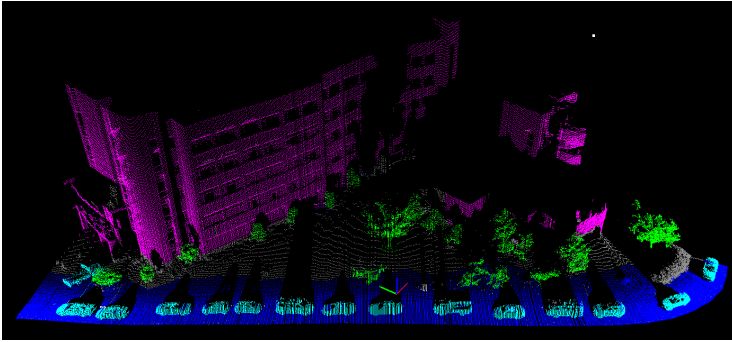


Fig. 8. Point clouds of 1st Patrol in KAIST campus

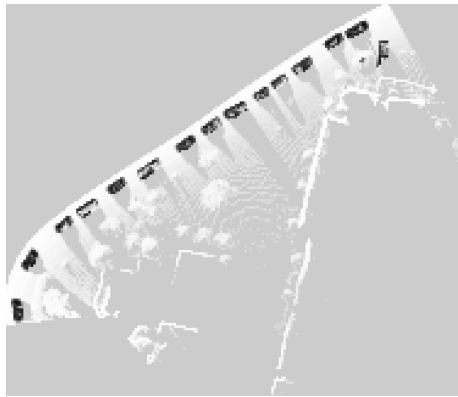


Fig. 9. 2D MOG Map (State = Car)

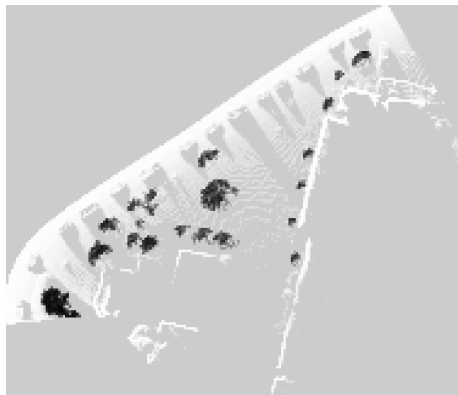


Fig. 10. 2D MOG Map (State = Tree)

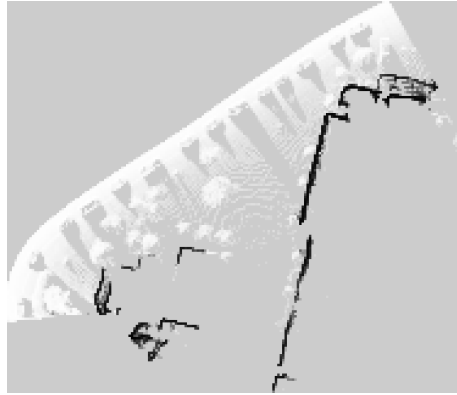


Fig. 11. 2D MOG Map (State = Building)

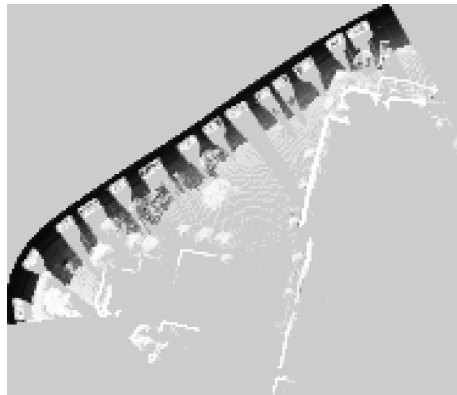


Fig. 12. 2D MOG Map (State = Road)

In Figure 9-12, it shows each class in the resulting 2D MOG Map made from point clouds in Figure 7. As can be seen, each class can be denoted by coloring from black (occupied) to white (non-occupied) according to its occupancy information. Black grids mean that corresponding class objects are occupied in the grid. This property is helpful to integrate information about the occupancy of various urban objects.

To test the proposed change detection method, point clouds of the 2nd patrol are modified from the 1st patrol point cloud as shown in Figure 13. In the 2nd patrol point clouds, several cars and road side trees were removed.

After building 2D MOG Maps of the 1st and 2nd patrol, the two 2D MOG Maps are compared by KL divergence to obtain change detection information. As shown in Figure 16, the change detection results between 2D MOG maps of the 1st and 2nd patrol show that the missing cars and trees are correctly denoted by gray scale colors. Therefore, we have shown that the proposed 2D MOG map can represent the occupancy of multi-class objects and its application as change detection successfully adopted.

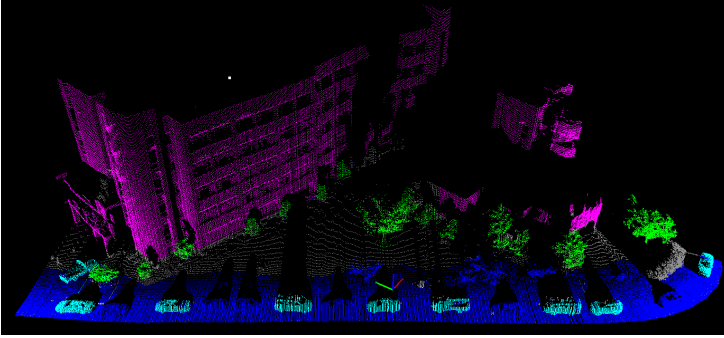


Fig. 13. 2nd Patrol in KAIST campus

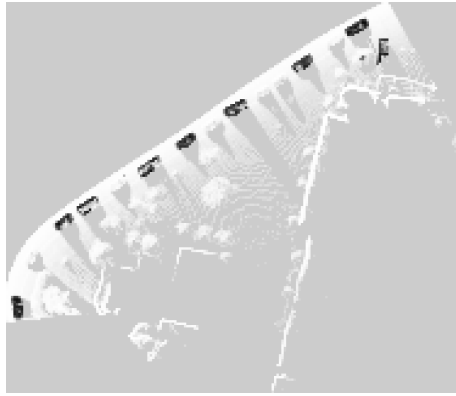


Fig. 14. 2D MOG Map of 2nd Patrol (State = Car)

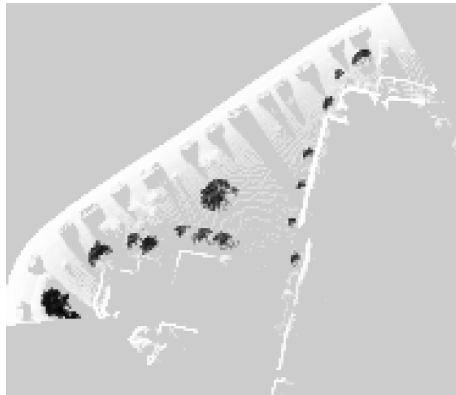


Fig. 15. 2D MOG Map of 2nd Patrol (State = Tree)

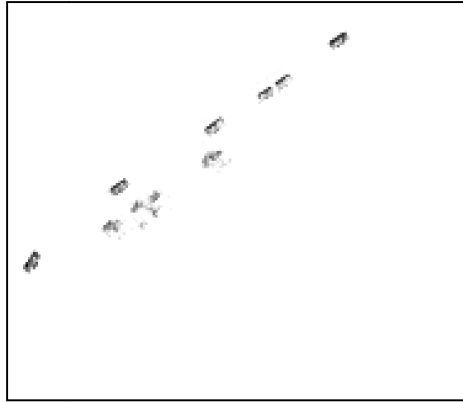


Fig. 16. Change Detection Result between 2D MOG maps of 1st and 2nd Patrol

(Change information is denoted by coloring from black (changed) to white (non-changed))

5 Conclusion

We propose 2D MOG map for the sake of security patrol robot surveillance. Occupancy of 3D objects can be simply represented in 2D grids according to classes. Since 2D MOG Map follows probability properties, we showed that 2D MOG Map can be adopted for updating map and change detection.

Acknowledgement. The Authors gratefully acknowledge the support from UTRC (Unmanned technology Research Center) at KAIST (Korea Advanced Institute of Science and Technology), originally funded by DAPA, ADD.

References

- [1] Birk, A., et al.: 3-D Perception and Modeling. *IEEE Robotics & Automation Magazine* (2009)
- [2] Durrant-Whyte, H., et al.: Simultaneous Localization and Mapping Part I. *IEEE Robotics & Automation Magazine* (2006)
- [3] Munoz, D., Bagnell, J.A., Vandapel, N., Hebert, M.: Contextual Classification with Functional Max-Margin Markov Networks. In: *IEEE Int. Conference on Computer Vision and Pattern Recognition*, Miami Beach, FL, pp. 975–982 (2009)
- [4] Weiming, H., et al.: A Survey on Visual Surveillance of Object Motion and Behaviors. *IEEE Transactions on Systems, Man, and Cybernetics—Part C* (2004)
- [5] Siciliano, B., Khatib, O. (eds.): *Handbook of Robotics. World Modeling* (W. Burgard, M. Hebert), ch. 36, pp. 853–869. Springer, Heidelberg (2008)
- [6] Andreasson, H., et al.: Has Something Changed Here? In: *Autonomous Difference Detection for Security Patrol Robots*, IROS (2007)
- [7] Núñez, P., et al.: Novelty Detection and 3D Shape Retrieval based on Gaussian Mixture Models for Autonomous Surveillance Robotics, IROS (2009)
- [8] Moravec, H.P., et al.: High resolution maps from wide angle sonar, ICRA (1985)

Trajectory Optimization Using Virtual Motion Camouflage and Particle Swarm Optimization*

Dong Jun Kwak, Byunghun Choi, and H. Jin Kim

School of Mechanical and Aerospace Engineering
Seoul National University
Seoul, Korea
djunkwak@gmail.com, {kysare,hjinkim}@snu.ac.kr

Abstract. This paper investigates a new numerical method to solve a nonlinear constrained trajectory optimization problem. Especially, we consider a problem constrained on the terminal angle and time. The proposed algorithm is based on the virtual motion camouflage (VMC) and particle swarm optimization (PSO) and is called VMCP SO. VMC changes the typical full space optimal problem to the subspace optimal problem, so it can reduce the dimension of the original problem by using path control parameters (PCPs). If the PCPs are optimized, then the optimal path can be obtained. Therefore, we employ PSO to optimize these PCPs. The optimization results show that the optimal path considering the terminal angle and time is effectively generated using VMCP SO.

Keywords: Trajectory optimization, virtual motion camouflage, particle swarm optimization.

1 Introduction

Requirements of the satisfactory trajectory planner in unmanned vehicle systems have been increased continuously in order to use the unmanned vehicles in complex environments. When the unmanned ground vehicle (UGV) passes through the mountainous terrain, the UGV should plan its next location and move to that position using allowable capabilities. This means that if the UGV utilizes all of the environmental information including its own information when it plans the trajectory, the planned path can improve the reliability while minimizing risks. This example is exactly same as the trajectory optimization problem. In the constrained trajectory optimization problem, minimizing the risks or maximizing the reliability can be the performance index, and the environmental information can be considered as constraints.

Many researchers have studied to solve the nonlinear constrained trajectory optimization and are still working on it. There are many numerical techniques

* This research was financially supported by a grant to Unmanned Technology Research Center funded by Defense Acquisition Program Administration, and by Samsung Thales.

for solving this problem, and it is helpful to divide into two parts: indirect or direct [1, 2]. Indirect methods are based on the calculus of variation or the maximum principle and seek a solution of the necessary conditions of optimality analytically. Thus, there is no requirement for discretization. Direct methods do not require analytical expression unlike to the indirect methods. Instead, direct methods discretize the original problem, then apply nonlinear programming (NLP) techniques to the resulting finite-dimensional optimization problem.

Recently, a virtual motion camouflage (VMC) subspace method was suggested in [3–6]. Idea of the VMC method came from observing biological phenomenon, in which an insect can actively camouflage its motion while it tracks another insect [7]. The typical nonlinear constrained trajectory optimization problem can be reformulated by applying the VMC method. Then, the existing problem with infinite dimension changes into the finite dimensional problem with path control parameters (PCPs). Arbitrary paths can be generated by only changing the PCPs. Therefore, the optimization problem can be solved by optimizing the PCPs.

In this paper, we propose a numerical algorithm to solve the nonlinear constrained trajectory optimization problem. As mentioned above, the original problem is changed into finding the optimal PCPs from the VMC formulation, so we utilize particle swarm optimization (PSO) [8] to optimize the PCPs. Before applying PSO in the VMC formulation, the constrained trajectory optimization problem is changed into the unconstrained trajectory optimization problem by using penalty functions. Then, the candidate PCPs converge on the optimal solution through local and global interactions with the other candidates depending on the number of iterations increases. The proposed algorithm will be validated by finding the optimal trajectory constrained on the terminal angle and time.

The rest of this paper is organized as follows: The problem description is given in Section 2. In Section 3, a basic nonlinear constrained trajectory optimization problem is introduced, and how to formulate VMC problem is explained. The details of the proposed algorithm are also described. Optimization results are discussed in Sections 4. Finally, in Section 5, conclusions are given.

2 Problem Description

In this paper, we focus on the optimal trajectory design in a two dimensional environment with terminal angle and time constraints, and also consider a constraint, in which the robot should not be collide with obstacles while they move to the terminal state. Here, we denote the terminal angle and time as γ_d and t_d , respectively. We also consider the kinematic model of a unicycle as follows:

$$\begin{bmatrix} \dot{x}(t) \\ \dot{y}(t) \\ \dot{\theta}(t) \end{bmatrix} = \begin{bmatrix} \cos \theta(t) & 0 \\ \sin \theta(t) & 0 \\ 0 & 1 \end{bmatrix} \begin{bmatrix} V(t) \\ w(t) \end{bmatrix} \quad (1)$$

where (x, y, θ) denote the position and heading angle of the robot, and (V, w) are the tangential and angular velocities. The robot's tangential and angular velocities are bounded with $|V| \leq V_{\max}$ and $|w| \leq w_{\max}$.

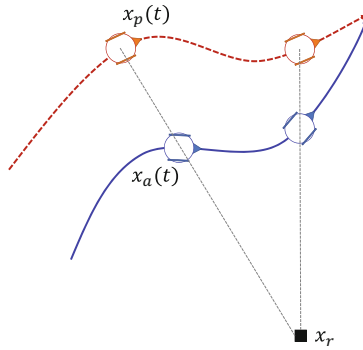


Fig. 1. Relationship between the reference point, the prey motion, and the aggressor motion

3 Optimal Trajectory Design

In this section, the problem for a basic nonlinear constrained optimal trajectory generation is considered, and a bio-inspired method is introduced to solve this problem more efficiently. In addition, our approach will be discussed.

3.1 Nonlinear Constrained Trajectory Optimization Problem

The nonlinear constrained trajectory optimization problem is defined by the following:

$$J = \Phi[\mathbf{x}(t_0), \mathbf{x}(t_f), t_0, t_f] + \int_{t_0}^{t_f} \mathcal{L}[\mathbf{x}(t), \mathbf{u}(t), t] dt \quad (2)$$

subject to the inequality constraints

$$\mathbf{g}(\mathbf{x}(t), \mathbf{u}(t), t) \leq 0, \mathbf{g} \in \mathbb{R}^{p \times 1} \quad (3)$$

and the equality constraints

$$\mathbf{h}(\mathbf{x}(t), \mathbf{u}(t), t) = 0, \mathbf{h} \in \mathbb{R}^{q \times 1}. \quad (4)$$

Here, the equality constraints include the boundary conditions

$$\Psi[\mathbf{x}(t_0), \mathbf{x}(t_f), t_0, t_f] = 0, \Psi \in \mathbb{R}^{l \times 1} \quad (5)$$

and the first-order dynamic constraints

$$\dot{\mathbf{x}}(t) = \mathbf{f}(\mathbf{x}(t), \mathbf{u}(t), t), \mathbf{x} \in \mathbb{R}^{n \times 1}, \mathbf{u} \in \mathbb{R}^{m \times 1} \quad (6)$$

where $(\mathbf{x}(t), \mathbf{u}(t), t, t_0, t_f)$ are the state, control, time, initial time, and final time, respectively. The optimal trajectory will be found by maximizing (or minimizing) the performance index J . The solution of this optimal problem might be locally or globally optimal depend on optimization methods.

3.2 VMC Formulation

Srinivasan and Davey [7] introduced *motion camouflage* (MC) for describing whether an agent can actively camouflage its motion while it tracks another agent and developed algorithms to determine agent's trajectories for a stationary or moving target. In [3–5], two moving agents which are an aggressor and a prey are considered, and the idea of MC is applied to the nonlinear constrained optimal control problem. As shown in Fig. 1, the path of the aggressor $\mathbf{x}_a(t)$ related to the motion of the prey $\mathbf{x}_p(t)$ and the reference point \mathbf{x}_r can be controlled by the path control parameter (PCP) $v(t)$ as follows:

$$\mathbf{x}_a(t) = \mathbf{x}_r + v(t)(\mathbf{x}_p(t) - \mathbf{x}_r) \quad (7)$$

and the derivatives of $\mathbf{x}_a(t)$ can be simply defined by the following:

$$\dot{\mathbf{x}}_a(t) = \dot{\mathbf{x}}_r + \dot{v}(t)(\mathbf{x}_p(t) - \mathbf{x}_r) + v(t)(\dot{\mathbf{x}}_p(t) - \dot{\mathbf{x}}_r) \quad (8)$$

$$\ddot{\mathbf{x}}_a(t) = \ddot{\mathbf{x}}_r + \ddot{v}(t)(\mathbf{x}_p(t) - \mathbf{x}_r) + v(t)(\ddot{\mathbf{x}}_p(t) - \ddot{\mathbf{x}}_r) + 2\dot{v}(t)(\dot{\mathbf{x}}_p(t) - \dot{\mathbf{x}}_r). \quad (9)$$

Before the VMC formulation, two assumptions are made as in [6].

Assumption 1. The state vector $\mathbf{x}(t) \in \mathbb{R}^{n \times 1}$ can be rearranged into two parts: the position state $\mathbf{x}_a(t) \in \mathbb{R}^{n_a \times 1}$ and the state rate $\mathbf{x}_{sr}(t) \in \mathbb{R}^{(n-n_a) \times 1}$. Correspondingly, the equations of motion $\dot{\mathbf{x}}(t) = \mathbf{f}(\mathbf{x}(t), \mathbf{u}(t), t)$ can be rewritten into two parts: $\dot{\mathbf{x}}_a(t) = \mathbf{f}_a(\mathbf{x}(t), t)$ and $\dot{\mathbf{x}}_{sr}(t) = \mathbf{f}_{sr}(\mathbf{x}(t), \mathbf{u}(t), t)$.

Assumption 2. The mappings from $(\mathbf{x}_a(t), \dot{\mathbf{x}}_a(t), t)$ to $\mathbf{x}_{sr}(t)$ and from $(\mathbf{x}(t), \dot{\mathbf{x}}(t), t)$ to $\mathbf{u}(t)$ are assumed to be injective, which means the control variables $\mathbf{u}(t)$ and the state rate $\mathbf{x}_{sr}(t)$ can be solved by $\mathbf{x}_{sr}(t) = \mathbf{f}_a^{-1}(\mathbf{x}_a(t), \dot{\mathbf{x}}_a(t), t)$ and $\mathbf{u}(t) = \mathbf{f}_{sr}^{-1}(\mathbf{x}(t), \dot{\mathbf{x}}_{sr}(t), t)$ either explicitly or implicitly using an iterative fashion.

The nonlinear constrained trajectory optimization problem stated in Section 3.1 can be reformulated by considering Assumption 1 and 2, and (7)-(9). Given \mathbf{x}_r and $\mathbf{x}_p(t)$, the variables $v(t), \dot{v}(t), \ddot{v}(t), \dots$, and t_f will be designed to minimize the performance index

$$J = \Phi[v(t), \dot{v}(t), \ddot{v}(t), \dots, t_f] + \int_{t_0}^{t_f} \mathcal{L}[v(t), \dot{v}(t), \ddot{v}(t), \dots, t] dt \quad (10)$$

subject to the state and control inequality constraints

$$\mathbf{g}(v(t), \dot{v}(t), \ddot{v}(t), \dots, t) \leq 0, \mathbf{g} \in \mathbb{R}^{p \times 1} \quad (11)$$

and the equality constraints

$$\mathbf{h}(v(t), \dot{v}(t), \ddot{v}(t), \dots, t) = 0, \mathbf{h} \in \mathbb{R}^{l \times 1} \quad (12)$$

In the VMC formula, the first-order dynamics constraints (6) are already taken into account when calculating $\mathbf{x}_{sr}(t)$ and $\mathbf{u}(t)$ based on Assumption 2, so the boundary conditions are only considered as the equality constraints.

To obtain the numerical solution, the VMC based nonlinear constrained trajectory optimization problem is directly formulated as a nonlinear programming via a pseudo-spectral based collocation method. The Legendre-Gauss-Lobatto (LGL) pseudo-spectral scheme is used to discretize the PCP $v(t)$ into the PCP nodes $v_k, k = 0, \dots, N$, and \mathbf{v} is the vector of the PCP nodes. Therefore, the discretized performance index can be described as

$$J = \Phi[v_N] + \left(\frac{t_f - t_0}{2}\right) \sum_{k=0}^N \mathcal{L}[\mathbf{v}, \dot{\mathbf{v}}, \ddot{\mathbf{v}}, \dots] \omega_k \tag{13}$$

where ω_k is the weights for the k^{th} LGL node. The state and control inequality and equality constraints can be written as

$$\mathbf{g}_k(\mathbf{v}, \dot{\mathbf{v}}, \ddot{\mathbf{v}}, \dots) \leq 0 \tag{14}$$

$$\mathbf{h}_k(\mathbf{v}, \dot{\mathbf{v}}, \ddot{\mathbf{v}}, \dots) = 0 \tag{15}$$

where the derivatives of the PCP vector is

$$\frac{d^k \mathbf{v}}{dt^k} = \left(\frac{2}{t_f - t_0}\right)^k \mathbf{D}^k \mathbf{v} \tag{16}$$

where the differentiation matrix \mathbf{D} can be found in [9]. Then, (7), (8) and (9) are rewritten by the following:

$$\mathbf{x}_a(k) = \mathbf{x}_r + v_k(\mathbf{x}_p(k) - \mathbf{x}_r) \tag{17}$$

$$\dot{\mathbf{x}}_a(k) = \dot{\mathbf{x}}_r + \dot{v}_k(\mathbf{x}_p(k) - \mathbf{x}_r) + v_k(\dot{\mathbf{x}}_p(k) - \dot{\mathbf{x}}_r) \tag{18}$$

$$\ddot{\mathbf{x}}_a(k) = \ddot{\mathbf{x}}_r + \ddot{v}_k(\mathbf{x}_p(k) - \mathbf{x}_r) + v_k(\ddot{\mathbf{x}}_p(k) - \ddot{\mathbf{x}}_r) + 2\dot{v}_k(\dot{\mathbf{x}}_p(k) - \dot{\mathbf{x}}_r). \tag{19}$$

The reference point \mathbf{x}_r will remain fixed, so (18) and (19) can be simply rewritten as follows:

$$\dot{\mathbf{x}}_a(k) = \dot{v}_k(\mathbf{x}_p(k) - \mathbf{x}_r) + v_k \dot{\mathbf{x}}_p(k) \tag{20}$$

$$\ddot{\mathbf{x}}_a(k) = \ddot{v}_k(\mathbf{x}_p(k) - \mathbf{x}_r) + v_k \ddot{\mathbf{x}}_p(k) + 2\dot{v}_k \dot{\mathbf{x}}_p(k). \tag{21}$$

In [6], the sequential VMC method involving two steps in an iteration process is proposed to solve this problem. In the first step, an optimal solution can be found quickly within subspace constructed by the PCP nodes, and a linear programming and a line search algorithm perform to improve the PCP nodes. The detailed algorithms and results can be found in [6].

3.3 The Proposed Approach

In our approach, the constrained optimization problem should be changed into an unconstrained optimization problem as follows:

$$\text{minimize}_{(\mathbf{v})} J = \left(\frac{t_f - t_0}{2}\right) \sum_{k=0}^N \mathcal{L}[\mathbf{v}, \dot{\mathbf{v}}, \ddot{\mathbf{v}}, \dots] \omega_k + C \sum_{k=0}^N \max_k(0, \mathbf{g}_k(\mathbf{v}, \dot{\mathbf{v}}, \ddot{\mathbf{v}}, \dots)) \tag{22}$$

where the second term of (22) is the penalty function to satisfy the inequality constraints, and C is the weighting parameter. Here, the boundary conditions such as the initial and final position can be included in (22) by setting $v_0 = 1$ and $v_N = 1$. As stated in Section 3.2, the most important task to find the optimal trajectory is how to determine the PCP nodes optimally. Thus, to deal with this parameter optimization problem, particle swarm optimization (PSO) is employed. PSO is a population-based stochastic optimization technique [8]. Every particle in the population travels in the search space looking for global minimum (or maximum) similar to the behavior of bird flocking and fish schooling. Each particle adjusts its velocity according to its own experience and its swarm's experience while particles search the global solution.

Let the particles be the candidate PCP vectors, then each particle in the population which begins with randomly selected position $\mathbf{v}_s \in \mathbb{R}^{(N+1) \times 1}$ and velocity $\boldsymbol{\nu}_s \in \mathbb{R}^{(N+1) \times 1}$ ($s = 1, 2, \dots, S$), where S is the swarm size, and iteratively moves in the problem space. To generate reliable candidate particles, i.e., the PCP vector \mathbf{v}_s , each candidate PCP node $v_{k,s}$ is computed with M the number of harmonic functions as follows:

$$v_{k,s} = 1 + r_0 \sum_{m=0}^M A_m \sin \left(m\pi \left(\frac{\omega_{\langle 0:k \rangle}}{\omega_{\langle 0:N \rangle}} \right) \right) \quad (23)$$

where $\langle a : b \rangle$ denotes $\sum_{i=a}^b \omega_i$, and A_m is constant to handle the range of the candidate paths. r_0 is chosen as uniform random values in the range $[-1, 1]$. The best previous position of the particle s is remembered and represented as $\mathbf{pBest}_s \in \mathbb{R}^{(N+1) \times 1}$. The position of the best particle among all the particles is represented as $\mathbf{gBest} \in \mathbb{R}^{(N+1) \times 1}$. At each iteration, the velocity $\boldsymbol{\nu}_s$ and position \mathbf{v}_s of each particle s can be updated by the following.

$$\begin{aligned} \boldsymbol{\nu}_s &= K[\boldsymbol{\nu}_s + c_1 r_1 (\mathbf{pBest}_s - \mathbf{v}_s) + c_2 r_2 (\mathbf{gBest} - \mathbf{v}_s)] \\ \mathbf{v}_s &= \mathbf{v}_s + \boldsymbol{\nu}_s \end{aligned} \quad (24)$$

where c_1 and c_2 are the acceleration constants, r_1 and r_2 are chosen as uniform random values in the range $[0, 1]$, K is the constriction factor to ensure the convergence of PSO [10], and it is determined by

$$K = \frac{2}{|2 - \varphi - \sqrt{\varphi^2 - 4\varphi}|} \quad (25)$$

where $\varphi = c_1 + c_2$, $\varphi > 4$. Typically, φ is set to 4.1.

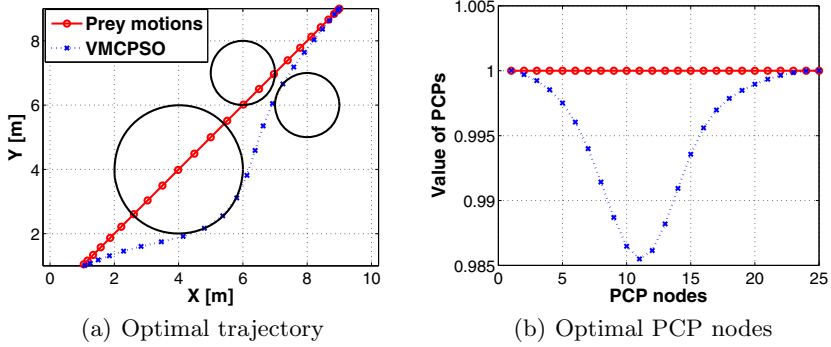


Fig. 2. VMCP SO results of minimum time problem

4 Optimization Results

As shown in Fig. 2(a), we consider a two-wheeled mobile robot minimum time collision avoidance trajectory planning problem given in [6].

$$\text{minimize } J = \left(\frac{t_f - t_0}{2} \right) \sum_{k=0}^N \omega_k \quad (26)$$

subject to $|V(k)| \leq V_{\max}$

$$|w(k)| \leq w_{\max}$$

$$(x(k) - 4)^2 + (y(k) - 4)^2 \geq 4$$

$$(x(k) - 6)^2 + (y(k) - 7)^2 \geq 1$$

$$(x(k) - 8)^2 + (y(k) - 6)^2 \geq 1$$

$$(x(0), y(0)) = (1, 1)$$

$$(x(N), y(N)) = (9, 9)$$

Table 1. Parameter values of VMCP SO

Parameter	Value
A_m	1
M	4
N	24
S	200
It_{\max}	150
V_{\max}	0.15 m/s
w_{\max}	135 deg/s
$C_1 \sim C_5$	100
t_0	0

Given (1), the position state \mathbf{x}_a and state rate \mathbf{x}_{sr} are set as $\mathbf{x}_a = [x, y]^T$ and $\mathbf{x}_{sr} = \theta$, respectively. Basically, the reference point is set as $\mathbf{x}_r = [100, -95]^T$ and the prey motion \mathbf{x}_p is given by the straight line shown in Fig. 2(a). From \mathbf{x}_r , \mathbf{x}_p and \mathbf{v} , $\dot{\mathbf{x}}_a = [\dot{x}, \dot{y}]^T$ and $\ddot{\mathbf{x}}_a = [\ddot{x}, \ddot{y}]^T$ are directly computed by (16)-(21) for each k -th LGL node, so the following results can be obtained.

$$V(k) = \sqrt{\dot{x}^2(k) + \dot{y}^2(k)} \quad (27)$$

$$\theta(k) = \text{atan} \left(\frac{\dot{y}(k)}{\dot{x}(k)} \right) \quad (28)$$

$$w(k) = \frac{\dot{x}(k)\ddot{y}(k) - \dot{y}(k)\ddot{x}(k)}{\dot{x}^2(k) + \dot{y}^2(k)}, (\dot{x}^2(k) + \dot{y}^2(k) \neq 0). \quad (29)$$

Thus, we can evaluate whether the constraints such as $|V| \leq V_{\max}$ and $|w| \leq w_{\max}$ are violated for each k -th LGL node by only using \mathbf{x}_a , $\dot{\mathbf{x}}_a$ and $\ddot{\mathbf{x}}_a$. To solve (26), we change the formula (26) into (22) as follows:

$$\begin{aligned} \text{minimize } J = & \left(\frac{t_f - t_0}{2} \right) \sum_{k=0}^N \omega_k + C_1 \sum_{k=0}^N \max_k (0, |V(k)| - V_{\max}) \quad (30) \\ & + C_2 \sum_{k=0}^N \max_k (0, |w(k)| - w_{\max}) \\ & + C_3 \sum_{k=0}^N \max_k (0, 1/d_1(k) - 1/2) \\ & + C_4 \sum_{k=0}^N \max_k (0, 1/d_2(k) - 1) \\ & + C_5 \sum_{k=0}^N \max_k (0, 1/d_3(k) - 1) \end{aligned}$$

where $d_i(k)$ denotes the distance between the position of i -th obstacle and $\mathbf{x}_a(k)$. Then, we apply VMCP SO to solve (30) for given the parameters in Table. 1. As shown in Fig. 2(a) the minimum time optimal trajectory is well generated, and the resulting optimal PCP nodes are shown in Fig. 2(b).

Now, our main problem which is the terminal angle and time constrained trajectory optimization problem is going to be discussed. Here, we consider the same environment, so the difference of cost functions between the minimum time problem and the terminal angle and time constrained problem is just the first term of (30). If we denote $\phi(\mathbf{g})$ the penalty function including all inequality constraints, our cost function can be defined by the following:

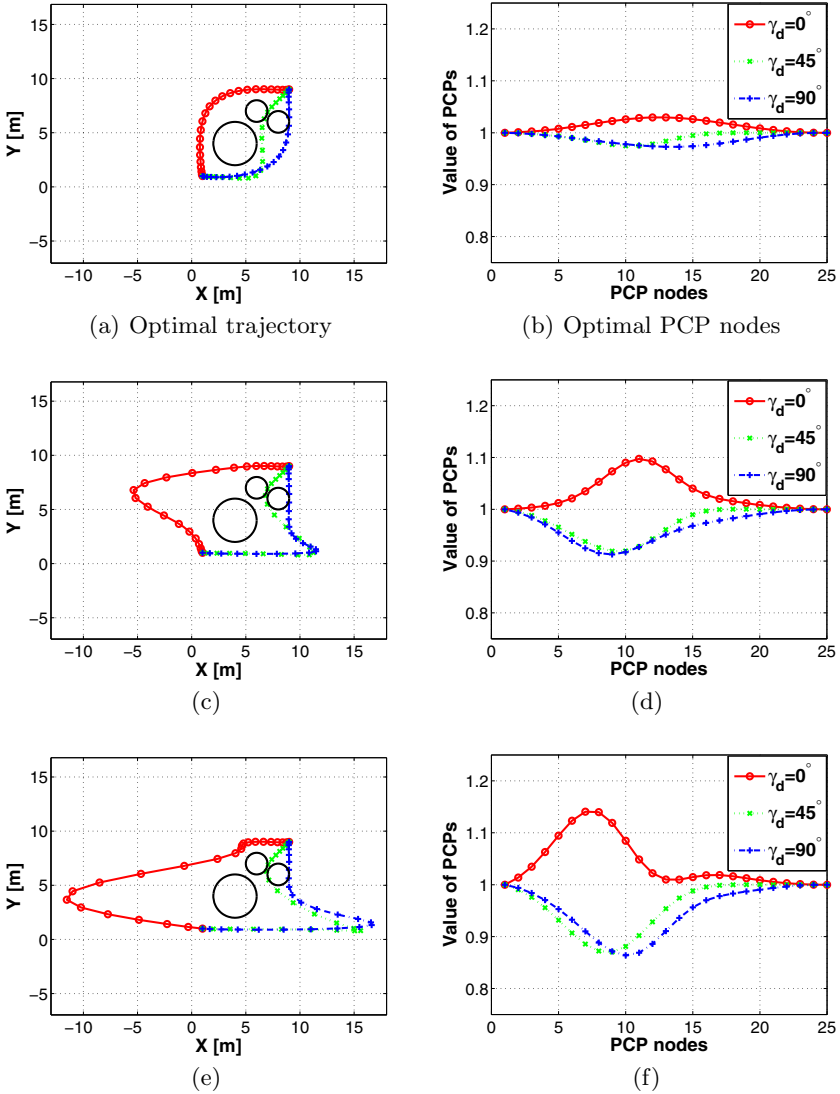


Fig. 3. VMCP SO results of terminal angle and time constrained problem (a,b) $t_d = 100$ sec, (c,d) $t_d = 200$ sec, (e,f) $t_d = 300$ sec

$$\text{minimize } J = I_T |t_{err}| + I_A \sum_{k=N-5}^{N-1} |\gamma_{err}| + \phi(\mathbf{g}) \quad (31)$$

where $t_{err} = t_d - \left(\frac{t_f - t_0}{2}\right) \sum_{k=0}^N \omega_k$ and $\gamma_{err} = \gamma_d - \text{atan}\left(\frac{y(N) - y(k)}{x(N) - x(k)}\right)$. The weighting parameters I_T and I_A are set to 2 and 1, respectively. The optimization is performed for $t_d = (100, 200, 300)$ [sec] and $\gamma_d = (0, 45, 90)$ [deg] by using VMCP SO with Table. 1. Fig. 3 shows that satisfactory results of the optimal trajectory and the PCP nodes for all the cases of t_d and γ_d . All of the trajectories are converged to minimize the cost function (31) by considering t_d and γ_d , and also to avoid collisions with the obstacles. As a result, our approach showed effectiveness to solve the terminal angle and time constrained trajectory optimization problem.

5 Conclusion and Future Works

In this paper, we focused on solving the nonlinear constrained trajectory optimization problem having the terminal angle and time constraints. To handle this problem, the new numerical algorithm called VMCP SO was proposed. The idea of VMCP SO came from the virtual motion camouflage (VMC) and particle swarm optimization (PSO). VMC has a role to change the typical full space optimal problem to the subspace optimal problem, and can reduce the dimensions of the problem by using the path control parameters (PCPs). If the PCPs are optimized, then the optimal path is generated. Therefore, we employed PSO to optimize these PCPs. In PSO, the candidate PCPs find the optimal solution during local and global interactions with the other candidates. From the optimization results, we found excellence of the proposed method. Next steps will be to extend the proposed algorithm to multi-agent path planning in a decentralized manner.

References

1. Stryk, O., Bulirsch, R.: Direct and indirect methods for trajectory optimization. *Annals of Operations Research* 37(1), 357–373 (1992)
2. Betts, J.T.: Survey of numerical methods for trajectory optimization. *Journal of Guidance, Control, and Dynamics* 21(2), 193–207 (1998)
3. Xu, Y.: Virtual motion camouflage and suboptimal trajectory design. In: *AIAA Guidance, Navigation and Control Conference and Exhibit* (2007)
4. Xu, Y.: Subspace optimal control and motion camouflage. In: *AIAA Guidance, Navigation and Control Conference and Exhibit* (2008)
5. Xu, Y., Basset, G.: Pre and post optimality checking of the virtual motion camouflage based nonlinear constrained subspace optimal control. In: *AIAA Guidance, Navigation, and Control Conference* (2009)
6. Xu, Y., Basset, G.: Sequential virtual motion camouflage method for nonlinear constrained optimal trajectory control. *Automatica* 48(7), 1273–1285 (2012)

7. Srinivasan, M.V., Davey, M.: Strategies for active camouflage of motion. Proceedings of the Royal Society of London. Series B: Biological Sciences 259(1354), 19–25 (1995)
8. Kennedy, J., Eberhart, R.C.: Particle swarm optimization. In: Proc. the 1995 IEEE International Conference on Neural Networks, pp. 1942–1948 (1995)
9. Fahroo, F., Ross, I.M.: Costate estimation by a legendre pseudospectral method. Journal of Guidance, Control, and Dynamics 24(2), 270–277 (2001)
10. Clerc, M., Kennedy, J.: The particle swarm explosion, stability, and convergence in a multidimensional complex space. IEEE Trans on Evolutionary Computation 6(1), 58–73 (2002)

3D Probability Map Building for UGV Navigation in Special Environment

Min-Ho Kim, Hee-Mu Lee, and Min-Cheol Lee

Control and Automation Systems Division, Pusan National University,
Busan, South Korea

xho1995@gmail.com, slm1023@nate.com, mclee@pusan.ac.kr

Abstract. In this study, a 3D probability map-building technique is proposed in order to UGV's navigation algorithm in the special environment like a battlefield. UGV's navigation algorithm needs an optimal path planning algorithm to navigate between some mission points and to avoid obstacles on the given map. However, although there are already a lot of researches on the path planning algorithm for UGV, they are mainly focused on finding the shortest path on the map. In some special environments, there may be other factors to be considered to find the optimal path. For example, enemy's location, terrain, obstacle, UGV's mobility may be some additional factors for path planning algorithm on the battlefield. Therefore, the integrated map building method is needed to combine all factors which might effect on the UGV's optimal path. 3D probability map is proposed how to integrate those information. And the simulation program has been developed to verify the proposed algorithm and the results are shown.

Keywords: UGV, Navigation, 3D Probability Map, Path Planning, Special Environment.

1 Introduction

UGV has been developed in order to navigate between mission points, observe unknown enemies, and battle on the battlefield. It must automatically avoid some obstacles and fight against the hidden enemies while reaching the goal point. The optimal path planning algorithm is needed to perform this mission. There have been already a lot of researches on the UGV's path planning. However, they are mainly focused on finding the shortest path on a given map. In some special environments, there may be other factors to consider finding the optimal path. The UGV's survival probability has been developed in order to consider other factors like enemy's location in the previous study. UGV's mobility and terrain may be some additional factors for path planning algorithm on the battlefield. Therefore, the integrated map building algorithm is needed to combine all those factors which might effect on the UGV's optimal path.

In this study, a 3D probability map building method is proposed in order to build the integrated map. The 3D terrain data is combined with the UGV's survival probability in the proposed map. And this map can be extended to combine other additional factors which might effect on the path planning algorithm.

First, in the next chapter, the method to build a 3D grid map from raw sensor data will be explained. 3D grid map becomes a basis of 3D probability map. Next, the survival probability being combined with the 3D grid map will be explained. The survival probability has been researched continuously since the previous studies. [1] Then, the developed simulation program and the path planning results are shown to verify the proposed algorithm.

2 3D Probability Map

A 3D probability map is a grid map which consists of triangle polygons. Grid maps are widely used in graph-tree search algorithm like A* in order to find the optimal path. [2] However, a grid consists of 4 points, thus it isn't suitable to model the 3D terrain surface, because a plane consists of 3 points. To solve this problem, each grid of the map has been divided into 8 triangle polygons. In subsequent sections, the proposed method to build a 3D grid map will be described.

2.1 Raw Point Cloud Data

This 3D grid map is made with point cloud data obtained by some sensors such as laser scanners. A sample of point cloud data obtained from Robotics Research lab at

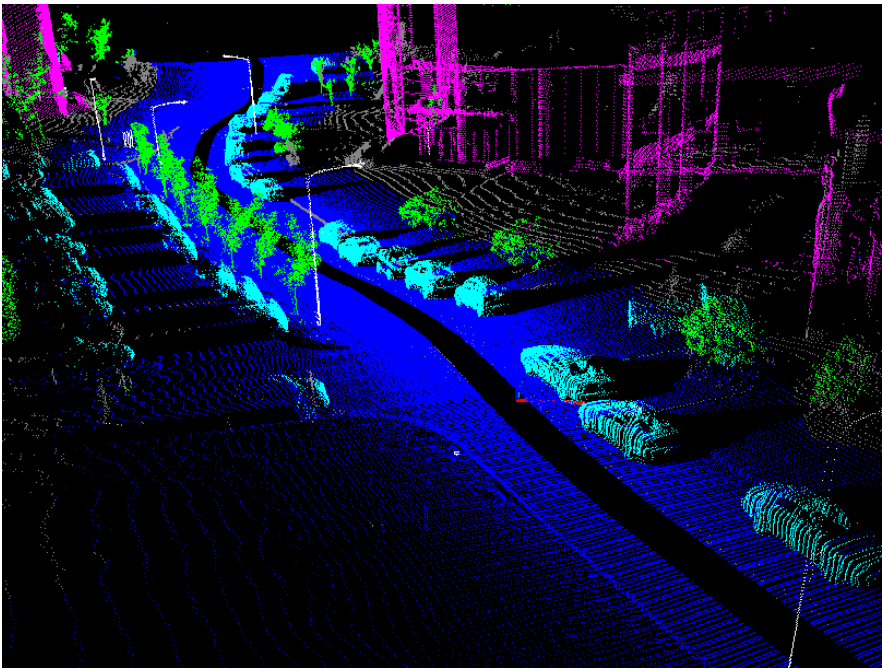


Fig. 1. Raw Point Cloud Data collected by Laser Scanners from RR Lab at KAIST

KAIST in South Korea has been shown in Fig 1. [3, 4] Using this raw point cloud data, a 3D probability map will be generated. However, this raw data have too many data with different density. Most of the point cloud data can be ignored during the path planning.

2.2 Simplification

Before building the 3D grid map, the point cloud data may be simplified to reduce ignorable data which aren't related with the UGV's path planning. By this, the storage space can be reduced and the algorithm operation speed can be improved. Because UGV moves along only the terrain surface, most of the points higher than UGV's height can be removed. The result of simplified point cloud data is shown in fig 2, there isn't any the top of tree or building.

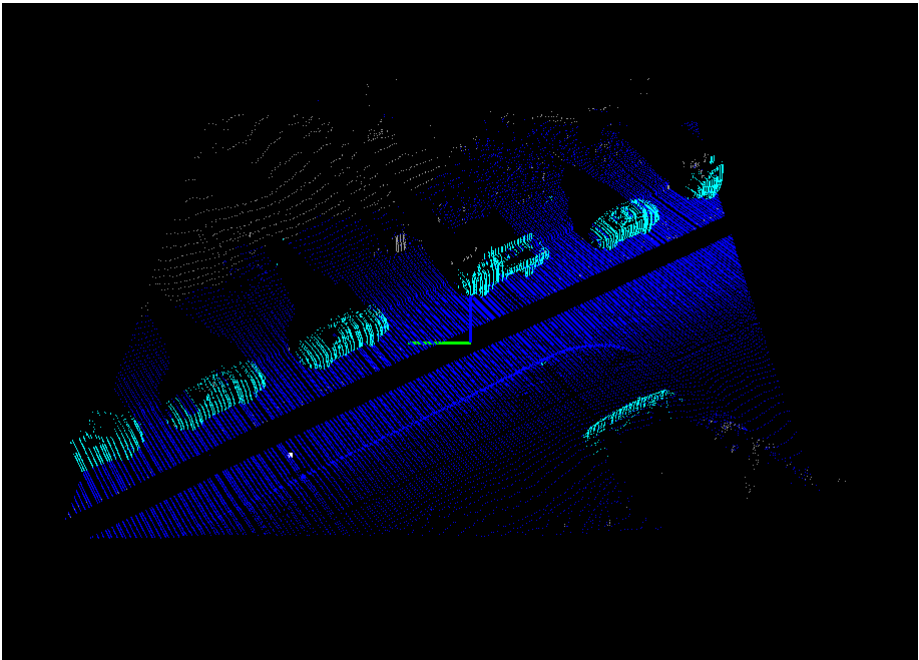


Fig. 2. Simplified Point Cloud Data

2.3 Quantization

Quantization process extracts the grid nodes of the map from the simplified point cloud data. First, it divides the point cloud data into some square regions, and then looks for the mean values of those regions respectively. The calculated mean values are the node values of the grid map. By connecting those nodes, the 3D grid map can be created. Fig. 3 shows the result nodes after the quantization process. While this process makes the grid map lose some details, it reduces the data storage space.

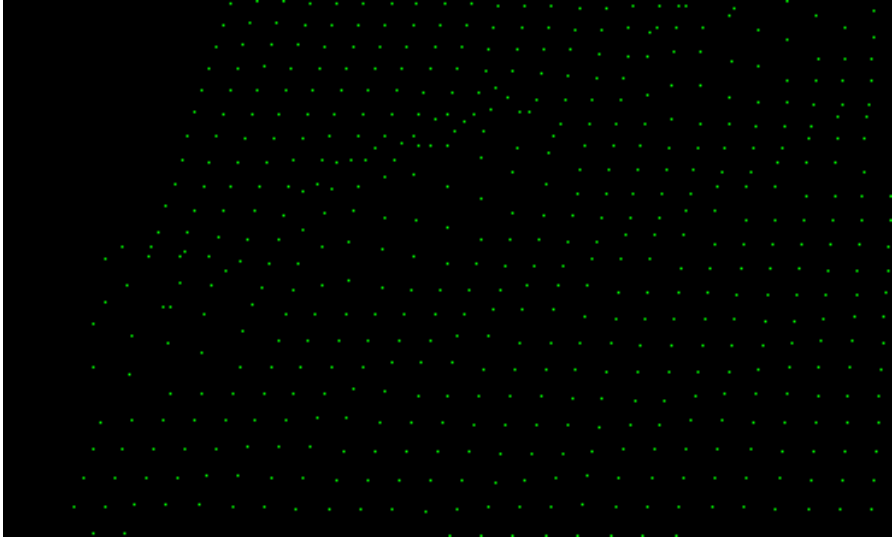


Fig. 3. Quantized Point Cloud Data

2.4 3D Grid Map

Simply, the 3D grid map seems to be able to create by connecting those nodes. However, there is a problem. A unit of 3D terrain consists of a triangle polygon because one plane consists of 3 points. On the other hand, a unit of grid map consists of 4 points. Thus, when the 3D grid map is created, the geometric ambiguity problem occurs. That problem is shown in Fig 4. The path between '1' and '3' nodes is not connected with the path between '2' and '4' nodes, because there isn't any geometric information about the unit terrain.

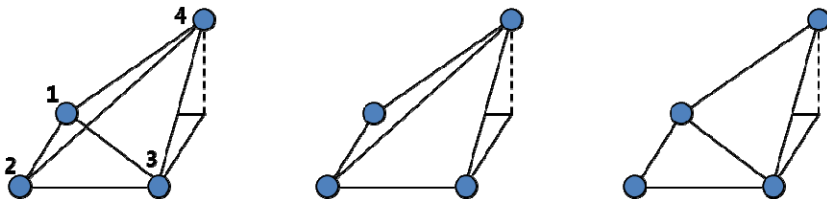


Fig. 4. Geometric ambiguity Problem; if 4 Points aren't on the one plane, there occurs two paths that can't be connected each other

Solution of the Geometric Ambiguity Problem. In order to solve this geometric ambiguity problem, a unit grid of the 3D grid map has been divided into the 8 triangle polygons shown as Fig. 5. In the Figure, colored region means a unit grid node, and one node is connected with adjacent 8 nodes. Between two nodes, an additional node has been inserted by mean value of adjacent nodes.

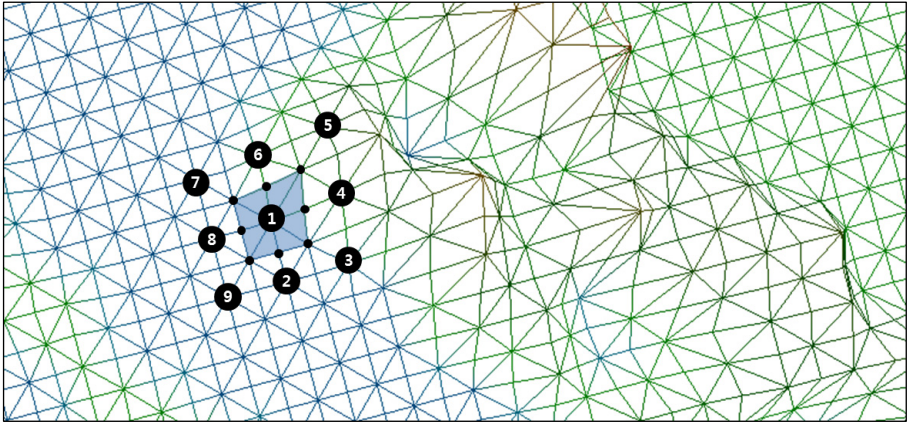


Fig. 5. The Solution of the Geometric Ambiguity Problem

Fig. 6 shows the result of 3D grid map which is created from the point cloud data of Fig. 2. It presents the geometric information of the 3D terrain by using the grid structure. By assigning a survival probability value at each node, a 3D probability map will be created.

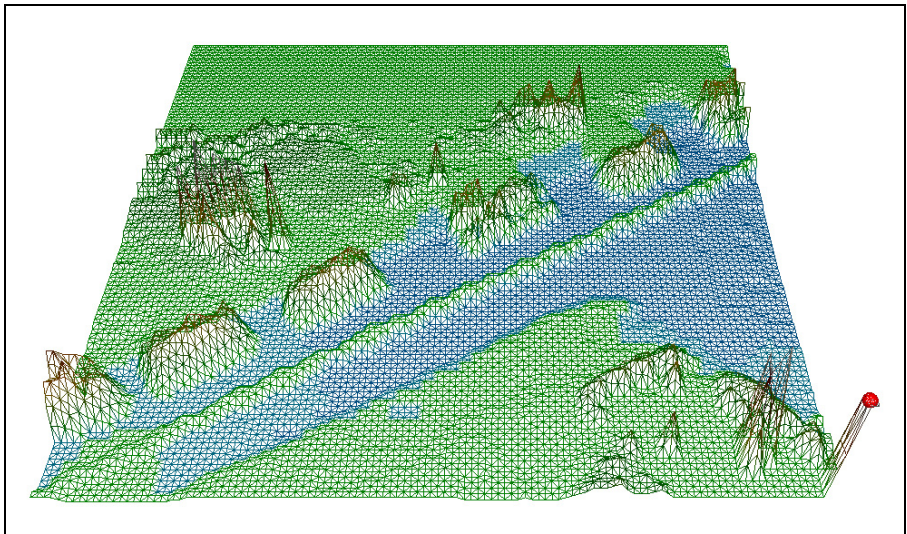
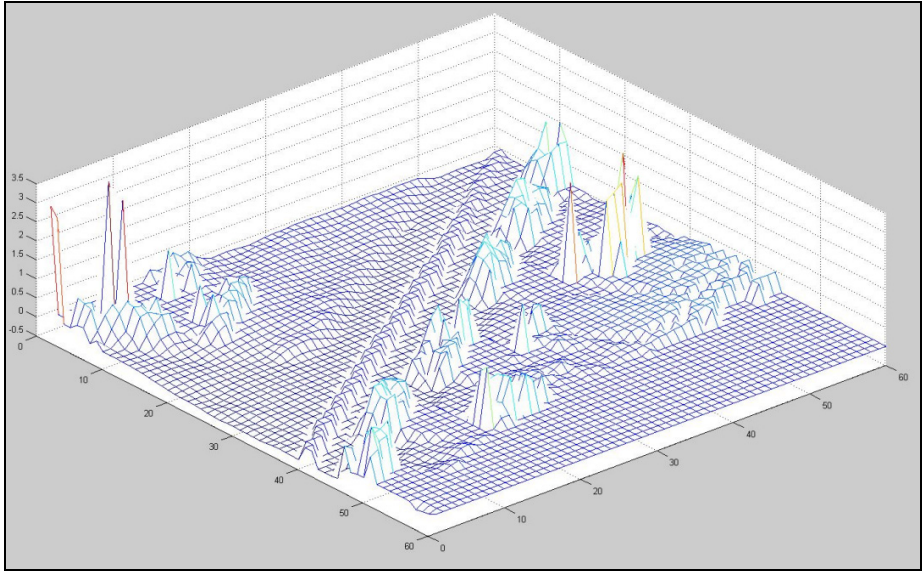
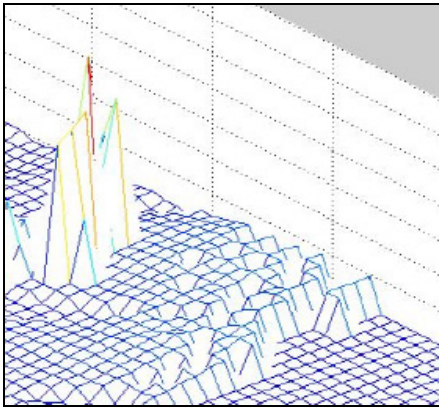


Fig. 6. The result of 3D Grid Map

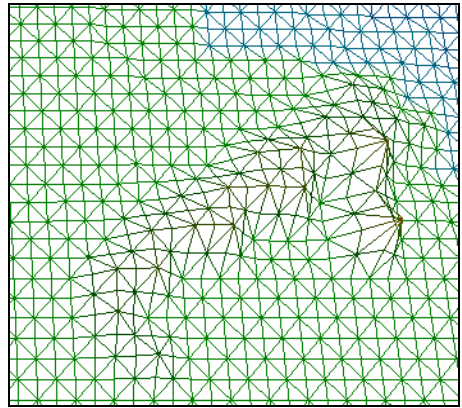
Compare with MATLAB 'Surf' Function. Fig. 7 shows the result of comparing the proposed algorithm with the MATLAB 'surf' function. In the Fig, (a) shows the result created by MATLAB with using same point cloud data, and the enlarged image (b) shows the geometric ambiguity problem well.



(a)



(b)



(c)

Fig. 7. This shows the 3D map building results of the MATLAB ‘surf’ Function and the Proposed Algorithm. (a) has been created by MATLAB with using the same point cloud data of Fig 5. (b) is the enlarged image of (a) and it shows the geometric ambiguity problem. (c) is the result of the proposed algorithm. There isn’t any disconnection between the nodes.

3 The Survival Probability

In order to build 3D probability map, the UGV’s survival probability should be defined. It has been defined in our previous study by using the classic definition of the probability shown as equation (1). [5]

$$P_s(A_i) = \frac{L_i - D_i}{L_i} = 1 - \frac{D_i}{L_i} \quad (1)$$

Where, $P_s(A_i)$ is the survivability of i -th UGV, L_i is the amount, called by 'Life', for the A_i to be able to resist the enemy's attack, and D_i is the amount which the enemies can damage the A_i . Now the damaged probability can be defined as;

$$P_d(A_i) = \frac{D_i}{L_i} \quad (2)$$

So, the survivability can be defined as 1 minus the damaged probability.

3.1 Damaged Probability

However, to determine the optimal, path we should compare the probabilities on the adjacent nodes at each time. Thus we should modify the definition of the damaged probability. It can be redefined as; [1]

$$P_d^k(A_i) = \sum_{j=1}^m \frac{\beta_j P_h(A_i)}{L_i} \quad (3)$$

Here, β_j is the coefficient of the power of the j -th enemy's weapon, m is the number of total enemies. And $P_h(A_i)$ is the probability that the enemy's attack can hit the A_i so called by 'the hit probability'.

The hit probability is related with the enemy's aim, thus it can be described with the Gaussian normal distribution. However, there is no direct solution of the integral of the normal distribution, therefore the hit probability can be approximated shown as equation (4) by using Arvind K. Sharh's method. [6]

$$P_h(A_i) = \begin{cases} z(4.4 - z) / 10 & 0 \leq z \leq 2.2 \\ 0.49 & 2.2 < z < 2.6 \\ 0.5 & z \geq 2.6 \end{cases} \quad (4)$$

3.2 Additional Cost Function for Optimal Path Planning

Finding the optimal path is implemented by searching the minimum cost function value on the map. Usually, the graph-tree searching algorithm like A* is used at finding the optimal path. [7] However the heuristic function of the normal A* is one of the distance value, thus we defined the additional cost function for the proposed algorithm shown as equation (5). [1]

$$P_s^t(A_i) = 1 - \sum_{k=0}^t \sum_{j=1}^m P_d^k(A_i | E_j) \quad (5)$$

4 Simulation and Result

The simulation program has been developed to verify the proposed algorithm by using C++ builder 2007 on the windows 7 environment. And the path planning result by proposed algorithm will be presented in the subsequent section. [8, 9, 10]

4.1 The Results

One of results of the proposed path planning algorithm is shown in the Fig. 8. In the Fig., the white balls between two red balls are the result path.

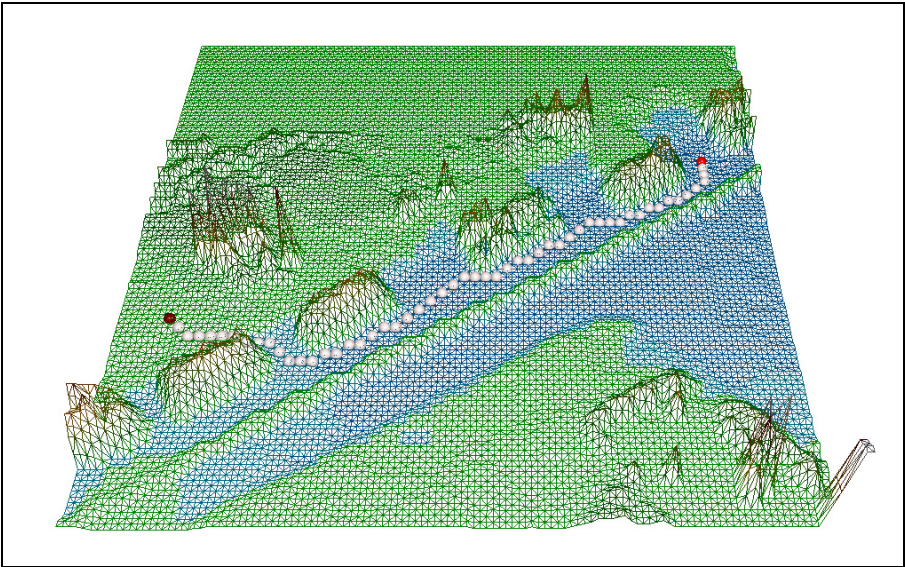


Fig. 8. One of the Path Planning Result on the 3D Grid Map

And the other path planning result on the 3D grid map is shown in the fig 9. if there are only some obstacles without enemy, the result is same as the normal A* algorithm.

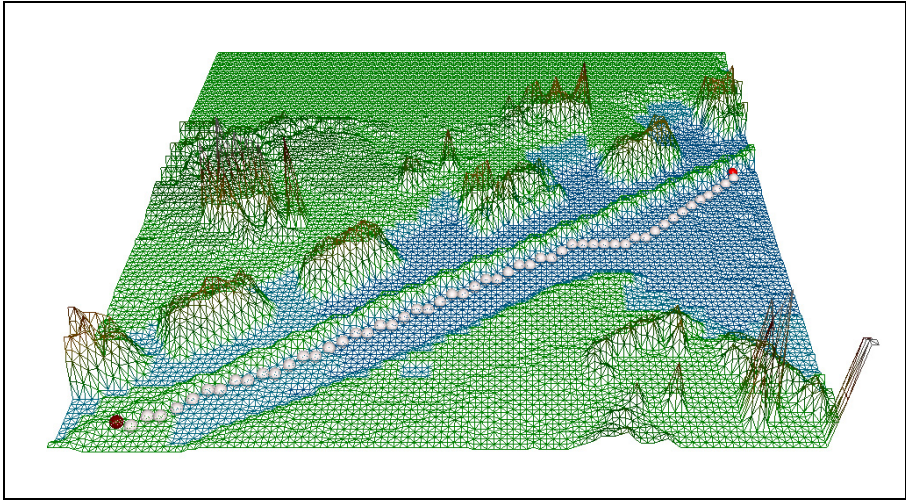


Fig. 9. The Other Result of the Proposed Algorithm on the 3D Grid Map

Fig. 10 shows the path planning result on the 3D probability map in which some enemies exist. Unlike the fig. 9, the value of each node isn't the elevation information. It means the dangerous probability similar with the potential energy at artificial potential field method. Thus, the path is generated like as if it avoids the higher value node.

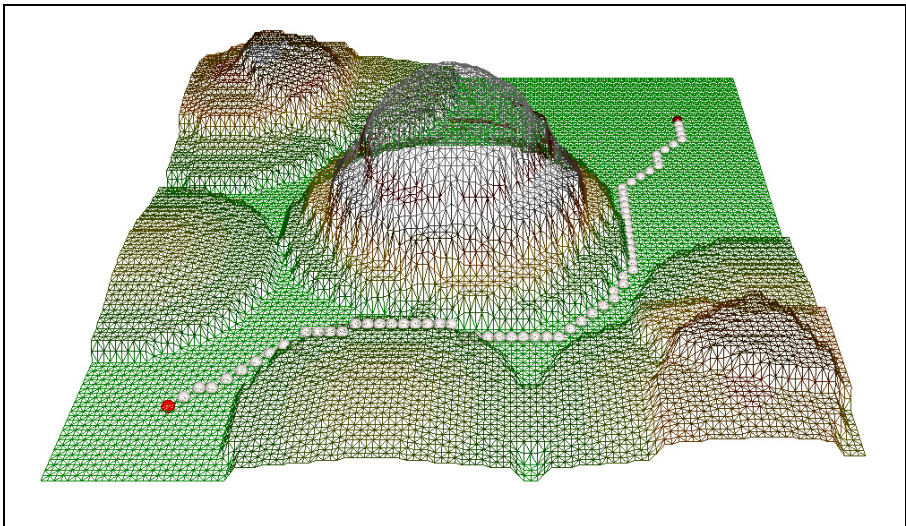


Fig. 10. The Path Planning Result on the 3D Probability Map

5 Conclusion

In this paper, the 3D probability map has been proposed in order to plan the optimal path for UGV in special environment like a battlefield. 3D probability map can be created by combining with the 3D grid map and the UGV's survival probability value. When building the 3D grid map from the point cloud data, the additional node is inserted between two grid nodes to solve the geometric ambiguity problem. The result map is symmetric of the eight directions and is connected with all adjacent nodes. Thus the cost value can be obtained within any direction without any geometric ambiguity.

The simulation program has been developed to verify the proposed algorithm, and the results were shown. The result shows that the optimal path planning algorithm works good with the 3D probability map. In future work, the proposed algorithm will be extended by combining other special environment factors like UGV's mobility.

Acknowledgments. The Authors gratefully acknowledge the support from UTRC (Unmanned technology Research Center) at KAIST (Korea Advanced Institute of Science and Technology), originally funded by DAPA, ADD.

References

1. Kim, M.-H., Lee, H.-M., Wei, Y., Lee, M.-C.: A Study of New Path Planning Algorithm Using Extended A* Algorithm with Survivability. In: Su, C.-Y., Rakheja, S., Liu, H. (eds.) ICIRA 2012, Part III. LNCS, vol. 7508, pp. 608–617. Springer, Heidelberg (2012)
2. Lester, P.: A* Pathfinding for Beginners, <http://www.policyalmanac.org/games/aStarTutorial.htm>
3. Choe, Y., Shim, I., Ahn, S., Chung, M.J.: Geometrical Featured Voxel based Urban Structure Recognition and 3-D Mapping for Unmanned Ground Vehicle. JICRS 14(8), 1–8 (2008)
4. Choe, Y., Ahn, S., Chung, M.J.: Fast Point Cloud Segmentation for an Intelligent Vehicle Using sweeping 2D laser scanners. URAI, 38–43 (2012)
5. Papoulis, A.S.: Unnikrishna Pillai: Probability, Random Variables and Stochastic Processes. McGraw-Hill Higher Education (2002)
6. Shah, A.K.: A Simpler Approximation for Areas Under the Standard Normal Curve. The American Statistician 39(1), 80 (1985)
7. Peter, E., Hart, N., Nilsson, J., Raphael, B.: A Formal Basis for the Heuristic Determination of Minimum Cost Paths. IEEE Transactions of Systems Science and Cybernetics 4(2), 100–107 (1968)
8. Gamma, E., Helm, R., Johnson, R., Vlissides, J.: Design Patterns. Addison-Wesley (1995)
9. Musser, D.R., Derge, C.J., Saini, A.: STL Tutorial and Reference Guide, 2nd edn. Addison-Wesley (2001)
10. Press, W.H., Teukolsky, S.A., Vetterling, W.T., Flannery, B.P.: Numerical Recipes in C++, 2nd edn. Cambridge University Press (2002)

Method and Development of Magnetic Positioning Device for Magnetic Guided Vehicle

Hyunhak Cho¹, Jaeyong Kim², Hajun Song², Moonho Park², Sungshin Kim^{2,*}

¹ Department of Interdisciplinary Cooperative Course: Robot, Pusan National University, Pusan, Korea

² Department of Electrical Engineering, Pusan National University, Pusan, Korea
{darkruby1004, arioner, darkhajun, 82akakak, sskim}@pusan.ac.kr

Abstract. In this paper, device development for AGV using magnet navigation and method of magnetic localization method are described. The most commercial AGV is using magnet navigation. This is more stable and lower cost of sensors than different navigation systems of AGV. However, the commercial magnet navigation devices use magnet hall sensor of digital type and those accuracy are decided by the number of magnet hall sensor and interval. The interval is about 10mm generally because interference occurs in the case of close interval, but the AGV using this interval has low accuracy. This AGV doesn't matter in straight driving, but occur breakaway or false operation in curve driving. Therefore, we create a magnet navigation device using magnet hall sensor of analog type and design fitting functions with the experimental results of magnet hall sensor in the work environment. Based on this, this paper proposes the method to detect magnet navigation line. In the result of proposed method, localization method accuracy is improved more about 16.73mm by this method than the commercial magnet navigation device and space to detect magnet navigation line is larger.

Keywords: Magnet Navigation Device, Magnet Hall Sensor, Fitting Function, Localization Method.

1 Introduction

In recently, the industry is possible larger supply of required product by production on a large scale. Common method that makes one product in manufacture line of production is difficult prompt response on small quantity batch production and is inefficient the unit cost of production[1-3]. Therefore flexible production system is required for flexible action on kind of production. This production system is classified workshop, materials handling system, control system, etc. The materials handling system that is important component with production cost means work of all filed that is related load and unload, transportation, storage of materials. In recently, dement of that is gradually incremental to satisfy flexible, efficiency of materials handling system. Commonly unmanned transfer system is autonomic ally work, decide load and unload, transportation of

* Corresponding author.

production or part materials of production. That is called automated guided vehicle (AGV)[4-7]. In technique of AGV, guided system is important technique with localization and driving control. The guided system of AGV is classified wire guided and wireless guided. Wire guided system is system that AGV move on designed position through wire guided device as magnetic measure device, camera and infrared light camera measure guideline attached and laid on floor[8-11]. The wireless navigation system is system that guide AGV using landmark information as laser navigation, stargazer, ultrasound satellite, GPS, RFID, etc. at work environment[12-14]. The wire guided system is large installed charge, very difficult maintenance. And that guide AGV designed line. On the other hand, the wireless system is possible autonomous driving not designed line, easy install and maintenance because using landmark information attached at work environment. However this has slow response time, expensive, low localization accuracy by comparison with wire guided system. Presently, AGV used on work environment has wire guided system because high accuracy, inexpensive than wireless guided system. Type of the wire guided system is magnetic guided AGV that guided on laid magnet, camera guided AGV that guided using camera on color tape and electromagnetic guided AGV that guided on electromagnetic line. Among these, electromagnetic guided AGV is most used because that is most low influence of damage of guided line and disturbance. Magnet positioning device measures magnetic line using magnet hall sensor. Magnet hall sensor is used 1-axis of digital type. Magnet positioning device has 8-type, 16-type on used hall sensor. Accuracy of magnet localization device is decided by interval of hall sensors. If interval of hall sensors is small, interference is happened. Accuracy is very low at large interval. Therefore, suitable Interval of hall sensors is required.

Digital magnetic localization is used because all sensor of analog type have disturbance by magnetic field of earth and magnetic field of current. Therefore, this paper proposes magnetic localization system using mapping and analog magnetic hall sensor for high accuracy magnetic localization sensor.

This research design and make magnetic localization device to measure position and angle of AGV using feature information of magnetic field. In the past magnetic localization device, we used and tested various bipolar analog magnetic hall sensor. To verify proposed method, we compared magnetic localization device of designed made by ourselves with commercialized production.

The organization of this paper is as follow. Section 2 analyze feature of magnetic hall sensor, section 3 describes the proposed magnetic localization device. Section 4 describes experiments to evaluate the proposed device. Finally, section 5 presents our conclusions and future study.

2 Magnetic Hall Sensor

In general, magnetic sensor which is applied to MGV(Magnetic guidance vehicle) or magnetic-gyro navigation AGV should be small and have high sensitivity for the real time operation. Take into account these merits, magnetic hall sensor has been used for magnetic localization of MGV. The feature of magnetic hall sensor can be divided into 2 parts: axis and direction information. In case of axis information, it can be divided into 3 parts, 1-axis, 2-axis, 3-axis, and they measure the magnetic field of

z-axis, x-y-axis, x-y-z axis in general, respectively. In case of direction information, it can be divided into two parts: on-direction and non-direction. With non-direction, it measures only the strength of magnetic field. However, with on-direction, it measures the magnetic field of the each opposite axis and calculates the difference or average using them. MGCV, using the wire navigation system, can measure the magnetic field of magnet constantly from magnetic path. For this reason, MGCV can use the low-cost magnetic hall sensor with no including direction information. At the first, we experiment the various magnetic hall sensors and analyze them to apply to MGCV. Two magnets are used for the experiment: magnetic tape for a guidance of MGCV and magnet for lying, and we only use the magnet which has the Gauss range from 5 to 10. However, in general, measuring range of magnetic hall sensor is wider than aforementioned range, e.g. SS411P and SS461A hall sensor had the range from -30 to 140 Gauss and from 5 to 80 Gauss, respectively. Digital hall sensor makes the on signal when it detects the objects which have the measurable range of Gauss of magnetic field, otherwise, it makes the Off signal. Sensors which can measure the polarity are classified as bipolar sensor and unipolar sensor. Magnetic hall sensor is commonly attached to MGCV with the height of 3 cm from the bottom. Base on this, experiment is done with 3cm height between 1-axis hall sensors and the bottom.

Table 1 shows the measurable range when the each hall sensor has the difference about 20mv from base voltage.

Table 1. Experimental result of measurable range of magnetic hall sensor

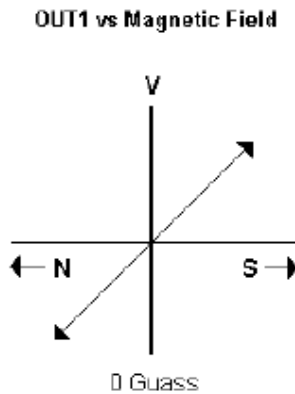
Magnetic hall sensor	Magnet Tape(unit: mm)	Laying magnet(unit: mm)
SS411P	5	8
SS40A	13	15
SS461C	10	12
A1101UA-T	X	5
WSH130	5	9
WSH130NL	3	8
WSH131	4	10
WSH133	7	15
WSH135	15	11
WSH136	35	33
WSH137	30	33
WSH138	50	45
WSH201	90	60
WSH315	10	10

Magnetic hall sensors that have the satisfied result are WSH136, WSH137, WSH138, WSH201, and WSH201 which has the longest measurable distance was used in this paper. Specification of WSH201 hall sensor is shown in Table. 2.

Table 2. Specification of WSH201 hall sensor

Parameter	Spec
Supply Voltage	2.2~12V
Measurement Range	5V : ± 200 Gauss 12V : ± 500 Gauss
Sensitivity	7.4 ~ 8.9 mv/Gauss
Low Temperature drift	± 1.0 mv/C(0G)
Communication	Analog Voltage
Polarity	Bipolar

Base voltage is increased about α when WSH201 hall sensor measures S polarity. Otherwise, it measures N polarity, base voltage is decreased as the same amount. WSH201 has the change of 20mv per a Gauss, and it only measures the z-axis magnetic field with no including direction information.

**Fig. 1.** Characteristic of magnet hall sensor (WSH201)

For experiments of WSH201 hall sensor, it moved per 2mm on x-axis from -91mm to 91mm with 3cm height from the bottom and measured the data. 10bit ADC is attached to WSH201 hall sensor for experiment. Using this, we measure the 100 data when the magnet was moved per 2mm and calculate the average of them. In Fig. 2 shows the data measurement system and experimental method, and result of experiment for magnetic tape and magnet for laying. There is no way to measure and exactly remove the external magnetic field between earth magnetic field and wire of measurement system. Because of this, experiment was done in clear space with no magnetic object in 2m radius and calculates the average of data which was measured during the 10 minutes. Based on this average, difference with measured data of WSH201 hall sensor was considered to experiment and N polarity was used for the test.

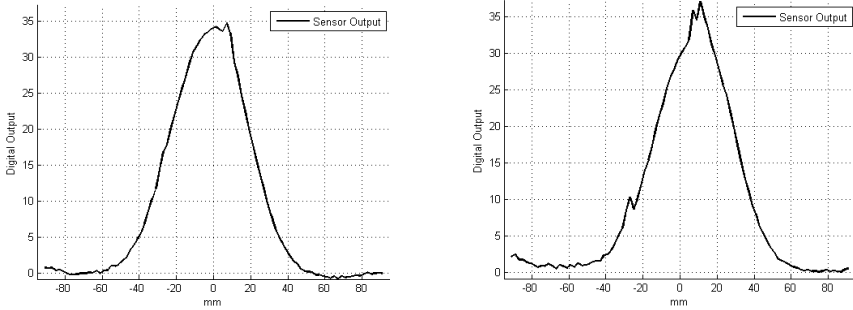


Fig. 2. Experimental Result of magnet hall sensor

Result of experimental graph forms the Gaussian function. At the experiment with 3cm height, magnetic tape has the max and min value as 37 and -1, respectively. In case of magnet for laying, it has the max and min value as 42 and -1, respectively. Converting these Gauss data, we get the max and min value of magnetic tape as 9.0332 and -0.2441, respectively. Along the same lines, magnet for laying has the max and min value as 10.2539 and -0.2441. ADC value is divided into 4.096 to calculate the converted ADC value. WSH201 hall sensor has the 20mv/G sensitivity. That is the why that if ADC value presents the 1024 and 4.096 when the voltage was 5V and 20mv in 10 bit ADC system, respectively.

3 Proposed Magnetic Position System and Position Decision

Magnetic Position System is designed and manufactured, that used 12 magnetic hall sensors of analog type. because set to 12 hall sensors through measurement time experiments to be less than driving control time(50 ~ 100 ms) of AGV, and we used ADC in MCU to reduce the time of the measurement of ADC device. Fig 3. is the form of designed and manufactured magnetic position device. That is included MCU, 12 hall sensors of analog type and max 232.

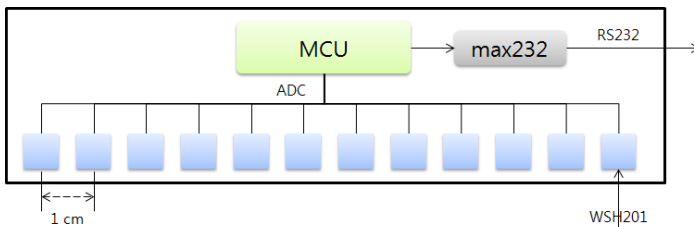


Fig. 3. Designed magnetic positioning device

Methods of position decision of the magnet are digital, center of gravity and fitting function used measured magnetic fields of magnets. It should be considered

surroundings and earth's magnetic field disturbances, therefore apply threshold magnetic field. These threshold values need to determine the magnetic field values appropriate to the environment in which the AGV. Digital decision method determines the position using the digital values (on/off data) by applying a threshold value to the measured magnetic field. Center of gravity method uses the magnetic value using the changed value (gauss data). The position decision method with fitting function method uses the maximum data the fitting function of the Gaussian type by the experimental data in the work environment.

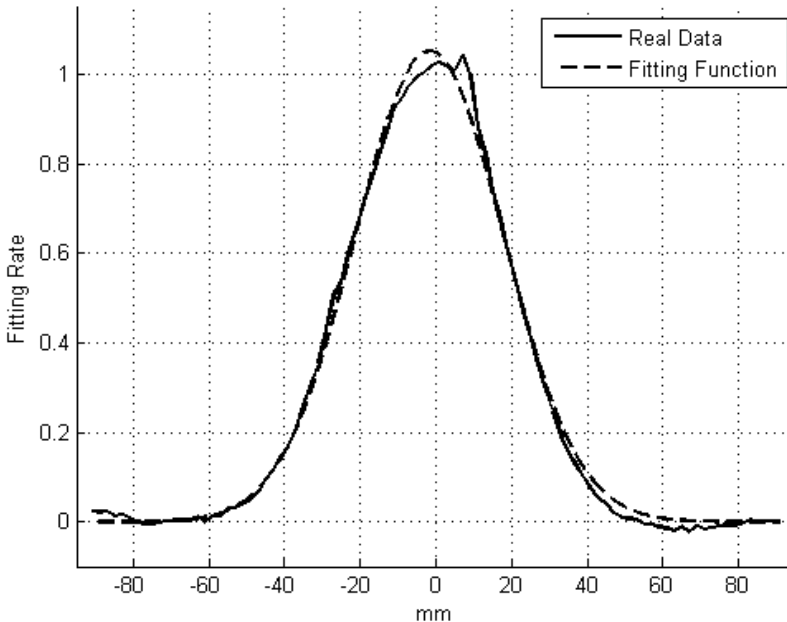


Fig. 4. Result of fitting Function using measured data

4 Experimental Result

4.1 Experimental Environment

To analyze the designed magnetic localization sensor with common sensor, we designed the experimental table using aluminum profile as shown in Fig. 5. Besides the experimental table, 400W BLDC motor was rotating about 300 RPM (Revolutions per minute) for making the oscillation to generate the effect such as the magnetic localization sensor is similar to attach the real AGV.

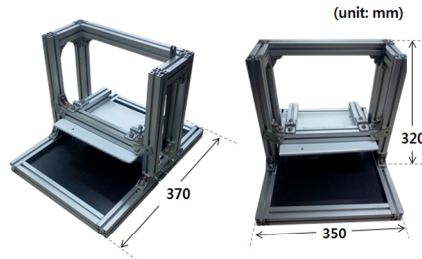


Fig. 5. Experimental equipment

4.2 Performance Experiment of the Position Method

To experiment the performance of proposed method, we set the center of magnetic localization sensor as 0 and the magnet was moved from -91mm to 91mm per each 2mm. Fig. 5 shows the experimental method.

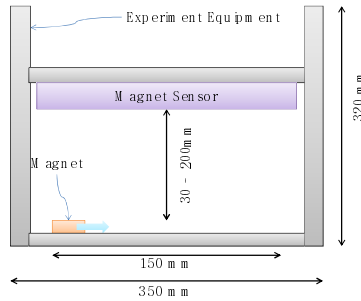


Fig. 6. Experimental method

The experiment results of the designed and manufactured magnetic position device are shown in the figure below. That is the result of calculated magnet position with digital, center of gravity and fitting function position using 100 times data. The digital position method are the calculated method of the commercially devices.

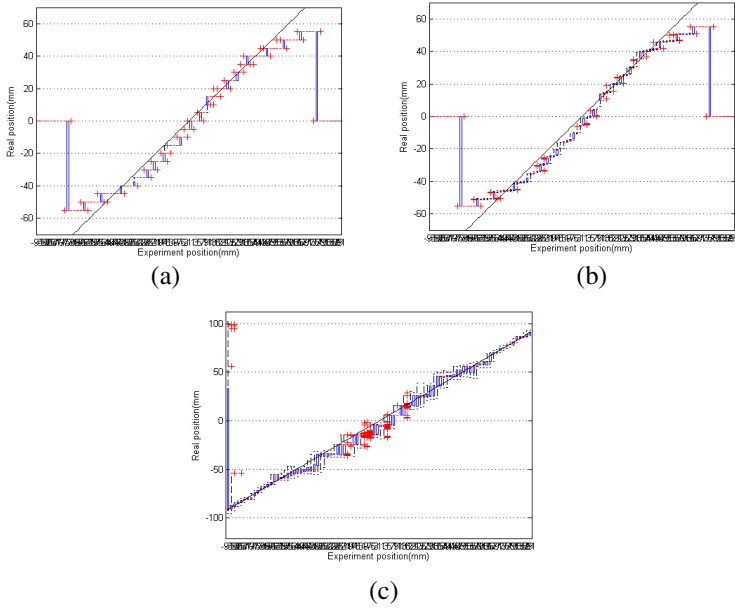


Fig. 7. Result of localization on magnet. (a) digital (b) center of gravity (c) fitting function

Fig 8 are the errors between the real position and the calculated position.

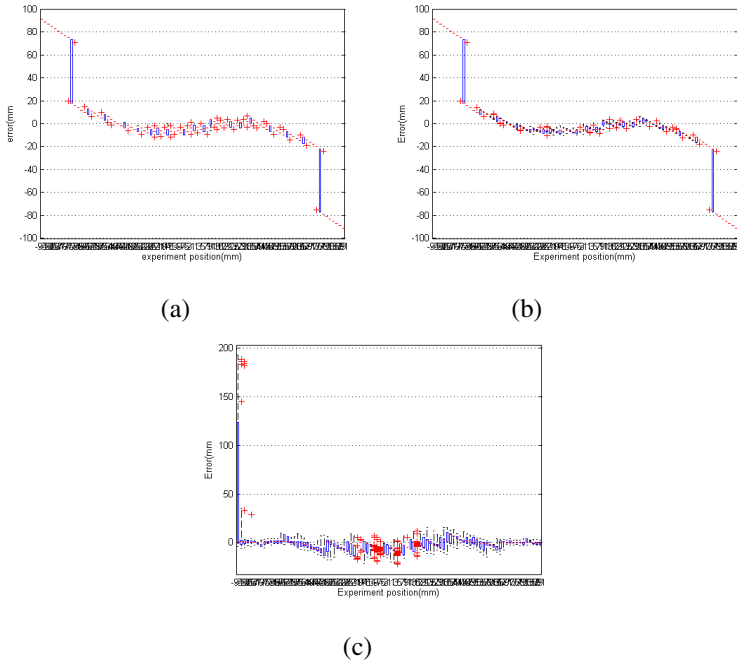


Fig. 8. Error of localization. (a) digital (b) center of gravity (c) fitting function

As can see from the experimental, digital and center of gravity position method are small than fitting function method, because it use the threshold magnetic field for in order to reduce disturbances and interference phenomenon between hall sensors. However, the fitting function method using the maximum data has the low accuracy than digital and center of gravity method in a certain interval because of the high sensitivity of hall sensor. From the experimental result, the accuracy of proposed magnetic position device is 3.25 mm, and we can verify that proposed method is similar to common magnetic localization device.

Table 3. Error result of magnet position method

Position of magnet	Digital	COG	Fitting Function
-91	91.00	91.00	1.25
-89	89.00	89.00	0.25
-87	87.00	87.00	0.13
-85	85.00	85.00	0.29
-83	83.00	83.00	0.24
-81	81.00	81.00	0.71
:			
-5	5.00	5.41	9.00
-3	7.00	7.04	11.82
-1	4.00	4.82	2.30
1	6.00	6.16	5.00
3	3.00	3.85	7.32
5	5.00	5.24	10.42
:			
81	81.00	81.00	0.69
83	83.00	83.00	2.40
85	85.00	85.00	0.33
87	87.00	87.00	0.39
89	89.00	89.00	1.31
91	91.00	91.00	0.38
AVG	19.98	19.76	3.25

5 Conclusion

It is a paper associated with development of magnetic position device for the magnet type AGV. In order to develop magnetic position device, we analyses sensor to measure magnetic field and choose suitable hall sensor for AGV and test repeatedly. We propose magnetic position device using WSH201 which is selected through continuous experiment. WSH201 which is chosen as hall sensor is easy to apply to AGV because WSH201 is a hall sensor of bipolar analog type, and it is also small and can measure wide magnetic field. We designed and manufactured 1 X 12 magnetic position device using hall sensors, set to fitting function to determine the position of magnet. From the experimental result, the accuracy of proposed magnetic position device is 3.25 mm, and we can verify that proposed method is similar to common magnetic localization device.

Acknowledgments. This research was supported by the MOTIE(The Ministry of Trade, Industry and Energy), Korea, under the Human Resources Development Program for Special Environment Navigation/Localization National Robotics Research Center support program supervised by the NIPA(National IT Industry Promotion Agency). (H1502-13-1001).

References

1. Yuste, H., Armesto, L., Tornero, J.: Benchmark tools for evaluating AGVs at industrial environments. In: 2010 IEEE/RSJ International Conference on Intelligent Robots and Systems, pp. 2657–2662 (2010)
2. Gutsche, R., Laloni, C., Wahl, F.M.: A flexible transport system for industrial environments using global sensor and navigation concepts. *Robotics and Autonomous Systems* 14(2–3), 85–98 (1995)
3. David, H.P., Humberto, M.B.: Decentralized coordination of autonomous AGVs in flexible manufacturing systems. In: 2008 IEEE/RSJ International Conference on Intelligent Robots and Systems, pp. 3674–3679 (2008)
4. Kim, J.M., Jung, K.H., Kim, J.Y., Song, H.J., Kim, S.S.: Positioning Accuracy Improvement of Laser Navigation using Unscented Kalman Filter: Intelligent Autonomous Systems. *Advances in Intelligent Systems and Computing* 193, 807–816 (2013)
5. Jung, S.Y., Kim, J.M., Kim, S.S.: Simultaneous localization and mapping of a wheel-based autonomous vehicle with ultrasonic sensors. *Artificial Life and Robotics* 14(2), 186–190 (2009)
6. Hung, N., Im, J.S., Jeong, S.K., Kim, H.K., Kim, S.B.: Design of a sliding mode controller for an automatic guided vehicle and its implementation. *International Journal of Control, Automation, and Systems* 8(1), 81–90 (2010)
7. Jia, Z., Balasuriya, A., Challa, S.: Sensor fusion-based visual target tracking for autonomous vehicles with the out-of-sequence measurements solution. *Robotics and Autonomous Systems* 56(2), 157–176 (2008)
8. Chan, C.Y.: A system review of magnetic sensing system for ground vehicle control and guidance: California PATH Research Report. UCB–ITS–PRR–2002–20 (2002)
9. Wakaumi, H., Nakamura, K., Matsumura, T.: Development of an automated wheelchair guided by a magnetic ferrite marker lane. *Journal of Rehabilitation Research and Development* 29(1), 27–34 (1992)
10. Chan, C.Y., Tan, H.T.: Evaluation of Magnetic Markers as a Position Reference System For Ground Vehicle Guidance and Control: California PATH Research Report (March 2003)
11. Ryoo, Y.J., Kim, E.S., Lim, Y.C., Mok, J.K., Chang, S.K.: Intelligent Positioning System for Magnetic Sensor Based Autonomous Vehicle. In: SCIS & ISIS (2004)
12. Woo, S.B., Jung, K.H., Kim, J.M., Park, J.J., Kim, S.S.: Velocity Control Method of AGV for Heavy Material Transport. *Journal of Korean Institute of Intelligent Systems* 20(3), 394–399 (2010)
13. Evans, D., Hu, L.: Localization for mobile sensor networks. In: Proceedings of the 10th Annual International Conference on Mobile Computing and Networking, pp. 45–57 (2004)
14. Thrun, S., Bennewitz, M., Burgard, W., Cremers, A.B., Dellaert, F., Fox, D.: MINERVA: A Second-Generation Museum Tour-Guide Robot. In: Proceeding of the IEEE Conference on Robotics and Automation, pp. 1999–2005 (1999)

Relative Pose Estimation for an Integrated UGV-UAV Robot System

Yongseop Jeong* and In So Kweon

Korea Advanced Institute of Science and Technology
291 Daehak-ro, Yuseong-gu, Daejeon 305-701, Korea
ysjeong@rcv.kaist.ac.kr, iskweon@kaist.ac.kr

Abstract. We have designed an integrated system of an UGV (Unmanned Ground Vehicle) and an UAV(Unmanned Aerial Vehicle), and propose a sensor-based relative pose estimation method for this system. Most of service robots are wheeled robots which can be easily controlled. However, due to the development of aerial vehicle technologies including sensors and wireless communication, recent UAVs can have lower weight, longer flight time and stabilized control system. Merging an UGV and an UAV for certain service can be a better choice for personal or public services, especially for effective surveillance. In this paper, a commercial μ UAV and a low-price, sensor-equipped mobile base are integrated to provide surveillance service. A fish-eye camera and an ultrasonic range finder sensor are utilized to estimate relative translation between two robots. Attitude and heading reference systems in both robots are utilized to estimate relative rotation between them. The probabilistic filter is applied to compensate sensor or camera measurement noises. The robustness of the proposed system is verified by a quad-camera stereo capture system. Also, practical application is provided with a scenario which performs the homing of the UAV from arbitrary location.

Keywords: UGV, UAV, relative pose, co-operation.

1 Introduction

1.1 Integration of UGV and UAV

The public demand for service robots is steadily increasing. According to *International Federation of Robotics(IFR)*, the number of service robots sold for personal and household was estimated more than 2.5 million in 2011, which was 15% more than that of 2010[1]. Most of the service robots move with attached wheels, which are stable and very easy to control.

However, wheels severely limit the movable range of service robots. For example, most of commercial bi-wheeled robotic vacuum cleaner cannot pass through

* This research was supported by the MOTIE (The Ministry of Trade, Industry and Energy), Korea, under the Human Resources Development Program for Convergence Robot Specialists support program supervised by the NIPA(National IT Industry Promotion Agency) (H1502-13-1001).

even a very low door sill. On outdoor application, automobiles cannot pass through a wall without making a hole. To overcome such obstacles, additional paths such as slopes or another moving means are required.

One of the candidate is wing. But due to difficulties, complexity and limits of the aerial vehicle control, they are not suitable to provide personal or household services. However, aerial vehicle technologies have been much developed these days. The weight of aerial vehicles have been decreased thanks to the advanced materials, and flight time has become longer with battery technologies. MEMS-based sensor equipments allow the stable control of aerial vehicles, and wireless communication technologies enable remote controllability and connectivity exchanging camera or sensory information between the robot and the station. These days, aerial vehicles are no longer a special technology. They are utilized not only for public transportation or military service, but also for hobbies and toys.

The wheeled robots are easy to control and comparatively free from the payload and energy limit, while aerial robots have much wider field of operations. Therefore, integrating two robots to provide surveillance services can take advantage of both of them. The ground one can patrol the desired region, and can deploy the aerial one to investigate unreachable regions. In this paper, a commercial μ UAV and a low-price, sensor-equipped mobile base are integrated to provide surveillance services.

1.2 Related Works

Recently, the aerial vehicle has become one of popular research fields of robotics. Researches for rapid and complex motion control of them[2], or their cooperation for manipulation or transportation[3] have been performed. Autonomous flight is also a popular issue. Autonomous flight with structured[4] or unstructured[5] environment was presented.

As mentioned in 1.1, the aerial vehicles are not free from the payload. This constraint limits the quantity of sensors or processors to be attached on the vehicle. Overcoming this limit and to achieve successful localization, the GPS-based method for outdoor environments[6] and artificial landmark-based method for indoors[7] are introduced. To compensate weak computational power, sensor data can be transferred to ground station[8].

To provide indoor service with the aerial vehicle, the aerial vehicle requires various sensors in small size. A commercial quadcopter, AR.Drone 2.0[9] is equipped with 2 cameras, a 9-axis inertial measurement unit(IMU), an ultrasonic altitude sensor with wireless communication ability. A periodical surveillance system have been introduced[10] utilizing this μ UAV and a mobile base. To localize the aerial vehicle, the bottom camera was utilized to observe the mobile base and the dead-reckoning method with internal IMU was applied. Because of the dead-reckoning method, the ground vehicle must stand still while the aerial vehicle is in flight.

1.3 Problem Definition

To perform services with multiple robots in cooperation, localizing both of them is one of the most important issues. Without an accurate localization, they might be crash into each other during the task, or their task paths could be overlapped unnecessarily. Relative localization is also an essential issue. With an absolute position of a robot and the relative position with another robot, the absolute position of the other can be determined.

In this paper, a commercial μ UAV and a low-price, sensor-equipped mobile base are integrated to provide surveillance services. To estimate the relative pose between them, a fish-eye camera, an ultrasonic range finder sensor, two IMUs are utilized.

The probabilistic filter is applied to compensate sensor/camera measurement noises. The robustness of the proposed system is verified by a quad-camera stereo capture system. Also, a practical application is provided with a scenario which performs the homing of the UAV from an arbitrary location.

2 Relative Pose Estimation Using Sensor Fusion

Pose estimation of certain object requires 2 elements; the rotation and the translation. To estimate relative pose of 2 objects, it is necessary to set a reference coordinate system. In this work, the camera center of the ground vehicle is the origin of overall coordinate system. The relative rotation and the translation can be easily calculated by estimating the position of aerial vehicle, (x_a, y_a, z_a) and the rotation of aerial vehicle, d_a in Fig. 2.

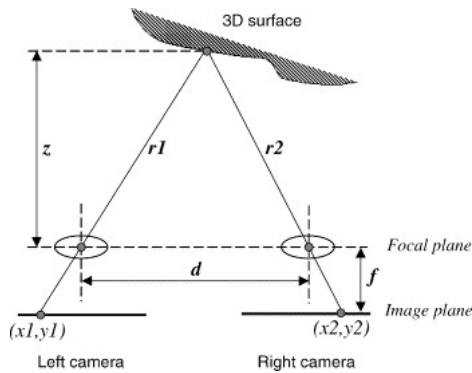


Fig. 1. Estimation of 3D position using 2-camera stereo system. x_1, y_1, x_2, y_2 : the position in the pixel plane. d : distance between cameras. f : focal length.

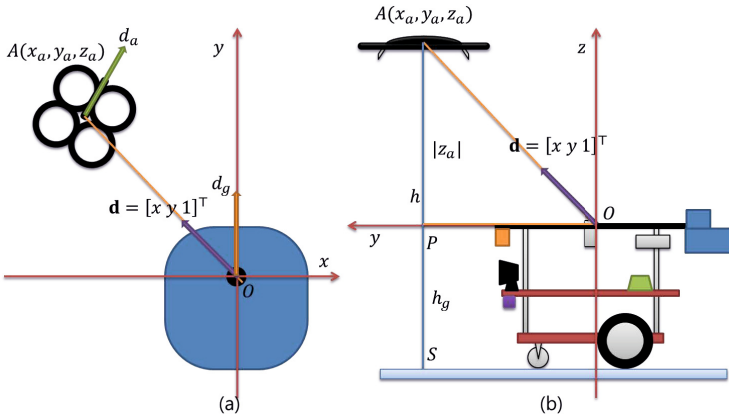


Fig. 2. The relative pose of two robots. (a) $x-y$ plane. (b) $y-z$ plane. h_g : predefined height of the ground vehicle, $\mathbf{d} = [x \ y \ 1]^T$: direction vector of the aerial vehicle from the ground vehicle, h : height of the aerial vehicle, d_a : direction of the aerial vehicle, d_g : direction of the ground vehicle.

2.1 Relative Rotation Using Inertial Measurement Units

An inertial measurement unit has three 3-axis sensors to estimate its rotation matrix; a gyroscope, an accelerometer and a magnetometer. If it is attached to a robot, its estimated rotation matrix can be treated as the robot rotation matrix. The rotation of a vehicle can be described with three variables, *roll*, *pitch* and *yaw* as in Fig. 3. So, the difference of the values of two vehicles can be treated as their relative rotation.

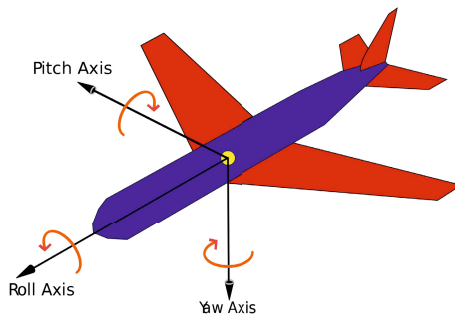


Fig. 3. Tait-Bryan notation of a vehicle

2.2 Relative Position Using Sensor Fusion

Among the methods to estimate three-dimensional position of an object[11], the most representative one is the 2-camera stereo. The 2-camera stereo system estimates the position of an object by triangulation, as in Fig. 1. To estimate the exact position, the distance between cameras d should be long enough. In the proposed system, upward camera system for observing the aerial vehicle is attached on top of the ground vehicle. So, it is not efficient to attach two or more cameras on the robot with ensuring large d , due to the limit of the size of ground vehicle.

Instead of the 2-camera stereo, we utilized a fish-eye camera and the altitude of the aerial robot. With the information of ray direction d and the altitude of the aerial vehicle h in Fig. 2, it is possible to estimate the relative position between two robots as (1) which is represented as $A(x_a, y_a, z_a)$.

$$\begin{aligned}
 x_a &= |z_a|x \\
 y_a &= |z_a|y \\
 z_a &= h - h_g
 \end{aligned}
 \tag{1}$$

2.3 Estimating Ray Direction From Fish-Eye Camera

If one can extract a target object from the image captured from a camera, it is possible to estimate the direction of the object from the camera center. Fig. 4 shows the geometric model of a pinhole camera. In this camera model, the real point X is projected to the point x on the image plane. From the properties of similar figures, the point $x = (x, y, f)$ can be represented with $X = (X, Y, Z)$ as $(fX/Z, fY/Z, f)$. It is possible to determine the ray direction of any projected points on the image plane after the camera calibration process[12].

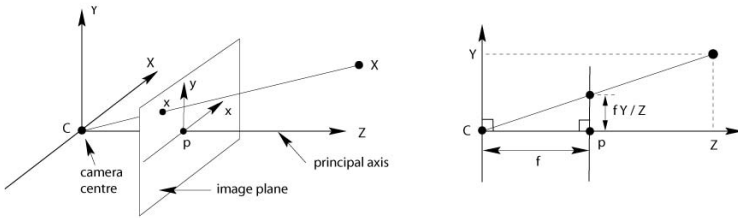


Fig. 4. Pinhole camera model

2.4 Estimating Altitude with Ultrasonic Sensor

The ultrasonic sensor range finder measures the distance between the sensor and a surface. If the sensor is attached to the bottom of an aerial vehicle and the vehicle is in flight, the sensor can estimate the altitude of the aerial vehicle. The response of the sensor is almost linear, but the response signal has uncertainties due to the ADC circuit noise or the temperature of the air.

3 Probabilistic Filter Compensating Measurement Error

Section 2 describes how to estimate the relative pose between two robots with the direction vector and the altitude of the aerial vehicle. But measurement errors can be occurred because of various reasons. Dominant errors are the altitude measurement error with the ultrasonic range finder and the image measurement error during the extraction the aerial vehicle from the fish-eye camera captured image. The probabilistic filter determines the relative position with the estimated pose and the model of noise from the image measurement and the ultrasonic sensor response.

Estimated position of the aerial vehicle at time t can be denoted as $X_t = [x_t \ y_t \ z_t]^T$. Also, observed position in t can be denoted as Z_t .

3.1 Probabilistic Model for Position Estimation

The objective of the probabilistic position estimation is updating X_t with respect to the variation of observation Z_t as (2) and Fig. 5.

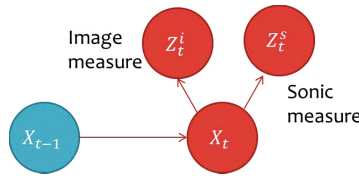


Fig. 5. Probabilistic Position Estimation

$$P(X_t|Z_{1:t}) = \eta P(Z_t|X_t)P(X_t|Z_{1:t-1}) \tag{2}$$

If the observed positions from $t = 0$ to $t - 1$ are known, the predicted position can be modeled as (3).

$$P(X_t|Z_{1:t-1}) = \int_{X_{t-1}} P(X_t|X_{t-1})P(X_{t-1}|Z_{1:t-1})dX_{t-1} \tag{3}$$

$P(X_t|X_{t-1})$ is called motion model and $P(Z_t|X_t)$ is called measurement model in (2) and (3).

3.2 Motion Model

Motion model describes the variations of relative position between two robots. To simplify the problem, conventional motion models assume the uniform velocity of robot or use sensors to observe exact velocity[13]. But in this research, two robots move separately. Also, the velocity of the aerial vehicle cannot be measured explicitly. So, it is impossible to assume uniform velocity or observe exact velocity. So, the motion model $P(X_t|X_{t-1})$ is modeled as Gaussian random variable.

3.3 Measurement Model

Measurement model with the position of the aerial vehicle in captured image pixel plane u_m and reprojection of X_t in image plane \hat{u} can be formulated as (4).

$$\exp\left(-\frac{\|u_m - \hat{u}\|}{2\sigma_p^2}\right) \quad (4)$$

Similar model can be derived as (5) for the ultrasonic measurement model.

$$\exp\left(-\frac{\|z - h\|}{2\sigma_h^2}\right) \quad (5)$$

The response of the ultrasonic sensor and the extraction from captured image are independent, so the measurement model can be derived by multiplying them as (6).

$$P(Z_t|X_t) = P(Z_t^i|X_t)P(Z_t^s|X_t) = \exp\left(-\frac{\|u_m - \hat{u}\|}{2\sigma_p^2}\right)\exp\left(-\frac{\|z - h\|}{2\sigma_h^2}\right) \quad (6)$$

4 Experiments

4.1 An Integrated System of an UGV and an UAV

Integrated robot system consists of two robots; an unmanned ground vehicle and an unmanned aerial vehicle. The bi-wheeled ground vehicle has a flat plate to carry the aerial vehicle. The aerial vehicle can take off or land on the station. A fish-eye camera is attached on the station.

The aerial vehicle is selected within the commercial small ones. AR.Drone 2.0[9] mentioned in 1.2 is a commercial quadcopter equipped with various sensors to be easily controlled. Also, with wireless communication technologies, users can not only control the robot but also retrieve sensory informations and camera images from the robot. To detect the aerial vehicle easily, we attached a LED array under the aerial vehicle. Fig. 6 shows the appearance of the integrated system.

4.2 Evaluation Setup

To evaluate the accuracy of the proposed method, we designed a quad-camera stereo capture system as Fig. 7. Four cameras are synchronized with the fish-eye camera and the ultrasonic altitude sensor of the UAV, to capture the path of the UAV. The captured path recorded by external four cameras is treated as the ground truth. The accuracy of proposed system is evaluated by calculating the error of Euclidean distance.



Fig. 6. Integrated Robots: Front view, Fisheye Camera, Landed aerial vehicle, Bottom view, Ultrasonic altitude sensor

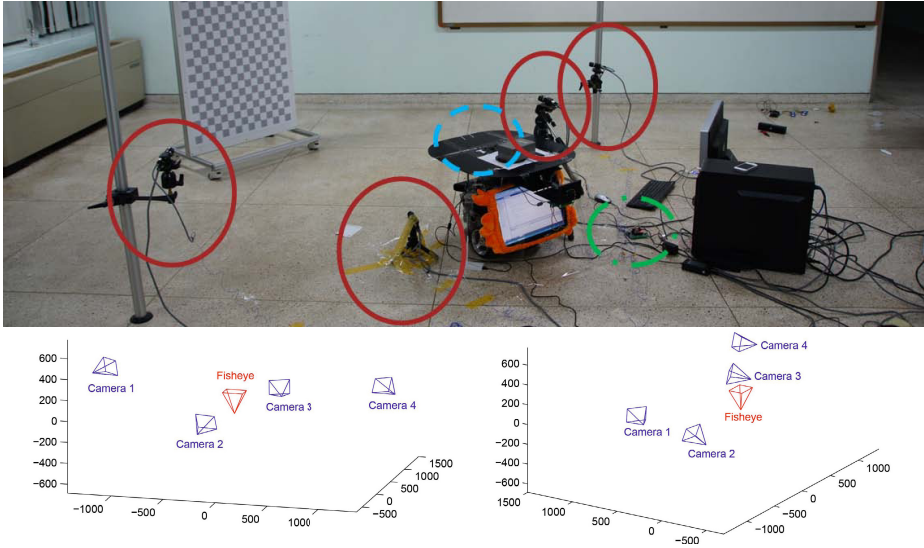


Fig. 7. Calibration of the quad-camera stereo capture system. Solid line: 4 cameras, Dashed line: fisheye camera attached to robot, Chain line: external synchronized trigger. Camera center of the fisheye camera is the origin of the world coordinates. 4 cameras are calibrated and firmly attached.

4.3 Experimental Result

Fig. 8 shows the result of estimation of relative position. The first one is the case of the smooth movement. In that case, the response of the ultrasonic sensor is comparatively stable. The second one is the case of the rapid movement, so the response of the ultrasonic sensor is distorted with noise. Table 1 is the error from the each experiment.

Table 1. Mean error of captured data

UAV Movement	Captured	Filtered
Smooth	106.38mm	103.51mm
Rapid	82.69mm	78.54mm

4.4 Autonomous Homing of the UAV

To show the possibility of practical application of the proposed method, we designed a scenario. To perform a surveillance service with this integrated system, each robot should perform its duty with different path. However, after the surveillance of the UAV, the aerial one must return to the base for safety and power issues. In this experiment, we perform the autonomous homing of the unmanned aerial vehicle.

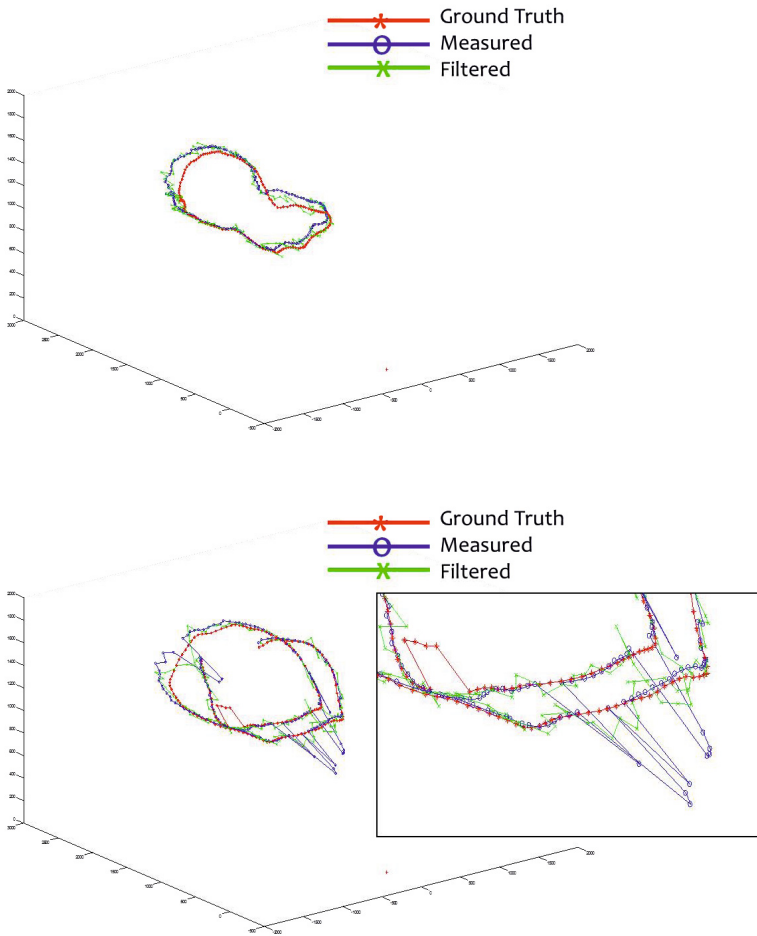


Fig. 8. Relative pose estimation result. (Top) Smooth moving(Stable sensor response), (Bottom) Rapid moving(Unstable sensor response)

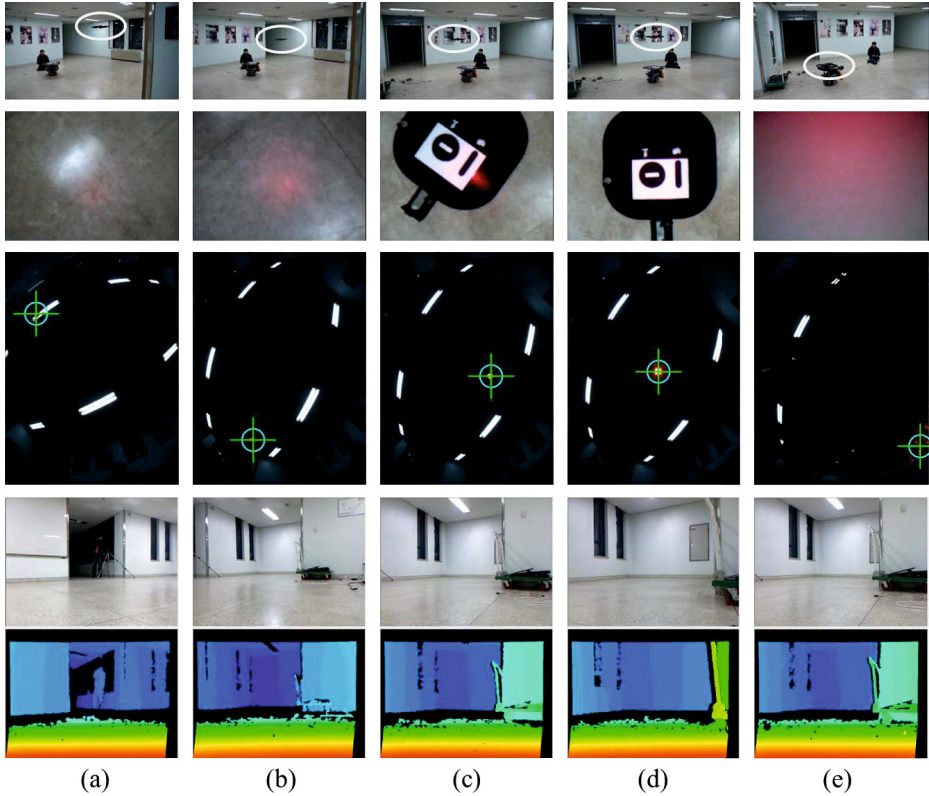


Fig. 9. Autonomous returning-to-base(homing) scenario. Row 1: Captured from external camera. Row 2: Captured by the bottom camera of the UAV. Row 3: Captured by the fisheye camera on the UGV. Row 4 5: Captured by Kinect attached on the UGV. (a) Order to return to base. (b) Moving toward the target (c) Pose correction with hovering target (d) Finish correcting hovering target (e) Landing completed.

The ground vehicle can track the relative position and rotation of aerial vehicle with the proposed method simultaneously. So, the integrated system can generate motions for the UAV, which makes the UAV return to the base. Fig. 9 shows the progress of returning to base. In this experiment, the aerial vehicle can return to the base not only the UGV is standing still, but also the UGV is wandering around.

5 Conclusion

We designed an integrated robot system consists of an UGV and an UAV for surveillance service, and proposed a method to estimate the relative pose between two robots using sensor fusion. With a fish-eye camera and an altitude sensor,

the relative position between two robots is successfully estimated. Probabilistic filter made the estimation algorithm robust. To evaluate the performance, a quad-camera stereo capture system is utilized. Also, an autonomous homing scenario is performed to show the possibility of a practical use of the proposed work.

References

1. IFR Statistical Department, World Robotics 2012 - Service Robots (2012)
2. Mellinger, D., Michael, N., Kumar, V.: Trajectory generation and control for precise aggressive maneuvers with quadrotors. In: International Symposium on Experimental Robotics, Delhi, India (December 2010)
3. Michael, N., Fink, J., Kumar, V.: Cooperative manipulation and transportation with aerial robots. In: Autonomous Robots (January 2011)
4. Bills, C., Chen, J., Saxena, A.: Autonomous MAV flight in indoor environments using single image perspective cues. In: IEEE International Conference on Robotics and Automation (May 2011)
5. Bloandsch, M., Weiss, S., Scaramuzza, D., Siegwart, R.: Vision based MAV navigation in unknown and unstructured environments. In: IEEE International Conference on Robotics and Automation (May 2010)
6. Ascending Technologies, <http://www.asctec.de/>
7. Motion Capture Systems, <http://www.vicon.com/>
8. Achtelik, M., Bachrach, A., He, R., Prentice, S., Roy, N.: Stereo vision and laser odometry for autonomous helicopters in GPS-denied indoor environments. In: SPIE Unmanned Systems Technology XI (2009)
9. Parrot, S.A.: AR.Drone 2.0 (2012)
10. Saska, M., Krajník, T., Přeučil, L.: Cooperative μ UAV-UGV autonomous indoor surveillance. In: 9th International Multi-Conference on Systems, Signals and Devices (March 2012)
11. Hartley, R., Zisserman, A.: Multiple View Geometry in Computer Vision. 2/e. Cambridge University Press (March 2004)
12. Zhang, Z.: A flexible new technique for camera calibration. In: Pattern Analysis and Machine Intelligence, vol. 22(11) (November 2000)
13. Kim, J., Yoon, K., Kweon, I.: Robust 3-D Visual SLAM in a Large Scale Environment. In: 14th International Symposium of Robotics Research (2009)

The Algorithm *Camera* Computing the Object Location

Tadeusz Szkodny

Silesian University of Technology,
Institute of Automatic Control, Akademicka 16 St.
44-100 Gliwice, Poland
Tadeusz.Szkodny@polsl.pl

Abstract. In this paper the algorithm *Camera* of calculation of the position and orientation coordinates of the object observed by the camera is presented. The camera is mounted above the technological station on which object appears. These coordinates are calculated relative to the station frame (coordinate system associated with the technological station) or relative to base frame (coordinate system associated with the base of robot). The orientation is described by the x - y - z fixed angles of rotation relative to station or base frame. In this algorithm the *perspective* model of camera is used. From the image on the camera matrix sensor of three characteristic points of the object are obtained $2D$ coordinates of these points. The location (position and orientation) of the object are calculated on the base of these coordinates. The calculated location coordinates allow the robot to automatically approach the object and carry out technological operations. For example, an object may be the car body and the technological operation sealing or welding. Creating of such algorithms is fundamental problem of computational intelligence for robots.

Keywords: Robot Vision, Computer Vision, Soft Computing, Robot Intelligence.

1 Introduction

Intelligent robots can do technological operations themselves, of course, in limited range. Independence that provides the appropriate software, called intelligent robots computer. This software includes the following algorithms: a) of image processing, b) of Cartesian trajectory generation, c) of the solutions of the inverse kinematics problem.

The image processing algorithms calculate a coordinates of the position and orientation of the object observed by the camera. The trajectory generation algorithms calculate Cartesian coordinates a via points of the trajectory. These points provide a proper approach of a robot to the observed object and take the appropriate operations technology. The solutions algorithm of the inverse kinematics computes actuator rotation angles from Cartesian coordinates calculated by the trajectory generation algorithm.

In this work focused on image processing algorithm. In the literature [1-4], we can find many descriptions of algorithms for the calculation of the Cartesian coordinates of the observed object by stereovision system of two cameras. In [5] is presented catadioptric stereovision systems with a single camera, but requiring additional mirrors.

In the proposed algorithm *Camera* here need only one camera, without additional mirrors. This algorithm calculates the homogeneous transformation matrix of camera frame relative to station frame, on which is the observed object.

The second section presents a description of the perspective camera model. The algorithm *Camera* which allows calculating the coordinates of the observed object relative to station frame, of on the basis of the coordinates in the camera coordinate system is formulated in the third section. Section four contains examples of calculations using this algorithm. The five section is a summary.

2 Perspective Model of Camera

In the perspective model of camera [6], we omit optical image distortion. This assumption simplifies the mathematical description of the observed point coordinates. Figure 1 illustrates the camera frame $x_c y_c z_c$, the, reference frame xyz and the coordinates of the point A.

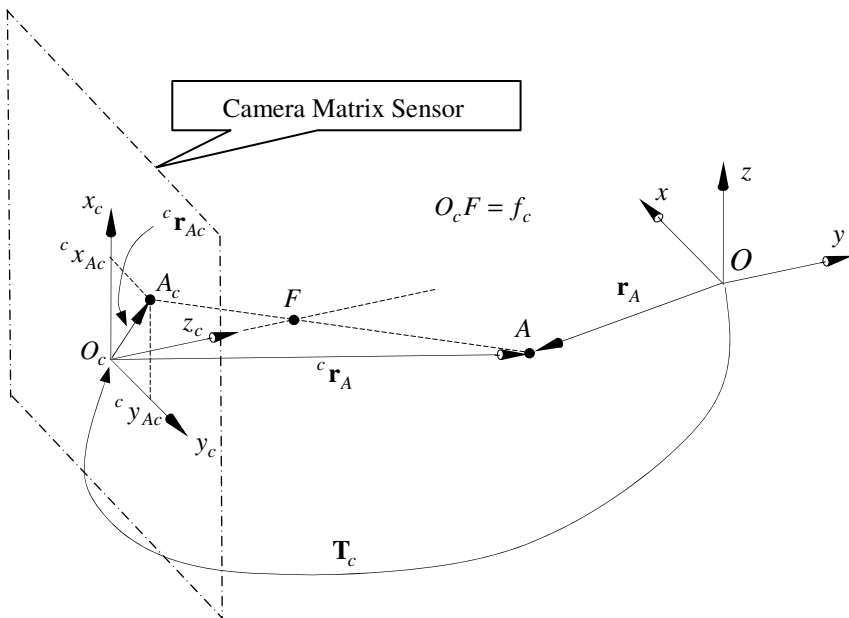


Fig. 1. The perspective model of camera

The plane $x_c y_c$ lies on the camera matrix sensor. The point F is the lens, away from the point O_c the focal length f_c of the lens. T_c is the homogeneous

transformation matrix [7,8] of frame $x_c y_c z_c$ relative to the frame xyz . The position coordinates of the point A in the frame xyz is given by equation (1a).

$$\mathbf{r}_A = \mathbf{T}_c {}^c \mathbf{r}_A = [x_A \ y_A \ z_A \ 1]^T . \tag{1a}$$

x_A, y_A, z_A are the coordinates of the position of point A in the frame xyz . ${}^c \mathbf{r}_A$ is the homogeneous form (1b) of the description of the point A in the frame $x_c y_c z_c$. ${}^c x_A, {}^c y_A, {}^c z_A$ are the coordinates of the position of point A in the frame $x_c y_c z_c$. From Fig. 2 it results the dependence of (2a) connecting the image coordinate ${}^c x_{Ac}$ of the point A with the coordinate ${}^c x_A$.

$${}^c \mathbf{r}_A = [{}^c x_A \ {}^c y_A \ {}^c z_A \ 1]^T . \tag{1b}$$

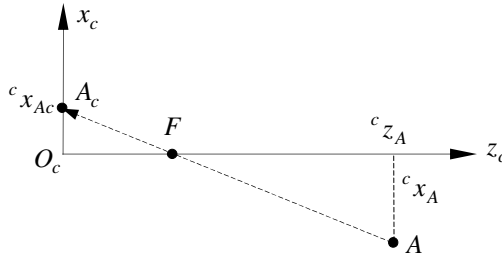


Fig. 2. The coordinates x of the point A in the camera frame

$$\frac{{}^c x_{Ac}}{f_c} = \frac{-{}^c x_A}{{}^c z_A - f_c} \rightarrow {}^c x_A = -{}^c x_{Ac} \left(\frac{{}^c z_A}{f_c} - 1 \right) . \tag{2a}$$

A similar relationship (2b) is valid for ${}^c y_A$ coordinate.

$${}^c y_A = -{}^c y_{Ac} \left(\frac{{}^c z_A}{f_c} - 1 \right) . \tag{2b}$$

The ${}^c x_{Ac}$ and the ${}^c y_{Ac}$ values read from the camera describe only straight half. The straight half is starting from point A_c and passes through point A. For these values, there are infinitely many points in this straight half, satisfying equation (2a) - (2b). A is one of the points. To unique definition of the point A coordinate ${}^c z_A$ is need.

We assume to describe the transformation matrix \mathbf{T}_c of the camera frame in the following form:

$$\mathbf{T}_c = \text{Trans}(d_x, d_y, d_z) \text{Rot}(z, \gamma) \text{Rot}(y, \beta) \text{Rot}(x, \alpha). \tag{3}$$

It is a record of successive transformations relative to the frame xyz . These transformations are: rotation around the x axis by an angle α , rotation around the y axis by an angle β , rotation around the z axis by an angle γ , displacement on d_z along the z axis, displacement on d_y along the y axis, displacement on d_x along the x axis. Orientation of the frame $x_c y_c z_c$ is described by the set x - y - z of fixed angles α , β , γ [7,8]. After taking the form (3) of the matrix \mathbf{T}_c in equation (1a), we obtain the geometric relationship:

$$\mathbf{r}_A = \text{Trans}(d_x, d_y, d_z) \text{Rot}(z, \gamma) \text{Rot}(y, \beta) \text{Rot}(x, \alpha) \begin{bmatrix} -{}^c x_{Ac} \left(\frac{{}^c z_A}{f_c} - 1 \right) \\ -{}^c y_{Ac} \left(\frac{{}^c z_A}{f_c} - 1 \right) \\ {}^c z_A \\ 1 \end{bmatrix},$$

which we write in the general form (4)

$$\mathbf{r}_A = \mathbf{g}(\alpha, \beta, \gamma, d_x, d_y, d_z, {}^c z_A). \tag{4}$$

The seven coordinates α , β , γ , d_x , d_y , d_z , ${}^c z_A$ are unknown. In equation (3) it is used a matrix of size 4×1 . From the fourth row of the matrix equation (4) results the identity $1 = 1$. Therefore, in equation (4) we omit the fourth row. This simplified relation describes the equation (4a).

$$\mathbf{r}_A = [x_A \ y_A \ z_A]^T = \underline{\mathbf{g}}(\alpha, \beta, \gamma, d_x, d_y, d_z, {}^c z_A). \tag{4a}$$

Equation (4a) is the basis for the calculation of the coordinates α , β , γ , d_x , d_y , d_z , occurring in the transformation matrix \mathbf{T}_c .

3 The Algorithm *Camera* for Calculations of Location Coordinates of the Object

To calculate the position and orientation of the camera in the system xyz are needed image coordinates x_c and y_c of a certain number of object points. These points we will call the characteristic. Let us assume that there are three characteristic points A , B , C . After the reading of the camera image coordinates ${}^c x_{Ac}$, ${}^c y_{Ac}$, ${}^c x_{Bc}$, ${}^c y_{Bc}$, ${}^c x_{Cc}$, ${}^c y_{Cc}$ we can calculate the coordinates α , β , γ , d_x , d_y , d_z occurring

in the matrix \mathbf{T}_c . These calculations allow the system of equations (5) formed from equation (4a) for characteristic points A, B, C .

$$\mathbf{G}(\alpha, \beta, \gamma, d_x, d_y, d_z, {}^c z_A, {}^c z_B, {}^c z_C) = \begin{bmatrix} -\underline{\mathbf{r}}_A + \underline{\mathbf{g}}(\alpha, \beta, \gamma, d_x, d_y, d_z, {}^c z_A) \\ -\underline{\mathbf{r}}_B + \underline{\mathbf{g}}(\alpha, \beta, \gamma, d_x, d_y, d_z, {}^c z_B) \\ -\underline{\mathbf{r}}_C + \underline{\mathbf{g}}(\alpha, \beta, \gamma, d_x, d_y, d_z, {}^c z_C) \end{bmatrix} = \mathbf{0}. \quad (5)$$

In equation (5) we have 9 unknown coordinates $\alpha, \beta, \gamma, d_x, d_y, d_z, {}^c z_A, {}^c z_B, {}^c z_C$. The relationship (5) is also a matrix description of nine scalar equations. Thus, the number of equations equals to the number of unknown coordinates. Using classical methods of solutions of nonlinear equations systems, we can calculate the unknown coordinates. The coordinates of characteristic points A, B, C in the frame xyz , appearing in matrices $\underline{\mathbf{r}}_A, \underline{\mathbf{r}}_B, \underline{\mathbf{r}}_C$ in equation (5), must be known.

For the calculation of the coordinates $\alpha, \beta, \gamma, d_x, d_y, d_z$ we can use a larger number of object characteristic points, for example A, B, C, D . After applying equation (4a) for these points we obtain the equation (6).

$$\mathbf{G}(\alpha, \beta, \gamma, d_x, d_y, d_z, {}^c z_A, {}^c z_B, {}^c z_C, {}^c z_D) = \begin{bmatrix} -\underline{\mathbf{r}}_A + \underline{\mathbf{g}}(\alpha, \beta, \gamma, d_x, d_y, d_z, {}^c z_A) \\ -\underline{\mathbf{r}}_B + \underline{\mathbf{g}}(\alpha, \beta, \gamma, d_x, d_y, d_z, {}^c z_B) \\ -\underline{\mathbf{r}}_C + \underline{\mathbf{g}}(\alpha, \beta, \gamma, d_x, d_y, d_z, {}^c z_C) \\ -\underline{\mathbf{r}}_D + \underline{\mathbf{g}}(\alpha, \beta, \gamma, d_x, d_y, d_z, {}^c z_D) \end{bmatrix} = \mathbf{0}. \quad (6)$$

In equation (6) we have an additional one unknown coordinate and three additional equations resulting from consideration of the point D . Therefore we have 10 unknowns coordinates and 12 equations.

In the general case for N object characteristic points will be $6 + N$ unknowns coordinates and $3N$ equations. Essential to solving the system of equations is to satisfy inequality

$$6 + N \leq 3N \rightarrow N \geq 3. \quad (7)$$

For the solution of this system of equations, satisfying the inequality (7), we can use iterative optimization [9-12] or geometric methods [13-17]. Usually in the methods of optimization a quadratic form $\mathbf{G}^T \mathbf{G}$ is minimized. In the geometric methods the system of linear equations resulting from the linearization function \mathbf{G} is solved. The main disadvantage of optimization methods is the large number of computations, and therefore the much time consuming. A large number of calculations resulting in large numerical errors. Geometric methods are free from such defects. For a well-chosen starting point geometric computation methods are faster and more precise than optimization methods.

From these considerations results, that it is best to use a geometric method with the minimum number of object points. From equation (7) results that the minimum number is 3. Thus, the calculation of coordinates $\alpha, \beta, \gamma, d_x, d_y, d_z$ will be

based on the matrix \mathbf{G} , described by equation (5). We will use the iterative geometric method of calculations, based on the linearized equation (5), in the form (8).

$$\mathbf{G}(\mathbf{x}) = \mathbf{G}(\mathbf{x}_0) + \left. \frac{\partial \mathbf{G}(\mathbf{x})}{\partial \mathbf{x}} \right|_{\mathbf{x}=\mathbf{x}_0} = \mathbf{0}, \quad (8)$$

$$\mathbf{x} = [\alpha, \beta, \gamma, d_x, d_y, d_z, {}^c z_A, {}^c z_B, {}^c z_C]^T.$$

\mathbf{x}_0 is a matrix describing the starting point of calculations. The matrix \mathbf{x} satisfying the equation $\mathbf{G}(\mathbf{x}) = \mathbf{0}$ is calculated by means of the algorithm *Camera*, described below in the step form (9).

The Algorithm *Camera*

Step 1. The choice of the starting point of the calculations $\mathbf{x} = \mathbf{x}_0$.

Step 2. Calculation of $\left. \frac{\partial \mathbf{G}(\mathbf{x})}{\partial \mathbf{x}} \right|_{\mathbf{x}=\mathbf{x}_0}$.

Step 3. Calculation of the matrix \mathbf{x} from following equation

$$\mathbf{x} = \mathbf{x}_0 - \left(\left. \frac{\partial \mathbf{G}(\mathbf{x})}{\partial \mathbf{x}} \right|_{\mathbf{x}=\mathbf{x}_0} \right)^{-1} \mathbf{G}(\mathbf{x}_0) = \mathbf{0}.$$

Step 4. The calculation of the norm $\|\mathbf{G}(\mathbf{x})\|$;

for $\|\mathbf{G}(\mathbf{x})\| > \Delta$ $\mathbf{x}_0 = \mathbf{x}$ and go to step 2,

for $\|\mathbf{G}(\mathbf{x})\| \leq \Delta$ matrix \mathbf{x} is the desirable solution. (9)

In this algorithm, a Δ is a calculation accuracy.

4 The Examples of Calculations

The algorithm *Camera* (9) can be applied to calculations of the matrices \mathbf{T}_c and \mathbf{x} for camera mounted above the technological station. Before those calculations, the observed object must be placed so that the object frame xyz coincides with the technological station frame $x_s y_s z_s$.

So the calculated matrix \mathbf{T}_c we denote by ${}^s \mathbf{T}_c$ (see Fig.3). The frame of object displaced and reoriented relative to the station frame $x_s y_s z_s$ we will be denoted by $x' y' z'$.

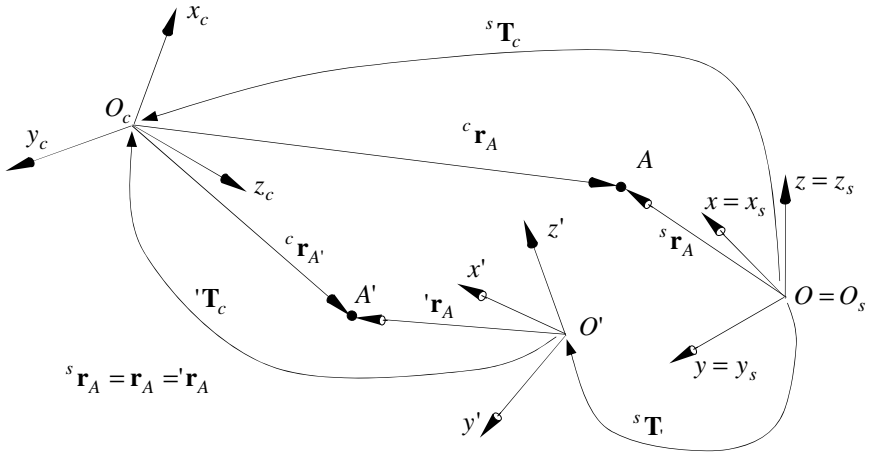


Fig. 3. The frames of: camera $x_c y_c z_c$, displaced and reoriented object $x' y' z'$, and station $x_s y_s z_s$.

After calculating the matrix ${}^s T_c$ each characteristic point observed by the camera can be calculated to the station frame. For example, after reading the image coordinates ${}^c x_{Ac}, {}^c y_{Ac}$, of characteristic point A we can calculate the coordinates ${}^s x_A, {}^s y_A, {}^s z_A$ of this point in the station frame, by using the equation (10).

$${}^s r_A = [{}^s x_A \quad {}^s y_A \quad {}^s z_A \quad 1]^T = {}^s T_c [{}^c x_{Ac} \quad {}^c y_{Ac} \quad {}^c z_A \quad 1]^T = {}^s T_c [{}^c x_A \quad {}^c y_A \quad {}^c z_A \quad 1]^T. \quad (10)$$

The coordinates ${}^s z_A$ is a 7-th element of matrix \mathbf{x} . Calculation of matrix ${}^s T_c$ is illustrated in Example 1

Another application of the algorithm Camera (9) is the calculation of the displacements and reorientations of the object relative to technological station. After the reading of the camera image coordinates of characteristic points A', B', C' , and using their in the algorithm Camera (9), we obtain the matrix $'T_c$. This matrix describes the transformation of the frame $x' y' z'$ to the camera frame $x_c y_c z_c$. From the matrices ${}^s T_c$ and $'T_c$ we can calculate the matrix ${}^s T$. This matrix describes displacement and reorientation of the object relative to the position frame $x_s y_s z_s$. The matrix ${}^s T$ results from dependence (11).

$${}^s T_c = {}^s T \cdot 'T_c \rightarrow {}^s T = {}^s T_c \cdot 'T_c^{-1}. \quad (11)$$

Now we can calculate the coordinates in the station frame $x_s y_s z_s$ of the points A' , B' and C' seen by camera. For example, the coordinates of the point A' can be calculated from the equation (12).

$${}^s\mathbf{r}_A = [{}^s x_A \ {}^s y_A \ {}^s z_A \ 1]^T = {}^s\mathbf{T} \cdot {}^s\mathbf{r}_A = {}^s\mathbf{T} \cdot [x^A \ y^A \ z^A \ 1]^T. \quad (12)$$

Additionally we can calculate the change of the coordinate matrices $\Delta\mathbf{x} = \mathbf{x}' - \mathbf{x}_0$. The matrices \mathbf{x}_0 and \mathbf{x}' are arguments of calculated matrices ${}^s\mathbf{T}_c$ and ${}^t\mathbf{T}_c$ respectively. The matrices ${}^s\mathbf{T}$ and $\Delta\mathbf{x}$ allow appropriate correction the position and orientation of the object to ensure coverage the frame $x'y'z'$ and the station frame $x_s y_s z_s$. These calculations can also be used to correction of the robot's movement to displaced and reoriented object. This correction is required to the proper doing of technological operations. The Example 2 illustrates the calculation of matrices ${}^t\mathbf{T}_c$, ${}^s\mathbf{T}_c$, ${}^t\mathbf{r}_A \div {}^t\mathbf{r}_C$, and $\Delta\mathbf{x}$.

In the Example 1 and 2 setting of the camera relative to station and distribution of the characteristic points A , B , C of object are similar to the real car factories (for example Skoda). The object is a car, the characteristic points are the means of technological holes in the car body. Coordinates of the points A , B , C in the object frame xyz are as follows:

$$\begin{aligned} x_A &= 795.4 \text{ mm}, \quad y_A = 1734.1 \text{ mm}, \quad z_A = 0 \text{ mm}; \\ x_B &= 795.4 \text{ mm}, \quad y_B = 2034.1 \text{ mm}, \quad z_B = 0 \text{ mm}; \\ x_C &= 795.4 \text{ mm}, \quad y_C = 1734.1 \text{ mm}, \quad z_C = 300 \text{ mm}. \end{aligned}$$

The camera has a focal length of $f_c = 5 \text{ mm}$. Calculations were made using an computer program *Camera* based on the algorithm *Camera* (9). This program was written in Matlab, on a computer with an processor Intel Pentium T3200 CPU, with a frequency of 2 GHz.

Example.1. Computing of Camera Location.

Before calculating the matrix ${}^s\mathbf{T}_c$, we have to set the body of the car so that the car frame xyz coincides with the station frame $x_s y_s z_s$. In addition, we must coarsely to measure the coordinates ${}^c z_A$, ${}^c z_B$, ${}^c z_C$ of characteristic points and coordinates α , β , γ , d_x , d_y , d_z of the camera frame in station frame. These coordinates can't be measured accurately and directly because the point O_c is inside the camera. The coarse values of these coordinates we in write to the matrix $\mathbf{x}_0 = [10^\circ, 240^\circ, 24^\circ, 2210 \text{ mm}, 2800 \text{ mm}, 1300 \text{ mm}, 2200 \text{ mm}, 2100 \text{ mm}, 2000 \text{ mm}]^T$. The

coordinates of points A, B, C in the camera frame are as follows: ${}^c x_{Ac} = 0mm$, ${}^c y_{Ac} = 0mm$, ${}^c x_{Bc} = 0.25mm$, ${}^c y_{Bc} = -0.59mm$, ${}^c x_{Cc} = -0.58mm$, ${}^c y_{Cc} = 0mm$.

For this matrix \mathbf{x}_0 the program *Camera* has calculated the exact value of the matrix ${}^s \mathbf{T}_c$ and matrix \mathbf{x} , which satisfies equation (5) with an accuracy of $\Delta = 10^{-6}$. These calculations lasted 0.094 seconds. These matrices describe the equations (13) and (14).

$${}^s \mathbf{T}_c = \begin{bmatrix} -0.4955 & -0.5711 & -0.6545 & 2259.1mm \\ -0.3447 & 0.8209 & -0.4553 & 2752.3mm \\ -0.7972 & 0 & -0.6036 & 1350.0mm \\ 0 & 0 & 0 & 1 \end{bmatrix}, \quad (13)$$

$$\mathbf{x} = [0.0^\circ, 232.9^\circ, 34.8^\circ, 2259.1mm, 2752.3mm, 1350.0mm, 2236.4mm, 2099.4mm, 2055.3mm]^T. \quad (14)$$

Example 2. Computing of Body Car Displacement and Reorientation.

In this example, we will calculate the displacement and reorientation of the body car relative to a technological station. Now the coordinate system associated to the car body we denote by $x'y'z'$ (see Fig. 3). For these calculations we use the program *Camera*. In the program the matrix \mathbf{x}_0 is equal to the matrix \mathbf{x} , described by equation (14) in the Example 1.

The coordinates of the displaced and reoriented body car points A', B', C' in the camera frame are as follows: ${}^c x_{A'c} = 0.44mm$, ${}^c y_{A'c} = -0.11mm$, ${}^c x_{B'c} = 0.75mm$, ${}^c y_{B'c} = -0.67mm$, ${}^c x_{C'c} = -0.15mm$, ${}^c y_{C'c} = -0.15mm$.

For these coordinates the program *Camera* has calculated the matrices ${}^s \mathbf{T}_c$, \mathbf{x}' , and coordinates of points A', B', C' in the station frame $x_s y_s z_s$. These calculations lasted 0.109 seconds with an accuracy of $\Delta = 10^{-6}$. These matrices describe the equations (15) and (16).

$${}^s \mathbf{T}_c = \begin{bmatrix} -0.3772 & -0.6499 & -0.6598 & 2209.1mm \\ -0.3749 & 0.7586 & -0.5329 & 2802.3mm \\ 0.8468 & 0.0463 & -0.5298 & 1330.0mm \\ 0 & 0 & 0 & 1 \end{bmatrix}, \quad (15)$$

$$\mathbf{x}' = [-5.0^\circ, 237.9^\circ, 44.8^\circ, 2209.0mm, 2802.3mm, 1330.0mm, 2206.6mm, 2046.7mm, 2047.7mm]^T. \quad (16)$$

The calculated coordinates of the points A', B', C' in the station frame are as follows:

$${}^s\mathbf{r}_A = \begin{bmatrix} 883.6 \text{ mm} \\ 1852.4 \text{ mm} \\ -135.5 \text{ mm} \\ 1 \end{bmatrix}, \quad {}^s\mathbf{r}_B = \begin{bmatrix} 914.0 \text{ mm} \\ 2150.8 \text{ mm} \\ -128.7 \text{ mm} \\ 1 \end{bmatrix}, \quad {}^s\mathbf{r}_C = \begin{bmatrix} 853.8 \text{ mm} \\ 1848.6 \text{ mm} \\ 163.0 \text{ mm} \\ 1 \end{bmatrix}. \quad (17)$$

${}^s\mathbf{T}$ matrix describing the car frame $x'y'z'$ in the station frame $x_s y_s z_s$ we obtain from the equation (11).

$${}^s\mathbf{T} = {}^s\mathbf{T}_c \mathbf{T}_c^{-1} = \begin{bmatrix} 0.9900 & 0.1013 & -0.0993 & -79.5 \text{ mm} \\ -0.1031 & 0.9946 & -0.0126 & 209.7 \text{ mm} \\ 0.0975 & 0.0227 & 0.9950 & -252.5 \text{ mm} \\ 0 & 0 & 0 & 1 \end{bmatrix}. \quad (18)$$

Changes of the matrix $\Delta\mathbf{x} = \mathbf{x}' - \mathbf{x}_0$ are as follows:

$$\Delta\mathbf{x} = [-5.0^\circ, 5.0^\circ, 10.0^\circ, -50.0 \text{ mm}, 50.0 \text{ mm}, -20.0 \text{ mm}, -29.8 \text{ mm}, -53.1 \text{ mm}, -7.6 \text{ mm}]^T \quad (19)$$

From the matrix $\Delta\mathbf{x}$ (19) result the following change of coordinates: $\alpha' - \alpha = -5.0^\circ$, $\beta' - \beta = 5.0^\circ$, $\gamma' - \gamma = 10.0^\circ$, $d_x' - d_x = -50.0 \text{ mm}$, $d_y' - d_y = 50.0 \text{ mm}$, $d_z' - d_z = -20.0 \text{ mm}$, ${}^c z_{A'} - {}^c z_A = -29.8 \text{ mm}$, ${}^c z_{B'} - {}^c z_B = -53.1 \text{ mm}$, ${}^c z_{C'} - {}^c z_C = -7.6 \text{ mm}$.

The calculated changes of coordinates can be used for automatic correction of motion of a robot that does operations with a fixed orientation and position relative to the body car.

5 Summary

The program *Camera* presented in this paper is an essential component of future computer intelligence robots. The results of researches described in Section 4 indicate the usefulness of the proposed algorithm (9) to calculate the transformation matrix of the camera frame relative to the station frame. The algorithm (9) is also useful for the calculation of displacements and reorientations of car body relative to station frame.

Above examples show the short time of calculation, which is the order of 100 milliseconds. This time can be reduced yet by writing the program *Camera* in one of the languages C, C++ or C#.

This program can be useful for calibrating the stereovision system of cameras [9,18-22].

The speed and accuracy of the calculations by means of the program *Camera* depends on the initial value of matrix \mathbf{x}_0 . When the matrix \mathbf{x}_0 too much differs from the solution \mathbf{x} it can happen longer time of calculations. Even the calculation of the matrix \mathbf{x} can be impossible. Therefore, before using this program, you must define the measurement area and prepare a set Ω of initial values of matrix \mathbf{x}_0 , which will be chosen automatically. Depending on the appropriate ranges in which are the coordinates of points A, B, C , read from the two cameras should be chosen from the set Ω of the matrix \mathbf{x}_0 , which guarantees the desired accuracy and speed of calculation.

The research presented here should be considered as the first necessary step to create applications for the real camera. The next step must be the experimental determination of the coordinates of the point O_c (see Fig.1) in pixels on the camera matrix sensor. The next experimental task is determination of a scale factors for the axis x_c and y_c . These factors allow convert the coordinates in pixels for coordinates in *mm*. The final experimental task is determination a factors occurring in mathematic model of the optical errors of the camera [23-25]. This mathematical model allows to determine the coordinates of the not distorted image. From the coordinates of distorted image, read from camera matrix sensor, we can determine the coordinates of the not distorted image, by means of the mathematical model of the optical errors.

Program *Camera* is valid only for the coordinates of not distorted image

References

1. Jähne, B.: Spatio-Temporal Image Processing. LNCS, vol. 751. Springer, Heidelberg (1993)
2. Kambhamettu, C., Goldgof, D.B., Terzopoulos, D., Huang, T.S.: Nonrigid Motion Analysis. In: Young, T. (ed.) Handbook of Pattern Recognition and Image Processing: Computer Vision, vol. 2. Academic Press (1994)
3. Seetharaman, G.S.: Image Sequence analysis for Three-Dimensional Perception of Dynamic Scenes. In: Young, T.Y. (ed.) Handbook of Pattern Recognition and Image Processing: Computer Vision, vol. 2. Academic Press (1994)
4. Sinha, S.S., Jain, R.: Range Image Analysis. In: Young, T.H. (ed.) Handbook of Pattern Recognition and Image Processing: Computer Vision, vol. 2. Academic Press (1994)
5. Google: Kalibracja kamery (2013) (in Polish), <http://etacar.put.poznan.pl/marcinKielczewski>
6. Edmund Industrial Optics. 2001 Optics and Optical Instruments Catalog (2001)
7. Paul, R.P.: Robot Manipulators: Mathematical Programming and Control. The MIT Press, Cambridge (2009)
8. Szkodny, T.: Podstawy robotyki. Wydawnictwo Politechniki Śląskiej. Gliwice, Poland (2012) (in Polish)
9. Craig, J.J.: Introduction to Robotics, 2nd edn. Addison Wesley Publ. Comp. (1986)
10. Chesi, G., Garulli, A., Vicino, A., Cipolla, R.: On the Estimation of the Fundamental Matrix: A Convex Approach to Constrained Least-Squares. In: Vernon, D. (ed.) ECCV 2000. LNCS, vol. 1842, pp. 236–250. Springer, Heidelberg (2000)

11. Golub, G.H., Van Loan, C.F.: *Matrix Computations*, 3rd edn. The Johns Hopkins University Press (1996)
12. Kaczorek, T.: *Wektory i macierze w automatyce i elektrotechnice*. WNT, Warszawa (1998) (in Polish)
13. Press, W.H., Teukolsky, S.A., Vetterling, W.T., Flannery, B.P.: *Numerical Recipes*. In: C. The Art. Of Scientific Computing, 2nd edn., Cambridge University Press (1999)
14. Black, M., Sapiro, G., Marimont, D.H., Hegger, D.: *Robust Anisotropic Diffusion*. IEEE Trans. On Image Processing 7(3), 421–432 (1998)
15. Faugeras, O.D., Luc, R.: *What can Two Images Tell us About a Third One?* INRIA Technical Report No.2018 (1993)
16. Faugeras, O.: *Three-dimensional Computer Vision. A Geometric Viewpoint* MIT (1993)
17. Faugeras, O., Holtz, B., Mathieu, H., Vieville, T., Zhang, Z., Fua, P., Theron, E., Moll, L., Berry, G., Vuillemin, J., Bertin, P., Proy, C.: *Real-Time Correlation-based Stereo: Algorithm, Implementations and Applications*, INRIA Technical Report No.2013 (August 1993)
18. Hartley, R.I.: *In Defense of the Eight-Point Algorithm*. IEEE Trans. on Pattern Analysis and Machine Intelligence 19(6) (1997)
19. Quan, L., Triggs, B.: *A Unification of Autocalibration Methods*. In: Asian Conference on Computer Vision, ACCV (2000)
20. Triggs, B.: *Autocalibration and the Absolute Quadric*. In: CVPR (1997)
21. Triggs, B.: *Camera Pose and Calibration from 4 or 5 Known 3D Points*. In: ICCV (1999)
22. Wojciechowski, K., Polański, A., Borek, A.: *Kalibrowanie Systemu Stereowidzenia. Algorytmy określania położenia i orientacji brył*. Nr. 763. Polska Akademia Nauk, Warszawa (1994) (in Polish)
23. Wojciechowski, K., Polański, A., Borek, A.: *Kalibrowanie Systemu Stereowidzenia. Podstawowa Procedura kalibracyjna stereoskopowego systemu widzenia maszynowego*. Nr. 776. Polska Akademia Nauk, Warszawa (1995) (in Polish)
24. Cyganek, B.: *Komputerowe przetwarzanie obrazów trójwymiarowych*. Akademicka Oficyna Wydawnicza EXIT. Warszawa, Poland (2002) (in Polish)
25. Hecht, E.: *Opics*. 3-th Edition. Addison Weseley (1998)

Quantitative Assessment of Uniformity in Particle Distribution

Xin Yuan, Lei Jia, Zhengyu Ba, Xinjun Sheng, and Zhenhua Xiong*

State Key Laboratory of Mechanical System and Vibration,
School of Mechanical Engineering, Shanghai Jiao Tong University,
Shanghai 200240, China
{kevin yuanxin, jerryjia, bazhengyu, xjsheng, mexiong}@sjtu.edu.cn

Abstract. Assessment of particle distribution has a wide range of applications in scientific researches and industrial processes. The knowledge of uniformity, density and agglomeration of distribution is essential for material, medical and many other fields. In this paper, we propose a set of parameters for evaluating the uniformity, density and agglomeration of particle distribution which is based on image processing. Distribution uniformity is evaluated by the value of coefficient of variation(cv) based on voronoi diagram, and by the eccentricity and deviation angle of particle distribution. The density of distribution is investigated via numerical density and area density which illustrate the area distribution at certain density levels. The assessment of agglomeration is carried out through the separation of particle distribution and the counting of different agglomeration situations. These three aspects of assessment will be demonstrated to fully describe the particle distribution. Microscopic images taken from chip on glass(COG) are used to show the assessment process, and the characteristics of distribution can be obtained clearly and comprehensively.

Keywords: Particle distribution, Image processing, Voronoi diagram, Eccentricity, Uniformity, Agglomeration.

1 Introduction

Assessment of particle distribution plays an important role in many industrial processes and scientific research fields. The distribution of second phase has a great influence on many properties of metal material in the particulate reinforced metal matrix composites (PMMC) [1]-[2]. Moreover, determination of particle distribution is also vital in mining and mineral processes [3]-[4], crystallization [5], fatigue crack formation processes [6], drug carriers [7], cancerous tissues inspection [8] and chip on glass(COG) technology[15].

In general, methods of assessment of particle distribution are based on the processing of images which are taken with microscopes and other optical instruments. Various methods have been developed to characterize the distribution

* Corresponding author.

of the particle. Some researches focused on distance characterization of images [9]-[10], Boselli[11] and Redon[12] etc. used finite body tessellation to generate polygons that contain particles, and computed the distance between border to border in order to analyze the distribution. Tessellation methods were widely researched in many studies, and several parameters belonging to spatial distribution such as aspect ratio, and cell area were used for evaluating the distribution [13]. These tessellation methods allowed the calculation of the distance to the first polygon, the average distance to the other polygon(cell). Meanwhile, Yotte[14] et al provided several parameters of various distances, such as intra-cluster inter-particle distance, inter-cluster distance and so on. However, due to the focus on the distance between neighbor particles, these methods require a large amount of computation and thus are very time-consuming. Also, the assessments of these methods are restricted to comparing the microstructures of identical particle size or shape. Therefore, a comprehensive assessment is needed to demonstrate the particle distribution more clearly.

In this paper, we propose a set of assessment parameters, which illustrate three aspects of characteristics - uniformity, density and agglomeration, to evaluate the particle distribution. These three aspects of the assessment can quantitatively illustrate the distribution with several parameters. Uniformity is evaluated by the value of coefficient of variation(cv) which comes from computing with voronoi diagram, and by the eccentricity and deviation angle of particle distribution. The value of coefficient of variation(cv) is prepared for measuring the global uniformity, the eccentricity and deviation angle are proposed for describing the symmetry of the distribution, which complements the coefficient of variation(cv). The numerical density is computed for assessing density of particles in monodisperse distribution and the area density is proposed to demonstrate the area of particle distribution with different densities. Three different degree of agglomeration are given to divide the distribution, and the number of particles in each degrees of agglomeration is counted to evaluate the degree of agglomeration of distribution. Several microscopic images which are taken with chip on glass applications are used to test this assessment.

2 Assessment of Particle Distribution

2.1 Uniformity Assessment

Uniformity is used for describing the dispersion of particle distribution. The particle distribution is a two-dimensional plane with fixed width and length. In order to describe the distribution clearly, each particle is represented by its centroid point of x and y coordinates. So the particle distribution plane is converted to the point-based plane. To evaluate and estimate the distribution, a method is required. Voronoi diagram is a widely applied tessellation method in many fields. Briefly, draw a line at mid distance between every two points in the plane and repeat this procedure. Consequently every two lines intersect each other and many intersections are generated. Then, a polygon is delineated around each point that encloses the part of the plane which is closer to that point than to

any other one. Finally, the voronoi diagram divides the two-dimensional plane into convex polygons(cells) and each polygon belongs to one point.

Let $K = \{k_1, k_2, \dots, k_i, \dots, k_n\}$ be a set of points that is defined in the two-dimensional plane. $V(k_i)$ is the polygon that relates to the point k_i . Based on this description, $V(k_i)$ is illuminated in Equation 1. Polygon $V(k_i)$ consists of all points that are closer to k_i than to any other point. Assuming the particle distribution is uniform and there is no agglomeration existing, the distance between every two points is the same. With each point being located on its own position, all of the points form the uniform array on the plane. Fig. 1(a) shows the uniform distribution of particles. Fig. 1(a) is the ideal uniformity distribution and Fig. 1(b) is the normal particle distribution, in which particles are irregularly dispersed on the two-dimensional plane. After the running of the voronoi diagram algorithm , Fig. 1(b) demonstrates these polygons and their inner points. The values of polygons are given in order to calculate not only the mean polygon area but also the standard deviation and the coefficient of variation(cv).

$$V(k_i) = \{x : |k_i - x| \leq |k_j - x|, \forall_j \neq i\} \tag{1}$$

$$S_{\sigma^2} = \frac{1}{n} \sum_{i=1}^n (s_i - s_{mean})^2 = \frac{1}{n} (\sum_{i=1}^n s_i^2 - ns_{mean}^2) \tag{2}$$

$$S_{\sigma} = \sqrt{\frac{1}{n} \sum_{i=1}^n (s_i - s_{mean})^2} = \sqrt{S_{\sigma^2}} \tag{3}$$

$$CV = \frac{S_{\sigma}}{s_{mean}} \tag{4}$$

Let $S = \{s_1, s_2, \dots, s_i, \dots, s_n\}$, with s_i representing the area of polygon which contains its point k_i . According to all coordinates of vertices in polygons, the area of each polygon is computed to compare with the average area that is demonstrated in Fig. 1(a). The mean polygon area increases or falls with the changing of the number of the particles. Let s_{mean} be the mean polygon area , S_{σ^2} be the variance of polygons' area, S_{σ} be the standard deviation and n be the number of particles. Equation 2 and Equation 3 show the calculation with these parameters. S_{σ} can evaluate the degree of deviation of the uniformity in distribution. It works exactly in the situation of the same average value or the same number of particles. However, different images have different distributions, and the numbers of particles also differs. In order to assess this situation, coefficient of variation(cv)(Equation 4) is introduced as a dimensionless quantity to reflect the dispersion and the uniformity of the distribution. The higher the number of particles is, the more reliable and accurate the coefficient of variation(cv) is. When the number of particles in the distribution is under a certain value(Fig. 2(b)), the coefficient of variation(cv) becomes unstable and the reliability of the value is low. In this situation, the symmetry of the distribution is very useful to support the measurement of uniformity.

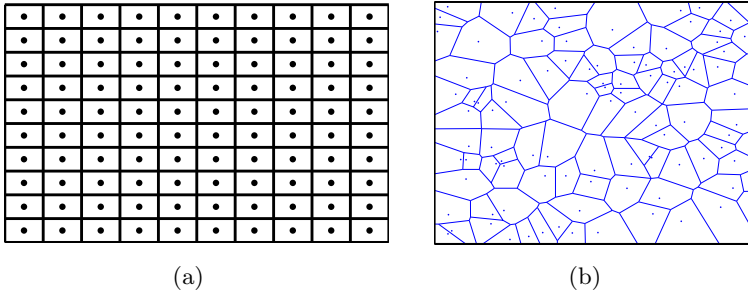


Fig. 1. Distribution of particles: (a) Uniformity distribution (b) Random or normal distribution

The symmetry and deviation of distribution are taken into account to support the uniformity of distribution. Given that each point is an object, the whole distribution is converted to be a plane with several objects containing mass. Define the two-dimensional plane to an x-y coordinate system, in which each point has its location. Meanwhile, define the mass of each point as 1 and the mass of the other points in the plane which are unrelated as 0. The two-dimensional plane has its center point with the coordinates of x_i and y_i . The centroid of the distribution has its coordinates of X_c and Y_c . Equation 5 is given to compute the value of centroid's coordinates. Since different distributions make different symmetries, the distance between centroid of distribution and center point of the image can be defined as eccentricity which can be used for measuring the deviation of the particle distribution. Moreover, the deviation angle θ is given to describe the orientation of deviation(Fig. 2(a)).

$$X_c = \frac{\sum_i x_i c_i}{\sum_i c_i}, Y_c = \frac{\sum_i y_i c_i}{\sum_i c_i} \tag{5}$$

Fig. 2(b) shows three different kinds of dispersion in the two-dimensional plane. Each distribution has its centroid and the red lines represent the eccentricities. In Fig. 2(b), the length of eccentricities measures the degree of deviation in distribution, and it also shows the distribution's location as well as the deviation angle. Label 1 disperses uniformly, and its eccentricity equals 0. This means, comparing to label 2 and label 3, it is dispersed in symmetry perfectly. The eccentricity of label 2 is longer than that of label 3, so the distribution of label 2 is more decentralized than that of label 3. According to the assessment of symmetry, the uniformity of distribution can be demonstrated clearly and comprehensively.

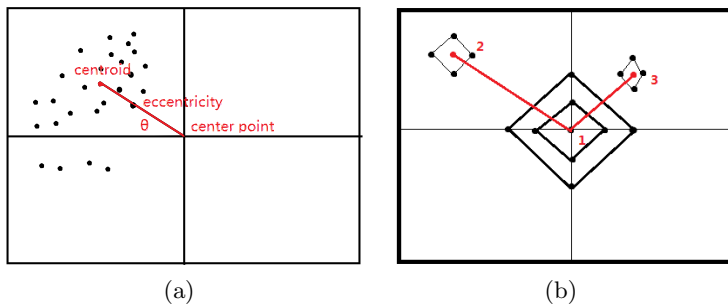


Fig. 2. (a) Schematic diagram of mass centroid and deviation angle (b) The eccentricity in different distributions

2.2 Density Assessment

Density is a very important parameter to assess particle distribution. In general, density assessment is based on image processing, and the number of particles in distribution is counted by the algorithm. However, if the number of particles is big enough and the size of each particle is close to micro-nano scale, agglomeration is found very often in distribution(Fig. 3(a)). However, the number of particles is not accurate enough for density assessment. Because the monodisperse particles are extremely useful in many fields, the D_{mono} is given to measure the density of monodisperse particles.

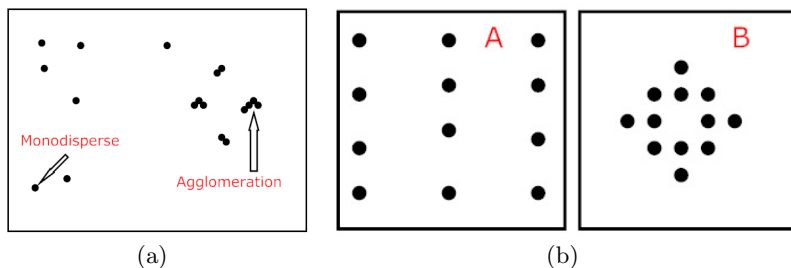


Fig. 3. (a) Schematic diagram of monodisperse and agglomeration in distribution (b) Schematic diagram of two different distribution with same particle density

The D_{mono} is the numerical density which displays the number of particles in certain plane. However, the same value of D_{mono} does not necessarily imply the same condition of distributions. Assuming distribution A and B in Fig. 3(b) have the same number of particles, and the D_{mono} of A and B are the same. By observing Fig. 3(b) we can know that the distribution in B is closer to the center point than the distribution in A. In other words, the distance between every two particles in A is larger than that in B. So, if we consider the local density or the

effective density (which refers to the density that is bigger than a certain value), the effective density in A is smaller than that in B. Fig. 4(a) illustrates the perfect uniformity of distribution, in which each point belongs to a square and the two-dimensional plane is segmented into many squares of the same area (each of which is defined as a monopoly square). As we know, under the equal two-dimensional plane, the area of each monopoly square decreases with the increasing of the number of points. According to the uniformity assessment above, the particle distribution we deal with is not the perfect uniform distribution. Instead, each point gets its own polygon obtained by the voronoi diagram (Fig. 4(b)). Comparing monopoly square to each polygon, points and polygons can be classified into several ranges with disparate colors. Based on voronoi diagram, the division of effective density area can be observed visually. Three different density levels distinguished by different sizes of area of monopoly squares are given to classify the distribution. The total area of polygons on each level is computed to compare with the whole area of plane. The area ratios of these different density levels can demonstrate the effective region of certain density. The parameters used in this method are named area densities, and AD_1 , AD_2 , and AD_3 are given to represent the three area ratios. The density of AD_1 is half of the density of AD_2 and the density of AD_2 is half of the density of AD_3 . With these three parameters, the identification of different densities in occupation is displayed clearly and effectively. With the combination of numerical density and area density, the global and local density of particle distribution can be better described.

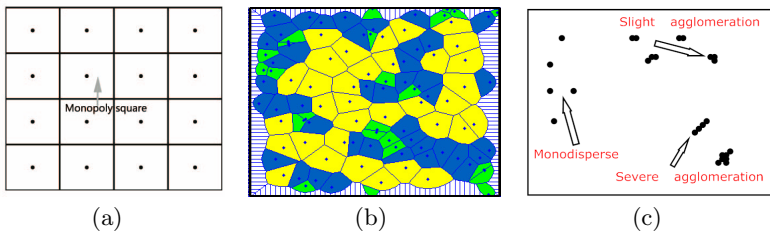


Fig. 4. (a) Schematic diagram of definition of monopoly square (b) Schematic diagram of area density and polygons filled with different colors (c) Schematic diagram of three different kinds of dispersion in distribution

2.3 Agglomeration Assessment

Agglomeration often appears in distribution, especially in the case of the micro and nano particles. Several particles adhere to one another and become a big block. In order to study this distribution, it is necessary to assess the degree of agglomeration. Each particle in distribution is represented by a connected domain in the binary image, and the agglomeration of particles is represented by a block connected domains. Based on image processing, the area of each single connected domain can be listed and the average area of the single particle connected

domain is obtained. With the same step, the area of each block connected domain which contains several particles is also obtained. In order to measure the degree of agglomeration, the distribution is divided into three situations(Fig. 4(c)). The first is monodisperse, namely, the separate dispersion of every particle. The second is slight agglomeration, in which each block connected domain contains two or three adhering particles. The third is severe agglomeration, in which each block connected domain contains more than three adhering particles.

With the help of this division, the whole area of connected domains in each situation is obtained. Meanwhile, the number of particles in the situation of monodisperse can be counted. Comparing the whole area of block connected domains in slight and severe agglomeration to the average area of connected domain in monodisperse, the number of particles in the two situations of agglomeration can be calculated. Define D_w as the density of all particles in distribution (including the situation of monodisperse and agglomeration), and R_{mono} , R_{sli} , R_{sev} as the ratios of the number of each dispersion situation to the number of all particles respectively. With these four parameters, the agglomeration can be demonstrated clearly.

3 Assessment Implementation

In the process of chip on glass(COG) technology, conductive particles contained in anisotropic conductive film(ACF) should be uniformly dispersed in XY direction so as to avoid the electrical short problem and to achieve certain density [15]. At the same time, certain density is required to ensure the electrical reliability in XY two-dimensional plane. Besides, specific areas, such as the top surface of the bump, need the particle distribution with effective and certain value of density. Considering these requirements, the assessment of uniformity, density and agglomeration in particle distribution is extremely important. A new method called electrospray is proposed to disperse these particles [16] due to its operability and low cost. Fig. 5 gives an example of the images with 768 x 576 array taken by microscope.

The assessment in this paper is used to analyze Fig. 6, and several parameters are given to evaluate the distribution. The assessment of agglomeration is measured by four parameters displayed in Table 1. According to Table 1, the density of particles in Fig. 5(a) is smaller than those in Fig. 5(b), but the monodisperse dispersion and the slight agglomeration in Fig. 5(a) are better than that in Fig. 5(b).

Moreover, two microscopic images are compared in terms of their coefficient of variation(cv), eccentricity and the deviation angle θ . The analysis of uniformity between two images is shown in Table 2. Firstly, the values of coefficient of variation(cv) are different: the smaller the cv is, the more uniform the image is. Therefore, distribution in Fig. 6(b) is more uniform than that in Fig. 6(a). Then, eccentricity reflects the deviation of the particle distribution. The distribution in Fig. 6(a) is further away from the center point of plane than the distribution in Fig. 6(b).

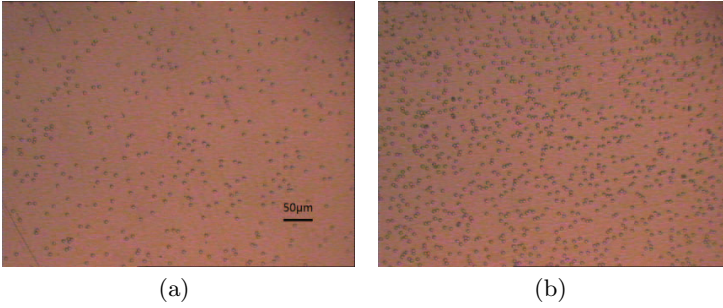


Fig. 5. Microscopic images of micro particles taken with chip on glass(COG) technology.

Table 1. Agglomerate parameters with three different levels of dispersion analyzed by the assessment based on Fig. 6

	$D_w (/mm^2)$	R_{mono}	R_{sli}	R_{sev}
Fig. 5(a)	975.81	0.79	0.17	0.03
Fig. 5(b)	2886.03	0.58	0.34	0.08

Table 2. Uniformity parameters analyzed by the assessment based on Fig. 7

	Coefficient of variation(cv)	Eccentricity	θ
Fig. 6(a)	0.770573	83.07	5°
Fig. 6(b)	0.491499	43.93	16.8°

The density of particles in monodisperse distribution is given. Let AD_3 be the ratio of density more than $3000/mm^2$, AD_2 be the ratio of density more than $2000/mm^2$ and AD_1 be the ratio of density more than $1000/mm^2$. In Fig. 7(b), the yellow polygons occupy more than 50% of the whole area of distribution. Additionally, the fact that the yellow polygons are more closely connected than the green and blue polygons means the area of AD_3 is more effective than the other two.

4 Case Study

Assessment of a single image is very useful for deeply understanding the uniformity and other characteristics of distribution. Fig. 8(a) is given to evaluate the comprehensive characteristics of distribution. The real meanings of and relationships among these parameters are displayed to explain the distribution clearly.

The assessment of uniformity is carried out with three parameters: cv, eccentricity and the deviation angle θ . The value of cv is 0.481244 and is far more

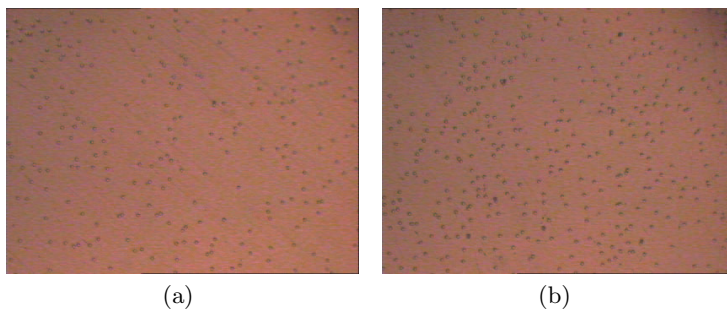


Fig. 6. Two microscopic images: (a) Smaller density of particle distribution (b) Larger density of particle distribution

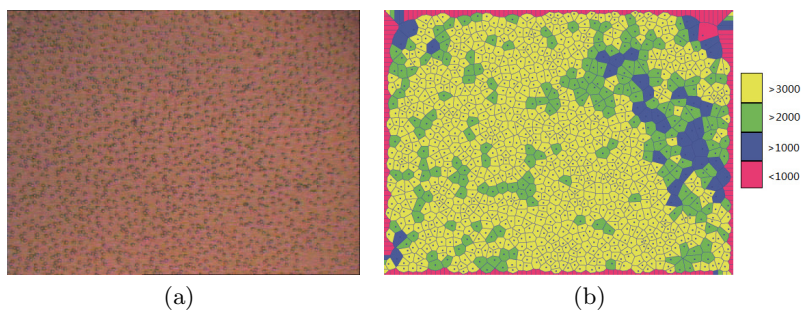


Fig. 7. (a) A microscopic image of particle distribution (b) Schematic diagram of area density

Table 3. Density parameters with different situations analyzed by algorithm in Fig. 7(a)

$D_{mono}(/mm^2)$	AD_3	AD_2	AD_1
2759.52	0.64	0.23	0.06

than 0, which shows that the distribution is nonuniform. Consider the eccentricity and the angle θ , the deviation distance and the deviation angle demonstrate the symmetry visually, and the whole distribution of particles is located in the lower left corner of the image. According to these three parameters, the degree and deviation of uniformity can be measured easily.

The assessment of density requires four parameters: D_{mono} , AD_3 , AD_2 and AD_1 . D_{mono} stands for the number of particles in monodisperse distribution which is widely applied and researched in many fields. AD_3 , AD_2 and AD_1 are the area density parameters, which can demonstrate the degree of density distribution visually and numerically. In this case, every area of agglomeration particles is considered to be a single point which is the centroid of their connected

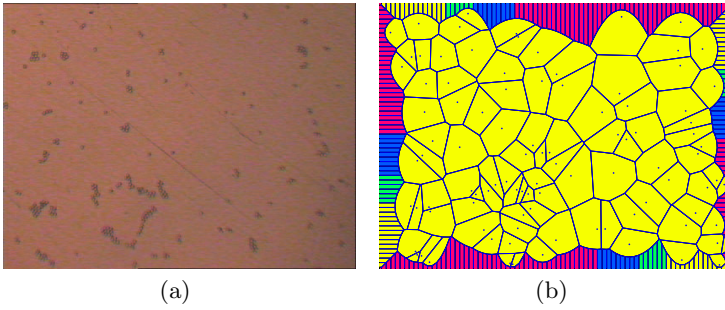


Fig. 8. (a) A case(image) taken by microscope (b) Schematic diagram of area density

Table 4. The assessment of uniformity, density and agglomeration with all parameters

CV	Eccentricity	θ	$D_{mono}(/mm^2)$	AD_3	AD_2	AD_1	$D_w(/mm^2)$	R_{mono}	R_{sli}	R_{sev}
0.481244	42.31	71°	149.94	0.8	0.00	0.00	603.39	0.25	0.36	0.39

domain. Based on this assumption, three area densities are calculated and compared. The yellow polygons cover the most area of the image, which suggests the density of the particles in yellow polygons is at AD_3 level($40/mm^2$) and the effective density area of these yellow polygons occupies 80% of the area of the whole image.

The assessment of agglomeration includes four parameters: D_w , R_{mono} , R_{sli} and R_{sev} . D_w is the number of all particles in the image that contains particles in monodisperse and agglomeration distribution. Comparing D_{mono} with D_w , if the two values are close to each other, the agglomeration is very slight in the distribution. However, in this case, D_w is almost five times larger than D_{mono} , which means particles are severely agglomerated in the distribution. At the same time, we can know from R_{mono} , R_{sli} and R_{sev} , the number of particles in monodisperse distribution is only a quarter of the number of whole particles in distribution. In sum, when combined together, these several parameters can demonstrate the uniformity, density and agglomeration in particle distribution effectively.

5 Conclusion

The assessment of particle distribution is a very important and usually difficult task, especially when agglomeration occurs, which happens very often among micro and nano particles. In this paper, a set of assessment parameters are proposed to evaluate the uniformity, density and agglomeration of particle distribution.

Uniformity of distribution is assessed by the coefficient of variation(cv) and the symmetry of particle distribution. The cv parameter, based on voronoi diagram, measures the degree of uniformity. The assessment of symmetry is measured

by the eccentricity and the deviating angle of distribution. The assessment of density consists of the evaluation of numerical density and area density which helps to describe the area distribution with certain density. In the assessment of agglomeration, three degrees of dispersion are defined, and the ratio of each one is computed. We have demonstrated that with the quantitative assessment from these three aspects, the distribution of particle can be understood clearly and comprehensively.

Acknowledgements. This work is supported in part by National Natural Science Foundation of China under Grant 51175344, the "Shu Guang" Program of Shanghai Municipal Education Commission and Shanghai Education Development Foundation under Grant 11SG14.

References

1. Mahmut, D., Mata, K.A.: Experimental and numerical investigation of effect of particle size on particle distribution in particulate metal matrix composites. *Appl.Math.Comput.* 177(1), 300–307
2. Liu, Z., Zu, G., Luo, H., Liu, Y., Yao, G.: Influence of Mg Addition on Graphite Particle Distribution in the Al Alloy Matrix Composites. *J. Mater. Sci. Technol.* 26(3), 244–250
3. Taty Costodes, V.C., Mause, C.F., Molala, K., Lewis, A.E.: A simple approach for determining particle size enlargement mechanisms in nickel reduction. *Int. J. Miner. Process.* 78(2), 93–100 (2006)
4. Schneide, C.L., Neumann, R.R., Souza, A.S.: Determination of the distribution of size of irregularly shaped particles from laser diffractometer. *Int. J. Miner. Process.* 82(1), 30–40 (2007)
5. Garciaa, E., Veessler, S., Boistellea, R., Hoffb, C.: Crystallization and dissolution of pharmaceutical compounds: An experimental approach. *J. Cryst. Growth.* 198(2), 1360–1364 (1999)
6. McDowella, D.L., Dunneb, F.P.E.: Microstructure-sensitive computational modeling of fatigue crack formation. *Int. J. Fatigue* 32(9), 1521–1542 (2010)
7. Lince, F., Marchisio, D.L., Barresi, A.A.: Strategies to control the particle size distribution of polycaprolactone nanoparticles for pharmaceutical applications. *J. Colloid. Interf. Sci.* 322(2), 505–515 (2008)
8. Thiran, J.P., Macq, B.: Morphological Feature Extraction for the Classification of Digital Image of Cancerous Tissues. *IEEE. T. Bio-Med. Eng.* 43(10), 1011–1020 (1996)
9. Schwaz, H., Exner, H.E.: The characterization of the arrangement of feature centroids in planes and volumes. *J. Microsc.* 129, 155–169 (1983)
10. Karnezis, P.A., Durrant, G., Cantor, B.: Characterization of reinforcement distribution in cast Al alloy/SiCp composites, *Mater. Charact.*, vol. 40, pp. 97–109 (1998)
11. Boselli, J., Pitcher, P.D., Gregson, P.J.: Sinclair II, Secondary phase distribution analysis via finite body tessellation. *J. Microsc.* 195, 104–112 (1999)
12. Redona, C., Chermanta, L., Chermanta, J.-L., Costera, M.: Automatic image analysis and morphology of fibre reinforced concrete. *Cement. Concrete. Comp.* 21(5-6), 403–412 (1999)

13. Bertram, M., Wendrock, H.: Characterisation of planar local arrangement by means of the Delaunay neighbourhood. *J. Microsc* 181, 45–53 (1996)
14. Yottea, S., Breysea, D.: Somnath GhoshbCluster, characterisation in a metal matrix composite. *Mater. Charact* 21(5-6), 403–412 (2001)
15. Li, Y., Wong, C.P.: Recent advances of conductive adhesives as a lead-free alternative in electronic packing: Materials, processing, reliability and applications. *Mater. Sci. Eng. R* 51, 1–35 (2006)
16. Lee, M.W., An, S., Kim, N.Y., Seo, J.H., Huh, J.-Y., Kim, H.Y., Yoon, S.S.: Effects of pulsing frequency on characteristics of electrohydrodynamic inkjet using micro-Al and nano-Ag particles. *Exp. Therm. Fluid. Sci* (in Press 2013)

Hand Gesture Recognition for Human-Computer Interaction Using Moment Invariants and Neural Network Classifier

Ran Chen, Shuangyuan Wang, Liang Gong, and Chengliang Liu

School of Mechanical Engineering, Shanghai Jiao Tong University, Shanghai, China
{happyweiyu, wsywsy86, gongliang_mi, chl1iu}@sjtu.edu.cn

Abstract. Gesture recognition is of utmost importance in intelligent human-computer interaction (HCI). In this paper, an algorithm using moment invariants and BP neural network classifier for hand gesture recognition is proposed. Seven invariant moments are extracted after the image segmentation, which quantitatively describes the targeted hand gesture, and then the trained BP neural networks are applied to recognize the gesture. The algorithm is validated and achieves a high recognition rate of 99% in experiments, which makes it feasible for practical HCI in some restricted environments.

Keywords: Hand gesture recognition, Human-computer interaction, Moment invariant, BP neural network.

1 Introduction

Gesture and vision is of great importance for human to communicate and get information. Motivated by developing more natural and efficient human-computer interfaces, a rapid growth of efforts has been put on vision-based gesture analysis [1] [2] [3]. Nhan Nguyen-Duc-Thanh *et al.* [4] introduced a two-stage hidden Markov model in gesture recognition for human-robot interaction in which not only the human can naturally control the robot by hand gestures, but also the robot can recognize what kind of task it is executing. Hyunsook Chung and Hee-Deok Yang [5] described a conditional random field-based gesture recognition approach with depth information, which can efficiently and effectively recognize body gestures. Sanin, A. *et al.* [6] developed an action and gesture recognition method based on spatio-temporal covariance descriptors and a weighted Riemannian locality preserving projection approach that takes into account the curved space formed by the descriptors. Ming-Hsuan Yang *et al.* [7] proposed a motion trajectories-based algorithm for extracting and classifying two-dimensional motion in an image sequence, which can accurately extract and recognize 40 hand gestures of American Sign Language. Motion patterns are learned from the extracted trajectories using a time-delay neural network. Zhaojie Ju and Honghai Liu [8] proposed a unified fuzzy framework of a set of recognition algorithms: time clustering, fuzzy active axis Gaussian mixture mode, and fuzzy empirical copula, from numerical clustering to data dependence structure in the

context of optimally real-time human-hand motion recognition. The algorithms were evaluated and performed well in terms of both effectiveness and efficiency criteria. Heung-Il Suk *et al.* [9] applied a method for recognizing hand gestures in a continuous video stream using a dynamic Bayesian network (DBN) model and a DP-based real-time decoding algorithm.

However, the above mentioned algorithms have limitations such as complex equipment or extensive computational resources. This paper introduces a hand gesture recognition algorithm using moment invariants and BP neural network classifier to recognize gestures taken by a Commercial Off-The-Shelf (COTS) camera. We apply the combination of complexion and moment invariants to the gesture recognition, and the classification correctness and the feature extraction process meet both of the accuracy and real-time performance demands in real practice.

The paper is organized as follows: Section 2 describes the preprocessing method and the approach for the hand gesture feature extraction. In Section 3, the gesture recognition is performed using a BP neural network classifier. Section 4 shows the experimental results. Finally, conclusion is given in Section 5.

2 Hand Gesture Feature Extraction

2.1 Hand Tracking and Positioning

To extract and recognize the hand gesture fast and accurately, obtaining the hand region in the images is a prerequisite, which consists 4 main steps. Firstly, the frame differential algorithm [10] is adopted to track the moving part in the frames; secondly, the differential operation in the motion area of the current frame image and the background image is applied to get a complete image of the moving target; thirdly, complexion information [11] is used to position the hand accurately; finally, morphological operations are optionally executed if there exist holes and glitches in the binary images of the target region.

2.2 HAND Gesture Feature Extraction

The hand gesture feature extraction is the most critical aspect of the gesture recognition.

Gesture images obtained contain a set of basic features of the given gesture (the original features), usually with large amount of dimensions. The gesture feature extraction is to select the most effective features from a set of the original ones, which can be defined as a transformation from the acquired-data space to a feature space:

$$X = AY \quad (1)$$

where Y is the data space, X is the feature space, and A is called the feature map or feature extractor [12].

Derived from the general theory of moments, moment invariants have been frequently used as features for shape recognition and classification. It was Hu (Hu, 1962), who first set up the mathematical foundation for two-dimensional moment

invariants and demonstrated their applications for shape recognition [13]. The moment invariant descriptors build up a new regional feature set per the rules of translation, scale and rotation invariance, which become a popular method in image processing, remote sensing, shape recognition, classification and other fields.

For the two-dimensional discrete image $f(x, y)$, the $(p+q)$ -order moments m_{pq} and central moments μ_{pq} are defined as

$$m_{pq} = \sum_x \sum_y x^p y^q f(x, y) \tag{2}$$

$$\mu_{pq} = \sum_x \sum_y (x - x_0)^p (y - y_0)^q f(x, y) \tag{3}$$

Where both p and q are natural numbers, $x_0 = \frac{m_{10}}{m_{00}}$, $y_0 = \frac{m_{01}}{m_{00}}$, x_0 is the barycenter in the horizontal direction of a two-dimensional image and the corresponding y_0 is the barycenter in the vertical direction.

Central moments can be represented by the regular moments, and they are independent of the translation. Let $\mu_{00} = m_{00}$ be the area of a region, which is used to measure the size of the region, then we can obtain

$$\left. \begin{aligned} \mu_{00} &= m_{00} \\ \mu_{01} &= \mu_{10} = 0 \\ \mu_{20} &= m_{20} - x_0 m_{10} \\ \mu_{11} &= m_{11} - y_0 m_{10} \\ &\dots \end{aligned} \right\} \tag{4}$$

In addition, the moments can be normalized, resulting in the descriptions that are independent of the scaling. The normalized central moments can be defined as

$$\eta_{pq} = \frac{\mu_{pq}}{\mu_{00}^{(p+q)/2+1}} \tag{5}$$

For the purpose of gaining feature moments which are translation, rotation and scaling unrelated, Hu *et al.* exploited the 2nd and 3rd order normalized central moments to obtain a set of seven values that can be calculated and defined by

$$\varphi_1 = \eta_{20} + \eta_{02} \tag{6}$$

$$\varphi_2 = (\eta_{20} - \eta_{02})^2 + 4\eta_{11}^2 \tag{7}$$

$$\varphi_3 = (\eta_{30} - 3\eta_{12})^2 + (3\eta_{21} - \eta_{03})^2 \tag{8}$$

$$\varphi_4 = (\eta_{30} + \eta_{12})^2 + (\eta_{21} + \eta_{03})^2 \tag{9}$$

$$\begin{aligned} \varphi_5 = & (\eta_{30} - 3\eta_{12})(\eta_{21} + \eta_{12})[(\eta_{30} + \eta_{12})^2 - 3(\eta_{21} + \eta_{03})^2] \\ & + (3\eta_{21} + \eta_{03})(\eta_{21} + \eta_{03})[3(\eta_{30} + \eta_{12})^2 - (\eta_{21} + \eta_{03})^2] \end{aligned} \quad (10)$$

$$\varphi_6 = (\eta_{20} - \eta_{02})[(\eta_{30} + \eta_{12})^2 - (\eta_{21} + \eta_{03})^2] + 4\eta_{11}(\eta_{30} + \eta_{12})(\eta_{21} + \eta_{03}) \quad (11)$$

$$\begin{aligned} \varphi_7 = & (3\eta_{21} - \eta_{03})(\eta_{30} + \eta_{12})[(\eta_{30} + \eta_{12})^2 - 3(\eta_{21} + \eta_{03})^2] \\ & + (3\eta_{12} - \eta_{30})(\eta_{21} + \eta_{03})[(\eta_{30} + \eta_{12})^2 - 3(\eta_{21} + \eta_{03})^2] \end{aligned} \quad (12)$$

The values of these seven-invariant moments are positively correlated with the recognition results. It indicates that the larger value of invariant moments have greater contribution to the recognition result.

3 Hand Gesture Recognition

After extracting the features, a BP neural network [14] is employed as an intelligent classifier to discriminate different gestures. An improved training algorithm [15] is used to enhance its convergence performance.

The BP neural network used is made up of three layers with the topology of $7 \times 22 \times 5$. The more nodes in the hidden layer, the more accurate the fitting results will be. However, excessive network nodes are also prone to over-fitting. On the contrary, too few nodes might result in under-fitting, which leads to lack of precision or loss of model generalization. Hereby we choose 22 nodes in the hidden layer, which is experimentally optimized to avoid the above-mentioned two situations. The structure of the BP neural network is shown in Fig. 1.

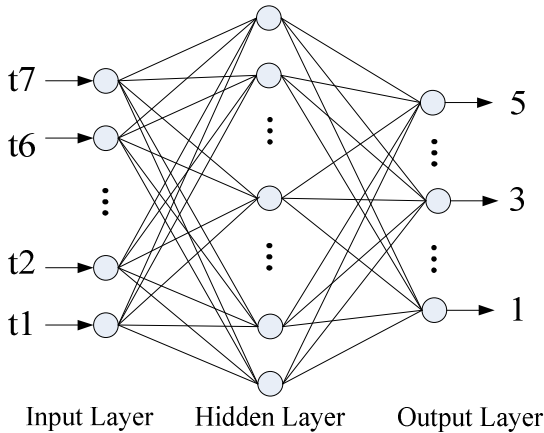


Fig. 1. Structure of the BP neural network

4 Experimental Results

In our experiments, the subjects, who make gestures with one hand, standing before the stationary background in normal illuminating condition. 5 different hand gestures, denoting the number of 1 to 5, are recorded. Each kind of gestures consists of a sequence of image frames capturing the hand with random size, location and moving directions. Each gesture is posted by 10 different individuals; hence 50 sample images are acquired. The size of each image is 640×512 , 24-bit true color with bmp format. All the sample images are shown in Fig. 2 (a).

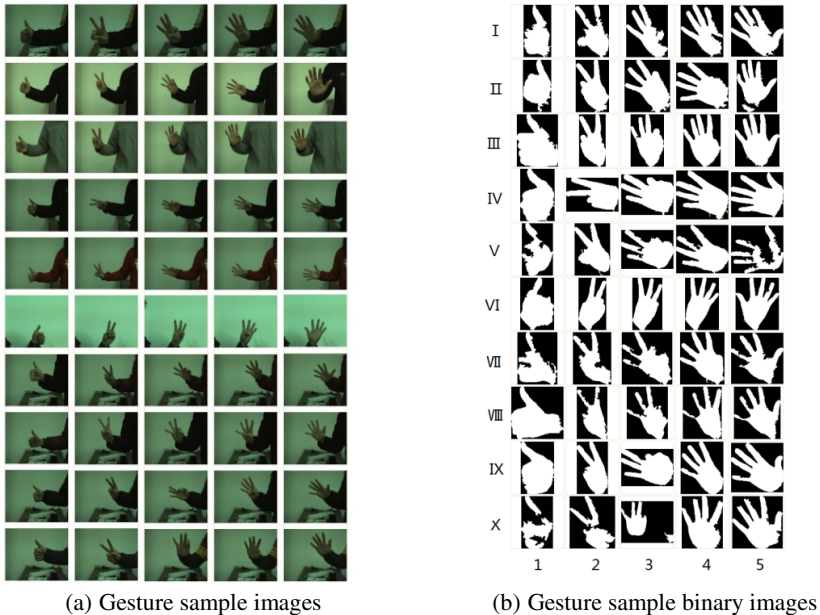


Fig. 2. Acquired raw images and their binary counterparts

Segmentation is performed on the images in Fig. 2 (a). We obtain the binary images of the samples, as are shown in Fig. 2 (b).

According to the fundamentals described in the second section, the seven invariant moments of each binary image are calculated. Part of the characteristics data is summarized as follows in Table 1.

Then we enlarge the number of sample images by resizing and rotating the original images, because of the rotation, scaling and translation invariance of the moment features. We gain another 40 groups of images through altering the original images with magnification of 1.2 times, deflation of 0.8 times, rotation of 90 degrees and rotation of 270 degrees. So a total of 250 sample images can be obtained, of which 200 used for training, 25 for validation and the last 25 for the test.

Table 1. Part of the characteristics of the samples

Samples	t1	t2	t3	t4	t5	t6	t7
I 1	0.6413	1.7788	2.4111	2.8958	5.5548	3.7874	6.3463
I 2	0.5623	1.6573	2.8315	2.5703	5.3110	3.3990	5.6594
I 3	0.5518	1.4445	3.1250	3.4671	6.8923	4.2849	6.9375
I 4	0.6119	1.7658	3.3636	4.0608	8.0138	4.9489	7.8601
I 5	0.6314	1.8742	3.3708	3.5724	7.0641	4.6229	7.5704
III1	0.7332	2.5495	2.9139	3.9029	7.3349	5.3760	7.8056
III2	0.6022	1.6130	3.2148	3.0531	6.2227	3.8942	6.5976
III3	0.6698	1.8836	3.9057	3.7501	7.6100	4.7356	8.0096
III4	0.6680	1.9507	4.1957	3.6868	7.8563	4.6712	7.7215
III5	0.6869	2.2790	4.9262	3.8092	8.6712	4.9672	8.2005
V 1	0.5908	1.7030	2.0672	2.5319	4.8384	3.4452	5.5834
V 2	0.6103	1.7249	2.9325	3.0475	6.0888	3.9240	6.3759
V 3	0.6152	1.7631	2.7307	2.8518	5.6433	3.7664	7.1127
V 4	0.6358	2.0216	3.5897	3.2570	7.2470	4.3366	6.6970
V 5	0.4332	2.0087	2.2778	2.9319	5.5938	4.0349	5.8547

Table 2 shows the network training, validation and test results of the gesture binary images. The correct rate of each term is greater than 99%.

Table 2. Recognition Results

	The number of samples	Root-mean-square error	Correct rate%
Training Set	200	7.83402e-5	99.9873
Validation Set	25	2.80237e-4	99.6501
Test Set	25	2.76744e-4	99.9595

5 Conclusions

This paper presents a hand gesture recognition algorithm, and its experimental results illustrate a high level of robustness and feasibility. With the proposed techniques, skin complexion is not sensitive to light intensity in the YCbCr color space, and the moments are invariant for translation, scale and rotation, which improve the robustness of the proposed algorithms. As a result of the simple background, small number of gestures and obvious differences between these gestures, the experimental results meet general-purpose application requirements. The source code can be embedded into actuator control systems, providing an attractive alternative to

cumbersome interface devices and realizing user-friendly human-computer interaction. Provided that a new gesture is needed to be recognized, the only job is to re-train the prescribed moment invariant descriptors due to the fact the relationships between new model and the original models are independent.

Acknowledgments. This research is supported partially by the National Natural Science Foundation of China (Grant No.61175038), and by the National High Technology Research and Development Program of China (Grant No. 2013AA100307).

References

1. Pavlovic, V.I., Sharma, R., Huang, T.S.: Visual Interpretation of Hand Gestures for Human-Computer Interaction: A Review. *IEEE Transactions on Pattern Analysis and Machine Intelligence* 19(7), 677–695 (1997)
2. Mitra, S., Acharya, T.: Gesture Recognition: A Survey. *IEEE Transactions on Systems, Man, and Cybernetics, Part C: Applications and Reviews* 37(3), 311–324 (2007)
3. Liu, H.: Exploring Human Hand Capabilities into Embedded Multifingered Object Manipulation. *IEEE Transaction on Industrial Informatics* 7(3), 389–398 (2011)
4. Nhan, N.D.T., Lee, S.Y., Kim, D.H.: Two-stage Hidden Markov Model in Gesture Recognition for Human Robot Interaction. *International Journal of Advanced Robotic Systems* 9(39), 1–10 (2012)
5. Chung, H., Yang, H.D.: Conditional random field-based gesture recognition with depth information. *Optical Engineering* 52(1) (2013)
6. Sanin, A., Sanderson, C., Harandi, M.T., Lovell, B.C.: Spatio-Temporal Covariance Descriptors for Action and Gesture Recognition. *IEEE Workshop on Application of Computer Vision*, 103–110 (2013)
7. Yang, M.H., Ahuja, N., Tabb, M.: Extraction of 2D Motion Trajectories and Its Application to Hand Gesture Recognition. *IEEE Transactions on Pattern Analysis and Machine Intelligence* 24(8), 1061–1074 (2002)
8. Ju, Z., Liu, H.: A Unified Fuzzy Framework for Human Hand Motion Recognition. *IEEE Transactions on Fuzzy Systems* 19(5), 901–913 (2011)
9. Suk, H.L., Sin, B.K., Lee, S.W.: Hand gesture recognition based on dynamic Bayesian network framework. *Pattern Recognition* 43(9), 3059–3072 (2010)
10. Luo, Z.S., Wang, L., Gao, X.R., Wang, Z.Y., Zhao, Q.K.: Analysis of Moving Object Detection and Tracking in Sequence Image. *Modern Electronics Technique* (11), 125–128 (2009)
11. Xu, Z.W., Zhu, M.L.: Color-based Skin Detection: A Survey. *Journal of Image and Graphics* 12(3), 377–388 (2007)
12. Liu, X.: Research on video-based sign language recognition algorithm, University of Science and Technology of China Master's degree paper, 29-32 (2008)
13. Keyes, L., Winstanley, A.: Using moment invariants for classifying shapes on large scale maps, *Computers, Environment and Urban Systems*, 25
14. Li, J., Ruan, Q.Q.: Research of Gesture Recognition Based on Neuron Networks. *Journal of Beijing Jiaotong University* 30(5), 32–36 (2006)
15. Gong, L., Liu, C.L., Yuan, F.Q.: Training Feedforward Neural Networks Using EBP with the Optimal Stepsize. *International Journal of Computational Information Systems* 9(4), 9–22 (2012)

Sum of Squares Based Range Estimation for Camera Systems

Cheol-Joong Kim and Dongkyoung Chwa*

Ajou University, Department of Electrical and Computer Engineering,
San 5 Wonchun-Dong Yeongtong-Gu, Suwon 443-749, South Korea
{cjoong,dkchwa}@ajou.ac.kr

Abstract. This paper presents a novel sum of squares based range estimation method for camera systems when the linear and angular velocities of camera are known. The proposed method converts the camera dynamics as a polynomial system whose system matrix are of linear and angular velocities of the camera. Then, state-dependent Luenberger-type estimator is designed to estimate unmeasurable state, which is distance between the camera and the object. In comparison to previous works, less restrict conditions are required for the proposed method. Simulation results are provided to demonstrate the performance of the proposed method.

Keywords: Range estimation, structure from motion, sum of squares, camera systems.

1 Introduction

The Euclidean geometry (i.e., range of 3D structure) of camera systems is most important information for the vision based control system. For example, we can solve more complex problems by estimating the Euclidean geometry when we develop the visual servoing or surveillance systems. Due to these necessities, many researchers have been interested in the “structure from motion (SfM)” problem, which provides the Euclidean geometry when the linear and angular velocities of camera are known.

The dynamics of the partially measurable state have been used quite much to solve the SfM problem [1]. Using the camera dynamics, [2] and [3] achieved uniformly ultimately bounded (UUB) and asymptotic stability results, respectively, using the sliding mode technique. And [4] developed the nonlinear estimator using converse Lyapunov theorem and achieved exponential convergence of the estimation error, but it has the limitation that the initial condition has to be within some bound of the ‘true’ depth. On the other hand, [5] developed the immersion and invariance (I&I) based estimator to solve the SfM problem. They computed the output injection functions by solving a camera dynamics and achieved a global exponential stability. However, the estimator in [5] requires camera acceleration measurements along with camera velocity and image

* Corresponding author.

feature measurements and cannot address all the camera motions. Recently, [6] proposed a globally exponentially stable estimator which can be globally exponentially stable under sufficient observability and exponential convergence is proven even under a relaxed observability condition which allows the camera motion to be zero along all three directions for sufficiently small duration of time. In addition, it was shown to be finite gain L_p stable with respect to an exogenous disturbance input. However, since the estimator uses the locally Lipschitz projection law, it requires the bounds of the camera velocity and the image size. On the other hand, unknown input observer is developed in [7] for “structure and motion from motion (SaMfM) problem. They separated the camera dynamics as linear and nonlinear parts, respectively, and considered the velocity of object as unknown input in the system. Then, the unknown input observer is designed using LMI method to estimate both unmeasurable state (i.e., range of 3D structure) and velocity of object. However, since LMI approach can only deal with constant system matrix, the nonlinear terms in dynamics should satisfy the Lipschitz condition; furthermore, an extra assumption is also required to design the observer.

In this paper, we propose a sum of squares based range estimation method. In the proposed method, the camera dynamics are converted as polynomial system whose system matrix has the polynomial linear and angular velocities of camera. Then, a state-dependent Luenberger-type estimator is designed and control gain matrix is obtained using sum of squares method. Unlike the literature work such as [6], it does not have to know the bounds of camera velocity. In addition, whereas [7] separated the camera dynamics as two parts, we can achieve the range estimation directly, because the proposed method based on sum of squares method which can obtain the estimator gain even when the system matrix has the polynomial time-varying variables. Moreover, as the proposed method can obtain the estimator gain via the numerical analysis, it can easily consider the further problems such as considering the uncertainties or estimating the motion of object. The simulation results with the similar scenarios of literature works in [6] and [7] are presented to demonstrate the validity of the proposed method.

The organization of this paper is as follows. First, we introduce the Euclidean and image space relationship and relative motion model between the camera and the object in Sections II and III, respectively. Section IV presents the proposed estimator using sum of squares method. Simulation results are provided to demonstrate the advantages of the proposed method in Section V. Finally, concluding remarks are stated in Section VI.

2 Euclidean and Image Space Relationships

Let F^* be an orthogonal coordinate system attached to the camera at the location corresponding to an initial point at the initial time t_o . After the initial time, let F_c be an orthogonal coordinate system attached to the camera which has changed through some rotation $\bar{R}(t) \in SO(3)$ and translation $\bar{x}_f \in \mathfrak{R}^3$ away from F^* . Let $\bar{m}(t) \in \mathfrak{R}^3$ denote the Euclidean coordinates of a feature point

observed by the moving camera expressed in the camera frame F_c as in (1) and $m(t) \in \mathbb{R}^3$ denote the normalized Euclidean coordinates as in (2).

$$\bar{m}(t) = [x_1(t), x_2(t), x_3(t)]^T \tag{1}$$

$$m(t) = \left[\frac{x_1(t)}{x_3(t)}, \frac{x_2(t)}{x_3(t)}, \frac{1}{x_3(t)} \right]^T \tag{2}$$

To facilitate the subsequent development, an auxiliary state vector $y(t) = [y_1(t), y_2(t), y_3(t)]^T \in Y$ with a closed and bounded set $Y \subset \mathbb{R}^3$ is defined from (2) as

$$y = \left[\frac{x_1(t)}{x_3(t)}, \frac{x_2(t)}{x_3(t)}, \frac{1}{x_3(t)} \right]^T \tag{3}$$

Using the projective geometry, the normalized Euclidean coordinates $m(t)$ can be related to the pixel coordinates in the image space as

$$p = A_c m \tag{4}$$

where $p(t) = [u, v, 1]^T$ is a vector of the image-space feature point coordinates $u(t), v(t) \in \mathbb{R}$ defined on the closed and bounded set $I \subset \mathbb{R}^3$ and $A_c \in \mathbb{R}^{3 \times 3}$ is a constant, known, invertible intrinsic camera calibration matrix [8]. From (4), $m(t)$ can be recovered using the information of p and A_c , which, in turn, can determine the first two components of $y(t)$. It should be noted that the last component of $y(t)$ is related to the relative Euclidean distance $x_3(t)$ between the camera and the feature point and thus should be estimated.

Assumption 1. *The camera velocities are assumed to be bounded, and the linear velocities are assumed to be continuously differentiable.*

Remark 1. We should note that the literature work [6] needs the bounds of the image size of camera to design the estimator. While the actual image size is finite, the proposed method does not have to know the bounds of image size.

3 Camera-Object Relative Motion Model

Fig. 1 shows that static object point q can be expressed in the coordinate system F_c as

$$\bar{m}(t) = \bar{x}_f + \bar{R}x_{Oq} \tag{5}$$

where x_{Oq} is a vector from the origin of coordinate system F^* to the static point q expressed in the coordinate system F^* . The time derivative of (5) gives the relative motion of q as observed in the camera coordinate system, which can be expressed by the following kinematics [8], [9].

$$\dot{\bar{m}}(t) = [w]_X \bar{m} + v_r \tag{6}$$

where $[w]_X \in \mathbb{R}^{3 \times 3}$ is a skew symmetric matrix in terms of the camera angular velocity $w(t) = [w_1(t), w_2(t), w_3(t)]^T \in W$ and $v_r(t)$ is a relative linear velocity of the camera with respect to the moving point, given by

$$v_r = v_c - \bar{R}\bar{v}_p \tag{7}$$

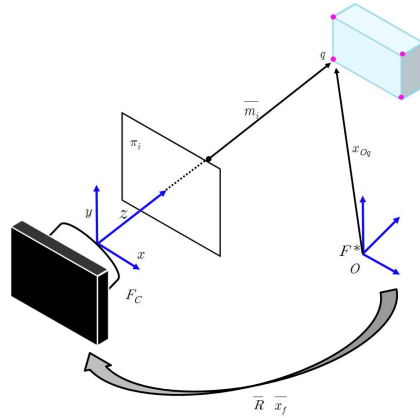


Fig. 1. Moving camera looking at the object

where $v_c = [v_{cx}, v_{cy}, v_{cz}]^T \in V_c \subset \mathfrak{R}^3$ is the camera velocity in the inertial reference frame, $\overline{R}\overline{v}_p \triangleq v_p(t) = [v_{px}, v_{py}, v_{pz}]^T \in V_p \subset \mathfrak{R}^3$ is the velocity of the moving point q expressed in camera reference frame F_c , and $\overline{v}_p = [\overline{v}_{px}, \overline{v}_{py}, \overline{v}_{pz}]^T \in \overline{V}_p \subset \mathfrak{R}^3$ is the velocity of the moving point q expressed in the inertial reference frame F^* . In the case of the static object, $\overline{v}_p(t) = 0$ holds, which results in $v_r = v_c$ from (7).

By substituting the vectors $w(t)$ and $v_r(t)$ into (6), the motion of a static point observed by a moving camera can be expressed as

$$\dot{\overline{m}}(t) = \begin{bmatrix} 1 & 0 & 0 & 0 & x_3 & -x_2 \\ 0 & 1 & 0 & -x_3 & 0 & x_1 \\ 0 & 0 & 1 & x_2 & -x_1 & 0 \end{bmatrix} \begin{bmatrix} v_c \\ w \end{bmatrix}. \tag{8}$$

Using (2) and (9), the dynamics of the partially measurable state vector $y(t)$ can be expressed as

$$\begin{cases} \dot{y}_1 = (v_{cx} - y_1 v_{cz})y_3 - y_1 y_2 w_1 + (1 + y_1^2)w_2 \\ \quad - y_2 w_3 - (v_{px} - y_1 v_{pz})y_3 \\ \dot{y}_2 = (v_{cy} - y_2 v_{cz})y_3 - (1 + y_2^2)w_1 + y_1 y_2 w_2 \\ \quad + y_1 w_3 - (v_{py} - y_2 v_{pz})y_3 \\ \dot{y}_3 = -y_3^2 v_{cz} - y_2 y_3 w_1 + y_1 y_3 w_2 + y_3^2 v_{pz} \end{cases} \tag{9}$$

where the states $y_1(t)$ and $y_2(t)$ can be measured as the output of the system through the invertible transformation given by (4). On the other hand, $y_3(t)$ is a function of unmeasurable state $x_3(t)$ and thus it should be estimated.

4 Range Estimation Design via Sum of Squares Method

Before designing the range estimator for the camera dynamics, a following assumption is needed.

Assumption 2. The object is assumed static (i.e., $v_p = 0$). The linear velocity of camera along to the Z-axis is assumed zero (i.e., $v_{cz} = 0$). And both angular velocities of camera along to the X and Y-axis are assumed zero (i.e., $w_1 = w_2 = 0$).

The camera motion dynamics in equation (9) can be expressed in the form of polynomial with zero object velocity (i.e., $v_p = 0$) as follows:

$$\begin{bmatrix} \dot{y}_1 \\ \dot{y}_2 \\ \dot{y}_3 \end{bmatrix} = \begin{bmatrix} w_2 y_1 & -w_3 - w_1 y_1 & v_{cx} - y_1 v_{cz} \\ w_2 y_2 + w_3 & w_1 y_2 & v_{cy} - y_2 v_{cz} \\ w_2 y_3 & -w_1 y_3 & -v_{cz} y_3 \end{bmatrix} \begin{bmatrix} y_1 \\ y_2 \\ y_3 \end{bmatrix}. \tag{10}$$

The equation (10) is the polynomial form of $\dot{y} = A(y, v_c, w)y$ where $A(y, v_c, w)$ is polynomial matrix.

Remark 2. We should note that [7] used camera dynamics which are separated as two parts. Thus, the nonlinear terms in dynamics should satisfy the Lipschitz condition and an extra assumption is also required to design the estimator. On the other hand, the proposed method can directly deal with the camera dynamics even, in the presence of the system states and the nonlinear terms.

The state-dependent Luenberger-type estimator can be designed to estimate the unmeasurable state y_3 as follows:

$$\begin{cases} \dot{\hat{y}} = A(\hat{y}, v_c, w)\hat{y} + L(e, v_c, w)(z - \hat{z}) \\ z = C\hat{y}. \end{cases} \tag{11}$$

where C is output matrix. In the camera systems, we can measure only $y_1(t)$ and $y_2(t)$; thus, the output matrix should be chosen as $C = \begin{bmatrix} 1 & 0 & 0 \\ 0 & 1 & 0 \end{bmatrix}$. Using the state estimator in equation (11), the error dynamics with $e = y - \hat{y}$ can be expressed as

$$\dot{e} = \tilde{A}(y, \hat{y}, v_c, w)e + \zeta(y, \hat{y}, v_c, w) - L(e, v_c, w)Ce \tag{12}$$

where

$$\tilde{A}(y, \hat{y}, v_c, w) = \begin{bmatrix} w_2(y_1 + \hat{y}_1) & -w_3 & v_{cx} \\ w_3 & -w_1(y_2 + \hat{y}_2) & v_{cy} \\ 0 & 0 & -v_{cz}(y_3 + \hat{y}_3) \end{bmatrix},$$

$$\zeta(y, \hat{y}, v_c, w) = \begin{bmatrix} -w_1(y_1 y_2 - \hat{y}_1 \hat{y}_2) - v_{cz}(y_1 y_3 - \hat{y}_1 \hat{y}_3) \\ w_2(y_1 y_2 - \hat{y}_1 \hat{y}_2) - v_{cz}(y_2 y_3 - \hat{y}_2 \hat{y}_3) \\ w_2(y_1 y_3 - \hat{y}_1 \hat{y}_3) + w_1(y_2 y_3 - \hat{y}_2 \hat{y}_3) \end{bmatrix}.$$

By the assumption 2, $\zeta(y, \hat{y}, v_c, w)$ becomes zero and the error dynamics can be represented simply as

$$\dot{e} = \bar{A}(v_{cx}, v_{cy}, w_3)e - L(e, v_c, w)Ce \tag{13}$$

where $\bar{A}(v_{cx}, v_{cy}, w_3) = \begin{bmatrix} 0 & -w_3 & v_{cx} \\ w_3 & 0 & v_{cy} \\ 0 & 0 & 0 \end{bmatrix}$.

If we obtain the estimator gain $L(e)$ to stabilize the error dynamics in equation (13), then the range estimation for camera systems can be achieved.

Theorem 1. For the error dynamics (13), suppose that there exist a symmetric matrix X , a polynomial matrix $M(e)$, a constant $\epsilon_1 > 0$, which satisfy the following conditions:

$$\nu^T (X - \epsilon_1 I) \nu > 0 \tag{14}$$

$$-\nu^T \begin{pmatrix} \bar{A}^T(v_c, w)X + X\bar{A}(v_c, w) \\ -C^T M^T(e, v_c, w) - M(e, v_c, w)C \end{pmatrix} \nu > 0 \tag{15}$$

where $\nu \in \mathbb{R}^N$ is vector independent of e . Then, estimator gain $L(e, v_c, w)$ can be obtained as

$$L(e, v_c, w) = X^{-1}M(e, v_c, w). \tag{16}$$

Proof. Assume that there exist solutions X and $M(e, v_c, w)$ for the conditions in equations (14) and (15). Also, define a positive definite function $V(e)$ as

$$V(e) = e^T X e \tag{17}$$

where X is a symmetric positive definite matrix. Then, the time derivative of $V(e)$ along the closed-loop system trajectories can be given by

$$\begin{aligned} \frac{dV(e)}{dt} &= \dot{e}^T X e + e^T X \dot{e} \\ &= e^T \begin{pmatrix} \bar{A}^T(v_c, w)X + X\bar{A}(v_c, w) \\ -C^T L^T(e, v_c, w)X - XL(e, v_c, w)C \end{pmatrix} e. \end{aligned} \tag{18}$$

By defining $M(e, v_c, w) = XL(e, v_c, w)$, we can conclude that the derivative of Lyapunov function is negative semidefinite for all e , and we can obtain the conditions of Theorem 1. This proves the stability of the closed-loop system. \square

SOS conditions in Theorem 1 are solved by reformulating them as semidefinite programs (SDPs). SOSTOOLS [10] which is recently developed toolbox of MATLAB can convert the SOS programs (SOSPs) to SDPs using SDP solver such as SeDuMi [11] or SDPT3 [12]. In this paper, we numerically find X and $M(e, v_c, w)$ satisfying the SOS conditions in Theorem 1 via SeDuMi along with SOSTOOLS. For more details of how to solve the SDPs using SeDuMi, see [10] and [11].

5 Simulation Results

This section shows the numerical simulation results to demonstrate the validity of the proposed method. For the simulation, we set the form of X as 3 by 3 constant matrix and the form of $L(e, v_c, w)$ as second order monomials of measurable variables such as e_1, e_2, v_{cx}, v_{cy} , and w_3 . Note that we could not use e_3 because y_3 is unmeasurable, and v_{cz}, w_1 , and w_2 are not employed from the assumption 2. Therefore, the obtained Lyapunov matrix X and estimator gain $L(e, v_c, w)$ are as follows:

$$X = \begin{bmatrix} 1.28 & 0.32 & 0 \\ 0.32 & 1.28 & 0 \\ 0 & 0 & 2.24 \end{bmatrix}, \tag{19}$$

$$L(e, v_c, w) = \begin{bmatrix} L_{11} & L_{12} \\ L_{21} & L_{22} \\ L_{31} & L_{32} \end{bmatrix}. \tag{20}$$

where

$$\begin{aligned} L_{11} &= 0.33 + 0.37w_3^2 + 0.21w_3 + 0.37v_{cy}^2 + 0.36v_{cx}^2 + 0.36e_1^2 - 0.024e_1e_2 + 0.098e_2^2, \\ L_{12} &= -0.087 - 0.092w_3^2 + 0.053w_3 - 0.091v_{cy}^2 - 0.092v_{cx}^2 - 0.024e_1^2 + 0.098e_1e_2 - \\ &0.090e_2^2, L_{21} = -0.087 - 0.092w_3^2 - 0.053w_3 - 0.092v_{cy}^2 - 0.091v_{cx}^2 - 0.090e_1^2 + \\ &0.098e_1e_2 - 0.024e_2^2, L_{22} = 0.32 + 0.37w_3^2 - 0.21w_3 + 0.36v_{cy}^2 + 0.37v_{cx}^2 + 0.098e_1^2 - \\ &0.024e_1e_2 + 0.36e_2^2, L_{31} = 0.57v_{cx} + 0.14v_{cy}, \text{ and } L_{32} = 0.14v_{cx} + 0.57v_{cy}. \end{aligned}$$

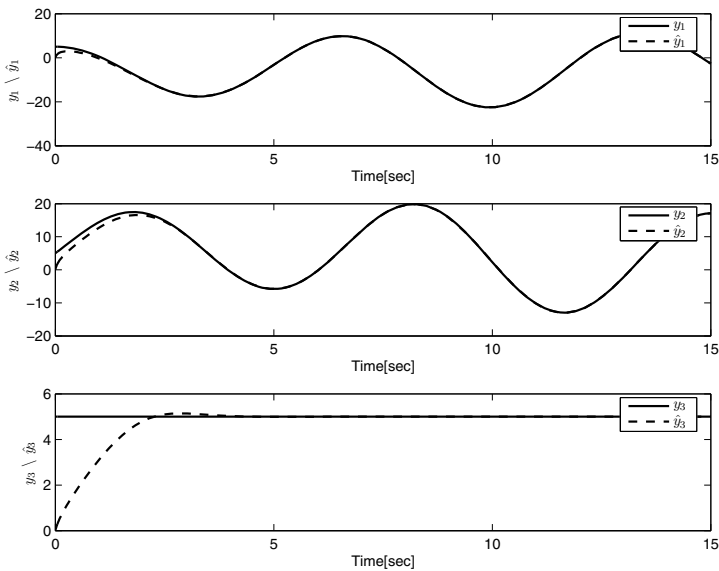
The original obtained estimator gains are more complicated, however, since the coefficients of estimator gains which does not mentioned before are too small, we omit them in this paper.

Table 1. Scenarios for the simulation

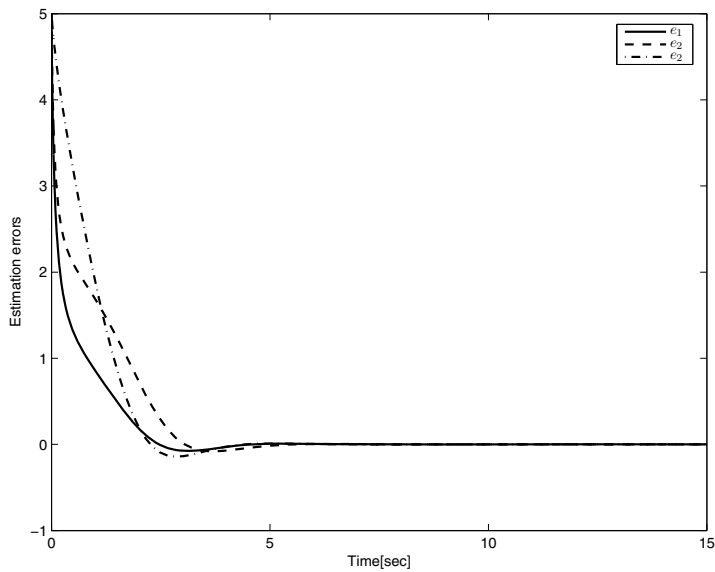
	$y(0)(m)$	$\hat{y}(0) (m)$	$v_c(t)(m/s)$	$w_c(t)(rad/s)$
i	$y(0) = [5, 5, 5]^T$	$\hat{y}(0) = [0, 0, 0]^T$	$v_{cx}(t) = 1 + 0.5 \sin(\pi t/8)$ $v_{cy}(t) = 1 + 0.5 \sin(\pi t/4)$ $v_{cz}(t) = 0$	$w_1(t) = 0$ $w_2(t) = 0$ $w_3(t) = 1$
ii	$y(0) = [5, 5, 5]^T$	$\hat{y}(0) = [0, 0, 0]^T$	$v_{cx}(t) = 1 + 0.5 \sin(\pi t/8)$ $v_{cy}(t) = 1 + 0.5 \sin(\pi t/4)$ $v_{cz}(t) = \sin(\pi t/4)$	$w_1(t) = 0.1 \sin(\pi t/4)$ $w_2(t) = 0.1 \sin(\pi t/4)$ $w_3(t) = 1$
iii	$y(0) = [5, 5, 5]^T$	$\hat{y}(0) = [0, 0, 0]^T$	$v_{cx}(t) = 3 \sin(\pi t/4)$ $v_{cy}(t) = 0$ $v_{cz}(t) = 0$	$w_1(t) = 0$ $w_2(t) = 0$ $w_3(t) = 0$

There are three scenarios shown in Table 1, which are similar to those of literature works [6], [7]. In the first scenario, we set the linear and angular velocities through the assumption 2 (i.e., $v_{cz} = w_1 = w_2 = 0$). And we added the bounded linear and angular velocities in the second scenario, which is not contained in the first scenario. Lastly, only v_{cx} exists in the third scenario which is similar to those in [7].

Figs. 2 through 4 show the simulation results using the proposed method. Each simulation achieves the range estimation successfully. It implies that the proposed method can achieve the range estimation and the unmeasurable states between the camera and the object are estimated. While the first scenario is set by the assumption 2, the additional linear and angular velocities are added in the second scenario. Even though these linear and angular velocities may be considered as the external disturbances of the closed-loop system, the proposed method can achieve the range estimation with small magnitude and bounded linear and angular velocities. It implies that the proposed method is robust against the bounded disturbances. On the other hand, the third simulation results show that only one linear velocity is needed to estimate the range in the camera dynamics. Since the third row of the estimator gains consists of v_{cx} and v_{cy} , the proposed method just needs v_{cx} or v_{cy} .



(a)



(b)

Fig. 2. Simulation results for the scenario i. (a) State response (solid line: state variables, dashed line: estimated states). (b) Error between the states and the estimated states.

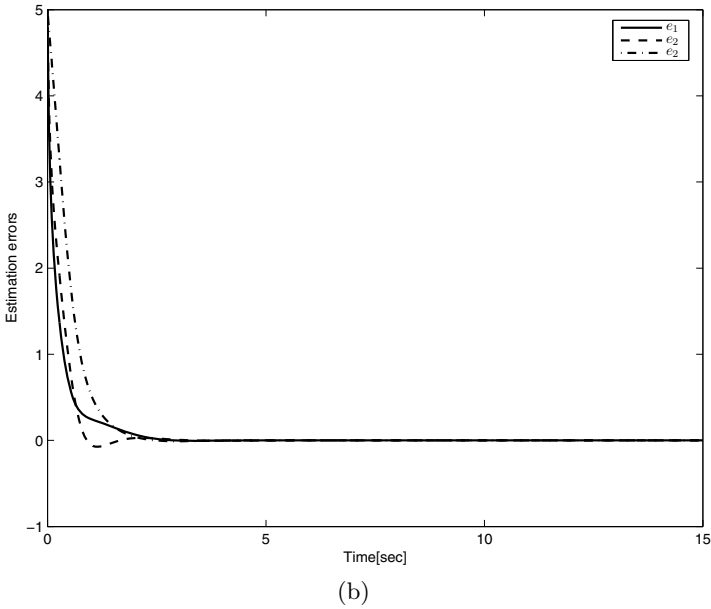
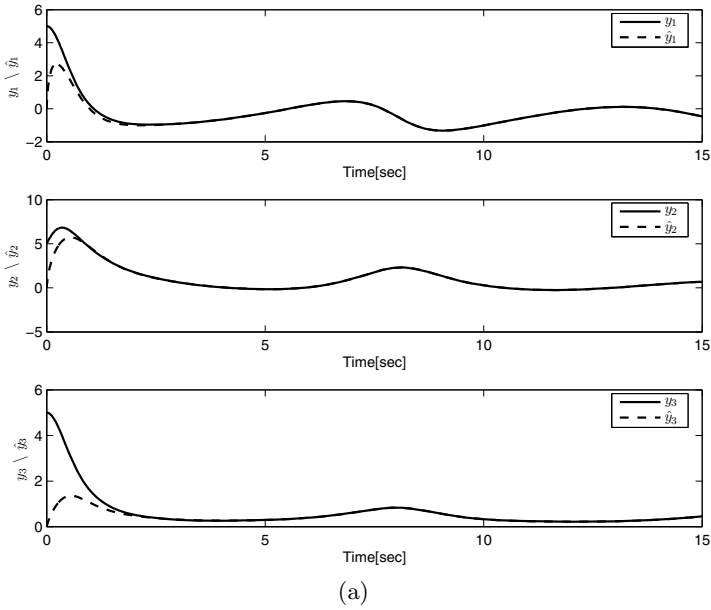
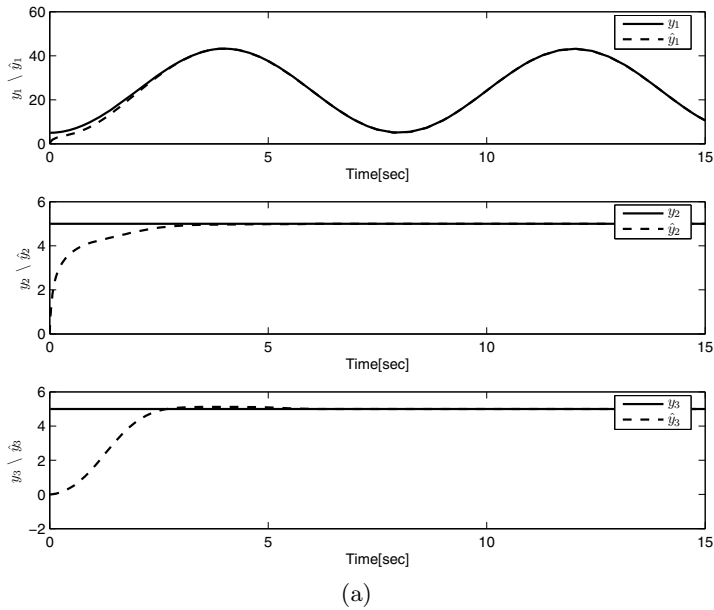
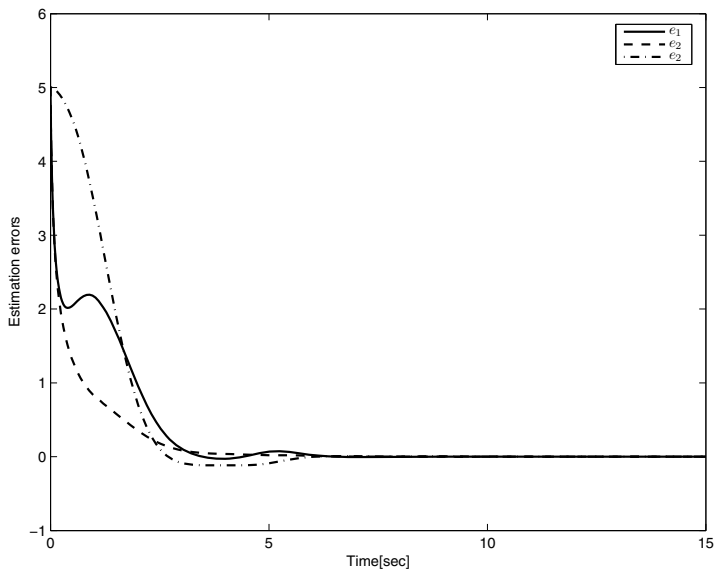


Fig. 3. Simulation results for the scenario ii. (a) State response (solid line: state variables, dashed line: estimated states). (b) Error between the states and the estimated states.



(a)



(b)

Fig. 4. Simulation results for the scenario iii. (a) State response (solid line: state variables, dashed line: estimated states). (b) Error between the states and the estimated states.

6 Conclusion

We have proposed a sum of squares based range estimation method for camera systems. The camera dynamics are converted as polynomial system whose system matrix consists of linear and angular velocities of camera. Then, Luenberger type state estimator is designed and the estimator gain matrix is obtained using sum of squares method. The simulation results show that the proposed method can achieve the range estimation well, even the system has the small magnitude bounded disturbance. In addition, the proposed method needs only v_{cx} or v_{cy} . Future works can include more complex problems such as considering the uncertainties or estimating the motion of moving object.

Acknowledgments. This research was supported by Basic Science Research Program through the National Research Foundation of Korea (NRF) funded by the Ministry of Education, Science and Technology (2012R1A1A2006233).

References

1. Dani, A.P., Fischer, N., Dixon, W.E.: Single Camera Structure and Motion Estimation. *IEEE Transactions on Automatic Control* 57, 241–246 (2012)
2. Chen, X., Kano, H.: State Observer for a Class of Nonlinear Systems and its Application to Machine Vision. *IEEE Transactions on Automatic Control* 49, 2085–2091 (2004)
3. Dixon, W.E., Fang, Y., Dawson, D.M., Flynn, T.J.: Range Identification for Perspective Vision Systems. *IEEE Transactions on Automatic Control* 48, 2232–2238 (2003)
4. Luca, A.D., Oriolo, G., Giordano, P.R.: Feature Depth Observation for Image-based Visual Servoing (Theory and experiments). *International Journal of Robotics Research* 27, 1093–1116 (2008)
5. Morbidi, F., Prattichizzo, D.: Range Estimation from a Moving Camera (an Immersion and Invariance Approach). In: *IEEE International Conference on Robotics and Automation*, pp. 2810–2815. IEEE Press, Kobe (2009)
6. Dani, A.P., Fischer, N., Kan, Z., Dixon, W.E.: Globally Exponentially Convergent Robust Observer for Vision-based Range Estimation. *Mechatronics (Special Issue on Visual Servoing)* 22, 381–389 (2012)
7. Dani, A.P.: Lyapunov-based Nonlinear Estimation Methods with Applications to Machine Vision. Ph.D. dissertation, University of Florida (2011)
8. Ma, Y., Soatto, S., Kosecka, J., Sastry, S.: *An Invitation to 3-D Vision*. Springer (2004)
9. Hutchinson, S., Hager, G., Corke, P.: A Tutorial on Visual Servo Control. *IEEE Transactions on Robotics and Automation* 12, 651–670 (1996)
10. Prajna, S., Papachristodoulou, A., Seiler, P., Parrilo, P.A.: *SOSTOOLS (Sum of Squares Optimization Toolbox for MATLAB)* (2004)
11. Sturm, J.F.: Using Sedumi 1.02, a Matlab Toolbox for Optimization over Symmetric Cones. *Optimization Methods Software* 11, 625–653 (1999)
12. Toh, K.C., Tutuncu, R.H., Todd, M.J.: On the Implementation of SDPT3(version 3.1)-a Matlab Software Package for Semidefinite-Quadratic-Linear Programming. In: *IEEE International Symposium on Computer Aided Control System Design*, Taipei, pp. 290–296 (2004)

Multi-Agent Fuzzy-Based Control Architecture for Autonomous Mobile Manipulators: Traditional Approaches and Multi-Agent Fuzzy-Based Approaches

Abdelfetah Hentout¹, Mohamed Ayoub Messous^{1,3},
Saliha Oukid², and Brahim Bouzouia¹

¹ Division of Computer-Integrated Manufacturing and Robotics (DPR)
Centre for Development of Advanced Technologies (CDTA)

BP 17, Baba Hassen, Algiers 16303, Algeria

² Research Laboratory for the Development of Computerized Systems (LRDSI)

³ University Saad Dahleb of Blida (USDB)

BP 270, Blida 09000, Algeria

ahentout@cdta.dz, mmessous@cdta.dz, mmessous@outlook.com

Abstract. This paper surveys the different control approaches for autonomous mobile manipulators (traditional control approaches and multi-agent heuristic-based control approaches), and focuses mainly on multi-agent fuzzy-based approaches. Directions are discussed and properties of the state-of-the-art in control approaches are classified and compared depending on the techniques used for controlling the robots. The conclusion of the paper presents our point of view about the current state of designing multi-agent fuzzy-based control approaches for such autonomous robots.

Keywords: Traditional control approaches, Fuzzy-based control approaches, Multi-agent control, Autonomous mobile manipulators.

1 Introduction

A mobile manipulator consists of one or more manipulators installed on a mobile base. This type of robots can perform most common tasks of robotics that require, at the same time, locomotion and manipulation capabilities. The mobility, offered by the mobile base, allows the robot to significantly expand its reachable workspace and incrementing, thus, its operational capabilities [1]. Mobile manipulators have applications in several fields such as handling tasks, grasping and transporting objects, forestry, mining, construction, etc. Recently, the environments of such robots have migrated from industrial and factory environments to human environments [2]. Such robots are well adapted to human tasks; they are currently present in hospitals, offices, homes for assisting elderly and/or disabled people, etc. [3].

An autonomous robot must be able to operate in complex, not-completely-known and changing worlds using its limited physical and computational resources with a reduced human intervention [4]. Two axes symbolize the needs related to autonomy [5]:

- *Ability to act with a reduced human intervention*: the task provided to the robot is, in general, of a high-level with a distant time horizon. Therefore, the robot must be able to make any decision to progress its task, and achieve its objective. If the introduced task cannot be accomplished directly, the robot must be able to deduce the intermediate operations to achieve this goal.
- *Variability of the environment*: this variability disturbs, in permanence, the operations plan of the robot. Therefore, mechanisms must exist to provide *robustness*¹. An autonomous robot must be able to perform its task properly, even if it encounters unexpected situations, without/with a reduced human intervention.

In an autonomous robotic system, two essential elements can be distinguished (*i*) *the robot* that consists of a mechanical structure and actuators, and (*ii*) *the robot controller* which is the part that provides the intelligence (by processing information and managing information issued from sensors) so that the robot can perform the tasks for which it was designed. Mataric [7] defines the *control of a robot* as the process of taking information about the environment through the sensors equipping the robot, processing it as necessary in order to make decisions about how to act, and executing actions in the environment.

The *control architecture* is defined by Mataric [6] as a methodology that supplies structure and imposes constraints on the way that robots are controlled. Caselli and colleagues [8] have defined it as an organized set of basic functionalities that the robot can accomplish. The control is the entity that will handle this architecture. The main objective of a control architecture is to simplify the development of basic modules and their composition, necessary to present complex behaviors. On the other hand, a *control approach* represents mathematical models and tools, and the manner of how these components are exploited in order to ensure the desired behavior.

These last years, there has been considerable research effort devoted to autonomous control of mobile manipulators. The works led to different approaches that have been proposed and developed. This paper reviews the various control approaches for such robots (traditional approaches and heuristic-based approaches). After surveying more than one hundred papers of current research, it was found that heuristic approaches (neural network, genetic algorithm, fuzzy logic, neuro-fuzzy, etc.) gave effective and suitable results for autonomous control of the robots evolving in unknown and dynamic environment compared to the classical techniques [9].

This article provided, first, some definitions related to autonomous robots, control and control architectures. Then, it proposes a classification of the main control approaches for autonomous mobile manipulators illustrated with examples from the literature. After that, the paper focuses on multi-agent fuzzy-based control approaches. This concept allows building an architecture by dividing it into a number of agents that are intelligent and capable of handling operations independently. Finally, the article presents our point of view about the current state of designing multi-agent control architectures for such robots.

¹ *Robustness* is the ability to make a correct service in a non-predictable situation of the environment (unexpected obstacle, closed door, etc.). *Fault tolerance* is the ability to give a correct service regardless of the faults affecting the components of the system (sensor or software error, etc.) [6].

2 Properties of Control Architectures

The control of a robot with a certain degree of autonomy and complexity, to achieve goals or to react to environment changes, is determined by the organization of its control architecture. This latter must ensure that the robot will accomplish, in real-time, its tasks despite all the encountered situations. The control is required to be reactively fast but, also, thorough while maintaining some properties (stability, robustness, etc.). A robot, to be usable, is required to meet some behavior specifications and design requirements. The main specifications and requirements are given as follows [4] [10] [11] [12]:

- *Reactivity to the environment and Adaptability*: as the state of the environment changes very quickly and unpredictably, the robot must be able to react to unexpected situations. Moreover, it must be capable to consider external and asynchronous events with time limits that are compatible with the correct, efficient and safe execution of the current task. In addition, the control architecture must be adaptable to switch smoothly and rapidly between the different strategies of control. Furthermore, the robot must be able to change its behavior, while taking into account all the current encountered circumstances. The robot must, therefore, have capacities to recognize situations and make decisions in order to select the most appropriate behavior.
- *Autonomy*: as the environment conditions are variable and imperfect, the robot must be able to perform a task through the management of its sub-systems.
- *Fusion of multiple sensors*: the narrow accuracy, reliability and applicability of individual sensor must be compensated by integrating the other sensors of the robot.
- *Resolving of multiple goals*: in case of robotic tasks, situations requiring conflicting concurrent actions are inevitable. The control architecture must ensure proper means to be able to fulfill those multiple goals.
- *Robustness, Reliability and Fault-tolerance*: the robot must handle imperfect inputs, unexpected events and sudden malfunctions. Furthermore, it must be able to operate without failures or performance degradation over a certain period. In addition, the robot must have some hardware and software redundancy, so that corrective strategies can be applied in case where the acting conditions of the robot change.
- *Programmability*: a useful robot should be able to achieve multiple tasks described at some abstraction level, instead of only one precise task. Furthermore, the robot must not be simply directed by external stimuli, but a programmable machine able to execute tasks assigned by the operator.
- *Modularity, Flexibility, Expandability, Scalability and Reconfigurability*: the control architecture must be divided into smaller sub-systems (individual components or modules) that can be separately and incrementally designed, implemented, tested, debugged and maintained. It must be mentioned that such phases require a long time and experimental robotics requires continuous changes during these phases (design, implementation, etc.). Therefore, flexible architectures are required to allow the design to be guided by the success or failure of individual elements, and designed to be scalable, since new features can

be developed and added progressively to the capabilities of the robot, new control algorithms can be tested, etc. without modifying the existing ones.

- *Global reasoning*: a control architecture should have a global high-level decision-making agent. This latter is responsible of understanding the overall situation and merging the partial available information while taking into account misinterpreted data issued from the sensors.
- *Intelligent and Consistent behavior*: the behavior of the robot and its reactions to external stimuli must be correct with the final purpose, guided by the objectives of its main task, and not only determined by the state that it perceives from the environment. Thus, its instant reaction to external events must be based on the general context (state of the robot and its environment) and the task which is performing.
- *Safety*: autonomous robots can interact with humans (museum guides, personal service robots, etc.) or intervene in sensitive areas (nuclear centrals, etc.), which introduces additional security measures.

3 Main Frames Attached to a Mobile Manipulator

The analysis of a mobile manipulator includes the interaction between its mobile base and manipulator. For modeling the robot, the following assumptions were made:

- The floor and the wheels are indeformable.
- The contact surface between the driving wheel and the floor is assimilated to a point.
- There is no slipping between the driving wheels and the floor.
- The manipulator is fixed rigidly on the mobile base.

The mathematical analysis of a mobile manipulator requires defining the main reference frames and transformation matrices as shown in Fig. 1 where [13]:

- *dof* (degrees-of-freedom): number of joints of the robot that may vary independently.
- $R_A = (O_A, \vec{x}_A, \vec{y}_A, \vec{z}_A)$: the absolute reference frame attached to the environment.
- $R_B = (O_B, \vec{x}_B, \vec{y}_B, \vec{z}_B)$: it is connected to the mobile base of the robot.
- $R_M = (O_M, \vec{x}_M, \vec{y}_M, \vec{z}_M)$: this frame is attached to the basis of the manipulator.
- $R_E = (O_E, \vec{x}_E, \vec{y}_E, \vec{z}_E)$: R_E is fixed to the end-effector of the robot.
- $R_k = (O_k, \vec{x}_k, \vec{y}_k, \vec{z}_k)$: it is attached to the joint k ($k=1, \dots, dof$) of the manipulator.
- ${}^M T_E$: this transformation matrix defines R_E in R_M .
- ${}^B T_M$: it defines R_M in R_B .
- ${}^A T_B$: the transformation matrix defining R_B in R_A .
- ${}^A T_E$: this transformation matrix defines R_E in R_A .
- *Effector* $_{AFin}(x_{EAFin}, y_{EAFin}, z_{EAFin}, \psi_{EAFin}, \theta_{EAFin}, \varphi_{EAFin})$: it is the final situation of the end-effector of the robot given in R_A . The first three values represent the position of the end-effector; the last three are its orientation according to Euler angles.
- *Base* $_{Fin}(x_{BFin}, y_{BFin}, \theta_{BFin})$: it represents the final situation of the mobile base in R_A .
- *Configuration* $_{Fin}(q_{1Fin}, \dots, q_{dofFin})$: it is the final configuration of the end-effector in R_M .

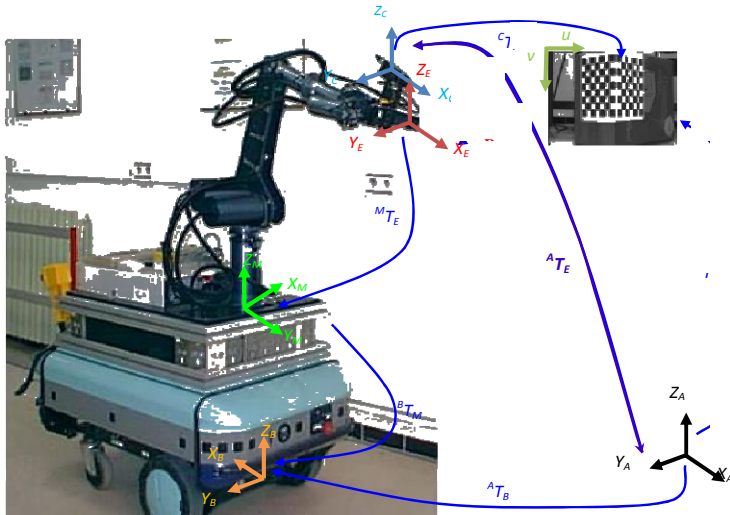


Fig. 1. Main reference frames attached to a mobile manipulator and the corresponding transformation matrices

The control architectures should be designed to meet all the requirements given previously. The existing research experience seems to have not yet performed a definitive paradigm for the distribution and/or coordination of the functionalities required for all the autonomous mobile manipulators [4].

In the literature, several studies have focused on proposing control architectures for such robots. Each proposition gives a specific way to solve the control problem. Some methods provide a total decoupling between the two sub-systems (mobile base and manipulator). While executing a task that requires the intervention of the two sub-systems, the control is carried out sequentially between the two disjointed entities. There exist, also, models for synchronizing the control of the mobile base and that of the manipulator.

To organize the operations that a mobile manipulator must perform and structure its internal functions in order to achieve the objectives assigned by the operator, each designer uses his own approach. The next sections review the different control approaches for autonomous mobile manipulators (traditional and multi-agent heuristic-based approaches) and discuss their major properties and characteristics, while focusing, primarily, on multi-agent fuzzy-based approaches.

4 Classical Control Approaches

This first class, considered as classical, is based on the study of mathematical models for both manipulator and mobile base mechanical sub-systems. Controlling a mobile manipulator consists of computing the motion of the manipulator joints and that of the mobile base. For this aim, the study of both *Direct (DKM)* and *Inverse (IKM) Kinematic* models of the robot is needed.

4.1 Direct Kinematic Model (DKM)

The *DKM* is the mathematical model that relates the variables of the joint space and the task space. It is written as follows where f is a non-linear function of the *DKM*:

$$Effector_{AFin} = f(Base_{Fin}, Configuration_{Fin}) \tag{1}$$

The computation of the *DKM* uses different matrices from the various frames (Figure 1). This means that each frame is considered moving relatively to the precedent one. Thus, R_B is considered moving relatively to R_A , R_E is considered moving relatively to R_M which moves relatively to R_B . Due to the transformation matrix ${}^A T_E$, the situation of the end-effector is given in R_A , by the following relation:

$${}^A T_E = {}^A T_B \cdot {}^B T_M \cdot {}^M T_E \tag{2}$$

4.2 Inverse Kinematic Model (IKM)

The *IKM* expresses the situation of the robot depending on the situation of its end-effector. It is written as follows:

$$(Base_{Fin}, Configuration_{Fin}) = f^{-1}(Effector_{AFin}) \tag{3}$$

The *IKM* of a mobile manipulator, operating in a three-dimension workspace, has as a purpose to compute the generalized coordinates $(x_{BFin}, y_{BFin}, \theta_{BFin}, q_{1Fin}, \dots, q_{dofFin})$, according to $Effector_{AFin}$. Unlike *DKM*, there are no specific rules to compute the *IKM* of a robot. However, it is up to the controller designers to choose specific strategies depending on the type of the robots. In most cases, *IKM* accept an infinite number of solutions since the robot presents geometric redundancy (the number of generalized coordinates is greater than the number of operational coordinates).

$Effector_{AFin}$ is completely defined in R_A . However, $Base_{Fin}$ as well as $Configuration_{Fin}$ can vary significantly as shown in Figure 2. In addition, the non-holonomic constraints of the mobile base can have an important effect on the form of the trajectory required to reach $Effector_{AFin}$. These last constraints cannot be resolved by using the *IKM*. It requires studying the differential-kinematic model and considering velocities [14]. This will further complicate the development of the control approach and requires considerable computation time, especially for real-time control.

A solution was proposed in [13] which partially decouples the robotic system. It begins with the motion of the mobile base, while considering the non-holonomic constraints of the mobile base and those related to the environment (obstacles avoidance), so that the robot can move its manipulator into a new situation where it may reach the imposed situation. Afterwards, the *IKM* of the manipulator is used, for, finally, placing the end-effector in the desired situation. Korayem [15] used the *Extended Jacobian Matrix* concept to solve the redundancy resolution and non-holonomic constraints. The authors formulated the problem as a *Trajectory*

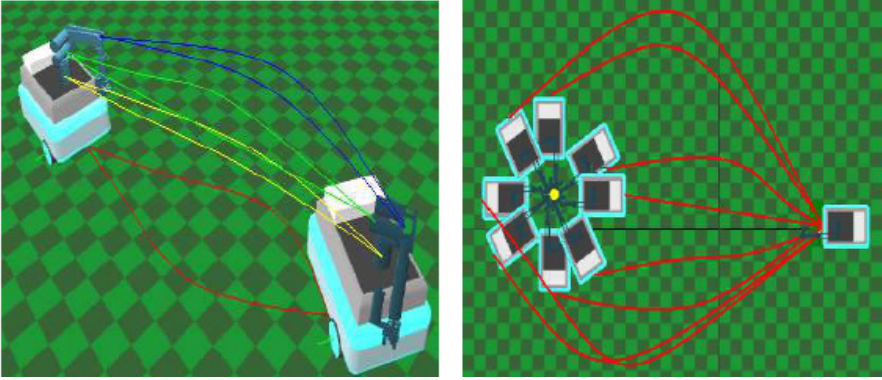


Fig. 2. Variations of $Base_{Fin}$ and its influence on $Configuration_{Fin}$ to reach $Effector_{AFin}$ [14]

Constrained non-linear Optimization Problem, and solved it by using the *Iterative Linear Programming* method, to find the *Maximum Dynamic Load* of the robot for a given two-end-point task. Nait-Chabane and colleagues [16] presented a global approach based on human-like behavior to help the disabled operator to understand the action of the robot. When the objective is close to the robot, the mobile base and the manipulator move together and the redundancy is used to maximize a *Manipulability criterion* [2].

4.3 Discussion of the Classical Approaches

Using the mathematical models to control mobile manipulators produces good and accurate results and offers a fairly exact control for repetitive tasks in controlled and known environments (industrial robotics). In this case, when the robot is required to repeat a trajectory thousands of times, very complicated calculation of these models is done, in most cases, off-line with the ability to optimize time and/or energy expended for performing a task. However, most robotic environments using mobile manipulators are not completely known but, per contra, evolutionary. Moreover, it should be noted that methods used for computing *DKMs* represented generic rules, whereas *IKMs* were constructed according to the mechanical structure of the robot. Also, these models do not tolerate any change in the mechanical structure of the robot (malfunction of one or more joints) without adding specific modes for failures treatment. When a fault occurs, the possibility of offering a *minimum service* until repairing the breakdown is a significant element of *Quality Of Service (QoS)* [17]. Furthermore, classical approaches have the disadvantage of computing time which is quite important depending on high number *dof* of the robot, especially in frequently-changed and not-completely-known environments. Finally, according to Brooks [10], *traditional robotics* seems unable to deliver real-time performances in a dynamic world.

5 Multi-Agent Heuristic-Based Approaches

When working with complex problems with large dimensions, the resolution of control problems for mobile manipulators is very difficult using traditional mathematical models. Several approaches have described the process allowing the end-effector of

such a robot to reach a position in its workspace, without using *IKM* or differential-equation solvers [18].

5.1 Multi-Agent Approaches

Multi-agent and *Distributed Artificial Intelligence (DAI)* techniques offer simple solutions [19]. Each joint is implemented as an agent. Every agent tries to align the position of the end-effector with that of the target, while being independent of the motions and positions of the other joints, and with no prior knowledge of the actions of the other agents. By acting recursively, the other agents, controlling the other joints, try to do the same job. A global behavior can emerge, consequently, from all the local agents which satisfy the desired objective.

Among the principal works done in this area, we find that developed by Delarue and colleagues [17]. They have built a control architecture adapted to the robotics of service (the *ARPH* robot), by using a multi-agent approach. This latter consists of two parts (i) the first concerns the manipulator and (ii) the second is assigned to the mobile base. This architecture has exploited the redundancy of the robot to offer tolerance to certain faults and breakdowns. The authors affirm, in their works, that each agent acts independently without any inter-synchronization. Each agent computes, first, the current position of the end-effector and, then, tries to match this position with the purpose to reach. By an approach of type “*Virtual movement-Check*”, each agent tends, with small local movements, to fulfill this constraint. If the imposed goal is outside the accessible workspace, each agent will align its joint with that objective. A global emergent behavior is then expected, which is to bring the robot to a fully-extended position, trying to get as close as possible to the objective. Fig. 3 shows an extension of this principle with a manipulator controlled by four agents and a mobile base controlled by a single agent.

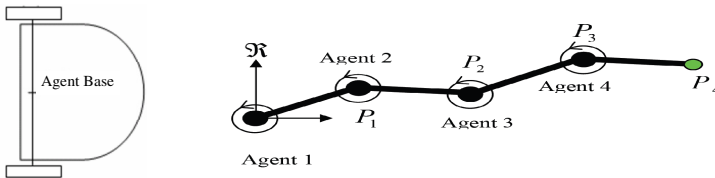


Fig. 3. Agents associated to a mobile manipulator as proposed in [19]

To solve a complex problem, a *Multi-Agent System (MAS)* can emerge global behaviors by using several agents. Each of these latter has a knowledge and a limited actions ability. Moreover, fuzzy logic, neural networks and/or genetic algorithms associated with *MAS*, can provide high-level control for such complex systems (mobile manipulators, etc.) [20] [21].

5.2 Multi-Agent Fuzzy-Based Approaches

Fuzzy logic is a mathematical formulation that copes with uncertainty in information [22]. Fuzzy control has proven to be a successful approach to many complex non-linear systems or even non-analytic ones. It has been suggested as an alternative approach to conventional or classical control techniques in many situations [23]. Such a control is characterized by the use of linguistic rules to manipulate and implement

human knowledge in control systems so as to handle the uncertainty present in the environment [24].

The model presented by Agah and Tanie [25] represents, to our knowledge, the first control architecture which is based on techniques of fuzzy logic with multiple distributed agents. The authors proposed a new approach in which the different agents cooperate and contend to control the system. By utilizing multiple software agents, they showed that the control design of the global system can be divided into small modules, in terms of the task, environment, or system status. These agents cooperate with each other to transform the input information (from sensors) into outputs information (control signals). Each agent was implemented using fuzzy-logic rules, and the agents were able to access all the available input information and, afterwards, suggest actions based on their knowledge and autonomy. The main controller (supervisor) evaluates the proposals of the contending agents according to their relevance, confidence and effect. Then, it selects the winner action that will be executed by the system. Finally, the winner agent controls the whole system alone.

This methodology was applied to control an inverted pendulum balanced by a robotic system, while being perturbed by a human force (similar to the system shown in Fig. 4). The practicality and feasibility of the proposed concepts were verified by applying the system to control a mobile manipulator in two-dimension handing over an object to an interacting human operator.

Three fuzzy-logic agents were developed for the robot pendulum balancing task (*i*) *Flexed* agent, (*ii*) *Mid-range* agent and (*iii*) *Extended* agent. For low values of robot length, *Flexed agent* is more relevant; for middle values, *Mid-range agent* is more relevant; and for high values, *Extended agent* is more relevant. Each agent is implemented as a fuzzy-logic controller with 21 rules. In these rules, the measured parameters are (*i*) the rotation angle of the pendulum, (*ii*) its rotation angle velocity, and (*iii*) the robot length. The control parameters determined by the system are (*i*) the magnitude and (*ii*) the direction of the force to be applied by the robot. The confidence of each action proposed by an agent is based on the fuzzy membership values of the sensory values (measure parameters).

In this work, the agents were defined according to the task to be done by the robot. Furthermore, one agent was active at a time. In such a scheme, it is more complicated to design and improve the control architecture for other systems.

5.3 Multi-Agent Fuzzy-Based Approaches Merged with other Heuristic

The most important drawbacks using fuzzy-logic to solve control problems are given hereafter [26]. These entire disadvantages have led to the idea of merging other heuristic approaches such as neural networks, genetic algorithms, etc. and the fuzzy technology.

- Standard and systematic method does not exist for the transformation of the human knowledge or experience into the rule base of a fuzzy inference system.
- There is no general procedure for choosing the optimal number of rules, since a large number of factors are involved in the decision (performance of the controller, efficiency of computation, human operator behavior, the choice of linguistic variables, etc.).
- In designing fuzzy-logic expert systems, a great deal of care and effort is required to obtain the rules.

- Even when human operators exist, their knowledge is often incomplete and episodic, rather than systematic.
- It is not possible to show the stability of the controlled system, since the model of the system is not known.
- There is no guarantee that rules are coherent and a no mismatch exists between the rules.
- Because of the complex operations (fuzzification and particularly defuzzification), computing time could be very long.

The work presented by Erden, Leblebicioglu and Halici in [27] fits into this context (merging fuzzy-logic and genetic algorithms). It describes a *MAS* approach to a service mobile manipulator that interacts with human during an object delivery and hand-over task in two dimensions. The required operations to achieve the overall objective are distributed between agents and each one fulfills its specific operation. The agents of the system are controlled using fuzzy control. The functions of the fuzzy controllers are tuned by using genetic algorithms.

The agents are identified as the *Base*, *Shoulder*, and *Elbow* of the robot. Each agent controls the movement of the junction referred by the name (Figure 4):

- *Base agent*: this first agent controls the displacement velocity of the mobile base (v_b) depending on horizontal and vertical distances d_x and d_y between the end-effector of the robot and the hand of the human operator.
- *Shoulder agent*: this agent controls the angular velocity of the shoulder (w_s) according to d_x and d_y distances and angle β . To compute this latter, the *Shoulder* agent needs information on the state of the *Elbow* agent (θ_e).
- *Elbow agent*: this last agent controls the angular velocity of the elbow (w_e) function of d_x and d_y distances and angle α .

In this work, an additional amelioration of the control has been performed by considering a criterion of improvement, with a focus on membership functions of the fuzzy controllers. This criterion is computed with a certain *fitness* function, which is a combination of (i) the distance traveled by the effector, (ii) the duration of the maneuver and (iii) the energy.

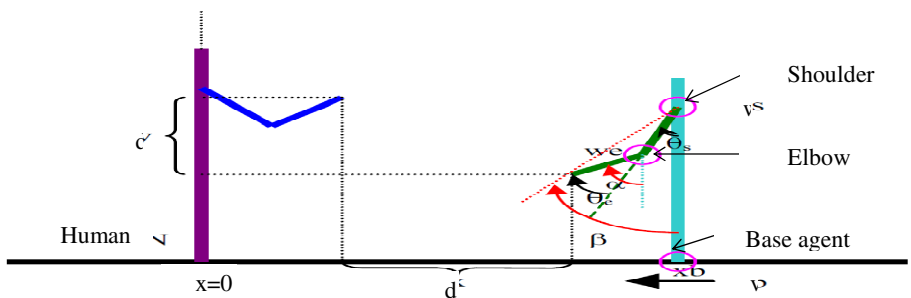


Fig. 4. Different agents associated to the system as proposed in [27]

5.4 Discussion of the Multi-Agent Approaches

In contrast to classical control approaches, multi-agent approaches offer methods that use the agent paradigm by proposing a decomposition of the robot control into a set of distinct agents. The *MAS* approaches benefit of all the advantages of distributed problem solving. The *MAS* perspective made it possible to consider the architecture as a compound of simpler modules, which gave way to easier design of the whole system. In addition, the need for massy mathematical models, *IKM* and differential-equation-solutions is overcome. Therefore, there is a considerable decrease in design effort and computation time compared to classical approaches. Moreover, with such a usage of *MAS*, the control architecture is more flexible to be applied to any robot [27].

The design phase of the development of a control architecture is the most strategic one. However, it is necessary to understand and to identify the needs to design and implement the approach in a proper manner. With the increasing complexity of architectures, using a development methodology is very necessary. Nevertheless, the absence of such a methodology covering the whole life cycle of a *MAS* makes the task very difficult and complicated [28]. The multi-agent approach poses, moreover, the problem of the management and control of agents and their shared resources. Another constraint that should not be overlooked when designing such a control system is the lack of information. This lack is mainly due to the measurement errors delivered by the physical sensors of the robot.

Multi-agent heuristic-based control approaches don't require a precise mathematical model of the robot to be controlled. However, if the model exists, it can be used for simulating and testing the control strategy. The main advantages of such controllers are given as follows [26] [29] [30]:

- No need to have a mathematical model of the robot (information is not available, information is not complete, the process is too complex, etc.).
- It is possible to implement expert-human knowledge and experience using comprehensible linguistic rules.
- Thanks to dedicated processors, it is possible to control fast processes.
- Such techniques allow developing robust and smooth controllers starting from heuristic knowledge and qualitative models.
- Such techniques allow considering imprecise, vague and unreliable information; and integrating symbolic reasoning and numeric processing in the same framework.

It should be mentioned that the aim of all the works presented in this section was to test the performances of the multi-agent heuristic-based design of control approaches in simulation. Moreover, all the studies were applied on a simple case of a service mobile manipulator interacting with human operators during hand-over tasks in two dimensions. Unfortunately, no works were done on real physical robots in three dimensions.

6 Conclusion

More than one hundred works have been surveyed in this paper covering the field of developing control approaches for autonomous mobile manipulators. We have tried to

bring together the major applications of multi-agent paradigm in the literature and come to conclusions about the nature of research in this field. The survey reveals that the application of heuristic methods, and especially fuzzy-based techniques merged with other heuristic approaches (neural networks, genetic algorithms, etc.), has increased due to their success in coping with the problems of combinatorial explosion.

This article presented a comparison between two different control approaches for autonomous mobile manipulators. The classical approaches use the mathematical models to control the robot. On the other hand, the second class is based on the *DAI* techniques for problem solving. Here, the control is mainly distributed on several concurrent agents, combining reactive and deliberative capacities. This class provides an alternative to use mathematical models to control such robots. It offers results that approximate human behaviors, and improves tolerance to certain faults and mechanical failures. Throughout the article, we have discussed some recent research which proposed interesting models for controlling mobile manipulators.

As remarked by Simmons [31], in many cases different approaches can be used for the same tasks. Fuzzy control can be adopted to coordinate the various system behaviors in response to the environment [32]. The combined use of fuzzy control with multi-agent approach, also, has another advantage of having a distributed fuzzy control system with smaller fuzzy sub-systems instead of one big centralized fuzzy system. Therefore, adopting an architecture/approach is a technological problem where the designer must consider the required degrees of reactivity, intelligent behavior and the related implementation cost. According to the type of robots and the necessary level of autonomy, different recommendations about the appropriate approach can be found in the literature. Typically, the differences are the ease with which approaches can be developed, and the efficiency with which tasks can be achieved [4].

The future works are dedicated to develop our own architecture for autonomous control of mobile manipulators. For this purpose, a multi-agent fuzzy-based approach is responsible for controlling the robot while sharing the control of the heterogeneous sub-systems.

References

1. Sugar, T., Kumar, V.: Decentralized Control of Cooperating Mobile Manipulators. In: The International Conference on Robotics and Automation (ICRA 1998), Leuven, Belgium, pp. 2916–2921 (1998)
2. Nagatani, K., Hirayama, T., Gofuku, A., Tanaka, Y.: Motion Planning for Mobile Manipulator with Keeping Manipulability. In: The International Conference on Intelligent Robots and Systems (IROS 2002), Switzerland (2002)
3. Alfaro, C., Ribeiro, M.I., Lima, P.: Smooth Local Path Planning for a Mobile Manipulator. In: The 4th Portuguese Robotics Festival Robotica 2004, Portugal (2004)
4. Medeiros, A.A.D.: A Survey of Control Architectures for Autonomous Mobile Robots. *Journal of the Brazilian Computer Society* 4(3) Campinas (April 1998)
5. Lussier, B.: Tolérance aux fautes dans les systèmes autonomes. Ph.D. Thesis in Computer Science System, Polytechnic National Institute of Toulouse, France (April 2007)
6. Mataric, M.J.: Behavior-Based Robotics as a Tool for Synthesis of Artificial Behavior and Analysis of Natural Behavior. *Trends in Cognitive Science* 2(3), 82–87 (1998)
7. Mataric, M.J.: Situated Robotics. *Encyclopaedia of cognitive science*, pp. 25–30. London Nature Publisher Group, Macmillan Reference (2002)

8. Caselli, S., Fantini, E., Monica, F., Occhi, P., Reggiani, M.: Toward a Mobile Manipulator Service Robot for Human Assistance. In: Robocare Workshop, Roma, Italy (October 30, 2003)
9. Mohanty, P.K., Parhi, D.R.: Controlling the Motion of an Autonomous Mobile Robot Using Various Techniques: a Review. *Journal of Advance Mechanical Engineering* 1(1), 24–39 (2013)
10. Brooks, R.A.: A Robust Layered Control System for a Mobile Robot. *IEEE Journal of Robotics and Automation* RA 2(1), 14–23 (1986)
11. Ferraz de Camargo, R.: Architecture matérielle et logicielle pour le contrôle d'exécution d'un robot mobile autonome. Ph.D. Thesis in Robotics, University of Toulouse III, France (1991)
12. Goût, J.: Intégration de la Planification Temporelle dans l'Architecture Décisionnelle d'un Robot Autonome. Ph. D. Thesis in Computer Science, University of Paul Sabatier, Toulouse, France (1999)
13. Hentout, A., Bouzouia, B., Akli, I., Toumi, R.: Mobile Manipulation: A Case Study. In: Lazinica, A., Kawai, H. (eds.) *Robot Manipulators, New Achievements*, pp. 145–167 (April 2010)
14. Akli, I., Haddad, M., Bouzouia, B., Achour, N.: Trajectory Generation for Operational Task Execution With Manipulability Analysis. In: *The International Conference on Advanced Robotics (ICAR 2011)*. Tallinn University of Technology, Estonia (2011)
15. Korayem, M.H., Ghariblu, H., Basu, A.: Maximum Allowable Load of Mobile Manipulators for Two Given end Points of End-effector. *International Journal of Advanced Manufacturing Technologies* 24, 743–775 (2004)
16. Nait-Chabane, K., Delarue, S., Hoppenot, P., Colle, E.: Strategy of Approach for Seizure of an Assistive Mobile Manipulator. *Robotics and Autonomous Systems* 57(2), 222–235 (2009)
17. Delarue, S., Hoppenot, P., Colle, E.: A Multi Agent Controller for a Mobile Arm Manipulator. In: *The 4th International Conference on Informatics in Control, Automation and Robotics (ICINCO 2007)*, Angers, France, May 9-12 (2007)
18. Duhaut, D.: Distributed Algorithm For High Control Robotics Structures. In: *International Conference on Artificial Intelligence*, vol. 1, pp. 45–50 (1999)
19. Colle, E., Nait Chabane, K., Delarue, S., Hoppenot, P.: ARPH: Comparaison d'une méthode classique et d'une méthode utilisant la coopération hommemachine pour exploiter la redondance de l'assistant robotisé. In: *The 4th Conference HANDICAP 2006*, France, June 7-9 (2006)
20. Tournassoud, P.: *Planification et contrôle en robotique: Application aux robots mobiles et manipulateurs*. Hermes Sciences Publications (September 1992)
21. Guessoum, Z.: A Hybrid Agent Model: a Reactive and Cognitive Behavior. In: *The 3rd International Symposium on Autonomous Decentralized Systems (ISADS 1997)*, Germany, pp. 25–32 (April 1997)
22. Klir, G.J., Folger, T.A.: *Fuzzy Sets, Uncertainty, and Information*. Prentice-Hall, Upper Saddle River (1992)
23. Precup, R.-E., Hellendoorn, H.: A Survey on Industrial Applications of Fuzzy Control. *Computers in Industry* 62(1), 213–226 (2011)
24. Passino, K.M., Yurkovich, S.: *"Fuzzy Control"*. Addison-Wesley, Menlo Park (1998)
25. Agah, A., Tanie, K.: Fuzzy-logic Controller Design Utilizing Multiple Contending Software Agents. *Fuzzy sets and systems* 106, 121–130 (1999)

26. Godjevac, J.: Comparative study of fuzzy control, neural network control and neuro-fuzzy control., Technical report n° 103/95, Federal Polytechnic School of Lausanne, Computer Science Department (February 1995)
27. Erden, M.S., Leblebicioglu, K., Halici, U.: Multi-agent System-Based Fuzzy Controller Design with Genetic Tuning for a Mobile Manipulator Robot in the Hand Over Task. *Journal of Intelligent and Robotic Systems* 39(3), 287–306 (2004)
28. Hentout, A., Bouzouia, B., Toukal, Z.: Modeling of Agent-based Architecture for Driving Mobile Manipulator Robots. In: *The International Conference on Distributed Human-Machine Systems (DHMS 2008)*, Greece, March 09-12 (2008)
29. Singh, M.K., Parhi, D.R., Bhowmik, S., Kashyap, S.K.: Intelligent Controller for Mobile Robot: Fuzzy Logic Approach. In: *The 12th International Conference of International Association for Computer Methods and Advances in Geomechanics (IACMAG)*, Goa, India, October 1-6 (2008)
30. Rashid, R., Elamvazuthi, I., Begam, M., Arrofiq, M.: Fuzzy-based Navigation and Control of a Non-Holonomic Mobile Robot. *Journal of computing* 2(3), 130–137 (2010)
31. Simmons, R.G.: Structured control for autonomous robots. *IEEE Transactions on Robotics and Automation* 10(1), 34–43 (1994)
32. Vadakkepat, P., Miin, O.C., Peng, X., Lee, T.H.: Fuzzy Behavior-Based Control of Mobile Robots. *IEEE Transactions on Fuzzy Systems* 12(4), 559–564 (2004)

Geometric Modeling of Any Obstacle Shapes for Robot Motion Planning

Md Nasir Uddin Laskar*, Seung Y. Choi,
Ishtiaq Ahmed, and TaeChoong Chung

Artificial Intelligence Lab, Dept. of Computer Engineering,
Kyung Hee University, 446-701, Republic of Korea
{nasir,sychoi84,ishtiaq.khu,tcchung}@khu.ac.kr

Abstract. We present an algorithm to model the workspace obstacles of a circular robot. Based on robot radius, we apply local geometry to model the obstacles and the operation is called offsetting. Result of our algorithm constructs an efficient configuration space and helps planning high-quality motion paths. Our method works in two major steps: it finds the raw offset curve for both lines and circular arcs in $O(n)$ times and then removes the global invalid loops in $O((n+k)\log m)$ times, where n is the number of vertices in the original polygon, k is the number of self-intersections, and m is the number of segments in the raw offset curve and always $m \leq n$. Local invalid loops are removed before generating the raw offset curve by invoking a pair-wise intersection detection test (PIDT). Our method is very fast, mathematically well defined, and overall complexity is approximately linear. By applying our simple and efficient approach, offsetting any shape of obstacles is possible to construct a configuration space that ensures optimized motion planning.

Keywords: Mobile robot, obstacle, polygon offsetting, motion planning, configuration space.

1 Introduction

The operation of Minkowski sum of polygons with a disc is called polygon offsetting. Most offsetting methods concentrate only for the convex polygons and they divide non-convex polygons into convex sub-polygons and offset them separately. Computing the Minkowski sum of two convex polytopes can have $O(n^2)$ time complexity [1], where n is the number of features of the polytopes. Minkowski sum of two non-convex polyhedra costs even more and can be as high as $O(n^6)$ combinatorial complexity. If a non-convex polygon is divided into m sub-polygons, their union can have $O(m^3)$ time complexity [2]. Our method applies local geometry and reduces the complexity to approximately linear.

Offsetting 2D point-sequence curve (PS-curve) is classified into four categories [3]: pair-wise, level set, Voronoi diagram and bisector based. Choi and Park [4] proposed a pair-wise offset algorithm for a polygon with no islands. Wein [5]

* Corresponding author.

presented a technique of Minkowski sum with a disc to compute exact and approximate offset of polygons. Another variant of Minkowski sum of two polygons is proposed by Guibas [1] to compute the convolution of the two bodies.

Bisector method is introduced by [6] which can automatically bridge the islands with main profile. It takes $O(n^2)$ time to compute the distance between two PS-curves, where n is the total number of curves. After that, Kim [7] and Kim *et al.* [8] used bisector method to calculate raw offset curve. They used the direction every time to report the global invalid loops.

Voronoi diagram implementation of polygon offsetting is another popular approach to the researchers. Q. Bo [9] introduced a recursive method to compute a trimmed offset of a polygon. Held [10] presented a $O(n \log n)$ algorithm to generate Voronoi diagram of curvilinear polygons and then finds the offset from the Voronoi diagram in $O(n)$ time, where n is the number of boundaries of the polygon. A circular arc extension to [10] is done based on a randomized incremental insertion [11].

S. McMains [12] presented an algorithm to build thin-walled parts in a fused deposition modeling machine. X. Chen and S. McMains [13] applied winding numbers to offset polygons. Their approach calculates the offset of multiple, non-overlapping polygons with islands and takes $O((n+k) \log n)$ time and $O(n+k)$ space, where n is the number of vertices in the input polygon and k is the number of self-intersections in the raw offset curve.

Robot motion planning has been studied extensively in the robotics literature for many years. There is a rich set of motion planning algorithms: grid-based search, cell decomposition, Minkowski sum, potential field method, sampling-based and some others. These algorithms deal with two approaches: sensor-based and model-based techniques [14]. A methodology for robot path planning among polygonal obstacles in a dynamic environment using mathematical modeling is introduced in [14] and [15]. These offsetting contradict with the smooth path properties of an optimized path in the workspace as described in [16] and cause the robot many sharp turns in the obstacle corners. Moreover, these methods can not handle a polygon that consists of both lines and arcs.

An approach to the coverage path planning problem called Boustrophedon Cellular Decomposition (BCD) is proposed by Choset [17]. Another approach to online complete coverage problem is proposed by [18]. Schwartz and Sharir [19] was the first to apply exact cell decomposition technique to solve the motion planning problem by their famous piano movers problem. For robot motion planning in the Euclidean space, different algorithms are proposed based on computing the Minkowski sum and the representation of the configuration space obstacles. Trapezoidal map of the free space with polygonal obstacles is presented by Berg *et al.* [20]. When the future locations are unknown, the planning problem is solved locally [21] or in conjunction with a global planner that guides the robot towards a goal [22], [23].

The remainder of the paper is organized as following manner. Section 2 describes our method in two subsections for offsetting lines and arcs respectively, and illustrates the way to handle global invalid loops. In section 3 we showed experimental results and performance analysis of our algorithm and finally, we conclude in section 4.

2 Computing Offsets

Input to our algorithm is a point-sequence curve with rational coordinates oriented counterclockwise (CCW), a curve type for each segment, and the robot radius d . Curve type is used to track the segments whether they are lines or arcs. Robot radius d works as the offset distance and we treat the polygon vertices differently depending on whether a vertex is convex or non-convex.

Throughout this paper, we indicate the points (or vertices) of the given polygon as p_i and the offset points as p'_j , where $i, j \in \mathbb{N}$. Since, in most of the cases, a vertex of the original polygon is associated with two points of the offset polygon, i and j are not necessarily be equal.

2.1 Offset Lines

A polygon can have convex as well as non-convex vertices. Fig. 1 demonstrates the possible offsetting cases for both convex and non-convex vertices of a polygon. Let a polygon P in Cartesian plane has n points $p_0(x_0, y_0), p_1(x_1, y_1), p_2(x_2, y_2)$ through $p_{n-1}(x_{n-1}, y_{n-1})$. Point $p_i(x_i, y_i)$ is directed to $p_{i+1}(x_{i+1}, y_{i+1})$. To offset the lines of the polygon P we shift each line segment by offset distance d along its normal direction or to the right side of the edge. As a result, we obtain n disconnected offset edges with $2n$ new points $p'_j(x'_j, y'_j)$ parallel to the original lines. For example, if we offset a line p_1p_2 we find the offset line $p'_1p'_2$, for line p_2p_3 we find the offset line $p'_3p'_4$ and for the line $p_{n-1}p_0$ we end up with the offset line $p'_{2n-2}p'_{2n-1}$. We tests the convexity of a vertex p_i by computing the angle $p_\theta = \angle(p_{i-1}, p_i, p_{i+1})$ at that vertex. A vertex is considered differently if it is start or end of a polygon arc.

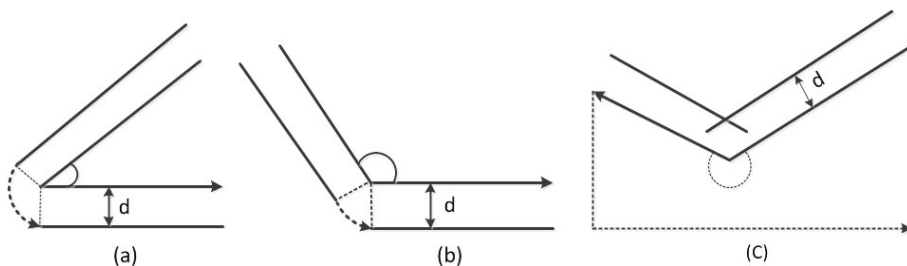


Fig. 1. Possible scenarios for offsetting polygon lines: (a) acute angle, (b) obtuse angle and (c) reflex angle

Theory of vector cross-product is used to the vectors $\overrightarrow{p_{i-1}p_i}$ and $\overrightarrow{p_i p_{i+1}}$ to find the angle p_θ based on the direction of the polygon (usually CCW). Every vertex has a z -component associated with it, which indicates the turning direction of the polygon at this vertex. Initially z -values of any vertex is zero and computing

Algorithm 1: Offset lines

```

input :  $p_i(x_i, y_i)$ ,  $p_{i+1}(x_{i+1}, y_{i+1})$  and offset distance  $d$ , which is the robot
radius
output:  $p'_j(x'_j, y'_j)$  and  $p'_{j+1}(x'_{j+1}, y'_{j+1})$  such that  $p'_j p'_{j+1}$  is parallel to  $p_i p_{i+1}$ 
with given distance  $d$ 

1 begin
2    $k \leftarrow 1$ 
3   for  $i = 0$  to  $(n - 1)$  do
4      $d_x \leftarrow x_{i+1} - x_i$ 
5      $d_y \leftarrow y_{i+1} - y_i$ 
6      $x_{perp} \leftarrow d_y$ 
7      $y_{perp} \leftarrow -d_x$ 
8      $i_{len} \leftarrow \sqrt{x_{perp}^2 + y_{perp}^2}$ 
9      $x'_{perp} \leftarrow (x_{perp} * d) / i_{len}$ 
10     $y'_{perp} \leftarrow (y_{perp} * d) / i_{len}$ 
11    for  $j = k$  to  $k + 1$  do
12       $x'_j \leftarrow x_i + x'_{perp}$ 
13       $y'_j \leftarrow y_i + y'_{perp}$ 
14       $x'_{j+1} \leftarrow x_{i+1} + x'_{perp}$ 
15       $y'_{j+1} \leftarrow y_{i+1} + y'_{perp}$ 
16    end
17     $k \leftarrow j + 1$ 
18  end
19 end

```

the cross-product $(p_i - p_{i-1}) \times (p_{i+1} - p_i)$ provides a non-zero value along the z -direction. Direction of vector cross-product is perpendicular to both the vectors being multiplied and normal to the plane containing them. If the z -value is positive, then $p_\theta < \pi$, we are turning left and the vertex is convex. If it is negative, then $p_\theta > \pi$, we are turning right and the vertex is non-convex.

If the vertex is convex as in Fig. 1(a) and (b) where outside lines are always the offset lines, adjacent two new points of offset edges will be connected by a circular arc centered in the corresponding vertex with radius d , which is the radius of the robot. For a vertex p_i , we draw an arc centered in p_i , between the points p'_{2i-2} and p'_{2i-1} , which are the end points of adjacent offset edges, induced by $p_{i-1}p_i$ and $p_i p_{i+1}$ respectively. The angle that defines such a circular arc is $\pi - \angle(p_{i-1}, p_i, p_{i+1})$.

Consider the line supporting $p_1 p_2$ is $ax + by + c = 0$, where $a, b, c \in \mathbb{R}$. Representation of the offset edge is based on the locus of all points lying at offset distance d from the line $ax + by + c = 0$ is given by

$$d = \frac{|ax + by + c|}{\sqrt{(a^2 + b^2)}}. \quad (1)$$

Algorithm 1 describes the process of finding two points which lie in the parallel to the given line segment in d distance. Line segments $p_i(x_i, y_i) p'_j(x'_j, y'_j)$ and

$p_{i+1}(x_{i+1}, y_{i+1})p'_{j+1}(x'_{j+1}, y'_{j+1})$ both are perpendicular to the given line segment $p_i(x_i, y_i)p_{i+1}(x_{i+1}, y_{i+1})$. d_x and d_y are the vector components of $\overrightarrow{p_i p_{i+1}}$ and its perpendicular vector components are x_{perp} and y_{perp} . Normalized vector components x'_{perp} and y'_{perp} are calculated applying vector magnitude i_{len} of the vector $\overrightarrow{p_i p_{i+1}}$. Offset coordinates x'_j and y'_j are found from the corresponding point (x_i, y_i) of the original polygon according to

$$\begin{aligned} x'_j &= x_i + x'_{perp} \\ y'_j &= y_i + y'_{perp}. \end{aligned} \tag{2}$$

For n lines of a polygon, we find n disconnected offset segments with $2n$ end points, as one point in the original polygon is corresponding to the end points of two offset lines. Starting point of a given line segment $p_i(x_i, y_i)$ is resulted with $p'_j(x'_j, y'_j)$ in d distance along its normal direction and the end point $p_{i+1}(x_{i+1}, y_{i+1})$ with $p'_{j+1}(x'_{j+1}, y'_{j+1})$ in the same d distance.

If the vertex is not convex, as in Fig. 1(c), PIDT test results positive as the offset lines of the adjacent two lines of non-convex vertex intersect each other. Since we are dealing with the outer offsetting only, it is most likely that, only non-convex vertices will cause two consecutive offset lines to intersect. For a non-convex vertex p_i , we find an intersection of two offset lines which causes a local invalid loop. We compute this intersection point to remove the local invalid loop caused by offset lines.

Consider two offset lines are of the form $a_1x + b_1y = c_1$ and $a_2x + b_2y = c_2$ respectively, where a_i, b_i and c_i are constants and $a_i, b_i \neq 0$. Then the determinant Δ is $a_1b_2 - a_2b_1$. If the intersection point is $p_s(x_s, y_s)$, we find $x_s = (b_2c_1 - b_1c_2)/\Delta$ and $y_s = (a_1c_2 - a_2c_1)/\Delta$.

2.2 Offset Circular Arcs

Arcs are handled way differently than the lines. Input point sequence curve has arc end points, center and direction of the circle along with curve type. Start angle θ_1 , end angle θ_2 and arc radius r are calculated from the given inputs. Local invalid loops are removed by invoking PIDT test. Compute intersections with neighboring offset segments and remove portions of the intersecting segments to find the final offsetting.

According to Fig. 2 (a) and (b), a circular arc can be clockwise (CW) or counterclockwise (CCW). Points $A(x_1, y_1)$, $C(x_2, y_2)$ and $O(c_x, c_y)$ are the start, end and center points of the arc ABC . Points $A'(x'_1, y'_1)$ and $C'(x'_2, y'_2)$ are the corresponding offset points for A and C respectively. Start angle θ_1 is calculated from OA as $\theta_1 = \tan^{-1}(\frac{y_1 - c_y}{x_1 - c_x})$ and end angle θ_2 from OC based on $\theta_2 = \tan^{-1}(\frac{y_2 - c_y}{x_2 - c_x})$. Arc angle $\theta_a = \theta_2 - \theta_1$. For a CCW arc, $\theta_2 > \theta_1$ and for a CW arc $\theta_2 < \theta_1$. If θ_1 and θ_2 become negative, then $\theta_1 = \theta_1 + 2\pi$ and $\theta_2 = \theta_2 + 2\pi$.

Finding the arc radius r is straight forward from the arc center (c_x, c_y) and the start (or end) point of the arc as $r = \sqrt{(c_x - x_1)^2 + (c_y - y_1)^2}$. If we consider the circle equation as

$$x^2 + y^2 + 2gx + 2fy + c = 0, \tag{3}$$

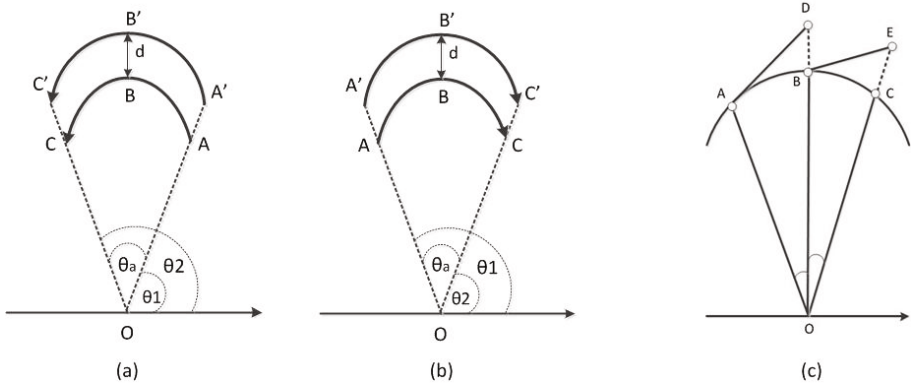


Fig. 2. Offsetting circular arcs: (a) CCW arc, $\theta_2 > \theta_1$, (b) CW arc, $\theta_2 < \theta_1$ and (c) draw the arc for offsets

where g, f and c are the constants, $(-g, -f)$ is the circle center and we can find the arc radius $OA = r$ from $\sqrt{g^2 + f^2 - c}$. However, radius of the offset arc OA' depends on arc direction. A CCW arc has its center inside the polygon area and the radius is $(r + d)$, where d is the offset distance. While a CW arc center resides outside the polygon area and the radius is $(r - d)$. Following derivation is performed considering the arc direction towards CCW. So, $OA' = (r + d)$ and a similar derivation can be done for CW arc considering $OA' = (r - d)$.

Start and end points of the offset arc is calculated according to θ_1, θ_2 and r . Start point $A'(x'_1, y'_1)$ of the offset arc $A'B'C'$ is calculated as

$$\begin{aligned} x'_1 &= c_x + (r + d) \cos \theta_1 \\ y'_1 &= c_y + (r + d) \sin \theta_1. \end{aligned} \tag{4}$$

To find the next point to the (x'_1, y'_1) , we apply the theory of circular motion. During each calculation, we move the point tangentially to the circle for a fixed distance AD and BE and then back towards the center of the circle for another fixed distance DB and EC , as shown in Fig. 2(c). At this point we store the new location and repeat the process.

Let θ be the angular length of a segment ahead of the previous point and x_t is the tangent of θ . If N_s is the number of segments (500 in our case) in the arc between start angle and end angle, $\theta = \theta_a / N_s$. We can easily turn the vector \vec{OA} by $\frac{\pi}{2}$ radians to CW direction that becomes tangent to the circle. Components of vector \vec{OD} is calculated as

$$\begin{aligned} x'_{new} &= x'_1 + x_t \tan \theta \\ y'_{new} &= y'_1 + y_t \tan \theta, \end{aligned} \tag{5}$$

Algorithm 2: Offset circular arcs

```

input : arcDirection,  $(x_1, y_1)$ ,  $(x_2, y_2)$  and  $(c_x, c_y)$  ; arc direction, start point,
        end point and center of the arc respectively.
output: An inflated arc between start and end point.

1 begin
2    $r \leftarrow \sqrt{(c_x - x_1)^2 + (c_y - y_1)^2}$ 
3   if (arcDirection == CW) then
4      $r \leftarrow r - d$ 
5   end
6    $r \leftarrow r + d$ 
7    $\theta_1 \leftarrow \tan^{-1}(\frac{y_1 - c_y}{x_1 - c_x})$ 
8   if ( $\theta_1 < 0$ ) then
9      $\theta_1 \leftarrow \theta_1 + 2\pi$ 
10  end
11   $\theta_2 \leftarrow \tan^{-1}(\frac{y_2 - c_y}{x_2 - c_x})$ 
12  if ( $\theta_2 < 0$ ) then
13     $\theta_2 \leftarrow \theta_2 + 2\pi$ 
14  end
15   $\theta_a \leftarrow \theta_2 - \theta_1$ 
16   $\theta \leftarrow \frac{\theta_a}{N_s}$ 
17  for  $i = 1$  to  $N_s$  do
18     $x'_1 \leftarrow c_x + r \cos \theta_1$ 
19     $y'_1 \leftarrow c_y + r \sin \theta_1$ 
20     $x_t \leftarrow -y'_1$ 
21     $y_t \leftarrow x'_1$ 
22     $x'_{new} \leftarrow x_{start} + x_t \tan \theta$ 
23     $y'_{new} \leftarrow y_{start} + y_t \tan \theta$ 
24     $x_{new} \leftarrow x'_{new} \cos \theta$ 
25     $y_{new} \leftarrow y'_{new} \cos \theta$ 
26  end
27 end

```

where (x'_{new}, y'_{new}) is the point D, θ is the angular length of a small segment of the arc, x_t and y_t are the tangent vector components of the radial vector (x_1, y_1) . Vector \vec{OB} is calculated as

$$\begin{aligned}
 x_{new} &= x'_{new} \cos \theta \\
 y_{new} &= y'_{new} \cos \theta,
 \end{aligned}
 \tag{6}$$

where (x_{new}, y_{new}) is the point B. At this point we are back where we started and repeating this process will fill the entire angular length θ_a . Algorithm 2 describes the process of offsetting the circular arc.

Now PIDT test will check whether this offset arc intersects with its neighboring offset segments. According to Fig. 3, one of the three scenarios can happen: (i) both the offset segments attached to the offset arc came from a single line as

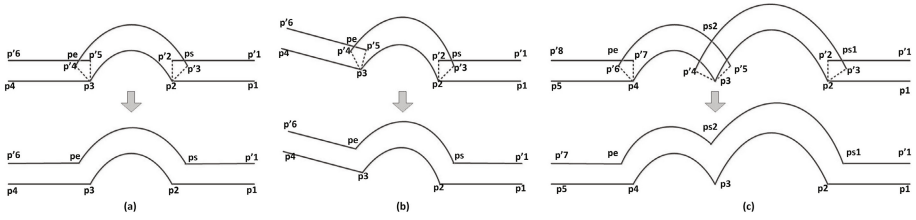


Fig. 3. Removing local invalid loops for arc offsets: (a) arc within a same line, (b) arc with different lines at its two ends and (c) two consecutive arcs in the main polygon.

in Fig. 3(a), (ii) offset arc intersects two different lines in its two sides as in Fig. 3(b), and (iii) an offset arc is a neighbor of another arc as in Fig. 3(c).

Finding the intersections between two offset lines or between an offset line and an offset arc can prevent local invalid loops before generating the raw offset curve, but still global invalid loops may exist. Instead of using the brute-force algorithm of $O(m^2)$, where m is the total number of segments in the raw offset curve, we use the well-known "Bentley-Ottmann Algorithm" [24] to find the global self-intersecting points which requires $O((n + k) \log m)$ time complexity, where n is the total number of vertices in the original polygon, k is the number of self-intersections and m is the number of valid segments in the raw offset curve and always $m \leq n$. We need to check for only the global self-intersection points instead of checking for all local and global self-intersection points, because local self-intersection points are already removed before generating the raw offset curve by PIDT test.

3 Experimental Results and Analysis

3.1 Experimental Results

We implemented our algorithm in GLUT for Win32 version 3.7.6 on a personal computer with Pentium(R) D CPU 3.00GHz and 2.00 GB RAM. We have tested our algorithm for various types of polygons and it can successfully handle any shapes of geometric objects. In the literature section, we have mentioned several times that, most of the algorithms can not handle non-convex shapes and circular arcs. However, our method deals such problems very efficiently with minimum computational cost we have seen so far.

Fig. 4 demonstrates the whole process of our proposed method. Input polygon has total eleven vertices ($n = 11$). Among them six are convex, three non-convex and remaining two are start and end point of the only arc. Fig. 4(a) is the original polygon. Fig. 4(b) shows disconnected offset segments for lines and arcs based on offset distance $d = 50$. Based on the type of the point sequence curve, angle between two neighboring segments are checked. For convex vertex, adjacent two new points of offset edges are connected by a circular arc centered in the corresponding vertex p_i as shown in Fig. 4(c). Pair-wise self-intersections are also

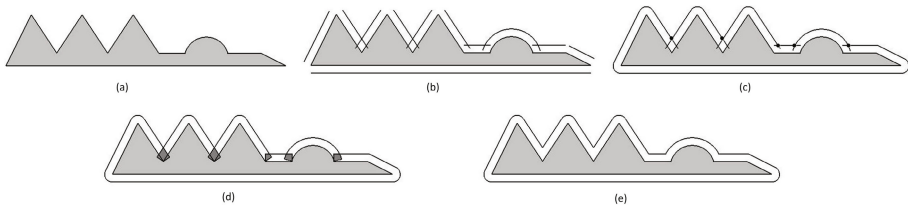


Fig. 4. Output of a polygon consists of convex vertex, non-convex vertex and arc: (a) input polygon (grayed), (b) disconnected offset segments for each lines and arcs, (c) for convex vertex, adjacent two offset points are connected by circular arcs of radius d . Self-intersection points caused by non-convex vertices and circular arc are indicated by black circles, (d) raw offset curve with local invalid loops (dark grayed) (e) final output.

shown for the non-convex vertices and circular arcs. A circular arc causes self-intersections with its two adjacent offset segments in its both ends. Fig. 4(d) is the raw offset curve for the original polygon with local invalid loops. Usually we remove the local invalid loops before generating the raw offset curves and in the raw offset curve, only global invalid loops remain. But in Fig. 4(d) local invalid loops are kept for better understanding of the whole process of getting the final output. After removing the local invalid loops, 4(e) shows the final output.

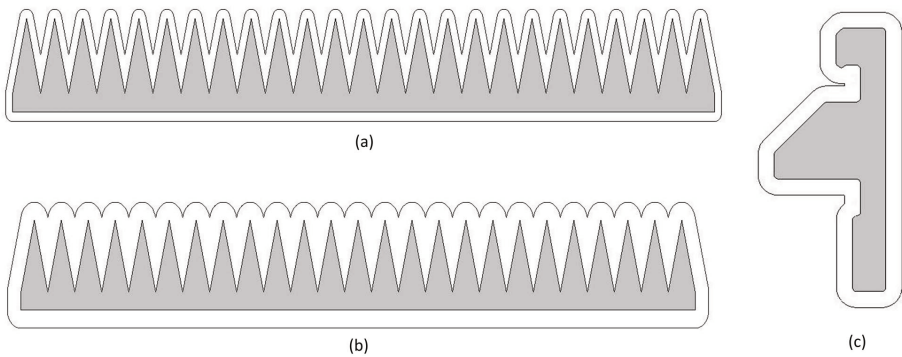


Fig. 5. Polygon consists of convex and non-convex vertices: (a) comb output, using offset distance $d = 50$, (b) comb output, using bigger offset distance ($d = 100$) and (c) pillar.

Fig. 5 shows the output of a comb for different d values and the case of a pillar. Fig. 6(a) is a shape of a duck with 19 lines and 66 arc segments and Fig 6(b) is a pocket profile with 9 non-convex vertices and 29 arc segments. Polygon statistics and algorithm execution times are shown in Table 1. Since the number of non-convex vertices and arc segments present in the polygon greatly influence the computation time, we mentioned them in Table 1. Running times are listed as the average of the maximum times taken by a single input from multiple executions. Fig. 7(a) is the plotted result of Table 1 that shows the running time is linear to the input size n . One may observe from the graph that the running time of pocket profile is comparatively higher. This is because of the large number of arc segments present in the pocket profile.

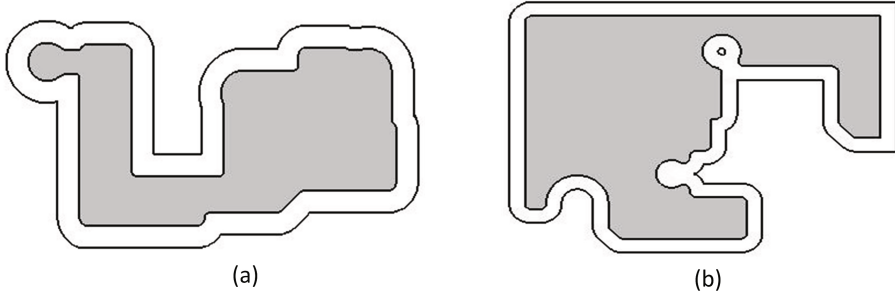


Fig. 6. (a) Shape of a duck, created with line and arc segments and (b) a pocket profile consists of arbitrary line and arc segments

Table 1. Running times (measured in milliseconds) for various types of input polygons

Input polygon	Size, n	Non-convex vertex, n_{nc}	Arc segment	Offset distance, d	Running time, ms
Output 1	11	3	1	75	2.21
Comb	53	24	0	100	7.18
Pillar	32	0	13	65	4.57
Duck	85	5	14	50	23.79
Pocket	66	9	25	50	21.25

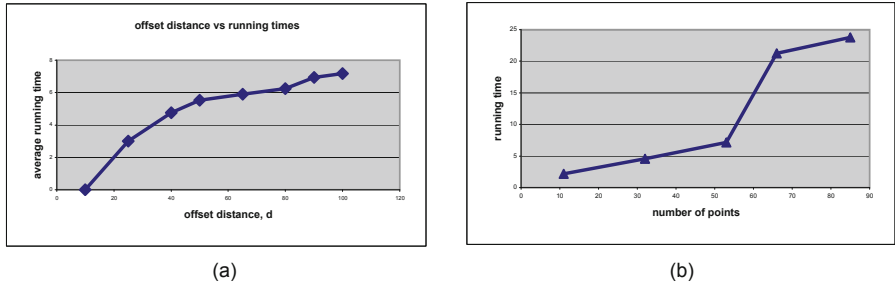


Fig. 7. (a) Running times for the outputs and (b) plotted result of Table 2. Effect of offset distance on the comb output.

Relation between algorithm running time and value of offset distance is a performance issue for polygon offsetting task. It is expected that, running time should not increase drastically for a bigger d value. We experimented our algorithm for different d values for all the shapes shown in this section and found our algorithm achieves this criteria. Fig. 5(a) and (b) is the comb output found using offset distance 50 and 100 respectively. Table 2 shows the running times based on different offset distances for the comb output. Fig. 7(b) shows the plotted result of Table 2.

Table 2. Running times for comb output based on different d values

Offset distance, d	Running time, ms
10	0.0
25	3.0
40	4.75
50	5.54
65	5.89
80	6.25
90	6.95
100	7.18

Table 3. Running times comparison with other methods

Input polygon Size, n	Non-convex vertex, n_{nc}	Offset distance, d	Running times, ms		
			Other method	Our method	
Comb	53	24	25	45	3.0
Wheel	40	14	50	35	2.55
Spiked	64	40	50	60	4.27

Table 3 shows the comparison of our method with [5] in case of computation time with the same experiment settings. Our method does not perform any redundant computation in the offsetting process, so it is way faster.

3.2 Complexity Analysis

Input of the algorithm is a polygon as point sequence curve and output is the offset polygon. The whole process performed in three steps: (1) raw offset curve generation, (2) checking for local invalid loops by invoking PIDT test and (3) removal of global invalid loops.

To generate the raw offset curve, each vertex is inserted only once. Time complexity to construct raw offset curve is $O(n)$, where n is the number of vertices in the input point sequence curve. This step also takes $O(n)$ space.

For second part, adjacent two offset segments are continuously checked for intersections if they come from non-convex vertices. Since we are dealing with outer offsetting, three situations will cause to create local invalid loops: (i) non-convex vertex (Fig. 1(c)), (ii) type variation of two adjacent offset curves, for example a line is adjacent to arc or vice versa (Fig. 3(a),(b)), and (iii) two adjacent offset arcs (Fig. 3(c)). A polygon has n total vertices and among them n_{nc} are non-convex and n_a vertices contain arcs, checking for local invalid loops with PIDT test will cost $O(n_{nc} + n_a)$ time and always $(n_{nc} + n_a) < n$.

In the third step, most of the time has been spent to report self-intersections. Time complexity to remove global invalid loops is $O((n+k) \log m)$ and uses $O(n+k)$ space, in which n is the total number of vertices in the original polygon, k is

the number of self-intersections, and m is the number of segments in the raw offset curve and always $m \leq n$. In practice, number of global invalid loop is very small and makes the complexity $O(n \log m)$. Moreover, point sequence curves contain a large number of interfering segments and the value of m become much smaller than n ($m \ll n$), so the time for this step becomes approximately linear.

4 Conclusions

A new algorithm to offset arbitrary shapes for efficient motion planning of a circular robot is presented in this paper. The algorithm is able to deal with convex, non-convex as well as arcs in an object. Line and arc segments are treated differently and local invalid loops are removed before generating the raw offset curve. Our method is simple, mathematically well defined, and produces consistent results. It handles the non-convex shapes very efficiently where prior methods impose redundant computations. Overall time complexity of the algorithm is approximately linear.

Acknowledgments. This work was supported a grant from the NIPA (National IT Industry Promotion Agency) in 2013 (Global IT Talents Program). This research was also partly supported by the Basic Science Research Program through the National Research Foundation of Korea (NRF) funded by the Ministry of Education, Science, and Technology (2010-0012609).

References

1. Guibas, L.J., Seidel, R.: Computing convolutions by reciprocal search. *Discrete and Computational Geometry* 2, 175–193 (1987)
2. Varadhan, G., Krishnan, S., Sriram, T.V., Manocha, D.: A simple algorithm for complete motion planning of translating polyhedral robots. *Int. Journal of Robotics Research* 24(11), 983–995 (2005)
3. Zhiwei, L., Jianzhong, F., Wenfeng, G.: A robust 2d point-sequence curve offset algorithm with multiple islands for contour-parallel tool path. *Computer-Aided Design* 45, 657–660 (2013)
4. Choi, B., Park, S.: A pair-wise offset algorithm for 2d point-sequence curve. *Computer Aided Design* 31, 735–745 (1999)
5. Wein, R.: Exact and approximate construction of offset polygons. *Computer-Aided Design* 39, 518–527 (2007)
6. Wong, T.N., Wong, K.W.: Toolpath generation for arbitrary pockets with islands. *Int. J. Journal of Advanced Manufacturing Technology* 12, 174–179 (1996)
7. Kim, H.C.: Tool path generation for contour parallel milling with incomplete mesh model. *Int. J. of Advanced Manufacturing Technology* 48, 443–454 (2010)
8. Kim, H.C., Lee, S.G., Yang, M.Y.: A new offset algorithm for closed 2d lines with islands. *Int. J. of Advanced Manufacturing Technology* 29, 1169–1177 (2006)
9. Bo, Q.: Recursive polygon offset computing for rapid prototyping applications based on voronoi diagrams. *Int. J. of Advanced Manufacturing Technology* 49, 1019–1028 (2010)

10. Held, M.: Voronoi diagrams and offset curves of curvilinear polygons. *Computer Aided Design* 30(4), 287–300 (1998)
11. Held, M., Huber, S.: Topology-oriented incremental computation of voronoi diagrams of circular arcs and straight-line segments. *Computer-Aided Design* 41, 327–338 (2009)
12. McMains, S., Smith, J., Wang, J., Sequin, C.: Layered manufacturing of thin-walled parts. In: *Proceedings of ASME Design Engineering Technical Conference*, Baltimore, MD (2000)
13. Chen, X., McMains, S.: Polygon offsetting by computing winding numbers. In: *Proc. of ASME Int. Design Engineering Tech. Conf, IDETC* (2005)
14. Esquivel, W., Chaing, L.: Nonholonomic path planning among obstacles subject to curvature restrictions. *Robotica* 20(1), 49–58 (2002)
15. Srivastava, A., Kartikey, D., Srivastava, U., Rajesh, S.: Non holonomic sortest robot path planning in a dynamic environment using polygonal obstacles. In: *Proc. of Int. Conf. on Ind. Tech (ICIT)*, India (2010)
16. Wein, R., Berg, J.P., Halperin, D.: The visibility-voronoi complex and its applications. In: *SCG Proc. of the twenty-first annual symposium on Computational Geometry*, pp. 63–72 (2005)
17. Choset, H.: Coverage of known spaces: The boustrophedon cellular decomposition. *Int.l Journal of Autonomous Robots* 9(1), 247–253 (2000)
18. Viet, H.H., Dang, V.H., Laskar, M.N.U., Chung, T.C.: Ba*: an online complete coverage algorithm for cleaning robots. *Int. Jour. of Applied Intelligence* (2012), doi:10.1007/s10489-012-0406-4
19. Schwartz, J.T., Sharir, M.: On the piano movers problem: Ii. general techniques for computing topological properties of real algebraic manifolds. *Advances of Applied Maths* 4, 298–351 (1983)
20. Berg, M., Cheong, O., Kreveld, M., Overmars, M.: *Computational Geometry: Algorithms and Applications*. Springer (2008)
21. Choset, H., Lynch, K.M., Hutchinson, S., Kantor, G., Burgard, W., Kavraki, L.E., Thrun, S.: *Principles of Robot Motion*. MIT Press, Cambridge (2007)
22. Clodic, A., Montreuil, V., Alami, R., Chatila, R.: A decisional framework for autonomous robots interacting with humans. In: *Proc. IEEE Int. Workshop Robot Human Interact. Commun.* (2005)
23. Xu, B., Stilwell, D., Kurdila, A.: A receding horizon controller for motion planning in the presence of moving obstacles. In: *Proc. IEEE Int. Conf. Robotics and Automation, ICRA* (2010)
24. Bentley, J.L., Ottmann, T.A.: Algorithms for reporting and counting geometric intersections. *IEEE Transactions on Computers* C-28(9), 643–647 (1979)

Path Planning Approach for Redundant Manipulator Based on Jacobian Pseudoinverse-RRT Algorithm

Yang Qian and Ahmed Rahmani

LAGIS UMR 8219 CNRS, Ecole Centrale de Lille
59650 Villeneuve d'Ascq, France
qianyang87@hotmail.com, ahmed.rahmani@ec-lille.fr

Abstract. The problem of collision-free path planning for redundant manipulator with the given desired pose is considered. For orientation, quaternion representation is applied to give singularity-free orientation control. A hybrid algorithm of combining the Jacobian pseudoinverse algorithm with Rapidly-Exploring Random Tree (RRT) method is proposed. The nearest configuration point to the task space with the goal pose is taken as the expanded node of the tree. The best expanding direction is calculated with the Jacobian pseudoinverse control algorithm. The velocity of the manipulator's end-effector is restricted by using the bisection gradient-decent extend algorithm to avoid the occurrence of joint velocity mutation. The simulation results from a 7 degrees of freedom robotic arm show the rapidity and validity of the proposed hybrid algorithm.

Keywords: Redundant manipulator, Path planning, Rapidly-Exploring Random Tree, Jacobian pseudoinverse, Quaternion.

1 Introduction

The project underway pursues the prototype development of a personal assistant robot for assistance tasks in household environments. This robot has two redundant manipulators. Redundant manipulator path planning in dynamic environment is a very important issue in the field of intelligent robot control. Researchers proposed a variety of planning algorithms, such as probabilistic roadmap method (PRM) [1, 2], Rapidly-Exploring Random Tree (RRT) [3, 4], artificial potential field method [5, 6], cell decomposition [7] and so on. Artificial potential field algorithm is often applied to local path planning. Cell decomposition method is mainly used for low-dimensional path planning. The search algorithm based on sampling techniques (PRM, RRT) can solve high-dimensional search problem. PRM algorithm is mainly used for the search problem in static environment. In configuration space RRT randomly samples some points to expand the tree until this search tree is connected to the goal point. Because of its ability to solve very complex, high dimensional planning problems and their relative ease of implementation, RRTs have been used for high-dimensional manipulation planning which is our current focus.

In practical applications, the goals are usually given in task space. For dealing with the uncertainty in configuration space an algorithm combining Jacobian pseudoinverse algorithm and RRT for redundant robot path planning is presented. The best expanding direction is calculated with the Jacobian pseudoinverse. And the velocity of the end-effector of the manipulator is restricted by using the bisection gradient-descent extend algorithm to avoid the occurrence of large change of joint velocity. In task space position control is rather straightforward, but orientation control is more complex. There are several representations for orientation such as the Euler angle convention [8]. But it inevitably contains singular points. In this paper, quaternion is applied for orientation control. Based on the above closed-loop feedback scheme, the simultaneous position/orientation control is achieved.

The paper is organized as follows. In section 2, we discuss the problems such as kinematics of redundant manipulator, quaternion-based orientation representation, and obstacle avoidance technique. Section 3 and section 4 present the hybrid algorithm of combining the Jacobian pseudoinverse control algorithm with RRT. Section 5 presents some simulation results. Finally, section 6 gives some concluding remarks.

2 Problem Formulation

2.1 Kinematics of a Manipulator

A manipulator is also considered as a linkage, which is defined to be a set of attached rigid bodies. Consider an n degrees of freedom (DOFs) manipulator. Each rigid body is referred to as a link, denoted by A . Let A_1, A_2, \dots, A_n denote a set of n links. The kinematic analysis mainly includes two sides, the forward kinematic analysis and the inverse kinematic analysis. The forward kinematic analysis means that the location and pose of the end of manipulator in a given reference coordinate system can be worked out with the given geometry parameters of the links and the variables of the joints for a robot. Let $\theta = \{\theta_1, \theta_2, \dots, \theta_n\}$ denote the set of angles of rotational joints, then θ yields an acceptable position and orientation of the links in the chain by using the homogeneous transformation matrix. Given the matrix ${}^{i-1}T_i$ expressing the difference between the coordinate frame of A_{i-1} and the coordinate frame of A_i , the application of ${}^{i-1}T_i$ transforms any point in A_{i-1} to the body frame of A_i . Repeating the above procedure, the location of any point $[x \ y \ z]^T \in A_n$ in the world frame is determined by multiplying the transformation matrices:

$$\begin{aligned} [x' \ y' \ z' \ 1]^T &= {}^0T_1 {}^1T_2 \dots {}^{n-1}T_n [x \ y \ z \ 1]^T \\ &= T [x \ y \ z \ 1]^T \end{aligned} \quad (1)$$

where $T = \begin{bmatrix} {}^0R_n & {}^0P_n \\ 0\dots 0 & 1 \end{bmatrix} = \begin{bmatrix} n_x & o_x & a_x & p_x \\ n_y & o_y & a_y & p_y \\ n_z & o_z & a_z & p_z \\ 0 & 0 & 0 & 1 \end{bmatrix}$, ${}^0R_n = \begin{bmatrix} n_x & o_x & a_x \\ n_y & o_y & a_y \\ n_z & o_z & a_z \end{bmatrix} \in \mathfrak{R}^{3 \times 3}$ and

${}^0P_n = [p_x \ p_y \ p_z]^T \in \mathfrak{R}^3$ give the rotation axis and the position in the base frame, respectively.

Eq. (1) represents the forward kinematics. The inverse of Eq. (1) forms the inverse kinematics problem in which a set of joint angles needs to be calculated corresponding to a given spatial constraint of the end-effector. In this paper the number of joint DOFs is seven and is more than the number of spatial constraints, the manipulator is redundant and there are multiple solutions.

2.2 Orientation Tracking

The position is well described by a position vector p , but there is no general method to describe the orientation. The application of unit quaternion [9] in robotics has increased in the latter years. Quaternion instead of Euler angles is used to estimate orientation (pitch, roll and yaw angles) because of its singularity-free orientation representation. It seems to be the preferred method to formulate the end-effector orientation tracking control problem. A quaternion has 4 components:

$$\mathbf{q} = (q_0 + iq_1 + jq_2 + kq_3) = q_w + \mathbf{q}_v \quad (2)$$

where $q_w = q_0, \mathbf{q}_v = (iq_1 + jq_2 + kq_3)$, $i^2 = j^2 = k^2 = -1, \quad jk = -kj = i, \quad ki = -ik = j, \quad ij = -ji = k$ and \mathbf{q} is subject to the constraint:

$$\mathbf{q}^T \mathbf{q} = 1. \quad (3)$$

As mentioned in the kinematic analysis section, the rotation axis can be represented with 0R_n . It also can be represented with composite product by a unit quaternion [10]:

$${}^0R_n(\theta) = (q_w^2 - \mathbf{q}_v^T \mathbf{q}_v)I_3 + 2\mathbf{q}_v \mathbf{q}_v^T - 2\mathbf{q}_v \times \mathbf{q}_v \quad (4)$$

where I_3 is a 3x3 identity matrix.

Similarly to Eq. (4), ${}^0R_{nd}$ which represents the desired orientation can be related to a desired unit quaternion, denoted by $[q_{wd} \ \mathbf{q}_{vd}]^T \in \mathfrak{R}^4$, as follows:

$${}^0R_{nd}(\theta) = (q_{wd}^2 - \mathbf{q}_{vd}^T \mathbf{q}_{vd})I_3 + 2\mathbf{q}_{vd} \mathbf{q}_{vd}^T - 2\mathbf{q}_{vd} \times \mathbf{q}_{wd} \quad (5)$$

To quantify the difference between the current and the desired end-effector orientations, we define the rotation matrix $\tilde{R} \in \mathfrak{R}^{3 \times 3}$ as follows:

$$\tilde{R} = RR_d^T \quad (6)$$

The unit quaternion tracking error $e_q \in \mathfrak{R}^4$ can be derived as follows [10]:

$$\mathbf{e}_q = \begin{bmatrix} e_w \\ \mathbf{e}_v \end{bmatrix} = \begin{bmatrix} q_w q_{wd} + \mathbf{q}_v^T \mathbf{q}_{vd} \\ q_w \mathbf{q}_{vd} - q_{wd} \mathbf{q}_v - \mathbf{q}_v \times \mathbf{q}_{vd} \end{bmatrix} \quad (7)$$

which satisfies the constraint:

$$\mathbf{e}_q^T \mathbf{e}_q = e_w^2 + \mathbf{e}_v^T \mathbf{e}_v = 1 \quad . \quad (8)$$

The control objective is formulated as follows:

$$\mathbf{e}_q = [\pm 1 \ 0 \ 0 \ 0]^T \quad . \quad (9)$$

The orientation error is defined using the quaternion and the coordinate transformation matrix. For orientation control, the orientation error is formulated using the unit quaternion as in [11]:

$$\mathbf{e}_0 = \mathbf{e}_v \quad . \quad (10)$$

2.3 Path Planning of a Manipulator

For grasping an object, several tasks have to be solved like reaching the desired grasping pose, solving the inverse kinematics and finding a collision-free grasping trajectory. The path planning problem can be described as follows: given an initial configuration θ_{init} in joint space and the desired pose (p_d, \mathbf{q}_d) of the end-effector in task space, find a collision-free path which satisfies the constraint equation:

$$(p_d, \mathbf{q}_d) = \text{Forwardkinematics}(\theta_{goal}) \quad . \quad (11)$$

where p_d and \mathbf{q}_d denote the desired position and orientation of the end-effector.

2.4 Obstacle Detection and Avoidance

To avoid obstacles, we have to determine that the minimum distance from the points on the manipulator to the obstacles is greater than a pre-set minimum value.

To generate a feasible path in an obstacle-ridden environment, the algorithm proposed by Sean Quinlan [12] is used for the present problem. The algorithm gives an upper bound for the distance and any point on the geometry of the manipulator can move for a given change in the configuration. This method is proposed for computing collision-free bubbles around the configurations of the manipulator with revolute joints. These bubbles represent the associated free space (Fig. 1).

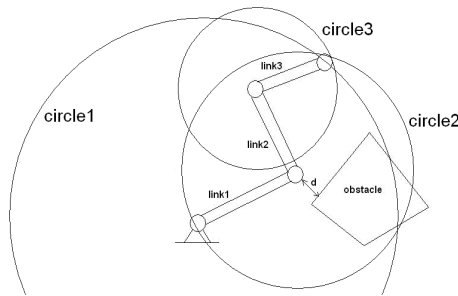


Fig. 1. Collision-free bubbles

Let d be the minimum distance between the manipulator and the obstacles in the environment. Suppose that for each joint of the manipulator, a radius r is determined such that the cylinder centered along the axis of the joint contains all the subsequent

links of the manipulator. The principle is shown in Fig. 1, consider a 3 DOFs manipulator, since the manipulator is planar, the bounding cylinder becomes a circle. Circle one contains the entire manipulator; circle two contains link 2 and link 3, and circle three only contains link 3. Consider moving the manipulator to a configuration θ by first rotating joint 1 to position θ_1^i . From the bounding cylinder at joint 1, we know that no part of the manipulator will move a distance greater than $r_1 |\theta_1^i - \theta_1|$. Next, joint 2 moves to θ_2^i (link 1 does not move), and the other links move a distance no greater than $r_2 |\theta_2^i - \theta_2|$. Each joint of the manipulator is moved in turn, and the total distance traveled by these motions is bounded by:

$$\sum_{i=1}^n r_i |\theta_i^i - \theta_i| \quad (12)$$

We can specify a joint space bubble by:

$$\beta_\theta = \left\{ \theta' : \sum_{i=1}^n r_i |\theta_i^i - \theta_i| < d \right\} \quad (13)$$

A set of bubbles are used to describe the local free space around the configuration of the manipulator.

3 Jacobian Pseudoinverse Algorithm

3.1 Inverse Kinematics Solution

The differential kinematic equation, in terms of either the geometric or the analytical Jacobian, establishes a linear mapping between the joint space velocities and the task space velocity, and it can be used to find the joint velocities. The differential kinematic equation that expresses the relation between the end-effector velocity and the joint velocities has the following form:

$$\dot{x} = \begin{bmatrix} v \\ \omega \end{bmatrix} = \begin{bmatrix} J_v \\ J_\omega \end{bmatrix} \dot{\theta} \quad (14)$$

where $\dot{\theta} = [\dot{\theta}_1 \ \dot{\theta}_2 \ \dots \ \dot{\theta}_n]^T$ is the joint velocity vector, $v = [\dot{p}_x \ \dot{p}_y \ \dot{p}_z]^T$ and $\omega = [\omega_x \ \omega_y \ \omega_z]^T$ are the linear and angular velocity vectors of the end-effector. J_v can then be written as:

$$J_v = \frac{\partial p}{\partial \theta^T} = \begin{bmatrix} \frac{\partial p_x}{\partial \theta_1} & \frac{\partial p_x}{\partial \theta_2} & \dots & \frac{\partial p_x}{\partial \theta_n} \\ \frac{\partial p_y}{\partial \theta_1} & \frac{\partial p_y}{\partial \theta_2} & \dots & \frac{\partial p_y}{\partial \theta_n} \\ \frac{\partial p_z}{\partial \theta_1} & \frac{\partial p_z}{\partial \theta_2} & \dots & \frac{\partial p_z}{\partial \theta_n} \end{bmatrix} \quad (15)$$

where $p = [p_x \ p_y \ p_z]^T$ denotes the position of the end-effector.

And J_ω can then be written as:

$$J_\omega = \begin{bmatrix} a_{1x} & a_{2x} & \dots & a_{nx} \\ a_{1y} & a_{2y} & \dots & a_{ny} \\ a_{1z} & a_{2z} & \dots & a_{nz} \end{bmatrix} . \tag{16}$$

where $[a_{ix} \ a_{iy} \ a_{iz}]^T$ which was mentioned in Eq.(1) denotes the rotation axis z of joint i in the base frame.

Based on the kinematic analysis, the end-effector orientation is expressed by the unit quaternion \mathbf{q} which is related to the angular velocity of the end-effector via the following differential equation [11]:

$$\dot{\mathbf{q}} = B(\mathbf{q})\omega . \tag{17}$$

The relation between the joint velocities and the end-effector velocity can also be expressed as follows:

$$\begin{bmatrix} \dot{p} \\ \dot{\mathbf{q}} \end{bmatrix} = \begin{bmatrix} J_v(\theta) \\ B(\mathbf{q})J_\omega(\theta) \end{bmatrix} \dot{\theta}, J = [J_v \ B(\mathbf{q})J_\omega]^T . \tag{18}$$

Due to the non-square Jacobian matrix for the redundant manipulator, the basic inverse solution of Eq. (14) is obtained by using the pseudoinverse J^\dagger of the matrix J and the inverse solution can then be written as:

$$\dot{\theta} = J^\dagger \dot{x} . \tag{19}$$

where the pseudoinverse J^\dagger can be computed as $J^\dagger = J^T (JJ^T)^{-1}$.

Without any obstacles, internal collisions, or joint limits, this simple controller is guaranteed to reach the goal. However, the pseudoinverse tends to have stability problems in the neighborhoods of singularities. If the configuration is close to a singularity, then the pseudoinverse method will lead to very large changes in joint angles, even for small movement in the target position. The pseudoinverse has the further property that the matrix $(I - J^\dagger J)$ performs a projection onto the null space of J .

A method including the null space in the solution is given by [13] as follows:

$$\dot{x} = J^\dagger \dot{y} + (I - J^\dagger J)z . \tag{20}$$

The first term is the particular solution to the inverse problem $J\dot{x} = \dot{y}$, and the second term represents the homogeneous solution to the problem $J(I - J^\dagger J)z = 0$.

Thus using Eq. (20) the general inverse solution for the redundant manipulator can be written as:

$$\dot{\theta} = J^\dagger \dot{x} + (I - J^\dagger J)\dot{\phi} . \tag{21}$$

where $\dot{\phi}$ is an arbitrary vector that can be used for optimization purposes and the matrix $(I - J^\dagger J)$ projects the joint vector $\dot{\phi}$ onto the null space $N(J)$.

3.2 Redundancy Resolution

In velocity based control, given the desired task space position p_d , orientation \mathbf{q}_d (as a quaternion), the linear velocity v and the angular velocity ω in task space are derived with position control and are defined as:

$$v = k_p(p_d - p) \tag{22}$$

$$\omega = k_0 \mathbf{e}_0 \tag{23}$$

where k_p and k_0 are positive.

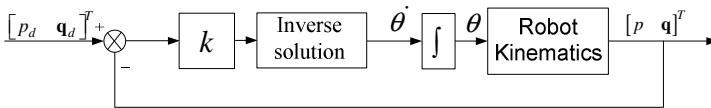


Fig. 2. Jacobian pseudoinverse algorithm

According to Fig. 2, we obtain the following control algorithm:

$$\dot{\theta} = kJ^\dagger e + (I - J^\dagger J)\dot{\phi} \tag{24}$$

where the position and orientation errors in task space are defined as

$$e = \begin{bmatrix} e_p \\ \mathbf{e}_0 \end{bmatrix} = \begin{bmatrix} p_d - p \\ \mathbf{e}_v \end{bmatrix} \in \mathfrak{R}^6 \text{ and } k = \begin{bmatrix} k_p & 0_{3 \times 3} \\ 0_{3 \times 3} & k_0 \end{bmatrix}.$$

A typical choice of the null space joint velocity vector is given by [13]:

$$\dot{\phi} = k_w \left(\frac{\partial w(\theta)}{\partial \theta} \right)^T \tag{25}$$

with $k_w > 0$. $w(\theta)$ is a scalar objective function of the joint variables and

$\left(\frac{\partial w(\theta)}{\partial \theta} \right)^T$ is the vector function representing the gradient of w .

By suitably choosing w , one can try to achieve secondary goals in addition to making the end-effector track the goal pose. In this research, just the joint limit avoidance is considered as the local optimization objective, and the objective function is the distance from the mechanical joint limits, which can be defined as:

$$w(\theta) = \frac{1}{n} \sum_{i=1}^n \left(\frac{\theta_i - \bar{\theta}_i}{\theta_{iM} - \theta_{iM}} \right)^2 \tag{26}$$

where $\theta_{iM}(\theta_{im})$ denotes the maximum (minimum) limit for θ_i , and $\bar{\theta}_i$ is the middle value of the joint range. Thus the redundancy may be exploited to keep the manipulator off the joint limits.

Note that the algorithm requires that all the expected joint angular velocities can be reached, but because of the joint angle constraints and the obstacles, the joint cannot change the configuration in any direction. To solve this problem, bisection method is used to choose the displacement of the end-effector and determine the feasibility of the joint angular velocities to limit the velocities of the joints and the end-effector.

4 RRT Method Based on Jacobian Pseudoinverse Algorithm

This section improves the basic RRT algorithm and uses this proposed method for the motion planning of the redundant manipulator. An RRT is a tree composed of nodes which represent configurations in the search space. The RRT growth process causes it to rapidly expand throughout the space. Considering the characteristic of multi-joint, we use this method in joint space. The basic principle of RRT algorithm can be described as follows.

Fig. 3 describes an example of how basic RRT works. The blue circles represent the configurations that are already in the tree. Initially the tree has only one node located at the starting state. Firstly a search tree is generated from this initial configuration q_{init} , and we take this configuration point as a parent node. Then we choose a point q_{rand} at random in configuration space. We find q_{rand} 's nearest neighbor in the tree and that configuration is denoted as q_{near} . Next we try to connect q_{rand} and q_{near} using a simple local planner, which essentially just moves from one configuration to the other until it encounters an obstacle. If the local planner succeeds in reaching q_{rand} , it is added as a new node in the tree. This step is repeated until the manipulator reaches the goal. Typically the search is only allowed to proceed in a small step δq , in which case the location reached (called q_{new}) is added instead. The new node q_{new} regards q_{near} as its parent node.

<p>Basic RRT algorithm</p> <pre> GENERATE_RRT(q_{init}, M, Δt) T.init(q_{init}); For $m = 1$ to M do $q_{rand} \leftarrow$ RANDOM_STATE(); $q_{near} \leftarrow$ NEAREST_NEIGHBOR(q_{rand}, T); EXTEND(q_{near}, q_{rand}) $\delta q \leftarrow$ SELECT_INTPUT(q_{rand}, q_{near}); $q_{new} \leftarrow$ NEW_STATE(q_{near}, δq, Δt); T.add(q_{new}); Return T; </pre>

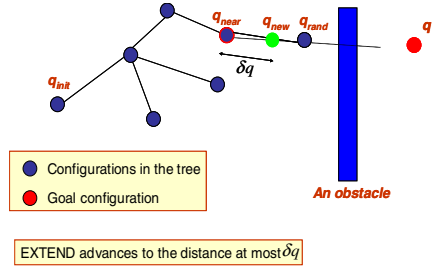


Fig. 3. Basic RRT principle

As seen from the above algorithm, a goal configuration should be given in joint space in advance before planning. In practice, the goal point is usually given in task space, and then the configuration is obtained by inverse kinematics. The Jacobian pseudoinverse is used to improve the RRT algorithm. During the expansion of the search tree, with probability p_r the tree is grown towards the goal and with probability $1 - p_r$ it is grown randomly in joint space. When growing randomly, it is exactly as in the basic RRT algorithm. When growing towards the goal, we select the node closest in task space to the goal pose x_{goal} and then use the pseudoinverse of Jacobian matrix on this node to determine the expansion direction. To avoid the occurrence of

mutations of joint and end-effector velocities in the expansion direction, RRT selects a new node along the expansion direction which is determined by the bisection gradient-decent extend algorithm. During the expansion, a failure count of a node is incremented when an attempt to add a new branch fails because the new node is not collision-free (computing collision-free bubbles) or does not yield a lower goal distance than the old node. When the number of failures exceeds the predetermined value, the node is removed from the search tree. This phenomenon indicates that there is not a feasible path from this node to the goal node. The parent node of this removed node is returned. Then RRT repeats the above process and randomly selects a node to expand the search tree until the distance between the end-effector and the goal is less than the preset value. The concrete realization of the algorithm is as follows:

① RRT method based on Jacobian pseudoinverse algorithm:

```

Qnew = {qstart}
while (DistanceToGoal(Qnew) > DistanceThreshold)
    p = Rand (0, 1)
    If p < pr
        Qnew = GradientDecentExtend ( )
    Else
        Qnew = BasicExtend ( )

```

② Gradient DecentExtend ()

```

qold = ClosestNodeToGoal();
Xold = KinematicsSolve ( qold ) //End-effector position and orientation
ΔX = Xgoal - Xold //Distance to goal
For j = 0: 1:N //Bisection gradient-decent extend
    ΔXstep = ΔP / 2j
    If |ΔXstep| < ΔXmax //Limiting the velocity of end-effector
        qnew = ComputeNewNode ( qold ,ΔXstep )
        Qnew = Qnew + { qnew }
        Break
    Else
        Continue

```

③ Expansion procedure:

```

ComputeNewNode ( qold ,ΔXstep )
If |ΔXstep| < ε
    return qold
Else
    J = ComputeJacobian ( qold )
    Δq = kJ† ΔXstep + (I - J†J)φ̇
    If |Δq| < Δqmax //Avoiding a sudden change of joints
        qnew = qold + Δq
    If
        CollisionFree(qnew) ∩ (DistanceToGoal(qnew) - DistanceToObstacle(qnew))
        < (DistanceToGoal(qnear) - DistanceToObstacle(qnear))
        return qnew

```

```

Else
    IncreaseFailureCount(qold, 1)
    If failureCount > f
        remove (qold)
        qold ← Parent(qold)
        return qold
    Else
        Continue
Else
    Continue

```

5 Simulation Results

The structure of 7 DOFs manipulator used in this paper is shown in Fig. 4. It is an important part of our service robot. This redundant manipulator is composed of a shoulder, an elbow and a wrist as the human arm.

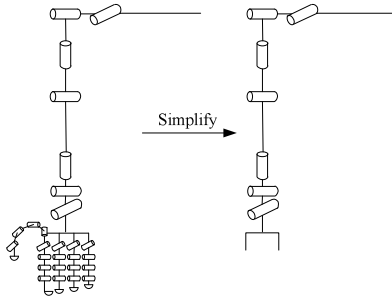


Fig. 4. Structure and dimensions of a 7 DOFs manipulator

The task is designed as follows: Given an initial configuration $\theta_{init} = [0 \ 0 \ 0 \ 0 \ 0 \ 0 \ 0]^T$ in configuration space and a desired posture (p_d, \mathbf{q}_d) of the end-effector in task space, then find a continuous collision-free path in the environment, where $p_d = [0.25 \ 0.3367 \ 0.349]^T$ and the unit quaternion \mathbf{q}_d can be obtained by the transformation of the desired Euler angles $[\frac{\pi}{2} \ 0 \ \frac{\pi}{2}]^T$.

For the validation of the proposed RRT path planning algorithm, a complete model of the mobile manipulator has been built in MATLAB. The structure of this robot is correspondent with the real one. All the links are simplified and are represented with lines.

Fig. 5 shows the simulation results based on the path planning approach. In these figures, the ball is taken as an obstacle. Fig. 5 (a) shows the initial state of the robot. From Fig. 5 (b), it can be seen that the pseudoinverse of the Jacobian matrix control algorithm to guide the expansion of search tree makes the robot continually move towards the goal and avoid the redundant movements of the joints. The quaternion based orientation control is successfully implemented. We achieve a good overall

performance in the regulation of the desired pose of the end-effector. The bisection gradient-decent extend algorithm limits each joint's angular velocity so that the movements of the joints are much smoother. The simulation results show the rapidity and validity of the proposed hybrid algorithm. From Fig. 5 (c), it is obvious that our improved RRT algorithm generates a collision-free path. The error is shown in Fig. 5 (d) which indicates that the desired position and orientation of the redundant manipulator are successfully achieved. The error curve in Fig. 5 (d) is obtained by $e^T e$, where $e = \begin{bmatrix} e_p \\ \mathbf{e}_0 \end{bmatrix} = \begin{bmatrix} P_d - P \\ \mathbf{e}_v \end{bmatrix} \in \mathfrak{R}^6$.

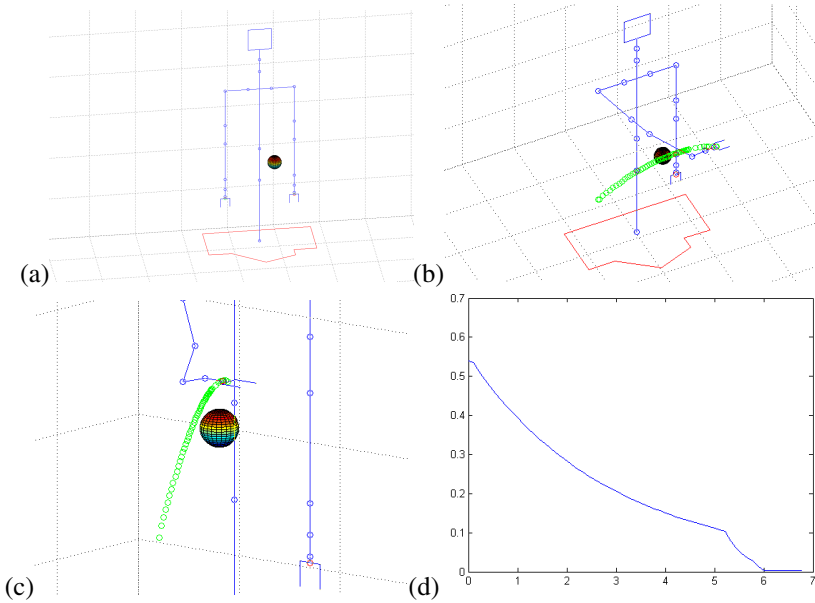


Fig. 5. Simulation results (a) Initial state of robot (b) Computed trajectory towards goal posture (c) Collision-free path (d) Error to the goal

6 Conclusions

We have presented an improved RRT algorithm based on inverse kinematics for motion planning. We have found it to be very effective for redundant manipulator path planning. RRT method can efficiently solve the collision-free path planning problem of high-dimensional robot. Quaternion is applied in the computation of orientation error, and its feedback is augmented into the control scheme for concurrent control. Jacobian pseudoinverse algorithm determines the optimal expansion direction of search tree, and this method speeds up the movement to the goal node. This method applies not only to the static environment, but also can solve the robot path planning in dynamic environment, especially for dynamic path planning of mobile manipulator.

References

1. Kavraki, L.E., Koulountzakis, M.N., Latombe, J.C.: Analysis of probabilistic roadmaps for path planning. *IEEE Trans. on Robotics and Automation* 14(1), 166–171 (1996)
2. Amato, N.M., Wu, Y.: A randomized roadmap method for path and manipulation planning. In: *IEEE International Conference on Robotics and Automation* (1996)
3. LaValle S.: Rapidly-exploring random trees: A new tool for path planning. *Comput. Sci. Dept., Iowa State Univ., Ames, IA, Tech. Rep. TR 98-11* (1998).
4. Kuffner, J., LaValle, S.: RRT-Connect: An efficient approach to single-query path planning. In: *Proc. IEEE International Conference on Robotics and Automation*, pp. 995–1001 (2000)
5. Ge, S.S., Cui, Y.J.: New potential functions for mobile robot path planning. *IEEE Trans. Robotics and Automation* 16(5), 615–620 (2000)
6. Koren, Y., Borenstein, J.: Potential field methods and their inherent limitations for mobile robot navigation. In: *Proc. IEEE Conference on Robotics and Automation*, pp. 1398–1404 (1991)
7. Lee, D.T.: Proximity and reachability in the plane. Ph. D. thesis,ampaign, IL, USA (1978)
8. Stuelpnagel, J.: On the parametrization of the three-dimensional rotation group, pp. 422–430. *SIAM review* (1964)
9. Kuipers, J.B.: Quaternions and rotation sequences: a primer with applications to orbits, aerospace, and virtual reality. Princeton University Press (1999)
10. Xian, B., Queiroz, M.S., Dawson, D.M., Walker, L.: Task-space tracking control of redundant robot manipulators via quaternion feedback. *IEEE. Transactions on Robotics and Automation* 20(1), 160–167 (2004)
11. Yuan, J.S.C.: Closed-loop manipulator control using quaternion feedback. *IEEE Journal of Robotics and Automation* 4(4), 434–440 (1988)
12. Quinlan, S.: Real-time modification of collision-free paths. Ph.D. dissertation. Stanford University (1994)
13. Liegeois, A.: Automatic supervisory control of the configuration and behavior of multibody mechanisms. *IEEE Trans. Systems, Man, and Cybernetics* 7(12), 868–871 (1977)

Dynamic Research of a Novel Exoskeleton with Level Walking

Dalei Pan and Feng Gao

Shanghai Jiao Tong University, Shanghai, China
pandalei100new@126.com, gaofengsjtu@gmail.com

Abstract. This article proposes a novel type of series-parallel lower extremity exoskeleton driven by hydraulic actuator. Each leg of the exoskeleton has 6 DOFs, which can walk like human and carry heavy loads. Inverse dynamic walking model is conducted to analyze the driving torques and driving power during the gait. The effects of different loads and speed are simulated and discussed. These performance analyses provide a basis to the design of the control law and the estimation of the hydraulic actuator parameters for the exoskeleton.

Keywords: Lower extremity exoskeleton, series-parallel mechanism, inverse dynamic, level walking, numerical simulation.

1 Introduction

Wheeled vehicles are the typical tools to carry heavy loads, but are often incapable of transporting over rough terrain, such as rocky slopes and staircases[1]. And people need enhance their strength, endurance and speed in many situations, such as rescue workers running on rough terrain, soldiers with heavy loads and persons with walking disabilities[2]. Within these settings, legged locomotion becomes attractive. Legged exoskeletons, worn by human, have been developed[3] to enhance the physical ability to carry heavy objects or fulfill daily life.

Lower extremity exoskeletons are generally for carrying heavy objects long distances and the paths are not passable by wheeled vehicles[4]. So the workspace of the mechanisms, the power and torques of the actuator, and the battery capacity are the three key technologies of lower extremity exoskeletons. Some exoskeletons[5] have already been developed and achieved good results, such as BLEEX[6], but are far from enough. In order to help wearer carry more heavy loads, it is a new topic to adopt series-parallel mechanisms to design a novel exoskeleton driven by hydraulic actuators, which can provide much more force and power with smaller volume compared to servo motor.

Walking is one of the basic capacities of human[7]. Many researchers focused on the effects of loads and speed on the joint torques and joint power of human walking[8]. Some biomechanical simulation softwares, such as Opensim[9] or Anybody[10], can also analyze human walking to get the joint torques and joint power. Walking is also the most important thing to do for the exoskeleton. However,

little research is done about the driving joint torques and driving joint power of exoskeleton during humanoid walking, which are required to know to design actuators.

In view of the development of legged exoskeleton, which can carry heavy loads and walk like human, this article proposes a novel type of lower extremity exoskeleton with series-parallel topology. The rest of this paper is organized as follows. Firstly, the exoskeleton mechanism is described. Then, a mapping from the positions of human lower extremity joints to exoskeleton joints is established, which provides data for dynamic simulation. Besides, Kane's method is used to conduct the exoskeleton inverse dynamics. In the last section, the typical humanoid gait, which is level walking, is simulated on the exoskeleton, and effects of loads and speed of level walking on driving torques and power are calculated. These performance analyses provide a basis to the design of the control law and the estimation of the hydraulic actuator parameters for the exoskeleton.

2 Description of the Novel Exoskeleton Mechanism

A three-dimensional draft model of the exoskeleton and DOF schematic of single leg is shown in Figure 1. Each leg has 6 DOFs and can be divided into $T-P$, $I-G$ and $J-Q$ parts. $T-P$ corresponds to the two human hip rotational degrees of freedom, where P is passive joint and T is driven by hydraulic actuator. $T-P$ can achieve that leg rotates around sagittal axis and vertical axis. $I-G$ is the main part of leg, which consists of 8 links. Between link BF and CE , there is a composite joint D . Link DJ can slide through joint D along line IG , which is angular bisector of BIC , but link DJ can't slide through joint G or rotate around joint G . $I-G$ contains 2 DOFs, which are rotation around I and slide along line IG in sagittal plane, so it can substitute for knee. Link IB and IC are driven by hydraulic actuators, which can rotate around joint I . $I-G$ is parallel structure, so it is weight-bearing. To simplify the mechanism, $J-Q$ corresponds to human foot and contains only two joints, where Q is passive joint and J is driven by hydraulic actuator. So joint T , joint J , link IB around joint I and link IC around joint I are actuated, the rest joint P and joint Q are unactuated and compliant.

3 Normal Gait Research

Before researching exoskeleton humanoid gaits, human gaits analysis is considered known. The objective of this section is to define a mapping from the positions of human lower extremity joints to exoskeleton joints.

3.1 Human Gaits Analysis

Level walking is the most important gait. The motion on vertical plane and coronal plane have little effect during walking, and the joint torques and joint power on them are much smaller. Therefore, to simplify the dynamic model, only sagittal plane motion of the exoskeleton will be researched. The hip, knee and ankle angle of right leg during gait cycle are shown in figure 2, and vertical reaction force and

anterior/posterior reaction force of ground and human foot are shown in figure 3. About former 60% of the cycle is stance phase, the rest is swing phase. The cycle duration of level walking is 1.1s, where walking speed of level walking is 1.3 m/s. Those data were collected from the OpenSim software and lots of experiments[11].

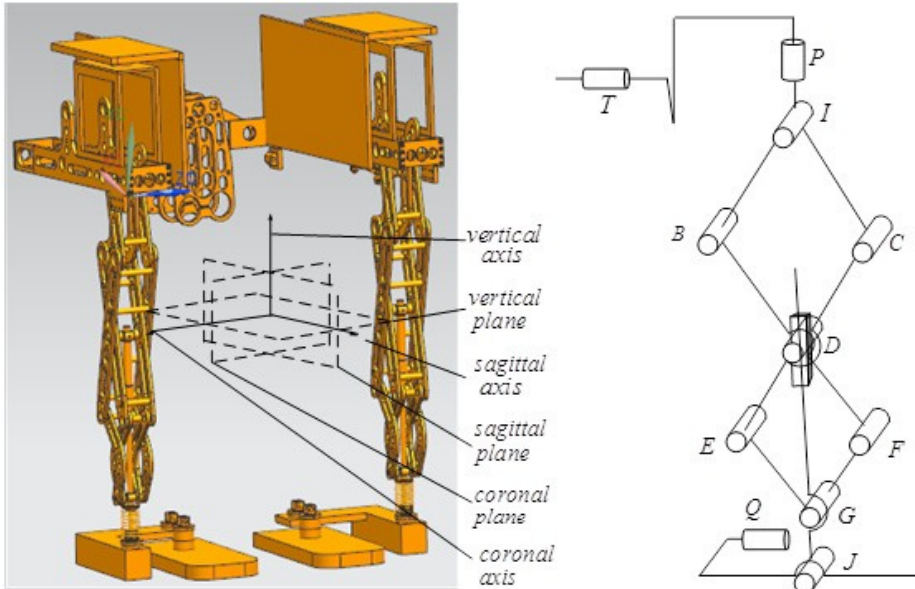


Fig. 1. 3D draft model of the exoskeleton and DOF schematic of single leg

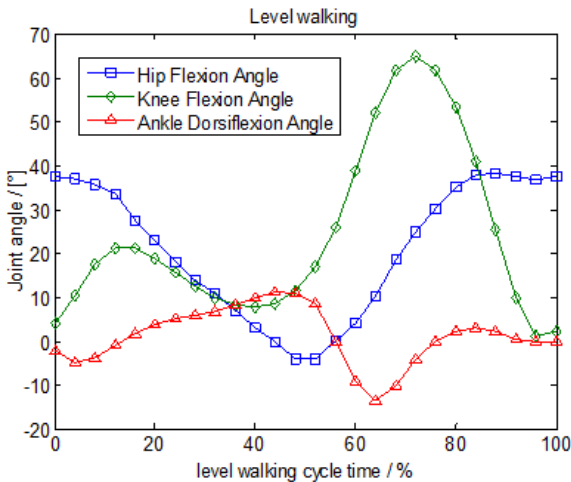


Fig. 2. Hip, knee and ankle angle of right leg during gait cycle

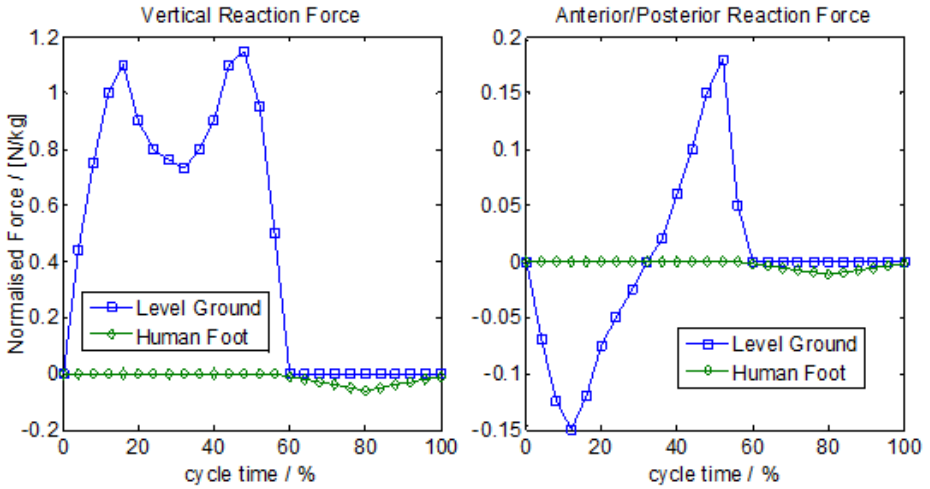


Fig. 3. Vertical and anterior/posterior reaction force of ground and human foot during gait cycle

F_v and F_{ap} , which are vertical and level force of human foot and ground on the exoskeleton during the gait cycle, can be written as

$$F_v = G \cdot F_{gv} + G_p \cdot F_{pv} \tag{1}$$

$$F_{ap} = G \cdot F_{ap} + G_p \cdot F_{pap} \tag{2}$$

where G is the total mass of human and the exoskeleton, G_p is the mass of human, F_{gv} and F_{pv} are vertical reaction force of ground and human foot, F_{ap} and F_{pap} are anterior/posterior reaction force of ground and human foot, which can be referred in Figure 3.

3.2 Position Analysis of Human Leg and Exoskeleton

Schematic of human lower extremity mechanisms is shown in Figure 4, where H is short for hip joint, K is short for knee joint and A is short for ankle joint. The coordinates of H , K and A are $(0,0)$, (x_k, y_k) and (x_a, y_a) respectively, and the expressions of point A can be written as

$$\begin{cases} x_a = l_t \sin(\theta_{hf}) + l_s \sin(\theta_k) \\ y_a = -l_t \cos(\theta_{hf}) - l_s \cos(\theta_k) \end{cases} \tag{3}$$

where θ_{hf} , θ_k and θ_a denote the angle of each joints and can be referred in Figure 2, and l_t , l_s and l_a denote the length or height of thigh, shank and foot.

Schematic of the exoskeleton in sagittal plane is shown in Figure 5, and point J can be generated as

$$\begin{cases} x_j = x_i - 2(L_1 + L_2) \sin\left(\frac{\alpha_2 + \alpha_1}{2}\right) \sin\left(\frac{\alpha_2 - \alpha_1}{2}\right) - l_1 \sin\left(\frac{\alpha_2 - \alpha_1}{2}\right) \\ y_j = y_i - 2(L_1 + L_2) \sin\left(\frac{\alpha_2 + \alpha_1}{2}\right) \cos\left(\frac{\alpha_2 - \alpha_1}{2}\right) - l_1 \cos\left(\frac{\alpha_2 - \alpha_1}{2}\right) \end{cases} \quad (4)$$

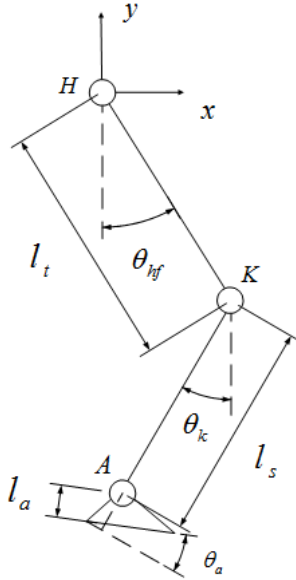


Fig. 4. Schematic of human lower extremity mechanisms

where L_1 denotes the length of links IB and IC , L_2 denotes the length of links EG and FG , and l_1 is the length of GJ . α_1 , α_2 and α_3 denotes the angle of the actuated joint IB , IC and J .

To solve α_1 and α_2 , make equations in (3) equal to equations (4), where joint J corresponds to human ankle joint A . That is

$$\begin{cases} x_j = x_a \\ y_j = y_a \end{cases} \quad (5)$$

The expressions of α_1 and α_2 can be solved by the MATLAB software. α_3 can be read from ankle dorsiflexion angle in Figure 2. The numerical solution of the derivative and second derivative of α_1 , α_2 and α_3 , which denote the speed and acceleration of joint IB , IC and J , can also be solved by the MATLAB software when

α_1 , α_2 and α_3 are numerical simulated or read. As part of input of numerical dynamic simulation, they are required to know.

4 Dynamic Modeling

Essentially all methods for obtaining dynamic equations of motion are equivalent[12]. However, the ease of use of the various methods differs and some are more suited for multi-body dynamics than others[13]. With the use of generalized forces the need for examining interactive and constraint forces between bodies is eliminated. The only differentiating required to compute velocities and accelerations can be obtained through the use of algorithms based on vector product. Kane's method offers an elegant means to develop the dynamics equations for multi-body systems that leads itself to automated numerical computation[14].

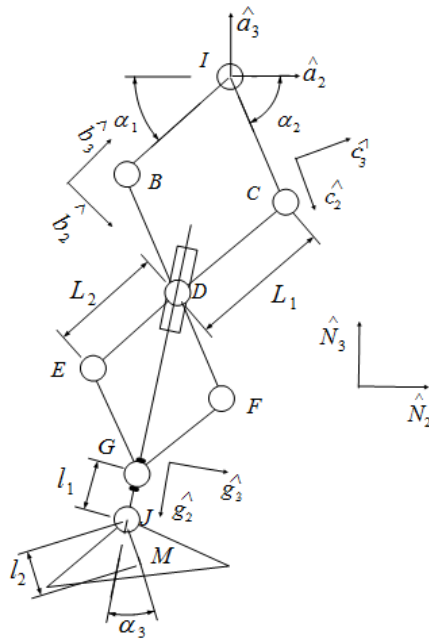


Fig. 5. Schematic of the exoskeleton in sagittal plane

For the purpose of analysis, the following notation and coordinate systems are defined, which are shown in Figure 5.

α_r : generalized coordinate, like α_1 , α_2 and α_3 ; u_r : generalized speed,

$$u_r = \frac{d\alpha_r}{dt} = \dot{\alpha}_r; \quad v^{N \rightarrow P} : \text{velocity of } P \text{ with respect to the } N \text{ reference frame ;}$$

v : velocity of the center of mass of link Q ; v_r : partial velocity,
 $v_r = \frac{\partial v}{\partial u_r}$; c_n or s_n : $\cos(n)$ or $\sin(n)$

Here are five coordinates, \hat{N} is world coordinate, \hat{a} , \hat{b} , \hat{c} , \hat{g} are local coordinates, $\hat{a} // \hat{n}$, $\hat{b}_3 // IB$, $\hat{c}_2 // IC$, $\hat{g}_2 // GJ$, $\hat{a}_1 // \hat{b}_1 // \hat{c}_1 // \hat{g}_1 // \hat{n}_1$.

The generalized active force F_r is defined as:

$$F_r = \sum_{r=1,2,3} \sum_{link} (F_{link} \cdot v_r + T_{link} \cdot \omega_r) \tag{6}$$

where F_{link} and T_{link} is active force and moment on each link.

So, F_r can be generated as:

$$\begin{aligned} F_r = & (F_v \hat{a}_3 - m_{MJ} g \hat{a}_3 + F_{ap} \hat{a}_2) \cdot v_r \\ & + T_j \hat{a}_1 \cdot \omega_r - m_{EG} g \hat{a}_3 \cdot v_r + T_{ic} \hat{a}_1 \cdot \omega_r \\ & - m_{FG} g \hat{a}_3 \cdot v_r - m_{BF} g \hat{a}_3 \cdot v_r - m_{GJ} g \hat{a}_3 \cdot v_r \\ & - m_{CE} g \hat{a}_3 \cdot v_r - [m_{IB} g \hat{a}_3 + \frac{1}{2} G_h (\hat{a}_2 + \hat{a}_3)] \cdot v_r \\ & + [\frac{1}{2} G_h (\hat{a}_2 - \hat{a}_3) - m_{IC} g \hat{a}_3] \cdot v_r + T_{ib} \hat{a}_1 \cdot \omega_r \end{aligned} \tag{7}$$

where T_j , T_{ib} , T_{ic} are driving torques of joint J , joint IB , joint IC , G_h is the load force of gravity, m_{MJ} , m_{GJ} , m_{EG} , m_{FG} , m_{BF} , m_{CE} , m_{IB} , m_{IC} are mass of each link.

The generalized active force F_r^* is defined as:

$$\begin{aligned} F_r^* = & \sum_{link} \{ (-m_{link} a) \cdot v_r - \\ & (I \cdot \alpha + \omega \times I \cdot \omega) \cdot \omega \} \end{aligned} \tag{8}$$

where m_{link} and I are the mass and inertia of each link, and each link does not spin about its longitudinal axis, the corresponding inertia parameter is set as zero[15]

$$\vec{I}^{link*} = m_{link} \begin{bmatrix} \frac{1}{12} L_{link}^2 & 0 & 0 \\ 0 & \frac{1}{12} L_{link}^2 & 0 \\ 0 & 0 & 0 \end{bmatrix}$$

Kane's equations can be constructed as:

$$F_r + F_r^* = 0, \quad r = 1, 2, 3 \tag{9}$$

Then solve the kane equations (9) by MATLAB, the expressions of T_j , T_{ib} , T_{ic} can be obtained. The driving power of each actuated joint can be written as

$$PowerT_j = T_j \cdot u_3 \tag{10}$$

$$PowerT_{ib} = T_{ib} \cdot u_1 \tag{11}$$

$$PowerT_{ic} = T_{ic} \cdot u_2 \tag{12}$$

5 Numerical Simulation

In this section, the exoskeleton humanoid gaits are simulated, and the driving torque and power computation are presented. The program based on the algorithm is developed using the MATLAB software.

The parameters of human lower extremity used for simulation are as follows: $l_t = 0.496m$, $l_s = 0.396m$, $l_a = 0.105m$, $G_p = 80kg$, which the height of person is about between 175 cm and 180 cm. Actually the exoskeleton can be worn by person of height between 165 cm and 185 cm. And the parameters of exoskeleton are based on the design criteria as follows: $l_1 = 0.05m$, $L_1 = L_2 = 0.232m$, $l_2 = 0.075m$, $G_h = 50kg$, $m_{MJ} = 2kg$, $m_{GJ} = 0.5kg$, $m_{EG} = 1kg$, $m_{FG} = 1.5kg$, $m_{IB} = 1kg$, $m_{IC} = 1kg$, $m_{BF} = 2kg$, $m_{CE} = 2kg$.

As shown in Figure 6, driving torques and driving power of joint J , IB and IC during level walking cycle are simulated. The walking speed is 1.3m/s and the load is 50kg.

Peak driving torques and driving power are very important for designing hydraulic actuators. Moreover, walking speed and loads are two important factors of driving torques and driving power. To observe the effects of them, the peak torques and power of level walking with different speed, while the load is 50 kg, is simulated and present in Figure7 and Figure 8. And the peak torques and power of level walking with different loads, while the speed is 1.3 m/s, is shown in Figure 9 and Figure 10. Some peak driving torques and power exponentially increase as speed increases, such as T_{ib} in Figure 7 and $PowerT_{ib}$ in Figure 8. Some peak driving torques and power linearly increase as the loads increases, such as T_{ic} in Figure 9 and

$PowerT_{ic}$ in Figure 10. And some peak torques and power seem to be effected little, like T_{ic} in Figure 7 and T_{ib} in Figure 9.

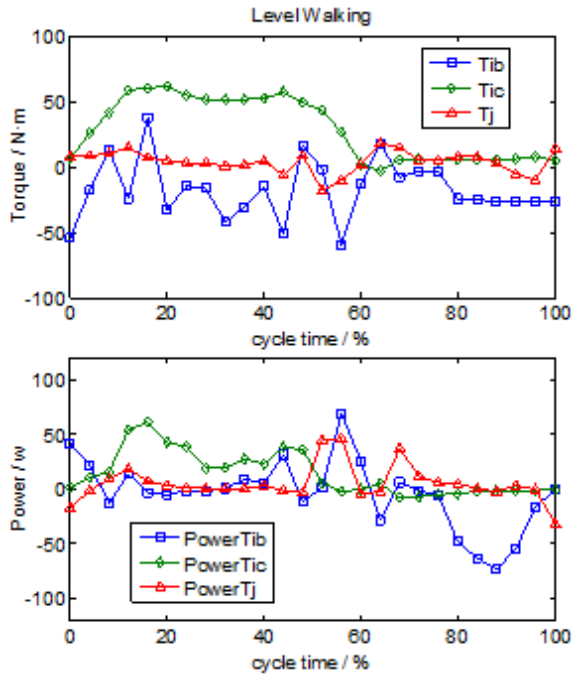


Fig. 6. The driving torques and power of joint J , IB and IC during level walking cycle

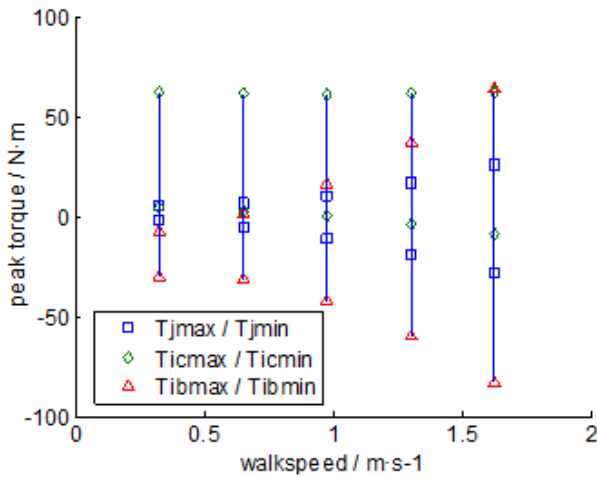


Fig. 7. Peak torques of joint J , IB and IC during level walking cycle with different speed

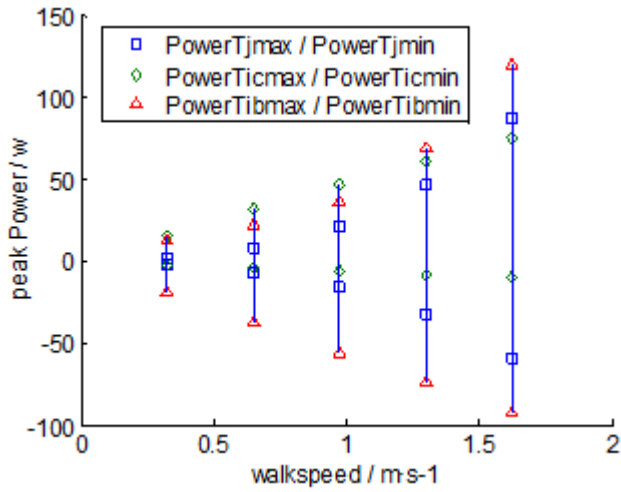


Fig. 8. Peak power of joint *J*, *IB* and *IC* during level walking cycle with different speed

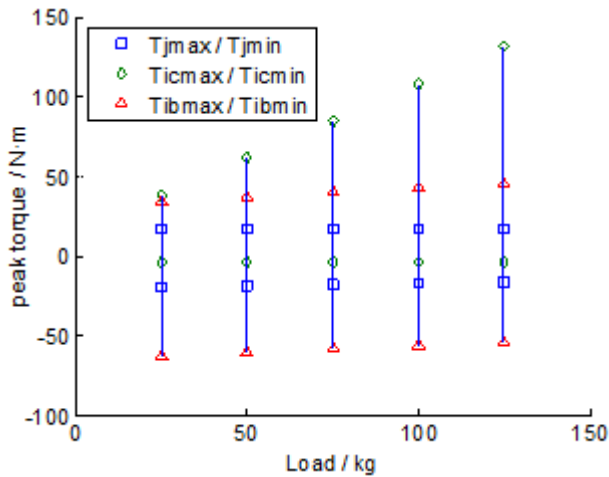


Fig. 9. Peak torques of joint *J*, *IB* and *IC* during level walking cycle with different loads

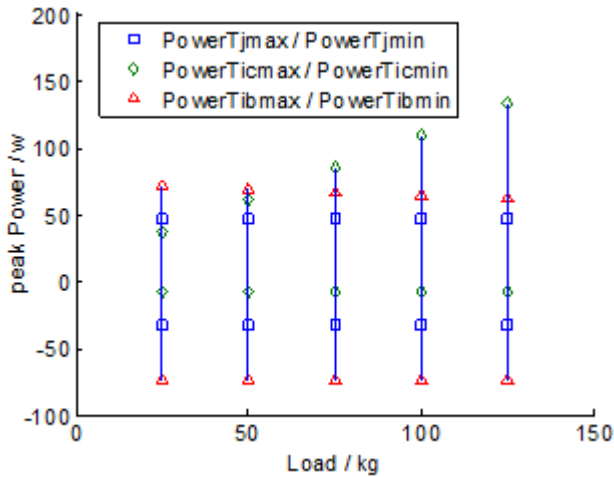


Fig. 10. Peak power of joint J , IB and IC during level walking cycle with different loads

6 Conclusion and Future Work

This novel series-parallel mechanisms is designed and firstly used in the legged exoskeleton, which can bear heavier loads than series mechanisms and have larger workspace than parallel mechanisms. Kane's method is used to conduct the exoskeleton inverse dynamics. Level walking gait is simulated on the exoskeleton, and effects of load and speed of level walking on driving torques and power are calculated. More gaits will be simulated in the future and these performance analyses provide a basis to the design of the control law and the estimation of the hydraulic actuator parameters for the exoskeleton.

References

1. Chu, A., Kazerooni, H., Zoss, B.A.: On the Biomimetic Design of the Berkeley Lower Extremity Exoskeleton. In: Proceedings of the 2005 IEEE International Conference on Robotics and Automation, pp. 4356–4363 (2005)
2. Veneman, J.F., Kruidhof, R., Hekman, E.E.G., et al.: Design and evaluation of the LOPES exoskeleton robot for interactive gait rehabilitation. *IEEE Transactions on Neural Systems and Rehabilitation Engineering* 15(3), 379–386 (2007)
3. Kazerooni, H., Racine, J.-L., Huang, L., et al.: On the control of the berkeley lower extremity exoskeleton (BLEEX). In: Proceedings of the 2005 IEEE International Conference on Robotics and Automation, pp. 4364–4371 (2005)
4. Kazerooni, H.: Hybrid Control of the Berkeley Lower Extremity Exoskeleton (BLEEX). *The International Journal of Robotics Research* 25(5-6), 561–573 (2006)
5. Banala, S.K., Kim, S.H., Agrawal, S.K., et al.: Robot assisted gait training with active leg exoskeleton (ALEX). *IEEE Transactions on Neural Systems and Rehabilitation Engineering* 17(1), 2–8 (2009)

6. Zoss, B., Kazerooni, A.: Biomechanical design of the Berkeley lower extremity exoskeleton (BLEEX). *IEEE/ASME Transactions on Mechatronics* 11(2), 128–138 (2006)
7. Abe, D., Muraki, S., Yasukouchi, A.: Ergonomic effects of load carriage on energy cost of gradient walking. *Applied Ergonomics* 39, 144–149 (2008)
8. Abe., D., Yanagawa., K., Niihata., S.: Effects of load carriage load position and walking speed. *Applied ergonomics* 35, 329–335 (2004)
9. Delp., S.L., Anderson., F.C., Arnold., A.S., et al.: OpenSim open-source software to create and analyze dynamic simulations of movement. *IEEE Transactions on Biomedical Engineering* 54(11), 1940–1950 (2007)
10. De Zee, M., Hansen, L., Wong, C., Rasmussen, J., Simonsen, E.B.: A generic detailed rigid-body lumbar spine model. *Journal of biomechanics* 40(6), 1219–1227 (2007)
11. Riener., R., Rabuffetti., M., Frigo., C.: Stair ascent and descent at different inclinations. *Gait and posture* 15, 32–44 (2002)
12. Shabana, A.A.: Flexible multibody dynamics review of past and recent developments. *Multibody System Dynamics* 1, 189–222 (1997)
13. Cuadrado., J., Cardenal., J., Bayo, E.: Modeling and solution methods for efficient real-time simulation of multibody dynamics. *Multibody System Dynamics* 1, 259–280 (1997)
14. Kane, T.R., Levinson, D.A.: The Use of Kane's Dynamical Equations in Robotics. *The International Journal of Robotics Research* 2(3), 3–21 (1983)
15. Bai, Y., Gao, F., Guo, W., Yue, Y.: Kinematic and dynamic analyses of the multi-actuated mechanical press with parallel topology. *Proceedings of the Institution of Mechanical Engineers, Part C: Journal of Mechanical Engineering Science* 226(10), 2573–2588 (2012)

Mobility Analysis of Two Exechon-Liked Parallel Mechanisms

Xinxue Chai, Qiaohong Chen, Jigang Ma, and Qinchuan Li*

Mechatronic Institute, Zhejiang Sci-Tech University,
Hangzhou, Zhejiang 310018, China
lqchuan@zstu.edu.cn

Abstract. Parallel mechanisms (PM) with two rotations and one translation (2R1T) have been used extensively. The parallel module of the Exechon robot is one of the most successful cases, which is equal to a 2-SPR-UPR PM. Few researchers mentioned what would happen to the PM's DOF if the arrangement of limbs were changed. Using screw theory, we investigate the mobility of the 2-SPR-UPR PM with two different arrangements of limbs. It is shown that the 2-SPR-UPR PM has two DOFs when its limbs are arranged to be symmetrical or to be parallel.

Keywords: Parallel mechanism, arrangement, mobility.

1 Introduction

The 3-DOF 2R1T PM is one of the significant members in the lower-mobility PMs. It has been used as telescope supporting device [1], motion simulator [2], micro-manipulator [3], coordinate measuring machine [4], Z3 head in machine tool [5]. Particularly, the parallel part of the Exechon[6], which is kinematically equal to a 2-UPR-SPR PM, is one of the most successful cases in the 2R1T PMs. It consists of two UPR limbs and one SPR limb, where U denotes the universal joint, P denotes the prismatic joint, R denotes the revolute joint, S denotes the spherical joint.

Researchers often focused on kinematics analysis [7-8], dimensional synthesis [9-10], singularity analysis [11-12] and dynamics [13-14] of 2R1T PMs. However, few of them mentioned what the DOF would change if the same limbs were arranged obeying different geometrical conditions. The Grübler-Kutzbach criterion [15-17] is a classic method but not applicable universally. Errorneous results may be obtained when it is applied to some overconstrained PMs. Screw theory [18] can be used to analyze the mobility of the spatial mechanisms.

In this paper, we analyzed the mobility of two Exechon-like parallel mechanism. The two PMs both were 2-SPR-UPR PMs, but the limbs were arranged differently. Using screw theory, we can get the constraint force and couple. Furthermore the mobility of this PM can be obtained.

* Corresponding author.

2 Mobility Analysis of a 2-SPR-UPR PM in Which Three Limbs Are Arranged Symmetrically

2.1 Description of Architecture

A 2-SPR-UPR PM contains two SPR limbs and one UPR limb. The SPR limb is consisting of a S joint, a P joint and a R joint. The UPR limb is consisting of a U joint, a P joint and a R joint. The 2-SPR-UPR PM in which three limbs are arranged symmetrically, namely, the angles between each limb's first revolute joint axis of U joint or S joint are equal to 120° , as shown in Fig. 1. Limb 1 and limb 3 are both SPR limbs. A_1 and A_3 are the central points of the S joint in limb 1 and limb 3. B_1 and B_3 are central points of the revolute joint which belongs to limb 1 and limb 3 respectively. The revolute joint axis of limb 1 and limb 3 is parallel to the second revolute joint axis of its S joint, respectively. Limb 2 is a UPR limb. A_2 is the central point of the U joint, B_2 is the central point of its revolute joint. The revolute joint axis of limb 2 is parallel to the second revolute joint of U joint.

According to the PM's structure, we set up the fixed reference frame as shown in Fig. 1. The x axis is coincident with A_1A_3 , the y axis is coincident with the first axis of U joint which also connects the fixed platform.

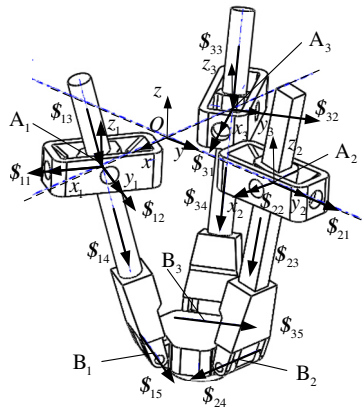


Fig. 1. 2-SPR-UPR PM are arranged symmetrically

2.2 Mobility Analysis

In the reference frame $O-xyz$ in Fig. 1, the coordinate of point A_1 is $(x_{A1}, 0, 0)$, the coordinate of point A_2 is $(0, y_{A2}, 0)$, and the coordinate of point A_3 is $(x_{A3}, 0, 0)$. Let point A_1 , A_2 and A_3 be the origin of the local reference frame of each limb, respectively. Axis x_i is parallel to the axis of its first revolute joint, and axis z_i is parallel to the z axis of the fixed frame ($i=1,2,3$), as shown in Fig. 1. The coordinate of point B_1 is (x_{B1}, y_{B1}, z_{B1}) in the local frame of limb1; The coordinate of point B_2 is

(x_{B2}, y_{B2}, z_{B2}) in the local frame of limb2; The coordinate of point B_3 is (x_{B3}, y_{B3}, z_{B3}) in the local frame of limb3.

The twist system of limb1 with respect to limb1's local frame is:

$$\begin{aligned}
 {}^1\mathcal{S}_{11} &= (1 \ 0 \ 0 \ ; \ 0 \ 0 \ 0) \\
 {}^1\mathcal{S}_{12} &= (0 \ m_{12} \ n_{12} \ ; \ 0 \ 0 \ 0) \\
 {}^1\mathcal{S}_{13} &= (l_{13} \ n_{12} \ -m_{12} \ ; \ 0 \ 0 \ 0) \\
 {}^1\mathcal{S}_{14} &= (0 \ 0 \ 0 \ ; \ l_{13} \ n_{12} \ -m_{12}) \\
 {}^1\mathcal{S}_{15} &= (0 \ m_{12} \ n_{12} \ ; \ n_{12}y_{B1} - m_{12}z_{B1} \ -n_{12}x_{B1} \ m_{12}x_{B1})
 \end{aligned} \tag{1}$$

where $l_{1i}, m_{1i}, n_{1i} (i = 1, 2, \dots, 5)$ are the direction cosines of the i th twist in limb1.

The reciprocal wrench of equation (1) is:

$${}^1\mathcal{S}_{11}^r = (0 \ m_{12} \ n_{12} \ ; \ 0 \ 0 \ 0) \tag{2}$$

${}^1\mathcal{S}_{11}^r$ in equation (2) denotes a constraint force that is parallel to the axis of the revolute joint connecting the moving platform. And the constraint force passes through point A_1 that is the central point of the S joint in limb 1, as shown in Fig. 2.

The twist system in limb 2 with respect to limb2's local frame is:

$$\begin{aligned}
 {}^2\mathcal{S}_{21} &= (0 \ 1 \ 0 \ ; \ 0 \ 0 \ 0) \\
 {}^2\mathcal{S}_{22} &= (l_{22} \ 0 \ n_{22} \ ; \ 0 \ 0 \ 0) \\
 {}^2\mathcal{S}_{23} &= (0 \ 0 \ 0 \ ; \ n_{22} \ m_{23} \ -l_{22}) \\
 {}^2\mathcal{S}_{24} &= (l_{22} \ 0 \ n_{22} \ ; \ n_{22}y_{B2} - n_{22}x_{B2} + l_{22}z_{B2} \ -l_{22}y_{B2})
 \end{aligned} \tag{3}$$

where $l_{2i}, m_{2i}, n_{2i} (i = 1, 2, \dots, 5)$ are the direction cosines of the i th twist in limb 2.

The reciprocal wrench of equation (3) is:

$$\begin{aligned}
 {}^2\mathcal{S}_{21}^r &= (l_{22} \ 0 \ n_{22} \ ; \ 0 \ 0 \ 0) \\
 {}^2\mathcal{S}_{22}^r &= (0 \ 0 \ 0 \ ; \ n_{22} \ 0 \ -l_{22})
 \end{aligned} \tag{4}$$

${}^2\mathcal{S}_{21}^r$ in equation (4) denotes a constraint force that is parallel to the axis of the revolute joint connecting the moving platform. And the constraint force passes through point A_2 which is the central point of the U joint. ${}^2\mathcal{S}_{22}^r$ denotes a constraint couple, whose direction is the common perpendicular of the first and the second revolute joint axis of limb2's U joint, as shown in Fig.2.

The twist system in limb3 with respect to limb3's local frame is:

$$\begin{aligned}
 {}^3\mathcal{S}_{11} &= (1 \ 0 \ 0 \ ; \ 0 \ 0 \ 0) \\
 {}^3\mathcal{S}_{32} &= (0 \ m_{32} \ n_{32} \ ; \ 0 \ 0 \ 0) \\
 {}^3\mathcal{S}_{33} &= (l_{33} \ n_{32} \ -m_{32} \ ; \ 0 \ 0 \ 0) \\
 {}^3\mathcal{S}_{34} &= (0 \ 0 \ 0 \ ; \ l_{33} \ n_{32} \ -m_{32}) \\
 {}^3\mathcal{S}_{35} &= (0 \ m_{32} \ n_{32} \ ; \ n_{32}y_{B3} - m_{32}z_{B3} \ -n_{32}x_{B3} \ m_{32}x_{B3})
 \end{aligned} \tag{5}$$

where $l_{3i}, m_{3i}, n_{3i} (i=1,2,\dots,5)$ are the direction cosines of the i th twist in limb3.

The reciprocal wrench of equation (5) is:

$${}^3\mathcal{S}_{31}^r = (0 \ m_{32} \ n_{32} \ ; \ 0 \ 0 \ 0) \tag{6}$$

${}^3\mathcal{S}_{31}^r$ in equation (6) denotes a constraint force being parallel to the axis of the revolute joint connecting the moving platform. And the constraint force passes through point A_3 which is the central point of the S joint, as shown in Fig.2.

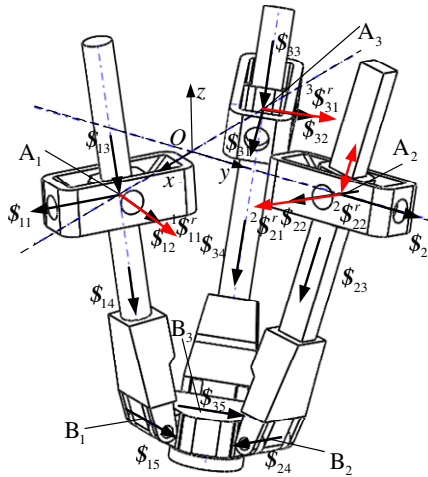


Fig. 2. The constraint force and couple of each limb

The rotation matrix 0R_1 of the local frame of limb 1 $A_1-x_1y_1z_1$ with respect to the fixed frame is:

$${}^0R_1 = R_{z, -\frac{\pi}{6}} = \begin{bmatrix} \sqrt{3}/2 & 1/2 & 0 \\ -1/2 & \sqrt{3}/2 & 0 \\ 0 & 0 & 1 \end{bmatrix} \tag{7}$$

Vector OA_1 can be expressed in a 3×3 skew-symmetric matrix with respect to the fixed frame :

$${}^0W_1 = \begin{bmatrix} 0 & 0 & 0 \\ 0 & 0 & -x_{A1} \\ 0 & x_{A1} & 0 \end{bmatrix} \tag{8}$$

Therefore, the transformation of screw coordinates [19] from local frame $A_1-x_1y_1z_1$ to the fixed frame can be expressed as follow:

$${}^0\tilde{T}_1 = \begin{bmatrix} {}^0R_1 & 0 \\ {}^0W_1 {}^0R_1 & {}^0R_1 \end{bmatrix} \tag{9}$$

Hence, reciprocal wrench ${}^1\mathcal{F}_{11}^r$ of limb1 can be written in the following form:

$${}^0\mathcal{F}_{11}^r = {}^0\tilde{T}_1 {}^1\mathcal{F}_{11}^r = (m_{12} \quad \sqrt{3}m_{12} \quad 2n_{12} \quad ; \quad 0 \quad -2n_{12}x_{A1} \quad \sqrt{3}m_{12}x_{A1}) \tag{10}$$

The rotation matrix 0R_2 of the local frame of limb 2 $A_2-x_2y_2z_2$ with respect to the fixed frame is:

$${}^0R_2 = R_{z,0} = \begin{bmatrix} 1 & 0 & 0 \\ 0 & 1 & 0 \\ 0 & 0 & 1 \end{bmatrix} \tag{11}$$

Vector OA_2 can be expressed in a 3×3 skew-symmetric matrix with respect to the fixed frame :

$${}^0W_2 = \begin{bmatrix} 0 & 0 & y_{A2} \\ 0 & 0 & 0 \\ -y_{A2} & 0 & 0 \end{bmatrix} \tag{12}$$

Hence, reciprocal wrench ${}^2\mathcal{F}_{21}^r$ and ${}^2\mathcal{F}_{21}^r$ of limb2 can be written in the following form:

$$\begin{aligned} {}^0\mathcal{F}_{21}^r &= {}^0\tilde{T}_2 {}^2\mathcal{F}_{21}^r = (l_{22} \quad 0 \quad n_{22} \quad ; \quad n_{22}y_{A2} \quad 0 \quad -l_{22}y_{A2}) \\ {}^0\mathcal{F}_{22}^r &= {}^0\tilde{T}_2 {}^2\mathcal{F}_{22}^r = (0 \quad 0 \quad 0 \quad ; \quad n_{22} \quad 0 \quad -l_{22}) \end{aligned} \tag{13}$$

The rotation matrix 0R_3 of the local frame of limb3 $A_3-x_3y_3z_3$ with respect to the fixed frame is:

$${}^0R_3 = R_{z, \frac{\pi}{6}} = \begin{bmatrix} \sqrt{3}/2 & 1/2 & 0 \\ -1/2 & \sqrt{3}/2 & 0 \\ 0 & 0 & 1 \end{bmatrix} \quad (14)$$

Vector OA_3 can be expressed in a 3×3 skew-symmetric matrix with respect to the fixed frame :

$${}^0W_3 = \begin{bmatrix} 0 & 0 & 0 \\ 0 & 0 & -x_{A3} \\ 0 & x_{A3} & 0 \end{bmatrix} \quad (15)$$

Hence, the reciprocal wrench ${}^3\mathcal{S}_{31}^r$ of the limb3 can be written in the following form:

$${}^0\mathcal{S}_{31}^r = {}^0\tilde{T}_3 {}^3\mathcal{S}_{31}^r = (-m_{32} \quad \sqrt{3}m_{32} \quad 2n_{32} \quad ; \quad 0 \quad -2n_{32}x_{A3} \quad \sqrt{3}m_{32}x_{A3}) \quad (16)$$

The reciprocal wrench of the twist system which consists of constraint forces and couples, namely the twist of the moving platform, is:

$$\begin{aligned} {}^0\mathcal{S}_1^{pm} = & (l_{22} \quad 0 \quad n_{22} \quad ; \quad -\frac{\sqrt{3}m_{12}m_{32}n_{22}^2(x_{A1} - x_{A3})}{2(m_{12}m_{32}n_{22} + l_{22}(m_{12}n_{32} - m_{32}n_{12}))} \\ & \frac{2l_{22}m_{32}n_{12}n_{22}x_{A3} - m_{12}n_{22}(2l_{22}n_{32}x_{A1} + m_{32}n_{22}(x_{A1} + x_{A3}))}{2(m_{12}m_{32}n_{22} + l_{22}(m_{12}n_{32} - m_{32}n_{12}))} \\ & \frac{\sqrt{3}l_{22}m_{12}m_{32}n_{22}(x_{A1} - x_{A3})}{2(m_{12}m_{32}n_{22} + l_{22}(m_{12}n_{32} - m_{32}n_{12}))}) \\ {}^0\mathcal{S}_2^{pm} = & (0 \quad 1 \quad 0 \quad ; \quad \frac{n_{22}(m_{32}n_{12}x_{A1} - m_{12}n_{32}x_{A3})}{m_{12}m_{32}n_{22} + l_{22}(m_{12}n_{32} - m_{32}n_{12})} \\ & \frac{m_{32}n_{12}n_{22}x_{A1} + m_{12}n_{32}(2l_{22}n_{12}(x_{A1} - x_{A3}) + m_{12}n_{22}x_{A3})}{\sqrt{3}(m_{12}m_{32}n_{22} + l_{22}(m_{12}n_{32} - m_{32}n_{12}))} \\ & \frac{l_{22}(m_{12}n_{32}x_{A3} - m_{32}n_{12}x_{A1})}{m_{12}m_{32}n_{22} + l_{22}(m_{12}n_{32} - m_{32}n_{12})}) \end{aligned} \quad (17)$$

Equation (17) denotes that the 2-SPR-UPR PM has two DOFs when its limbs are arranged symmetrically. One is ${}^0\mathcal{S}_1^{pm}$ indicating a rotation about the axis along the unit vector $(l_{22} \quad 0 \quad n_{22})$ which is parallel to the revolute joint of limb2, the other is ${}^0\mathcal{S}_2^{pm}$ indicating a helical motion about the axis along the unit vector $(0 \quad 1 \quad 0)$ which is parallel to axis y.

3 Mobility of a 2-SPR-UPR PM in Which Three Limbs Are Arranged Parallely

3.1 Description of Architecture

A 2-SPR-UPR PM which three limbs are arranged parallely, namely, each limb's first revolute joint axis of U joint or S joint are parallel to each other, as shown in Fig.3. Others are the same with the 2-SPR-UPR PM in which three limbs are arranged symmetrically.

According to the PM's architecture, we set up the fixed reference frame as shown in Fig. 3. The x axis is coincident with A_1A_3 , the y axis is coincident with the first axis of the U joint which also connects with the fixed platform.

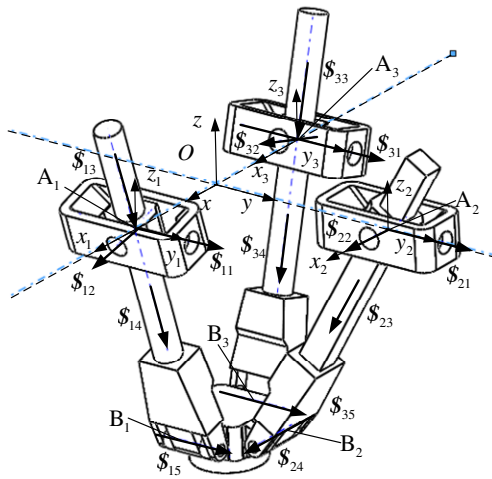


Fig. 3. 2-SPR-UPR PM are arranged parallely

3.2 Mobility Analysis

In the reference frame $O-xyz$ in Fig. 3, the coordinate of point A_1 is $(x_{A1}, 0, 0)$, the coordinate of point A_2 is $(0, y_{A2}, 0)$, and the coordinate of point A_3 is $(x_{A3}, 0, 0)$. Let point A_1 , A_2 and A_3 be the original of local reference frame of each limb, respectively. Axis y_i is parallel to the axis of its first revolute joint, axis z_i is parallel to the z axis of the fixed frame ($i=1,2,3$), as shown in Fig. 3. Coordinate of point B_1 is (x_{B1}, y_{B1}, z_{B1}) in the local frame of limb1; Coordinate of point B_2 is (x_{B2}, y_{B2}, z_{B2}) in the local frame of limb2; Coordinate of point B_3 is (x_{B3}, y_{B3}, z_{B3}) in the local frame of limb3.

The twist system in limb1 with respect to limb1's local frame is:

$$\begin{aligned}
 {}^1\mathcal{S}_{11} &= (0 \quad 1 \quad 0 \quad ; \quad 0 \quad 0 \quad 0) \\
 {}^1\mathcal{S}_{12} &= (l_{12} \quad 0 \quad n_{12} \quad ; \quad 0 \quad 0 \quad 0) \\
 {}^1\mathcal{S}_{13} &= (n_{12} \quad m_{13} \quad -l_{12} \quad ; \quad 0 \quad 0 \quad 0) \\
 {}^1\mathcal{S}_{14} &= (0 \quad 0 \quad 0 \quad ; \quad n_{12} \quad m_{13} \quad -l_{12}) \\
 {}^1\mathcal{S}_{15} &= (l_{15} \quad 1 \quad \frac{m_{13} + l_{15}n_{12}}{l_{12}} \quad ; \quad \frac{m_{13}y_{B1}}{l_{12}} + \frac{l_{15}n_{12}y_{B1}}{l_{12}} - z_{B1} \\
 &\quad - \frac{m_{13}x_{B1}}{l_{12}} - \frac{l_{15}n_{12}x_{B1}}{l_{12}} + l_{15}z_{B1} \quad x_{B1} - l_{15}y_{B1})
 \end{aligned} \tag{18}$$

where $l_{1i}, m_{1i}, n_{1i} (i=1,2,\dots,5)$ are the direction cosines of the i th twist in limb 1.

The reciprocal wrench of equation (18) is:

$${}^1\mathcal{S}_{11}^r = (l_{15} \quad 1 \quad \frac{m_{13} + l_{15}n_{12}}{l_{12}} \quad ; \quad 0 \quad 0 \quad 0) \tag{19}$$

${}^1\mathcal{S}_{11}^r$ in equation (19) denotes a constraint force that is parallel to the axis of the revolute joint connecting the moving platform. And the constraint force passes through point A_1 that is the central point of the S joint in limb 1, as shown in Fig. 4.

Because of the local frame of limb 2 when limbs arranged parallelly and when limbs arranged symmetrically are the same, the twist system in limb2 with respect to limb2's local frame is equal to equation (3), and its reciprocal wrench is equal to equation (4). ${}^2\mathcal{S}_{21}^r$ and ${}^2\mathcal{S}_{22}^r$ also has the same direction and position, as shown in Fig. 4.

The twist system in limb3 with respect to limb3's local frame is:

$$\begin{aligned}
 {}^3\mathcal{S}_{31} &= (0 \quad 1 \quad 0 \quad ; \quad 0 \quad 0 \quad 0) \\
 {}^3\mathcal{S}_{32} &= (l_{32} \quad 0 \quad n_{32} \quad ; \quad 0 \quad 0 \quad 0) \\
 {}^3\mathcal{S}_{33} &= (n_{32} \quad m_{33} \quad -l_{32} \quad ; \quad 0 \quad 0 \quad 0) \\
 {}^3\mathcal{S}_{34} &= (0 \quad 0 \quad 0 \quad ; \quad n_{32} \quad m_{33} \quad -l_{32}) \\
 {}^3\mathcal{S}_{35} &= (l_{35} \quad 1 \quad \frac{m_{33} + l_{35}n_{32}}{l_{32}} \quad ; \quad \frac{m_{33}y_{B3}}{l_{32}} + \frac{l_{35}n_{32}y_{B3}}{l_{32}} - z_{B3} \\
 &\quad - \frac{m_{33}x_{B3}}{l_{32}} - \frac{l_{35}n_{32}x_{B3}}{l_{32}} + l_{35}z_{B3} \quad x_{B3} - l_{35}y_{B3})
 \end{aligned} \tag{20}$$

where $l_{3i}, m_{3i}, n_{3i} (i=1,2,\dots,5)$ are the direction cosines of the i th twist in limb3.

The reciprocal wrench of equation (20) is:

$${}^3\mathcal{S}_{31}^r = (0 \quad m_{32} \quad n_{32} \quad ; \quad 0 \quad 0 \quad 0) \tag{21}$$

${}^3\mathcal{S}_{31}^r$ in equation (21) denotes a constraint force, that is parallel to the axis of the revolute joint connecting the moving platform. And the constraint force passes through point A_3 which is the central point of the S joint, as shown in Fig. 4.

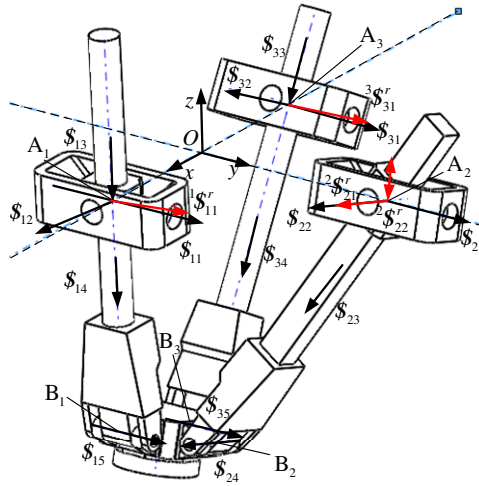


Fig. 4. The constraint force and couple of each limb

The rotation matrix ${}^0R_1, {}^0R_2, {}^0R_3$ of its local frame is:

$${}^0R_1 = {}^0R_2 = {}^0R_3 = R_{z,0} = \begin{bmatrix} 1 & 0 & 0 \\ 0 & 1 & 0 \\ 0 & 0 & 1 \end{bmatrix} \tag{22}$$

Vector OA_1 can be expressed in a 3x3 skew-symmetric matrix with respect to the fixed frame :

$${}^0W_1 = \begin{bmatrix} 0 & 0 & 0 \\ 0 & 0 & -x_{A1} \\ 0 & x_{A1} & 0 \end{bmatrix} \tag{23}$$

Hence, reciprocal wrench ${}^1\mathcal{S}_{11}^r$ of limb1 can be written in the following form:

$${}^0\mathcal{S}_{11}^r = {}^0\tilde{T}_1 {}^1\mathcal{S}_{11}^r = (l_{15} \quad 1 \quad \frac{m_{13} + l_{15}n_{12}}{l_{12}} ; 0 \quad -\frac{m_{13} + l_{15}n_{12}}{l_{12}}x_{A1} \quad x_{A1}) \tag{24}$$

Vector OA_2 can be expressed in a 3x3 skew-symmetric matrix with respect to the fixed frame :

$${}^0W_2 = \begin{bmatrix} 0 & 0 & y_{A2} \\ 0 & 0 & 0 \\ -y_{A2} & 0 & 0 \end{bmatrix} \quad (25)$$

Hence, reciprocal wrench ${}^2\mathcal{F}_{21}^r$ and ${}^2\mathcal{F}_{21}^r$ of limb2 can be written in the following form:

$$\begin{aligned} {}^0\mathcal{F}_{21}^r &= {}^0\tilde{T}_2 {}^2\mathcal{F}_{21}^r = (l_{22} \quad 0 \quad n_{22} \quad ; \quad n_{22}y_{A2} \quad 0 \quad -l_{22}y_{A2}) \\ {}^0\mathcal{F}_{22}^r &= {}^0\tilde{T}_2 {}^2\mathcal{F}_{22}^r = (0 \quad 0 \quad 0 \quad ; \quad n_{22} \quad 0 \quad -l_{22}) \end{aligned} \quad (26)$$

Vector OA_3 can be expressed in a 3×3 skew-symmetric matrix with respect to the fixed frame :

$${}^0W_3 = \begin{bmatrix} 0 & 0 & 0 \\ 0 & 0 & -x_{A3} \\ 0 & x_{A3} & 0 \end{bmatrix} \quad (27)$$

Hence, the reciprocal wrench ${}^3\mathcal{F}_{31}^r$ of limb3 can be written in the following form:

$${}^0\mathcal{F}_{31}^r = {}^0\tilde{T}_3 {}^3\mathcal{F}_{31}^r = (l_{35} \quad 1 \quad \frac{m_{33} + l_{35}n_{32}}{l_{32}} \quad ; \quad 0 \quad -\frac{m_{33} + l_{35}n_{32}}{l_{32}}x_{A3} \quad x_{A3}) \quad (28)$$

The reciprocal wrench of the twist system which consisting of constraint forces and couples, namely the twist of the moving platform, is:

$$\begin{aligned} {}^0\mathcal{F}_1^{pm} &= (l_{22} \quad 0 \quad n_{22} \quad ; \quad \frac{l_{12}l_{32}n_{22}^2(x_{A3} - x_{A1})}{l_{12}l_{32}(l_{15} - l_{35})n_{22} + l_{22}(l_{12}(m_{33} + l_{35}n_{32}) - l_{32}(m_{13} + l_{15}n_{32}))} \\ &\quad \frac{l_{12}l_{32}(m_{13} + l_{15}n_{32})n_{22}x_{A3} - l_{12}n_{22}(l_{22}(m_{33} + l_{35}n_{32})x_{A1} + l_{32}n_{22}(l_{15}x_{A3} - l_{35}x_{A1}))}{l_{12}l_{32}(l_{15} - l_{35})n_{22} + l_{22}(l_{12}(m_{33} + l_{35}n_{32}) - l_{32}(m_{13} + l_{35}n_{32}))} \\ &\quad \frac{l_{12}l_{22}l_{32}n_{22}(x_{A1} - x_{A3})}{l_{12}l_{32}(l_{15} - l_{35})n_{22} + l_{22}(l_{12}(m_{33} + l_{35}n_{32}) - l_{32}(m_{13} + l_{35}n_{32}))}) \\ {}^0\mathcal{F}_2^{pm} &= (0 \quad 1 \quad 0 \quad ; \quad \frac{n_{22}(l_{32}(m_{13} + l_{15}n_{32})x_{A1} - l_{12}(m_{33} + l_{35}n_{32})x_{A3})}{l_{12}l_{32}(l_{15} - l_{35})n_{22} + l_{22}(l_{12}(m_{33} + l_{35}n_{32}) - l_{32}(m_{13} + l_{35}n_{32}))} \\ &\quad (n_{22}(l_{32}l_{35}(m_{13} + l_{15}n_{32})x_{A1} - l_{12}l_{15}(m_{33} + l_{35}n_{32})x_{A3}) \\ &\quad - l_{22}(m_{13} + l_{15}n_{32})(m_{33} + l_{35}n_{32})(x_{A1} - x_{A3}))) / (l_{12}l_{32}(l_{15} - l_{35})n_{22} \\ &\quad + l_{22}(l_{12}(m_{33} + l_{35}n_{32}) - l_{32}(m_{13} + l_{35}n_{32}))) \\ &\quad \frac{l_{22}(l_{32}(m_{13} + l_{35}n_{32})x_{A1} - -l_{12}(m_{33} + l_{35}n_{32})x_{A3})}{l_{12}l_{32}(l_{15} - l_{35})n_{22} + l_{22}(l_{12}(m_{33} + l_{35}n_{32}) - l_{32}(m_{13} + l_{35}n_{32}))}) \end{aligned} \quad (29)$$

Equation (29) denotes that the 2-SPR-UPR PM has two DOFs when its limbs are arranged parallelly. One is ${}^0\mathcal{S}_1^{pm}$ indicating a rotation about the axis along the unit vector $(l_{22} \ 0 \ n_{22})$ which is parallel to the revolute joint of limb2, the other is ${}^0\mathcal{S}_2^{pm}$ indicating a helical motion about the axis along the unit vector $(0 \ 1 \ 0)$ which is parallel to axis y .

4 Conclusion

The mobility analysis of a 2-SPR-UPR PM with two different arrangements of limbs is discussed. When the limbs are arranged symmetrically, the 2-SPR-UPR PM has two DOFs. One is a rotation about the axis along the unit vector $(l_{22} \ 0 \ n_{22})$, the other is a helical motion about the axis along the unit vector $(0 \ 1 \ 0)$. When the limbs are arranged parallelly, the 2-SPR-UPR PM also has a rotation and a helical motion. Note that the rotational axis is parallel to the unit vector $(l_{22} \ 0 \ n_{22})$ and the helical axis is parallel to the unit vector $(0 \ 1 \ 0)$. Future work will involve further mobility analysis of other lower-mobility PMs with different arrangement of limbs.

Acknowledgments. This work was supported by the National Natural Science Foundation of China (NSFC) under Grant 51075369 and by Natural Science Foundation of Zhejiang Province under Grant LY12E05029.

References

1. Carretero, J.K., Nahon, M., Gosselin, C.M., Buckham, B.: Kinematic analysis of a three-dof parallel mechanism for telescope applications. In: ASME Design Automation Conference, Sacramento, California (1997)
2. Poulthiot, N.A., Nahon, M., Gosselin, C.M.: Motion Simulation Capabilities of Three-Degrees-Of-Freedom Flight Simulators. *Journal of Aircraft* 35, 9–17 (1998)
3. Yu, J.J., Hu, Y.D., Bi, S.S., Zong, G.H., et al.: Kinematics feature analysis of a 3 DOF in-parallel compliant mechanism for micro manipulation. *Chinese Journal of Mechanical Engineering* 17, 127–131 (2004)
4. Liu, D., Che, R., Li, Z., Luo, X.: Research on the theory and the virtual prototype of 3-DOF parallel-link coordinatng-measuring machine. *IEEE Trans. Instrum. Meas.* 52, 119–125 (2003)
5. Wahl, J.: Articulated tool head: EPO WO/2000/025976 (2011)
6. Bi, Z.M., Jin, Y.: Kinematic modeling of Exechon parallel kinematic machine Original Research Article. *Robotics and Computer-Intergrated Munufacturing* 27, 186–193 (2011)
7. Tsai, M.S., Shiau, T.N., Tsai, Y.J., Chang, T.H.: Direct kinematic analysis of a 3-PRS parallel mechanism. *Mech. Mach. Theory* 38, 71–83 (2003)
8. Li, Y.M., Xu, Q.S.: Kinematics and inverse dynamics analysis for a general 3-PRS spatial parallel mechanism. *Robotica* 23, 219–229 (2007)

9. Tsai, L.W., Kim, H.S.: Kinematic synthesis of a spatial 3-RPS parallel manipulator. *ASME J. Mech. Des.* 125, 92–97 (2003)
10. Rao, N.M., Rao, K.M.: Multi-position dimensional synthesis of a spatial 3-RPS parallel manipulator. *ASME J. Mech. Des.* 128, 815–819 (2006)
11. Joshi, S.A., Tsai, L.W.: Jacobian analysis of limited-DOF parallel manipulator. *ASME J. Mech. Des.* 124, 254–258 (2002)
12. Liu, C.H., Cheng, S.: Direct singular positions of 3RPS parallel manipulator. *ASME J. Mech. Des.* 126, 1006–1016 (2006)
13. Lee, K., Shah, D.K.: Dynamic analysis of a three degrees of freedom in-parallel actuated manipulator. *IEEE Trans. Rob. Autom.* 4, 361–367 (1988)
14. Farhat, N., Mata, V., Page, A., Valero, F.: Identification of dynamic parameters of a 3-DOF RPS parallel manipulator. *Mechanism and Machine Theory* 43, 1–17 (2008)
15. Grübler, M.: Allgemeine Eigenschaften der zwanglaufigen ebenen kinematische kette. *Civilingenieur* 29, 167–200 (1883)
16. Kutzbach, K.: Einzelfragen aus dem Gebiet der Maschinenteile. *Zeitschrift der Verei Deutscher Ingenieur* 77, 1168 (1933)
17. Hunt, K.H.: Kinematic geometry of mechanisms. Oxford University Press, Oxford (1990)
18. Huang, Z., Li, Q.C.: Type synthesis of symmetrical Lower-mobility parallel mechanisms using constraint-synthesis method. *The International Robotics Research* 22, 59–79 (2003)
19. Tsai, L.W.: Robot Analysis. Morgan Kaufmann. John Wiley & Sons, Inc., Canada (1999)

A Method for Inverse Kinematic Solutions of 3R Manipulators with Coupling

Byoung-Ho Kim

Biomimetics and Intelligent Robotics Lab.
Department of Mechatronics Eng., Kyungshung Univ., Busan, 608-736
Korea
`kimbh@ks.ac.kr`

Abstract. In order to control a robot manipulator, we need to determine the joint combination of the manipulator for the given end-effector's position. This paper presents a neural learning-based method for the inverse kinematic solutions of a 3R manipulator that has three revolute joints with a coupling. Especially, we use a neural learning algorithm for effective learning of a multi-layered neural network. The usefulness of the proposed approach is verified by simulations.

Keywords: Inverse kinematic solution, 3R manipulator, Neural learning scheme.

1 Introduction

For the manipulation of a robot manipulator or a finger, we need to know the combination of joints [1][2]. Thus, a method is necessary to get the joint combination of the manipulator for the given end-effector's position.

For instance, in the cases of a redundant manipulator or a manipulator with a coupling among joints, there exists a certain preferable configuration depending on the task, and it is not easy to take such an effective joint configuration due to the redundancy or the constraint. So, some ideas have been proposed for solving the inverse kinematics of manipulators or fingers [3]-[5]. Yoshikawa [3] and Chiu [4] suggested a performance index-based algorithm using a manipulability criterion or a compatibility index, respectively, to determine an effective posture of robot manipulators. These methods have an advantage to resolve the singularity posture of a manipulator as well as to avoid obstacles. However, unbalanced joint configurations can be made by such a performance index-based algorithm. Secco, *et al.* [5] solved the inverse kinematic problem for a prosthetic finger by adopting a physiological constraint among joints. Secco's method is helpful for a simple closed-form solution of a three-jointed robot manipulator, but it may not be applicable if their relation among joints is not identical.

In this paper, we present a neural learning-based method to get the inverse kinematic solution of a 3R manipulator that has three revolute joints with a coupling.

2 Model of 3R Robot Manipulators with Coupling

Consider a 3R manipulator that has three revolute joints with a coupling, as shown in Fig. 1. Practically, the motions of joints of the robot manipulator can be limited in the following ranges: $0 \leq \theta_1 \leq \theta_{1max}$, $0 \leq \theta_2 \leq \theta_{2max}$, and $0 \leq \theta_3 \leq \theta_{3max}$.

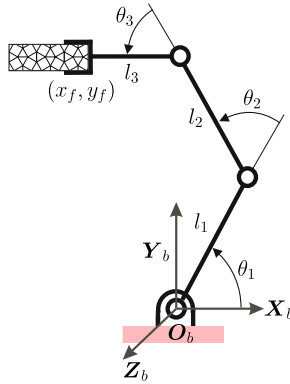


Fig. 1. A model of 3R robot manipulators with a coupling, $\theta_3 = k_\theta \theta_2$

The forward kinematic relations of the manipulator are described by

$$x_f = l_1 \cos \theta_1 + l_2 \cos(\theta_1 + \theta_2) + l_3 \cos(\theta_1 + \theta_2 + \theta_3) \tag{1}$$

$$y_f = l_1 \sin \theta_1 + l_2 \sin(\theta_1 + \theta_2) + l_3 \sin(\theta_1 + \theta_2 + \theta_3) \tag{2}$$

where x_f and y_f denote the x - and y -directional tip positions of the manipulator, respectively.

For the manipulation of the robot manipulator, we need to get the actual combination of joints by solving the inverse kinematics. In general, a robot manipulator with three independent revolute joints has one redundancy for a motion in the two-dimensional space. However, the robot manipulator shown in Fig. 1 has no redundancy because of the coupling between the third joint and the second joint. If the coupling is identical, the solution of the manipulator’s inverse kinematics can be obtained by using the Secco’s method. If it is not identical, however, it is usually not easy to have the inverse kinematic solution.

In this study, we try to use the advantage of neural learning for the inverse kinematic solution.

3 Neural Learning Scheme for Inverse Kinematics

This section describes a neural learning scheme for the inverse kinematic solutions of a 3R manipulator with a coupling, as shown in Fig. 1.

3.1 Neural Learning Scheme

The neural learning scheme proposed for the inverse kinematic solution of the 3R manipulator is shown in Fig. 2, where the neural network is constructed as Fig. 3.

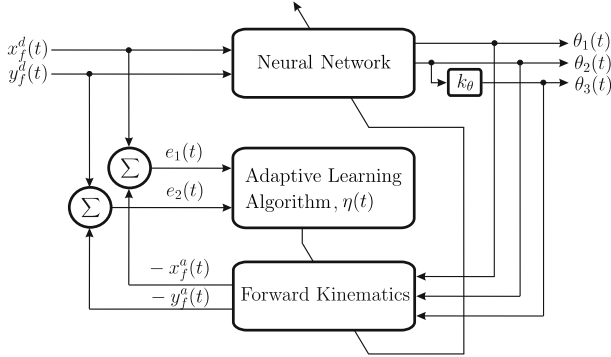


Fig. 2. A neural learning scheme for inverse kinematic solution

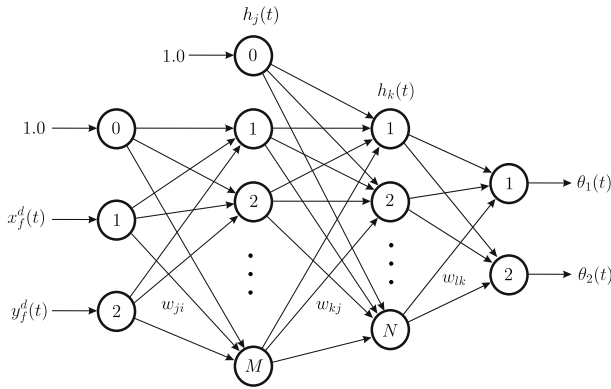


Fig. 3. A multi-layered neural network

The overall learning scheme shown in Fig. 2 is described as follows. The input neurons are assigned by the desired positions, x_f^d and y_f^d , of the manipulator. The output neurons are assigned by the two joint angles, θ_1 and θ_2 . The third joint is made by the operation of the second joint based on the coordination parameter. The actual tip positions of the manipulator are computed by the forward kinematics using the joint angles which have been obtained by the neural network. By using the position error of each direction, the adaptive learning algorithm estimates a proper learning rate for the learning of the neural network. Thus, the neural network is recursively learned by the conventional error back propagation method. If the maximum position error assigned in the tip space is satisfied, the learning process is terminated, and the output of the neural network is finally accepted as the solution of the inverse kinematics.

The signal processing of the neural network shown in Fig. 3 is described as follow. The input of the network $z_i(t)$ is assigned by

$$z_i(t) = \begin{cases} 1.0, & i = 0 \\ x_f^d(t), & i = 1 \\ y_f^d(t), & i = 2 \end{cases} \tag{3}$$

where $x_f^d(t)$ and $y_f^d(t)$ denote the x - and y -directional positions desired in the tip space, respectively. The term $z_0(t)$ represents a bias input that affects the output function of the first hidden layer. The function of the input layer is only to pass the input to the first hidden layer.

The output of the first hidden layer $h_j(t)$ is determined by

$$h_j(t) = \begin{cases} 1.0, & j = 0 \\ \frac{1}{1+e^{-s_j(I_j(t))}}, & j = 1, 2, \dots, M \end{cases} \tag{4}$$

where

$$I_j(t) = \sum_{i=0}^2 w_{ji}(t)z_i(t) \tag{5}$$

here $w_{ji}(t)$ denotes the weighting factor between the i -th input layer and the j -th first hidden layer. The parameter s_j implies the slope of the j -th sigmoid function at the first hidden layer and M indicates the number of neurons placed at the first hidden layer.

The final output of the network $\theta_l(t)$ is determined by

$$\theta_l(t) = \begin{cases} \sum_{k=1}^N w_{lk}(t)h_k(t), & l = 1 \\ \left(\sum_{k=1}^N w_{lk}(t)h_k(t)\right)^2, & l = 2 \end{cases} \tag{6}$$

where $w_{lk}(t)$ denotes the weighting factor between the second hidden layer and the output layer. As a result, the second joint angle of the manipulator is at least positive and thus the third joint also has positive angle. This is to consider the structural motion constraint of the given robot manipulator.

3.2 Learning Algorithm

The basic concept of the learning algorithm is to change the learning rate by considering the state of the neural learning. For the learning of the neural network in Fig. 3, define an error function as follows:

$$J(t) = \frac{1}{2} \sum_{m=1}^2 (e_m(t))^2 \tag{7}$$

where

$$e_1(t) = x_f^d(t) - x_f^a(t) \tag{8}$$

$$e_2(t) = y_f^d(t) - y_f^a(t). \tag{9}$$

In fact, the error function implies the sum of each position error at the tip space.

Through the conventional error back propagation [6], all of the weights at each layer can be updated by the following rule:

$$w_{lk}(t+1) = w_{lk}(t) + \eta(t)\delta_{ol}(t)h_k(t) \quad (10)$$

$$w_{kj}(t+1) = w_{kj}(t) + \eta(t)\delta_{h2k}(t)h_j(t) \quad (11)$$

$$w_{ji}(t+1) = w_{ji}(t) + \eta(t)\delta_{h1j}(t)z_i(t) \quad (12)$$

where $\delta_{ol}(t)$, $\delta_{h2k}(t)$, and $\delta_{h1j}(t)$ denote the error terms propagated back from the tip space of the manipulator to the output and hidden layers. The parameter $\eta(t)$ is the learning rate to update the weights of the neural network and the detail procedure to determine the learning rate is referred to the previous research [7].

4 Simulation Results

This section shows the resultant inverse kinematic solution of the 3R manipulator shown in Fig. 1 by using the above-mentioned neural learning scheme.

For the simulation study, the link parameters of the manipulator are set as $l_1=0.058$ m, $l_2=0.035$ m, and $l_3=0.028$ m. The joint coupling parameter k_θ is assigned as 0.47. We assumed that the motions of the first and second joints of the robot manipulator are limited in the following ranges: $0 \leq \theta_1 \leq 90^\circ$, $0 \leq \theta_2 \leq 120^\circ$, and $0 \leq \theta_3 \leq 60^\circ$. Also, some test points on the following curve are assigned for the simulation:

$$y_f = -9.73x_f^2 + 0.56x_f + 0.08. \quad (13)$$

The neural network employed in this simulation has four layers as shown in Fig. 3. The neurons at the input layer, the first hidden layer, the second hidden layer, and the output layer are assigned by 2, 5, 3, and 2, respectively. The parameters for the learning algorithm, β , σ , P, and Q, are assigned by 0.0015, 0.5, 3, and 5, respectively. In the neural learning process, the range of the tip position error is actually determined by the desired accuracy of the given manipulation task. In this simulation, it is assigned as ± 0.5 mm. Thus, the learning process for each trajectory is completed if the maximum value of the tip position errors is less than the assigned range.

Fig. 4 shows the x - and y -directional tip trajectories of the robot manipulator used in the neural learning process, where each trajectory has been assigned successively after having the previous inverse kinematic solution, and the actual tip trajectories have been taken by the forward kinematics using the joint angles which are resultantly obtained by the neural learning. Those inverse kinematic solutions for the given tip positions have been shown in Fig. 5.

From Fig. 4, we can see that the actual tip positions gradually approached the desired positions by learning. In fact, the inverse kinematic process is completed at the moment of each circle in Fig. 4 and the corresponding joint angles of the neural network have been taken as the actual inverse kinematic solution. In particular, it is noted from Figs. 4 and 5 that somewhat long learning has

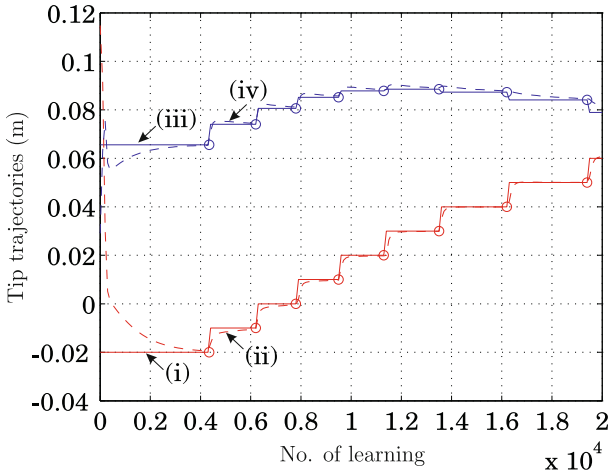


Fig. 4. Tip trajectories of the 3R robot manipulator: (i) given x -directional trajectory(x_f^d), (ii) actual x -directional trajectory followed by the proposed neural learning(x_f^a), (iii) given y -directional trajectory(y_f^d), and (iv) actual y -directional trajectory followed by the neural learning(y_f^a). Note that the inverse kinematic process for each trajectory has been completed at the moment of each circle.

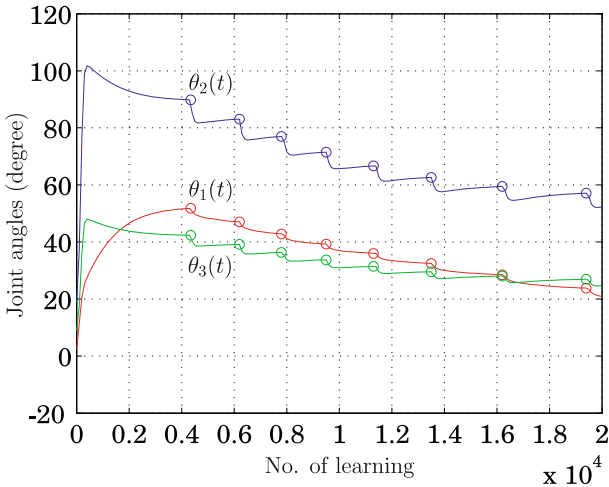


Fig. 5. Joint angles obtained by the neural learning-based inverse kinematics. Note that the joint angles at the moment of each circle are the actual inverse kinematic solution.

been required for the first positioning. The period actually means the initial positioning process of the manipulator and thus it is practically not related to the computing load in the manipulation process. Actually, the effort to reduce the learning time in the cases of neural network approaches is very important

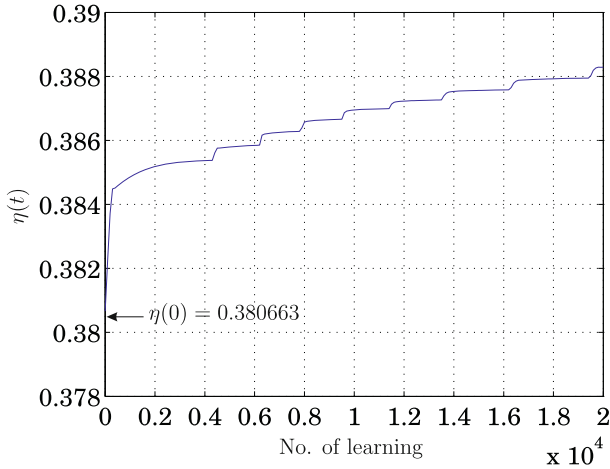


Fig. 6. Trace of the learning rate for the given motion

in the implementation aspect [8]-[10]. It is remarkable that the learning rate algorithm can improve the speed of learning. The trace of the learning rate during the learning process has been shown in Fig. 6.

Thus, it is expected that the proposed approach can be applied to the effective motion control of 3R manipulators with a coupling, as shown in Fig. 1.

5 Concluding Remarks

A neural learning-based solution of the inverse kinematics of 3R manipulators with a coupling has been presented in this paper. Especially, we used a four-layered neural network utilizing an effective learning algorithm to show the usefulness of the proposed approach. Through simulations, we showed that the inverse kinematics of a 3R manipulator with a proper coupling can be solved by the neural learning approach, and its accuracy is satisfactory. Finally, it is concluded that the proposed approach is useful for the solution of the inverse kinematics of 3R manipulators with a coupling.

Acknowledgments. This research was supported by Kyungshung University Research Grants in 2013.

References

1. Pons, J.L., Ceres, R., Pfeiffer, F.: Multifingered dexterous robotics hand design and control: a review. *Robotica* 17, 661-674 (1999)
2. Butterfass, J., Grebenstein, M., Liu, H., Hirzinger, G.: DLR-Hand II: Next generation of destrous robot hand. In: Proc. of IEEE Int. Conf. on Robotics and Automation, pp. 109-114 (2001)

3. Yoshikawa, T.: Analysis and control of robot manipulators with redundancy. In: Brady, M., Paul, R. (eds.) *Robotics Research: The First International Symposium*, pp. 735–747. MIT Press, Cambridge (1984)
4. Chiu, S.L.: Task compatibility of manipulator postures. *Int. Jour. of Robotics Research*. 7(5), 13–21 (1988)
5. Secco, E.L., Visioli, A., Magenes, G.: Minimum jerk motion planning for a prosthetic finger. *Jour. of Robotic Systems*. 21(7), 361–368 (2004)
6. Nielsen, R.H.: *Neurocomputing*, pp. 183–191. Addison-Wesley (1990)
7. Kim, B.-H.: Characteristics modeling of dynamic systems using adaptive neural computation. *Jour. of Control, Automation, and Systems*. 13(4), 309–314 (2007)
8. Wojitara, T., Nonami, K.: Hand posture detection by neural network and grasp mapping for a master slave hand system. In: *Proc. of IEEE Int. Conf. on Robotics and Automation*, pp. 866–871 (2004)
9. Afshar, P., Mastuoka, Y.: Neural-based control of a robotic hand: evidence for distinct muscle strategies. In: *Proc. of IEEE Int. Conf. on Robotics and Automation*, pp. 4633–4638 (2004)
10. Kim, S.S., Jung, S.: Hardware implementation of a real time neural network controller with a DSP and an FPGA. In: *Proc. of IEEE Int. Conf. on Robotics and Automation*, pp. 4639–4644 (2004)

Author Index

- Afzal, Muhammad Raheel I-154
Aghaei, Morteza II-54
Aghili, Farhad II-121
Ahmad, Mehran II-569
Ahmed, Ishtiaq I-693
Aljanaideh, Omar II-635
- Ba, Z. II-397
Ba, Zhengyu I-649
Bae, Joonbum II-257
Baek, Joo-Won II-327
Baek, Ju-Won II-320
Baek, Seung-Hwa I-8
Bashir, Ali Kashif I-105, II-454
Bouzouia, Brahim I-679
Broecker, Bastian II-108
Butt, Khurram II-569
- Cai, Hui II-513
Cai, Maojiao II-535
Chai, Xinxue I-730
Chang, Hyunjin I-540
Chen, Genliang I-384
Chen, Puwei II-503
Chen, Qiaohong I-730
Chen, Ran I-661
Chen, Weidong I-295, I-307, II-535
Chen, Wenbin I-339
Chen, Xinkai II-666
Chen, Zhiyong II-525
Chen, Zichen I-475
Cheng, Liling I-129, I-500
Cheng, Pi-Ying I-258
Cheng, Xiaoying I-500
Cheon, Byungsik I-237
Cho, Chullhee II-310
Cho, Hyunhak I-615
Cho, Kyu-Jin II-302
Choe, Yungeun I-584
Choi, Byunghun I-594
Choi, Hyeung-Sik II-289
Choi, Joon-Young I-267
Choi, Seunghwan I-66
Choi, Seung Y. I-693
- Choi, Tae Yong II-74, II-155
Choi, Wan Sik I-105
Chung, Kwangcho II-155
Chung, Myung Jin I-584
Chung, TaeChoong I-693
Chwa, Dongkyoung I-668
Claes, Daniel II-108
Cui, Yuding I-484
Czeczot, Jacek II-178
- Dadkhah, Mohammad I-177
Dai, Mengyuan I-520
Dai, Yu I-475
Defoort, M. II-202
Deng, Hua I-415
Deng, W.H. II-189
Ding, Han II-365, II-397, II-491, II-503, II-525, II-592
Do, Hyun-Min II-74, II-155
Du, Yuheng I-463
Duan, Xiaogang I-415
- Fang, Yinfeng I-405
Farshchi, Seyyed Mohammad Reza II-54
Fei, Ling II-470
Feng, Mingchi II-417
Feng, Pingfa II-614
Feng, Ying II-623
Fossil, Joscha II-108
Fu, Xin I-129, I-427, I-500, I-509
Fu, Z. II-16, II-189, II-214
- Gao, Feng I-718, II-132
Gao, Ming I-520
Ge, Yang II-470
Glowa, Christoph II-84
Go, Seok-Jo II-442
Gong, Liang I-661
Gonzalez, Jose I-318
Gu, Dong-Yun I-273
Gu, Guo-Ying II-385, II-644, II-678
Gulraiz, Shiraz II-1

- Guo, Weizhong II-41
 Guo, Yalei II-41
- Ha, Hyunuk I-45
 Haider, Nauman K. II-1
 Han, HyeYoung II-375
 Han, Sung Hyun II-265
 Han, Youngjae I-97
 Hashizume, Makoto I-237
 Hassan, Syed I-154, I-204
 He, Jiayuan I-396
 Hennes, Daniel II-108
 Hentout, Abdelfetah I-679
 Heo, Seong-Min I-38
 Heo, Shin-nyeong I-562
 Hong, Jaesung I-237
 Hu, Liang I-509
 Huan, Zhang II-720
 Huang, Feng I-427
 Huang, Qi I-216
 Huang, Xinda II-491
 Huo, Junzhou II-700
 Hur, Kook-Sung I-1
 Hussain, Irfan I-165
 Hussain, Sajjad I-105
 Hwang, Seungik I-562
 Hwang, Won Jun II-265
- Imamoglu, Nevrez I-318
 Izhar, Umer II-1
 Izumi, Kiyotaka II-96
- Jan, Yasir I-154
 Jeong, Dong-Keun II-327
 Jeong, Heein I-330
 Jeong, Jae-Hun I-1
 Jeong, Yang Keun I-136
 Jeong, Yongseop I-625
 Ji, DaeKeun I-237
 Jia, L. II-397
 Jia, Lei I-649
 Jiang, Hua II-166
 Jiang, Jun II-429
 Jiang, Li I-216
 Jiang, Ning II-63
 Jin, Taeseok I-540
 Jin, Yi II-417
 Jirattigalachote, Wisit I-434
 Jo, Jeongmin I-97
 Jun, Du II-727
- Jung, Seoul II-274
 Jung, Sung Won I-136
 Jung, Yeongtae II-257
- Kamashima, Tsutomu I-532
 Kang, Eun Uk II-265
 Kang, Sun-Kyun I-56, I-85
 Kim, Byoung-Ho I-742
 Kim, Byung In II-74
 Kim, Cheol-Joong I-668
 Kim, Chi Yen I-227
 Kim, Dong-Hyun I-25, I-31
 Kim, Dong-Il I-576
 Kim, Doo-Hyung II-155
 Kim, Hee-Je I-1, I-8, I-18, I-25, I-31, I-38, II-320, II-327, II-334, II-338, II-345
 Kim, H. Jin I-594
 Kim, Ho-Sung II-320
 Kim, Hyoung-Woo I-267
 Kim, Hyun-Min I-8
 Kim, Jaeyong I-615
 Kim, Jonggeun II-375
 Kim, Jong-Hyun II-320, II-334
 Kim, Jongmoo I-45
 Kim, Kijung I-66
 Kim, Ki-Ryong I-25, I-31, I-38
 Kim, Kyung-Sik II-310
 Kim, Min-Ho I-605
 Kim, Myeong Ok I-204
 Kim, Myong-hwan I-18
 Kim, Sungshin I-615, II-375
 Kim, Tae-Jin II-338
 Kim, Yeoun-Jae II-237
 Kim, Yunki I-66
 Klopot, Tomasz II-178
 Klopot, Witold II-178
 Kumar, Naveen I-177
 Kwak, Dong Jun I-594
 Kweon, In So I-625
 Kyung, Jin Ho II-74
- Lai, Lei-Jie II-385, II-644
 Lai, Po-Ying I-258
 Laskar, Md Nasir Uddin I-693
 Laszczyk, Piotr II-178
 Lee, Changyoung I-97
 Lee, Dong-Hyuk I-56, I-85
 Lee, Hansoo II-375

- Lee, Hee-Mu I-605
 Lee, Jangmyung I-45, I-56, I-66, I-77,
 I-85, I-145, I-562, I-330
 Lee, Jinho I-97
 Lee, Jong-Pil II-338, II-345
 Lee, Joon-Yong II-237
 Lee, Ju-Jang II-237
 Lee, Kok-Meng I-509
 Lee, Kyoung-Jun II-338, II-345
 Lee, Min-Cheol I-227, I-605
 Lee, Sang-Hyo II-310
 Lee, Sang-Il II-454
 Lee, Sang-Seob II-289
 Lee, Sangyong I-330
 Lee, Woo Song II-265
 Lee, Wongryol II-454
 Lee, Young-Jin II-442
 Li, Bin II-513
 Li, Chun-Xia II-644, II-678
 Li, Kang I-295, I-307, II-470, II-535
 Li, Meng II-535
 Li, Qinchuan I-730
 Li, Weimin II-63
 Li, Wen-long II-555
 Li, Xiuliang II-409
 Li, Zhi II-656
 Li, Zicheng II-545
 Liang, Guanhao I-475
 Liao, Wenlong I-295
 Lim, Hyun-Seop I-562
 Lim, Jeong Geun II-274
 Lin, Chin-Teng I-246
 Lin, Sen II-481
 Lin, Zhongqin I-384
 Ling, Jingxiu II-700
 Liu, Chao II-33, II-353
 Liu, Chengliang I-661
 Liu, Guoqing II-143
 Liu, Hong I-216
 Liu, Honghai I-405
 Liu, Huan I-463
 Liu, J.H. II-189
 Liu, Jia II-353
 Liu, Kai I-363
 Liu, Pin-kuan II-365
 Liu, Sining II-656
 Liu, Wei-ting I-129, I-500, I-509
 Liu, Yizhi II-481
 Liu, Yong-Hua II-623
 Liu, Yuzhang I-373
 Luo, Bo II-513
 Luo, Tao II-417
 Ma, Jigang I-730
 Mai, Ba-Loc II-289
 Manurung, Auralius I-165
 Mao, Jianyu II-41
 Mao, Xinyong II-513
 Mehmood, Ayaz II-1
 Mei, Deqing I-475
 Meng, Jianjun I-453
 Merat, Pooya II-121
 Mertsching, Bärbel I-117, I-550
 Messous, Mohamed Ayoub I-679
 Metzger, Mieczyslaw II-178
 Miao, Yunjie II-132
 Mirabdollah, Mohammad Hossein
 I-117, I-550
 Moon, Seong-eun I-532
 Moon, Wae-Shik II-580
 Mou, Haikuo II-491
 Mu, Hua I-520
 Munawar, Majid II-569
 Nagai, Isaku II-96
 Nakadai, Kazuhiro I-532
 Nergui, Myagmarbayar I-318, I-532
 Nie, Hua II-246
 Noh, Kyung-Wook I-56
 Oh, Mingyun I-188
 Otake, Mihoko I-532
 Oukid, Saliha I-679
 Pan, Dalei I-718, II-132
 Pan, Lizhi I-493
 Pan, Minghua II-710
 Pan, Xianfei I-520
 Park, Chanhun II-74
 Park, Chan-Ik I-145
 Park, In Man I-136
 Park, Jang Sik II-450
 Park, Jinseop II-454
 Park, Kang-Il I-145
 Park, Kyoung-Taik I-85
 Park, Kyung-Taik II-155
 Park, Min-Kyu II-436, II-442, II-466
 Park, Moonho I-615
 Park, Moon Yeol I-136
 Park, Myong-Soon I-105, II-454

- Park, Yong-Jai II-302
 Peng, Fangyu II-481, II-513
 Prasad, Mukesh I-246
 Pyo, Sanghun I-188
- Qi, Geng II-727
 Qian, Wenwei I-427
 Qian, Yang I-706
 Qin, Guohua II-246
 Qiu, Dong I-351
 Qiu, Zhongyi I-444
- Rahmani, Ahmed I-706
 Rakheja, Subhash II-635
 Rath, J.J. II-202
 Ren, Jie II-41
 Ren, Yong II-226
 Rovetta, Alberto II-281
 Ruan, Xiaodong I-427
 Ryu, Myung-Hyo II-320, II-327, II-334
 Ryuh, Youngsun II-310
- Saxena, Amit I-246
 Schlegl, Thomas II-84
 Seo, Jonghyun I-77
 Shah, Sayed Chhatten II-454
 Shah, Sayed Chhatten I-105
 Shahzad, Waseem II-569
 Shan, Qingchuan I-500
 Shao, Chengjun II-409
 Shen, Hui-Min I-509
 Sheng, X. II-397
 Sheng, Xinjun I-396, I-453, I-463, I-493, I-649
 Shim, Byung Kyun II-265
 Shin, Dongsul II-338, II-345
 Shin, Hang Bong I-136
 Shu, Xiaokang I-453
 Shull, Pete B. I-434
 Song, Hajun I-615
 Song, Jae-Bok I-576
 Song, Jong Kwan II-450
 Su, Chun-Yi II-121, II-623, II-635, II-656, II-666
 Su, Hongye II-409
 Sun, Ronglei I-484, II-246
 Sun, Wei II-700
 Sung, Ji-Hun II-580
 Sung, Ki Won II-265
 Sung, Kum-Gil II-466
- Sung, Young-Hoon II-580
 Szkodny, Tadeusz I-637
- Takagi, Kentaro I-532
 Tao, Yuebang I-129
 Tesar, Delbert II-436
 Tomikawa, Morimasa I-237
 Tran, Ngoc-Huy II-289
 Tuyls, Karl II-108
- Ullah, Ikram I-204
- Veluvolu, K.C. II-202
- Wang, Can I-373
 Wang, Gang I-373
 Wang, Hao I-384, II-33
 Wang, Hesheng II-535
 Wang, Hui II-353
 Wang, Huiyu I-307
 Wang, Jingcheng II-470
 Wang, Jingchuan I-295, I-307
 Wang, Shuangyuan I-661
 Wang, Xiaohui II-63
 Wang, Y. II-16
 Wang, Yancheng I-475
 Wang, You I-351
 Watanabe, Keigo II-96
 Wei, Jian-He I-273
 Wei, Zhixuan I-295, I-307
 Wu, Jian-hua II-353, II-365
 Wu, Xinyu I-373
 Wu, Yu I-273
- Xie, Le II-429
 Xiong, Caihua I-339, I-363, I-484
 Xiong, You-lun II-545, II-555
 Xiong, Zhenhua I-649, II-353, II-397
 Xu, Jiahang II-166
 Xu, Kai I-351, I-463, II-143
- Yan, Hua I-284
 Yan, Rong II-481
 Yan, W.X. II-16, II-189, II-214
 Yan, Yonghua II-166
 Yang, Canjun I-284
 Yang, Chien-Ting I-246
 Yang, Dapeng I-216
 Yang, Gi-Hun II-310
 Yang, Mei-Ju II-678

- Yang, Sheng II-481
 Yao, Jin II-720
 Yao, Lin I-453
 Yao, Yan-An II-33
 Yasuda, Gen'ichi II-602
 Yi, Hyun-Chul I-267
 Yimin, Xia II-720
 Yin, Zhouping II-545
 Yiping, Tang II-727
 Yongliang, Cheng II-720
 Yoon, Byung Woo II-450
 Yoon, Jungwon I-154, I-165, I-177,
 I-188, I-204
 Yoon, Sung Min I-227
 Yoshida, Yuki I-318
 Yousaf, Kamal II-569
 Yu, Haidong II-690
 Yu, Hailong II-429
 Yu, Huiyang II-246
 Yu, Jungwon II-375
 Yu, Pin I-500
 Yu, Wenwei I-318
 Yuan, X. II-397
 Yuan, Xin I-649
 Yun, Hyeok-Jin II-334

 Zain, Zainah Md. II-96
 Zhai, Chao II-417
 Zhai, Jie II-503
 Zhai, Mei-Li II-33
 Zhan, S.T. II-189, II-214
 Zhang, Chuncao II-710

 Zhang, D. II-202
 Zhang, Dingguo I-396, I-444, I-493,
 II-226
 Zhang, Gang II-365
 Zhang, Hai-Tao II-503, II-525
 Zhang, Jianbo II-710
 Zhang, Jianfu II-614
 Zhang, Jianjun II-63
 Zhang, Jianrong II-166
 Zhang, Langwen II-470
 Zhang, Mingyong II-166
 Zhang, Q. II-202
 Zhang, Qing II-226
 Zhang, Wenxi I-295
 Zhang, Xiaoming II-491, II-503, II-592
 Zhang, Xu II-700
 Zhao, Chunzhang II-690
 Zhao, Yanmin II-614
 Zhao, Yan-Zheng II-16, II-189, II-214
 Zhao, Yong II-690
 Zheng, Duan I-373
 Zhengying, Wei II-727
 Zhou, Hang II-385
 Zhou, H.F. II-16
 Zhou, Li-ping II-555
 Zhou, Maoying I-129
 Zhu, Gaoke I-415
 Zhu, Guoli II-710
 Zhu, Li-Min II-385, II-644, II-678
 Zhu, Xiangyang I-396, I-405, I-434,
 I-444, I-453, I-463, I-493
 Zhuang, Kejia II-592